

Single Layer Meta-material Lens with Graded Refractive Index

M. A. Bitar, Y. Nasser, M. Al-Husseini, and K. Y. Kabalan
ECE Department, American University of Beirut, Beirut 1107 2020, Lebanon

Abstract— A new single layer meta-material lens design with frequency-dependent focal points is investigated. In the proposed design, the surface of the single layer dielectric material is divided into zones in the same plane with perforations of different specifications. The focal point for each frequency is achieved through varying the permittivity coefficient of each zone. The variation of the permittivity of each zone is based on the changes of the perforations' specifications in the dielectric material. The paper presents a conceptual design of a lens with two zones; each zone is optimized for a specific frequency. The design can be optimized to provide several focal points, each for a specific frequency, meeting pre-defined size constraints.

1. INTRODUCTION

Meta-material lenses are of great importance in radiometry process, which allows the measurement of the temperature profile in magnetic confinement fusion devices [1]. In practice, optical systems are optimized for a single frequency leading to losses in the transverse resolution at other frequencies. Thus, the increase and optimization of the transverse resolution require different focal points for different frequencies.

In the literature, meta-material lenses with frequency-dependent focal points have been proposed [2] to replace conventional optical systems. In the former, the surface of the lens is divided into several zones; each provides a certain phase-shift for a certain frequency. As a result, each frequency would have a specific focal point [6–8]. This was achieved using layered structure, consisting of periodic arrangements of capacitive patches and inductive wire grids, separated by a dielectric material. In each zone the capacitive patches and inductive wire grids act as band pass filters allowing certain frequencies and providing a specific phase-shift [3]. However, this appeared to be complex to design and manufacture due to the layered structure [2–5].

In this paper, we propose a new design of the meta-material lens with frequency dependent focal points. Opposed to designs seen in the literature, we propose to use a single dielectric layer with different zones in the same plane. The phase-shift for each frequency is achieved through having a different refractive index in each zone. This reduces the complexity of both design and manufacture.

This paper is divided into three main sections. Section 2 presents the unit cell characteristics and describes the effect of the change in unit cell perforations diameter on the permittivity and on the optimal frequency of the unitcell. Section 3 describes the theory behind the lens design proposed in this paper. Finally, Section 4 discusses the conceptual design of the proposed two zones lens.

2. UNIT CELL CHARACTERIZATION

In this section, we start investigating the square unit cell element of dielectric material of permittivity equals to 10.2 as it is used for the design of the whole lens. The unit cell element presented in Figure 1 proved to resemble a change in permittivity upon the change of perforation diameter d and/or distance s separating perforations [4]. This change is described by formulas (1) and (2) below, whose results are given in Figure 2:

$$\varepsilon_{eff} = \varepsilon_r (1 - \alpha) + \alpha \quad (1)$$

$$\alpha = \frac{\pi}{2\sqrt{3}} \left(\frac{d}{s} \right)^2 \quad (2)$$

The electromagnetic characterization of the unit cell, simulations on HFSS-Ansoft showed that each unit cell is optimized for a specific frequency, at which it provides a specific phase-shift. Figure 3(b) shows the S_{11} parameter with respect to the incident wave frequency. It is clear from the figure that the unit cell with 4 mm perforations diameter and 7.5 mm distance between perforations is optimized for a frequency of 11.1444 GHz.

Similarly, we could also investigate some results of a square unit cell of side equal to 1.5 cm, where s equals 7.5 mm. As expected, Table 1 shows that perforation diameter could be optimized for a pre-defined phase shift and target frequency.

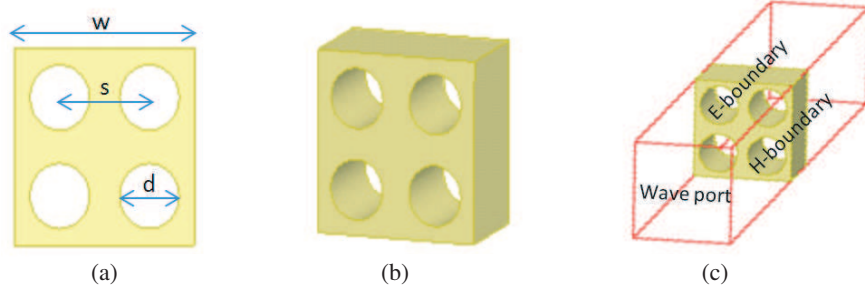


Figure 1: (a) Unit cell front view. (b) Unit cell side view. (c) Waveguide assignments.

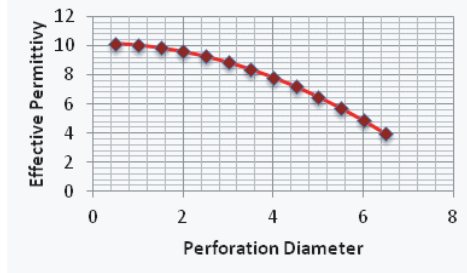


Figure 2: Effective permittivity as function of perforation diameter.

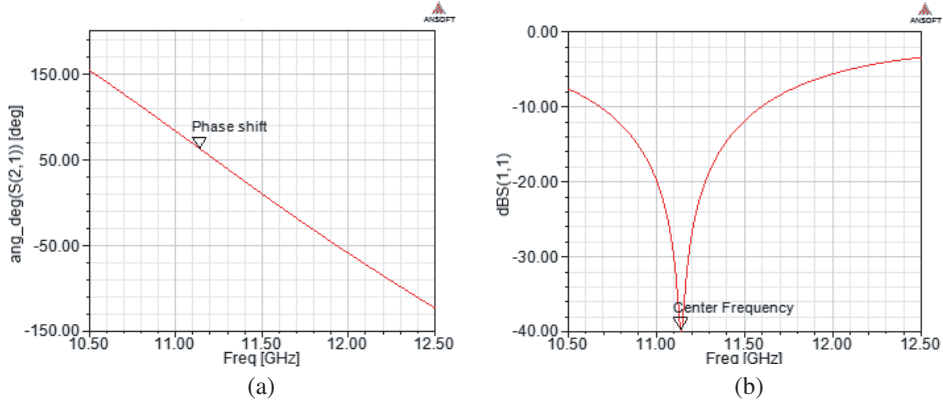
Figure 3: Unitcell with 4 mm perfocation diameter $S(1,1)$ value and Phase-shift values.

Table 1: Frequency optimization results as a function of the perforation diameter.

Perforation diameter (mm)	Center Frequency (GHz)	$S(1,1)$ (dB)	Phase-shift (deg)
2	10.2222	-40.0946	146
4	11.1444	-39.9772	62
6	13.2833	-40.4147	35

3. LENS CONCEPT

In this section, we utilize the conclusions obtained in Section 3 to describe the concept of one zone lens design. From Gaussian optics, the phase-shift experienced by a wave is directly related to the point at which the wave converges [6, 7]. This is illustrated by the following relation:

$$\varphi(f) = \frac{\pi f}{c} \frac{r^2}{R} + \varphi_0(f) \quad (3)$$

where, φ is the phase-shift, f is the frequency, c is the speed of light, r is the radial distance from the optical axis, R is the radius of curvature of the lens, and φ_0 is an arbitrary constant that varies with frequency but remains the same in all zones [6].

Furthermore, the focal length for a thin lens is related to the index of refraction [8] by the following approximation:

$$\frac{1}{l} = (n - 1) \left(\frac{1}{R_1} + \frac{1}{R_2} \right) \quad (4)$$

where, l is the focal length, n is the refractive index, and R_1 and R_2 are the incidence and transmittance radius of curvature. For a plane lens, the incident radius of curvature is infinite [8]. Hence, (4) would transform to:

$$\frac{1}{l} = (n - 1) \left(\frac{1}{R} \right) \quad (5)$$

where, $R = R_2$ is the same as in Equation (4) (i.e., transmitted radius of curvature) optimized for a focal point l ; Using Maxwell equations, we could derive the relation between the permittivity and the refractive index of a material [8] by the approximation formula: $n = \sqrt{\epsilon}$ and then relate it to (1) through:

$$n = \sqrt{\epsilon_{eff}} \quad (6)$$

Eventually, combining Equations (1), (3) and (5), we obtain:

$$\varphi(i, f) = \frac{\pi f}{c} \frac{r_i^2}{l(\sqrt{\epsilon_{eff}} - 1)} + \varphi_0(f) \quad (7)$$

In the above equation r_i represents the location of the i th zone on the surface of the lens and it corresponds to the distance from the center of the lens to the midpoint between the inner and outer radius of a zone [2]. This determines the size of the lens.

Using (7), it is now possible to design a single layer lens composed of several zones. Each zone is optimized for a specific frequency f at which it provides a specific phase-shift φ , and have a specific index of refraction $n = \sqrt{(\epsilon_{eff})}$, contributing to a focal distance l .

4. TWO ZONE LENS CONCEPTUAL DESIGN

Consider a lens composed of two zones. Zone 1 has a radial distance r_1 equal to 2.25 cm, and perforations of diameter equal to 4 mm ($\epsilon_{eff} = 7.826$), optimized for 11.1444 GHz. Zone 2 has r_2 equal to 3.75 cm, and perforations of diameter 6 mm ($\epsilon_{eff} = 4.860$), optimized for 13.2833 GHz. Substitution in (7), and assuming φ_0 equal to 0 (for simplicity) leads to the results presented in Table 2 below:

Table 2: Focal point corresponding to zone frequency.

Frequency (GHz)	Focal Point (cm)
11.1444	3.03
13.2833	26.58

Reversely, it is possible to design a lens starting with specifying dimensions, and frequencies of operation and their corresponding focal points. Accordingly, we could determine the size constraints of each zone, and optimize the unit cell dimensions, perforation diameters, and phase-shift attained from a specific unit cell, in such a way to minimize the difference between the two sides of formula (7).

Figure 4 below shows a diagram of the proposed conceptual lens design.

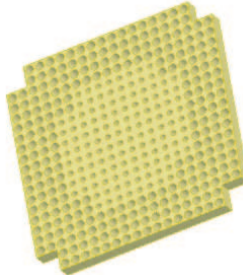


Figure 4: Two zones lens design.

5. CONCLUSION

In summary, the proposed design benefits from the effect of perforations on the dielectric material and uses it in an innovative way to design a lens which can provide specifiable frequency dependent focus. Unitcells having different dimensions and different perforation diameters can be optimized for a specific frequency with a specific phase-shift, i.e., focal distance. This allows having a lens with several frequency zones, which can provide a specific focal point for each frequency.

The concept of the design is proved through theoretical formulation, which can guide easy and simple manufacturing. This can be further investigated, optimized, and customized to produce lenses for radiometry or other diagnostic purposes that require having a high resolution at more than one frequency.

ACKNOWLEDGMENT

Thanks to professor Francesco Volpe, Kenneth Hammond and Scott Massidda of Columbia University and thanks to Ferhad Kassem, Professor Ali El Hajj, and professor Joseph Constantine of the American University of Beirut for their support and comments.

REFERENCES

1. Hutchinson, *Principles of Plasma Diagnostics*, Cambridge Univ. Press, 2002.
2. Capecchi, W. J., N. Behdad, and F. A. Volpe, "Numerical optimization of reverse chromatic aberration in planar metamaterial lenses," *Optics Express*, Vol. 20, 8761, 2012.
3. Al-Joumayly, M. and N. Behdad, "A generalized method for synthesizing low-profile, band-pass frequency selective surfaces with non resonant constituting elements," *IEEE Transactions on Antennas and Propagation*, Vol. 58, 4033–4041, 2010.
4. Muldavin, J. B. and G. M. Rebeiz, "Millimeter-wave tapered-slot antennas on synthesized low permittivity substrates," *IEEE Transactions on Antennas and Propagation*, Vol. 47, 1999.
5. Zainud-Deen, S. H., S. M. Gaber, and K. H. Awadalla, "Transmitarray using perforated dielectric material for wideband applications," *Progress In Electromagnetics Research M*, Vol. 24, 1–13, 2012.
6. Hammond, K., W. J. Capecchi, S. Massidda, and F. A. Volpe, "Metamaterial lens of specifiable frequency-dependent focus and adjustable aperture for electron cyclotron emission in the DIII-D tokamak," *J. Infrared Millim. THz Waves*, 2013, Submitted.
7. Goldsmith, P. F., *Quasioptical Systems: Gaussian Beam Quasioptical Propagation and Its Applications*, IEEE Press, 1998.
8. Hecht, E., *Optics*, 4th Edition, Addison-Wesley, 2002.

Stability of Nonlinear 2D-tunnel Bifurcations in Systems of Interacting Quantum Molecules in the Metamaterial Matrix

V. D. Krevchik¹, V. I. Volchikhin¹, I. I. Artemov¹, M. B. Semenov¹, R. V. Zaitsev¹, A. V. Razumov¹, A. K. Aringazin², K. Yamamoto³, and T. A. Gubin¹

¹Penza State University of Russia, Russia

²Eurasian National University, Kazakhstan

³International Medical Center, Japan

Abstract— The problem of controllability for 2D-tunnel bifurcations in systems with quantum molecules in a dielectric matrix of a metamaterial in the external electric field at finite temperature has been investigated. Usage of the quantum tunneling with dissipation theory to study the interaction of quantum molecules with contact environment is productive, because, despite of the instanton approach usage, it is possible to obtain the main results in the analytical form with account of the environment influence on the process of tunneling, whereas other commonly used approaches give not such possibility. A theoretical study of the electric field influence on the 2D-quantum tunneling for quantum molecules in the matrix of a metamaterial (with negative effective permittivity) at finite temperature has been fulfilled in the instanton approximation. It is shown that a stable regime of 2D-bifurcations in such matrix can take place in a more narrower range of parameters than in case of usual dielectric matrix. An important problem in this case is to identify the range of experimentally realizable values of the relative dielectric permittivity (including negative values) for the matrix environment, which allow to realize the 2D-bifurcations regime. A range of the control parameters (electric field, temperature, and the relative permittivity of the metamaterial matrix), in which the regime of stable 2D-bifurcations in the system of quantum molecules, as well as in the system “AFM/STM cantilever-quantum dot or quantum molecule” can take place, has been theoretically investigated. The “phase diagram” for the stable 2D-bifurcations regime for tunnel current in the matrix of a metamaterial in dependence on controllable parameters (the inverse temperature, electric field intensity and values of the (negative) relative permittivity for the heat-bath environmental matrix), has been represented. It is shown that in contrast to usual dielectric matrices in case of the metamaterial matrix the region of stable 2D-bifurcation is significantly narrowed, which is probably due to inversion of the sign of the tunneling particles interaction.

1. INTRODUCTION

Currently, a new class of materials, known as metamaterials [1], with unique properties in a certain frequency range, is of great interest. Metamaterials are the artificial composite materials consisting of a dielectric or conductive elements that form a regular structure, which are characterized by a negative effective permittivity and permeability (ϵ and μ) and, accordingly, a negative refractive index. On the basis of such materials it is possible to develop a number of unique devices [1], such as flat electromagnetic lenses that do not have the diffraction limit (superlens), masking the shell, and so such properties cause the increased interest in their practical implementation. In addition, the problem of control for nanostructures, which are in the matrices of metamaterials, is of great interest. In this paper, we investigate the problem of controllability for 2D-tunnel bifurcations in systems with quantum molecules in a dielectric matrix of the metamaterial in the external electric field at finite temperature. Usage of the quantum tunneling with dissipation theory to study the interaction of QM with contact medium is productive, because, despite of usage of the instanton approach it is possible to get the main results in an analytical form with account of the environment effects on the tunneling process, which it is not possible in other often used approaches [2]. It is experimentally possible to observe earlier theoretically predicted 2D-bifurcations for QD from colloidal gold in the matrix of a conventional insulator on the tunneling current-voltage characteristics in the system of combined AFM/STM [2]. An important problem is to reveal the experimentally realizable range of values of the relative dielectric constant for the matrix environment, allowing 2D-bifurcations regime, including negative values, which corresponds to the matrix of metamaterials.

The aim of this work is to theoretically study the range of control parameters (electric field strength, temperature, and the relative dielectric constant of matrix of the metamaterial), in which the regime of stable 2D-bifurcations in the QM system can be realized, as well as in system with “the

cantilever needle of combined AFM/STM — QD or QM". Special attention is paid to the problem of control in a two-dimensional dissipative tunneling for system of interacting QM, simulated by 2D-oscillator potential in the medium with negative dielectric permittivity in an external electric field.

2. PROBABILITY OF 2D-TUNNELING UNDER EXTERNAL ELECTRIC FIELD IN MATRIX OF THE METAMATERIAL

We consider the simultaneous tunneling transfer of two particles which weakly interact with each other. If there is no interaction, each of the particles moves independently in its own double-well potential. We will study the effect of the particle interaction on the tunneling regime change from synchronous to asynchronous (the effect of 2D-bifurcation ([2-9])) as a function of interaction with the heat-bath in an external electric field. With the introduction of the interaction between particles in the dipole-dipole approximation, we choose V_{int} in the form of a harmonic "attraction" potential

$$V_{\text{int}} = -\frac{\alpha(q_1 - q_2)^2}{2}. \quad (1)$$

The function of the potential energy for interaction can be represented as a series in powers of parameter $\frac{(q_{1t} - q_{2t})^2}{R_0^2}$, where q_{1t} and q_{2t} — are tunnel coordinates, R_0 — the distance between the tunneling "channels". For the Coulomb repulsion of the particles in the medium (ε_0 — dielectric constant, ε — relative dielectric constant) we get

$$V_{\text{rep}} = \frac{e^2}{\varepsilon\varepsilon_0|R|} = \frac{e^2}{\varepsilon\varepsilon_0[R_0^2 + (q_{1t} - q_{2t})^2]^{1/2}} \approx \frac{e^2}{\varepsilon\varepsilon_0 R_0} - \frac{1}{2} \cdot \frac{e^2}{\varepsilon\varepsilon_0 R_0} \cdot \frac{(q_{1t} - q_{2t})^2}{R_0^2}. \quad (2)$$

Hence, $\alpha = \frac{e^2}{\varepsilon\varepsilon_0 R_0^3}$ (where $\varepsilon < 0$ for the metamaterial matrix).

Negative harmonic potential energy (the second term in the expansion) appears, therefore, as an effective attractive interaction, although the potential is always repulsive. This negative contribution reduces repulsive potential of its maximum value in R_0 . The constant component $U(R_0) = \frac{e^2}{\varepsilon\varepsilon_0 R_0}$ may be included in the definition of the potential energy for the individual particles $U(q_1)$ and $U(q_2)$. The influence of an electric field can be accounted for by the renormalization parameter $a = \tilde{a} = a_0 + \frac{|e|E}{\omega_0^2}$, $b = \tilde{b} = b_0 - \frac{|e|E}{\omega_0^2}$.

For 2D-parallel transfer with account of the particles interaction and with the renormalization of the potential parameters in an external electric field, we obtain the renormalized potential in the next form

$$\begin{aligned} U_p(q_1, q_2) = \frac{2\tilde{U}_p(q_1, q_2)}{\omega^2} &= (q_1 + a)^2 \theta(-q_1) + \left[-(b^2 - a^2) + (q_1 - b)^2 \right] \theta(q_1) + (q_2 + a^2) \theta(-q_2) \\ &+ \left[-(b^2 - a^2) + (q_2 - b)^2 \right] \theta(q_2) - \frac{\alpha^*}{2} (q_1 - q_2)^2. \end{aligned} \quad (3)$$

We assume that two particles interact independently with the harmonic thermostat (a heat-bath). This interaction is considered in the bilinear approximation. Oscillatory dynamics of the medium is described by the Hamiltonian (we have used the system of units, in which $\hbar = 1$, $k_B = 1$, and the mass of the oscillators are 1).

$$H_{\text{ph}} = \frac{1}{2} \sum_i (P_i^2 + \omega_i^2 Q_i^2). \quad (4)$$

Each of the tunneling particles (electrons or effective charges) interacts with the oscillator thermostat as follows:

$$V_{p-ph}^{(1)}(q_1, Q_i) = q_1 \sum_i C_i Q_i, \quad V_{p-ph}^{(2)}(q_2, Q_i) = q_2 \sum_i C_i Q_i, \quad (5)$$

As in [3], we are interested in the probability of transfer per unit time or, strictly speaking, only in the exponential part of it, which can be written in the Langer form

$$\Gamma = 2T \frac{\text{Im}Z}{\text{Re}Z}. \quad (6)$$

To calculate Γ , it is convenient to represent the partition function in the form of the path integral [1–9]

$$Z = \prod_i \int Dq_1 Dq_2 DQ_i \exp [-S \{q_1, q_2, Q_i\}]. \quad (7)$$

Here S is the sub-barrier action for the entire system. The imaginary part $\text{Im}Z$ appears due to the decay of the energy levels in the initial well of the potential energy. The validity of this approach requires that the dissipation would be enough strong, so, the only incoherent decay is realized [3].

The integral (7) can be taken over the phonon coordinates [3], in result we obtain

$$S \{q_1, q_2\} = \int_{-\beta/2}^{\beta/2} d\tau \left[\frac{1}{2} q_1^2 + \frac{1}{2} q_2^2 + V(q_1, q_2) + \int_{-\beta/2}^{\beta/2} d\tau' D(\tau - \tau') [q_1(\tau) + q_2(\tau)] \times [q_1(\tau') + q_2(\tau')] \right], \quad (8)$$

where

$$D(\tau) = \frac{1}{\beta} \sum_{n=-\infty}^{\infty} D(v_n) \exp(i\nu_n\tau), \quad (9)$$

$\beta = \hbar / (k_B T)$ — inverse temperature (we assume that $\hbar = 1$ and $k_B = 1$), $v_n = 2\pi n/\beta$ is the Matsubara frequency, and

$$D(v_n) = - \sum_i \frac{C_i^2}{\omega_i^2 + v_n^2} - \sum_i \frac{C_i^2}{\omega_i^2} + \xi_n. \quad (10)$$

The trajectory that minimizes the Euclidean action S , can be found from the equations of motion. The moments of time, τ_1 and τ_2 , in which particles transfer the top of the barrier, are determined by the following equations:

$$q_1(\tau_1) = 0, \quad q_2(\tau_2) = 0. \quad (11)$$

Once a path is found, the Equation (11) can be represented in the following form:

$$\begin{aligned} & \sinh \varepsilon [\cosh \tau \coth \beta^* - \sinh \tau - \coth \beta^*] + \frac{1}{1 - \alpha^*} \sinh (\varepsilon \sqrt{1 - \alpha^*}) [\cosh (\tau \sqrt{1 - \alpha^*}) \\ & \times \coth (\beta^* \sqrt{1 - \alpha^*}) - \sinh (\tau \sqrt{1 - \alpha^*}) + \coth (\beta^* \sqrt{1 - \alpha^*})] = 0, \\ & 3 - \frac{4}{1 + b^*} - \frac{1}{1 - \alpha^*} + \cosh \varepsilon [\sinh \tau \coth \beta^* - \cosh \tau - 1] + \sinh \tau \coth \beta^* - \cosh \tau \\ & + \frac{1}{1 - \alpha^*} \cosh (\varepsilon \sqrt{1 - \alpha^*}) [\sinh (\tau \sqrt{1 - \alpha^*}) \coth (\beta^* \sqrt{1 - \alpha^*}) - \cosh (\tau \sqrt{1 - \alpha^*}) + 1] \\ & - \frac{1}{1 - \alpha^*} [\sinh (\tau \sqrt{1 - \alpha^*}) \coth (\beta^* \sqrt{1 - \alpha^*}) - \cosh (\tau \sqrt{1 - \alpha^*})] = 0. \end{aligned} \quad (12)$$

As we have shown in [2], the solution of this system reveals the bifurcation of the 2D-tunneling trajectories, i.e., at a certain temperature β^* or the potential asymmetry parameter associated with the applied electric field $b^* = b/a$, or the interaction factor $\alpha^* = 2\alpha/\omega^2$ (where $\alpha = \frac{e^2}{\varepsilon \varepsilon_0 R_0^3}$ depends on the relative permittivity of the medium (a heat-bath) for metamaterials $\varepsilon < 0$). Numerical analysis of the system (12) can also allow to identify the fine structure for tunnel transition in the vicinity of the bifurcation point, namely the regime of quantum beats for the parallel transport of tunneling particles. As a result, the probability of 2D-tunneling with exponential accuracy is defined as $\Gamma = \exp(-S)$.

The system of Equation (12) decision reveals the bifurcation for 2D-tunnel paths for certain values of temperature or for the potential asymmetry parameter (which is connected with the value of an external electric field), or for the interaction factor α , which depends on the relative negative dielectric constant for metamaterials. Numerical analysis of the system (12) can also identify the fine structure for transition in the vicinity of the bifurcation point, i.e., regime of quantum beats for the parallel transport of tunneling particles (in this case apart from the trivial solutions of (12), additional solutions are appeared).

The dependence of the tunneling probability on the electric field is shown in Fig. 1. In this figure, the area of the stable 2D-bifurcations is realized. In the vicinity of this point (as in the

neighborhood of interruption point for 2D-bifurcation) the quantum beats mechanism is realized, where mechanisms for synchronous and asynchronous transfer for tunneling particles are competing. Region for realization of the 2D-bifurcations stable effect is revealed, as also corresponding limits of the 2D-bifurcation existence are analyzed under change of the control parameters (the inverse temperature β , the relative dielectric constant of the heat-bath — ε for the metamaterial matrix, and the asymmetry parameter for 2D-potential of interacting QM b, which is weakly nonlinear depended on the magnitude of the external electric field).

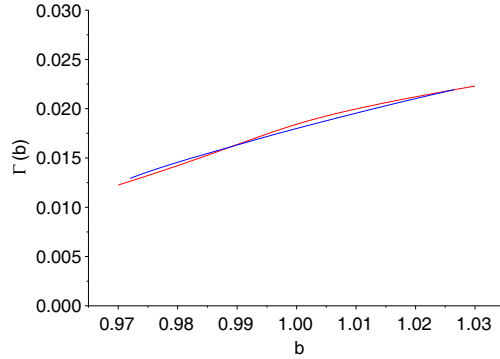


Figure 1: The dependence of the tunneling probability on the electric field.

3. CONCLUSION

Thus, the dependence of the electric field strength, at which the stable 2D-bifurcations are realized, on the value of the inverse temperature, has been investigated in this work. In contrast to conventional dielectric matrix in the case of the metamaterial matrix, region of the stable 2D-bifurcations is narrowed considerably, probably due to the sign inversion of the tunneling particles interaction. It should be noted, that the theoretical results, obtained in this article, do not have any quantitative comparison with the experiment, and are only qualitative meaning.

REFERENCES

1. Vendik, I. B., O. G. Vendik, and M. A. Odit, "Isotropic metamaterial based on ferro — Ceramic spherical inclusions," *FSS*, Vol. 51, No. 8, 1499–1503, 2009.
2. Leggett, A. J., V. D. Krevchik, V. Y. Krivnov, M. B. Semenov, and K. Yamamoto, *Transfer Processes in Low-dimensional Systems*, 690, UT Research Institute Press, Tokyo, Japan, 2005.
3. Caldeira, A. O. and A. J. Leggett, "Influence of dissipation on quantum tunneling in macroscopic systems," *Phys. Rev. Lett.*, Vol. 46, No. 4, 211–214, 1981.
4. Larkin, A. I. and Y. N. Ovchinnikov, "Quantum tunneling with dissipation," *JETP Letters*, Vol. 37, No. 7, 322–325, 1983.
5. Ivlev, B. I. and Y. N. Ovchinnikov, "The decay of metastable states in the presence of close-barrier trajectories," *JETP*, Vol. 93, No. 2(8), 668–679, 1987.
6. Kagan, Y. and N. V. Prokofyev, "About tunneling with 'dissipation,'" *JETP Letters*, Vol 43, No. 9, 434–437, 1986.
7. Benderkii, V. A., V. I. Goldanskii, and A. A. Ovchinnikov, "Effect of molecular motion on low-temperature and other anomalously fast chemical reactions in the solid phase," *Chem. Phys. Lett.*, Vol. 73, No. 3, 492–495, 1980.
8. Benderskii, V. A., E. V. Vetoshkin, E. I. Kats, and H. P. Trommsdorff, "Competing tunneling trajectories in a 2D potential with variable topology as a model for quantum bifurcations," *Phys. Rev. E*, Vol. 67, 026102, 2003.
9. Kiselev, M. N., K. Kikoin, and L. W. Molenkamp, "Resonance Kondo tunneling through a double quantum dot at finite bias," *Phys. Rev. B*, Vol 68, 155323, 2003.

Slotted Patch Antenna Loaded with Metamaterial

Surabhi Dwivedi¹, Vivekanand Mishra¹, and Yogesh P. Kosta²

¹ECED, S.V.N.I.T., Surat, India

²Marwadi Education Foundation's Group of Institutions, Rajkot, India

Abstract— Two ways to simulate a patch antenna has been demonstrated. The return loss is obtained for simple and slotted patch and compared with the metamaterial included slotted patch response. The deviation in solution time and the results are the important factors that are considered. Miniaturization of the patch antenna is to the core of our effort and the enhancement of bandwidth is obtained by slotting of the patch. Microstrip antennas are a relatively new generation of antennas and are preferable for many applications over the broad frequency range from 500 MHz to 50 GHz also called “patch antennas” or “printed antennas” or “planar antennas”.

1. INTRODUCTION

The objective is to develop a methodology to analyze and design a metamaterial substrate for a slotted microstrip antenna. Numerical simulation and theoretical studies are used first to design a metamaterial structure that is suitable for the antenna substrate; then use experiments to prove the prediction. Since simulating the real size structure requires full wave analysis which needs more memory and takes longer time. With the effective permittivity and permeability, one can use analytic formula to obtain far-field results. Symmetrical slotted patch antenna using four slots is introduced to design an antenna resonating at three resonant frequencies. Moreover, the design of patch antenna with slots has been presented for different wireless communication applications, e.g., triband circular polarized antennas for the UHF band. This study also shows the effect of different parameters on the antenna structure.

The primary aim is at simulation of combined metal-dielectric structures. A typical patch antenna structure consisting of a single patch above a finite ground plane was mostly considered in the present study. The performance of the antenna is studied for different mesh configurations, different dielectric constants and dimension of the substrate. Other straightforward applications of the present solver include simulation of antennas embedded in metamaterial.

2. CONCEPT OF METAMATERIALS

A metamaterial (or meta material) is a material which gains its properties from its structure rather than directly from its composition. Metamaterials are a broader class of materials which enables us to manipulate the permittivity and permeability for optimizing physical properties of radiating patch primarily for improvement in radiation from antenna. Recently, there has been growing interest in both the theoretical and experimental study of metamaterials. Metamaterials, also known as left-handed metamaterial (LHM) where the permeability and permittivity were simultaneously negative. LHM is an interesting material to be investigated where this artificial material has several unique properties such as the backward wave and the focusing effect inside it slab.

3. APPROACH AND METHODOLOGY

- Array of Unit Cell to Be Placed in the Substrate
 - PHASE 1: Unit cell development.
 - PHASE 2: Arbitrary shaped conducting sheet insertion.
 - PHASE 3: Chopping: Circular Polarisation.
 - PHASE 4: Slotting: Miniaturization, Multiband Operation, Tuning, Shifting frequency down to 2 GHz, Bandwidth is increased.
 - PHASE 5: Metamaterial Induced Patch Antenna.

Steps of designing

- (1 To obtain triband operation of slotted and chopped miniaturized patch within desired frequency band.

Table 1: Design parameters.

User Inputs	Outputs
Operating Frequency (f_r)	Radiation Resistance
Characteristic Impedance (Z_0)	Effective dielectric constant
Substrate's dielectric constant (ϵ_r)	Phase Constant
Height (h)	Input Impedance
Loss tangent	Beam width, Bandwidth, Directivity, Gain, Efficiency

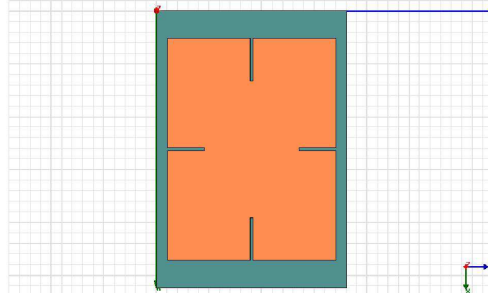


Figure 1: Top view of slotted patch.

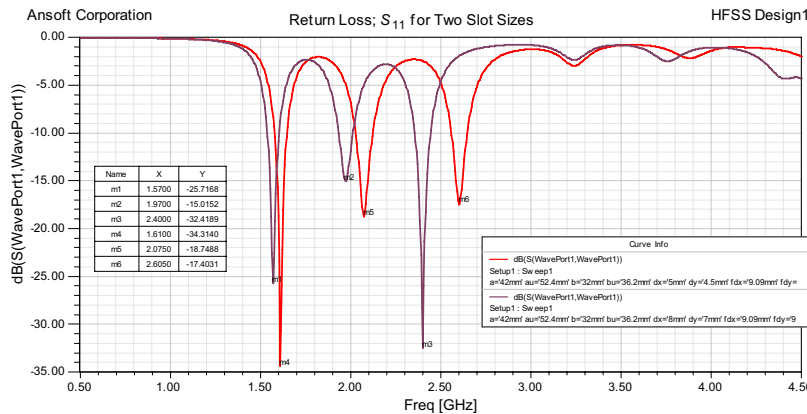


Figure 2: Return loss plot for two slot sizes of slotted patch antenna.

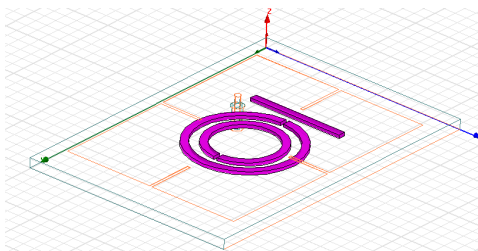
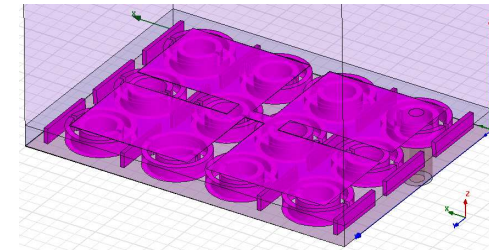
Figure 3: SRR-TW in FR₄ dielectric substrate of antenna.

Figure 4: Resonating structure in microwave band regimes for dual frequencies.

- (2) To enhance the response using metamaterials which is used as artificial substrate.
- (3) To observe the effect of varying the slot dimensions on the performance of slotted MSA is described.
- (4) Miniaturization of the overall antenna size.

4. SLOTTED PATCH IN HFSS

4.1. Significance of Slotting

The slotting in the patch caused the antenna to respond at frequency lower than that of the simple patch without slots. Also, by changing slot size, frequencies can be tuned.

Table 2: Highlighted portion shows optimum desired band 1.4910–2.6810 GHz.

a_p (mm)	No. of Bands	Band-1		Band-2		Band-3	
		Max Freq (GHz)	S11(dB)	Max Freq (GHz)	S11 (dB)	Max Freq (GHz)	S11 (dB)
40	3	1.6600	-15.6078	2.0850	-10.2846	2.5000	-12.3866
43.04	3	1.5100	-13.5812	2.0950	-13.0829	2.4100	-16.1982
45	3	1.4450	-15.2823	2.1050	-15.9902	2.4050	-22.2767
45.9	3	1.4200	-15.5753	2.0950	-19.0988	2.3850	-20.9514
50	3	1.3100	-31.8061	2.0950	-24.4716	2.3500	-15.5596
51	3	1.3000	-14.5347	2.0850	-17.7834	2.3500	-9.5395

4.2. Slotted Patch with Unit Cell in HFSS

A pair of Split Ring Resonator (SRR) and Thin Wire (TW) was inserted in the dielectric substrate of the slotted patch antenna.

4.3. Significance

The figure shows the shape, size and position of the SRR-TW in FR4 substrate. The antenna dimensions are yet to be changed. But the response shows the resonant frequencies to be lowered due to insertion of SRR-TW.

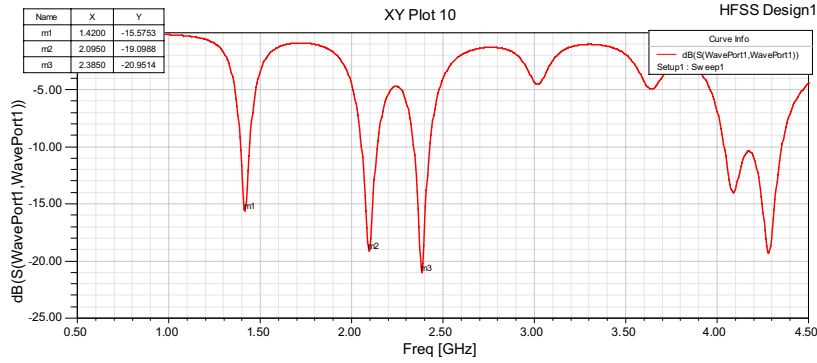
5. METAMATERIAL ARRAY IN SLOTTED PATCH

5.1. Slot Dimensions

For different dimensions of patch: After simulating various models, best results are displayed below. $d_y \times w_x = 8 \text{ mm} \times 0.5 \text{ mm}$, $d_x \times w_y = 8 \text{ mm} \times 0.5 \text{ mm}$. Varying $a_p, b_p = 30 \text{ mm}$;

5.2. Simulated Result

Return loss/S parameter:



6. RESULT ANALYSIS

Slotted Patch responds between 1.4910–2.6810 GHz which is optimized for patch dimensions 30 mm × 50 mm. Tribands are made to be shifted for the application of LEO and MEO satellite.

7. CONCLUSION

Triband Operation of slotted patch antenna for 1 to 4 GHz of frequency band is obtained with optimized results in terms of return loss. It can be concluded that after appropriate slotting the patch the triband is shifted more towards left of the frequency axis, i.e., upto 1.4910 GHz. Moreover all the three bands are obtained between 1.4450–2.4100 GHz. Modeling of patch antennas on arbitrary dielectric substrates using surface/volume RWG elements and the Method of Moments was implemented. Performance of the solver was tested for different mesh configurations and for different dielectric constants of the substrate. Further scope for improvement lies in the investigation of boundary conditions at the metal-dielectric interface and the optimization of the Matlab scripts.

Metamaterial Included Slotted Patch Antenna versus Metamaterial Cover over Patch

Surabhi Dwivedi¹, Vivekanand Mishra¹, and Yogesh P. Kosta²

¹ECED, S.V.N.I.T., Surat, India

²Marwadi Education Foundation's Group of Institutions, Rajkot, India

Abstract— A metamaterial is introduced into the cover of a patch antenna and its band structure is analyzed. The metamaterial cover with correct selection of the working frequency increases the patch antenna's directivity. Based on the methodology, optimization of structure is proposed for the application of metamaterials as antenna substrate to primarily enhance directivity by minimizing its refractive index. The experimental results are presented thoroughly and compared with the analytic calculations. This paper aims to review and critically discuss the comparison of a metamaterial included patch and metamaterial cover over the patch. An analytical method is used to predict the features of the simulation results, implying that within a certain frequency range, comparison can be made between these two models. The *S*-parameters as a performance matrix are obtained from antenna simulations carried on CADFEKO Silverlite version 5.5. Simulations have been carried out for different shapes of microstrip patch antenna in the microwave regime in HFSS 13.0.

1. INTRODUCTION

Metamaterials are a broader class of materials which enables us to manipulate the permittivity and permeability for optimizing physical properties of radiating patch primarily for improvement in radiation from antenna. Recently, there has been growing interest in both the theoretical and experimental study of metamaterials. Many properties and potential applications of left-handed metamaterials have been explored and analyzed theoretically. Emission in metamaterials using an antenna was presented in 2002 by Enoch et al. An MSA in its simplest form consists of a radiating patch on one side of a dielectric substrate and a ground plane on the other side. Radiation from the MSA can occur from the fringing fields between the periphery of the patch and the ground plane. In 1953, Deschamps first proposed the concept of the MSA. Practical antennas were developed by Munson and Howell in the 1970s. The numerous advantages of MSA led to the design of several configurations for various applications, which includes its low weight, small volume, and ease of fabrication. With increasing requirements for personal and mobile communications, the demand for smaller and low-profile antennas has brought the concept of MSA.

Another objective of this paper is to develop a methodology to analyze, design and compare a metamaterial substrate for a microstrip antenna with a patch cover. We will use numerical simulation and theoretical studies first to design a metamaterial structure that is suitable for the antenna substrate; then use experiments to prove our prediction for the comparison purpose.

MSAs are manufactured using printed-circuit technology, so that mass production can be achieved at a low cost.

A metamaterial (or meta material) is a material which gains its properties from its structure rather than directly from its composition.

DPS-Double Positive material, ENG- ϵ (Electrically) negative material, MNG- μ (Magnetically) negative material, DNG-Double Negative material.

2. PARAMETRIC STUDY OF MSAs

2.1. Effect of b_p

The width b_p of the RMSA has significant effect on the input impedance, BW, and gain of the antenna. With an increase in b_p the following effects are observed: the resonance frequency decreases from 3.14 GHz to 2.46 GHz. The BW of the antenna increases by 8.7%. The aperture area of the antenna increases resulting in an increase in the directivity, efficiency, and gain.

2.2. Effect of ϵ_r

With an increase in ϵ_r the following effects are observed: BW increases due to a decrease in ϵ_r and an increase in h/λ_0 , because the resonance frequency has increased. A better comparison of effect of ϵ_r is obtained when the antenna is designed to operate in the same frequency range for different values of ϵ_r .

2.3. Effect of Finite Ground Plane

The finite ground plane effect can be taken into account by numerical techniques. However, it should be noted that the simulation time is least when the ground plane is infinite because then only the patch is analyzed with its perfect image. For the finite ground plane, on the other hand, both the patch and the ground plane are divided into number of segments and hence the simulation time increases. Also, as the size of the ground plane increases, the simulation time increases [3].

3. DESIGNED MODEL

3.1. Slotted Patch Antenna

Figure 1 indicates generalized patch antenna with four slots modelled in CADFEKO with following dimensions: Substrate dimensions:

52.4 mm × 36.2 mm × 1.56 mm;
Patch dimensions: 40 mm × 20 mm;
Slot dimensions: 8 mm × 0.5 mm.

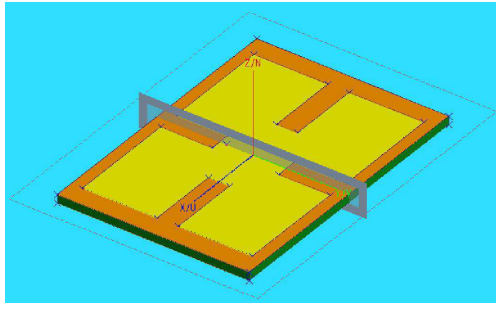


Figure 1: Slotted patch antenna modeled in CADFEKO.

3.2. Slotted Patch with Metamaterial

For different dimensions of the patch, after simulating various models, best results are displayed below:

$$d_y \times w_x = 7 \text{ mm} \times 0.5 \text{ mm}, d_x \times w_y = 8 \text{ mm} \times 0.5 \text{ mm}, a_p = 45.9 \text{ mm}, b_p = 30 \text{ mm};$$

Figure 2 represents simulated result with return loss/S-parameter and tribands in the range of 1–4 GHz. Result analysis shows slotted patch with metamaterial responds between 1.4450–2.4150 GHz for patch dimensions 30 mm × 45.9 mm. Tribands are further shifted towards left of the frequency axis with good results of return loss.

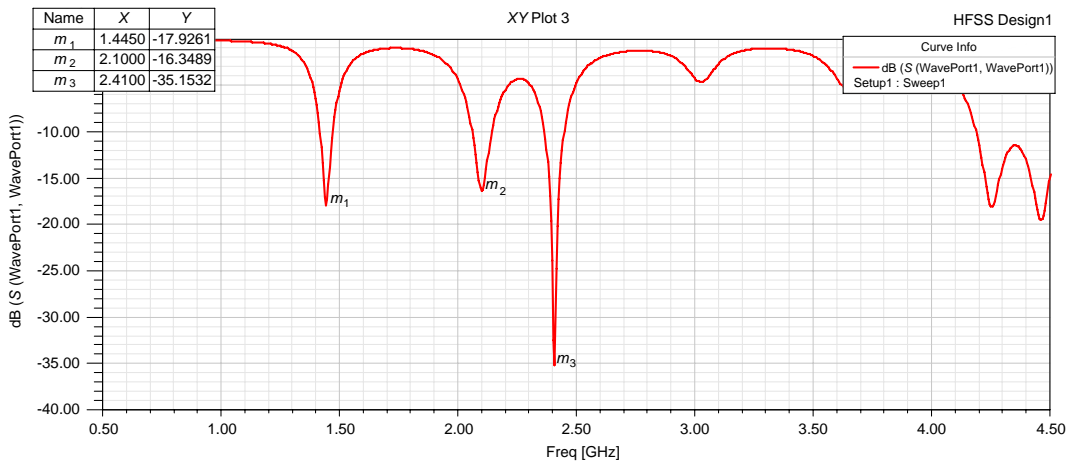


Figure 2: Return loss of slotted patch with MTM.

3.3. Metamaterial Cover over Patch

SRR and rod is used as patch cover and return loss is analysed.

Figure 3 shows tri-band operation of slotted patch antenna for 1 to 4 GHz of frequency band is obtained with optimized results in terms of return loss. It can be concluded that after appropriate slotting the patch the tri-band is shifted more towards left of the frequency axis, i.e., upto 1.4910 GHz. Moreover all the three bands are obtained between 1.4450–2.4100 GHz. The improved gain curve is as shown in the Figure 4 and Figure 5 respectively.



Figure 3: Return loss of metamaterial cover.

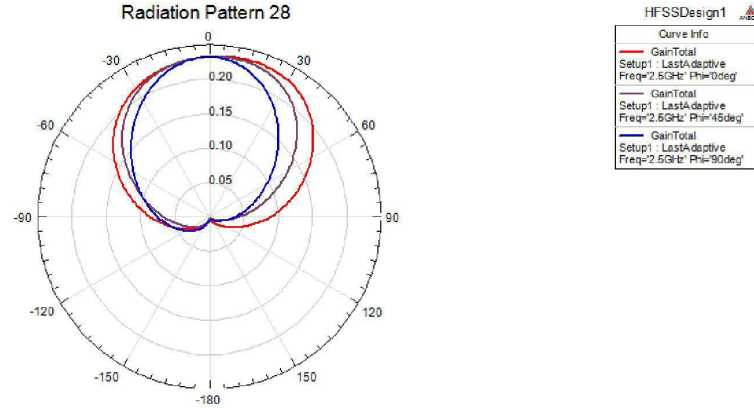


Figure 4: Gain curve.

Special design of the metamaterial is composed of tiny metallic inclusions and these elements are significantly smaller than the free space wavelength λ_o so as to prevent diffraction effects. Then the array of unit cells are formed and by increasing array dimensions return loss S_{11} improves and bandwidth widens as a result of different coupling effects.

4. CONCLUSION

This paper has demonstrated two ways to simulate a patch antenna. The return loss is obtained for metamaterial include slotted patch and compared with the patch cover response. Applying metamaterial to patch antenna is an important development of new high-directivity patch antenna.

The results showed that the metamaterial cover, which works like a lens, could effectively improve the patch antenna's directivity. The physical reasons for the improvement are also given.

Miniaturization of the patch antenna is to the core of our effort and the enhancement of bandwidth is obtained by slotting of the patch. After inclusions of the metamaterial the bandwidth increment is 11.13% as compared to the substrate with teflon as the dielectric. Future scope of metamaterials hold great promise for new applications in the megahertz to terahertz bands, as well as optical frequencies which includes super-resolution imaging, cloaking, hyperlensing, and optical transformation.

Snow Cover Effect on Brightness Temperature of Arctic Ice Fields Based on SSM/I Data

V. V. Tikhonov¹, D. A. Boyarskii¹, I. A. Repina^{1, 2},
M. D. Raev¹, E. A. Sharkov¹, and T. A. Alexeeva³

¹Remote Sensing of the Earth Department, Space Research Institute, Russian Academy of Sciences, Russia

²A. M. Obukhov Institute of Atmospheric Physics, Russian Academy of Sciences, Russia

³Arctic and Antarctic Research Institute, Russia

Abstract— The presence of snow on the surface of ice considerably influences the radiation characteristics of the “water surface — ice cover — snow cover — atmosphere” system. This work discusses the effect of snow cover on brightness temperature of Arctic ice fields.

1. INTRODUCTION

The studies of the spatial and temporal characteristics of Arctic ice fields provide the basis for monitoring global change of the environment. Employing remote sensing techniques is the most feasible way to investigate the ice cover. These techniques include passive microwave sensing aimed at defining spatial distribution, types, thickness and snow cover of ice. The presence of snow on the surface of ice considerably influences the radiation characteristics of the “water surface — ice cover — snow cover — atmosphere” system.

2. ELECTRODYNAMIC MODEL

The radiating system is represented by a water surface covered by several layers of ice and snow with a thick atmospheric layer atop. Brightness temperature of such system can be derived from the following expressions [1]:

$$T_{br}^v = \sum_{j=1}^N \frac{T_j |W_j|^2}{|1 - R_j^- R_j^+ \exp(2i\psi_j)|^2} \times \left[(1 - \exp(-2\text{Im}\psi_j)) \left(1 + |R_j^- \exp(i\psi_j)|^2 \right) \right. \\ \left. + 4 \frac{\text{Im}\psi_j}{\text{Re}\psi_j} \text{Re}(R_j^- \exp(i\psi_j)) \text{Im}(\exp(i\psi_j)) \times \left(\frac{|k_{zj}|^2 - k_x^2}{|k_j|^2} \right) \right] \frac{\text{Re}Z_j}{\text{Re}Z_0} + T_{N+1} |W_{N+1}|^2 \frac{\text{Re}Z_{N+1}}{\text{Re}Z_0}, \quad (1)$$

$$T_{br}^h = \sum_{j=1}^N \frac{T_j |W_j|^2}{|1 - R_j^- R_j^+ \exp(2i\psi_j)|^2} \times \left[(1 - \exp(2\text{Im}\psi_j)) \left(1 + |R_j^- \exp(i\psi_j)|^2 \right) \right. \\ \left. + 4 \frac{\text{Im}\psi_j}{\text{Re}\psi_j} \text{Re}(R_j^- \exp(i\psi_j)) \text{Im}(\exp(i\psi_j)) \right] \frac{\text{Re}Z_j}{\text{Re}Z_0} + T_{N+1} |W_{N+1}|^2 \frac{\text{Re}Z_{N+1}}{\text{Re}Z_0}, \quad (2)$$

where subscripts *v* and *h* indicate vertical and horizontal polarizations; T_j — layer *j* temperature; R_j^+, R_j^- — electric field amplitude reflection coefficients for the upper and lower boundaries of layer *j*, respectively; W_j — electric field amplitude transmission coefficients from the inner side of layer *j* upper boundary to the boundary of the medium; Z_j — wave impedance of layer of permittivity ϵ_j , $k_j = 2\pi/\lambda \times \{\sin\theta_j, 0, \cos\theta_j\}(\epsilon_j)^{1/2}$ — wave vector, $\Psi_j = k_{jz}h_j$, h_j — layer thickness. N — number of layers. Index $j = 1$ stands for the atmosphere; index $j = N + 1$ — the water surface.

The signal received by radiometer is determined by dielectric properties of each layer of the system. Dielectric properties of Arctic ice strongly depend on its age and meteorological conditions during formation stage. Young ice includes large quantities of air bubbles known to scatter microwaves. Old ice is less porous and scatters less radiation. At temperatures close to 0°C air pores in ice start to be filled with liquid brine. Brine bubbles in ice not only scatter but also absorb electromagnetic radiation. Radiation scattering and absorption in ice strongly affect its dielectric properties. Snow cover on ice also influences radiation properties of the whole system. When penetrating snow, radiation is absorbed and scattered by snow crystals, whereas appearance of moisture in snow results in a drastic change of its radiophysical characteristics.

A model of multi-phase disperse medium [2, 3] has been employed to determine dielectric properties of ice and snow layers. The model takes into account physical and structural properties of a medium as well as radiation scattering and absorption on impurities. According to the model, sea ice is represented as a continuous ice medium containing spherical inclusions of air and liquid brine, while snow cover is viewed as an air medium containing spherical ice grains covered with water film and water drops.

Based on this model, effective permittivity of sea ice layer is derived from the expression:

$$\varepsilon_{eff} = \varepsilon_i \left[1 - \frac{4\pi n_a (\varepsilon_a + 2\varepsilon_i) \frac{\langle f_\omega \rangle_a}{k^2}}{2\varepsilon_{eff} + \varepsilon_a} - \frac{4\pi n_{sw} (\varepsilon_{sw} + 2\varepsilon_i) \frac{\langle f_\omega \rangle_{sw}}{k^2}}{2\varepsilon_{eff} + \varepsilon_{sw}} \right]^{-1}, \quad (3)$$

where k is wave number, n_a , and n_{sw} — concentrations of air pores and brine drops, respectively; ε_i , ε_a and ε_{sw} — permittivities of ice, air and liquid brine, respectively; $\langle f_\omega \rangle_a$ and $\langle f_\omega \rangle_{sw}$ — size-averaged amplitudes of forward scattering on air pores and brine drops, respectively.

Proceeding from these assumptions, effective permittivity of snow medium is derived from the expression:

$$\varepsilon_{eff}^{-1} = 1 - \frac{4\pi n_i (\varepsilon_i^w + 2) \frac{\langle f_\omega \rangle_i}{k^2}}{2\varepsilon_{eff} + \varepsilon_i^w} - \frac{4\pi n_w (\varepsilon_w + 2) \frac{\langle f_\omega \rangle_w}{k^2}}{2\varepsilon_{eff} + \varepsilon_w}, \quad (4)$$

where n_i and n_w are concentrations of ice grains and water drops, respectively; ε_i^w — effective permittivity of an ice grain covered with water film; ε_w — permittivity of snow; $\langle f_\omega \rangle_i$ and $\langle f_\omega \rangle_w$ — size-averaged amplitudes of forward scattering on an ice grain covered with water film and a water drop, respectively. Amplitudes of forward scattering in expressions (3) and (4) are computed according to the Mie theory. Sizes of inclusions in sea ice and snow cover are assumed to obey the logarithm normal distribution [4].

Variations of dielectric properties of sea ice and snow cover are illustrated in Fig. 1. Frequency dependencies of the real (solid lines) and imaginary (dashed lines) parts of permittivities are drawn for: water — blue color, solid freshwater ice — light blue color, sea ice with pores filled with air — red color, sea ice with pores filled with liquid brine — green, dry snow — orange; maximum wetness snow — magenta. The curves for sea ice and snow are derived from (3) and (4), while those for water and solid freshwater ice at 0°C are taken from [5, 6]. Fig. 1(a) shows that with the occurrence of air pores in ice, the imaginary part of ice permittivity drastically increases, while the real part slightly decreases. With liquid brine filling up the pores, the permittivity real and imaginary parts strongly increase, while the shape of the dependencies completely mimics that of permittivity real and imaginary parts of water. Fig. 1(b) demonstrates that the effect of radiation scattering on ice grains is very important in dry snow cover. This results in strong rise of the imaginary part of dry snow complex permittivity compared to that of solid freshwater ice. The appearance of liquid water in snow leads to a significant increase of the real and imaginary parts of

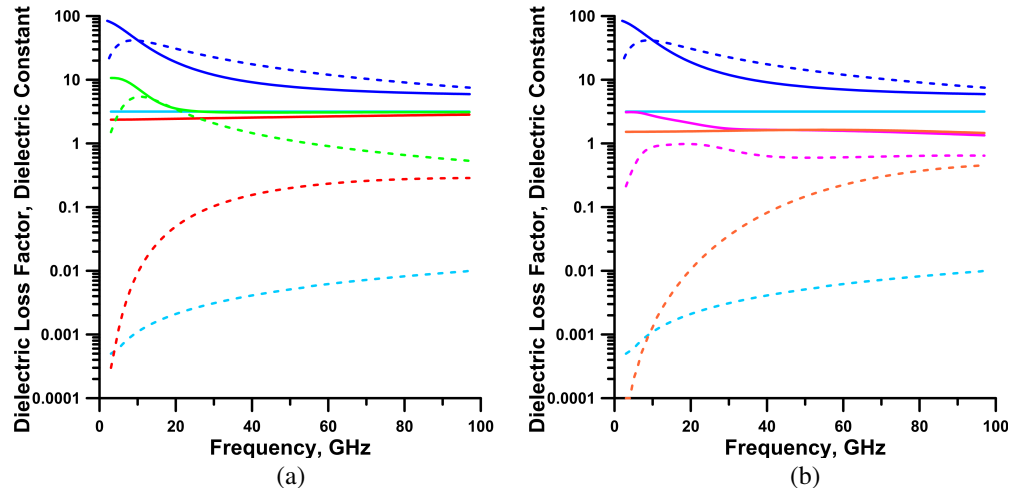


Figure 1: Dielectric properties of ice and snow: (a) — sea ice, (b) — snow.

wet snow permittivity, with the shape of the dependencies completely mimicking that of the real and imaginary parts of water permittivity.

Dielectric properties of sea ice and snow allow us to calculate the corresponding thicknesses of effective radiating layer (depth of radiation formation) for microwave frequencies. The depth of radiation formation, that is the thickness of medium, across which the amplitude of electromagnetic wave decreases e times, is derived from the relation [7]: $h = \lambda/(4\pi n^{\parallel})$, where λ is the wavelength, n^{\parallel} is the imaginary part of complex refraction index of the medium. Fig. 2 presents dependencies of the depth of radiation formation on microwave frequency for: snow cover — red color, sea ice — green color, solid freshwater ice — light blue color. Solid curves refer to the temperature of -20°C , when no liquid phase exists either in snow or ice, dashed curves refer to 0°C , when there is the largest possible liquid phase both in snow and ice. Thin vertical lines mark SSM/I frequencies (19.35, 22.235, 37 and 85.5 GHz).

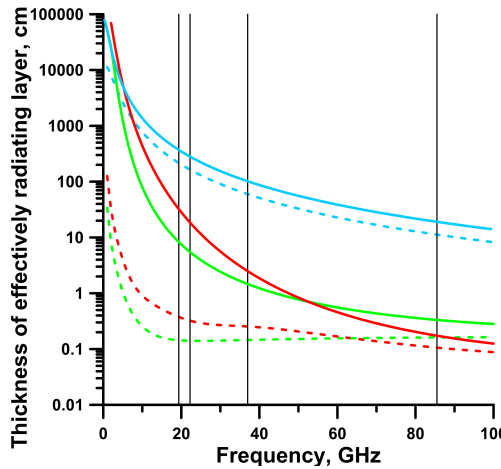


Figure 2: Depth of radiation formation for sea ice and snow cover.

It is clear from the figure, that the thickness of effectively radiating layer is considerably smaller for sea ice than for solid ice. This is explained by stronger radiation scattering in sea ice in the presence of air bubbles as well as stronger absorption in the presence of liquid brine. Hence, the imaginary part of complex refraction index of sea ice rises. The same effects (radiation scattering and absorption on impurities) determine the depth of radiation formation of snow cover. For wet snow, it is only a few centimeters for microwaves. For dry snow, it does not exceed 30 cm. Therefore, within the SSM/I frequency range, the radiation of the “water surface — sea ice — snow cover — atmosphere” system is conditioned only by a thin upper layer of solid ground: from 20–30 cm at 19.35 GHz to a few millimeters at 85.5 GHz.

3. RESULTS

The differences in dielectric properties of sea ice and snow must be reflected in the radiating characteristics of the “water surface — sea ice — snow cover — atmosphere” system, the SSM/I brightness temperature values, in particular. Model estimates of the brightness temperature of Arctic ice cover assimilating *in situ* data have been compared with SSM/I data (Fig. 3).

The model input data were retrieved from the databank of sea ice observations collected by the Arctic and Antarctic Research Institute [8]. Satellite data were provided by the POLE-RT-Fields SSM/I database for polar regions built on the basis of the GLOBAL-RT database [1] developed at the Space Research Institute RAS.

We can see from the figures, that model results agree well with satellite data. The presence of snow cover on ice attenuates the steepness of the dependencies at 19.35 and 22.235 GHz (c, f). The thickness of the effectively radiating layer for these frequencies makes only 20–30 cm. Therefore, if ice is covered with a thin layer of snow, this layer gives the main contribution into brightness temperature of the “water surface — sea ice — snow cover — atmosphere” system at frequencies higher than 10 GHz. Permittivity of snow, either wet or dry, is significantly less than that of water or sea ice (Fig. 1). This fact results in attenuation of brightness temperature dependence at lower frequencies of the given range.

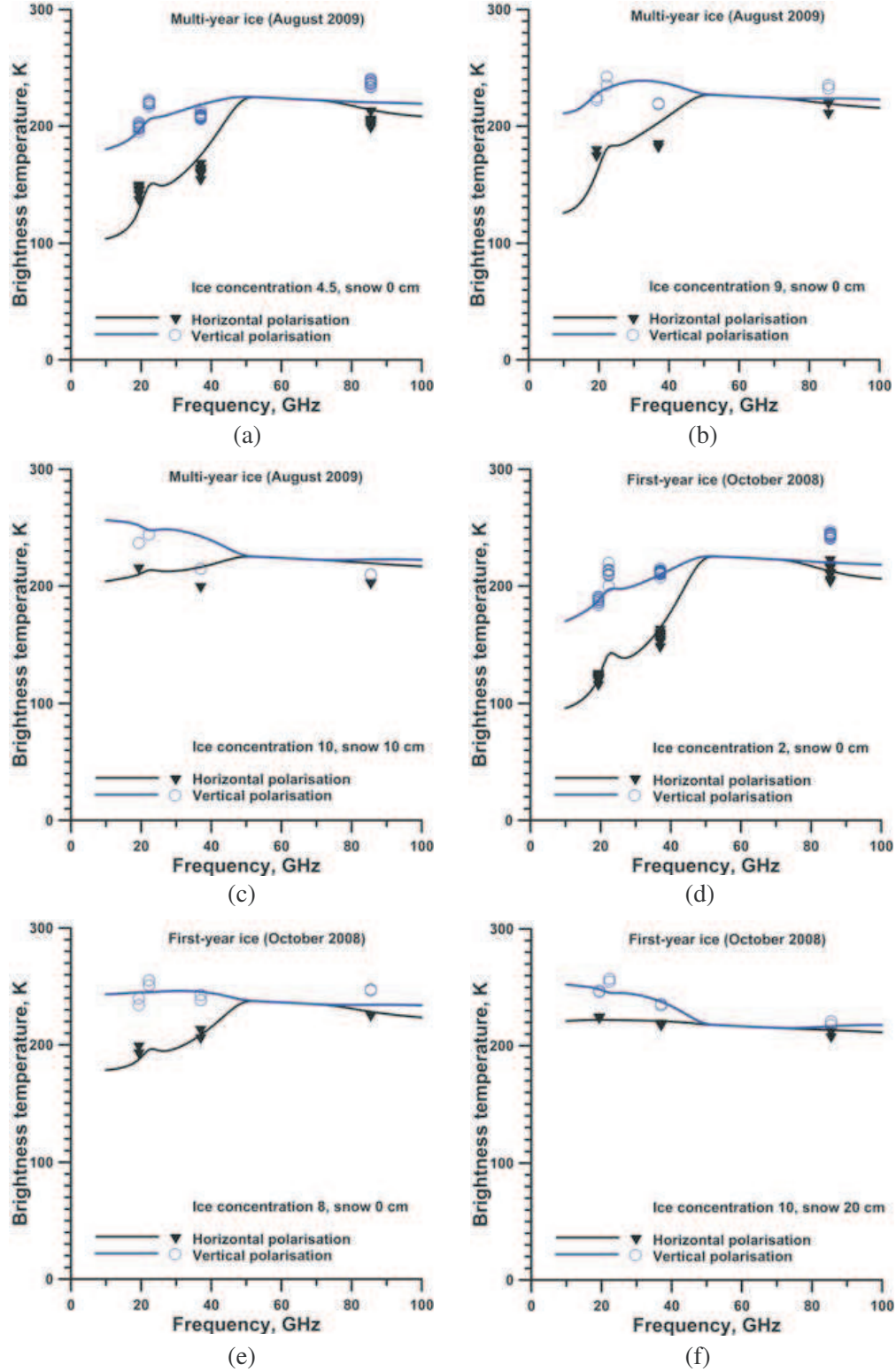


Figure 3: Frequency dependencies of brightness temperature of Arctic ice cover. Solid lines — model results, triangles and circles — SSM/I data.

4. CONCLUSION

The presence of snow cover on ice has a dramatic impact on radiating characteristics of the “water surface — sea ice — snow cover — atmosphere” system. This fact should be taken into consideration when estimating the characteristics of Arctic ice fields from satellite radiometry data.

5. ACKNOWLEDGEMENT

The work was performed with the support of RFBR projects N 13-05-00272 and N 11-05-00679 as well as the Russian Federation Governmental grant (Agreement N 11.G34.31.0078) for investigations guided by outstanding scientists and the Ministry of Education and Science grant (Agreement N 8833).

REFERENCES

1. Sharkov, E. A., *Passive Microwave Remote Sensing of the Earth: Physical Foundations*, 613, Springer/PRAXIS, Berlin, Heidelberg, London, New York, etc., 2003.
2. Boyarskii, D. A., V. V. Tikhonov, N. I. Kleeorin, and V. G. Mirovskii, “Inclusion of scattering losses in the models of the effective permittivity of dielectric mixtures and applications to wet snow,” *Journal of Electromagnetic Waves and Applications*, Vol. 8, No. 11, 1395–1410, 1994.
3. Boyarskii, D. A., V. V. Tikhonov, and N. Yu. Komarova, “Model of dielectric constant of bound water in soil for applications of microwave remote sensing,” *Progress In Electromagnetics Research*, Vol. 35, 251–269, 2002.
4. Colbeck, S. C., “Snow metamorphism and classification,” *Seasonal Snowcovers: Physics, Chemistry, Hydrology. NATO ASI Series*, Vol. 211, 1–35, 1987.
5. Hufford, G., “A model for the complex permittivity of ice at frequencies below 1 THz,” *Intern. J. Infrared and Millimeter Waves*, Vol. 12, No. 7, 677–682, 1991.
6. Ray, P. S., “Broadband complex refractive indices of ice and water,” *J. Applied Optics*, Vol. 11, No. 8, 1836–1844, 1972.
7. Feinberg, E. L., *Propagation of Radiowaves along the Terrestrial Surface*, 496, Nauka, Moscow, 1999.
8. Polyakov, I. V., et al., “Observational program tracks Arctic Ocean transition to a warmer state,” *Eos, Transactions American Geophysical Union*, Vol. 88, 398–399, 2007.

Impact of Counselling Programs on the Academic Results at Telecommunication Engineering Degree

E. de Lorenzo, A. Mojón, G. F. Manín, C. L. Bravo, and I. Cuiñas

School of Telecommunication Engineering, Universidade de Vigo, Spain

Abstract— Traditionally, academic results of undergraduates at engineering degrees seem to be far from the aptitudes and competences of such selected students. And this occurs mainly during the first year of the University degree. However, our schools and faculties are receiving, year by year, most of the best secondary school students.

A first analysis would highlight a common behaviour of such students: Their academic results are better once they have adapted their study skills to those required in the University, and when they feel themselves as residents at the campus. So, different strategies could be applied to help students in landing on campus and adapting their habits to the University lifestyle.

The objective of this contribution is to share our experience in the Telecommunication Engineering School, at the University of Vigo. The impact of counselling when new students arrive at the School by helping them to get a fast adaptation to their new stage of education is presented herein. Academic results as well as satisfaction surveys indicate promising future for such experience.

1. INTRODUCTION

For years, Telecommunication Engineering degrees (also called Electrical or Computer Science Engineering out of Spain) are receiving the best pre-university students: Our 18-years-old arriving students are proud of their previous level qualifications, and they are used to pass with honours most of the topics they have followed at high school. So, the aptitudes and competences of such selected students are supposed to be outstanding, and the staffs of the Schools and Faculties are very confident on the future results they could obtain. However, the first year at the University degree appears to be a wall where many high-level students beat and beat, instead of jumping it.

The scenario is simple: We have good or very good students obtaining bad or very bad qualification. That contradictory situation becomes a bit more explainable when we test that the academic results are better after six or twelve months. It seems to be a period of time needed by the students to adjust their study skills and techniques to those required at the University. Thus, they have to change from feeling themselves as visitors to become residents at the campus. Probably, the citizenship is the key to obtain better results in academic terms, but also to live comfortably among their classmates and professors.

Taking into account this evidence, different strategies could be applied to help the students to land on the campus and to become citizens of it. And those strategies do not only involve the students, but the whole academic institution: The people in the teaching staff must change their mind from only transmitting knowledge to work towards an integral formation. This new education paradigm tends to integrate some ideas that are continuously used in re-cycling courses in other areas as entrepreneurship, leadership, networking, walking towards a multidisciplinary set. Talent, inventiveness, creativity, compromise, implication, are becoming musts in the curricula of future professionals, and all them have to be involved in the new education programs. We are not in changing times, we are changing of time! Thus, a deep reflection and analysis work is mandatory as our education programs need integral changes, not yet a superficial adaptation in order to survive.

All that previous reflection could be applied to the recent experience of our School of Telecommunication Engineering, at the University of Vigo. For years, the students arrived first time the School without any help, and they began attending lessons. And Darwin theory of evolution was demonstrated: Only those students with adaptation skills survived in the degree after one or two years, and their academic results were commonly worse than expected taking into account their pre-university marks. Some years ago, an incipient counselling program was implemented, and few results were obtained, as commented in Section 2.

Recently, a full counselling program has been implemented, with mandatory registration for students and an organized timetable for the activities. Professors in charge receive support by Counselling Coordinator and the School Direction, and all the activities are planned in advance taking into account the academic duties for students along the year. This program is also supported

by a full coordination among topics, in terms of both contents and assessments. Last years statistics support an increasing number of students attending the different tests along the season and the final exams, but also an improvement in the qualifications our students obtain, related to their participation in the counselling program. The explanation of our personal and group tutoring plan, the analysis of its effects in terms of students and tutors satisfaction, and the evaluation of the improvement in academic results are the contents of Sections 3, 4 and 5.

2. THE FIRST ATTEMPT IN COUNSELING PLAN

The first attempt to promote a tutoring/counselling plan among the new arriving students was implemented in 2000/2001 academic year. This plan was completely voluntary for both students and staff, which includes a counsellor-professor and also some counsellor-students. At that time, the plan was focused on students arriving first time the School, for following first year topics. The students that decided to join the plan were assigned to a group, which was leaded by a professor helped by one or two veteran students, coursing third or fourth year. The rhythm of the meetings, their contents, and the materials to use were open and the group leaders have a lot of responsibility.

Different difficulties were detected in those initial years that set hurdles to the well development of the tutoring plan:

- Lack of communication and coordination between tutor-students and tutor-profs, which causes an overlap in functions, information, support materials, etc. offered by both kind of tutors.
- Limitations in monitoring the program performance by School Direction.
- Psychological distance from the professor regarding the students of first years that encourages little participation.
- Availability of time and infrastructure to carry out the tutorials.
- Mixture with academic tutoring (contents, exams).
- Academic recognition of tutor-profs, who are using several workable hours “for free”.

3. PERSONAL AND GROUP COUNSELING PLAN

The limitations of that first attempt were early analysed and around 2003, the objectives of a more ambitious plan had been enunciated, including the main aims, the coordination scheme, and a long-life formation program for tutor-profs. However, these ideas were not implemented, and the utility of the plan was going down.

Around 2010/11, an improvement has been applied to the tutoring/counselling plan. The focus was put in an important change: The students were not only expected to chat, but they also have to be listened to. This means that the objective is not just to maintain chats or meetings with a group of students, as a sort of group therapy; the counsellor has to attend the opinion of the students to take into account their problems and their ideas to solve them. This strategy must have a direct impact on the coordination among topics, in terms of contents and timing, qualification methods, didactic materials, and any other academic issue.

Now, each new arriving student is mandatorily assigned to a tutoring/counselling group, led by a professor or associate professor, who has a complete a priori planning of meetings along the year:

- At the beginning, to help the students in the first landing on the University.
- After two months, to detect organization/timing problems at both sides: The own new student, but also the topics.
- After the exams of the first semester, to analyse the results, and to plan the second semester.
- In the middle of the second semester, to check the planning done and some partial test results.
- At the end of the academic year, to analyse second semester results.

This scheme resulted to be well accepted in terms of student satisfaction, but also promising in terms of academic results [1, 2].

Different topics including general institutional information, different services offered (cultural programs, sports, foreign languages, psychological assistant, etc.), keys about bibliographical search or how to use computer labs are presented the first weeks of classes for a big group of students. Afterwards the counsellor-students meetings are small group meetings and individual time is considered also for first year students. This counselling plan includes different group meetings for the next years when such a near and deep relation is not needed. In relation with this information

and counselling about rules related with academic effort and meetings for explaining the different specialization in the degree are included. At last year, workshops about employment, interview preparation, resume redaction, and so on are considered too.

But the current plan is no more than an improvement of the initial one. Nowadays, a new tutoring/mentoring plan is being prepared for next academic year. One important characteristic is based on previous training for the people involved in counselling, and the second is including mentoring. Two levels of counselling are considered: Teachers and last-year students for mentoring. With this aim, a group of 25 students have attended a course on transversal competences and personal skills development to acquire the background they are going to need in their mentoring tasks. In parallel, the set of counsellors is being prepared with a course on group techniques, personal development, some psychological topics, and in general non-technical knowledge that could be useful for wearing the shoes of next year new students.

Mentors are near new students because of age and situation; they can communicate better and know well the situation their colleagues are at that moment. The background acquired will help the older students in leading the meetings, in encouraging the new students and help them in become part of the campus and to get involved easily in this new time of their lives. Besides that they can help them in changing some studying techniques, time-planning and self-organization. The teachers, that can be seen farther, are helping the mentors and giving different advices that are also needed.

Besides that the mentors acquired new skills that will help them at the moment they finish the degree and get an employment and the work as volunteers, helping their colleagues. It is not only to get new skills, but to learn about solidarity and knowing other people process, with the self-enrichment that this chance will give them for a near future.

4. SOME ACADEMIC RESULTS

The main objective of the tutoring/counselling plan is to provide some aid to the students during their life at the University. And a fast adaptation to this life would be accompanied by better performance in their time management, and improved academic results. Besides, the information provided by the counsellors of the current plan has to be used to improve the coordination and organization of the topics, what must be related to the work of the students.

Trying to analyse the possible effect on the academic results, a collection of academic data has been processed, and presented in Figures 1 and 2. Both lines represent the percentage of students that passed some topics, related to the total number of students of the topic. They are typical topics at Electrical Engineering first year: Calculus and Linear Algebra. Calculus data is depicted in blue line and Algebra in red line.

Figure 1 is focused in the period when the first attempt began, around year 2000/01. An improvement in academic results could be observed in both topics, but it shows a clear dependence on the topic, which it could be interpreted as there are more factors influencing such improvement: Probably a change in the teachers or in the topic organization in Algebra.

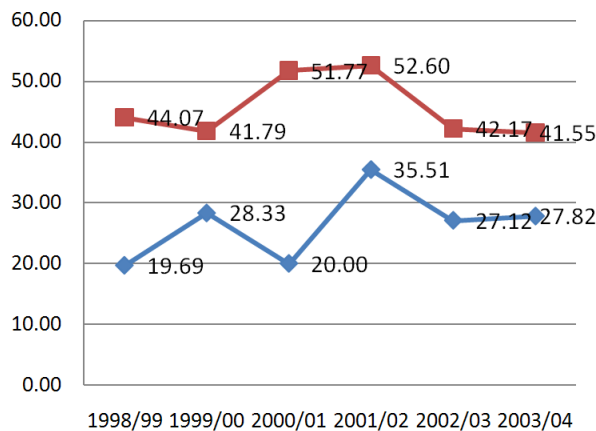


Figure 1: Evolution of academic results in Algebra (blue line) and Calculus (red line), period 1998–2004.

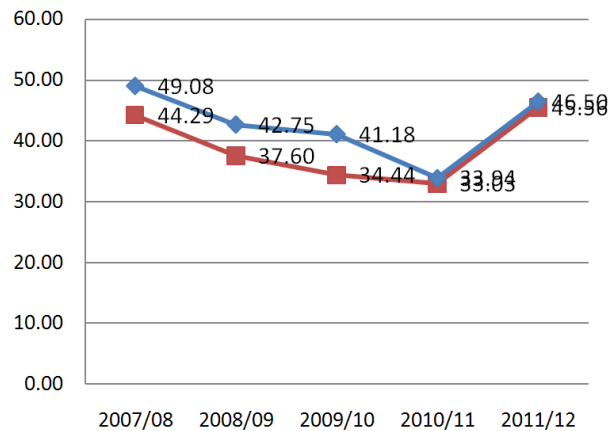


Figure 2: Evolution of academic results in Algebra (blue line) and Calculus (red line), period 2007–2012.

On the other hand, results at Figure 2 are centred on the beginning of the current plan, 2010/11. The effects on the coordination of the topics and the better organization of their contents are reflected in similar behaviours in the evolution of academic results related to both Algebra and Calculus. Preliminary results of the current academic year, 2012/13, confirm such a trend. The difference with Figure 1 values could be attributed to the importance that current counselling plan gives to use the opinions from the students to track the educative process, to check the coordination between topics, and to obtain feedback to modifying such academic techniques. Besides, the confrontation of results among the different members of the group helps the students to maintain the connection to the topics and to study day a day, being more participative during the lessons and performing more efficient homework, in many cases in a group learning process.

We expect that the coming soon counselling-mentoring plan will help in progressing towards a more efficient learning experience, involving students, professors and veteran students in a process that go further than Electrical Engineering education, trying to provide horizontal skills, and useful competence for daily life [3, 4].

5. CONCLUSIONS

An analysis on the academic results and university life integration of first year students at Engineering degrees is presented along this paper. The evolution along years of such land on a new paradigm of education is commented, using the different tutoring programs at the School of Telecommunication Engineering at University of Vigo as thread.

The satisfaction analysis of the tutoring program actors indicates that good planning of a variety of meetings (including informative and counselling) help the students in feeling more integrated in the university world. Students are more assertive confronting this challenge and being near teachers facilitates and enhances communication among them. This produces a more active participation at classes, facilitating teachers work and students become more confident.

Besides, the set of meetings provide direct information about found difficulties: topic contents coordination, planning imbalance, and student workload. This helps the coordination staff to solve present problems for the next year. The students appreciate to be taken into account (comments, suggestions, complains) and feel more comfortable and reinforced, contributing to a continuous improvement process. All these will end in better academic results and reinforced skills (not only the technical and scientific ones) for future professionals.

Analyzing the academic results in two basic first year topics (Algebra, and Calculus) at two different periods (1998/2004, and 2007/2012) supports the importance of tutoring programs, harmonized to coordination plans, in the improvement of academic results and in helping the students to be integrated as soon as possible in campus life.

ACKNOWLEDGMENT

This work was partially funded by the Galician Regional Government under project CN 2012/260 “Consolidation of Research Units: Atlant TIC”.

REFERENCES

1. Falchikov, N., *Learning Together. Peer Tutoring in Higher Education*, Routledge Falmer, London, England, 2001.
2. Fernández Martín, F. D., J. L. Arco Tirado, S. López Ortega, and V. A. HeilbornDíaz, “Prevención del fracaso académico universitario mediante tutoría entre iguales,” *Revista Latinoamericana de Psicología*, Vol. 43, No. 1, 59–71, 2011.
3. Higgins, B., “Relationship between retention and peer tutoring for at-risk students,” *Journal of Nursing Education*, Vol. 43, No. 7, 319–321, 2004.
4. Tobajas, F. B. and V. de Armas, “Criterios para medir la eficacia de un programa de mentorías en la orientación de los estudiantes de nuevo ingreso,” *Mentoring & Coaching*, No. 2, 185–198, 2009.

Understanding Matching Circuits; Plastic Made Quasioptical Multilayer Matching Unit Design at X-band

Tugrul Aydogmus, Inan Kopcal, Gizem Kahya, Yalcin Albayrak,

Selcuk Helhel, and Sukru Ozen

Electrical and Electronics Engineering Department

Akdeniz University, Campus, Antalya 07058, Turkey

Abstract— 1 mm thick rectangular plastic cards having a dimension of 800 mm × 500 mm have been used as quasi-optical matching unit at X-band frequencies. Varying number of plastic cards were placed in varying positions between transmitting and receiving antennas, and complex S_{21} and S_{11} parameters were measured for each position in order to calculate transmission and reflection coefficient of designed setup. Obtained results showed that increased number of plastic cards from 1 to 6 resulted in decreasing transmission as expected, but certain number of plastic (5 plastics) at a frequency range of 7 GHz–9 GHz behaves as resonating circuit. Manually adjusted multilayered plastic slots can be atomized as continuous microwave adaptation, and proposed setup is quite understandable by students.

1. INTRODUCTION

Many applications of electromagnetic theory are related with electromagnetic waves' reflection and transmission on dielectric interfaces with different characteristics [1, 2]. Measuring dielectric permeability of different materials by means of dielectric interfaces is one of the important practical applications. Vector network analyzer is a 2 or 4 port microwave receiver which was designed to measure amplitudes and phases of the waves which are transmitted to or received from the network. An inner computer computes some values such as standing wave ratio, return loss, group delay, impedance by using scattering parameters and shows them on the screen.

Kurnaz [3] used same setup for detecting metals embedded in non-conductive materials by radar measurement at X-Band, and Kurnaz et al. [4, 5] proposed two studies using same setup. Kurnaz et al. [5] investigated transmittance and reflection dependence of monstera leaf on moisture at X-band. In measurement campaign, forward transmission and forward refection coefficients S_{21} and S_{11} were observed with respect to the change of moisture content within the leaf.

It is well known that in millimeter waves, the analysis of electro dynamical systems should be carried out taking into account the structural features of the real electromagnetic field. The resultant field can be characterized by in-homogeneity amplitude and phase in transverse direction [2].

In this study, varying number of plastic made cards were placed at varying distances that they are following each other, and a vector network analyzer has been used for scanning at X-band. Scope of this study is mainly to teach how multiple interfaces (including distance between layer) affect reflection and transmission of electromagnetic waves passing through the system.

2. THEORY

2.1. Multilayer Structures

Vertiy et al. [2] proposed a study about high-quality open resonator system which allow to study, control and affect on the physical process proceeding in the material medium under the influence of various factors. As he proposed, an effective resonator method, where multiple cuvette placed in resonator volume employing operational measurements of permittivity of weakly absorbing liquids by means of analyzing the resultant spectrum when the liquid is following through the cuvette was described.

An equivalent reflection coefficient equation for a multilayer structure (Fig. 1) is given as below [1]

$$\Gamma_{in} \approx \Gamma_0 + \Gamma_1 e^{-i2\beta_1 d_1} + \Gamma_2 e^{-i2(\beta_1 d_1 + \beta_2 d_2)} + \dots + \Gamma_N e^{-i2(\beta_1 d_1 + \beta_2 d_2 + \dots + \beta_N d_N)} \quad (1)$$

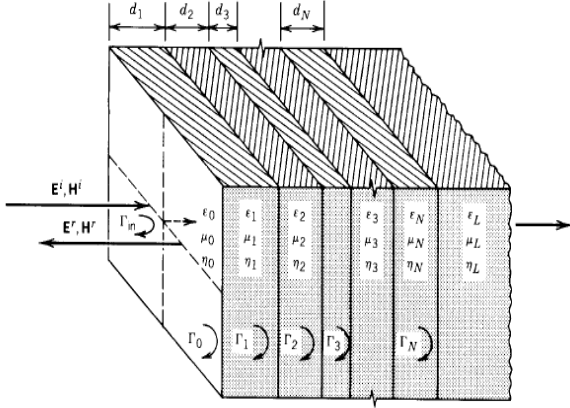


Figure 1: Multilayer structures [Balanis, 1].

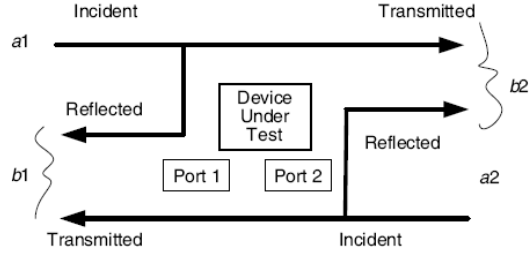


Figure 2: Two port network representation.

where

$$\begin{aligned} \Gamma_1 &= \frac{\eta_1 - \eta_0}{\eta_1 + \eta_0} \\ \Gamma_2 &= \frac{\eta_2 - \eta_1}{\eta_2 + \eta_1} \\ &\vdots \\ \Gamma_n &= \frac{\eta_L - \eta_N}{\eta_L + \eta_N} \end{aligned} \quad (2)$$

2.2. Measurement of Transmission

In a linear electrical system, the relationship between the input/output terminals is expressed in terms of S parameters. In an n -port network system, there are n^2 times S -parameters, which are S_{11} , S_{12} , S_{21} and S_{22} . A sample two-port network is shown in Fig. 1 as below For a 2-port network, the relationship between the ports can be expressed as in Equation (3) [6]. Keep in mind that S parameter values are complex.

$$b_1 = S_{11}a_1 + S_{12}a_2 \quad (3a)$$

$$b_2 = S_{21}a_1 + S_{22}a_2 \quad (3b)$$

where S_{11} is forward refection coefficient and expressed as

$$S_{11} = \left. \frac{b_1}{a_1} \right|_{a_2=0} \quad (4)$$

where S_{21} is forward transmission coefficient and expressed as

$$S_{21} = \left. \frac{b_2}{a_1} \right|_{a_2=0} \quad (5)$$

3. TEST MECHANISM

Measurements were assessed in Near Field Antenna Measurement Laboratory at the EMUMAM, Akdeniz University. Dielectric permeability measurement mechanism consists of Horn antennas used as receivers and transmitters, wave antennas and a vector network analyzer which works between 10 MHz and 9 GHz. Measurement was done by putting the material — first examined, by connecting the network receiver and transmitter directly, and calibrated — between the Horn antennas. “ L ” is the distance between the sample material and the antennas, “ D ” is the maximum length, “ λ ” is wave length; it is tried to sustain the $L \gg 2D^2/\lambda$, the planar wave approach. Another important aspect of the mechanism is that sustaining the materials to be infinite at x -axis is required. This requirement is tried to meet by assessing “ D ” and “ 5λ ” at minimum. The mechanism is shown at Fig. 3 and Fig. 4.

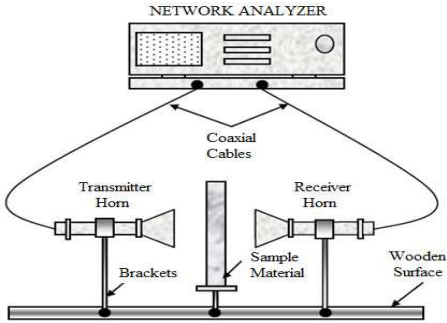


Figure 3: Measurement setup.



Figure 4: Test environment.

One of the step motors makes $\pm x$ movement and the other one makes $\pm y$ movement; so that a square field is scanned. A third motor is able to turn the scanning mechanism 360° ; however it is not used as not needed. Measurement probe assessed its measurements on just one polarization.

As measurement probe; an open ended, rectangle shaped wave guide — measuring between 7 GHz and 9 GHz — is used. Transmitting Horn antenna, distributes the electromagnetic wave that comes from the network analyzer at the top of the scanning mechanism. The wave receiving measurement probe at the middle of the scanning mechanism, sends the electromagnetic wave that scatters back to network analyzer. The Horn antenna at the top, stabilized to the measurement probe, moves with the scanner.

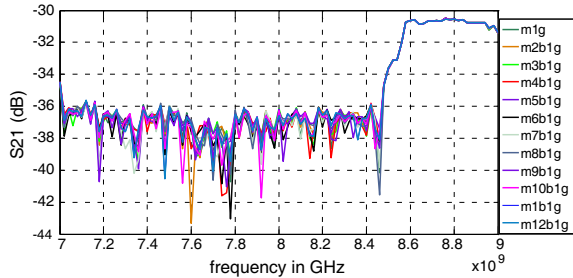


Figure 5: Amplitude variation with respect to frequency.

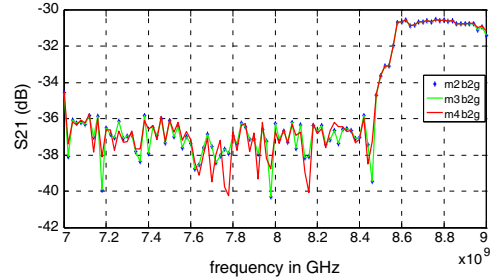


Figure 6: Amplitude variation with respect to frequency.

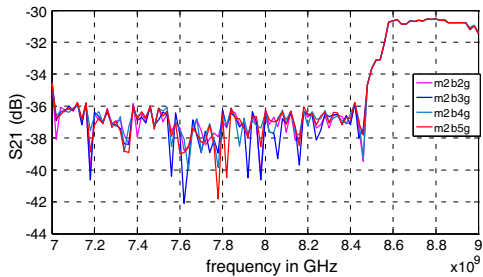


Figure 7: Amplitude variation with respect to frequency.

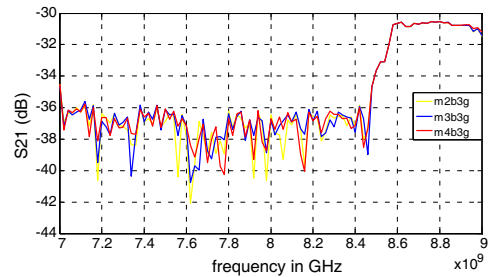


Figure 8: Amplitude variation with respect to frequency.

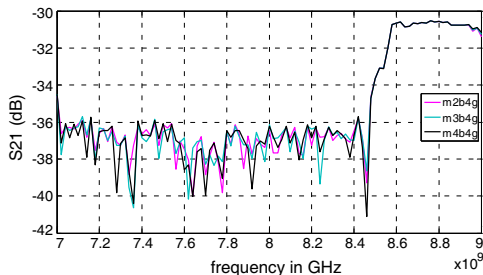


Figure 9: Amplitude variation with respect to frequency.

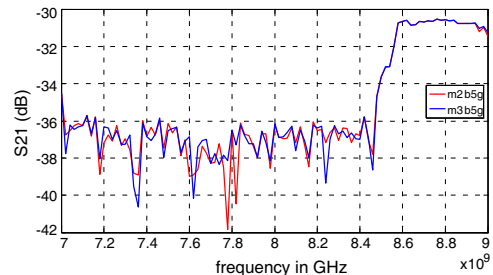


Figure 10: Amplitude variation with respect to frequency.

4. RESULTS AND CONCLUSION

The measurement values assessed by the test mechanism have been evaluated in MATLAB, and the differences in the dielectric coefficient for different material amount and increase at the distance. Fig. 5. represents the transmission in dB with respect to frequency in GHz. Number of plates is changing between 1 to 12, while two parallel plates are located 1 cm apart from each other.

Figure 6 represents the transmission in dB with respect to frequency in GHz. Number of plates is changing between 2 to 4, while two parallel plates are located 2 cm apart from each other.

Figure 7 represents the transmission in dB with respect to frequency in GHz. In this configuration, two parallel plates are used, while distance between them varies between 2 cm and 5 cm.

Figure 8 represents the transmission in dB with respect to frequency in GHz. In this configuration, distance between two pales is kept as 3 cm while number of parallel plates varies from 2 to 4.

Figure 9 represents the transmission in dB with respect to frequency in GHz. In this configuration, distance between two pales is kept as 4 cm while number of parallel plates varies from 2 to 4.

Figure 10 represents the transmission in dB with respect to frequency in GHz. In this configuration, distance between two pales is kept as 6 cm while number of parallel plates is 2.

As shown in this work, amplitude, so is loss, increases as the amount of plastic cards on insulated foam increase. When comparing Fig. 5 and Fig. 6, it is seen that the increase space length causes an increase at loss, too. If the adaptation circuit designed with plastic cards ($800 \times 500 \times 1$ mm) is automated, an adaptive filter would be made by changing the space length and the amount of materials.

REFERENCES

1. Balanis, C. A., *Advanced Engineering Electromagnetics*, John Wiley and Sons, 1989.
2. Vertiy, A. A., S. P. Gavrilov, S. Helhel, B. Colak, and R. Samedov, “Quasioptical multilayered interferometer for gasoline testing,” *International Journal of Infrared And Millimeter Waves*, Vol. 17, 543–557, Mar. 1996.
3. Kurnaz, O., “Determination of buried metals inside the dielectric block by using X-band radar measurements,” M.S. Thesis, Institute of Natural Science, Akdeniz University, 2012.
4. Kurnaz, O., S. Helhel, and S. Ozen, “Embedded object detection by using planar antenna measurement system,” *PIERS Proceedings*, 208–211, Moscow, Russia, Aug. 19–23, 2012.
5. Kurnaz, O., Y. E. Yoruk, and S. Helhel, “Electrical characteristics dependence of monstera leaf on moisture content,” *PIERS Proceedings*, 653–655, Moscow, Russia, Aug. 19–23, 2012.
6. Riad, T. and Q. Jing, “A nonlinear S-parameters behavioral model for RF LNAs,” *2010 2nd Asia Symposium on Quality Electronic Design*, Aug. 3–4, 2010, Paper DOI: 10.1109/ASQED.2010.5548227.

Virtual Laboratory for Microwave Devices

D. S. Gubsky, I. V. Mamay, and V. V. Zemlyakov

Physics Department, Southern Federal University, Russia

Abstract— The method of computer simulation of microwave devices and special laboratory workshops is described. Simulated laboratory has a module structure. The basis for constructing a model of the specific workshop is a concept of the abstract “device” with layout is identical to the installation of a real one. As an example the laboratory work which includes sweep frequency generator, VSWR/Attenuation Scope and a band-pass waveguide filter was simulated. The software interface allows changing the frequency tags and filter configuration to carry out all necessary measuring characteristics.

1. INTRODUCTION

Nowadays, computer simulation of operating principles of measurements equipment and microwave devices is of great importance [1–3]. It allows making computer simulators of laboratory works with practically no difference between the simulation and real equipment behavior. Virtually created laboratory works represent operating principles of measurement units, test devices and their interactions which is enough to gain operational experience and to study basic physical properties of test devices. It is also significant that virtual laboratory works can find their application also in distance and online education [3]. It is important to note that alternatively to “real” laboratory work virtual laboratory work has no limits in a number of working places. First of all, virtual laboratory works should be aimed at studying physical processes of test devices and training student to operate laboratory equipment which means that there must be practically no difference in interface and execution order between the “real” laboratory work and virtual one.

In this paper the technology of computer simulations of microwave equipment, devices and special laboratory works is presented.

2. LABORATORY WORKSHOP STRUCTURE

Any laboratory work comes with measurement units and test devices combined in a single installation. Each measurement unit could be described with the set of input and output signals (e.g., indicator unit receives signal from test device and management signals from generator). Additionally, each measurement unit has determinated functions. Moreover, microwave test devices also could be described with sets of input and output signals and functions (e.g., signal of defined frequency and value at the input of the filter is converted to output signal according to filter “function”). Therefore, the behavior of device can be described by set of input and output signals and their transfer function (Figure 1).

Simulated laboratory works have modular construction. At the basis of laboratory works simulations a conception of abstract “device” is used. Those abstract devices could be combined into installation, identically to real devices, i.e., connection of output signals with input signals. Device’s behavior is described with notion of “signal” and “function”. Each device has set of input and output signals and it is possible to connect devices to each other in a certain way. Each device module is an autonomous software element. For this reason the functionality of software package is easily expandable and depends only on module set.

A laboratory work for software package is information about set of essential modules, number of copies of each device and the way they are connected with each other. Therefore, it is possible to construct function chains and trees, there first members are independent and last are recursive dependent on all previous (Figure 2). By this means any measurement unit and test device could be assembled from modules and their behavior is described by sets of functions which transform input signals into output signals. The process of input signals transformation to output signals depend only on way of device realization.

For software package any test device could be represented in form of abstraction with define property set and behavior with reference to other devices. Device’s properties are: type, name, input signals, output signals, unique identifier.

In case of connection the correspondence is established between input signal of receiving device and output signal of transmitting device. Therefore, any input signal of the device unlike output

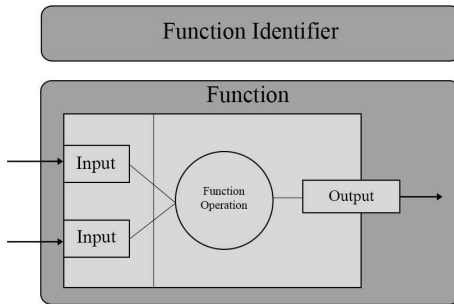


Figure 1: Signals and functions organization.

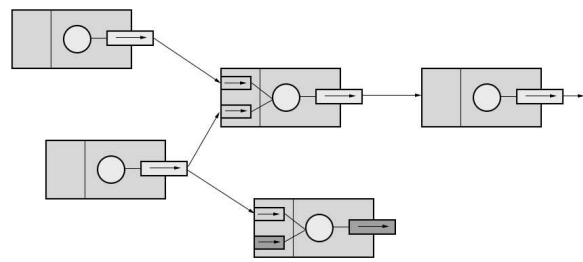


Figure 2: Signal interaction.

signal is not an autonomous object but it is a pointer to output signal of another device. That allows connecting devices with each other in unspecified way.

Device's modules are dynamic libraries with common public interface which is a functional of abstract device's "factory". Device's "factory" creates a sample of the device. Modules are loaded and used during the main application execution and don't have direct connection with package's core. This conception allows making package core independent from device's modules set. Moreover, common abstract interface makes possible modules development totally independent from each other which mean that functionality of one module is totally independent from functionality of another.

So the target device is inheritor of abstract device and has a set of output signals which could be connected to other modules, and set of input signals which are necessary for device self functionality. Those signals mostly determine functionality of whole device. Certain "factory" has information about existence of target device and can create any number of its samples. The "factory" itself is inheritor of abstract device "factory". So, for user the interface of abstract "fabric" is available which allows making realization of devices with abstract device interface.

Software package for microwave device simulations and connection of microwave device modules is developed with programming language C++ on Microsoft Visual Studio IDE 2008. As package's basis a cross-platform toolkit for applications and user interface development Nokia Qt 4.7.3 was chosen. Because of small volume of stored information the database SQLite 3.7 was used.

3. VIRTUAL LABORATORY WORK EXAMPLE

Let us describe a process of laboratory works creation. The measurement units which were created before and represented in a package as device's modules or new measurement units could be used.

Let us consider a process of new measurement units design to study the parameters of waveguide filter which consists of Sweep Frequency Generator, VSWR/Attenuation Scope and filter model.

Abstract device "Sweep Frequency Generator (SFG)" act as control program interface which operates with start and stop scanning frequency values and frequency markers. Abstract device "VSWR/Attenuation Scope" act as control program interface which operates with markers, test line position values and the range of measurement values. This unit controls abstract grid area by applying the above values.

At this stage of simulation there is no sets of output and input signals but it is expected that indicator unit won't have any of output signals.

So, by combining devices listed above it is possible to create one of the most simple laboratory works which scheme is represented at Figure 3.

For the module "Sweep Frequency Generator" operator can perform such actions: shifting between start and stop scanning frequency values and markers values to visualize data on digital display; changing start and stop scanning frequency values and markers values. For the module "VSWR/Attenuation Scope" operator can perform such actions: changing position of test line (in this case attenuation value will be displayed on certain display panel); changing markers position; changing value of additional signal gain.

The test device — "Blackbox" is of special interest. This abstract device doesn't provide any additional universal program interface. All functionality of "Blackboxes" should be contained in its output signals which behavior is studied in corresponding laboratory work. For "Blackbox" the basic data are: analytical transformations of input signal values; experimental data, saved in

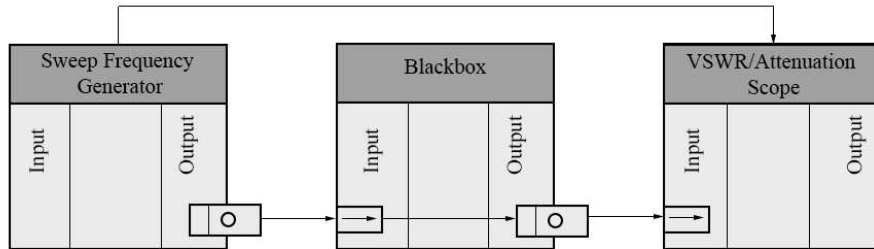


Figure 3: Simplest laboratory work.

certain unify format; computation data obtained from external application packages for microwave device simulations (for example CST Microwave Studio).

Analytic transformations of input signal values are the software implementation of analytical expressions. Experimental or computation data are convenient to report in binary data. The final format of such data depends on certain sets of values and number of such sets.

In this work the target module of “Blackbox” device — the “band-pass filter” was created. This device has one output signal and expects connection of one input signal.

The model of band-pass filter is a section of rectangular waveguide with grating and two rods with user-defined insertion. *S*-parameters describing electrodynamic properties of filter were calculated for series rods positions with certain step.

Band-pass filter was simulated with CST Microwave Studio software. Received simulation data was converted to binary form and exported to module of abstract device “Blackbox”.

Since the set of received values is discrete for proper construction of amplitude-frequency characteristic it is necessary to interpolate the received values. It is shown that Newton’s quadratic polynomial interpolation is good enough for this purpose. The operator can change the rods insertion depth. After changing insertion depth the certain set of corresponding values are loaded and polynomials are calculated.

By using interactive configuration tool all simulated devices are combined together and create laboratory work for studying properties of microwave filter based on rectangular waveguide. After launching laboratory work and loading all necessary modules the laboratory unit user interface is displayed on PC monitor (Figure 4). User can change the range of signal, frequency markers, rods insertion depth in test filter and calculate all necessary properties.

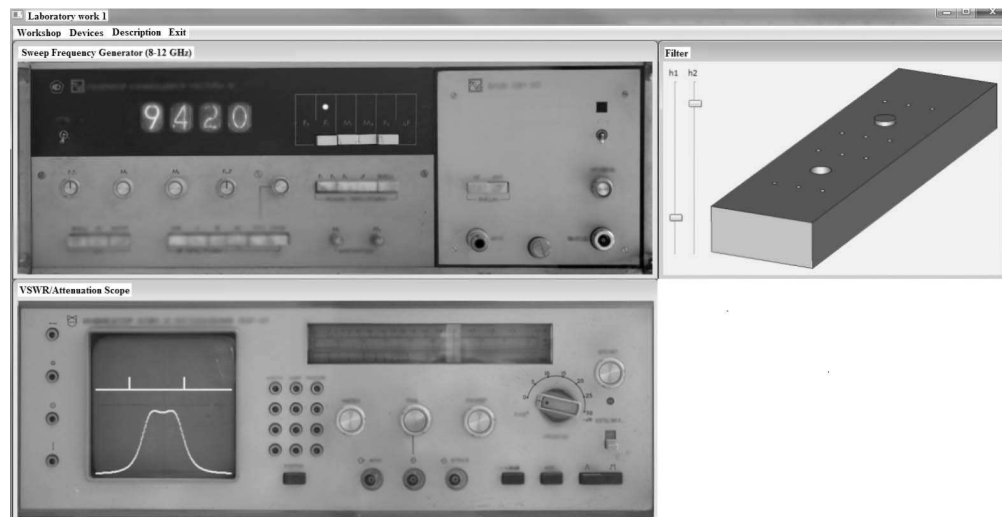


Figure 4: Laboratory unit interface.

4. CONCLUSION

As a result of current investigation the software package for constructing virtual laboratory workshop was designed. It could be used in education process as interactive tutorial. Designed virtual laboratory is based on autonomous independent components modules which allows to expand and edit the set of devices used for simulations without interactions with package core. The main feature of this realization is representing test devices as “Blackboxes” which behavior depends on mathematical model or on output values of external applications for microwave device simulations and also could be based on real experimental data. All components included in presented laboratory work are identical to real devices.

REFERENCES

1. Gupta, T., A. S. M. Prachi, M. J. Akhtar, and K. V. Srivastava, “Development of the virtual lab module for understanding the concepts of electric and magnetic field patterns in rectangular waveguides and cavities,” *International Journal of Online Engineering*, Vol. 8, No. 3, 12–21, 2012.
2. Gomez-Tornero, J. L., D. Canete-Rebenaque, F. D. Quesada-Pereira, and A. Alvarez-Melcon, “Interactive lab to learn radio astronomy, microwave & antenna engineering at the Technical University of Cartagena (Spain),” *International Journal of Online Engineering*, Vol. 7, No. 1, 10–18, 2011.
3. Kara, A., E. Aydin, M. E. Ozbek, and N. Cagiltay, “Design and development of a remote and virtual environment for experimental training in electrical and electronics engineering,” *9-th International Conference on Information Technology Based Higher Education and Training, ITHET 2010*, 194–200, 2010.

Characterization of Snow Cover Areas by Change Detection Applied to COSMO-SkyMed Images

S. Pettinato¹, E. Santi¹, S. Paloscia¹, B. Aiazzi¹, and A. Garzelli²

¹Institute of Applied Physics, National Research Council, Firenze, Italy

²Department of Information Engineering and Mathematical Sciences
University of Siena, Siena, Italy

Abstract— An experimental study on the characterization of snow cover areas from multi-temporal COSMO-SkyMed (CSK) images is presented. Himage and PingPong data in Stripmap acquisition mode from the CSK constellation are processed by applying two alternative approaches: a classical threshold method and an effective change-detection method. The proposed information-theoretic approach to change detection provides very promising results on multi-temporal 1-look SAR images at very high spatial resolution.

1. INTRODUCTION

The use of satellite data for a timely monitoring of the Earth's surface has become ever more appealing and effective in the last decades. Quantitative snow cover investigation can provide important information on global changes and water resource management, as well as flood and avalanche risk prevention. Optical sensors have been proven capable of monitoring snow cover in cloud-free conditions, and several systems have been developed for operational monitoring of snow parameters from remote sensing data [1]. However, only microwave sensors are able to acquire data independently of daylight and in adverse weather conditions. In particular, spaceborne X-band SAR systems (e.g., COSMO-SkyMed and TerraSAR-X) can provide accurate localization of snow-covered areas and exploit high/low penetration in dry/wet snow [2, 3]. The estimation of the snow water equivalent (SWE) is possible in the case of dry snow only. In general, backscattering coefficients higher than the snow-free case can be detected, by assuming that the backscattering increase is due to snow characterized by a snow depth greater than 60–70 cm (SWE greater than 100 mm) and therefore able to contribute to the radar response at the X-band [4].

The paper presents an experimental study on the characterization of snow cover areas on COSMO-SkyMed images. Two different data processing approaches are tested and experimentally compared: 1) Process multi-temporal SAR images to detect a backscattering increase due to dry snow with respect to snow-free soil [4]; 2) Apply a non-parametric information-theoretic change detection algorithm on two-date SAR images [5].

2. THRESHOLD METHOD

The acquired images, listed in Table 1, have been processed by using the following procedure. Multi-look detected images were generated from single look complex data by averaging the intensity in azimuth and range directions. The number of looks was chosen in order to reduce the speckle and retrieve a square pixel in the multilooked image. The geocoding was performed to convert the position of the backscatter elements from SAR geometry to three-dimensional object coordinates by using a DEM (derived from SRTM mission) and the satellite orbital parameters. The geocoded images have a pixel size of $10 \times 10 \text{ m}^2$. Layover and shadow effects in every acquired image were identified. Forest classification was derived by Normalized Difference Vegetation Index (NDVI) and through the Coordination of Information on the Environment (CORINE) land cover data. The backscattering values were converted in dB and the difference between the winter image and the reference image was computed. A pixel was classified as dry snow when the corresponding difference was greater than 0 dB (i.e., $10 * \log(winter_{image}) - 10 * \log(ref_{image}) > 0$).

3. INFORMATION-THEORETIC CHANGE DETECTION APPROACH

The change detection algorithm proposed in [5] is based on the computation of the negative of the logarithm of the estimated probability of a mean amplitude level in one image conditional to the mean amplitude level of the same pixel in the other image. This value measures the amount of information associated to the pixel change and hence the amount of change, which may be related to the conditional information of couples of symbols emitted by two information sources.

It should be noted that the method has been applied directly on the SCS-B image data, thanks to its robustness to speckle noise. The output of the method is the pixel-wise feature $\mathcal{C}(m, n)$ whose values increase from 0, corresponding to unchanged pixels, to higher values, corresponding to changed pixels. Change detection maps can be obtained by properly thresholding $\mathcal{C}(m, n)$: the selection of the threshold value T is application dependent and in this study has been experimentally set to $T = 0.045$ for both Himage and PingPong SAR images, as shown Section 5. The output of the change detection approach has been finally geocoded to locate each pixel on a cartographic map.

4. DATASET

Table 1 reports the main characteristics of the two Level-1A Single-Look-Complex Slant (SCS-B) datasets selected for the experiments. The images have been acquired over a mountain region in the eastern Italian Alps (Cordevole basin, central geographic coordinates: 11.87 East, 46.51 N) where meteorological and conventional snow measurements are available as well. The first dataset is composed of a SAR image pair acquired in dual-polarimetric Ping Pong mode on August 2nd, 2010 and January 1st, 2011. Three images acquired in Himage mode on September 9th, 2011, December 25th, 2011 and January 2nd, 2012 form the second dataset. Both acquisition modes provide 1-look image data, but having different ground-range and azimuth resolutions: 3 m for Himage and 15 m for Ping Pong. Hence, the two datasets allow to test the capabilities of snow-cover characterization in different conditions, also concerning the assessment of change detection and localization accuracy. The Ping Pong Stripmap images can be also objectively assessed thanks to the availability of ground truth data.

Table 1: Available images for the experiments.

Sensor	Mode	Looking	Pol.	Orbit	Date	Time (UTC)
CSK1	PingPong	Right	VV/VH	Asc	02/08/10	4:56:20 AM
CSK2	PingPong	Right	VV/VH	Asc	01/01/11	4:54:34 AM
CSK4	HIMAGE	Right	VV	Asc	08/09/11	5:04:06 AM
CSK2	HIMAGE	Right	VV	Asc	25/12/11	5:03:06 AM
CSK1	HIMAGE	Right	VV	Asc	02/01/12	5:02:59 AM

Table 2 presents the list of the automatic meteo station that can be used in the experiment. In case of Himage dataset, the available ground truth are available, however only a portion of the entire image was processed in this work, because this method is very time-consuming. In this latter dataset, only one ground station could be used for validation. In Table 3 the snow depth of each meteo station for each satellite passage is reported.

Table 2: List of the automatic meteo stations.

Station ID	Altitude	Longitude (E)	Latitude (N)
Malga Losch	1735	11.95805556	46.26194444
Col dei Baldi	1900	12.07388889	46.41694444
Monti Alti Ornella	2250	11.88555556	46.47583333
Ravales	2615	12.08	46.54666667
Cima Pradazzo	2200	11.82222222	46.35666667
Cherz	2000	11.879071	46.515284

5. EXPERIMENTAL RESULTS

Figure 1 shows visual representations of the map values by considering the position of the correspondent image point in the filtered scatterplots of the mean amplitude levels for the reference image against the mean amplitude levels for the changed image, in the case of CSK in Himage

Table 3: Snow depth (cm) for each satellite data pass (* indicates no data available).

Date	Malga Losch	Col dei Baldi	Monti Alti Ornella	Ravales	Cima Pradazzo	Cherz
02/08/10	0	0	0	0	0	0
01/01/11	96	145	166	163	112	106
08/09/11	0	0	0	0	0	0
25/12/11	25	22	28	40	*	18
02/01/12	27	25	33	42	*	40

mode and CSK Ping Pong mode, respectively. Each mean is computed by considering a sliding window of 7×7 pixels centered on the current pixel. The scatterplots are quantized in $L \times L$ bins, where $L = 256$, so that a 3D histogram is delivered, by counting the number of scatterpoints in each bin. The 3D histogram is successively filtered by means of a normalized triangular kernel of size 17 according to the Parzen window method, in order to obtain an estimation of the joint density probability $p(a, b)$, where a denotes the mean amplitude levels reference image and b denotes the mean amplitude levels of the changed image. Estimations of the conditional probabilities $p(a|b)$ and $p(b|a)$ are obtained by dividing for the maximum of each row and the maximum of each column, respectively. A pixel is considered to have a high probability to be changed if almost one of the conditional probabilities is low, i.e., difficult to predict given the levels of the other image. To obtain this, the minimum of $p(a|b)$ and $p(b|a)$ is taken for each bin and a change feature value $\mathcal{C}(m, n)$ computed by the negative logarithm of this minimum is assigned to all the scatterpoints in the bin. Figures 1(a) and 1(b) show that the range of the change feature is between 0 (high probability) and 5–6 (very low probability), with the high probability values that are placed around to the main diagonal (unchanged points), and the low probability values that are dispersed through all the rest of the scatterplot. A suitable threshold of 0.045 is taken to obtain the final maps. The optimal separation between change-no change points is visible in the reported Figures 1(a) and 1(b), where the unchanged pixels whose feature values are lower than the threshold are represented in blue and are grouped near the diagonal, while the change points are represented in yellow-red colors.

In Figure 2 the snow covered map generated by the PingPong dataset is presented. The ground conditions of this map have to be related to the January 1st 2011, where the snow was abundant as it can be observed in Table 3. The maps obtained by using the two methods are similar, mainly because the presence of high snow depth values increases the backscattering of the January 2011 image. However, the change detection algorithm is able to retrieve more homogeneous snow coverage. Figures 3 and 4 present different snow coverage maps by using the two methods for Himage data. This fact can be attributed to the different snow deposition on ground in the date of December 25th, 2011 and January 2, 2012 (see Table 3). In fact, in that time period, the snow depth was not enough high to be detected with the more simple threshold method, while the change detection allows to identify snow extension in more appropriate way according the ground truth

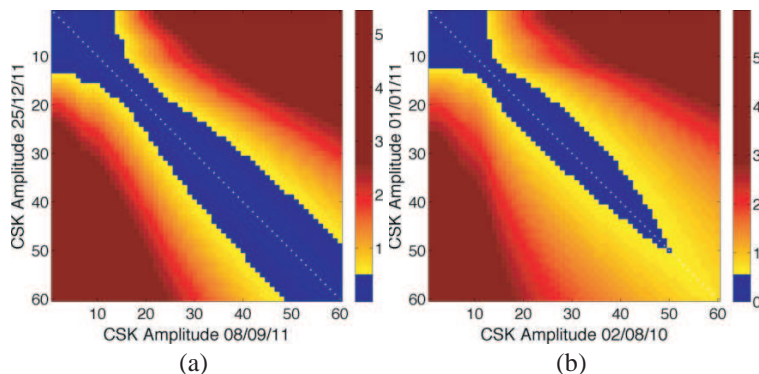


Figure 1: The most populated parts of the scatterplots of the amplitude image pairs (bins from 0 to 60): (a) September vs December in Himage mode; (b) August vs January in PingPong mode.

data and the seasonal conditions.

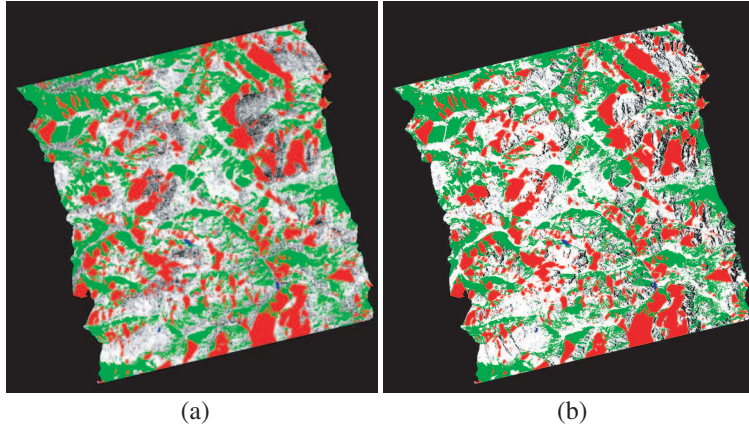


Figure 2: Snow cover extension on January 1st, 2011 from the PingPong image pair: (a) threshold 0 dB; (b) from the IT-based change detection feature. Legend: white: snow, black: no-snow, red: layover/shadow, green: forest, blue: water.

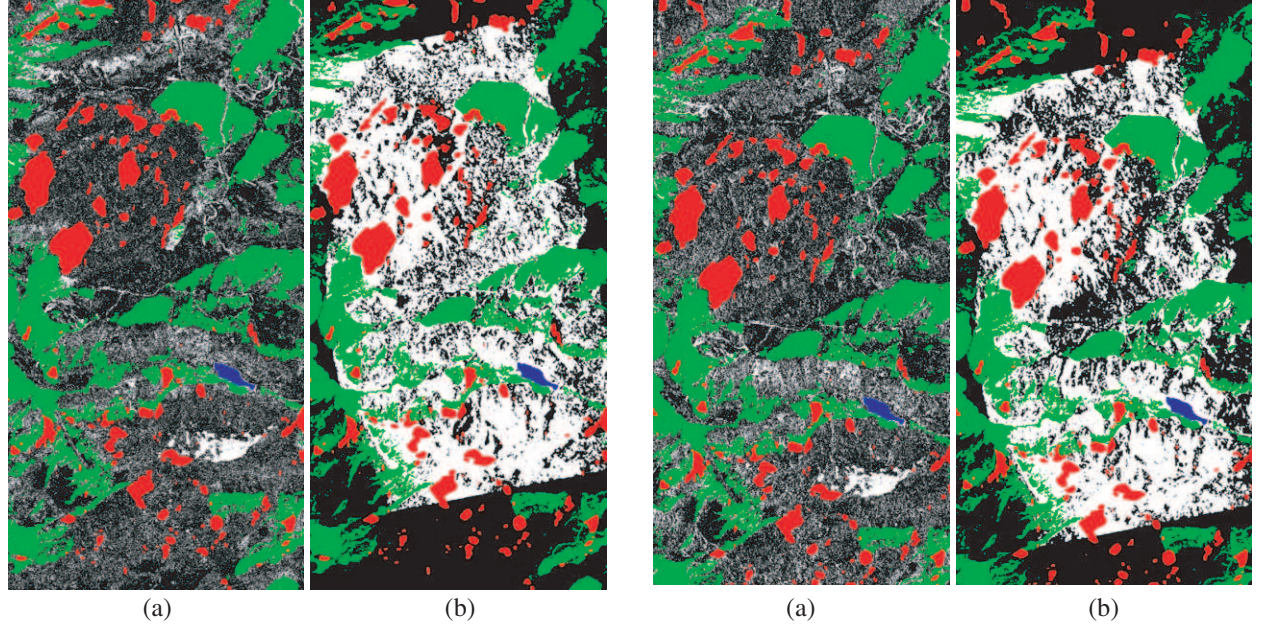


Figure 3: Snow cover extension on December 25th, 2011 from the Dec-Sept Himage image pair: (a) threshold 0 dB; (b) from the IT-based change detection feature. The same colormap of Fig. 2 is applied.

Figure 4: Snow cover extension on January 2nd, 2012 from the Jan-Sept Himage image pair: (a) threshold 0 dB; (b) from the IT-based change detection feature. The same colormap of Fig. 2 is applied.

6. CONCLUSIONS

In this paper, two different approaches to generate snow coverage maps were presented. The different methodologies were applied on Cosmo-SkyMed data acquired in stripmap mode (Himage and PingPong). The discrepancies between the two methods are more evident in case of low snow depth values on ground, that is the case of Himage data. However, regardless of the snow depth conditions, the IT change detection approach is able to retrieve more snow coverage that is in line with what expected with the season and the available ground data areas with an improved homogeneity, as it can be observed in maps generated by PingPong data. Experimental results on Single-Look-Complex CSK ® images (Himage data) acquired in September, December and January on an alpine region in Northern Italy show that the results obtained by applying the

second approach are promising since they provide an improved localization of the snow covered areas and reduced false alarm rate with respect to the first classical approach.

ACKNOWLEDGMENT

The authors want to thank the Italian Space Agency (ASI) for providing Cosmo-SkyMed ® data in the framework of the AO-Project Hydrocosmo (ID 1720).

REFERENCES

1. Salomonson, V. V. and I. Appel, "Development of the Aqua MODIS NDSI fractional snow cover algorithm and validation results," *IEEE Trans. Geosci. Remote Sens.*, Vol. 44, No. 7, 1747–1756, 2006.
2. Nagler, T. and H. Rott, "Retrieval of wet snow by means of multitemporal SAR data," *IEEE Trans. Geosci. Remote Sens.*, Vol. 38, No. 2, 754–765, 2000.
3. Pettinato, S., P. Poggi, G. Macelloni, S. Paloscia, P. Pampaloni, and A. Crepaz, "Mapping snow cover in alpine areas with ENVISAT/SAR images," *Envisat & ERS Symposium, Proceedings ESA*, Salzburg, Austria, CD-rom, 2004, ISBN 92-9092-883-2.
4. Pettinato, S., E. Santi, M. Brogioni, S. Paloscia, E. Palchetti, and C. Xiong, "The potential of COSMO-SkyMed SAR images in monitoring snow cover characteristics," *IEEE Geosci. Remote Sens. Lett.*, Vol. 10, No. 1, 9–13, 2013.
5. Aiazzi, B., L. Alparone, S. Baronti, A. Garzelli, and C. Zoppetti, "Non-parametric change detection in multitemporal SAR images based on mean-shift clustering," *IEEE Trans. Geosci. Remote Sens.*, Vol. 51, 2022–2031, 2013.

An Alternative Derivation of the Equivalent Networks for Spherical Modes Using the Extended Kuroda Transform

J. S. McLean¹, R. Sutton¹, and H. D. Foltz²

¹TDK R. & D. Corp., Cedar Park, TX, USA

²Department of Electrical Engineering, University of Texas Pan-American, Edinburg, TX, USA

Abstract— The one-port, lumped-element equivalent networks first derived by Chu for the electromagnetic spherical modes are considered along with the two-port equivalent network for spherical wave propagation in a spherical shell given by Thal. We show that the impedances associated with the spherical, small-signal, acoustic, compressional modes can also be represented by similar one-port, lumped-element networks with these networks degenerating to the well-known first-order, lumped-element network representing the zeroth-order acoustic spherical wave impedance. The impetus for this is that the first-order equivalent network for the zeroth-order acoustic spherical mode is similar to, but simpler than, the second-order equivalent networks for the TE₀₁ and TM₀₁ electromagnetic dipole modes. Using Thal's approach, we then derive a two-port model for zeroth-order acoustic spherical wave propagation in a spherical shell and show that this model is equivalent to the one derived by Benade for zeroth-order acoustic wave propagation in a rigid-walled, conical horn. Thus, Thal's model and Benade's two-port models are equivalent when the proper electro-acoustic analogies are employed. Finally, we show that the equivalent two-port network representing spherical wave propagation in a spherical shell can be derived using Kobayashi's extended Kuroda transform. Although we have not derived a general relationship between Kobayashi's extended Kuroda transform and the Thal's two-port representation of a spherical mode of arbitrary order, we have derived one specific case and provide a rationale for the equivalence in the general case.

1. INTRODUCTION: EQUIVALENT NETWORKS FOR SPHERICAL WAVES

The wave impedances¹ associated with outgoing spherical modes are given directly from solutions to Maxwell's equations as [1]:

$$Z_{+R}^{\text{TM}} = \frac{E_\theta^+}{H_\phi^+} = -\frac{E_\phi^+}{H_\theta^+} = j\eta \frac{\hat{H}_n^{(2)\prime}(kR)}{\hat{H}_n^{(2)}(kR)} \quad (1)$$

$$Z_{+R}^{\text{TE}} = \frac{E_\theta^+}{H_\phi^+} = -\frac{E_\phi^+}{H_\theta^+} = -j\eta \frac{\hat{H}_n^{(2)}(kR)}{\hat{H}_n^{(2)\prime}(kR)} \quad (2)$$

where η is the free space wave impedance and $\hat{H}_n^{(2)}$ is the Schelkunoff- or Riccati-Hankel function of the second kind. Thus, the TM wave impedance is proportional to the logarithmic derivative of the Riccati-Hankel function and the TE wave impedance is proportional to the reciprocal of this quantity [2]. One could argue that all of the physics associated with the spherical modes is contained within the modal solutions to Maxwell's equations as given in Ref. [1] and thus in the wave impedances given in Eqs. (1) and (2). Nevertheless, some aspects, such as the separation of propagating and non-propagating energy, have been perennially difficult to understand. The equivalent lumped-element ladder networks originally derived by Chu [1, 3, 4], which represent electromagnetic spherical modes, are invaluable for the understanding of numerous phenomena, including radiation from electrically-small antennas. One strong impetus for this approach is that it enables the application of the rigorous Fano-Bode theory, which predicts limitations on impedance matching and bandwidth, but which applies strictly to lumped-element networks [5–7]. Another is that it facilitates the evaluation of the inverse Laplace transform via a partial fraction expansion, thus enabling time-domain response to be analytically modeled. Specifically, what is sought here is a rational frequency-domain antenna transfer function such as is defined as in Ref. [8].

The one-port, lumped-element equivalent networks in Refs. [1, 3, 4] were derived entirely using only the recursion relations for the spherical Bessel functions or, equivalently, the recursion relations

¹As in Ref. [1], we use the term wave impedance to denote the ratio of the components of electric and magnetic field that form the Poynting vector product which gives power density.

for the logarithmic derivative of the spherical Bessel functions [2]. The networks originally derived by Chu are fundamentally one-port networks describing only the relationship between electric and magnetic field components of the spherical modes at a particular value of radial coordinate R and for a particular direction of propagation, namely outward. The networks are shown in Fig. 1 and Fig. 2. As noted in Harrington's book, "The dissipation in the resistive element at the end of the network represents the transmitted power in the field problem." However, it would be incorrect to assume that the two-port network obtained by cutting the network at the resistive load and taking the terminals across which the resistive load was connected as the second port provides a two-port representation of spherical wave propagation. Instead, for a given equivalent network from Fig. 1 or Fig. 2, the input impedance represents the outward-traveling wave impedance for the mode to which the circuit corresponds at $R = a$. Note that as the radial mode index is increased reactive elements are inserted in between the existing reactive network and the resistive load. Thus, the TM circuits are all minimum susceptance and the TE modes are all minimum reactance. A separate network must be drawn to represent each mode.

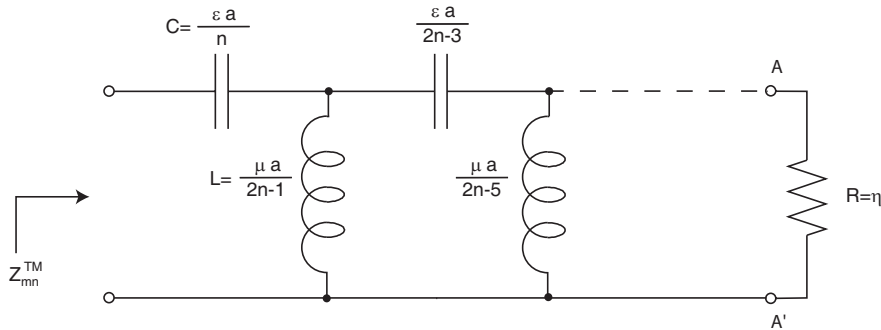


Figure 1: Equivalent circuit for spherical TM-to- R modes at $R = a$ as shown in Figs. 5–6 of Ref. [3] and Ref. [1]. Note that a separate network must be drawn for each mode as additional sections are inserted in between the load and the existing network as the order is increased. On the right hand end of the network is a load which does represent far field radiation of power. However, the port comprised by the two terminals shown on the right is fictitious in the sense that neither the voltage across nor the current through the resistor represents a field quantity at some value of R .

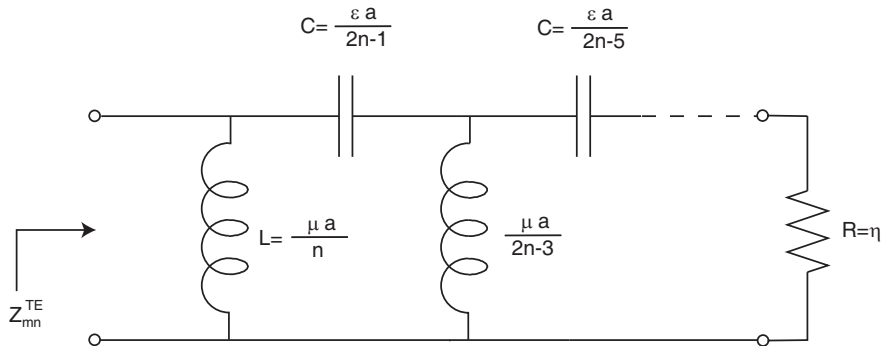


Figure 2: Equivalent circuit for spherical TE-to- R modes as shown in Figs. 5–6 of Ref. [3] and Ref. [1]. These networks are the duals of the ones shown in Fig. 1 and thus only one set is required.

Thal [4] derived a much more complete and physically meaningful equivalent network, which is shown in Fig. 1. Fig. 1 should be compared with Fig. 1 of Ref. [4]. This circuit follows from the recursion relations for the logarithmic derivative of the Schelkunoff- or Riccati-Hankel functions denoted here as C_n [2], although Thal derived it directly from the recursion relations for the spherical Bessel functions. The logarithmic derivative of the Schelkunoff-Hankel function is given by:

$$C_n = \frac{d \ln (\hat{H}_n^{(2)}(kR))}{d(kR)} = \frac{\hat{H}_n^{(2)\prime}}{\hat{H}_n^{(2)}} = \frac{\hat{H}_{n-1}^{(2)}}{\hat{H}_n^{(2)}} - \frac{n}{kR} = \rho_{n-1} - \frac{n}{kR} \quad (3)$$

where

$$\rho_n = \frac{\hat{H}_n^{(2)}}{\hat{H}_{n+1}^{(2)}} = \frac{h_n^{(2)}}{h_{n+1}^{(2)}}. \quad (4)$$

Therefore, using the recursion relations for spherical Bessel functions we obtain recursion relations for the logarithmic derivatives of the Schelkunoff spherical Bessel functions [2]:

$$\begin{aligned} C_n &= -\frac{n}{kR} + \frac{1}{\frac{n}{kR} - C_{n-1}} && \text{downward recursion, and} \\ C_n &= \frac{n+1}{kR} - \frac{1}{\frac{n+1}{kR} + C_{n+1}} && \text{upward recursion} \end{aligned} \quad (5)$$

In Thal's equivalent network each LC section of the ladder network actually represents the input impedance or admittance (at the same value of R) for a different spherical mode with the TE and TM modes interlaced. This alternation of the TE and TM modes (or between the logarithmic derivative and its reciprocal) at successive terminal planes can be seen in the recursion relations for the logarithmic derivative of the Schelkunoff-Bessel functions, Eq. (5). The current and voltages in Thal's network are analogous to components of the electric and magnetic field that form the Poynting vector product. Moving to the load (the terminal plane labeled "0" in Thal's paper) actually provides the ratio of $\frac{\hat{H}'_0(ka)}{\hat{H}_0(ka)} = j \tan ka$, which corresponds to the normalized impedance of the TEM mode in a biconical structure.

The impedance looking right at a given terminal plane in Fig. 3 (left in Fig. 1 of Ref. [4]) is the outward-traveling impedance of the corresponding spherical mode at a particular value of R , while the impedance looking left (right in Fig. 1 of Ref. [4]) at the same terminal plane is the inward-looking impedance of the corresponding mode. Thus, Thal's network gives the behavior of a spherical transmission line [9] at a particular value of R . Insertion of the proper source at this point then immediately provides a model for an idealized spherical wire antenna [10], including the interior fields.

To summarize, Chu's one-port networks can provide the complex wave impedance looking in a particular direction, namely outward, while Thal's network provides both simultaneously. Nevertheless, the network in Fig. 1 of Ref. [4] does not provide a two-port description of a spherical wave propagation—the field values are predicted only for a particular value of R ; that is the model represents a particular point or value of R on a spherical transmission line.

The foregoing does not imply that two-port network theory cannot be advantageously applied to the equivalent networks given by Chu and Thal. As Thal states in Ref. [4], the lumped equivalent networks "allow circuit concepts and theorems to be brought to bear ...". In fact, in Refs. [6, 7], Darlington's theorem [11] is used in conjunction with these circuits in the application of the Fano-Bode theory in order to rigorously determine the limitations on impedance matching and bandwidth. Still, the equivalent networks cannot be used to determine a two-port antenna transfer function as defined in Ref. [8] without some modification.

The lumped element equivalent networks in Figs. 1, 2, and 3 give the proper wave impedances for the associated modes and directions for *all* frequencies. Thus, one might anticipate that the only two types of ideal elements that could be added to these networks without changing the correctly predicted impedances would be uniform transmission lines and ideal transformers. This turns out to be the case and all of the one- and two-port networks described in the next section composed of lumped elements, uniform transmission lines, and ideal transformers representing spherical wave propagation can be thought of as arising from the following expression for the spherical Hankel function given in Ref. [12], which is the product of a rational function (which can be represented by a lumped ladder network) and a complex exponential with the purely imaginary argument iz (which can be represented by a lossless uniform transmission line):

$$h_n^{(2)}(z) = (i)^{n+1} \frac{e^{-iz}}{z} \sum_{s=0}^n \frac{i^s}{s! (2z)^s} \frac{(n+s)!}{(n-s)!}. \quad (6)$$

Clearly, the logarithmic derivative is a rational function as the same complex exponential factor appears in both the numerator and the denominator. Thus, we anticipate that the lumped-element

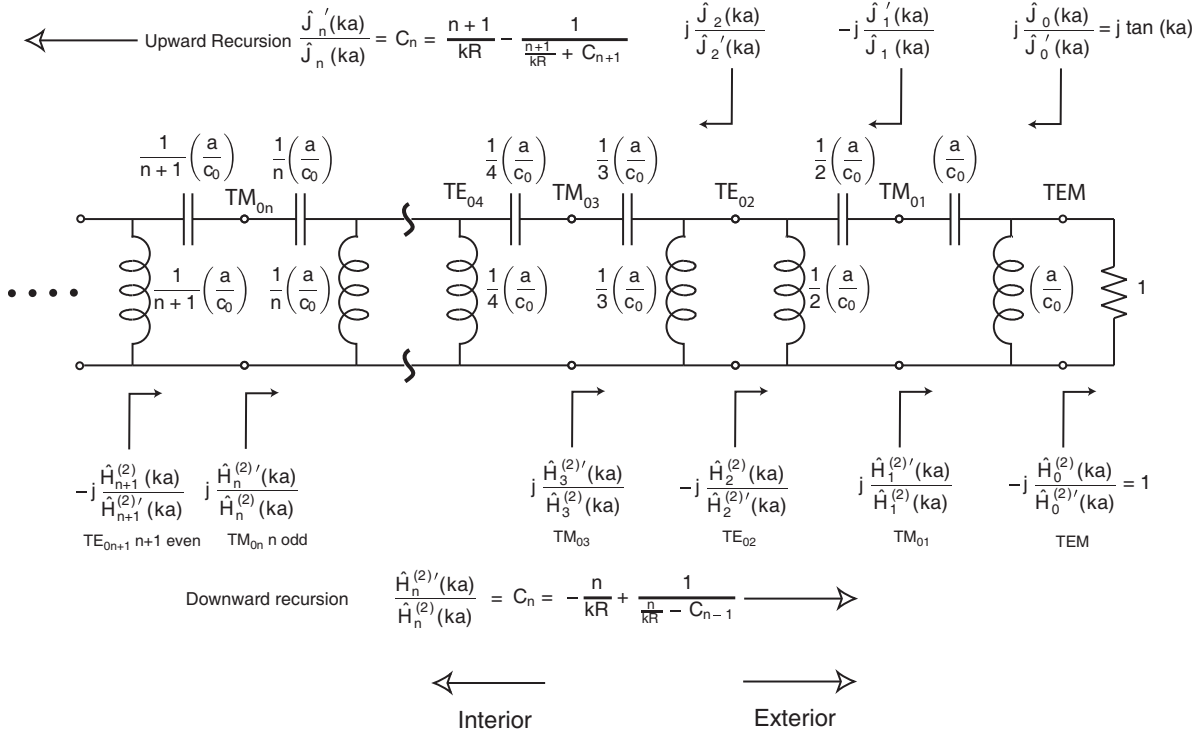


Figure 3: Equivalent circuit for spherical TM-to- R modes with odd radial index and TE-to- R modes with even radial index, as shown in Fig. 1 (top) of Ref. [4]. Note that the network is flipped right to left compared to Fig. 1 in Ref. [4]. As in Ref. [4], all impedances in this circuit are normalized to η_0 . Finally, note that the interleaving of the TE and TM mode impedances can be seen in Eq. (3), the recursion relation for the logarithmic derivative of the Riccati-Hankel functions.

networks can be modified to represent spherical wave propagation by the addition of ideal transformers and uniform, non-dispersive transmission lines or unit elements. Before dismissing such a model as obvious, one might consider the equivalent spherical transmission line model in Ref. [9] in which the local characteristic impedance and wave number are both functions of frequency as well as radial coordinate R .

2. TWO-PORT EQUIVALENT NETWORKS FOR SPHERICAL MODES

Thal [4] actually did provide just such a two-port network describing the propagation of the spherical modes within a spherical shell. The network could be described in microwave terminology as a mixed lumped and distributed network and is a combination of lumped elements and *uniform, dispersionless* transmission lines. The equivalent circuits for the TM_{01} and TE_{01} modes for a spherical shell of inner radius a and outer radius b are given in Ref. [4] and Ref. [13] and are shown here in Figs. 4 and 5. Note that Thal's two-port model of a spherical shell contains positive lumped elements (positive inductances and capacitances) on one end of a uniform transmission line and negative lumped elements (negative inductors and capacitors) on the other, such that the proper cascade of two such networks results in a similar, larger network.

The value of the explicit two-port model given by Thal cannot be overstated. It clearly separates a lumped-element filtering effect and pure time delay. Again, the lumped element model is amenable to impedance matching techniques and bandwidth/tolerance computations which require a rational function representation. However, one might note that this model does not give the correct values for electric and magnetic field at both values of radial coordinate R . This can be seen by allowing the frequency to become very large, or rather, allowing ka and kb to both become much greater than one. Then, the lumped elements “disappear” and one is left with only the unit element. However, spherical spreading of the field should cause the electric and magnetic fields at a and b to differ by a factor of $\frac{b}{a}$. It would appear that this could be accounted for with an ideal transformer. On the other hand, if the terminal voltages in Thal’s equivalent network are taken as being analogous to spherical transmission line voltages given in Ref. [9] and the currents in Thal’s network are taken as

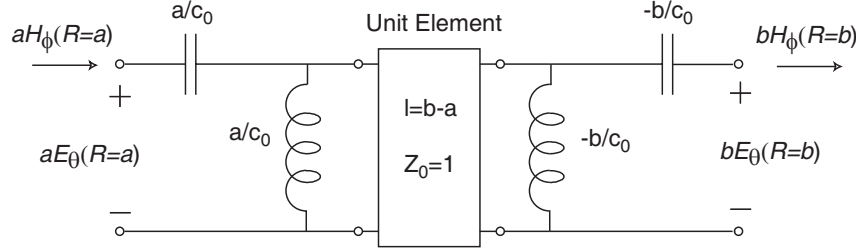


Figure 4: Equivalent circuit for spherical shell supporting TM_{01} modes with inner radius a and outer radius b as given in Ref. [4]. Note that the lumped elements on the right side of the unit element are negative. Also note the directions of the currents. Finally note that the network in Ref. [4] is flipped right to left in relation to this one. As noted in Ref. [4], if two spherical shells were cascaded, these elements would cancel with the positive counterparts on the next shell. If $b \rightarrow \infty$, the negative series capacitance would become a short while the negative shunt inductance would become an open circuit.

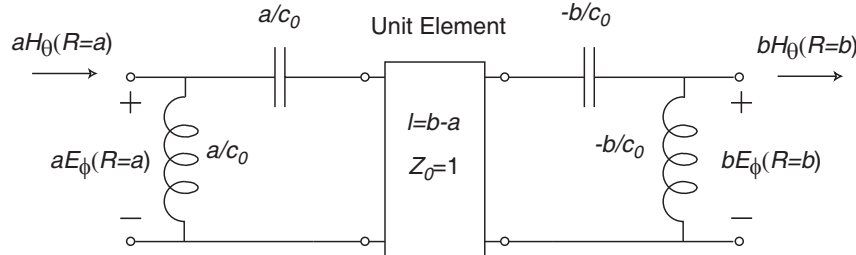


Figure 5: Equivalent circuit for spherical shell supporting TE_{01} modes with inner radius a and outer radius b as given in Ref. [4]. Again, note that the network in Ref. [4] is flipped right to left in relation to this one.

being analogous to the spherical transmission line currents again in Ref. [9], the model is consistent. This is shown in Figs. 4 and 5 in terminal voltages and currents. Finally, note that the spherical transmission line voltages and currents given in Ref. [9] are true power conjugate variables.

3. ACOUSTIC SPHERICAL WAVE PROPAGATION

It would seem plausible that similar lumped-element equivalent networks could be developed for the small-signal, acoustic compressional spherical modes [14] since these are solutions to the Helmholtz equation. In fact, a model for the zeroth-order acoustic monopole mode has been given by Benade [15]. The analogous work in the area of linear acoustics bolsters the model developed by Thal and provides an interesting alternative derivation.

3.1. Acoustic Impedance of Spherical Modes

It is necessary to draw an analogy between field quantities in order to develop equivalent networks for the acoustic spherical modes. When employing an equivalent circuit, an arbitrary choice exists in selection of power conjugate variables. Reversing this choice results in a dual equivalent circuit. In Ref. [16] and Ref. [17], acoustic pressure is chosen as the across variable and volume velocity as the through variable. This analogy is intuitive but is sometimes rejected in favor of choosing volume velocity as the across variable and pressure as the through variable [17–19]. The analogy used here makes analogy between electric potential and acoustic pressure and between electric current and volume velocity. This analogy is sometimes referred to as the acoustic impedance analogy [17, 18].

When using the acoustic-impedance analogy, acoustic impedance is defined as:

$$Z_A(\omega) = \frac{p}{U} \text{ MKS acoustic Ohms}$$

where p is the acoustic pressure and U is the volume velocity. The specific acoustic impedance is defined as the ratio of acoustic pressure to particle velocity. Thus, the specific acoustic impedance of the n th order spherical mode is given by the reciprocal of the logarithmic derivative of the conventional spherical Hankel function:

$$z(\omega) = \frac{p}{u} = \frac{p}{j \frac{1}{\omega \rho_0} \frac{\partial p}{\partial R}} = \frac{p}{j \frac{k}{\omega \rho_0} \frac{\partial p}{\partial kR}} = -j \frac{p}{c_0 \rho_0 \frac{\partial p}{\partial kR}} = -j z_0 \frac{h_n^{(2)}(kR)}{h_n^{(2')} (kR)} \quad (7)$$

where u is the particle velocity, ρ_0 is the quiescent density, and c_0 is the small-signal sound speed. Also, z_0 is the wave impedance $\rho_0 c_0$ and is analogous to η_0 for electromagnetic plane waves. If the Firestone or acoustic-mobility analogy were employed, the specific acoustic impedance would be the reciprocal of this quantity.

It can be shown that the reciprocal of the logarithmic derivative of the conventional spherical Hankel function is related to that of the Schelkunoff spherical hankel function as follows:

$$\frac{h_n^{(2)}(kR)}{h_n^{(2)\prime}(kR)} = \left[\frac{\hat{H}_n^{(2)\prime}(kR)}{\hat{H}_n^{(2)}(kR)} - \frac{1}{kR} \right]^{-1} \quad (8)$$

and therefore the acoustic impedance is given by the TE mode equivalent network with one additional leading shunt reactive branch:

$$-j z_0 \frac{h_n^{(2)}(kR)}{h_n^{(2)\prime}(kR)} = -j z_0 \frac{\hat{H}_n^2(kR)}{\hat{H}_n^{(2)\prime}(kR)} \parallel (j z_0 kR) \text{ shunt branch.} \quad (9)$$

Thus, an equivalent ladder network for the wave impedance of the outgoing spherical modes using the acoustic impedance analogy is given in Fig. 6: When the radial index is zero, $n = 0$, only the leading shunt inductance and the resistive termination are present and the equivalent network is identical to the one shown on page 117 of Ref. [17] for the radially pulsating sphere. In any case, with this simple modification (an additional shunt or series branch depending on the analogy employed) we can then borrow intact the equivalent networks of Chu, Harrington, and Thal for the analysis of acoustic spherical modes.

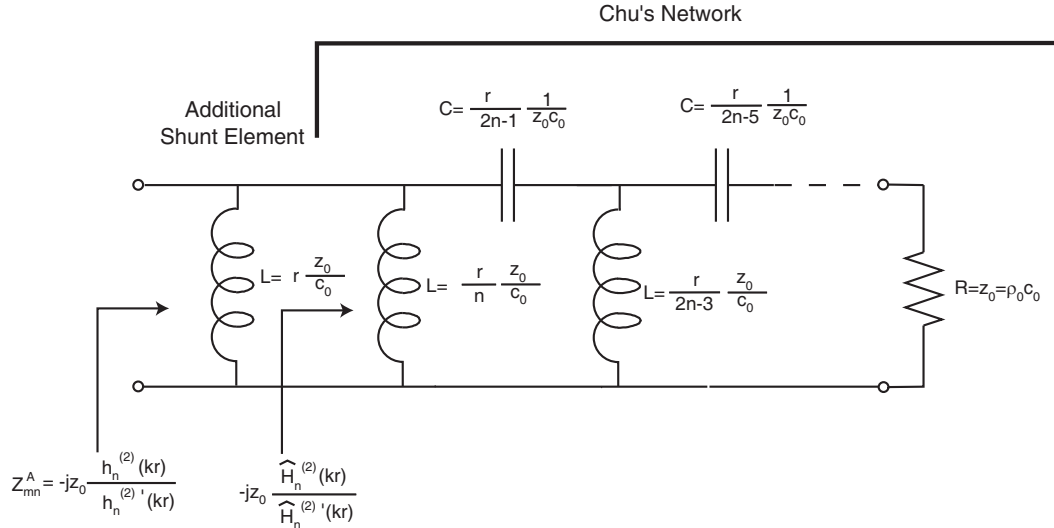


Figure 6: Equivalent circuit for specific acoustic impedance [17], $Z_s = \frac{p}{u}$ ($\frac{\text{Newton}\cdot\text{sec}}{\text{m}^3}$ or mks Rayls) of the acoustic spherical modes when the acoustic impedance analogy is employed. The specific acoustic impedance is analogous to the wave impedance in electromagnetics. This circuit can be obtained from Chu's equivalent circuit for the TE modes with an additional shunt branch. As with the spherical electromagnetic modes, the wave impedance does not depend on azimuthal index.

4. BENADE'S EQUIVALENT NETWORK FOR THE RIGID-WALLED CONICAL HORN

A rigid-walled conical horn as shown in Fig. 7 supporting Neumann boundary conditions for the acoustic pressure at the wall is a spherical waveguide. Solutions to the Webster horn equation or nonuniform transmission model have been known for some time [16, 17, 20, 21]. In Benade's analysis, the radial coordinate of the spherical wave is replaced by the apical distance in the conical horn. Benade's equivalent network is reproduced in Fig. 8. The circuit in Fig. 8 degenerates to a section of transmission line in cascade with an ideal transformer as the radii at both ends of the horn become large with respect to a wavelength. Benade's equivalent network gives predictions for conical horn behavior that match the analysis in Refs. [22–24]. Note that acoustic pressure and volume velocity

comprise a pair of power conjugate variables. The ratio of electric to magnetic field has units of Ohms as does the ratio of voltage to current. However, while the ratio of acoustic pressure to particle velocity has units of MKS Rayls, the ratio of acoustic pressure to volume velocity has units of MKS acoustic Ohms. Finally, note that the model given in Fig. 8 is exactly the same as that given in Fig. 7 of Ref. [25] for the inverse quadratic impedance taper. To show this, one makes the following substitutions in Fig. 7 of Ref. [25]: $l = b - a$ (meters), $\nu = c_0$ (meters/second), $W = 1$ (Ω), $L_0 = \frac{a}{b-a}$ (Ω), $m = \frac{L_0+W}{L_0} = \frac{\frac{a}{b-a}+1}{\frac{a}{b-a}} = \frac{a+b-a}{a} = \frac{b}{a}$ (dimensionsless).

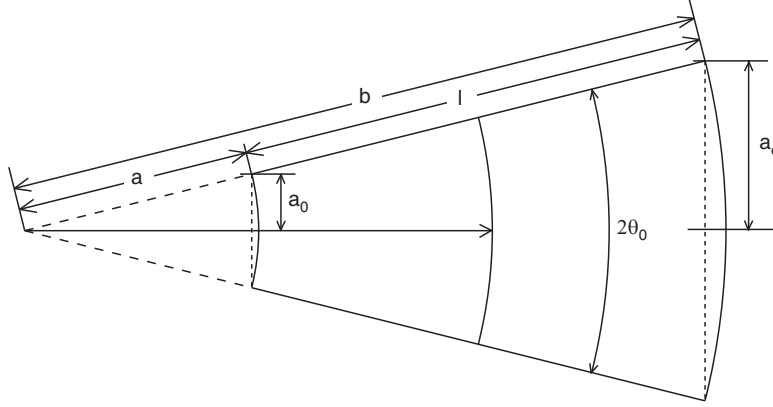


Figure 7: Equivalent circuit for conical acoustic waveguide with rigid walls given in Ref. [15].

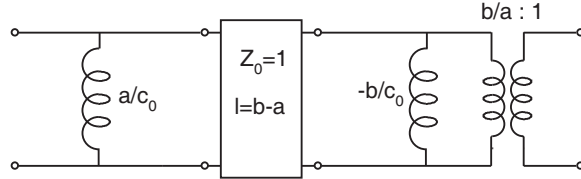


Figure 8: Equivalent circuit for finite-length, rigid-walled conical acoustic horn. All impedances are scaled by a factor $\frac{\rho_0 c_0}{\pi a_0^2 F(\theta_0)}$ where $F(\theta_0) = \frac{2(1-\cos \theta_0)}{\sin^2 \theta_0}$ where $a_0 = a \sin(\theta_0)$. That is, $\frac{\rho_0 c_0}{\pi A}$ where A is the area of the spherical wavefront at the smaller end of the horn. More details are given in Ref. [15].

5. CONCLUSION

The equivalent networks given by Thal [4] for the TE_{nm} and TM_{nm} spherical mode propagation in spherical shells, with the addition of an ideal transformer, are similar to and most likely equivalent to those which can be derived using Kobayashi's extended Kuroda identities [25], given the requisite associated local characteristic impedance distribution for each mode. The characteristic impedance distribution for Kobayashi's nonuniform transmission line representation is not the same as that given in the nonuniform transmission line model for spherical modes in Ref. [9], as this model is a nonuniform transmission line in which the characteristic impedance and wave number are both functions of the longitudinal coordinate whereas in Kobayashi's model the nonuniform transmission line has a wave number (or phase velocity) independent of the longitudinal position; i.e., it is dispersionless. Also, both sets of networks are similar to the one derived for zeroth-order acoustic spherical wave propagation derived by Benade [15]. Here we have shown the rigorous equivalence of Benade's model, Thal's model, and Kobayashi's model for the zeroth-order acoustic mode. A general equivalence for all orders of electromagnetic spherical modes and Kobayashi's approach is not complete, but appears to be sound.

REFERENCES

1. Harrington, R. F., *Time Harmonic Electromagnetic Fields*, McGraw-Hill, New York, 1961.
2. Cantrell, C. D., "Numerical methods for the accurate calculation of spherical Bessel functions and the location of MIE resonances," Technical Report, University of Texas at Dallas, Richardson, TX, 2006.

3. Chu, L. J., "Physical limitations on omnidirectional antennas," *Journal Applied Physics*, Vol. 19, 1163–1175, 1948.
4. Thal, Jr., H. L., "Exact analysis of spherical waves," *IEEE Trans. Antennas Propagat.*, Vol. 26, No. 2, 282–287, 1978.
5. R. M. Fano, "Theoretical limitations on the broadband matching of arbitrary impedances," *J. Franklin Institute*, Vol. 249, 57–83, Jan. 1950, and 139–155, Feb. 1960.
6. Villalobos, M. C., H. D. Foltz, J. S. McLean, and I. Sen Gupta, "Broadband tuning limits on uwb antennas based on fanos formulation," *Proc. 2006 IEEE Antennas and Propagation International Symposium*, 171–174, Albuquerque, NM, Jul. 9–14, 2006.
7. Villalobos, M. C., H. D. Foltz, and J. S. McLean, "Broadband matching limitations for higher order spherical modes," *IEEE Trans. Antennas Propagat.*, Vol. 57, No. 4, 1018–1026, Apr. 2009.
8. McLean, J. S., R. Sutton, and H. Foltz, "Pattern descriptors for UWB antennas," *IEEE Trans. Antennas Propagat.*, Vol. 53, No. 1, 553–559, Jan. 2005.
9. Marcuvitz, N., *Waveguide Handbook*, 47–54, 96–100, Peter Peregrinus, Ltd, on behalf of the Institution of Electrical Engineers, 1986.
10. Thal, Jr., H. L., "New radiation Q limits for spherical wire antennas," *IEEE Trans. Antennas Propagat.*, Vol. 54, No. 2, 2757–2763, Oct. 2006.
11. Darlington, S., "Synthesis of reactance 4-poles," *J. Math. Phys.*, Vol. 18, 275–253, Sep. 1939.
12. Arfken, G., *Mathematical Methods for Physicists*, 623–630, Academic Press, Inc., 1985
13. Thal, Jr., H. L., "A circuit model for spherical wheeler cap measurements," *IEEE Trans. Antennas and Propagat.*, Vol. 59, No. 10, 3638–3645, 2011.
14. Pierce, A. D., "Basic linear acoustics," *Springer Handbook of Acoustics*, T. D. Rossing, ed., 65–75, Springer, New York, 2007.
15. Benade A. H., "Equivalent circuits for conical waveguides," *J. Acoust. Soc. Am.*, Vol. 83, No. 5, 1764–1769, May 1988.
16. Olson, H. F., *Elements of Acoustical Engineering*, 95–12, D. Van Nostrand Company, Inc., New York, 1947.
17. Beranek, L. L., *Acoustics*, 268–278, McGraw-Hill, New York, 1954.
18. Busch-Vishniac, I. J., *Electromechanical Sensors and Actuators*, 16–52, Springer-Verlag, New York, 1999.
19. Firestone, F. A., "A new analogy between mechanical and electrical systems," *J Acoust. Soc. Am.*, Vol. 4, 249–267, 1933.
20. Blackstock, D. T., *Fundamentals fo Physical Acoustics*, 46–51, John Wiley & Sons, New York, 2000.
21. Kinsler, L. E. and A. R. Frey, *Fundamentals of Acoustics*, 163–165, John Wiley & Sons, New York, 1962.
22. Caussé, R., "Input impedance of brass musical instruments — Comparison between experiment and numerical models," *J. Acoust. Soc. Am.*, Vol. 75, No. 1, 241–254, Jan. 1984.
23. Kulik, Y., "Transfer matrix of conical waveguides with any geometric parameters for increased precision in computer modeling," *Journal of the Acoustical Society of America, Express Letters*, Published Online, October 2, 2007.
24. Mapes-Riordan, D., "Horn modeling with conical and cylindrical transmission line elements," *Proc. Audio Engineering Society Convention*, Vol. 91, Oct. 1991.
25. Kobayashi, K., Y. Nemoto, and R. Sato, "Kurodas identity for mixed lumped and distributed circuits and their application to nonuniform transmission lines," *IEEE Trans. Microwave Theory Tech.*, Vol. 29, No. 2, 81–86, 1981.

Design of Miniature Multiband Fractal CPW-fed Antenna for Telecommunication Applications

I. Rouissi¹, I. Ben Trad^{2,3}, J. M. Floc'h³, M. Sheikh⁴, and H. Rmili⁴

¹SYSCOM, ENIT, Université de Tunis-El Manar, Tunis 1002, Tunisia

²INNOV'COM, Sup'Com, City of Communication Technologies, Ariana 2083, Tunisia

³IETR, INSA Rennes, 20 Avenue Buttes des Coësmes, Rennes 35043, France

⁴Faculty of Engineering, Electrical and Computer Engineering Department
King Abdulaziz University, P. O. Box 80204, Jeddah 21589, Saudi Arabia

Abstract— A miniature planar fractal antenna has been introduced in this paper for multistandard wireless communication systems. The multifrequency structure was based on Hilbert curve at the second iteration and fed using the CPW technology. The performed monopole was designed using the EM Simulator HFSS v11 from Ansoft. Simulation results show that it resonates at several frequencies such as GSM900, WLAN, ISM, WiFi, WiMAX bands. A prototype was manufactured and characterized and measurements show that this compact monopole antenna can be used for a wide variety of telecommunication applications.

1. INTRODUCTION

With the increasing development of wireless communication technologies in recent years the need for small size and multiband antennas has risen drastically. A lot of approaches have been developed to design compact antennas able to cover the maximum of telecommunication standards. Among the most investigated ones, the fractal approach has received a significant attention from the academic and industrial communities [1].

Thanks to their advantages, fractal antennas allow us to ovoid the refuge to traditional way of using different antennas for different frequency bands which causes a limited space problem and to miniaturize antennas by capitalizing on their space filling ability to fit large electrical lengths into small physical volume [2–4]. Especially, the planar printed fractal antennas have been extensively studied because of their low profile multi-frequency behavior, ease of fabrication and integration and low cost which are the main requirements for all modern wireless application system [5–8].

In this paper, a planar multiband Hilbert curve CPW-fed antenna was designed and performed. The parameters of the proposed structure have been studied and adjusted to make the antenna operating at 0.8–1.02 GHz, 1.2–1.5 GHz, 2.1–3.9 GHz and 4.4–4.9 GHz bands. Then a prototype of the printed multiband antenna has been manufactured and measured. This structure is a suitable candidate for wireless communication.

2. ANTENNA DESIGN

The compact fractal second-iteration antenna of size $27 \times 28 \text{ mm}^3$ based on Hilbert curve is shown in Figure 1(a). It is printed on FR4 substrate with relative permittivity $\epsilon_r = 4.4$ and thickness $h = 1.6 \text{ mm}$. The CPW fed monopole antenna has been supplied by a 50Ω SMA connector. The

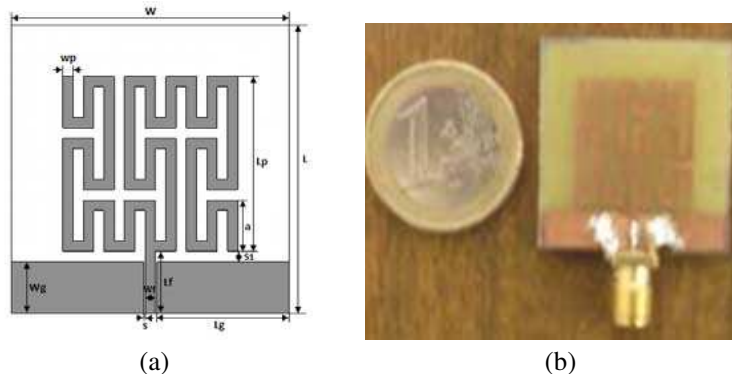


Figure 1: The planar fractal CPW-fed antenna: (a) geometry and (b) prototype.

optimized design parameters are as following: $a = 5 \text{ mm}$, $W_p = 1 \text{ mm}$, $L_p = 17 \text{ mm}$, $L_f = 6 \text{ mm}$, $W_f = 1 \text{ mm}$, $s = 0.11 \text{ mm}$, $W_g = 5 \text{ mm}$, $L_g = 12.89 \text{ mm}$, $S_1 = 1 \text{ mm}$. Figure 1(b) depicts the photo of the prototyped planar antenna.

3. RESULTS

In this section, the simulation results are carried out to show the performance of the optimized design. It can be clearly concluded from the Figure 2 that by fixing $a = 5 \text{ mm}$, the position of the feed line on the middle (the positions of the feed line on the far left, on the middle and on the far right correspond to position 1, position 2 and position 3 respectively) and $W_g = 5 \text{ mm}$, a multiband and UWB behaviors were well obtained ($0.8\text{--}1.02 \text{ GHz}$, $1.2\text{--}1.5 \text{ GHz}$, $2.1\text{--}3.9 \text{ GHz}$ (the achieved UWB frequency band) and $4.4\text{--}4.9 \text{ GHz}$). Almost desired standards are successfully covered, the achieved simulated frequency bands can meet the requirement of GSM850, GSM900, UMTS, WLAN, LTE, Bluetooth, WiFi, WiMAX

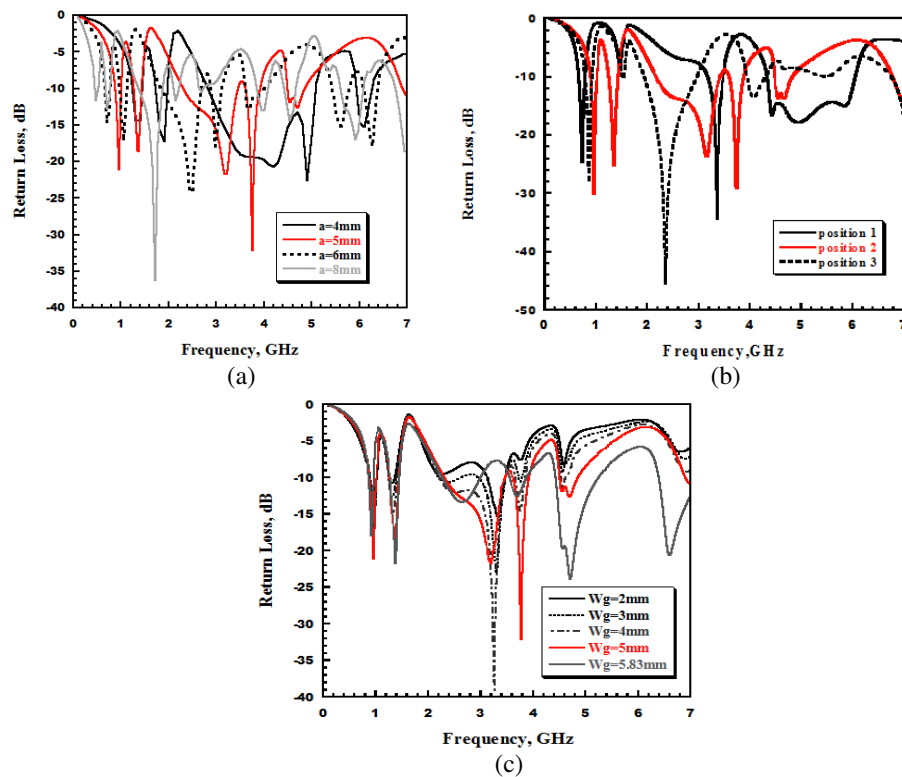


Figure 2: Simulated return loss S_{11} for different (a) values of “ a ”; (b) positions of the feeding line and (c) widths of W_g .

The Hilbert curve fractal antenna was realized and measured results agree well with simulation ones as it can be seen in Figure 3. Actually, the compact structure has a multiband behavior as it was expected, almost the desired bands were achieved. The measured results show however three operating bands which are $0.9 \sim 1.1 \text{ GHz}$, $2.8 \sim 3.39 \text{ GHz}$ and $4.6 \sim 4.9 \text{ GHz}$. This can be explained by the energy losses caused by the fact that the connector was not taken into account in the simulation.

Simulated results of the antenna surface currents at six frequencies $F_1 = 0.96 \text{ GHz}$, $F_2 = 1.36 \text{ GHz}$, $F_3 = 3.2 \text{ GHz}$, $F_4 = 3.76 \text{ GHz}$, $F_5 = 4.54 \text{ GHz}$ and $F_6 = 4.7 \text{ GHz}$ are presented in Figure 4. The surface current distribution changes depending on the operating frequency. For example, in Figure 4(a), the surface current distribution at the 0.96 GHz frequency is localized along the micro strip line due to the existing EM coupling with the ground plane and chiefly at the center of the Hilbert curve. At the other frequencies, the current distributions are mainly localized in the right and/or left edge sides of the radiating patch. The printed antenna has a monopole-like behavior.

The 2D measured radiation patterns of the printed fractal CPW-fed antenna have been measured in the anechoic chamber at the site of the IETR-INSA Rennes and the experimental results on

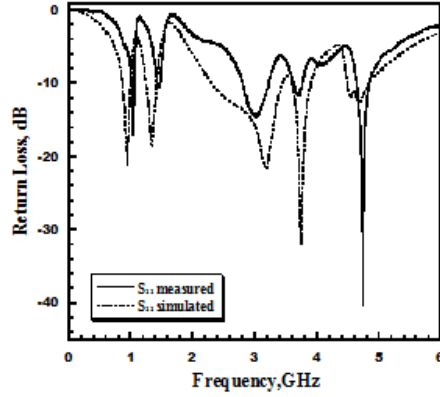
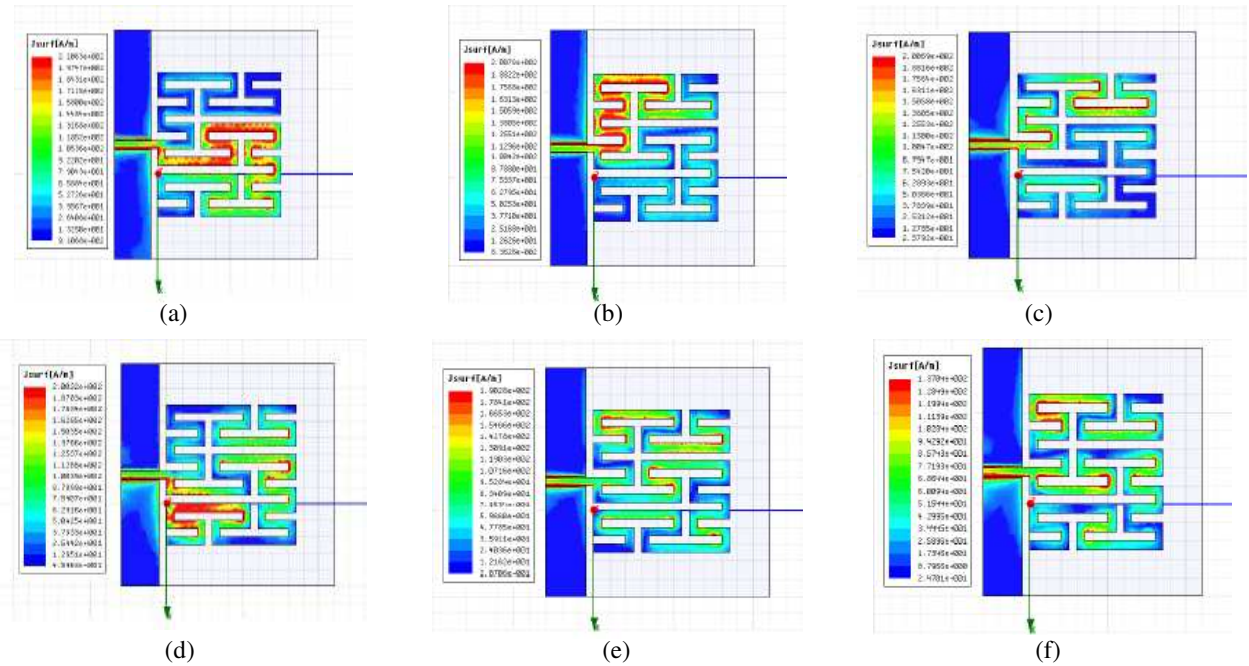


Figure 3: Measured and simulated return loss.

Figure 4: Surface current distribution for (a) $F_1 = 0.96$ GHz; (b) $F_2 = 1.36$ GHz; (c) $F_3 = 3.2$ GHz; (d) $F_4 = 3.76$ GHz; (e) $F_5 = 4.54$ GHz and (f) $F_6 = 4.7$ GHz.

E -plane and H -plane at 1.03 GHz, 3.02 GHz and 4.73 GHz frequencies are depicted in Figure 5. It can be concluded that the antenna has almost an Omni-directional radiation pattern at these frequencies and behaves as a monopole. It's important to notice that at the first frequency 1.03 GHz

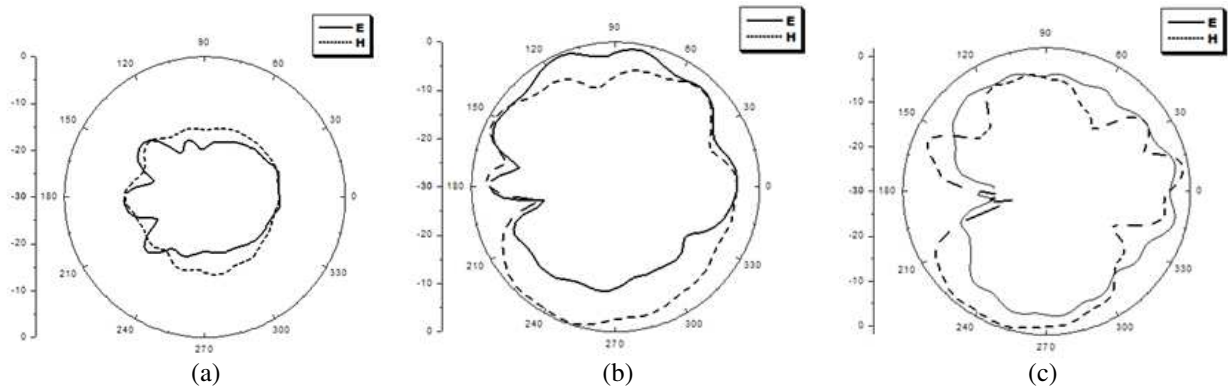


Figure 5: Measured radiation patterns at frequencies: (a) 1.03 GHz; (b) 3.02 GHz; (c) 4.73 GHz.

(Figure 5(a)), the injected power still stored in the antenna and will not be radiated which explain the observed gain drop. Otherwise, the radiation performances are maintained over the operating bands.

4. CONCLUSION

A compact fractal monopole CPW-fed antenna was proposed and performed for multistandard wireless communication systems. The simulation results show that the multiband antenna covers well different desired bands required for GSM85, GSM900, WiMAX, LTE, WiFi, WLAN A prototype has been manufactured and measured, and the experimental results match well with the simulated ones. The printed antenna has a monopole like behavior all over the operating bands. In addition, the antenna size is small which make easy its integration into multistandard telecommunication systems.

REFERENCES

1. Werner, D. H. and S. Ganguly, "An overview of fractal antenna engineering research," *IEEE Antennas and Propagation Magazine*, Vol. 45, No. 1, 38–57, 2003.
2. Elkamchouchi, H. and M. Abu Nasr, "3D fractal hilbert antennas made of conducting plates," *International Conference on Microwave and Millimeter Wave Technology ICMMT*, 2007.
3. Anagnostou, D., M. Khodir, J. Lyke, and C. Christodouliou, "Fractal antenna with RF MEMS switches for multiple frequency application," *IEEE Antennas and Propagation Society International Symposium*, Vol. 2, 2002.
4. Waqas, M., Z. Ahmed, and M. Bin Ihsan, "Multiband sierpinski fractal antenna," *IEEE Antenna and Wireless Propagation Letters*, 1–6, 2009.
5. Suganthi, S., S. Raghavan, D. Kumar, and S. Hosimin Thilagar, "A compact hilbert curve fractal antenna on metamaterial using CSRR," *PIERS Proceedings*, 136–140, Kuala Lumpur, Malaysia, Mar. 2012.
6. Dalsonia, P., B. Shar, T. Upadhyaya, and V. V. Dwivedi, "Analysis of multiband behaviour on square patch fractal antenna," *International Conference on Communication Systems and Network Technologies*, 2012.
7. Ali, J. K., Z. A. Abed AL-Hussain, A. A. Osman, and A. J. Salim, "A new compact size fractal based microstrip slot antenna for GPS applications," *PIERS Proceedings*, 700–703, Kuala Lumpur, Malaysia, Mar. 2012.
8. Giianvittoria, J. and Y. Rahmat-Sami, "Fractal element antennas: A compilation of configurations with novel characteristics," *IEEE APS Conference Antennas and Propagation for Wireless Communication*, 129–132, 2000.

A Stacked Microstrip Antenna with CSRR Arrays for Beidou Navigation System

Baiqiang You, Lizhi Li, Yang Zhao, Jianhua Zhou, and Jie Li

Department of Electronic Engineering, Xiamen University, Xiamen, Fujian 361005, China

Abstract— A double-feeding and dual-band circularly polarized microstrip antenna is presented for Beidou Navigation System. CSRR (complementary split ring resonator) arrays are used for the miniaturization of the proposed antenna, together with slotting and corner cutting for circular polarization. Simulation results show that the designed antenna covers two frequency bands, with obviously widened bandwidths caused by the stacked structure. The 10 dB impedance bandwidth and 3 dB axial-ratio bandwidth for lower band are 11.8 MHz and 2.8 MHz respectively, and that for higher band are 165 MHz and 65.7 MHz respectively. There has been good agreement between stimulation and measurement results, confirming the suitability for Beidou navigation application.

1. INTRODUCTION

In recent years, with the rapid progress in satellite navigation systems, demands for multi-frequency circularly polarized antennas are increasing [1]. In order to realize the miniaturization of microstrip antenna, some novel structures had been proposed, such as introducing fractals, splits and slots, and PBGs (photon bandgap) on the patch. Based on the study of SRR (split ring resonator) structure, Falcon and Marques created a new structure — CSRR (complementary split ring resonator) in 2004 [2, 3]. Then, Juan Domingo Baena et al. discussed the high-frequency selective characteristics of CSRRs and gave the equivalent circuit [4]. In 2008, H. Zhang and Y.-Q. Li found that when the splits of a CSRR were asymmetric to the surface current paths of antenna, a circularly polarized (CP) wave would be activated [5]. In addition, CSRRs also possess a band rejection characteristic. Therefore, many UWB antennas are implemented by etching complementary split-ring resonator on the feed line or inner patch to obtain a band-notched function [6–8]. CSRRs are introduced on ground plates or feeders in most of relative research reports [9], and many studies on split rings for metamaterials and microwave circuit designs have been done [10].

Considering the great advantages of CSRR constructs, we employ CSRR arrays and a stacked structure to realize a compact antenna with improved gain. Applying two stacked patches, the proposed antenna with wide bandwidth could be realized.

2. ANTENNA DESIGN

The geometry of the proposed stacked microstrip patch antenna is shown in Fig. 1, with two patches etched on separate rectangle substrates. The top patch is used as a receiving antenna at higher band (S-band), and the bottom one as a transmitting antenna at lower band (L-band). For convenience in practical design, the thickness h and dielectric permittivity ϵ_r of both substrates are set as 3 mm and 10 respectively. As shown in the figure, the dimensions of the designed antenna are selected as following according to the simulation.

$L_{top} = 28$ mm, $W_{top} = 26.78$ mm, $L_{11} = 15.82$ mm, $L_{12} = 3.46$ mm, $W_{12} = 0.8$ mm, $L_{cut} = 3.23$ mm, $L_s = 4.4$ mm, $L_{cs} = 2$ mm, $D_c = W_c = 0.4$ mm, $X_f = 2.98$ mm, $L_{bottom} = 36.6$ mm, $W_{bottom} = 32.56$ mm, $L_{21} = 26$ mm, $L_{22} = 5$ mm, $W_{22} = 3$ mm, $S_{cut} = 1.23$ mm, $X_d = 2.18$ mm.

The top patch is comprised of a corner-cutting rectangle with an array of CSRR locating at the center, in which there are four CSRRs of the same size in symmetric arrangement. Since each CSRR can be equivalent to a RLC resonance circuit of a high Q value [4], we use three parameters, R_c , L_c , C_c , which stand for the resistance and capacitance of the inner square surrounded by a ground plane at a distance W_c of its edge and the inductance connecting the inner square to the ground respectively. So the resonant frequency of each CSRR can be expressed as

$$f_c = \frac{1}{2\pi\sqrt{L_c C_c}} \quad (1)$$

The coupling between the four CSRRs would make the resonant frequency of the patch (f_0) shift downward, and also the negative permittivity characteristics of CSRRs make the resonance electrical length become much shorter than that without CSRR. While the rational distribution of the

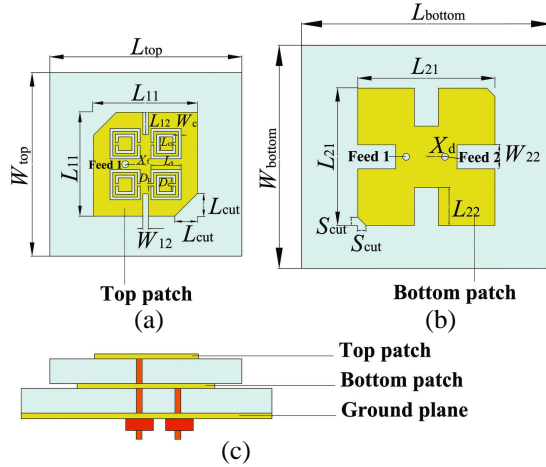


Figure 1: Geometry scheme of the proposed stacked microstrip antenna with (a) top view, (b) bottom view and (c) side view.

CSRR array could strengthen these performances, that promises much smaller antenna. To produce right-handed CP radiation, a corner cutting is introduced in the antenna element, by which the fundamental resonance mode TM_{10} is divided into two orthogonal degenerate modes with a 90° phase shift. Further miniaturization can be achieved by adding two rectangle slots (length L_{12} and width W_{12}) at the edges of the patch. Due to the introduction of the slots, the current path in the patch becomes longer and the resonant frequency decreases, equivalent to the introduction of C_f/L_f resonant circuit. Meanwhile, the circular polarization also can be adjusted by changing the dimensions of the slots. The equivalent circuit of the top patch is provided as in Fig. 2(a), ignoring the corner cut and the impact of the bottom patch on the top one.

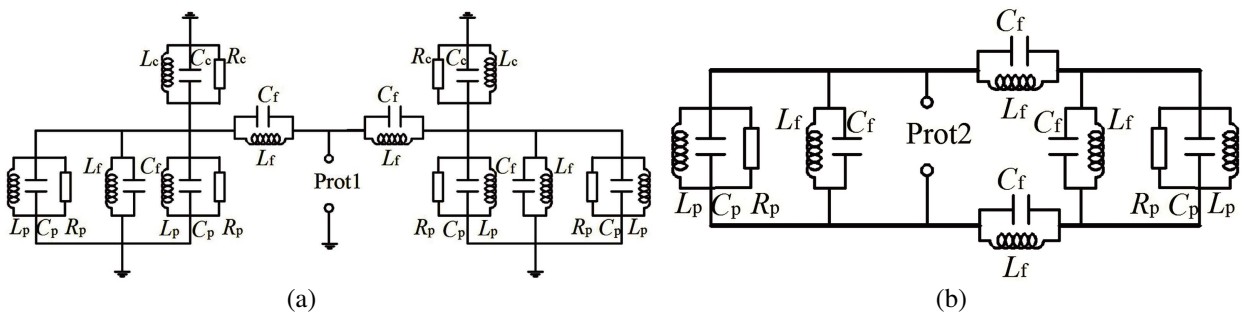


Figure 2: The equivalent circuits of (a) top patch and (b) bottom patch.

Besides corner cuttings introduced in the design of the bottom patch, four rectangular slots (length L_{22} and width W_{22}) are added at four edges of the patch, equivalent to the introduction of C_f/L_f resonant circuit. By adjusting the dimensions of the corner cuttings and slots, the perturbed TM_{01} and TM_{10} modes can be split into two near-degenerate modes with equal amplitude and a 90° phase shift for dual CP radiation. Similarly, the equivalent circuit of the bottom patch is provided as in Fig. 2(b), ignoring the corner cut, via hole and the impact of the top patch on the bottom.

3. SIMULATED AND MEASURED RESULTS

In order to learn the influence of the CSRR array on the designed antenna, a detailed parameter study is carried out. The simulated return loss for different values of L_{cs} (length of inner square) is depicted as in Fig. 3(a). It can be seen that the higher resonant frequency decreases when the dimension of L_{cs} increases, due to the increasing of C_c and L_c values. The simulated return loss for different values of D_c (width of slots) is depicted in Fig. 3(b), which illustrates that with the increasing of D_c value, the higher frequency also increases due to the decreasing of C_c and L_c values. According to the simulated axial ratio against frequency at lower band in the broadside direction as shown in Fig. 4(a), there is a 3 dB axial ratio bandwidth of about 3 MHz from 1.613 GHz to

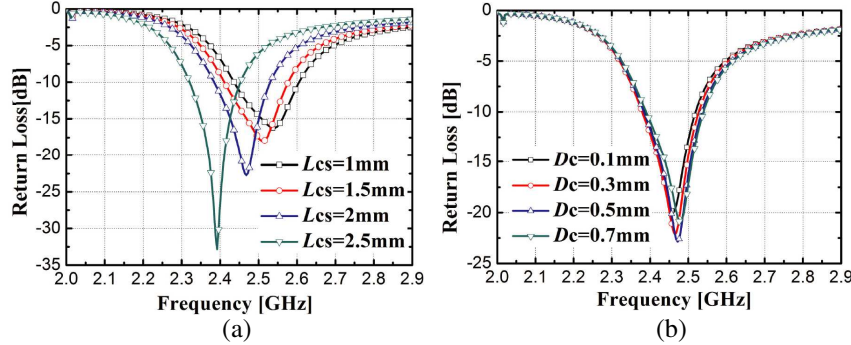


Figure 3: The simulated return loss for different values of (a) L_{cs} and (b) D_c .

1.616 GHz for LHCP, about 0.18% with respect to the center point of 1.61 GHz. While according to that at higher band as shown in Fig. 4(b), there is a 3 dB axial ratio bandwidth of about 66.4 MHz from 2.519 GHz to 2.586 GHz for RHCP, about 2.66% with respect to the center point of 2.49 GHz. It is obvious that due to the introduction of the stacked structure, the -10 dB bandwidth and 3 dB axial-ratio bandwidth at the higher band are all widened greatly. From the simulated radiation patterns on XZ -plane and YZ -plane at 1.61 GHz and 2.49 GHz, as shown in Figs. 5(a) and (b) apartly, the gains with LHCP and RHCP in the positive z -direction are about 0.5 dB and 4.7 dB, both of which could be adjusted with the parameters of the structure and material. Note that the radiation patterns are symmetrical with a 3-dB beam-width of 104° at 2.49 GHz.

Figures 6(a) and (b) show the top view and side view of the fabricated sample antenna, based on two ceramic substrates with the same ϵ_r of 10 and h of 3 mm, which are CER-10 high performance plates provided by Taconic Company. As shown in Figs. 7(a) and (b), the measured and simulated return losses suggest that the lower band has a -10 dB bandwidth of 11 MHz from 1.604 GHz to

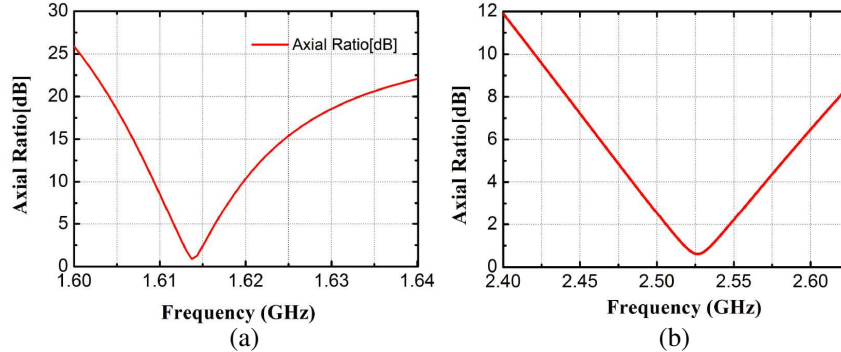


Figure 4: The simulated axial ratio against frequency at (a) lower band and (b) higher band.

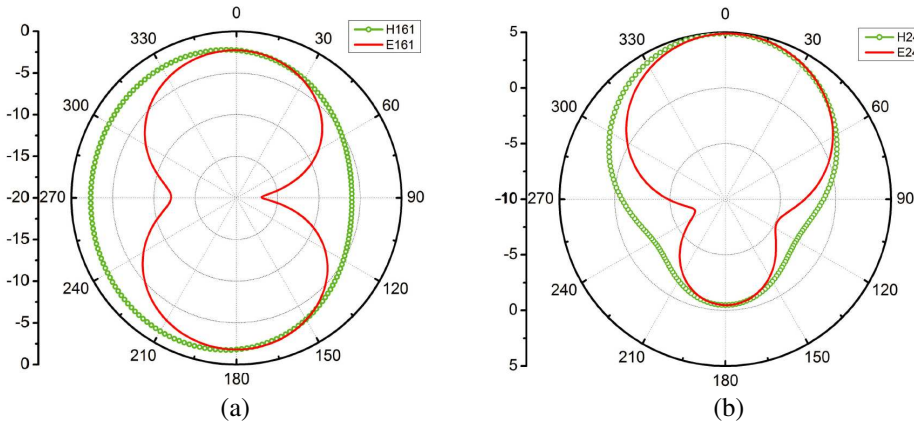


Figure 5: The simulated radiation patterns at (a) lower band and (b) higher band for different values of L_{cs} .

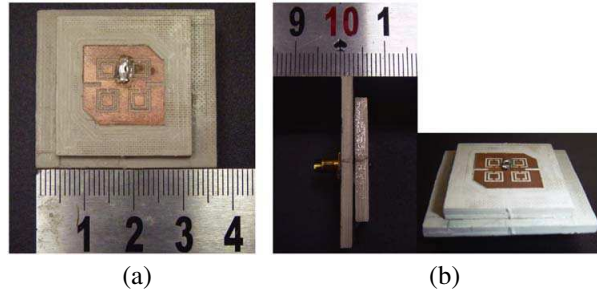


Figure 6: The photograph of the fabricated antenna with (a) top view and (b) side view.

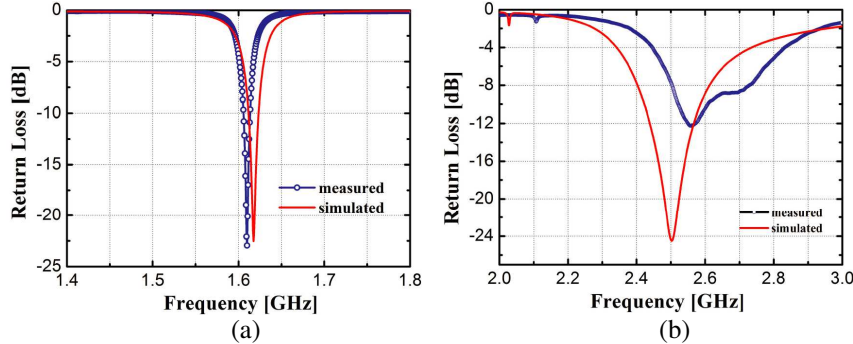


Figure 7: The measured and simulated return losses at (a) lower band and (b) higher band.

1.615 GHz, and the higher band has a -10 dB bandwidth of 87 MHz from 2.521 GHz to 2.608 GHz. Moreover, it can be found that the measured data are greatly lower than the simulated data at the higher band, which is caused by the CSRR structure too fine to be implemented using mechanical engraving and the base materials loss, while there is a little shift between the similar curves of the measured and simulated at the lower band. It may result from the inaccuracy of implementing.

4. CONCLUSION

This paper proposes a double-feed, dual-band circularly polarized microstrip antenna. The design of introduced CSRR array is optimized to reduce the size of the antenna and enhance the gain. By applying the corner cutting technique into the proposed antenna, good CP bandwidths could be acquired in all bands. Due to the stacked structure, the designed antenna can provide wider impedance bandwidths and higher gain for the higher band at 2.49 GHz. The antenna parameters are relatively independent and easy to tune for the miniaturization and gain improvement. Since it is not difficult to fabricate the proposed antenna based on ceramic substrates with total dimension of only 36 mm \times 33 mm \times 6 mm, it is a potential candidate for the terminal application in Beidou navigation systems.

ACKNOWLEDGMENT

This work is supported by Fujian Provincial Key Sci-Tech Project (2010HZ0004-1) of China.

REFERENCES

- Doust, E. G., M. Clenet, V. Hemmati, et al., "An aperture-coupled circularly polarized stacked microstrip antenna for GPS frequency bands L1, L2, and L5," *IEEE Trans. Antennas and Propagation Society International Symposium*, 1–4, 2008.
- Falcone, F., T. Lopetegi, J. D. Baena, et al., "Babinet principle applied to the design of metasurfaces and metamaterials," *Phys. Rev. Lett.*, Vol. 93, No. 19, 197–201, 2004.
- Falcone, F., T. Lopetegi, J. D. Baena, et al., "Effective negative- ϵ stop-band microstrip lines based on complementary split-ring resonators," *IEEE Microwave Wireless Compon. Lett.*, Vol. 14, No. 6, 280–282, 2004.
- Baena, J. D., J. Bonache, F. Martín, et al., "Equivalent-circuit models for split-ring resonators and complementary split-ring resonators coupled to planar transmission lines," *Microwave Theory and Techniques*, Vol. 53, No. 4, 1451–1461, 2005.

5. Zhang, H., Y.-Q. Li, X. Chen, Y.-Q. Fu, et al., “Design of circular polarisation microstrip patch antennas with complementary split ring resonator,” *IET Microwaves, Antennas & Propagation*, Vol. 3, No. 8, 1186–1190, 2009.
6. Li, W. T., Y. Q. Hei, W. Feng, et al., “Planar antenna for 3G/bluetooth/WiMAX and UWB applications with dual band-notched characteristics,” *IEEE Antennas and Wireless Propagation Letters*, Vol. 11, 61–64, 2012.
7. Jiang, D., Y. Xu, R. Xu, et al., “Compact dual-band-notched UWB planar monopole antenna with modified CSRR,” *Electronics Letters*, Vol. 48, 1250–1252, 2012.
8. Kim, J.-Y., N. Kim, S. Lee, et al., “Triple band-notched UWB monopole antenna with two resonator structures,” *Microwave and Optical Technology Letters*, Vol. 5, No. 1, 4–6, 2013.
9. Oh, J.-H., Y.-P. Hong, and J.-G. Yook, “Dual circularly-polarized stacked patch antenna for GPS/SDMB,” *IEEE Antennas and Propagation Society International Symposium*, 1–4, 2008.
10. Duran-Sindreu, M., J. Naqui, J. Bonache, et al., “Split rings for metamaterial and microwave circuit design: A review of recent developments,” *International Journal of RF and Microwave Computer-aided Engineering*, Vol. 22, No. 4, 439–458, 2012.

Single Layer Cylindrical Frequency Selective Structures for Radome Applications

E. Di Salvo, F. Frezza, E. Stoja, and N. Tedeschi

Department of Information Engineering, Electronics and Telecommunications
Sapienza University of Rome, Via Eudossiana 18, Rome 00184, Italy

Abstract— An analysis method is proposed for Cylindrical Frequency Selective Surfaces (CFSS), at microwave wavelength, particularly useful for antenna radome applications. The structures are made by conducting rectangular patches or slots, conformed to a cylindrical surface. Appropriate relations are employed to analyze, in particular, structures with many elements. The opacity or transparency of the surfaces for a suitable frequency range in terms of transmission/reflection coefficients is computed. Comparisons with previous results given in the literature and with data obtained through Electromagnetic Simulators have been performed.

1. INTRODUCTION

With the name of Frequency Selective Surfaces (FSS) are commonly indicated some particular resonant structures composed by metallic array elements (“patch”), and/or openings (“slot”) on metal sheets. Basically FSSs are filters designed to show, when lighted by an incident wave, some transmission and reflection properties at different frequency values. FSS have been an extensive research topic since a long time [1, 2] but the case of Cylindrical Frequency Selective Surfaces (CFSS), which may be of interest for curved surfaces and in particular for antenna radome applications, has been less studied in the literature [3, 4]. In the present paper an analysis technique is explained, particularly useful for structures with many circumferential constitutive elements.

2. ANALYSIS METHOD EMPLOYED

Figure 1 shows the infinitely long cylindrical structure we have considered. It may consist of free-standing lossless conducting rectangular patches, or of a perfectly conducting circular cylinder perforated with axial slots. Patches or slots are located periodically along the circumferential direction ϕ (T_ϕ periodicity) and along the axial direction z (T_z periodicity). Because of bidirectional periodicity, the scattered fields are computed by analyzing the unit cell shown in Figure 1(b). Moreover it is assumed $w < l/10$ and $w < \lambda/20$ where λ is the wavelength of the incident field.

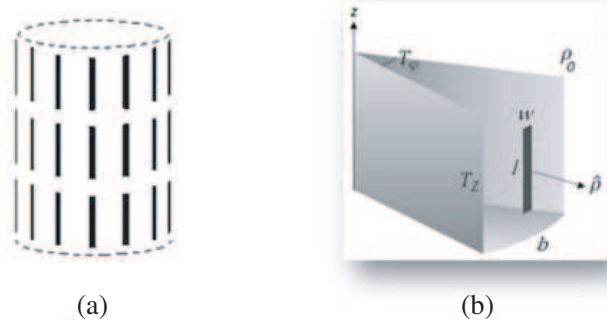


Figure 1: (a) Cylindrical Frequency Selective Surface, made by conducting patches or slots; (b) relevant unit cell parameters.

For the case of free-standing conducting patches, a cylindrical wave with TM polarization ($E_\phi = 0$; $H_z = 0$), generated by an electric line current located on the cylinder axis, is considered:

$$\mathbf{I} = \hat{z} I_0 e^{-i\beta_0 z} \quad (1)$$

in which β_0 denotes a linear phase variation along the z axis and I_0 is the current amplitude. With the above written hypotheses the ϕ component of the electric surface current is considered

constant: consequently, only the z component of the scattered electric field and the ϕ component of the scattered magnetic field are taken into account.

Being the structure under consideration periodical along ϕ and the z axis, the scattered fields are expressed as infinite sums of cylindrical Floquet modes. The amplitude coefficients of the cylindrical waves composing the scattered field are function of the surface current induced on the conducting patch. This relation is found applying the boundary conditions on the tangential component of the electric field, that should be continuous at $\rho = \rho_0$, and on the tangential component of the magnetic field, that should be discontinuous at $\rho = \rho_0$ by an amount equal to the induced current density J_z . Finally, equating the total tangential electric field to zero on a strip surface, an integral equation is obtained, where the unknown quantity is the current distribution. This integral equation may be solved numerically by using a method of moments technique. To obtain a numerical solution, the current is expanded into seven entire domain sinusoidal basis functions for narrow strips.

For the case of free-standing slots, a cylindrical wave with TE polarization ($E_z = 0$; $H_\phi = 0$) generated by a magnetic line current located on the cylinder axis is considered:

$$\mathbf{M} = \hat{z} M_0 e^{-i\beta_0 z} \quad (2)$$

in which β_0 denotes a linear phase variation along the z axis and M_0 is the magnetic current amplitude.

The slot size is the same as for the patch case and the conclusions for the field components are dual, that is only the z component of the scattered magnetic field and the ϕ component of the

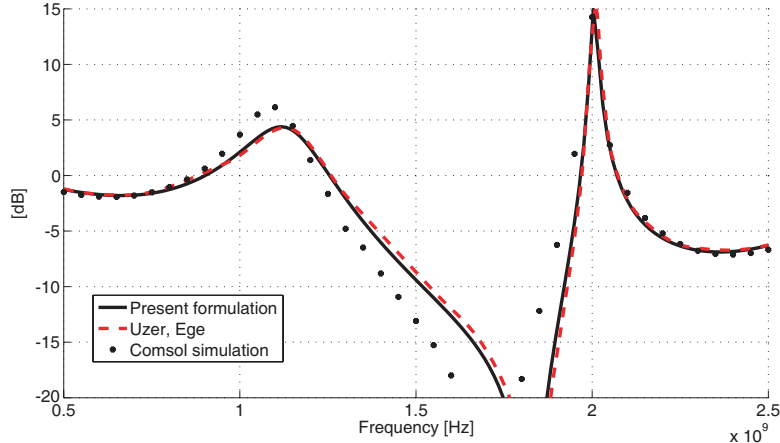


Figure 2: Ratio (dB) between radiated power measured away from the electric line current, with and without the CFSS, with $N = 16$ circumferential patches. Unit cell parameters: $b = 50$ mm, $T_z = 100$ mm, $l = 90$ mm, $w = 4$ mm.

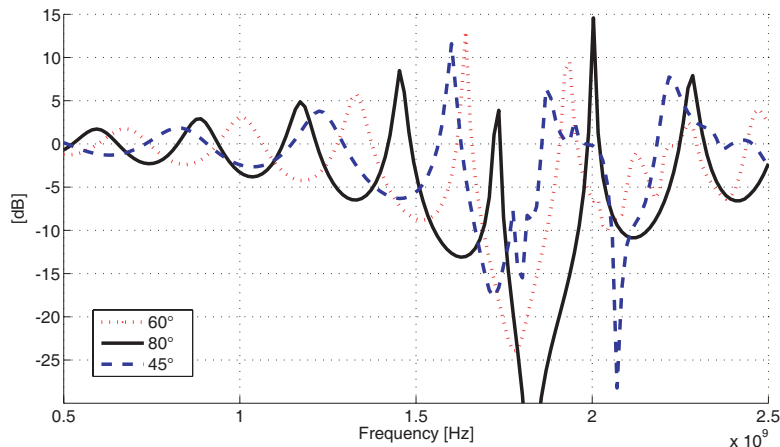


Figure 3: Ratio (dB) between radiated power measured on the cylinder axis with and without the CFSS, with $N = 64$ circumferential patches varying the incident angle. Unit cell parameters: $b = 50$ mm, $T_z = 100$ mm, $l = 90$ mm, $w = 4$ mm.

scattered electric field are taken into account. For the numerical solution, the electric slot field is expanded into seven entire domain sinusoidal basis functions. Scattered fields are calculated according to the procedure described in [4] but we have extended this formulation for structures with a larger number of circumferential patches/slots (e.g., more than 64).

This improvement has been achieved using for Bessel-Hankel functions calculation:

- high order/high argument approximated expressions [5, 6].
- recurrence relations in conjunction with Millers algorithm [5], to maintain numerical stability and to avoid overflow and underflow problems due to large-order and large-argument Bessel functions calculation.

3. NUMERICAL RESULTS

Figure 2 shows a comparison between a plot in [4] and our results achieved: with a Matlab code implementing our formulation; with the commercial simulation tool COMSOL Multiphysics.

Figure 3 has been obtained with our formulation and shows the effect of changing the incident angle when a radiating electric line current is located far away from the CFSS. Resonance degradation is highlighted moving from the condition of normal incidence. This is due to the smaller induced current on the metallic patches. In both the figures we can see that near $l = 0.5\lambda$ the CFSS does not allow the power to flow out or to seep into.

The plots in Figure 4 and in Figure 5 are related to a conducting cylinder periodically drilled with axial slots. On the cylinder axis is located a magnetic line current that generates a cylindrical

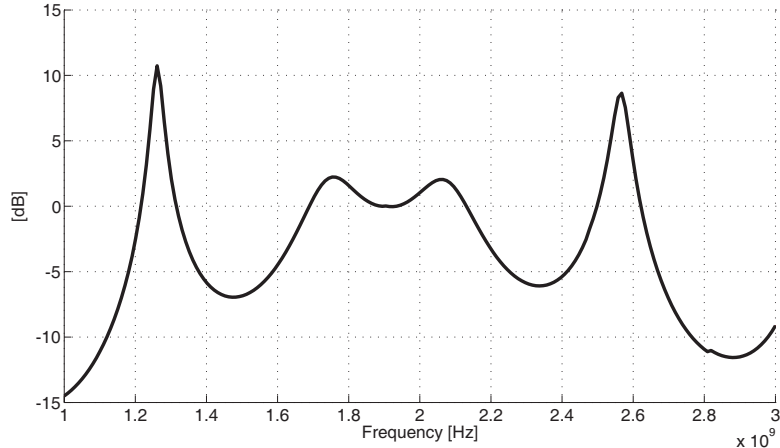


Figure 4: Ratio (dB) between longitudinal magnetic field measured away from the magnetic line current, with and without the CFSS, with $N = 32$ slots. Unit cell parameters: $b = 50$ mm, $T_z = 100$ mm, $l = 90$ mm, $w = 4$ mm.

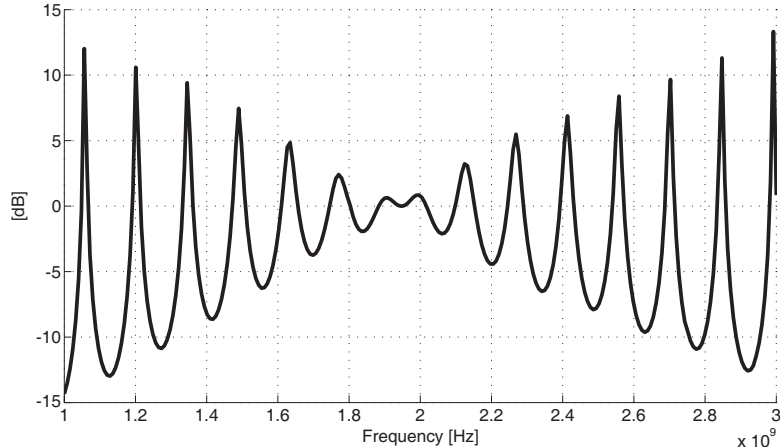


Figure 5: Same as Figure 4 for $N = 128$ circumferential slots.

wave TE polarized. Near $l = 0.6\lambda$ the CFSSs allows the whole longitudinal magnetic field to flow out.

4. CONCLUSION

The described technique is able to analyze cylindrical frequency selective structures with a large number of elements, useful for antenna radomes. Further developments may concern the application of the technique to different patch/slot geometries and to sandwiched structures.

REFERENCES

1. Vardaxoglou, J. C., *Frequency Selective Surfaces: Analysis and Design*, Wiley, New York, 1997.
2. Mittra, R., T. Cwik, and C. H. Chan, “Techniques for analyzing frequency selective surfaces,” *Proceedings of IEEE*, Vol. 76, No. 12, December 1988.
3. Cwik, T., “Coupling into and scattering from cylindrical structures covered periodically with metallic patches,” *IEEE Transactions on Antennas and Propagation*, Vol. 38, 220–226, February 1990.
4. User, A. and T. Ege, “Radiation from a current filament located inside a cylindrical frequency selective surface,” *ETRI Journal*, Vol. 26, No. 5, 481–485, October 2004.
5. Abramowitz, M. and I. A. Stegun (editors), *Handbook of Mathematical Functions: With Formulas, Graphs, and Mathematical Tables*, Dover, New York, 1972.
6. Watson, G. N., *A Treatise on the Theory of Bessel Functions*, Cambridge University Press, London, 1962.

Comparison between Two Methods for Directivity Enhancement of Antennas through 2-D EBGs

S. Ceccuzzi, L. Pajewski, C. Ponti, and G. Schettini

Department of Engineering, "Roma Tre" University, Roma, Italy

Abstract— Among the uses of Electromagnetic Band-Gap (EBG) materials to enhance the directivity of single radiators, thus avoiding the use of complex arrays relying on troublesome feeding networks, two methods are particularly effective. One realizes a resonator antenna by sandwiching the radiator in between a ground plane and an EBG material working in the band-gap, while the other embeds it inside an EBG structure working at the edge of the band-gap. In the former case a cavity is created and the periodically spaced elements act as a partially reflecting surface, while in the latter configuration, the EBG structure behaves like an epsilon near zero material and can generate equi-phase wavefronts at its boundaries. This paper pushes forward a benchmark between the two approaches by comparing their performance for a set of two-dimensional EBG structures, consisting of either triangular or square arrangements of dielectric cylinders, excited by a 8 GHz, TM-polarized, line source. Different finite-size configurations, obtained by changing the number of layers as well as the amount of cylinders per layer, are optimized with a full-wave solver. The resonator antenna generally gives the highest directivities, but there are operative conditions in which it is outperformed by the method with embedded source. In details, the former approach results more suitable in case of low-profile arrangements, i.e., very few layers with many rods, while the latter one better fits compact configurations, having more layers with few cylinders. The radiation patterns of the most attractive configurations are reported together with a discussion about the strengths and weaknesses of the methods.

1. INTRODUCTION

Exactly like the periodic spatial distributions of electrostatic potential can affect and control the motion of electrons, materials featuring spatially periodic electromagnetic properties offer the possibility to control photons, i.e., the light. In this sense, one of the most surprising phenomena (known since 1887 and explained in terms of multiple reflection) is the existence of band-gaps where wave propagation is forbidden; for this reason structures exhibiting such a behaviour at microwave frequencies are often called Electromagnetic Band-Gap (EBG) materials [1].

In the last three decades EBG materials received considerable attention and their use was proposed in a wide variety of applications as components in the microwave and millimeter wave devices (e.g., shields, filters, waveguides, etc.), as well as in antennas [2]. Concerning the latters, EBG structures have been successfully employed in combination with several radiator types, e.g., printed [3], slot [4] or wire [5] antennas, with different roles such as ground plane or substrate, namely aiming at suppressing surface waves or at implementing ground planes with a proper phase reflection. Another profitable use of EBG materials with antennas is their ability of enhancing directive radiation by behaving like filters in the spectrum of wavevectors. In this sense periodic structures were mainly adopted as antenna cover to realize cavity resonator [6] and as hosting medium of the radiating source to embed it inside an epsilon near zero material [7].

Both methods are fairly documented in literature from theoretical and experimental viewpoint [8–10], but they have been rarely compared. We present a study of this kind for two-dimensional geometries. Square and triangular arrangements of dielectric rods are studied when excited by a thin current wire of infinite length, aligned with the cylinders axis. The advantages and limitations of the different mechanisms and lattices are analysed to understand the operational conditions they are more suitable for.

The first step to be performed is a preliminary design of the lattices; it is described in Section 2, taking the square lattice as example. The next step is the conversion of the periodic arrangements from infinite to finite extension: it implies the need to optimize every single configuration to make it deliver its best performance; these concepts are clarified in Section 3. Then results are compared and discussed in Section 4 and conclusions are given in Section 5.

2. LATTICE DESIGN

The field radiated by an infinitely long, cylindrical, current distribution in harmonic regime can be described with the product between an exponential term and a scalar function V , which is often

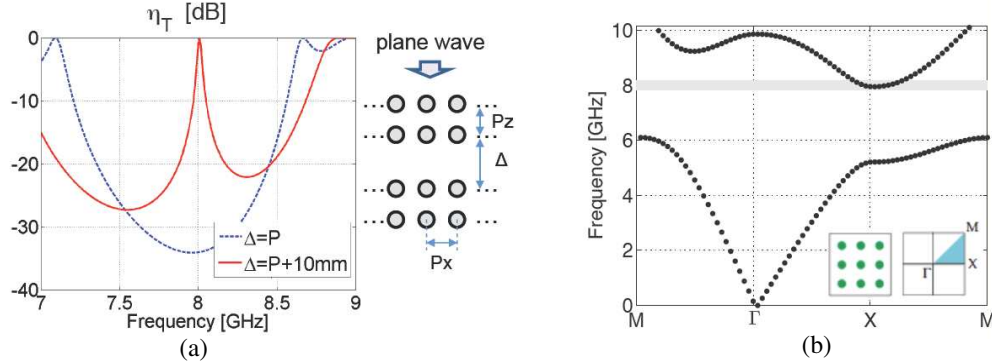


Figure 1: (a) Transmission efficiency vs. frequency of a square arrangement of dielectric rods in a vacuum with lattice periods $P_x = P_z = 24\text{ mm}$, rod diameter $d = 8.5\text{ mm}$ and relative permittivity $\epsilon_r = 9$. (b) Band diagram of a similar lattice with $P_x = P_z = 18\text{ mm}$, $d = 6.5\text{ mm}$ and $\epsilon_r = 9$.

expressed through a series expansion. In case of a source aligned with the y -axis, the former term is $e^{j(\omega t - k_y y)}$ and the latter one, being the y component of the E-field, only depends on the in-plane polar coordinates ρ and θ . More precisely, the radial dependence is described by Hankel functions and the azimuthal variation through exponential functions; the coefficients of the series expansion account for the wire radius a by means of Bessel functions of the first kind. For very thin wires, only the 0-th order of the Bessel functions holds, namely

$$V = \sum_n V_n(k_t a) H_n^{(2)}(k_t \rho) e^{jn\theta} \approx V_0 H_0^{(2)}(k_t \rho) \quad (1)$$

and the radiated field pattern in the H -plane becomes omnidirectional since the azimuthal dependence disappears. This pattern can be enhanced by means of two-dimensional EBG structures. In the present case, dielectric cylinders, aligned with the current wire (i.e., TM polarization) and arranged in either triangular or square lattices, have been employed. Their periodical distribution has been designed as required by the mechanisms to be compared, which, in the following, will be referred to as “cavity” and “embedded source” method.

The former relies on an EBG working in the band-gap and a defect is introduced to generate a transmission peak inside the forbidden band. This behaviour can be clearly seen when studying the propagation of a plane wave across the structure and looking at the transmission efficiency η_T , i.e., the ratio between transmitted and incident power. The result for the square lattice is shown in Figure 1(a), where the simulated geometry is also sketched aside. The filtering performance of the EBG material can be finely adjusted through several techniques [11] so as to achieve, e.g., a 8 GHz bandpass behaviour for normal incidence. Here the cavity width has been used to this aim: in absence of defect, the structure holds its periodicity and the plane wave is totally reflected in the forbidden band (blue dashed curve), while by increasing the spacing of 10 mm, a transmission peak appears in the band-gap (solid red curve).

The second method adopts an EBG working at the edge of the band-gap, where only a particular mode of the crystal can propagate. The preliminary design is done using the band diagram; Figure 1(b) shows the dispersion plot of a square lattice as calculated with an in-house code based on the a Plane Wave Expansion (PWE) method [1]. Lattice parameters have been adjusted so that the lower edge of the second band falls at exactly 8 GHz. Under this condition the wave in the crystal is allowed to propagate only towards the “X” point of the irreducible Brillouin Zone. Due to the symmetry of the lattice, it means that the radiation pattern of such a structure shows four main lobes aligned with the x and y axes.

3. FINITE-SIZE GEOMETRIES

Real structures have finite dimensions and perfect electric conductors (PEC) must be used to keep only the desired lobe. So, to compare the two methods, lattices have been truncated, ground planes used and current wires inserted as shown in Figure 2. In the cavity method, the reflector breaks the structure in two identical halves: it is placed in the middle of the crystal defect. The source is located inside the cavity and the structure works like a resonator, while the EBG material acts as a partially reflecting surface. The source is at a quarter wavelength from the ground plane; anyway

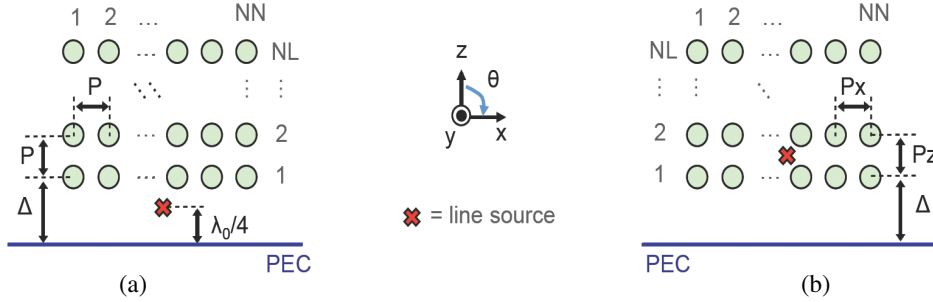


Figure 2: Finite-size geometries for (a) the configurations with the cavity and (b) the embedded source.

this spacing was found not to have much impact on the performances, provided that a minimum distance (about $\lambda_0/20$) is preserved. As far as the embedded source is concerned, the reflecting plane is simply leant behind the structure and the current wire is embedded in the crystal. Several full-wave simulations indicated as a good choice to place the source in between the first and the second layer of rods.

Finite dimensions slightly modify structure performance, for example detuning the cavity. In order to attain a meaningful comparison between the methods, each structure under consideration must be optimized. Several geometries with different number of layers (from 1 to 4) and rods per layer (from 4 to at least 20) have been studied; the optimization method was launched for each of them. Since a preliminary design has been already done, the assumption to be quite close to the optimum configuration is reasonable and a local optimization algorithm should be enough for the present purpose. With reference to the cavity, the distance between the ground plane and the first layer of cylinders has been optimized because performances are very sensitive to the cavity width. Concerning the embedded source method, the most sensitive parameters are the lattice periods (the distances between two adjacent cylinders in horizontal and vertical direction), so the optimization was done with respect to them. All computations have been performed with a full-wave software (CST Microwave Studio) using one of its local optimizers.

4. RESULTS

The results for the square arrangement is given in Figure 3 in terms of maximum in-plane directivity, which is calculated in two dimensions, so that an isolated line source achieves 0 dB. In the present case, directivity corresponds to antenna gain since ideal conditions have been assumed; nevertheless, when this approximation is removed, besides the finite conductivity of the radiator, a small imaginary part of the rod permittivity must be considered too. The number of cylinders, namely of lossy dielectrics, becomes therefore a fundamental parameter since it is tightly related to the structure efficiency.

As a term of comparison, it must be said that the directivity of a current wire without cylinders, but with a reflector, is 4.9 dB. As far as the cavity is concerned, the green and red curves start at respectively 8 and 12 rods per layers: results at lower values are not shown because the maximum directivity is not in broadside direction. Layers number (NL) in the cavity method has been limited to 3 since the larger NL, the sharper the transmission peak of the cavity, making device tuning difficult.

By comparing the curves with the same number of layers, like c2 with e2 or c3 with e3, it stands out that:

- the cavity method achieves the highest performances. For a low number of cylinders per layer (NN) it is worse, but at higher abscissa values it overpasses the method with the embedded source;
- at lower number of cylinders per layer, the current wire embedded in the EBG material gives the best results, but when NN is increased, the directivity seems to saturate quite soon.

Everything was repeated for triangular lattices. The relevant results led to similar conclusions with the peculiarity that the triangular arrangement is slightly more favourable to the method of the embedded source. For a directivity enhancement of about 9 dB, the cavity requires indeed at least two layers of rods; furthermore, provided that $NN < 12$, the mechanism with the embedded source is definitely better than the other.

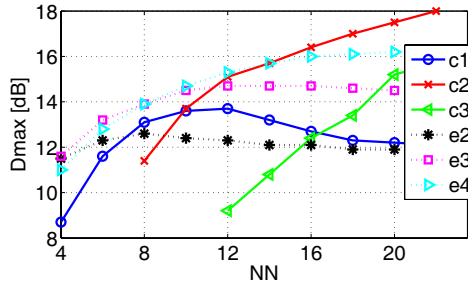


Figure 3: Maximum directivity vs. the number of rods per layer for square lattices. Curve acronyms are in the form of a letter plus a number, which respectively represent used method (c = cavity, e = embedded source) and number of layers (NL).

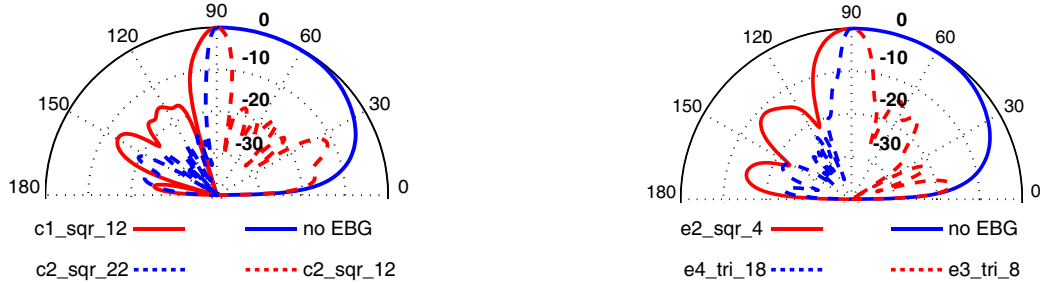


Figure 4: H -plane radiation patterns for some selected configurations. Legend reads as before and the last two new fields stand for lattice type (sqr = square, tri = triangular) and number of cylinders per layer (NL).

In general, given a number of layers, all geometries have an optimal value of NN , above which the directivity keeps constant or presents very little variation. Keeping this in mind and looking at the full set of results, a selection of the configurations exhibiting the best trade-off between radiation performances and geometrical parameters (i.e., size and number of scatterers) has been carried out. The radiation patterns of such configurations are plotted in Figure 4; the pattern of a current wire with a ground plane (blue solid curve) is also shown to get a better picture. The EBG structures clearly modify the radiation pattern, making it more directive. Due to the symmetry only half of the pattern is shown: on the left there are the cases pertaining to the cavity method, while on the right, the ones relevant to the embedded source method.

Finally, concerning a possible extension of the methods to a dual band behaviour, the cavity concept seems to be more favourable from a preliminary analysis. New transmission peaks can be indeed obtained by playing with defects; on the contrary, with the embedded source method, it is rather difficult to find suitable band-gap edges at different frequencies and to properly excite the corresponding modes.

5. CONCLUSION AND PERSPECTIVES

Two methods to improve the directivity of line sources by means of two-dimensional EBG structures have been compared. They use square or triangular arrangements of dielectric rods in a vacuum as superstrate or hosting medium.

The first mechanism (cavity) results the most suitable for low profile structures, while the second one (embedded source) is attractive for more compact, i.e., taller but less extended structures. When many rods per layer are employed, the cavity method outranks the radiation performance of the other method. Future developments of the present work could be a systematic benchmark between dual band structures and an extension to three-dimensional geometries.

REFERENCES

1. Joannopoulos, J. D., R. D. Meade, and J. N. Winn, *Photonic Crystals: Molding the Flow of Light*, Princeton University Press, Princeton, 1995.
2. de Maagt, P., R. Gonzalo, Y. C. Vardaxoglou, and J.-M. Baracco, “Electromagnetic bandgap antennas and components for microwave and (sub)millimeter wave applications,” *IEEE Trans. Antennas Propag.*, Vol. 51, No. 10, 2667–2677, 2003.

3. Brown, E. R., C. D. Parker, and E. Yablonovitch, "Radiation properties of a planar antenna on a photonic-crystal substrate," *J. Opt. Soc. Am. B*, Vol. 10, No. 2, 404–407, 1993.
4. Leung, W. Y., R. Biswas, S. D. Cheng, M. M. Sigalas, J. S. McCalmont, G. Tuttle, and K. M. Ho, "Slot antennas on photonic band gap crystals," *IEEE Trans. Antennas Propag.*, Vol. 45, No. 8, 1569–1570, 1997.
5. Yang, F. and Y. Rahmat-Samii, "Reflection phase characterizations of the EBG ground plane for low profile wire antenna applications," *IEEE Trans. Antennas Propag.*, Vol. 51, No. 10, 2691–2703, 2003.
6. Thévenot, M., C. Cheype, A. Reineix, and B. Jecko, "Directive photonic-bandgap antennas," *IEEE Trans. Microwave Theory Tech.*, Vol. 47, No. 11, 2115–2122, 1999.
7. Enoch, S., G. Tayeb, and D. Maystre, "Dispersion diagrams of Bloch modes applied to the design of directive sources," *Progress In Electromagnetics Research*, Vol. 37, 61–81, 2002.
8. Cheype, C., C. Serier, M. Thévenot, T. Monèdier, A. Reineix, and B. Jecko, "An electromagnetic bandgap resonator antenna," *IEEE Trans. Antennas Propag.*, Vol. 50, No. 9, 1285–1290, 2002.
9. Enoch, S., G. Tayeb, P. Sabouroux, N. Guérin, and P. Vincent, "A metamaterial for directive emission," *Phys. Rev. Lett.*, Vol. 89, No. 21, 213902-1–213902-4, 2002.
10. Frezza, F., L. Pajewski, E. Piuzzi, C. Ponti, and G. Schettini, "Analysis and experimental characterization of an alumina woodpile-covered planar antenna," *Proceedings of the 40th European Microwave Conference (EuMC)*, 200–203, Paris, France, September–October 2010.
11. Frezza, F., L. Pajewski, and G. Schettini, "Periodic defects in 2D-PBG materials: Full-wave analysis and design," *IEEE Trans. on Nanotechnology*, Vol. 2, No. 3, 126–134, 2003.

Manufacturing and Applications of Screen-printed RFID Tags on Paper Substrate

Johanna Virkki¹, Toni Björninens¹, Sari Merilampi², Lauri Sydänheimo¹, and Leena Ukkonen¹

¹Department of Electronics and Communications Engineering
Tampere University of Technology, P. O. Box 692, Tampere 33101, Finland

²Faculty of Technology and Maritime Management
Satakunta University of Applied Sciences, Tekniikantie 2, Pori 28600, Finland

Abstract— We manufactured quarter-wave dipole antennas for passive UHF RFID tags by screen printing polymer thick film silver ink on paper. The performance of the fully assembled tags was evaluated in threshold power measurements. The associated uncertainty was assessed based on the hardware specification and variability in repeated measurements. In free-space, the tag achieved the peak read range of 9.5 m at 960 MHz, referred to the emission limit EIRP = 4 W. When embedded in a stack of books, the read range higher than 2.5 meters within the frequency range of 800–1000 MHz was measured all around the stack. This performance is without a doubt sufficient for the applications of paper-based tags in packaging industry, libraries, and postal services, for instance.

1. INTRODUCTION

Radio-frequency identification is an automatic identification technology. RFID systems consist of tags, reader(s), and a background system. Tags are attached or embedded in the objects that are to be identified or tracked. Passive tags are composed of an antenna and a microchip containing the identification data which can be read and modified remotely. They do not contain an on-board energy source, but are remotely powered by the reader. The use of propagating electromagnetic waves to power and communicate with the tags enables the rapid identification of a large number of items from the distances of several meters. Identification can be done through most of the everyday materials, excluding good conductors. To enable ultra-low-power operation, data transmission from the tags to the reader is based on communication by means of reflected power [1].

Paper is ubiquitous in everyday life and a truly environmental-friendly and low-cost material. Hence it is a fit platform for RFID tags. However, applying electronics on paper is challenging [2]. The paper surface is not only very rough compared to plastics, but is also porous. This is detrimental for most electronic devices manufactured directly on paper, but there are approaches, such as screen-printing, which are compatible with the rough and absorptive paper surface [2–4]. In this work, we present screen-printed antennas for passive ISO 18000-6 compliant RFID tags operating in the regionally regulated sub-bands of the 860–960 MHz frequency range. We fabricated the antennas by screen-printing polymer thick film silver ink on paper.

2. EFFECT OF PAPER SUBSTRATE ON TAG PERFORMANCE

Generally the dielectric substrate affects the tag performance through its electrical properties such loss tangent and relative permittivity. Porous substrates like paper also have an indirect effect on the tag through the ink film morphology. Morphology of a printed film depends on the printing method, substrate, and composition of the ink. On porous substrates, the ink is partially absorbed into the substrate and the average thickness of the printed film depends thus on the substrate material. The cross-section area of the conductive film is an important parameter determining the effective conductivity of the printed pattern that affects the electrical performance of films printed with conductive inks [5, 6].

The substrate material also interacts with electromagnetic fields. When insulating dielectric material is subjected to an electric field, a displacement of charge takes place at the atomic, molecular and bulk material levels. This phenomenon is known as polarization. Relative permittivity is a parameter that indicates the relative charge (energy) storage capability of the dielectric material. An ideal dielectric would release all the stored energy when the electric field is removed, but in practice dielectrics dissipate part of the energy as heat and free charge carriers cause ohmic loss when an electric field is applied. In addition, dielectric losses occur. In an electromagnetic wave the direction of the electric field vector changes. This causes the dipole molecules of the dielectric

medium to rotate and charged particles to displace according to the applied field vector. As the frequency increases, the inertia of the charged particles tends to prevent the particle displacements from keeping in phase with the field changes, leading to a frictional damping mechanism that causes power loss (dielectric losses) since work must be done to overcome the damping forces. The loss tangent is a measure of the conversion of the reactive power to the real power, expressed as heat. Some values for relative permittivity and loss tangent for paper are reported, e.g., in [7, 8].

3. FABRICATION OF RFID TAGS

In this study, the tags were manufactured by screen printing polymer thick film silver ink, mainly consisting of silver particles mixed in polyester resin (particle sizes of 3-to-15 μm), on the paper substrate. Plain copy paper (80 g/m^2) was used as the substrate material. After printing, the tags were sintered in an oven (120°C , 20 min). The tag geometry (a) and the sintered ink layer on a paper substrate (b) are shown in Figure 1. After printing and curing, NXP UCODE G2iL ICs were attached to the samples using a conductive silver epoxy resin.

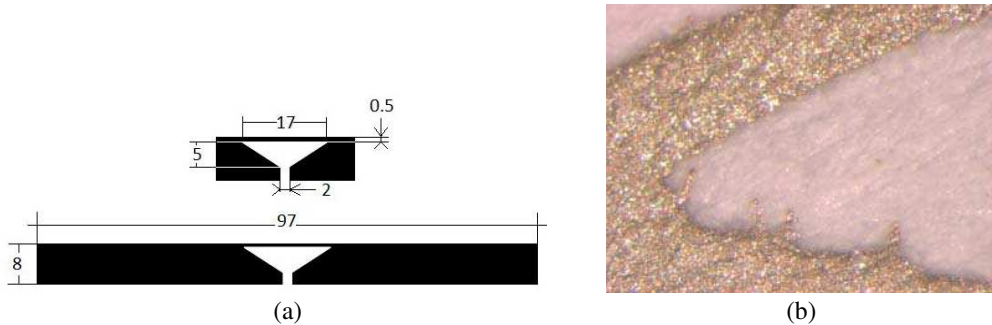


Figure 1: (a) Studied antenna (dimensions in millimetres), (b) sintered antenna on a paper substrate (magnification X57).

4. MEASUREMENTS

We characterized the tags by recording the minimum of the transmitted carrier power (threshold power), which enabled a valid response from the tag under test to ISO 18000-C6 ‘query’ command. The tag responds to this command with its identification code. The measurement can be done with readers with adjustable output power and RFID testers [9]. We conducted the measurement with Voyantic Tagformance measurement system. The measurement setup can be seen in Figure 2.

First, we measured 4 sample tags in free-space. Second, we chose one sample tag and measured it inside a 0.8 cm thick book. Next, this sample tag was measured so that it was next to another book with a tag inside. This was then repeated with a stack of two and three added books with tags inside. This was done to simulate a situation where several books with tags may lie in close proximity, e.g., in a bookshelf. As tags are brought closer to one another, their operation characteristics can alter significantly [10]. Finally, the radiation patterns for all these book stack combinations were measured.

First, we characterized the wireless measurement channel in terms of the measured power loss factor (L_{iso}) from the generator’s output port to the input port of an equivalent polarization-matched isotropic antenna placed at a reference location. We computed L_{iso} as

$$L_{iso} = \frac{\Lambda}{P_{th*}} \quad (1)$$

where Λ is a known constant describing the sensitivity of the reference tag and P_{th*} is the measured threshold power of the reference tag in polarization-matched configuration. Using this information, we obtained the power density generated at the reference location with an arbitrary generator output power P_{tx} :

$$S_{inc} = \frac{L_{iso} P_{tx}}{\lambda^2 / 4\pi} = \frac{4\pi\Lambda}{\lambda^2 P_{th*}} P_{tx} \quad (2)$$

In particular, during the threshold measurement of the tag under test, Equation (2) gives the threshold power density $S_{inc,th}$ corresponding to $P_{tx} = P_{th}$. In this formulation P_{th} implicitly

includes the possible polarization mismatch power loss. However, in the measurement, we used a linearly polarized transmit-antenna aligned for polarization matching with the measured dipole tags.

On the other hand, in free space conditions, at the critical transmit-antenna — tag separation: $d = d_{tag}$, the power delivered to the tag IC equals the wake-up power of the chip. Correspondingly, the incident power density is equal to the threshold power density. Thus,

$$\frac{EIRP}{4\pi d_{tag}^2} = \frac{4\pi\Lambda}{\lambda^2 P_{th^*}} P_{th} = S_{inc,th}, \quad (3)$$

where $EIRP$ is the regionally regulated equivalent isotropically radiated power. This implies

$$d_{tag}(P_{th}, P_{th^*}) = \sqrt{\frac{EIRP}{4\pi S_{inc,th}}} = \frac{\lambda}{4\pi} \sqrt{\frac{EIRP}{\Lambda} \frac{P_{th^*}}{P_{th}}}, \quad (4)$$

which is a fully measurement based estimate of the theoretical read range of the tag. In practice, the properties of the transmit-antenna — tag wireless channel vary from site to site. Thus, in order to provide a universal characterization, we chose to evaluate the tags in terms of the theoretical read range. All the measurement results presented below were obtained following the emission regulation: $EIRP = 4$ W.

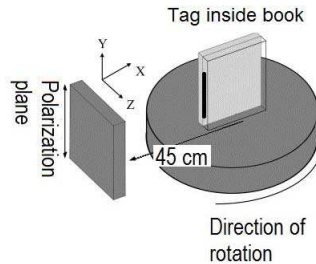


Figure 2: The measurement setup.

To assess the measurement uncertainty, we considered both static and dynamic variations. Firstly, we computed the bounds for $d_{tag}(P_{th}, P_{th^*})$ under the maximum variability of $-0.09\dots+0.14$ dB in the output power of the measurement device in the 800–1000 MHz range during the measurement of P_{th} and P_{th^*} . This device-specific information was provided by the manufacturer based on output power calibration. In addition, from 20 repeated measurements, we computed the sample averages and sample standard deviations (μ, U) and (ν, V) of P_{th} and P_{th^*} , respectively, to estimate the expectation and standard deviation of the governing probability distribution. To estimate how the measurement uncertainty propagates from the measured quantities P_{th} and P_{th^*} to the theoretical read range through the non-linear Equation (4), we linearized it in the neighborhood of the measured sample averages using the first order Taylor Expansion. As a result, we obtained the first order approximations

$$d_{tag}(\mu, \nu) \quad \text{and} \quad \frac{d_{tag}(\mu, \nu)}{2} \sqrt{\frac{U^2}{\mu^2} + \frac{V^2}{\nu^2}} \quad (5)$$

of the expectation of and standard deviation in $d_{tag}(P_{th}, P_{th^*})$, respectively.

5. RESULTS

Figure 3 shows the results for all 4 sample tags, measured in free-space. According to these measurement results, there is little variation in the performance among the tested tag samples. Furthermore, the maximum read range of the tags is almost 10 meters (at 960 MHz). Read ranges of 4-to-10 meters were measured throughout the global UHF RFID band.

Figure 4(a) shows the results from measurements where one sample tag is (a) in free-space, (b) inside a 0.8 cm thick book, (c) inside a book next to another book with a tag inside, (d) inside a

book next to two books with tags inside, and (e) inside a book next to three books with tags inside. Figure 4(b) shows the radiation patterns for all these combinations. When the tag was measured inside a book, the point of optimal impedance matching shifted to a lower frequency compared to measurements in free-space. Thus, also the maximum read range shifted from 960 MHz to 890 MHz. When one, two, or three books are added around the measured book, the maximum read ranges are dropped from 10 meters to 5, 4, and 3 meters, respectively. According to Figure 4(b), adding other books around the measured book shortens the read range of the tag from all directions. However,

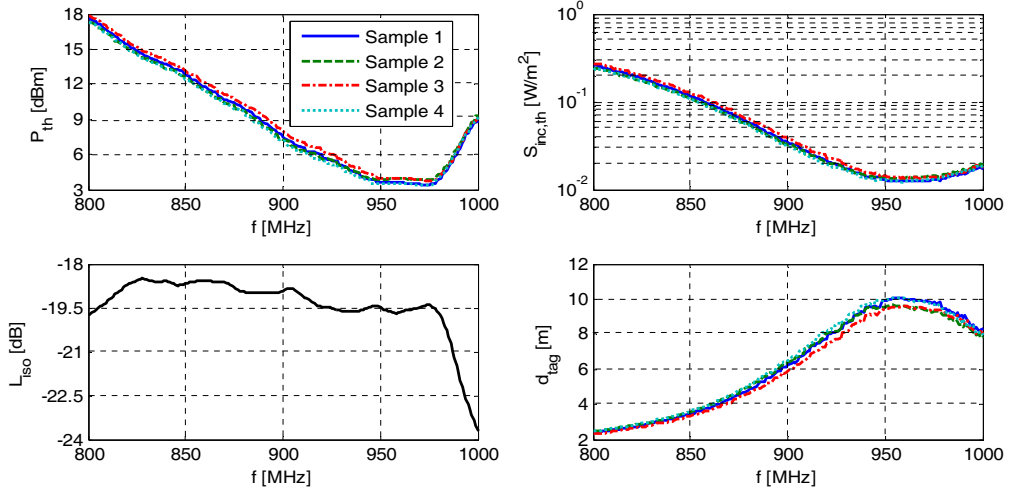


Figure 3: Measurement results for all 4 sample tags in free-space.

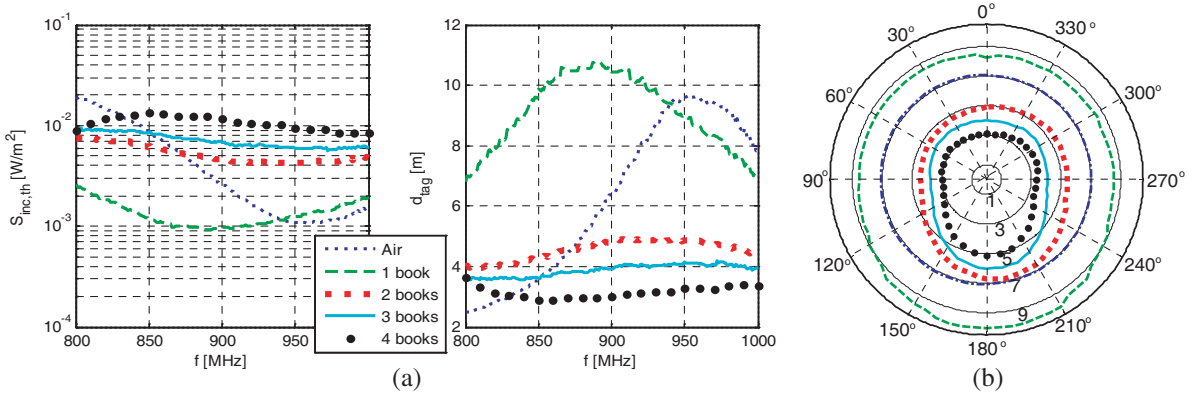


Figure 4: (a) Measurement results and (b) radiation pattern results from different combinations.

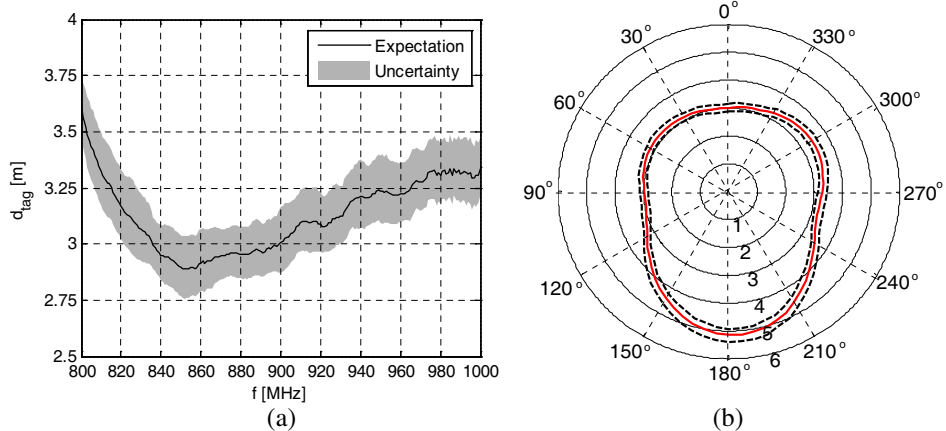


Figure 5: A tag inside a book next to three other books; (a) theoretical read range and (b) radiation pattern with uncertainty represented with the dashed lines.

the tag is readable from the distance of approximately 3 meters from all directions, even when surrounded by three other books with tags inside.

Figure 5 shows the theoretical read range of a tag inside a book next to three other books that have tags inside. In Figure 5, the static and dynamic variations in measurements are considered as uncertainty in presented results. As can be seen, the difference between the upper and lower uncertainty limit is approximately 30 cm.

6. CONCLUSION

Paper is ubiquitous in everyday life and it offers a huge potential when used as an environmental-friendly, low-cost substrate for electronics. In this study, UHF RFID tags were fabricated by screen printing polymer thick film ink on paper substrates. These tags offer a great potential, e.g., for packaging industry, libraries, and postal services. Our experimental results showed that the performance of the paper-based tags is sufficient for such field applications.

REFERENCES

1. Stockman, H., "Communication by means of reflected power," *Proceedings of the IRE*, Vol. 36, No. 10, 1196–1204, 1948.
2. Tobjörk, D. and R. Österbacka, "Paper electronics," *Advanced Materials*, Vol. 23, No. 17, 1935–1961, 2011.
3. Blayo, A. and B. Pineaux, "Printing processes and their potential for RFID printing," *Conference on Smart Objects and Ambient Intelligence: Innovative Context-aware Services: Usages and Technologies*, 2005.
4. Shaker, G., S. Safavi-Naeini, N. Sangary, and M. M. Tentzeris, "Inkjet printing of ultrawideband (UWB) antennas on paper-based substrates," *IEEE Antennas and Wireless Propagation Letters*, Vol. 10, 111–114, 2011.
5. Merilampi, S., T. Björninen, A. Vuorimäki, L. Ukkonen, P. Ruuskanen, and L. Sydänheimo, "The effect of conductive ink layer thickness on the functioning of printed UHF RFID antennas," *IEEE Special Issue, RFID — A Unique Radio Innovation for the 21st Century, Proceedings of the IEEE*, Vol. 98, No. 9, 1610–1619, 2010.
6. Merilampi, S., T. Björninen, L. Ukkonen, P. Ruuskanen, and L. Sydänheimo, "Characterization of UHF RFID tags fabricated directly on convex surfaces by pad printing," *The International Journal of Advanced Manufacturing Technology*, Vol. 53, No. 5, 577–591, 2009.
7. Yang, L., A. Rida, R. Vyas, and M. M. Tentzeris, "RFID tag and RF structures on a paper substrate using inkjet-printing technology," *IEEE Transactions on Microwave Theory and Techniques*, Vol. 55, No. 12, 2894–2901, 2007.
8. Fraden, J., *Handbook of Modern Sensors — Physics, Designs and Applications*, 3rd Edition, Springer — Verlag, 2004.
9. Nikitin, P., K. V. S. Rao, and S. Lam, "UHF RFID tag characterization: Overview and state-of-the-art," *34th Antenna Measurement Techniques Association Symposium Digest*, 289–294, Bellevue, WA, USA, Oct. 21–26, 2012.
10. Lu, F., X. Chen, and T. T. Ye, "Performance analysis of stacked RFID tags," *IEEE International Conference on RFID*, 330–337, 2009.

Printable RFID Antenna with Embedded Sensor and Calibration Functions

**Y. Amin^{1,2}, R. K. Kanth³, P. Liljeberg³, A. Akram²,
Q. Chen¹, L.-R. Zheng¹, and H. Tenhunen^{1,3}**

¹iPack VINN Excellence Center, Royal Institute of Technology (KTH), Stockholm, Sweden

²Telecommunication Engineering Department, University of Engineering and Technology Taxila, Pakistan

³Turku Centre for Computer Science, University of Turku, Finland

Abstract— An RFID antenna with integrated humidity sensor and calibration functionality for wireless sensor network is proposed. The antenna is composed of series and shunt stubs for impedance matching and reliability for near-field communication. The innovative ladder contour structure plays the key role for humidity sensing, and sensor calibration. The quadrangular end-tip loading is employed to offer capacitance and stability for far-field communication. The prototypes of the antenna are fabricated and tested: antenna effectively senses the ambient humidity levels while demonstrating stable behavior for RFID communication. The antenna has a compact size of 1×10 cm for 902–928 MHz RFID band.

1. INTRODUCTION

RFID is an emerging and disruptive compact wireless technology for the identification of physical objects and is reckoned as an eminent candidate, for the realization of ubiquitous wireless sensor networks [1, 2]. The prima challenges which are presently hampering the effective RFID implementation are: cost, reliability, and environmental-friendliness that could countenance for the implementation of “green” and “robust” RFID solutions. The employment of additional RFID tags [1] or sensing material [3, 4] to develop a sensor module has extended the ambit of RFID practice in assorted segments of industrial applications. This concept gets “green” by integrating paper substrate with conductive ink [5], and multiple set of discrete components to accomplish RFID-enabled sensor tags [2]. These sensor based solutions either involve additional tag, sensing material or components in accession to RFID tag, which not only increases the overall size but also cost effectiveness is an issue. Furthermore, the capability of customizable calibration is a prime aspect for an efficient sensor-enabled solution [6].

In this paper, an RFID tag antenna which has incorporated humidity sensor functionality along with calibration mechanism due to distinctiveness of its structural behavior, is proposed. The sensor-enabled antenna is directly printed on paper substrate using state-of-the-art inkjet printing technology for realizing the eco-friendly and ultra-low cost wireless sensor network (WSN) module. The antenna has reduced profile that paves the way for small item-level tagging and monitoring. The effect of humidity on paper-based antenna characteristics along with other electromagnetic parameters is investigated to evaluate the antenna performance under realistic operating conditions. The proposed antenna exhibits wider operational bandwidth and extended read range while at the same time provides an additional degree of freedom for sensor calibration.

2. ANTENNA AS A SENSOR DESIGN

The antenna has to counter the dielectric variations of the substrate in a precise, controlled mode while demonstrating linear parametric change for realizing humidity sensor and its calibration relative to specified humidity levels without being undetected. Consequently, the antenna is composed of four classifiable elements which provide stability as well as variability in order to exhibit sensory and radiating physiognomies. The substrate adopted is Kodak photopaper of $250 \mu\text{m}$ thickness (280 gm/m^2) with dielectric permittivity of $\epsilon_r = 3.2$, and loss tangent $\tan \delta = 0.077$, characterized at $1 \text{ GHz}@25^\circ\text{C}$, and NXP UCODE G2XM RFID Al strap is selected, for instance the goal IC impedance at 915 MHz is $13.3 - j122 \Omega$ is preferred. However, the principle of operation for the proposed antenna is not IC dependent.

The novel progressive ladder contours (Figure 1) play the important role for customizing the sensor calibration by varying the lengths of $D-H$ segments. It is observed that the coupling between electromagnetic characteristics of the paper substrate and radiating elements is significantly aided by these contours. The coupling features and stabilized performance in the far-field region are

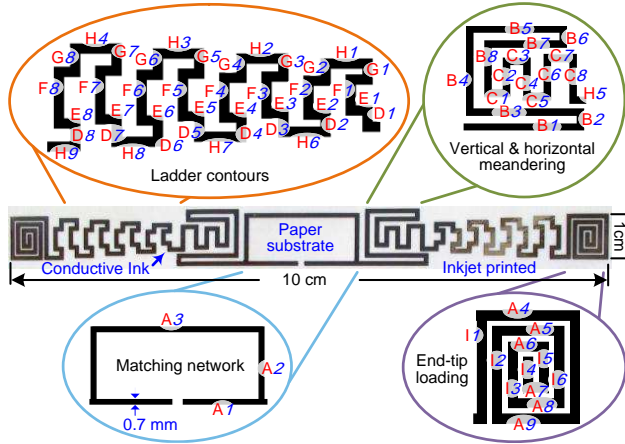


Figure 1: Geometry & structural components of RFID sensor antenna.

likewise alleviated by quadrangular end-tip loading by adjusting the length and spacing of segments from A_4 – A_9 & I . Moreover, the length of segments (B – C) forming the progressive & horizontal meandering structure is optimized to improve the input impedance matching in collaboration with series and shunt stubs (A_1 – A_3). The computer-aided design of the antenna is performed by using the commercial full-wave simulator ANSYS HFSS™.

3. FABRICATION PROCESS

The prototype antenna is directly printed on paper (Figure 1) by employing Dimatix DMP-2800 printer with silver nano particles based ink (CCI-300) by Cabot Corp., which contains 19–21% weight of nano-silver particles of less than 50 nm diameter. This ink is selected due to the large ratio of the area to volume of its nano particles which exhibit significantly lower melting point and provides steadiness against humidity effects. Three layers are printed (each of 600 nm thickness) by considering skin depth effect and sheet resistance [7]. After printing, the deposited ink is dried at room temperature and subsequently annealed in a ventilated thermal oven for two hours at 120°C. This aftermaths in conductivity of around 9×10^6 S/m (measured by deploying Four Probe Method along with Profilometer measurements). The dimensions of the proposed antenna are optimized (Table 1) and calibrated for measuring every 20% RH change.

Table 1: Dimensions of antenna for sensing every 20% RH change.

(mm)	A	B	C	D	E	F	G	H	I
1	9.50	12.1	2.42	0.40	1.85	2.8	0.39	3.55	6.30
2	8.40	0.70	2.22	0.46	1.85	3.0	0.46	3.55	5.25
3	18.8	11.0	2.60	0.53	1.85	3.2	0.53	3.50	3.15
4	7.01	7.00	2.56	0.60	1.80	3.4	0.60	3.50	1.75
5	4.90	9.40	2.60	0.67	1.80	3.6	0.67	3.10	2.10
6	2.80	0.70	2.90	0.74	1.80	3.8	0.74	3.55	4.20
7	1.75	7.70	3.10	0.81	1.80	4.0	0.81	3.55	
8	3.85	3.80	3.24	0.88	1.80	4.2	0.88	3.50	
9	5.95							3.50	

4. EXPERIMENTAL VERIFICATION OF ANTENNA PERFORMANCE

Firstly, the antenna characteristics are measured standalone in an anechoic chamber setup with Impinj's UHF RFID reader kit in order to verify the standard communication characteristics of the proposed RFID tag. The impedance is measured by using S -parameter method [8, 9] whereas the return loss, and radiation patterns are measured by employing Imaging Method to achieve ameliorated measurement accuracy. The effect of humidity on antenna is foremost characterized using climate chamber (Weiss Technik WK 11-180), and then for demonstrating results under normal room conditions, measurements are carried out in the anechoic chamber by deploying humidifier

and hygrometer while maintaining the fixed distance between the reader and the sensor tag. The computed and measured impedance variations of the antenna against distinct humidity levels are shown in Figure 2(a). The resistance and reactance exhibit controlled linear curves of overall 9% and 7% variation, respectively. The measurements are reiterated several times for extracting reliability parameters and corroborating the sensor functionality.

Secondly, the calibration mechanism on the tag side alleviates in enforcing unpretentious and more reliable modes to formulate the entire humidity sensing system. The gain of the antenna varies with respect to ambient humidity levels as showed in Figure 3(a), and as a result, the received backscattered power (while placed in boresight) to the reader varies, which is conveniently scaled to determine the relative humidity (RH%) change. Figure 3(b) shows the return loss which is better than -15 dB in the complete FCC RFID ISM band. The distortion is possibly due to the effect of metal ground fixture used for Imaging Method. The normalized computed and measured radiation pattern, which are almost uniform (omnidirectional) at 915 MHz, are plotted in Figure 2(b). A good agreement is observed between the computations and measurements, which can also be verified for other frequencies within the antenna's bandwidth. The proposed sensor tag exhibits extended portable read range of 11 m and fixed 6.5 m as a standalone RFID tag and with full humidity sensing capability, respectively. Moreover, the gain of sensor antenna can be improved by increasing the size depending upon the particular application.

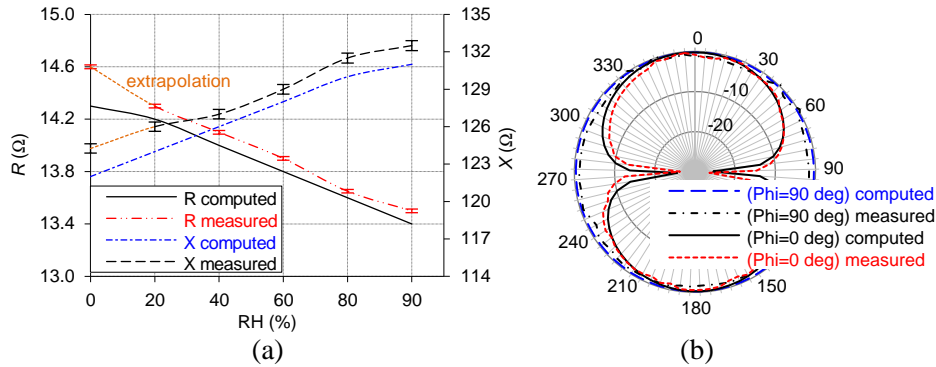


Figure 2: (a) Resistance and reactance variation. (b) Radiation patterns of RFID sensor antenna at 915 MHz.

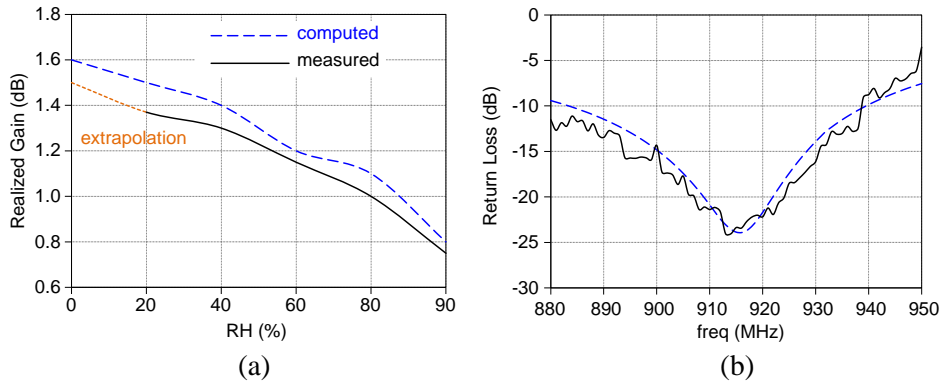


Figure 3: (a) Gain variation due to change in humidity level. (b) Measured and computed return loss.

5. CONCLUSION

An RFID tag antenna which has instinct characteristics of a humidity sensor and potentiality of customizable calibration, is designed, fabricated and validated. It is observed that the explicit incorporation of ink and paper substrate is crucial for igniting the destabilisation effect, which is exploited in a regulated mechanism by the structural alignment of the proposed antenna. The design flexibility of the antenna resourcefully provides the effective calibration of the humidity sensor in accordance with defined requirements. In addition, this structure is eco-friendly, flexible

and ultra-low cost, thus making this antenna well suited for realizing ubiquitous wireless sensor networks.

ACKNOWLEDGMENT

This work was financially supported by Vinnova (The Swedish Governmental Agency for Innovation Systems) through the Vinn Excellence centers program.

REFERENCES

1. Bhattacharyya, R., C. Floerkemeier, and S. Sarma, “Low-cost, ubiquitous RFID-tag-antenna-based sensing,” *Proc. IEEE*, Vol. 98, No. 9, 1593–1600, 2010.
2. Lakafosis, V., A. Rida, R. Vyas, Y. Li, S. Nikolaou, and M. M. Tentzeris, “Progress towards the first wireless sensor networks consisting of inkjet-printed, paper-based RFID-enabled sensor tags,” *Proc. IEEE*, Vol. 98, No. 9, 1601–1609, 2010.
3. Gao, J., J. Siden, and H.-E. Nilsson, “Printed electromagnetic coupler with an embedded moisture sensor for ordinary passive RFID tags,” *IEEE Electron Device Lett.*, Vol. 32, No. 12, 1767–1769, 2011.
4. Manzari, S., C. Occhiuzzi, S. Nawale, A. Catini, C. Di Natale, and G. Marrocco, “Humidity sensing by polymer-loaded UHF RFID antennas,” *IEEE Sensors J.*, Vol. 12, No. 9, 2851–2858, 2012.
5. Andersson, H., A. Manuilskiy, T. Unander, C. Lidenmark, S. Forsberg, and H. Nilsson, “Inkjet printed silver nanoparticle humidity sensor with memory effect on paper,” *IEEE Sensors J.*, Vol. 12, No. 6, 1901–1905, 2012.
6. Wang, Y. I., C. J. Simonson, R. W. Besant, and W. Shang, “Transient humidity measurements — Part I: Sensor calibration and characteristics,” *IEEE Trans. Instrum. Meas.*, Vol. 56, No. 3, 1074–1079, 2007.
7. Huang, Y. and K. Boyle, *Antennas from Theory to Practice*, John Wiley & Sons Ltd., New York, 2008.
8. Kuo, S.-K., S.-L. Chen, and C.-T. Lin, “An accurate method for impedance measurement of RFID tag antenna,” *Progress In Electromagnetics Research*, Vol. 83, 93–106, 2008.
9. Qing, X., C. K. Goh, and Z. N. Chen, “Impedance characterization of RFID tag antennas and application in tag co-design,” *IEEE Trans. Microw. Theory Techn.*, Vol. 57, No. 5, 1268–1274, 2009.

On the Influence of Edge Roughness in High-speed RFID Antenna Manufacturing Processes

J. Gao, J. Sidén, and H.-E. Nilsson

Mid Sweden University, Sundsvall, Sweden

Abstract— High speed manufacturing processes are commonly associated with high mechanical tolerances. For RFID antennas, mechanical manufacturing tolerances imply uncertainties in the antennas outer dimensions as well as in the surface- and line-roughness of the antennas geometry. Rough edges can for example be caused by high speed dry patterning processes. This work investigates the impact that rough patterns along the edges of an antenna structure have on UHF RFID tags' communication capabilities. The work characterizes the negative influence that edge roughness of different levels has on standard RFID dipoles. Results show that, as expected, the performance degradation for an RFID tag antenna increases with increased edge roughness amplitude. The results also show that the performance degradation due to edge roughness is almost identical for the investigated antennas' different line widths when the roughness level is normalized to its specific antenna line width, i.e., an antenna with a wider line width is more robust and can withstand a higher degree of edge roughness.

1. INTRODUCTION

Antenna robustness is becoming an ever more important issue. An originally great antenna design can suffer from physical damages when used in a harsh environment or being unintentionally detuned due to unforeseen nearby materials or environmental factors. High-speed and low-cost manufacturing processes can likewise introduce unintentionally high mechanical tolerances. Much of previous research on antenna manufacturing tolerances and random damages has primarily been directed toward arrays [1] and reflector antennas [1–3] where a longer list of references for example can be retrieved from [4, 5]. Other work on characterizing the robustness of antenna designs includes a characterization of mechanical robustness performance for an embedded annular ring type antenna for GPS applications by using drop weight impact tests [6]. The work in [7] studies the effect of environmental stress by exposing antennas to physical bending, high humidity levels and temperature cycling and how different stresses may accelerate the effects of another stress. The work in [8] also shows how a wideband antenna is less affected by bending than its narrowband counterpart. Performance degradation due to elongation of electrical structures is investigated in [9, 10] where antennas are printed with silver ink on stretchable PVC. [4] presents a statistical methodology for the evaluation of antenna susceptibility to various types of random physical damages and exemplifies the method for respectively “buck shots” [4] and “scratches” [5].

The last decades rapid expansion of RFID-technology has constituted a driving force for low-cost antenna manufacturing methods. Printed RFID tag antennas have received high attention in the literature while etched and milled antennas so far represent the largest amount of manufactured tag antennas. Printed antennas commonly receive a significantly higher surface roughness as compared to their etched counterparts. Screen-printed antennas for example suffer from two different length scales of surface roughness, one due to the nature of the conductive ink itself and one due to mesh traces. Surface roughness for screen printed RFID antennas is further described in [11] where an increase of the AC resistance per unit length by approximately 10% is observed, and with an overall resonant frequency shift of about 1%.

[12] looks into surface roughness created by substrates based on the fact that cellulose based substrates can be very rough, which may not allow the conductive ink particles to touch and thus not provide a good substrate for conductive continuity without increasing the ink film thickness to a point where cost benefits are lost. [13] specifically focuses on the interaction mechanisms of printed conductive inks and substrates.

The work that is presented in this article characterizes performance degradation for RFID tag antennas with a smooth surface but whose edges has received a rough pattern. Such rough patterns can for example occur in the subtractive production process in which high-speed milling is used on metallic foils (Figure 1).

Earlier work on edge roughness has primarily been related to microwave remote sensing. The concept of stochastic theory of edge diffraction (STED) provides one of the newer examples in the

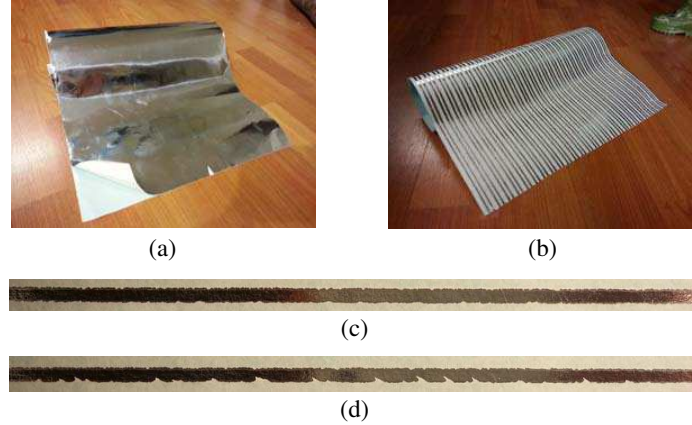


Figure 1: Antennas manufactured from metallic foils with high speed milling processes are susceptible to receiving a large edge roughness. (a) Roll of label material with paper as carrier and aluminum as electrical conductor. (b) Roll that has received straight line patterns by a high speed milling process. (c)–(d) Snapshots of edge roughness. In this case, the roughness caused by the milling process is mainly due to mechanical movements between the label material and its protective carrier.

literature [14, 15]. The work in [14, 15] focus on fields that are scattered by a half plane with a randomly rough edge. The fields are evaluated for both roughness parameters that is very low as compared to λ and for rough edges where the roughness is comparable to λ . [14] and [15] also illustrate the relation between the proposed STED methods and the classical uniform geometrical theory of diffraction (UTD). Methods for using resistive loading to suppress edge-diffraction effects in numerical modeling of microwave scattering from arbitrary rough surfaces is exemplified in [16] and [17]. [16] and [17] discuss solutions to the problem that finite computer resources limit the size of the surface that may be numerically treated and that simply truncating the surface without further consideration introduces undesired artificial edges.

As compared to the statistical approaches in for example [4, 5] and [14], this work follows a deterministic approach when applying distortions to antenna structures.

2. EXPERIMENTAL SETUP

Surface roughness and edge roughness are commonly quantified as the root mean square (RMS) of the geometrical deviations that cause the roughness. In this investigation, deviations are introduced to an antenna structure by applying a triangular wave pattern that is uniformly distributed around the ideal edges of the antenna. The triangular pattern causing the roughness is quantified in Figure 2 by four parameters r , α , β and p . Parameter r is the wave's peak amplitude and α and β are the angles formed by the triangle wave and the ideal edge of the antenna. Parameter p is the wave's period length and can be calculated by the other three parameters, i.e., $p = 2r * (\cot\alpha + \cot\beta)$. The specific antenna illustrated in Figure 2 has an original line width of 2.0 mm and has received a roughness pattern with $r = 0.5$ mm, $\cot\alpha = 1$, $\cot\beta = 3$ and $p = 4$ mm, which gives a triangle wave RMS value of $r_{rms} = 0.5/\sqrt{3} = 0.29$ mm.

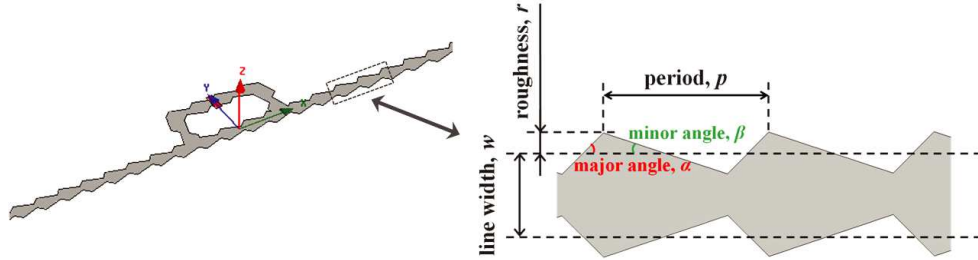


Figure 2: Illustration of the designed edge roughness pattern for investigating the edge roughness on an antenna.

The present work characterizes the influence that edge roughness has on the performance of

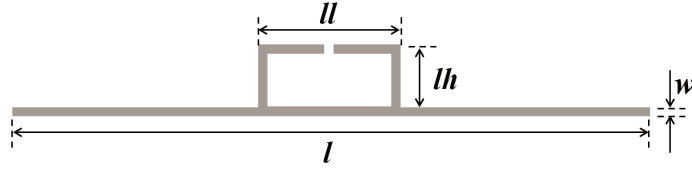


Figure 3: The RFID antenna used in the experiments before receiving rough edges.

the RFID tag antenna illustrated in Figures 2 and 3. The antenna under test has dimensions $l = 175 \text{ mm}$, $ll = 17 \text{ mm}$, $lh = 7.5 \text{ mm}$ and a line width w that varies from 1.0 mm to 3.0 mm . The experimental setup uses the triangle wave pattern's period length and amplitude as input parameters for describing the level of edge roughness while the input return loss, bandwidth and ohmic losses are used as output parameters.

As different line widths produce different input impedances, the input impedance of a rough-edged antenna with a certain line width is compared to the input impedance of an antenna with the same line width but without rough edges. If the antenna without rough edges has a perfect impedance match, i.e., the return loss is minus infinite dB, then the rough-edged antennas will be detuned and their return loss will be a larger value. In addition, edge roughness will also cause changes in antenna bandwidth and radiation efficiency. All experiments are performed by utilizing full-wave simulations.

3. RESULTS

The antenna in Figure 3 is simulated for the original line widths of 1.0 , 2.0 and 3.0 mm . The triangular patterns that are applied in these experiments have a parameter α that always equals 45° , i.e., $\cot\alpha = 1$, and a parameter β that equals either α or 0.41α , i.e., $\cot\beta = 1$ or $\cot\beta = 3$. The roughness pattern's amplitude is swept from a relatively small value that hardly affects the original antenna properties up to the extreme case where the roughness' subtractive parts meet each other, that is, up to the point where the conductive traces cease to be connected. Antennas with wide lines can thus be simulated with a higher maximum edge roughness than is the case for antennas with thin lines.

3.1. Input Return Loss

The input return loss is commonly used for evaluating the antenna input impedance matching. The input return loss for each simulated rough antenna is shown in Figure 4(a). It is observed that the input return loss for all six antennas shows a relatively good impedance match for a low level of edge roughness. The input return loss then increases with the roughness amplitude in an almost linear fashion, for the highest possible roughness with the defined triangular wave pattern.

Figure 4(b) shows the same result as Figure 4(a) but with the RMS roughness amplitude normalized to the corresponding line widths. In Figure 4(b), when the roughness patterns have a certain triangle shape, i.e., have a fixed α and β , almost identical changes in input return loss are observed for the different antenna line widths. For the specific antenna structure used in this work,

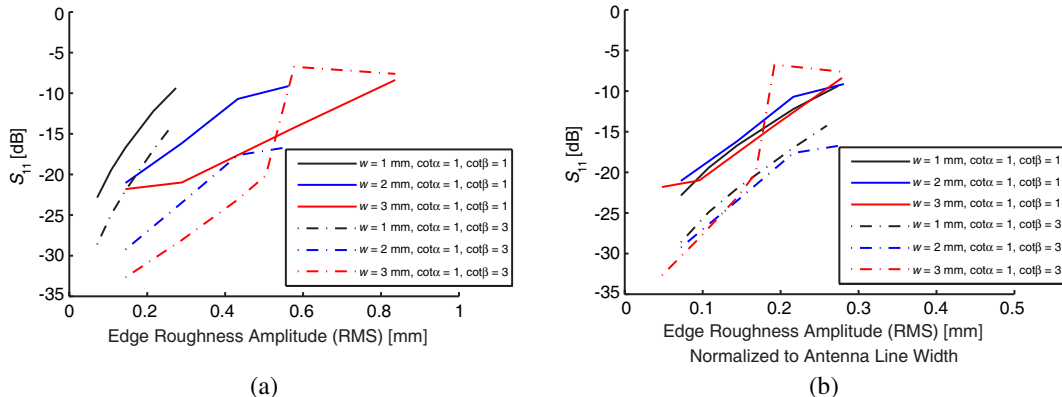


Figure 4: Input return loss for different levels of edge roughness, at 868 MHz.

it is thus concluded that the level of performance degradation due to edge roughness, in terms of input return loss, is related to the structure's line width and not only related to the level of roughness amplitude.

When the roughness patterns have different triangle shapes, i.e., have different α and β , the input return loss is less for the rough antennas with a larger wave period p . Therefore, the level of performance degradation due to edge roughness is also related to the wave period of the roughness pattern.

The exception occurs when the wave period of the roughness pattern is larger than the height of the antenna loop, since the mean line-width of the loop will become larger and the inner area of the loop will become smaller.

Similar experiments should be conducted with other antenna structures to determine if this argument is universal or only holds for certain antenna structures.

3.2. Bandwidth

The previous subsection considered the deviations of the impedance for a rough-edged antenna from that of a smooth-edged antenna with the same line width at a single frequency. This subsection evaluates the impedance deviations at various frequencies from the impedance at 868 MHz for the individual antenna, in terms of bandwidth. That is, the bandwidth of an antenna with a specific line width and a specific degree of edge roughness is calculated with the base in its own input impedance at 868 MHz and is not based upon comparisons with the smooth-edged original antenna. The bandwidth was calculated with a critical condition of $VSWR \leq 1.5$ ($VSWR$: voltage standing wave ratio). It was observed that the bandwidth decreases with increased edge roughness for the specific antenna under test. This is shown in Figure 5 where the bandwidth decreases from about 60 MHz to about 40 MHz for each simulated antenna line width.

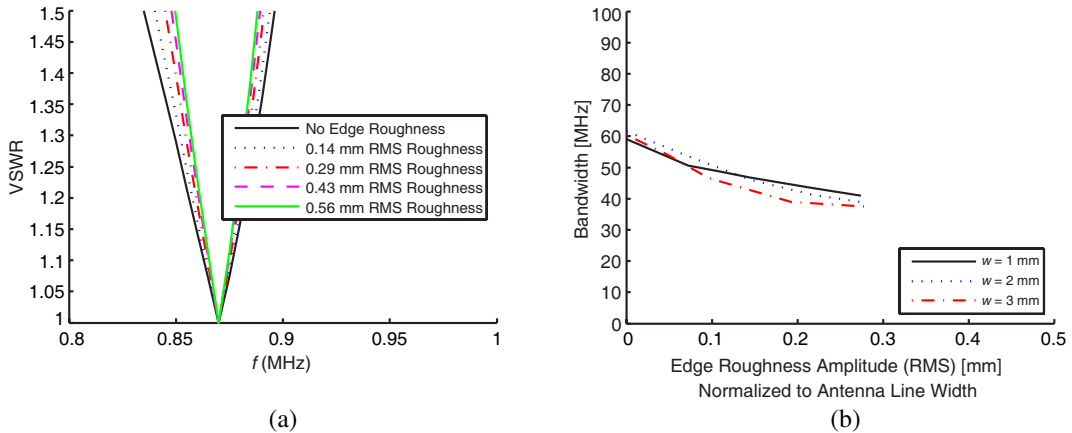


Figure 5: (a) VSWR for the antennas with different levels of edge roughness, when they have a line width of 2 mm and a triangular edge roughness pattern with parameters $\alpha = \beta = 45^\circ$. (b) Bandwidth decreases with increased edge roughness, when the triangular edge roughness pattern has parameters $\alpha = \beta = 45^\circ$.

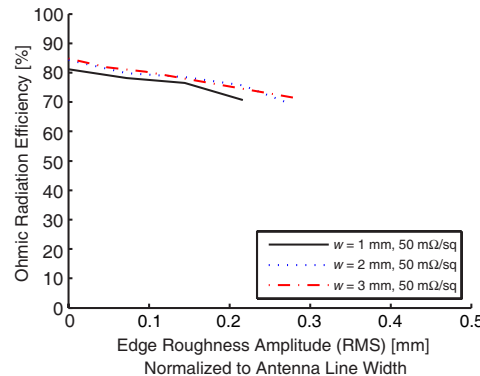


Figure 6: Radiation efficiency due to ohmic losses for antennas with different levels of edge roughness, when they have a triangular edge roughness pattern with parameters $\alpha = \beta = 45^\circ$.

3.3. Ohmic Losses

A great deal of previous work on RFID tag antennas has focused on printing the antennas with electrically conductive ink, with a conductivity that is significantly lower than the antennas that are etched or milled from solid metal. It is therefore of interest to investigate what effect a hypothetical printing process that creates traces with finite conductivity and rough edges would have on an RFID tag antenna. The results of simulating antennas with a sheet resistance of $50 \text{ m}\Omega/\square$ are shown in Figure 6 where it is seen that ohmic losses increase with the roughness amplitude in a linear way and the effect is almost identical for different line widths if the roughness amplitudes are normalized to the line widths. The effect of the edge roughness on the ohmic losses is relatively mild compared to that on input return loss.

4. CONCLUSION

For an RFID tag antenna, the edge roughness is commonly relatively small and will not reach the extreme case investigated. However, it can be concluded that an antenna with a wider line width is more robust and can withstand a higher degree of edge roughness. Antennas that are at risk of receiving a high degree of edge roughness should be designed to be electromagnetically robust against this kind of manufacturing issue. While this initial investigation on the subject utilized relatively simple roughness models, more advanced statistical models such as those presented in [4] could indeed be utilized in order to characterize the effects of random edge roughness. It should be evaluated whether different types of RFID tag antennas are more and less sensitive to edge roughness. The results of such an evaluation could advantageously constitute the basis for creating design guidelines for antennas that are robust against edge roughness.

ACKNOWLEDGMENT

KK Foundation and the Swedish Research Council Formas are acknowledged for their financial support.

REFERENCES

1. Schjaer-Jacobsen, H., "Worst-case tolerance optimization of antenna systems," *IEEE Trans. Antennas Propag.*, Vol. 28, No. 2, 247–250, Mar. 1980.
2. Xiao, J., X.-W. Xu, and T. Dong, "A study on the radiation characteristics of a shaped beam reflector antenna subjected to the single-hole damage," *Trans. Beijing Inst. Technol.*, Vol. 23, No. 6, 768–771, 2003.
3. Dong, T. and X.-W. Xu, "Hybrid method to predict damage effects of reflector antenna with a hole perforation on its feed," *Trans. Beijing Inst. Technol.*, Vol. 20, No. 3, 378–380, 2005.
4. Olsson, T. and A. Koptioug, "Statistical analysis of antenna robustness," *IEEE Trans. Antennas Propag.*, Vol. 53, No. 1, 566–570, Jan. 2005.
5. Olsson, T., M. Hjelm, J. Siden, and H. E. Nilsson, "Comparative robustness study of planar antennas," *IET Microw. Antennas Propag.*, Vol. 1, No. 3, 674–680, Jun. 2007.
6. Shin, D. S., J. Kim, W. S. Park, and W. B. Hwang, "Investigation for impact behavior of composite surface antenna," *2011 IEEE Int. Symp. Antennas Propag. (APSURSI)*, 461–463, Jul. 2011.
7. Saarinen, K., L. Frisk, and L. Ukkonen, "Effects of different combinations of environmental tests on the reliability of UHF RFID tags," *18th European Microelectron. and Packag. Conf. (EMPC)*, 1–5, Sep. 2011.
8. Sidén, J., P. Jonsson, T. Olsson, and G. Wang, "Performance degradation of RFID system due to the distortion in RFID tag antenna," *11th Int. Conf. Microw. Telecommun. Technol., CriMiCo 2001*, 371–373, Sep. 2001.
9. Merilampi, S., T. Björninen, V. Haukka, P. Ruuskanen, L. Ukkonen, and L. Sydänheimo, "Analysis of electrically conductive silver ink on stretchable substrates under tensile load," *Microelectronics Reliability*, Vol. 50, No. 12, 2001–2011, 2010.
10. Merilampi, S., P. Ruuskanen, T. Björninen, L. Ukkonen, and L. Sydänheimo, "Printed passive UHF RFID tags as wearable strain sensors," *2010 3rd Int. Symp. Applied Sciences in Biomedical and Communication Technologies (ISABEL)*, 1–5, Nov. 2010.
11. Shin, D.-Y., Y. Lee, and C. H. Kim, "Performance characterization of screen printed radio frequency identification antennas with silver nanopaste," *Thin Solid Films*, Vol. 517, No. 21, 6112–6118, 2009.

12. Cruz, M. A., M. Joyce, P. D. Fleming, M. Rebros, and A. Pekarovicova, "Surface topography contribution to RFID tag efficiency related to conductivity," *Coating and Graphic Arts Conference, TAPPI*, 2007.
13. Andersson, H., A. Manuilskiy, C. Lidenmark, J. Gao, and T. Unander, "The influence of paper coating content on room temperature sintering of silver nanoparticle ink," submitted to *IOP Nanotechnology*.
14. Franceschetti, G., A. Iodice, A. Natale, and D. Riccio, "Stochastic theory of edge diffraction: Its physical reading," *IEEE Trans. Antennas Propag.*, Vol. 58, No. 12, 4078–4081, Dec. 2010.
15. Franceschetti, G., A. Iodice, A. Natale, and D. Riccio, "Stochastic theory of edge diffraction," *IEEE Trans. Antennas Propag.*, Vol. 56, No. 2, 437–449, Feb. 2008.
16. Zhao, Z. and J. West, "Resistive suppression of edge effects in MLFMA scattering from finite conductivity surfaces," *IEEE Trans. Antennas Propag.*, Vol. 53, No. 5, 1848–1852, May 2005.
17. West, J., "On the control of edge diffraction in numerical rough surface scattering using resistive tapering," *IEEE Trans. Antennas Propag.*, Vol. 51, No. 11, 3180–3183, Nov. 2003.

Design of Sierpinski Grid Patch Antenna for Multiband Application

R. K. Kanth¹, P. Liljeberg¹, H. Tenhuen¹, Y. Amin²,
Q. Chen², A. Janstch², L. R. Zheng², and H. Kumar³

¹Turku Centre for Computer Science, University of Turku, Joukahaisenkatu 3-5 B, Turku 20520, Finland

²School of Information and Communication Technology

Royal Institute of Technology, KTH Forum, Isafjordsgatan 39, Kista, Stockholm 164 40, Sweden

³Department of Electronics and Communication Engineering, Bhagwant Institute of Technology
Muzaffarnagar, UP, India

Abstract— The purpose of this paper is two-fold. Firstly, we have attempted to design a planar Sierpinski fractal antenna with stacked configuration for multiband applications. The stacked configuration of Sierpinski fractal patch and Sierpinski grid are employed to improve the multiband characteristics. The operating frequencies obtained are at 3.3 GHz, 5 GHz, 5.74 GHz and 5.9 GHz which covers the bands useful for HIPERLAN2 frequencies and for implementation in futuristic WiFi enabled devices and PCI Cards for mobile internet. The Simulated results show that the operating frequencies obtained are spread over a wide range of frequency band compared to the simple Sierpinski fractal patch antenna. Secondly this paper aims at evaluating the sustainability and life cycle management of proposed antenna.

1. INTRODUCTION

The rapid progress in telecommunication technology deals with a great variety of communication systems like cellular, global positioning, and satellite communication systems. Each of these systems operates at several frequency bands employing a number of small to large antennas depending on the choices of applications. Printed antennas offer an excellent performance in a wide variety of wireless communication applications. Moreover, due to low weight, low profile and low cost production of patch and fractal structures, these antennas are becoming more popular in wireless and telecommunication industry. Various multiband designs employing parasitic patches or shorting pins have been proposed to date [1, 2]. However, these techniques usually lead to an increase in antenna size or manufacturing cost. The recent trends establish evidence that production of antennas for different applications are growing rapidly. This has initiated antenna research in various directions, one of which is using fractal shaped antenna elements.

Fractal geometries have two common properties, space-filling and self-similarity. The self-similarity properties of certain fractals result in a multi-band behavior [3–6], while the space-filling properties of fractals make possible to reduce antenna size [7]. Fractal objects have self-similar shapes, which mean that some of their parts have the same shape as the whole object but at a different scale. In this paper the Sierpinski patch antenna has been considered for the investigation. The Sierpinski gasket is named after the Polish mathematician Sierpinski who described some of the main properties of this fractal shape in 1916 [8]. The original gasket is constructed by subtracting a central inverted triangle from a main triangle shape as shown in Fig. 1. After the subtraction, three equal triangles remain on the structure, each one being half of the size of the original one. This is the first iteration of the Sierpinski fractal generation. One can iterate the same subtraction procedure on the remaining triangles and if the iteration is carried out an infinite number of times, the ideal fractal Sierpinski gasket is obtained. In such an ideal structure, each one of its three main parts is exactly equal to the whole object, but scaled by the factor of two and so is each of the three gaskets that compose any of those parts. Due to this particular similarity property, shared with many other fractal shapes, it is said that the Sierpinski gasket is self-similar [9, 10]. The following sections constitute the whole paper. The next two sections describe the antenna design criteria and the results obtained respectively. Section 4 deals with sustainability model and explores environmental impacts assessment. Section 5 give a conclusion of our work.

2. ANTENNA DESIGN

In this paper, only up to the second stage of the Sierpinski gasket is considered. For the first stage, which is a simple triangular patch with the length of each side 32 mm is placed on a substrate of thickness 1.6 mm and permittivity 4.4. Location of the coax feed placed on the patch is $-3, 20.5$ (x_f, y_f) from the centre of the patchs base (offset). Resonant frequencies obtained were 5.07

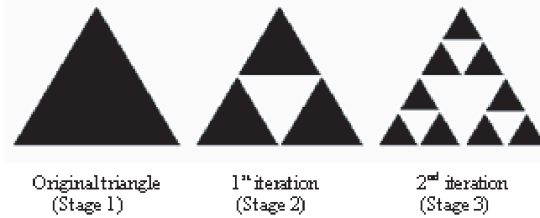


Figure 1: Sierpinski fractal generation up to 2nd iteration.

and 5.72 GHz. The second stage of the Sierpinski gasket (1st iteration) is then obtained using the Sierpinski gasket design method described above. With this configuration the resonant frequencies obtained were at 5.51 and 5.62 GHz. But in this case, too, there were only two operating frequencies with the slight frequency shift.

In the next step a grid with the width of 1.0 mm is formed, whose dimensions are same as that of the second stage of the Sierpinski gasket. This Grid is constructed on a foam substrate of thickness 1.6 mm and permittivity of 1.06 and is placed over the previous structure. This way a stacked configuration is obtained in which the lower structure is Sierpinski gasket on FR4 where the upper structure is grid on a foam of thickness 1.6 mm. The lower patch is coaxially fed. This final configuration of the antenna is shown in Fig. 2. With this configuration the operating frequency obtained are 3.3 GHz, 5 GHz, 5.75 GHz and 5.9 GHz, which are widely spreaded over the frequency band.

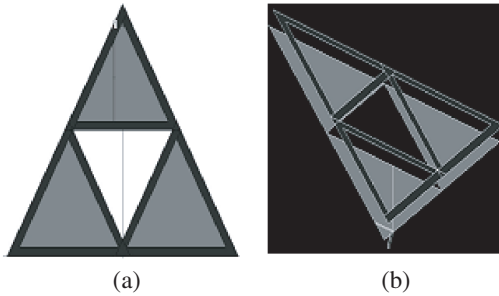


Figure 2: Sierpinski grid patch antenna in stacked configuration. (a) Top view and (b) 3-D view.

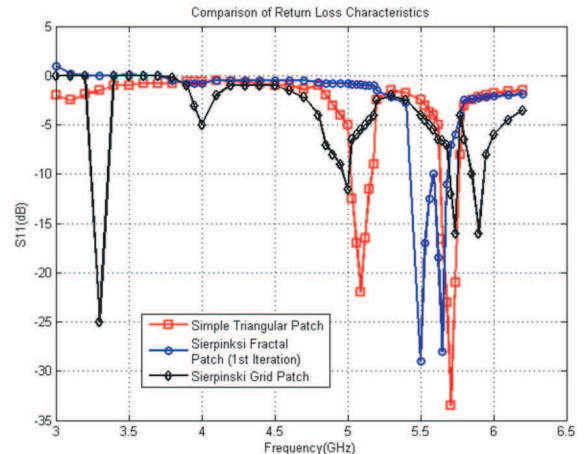


Figure 3: Comparison of return loss characteristic of three structures.

3. RESULTS AND DISCUSSION

Return loss characteristics of the three structures are shown in Fig. 3. It is evident from the figure that within the range of 6 GHz, only two operating frequencies were obtained with the simple triangular patch and the Sierpinski fractal patch (1st iteration). With the Sierpinski fractal patch (1st iteration) resonant frequencies were at 5.51 and 5.62 GHz and give rise to a wide band antenna whose return loss is less than -10 dB from 5.49 GHz to 5.67 GHz.

The third configuration in which Sierpinski fractal patch and Sierpinski grid were considered in the stacked configuration, with Sierpinski fractal patch as probe fed and Sierpinski grid as parasitic patch, the resonant frequency obtained are four, which are at 3.3 GHz, 5 GHz, 5.75 GHz and 5.9 GHz.

Characteristics related to these frequencies are tabulated in the Table 1. The gain of this novel antenna is, within the desired frequency, always more than 5.5 dBi. The simulated radiation pattern in E and H plane at four frequencies 3.3 GHz, 5 GHz, 5.75 GHz and 5.9 GHz are shown in the Fig. 4, Fig. 5, Fig. 6 and Fig. 7 respectively.

The radiation pattern characteristics at all the frequencies are almost same. At frequency

5.9 GHz the gain is slightly reduced but is still greater than 5 dBi.

Table 1: Return loss, VSWR and gain characteristics of sierpinski grid patch antenna in stacked configuration.

S.N	Frequency	Return Loss (dB)	Bandwidth (MHz)	Gain (dBi)
1	3.3 GHz	-24.8	100	6.37
2	5 GHz	-11.6	70	6.47
3	5.75 GHz	-15.3	120	6.18
4	5.9 GHz	-15.9	50	5.6

—○— f=3.3(GHz), E-total, phi=0 (deg)
—○— f=3.3(GHz), E-total, phi=90 (deg)

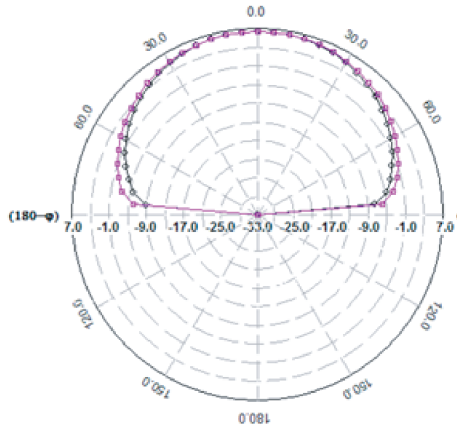


Figure 4: E and H plane radiation pattern of Sierpinski grid patch antenna in stacked configuration at 3.3 GHz.

—○— f=5(GHz), E-total, phi=0 (deg)
—○— f=5(GHz), E-total, phi=90 (deg)

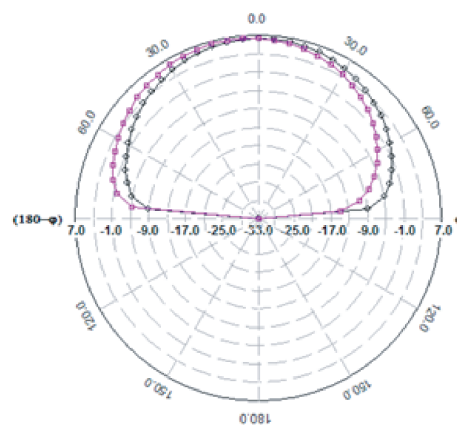


Figure 5: E and H plane radiation pattern of Sierpinski grid patch antenna in stacked configuration at 5 GHz.

—○— f=5.7(GHz), E-total, phi=0 (deg)
—○— f=5.7(GHz), E-total, phi=90 (deg)

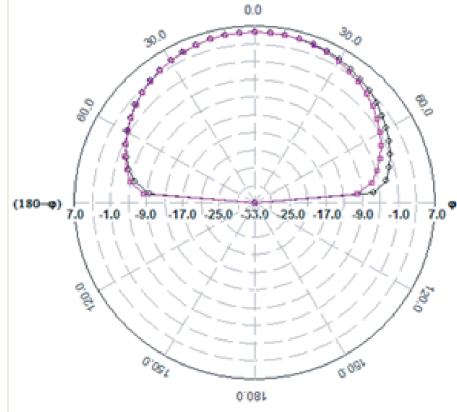


Figure 6: E and H plane radiation pattern of Sierpinski grid patch antenna in stacked configuration at 3.75 GHz.

—○— f=5.9(GHz), E-total, phi=0 (deg)
—○— f=5.9(GHz), E-total, phi=90 (deg)

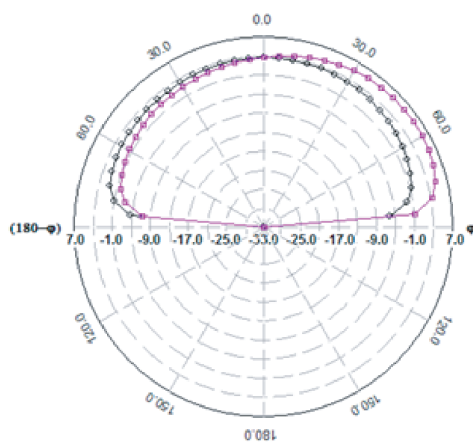


Figure 7: E and H plane radiation pattern of Sierpinski grid patch antenna in stacked configuration at 5.9 GHz.

4. SUSTAINABILITY ANALYSIS

This section provides an overview of sustainability and environmental impacts assessment [11–15] in production process of Sierpinski structure based microstrip printed antennas. The sustainable model for this antenna has been made using Gabi 5.0 environmental assessment tool. In this work,

we have considered two stages of life cycle analysis: production stage and end-of-life stage. The model in question has been depicted in Fig. 8. The numerical analysis of environmental emissions in these stages employed several materials the printed antenna has been composed of. Substrate, antenna trace material (may be copper, silver ink, or aluminum) and the associated energy have been taken into consideration as vital components as they cause most environmental impacts. The recent trends of using conductive inks for tracing antenna patterns are gradually turning toward low cost printing material such as copper. Although this element has several limitations for example poisoning the circuits, copper oxidation, and high temperature annealing process. The higher demand of silver conductive ink for tracing massive amount of UHF antennas and billions of RFID tags caused shortage of silver nano ink. Hence manufacturers are considering of using copper nano inks with improved performance. In this work inkjet printing technology has been employed to trace the required Sierpinski fractal pattern. Our previous work [16–20] presents the environmental impacts in different antenna systems. The mass of FR4 (flame retardant epoxy material), copper antenna trace and the manufacturing energy have been estimated on the basis of antenna structure and its Sierpinski fractal layout. The model that have been developed for this research comprises of copper and epoxy masses 3 nanogram and 5gm respectively.

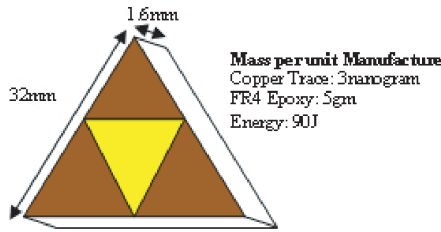


Figure 8: Model and mass of the antenna materials.

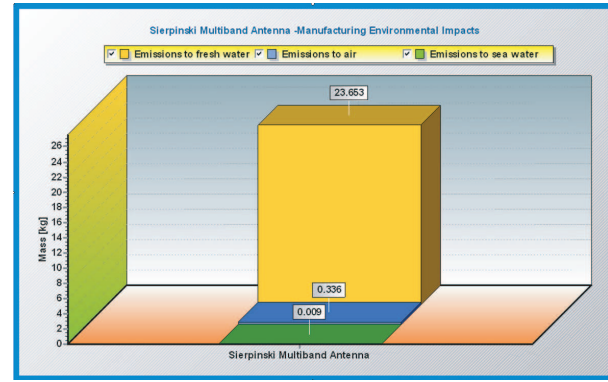


Figure 9: Environmental emissions during manufacturing of Sierpinski multiband antenna.

The inkjet printing methodology consumes 90 Joule of energy for tracing one pattern. The equivalent environmental emissions during the manufacturing process have been depicted in Fig. 9. The relative contribution shows that the impact on emissions to fresh water is larger than emissions to air and sea water.

5. CONCLUSION

In this paper, we have attempted to give an overview of designing fractal patch antennas in stacked configuration as well as environmental impacts during its manufacturing process. The proposed antenna is designed in such a way that second stage of the Sierpinski gasket (1st iteration) is used as a the lower patch and fed with coaxial probe, where as the Sierpinski grid has been used as the upper parasitic patch. This antenna has four operating frequencies 3.3 GHz, 5 GHz, 5.75 GHz and 5.9 GHz. The major applications of this antenna falls within area of HIPERLAN2, WiFi enabled devices and PCI Cards for mobile internet. We have also explored the environmental impacts in manufacturing process of this Sierpinski type multiband printed microstrip antenna.

ACKNOWLEDGMENT

The authors acknowledge iPack Vinn Excellence Centre, Royal Institute of Technology (KTH) for supporting the necessary tools and equipments to carry out these investigations. We would like to thank Turku Centre for Computer Science for assisting the financial support.

REFERENCES

1. James, J. R. and P. S. Hall, *Handbook of Microstrip Antennas*, Vol. 1, Peter Peregrinus, London, UK, 1989.
2. Kumar, H., M. D. Upadhyay, V. K. Rai, L. Varshney, and R. K. Kanth, "Multiband planar mircostrip antenna," *Proceeding of the IEEE International Conference on Antenna & Prop-*

- agation in Wireless Communication*, Vol. 2, 1360–1363, Sept. 16–20, 2011, 978-1-4577-0048-4/11//\$26.00.
3. Best, S. R., “On the significance of self-similar fractal geometry in determining the multiband behavior of the Sierpinski gasket antenna,” *IEEE Antennas and Wireless Propagation Letters*, Vol. 1, No. 1, 22–25, 2002.
 4. Puente, C., J. Ponmeu, R. Pous, and A. Cardama, “On the behavior of the Sierpinski Multi-band Antenna,” *IEEE Transactions on Antennas and Propagation*, Vol. 46, No. 4, 517–524, Apr. 1998.
 5. Yeo, J. and R. Mittra, “Design of conformal multiband antennas based on fractal concepts,” *Microwave and Optical Technology Letters*, Vol. 36, No. 5, 333–338, 2003.
 6. Luintel, T. and P. F. Wahid, “Modified Sierpinski fractal antenna,” *IEEE/ACES International Conference on Wireless Communications and Applied Computational Electromagnetics*, 578–581, Apr. 3–7, 2005.
 7. Biswas, B. N., R. Ghatak, R. K. Mishra, and D. R. Poddar, “Characterization of a self-complementary Sierpinski gasket microstrip antenna,” *PIERS Online*, Vol. 2, No. 6, 698–701, 2006.
 8. Kanth, R. K., W. Ahmad, S. Shakya, P. Liljeberg, L.-R. Zheng, and H. Tenhunen, “Autonomous use of fractal in structure low cost, multiband and compact navigation antenna,” *Proceeding of MMS*, 135–138, Cyprus, Aug. 2010.
 9. Kumar, H., R. K. Kanth, P. Liljeberg, and H. Tenhunen, “Metamaterial based slotted patch antenna,” *Proceedings of the IEEE 10th International Conference on Telecommunication in Modern Satellite Cable and Broadcasting Services*, Vol. 2, 536–539, 2011.
 10. Puente, C., “Fractal antennas,” Ph.D. Dissertation, Dept. Signal Theory Communicat., Universitat Politecnica de Catalunya, Jun. 1997.
 11. Wang, X. and G. Gaustad, “Prioritizing material recovery for end-of-life printed circuit boards,” *Proceedings of 2011 International Symposium on Sustainable Systems and Technology (ISSST)*, 1, Golisano Institute of Sustainability, RIT, 2011.
 12. Maruschke, J. and B. Rosemann, “Measuring environmental performance in the early phase of product design using life cycle assessment,” *Environmentally Conscious Design and Inverse Manufacturing*, 248–249, 2005.
 13. Pekkanen, V., M. Mntysalo, and P. Mansikkamki, “Design considerations for inkjet printed electronic interconnections and packaging,” *Proceedings of the Imaps 40th International Symposium on Microelectronics*, 1076–1083, California, USA, 2007.
 14. Griese, H., L. Stobbe, A. Middendorf, and H. Reichl, “Environmental compatibility of electronics — A key towards local and global sustainable development,” *Proceedings of 2004 International IEEE Conference on the Asian Green Electronics*, 158–163, 2004.
 15. Bailey, C., C. babbitt, and G. Gaustad, “Tracking the material, energy, and value flow for end-of-life lithium ion batteries in the US,” *Proceedings of 2011 International Symposium on Sustainable Systems and Technology (ISSST)*, 1, Rochester Institute of Technology, 2011.
 16. Kanth, R. K., P. Liljeberg, H. Tenhunen, W. Qiansu, Y. Amin, B. Shao, Q. Chen, L. Zheng, and H. Kumar, “Evaluating sustainability, environmental assessment and toxic emissions during manufacturing process of RFID based systems,” *2011 IEEE 9th International Conference on Dependable, Autonomic and Secure Computing (DASC)*, J. Chen, Ed., 1066–1071, IEEE Computer Society, 2012, DOI: 10.1109/DASC.2011.175.
 17. Kanth, R. K., P. Liljeberg, Y. Amin, Q. Chen, L. Zheng, and H. Tenhunen, “Comparative end-of-life study of polymer and paper based radio frequency devices,” *International Journal of Environmental Protection*, Vol. 2, No. 8, 2327, 2012, Online ISSN: 2224-7777, Print ISSN: 2226-6437.
 18. Kanth, R. K., Q. Wan, H. Kuamr, P. Liljeberg, Q. Chen, L. Zheng, and H. Tenhunen, “Evaluating sustainability, environment assessment and toxic emissions in life cycle stages of printed antenna,” *Procedia Engineering*, Vol. 30, No. 1, 508–513, Elsevier, 2012.
 19. Kanth, R. K., P. Liljeberg, H. Tenhunen, Q. Chen, L. Zheng, and H. Kumar, “Comparative toxic emission analysis in production process of polymer and paper based RFID tags,” *11th International Conference on Environment and Electrical Engineering*, M. Caciotta and Z. Leonowicz, Eds., 184–187, IEEE, 2012, DOI: 10.1109/EEEIC.2012.6221570.

20. Kanth, R. K., P. Liljeberg, H. Tenhunen, Q. Chen, L. Zheng, and H. Kumar, "Study on glass epoxy based low cost and compact tip-truncated triangular printed antenna," *International Journal of Antennas and Propagation* 2012, Vol. 2012, Article ID 184537, 18, Hindawi Publication, 2012, DOI:10.1155/2012/184537.

A Battery Free RFID Sensor for Quality Detection of Food Products

Dat-Son Nguyen^{1, 2}, Gia-Tam Phan¹, Tien-Thong Pham¹, Nguyen-Ngan Le¹, Mau-Chien Dang¹, and Smail Tedjni²

¹Laboratory for Nanotechnology, Vietnam National University — Ho Chi Minh City Community 6, Linh Trung Ward, Thu Duc District, Ho Chi Minh City, Vietnam

²Laboratoire de Conception et d'Intégration des Systèmes, Université de Grenoble 50 rue Barthélémy de Laffemas, BP 54, 26902 Valence Cedex 9, France

Abstract— In this paper, we propose the use of passive UHF RFID tags as a sensor in order to detect the quality of food products. The sensor RFID tag includes plural pairs of antenna/chip where each pair of antenna/chip is designed to operate over a range of the permittivity value of the food. Knowing the variation of the permittivity of food over time (due to aging), we can detect when the food becomes contaminated with the measurement of each pair's read-range. The ultimate goal of this study is to develop a wireless sensor based on low-cost UHF RFID passive tags that can detect the quality of a food product. The experimental and simulation results have shown the potential of this technique for real-world applications of food traceability. In addition, the results of this work allow considering the use of this approach for medical applications in real-world. As we known, the permittivity of human muscle and tissue is very close to the permittivity of meat such as pork or beef. Sensitivity study should be conducted in order to better optimize the sensor and predict its performance.

1. INTRODUCTION

Nowadays, RFID technology is growing rapidly and has many applications in various areas of daily life. This technology offers many advantages with automatic capture and contactless data in a smart label (commonly called tag) [1]. Indeed, it allows saving time and considerable labor cost. In this context, RFID Ultra High Frequency (UHF) passive can store large amounts of data and have a potentially unlimited lifespan. The combination of RFID tags with sensing capability is a recent development in the field of RFID and very interesting approach in the world. From literature [2, 3], some applications of electromagnetic techniques in monitoring the freshness of food products have been introduced. Keat Ghee Ong et al. [2] proposed an analytical formula to calculate the permittivity of food products during the increasing of bacteria concentration through the impedance of embedded structure in food products. In another way, Ghatass et al. [3] estimated the freshness of beef by calculating the permittivity and conductivity from measured capacitance and inductance.

In this paper, we present an approach to evolve the RFID passive tags that ultimately transforms them into sensor with the aim to apply for food quality detection. For this work, we use conventional tags and exploit the sensitivity of the tag antenna to its environment to measure the properties of the immediate environment of the tag. This paper is organized as follows: Section 2 presents the theoretical background to explain the operational mode of detection for passive UHF RFID tags. Then, the method of design is presented in Section 3. The experimental results and discussions are presented in Section 4 and finally, the conclusions are in Section 4.

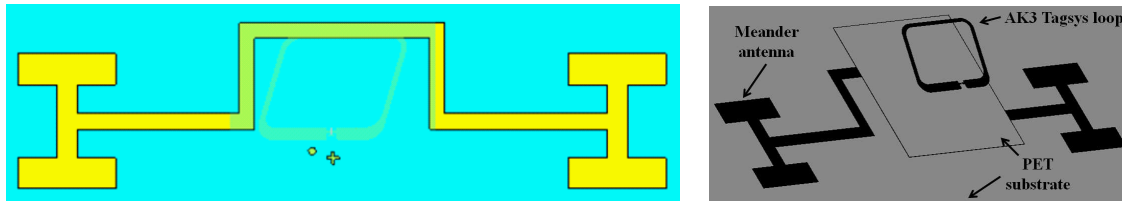


Figure 1: The proposed geometry of antenna for tag.

2. THEORETICAL BACKGROUND

In Fig. 1, we present the geometry of a typical RFID tag which is designed to be sensitive to its environment represented by direct contact with food to be monitored and assumed to be 1-cm

thickness. We considered a product whose permittivity is between 40 and 80 to simulate a food product, based on data from literature [4, 5]. We present in Fig. 2 the change of the impedance of the antenna for this range of permittivity. There has been a significant change in both the real and the imaginary parts of the impedance of the tag antenna. This change modifies also the matching between the antenna and the RFID chip and leads to a final modification of power transmission coefficient τ between RFID chip and antenna.

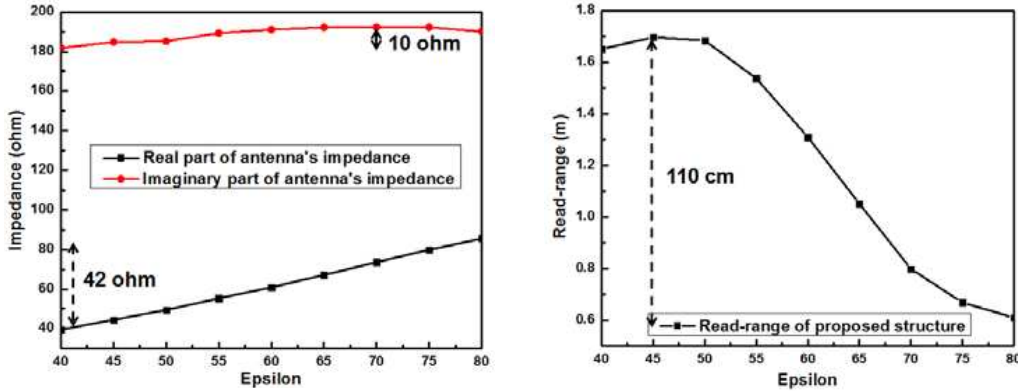


Figure 2: The impedance and read-range of proposed tag design in function to permittivity.

As the results, this change leads to a modification of the read-range given by the following expression [1]:

$$r = \frac{\lambda}{4\pi} \sqrt{\frac{P_t G_t G_r \tau}{P_{th}}} \quad (1)$$

where r is the read-range of the tag, λ is the wavelength, $P_t G_t$ is the maximum transmission power depending on the regulation, G_r is the gain of tag's antenna, τ is the power transmission coefficient between the chip and antenna, P_{th} is the activation power of the chip (-15 dBm here for NXP chip).

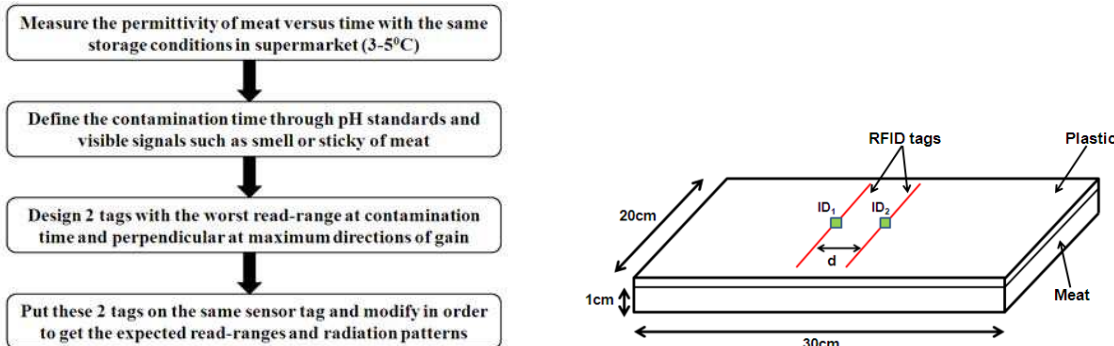


Figure 3: The design method and simulation model of sensor RFID tag.

To design the sensor tag, we use essentially the variation of read-range distance. We also use the concept of multi-tag developed in the literature [6]. Thus, we use two tags that are designed for different values of permittivity. In fact, when food products such as meat, cheese, tofu ... change in quality from a fresh to a contaminated state, their values of permittivity vary significantly. In this work, we consider the beef on which will be deposited the sensor tag. As known, the beef will lose its freshness to reach the state of contamination in function to time. The sensor tag has been designed to meet the minimum read-range at the state of contamination and the system can detect the contamination of food with only one tag. However, we can add another tag with the distance d from the first tag to increase the reliability of the system as in Fig. 3. The second tag is also designed to have the minimum read-range at the contamination time but the radiation pattern will have the perpendicular direction in comparison to the maximum direction of gain in case of first tag. All the simulations focus on just ETSI regulation of UHF RFID with the resonant frequency

of 868 MHz). The remarkable point is that both of 2 tags are designed to have the worst read-range in corresponding to the permittivity of contaminated state of food product. As in Fig. 4, we can see that the chosen value of contaminated meat will be $61.8023 + j23.9777$ and the aim of this technique is to have the worst read-range of 2 tags at this value of permittivity.

3. DESIGN OF SENSOR TAG

Figure 3 describes the design process which is primarily based on data on the permittivity of foods. The database of meat's permittivity will be measured by the coaxial probe HP85070B of Agilent[®] [7] under the same conditions as supermarket (3–5°C). The beef to be used is the sample in the supermarket of METRO[®] France and it is sampled the pH and permittivity everyday from the fresh state to the contamination state (7 consecutive days). From the visible signals and the pH standard [8], we can detect the moment of beef contamination is between 90 h and 120 h like in Fig. 4. In Fig. 3, we also describe the simulation model for the design of RFID tag-sensor for monitoring the quality of beef. The simulation parameters are then imported in CST Microwave Studio[®]. The distance d between the two RFID tags will be optimized from 1 cm to 8 cm and the two tags are mounted on the meat with the imported permittivity from experimental results above in Fig. 4. The optimized results show that the optimized distance between two tags is 3 cm in order to keep the desired conditions in radiation patterns of them.

MEASURED PERMITTIVITY OF BEEF VS TIME			
Time	Dielectric constant	Loss factor	pH
0h	56.8473	22.6368	5.75
30h	59.4764	19.4102	5.78
60h	59.0539	21.0592	5.69
90h	58.006	22.6277	5.93
120h	61.8023	23.9777	6.09
150h	57.103	21.2671	6.33
180h	59.1214	21.3047	6.52
210h	57.775	20.4042	6.8
240h	57.4604	19.3841	6.68

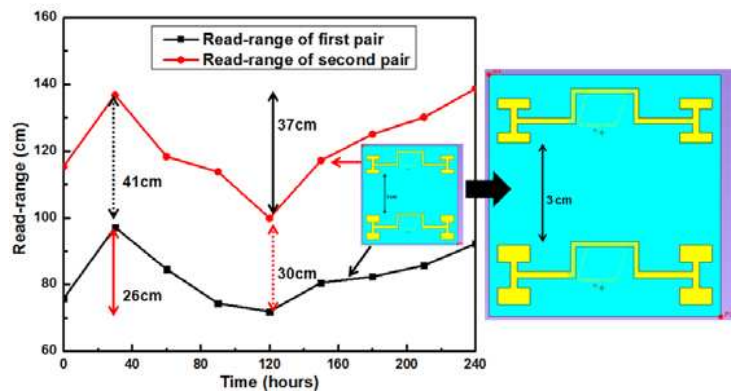


Figure 4: The measured permittivity for simulation and read-range of sensor tag at maximum direction in function to time.

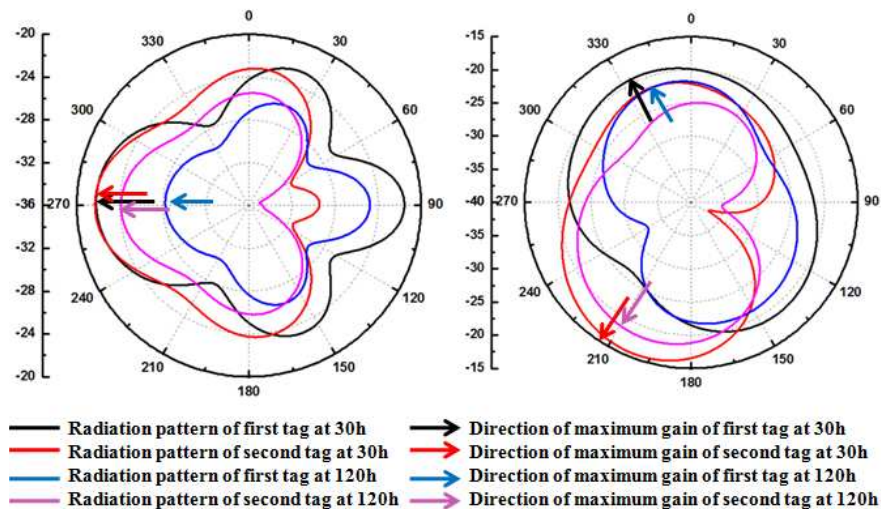


Figure 5: The radiation pattern of tags on Thêta-plan and Phi-plan.

According to Fig. 4 and Fig. 5, we can see that the read-range of each tag reaches the minimum value at 120 hours and the radiation pattern of each tag keeps the same shape over time. From

Fig. 5, we can see that the radiation pattern of each tag are almost unchanged and it leads to the direction of maximum radiation for each tag is also the same in function to time. However, the gain of the antenna is changed but the directions of maximum radiation are almost perpendicular to each other. In addition, the difference between the maximum and minimum read-range of each tag is acceptable and feasible in practice (37 cm and 26 cm). For the scenario of application, because the maximum read-range is obtained after 30 hours and the minimum one is obtained after 120 hours, in perpendicular directions to each other, we can use two UHF RFID readers installed in perpendicular directions to detect the state of contamination in function to time.

4. EXPERIMENTAL RESULTS AND DISCUSSIONS

Fabricated sensor tag (with the dimensions of 67 mm × 63 mm) will be measured in 3D with the measurement setup as in Fig. 6. The reader for characterization is Speedway Revolution R420 of Impinj® [9]. The sensor tag will be mounted on the beef sample in order to define the 3D read-range from the fresh state to the contamination state (7 consecutive days). From the measured read-range described in Fig. 6, the difference between simulated and measured read-range can be explained by the accuracy between permittivity's database (caused by the difference in temperature and thickness of beef sample).

Furthermore, the contamination time of sensor tag is still between 96 hours and 120 hours as from simulation like in Fig. 6. From Fig. 7, we can see that the directions of maximum read-range corresponding to each tag are quasi-perpendicular each to other. This agreement proves the feasibility of this system for food quality detection in real application. In another point, the mismatch between the simulation and the measurement can be explained from the theories of literature. In fact, we know that the permittivity of contamination time will be changed if the environmental conditions such as temperature and moisture content are fluctuated [5].

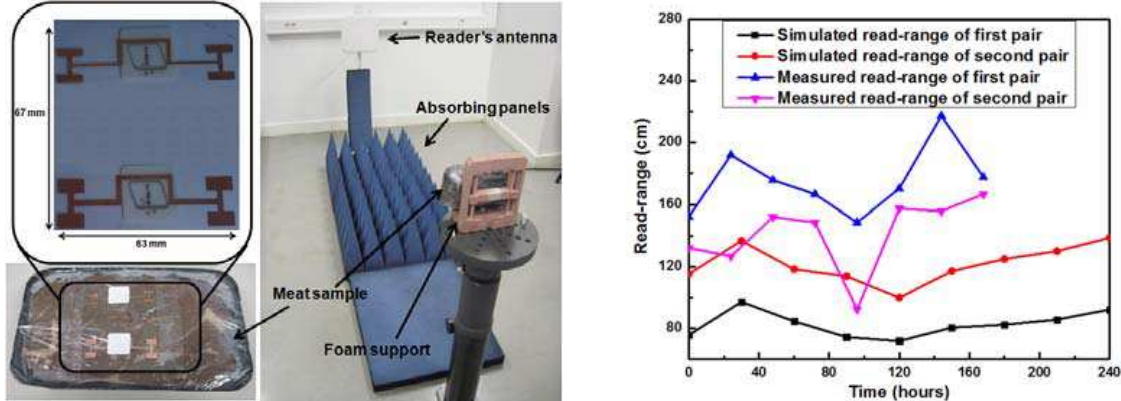


Figure 6: The measured read-range in comparison to the simulation results of sensor tag.

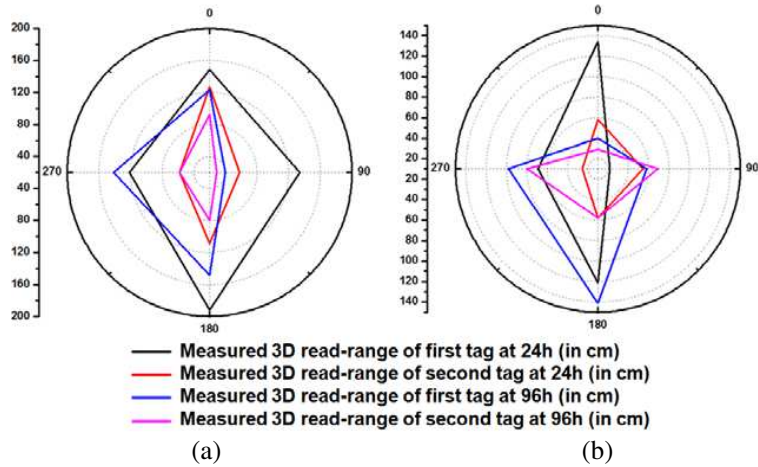


Figure 7: The read-range of sensor tag in (a) Theta-plan and (b) Phi-plan.

In future step, the consideration of read-range and permittivity in function to environmental factors such as temperature and moisture content should be executed in order to define the sensitivity and also the error in performance of RFID sensor tag. Another limitation is that the dimensions of meat sample in simulation and the ones of measured sample are a bit different in thickness. This different can lead to the tolerance in the radiation gain and change the read-range in experimental measurement. The last remark is the difference between the fabricated antennae and simulated dimensions (the tolerance is ± 0.05 mm) can be one of the reasons in mismatch between the simulation and the measurement.

5. CONCLUSIONS

In this paper, we proposed an approach for using passive UHF RFID tags to detect contamination and meat quality. The experimental and simulation results have shown the potential of this technique for real-world applications of food traceability. In addition, the results of this work allow considering the use of this approach for medical applications in real-world. Sensitivity study should be conducted in order to better optimize the sensor and predict its performance. One of the perspectives of this work can be biomedical application as wearable antenna to detect the cancer tumor under the muscle. As we known, the permittivity of human muscle and tissue is very close to the permittivity of meat such as pork or beef.

ACKNOWLEDGMENT

This work is supported under the grant of Vietnam National Foundation for Science and Technology Development (NAFOSTED). The AK3 Tagsys loops and simulation tools were kindly provided by Laboratory LCIS (Valence, France) and Mr. Christophe Loussert in the frame of our collaboration.

REFERENCES

1. Dobkin, D., *RF in RFID: Passive RFID UHF in Practice*, Newnes, Ed., 2008.
2. Ong, K. G., J. S. Bitler, C. A. Grimes, et al., "Remote query resonant-circuit sensors for monitoring of bacteria growth: Application to food quality control," *Sensor MDPI*, 219–232, Feb. 2002.
3. Ghatass, Z. F., M. M. Soliman, and M. M. Mohamed, "Dielectric technique for quality control of beef meat in the range 10 kHz–1 MHz," *American-Eurasian Journal of Scientific Research*, Vol. 3, 62–69, 2008, ISSN 1818-6785.
4. Ryynänen, S., "The electromagnetic properties of food materials: A review of the basic principles," *Journal of Food Engineering*, Vol. 26, 409–429, 1995.
5. Komarov, V., S. Wang, and J. Tang, "Permittivity and measurement," *The Wiley Encyclopedia of RF and Microwave Engineering*, 3693–3711, John Wiley & Sons, New York, 2005.
6. Marrocco, G., L. Mattioni, and C. Calabrese, "Multiport sensor RFIDs for wireless passive sensing of objects — Basic theory and early results," *IEEE Transactions on Antennas and Propagation*, Vol. 56, No. 8, 2008
7. [Http://cp.literature.agilent.com/litweb/pdf/5091-6247EUS.pdf](http://cp.literature.agilent.com/litweb/pdf/5091-6247EUS.pdf).
8. [Ftp://ftp.fao.org/docrep/fao/010/ai407e/ai407e12.pdf](ftp://ftp.fao.org/docrep/fao/010/ai407e/ai407e12.pdf).
9. [Http://www.impinj.com/support/downloadable_documents.aspx#Speedway%20Revolution%20Reader](http://www.impinj.com/support/downloadable_documents.aspx#Speedway%20Revolution%20Reader).

A Microstrip-fed Printed Slot Antenna for 3G/Bluetooth/WiMAX and UWB Applications with 3.6 GHz Band Rejection

Mohamed Mamdouh M. Ali¹, Ayman Ayd R. Saad², and Elsayed Esam M. Khaled¹

¹Electrical Engineering Department, Assiut University, Assiut, Egypt

²Kosseir Radio, Telecom Egypt, Kosseir 84712, Egypt

Abstract— In this paper, a compact slot antenna fed by microstrip-line for 3G/Bluetooth/WiMAX and UWB applications with 3.6 GHz band-notched function is presented. A rectangular wide-slot etched off the ground plane is used to control the low frequency band and impedance matching of the proposed antenna. A modified rectangular tuning stub is used to enhance and control the operating bandwidth at the high frequency band. To reduce unwanted interference between IEEE 802.16e standard (3.3–3.9 GHz) and UWB communication systems, the antenna employs a U-shaped slot in the microstrip feeding line which provides a band-rejection performance at 3.6 GHz in the UWB frequency band. The proposed antenna is designed and simulated. Also the antenna is fabricated. The simulated results and measured data show an impedance bandwidth about 7.75 GHz (from 1.9 to 9.65 GHz) for UMTS (1.920 ~ 2.170 GHz)/Bluetooth (2.4 ~ 2.484 GHz)/WiMAX (2.5 ~ 2.96 GHz) and UWB (3.1 ~ 9.65 GHz) applications with good radiation characteristics, except at the narrow band notch (3.2 ~ 4.0 GHz). Moreover, an equivalent circuit model of the proposed antenna is presented through the use of a Vector Fitting (VF) technique for a rational function approximation that is compatible with time-domain circuit simulators.

1. INTRODUCTION

Since the Federal Communications Commission (FCC) approved rules for the commercial use of the ultra-wideband (UWB) with a frequency range of 3.1–10.6 GHz for commercial purposes, in 2002 [1], the feasible design and implementation of UWB system has become a highly competitive topic in both academy and industry communities of telecommunications. As the front-end equipment of the UWB communication systems, the UWB antenna is of course very vital. A suitable UWB antenna is supposed to fulfill many requirements such as small size, omnidirectional radiation patterns, constant group delay and a high and stable gain across the whole band.

In practical, it is desired to design an ultra bandwidth antenna that can operate in multifunctional wireless communication systems without performance distortion, such as wireless cellular telephone technology (2G ~ 4G), Bluetooth, WiMAX and the UWB technology [2, 3]. However, this antenna requires rejection of certain frequencies that already occupy narrow bands in the frequency spectrum, such as WLAN (5–6 GHz) and WiMAX (3.3–3.9 GHz) technologies, that interfere with the UWB frequency band [4, 11].

In this paper, a new printed slot antenna that covers 3G, Bluetooth, WiMAX, and the UWB but exhibits single band-notched characteristic at 3.6 GHz is proposed and studied. The design produces an ultra-wide bandwidth with return loss less than 10 dB in the frequency range of 1.9–9.65 GHz for UMTS (1.920 ~ 2.170 GHz)/Bluetooth (2.4 ~ 2.484 GHz)/WiMAX (2.5 ~ 2.96 GHz) and UWB (3.1 ~ 9.65 GHz) applications. Also it provides band-notch function at IEEE 802.16e standard narrowband (3.2 ~ 4.0 GHz). An electrical lumped-elements equivalent circuit is obtained for the proposed antenna. Also the antenna is fabricated. The mechanism of the antenna design accomplished with simulated results, measured data and equivalent circuit results are presented and discussed in the following sections.

2. ANTENNA DESIGN

In Fig. 1, the geometry of the proposed antenna is shown. It is built on a FR4 substrate with a thickness of $h = 1.5$ mm, a relative permittivity of $\epsilon_r = 4.7$, dielectric loss tangent $\tan \delta = 0.025$ and an overall dimensions of $L \times W = 40 \times 30$ mm². The antenna consists of a main rectangular wide-slot etched off the ground plane with size of $L_s \times W_s = 17 \times 28$ mm² at a distance $Y_r = 9$ mm from the top of the ground plane, that operates at low frequency mode. The 50 Ohm microstrip line having a width $W_f = 3$ mm and a length $L_f = 21$ mm, excite a manipulated rectangular patch with size of $L_p \times W_p = 6 \times 11$ mm² in conjunction with a reversed U-shaped strip of dimensions $L_{u1} = 10$ mm, and $L_{u2} = L_{u3} = 1$ mm of a uniform width $W_{up} = 1$ mm, as shown in Fig. 1(a). To

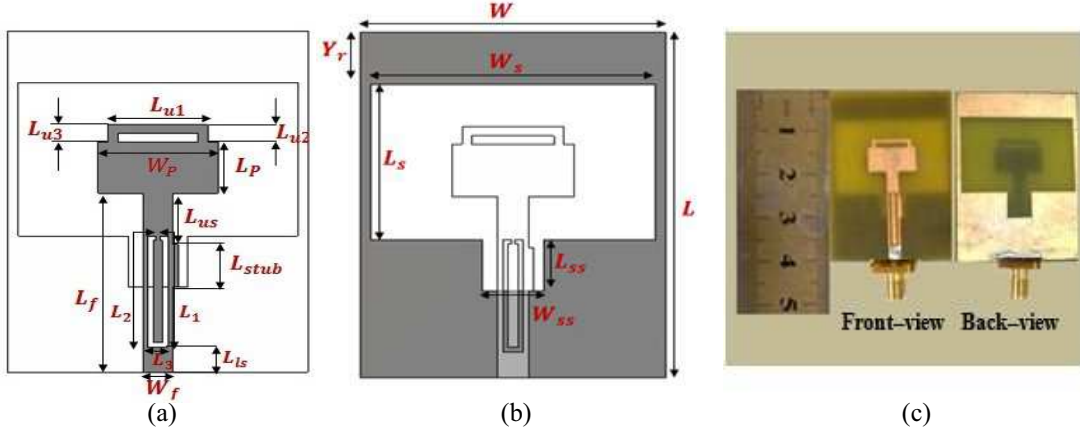


Figure 1: Geometry of the proposed antenna. (a) Front-view. (b) Back-view. (c) Photograph of the fabricated antenna.

improve the impedance matching at high frequency mode a rectangular slot with size of $L_{ss} \times W_{ss} = 6.5 \times 6 \text{ mm}^2$ is etched off the ground plane at the bottom of the rectangular wide slot underneath the microstrip fed line located in the other side of the antenna substrate as shown in Fig. 1(b). For further improving the impedance matching at high frequency mode a single shunt stub with length $L_{stub} = 5 \text{ mm}$ and a uniform width 1 mm is connected to the microstrip line at a distance $L_{us} = 7 \text{ mm}$ from the end of the patch. The proposed antenna achieve ultra wide operation frequency band for multi-band applications. By inserting a nearly half-wavelength U-shaped slot in the microstrip feeding line with total length $L_t = L_1 + L_2 + L_3 = 25.6 \text{ mm}$ of uniform width 0.5 mm at distance $L_{ls} = 3 \text{ mm}$ from the end of the line, the frequency band notch at 3.6 GHz of IEEE 802.16e WiMAX standard is created to minimize the interference with UWB operation. The proposed antenna is fabricated after optimizing its shape and dimensions. A photograph of the implemented antenna is shown in Fig. 1(c).

3. RESULTS AND DISCUSSION

In order to consider the effect of integrating the proposed antenna with a whole communication system simulation, the equivalent circuit of the proposed antenna is obtained based on the VF technique. The method is described as follows: First, the response of the input admittance of the proposed antenna obtained by simulation is calculated in the frequency range of interest. Second, the simulated response of the input admittance is fitted by means of the VF technique. Finally, the rational function is converted into a SPICE-compatible lumped-element equivalent circuit and the synthesized components values are obtained.

The rational approximation of a certain frequency domain response can be expressed as [5]:

$$F(s) = \sum_{k=1}^N \frac{res_k}{s - p_k} + d + se \quad (1)$$

where res_k and p_k denote the k th residues and poles, respectively which are either real quantities or complex conjugate pairs of N identical set of poles (order of approximation), $s = j\omega$ represents the complex frequency, d is a real constant term and e is a real proportional term. The terms d and e are optional.

Approximating rational functions through VF is a great tool that can be used to create equivalent circuits based on scattering parameter data. A major limitation in the creation of these equivalent circuits is the presence of negative resistors which makes the circuit non-physical [6, 7], although the stability and enforcing of passivity [8], due to the fact that this technique is not systematic. In other words, the method does not contain a physics-based approach, and therefore, it is expected that this method may not provide accurate results for all geometries. Nevertheless, it is stressed that this method can be used as a tool to aid engineers in designing an actual passive circuit that can be used to mimic the scattering parameter response of an antenna [7]. The details of this procedure to obtain the equivalent circuit of UWB antenna can be found in [9-11].

In this paper, to avoid the non-physical circuit elements, a different circuit representation for complex pairs is employed for the generation of SPICE compatible equivalent circuit of UWB

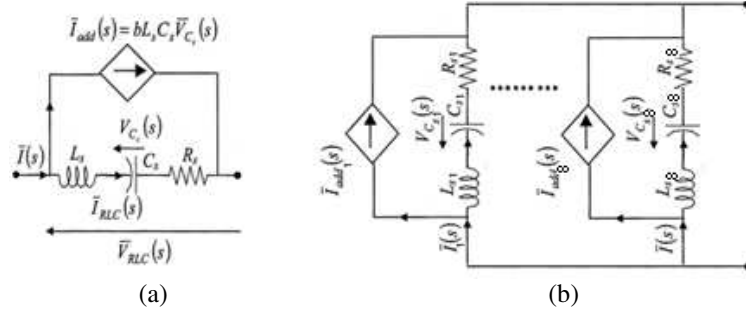


Figure 2: (a) Equivalent series RLC circuit for complex pole pair synthesis. (b) Overall synthesized equivalent circuit of the proposed antenna.

antenna [12]. The overall equivalent circuit of the function $F(s)$ is shown as a series RLC circuit in parallel with a voltage-controlled current source (VCCS) whose voltage is $V_{cs}(s)$ and controlling factor $bL_s C_s$ in which b is frequency independent and given as in [12]. The resulting equivalent circuit is shown in Fig. 2(a).

Without loss of generality, $F(s)$ is applied to the simulated admittance-type function, $Y(s)$ of the proposed antenna. The set of the initial poles is found to be 8 complex pairs ($N = 16$) linearly spaced over the frequency range of interest (1 to 10 GHz) with 3 iterations to refine the fitting to a very accurate approximation. The fitting procedure provides 8 complex conjugate pairs when $d = e = 0$. The computed *rms*-error of the magnitude is found to be 7.5314e-004. Table 1 shows the component values for the equivalent circuit of the proposed antenna corresponding to the rational approximation (poles and residues). Consequently, the equivalent circuit model of the proposed antenna is synthesized as shown in Fig. 2(b).

Table 1: Synthesized component values of the proposed antenna.

Type and No. of poles	R_s (Ω)	L_s (H)	C_s (F)	$bL_s C_s$ (S)
Complex 1	0.9041	0.0901E-07	0.1478E-11	0.0000
Complex 2	48.8439	0.1317E-07	0.0407E-11	-0.0024
Complex 3	47.0866	0.1104E-07	0.0255E-11	0.0038
Complex 4	32.8314	0.1288 E-07	0.0139E-11	-0.0030
Complex 5	60.4830	0.1004 E-07	0.0102E-11	0.0000
Complex 6	52.4736	0.1188E-07	0.0049E-11	-0.0006
Complex 7	55.5881	0.0498E-07	0.0073E-11	0.0005
Complex 8	1.5312	0.0078E-07	0.0201E-11	0.0015

It is observed that, the proposed is suitable for providing equivalent circuits of UWB antenna with physical and passive circuit elements.

The electromagnetic software CST Microwave Studio 2010 is employed to perform the design and optimization process. The measurement of VSWR of the fabricated antenna is carried out with a vector network analyzer, Agilent HP8719ES. Fig. 3(a) shows the characteristics of the measured and simulated VSWR of antenna along with the equivalent circuit results. A good agreement between measurements and calculations can be observed. It is found that the proposed antenna is well matched in the bandwidth of 1.9 ~ 9.65 GHz for $VSWR < 2$, which is suitable for UMTS (1.920 ~ 2.170 GHz)/Bluetooth (2.4 ~ 2.484 GHz)/WiMAX (2.5 ~ 2.96 GHz) and UWB (3.1 ~ 9.65 GHz) applications, and exhibited a notched band at (3.2 ~ 4.0 GHz) for existence of the IEEE 802.16e standard.

Figure 3(b) shows the input impedance of the proposed antenna with and without shunt stub. It is apparent that the input impedance of the proposed antenna with the shunt stub is more adjusted with better performance than that of the antenna without the shunt stub, which enhances the impedance matching of the antenna in higher frequencies.

Figure 4 shows the normalized far field radiation patterns of E_θ and E_φ in the yz (E -plane) and xz (H -plane) planes of the proposed antenna at frequencies 2.5 and 7.5 GHz. It is observed that the simulated patterns exhibits a relatively omidirectional radiation in the xz plane at these

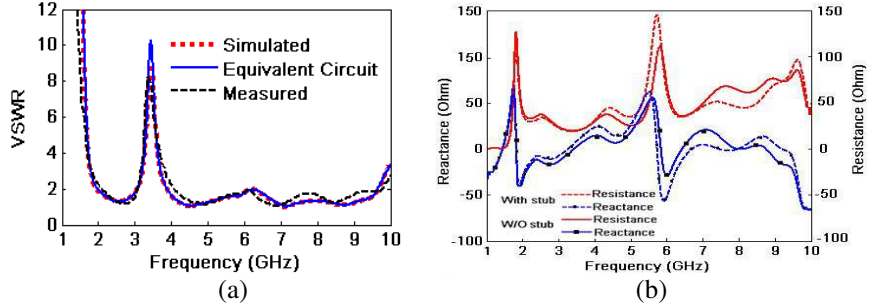


Figure 3: (a) VSWR characteristics of the proposed antenna. (b) Simulated input impedance versus frequency of the proposed antenna with and without open shunt stub.

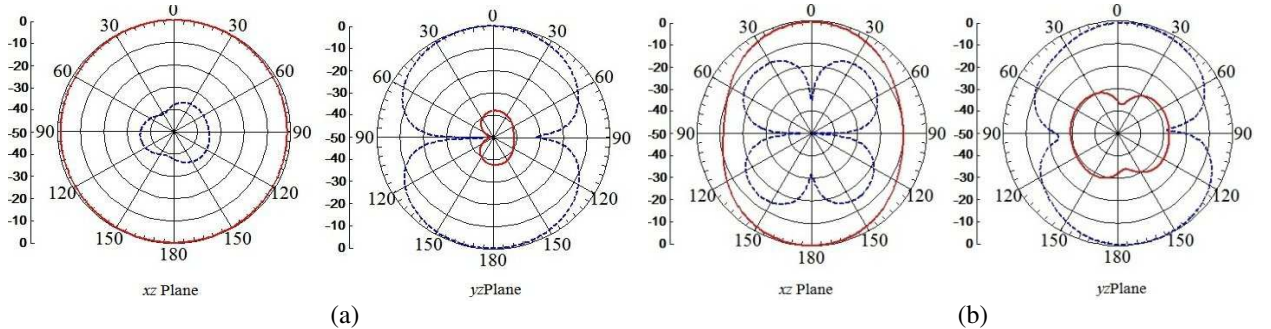


Figure 4: Simulated radiation patterns of E_θ (dashed line) and E_φ (solid line) in the yz and xz planes of the proposed antenna at different frequencies, (a) 2.5 GHz, (b) 7.5 GHz.

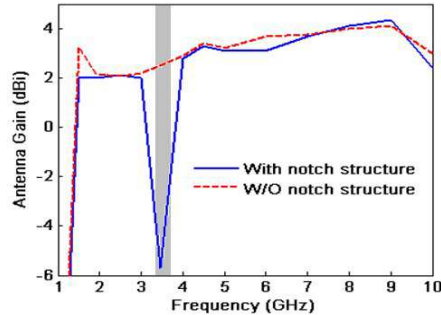


Figure 5: Simulated peak gain of the proposed antenna with and without the resonating U-slot.

frequencies whereas, the simulated patterns in the yz plane illustrates radiations, look like E -plane radiation pattern of a vertical dipole.

The simulated peak gain of the proposed antenna is shown in Fig. 5. Stable gain with an average of about 3.5 dBi is obtained throughout the operating band. Significantly drop of the antenna gain is observed at the notched frequency band in the vicinity of 3.6 GHz.

4. CONCLUSION

A compact design of a wide-band operations slot antenna for personal and mobile or medical UWB applications is designed and implemented. In this design, the antenna can cover UMTS (1.92 ~ 2.17 GHz), Bluetooth (2.4 ~ 2.484 GHz), WiMAX (2.5 ~ 2.96 GHz), and the UWB (3.1 ~ 9.65 GHz) frequency bands. The proposed antenna satisfies the necessity of using a single antenna to cover several allocations wireless frequency-band applications. Moreover, the proposed antenna provides a band-notch feature at (3.2 ~ 4.0 GHz) for IEEE 802.16e standard to reduce the potential interference with UWB operations. The presented simulated and measured results are showing that the proposed antenna has a good and stable gain. Also the proposed antenna provides good and almost omnidirectional radiation patterns across all the relevant bands except the notched one. In

addition, the equivalent circuit model of the proposed antenna is obtained for further comprehension of the antenna performance, when integrated with the whole communication system.

REFERENCES

1. Federal Communications Commission, "First report and order," Revision of Part 15 of the Commission's Rule Regarding Ultra-wideband Transmission Systems, Feb. 2002.
2. Li, W. T., Y. Q. Hei, W. Feng, and X. W. Shi, "Planar antenna for 3G/Bluetooth/WiMAX and UWB applications with dual band-notched characteristics," *IEEE Antennas Wireless Propag. Lett.*, Vol. 11, 61–64, 2012.
3. Xu, L., B. Yuan, and S. He, "Design of novel UWB slot antenna for bluetooth and UWB applications," *Progress In Electromagnetics Research C*, Vol. 37, 211–221, 2013.
4. Khaled, E. E. M., A. A. R. Saad, and D. A. Salem, "A proximity-fed annular slot antenna with different a band-notched manipulations for ultra-wideband applications," *Progress Electromagnetics Research B*, Vol. 37, 289–306, 2012.
5. Gustavsen, B. and A. Semlyen, "Rational approximation of frequency domain responses by vector fitting," *IEEE Trans. Power Delivery*, Vol. 14, 1052–1061, Jul. 1999.
6. DeJean, G. R. and M. M. Tentzeris, "Modeling and optimization of circularly-polarized patch antennas using the lumped element equivalent circuit approach," *IEEE Antennas Propag. Society Int. Symp.*, Vol. 4, 4432–4435, Jun. 2004.
7. DeJean, G. R. and M. M. Tentzeris, "The application of lumped element equivalent circuits approach to the design of single-port microstrip antennas," *IEEE Trans. Antennas Propag.*, Vol. 55, No. 9, 2472–2468, Sep. 2007.
8. Gustavsen, B. and A. Semlyen, "Enforcing passivity for admittance matrices approximated by rational functions," *IEEE Trans. Power System*, Vol. 16, 97–104, Feb. 2001.
9. Saad, A. A. R., D. A. Salem, and E. E. M. Khaled, "Design and circuit-modeling of a novel printed split-ring resonator antenna with 5.5 GHz band-notched characteristics," *30th National Radio Science Conference (NRSC 2013)*, 100–108, National Telecommunication Institute (NTI), Cairo, Egypt, Apr. 2013.
10. Saad, A. A. R., E. E. M. Khaled, and D. A. Salem, "A novel proximity-fed UWB printed slot antenna with 3.6/5.5 GHz dual band-notched characteristics: Design and circuit-modeling," *30th National Radio Science Conference (NRSC 2013)*, 90–99, National Telecommunication Institute (NTI), Cairo, Egypt, Apr. 2013.
11. Mahmoud Ali, M., A. R. Saad, and E. M. Khaled, "A design of miniaturized ultra-wideband printed slot antenna with 3.5/5.5 GHz band-notched characteristics: Analysis and implementation," *Progress In Electromagnetics Research B*, Vol. 52, 37–56, 2013.
12. Antonini, G., "SPICE equivalent circuits of frequency-domain responses," *IEEE Trans. Electromagnetic Compatibility*, Vol. 45, No. 3, 502–512, Aug. 2003.

Symmetrical T-stubs Coupled Miniature Square Open-loop Dual-band Bandpass Filter for C- and X-band Applications

Ram Krishna Maharjan and Nam-Young Kim

RFIC Center, Kwangwoon University

447-1 Wolgye-dong, Nowon-ku, Seoul 139-701, Korea

Abstract— A compact microstrip symmetrical T-stubs coupled dual-band square open-loop bandpass filter (BPF) with asymmetrical feed lines is proposed. English letter T-shaped stub is inserted inside-wall of each square loop resonator. The maximum coupling can be possible by optimizing the open-loop gap, the spacing of the two open-loop resonators, the orientation of the loaded T-stubs, and controlling parameters of T-stubs itself. The asymmetrical port terminals also enhance to couple electromagnetic (EM) energy to maintain 50Ω impedance matching with input/output devices. The open gap between the two loops of the filter structure strongly inhibits the flow of DC current and out-of-band signals. The face-to-face open sides of the loops orientation build up strong electric fields and inserted T-stubs are subjected to generate the magnetic coupling through the open gaps; as a result, the combined coupling gives an effective EM coupling in the proposed filter with adequate transmission and reflection coefficients for dual-band frequencies. The first and second band resonant frequencies were measured at 5.85 GHz and 9.35 GHz, respectively. The measured return losses (S_{11}) of the fabricated filter are of -14.6 dB and -14.8 dB ; and insertion losses (S_{21}) are of -1.5 dB and -1.7 dB , at the first and the second resonant frequencies of the dual-band bandpass filter, respectively. The spurious suppression was measured to be more than -35 dB at out-band frequencies in all of four transmission zeros. The design analysis for this research primarily focuses on applying the highly compatible size and planarity of a type reliable bandpass filter utilized for the combined C- and X-band frequencies in a single communication system, and therefore this proposed bandpass filter can be used for fusion application in modern remote sensing satellite systems.

1. INTRODUCTION

Recently, remote sensing satellite systems have been more widely used in disaster management and other signal detection from the earth's surface. However, because of cloud cover and fog, using optical imagery for detection is not always feasible for general identification at the target location. Therefore, it could be more practical to apply all-weather RF imaging instead of weather dependent optical imaging [1]. Remote sensing satellites that use RF signals to receive images of targeted areas can provide better resolution even in worse weather conditions. Currently, the combined RF footprint coverage of C- and X-band for remote sensing applications is an emerging technology. They are mostly used for RF data collection for image identification of the earth's surface. In some countries, it is quite common to have dual coverage from both C- and X-band radars installed in the same remote sensing satellite. Because, a combined C- and X-band filter has a single purpose with dual band capability, it can be considered a fusion technology for remote sensing satellite systems and can be used for RF data collection during image identification on the earth's surface [2]. In this work, for this research primarily focuses on applying the highly compatible size and planarity of a type reliable BPF that can be utilized for combined C- and X-band frequencies for remote sensing purpose in a single communication system [2, 3]. The proposed BPF can be very useful to the system by reducing the cost and size, as well as enhancing the overall system performance. This type of microstrip filter can be a desired size and is easily mounted on a dielectric substrate using printed circuit technology. These planar filters have the advantages of a low profile, high selectivity and good reliability. They are also compact and light-weight and can conform to the mounting structure, integrate with solid-state devices and be easily fabricated at low cost. This makes them attractive not only for satellite remote sensing systems but also in military applications and space communications.

2. DESIGN ANALYSIS OF DUAL-BAND BPF

In this design analysis, we utilized a commercially available EM simulator of the Sonnet tool to realize the desired filter characteristics. Figure 1 shows the schematic design layout of the dual-band BPF with the appropriate dimensions. The electric coupling and magnetic coupling phenomena in the design structure can also be seen in the illustrated figure. The T-stubs mounted on the inner

wall of each square loop resonator help to enhance and combine the magnetic coupling effectively, and the open-gap of the parallel square loops has also strong capacitive effects resulting to produce the electric coupling phenomena. Each T-stub loaded square open-loop structure is tied with the asymmetric feeder lines for proper excitation at the desired resonant frequencies in the dual-band response and to maintain 50Ω impedance matching with input/output devices [46]. The loaded T-stubs play an important role to convert the single-band filter characteristic into a dual-band response. The rectangular-bar that forms the T-stub is only $0.4 \times 2.0\text{ mm}^2$ and is very important in the dual-band response with effective and useful scattering parameters.

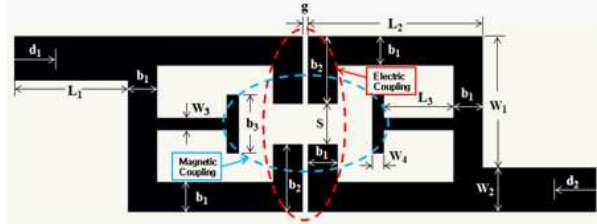


Figure 1: Schematic design layout of the proposed dual-band filter.

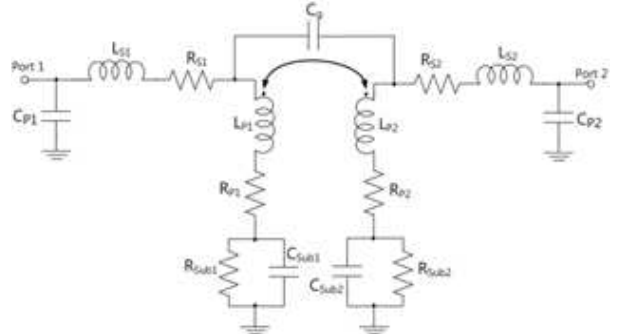


Figure 2: Equivalent circuit of the filter.

The electric and magnetic coupling phenomena due to the capacitive and magnetic behaviors of the given resonators will be clearly demonstrated with the use of an equivalent circuit model, as shown in Figure 2. For simplicity in the equivalent model, we introduce R_{S1} , L_{S1} and R_{S2} , L_{S2} as two symmetrical branches belonging to the respective feeders, which can model the surface layer resistance and the inductance of the corresponding square loops. L_{P1} and L_{P2} are models of the equivalent inductances, which are mutually coupled with each other in terms of their magnetic connection as a reflection of a virtual planar transformer. In this analysis, the parallel resistances in the model corresponding to L_{P1} and L_{P2} are represented by R_{P1} and R_{P2} , respectively, as small resistive effects of mutual inductors. The overall equivalent capacitance for the two open loops is modelled by a capacitor, C_g , in the centre of the circuit model. The substrate circuits of R_{Sub1} , C_{Sub1} and R_{Sub2} , C_{Sub2} are the equivalent metal-to-substrate connections of an RC network. The ohmic (I^2R) loss in the conductive substrate is, due to the displacement current conducted through the metal-to-substrate capacitance that is contributed by the model substrate-resistance, R_{Sub} . It can be modelled by the substrate RC network, which is composed of both sides of R_{Sub} and C_{Sub} in the parallel circuit. C_{P1} and C_{P2} are the respective pad capacitances of port 1 and port 2.

3. FABRICATION AND RESULTS

The actual physical structure of the proposed device is mentioned as in Figure 1. The photograph of the fabricated BPF is demonstrated in Figure 3. It was developed by photolithographic techniques and wet-etching process in the printed circuit technology. The filter was designed and fabricated on the Teflon substrate with a thickness, h of 0.504 mm and a relative dielectric constant, ϵ_r of 2.52 . The last optimized geometric dimensions were fixed in which the actual physical dimensions of the proposed device mentioned as in Figure 1 are as follows: $W_1 = 4.5\text{ mm}$, $W_2 = 1.5\text{ mm}$, $W_3 = 0.4\text{ mm}$, $W_4 = 0.4\text{ mm}$, $L_1 = 3.9\text{ mm}$, $L_2 = 6.0\text{ mm}$, $L_3 = 2.4\text{ mm}$, $d_1 = 1.5\text{ mm}$, $b_1 = 1.0\text{ mm}$, $b_2 = 2.4\text{ mm}$, $b_3 = 2.0\text{ mm}$, $S = 1.2\text{ mm}$ and $g = 0.2\text{ mm}$ (units are all in mm). The overall device size of the fabricated filter is $6 \times 20\text{ mm}^2$ which equals approximately $0.12\lambda_{g1} \times 0.39\lambda_{g1}$ for the first band and approximately $0.19\lambda_{g2} \times 0.62\lambda_{g2}$ for the second band, where λ_{g1} and λ_{g2} are the guided wavelengths of center operating frequencies of the first and the second band, respectively. Thus, the proposed T-stub loaded filter is able to be miniaturized comparing with the previous design works [7–10]. The fabricated filter was tested and characterized using an Agilent 8510C vector network analyzer (VNA). The filter was originally simulated and designed at 6.0 GHz and 9.5 GHz . The measured S_{11} of the both bands became a little wider and a lower reflection amplitude than predicted simulations results. The measured and simulated S -parameter responses of the dual-band BPF are compared in Figure 5.23. The first and second band resonant frequencies are measured at 5.85 GHz and 9.35 GHz , respectively. These center frequencies are shifted down from their simulated results. The measurement results showed the S_{11} equal to -14.6 dB and -14.8 dB ; similarly, S_{21} were measured -1.5 dB and -1.7 dB for the

first and the second resonant frequencies, respectively.

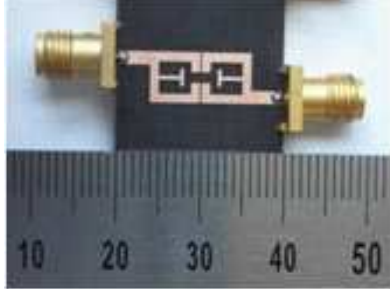


Figure 3: Photograph of the fabricated filter.

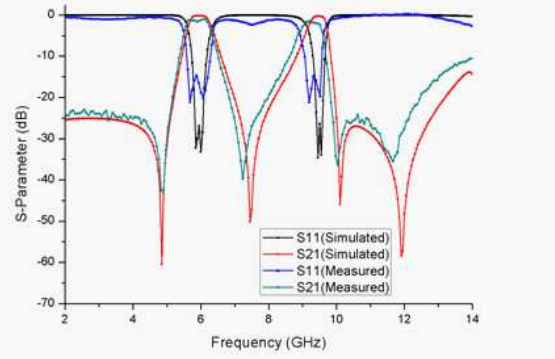


Figure 4: Comparison of S -parameter responses.

4. CONCLUSIONS

The SOL BPF was designed, fabricated, measured and compared with the predicted simulation results. The compact BPF with inserted T-stubs on the inner walls of the symmetric square open-loop structures was presented. The proposed filter can be useful to reduce the cost and enhance the system performance. In addition, it can easily be conformable to the mounting structure, where space is very critical, such as in spacecraft and satellites. Due to the inserted-stubs inside the proposed SOLs, a dual-band filter with four transmission zeros was possible. These types of BPF can be attractive in fixed satellite service and remote sensing satellite systems.

ACKNOWLEDGMENT

This research work was supported by the National Research Foundation of Korea (NRF) and a Grant supported from the Korea government (MESH) (No. 2012-0009224) and (No. 2012R1A1A200-4366). This work was also supported by a Research Grant of Kwangwoon University in 2013.

REFERENCES

1. Lau, S. W., "Comparison and fusion of space borne L-, C- and X-band SAR images for damage identification in the 2008 Sichuan earthquake," *Division of Geodesy and Geoinformatics, Royal Institute of Technology (KTH)*, TRITA-GIT EX 11-003 Report, Stockholm, June 2011.
2. Pellarin, T., Y. H. Kerr, and J. P. Wigneron, "Global simulation of brightness temperatures at 6.6 and 10.7 GHz over land based on SMMR data set analysis," *IEEE Tran. on Geoscience and Remote Sensing*, Vol. 44, 2492–2505, 2006.
3. Pozar, D. M., *Microwave Engineering*, 3rd Edition, New York, 2004.
4. Maharjan, R. K. and N.-Y. Kim, "Compact stub-coupled square open-loop bandpass filter for Ku-band applications," *Journal of Electromagnetic Waves and Applications*, Vol. 26, Nos. 5–6, 603–614, 2012.
5. Maharjan, R. K., B. Shrestha, and N. Y. Kim, "Compact microstrip square open-loop bandpass filter using open-stub," *IET Electron. Lett.*, Vol. 48, No. 6, 333–334, 2012.
6. Maharjan, R. K. and N. Y. Kim, "Microstrip dual I-band bandpass filter with symmetrical twininductor resonators," *Microw. and Optical Techn. Lett.*, Vol. 54, No. 3, 638–641, 2012.
7. Mondal, P. and M. K. Mandal, "Design of dual-band bandpass filters using stub-loaded open-loop resonators," *IEEE Trans. Microw. Theory Tech.*, Vol. 56, No. 1, 150–155, 2008.
8. Singh, Y. K. and A. Chakrabarty, "Miniaturized dual-mode band-pass filter using stub-loaded square ring resonator," *Microw. and Optical Techn. Lett.*, Vol. 51, No. 8, 1927–1929, 2009.
9. Chen, F.-C., Q.-X. Chu, and Z.-H. Tu, "Tri-band bandpass filter using stub loaded resonators," *IET Electron. Lett.*, Vol. 44, 747–749, 2008.
10. Deng, H.-W., Y.-J. Zhao, X.-S. Zhang, L. Zhang, and S.-P. Gao, "Compact wide upper-stopand BPF using open stub loaded dual-mode resonator," *Microw. and Optical Techn. Lett.*, Vol. 52, 2185–2188, 2010.

Theoretical Study of the Coupling Factor of Open-ended Coupled Transmission Lines at First Resonant Frequencies under Quasi-TEM Propagation

E. Bronchalo¹, M. A. Sánchez-Soriano², G. Torregrosa¹, and A. Coves¹

¹Departamento de Ingeniería de Comunicaciones, Universidad Miguel Hernández de Elche
Elche, Alicante 03202, Spain

²Lab-STICC, Université Bretagne Occidentale, Brest, France

Abstract— In this work we present the results of a theoretical study on identical, open-ended transmission lines coupled with arbitrary coupling strength under the assumption of quasi-TEM propagation. The study focuses on the coupling factor between resonant lines, as this parameter has a great practical interest in the design of RF and microwave filters. The coupling factor of a pair of identical resonators is usually calculated from the two resonant frequencies into which the fundamental frequency of the isolated resonators is split. This method leads a unique coupling factor for the two resonant frequencies. In this work, we have used the definitions of electric, magnetic and total coupling factors based on the ratio of coupled and uncoupled energies at a given resonance. Exact expressions for the resonant frequencies, voltage and current distributions have been used to calculate the different energies and the coupling factors at the two first resonant frequencies split from the fundamental one as a consequence of the coupling. The theoretical expressions obtained have been used to compare the behavior of several definitions of coupling coefficients as functions of the coupling length.

1. INTRODUCTION

The wave propagation in coupled transmission lines and the electromagnetic coupling between resonators are classical topics of applied electromagnetics [1–3]. The coupling strength between propagating modes on coupled transmission lines is usually expressed in terms of per-unit-length circuital parameters, and the formalism describing the propagation of voltage and current waves in coupled lines, supposing TEM or quasi-TEM propagation, is well established. For a pair of identical, lossless coupled lines, the circuit model, shown in Figure 1, is especially simple. The parameters L and L_m denote the self-inductance of each line and their mutual inductance, respectively, while $C-C_m$ and C_m denote the line capacitance and mutual capacitance. All these parameters are per-unit-length parameters. One of the two TEM or quasi-TEM propagating modes has even symmetry and the other one odd symmetry. As is well known, their velocities and characteristic impedances can be easily expressed in terms of the circuital parameters:

$$v_e = \frac{v}{\sqrt{LC(1 + k_L)(1 - k_C)}}, \quad v_o = \frac{1}{\sqrt{LC(1 - k_L)(1 + k_C)}} \quad (1a)$$

$$Z_e = \sqrt{\frac{L}{C}} \sqrt{\frac{1 + k_L}{1 - k_C}}, \quad Z_o = \sqrt{\frac{L}{C}} \sqrt{\frac{1 - k_L}{1 + k_C}} \quad (1b)$$

Here we have introduced the capacitive and inductive coupling coefficients:

$$k_C \equiv \frac{C_m}{C}, \quad k_L \equiv \frac{L_m}{L} \quad (2)$$

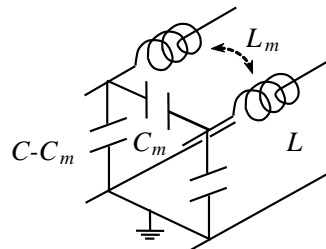


Figure 1: Circuit model of a pair of identical, lossless coupled transmission lines.

For pure TEM propagation, $k_C = k_L$ as a consequence of the equality between v_e and v_o . The coefficients k_C and k_L are local in nature, and therefore we will refer to them as local coupling coefficients to distinguish from the global coupling coefficients to be defined later.

For coupled resonators, coupling coefficients analogous to k_L and k_C can be defined. Coupled resonators play an essential role as building elements of passband filters. The canonical filter coefficients determining the filter response are related to the coupling coefficients between the resonators that make up the filter by well-known expressions [4–6]. Besides, the control of coupling coefficients at spurious resonances can be used to enhance the out-of-band filter performance [7]. Here we are concerned with resonators consisting of a pair of identical, lossless, open-ended transmission lines coupled by proximity along a part of their length. In the following sections we will study the resonant frequencies, current and voltage distributions of these resonators, we will present some definitions of coupling coefficients for coupled resonators, and we will use the analytical current and voltage distributions to calculate and compare those different coupling coefficients.

2. STUDY OF VOLTAGE AND CURRENT DISTRIBUTION OF A PAIR OF IDENTICAL, COUPLED, OPEN ENDED TRANSMISSION LINES

The system under study is schematically shown in Figure 2. The subscript in the impedances and the velocities are e and o for the even and odd propagating modes in the coupling region of length l_c , and u for the uncoupled parts of the lines. The complete knowledge of the voltage and current distributions in the lines requires finding eight wave amplitudes (forward and backward amplitudes for the two uncoupled regions and for the two modes in the coupled region). The open-circuit conditions in the lines ends plus the voltage and current continuity conditions in the coupled-uncoupled frontiers lead to an eigenvalue problem.

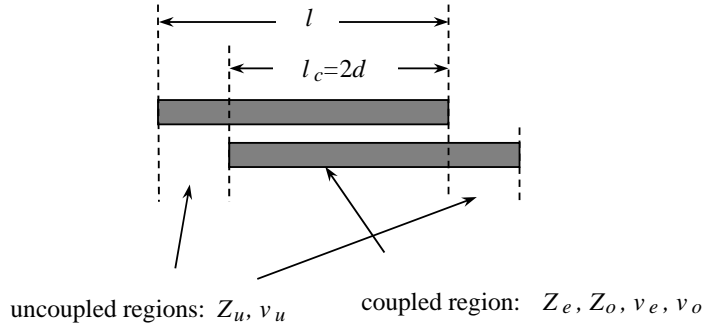


Figure 2: A pair of identical, coupled, open-ended transmission lines.

There are two infinite set of solutions, or resonances, whose resonant frequencies fulfill the following equations:

$$2Z_u \operatorname{ctg}(\beta_u(l - l_c)) = Z_i \operatorname{tg}(\beta_i d) - Z_p \operatorname{ctg}(\beta_p d) \quad (3a)$$

$$2Z_u \operatorname{ctg}(\beta_u(l - l_c)) = Z_p \operatorname{tg}(\beta_p d) - Z_i \operatorname{ctg}(\beta_i d) \quad (3b)$$

where β_k are the phase constant ($= \omega/v_k$) at the resonant frequencies. The corresponding voltage and current distributions are linear combinations of sinusoidal functions fulfilling the boundary and continuity conditions. Figure 3 shows an example corresponding to the following parameters: $k_C = 0.25$, $k_L = 0.35$, $l_c/l = 0.6$, $Z_u = (Z_p Z_i)^{1/2}$.

These current and voltage distributions can be used to calculate the coupling coefficients between the two coupled-line resonators, as we will see in the following sections.

3. GLOBAL COUPLING COEFFICIENTS

The coupling coefficients for two coupled resonators have been defined in several ways by different authors. Hong and Lancaster [5] use the following definition:

$$K = \frac{U_{M12}}{2\sqrt{U_{M1}U_{M2}}} + \frac{U_{E12}}{2\sqrt{U_{E1}U_{E2}}} \quad (4a)$$

where the subscripts 1 and 2 denote the resonators, U_{M1} , U_{M2} , U_{E1} , U_{E2} are magnetic and electric energies stored in each resonator, and U_{M12} and U_{E12} are coupled magnetic and electric energies.

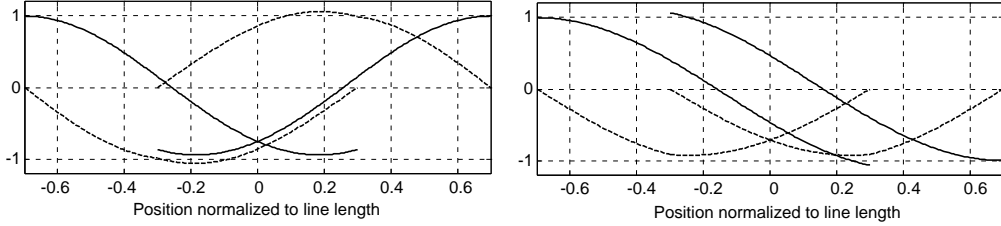


Figure 3: Voltage (solid) and current (dashed) distributions for the two resonances of a pair of open-ended coupled lines (see text). The currents have been multiplied by an impedance to use the same scale as the voltage. The plots do not show a 90° phase difference between currents and voltages. Arbitrary voltage units have been used for the vertical axis.

The first term in the sum can be considered a magnetic coupling coefficient and the second one an electric coupling coefficient, denoted by K_M and K_E , respectively, on what follows. Tyurnev [8] presents an alternative definition:

$$K_M = \frac{K_{M12}}{\sqrt{(U_{M1} + U_{E1})(U_{M2} + U_{E2})}}, \quad K_E = \frac{U_{E12}}{\sqrt{(U_{M1} + U_{E1})(U_{M2} + U_{E2})}} \quad (5a)$$

The total coupling coefficient used by Tyurnev is

$$K = \frac{K_M + K_E}{1 + K_M K_E} \quad (6)$$

This equation can be considered as a generalization of a result obtained for LC resonant circuits with inductive and capacitive coupling [5].

All those coupling coefficients are related to the energy exchange between the whole resonators, and therefore we will refer to them as global coupling coefficients. For isolated identical resonators the Hong-Lancaster definition reduces to

$$K_M = \frac{U_{M12}}{2U_{M1}}, \quad K_E = \frac{U_{E12}}{2U_{E1}} \quad (4b)$$

and the Tyurnev definition gives

$$K_M = \frac{U_{M12}}{U_{M1} + U_{E1}}, \quad K_E = \frac{U_{E12}}{U_{M1} + U_{E1}} \quad (5b)$$

In the limit of weak coupling, the coupled energies represent a small amount of the total energy. In that case, and taking into account that the mean magnetic and electric energies are equal at resonance, (4b) and (5b) give similar results for identical resonators, as those considered in this work.

From a practical point of view, the total coupling coefficient for identical resonators can be obtained from the two resonant frequencies f_1 and f_2 in which the fundamental frequency f_0 of the isolated resonators is split [5]:

$$K = \frac{f_2^2 - f_1^2}{f_2^2 + f_1^2} \quad (7)$$

This formula provides a unique coefficient for the two resonances, while (4a), (4b) and (5a), (5b) can be calculated separately at each resonance. Therefore, for strong coupling, when $f_2 - f_1$ is a relatively large fraction of f_0 , the meaning of this coefficient is somewhat ambiguous.

In order to compare the different coupling coefficients presented here, we have used the exact voltage and current distributions of a pair of isolated, identical and lossless open-ended coupled-line resonators at the first resonant frequencies given by (3a) and (3b). With these distributions, we have calculated the energies involved in (4b) and (5b) and the corresponding coupling coefficients as functions of the coupling length to resonator length ratio. The results are presented in the following section.

We have to mention that for simplicity we have not taken into account the capacitive effects associated to the line ends. These effects, however, are not difficult to include in the model.

4. ENERGETIC CALCULATION AND RESULTS

From the circuit model of Fig. 1, the different energies used in the definitions (4a), (4b) and (5a), (5b) can be calculated as

$$U_{Ek} = \frac{1}{2} \int_{line\ k} CV_k^2(x)dx \quad U_{Mk} = \frac{1}{2} \int_{line\ k} LI_k^2(x)dx \quad (8a)$$

$$U_{E12} = - \int_{coupling\ region} C_m V_1(x)V_2(x)dx \quad U_{M12} = \int_{coupling\ region} L_m I_1(x)I_2(x)dx \quad (8b)$$

Real voltage and current functions have been used. As these functions are linear combinations of sinusoids, the integrals in (8a) and (8b) can be easily solved, the results being functions of l , l_c and of the circuital parameters of Figure 1.

We have applied this theoretical scheme to calculate the global coupling factor of two identical microstrip resonators whose geometrical and material parameters are the following: relative permittivity of the substrate: 9.8 (alumina); loss tangent; 10^{-4} ; substrate height: 700 μm ; conductor: copper; conductor thickness: 25 μm ; strips width: 550 μm ; strips separation: 170 μm ; strips length: 20 mm. The local coupling parameters have been calculated using the parametrization given in [9], the result being $k_L = 0.3966$ and $k_C = 0.2927$.

Figure 4 shows a plot of the total coupling factors between the two microstrip resonators as given by formulas (4b) (Hong and Lancaster, red lines), (5b) (Tyurnev, blue lines) and (7) (black line). The solid lines are for the resonance of higher frequency, and the dashed lines for the lower one. Formulas (4b) and (5b) have been used along with the addition rule (6), although the difference respect a direct sum is not very important in this example.

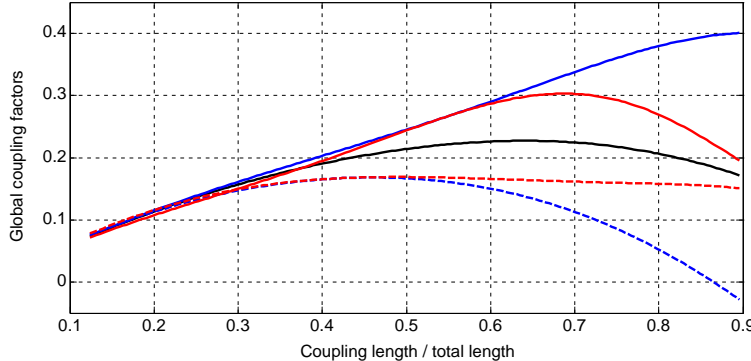


Figure 4: Total coupling factors following (4b) (red), (5b) (blue) and (7) (black) as functions of l_c/l . Solid lines: higher frequency resonance. Dashed lines: lower frequency resonance.

Some relevant consequences can be extracted from this graph. 1) Even for a moderate local coupling strength, the differences between Tyurnev and Hong-Lancaster coupling coefficients are not very important for coupling lengths lower than 50%, but this difference increases strongly for higher coupling lengths. 2) The coupling coefficient (5b) for the lower frequency resonance presents a null for $l_c/l = 0.865$. In order to test the existence of such a coupling null, we have simulated using the electromagnetic simulator Sonnet the coupled microstrip resonators with the dimensions given below and several l_c/l values around 0.865. Input and output 50 Ω microstrip lines with a very weak coupling to the resonators have been used to excite the resonators. Special care has been taken to avoid any significant level of cross-coupling between the I/O lines and the non-adjacent resonators. In all cases two well defined peaks near the theoretical resonant frequencies given by (3a)–(3b) were present, indicating the absence of coupling nulls. The small differences between the resonant frequencies obtained in the simulations and (3a)–(3b), in the range of 0.5–1.5%, could be due to the end-line capacitive effects, not taken into account in the model. But the important fact is that the coupling null predicted by (5b) has not been founded in the simulations.

Although not shown in the graph to facilitate its understanding, the mean between the coupling coefficients of the two resonances has been calculated for (4b) and (5b). In both cases, the resulting curves are close to the curve (7), the difference being less than 8% with for $l_c/l < 0.9$.

5. CONCLUSIONS

Using analytical expressions for resonant frequencies, current and voltage distributions, the different energies involved in the resonance of two identical, open-ended coupled-lines have been calculated. With these energies, the global coupling coefficients given by three different approaches have been compared for a pair of coupled microstrip lines. The results show that the different approaches give similar results for coupling lengths lower than half the resonators length, but they differ significantly for higher coupling lengths. In the example analyzed, one of the approaches (5b) gives a coupling null for one of the two resonances generated from the fundamental frequency by the coupling at a coupling length around $0.865l$. The simulations do not show any evidence of this coupling null.

ACKNOWLEDGMENT

This work was supported by the Ministerio de Ciencia e Innovación, Spanish Government, under the coordinated project TEC2010-21520-C04-02.

REFERENCES

1. Krage, M. K. and G. I. Haddad, “Characteristics of coupled microstrip transmission lines — I, Coupled mode formulation of inhomogeneous lines,” *IEEE Trans. Microw. Theory Tech.*, Vol. 18, No. 4, 217–222, Apr. 1970.
2. Tripathi, V. K., “Asymmetric coupled transmission lines in an inhomogeneous medium,” *IEEE Trans. Microw. Theory Tech.*, Vol. 23, No. 9, 734–739, Sep. 1975.
3. Speciale, R. A., “Even- and odd-mode waves for nonsymmetrical coupled lines in nonhomogeneous media,” *IEEE Trans. Microw. Theory Tech.*, Vol. 23, No. 11, 897–907, Nov. 1975.
4. Matthaei, G., E. M. T. Jones, and L. Young, *Microwave Filters, Impedance-matching Networks, and Coupling Structures*, Artech House, 1980.
5. Hong, J.-S. G. and M. J. Lancaster, *Microstrip Filters for RF/Microwave Applications*, John Wiley & Sons, New York, 2001.
6. Mongia, R. K., I. J. Bahl, P. Bhartia, and J. Hong, *RF and Microwave Coupled-line Circuits*, Artech House, 2007.
7. Sánchez-Soriano, M. A., E. Bronchalo, and G. Torregrosa-Penalva, “Parallel-coupled line filter design from an energetic coupling approach,” *IET Microw. Antennas Propag.*, Vol. 5, No. 5, 568–575, 2010.
8. Tyurnev, V. V., “The coupling coefficients of an asymmetric pair of microwave resonators,” *J. of Communications Technology and Electronics*, Vol. 47, No. 1, 1–8, 2002.
9. Kirschning, M. and R. H. Jansen, “Accurate wide-range design equations for the frequency-dependent characteristic of parallel coupled microstrip lines,” *IEEE Trans. Microw. Theory Tech.*, Vol. 32, No. 1, 83–90, Jan. 1984, Corrections in *IEEE Trans. Microw. Theory Tech.*, Vol. 33, No. 3, 288, Mar. 1985.

A V-band Low Noise Amplifier with 18.1 dB Gain and 6.3 dB NF in 90-nm CMOS Process Technology

Chiu-Hsiang Hsu and Yen-Chung Chiang
National Chung Hsing University, Taiwan

Abstract— A three-stage low noise amplifier (LNA) implemented in the TSMC 90-nm CMOS process technology for V-band applications is proposed in this paper. The proposed low noise amplifier consists of three commonsource stages with inductive degeneration. We use microstrip lines for input/output matching and as loads for all stages. The chip size of the proposed low noise amplifier is $0.608 \times 0.636 \text{ mm}^2$. The measured peak gain is 18.1 dB at 59.9 GHz with 3 dB bandwidth from 58 to 62.4 GHz. The lowest measured noise figure (NF) is 6.3 dB at 61 GHz and 63.5 GHz, respectively, and NF is from 6.3 dB to 8 dB for the 57–64 GHz frequency range. The measured input 1 dB compression point (P1 dB) is -19 dBm and input third intercept point (IIP3) is -10 dBm . The proposed circuit draws a 32.6 mW dc-power from a 1.2-V supply.

1. INTRODUCTION

Recently, progress in semiconductor technologies and wireless communication techniques make it possible to transfer large capacity of information via wireless communication systems. At the same time, various application programs are developed for peoples to use through different portable devices and this in turn requires more and more large capacity and high speed of data transfer via wireless systems. Wireless communication technologies that we used nowadays, such as bluetooth, WLAN 802.11, Wi-Fi, and so on, are relatively mature and these systems are well defined. However, the bands used by these systems within 10 GHz become too crowded and do not meet people's rapid growing requirement. This situation sparked interests in V-band (60 GHz band) operation [1]. With the 7-GHz unlicensed spectrum in the 60 GHz band, V-band wireless system owns some attractive characteristics for indoor wireless applications including high data rate, good data security, low inference, and so on. Different equipments including personal computers, consumer devices, and handheld devices can be supported by this V-band wireless technology which provides at least 1 Gb/s data rate within 10 meters distance.

In the RF front end, the low-noise amplifier (LNA) is an essential component and plays a key role in the receiver front end. The LNA in general is the first stage, and it is required to provide a sufficient power gain with low noise figure (NF) and high linearity. Due to the relatively low cost and easy integration with digital baseband, the CMOS technology is a strong candidate among the technologies for implementing the V-band LNA. There have been many LNAs proposed for the V-band applications [1–8]. In this paper, we adopted the three-stage architecture and design a V-band LNA by using the 90-nm CMOS process technology. Although it is not impossible to design a V-band LNA by using on-chip inductors [6], most of LNAs designed for such applications adopted transmission lines rather than inductors for impedance matching, source degeneration, and as the loads. We also use on-chip microstrip line in our LNA design. The microstrip transmission line and LNA design considerations are presented in Section 2, measured results of the proposed LNA are shown in Section 3, and then a simple conclusion is made in Section 4.

2. CIRCUIT DESIGN

The geometrical structure of microstrip transmission line (MTL) is shown in Figure 1. In layered structures, microstrip lines and coplanar waveguides (CPW) are most commonly used as the transmission lines. Compared with the CPW structure, the MTL has lower Q -factor. However, the coupling between MTL is relatively small and it is easy to layout and to integrate [4]. Thus we choose the MTL structure as the transmission lines in our design of the V-band LNA. Due to the chip size and system consideration, the characteristic impedance Z_0 of the MTL is chosen to be 50Ω . Referring to Figure 1, the characteristic impedance of the microstrip line is determined by the effective dielectric constant (ϵ_{eff}) of the dielectric between metal layers, the signal line width (W), and the distance between the signal line and the ground plane (h). The signal line is implemented by using metal 9 layer with width being $9 \mu\text{m}$ and the ground plane is formed by the metal 1 layer. The simulated Z_0 of the microstrip line is close to 50Ω as shown in Figure 2. In the design of the

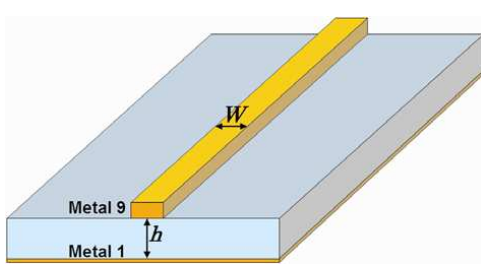


Figure 1: Geometry of the microstrip transmission line.

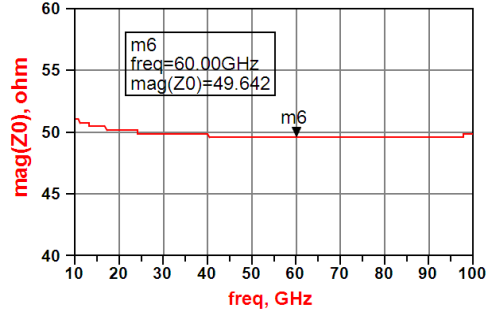


Figure 2: Simulated characteristic impedance of the microstrip transmission line.

whole circuit, we use microstrip line sections with the same Z_0 , including RF chokes and matching networks.

The common-source (CS) amplifier with source inductive generation is the most common structure for the low noise amplifier design and the noise figure (NF) of such CS stage becomes [9]:

$$F_{CS} = 1 + \frac{R_l}{R_s} + \frac{R_g}{R_s} + \frac{\gamma}{\alpha} \frac{\chi}{Q_L} \frac{\omega_o}{\omega_T}, \quad (1)$$

in which R_s is the source resistance seen into the signal source, R_l represents the effective series resistance of the gate inductor L_g , R_g is the gate resistance of input MOS transistor, ω_o is the operating angular frequency, and α and γ are bias-dependant parameters [10]. From Equation (1), we know that reducing R_l and R_g can improve NF performance, but we also need to match the input impedance. Thus using the source degeneration inductor L_s help optimizing NF and power matching.

The common source-common gate (CS-CG) amplifier structure is also usually used in LNA design which provides better reverse isolation and higher gain. The NF equation of the CS-CG amplifier can be expressed as:

$$F \cong F_{CS} + 4R_s \gamma_2 g_{d02} \left(\frac{\omega_o^2 C_x}{\omega_T g_{m2}} \right)^2, \quad (2)$$

in which F_{CS} is give by Equation (1), g_{m2} is the transconductance of the cascaded MOS transistor, g_{d02} is the zero-bias drain conductance and γ_2 is the process parameter. The major contribution of the NF is from the input stage F_{CS} , and the second term in Equation (2) is a minor term. Some previous researches indicated that the additional gain benefited from the cascaded stage for V-band is not significant as lower frequencies, thus we adopted CS with inductive degeneration in our design for NF consideration.

The complete circuit of the proposed V-band LNA is depicted in Figure 3 which is composed of three CS stages with inductive degeneration. Since the design of first stage focuses on the NF and input matching, the gain cannot meet the required specification. The main considerations of the second and third stages are the gain and the linearity under acceptable power consumption. We choose the same device size of $20 \mu\text{m}/100 \text{ nm}$ for transistors M_1 to M_3 . And the capacitances C_1 to C_4 function as both dc blocking and impedance matching. The other load impedance and

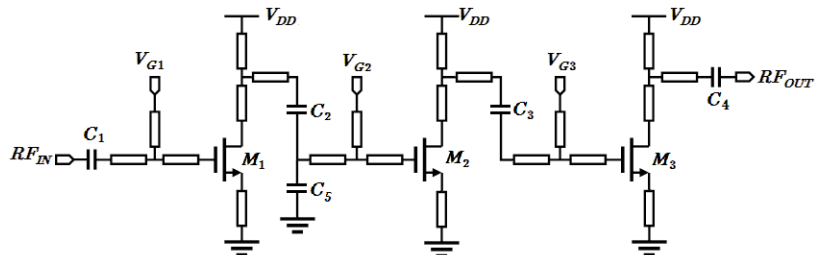


Figure 3: Schematic of the proposed V-band low-noise amplifier.

matching components are composed of the microstrip transmission lines introduced in the previous paragraphs. The source degeneration inductors are also implemented by MTLs, and the length of each stage are chosen by balancing between NF and gain.

The proposed LNA is implemented in the 90-nm CMOS process technology. The micrograph of the circuit is as shown in Figure 4 and the chip size is $0.608 \times 0.636 \text{ mm}^2$.

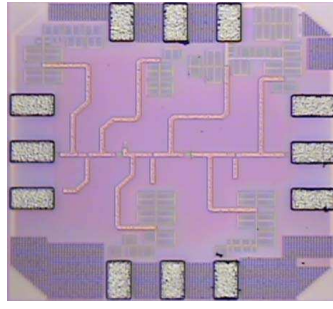


Figure 4: Micropgrah of the proposed V-band LNA.

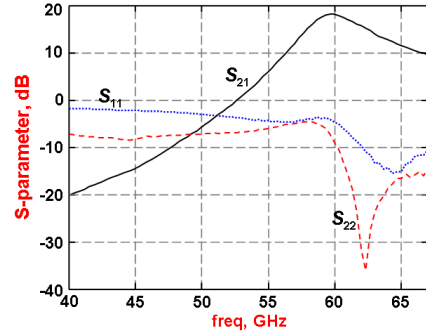


Figure 5: Measured S -parameters of the proposed LNA.

3. MEASURED RESULTS

The supply voltage (V_{DD}) and total power consumption are 1.2 V and 32.6 mW, respectively. Figure 5 shows the measured S -parameters, in which the gain (S_{21}) has a peak of 18.1 dB at 59.9 GHz and its 3 dB bandwidth is from 58 GHz to 62.4 GHz. It also shows the measured input and output matching (S_{11} and S_{22}), and it can be seen that the input bandwidth for S_{11} less than -10 dB is from 62.5 GHz to 67 GHz and the output band width for S_{22} less than -10 dB is only from 60 GHz over 67 GHz. Both input and output matching are drifted to a higher band and it need be further improved.

The measured NF of the proposed LNA is as shown in Figure 6 and the measured gain is also shown in the same figure. The lowest measured noise figure (NF) is 6.3 dB at 61 GHz and 63.5 GHz, respectively, and NF is from 6.3 dB to 8 dB for the 57–64 GHz frequency range. The peak gain is 18.795 dB at 59.04 GHz while the gain is 17.98 dB at 60 GHz. The input 1 dB compression point (P1 dB) is -19 dBm as shown in Figure 7. The measured input third intercept point (IIP3) is -10 dBm .

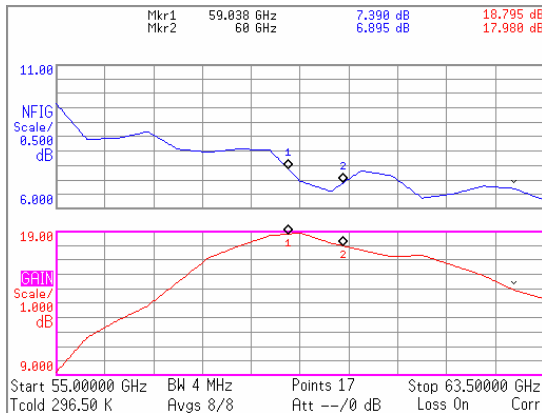


Figure 6: Measured NF and gain of the proposed V band LNA.

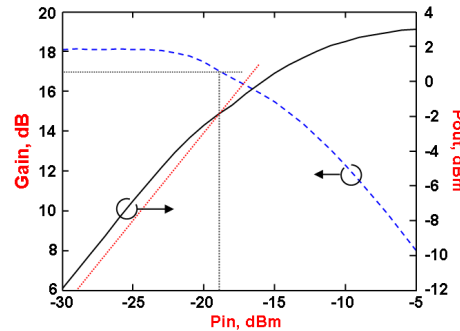


Figure 7: Measured output power versus input power and 1 dB compression point (P1 dB).

4. CONCLUSIONS

In this paper, we have proposed a V-band low noise amplifier in the 90-nm CMOS process technology. By using three common source stages with inductive degeneration, the proposed LNA achieves a 18.1 dB peak gain with NF from 6.3 to 8 dB within 57 to 64 GHz. The measured P1 dB

is -19 dBm and the IIP3 is -10 dBm. The proposed LNA draws 32.6 mW power from a 1.2 -V supply.

ACKNOWLEDGMENT

This work was supported in part by the Ministry of Education, Taiwan, R.O.C. under the ATU plan and by the National Science Council of the Republic of China under Grant NSC101-2220-E-005-010. The authors would like to thank the National Chip Implementation Center (CIC) in Hsinchu, Taiwan for the chip fabrication, measurement and other technical supports.

REFERENCES

1. Wang, C. S., J. W. Huang, K. D. Chu, and C. K. Wang, "A 60 GHz phased array receiver front-end in $0.13\text{ }\mu\text{m}$ CMOS technology," *IEEE Trans. on Circuits and Systems I*, Vol. 56, No. 10, 2341–2352, 2009.
2. Hung, H. L. A., G. M. Hegazi, T. T. Lee, F. R. Phelleps, J. L. Singer, and H. C. Huang, "V-band GaAs MMIC low-noise and power amplifiers," *IEEE Trans. on Microwave Theory and Tech.*, Vol. 36, No. 12, 1966–1975, 1988.
3. Nishikawa, K., B. Piernas, K. Kamogawa, T. Nakagawa, and K. Araki, "Compact LNA and VCO 3-D MMICs using commercial GaAs PHEMT technology for V-band single-chip TRX MMIC," *IEEE MTT-S Int. Microwave Symp. Dig.*, Vol. 3, 1717–1720, Aug. 2002.
4. Sun, Y., J. Borngräber, F. Herzl and W. Winkler, "A fully integrated 60 GHz LNA in SiGe:C BiCMOS technology," *Proc. of the IEEE Bipolar/BiCMOS Circuits and Technology Meeting (BCTM2005)*, 14–17, Santa Barbara, USA, 2005.
5. Floyd, B. A., S. K. Reynolds, U. R. Pfeiffer, T. Zwick, T. Beukema, and B. Gaucher, "SiGe bipolar transceiver circuits operating at 60 GHz," *IEEE J. Solid-State Circuits*, Vol. 40, No. 1, 156–167, 2005.
6. Cohen, E., S. Ravid, and D. Ritter, "An ultra low power LNA with 15 dB gain and 4.4 dB NF in 90 nm CMOS process for 60 GHz phase array radio," *IEEE Radio Frequency Integrated Circuits Symposium (RFIC2008)*, Atlanta, USA, Jun. 15–17, 2008.
7. Pellerano, S., Y. Palaskas, and K. Soumyanath, "A 64 GHz LNA with 15.5 dB gain and 6.5 dB NF in 90 nm CMOS," *IEEE J. Solid-State Circuits*, Vol. 43, No. 7, 1542–1552, 2008.
8. Jen, Y. N., J. H. Tsai, T. W. Huang, and H. Wang, "Design and analysis of a 55 – 71 -GHz compact and broadband distributed active transformer power amplifier in 90-nm CMOS process," *IEEE Trans. on Microw. Theory and Tech.*, Vol. 57, No. 7, 1637–1646, 2009.
9. Fan, X., H. Zhang, and E. Sanchez-Sinencio, "A noise reduction and linearity improvement technique for a differential cascode LNA," *IEEE J. Solid-State Circuits*, Vol. 43, 588–599, 2008.
10. Sheffer, D. K. and T. H. Lee, "A 1.5 V , 1.5 GHz CMOS low-noise amplifier," *IEEE J. Solid-State Circuits*, Vol. 32, No. 5, 745–759, 1997.

The Band-pass SIW-filter Based on L-ridged Rectangular Waveguide

V. V. Zemlyakov

Faculty of Physics, Southern Federal University, Russia

Abstract— The problem of electrodynamic analysis and synthesis of band-pass filters based on waveguide of complex cross-section is solved. The possibilities of a new class of SIW structures implementation for ridged rectangular waveguides are discussed. A new type of waveguide — L-ridged rectangular waveguide is investigated both in classical and in SIW versions.

1. INTRODUCTION

The waveguide filters are actively applied in modern microwave equipment. In comparison with other selective devices the waveguide filters possess a number of advantages, in particular high power level, small losses and high Q-factor of resonators.

The filters implementation based on waveguides of complex cross-section, for example ridged waveguides, allows improving a mass-dimensions indicator and a single-mode operating range. The approaches to the design of band-pass filters on single- and double-ridge waveguides are considered in paper [1]. The most popular waveguide frequency selective structures are created using transverse irregularities like thin diaphragms [1], or junctions of waveguides of various cross-sections. In the filter in this case the series of volume resonators are connected by segments of waveguides, playing a role of impedance inverters [1, 2]. The evanescent waveguides, i.e., waveguides with operating frequency below the cutoff, can act as impedance inverters of the waveguide band-pass filters. For ridged waveguides the rectangular waveguide of similar cross section can be such evanescent waveguide. Filters with evanescent waveguide sections possess the smaller dimensions and a high stop-band attenuation level [2, 3].

Besides the classical waveguides with rectangular ridges, there is a possibility for constructing band-pass filters on waveguides with ridges of a complex form [3]. One of such waveguides is the rectangular waveguide with two L-ridges [4].

In this work the problem of electrodynamic analysis and synthesis of band-pass filters on L-ridged waveguide with the evanescent-mode sections on a rectangular waveguide of similar cross-section is solved. The calculation of cutoff wave numbers and components of the electromagnetic fields of L-ridged waveguide was carried out by the method of partial regions including field singularities at the edge [4].

2. ELECTRODYNAMIC ANALYSIS OF L-RIDGED RECTANGULAR WAVEGUIDE

According to the method of partial regions including field singularities at the edge the waveguide cross-section (Fig. 1) is separated into seven partial rectangular regions. In each partial region the solution of the two-dimensional Helmholtz equation is given in a series form with unknown coefficients on eigen functions of partial regions. Eigen functions for all partial regions are used according to the boundary conditions, and unknown decomposition coefficients are defined by values of unknown functions set on all separation lines of partial regions [4].

From a condition of continuity of a magnetic field longitudinal component on separation lines of partial regions a system of Fredholm integral equations of the first kind is derived with the kernels having logarithmic singularity. This system of integral equations is solved by Galerkin's method taking into account electromagnetic field singularities at the edges of a boundary surface of the waveguide [4]. According to Galerkin's method the unknown functions are represented in the series form with unknown coefficients on a complete and orthogonal system of functions with the weight considering singularity on the corresponding edge. As a result the system of linear algebraic equations is derived. Equating its determinant to zero the normalized cutoff wave numbers $k_c \cdot a$ could be calculated from the corresponding transcendental equation.

The dependences of normalized cutoff wave numbers of the first four TE waves on waveguide L-ridges gap c/a change are given in Fig. 2. The single-mode operating range is seen to be narrowed with L-ridges gap increase and cutoff wave numbers of the second and third mode dependence is changed very little.

Figure 3 demonstrates the electric fields contour lines in the L-ridged waveguide cross-section in a cutoff mode for the first two TE waves. Apparently the electric field of the dominant mode of a

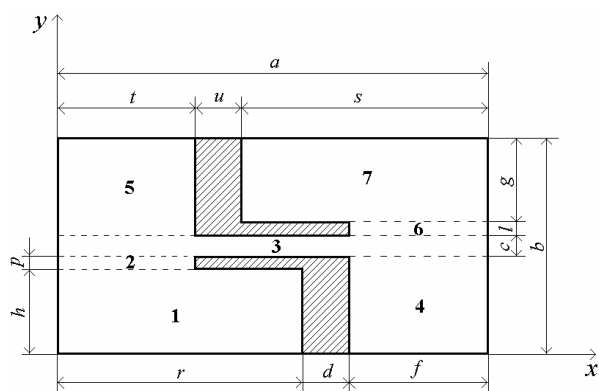


Figure 1.

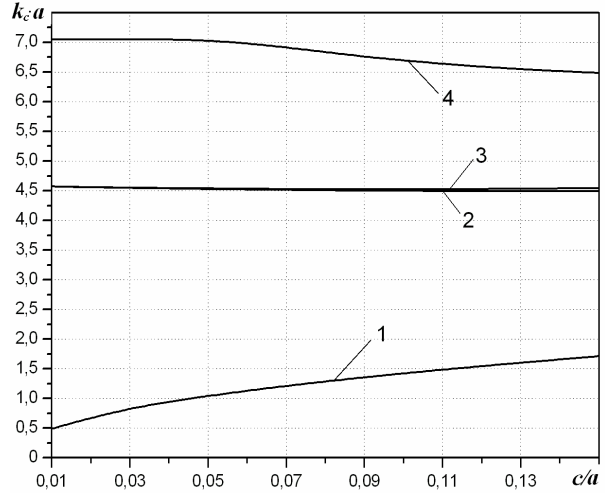


Figure 2.

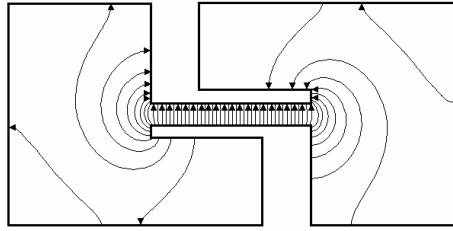


Figure 3.

waveguide (on the left) is almost completely concentrated in a gap between ridges and has uniform structure and electric field of the second mode (on the right), on the contrary, is forced completely out of this gap.

Thus, L-ridged waveguide possesses the following characteristics which in some cases exceed characteristics of single and double rectangular ridges waveguides: The wide single-mode operating range, low dominant mode frequency, low wave impedance, the form of a ridge allowing to reduce the mass of the device, favorable distribution of an electromagnetic field on cross-section for frequency selective structures development.

3. CALCULATION OF CHARACTERISTICS OF SINGLE AND BOUNDED TRANSVERSE JUNCTIONS OF WAVEGUIDES

Let's consider any electromagnetic wave with the serial number — p from the spectra of eigen TE- and TM-modes incidence on transverse junction in the positive direction of z -axis. Taking into account orthogonality of eigen vector functions of waveguides the coefficients of reflection r_{qp}^{ba} and transmission t_{qp}^{ba} of all modes on a junction aperture [1] are:

$$\begin{aligned} 1 + r_{pp}^{Ia} &= \int_s \vec{E}_p(x, y) \rho_p^{Ia} \vec{E}_p^{Ia}(x, y) ds, r_{qp}^{Ia} = \int_s \vec{E}_p(x, y) \rho_q^{Ia} \vec{E}_q^{Ia}(x, y) ds, t_{qp}^{IIa} \\ &= \int_s \vec{E}_p(x, y) \rho_q^{IIa} \vec{E}_q^{IIa}(x, y) ds, \end{aligned} \quad (1)$$

where: $\vec{E}_p^{Ia}(x, y)$ — the vector electric field of a wave incidence on the waveguides junction, $\vec{E}_p(x, y)$ — the unknown vector electric field on a junction aperture — s ; ρ_q^{ba} — the normalizing coefficient defined from orthogonality condition of eigen vector functions, $b = I, II$ — waveguide number; the index $a = h, e$ — means belonging to a class of TE- or TM-modes respectively.

Let's write $\vec{E}_p(x, y)$ in a junction aperture — s in a form:

$$\vec{E}_p(x, y) = \sum_{i=1}^N U_{ip} \vec{Q}_i(x, y), \quad (2)$$

where U_{ip} — unknown coefficients of p -th wave field decomposition; $\vec{Q}_i(x, y)$ — the electric eigen vector functions satisfying boundary conditions on a contour of a junction aperture.

Using the circuit theory it is possible to present the transverse irregularity in a waveguide in the form of multiport device with a number of inputs and outputs equal to a number of waves exciting the irregularity. Such multiport device is described by the generalized scattering matrix. The relation between scattering matrix elements and coefficients of reflection r_{qp}^{ba} and transmission t_{qp}^{ba} of waves exciting irregularity is defined by ratios [1] (σ_q^b — the wave impedance of the line b for q -th wave):

$$S_{np}^{11} = \left(\frac{\sigma_p^I}{\sigma_n^I} \right)^{1/2} \cdot r_{np}^{Ia}, \quad S_{np}^{12} = \left(\frac{\sigma_p^{II}}{\sigma_n^I} \right)^{1/2} \cdot t_{np}^{Ia}, \quad S_{np}^{21} = \left(\frac{\sigma_p^I}{\sigma_n^{II}} \right)^{1/2} \cdot t_{np}^{IIa}, \quad S_{np}^{22} = \left(\frac{\sigma_p^{II}}{\sigma_n^{II}} \right)^{1/2} \cdot r_{np}^{IIa}, \quad (3)$$

Using formulas for scattering matrix of each connected multiport a scattering matrix in a case of cascade connection of two and more multiport device is derived.

4. SYNTHESIS OF BAND-PASS FILTERS ON EVANESCENT-MODE WAVEGUIDES

The T-shaped equivalent circuit [3] is widely used as a representation of the ideal impedance inverter. Its characteristics are related with elements of a matrix of S -parameters by the following ratios:

$$Z_1 = \frac{1 - S_{12} + S_{11}}{1 - S_{11} + S_{12}}, \quad Z_2 = \frac{2 \cdot S_{12}}{(1 - S_{11})^2 - S_{12}^2}. \quad (4)$$

The phase shift φ and the coupling coefficient of the inverter K can be calculated by formulas [2]:

$$\varphi = -\text{arth}(2 \cdot Z_2 + Z_1) - \text{arth}(Z_1), \quad K = |\text{th}(\varphi/2 + \text{arth}(Z_1))| \quad (5)$$

As it was mentioned above the section of an evanescent-mode waveguide possesses the properties of the impedance inverter.

In this work the impedance inverter is created by a section of the rectangular waveguide between two volume resonators on the L-ridged waveguide. The calculation of S -parameters matrix of such junction can be made by means of the technique described above. The procedure of filter synthesis of the evanescent-mode waveguides is described in detail in [3].

5. RESULTS OF FILTERS SYNTHESIS

Let's describe the results of synthesis of band-pass filters on L-ridge rectangular waveguides. Fig. 4 demonstrates the structure of the synthesized band-pass filters on three and five resonators. The dependences of S -parameters on normalized wave number $k \cdot a_0$ are given on Fig. 5, where a_0 — the wide wall dimension of an input rectangular waveguide. Apparently the received band-pass filters possess an ultra narrow pass-band (0.92% and 0.65% respectively) and a wide stop-band with high attenuation level in it. The longitudinal filters dimensions are 0.7λ and 1.6λ respectively, where λ — the operating wave length.

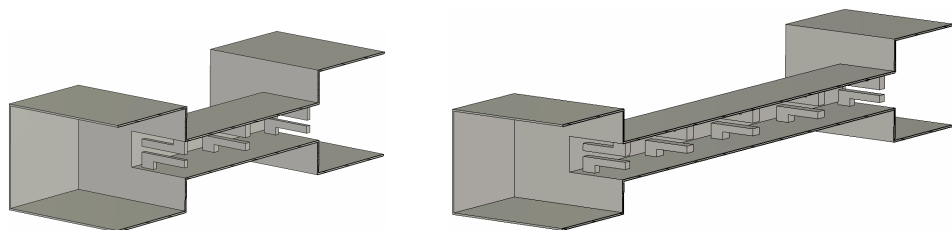


Figure 4.

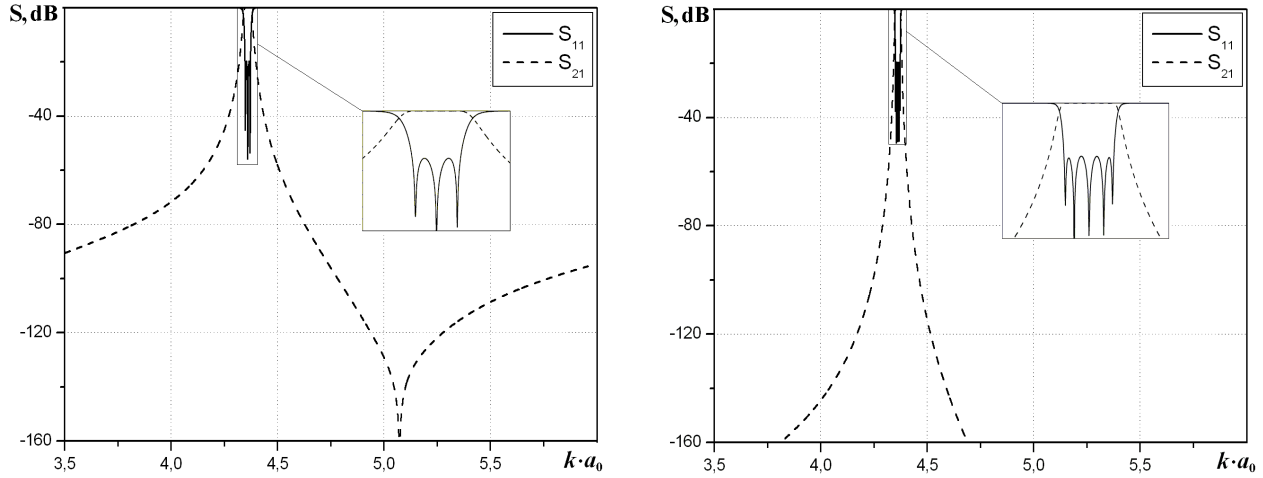


Figure 5.

6. SIW-FILTER DEVELOPMENT

The modern technologies of design and production of integrated circuits open up possibilities of integration in the structure of 3-D elements, in particular rectangular waveguides and cavity resonators on their basis. Such technology is called — SIW (Substrate Integrated Waveguide). The main feature of SIW structures is that they retain the advantages of classical waveguides (high power transmission, low losses, completely shielded structure, high Q-factor of resonators) gaining features of planar structures (the small sizes and weight, low cost of production) [5]. The SIW technology can be successfully used for developing compact band-pass filters.

The filter synthesis was carried out on the basis of the methods described above for classical waveguides, and the subsequent transfer of geometry on SIW structure. The dielectric substrate with permittivity — 2.33 and thickness — 0.508 mm was used. The parameters of final device were calculated by CST Microwave Studio. The total length of the filter is 28 mm and the band-width 4%. The in-band return loss is below −20 dB.

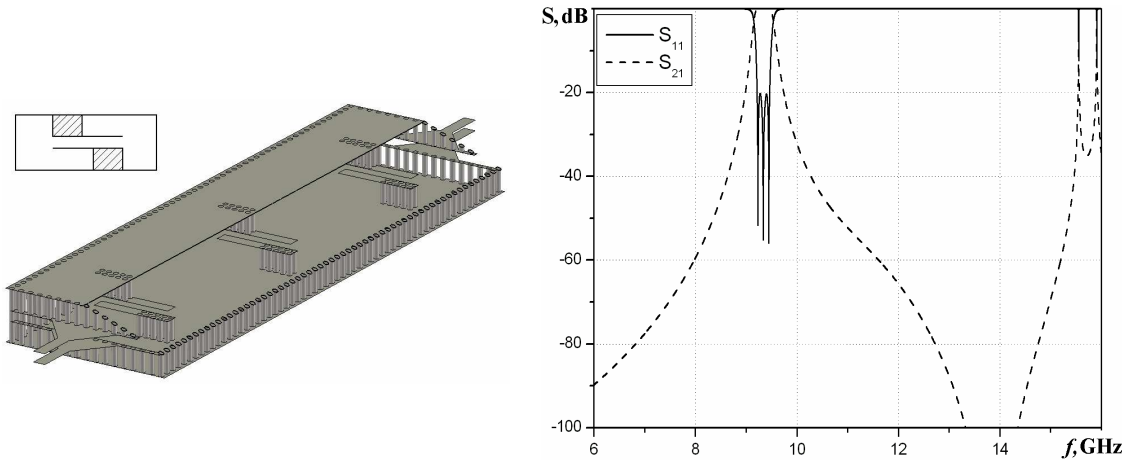


Figure 6.

7. CONCLUSION

Thus, in this work the problem of the electrodynamic analysis and synthesis of band-pass filters on L-ridged rectangular waveguides is solved. The comparison of calculated data with the data received by CST Microwave Studio software shows coincidence not worse than 99%. The high-speed algorithms allowing design effectively filters with sections of evanescent-mode waveguides are realized. The implementation possibilities of a new class of SIW frequency selective structures based on L-ridged rectangular waveguides are discussed.

ACKNOWLEDGMENT

The reported study was partially supported by RFBR, research project No. 12-07-31003-mol_a.

REFERENCES

1. Zargano, G. F., V. V. Zemlyakov, and G. P. Sinyavskii, "Electrodynamics analysis and synthesis of selective devices based on thin diaphragms in ridge waveguides," *Journal of Communications Technology and Electronics*, Vol. 54, No. 4, 381–390, 2009.
2. Nanan, J.-C., J.-W. Tao, H. Baudrand, and B. Theron, "A two-step synthesis of broadband ridged waveguide bandpass filter with improved performances," *IEEE Trans. on Microwave Theory and Techniques*, Vol. 39, No. 12, 2192–2197, 1991.
3. Labay, V. A. and J. Bornemann, "CAD of T-septum waveguide evanescent-mode filter," *IEEE Trans. on Microwave Theory and Techniques*, Vol. 41, No. 4, 731–733, 1993.
4. Zargano, G. F., V. V. Zemlyakov, and V. V. Krivopustenko, "Electrodynamics analysis of eigenmodes in a rectangular waveguide with two L-shaped septa," *Journal of Communications Technology and Electronics*, Vol. 56, No. 3, 259–268, 2011.
5. Bozzi, M., L. Perregini, and K. Wu, "Modeling of conductor, dielectric, and radiation losses in substrate integrated waveguide by the boundary integral-resonant mode expansion method," *IEEE Trans. on Microwave Theory and Technique*, Vol. 56, No. 12, 3153–3161, 2008.

Cooperative Communications Based on Smart Antenna Systems Using PSO Algorithm

Ahmed Magdy¹, K. R. Mahmoud¹, and S. Sayed^{1, 2}

¹Department of Electronics, Communications, and Computers Engineering
Helwan University, Cairo, Egypt

²Department of Electronic and Electrical Engineering University College London, London, UK

Abstract— In this paper, a multi-relay cooperative diversity transmission technique is proposed based on smart antenna design using the Particle Swarm Optimization (PSO) algorithm. In the proposed protocol, a source node sends its information omnidirectionally to relay terminals and its destination in the first time slot. After receiving the source information, the relay terminals forward this information to the desired destination also omnidirectionally in the second time slot. To overcome the interference problem at the destination node, the beam pattern at that node is synthesized with number of main-lobs directed to the corresponding relay terminals located at different positions. A uniform circular array (UCA) geometry is designed at the destination node to achieve the desired beam pattern. Therefore, the proposed protocol can achieve full diversity gain for the same channel resources. Simulation results show that the diversity gain is monotonically increased as the number of relay nodes increases.

1. INTRODUCTION

In a world of increasing mobility, wireless communication received incredible growth in recent years. The number of mobile subscribers worldwide increased from 215 million in 1997 to 6.8 billion in 2013 according to the international telecommunication union (ITU) report [1]. The ITU expects that the number of the subscriptions will be 7.3 billion in early 2014 which exceeds the world population. This requires to guarantee both Quality of Service (QoS) and high transmission rate. However, transmission over wireless channel undergoes multipath fading which degrades the system performance. Temporal, frequency, and spacial diversity techniques are the powerful approaches to mitigate the degrading effects of multipath fading. Among those, spatial diversity is particularly attractive because it requires no additional bandwidth and it improves the signal to noise ratio (SNR). The spatial diversity can be exploited by using multiple antennas at the transmitter and/or the receiver with difficulties of installing multiple antennas on small communication nodes.

Recently, cooperative communication emerged to mitigate the negative effects of multipath fading and resolving the difficulties of installing multiple antennas on small size terminals. Whereas, cooperative communication allows multiple users or stations in a wireless network to coordinate their transmissions and share each other's resources, thus achieving cooperative diversity or user cooperative diversity [2–7]. The source node uses neighbouring nodes as relays to forward its information to its destination, hence forming a virtual antenna array realizing spatial diversity in distributed manner. Cooperative networks based on single relay terminal have been introduced and analyzed in [8–11]. The full spatial diversity gain can be achieved using multi-relay cooperative networks [12–14]. However, the spectral efficiency is reduced by increasing the number of relays. This is because each relay uses separate channel to avoid interference with other relay nodes. Therefore, when the number of relays is N , it is required N orthogonal channels for achieving full diversity gain.

The problem of channel bandwidth inefficiency can be mitigated by conjunction cooperative communication with smart antenna systems. Smart antennas surprised the world by their improvements in interference reduction and increasing channel capacity [15–17]. Adaptive beamforming capability in smart antenna arrays is very powerful in the suppression of interference and maximizing the gain in the desired direction. This feature can be used to improve the spectral efficiency by placing nulls in the antenna patterns to suppress the transmission and/or receiving in the undesired direction. Variety of optimization algorithms such as Genetic Algorithm (GA) [18], Particle Swarm Optimization (PSO) [19], and Gravitational Search Algorithm (GSA) [20] are exploited in electromagnetic and antenna design problems [21–24].

In this paper, a multi-relay cooperative diversity transmission technique is proposed based on smart antenna design using PSO algorithm. The PSO algorithm is considered a practical and powerful optimization tool that requires minimum mathematical processing compared with other

algorithms such GA algorithm. The PSO is used to optimize the complex excitations of the array elements to synthesize the beam pattern at the destination node. In the proposed protocol, a source node sends its information omnidirectionally to relay terminals and its destination in the first time slot. After receiving the source information, the relay terminals forward this information to the desired destination also omnidirectionally in the second slot. To overcome the interference problem at the destination node, the beam pattern at that node is synthesized with number of main-lobes directed to the corresponding relay terminals, located at different positions, based on the concept of space division multiple access (SDMA). Therefore, the proposed protocol can achieve full diversity gain for the same channel bandwidth. A uniform circular array (UCA) geometry is designed at the destination node. The advantage of UCA geometry is that it can be electronically rotated in the plane of the array without significant changes in the beam shape [25].

The rest of the paper is organized as follows. Section 2 presents the system model. Section 3 introduces the smart antenna array beamforming. The performance analysis of the proposed protocol is given in Section 4. Simulation results are presented and discussed in Section 5, followed by conclusions in Section 6.

2. SYSTEM MODEL

In this paper, a wireless communication system is considered in Figure 1. In the first time slot, the source node S sends its information to its destination D and L relay nodes R_i , where $i = 1, 2, \dots, L$ as shown in Figure 1(a). The destination stores this information for future processing. Each relay node R_i uses Amplify and Forward (AF) technique and broadcasts the received signal from the source node in the second time slot. The destination D synthesizes its beam pattern with L main-lobes towards the corresponding L relay nodes as shown in Figure 1(b). This is achieved by using smart antenna system based on UCA. Then, the received L signals from relay nodes and the delayed signal received from the source node are processed at the destination D using Maximal Ratio Combining (MRC) technique. Finally, this paper uses Rayleigh fading channel model in the analysis.

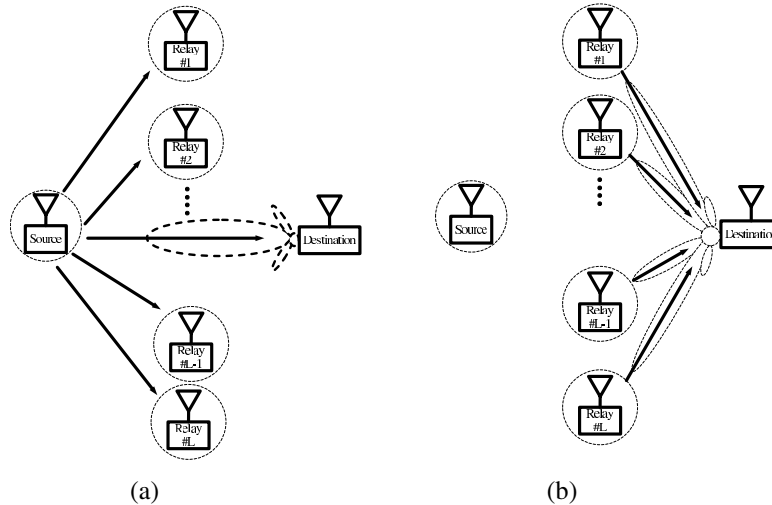


Figure 1: Multi-relay cooperative communication system. (a) Source transmission during first time slot. (b) Relays transmission during second time slot.

3. SMART ANTENNA ARRAY BEAMFORMING

To achieve the desired goal of the proposed protocol to achieve full diversity gain from multi-relays, a UCA antenna array is proposed at the destination node. The array structure consists of M isotropic elements uniformly distributed along the perimeter of a circle of radius $r = (M/2) * \lambda/2\pi$. For beam-forming synthesis, the feeding of each antenna element (amplitude and phase) needs to be optimized to maximize the main-lobe in the direction of relay nodes using the PSO algorithm. The PSO has attracted a lot of attention since its introduction in 1995 [23]. In the PSO, each solution is a point in the search space called a particle in the algorithm. Each particle flies through the N dimensional problem space learning from the best experiences of all particles. For a N

dimensional problem, the position of i th particle is represented as $X_i = (x_{i1}, x_{i2}, \dots, x_{iN})$. The particles move to the next position by a rate of position change $V_i = (v_{i1}, v_{i2}, \dots, v_{iN})$. The next position $x_{iN}^{k+1} = x_{iN}^k + v_{iN}^{k+1} \Delta t$, where Δt is a unit time step. The objective function given in Equation (1) is considered for maximizing the received power at the destination D from the relay R_i located at θ_i .

$$\text{Obj-fun} = \sum_{i=1}^L a_i AF(\theta_i) \quad (1)$$

where $AF(\theta_i)$ is the antenna array factor at the angle θ_i and a_i is the weight that controls the priority of maximizing the power to a certain direction rather than others. In the first time slot, the destination has a main lobe toward the source node direction. In the second time slot, the destination node has number of main lobes towards the relay nodes as shown in Figure 1.

4. PERFORMANCE ANALYSIS

In this section, the Signal to Noise Ratio (SNR) is calculated for multi-relay cooperative communication system. In the first time slot, the source S broadcast its information in the direction of relay nodes R_i , $i = 1, 2, \dots, L$ and destination D . The signal received at the destination D in the first time slot is given by

$$y_{D,S} = \sqrt{P_S} u_{SD} h_{SD} x + n_{D,S} \quad (2)$$

where P_S is the average transmitted power from source S , u_{SD} is the feeding weights (amplitudes and phases) of antenna array that controls the beamforming of D to receive maximum power from S , h_{SD} is the source-destination channel coefficient, x is the transmitted symbol with unit average energy, and $n_{D,S}$ is the additive white noise between S and D . The signal received at each relay node in the first time slot is given by

$$y_{R_i,S} = \sqrt{P_S} h_{SR_i} x + n_{R_i,S}, \quad i = 1, 2, \dots, L \quad (3)$$

where h_{SR_i} is the channel coefficient between the source S and the relay R_i , and $n_{R_i,S}$ is the additive white noise between S and R_i . In the second time slot, the relay nodes normalize the received signal by a factor of $\sqrt{E(|y_{R_i,S}|^2)}$ to ensure that the average energy at the output of relay node i is unity. The value of $E(|y_{R_i,S}|^2)$ is given by

$$E(|y_{R_i,S}|^2) = P_S |h_{SR_i}|^2 + N_o, \quad i = 1, 2, \dots, L \quad (4)$$

where N_o is the white noise variance. After that, the relay terminals retransmit the signal during the second time slot. The received signal at the destination D is given by:

$$y_{D,R_i} = \sqrt{P_{R_i}} u_{R_i,D} h_{R_i,D} \frac{y_{R_i,S}}{\sqrt{E(|y_{R_i,S}|^2)}} + n_{D,R_i}, \quad i = 1, 2, \dots, L \quad (5)$$

where P_{R_i} is the average transmitted power from the relay R_i , $u_{R_i,D}$ is the feeding weights (amplitudes and phases) of antenna array that controls the beamforming of D to receive maximum power from R_i , $h_{R_i,D}$ is the channel coefficient between the relay R_i and destination D , and n_{D,R_i} is the white gaussian noise between D and R_i .

By substituting Equations (3) and (4) into Equation (5) we get

$$y_{D,R_i} = \sqrt{P_{R_i}} u_{R_i,D} h_{R_i,D} \frac{(\sqrt{P_S} h_{SR_i} x + n_{R_i,S})}{\sqrt{P_S |h_{SR_i}|^2 + N_o}} + n_{D,R_i}, \quad i = 1, 2, \dots, L \quad (6)$$

To mitigate the channel effect, the channel state information (CSI) must be available at the destination D . The destination node obtains the CSI from the signals sent by the relay nodes and the source node to other stations in the network because of the nature of wireless transmission. If this information is not updated, pilot signals can be sent from the source and relay nodes to the destination. The pilot signals are known pattern to the destination node. Then the CSI can

be extracted from received signals in this acquisition period. Then the received signals at the destination node will be weighted by the collected CSI and are given as follows

$$r_{D,S} = w_{SD} y_{D,S} \quad (7)$$

$$r_{D,R_i} = w_{R_i} y_{D,R_i}, \quad i = 1, 2, 3, \dots, L \quad (8)$$

In this paper, the weights w_{SD} and $w_{R_i D}$ are obtained by using the PSO optimization technique. Once $r_{D,S}$ and r_{D,R_i} have been obtained, the MRC is used to compute the composite received signal r_C as follows

$$r_C = a_S r_{D,S} + \sum_{i=1}^L a_{R_i} r_{D,R_i} \quad (9)$$

where a_S and a_{R_i} are the optimum weight of the MRC and are given as follows assuming equal noise power

$$a_S = \frac{\sqrt{P_S} h_{SD}^* (w_{SD}^H u_{SD})^*}{\| w_{SD} \|^2 N_o}$$

$$a_{R_i} = \frac{\sqrt{P_{R_i} P_S} h_{SR_i}^* h_{R_i D}^* (w_{R_i D}^H u_{R_i D})^*}{\sqrt{P_S |h_{SR_i}|^2 + N_o} \left(\| w_{R_i D} \|^2 + \frac{|\sqrt{P_{R_i}} w_{R_i D}^H u_{R_i D} h_{R_i D}|^2}{P_S |h_{SR_i}|^2 + N_o} \right) N_o}$$

5. SIMULATION RESULTS

To validate the above analysis, we have developed Mont-Carlo simulation of the system model shown in Figure 1 using Matlab package. The PSO simulator is used to optimize the antenna feeding (amplitude and phase) for maximizing the received power from the desired directions at

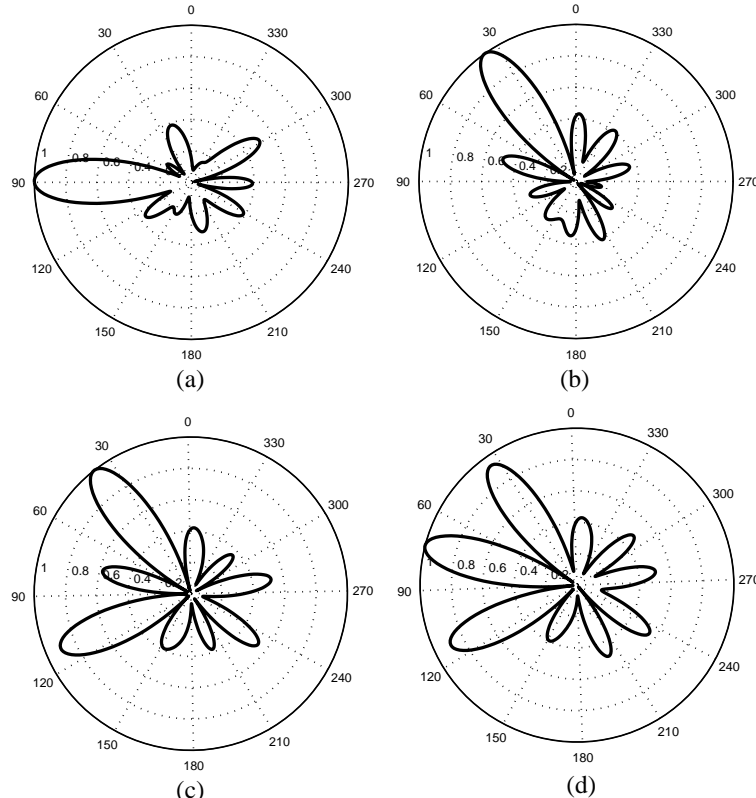


Figure 2: Polar beam patterns of the smart antenna 12 elements system. (a) Destination-source beam pattern. (b) Destination-(one-relay) beam pattern. (c) Destination-(two-relays) beam pattern. (d) Destination-(three-relays) beam pattern.

the destination. In addition, the PSO is used to optimize the weights of the channel to mitigate the fading effect. For simplicity, the power allocated for source node and the relay nodes are normalized to one watt, $P_s = P_{R_i} = 1$. The Raleigh fading wireless channel is simulated using Jake's model [26] with a normalized Doppler shift of 5000 Hz. BPSK and QPSK are used for source node and relay nodes transmission, respectively. The channel variances between source and relays ($E(|h_{SR_i}|^2)$), source and destination ($E(|h_{SD}|^2)$), and relays and destination ($E(|h_{R_iD}|^2)$) are set to one. Furthermore, the number of pilot signals during the acquisition period is chosen to be 500 bits, the number of array's antenna elements is $M = 12$; and the directional of arrivals (DOAs) are 90° , 35° , 70° , and 115° from destination to source, first relay, second relay, and third relay, respectively. The amplitude and phase of the antenna array at the destination are allowed to vary between 1 and 3 and between $-\pi$ to π , respectively.

Figure 2 shows normalized beam patterns of smart antenna for UCA geometry from destination node to source, to one relay, to two relays, and to three relays at angles 90° , 35° , 35° and 115° , and 35° and 70° and 115° , respectively. It is clear that the UCA array based on PSO algorithm can direct the main beam from destination towards the incoming signals from source and relays.

To study the effect of increasing number of relays on the system performance, Figure 3 shows the relation between the bit error rate (BER) and average bit energy to noise ratio E_b/N_o . It can be noticed that the BER reduces significantly by increasing the number of relay nodes. For example at $E_b/N_o = 10$ dB, the BER reduced from 9×10^{-2} with the signal received from the source only to 5×10^{-3} , 10^{-3} , and 2×10^{-4} with signals received from one, two, and three relays, respectively. Therefore, the diversity gain increases as the number of relay nodes increases.

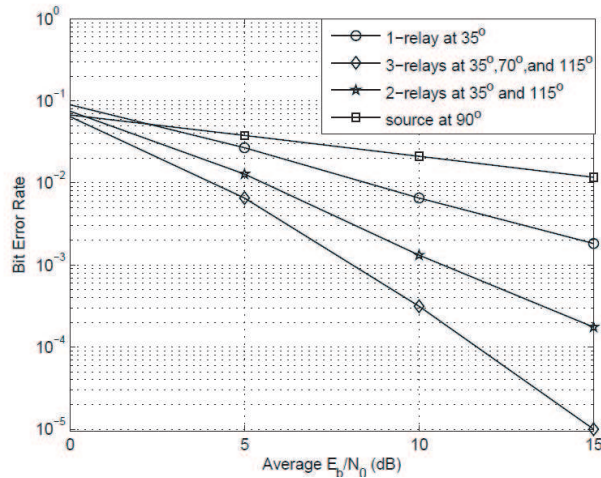


Figure 3: BER vs. E_b/N_o for using different numbers of relays.

6. CONCLUSIONS

In this paper, a cooperative communication protocol with multi-relay terminals based on smart antenna array using PSO optimization algorithm is proposed. To overcome the interference problem at the destination node, the beam pattern at that node is synthesized with number of main-lobs directed to the corresponding relay terminals. UCA geometry is designed at the destination node to achieve the desired beam pattern. Therefore, the proposed protocol can achieve full diversity gain for the same channel bandwidth. Simulation results show that the diversity gain is monotonically increased as the number of relay nodes increases.

REFERENCES

1. Sanou, B., "ICT facts and figures," *ITU*, 2013, Online Available: <http://www.itu.int/en/ITU-D/Statistics/Documents/facts/ICTFactsFigures2013.pdf>.
2. Hunter, T. E. and A. Nosratinia, "Coded cooperation under slow fading, fast fading and power control," *Asilomar Conference on Signals, Systems, and Computers*, Nov. 2002.
3. Laneman, J. N. and G. W. Wornell, "Distributed space-time coded protocols for exploiting cooperative diversity in wireless networks," *IEEE Trans. Inform. Theory*, Vol. 49, 2415–2425, Oct. 2003.

4. Sendonaris, A. and B. Aazhang, "User cooperation diversity — Part I: System description," *IEEE Trans. Comm.*, Vol. 51, 1927–1938, Nov. 2003.
5. Janani, T. E. H. M., A. Hedayat, and A. Nostratinia, "Coded cooperation in wireless communications: Space-time transmission and iterative decoding," *IEEE Trans. Signal Processing*, Vol. 52, No. 1, 362–371, Feb. 2004.
6. Laneman, J. N., D. N. C. Tse, and G. W. Wornell, "Cooperative diversity in wireless networks: Efficient protocols and outage behavior," *IEEE Trans. Inf. Theory*, Vol. 50, No. 12, 3062–3080, Dec. 2004.
7. Hunter, T. E. and A. Nosratinia, "Diversity through coded cooperation," *IEEE Transactions on Wireless Comm.*, Vol. 5, No. 2, 283–289, 2006.
8. Gunawardena, S. and N. Rajatheva, "SEP formula for single relay selection in a multiple relay environment over rayleigh fading channels," *Canadian Conference on Electrical and Computer Engineering (CCECE)*, 1931–1936, 2008.
9. Menghwar, G. D., "Alamouti based cooperative communications with a relay node using network coding: A diversity-multiplexing tradeoff perspective," *11th European Wireless Conference-sustainable Wireless Technologies (European Wireless)*, 1–4, 2011.
10. Mannai, U. N., M. M. Eddaghel, F. A. M. Bribesh, and J. A. Chambers, "Outage probability analysis of a multi-path cooperative communication scheme based on single relay selection and amplify-and-forward relaying," *20th International Conference on Software, Telecommunications and Computer Networks (SoftCOM)*, 1–5, 2012.
11. Hakim, H., H. Boujemaa, and W. Ajib, "Single relay selection schemes for broadcast networks," *IEEE Transactions on Wireless Comm.*, Vol. 12, No. 6, 2646–2657, 2013.
12. Asaduzzaman and H. Y. Kong, "Multi-relay cooperative diversity protocol with improved spectral efficiency," *Journal of Communications and Networks*, Vol. 13, No. 3, 240–249, 2011.
13. Kim, S.-I. and J. Heo, "Outage performance of cooperative wireless networks with varying number of relays," *IEEE 23rd International Symposium on Personal Indoor and Mobile Radio Communications (PIMRC)*, 1791–1795, 2012.
14. Renzo, M. D., M. Iezzi, and F. Graziosi, "Error performance and diversity analysis of multi-source multi-relay wireless networks with binary network coding and cooperative MRC," *IEEE Transactions on Wireless Comm.*, Vol. 12, No. 6, 2883–2903, 2013.
15. Rao, T. and V. Rao, "Evaluation of MUSIC algorithm for a smart antenna system for mobile communications," *International Conference on Devices, Circuits and Systems (ICDCS)*, 67–71, 2012.
16. Chang, D.-C. and C.-N. Hu, "Smart antennas for advanced communication systems," *Proceedings of the IEEE*, Vol. 10, No. 7, 2233–2249, 2012.
17. Liu, H., S. Gao, and T. Loh, "Small director array for low-profile smart antennas achieving higher gain," *IEEE Transactions on Antennas and Propagation*, Vol. 61, No. 1, 162–168, Jan. 2013.
18. Johnson, J. M. and Y. Rahmat-Samii, "Genetic algorithm optimization and its application to antenna design," *Antennas and Propagation Society International Symposium, AP-S. Digest*, Vol. 1, 326–329, 1994.
19. Kennedy, J. and R. Eberhart, "Particle swarm optimization," *IEEE International Conference on Neural Networks*, Vol. 4, 1942–1948, Perth, Australia, 1995.
20. Rashedi, E., H. Nezamabadi-Pour, and S. Saryazdi, "GSA: A gravitational search algorithm," *Information Sciences*, Vol. 179, No. 13, 2232–2248, 2009.
21. Boeringer, D. and D. Werner, "Particle swarm optimization versus genetic algorithms for phased array synthesis," *IEEE Trans Antennas Propag.*, Vol. 52, 771–779, 2004.
22. Mani, V. V. and R. Bose, "Genetic algorithm based smart antenna design for UWB beamforming," *IEEE International Conference on Ultra-Wideband (ICUWB)*, 2007.
23. Mahmoud, K. R., M. El-Adawy, R. Bansal, S. H. Zainud-Deen, and S. M. M. Ibrahim, "Analysis of uniform circular arrays for adaptive beamforming applications using particle swarm optimization algorithm," *International Journal of RF and Microwave Computed Aided Eng.*, Vol. 18, 42–52, 2008.
24. Magdy, A., S. Sayed, and K. R. Mahmoud, "Modified cooperative access with Relay's data protocol using smart antenna," Accepted in *Journal of Engineering Sciences*, 2013.
25. Ioannides, P. and C. Balanis, "Uniform circular and rectangular arrays for adaptive beamforming applications," *IEEE Antennas Wireless Propag. Lett.*, Vol. 4, 351–354, 2005.
26. Proakis, J. G., *Digital Communications*, 4th Edition, McGraw-Hill, 2001.

Evaluation of UWB Chipless RFID System Performance Considering Indoor Multipath Propagation Channel and Real World Aspects

M. El-Hadidy¹, A. Fawky¹, B. Nagy¹, M. Khaliel¹, E. Abdallah²,
H. Elhennawy³, and T. Kaiser¹

¹Institute of Digital Signal Processing, Duisburg-Essen University, Germany

²Ain-Shams University, Cairo, Egypt

³Electronic Research Institute, Cairo, Egypt

Abstract— Main objective of this contribution is to evaluate the overall performance of the Ultra Wide Band (UWB) Radio Frequency Identification (RFID) system based on chipless RFID tags, within the UWB range from 3.1 to 10.6 GHz. In this work, a ray-tracing tool “*Wireless Insite*” is used to consider the channel multipath components and the real environmental effects as fading, frequency dependence, transmission, reflections, diffractions and polarization dependence. Furthermore, an Electromagnetic (EM) simulation tool “*CST Microwave Studio*” is used to compute the Frequency Coding Response (FCR) and the Radar Cross Section (RCS) of the UWB-chipless-RFID tag. The system is based on an 8-bit FCR concept of a compact printable orientation independent chipless RFID tag. The tag consists of a circular patch loaded with N multiple slot ring resonators, where each resonator is relevant to a frequency component in the FCR. Simulation results show constructive guidelines for designing multiuser UWB RFID communications and enhancing the channel estimation process of the chipless RFID tag systems. System evaluation would consider several parameters as Bit Error Rate (BER), FCR word length, and the maximum reader-tag range. This enables the insertion of the advanced communication techniques as Interference Alignment (IA), Cognitive Radio (CR) and Massive Multiple Input Multiple Output (MIMO) for passive RFID systems.

1. INTRODUCTION

Passive Radio-frequency identification (RFID) tags are increasingly being used in everyday scenarios, ranging from inventory control and tracking, to medical-patient management. A business can also use this technology to make its internal processes more efficient and optimize its supply chain. RFID technology can modernize all phases of the production cycle, including pre-production activities, asset management, inventory control, production tracking, shipping, recalls and warranty authorization [1, 2]. The key driver behind this widespread adoption is the simplicity of the tags, which enables very low (nearly zero) cost at high volumes.

Passive RFID tags can be generally classified into chipped passive tags, and chipless RFID tags. Chipped-passive tag usually consists of both active components (e.g., transistors) and passives (e.g., antenna). The expensive fabrication cost of an RFID tag is not only attributed to the high cost of silicon chips, but also to the considerable expenditure for assembly process to integrate chips with tag antennas. For realizing low cost RFID tags, one of the most promising techniques is printable chipless RFID tags [3–5]. Benefit from the removal of chips, the price of a unit chipless tag is expected to be significantly lower than the chip based tags. Moreover, incorporating high-throughput printing techniques and low cost paper substrates, these chipless tags can be massively produced at extremely low expense [6].

The challenge that researchers face when designing chipless RFID transponders is how to perform data encoding without the presence of a chip. In overcome problem, two general types of RFID transponders can be identified: time domain reflectometry (TDR)-based and spectral (frequency) signature-based chipless RFID transponders [7]. TDR-based chipless RFID transponders are interrogated by sending a signal by the reader in the form of a pulse and listening to the echoes of the pulse sent by the tag. Examples of TDR chipless RFIDs are Thin-Film-Transistor Circuits (TFTC) [8] and Delay-line based chipless RFID tags [9–11]. However, low cost manufacturing processes and high bit rate has not yet been realized in chipless TDR RFID.

Spectral signature-based chipless transponders (SSBCT) encoded data into the spectrum using resonant structures. Each data bit is usually associated with the presence or absence of a resonant peak at a predetermined frequency in the spectrum. So far, two main spectral based planar circuit

tags have proven to be reliable and offer high data rates. The first type of chipless RFID transponder consists of a vertically polarized UWB disc-loaded monopole receiving (Rx) tag antenna, a multiresonating circuit and a horizontally polarized UWB disc-loaded monopole transmitting (Tx) tag antenna [12]. The 32-bit multiresonating circuit encodes data bits using cascaded spiral resonators, which introduce attenuations and phase jumps at particular frequencies of the spectrum. However, all model are needed to be aligned with the linearly polarized reader antennas. A novel compact easily-printable slot ring resonator loaded chipless RFID tag proposed in [13] is used in our simulation to overcome the limitations of the other chipless tags suggested in the previous studies as shown in Figure 1.

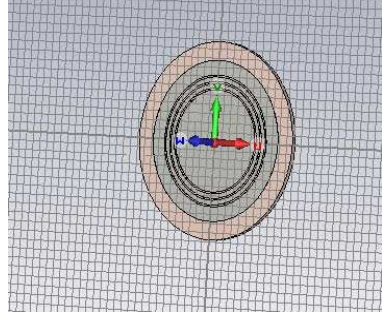


Figure 1. Printable chipless RFID.

In this paper, the overall performance of the Ultra Wide Band (UWB) RFID system based on chipless RFID tags in [7], within the UWB range from 3.1 to 10.6 GHz, shown in Figure 1. We contribute to the state of the art by considering the channel estimation between each reader antenna and each RFID tag using Deterministic Channel Analysis (DCA), and the tag radar cross section variation regarding the received power.

The paper is organized as follows: Section 2 describes the RCS of chipless tag, deterministic channel, and proposed algorithm, Section 3 presents the results of the performed simulations and the received frequency response after equalization, finally Section 4 presents the main conclusions of this work.

2. ANALYSIS AND DESIGN

In this paper, the chipless RFID was designed using “*CST Microwave Studio*” were the RCS was calculated. The chip was then placed in a virtual warehouse in the “*Wireless Insite*” were the CIR was calculated. The CIR with the effect of the RCS was then calculated using “*Matlab*” and it was shown the effect of a Zero Forcing (ZF) equalizer on the signal received.

2.1. Radar Cross Section (RCS)

The backscatter channel is modeled as the product of the independent deterministic channels and a frequency-dependent differential RCS [14, 15]. RCS is the amount of the radiated energy proportional to the target size, orientation, physical shape, and material, which are all lumped together in one target-specific parameter represented by the following equation.

$$\sigma = 4\pi \frac{P_s}{P_i}$$

Were σ is the RCS and P_s is the backscattered power of the object and P_i is the intercepted power of the object. In this work, the RCS of the chipless tag, was calculated using CST microwave studio, shown in Figure 2. Shown in the graph is a 3 resonance (bits) RCS of a chipless RFID at 4.5, 5.4, 6.48 GHz. In this simulation the frequency from 4 to 5 GHz was analyzed.

2.2. Deterministic Channel Model

The performance of the RFID communication system is limited by intermittent power losses, or “deep fades”, associated with the fading channel. The transmission path between the transmitter and the receiver can include fading, frequency dependence, transmission, reflections, diffractions and polarization dependence by terrain configuration and the man-made environment. In this paper, the deterministic channel was modeled using “*Wireless Insite*” in a small $10\text{ m} \times 10\text{ m}$ warehouse shown in Figure 3. Wooden boxes and desks were modeled in the software to simulate a real warehouse environment.

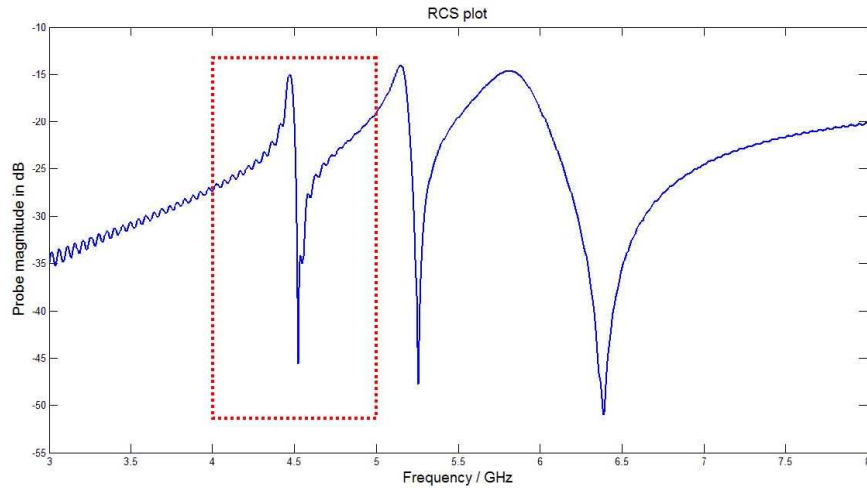


Figure 2. RCS of the chipless RFID.

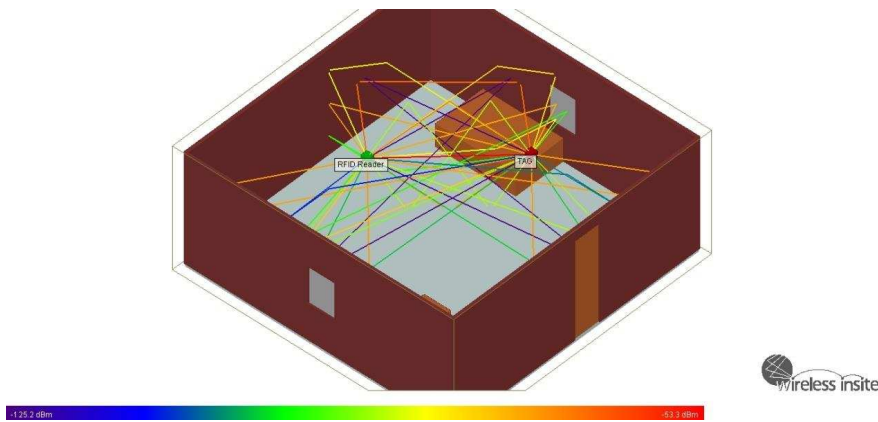


Figure 3.

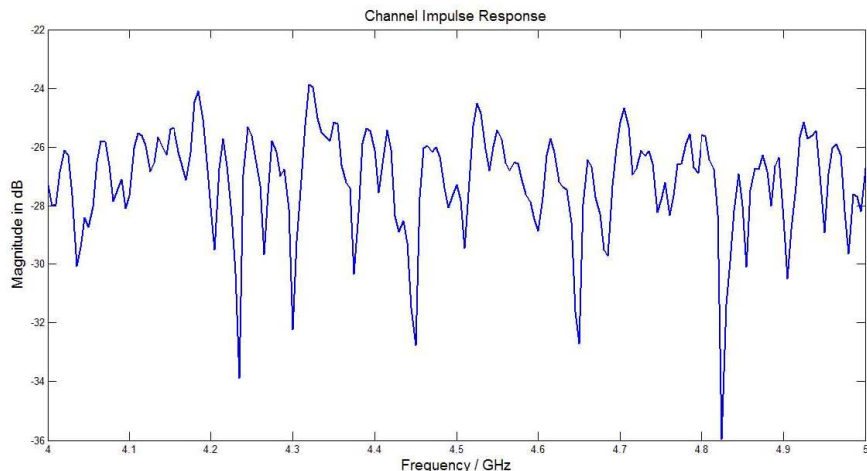


Figure 4. Absolute value of CIR using Freq sweep algorithm.

3. SIMULATION RESULTS

To test the effect of adding the RCS to the CIR, a “Matlab” simulation was done to simulate the effect of the channel on the RCS as shown in Figure 5.

As shown in the graph the channel added 2 extra undesired resonances at 4.25 and 4.81 GHz (marked in red) rather than resonance at 4.51 GHz caused by the tag at which will cause misdetection in the reader. To mitigate the channel effect a ZF equalizer has been implemented at the

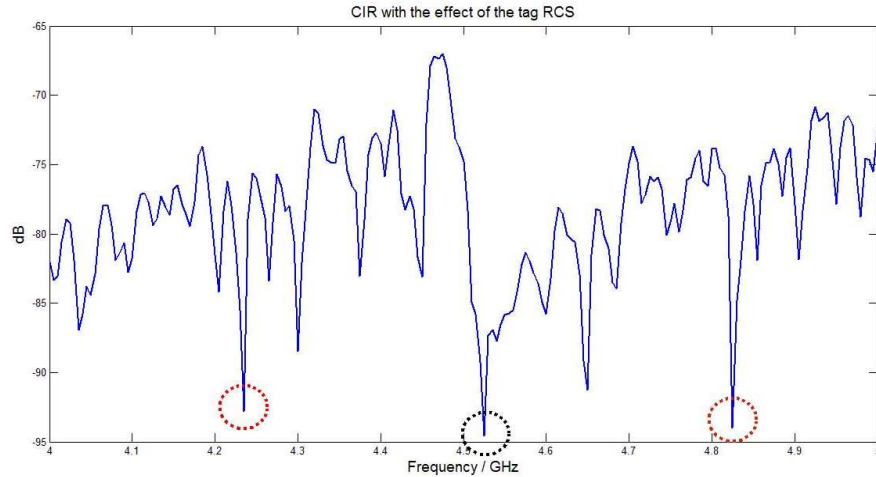


Figure 5. CIR with the effect of the Chipless RCS.

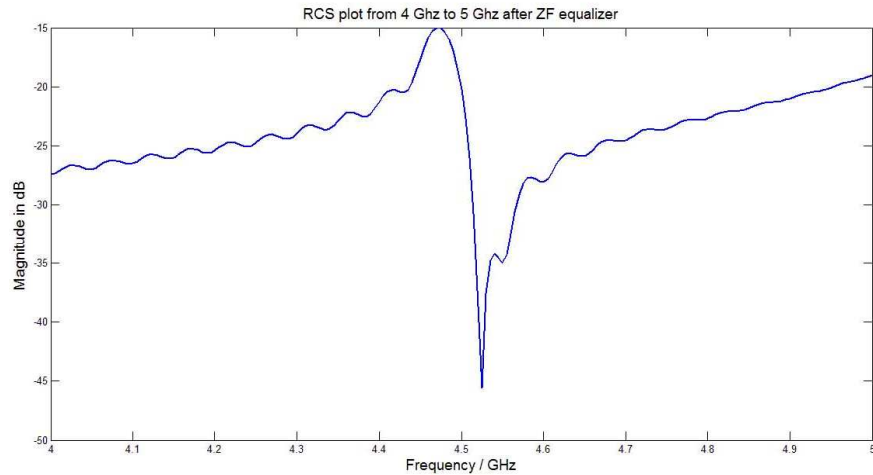


Figure 6. RCS plot after using equalizer at the reader.

reader.

4. CONCLUSION

It is shown that the channel has a great effect on the signal received by the RFID reader. An equalizer is vital to increase the accuracy of the reader in an indoor environment and to mitigate the multipath effect. Further research should be performed for channel estimation and equalization in the RFID system. This will enable the integration of more complex as Interference Alignment (IA), Cognitive Radio (CR) and Massive Multiple Input Multiple Output (MIMO) algorithms for enhancing the passive RFID systems.

REFERENCES

- Min, H. and G. Zhou, "Supply chain modeling: Past, present and future," *Journal of Computer and Industrial Engineering, Elsevier Science Direct*, Vol. 43, Nos. 1–2, 231–249, Jul. 2002.
- Angeles, R., "RFID technologies: Supply-chain applications and implementation issues," *Information Systems Management*, Vol. 22, No. 1, 51–65, 2005.
- Subramanian, V., P. C. Chang, D. Huang, J. B. Lee, S. E. Molesa, D. R. Redinger, and S. K. Volkman, "All-printed RFID tags: Materials, devices, and circuit implications," *19th International Conference on Vlsi Design, Proceedings*, 709–714, 2005.
- Preradovic, S. and N. C. Karmakar, "Chipless RFID: Bar code of the future," *IEEE Microwave Magazine*, Vol. 11, 87–97, 2010.

5. Tedjini, S., E. Perret, V. Deepu, and M. Bernier, “Chipless tags, the next RFID frontier,” *The Internet of Things*, 239–249, 2010.
6. Zou, Z., B. Shao, Q. Zhou, C. Zhai, J. Mao, M. Baghaei-Nejad, Q. Chen, and L. Zheng, “Design and demonstration of passive UWB RFIDs: Chipless versus chip solutions,” *2012 IEEE International Conference on RFID-Technologies and Applications (RFID-TA)*, 6–11, Nov. 5–7, 2012.
7. Preradovic, S. and N. C. Karmakar, *Multiresonator-based Chipless RFID*, 9–24, eBook, Springer, US, 2012.
8. Das, R. and P. Harrop, “Chip-less RFID forecasts, technologies & players 2006–2016,” IDTechEx Internet Article, Feb. 2006, <http://www.idtechex.com/products/en/view.asp?productcategoryid=96>.
9. Chamarti, A. and K. Varahramyan, “Transmission delay line-based ID generation circuit for RFID applications,” *IEEE Microw. Wireless Compon. Letters*, Vol. 16, No. 11, 588–590, Nov. 2006.
10. Vemagiri, J., A. Chamarti, M. Agarwal, and K. Varahramyan, “Transmission line delay-based radio frequency identification (RFID) tag,” *Microw. Opt. Technol. Lett.*, Vol. 49, No. 8, 1900–1904, 2007.
11. Shrestha, S., J. Vemagiri, M. Agarwal, and K. Varahramyan, “Transmission line reflection and delay-based ID generation scheme for RFID and other applications,” *Int. J. Radio Freq. Identification Technol. Appl.*, Vol. 1, No. 4, 401–416, 2007.
12. Preradovic, S., I. Balbin, N. C. Karmakar, and G. Swiegers, “A novel chipless RFID system based on planar multiresonators for barcode replacement,” *2008 IEEE International Conference on RFID*, 289–296, Apr. 16–17, 2008.
13. Nikitin, P. V., K. V. S. Rao, and R. D. Martinez, “Differential RCS of RFID tag,” *Electronics Letters*, Vol. 43, No. 8, 431–432, 2007.
14. Loo, C. H., K. Elmahgoub, F. Yang, A. Z. Elsherbeni, D. Kajfez, A. A. Kishk, T. Elsherbeni, L. Ukkonen, L. Sydanheimo, M. Kivikoski, S. Merilampi, and P. Ruuskanen, “Chip impedance matching for UHF RFID tag antenna design,” *Progress In Electromagnetics Research*, Vol. 81, 359–370, 2008.

On the Use of Huygens' Sources for Synthetic Propagation Environments with the Application in MIMO Over-the-air Testing

Afroza Khatun and Keijo Nikoskinen

SMARAD, Department of Radio Science and Engineering, School of Electrical Engineering
Aalto University, P. O. Box 13000, AALTO, Espoo 00076, Finland

Abstract—Standardization work for multiple-input multiple-output (MIMO) over-the-air (OTA) testing is ongoing. This paper presents mainly from the electromagnetic viewpoint, a theoretical study on the generation of the plane-wave conditions in the test zone with a finite number of elementary antennas. In particular, such a MIMO-OTA test system is considered, where electric and magnetic dipole antennas are placed at the vertices of a dodecahedron test zone surface.

1. INTRODUCTION

To support the increased demand for higher data rate transmission, new multi-antenna terminals are being emerged exploiting the advances in multiple-input multiple-output (MIMO) technique. New wireless technologies such as LTE, LTE-Advanced, WiMAX with MIMO technology are already in operation. MIMO technique not only opens up new opportunities, but also needs a realistic test methodology to evaluate the MIMO terminal performances. Since the MIMO terminal performance is a combination of antenna characteristics, multi-path radio propagation conditions, radio frequency, baseband hardware and software, it needs to be tested in a controlled environment. The most realistic way to test MIMO terminals is to test them as they are used in real life by an end user. Over-the-air (OTA) testing, that has been used for single-input single-output (SISO) performance evaluation [1, 2], is an obvious choice also for MIMO performance evaluation, but additionally radio-propagation channel must be taken into account.

Standardization works for MIMO-OTA test procedures started several years ago and are still on-going at the Wireless Association (CTIA), the Third generation Partnership project (3GPP) and the European Cooperation in Science and technology (COST). Several possible MIMO-OTA test methodologies have been proposed in research and standardization forums with the purpose to be capable of creating such an electromagnetic field environment which represents the true environment where the device is exposed during its normal operation [3].

One possible way to achieve the conditions representing the actual radio-channel environment is through exploitation of multi-probe technology where probes are placed on a circle in 2-D case or on a sphere in 3-D case around the device under test (DUT) in an anechoic chamber. With the help of the channel models developed for different radio-propagation environments, these probes are used to synthesize such radio-channel conditions inside the test volume that emulate the actual conditions where the device would be used in practice. One of the key issues addressed in anechoic chamber based method is the optimum distance between the DUT and the probe circle (sphere) which directly defines the required size of the chamber as well as the cost of the MIMO-OTA testing.

The purpose of this paper is, from the electromagnetic viewpoint, to discuss the synthesis of the test zone fields with the Huygens' Principle with the emphasis on 3-D field synthesis. With the proper electronics, it may possible to map the existing field environment into such excitation currents at the Huygens' sources on the test surface enclosed the DUT. Since by this principle the field outside the test volume is ideally zero, the actual radio-channel environment may be created inside a test volume in any laboratory conditions. Hence, fundamentally no anechoic chamber is required for synthesizing the fields which indicates the reduction of cost significantly. In Fig. 1, an illustration of a 2-D MIMO-OTA test system using Huygens' sources located on a circle around the test zone is presented.

2. HUYGENS PRINCIPLE

The Huygens' Principle state that “*each point on a primary wavefront can be considered to be a new source of a secondary spherical wave and that a secondary wavefront can be constructed as the envelope of these secondary spherical wave* [4].” By this principle, the electromagnetic field can be preserved inside an imaginary closed surface S , and annihilated outside it, if the appropriate equivalent surface sources are placed on the surface (boundary). Additionally, all the field sources inside S should remain in place, while all the field sources outside S should be turned off [5–7]. An

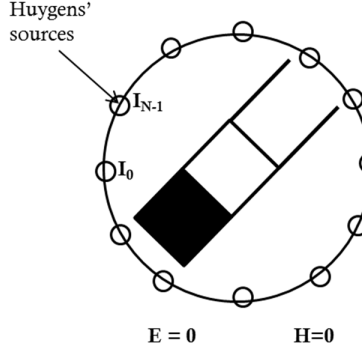


Figure 1: An illustration of a possible MIMO-OTA test system with N equally spaced Huygens' sources placed on a circle around the test zone where the DUT is located.

alternative formulation is possible, in which the field is annihilated inside S , and preserved outside S . In that case, the equivalent sources have the opposite sign with respect to the first formulation, the field sources inside S should be turned off, while the field sources outside S should remain intact. In the electrodynamics case, the equivalent sources are electric surface currents, \mathbf{J}_s , and magnetic surface currents \mathbf{M}_s defined as

$$\mathbf{J}_s = \vec{n} \times \mathbf{H}, \quad \mathbf{M}_s = -\vec{n} \times \mathbf{E}, \quad (1)$$

respectively. Here \vec{n} is the unit inward normal on the surface, \mathbf{E} is the complex electric field vector, and \mathbf{H} is the complex magnetic field vector on S . Then these equivalent currents are integrated with the Green's dyadic weighting to obtain the field quantities inside or outside the surface S .

3. SIMULATION AND RESULTS

3.1. Plane Wave Description and Equivalent Source Currents

The test zone in this paper is a volume bounded by a dodecahedron with the radius R of a circumscribed sphere such that the centre of the dodecahedron is located in the origin of the coordinate system. Assuming, for example, that there is a time harmonic plane wave propagating in the y direction then the electromagnetic fields on the surface of the dodecahedron are

$$\mathbf{E}(\mathbf{r}') = \hat{u}_{z'} E e^{-jky'}, \quad \mathbf{H}(\mathbf{r}') = \hat{u}_{x'} \frac{E}{\eta} e^{-jky'}, \quad (2)$$

where E is the amplitude of the plane wave, k is the wave number, \mathbf{r}' vector contains the coordinates (x', y', z') of the vertices of the dodecahedron, η is the impedance of the medium. Then using Eq. (1) the Huygens' source currents (electric and magnetic) can be easily calculated as follows

$$\mathbf{J}_s(\mathbf{r}') = \vec{n} \times \hat{u}_{x'} \frac{E}{\eta} e^{-jky'}, \quad \mathbf{M}_s(\mathbf{r}') = -\vec{n} \times \hat{u}_{z'} E e^{-jky'} \quad (3)$$

3.2. Synthetic Procedure

The continuous Huygens' sources in Eq. (3) can be approximated and realized by a set of small electric and magnetic dipoles, whose positions can be set at the vertices of a dodecahedron because of symmetry. The electromagnetic fields at the observation point \mathbf{r} generated by a radiating electric dipole with source current $\mathbf{J}_s(\mathbf{r}')$ located at the source point can be calculated by integrals of the Green dyadic:

$$\mathbf{E}(\mathbf{r}) = -j\omega\mu \int_V \bar{\bar{G}}(\mathbf{r} - \mathbf{r}') \cdot \mathbf{J}_s(\mathbf{r}') dV', \quad (4)$$

$$\mathbf{H}(\mathbf{r}) = \int_V \nabla G(\mathbf{r} - \mathbf{r}') \times \mathbf{J}_s(\mathbf{r}') dV'. \quad (5)$$

From duality, the fields from a magnetic dipole with source current $\mathbf{J}_m(\mathbf{r}')$ are

$$\mathbf{H}(\mathbf{r}) = -j\omega\epsilon \int_V \bar{\tilde{G}}(\mathbf{r} - \mathbf{r}') \cdot \mathbf{J}_m(\mathbf{r}') dV', \quad (6)$$

$$\mathbf{E}(\mathbf{r}) = - \int_V \nabla G(\mathbf{r} - \mathbf{r}') \times \mathbf{J}_m(\mathbf{r}') dV'. \quad (7)$$

3.3. Computer Calculation and Results

Computer calculations are performed with a dodecahedron with 12 faces, 30 edges, and 20 vertices as shown in Fig. 2. The radius of the circumscribed sphere by the dodecahedron is 0.2 cm. The time harmonic plane wave fields explained in Eq. (2) with $E = 1$ is considered to be synthesized into the test volume by the Huygens' sources. We placed two tangential (tangential to the plane wave fields) electric and two tangential magnetic dipole sources at the vertices of the dodecahedron. Hence, the total number of dipole sources is $N = 20 \times 4$. The dipole currents are calculated from Eq. (3). Finally the resultant electromagnetic fields generated by the radiating dipole sources located on the surface are calculated through the Eqs. (4)–(7) at the observation points (inside and outside of the test volume). The calculation is performed at the frequency $f = 0.3$ GHz. Importantly, this synthesis technique with the Huygens' Principle is frequency dependent. Hence, synthesizing the fields at higher frequency requires more samples of Huygens' sources for the fixed test zone size in order to meet the accuracy.

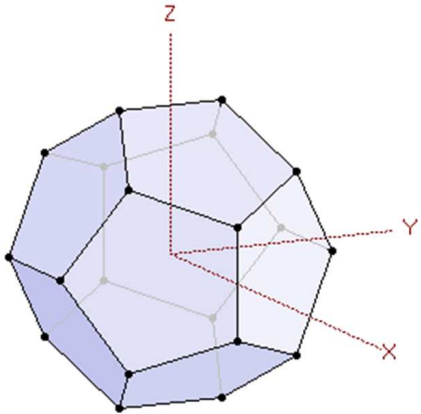


Figure 2: Dodecahedron test zone. Huygens' sources are placed at the vertices.

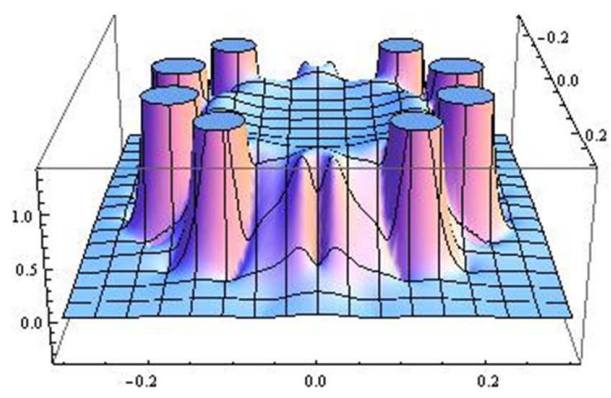


Figure 3: The absolute value of the electromagnetic field inside and outside of the test zone.

The Fig. 3 shows the XY cut of absolute value of the electromagnetic fields. It can be easily shown from the Fig. 3 that the field outside the test volume of the dodecahedron is zero and equal to one inside the volume which indicates the perfect synthesize of the plane wave field inside the test zone. The singular points in Fig. 3 are showing the positions of the dipole sources at the vertices.

4. CONCLUSIONS

Huygens' Principle for the synthetic propagation environment with the application to MIMO-OTA testing has been considered in this paper. The result shows that placing the Huygens' sources over a dodecahedron surface provides the generation of plane wave conditions in the test zone. In this way, the actual radio-channel environment may be created inside a test volume in laboratory conditions. As the Huygens' sources are placed on the surface of the test volume then the required chamber will be small enough in size which reduces the cost of the MIMO-OTA test set-up significantly. On the contrary, the mutual coupling between the sources will be increased for such a large number of sources placed on the test surfaces. A point, which deserves further study though, is the possibility of extending the analysis to reduce the number of Huygens' sources required for the synthetic environments and to deal with the influences of the real sources in laboratory condition.

REFERENCES

1. 3GPP TS 34.114, “User equipment (UE)/mobile station (MS) over the air (OTA) antenna performance; conformance testing (Release 7),” Sep. 2009.
2. CTIA Certification, “Test plan for mobile station over the air performance, method of measurement for radiated RF power and receiver performance,” Rev 2.2.2, Dec. 2008.
3. 3GPP TR 37.976, “Measurement of radiated performance for MIMO and multi antenna reception for HSPA and LTE terminals (Release 10),” V1.1.0, R4-102357, May 2010.
4. Huygens, C., *Traite de la Lumiere*, Leyden, 1690; Translated in English by S. P. Thompson, London, 1912; reprinted by The University of Chicago Press.
5. Harrington, R. F., *Time-harmonic Electromagnetic Fields*, McGraw-Hill Book Company, New York, 1961.
6. Popvić, B. D., “Electromagnetic field theorems (a review),” *Proceedings IEE*, Part A, 47–63, 1981.
7. Lindell, I. V., “On Huygens’ principle in electromagnetic,” *IEE Proc. Sci. Meas. Tech.*, Vol. 143, No. 2, 103–105. 1996.

Variability of Radio Channel Characteristics in Different Indoor Environments

Hassan El-Sallabi¹, Khalid Qaraqe¹, and Erchin Serpedin²

¹Wireless Communications Laboratory, Electrical Engineering Department
Texas A&M University at Qatar, Qatar

²Electrical and Computer Engineering Department, Texas A&M University, College Station, TX, USA

Abstract— This work presents a characterization of the radio channel of the next evolution of Wi-Fi standard IEEE802.11ac with a bandwidth of 80 MHz around the frequency range of 5 GHz for three different indoor environments: a lecture hall, corridor and banquet hall. These environments are selected to represent three different levels of dispersion in the delay and direction domains. The very wide bandwidth results in high resolution in the delay domain and leads to splitting delay clusters as the distance between transmitter and receiver increases. The radio channel of this system is expected to have a variable number of delay clusters with different excess delays per cluster. The spread and geometric distance distribution of scatterers are the main factors that determine the cluster characteristics of this radio channel.

1. INTRODUCTION

Radio channel characteristics in different domains are determined by scatterers distribution, locations of transmitter and receiver, their antenna patterns, frequency, bandwidth and mobility in the channel either at one end of the radio communication link, or at both and/or scatterers in the environment. The distribution of scatterers varies for indoor and outdoor, which would be reflected on the radio channel characteristics (RCC). The impact of antenna patterns at transmitter and receiver on RCC of a single-input single-output channel is determined by the antenna pattern parameters: 1) horizontal and vertical beam-width, which determines the directionality properties of the antenna, 2) pointing direction, 3) antenna tilt, and 4) antenna rotation. The movement of the mobile device introduces different temporal and directional variations on the RCC. The amount of variation depends on the aforementioned parameters in addition to the mobility speed and amount of randomness and distributions of scatterers in the communications channel. The personnel movements in the indoor channel are also a major source of temporal and spatial variability in the radio channel.

The next evolution of the Wi-Fi standard is IEEE802.11ac [1]. This standard is expected to meet the increasing demand for video content data. It is a high-throughput extension to IEEE802.11n WLAN standard, where a single-STA should be capable of throughput greater than 500 Mbps. It has a mandatory operation at the 5 GHz frequency range and bandwidth of 80 MHz with 160 MHz available optionally. The standard group approved TGac Channel Model Addendum v12 [2], which are mainly modifications of the IEEE802.11n channel models [3] for wide bandwidth. Some additional technical details are available in [4]. The adopted models assume fixed tapped delay line channel models with a tap spacing of 5 ns and with some defined directional clusters. The directional clusters parameters are defined for angle of arrival and its angular spread and angle of departure and its angular spread for every tap within its directional cluster.

In this work, we characterize the radio channel as specified by IEEE802.11ac, e.g., frequency range is 5 GHz and bandwidth is 80 MHz. The characterization is based on a physics based model. The focus of our studies is on three different indoor environments representing lecture hall, corridors and banquet hall. The lecture hall environment represents a scenario where the delay and directional properties are comparably affected due to closeness of walls, ceiling and floor. The corridor represents a scenario where the spacing between two reflecting surfaces is at a larger distance from each other relative to the spacing between the other opposite walls. Their effect will represent a couple of far indoor scatterers that may result in isolated clusters at large delays and opposite angles of arrival relative to the tested geometry. The third tested indoor environment is the banquet hall. This represents a scenario where every two opposite surfaces are far from each other in terms of the indoor dimensions. The large distances between the opposite surfaces will be reflected in terms of the delay and directional properties of the channel as well as transmitter and receiver.

In this work, we describe how the radio channel characteristics of these environments vary with the mobile speed and local movements for small spatial variations. The results will be presented in terms of 1) channel dispersion metrics (delay and directional) and 2) temporal correlation properties

2. CHANNEL MODEL

Radio wave propagation in an indoor environment is confined by the scatterers from different directions such as side walls, opposite walls, floor and ceiling. For indoor line of sight propagation, signals arrive at the receiver via line of sight rays, signals bounce between opposite walls, side walls, ceiling and floor or any combinations between these different surfaces. This makes the signal arrive from almost all possible azimuthal angles with large directional dispersion in the vertical plane. These different rays would experience different antenna gains and losses as a function of angular information, azimuthal and co-elevation departure and arrival directions. The adopted channel model in this work is based on the physics of the specular reflection propagation mechanism in addition to the line of sight component. These propagation mechanisms are presented in terms of multi-rays that exhibit multi-dimensional parameters. This work models also the RF propagation in a cubical shaped indoor environment. This particular shape of indoor environment includes different propagation scenarios such as a corridor, office, lecture hall, convention center, etc.. The tested model essentially presents similar features to the model presented in [5]. The simulated propagation characteristics are determined by the input parameters to the model and communications link setup. The input parameters to the channel model include operating frequency, system bandwidth, antenna's polarization and the heights of transmitter and receiver, antennas' field pattern, electrical properties of scatterers, etc.. The communication link setup includes the locations of transmitter and receiver antennas with respect to the scatterers and reflecting surfaces such as ceiling, side and opposite walls, etc.. In this physical model, each ray is determined by its parameters defined by its delay, azimuth-coelevation angle of arrival, and azimuth-coelevation angle of departure. The complex amplitude of each ray is computed with electromagnetic formulations for free space loss and loss due to the interaction with the scatterers in the environment. The interaction loss depends on the interaction, wave-front and geometrical properties of impinging rays and physical properties of reflecting surfaces. Different coefficients can be used to capture the interaction losses that depend on the transmit waveform type: plane wave, cylindrical wave or spherical wave. The most commonly used reflection coefficient is the Fresnel plane wave reflection coefficient, which is valid for flat surfaces and is function of the incidence angle and electrical properties of the reflecting surface. The RF propagation characteristics depend on how the multi-ray components interact with each constructively or destructively to create different fading profiles. The multi-domain RF characteristics depend on the dispersion pattern in their corresponding domain such as delay, direction and Doppler. The received signal is obtained as a sum of multi-ray components as vector superposition of the N individual rays, which can be represented as follows:

$$h(t) = \sum_{n=1}^N A_n \delta(t - \tau_n) e^{-jk(r_n - \mathbf{V} \cdot \Psi_n t)} \quad (1)$$

where k is wave number given as $k = \frac{2\pi}{\lambda}$, λ denotes to wavelength of the operating frequency, \mathbf{V} stands for the velocity vector of the UE, which is assumed as the receiver in this notation, and defined by $\mathbf{V} = v_x \vec{x} + v_y \vec{y} + v_z \vec{z}$ and Ψ_{Rx} is the arrival direction vector defined for ray n as

$$\Psi_n = \cos(\phi_n) \sin(\theta_n) \vec{x} + \sin(\phi_n) \sin(\theta_n) \vec{y} + \cos(\theta_n) \vec{z} \quad (2)$$

where ϕ_n is the horizontal arrival angle relative to the x -axis of ray n , and θ_n is the elevation arrival angle relative to z -axis of ray n , r_n is the path length of ray n

$$r_n = \sum_{p=1}^{P_n} d_{n,p}. \quad (3)$$

Parameter $d_{n,p}$ denotes the distance traversed by the specular wave between the $(p-1)$ and p -th boundary intersections and the complex amplitude A_n is defined as

$$A_n = \frac{\lambda}{4\pi r_n} \sqrt{G_{tx}(\varphi_n, \vartheta_n) G_{rx}(\phi_n, \theta_n)} \prod_{p=1}^{P_n} \Gamma_p e^{-jkd_{n,p}} \quad (4)$$

Γ_p stands for the surface reflection coefficient for the p -th wave-interface intersection, while the term $\frac{\lambda}{4\pi r_n}$ is the free space path loss that accounts for the wave spreading loss, and $G_{tx}(\varphi_n, \theta_n)$ and $G_{rx}(\phi_n, \theta_n)$ are the transmitter and receiver antenna gain, respectively.

3. NUMERICAL RESULTS

The following results are for three different indoor environments, where the IEEE802.11ac system may operate. These indoor environments are 1) lecture hall with dimensions, height (H) = 4 m, width (W) = 8 m, length (L) = 10 m, 2) corridor with dimensions: H = 4 m, W = 2 m, and L = 30 m, and 3) banquet hall with dimensions: H = 10 m, W = 15 m, and L = 50. The simulations are set-up for an antenna access point (AP) on ceiling and client station antenna height is 1.7 m. It is assumed that AP is the transmitter and client station is the receiver. The receiver speed is 3 km/hr, which is defined as the pedestrian speed in 3GPP standard. Reflection orders of up to 6 per reflecting surface are included in addition to the line of sight component. This means that when the signal bounces between two walls, then rays of up to 12 reflection orders could result and so on for rays bouncing between three surfaces would result in rays of up to 18 reflection orders. Reflecting surfaces have relative permittivity of 5 and conductivity of 0.02. The simulated temporal range is for one second for every spatial location. The temporal sampling rate is 26,000 samples/sec. In order to investigate the effect of the environment on similar communication link setups, the three indoor environments have been tested for same route from the access point. A route starting from a horizontal distance of 2 m from AP till 9.5 m with spatial resolution of about 2.5 cm is used in the study. Since the AP is assumed on the ceiling, then there would be a difference in terms of transmitter antenna height in a banquet hall with respect to other two indoor environments. It is assumed that both antennas are vertically polarized. The three dimensional antenna pattern is the well-known omnidirectional pattern, where signals propagating in the xy -plane experience no antenna loss irrespective of the azimuthal angles but the attenuation takes place in the non-horizontal plane propagation, where the amount of antenna loss depends on the elevation angles. The antenna loss increases as the elevation angle of the arrived signal gets away from the 90-degrees plane (i.e., xy -plane).

Mobile channels have dynamic behavior and representing the channel by tapped delay line channel model is just representing it by a snapshot of the spatial variant radio channel impulse response. As the client station moves, the distance to the AP changes, and as a result the spacing between the multipath components will change too. Figure 1 shows the spatial variant of the power delay profiles for the three tested indoor environments. The spatial variant power delay profile represents the received power in the delay domain as a function of distance. It can be well seen as expected that the excess delay increases with the environment dimensions due to the longer path delays. The lecture hall has confined one delay cluster of multipath components. However, some of the multipath components cluster themselves in small delay clusters as the distance between the two terminals of the communication link increases. The delay clusters effect is pretty clear with corridor and banquet hall indoor environments. One can clearly see the splitting of delay clusters in two other delay spaced clusters as the client station moves further from AP. Since the bandwidth is quite large, i.e., 80 MHz, the resolution of multipath components in the delay domain is clearly

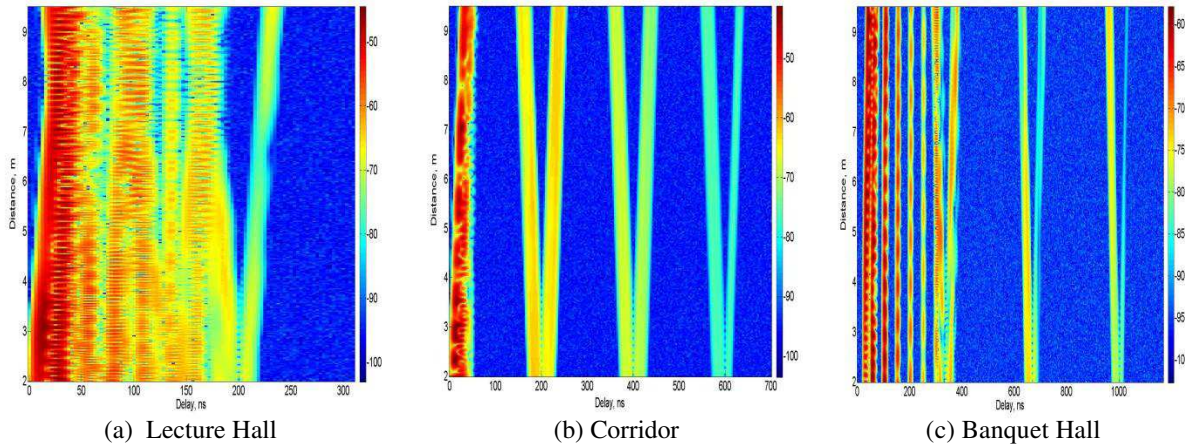


Figure 1: Spatial variant power delay profiles in three different indoor environment.

visible. The measurements carried out for the three indoor environments indicate that the larger the dimensions are, more delay clusters will be generated in the multipath radio channel. Figure 2 shows a sample of the power delay profile (PDP) at a particular distance. It can be observed that the noise floor is around -95 dBm, which is due to the large bandwidth. The early arrival components in the banquet hall environment suffer the strongest loss. Due to its highest ceiling, this leads to the largest offset from the xy -plane, where the omni-directional antenna exhibits a minimum. The PDP presented in Figure 2 shows clearly separated multipath components for the corridor and banquet hall. The large separation between opposite walls relative to separation between side walls make the signals bounce between them before traveling long distance, which results in delay domain clusters. The bouncing between opposite walls and largely separated side walls as in the case of the banquet hall results in larger delayed multipath components. The large difference in the delay domain characterization of multipath components can be described by the root mean square (rms) delay spread (rDS), which is the second central moment of the PDP. It depends on the delay difference and power ratios of the rays. The rDS for the tested indoor environments is presented in Figure 3. The computation is based on signals above noise floor (i.e., -95 dBm) and within 30 dB from the strongest multipath component. The rDS is a measure for the frequency selectivity of the radio channel. The rDS for lecture hall is quite confined between 20 nsec and about 60 nsec. The range of variation is wider for corridor environments about 100 nsec starting from 35 nsec till about 140 nsec. The highest level of rDS for the tested environments is obviously that corresponding to the banquet hall but the largest standard deviation of variability of rDS is that corresponding to the corridor. The formula to calculate the rDS can be found in [6]. Figure 4 depicts a sample of the temporal correlation of the channel for the three environments. The temporal correlation is calculated as in [7, 8]. This function can be used to compute the coherence time of the three different channels. The correlation decreases with time and then starts to oscillate with different rates for different environments. The coherence time is computed as the correlation time where 0.5 of temporal correlation value is reached. The cumulative distribution function of coherence time of temporal channel time series at every spatial location is presented in Figure 4. The highest range of coherence time is observed for corridor, while comparable and lower values can be seen for lecture hall and banquet hall. The highest coherence time of corridor could be due to the narrow width and large distance of bouncing between the two opposite walls, which causes dispersion in the horizontal angular spread, and it is small as can be seen in Figure 6. The arrival angles are primarily as two directional clusters around the line of sight direction and around the opposite direction due to bouncing back. Due to close distances of reflecting surfaces in lecture hall, the arrival angles of high reflection orders would arrive with larger dispersion in azimuth angles of arrivals (AoA). This is easily seen in blue dots in Figure 6. Similar explanation applies for the banquet hall environment but their received power is lower. The impact of the received power is illustrated in azimuthal angular spread (rAS) in Figure 7, where the lowest range of rAS is observed to corridor. 50% of the CDF of rAS are at $30^\circ, 68^\circ, 82^\circ$ for corridor, banquet hall, and lecture hall, respectively. The azimuthal rAS is computed as in [8].

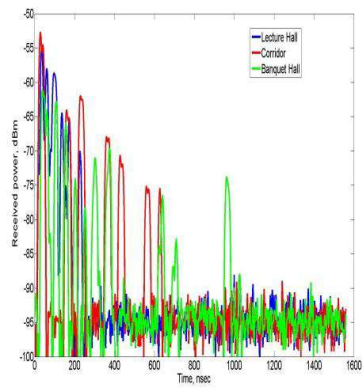


Figure 2: Sample of PDP.

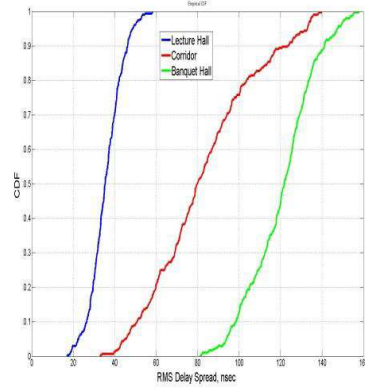


Figure 3: CDF of RMS delay spread.

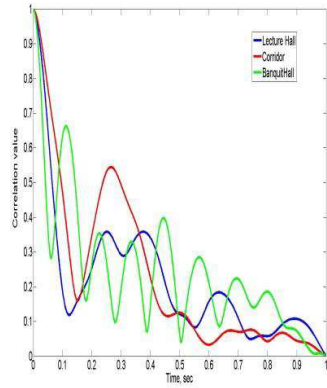


Figure 4: Temporal correlation.

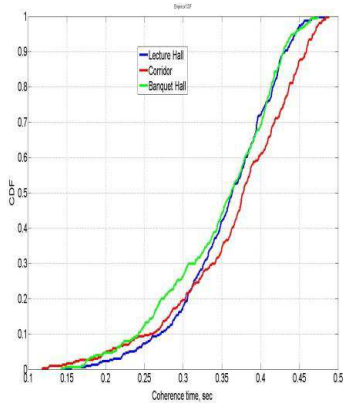


Figure 5: CDF of coherence time.

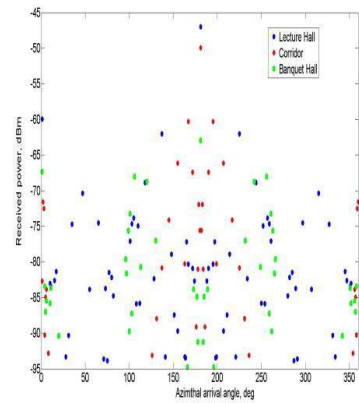


Figure 6: Sample of azimuthal AoA.

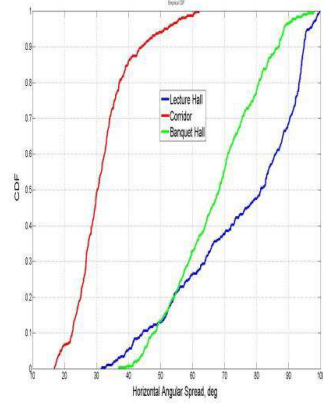


Figure 7: Azimuthal angular spread.

4. CONCLUSIONS

Characterization of the radio channel for the next evolution of Wi-Fi standard IEEE802.11ac, which has a bandwidth of 80 MHz around the frequency range of 5 GHz for three different indoor set-ups has been presented. We showed how delay clusters split into different delay clusters as distance between two terminals increase and generate more delay clusters. The large system bandwidth increases the multipath delay resolution, which creates more delay clusters with dynamics in the channel variations. Delay and direction dispersion are characterized by their second central moment using rDS and rAS. Coherence time is the largest for corridor. The lecture hall and banquet hall have in general comparable coherence times. The smallest azimuthal angular spread is for the corridor due to its narrow width.

ACKNOWLEDGMENT

This publication was made possible by NPRP grants 09-341-2-128 and 4-1293-2-513 from the Qatar National Research Fund (a member of Qatar Foundation). The statements made herein are solely the responsibility of the authors.

REFERENCES

1. Official IEEE 802.11 Working Group Project Timelines — May 18, 2013, Online: http://grouper.ieee.org/groups/802/11/Reports/802.11_Timelines.htm.
2. Breit, G., et al., "TGac channel model addendum," Institute of Electronic and Electrical Engineers, IEEE 802.11-09/0308r12, Mar. 18, 2010, Online: Available: <https://mentor.ieee.org/802.11/dcn/09/11-09-0308-12-00ac-tgacchannel-model-addendum-document.doc>.
3. Erceg, V., et al., "TGN channel models," Doc. IEEE802.11-03/940r4, 2004.
4. Breit, G., et al., "TGac channel model addendum supporting material," Doc. IEEE802.11-09/0569r0, 2009.
5. Malik, W. Q., C. J. Stevens, and D. J. Edwards, "Spatio-temporal ultrawideband indoor propagation modelling by reduced complexity geometric optics," *IET Commun.*, Vol. 1, No. 4, 751–759, 2007.
6. Kaya, A. O., L. J. Greenstein, and W. Trappe, "Characterizing indoor wireless channels via ray tracing combined with stochastic modeling," *IEEE Trans. on Wireless Comm.*, Vol. 8, No. 8, 4165–4175, Aug. 2009.
7. Moraitis, N. and P. Constantinou, "Measurements and characterization of wideband indoor radio channel at 60 GHz," *IEEE Trans. on Wireless Comm.*, Vol. 5, No. 4, 880–889, Apr. 2006.
8. Fleury, B. H., "First- and second-order characterization of direction dispersion and space selectivity in the radio," *IEEE Trans. on Information Theory*, Vol. 46, No. 6, 2027–2044, Sep. 2000.

Novel Methodology for Increasing the Reading Range of the UWB Passive RFID Chipless Tags Considering Power Regulations

M. El-Hadidy¹, B. Nagy¹, M. Khalil¹, A. Fawky¹,
E. Abdallah², H. Elhennawy³, and T. Kaiser¹

¹Institute of Digital Signal Processing

Duisburg-Essen University, Germany

²Ain-Shams University, Cairo, Egypt

³Electronic Research Institute, Cairo, Egypt

Abstract— This paper presents a reading methodology for RFID readers to overcome the problem of the limited reading range and enhance the reading efficiency of the UWB chipless tags in a noisy environment. We apply this methodology on passive UWB chipless tag consists of a circular patch loaded with multiple rings resonators. The main problem of these passive chipless tags is that the reflected UWB power is hardly detected, because the transmitted UWB power is dramatically low by the FCC regulations. In this work, is a new methodology has been developed to make the best use of the restricted UWB regulations to increase the effective radiated power by the RFID reader. This leads to a significant improvement of the reader range and the overall system performance. The FCC regulation states that the maximum allowed limit for the Effective Isotropic Radiated Power (EIRP) for an UWB device operating in the 3.1–10.6 GHz must not exceed than -41.3 dBm/MHz . However, the FCC regulations allows a peak level of emission with a maximum of 0 dBm , contained within a bandwidth of 50 MHz centered at the frequency at which the highest emission occurs. Therefore, the methodology depends on detecting the presence of a tag in a carrier sense manner using frequency sweeping and hoping techniques, instead of sending an UWB signal. The link budget analysis shows a considerable enhancement in the RFID system range and improving the signal to noise ratio at the reader. Simulation results show the expected improvement of the overall system performance.

1. INTRODUCTION

Radio Frequency Identification (RFID) system consists of a reader and tags applied to objects. The cheapest tag with the largest commercial potential are passive or semi-passive, where the energy necessary for tag–reader communication is harvested from the reader’s signal or the surrounding environment [1]. However, the chip found in these tags limits the tag operation and increase the tag price.

Recently, UWB Passive RFID Chipless Tags proposed to replace barcodes [2], but the main limitations of these tags are the read range and the memory capacity. The solution of the memory capacity is to optimize the tag structure to have a sharp and small bandwidth tuned frequencies, which is not the scope here. On the other hand, there is no other research tried to overcome the problem of read range of such system. This extremely low read range in an UWB system not only affected by the parameters of the link budget equation but also affected by the pulse shaping devices, the channel response, and the correlation receiver. This paper presents a reading methodology for RFID readers to overcome the problem of the limited reading range and enhance the reading efficiency of the UWB chipless tags. We apply this methodology on the tag presented in [2], this tag consists of a circular ring resonant structure that absorb the modulated carrier and reradiate the unmodulated one as shown in Figure 1. This tag operates in the frequency range from 6 GHz to 14 GHz as shown in Figure 2. So to identify this tag we have to illuminate it with UWB pulse covering this range and comparing the incident and reflected wave we can extract the tag identification number.

In the following sections, the link budget equation for RFID reader systems introduced in the second section. In third section, the link budget equation applied to the proposed system for calculating the read range and make comparison. The fourth section, gives the work conclusion.

2. THE LINK BUDGET ANALYSIS

The link budget equation cannot directly applied to an UWB system as the formula expressed as a function of frequency [3]. The suggested methodology depends on detecting the presence of a tag in a carrier sense manner using frequency sweeping and hoping techniques, instead of sending

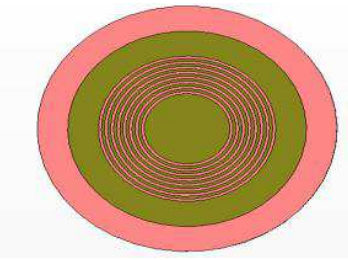


Figure 1: Orientation independent chipless tag [1].

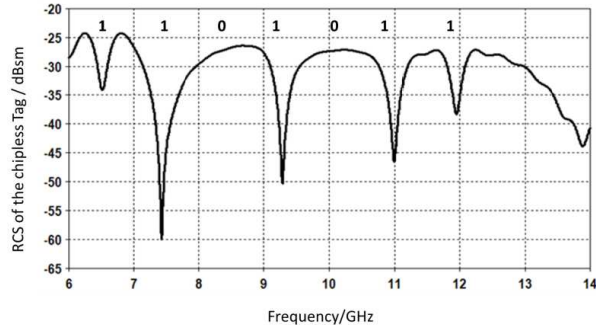


Figure 2: Radar cross section (RCS) of the tag [1].

an UWB signal so we can use the link budget formula in read range calculation. The three types of link budget used in backscatter radio are the power up link, the monostatic, and the bistatic backscatter-Link Budgets [4]. The studied chipless tag does not need the power up link as it depends on modulating the radar cross section of the tag structure without using any silicon device.

2.1. The Link Budget Equation

The read range calculated against the reflected power from Equation (1) [5]:

$$P_{Dr} = \frac{P_t G_t G_r \lambda^2 \sigma}{(4\pi)^3 R_t^2 R_r^2} \quad (1)$$

where P_{Dr} is the power delivered to the reader signal processor, R_t is the transmitter distance, R_r is the read range, G_t , G_r are the gain of the transmitter and reader antenna, λ is the carrier wavelength, σ is the tag radar cross section, and P_t is the effective radiated power of the reader antenna. The effective radiated power in case of UWB system is -54.3 dB/50 MHz but in the proposed method, it will be -30 dB/50 MHz. The radar cross section calculated using the CST — microwave studio, and the comparison graphs are plotted using matlab program as shown in Figures 3, 4.

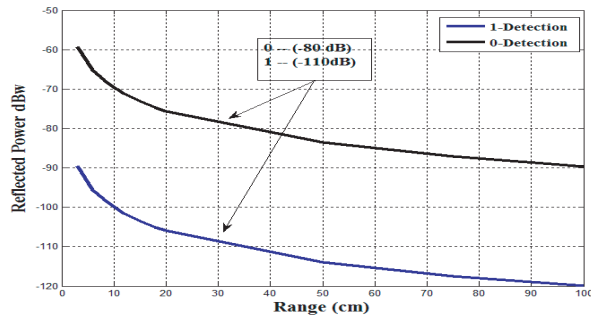


Figure 3: Read range against reflected power in case of UWB transmission.

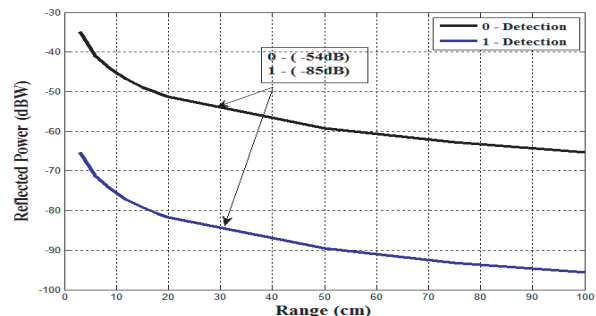


Figure 4: Read range against reflected power in case of narrowband transmission.

3. LINK BUDGET CALCULATION

To make comparison between the proposed methodology and the UWB identification method we read the reflected power at 30 cm away from the tag in both cases. The reflected power of (zero and one) transmission in case of UWB transmission is (-80 dB and -110 dB) and in case of narrowband transmission (-54 dB and -85 dB) respectively. These results in Figures 3, 4 show that the reflected power from zero detection in case of narrowband transmission is 400 times the power reflected in case UWB transmission at 30 cm distance.

4. CONCLUSION

In this paper, we present a suggested design methodology to increase the reading range of the UWB chipless tags. The methodology suggests that the UWB spectrum can be divided into 150-carrier

frequency with bandwidth of 50 MHz. This division allow us to send 0 dBm/50 MHz power at the carrier frequency instead of sending -24.3 dBm/50 MHz over the UWB spectrum. Therefore, the methodology depends on detecting the presence of a tag in a carrier sense manner using frequency sweeping and hoping techniques, instead of sending an UWB signal. The link budget analysis shows a considerable enhancement in the RFID system range and improving the signal to noise ratio at the reader. Simulation results show the expected improvement of the overall system performance.

REFERENCES

1. Dardari, D., R. D'Errico, C. Roblin, A. Sibille, and M. Z. Win, "Ultrawide bandwidth RFID the next generation," *Proceedings of the IEEE*, Vol. 98, No. 9, 1570–1582, Sep. 2010.
2. Islam, M. A., Y. Yap, N. Karmakar, and A. K. M. Azad, "Orientation independent compact chipless RFID tag," *IEEE International Conference on RFID - Technologies and Applications (RFID-TA)*, 137–141, 2012.
3. Promwong, S., W. Hachitani, and J.-I. Takada, "The link budget evaluation of ultra wideband impulse radio transmission systems," *IEEE ISCIT*, 474–478, 2009.
4. Griffin, J. D. and G. D. Durgin, "Complete link budgets for backscatter-radio and RFID systems," *IEEE Antennas and Propagation Magazine*, Vol. 51, No. 2, Apr. 2009.
5. Mahafza, B. R., "Radar systems analysis and design using matlab," Chapman and Hall/CRC, ISBN 1-58488-182-8, 2000.

Reduced Volume Integral Formulations for an Open Waveguide Based on the Cylindrical Vector Wave Expansion

S. Nordebo, A. D. Ioannidis, and B. Nilsson

Linnaeus University, Sweden

Abstract— A Fourier representation of the electric field volume integral equation for an open and cylindrically symmetrical waveguide is given in this paper. The waveguide material is assumed to be isotropic, non-magnetic and with an arbitrary radial variation in the relative permittivity. The Fourier representation yields a system of one-dimensional integral equations, one system for each azimuthal index and where the Fourier variable for the longitudinal direction plays the role of a spectral parameter. The integral equation is of the second kind and has a kernel that is generally discontinuous on the diagonal and singular at the origin. In the axial symmetric case, it can readily be shown that the elements of the matrix kernel belong to an L^2 -space, and hence that the integral operator is compact and the analytic Fredholm theorem is applicable.

1. INTRODUCTION

The analysis of the dispersive behavior of open waveguides is a research field that raises many interesting questions regarding the qualitative properties of the spectrum [9, 15], and which has important applications in fiber optic communications [1, 8], as well as with the modeling of propagating waves on a power cable [11]. As an example is given in [9] a spectral characterization of the generalized natural modes of an inhomogeneous optical fiber with arbitrary cross-section without a sharp boundary. The volume equivalence principle in connection with the strongly singular free-space Green's dyadic for Maxwell's equations is a generic technique to derive integral equations in scattering theory, see e.g., [3, 4, 5, 7, 14]. A discussion on several different derivations is given in [14] regarding general composite volume media. A rigorous mathematical derivation of the electric field volume integral equation under the hypothesis of a discontinuity of the electric permittivity across the dielectric boundary and no electric conductivity is given in [7]. Numerical aspects involving Galerkin formulations for general inhomogeneous scatterers are treated in [3] including comparative numerical results for higher-order basis functions.

In this paper, we give a reduced volume integral formulation for an open and cylindrically symmetrical waveguide based on the cylindrical vector wave expansion. The waveguide material is assumed to be isotropic, non-magnetic and with an arbitrary radial variation in the relative permittivity. Based on the expansion of the free-space Green's dyadic in terms of the cylindrical vector waves [6], it is shown that the volume integral equation [7, 14] reduces to a system of one-dimensional integral equations, one system for each azimuthal index and each with a discontinuous kernel which is singular at the origin. The Fourier variable of the cylindrical vector wave expansion plays the role of a spectral parameter. Spectral issues, asymptotic properties and numerical issues are discussed.

2. PRELIMINARIES

Consider an open circularly symmetrical cylindrical waveguide of radius a which is filled with an isotropic and inhomogeneous dielectric material with relative permittivity ϵ . The material is assumed to be non-magnetic with relative permeability $\mu = 1$. The waveguide constitutes an open structure placed in vacuum.

Let μ_0 , ϵ_0 , η_0 and c_0 denote the permeability, the permittivity, the wave impedance and the speed of light in vacuum, respectively, and where $\eta_0 = \sqrt{\mu_0/\epsilon_0}$ and $c_0 = 1/\sqrt{\mu_0\epsilon_0}$. The wave number of vacuum is given by $k_0 = \omega\sqrt{\mu_0\epsilon_0}$ where $\omega = 2\pi f$ is the angular frequency and f the frequency. The cylindrical coordinates are denoted by (ρ, ϕ, z) , the corresponding unit vectors $(\hat{\rho}, \hat{\phi}, \hat{z})$, the transversal coordinate vector $\boldsymbol{\rho} = \rho\hat{\rho}$ and the radius vector $\mathbf{r} = \boldsymbol{\rho} + z\hat{z}$. The permittivity ϵ is assumed to have a radial variation and to be independent of the transversal coordinates, which motivates the notation $\epsilon = \epsilon(\rho)$.

Let $\mathbf{E}(\mathbf{r})$ and $\mathbf{H}(\mathbf{r})$ denote the electric and magnetic fields, respectively, where the time-harmonic factor $e^{-i\omega t}$ has been suppressed. Maxwell's equations [6] for this situation are given by

$$\begin{cases} \nabla \times \mathbf{E}(\mathbf{r}) = i\omega\mu_0\mathbf{H}(\mathbf{r}), \\ \nabla \times \mathbf{H}(\mathbf{r}) = \mathbf{J}(\mathbf{r}) - i\omega\epsilon_0\epsilon(\rho)\mathbf{E}(\mathbf{r}), \end{cases} \quad (1)$$

where \mathbf{J} is the electric current source. The Maxwell's Equation (1) are also supplemented with a radiation condition [6]. Taking the curl of the first equation in (1) (Faraday's law) yields

$$\nabla \times \nabla \times \mathbf{E}(\mathbf{r}) - k_0^2\epsilon(\rho)\mathbf{E}(\mathbf{r}) = ik_0\eta_0\mathbf{J}, \quad (2)$$

where $k_0\eta_0 = \omega\mu_0$. The wave Equation (2) can be rearranged as

$$\nabla \times \nabla \times \mathbf{E}(\mathbf{r}) - k_0^2\mathbf{E}(\mathbf{r}) = k_0^2(\epsilon(\rho) - 1)\mathbf{E}(\mathbf{r}) + ik_0\eta_0\mathbf{J}. \quad (3)$$

According to the volume equivalence principle [3–5, 7, 14], the solution to (3) can now be expressed in terms of the free-space Green's dyadic $\mathbf{G}_e(\mathbf{r}, \mathbf{r}')$ for the electric field. The following integral equation of the second kind is obtained

$$\mathbf{E}(\mathbf{r}) = k_0^2 \int_{V_m} \mathbf{G}_e(\mathbf{r}, \mathbf{r}') \cdot \{(\epsilon(\rho') - 1)\mathbf{E}(\mathbf{r}')\} d\mathbf{v}' + ik_0\eta_0 \int_{V_s} \mathbf{G}_e(\mathbf{r}, \mathbf{r}') \cdot \mathbf{J}(\mathbf{r}') d\mathbf{v}', \quad (4)$$

where the integrals extend over the support of the material, V_m , and the source, V_s , respectively.

3. VECTOR WAVE EXPANSION OF THE FREE-SPACE GREEN'S DYADIC

Consider a homogeneous and isotropic cylindrical region with relative permittivity ϵ , relative permeability μ and wave number $k = k_0\sqrt{\mu\epsilon}$. The cylindrical vector waves are defined here by

$$\begin{cases} \chi_{1m}(\mathbf{r}, \alpha) = \frac{1}{\kappa} \nabla \times (\hat{\mathbf{z}}\psi_m(\kappa\rho)e^{im\phi}e^{i\alpha z}), \\ \chi_{2m}(\mathbf{r}, \alpha) = \frac{1}{k} \nabla \times \chi_{1m}(\mathbf{r}), \end{cases} \quad (5)$$

where $\psi_m(\kappa\rho)$ is a Bessel function or a Hankel function of the first or second kind and order m , cf., [2, 6]. Here, α is the longitudinal wave number and $\kappa = \sqrt{k^2 - \alpha^2}$ the transversal wave number where the square root is chosen such that $0 < \arg \kappa \leq \pi$ and hence $\text{Im } \kappa \geq 0$. The following notation will be used

$$\chi_{\tau m}(\mathbf{r}, \alpha) = \chi_{\tau m}(\rho, \alpha)e^{im\phi}e^{i\alpha z}, \quad (6)$$

where $\tau = 1, 2$, and the vectors $\chi_{\tau m}(\rho, \alpha)$ are given explicitly in cylindrical coordinates as

$$\begin{cases} \chi_{1m}(\rho, \alpha) = \hat{\rho}\frac{im}{\kappa\rho}\psi_m(\kappa\rho) - \hat{\phi}\psi'_m(\kappa\rho), \\ \chi_{2m}(\rho, \alpha) = \hat{\rho}\frac{i\alpha}{k}\psi'_m(\kappa\rho) - \hat{\phi}\frac{m\alpha}{k\kappa\rho}\psi_m(\kappa\rho) + \hat{\mathbf{z}}\frac{\kappa}{k}\psi_m(\kappa\rho). \end{cases} \quad (7)$$

Let the regular and the outgoing (radiating) cylindrical vector waves $\mathbf{v}_{\tau m}(\mathbf{r}, \alpha)$ and $\mathbf{u}_{\tau m}(\mathbf{r}, \alpha)$ be defined as in (5) by using the Bessel functions and the Hankel functions of the first kind, $J_m(\kappa\rho)$ and $H_m^{(1)}(\kappa\rho)$, respectively. The electric field in a source-free cylindrical region can then generally be expanded as

$$\mathbf{E}(\mathbf{r}) = \frac{1}{2\pi} \int_{-\infty}^{\infty} \sum_{m=-\infty}^{\infty} \sum_{\tau=1}^2 [a_{\tau m}(\alpha)\mathbf{v}_{\tau m}(\mathbf{r}, \alpha) + b_{\tau m}(\alpha)\mathbf{u}_{\tau m}(\mathbf{r}, \alpha)] d\alpha, \quad (8)$$

where $a_{\tau m}(\alpha)$ and $b_{\tau m}(\alpha)$ are complex valued expansion coefficients [2, 6]. Note that an interior region containing the origin is represented solely by the regular waves $\mathbf{v}_{\tau m}(\mathbf{r}, \alpha)$, and an exterior region extending to infinity is represented solely by the outgoing radiating waves $\mathbf{u}_{\tau m}(\mathbf{r}, \alpha)$.

The free-space Green's dyadic for the electric field satisfies

$$\begin{cases} \nabla \times \nabla \times \mathbf{G}_e(\mathbf{r}, \mathbf{r}') - k^2 \mathbf{G}_e(\mathbf{r}, \mathbf{r}') = \mathbf{I}\delta(\mathbf{r} - \mathbf{r}'), \\ \nabla \times \mathbf{G}_e(\mathbf{r}, \mathbf{r}') - ik\hat{\mathbf{r}} \times \mathbf{G}_e(\mathbf{r}, \mathbf{r}') = o((kr)^{-1}), \end{cases} \quad (9)$$

where k is the wave number of the free space, \mathbf{I} the identity dyadic, $\delta(\cdot)$ the Dirac delta function and the second line gives the radiation condition [2, 6]. The free-space Green's dyadic can be expanded in cylindrical vector waves as

$$\mathbf{G}_e(\mathbf{r}, \mathbf{r}') = \frac{i}{8\pi} \int_{-\infty}^{\infty} \sum_{m=-\infty}^{\infty} \sum_{\tau=1}^2 \mathbf{v}_{\tau m}(\mathbf{r}_<, \alpha) \mathbf{u}_{\tau m}^\dagger(\mathbf{r}_>, \alpha) d\alpha - \frac{1}{k^2} \hat{\rho} \hat{\rho} \delta(\mathbf{r} - \mathbf{r}'), \quad (10)$$

where $\mathbf{r}_<$ and $\mathbf{r}_>$ denote the vector in $\{\mathbf{r}, \mathbf{r}'\}$ having the smallest and largest radial coordinate, respectively, i.e., $\rho_< = \min\{\rho, \rho'\}$ and $\rho_> = \max\{\rho, \rho'\}$, cf., [2, 6]. Here, the dagger $\{\cdot\}^\dagger$ refers to a sign-shift in the exponentials in the definition (5), and which can be placed on any of the two vectors in the expression (10), cf., [2]. Note that the expression (10) also contains a Dirac delta function and a dyadic taking the source point into account, cf., [6]. By employing the notation defined in (6) the Green's dyadic can also be expressed as

$$\mathbf{G}_e(\mathbf{r}, \mathbf{r}') = \frac{1}{2\pi} \frac{i}{4} \int_{-\infty}^{\infty} \sum_{m=-\infty}^{\infty} \mathbf{a}_m(\boldsymbol{\rho}, \boldsymbol{\rho}', \alpha) e^{im(\phi-\phi')} e^{i\alpha(z-z')} d\alpha - \frac{1}{k^2} \hat{\rho} \hat{\rho} \delta(\mathbf{r} - \mathbf{r}'), \quad (11)$$

where the dyadic $\mathbf{a}_m(\boldsymbol{\rho}, \boldsymbol{\rho}', \alpha)$ is given by

$$\mathbf{a}_m(\boldsymbol{\rho}, \boldsymbol{\rho}', \alpha) = \begin{cases} \sum_{\tau=1}^2 \mathbf{u}_{\tau m}(\boldsymbol{\rho}, \alpha) \mathbf{v}_{\tau m}^\dagger(\boldsymbol{\rho}', \alpha) & \rho' < \rho, \\ \sum_{\tau=1}^2 \mathbf{v}_{\tau m}(\boldsymbol{\rho}, \alpha) \mathbf{u}_{\tau m}^\dagger(\boldsymbol{\rho}', \alpha) & \rho' > \rho, \end{cases} \quad (12)$$

and where the dagger $(\cdot)^\dagger$ has been placed on the vector with primed coordinates. It follows from the definition (7) that the dyadic $\mathbf{a}_m(\boldsymbol{\rho}, \boldsymbol{\rho}', \alpha)$ can be represented by the following matrices

$$A_m(\rho, \rho', \alpha) = \begin{pmatrix} \frac{m^2}{\kappa^2 \rho \rho'} H_m^{(1)} J_m + \frac{\alpha^2}{k_0^2} H_m^{(1)\prime} J_m' & -\frac{im}{\kappa \rho} H_m^{(1)} J_m' - \frac{im \alpha^2}{k_0^2 \kappa \rho'} H_m^{(1)\prime} J_m & \frac{i \alpha \kappa}{k_0^2} H_m^{(1)\prime} J_m \\ \frac{im}{\kappa \rho'} H_m^{(1)\prime} J_m + \frac{im \alpha^2}{k_0^2 \kappa \rho} H_m^{(1)} J_m' & H_m^{(1)\prime} J_m' + \frac{m^2 \alpha^2}{k_0^2 \kappa^2 \rho \rho'} H_m^{(1)} J_m & -\frac{m \alpha}{k_0^2 \rho} H_m^{(1)} J_m \\ -\frac{i \alpha \kappa}{k_0^2} H_m^{(1)} J_m' & -\frac{m \alpha}{k_0^2 \rho'} H_m^{(1)} J_m & \frac{\kappa^2}{k_0^2} H_m^{(1)} J_m \end{pmatrix}, \quad (13)$$

for $\rho' < \rho$, and

$$A_m(\rho, \rho', \alpha) = \begin{pmatrix} \frac{m^2}{\kappa^2 \rho \rho'} J_m H_m^{(1)} + \frac{\alpha^2}{k_0^2} J_m' H_m^{(1)\prime} & -\frac{im}{\kappa \rho} J_m H_m^{(1)\prime} - \frac{im \alpha^2}{k_0^2 \kappa \rho'} J_m' H_m^{(1)} & \frac{i \alpha \kappa}{k_0^2} J_m' H_m^{(1)} \\ \frac{im}{\kappa \rho'} J_m' H_m^{(1)} + \frac{im \alpha^2}{k_0^2 \kappa \rho} J_m H_m^{(1)\prime} & J_m' H_m^{(1)\prime} + \frac{m^2 \alpha^2}{k_0^2 \kappa^2 \rho \rho'} J_m H_m^{(1)} & -\frac{m \alpha}{k_0^2 \rho} J_m H_m^{(1)} \\ -\frac{i \alpha \kappa}{k_0^2} J_m H_m^{(1)\prime} & -\frac{m \alpha}{k_0^2 \rho'} J_m H_m^{(1)} & \frac{\kappa^2}{k_0^2} J_m H_m^{(1)} \end{pmatrix}, \quad (14)$$

for $\rho' > \rho$, and where the rows and columns of the matrices represent the corresponding unprimed and primed cylindrical coordinates, respectively. Here, the arguments of the Bessel and Hankel functions have been omitted with the convention that arguments are ordered with $\kappa \rho$ first and $\kappa \rho'$ second.

4. FOURIER REPRESENTATION OF THE VOLUME INTEGRAL EQUATION

Let the Fourier (integral and series) representation of the electric field $\mathbf{E}(\mathbf{r})$ be given by

$$\mathbf{E}(\mathbf{r}) = \frac{1}{2\pi} \int_{-\infty}^{\infty} \sum_{m=-\infty}^{\infty} \mathbf{E}_m(\boldsymbol{\rho}, \alpha) e^{im\phi} e^{i\alpha z} d\alpha, \quad (15)$$

where $\mathbf{E}_m(\boldsymbol{\rho}, \alpha) = \hat{\rho} E_{m\rho}(\rho, \alpha) + \hat{\phi} E_{m\phi}(\rho, \alpha) + \hat{\mathbf{z}} E_{mz}(\rho, \alpha)$, and similarly for the source $\mathbf{J}(\mathbf{r})$. The following Fourier representation of the volume integral Equation (4) is obtained

$$\begin{aligned} (\mathbf{I} + (\epsilon(\rho) - 1)\hat{\rho}\hat{\rho}) \cdot \mathbf{E}_m(\boldsymbol{\rho}, \alpha) &= k_0^2 \frac{i\pi}{2} \int_0^a \mathbf{a}_m(\boldsymbol{\rho}, \boldsymbol{\rho}', \alpha) \cdot \{(\epsilon(\rho') - 1) \mathbf{E}_m(\boldsymbol{\rho}', \alpha)\} \rho' d\rho' + \mathbf{F}_m(\boldsymbol{\rho}, \alpha) \\ &= K_m(\alpha) \mathbf{E}_m(\boldsymbol{\rho}, \alpha) + \mathbf{F}_m(\boldsymbol{\rho}, \alpha), \end{aligned} \quad (16)$$

where (11) and (15) and the convolution theorem have been used, and where $\mathbf{F}_m(\boldsymbol{\rho}, \alpha) = -k_0 \eta_0 \frac{\pi}{2} \int_0^a \mathbf{a}_m(\boldsymbol{\rho}, \boldsymbol{\rho}', \alpha) \cdot \mathbf{J}_m(\boldsymbol{\rho}', \alpha) \rho' d\rho' - i \frac{\eta_0}{k_0} \hat{\rho}\hat{\rho} \cdot \mathbf{J}_m(\boldsymbol{\rho}, \alpha)$. Here, the dyadic $\mathbf{a}_m(\boldsymbol{\rho}, \boldsymbol{\rho}', \alpha)$ is defined as in (12), (13) and (14) with transversal wave number $\kappa = \sqrt{k_0^2 - \alpha^2}$. It is noted that (16) is a reduced (one-dimensional) volume integral equation of the second kind, and where the singularity behavior of the operator $K_m(\alpha)$ will govern the applicability of the analytic Fredholm theorem [13], as well as the convergence properties of various numerical methods [10].

5. BASIC OBSERVATIONS ON CONVERGENCE AND COMPACTNESS

The natural modes are defined as the nontrivial solutions to (16) when there are no sources present, and which may occur for some specific values of α referred to as propagation constants. Assume now that the material is homogeneous in a neighborhood of the origin. In this neighborhood the natural modes can be expanded in regular vector waves as in (8), and it follows from (7) that the asymptotic behavior of the fields close to the origin $\rho = 0$ is given by

$$\begin{cases} E_{0\rho}(\rho, \alpha) = \mathcal{O}\{\rho\} & E_{m\rho}(\rho, \alpha) = \mathcal{O}\{\rho^{m-1}\} \quad m \geq 1 \\ E_{0\phi}(\rho, \alpha) = \mathcal{O}\{\rho\} & E_{m\phi}(\rho, \alpha) = \mathcal{O}\{\rho^{m-1}\} \quad m \geq 1 \\ E_{0z}(\rho, \alpha) = \mathcal{O}\{1\}, & E_{mz}(\rho, \alpha) = \mathcal{O}\{\rho^m\} \quad m \geq 1, \end{cases} \quad (17)$$

and where $\mathbf{J}_m(\kappa\rho) = \mathcal{O}\{\rho^m\}$ has been used for $m \geq 0$, and $\mathbf{J}'_0(\kappa\rho) = -J_1(\kappa\rho)$, see e.g., [12]. Under the assumptions given in (17) it follows that the integral in (16) converges as an improper integral. For $m > 0$ it is also useful to introduce

$$\begin{cases} X_{m\rho}(\rho, \alpha) = \rho^{-m+2} E_{m\rho}(\rho, \alpha) = \mathcal{O}\{\rho\} \quad m \geq 1 \\ X_{m\phi}(\rho, \alpha) = \rho^{-m+2} E_{m\phi}(\rho, \alpha) = \mathcal{O}\{\rho\} \quad m \geq 1 \\ X_{mz}(\rho, \alpha) = \rho^{-m+1} E_{mz}(\rho, \alpha) = \mathcal{O}\{\rho\} \quad m \geq 1, \end{cases} \quad (18)$$

which is a substitution of minimum order that cancels the logarithmic singularity that results from the integration. In the same way, it can be shown that the collocation method as well as the Galerkins method [10] based on linear interpolation functions will yield convergent elemental integrals.

The branch-point for the square root $\kappa = \sqrt{k_0^2 - \alpha^2}$ is given by $\alpha = \pm k_0$. It is observed that the elements of the matrix $A_m(\rho, \rho', \alpha)$ defined in (13) and (14) are either continuous or discontinuous at $\rho = \rho'$ when $\alpha \neq \pm k_0$, and the properties of the integral operator $K_m(\alpha)$ is governed by the singularity behavior at $\rho = 0$. For $m = 0$, all the matrix elements of the kernel $\rho'(\epsilon(\rho') - 1) A_0(\rho, \rho', \alpha)$ or $\rho'(\epsilon(\rho') - 1) A_0(\rho, \rho', \alpha)/\epsilon(\rho)$ defined by (13), (14) and (16), belong to the space $L^2([0, \infty] \times [0, \infty])$ when $\alpha \neq \pm k_0$, and the operator $K_0(\alpha)$ is hence compact [10, 13]. To see this, consider e.g., the $z\rho'$ -component of the matrix $A_0(\rho, \rho', \alpha)$, yielding the following integral for the corresponding kernel element

$$\begin{aligned} &\int_{\rho'=0}^a \int_{\rho=0}^{\rho'} \rho'^2 |\epsilon(\rho') - 1|^2 |J_0(\kappa\rho)|^2 \left| H_0^{(1)'}(\kappa\rho') \right|^2 d\rho d\rho' \\ &= \int_{\rho'=0}^a d\rho' \rho'^2 \underbrace{|\epsilon(\rho') - 1|^2}_{=\mathcal{O}\{(1)\}} \underbrace{\left| H_0^{(1)'}(\kappa\rho') \right|^2}_{=\mathcal{O}\{\rho'^{(-2)}\}} \underbrace{\int_{\rho=0}^{\rho'} d\rho |J_0(\kappa\rho)|^2}_{=\mathcal{O}\{\rho'\}} = \int_{\rho'=0}^a d\rho' \mathcal{O}\{\rho'\} < \infty, \end{aligned} \quad (19)$$

where the integration is over the domain $D_1 = \{(\rho, \rho') | \rho' \leq a, \rho' > \rho\}$, as depicted in Fig. 1. It is assumed here that $\epsilon(\rho') - 1$ is square integrable and well behaved at the origin, e.g., $\epsilon(\rho') - 1 = \mathcal{O}\{1\}$ as $\rho' \rightarrow 0$. The integral over the domain $D_2 = \{(\rho, \rho') | \rho \leq a, \rho' < \rho\}$ is treated in a similar way,

and where the asymptotics $H_0^{(1)}(\kappa\rho) = \mathcal{O}\{\ln \rho\}$ as $\rho \rightarrow 0$, is used. For the integration over the domain $D_3 = \{(\rho, \rho') | \rho' \leq a, a \leq \rho\}$, it is noted that the Hankel function $H_0^{(1)}(\kappa\rho)$ has exponential decay for large ρ . Note that the integration over all the domains D_1-D_3 depicted in Fig. 1 are with $\rho' \leq a$ since $\epsilon(\rho') - 1 = 0$ for $\rho' > a$.

It is observed that for $m = 0$, the two cases with TE₀ (E_ϕ) and TM₀ (E_ρ, E_z) are decoupled and the corresponding operators $K_m^{\text{TE/TM}}(\alpha)$ are compact for every $\alpha \neq k_0$. For $m > 0$, the elements of the kernel $\rho'(\epsilon(\rho') - 1) A_m(\rho, \rho', \alpha)$ or $\rho'(\epsilon(\rho') - 1) A_m(\rho, \rho', \alpha)/\epsilon(\rho)$ defined in (16), are generally not in $L^2([0, \infty] \times [0, \infty])$.

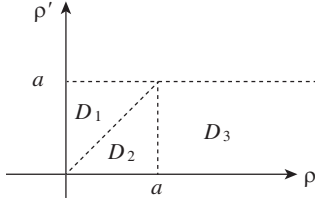


Figure 1: Integration domains for the kernel $\rho'(\epsilon(\rho') - 1) A_m(\rho, \rho', \alpha)$ in $[0, \infty] \times [0, \infty]$.

6. SUMMARY AND CONCLUSIONS

A Fourier representation of the electric field volume integral equation for an open and cylindrically symmetrical waveguide has been given in this paper. In the axial symmetric case with azimuthal index $m = 0$, it can readily be shown that the elements of the matrix kernel belong to an L^2 -space, and hence that the integral operator is compact and the analytic Fredholm theorem is applicable.

REFERENCES

1. Agrawal, G. P., *Fiber-optic Communication Systems*, John Wiley & Sons, Inc., Hoboken, New Jersey, 2010.
2. Boström, A., G. Kristensson, and S. Ström, "Transformation properties of plane, spherical and cylindrical scalar and vector wave functions," *Field Representations and Introduction to Scattering, Acoustic, Electromagnetic and Elastic Wave Scattering*, V. V. Varadan, A. Lakhtakia, and V. K. Varadan, ed., Chap. 4, 165–210, Elsevier Science Publishers, Amsterdam, 1991.
3. Botha, M. M., "Solving the volume integral equations of electromagnetic scattering," *Comput. Phys.*, Vol. 218, 141–158, 2006.
4. Budko, N. V. and A. B. Samokhin, "On the eigenvalues of the volume integral operator of electromagnetic scattering," *SIAM J. Sci. Comput.*, Vol. 28, No. 2, 682–700, 2006.
5. Chew, W. C., *Waves and Fields in Inhomogeneous Media*, IEEE Press, Piscataway, NJ, 1995.
6. Collin, R. E., *Field Theory of Guided Waves*, 2nd Edition, IEEE Press, New York, 1991.
7. Costabel, M., E. Darrigrand, and E. H. Koné, "Volume and surface integral equations for electromagnetic scattering by a dielectric body," *Comput. Appl. Math.*, Vol. 234, 1817–1825, 2010.
8. Joannopoulos, J. D., S. G. Johnson, J. N. Winn, and R. D. Meade, *Photonic Crystals*, Princeton University Press, New Jersey, 2008.
9. Kartchevski, E. M., A. I. Nosich, and G. W. Hanson, "Mathematical analysis of the generalized natural modes of an inhomogeneous optical fiber," *SIAM J. Appl. Math.*, Vol. 65, No. 6, 2033–2048, 2005.
10. Kress, R., *Linear Integral Equations*, 2nd Edition, Springer-Verlag, Berlin Heidelberg, 1999.
11. Nordebo, S., B. Nilsson, T. Biro, G. Cinar, M. Gustafsson, S. Gustafsson, A. Karlsson, and M. Sjöberg, "Wave modeling and fault localization for underwater power cables," *International Conference on Electromagnetics in Advanced Applications (ICEAA11)*, 698–701, 2011.
12. Olver, F. W. J., D. W. Lozier, R. F. Boisvert, and C. W. Clark, *NIST Handbook of Mathematical Functions*, Cambridge University Press, New York, 2010.
13. Reed, M. and B. Simon, *Methods of Modern Mathematical Physics, Volume I: Functional Analysis*, Academic Press, New York, 1980.
14. Sancer, M. I., K. Sertel, J. L. Volakis, and P. V. Alstine, "On volume integral equations," *IEEE Trans. Antennas Propagat.*, Vol. 54, No. 5, 1488–1495, 2006.
15. Shestopalov, V. and Y. Shestopalov, *Spectral Theory and Excitation of Open Structures*, Peter Peregrinus, Ltd., London, 1996.

Plasmonic Cavity Modes: Black-hole Phenomena Captured by Perfectly Matched Layers

A.-S. Bonnet-Ben Dhia¹, C. Carvalho¹, L. Chesnel², and P. Ciarlet, Jr.¹

¹POEMS, UMR 7231 CNRS-INRIA-ENSTA, France

²Department of Mathematics and Systems Analysis, Aalto University, Finland

Abstract— We study a 2D dielectric cavity with a metal inclusion and we assume that, in a given frequency range, the metal permittivity $\epsilon = \epsilon(\omega)$ is a negative real number. We look for the plasmonic cavity resonances by studying the linearized eigenvalue problem (dependence in ω of ϵ frozen). When the inclusion is smooth, the linearized problem operator has a discrete spectrum which can be computed numerically with a good approximation, e.g., by a classical Finite Element Method. However, when the inclusion has corners, due to very singular phenomena, we loose the operator properties and numerical approximations are not stable. Paradoxically there is a theoretical and a numerical need to take into account these singularities in order to compute the modes, even the regular ones. Then we propose an original use of PMLs (Perfectly Matched Layers) at the corners to capture these plasmonic waves.

1. INTRODUCTION

Consider a cavity Ω made of a dielectric material Ω_1 with a metal inclusion Ω_2 , which are separated by an interface Σ . We consider the time-harmonic Maxwell equations for the Transverse Magnetic polarization. In the metal the permittivity ϵ depends on the frequency ω but for simplicity we study the *linearized* eigenvalue problem:

$$\left| \begin{array}{l} \text{Find } u \in H^1(\Omega), u \neq 0, \omega \in \mathbb{C} \text{ such that:} \\ -\operatorname{div}\left(\frac{1}{\epsilon} \nabla u\right) = \omega^2 \mu u \quad \text{in } \Omega \\ u = 0 \quad \text{on } \partial\Omega \end{array} \right. \Leftrightarrow \left| \begin{array}{l} \text{Find } u \in H_0^1(\Omega), u \neq 0, \omega \in \mathbb{C} \text{ such that:} \\ \int_{\Omega} \frac{1}{\epsilon} \nabla u \cdot \nabla \bar{v} d\Omega = \omega^2 \int_{\Omega} u \bar{v} d\Omega \quad \forall v \in H_0^1(\Omega) \end{array} \right. \quad (1)$$

where μ denotes the magnetic permeability. We take ϵ and μ piecewise constant functions, $\mu > 0$ almost everywhere and ϵ sign changing through the interface Σ . Let's define the operator:

$$A : \left| \begin{array}{rcl} D(A) \subset L^2(\Omega) & \longrightarrow & L^2(\Omega) \\ u & \longmapsto & -\frac{1}{\mu} \operatorname{div}\left(\frac{1}{\epsilon} \nabla u\right) \end{array} \right. \text{ with } D(A) = \{u \in H_0^1(\Omega) / -\frac{1}{\mu} \operatorname{div}\left(\frac{1}{\epsilon} \nabla u\right) \in L^2(\Omega)\}.$$

Our goal is to find the eigenvalues of A . When ϵ is not sign changing, one can easily prove that A is symmetric, self-adjoint and has a compact resolvent (called SC. properties in the rest of the paper). When ϵ changes sign at the interface, these properties can still be satisfied under some conditions on ϵ and the geometry of Σ [1]. These conditions lead to the existence of an isomorphism T of $H_0^1(\Omega)$ such that the sesquilinear form is T -coercive : $\int_{\Omega} \frac{1}{\epsilon} \nabla u \cdot \nabla \bar{T}u d\Omega \geq \alpha \|u\|_{H_0^1(\Omega)}^2$ with $\alpha > 0$, α independent of u . Then the operator is self-adjoint and with compact resolvent. When these conditions are not satisfied, the operator A is no longer self-adjoint and neither has compact resolvent. Due to singular phenomena occurring at the corners, a new functional framework is required. In [2, 3] an extension of the operator A is given which recovers the resolvent's compactness property. It takes into account singular functions whose gradient is not square integrable at the corners. Numerically, a specific treatment is required at the corners to capture these singularities. The first section is dedicated to solving the self-adjoint case, the next one to solving the non self-adjoint case, and the last one handles the non linear eigenvalue problem by taking into account the dependence in ω of the permittivity.

2. THE SELF-ADJOINT CASE

When ϵ changes sign, one can still have SC. properties for A if and only if [1] the ratio κ_ϵ of permittivities between the dielectric and the metal (called the contrast) is such that:

- $\kappa_\epsilon \neq -1$ for a smooth interface Σ (see Fig. 1)

- κ_ϵ doesn't belong to a *critical interval* I_c containing $\{-1\}$ when the interface Σ has corners (see Fig. 1)

I_c is a function of the sharpest corner θ ($\theta < \pi$) given by $I_c = [\frac{\theta-2\pi}{\theta}, \frac{\theta}{\theta-2\pi}]$. Notice that when $\theta \rightarrow \pi$, $I_c \rightarrow \{-1\}$ and when $\theta \rightarrow 0$, $I_c \rightarrow \mathbb{R}^-$. Having a sign changing permittivity yields the existence of both positive and negative eigenvalues. More precisely, the eigenvalues $(\omega_i^2)_i$ have finite multiplicity and consist in two sequences of real numbers tending respectively to $\pm\infty$ (see Fig. 7).

2.1. Approximation of the Eigenvalues outside the Critical Interval

In order to approximate the problem (1), we use standard conforming Lagrange Finite Elements of order 2. Under some conditions on the mesh [4], we can prove the convergence toward the exact eigenvalues without spurious modes [5]. We have made computations for the geometry of Fig. 2. We observe stability of the results with respect to the mesh size (see Fig. 3). The bigger in modulus the eigenvalue becomes, the more confined are the associated modes: in the metal for a negative eigenvalue, respectivlty in the dielectric for a positive one (see Fig. 4).

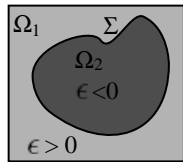


Figure 1: Example of a cavity with a smooth interface.

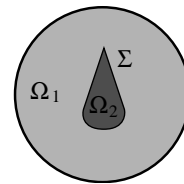


Figure 2: Example of a cavity where the interface has corners.

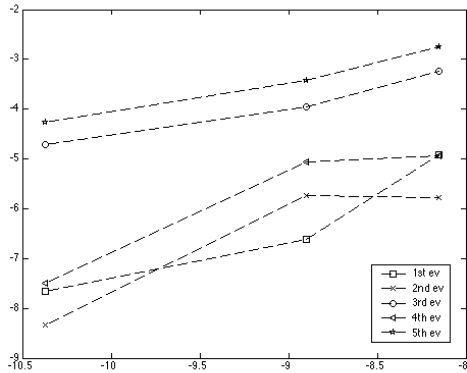


Figure 3: Approximation of the first eigenvalues $\log(|\lambda_{\text{finer mesh}} - \lambda_{\text{coarser mesh}}|)$ for several mesh sizes. The numerical illustrations are realized with the following parameters: the metal's shape is a droplet with a sharp angle of $\frac{\pi}{6}$, and permittivities $\epsilon_1 = 1$, $\epsilon_2 = -13$.

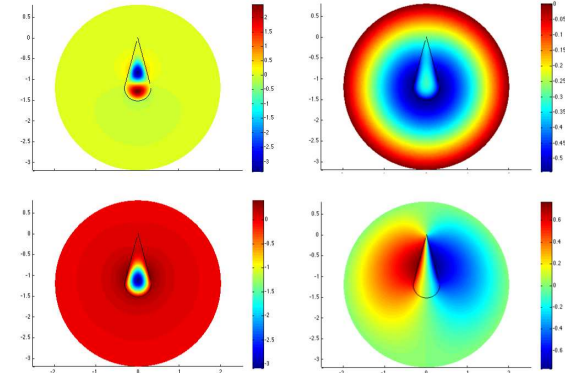


Figure 4: First modes of the SC. operator, associated to the first eigenvalues (the smallest in modulus): the two on the left are associated to a negative eigenvalue, and the two on the right to a positive one. The numerical illustrations are realized on the finer mesh with the same parameters as Fig. 3.

3. THE NON SELF-ADJOINT CASE: AN ORIGINAL USE OF PMLS

For a contrast κ_ϵ chosen in the critical interval (excluding -1), since the problem (1) is ill-posed, there is no convergence of the Finite Element Method (see Fig. 5), and particular phenomena occur at the corner.

Near the corner, an asymptotic analysis [2] let us know that, for κ_ϵ in the critical interval, the magnetic field is a combination of separated variables functions plus a regular part:

$$u(r, \theta) \simeq u_{\text{cst}} + u_{\text{reg}} + c^+ s^+ + c^- s^-, \quad c^+, c^- \in \mathbb{C} \quad (2)$$

where u_{cst} is a constant number and $s^\pm(r, \theta) = \phi(\theta)r^{\pm i\eta}$ ($\eta \in \mathbb{R}$) can be interpreted as propagative waves propagating towards the corner, or from the corner: s^\pm are called black-hole waves. These

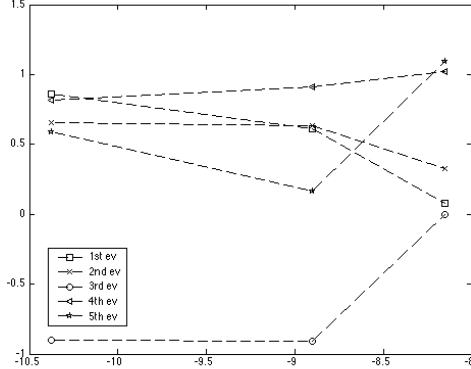


Figure 5: Approximation of the first eigenvalues $\log(|\lambda_{\text{finer mesh}} - \lambda_{\text{coarser mesh}}|)$ for several mesh sizes inside the critical interval. The numerical illustrations are realized with a contrast $\kappa_\epsilon = -\frac{1}{0.7} \in I_c$.

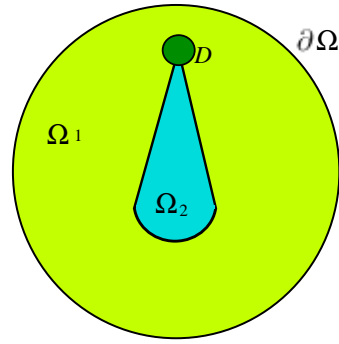


Figure 6: Scheme of the whole domain minus a small disk D_ρ at the corner.

singularities are responsible for the ill-posedness of the problem and their existence characterizes the critical interval. In [2, ?] extensions of the operator A are given that take into account the singularities s^\pm . We define an extension family A_γ of A such that $D(A_\gamma) = D(A) \oplus \text{span}\{s_\gamma = s^+ + \gamma s^-\}$. Then $\forall u \in D(A_\gamma)$, $u = u_A + \beta s_\gamma$, with $u_A \in D(A)$ and $\beta \in \mathbb{C}$. All extensions have compact resolvent, thus the extended operator spectrum will be discrete. If $|\gamma| = 1$, A_γ is a self-adjoint extension according to [4]. Here we're going to choose a non self-adjoint extension in order to have an efficient numerical method. Let's motivate our choice by calculating the energy flux. In order to estimate the energy that goes towards the corner, let's take the whole domain minus a small disk D_ρ centered at the corner (see Fig. 6). In particular the magnetic field satisfies the following equation:

$$\begin{aligned} -\text{div} \left(\frac{1}{\epsilon} \nabla u \right) &= \omega^2 \mu u && \text{in } \Omega / D_\rho \\ u &= 0 && \text{on } \partial\Omega \end{aligned} \tag{3}$$

By multiplying the equation by \bar{u} and integrating, after applying the Green's formula we obtain:

$$\int_{\Omega} \frac{1}{\epsilon} |\nabla u|^2 d\Omega - \int_{\partial D_\rho} \frac{1}{\epsilon} \frac{\partial u}{\partial n} \bar{u} d\Gamma = \omega^2 \int_{\Omega} |u|^2 d\Omega \tag{4}$$

Since $u \in D(A_\gamma)$, when $\rho \rightarrow 0$, one can assimilate the magnetic field to its asymptotic behaviour near the corner given by (2). After some calculus, one can check that the boundary term tends to $-\eta|\beta|^2(1 - |\gamma|^2) \int_{\theta=0}^{2\pi} \frac{1}{\epsilon} |\phi(\theta)|^2 d\theta$. By taking the imaginary part of (4) we obtain for $\rho \rightarrow 0$:

$$-\eta|\beta|^2(1 - |\gamma|^2) \int_{\theta=0}^{2\pi} \frac{1}{\epsilon} |\phi(\theta)|^2 d\theta = \text{Im}(\omega^2) \int_{\Omega} |u|^2 d\Omega \tag{5}$$

Despite the change of sign of ϵ , one can prove the non trivial result: $\eta \int_{\theta=0}^{2\pi} \frac{1}{\epsilon} |\phi(\theta)|^2 d\theta \geq 0$ [2]. Then $\text{Im}(\omega^2)$ has the same sign as $-\beta^2(1 - |\gamma|^2)$. The Equation (5) gives us lots of informations. Indeed, if we choose $|\gamma| = 1$, we see that ω^2 is real, which is coherent with the self-adjointness mentioned above. Let's take $|\gamma| \neq 1$. If ω^2 is real, then the left-hand side is equal to zero which implies that $\beta = 0$ and $u = u_A \in D(A)$. It means that no real eigenvalue (ω_i^2) is exciting the singularity s_γ , so they correspond to the eigenvalues of the initial operator A . This wouldn't be the case for self-adjoint extensions. All the complex eigenvalues have the same sign for their imaginary part: if $|\gamma| > 1$ then $\text{Im}(\omega^2) \geq 0$, whereas if $|\gamma| < 1$ then $\text{Im}(\omega^2) \leq 0$. For simplicity we choose here $\gamma = 0$ such that the extended operator A_0 takes only one singularity into account, and also $\text{Im}(\omega_i^2) \leq 0 \forall i$. This singularity can be captured numerically using Perfectly Matched Layers (PMLs).

An Efficient Numerical Method to Capture the Black-hole Waves

Usually, PMLs are used to bound infinite domains, for instance to truncate waveguides. Here we operate an original use of PMLs by putting them at the corners in order to capture the black-hole waves. Indeed, for each disk D_ρ centered at a corner, by the Euler change of variables $(r, \theta) \mapsto (\log(r), \theta)$ we transform the disk into a semi-infinite waveguide:

$$\begin{aligned} -\operatorname{div}\left(\frac{1}{\epsilon} \nabla u\right) &= \omega^2 \mu u \quad \text{in } D_\rho \quad (x, y) \\ &\Updownarrow \\ -\frac{1}{\epsilon} \left(\frac{\partial u}{\partial r}\right)^2 - \frac{\partial}{\partial \theta} \left(\frac{1}{\epsilon} \frac{\partial u}{\partial \theta}\right) &= \omega^2 \mu r^2 u \quad \text{in } D_\rho \quad (r, \theta) \\ &\Updownarrow z = \log\left(\frac{r}{\rho}\right) \\ -\operatorname{div}\left(\frac{1}{\epsilon} \nabla u\right) &= \omega^2 \mu e^{2z} u \quad \text{in }]-\infty, 0] \times [0, 2\pi] \quad (z, \theta) \end{aligned}$$

Then we use PMLs in a standard way. Basically, it consists in stretching the propagation direction z by a complex number α , $\operatorname{Re}(\alpha) > 0$:

$$\begin{aligned} -\operatorname{div}\left(\frac{1}{\epsilon} \nabla u\right) &= \omega^2 \mu e^{2z} u \quad \text{in }]-\infty, 0] \times [0, 2\pi] \quad (z, \theta) \\ &\Downarrow z \rightarrow \frac{z}{\alpha} \\ -\frac{\alpha^2}{\epsilon} \frac{\partial^2 u}{\partial z^2} - \frac{\partial}{\partial \theta} \left(\frac{1}{\epsilon} \frac{\partial u}{\partial \theta}\right) &= \omega^2 \mu e^{2z/\alpha} u \quad \text{in }]-\infty, 0] \times [0, 2\pi] \quad (z, \theta) \end{aligned}$$

When α is suitably chosen, the asymptotic behaviour (2) leads to a sum of evanescent modes, even s^+ (and a constant mode) such that we can truncate the waveguide at $z = -L$: we put a Neumann condition at $z = -L$ to avoid reflexion of the constant mode. For an implementation point of view, we split the problem in two: the problem in the whole domain minus D_ρ , and the problem at the corner transformed into a strip. It requires matching conditions between the two solutions. Computations confirm that the PMLs' method is efficient to ensure the stability of the Finite Elements approximation. Note that the A_0 spectrum contains complex eigenvalues which clearly proves its non self-adjointness. All the eigenvalues belong to $\{z \in \mathbb{C} \text{ s.t. } \operatorname{Im}(z) \leq 0\}$, which is numerically almost satisfied (see Fig. 8).

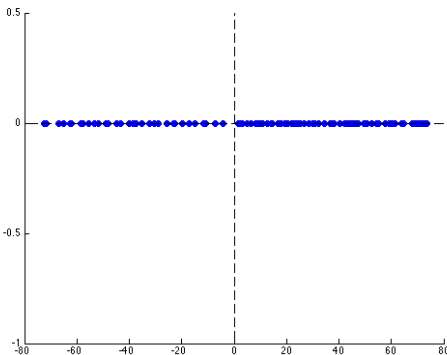


Figure 7: Spectrum of the SC. operator in the complex plane.

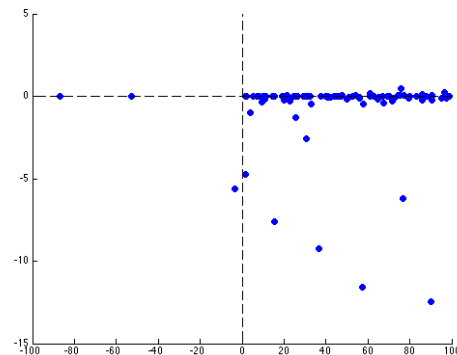


Figure 8: Spectrum of operator A_0 in the complex plane.

4. TOWARDS THE NON LINEAR EIGENVALUE PROBLEM

Considering the dispersionless Drude's model permittivity, one can rewrite the time-harmonic Maxwell equations for the Transverse Magnetic polarization as a non linear eigenproblem:

$$\begin{aligned} -\operatorname{div}\left(\frac{1}{\epsilon(\omega)} \nabla u\right) &= \omega^2 \mu u \quad \text{in } \Omega \\ u &= 0 \quad \text{on } \partial\Omega \end{aligned} \tag{6}$$

with $\epsilon(\omega) = \begin{cases} \epsilon_1 > 0 & \text{in } \Omega_1 \\ \epsilon_2(\omega) = \epsilon_\infty(1 - \frac{\omega_p^2}{\omega^2}) & \text{in } \Omega_2 \end{cases}$ where ω_p is the plasma frequency, $\epsilon_\infty > 0$ the limit behaviour of the metal at high frequencies: for $\omega < \omega_p$, $\epsilon_2(\omega) < 0$. Let's write the variational formulation:

Find $u \in H_0^1(\Omega)$ such that:

$$\frac{1}{\epsilon_1} \int_{\Omega_1} \nabla u \cdot \nabla \bar{v} d\Omega + \frac{1}{\epsilon_\infty} \frac{\omega^2}{\omega^2 - \omega_p^2} \int_{\Omega_2} \nabla u \cdot \nabla \bar{v} d\Omega = \omega^2 \int_{\Omega} u \bar{v} d\Omega \quad \forall v \in H_0^1(\Omega) \tag{7}$$

We multiply (7) by $\omega^2 - \omega_p^2$ [6] and sort the terms. This leads to a polynomial equation in ω :

$$\omega^4 \mathcal{M}_2(u, v) + \omega^2 \mathcal{M}_1(u, v) + \mathcal{M}_0(u, v) = 0$$

with

$$\begin{aligned} \mathcal{M}_0(u, v) &= \int_{\Omega} \tilde{\omega} \nabla u \cdot \nabla \bar{v} d\Omega, \quad \tilde{\omega} = \begin{cases} \frac{\omega_p^2}{\epsilon_1} & \text{in } \Omega_1 \\ 0 & \text{in } \Omega_2 \end{cases} \\ \mathcal{M}_1(u, v) &= \int_{\Omega} \frac{1}{\tilde{\epsilon}} \nabla u \cdot \nabla \bar{v} d\Omega + \omega_p^2 \int_{\Omega} u \bar{v} d\Omega, \quad \tilde{\epsilon} = \begin{cases} \epsilon_1 & \text{in } \Omega_1 \\ \epsilon_\infty & \text{in } \Omega_2 \end{cases} \\ \mathcal{M}_2(u, v) &= \int_{\Omega} u \bar{v} d\Omega \end{aligned}$$

One can reformulate this problem into a system with the two unknowns (u, w) , $w = \omega^2 u$. After discretization, we obtain a linear eigenvalue problem:

$$\begin{pmatrix} \mathbb{M}_0 & 0 \\ 0 & \mathbb{I} \end{pmatrix} \begin{pmatrix} \mathbf{u} \\ \mathbf{w} \end{pmatrix} = \omega^2 \begin{pmatrix} -\mathbb{M}_1 & -\mathbb{M}_2 \\ \mathbb{I} & 0 \end{pmatrix} \begin{pmatrix} \mathbf{u} \\ \mathbf{w} \end{pmatrix} \tag{8}$$

which we can solve as the previous one. Recent works on computations with Finite Elements shows an accumulation point of the eigenvalues at 0 which seems coherent with [6].

ACKNOWLEDGMENT

We thank the DGA for financial support.

REFERENCES

1. Bonnet-Ben Dhia, A.-S., L. Chesnel, and P. Ciarlet, Jr., "T-coercivity for scalar interface problems between dielectrics and metamaterials," *Math. Mod. Num. Anal.*, Vol. 46, 1363–1387, 2012.
2. Bonnet-Ben Dhia, A.-S., L. Chesnel, and X. Claeys, "Radiation condition for a non-smooth interface between a dielectric and a metamaterial," *Math. Mod. Meth. App. Sci.*, 2013.
3. Bonnet-Ben Dhia, A.-S., M. Dauge, and K. Ramdani, "Analyse spectrale et singularités d'un problème de transmission non coercif," *C. R. Acad. Sci. Paris, Ser. I*, Vol. 328, 717–720, 1999.
4. Chesnel, L. and P. Ciarlet, Jr., "T-coercivity and continuous Galerkin methods: Application to transmission problems with sign changing coefficients," *Numer. Math.*, Vol. 124, 1–29, 2013.
5. Babuska, I. and J. E. Osborn, "Eigenvalue Problems," *Handbook of Numerical Analysis*, 1991.
6. Vial, B., M. Commandre, F. Zolla, A. Nicolet, and S. Tisserand, "Analysis of diffraction gratings via their resonances," *AIP*, 109111, doi :10.1063/1.3644228. URL: <http://link.aip.org/link/?APC/1398/109/1>, contributed talk.

The Reconstruction of Dielectric Profile of a Layer for the Harmonic Wave Case

N. B. Pleshchinskii and D. N. Tumakov

Kazan Federal University, Russia

Abstract— The problem of reconstruction of a dielectric profile of a layer for single frequency is considered. The residual functional is constructed. The purpose of the paper is to select the frequency for which the functional becomes a more stable. It is shown that the frequency corresponds to the frequency of the minimum of the transited energy through a layer. Numerical experiments performed for ridge-shaped and complex profiles confirm correctness of the selected frequency.

1. INTRODUCTION

The reconstruction of one-dimensional profile $\varepsilon(x)$ or $n(x)$ of a layer is one of the general problem in electrodynamics and is the inverse problem. Different sets of data may be used for the reconstruction of unknown profile. These data may be reflection coefficients, input impedance, scattered electric or magnetic fields. The very complete review of various techniques of reconstructing of different profiles is given in [1].

In this article the reconstruction problem is reduced to the minimization of some functional. To minimize the functional we solve the direct problem iteratively. The algorithm for the reconstruction of the refractive index is tested by experiments with the single frequency. Firstly, we consider the case in which refractive index (permittivity) of a layer monotonically increases and then monotonically decreases. Secondly, we consider the layer with the periodical dielectric profile and the layer with the complex profile.

We make the conclusion, that our method gives the optimum approximation for the case of experiments with the single frequency for which the transited energy attains the minimum.

2. PROBLEM STATEMENT

Let the plane electromagnetic harmonic wave of type $u_0(x, t) = A_0 \exp\{-ik_0 n_1 x + i\omega_j t\}$ fall on a layer of thickness L with unknown refractive index $n_2(x)$ from a homogenous isotropic medium (see Figure 1). We change variable t by ω and will suppose that functions depend on variables x and ω . It is necessary to reconstruct the refractive index $n_2(x)$, by assumption that the reflected $u_1(x, \omega_j)$ and the transmitted $u_3(x, \omega_j)$ waves are known for several frequencies ω_j . We suppose that profile of the refractive index $n_2(x)$ is varied continuously.

We have measurements on M of different frequencies ω_j , $j = 1 \dots M$ for intensity of magnetic and electric fields. Measured values of intensities are real numbers. We obtain M of complex values for $u_1(0, \omega_j)$ and $u_3(L, \omega_j)$ (for example, for TE-polarisation it is intensity of electric field), by the method of over-determined boundary value problems [2].

So, we have M sets of complex numbers $\hat{u}_0^j = u_0(0, \omega_j) + u_1(0, \omega_j)$ for the values of the field in the layer at $x = 0$ and $\hat{u}_L^j = u_3(L, \omega_j)$ for values of the field at $x = L$. Solving the direct problem of the diffraction by a layer with some $n_2(x)$, we should variate $n_2(x)$ so, that the field, which is the solution of the direct problem give values \hat{u}_0^j and \hat{u}_L^j on boundaries of the layer.

3. DIRECT PROBLEM

We will solve the direct problem for a harmonic wave with frequency ω_j [3]. In this section, we will neglect the variable ω_j , considering it as the parameter. Let the plane electromagnetic wave of type $u_0(x) = A_0 \exp\{-ik_0 n_1 x\}$ falls on a layer of thickness L , which given known refractive index $n_2(x)$ from a homogenous isotropic medium (see Figure 1). It is necessary to find the diffracted field or, more precisely, the reflected, transited waves and a field in a layer $u_2(x)$.

The function $u(x)$ which is continuous everywhere with its derivatives, satisfies the equation

$$u''(x) + k_0^2 n^2(x) u(x) = 0, \quad x \in \mathbf{R}$$

with a given continuous function $n(x)$. For regions 1 and 3 of the medium, function $n(x)$ is constant and the equation for these cases is solved explicitly.

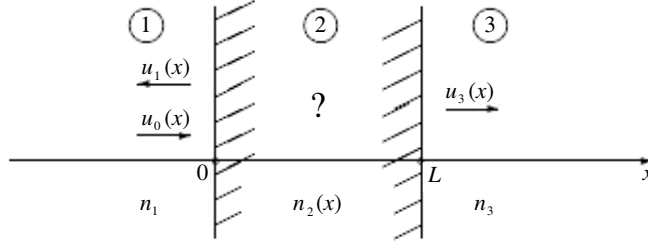


Figure 1: Geometry of the problem.

Thus, the diffraction problem is reduced to an ordinary differential equation

$$u_2''(x) + k_2^2(x)u_2(x) = 0, \quad 0 < x < L, \quad (1)$$

with boundary conditions

$$u_2'(0) - ik_1 u_2(0) = -2ik_1 A_0, \quad u_2'(L) + ik_3 u_2(L) = 0, \quad (2)$$

where $k_j = k_0 n_j$ are wavenumbers of the media. We solved the direct problem numerically. The method of approximating an integral identity [4] is applied to increase accuracy of the grid solution to the obtained boundary problem.

4. INVERSE PROBLEM

Let's assume that the M measurements are executed and as a result of which are obtained the values of fields on the layer's bounders. We will solve the direct problem iteratively in order to solve the inverse problem. The direct problem is solved with the refractive index obtained on a previous iteration. The initial approximation for $n(x)$ is the straight line which connect points $x = 0$ and $x = L$ with values n_1 and n_3 . If $n_1 = n_3$ then $n(x) \equiv n_1$. We will minimize the functional defined by

$$F[n(x)] = \sum_{j=1}^M \left| u^j(0) - \hat{u}_0^j \right|^2 + \sum_{j=1}^M \left| u^j(L) - \hat{u}_L^j \right|^2 + \alpha \|n(x)\| + \beta_1 |n(0) - \hat{n}_0|^2 + \beta_2 |n(L) - \hat{n}_L|^2,$$

where \hat{u}_0^j and \hat{u}_L^j are known values of the measured field for j th experiment, $u^j(0)$ and $u^j(L)$ are calculated values of the field on the current iterative step on both sides of the layer (at $x = 0$ and $x = L$). The values α , β_1 and β_2 are regularization parameters; values \hat{n}_0 and \hat{n}_L are known values of refractive index on the layer's bounders. In our case $\hat{n}_0 = n_1$ and $\hat{n}_L = n_3$.

The function $n(x)$ is changed by the vector $\mathbf{n} = \{n_i, i = 0 \dots N\}$. New functional is

$$F[\mathbf{n}] = \sum_{j=1}^M \left| u_0^j - \hat{u}_0^j \right|^2 + \sum_{j=1}^M \left| u_N^j - \hat{u}_L^j \right|^2 + \alpha \|\mathbf{n}\|_{\ell_2} + \beta_1 |n_0 - \hat{n}_0|^2 + \beta_2 |n_N - \hat{n}_L|^2,$$

where the norma of the vector is defined by

$$\|\mathbf{n}\|_{\ell_2} = \sum_{i=0}^N |n_i|^2.$$

The method of golden section is used for minimization of our functional. Also we use the next condition about n_i : $n_{\min} \leq n_i \leq n_{\max}$.

We will use the relative error of the found refractive index $\{n_i\}$ for the checking of the accuracy of the approximation:

$$r = \sum_{j=0}^N |n(x_i) - n_i|^2 / \sum_{j=0}^N |n(x_i)|^2.$$

5. RECONSTRUCTION OF RIDGE-SHAPED PROFILES OF REFRACTIVE INDEX

Let's consider layers with ridge-shaped profile of refractive index. The propagation of electromagnetic wave through layers with ridge-shaped profiles from Figure 2 give the specifical frequency-response characteristics [5]. Transited energy has the accurately expressed minimum. For example, the minimum value of transited energy is reached at $\omega = 283$ THz for the linear profile of permittivity.

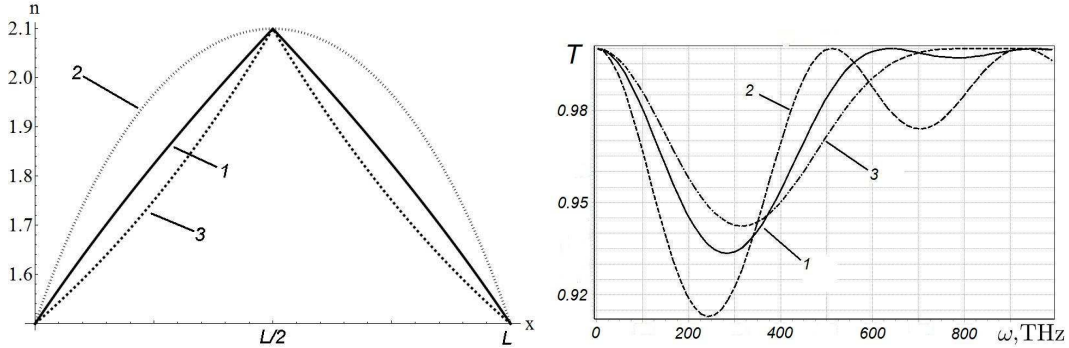


Figure 2: Distribution and frequency-response characteristic of transited energy for refractive index in the gradient layer: 1 — linear permittivity, 2 — parabolic permittivity, 3 — exponential permittivity.

In this work in all numerical experiments we will assume $n_1 = n_3 = 1.5$ and $\beta_1 = \beta_2 = 2$. Also in this section we will fix the number of points of an unknown profile of $N = 50$. We will reconstruct the profile for the one chosen frequency. We investigate the dependence of the accuracy of reconstruction on the chosen frequency. We will make comparisons for three frequencies: the first corresponds to the global minimum of T , the second and the third frequencies select of less and more than the first frequency.

We begin the analysis with a smooth parabolic profile (graphic 2 in Figure 2). Let's choose frequency $\omega = 243$ THz, 100 THz and 500 THz. Here $\omega = 243$ THz corresponds to the minimum of transited energy. We will try to minimize the functional with $\alpha = 0$. Results are presented in Figure 3. The functional constructed for the frequency, where T has the minimum, is stable. The reconstructed profile is the closest profile to the true value of $n(x)$. The profiles, which are reconstructed for other frequencies, have jumps on the ends of the layer and approach the justify value of $n(x)$ significantly badly.

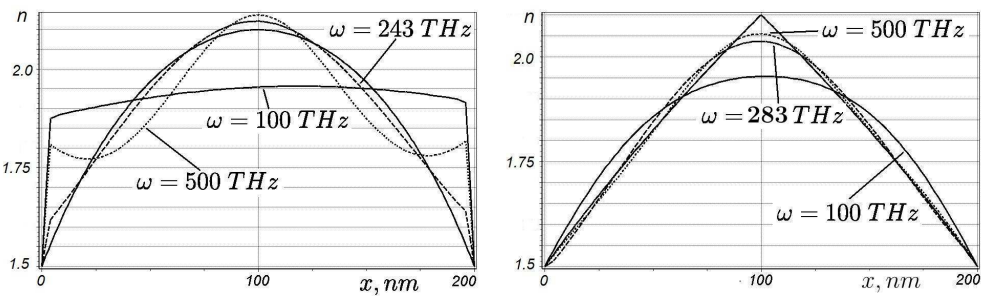


Figure 3: Results of the reconstruction of profiles 2 and 3 from Figure 2.

Results of approximation of the piecewise smooth profile of $n(x)$ with the optimum parameter α for each frequency are given in Figure 3. Better results of the approximation of $n(x)$ are obtained for frequencies $\omega = 283$ and $\omega = 500$ THz. For these cases the regularization parameter is $\alpha = 0$ and $\alpha = 0.015$, the error is $r = 2 \cdot 10^{-4}$ and $r = 7.6 \cdot 10^{-5}$. If $\omega = 100$ THz, then optimal value of $\alpha = 0.035$ and error $r = 1.7 \cdot 10^{-2}$.

Let's provide in the Table 1 results of reconstruction of all profiles from Figure 3. The results of the reconstruction of the profile are shown at the optimum single frequency and at the frequency interval from 500 THz to 1000 THz with the step $\Delta\omega = 50$ THz.

Table 1: Results of optimization for several profiles. Number of points $N = 50$, $\beta_i = 2$.

profile type	ω , THz	α	r
linear	283	0.0	$2.0 \cdot 10^{-4}$
	[500, 1000], $\Delta\omega = 50$	0.35	$4.5 \cdot 10^{-5}$
parabolic	243.6	0.035	$2.3 \cdot 10^{-5}$
	[500, 1000], $\Delta\omega = 50$	0.35	$4.75 \cdot 10^{-6}$
exponential	315.8	0.0	$6.7 \cdot 10^{-4}$
	[500, 1000], $\Delta\omega = 50$	0.35	$1.3 \cdot 10^{-4}$

6. RECONSTRUCTION OF COMPLEX PROFILES OF REFRACTIVE INDEX

At first, let's consider the reconstruction of the periodic profile $n(x)$, which is formed by three parabolic layers (see Figure 4), presented on graphic 2 of Figure 2. We obtained the following results. If $\omega = 361$ THz, then optimal value $\alpha = 0.1$ and error $r = 3.6 \cdot 10^{-3}$; if $\omega = 200$ THz, then optimal value $\alpha = 0.01$ and error $r = 1.7 \cdot 10^{-2}$; if $\omega = 500$ THz, then optimal value $\alpha = 0.05$ and error $r = 3.2 \cdot 10^{-2}$. In this case, we can see that only for the frequency $\omega = 361$ THz the constructed $n(x)$ is the really closed shape to the justify profile.

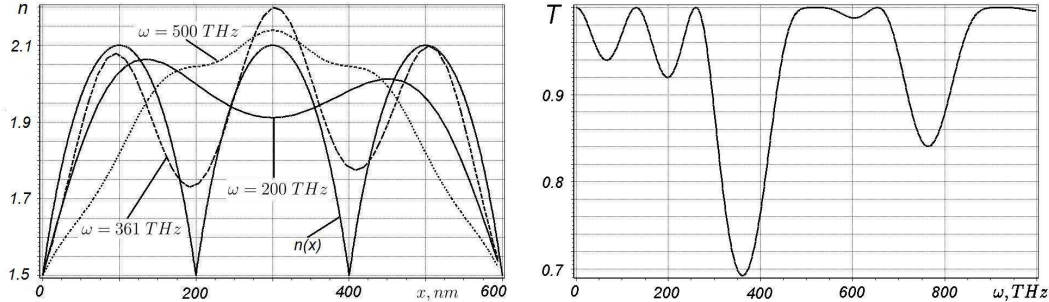


Figure 4: Results of the reconstruction and frequency-response characteristic of transited energy of the periodical profile.

The example of reconstruction of more profile is given in Figure 5. Here the initial profile is more smooth, and the reconstruction is better carried out with all frequencies. If $\omega = 788$ THz, then optimal value $\alpha = 0.2$ and error $r = 1.2 \cdot 10^{-3}$; if $\omega = 560$ THz, then optimal value $\alpha = 0.01$ and error $r = 2.4 \cdot 10^{-3}$; if $\omega = 1000$ THz, then optimal value $\alpha = 0.2$ and error $r = 9.6 \cdot 10^{-3}$. But, as well as in the previous example, we have the best approximation with the frequency which corresponds to the minimum of the transited energy.

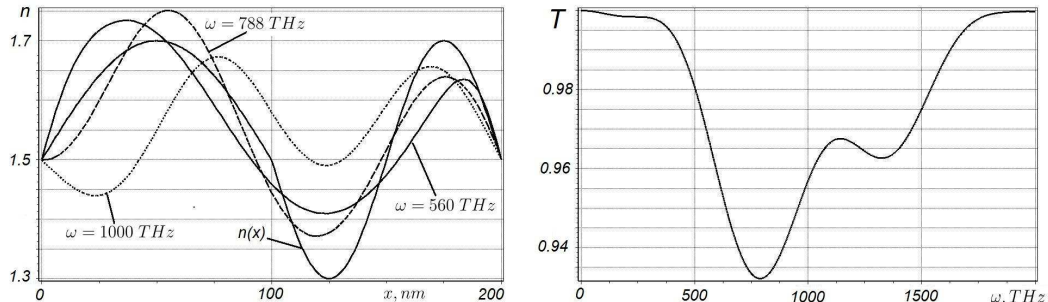


Figure 5: Results of the reconstruction and frequency-response characteristic of transited energy of the complex profile.

7. CONCLUSIONS

Our functional gives the optimum approximation for the case of $M = 1$ with the frequency for which the transited energy attains the minimum. The regularization parameter can be chosen as the small value. We have especially good results for the ridge-shaped profile. The reconstruction with frequencies smaller than the specified frequency significantly degrade the quality of the reconstruction; for big frequencies it is necessary to increase parameter α .

ACKNOWLEDGMENT

This work was supported by RFBR 12-01-97012-r-povolzh'e.a.

REFERENCES

1. Emad Eldin, A. M., E. A. H. Hashish, and M. I. Hassan, "Inversion of lossy dielectric profiles using particle swarm optimization," *Progress In Electromagnetics Research M*, Vol. 9, 93–105, 2009.
2. Pleshchinskii, N. B., I. E. Pleshchinskaya, and E. M. Karchevskiy, "The over-determined boundary value problem method in the electromagnetic waves propagation and diffraction theory," *PIERS Proceedings*, 132–136, Moscow, Russia, August 18–21, 2009.
3. Pleshchinskii, N. B. and D. N. Tumakov, "Analysis of electromagnetic wave propagation through a layer with graded-index distribution of refractive index," *PIERS Proceedings*, 425–429, Moscow, Russia, August 19–23, 2012.
4. Anufrieva, A. V., V. L. Kipot, and D. N. Tumakov, "Elastic wave propagation through a layer with graded-index distribution of density," *Days on Diffraction 2012*, 21–26, Spb, Russia, May–June 2012.
5. Anufrieva, A. V. and D. N. Tumakov, "Peculiarities of electromagnetic wave propagation through layers with ridge-shaped refractive index distribution," *2012 Int. Conf. on Mathematical Methods in Electromagnetic Theory, MMET*, 386–389, Kharkiv, Ukraine, August 2012.

Adaptive Artificial Boundary Conditions for Schrödinger Equation with Un-instantaneous Nonlinearity

V. A. Trofimov, A. D. Denisov, M. V. Fedotov, and A. S. Prokopenko

Lomonosov Moscow State University, Moscow 119992, Russia

Abstract— Enhancement of a computer simulation performance is one of the urgent problems. A possible way to do this consists in implementing artificial boundary conditions applied for the numerical solution of equation under consideration. As it well-known, such approach is widely applied for computer simulation of wave propagation in linear and nonlinear medium. In particular, various types of artificial boundary conditions were proposed for Schrödinger equation. Mainly, such conditions were developed for such equation with instantaneous nonlinear response of medium or in the linear case. In present report [7], we proposed the adaptive artificial boundary conditions for Schrödinger equation describing a nonlinear propagation of terawatt laser pulse in glass taking into account the multi-photon absorption and non-stationary generation of free carriers of charges and Kerr nonlinear response of medium. This process is described by the nonlinear Schrödinger equation together with time-dependent equation with respect to concentration of free electrons. For considering set of the equations in 1D case, we constructed two-layer non-explicit scheme, which is conservative one in the case of transparent medium. To realize the adaptive artificial boundary conditions, the analysis of instantaneous frequency of optical pulse near the boundaries of time interval under consideration is provided. This value of frequency is used in the boundary conditions. Obviously, the instantaneous frequency depends on propagation coordinate and time. Therefore, using the constant value of frequency in the boundary conditions is ineffective way for developing of the artificial boundary conditions. On the base of computer simulation, we show high efficiency of an approach, developed by us.

1. INTRODUCTION

Modern problems of ultrashort laser pulse propagation require a lot of computations, which can be associated with multidimensionality of considered problem or necessity of computational domain enlarging due to physical features of the problem. A possible way to increase the efficiency of computer simulation consists in using of artificial boundary condition [1–7]. Such kind boundary conditions are used usually for solution of Schrödinger equation with instantaneous nonlinear response. Below we consider a possibility of applying adaptive artificial boundary conditions if a laser pulse propagates in nonlinear medium with un-instantaneous nonlinearity. The medium can be, for example, glass, in which the high-intensive femtosecond pulse propagates. As it is well-known, the time-dependent generation of free-electrons takes place under such conditions.

2. STATE OF PROBLEM

Dimensionless Schrödinger equation with un-instantaneous nonlinearity can be written in the following manner:

$$\frac{\partial u}{\partial z} + iD \frac{\partial^2 u}{\partial t^2} + i\alpha\rho u + \delta|u|^2 u = 0, \quad z > 0, \quad 0 < t < L_t, \quad (1)$$

$$\frac{\partial \rho}{\partial t} + \frac{\rho}{\tau_\rho} = q|u|^4, \quad (2)$$

$$u_{z=0} = e^{-(t-\theta L_t)^2}, \quad \rho_{t=0} = 0,$$

where u — is slowly varying envelope amplitude of laser pulse, D — parameter characterizing second order dispersion, function $\rho > 0$ describes free electrons concentration, q means the generation of plasma, τ_ρ — characterizes time of free electron relaxion. Parameter θ defines pulse center position.

Let us define two type of boundary conditions for the problem above. The first type is zero-value boundary conditions:

$$u(z, 0) = u(z, L_t) = 0. \quad (3)$$

Using of these conditions is possible only if the case of zero-value solution near the boundary takes place. In opposite case, the adaptive artificial boundary conditions can be used. Let us introduce

this condition for the left boundary:

$$\begin{aligned} \left(\frac{\partial u}{\partial z} - 2D\Omega_L \frac{\partial u}{\partial t} + iD\Omega_L^2 u + i\alpha\rho u + \delta|u|^2 u \right)_{t=0} &= 0, \\ u(z, L_t) &= 0. \end{aligned} \quad (4)$$

Here Ω_L means the instantaneous frequency of the light pulse on the left boundary in time domain. In general case it depends on current solution near the boundary.

3. FINITE-DIFFERENCE SCHEME

In the domain $\Omega = [0, L_z] \times [0, L_t]$ we define mesh function A and ρ on uniform grids $\omega = \omega_z \times \omega_t$ and $\tilde{\omega} = \omega_z \times \tilde{\omega}_t$ correspondingly,

$$\begin{aligned} \omega_z &= \{z_j = jh, j = 0, 1, \dots, N_z, h = L_z/N_z\}, \quad \omega_t = \{t_k = k\tau, k = 0, 1, \dots, N_t, \tau = L_t/N_t\}, \\ \tilde{\omega}_t &= \{t_k = k\tau - \tau/2, k = 0, \dots, N_t + 1, \tau = L_t/N_t\}. \end{aligned}$$

Let us introduce the following index-free notations:

$$\begin{aligned} A &= A_{j,k} = A(z_j, t_k), \quad \hat{A} = A(z_{j+1}, t_k), \quad \overset{0.5}{A} = 0.5(\hat{A} + A), \quad \left| \overset{0.5}{A} \right|^2 = 0.5(|\hat{A}|^2 + |A|^2), \\ \rho &= \rho_{j,k} = \rho(z_j, t_k), \quad \hat{\rho} = \rho(z_j, t_{k+1}), \quad \overset{0.5}{\rho} = 0.5(\hat{\rho} + \rho), \quad \Lambda_{\bar{t}t} A = (A_{k+1} - 2A_k + A_{k-1})/\tau^2. \end{aligned}$$

Using these notations, one can write the following finite-difference scheme for (1) with iterative process:

$$\begin{aligned} \frac{\overset{s+1}{\hat{A}} - A}{h} + iD\Lambda_{\bar{t}t} \overset{0.5}{A} + i\alpha \overset{0.5}{\rho} \overset{0.5}{A} + \delta \left| \overset{0.5}{A} \right|^2 \overset{0.5}{A} &= 0, \\ \frac{\hat{\rho} - \rho}{\tau} + \frac{\overset{0.5}{\rho}}{\tau_\rho} &= q \left| \overset{0.5}{A} \right|^4, \\ \rho_{j,0} &= 0. \end{aligned} \quad (5)$$

Approximation of the condition (4) is chosen as:

$$\frac{\overset{s+1}{\hat{A}}_0 - A_0}{h} - 2D\Omega \frac{\overset{s+1}{\hat{A}}_1 - \overset{s+1}{\hat{A}}_0}{\tau} + iD\Omega^2 \overset{s+1}{\hat{A}}_0 + i\alpha \overset{0.5}{\rho} \overset{0.5}{A}_0 + \delta |\overset{0.5}{A}_0|^2 \overset{0.5}{A}_0 = 0. \quad (6)$$

Value of the functions at zero iteration is defined as

$$\overset{0}{\hat{A}}_k = A_k, 0 \leq k \leq N_t.$$

The criterion of the iterations stopping is

$$\max_{0 \leq k \leq N_t} \left| \overset{s+1}{\hat{A}}_k - \overset{s}{A}_k \right| \leq \varepsilon_1 \max_{0 \leq k \leq N_t} \left| \overset{s}{\hat{A}}_k \right| + \varepsilon_2, \quad \varepsilon_2 = 0.1\varepsilon_1, \quad \varepsilon_1 = 0.001. \quad (7)$$

To control the finite-difference solution near the boundary with adaptive artificial boundary condition (6) we will compare this solution with solution of Schrödinger equation with zero-value boundary conditions. The difference between these two solutions is estimated by:

$$\xi = \left\| |u|^2 - |A|^2 \right\|_c = \max_{z,t \in \omega} \left| |u|^2 - |A|^2 \right|.$$

4. COMPUTER SIMULATION RESULTS

To avoid non-physical behaviour of the solution of finite-difference problem, it is important to control invariants. One of the laws is energy law. But the problem (1) is nonstationary. Taking into account this feature we can check (if parameter δ in (1) is not equal to zero, in opposite case the invariant can be found) the difference between $|A(j, \theta N_t)|^2$ and analytical solution for Equation (1). This solution can be written as: $\frac{1}{2\delta z + 1/|u(0, \theta L_t)|^2}$ in the case when second order dispersion is equal to zero. In Figure 1, we show the evolution of these solutions for $D = 0.1$, $\alpha = 20$, $\delta = 10$, $\theta = 0.5$ and mesh steps $h = \tau = 0.001$ for $L_z = 2$, $L_t = 20$.

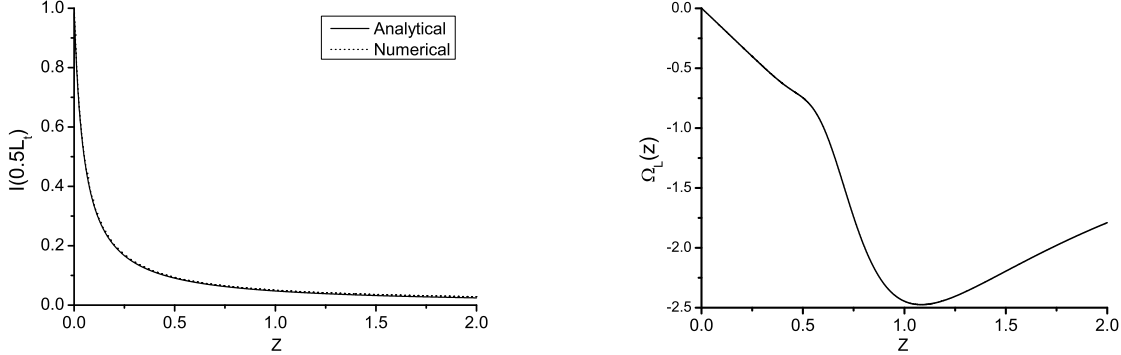


Figure 1: Evolution of maximal intensity (here and below $I(j, k) = |A|^2$) along z coordinate for $D = 0.1$, $\alpha = 20$, $\delta = 10$, $q = 1$, $\tau_\rho = 1$ with $h = \tau = 0.001$.

Figure 2: Evolution of the instantaneous frequency Ω_L along z coordinate for $D = 0.1$, $\alpha = 20$, $\delta = 10$ and $h = \tau = 0.001$ and $\theta = 0.2$, $L_t = 10$.

Our consideration shows the necessity of computing parameter Ω_L along z coordinate. Changing of Ω_L in depending on z coordinate is shown on the Figure 2. It is well seen that the character of $\Omega_L(z)$ is nonlinear (for definiteness we assign considered domain as: $L_z = 2$, $L_t = 20$ everywhere later). That is why we can not choose Ω_L equals to constant value. To verify that, let us turn to the Figure 3 in which it is clearly seen that the result of computation for $\Omega_L = 1$ in (4) leads to worse result.

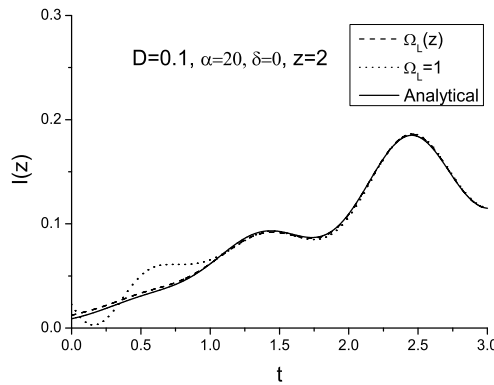


Figure 3: Pulse shape computed for $\Omega_L(z)$ and for $(\Omega_L = 1)$ with mesh steps $h = \tau = 0.001$.

Table 1: Dependence of assessment ξ on time for the problem (1), (2), (4) with $\theta = 0.05$ for $h = 0.01$, $D = 0.1$; $\alpha = 20$; $\delta = 0$; $\tau_\rho = 1$; $q = 1$; $L_t = 40$.

$\tau = 0.1$	$\tau = 0.01$	$\tau = 0.001$
3.03E-02	3.56E-03	3.44E-03

It is interesting to review simulation for the problem (1), (3) depending on parameters τ_ρ and δ . On the Figure 4 the results are presented. On the Figure 5 the results for fixed parameters: $D = 0.1$, $\alpha = 20$, $\delta = 10$, $\tau_\rho = 1$, $q = 1$ are shown. For these sets of parameters, norm ξ is

represented in Tables 1, 2. Parameter Ω_L from (4) was computed from the finite-difference solution of (1), (3) in the section of supposed artificial boundary.

Table 2: Same as in Table 1 for $D = 0.1$, $\alpha = 20$, $\delta = 10$, $\tau_\rho = 1$, $q = 1$.

$\tau = 0.1$	$\tau = 0.01$	$\tau = 0.001$
3.97E-03	2.25E-03	2.19E-03

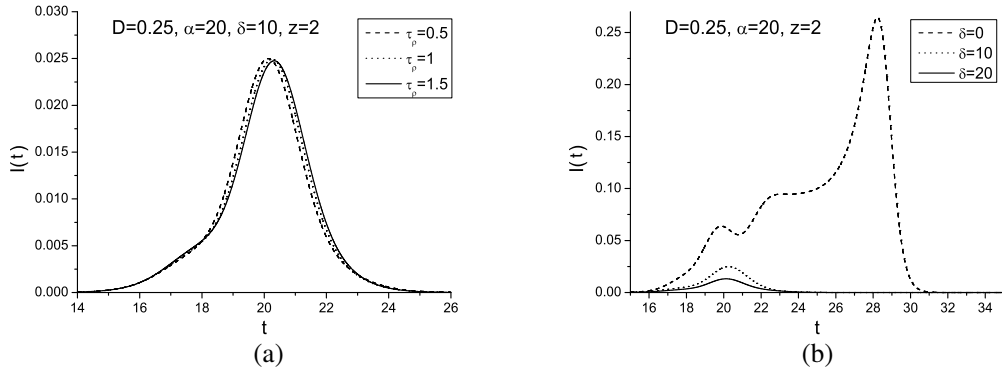


Figure 4: Intensity distributions depending on parameters (a) τ_ρ and (b) δ for $q = 1$ and $h = \tau = 0.001$.

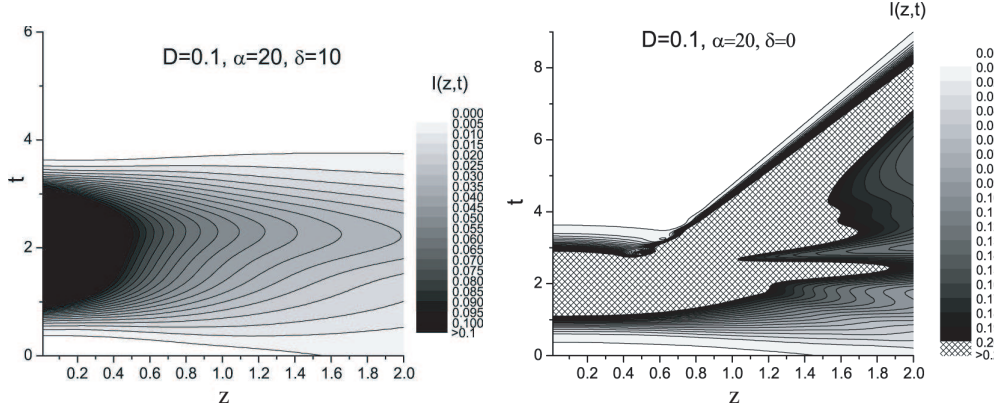


Figure 5: Laser pulse intensity distribution on the plane (z, t) for $D = 0.1$, $\alpha = 20$, $\delta = 0$ and $h = \tau = 0.001$.

5. CONCLUSIONS

Proposed adaptive artificial boundary conditions are able to be used for the considered problem. They demonstrate high efficiency for the case of un-instantaneous nonlinear response. To achieve this efficiency it is necessary take into account the evolution of instantaneous frequency along z coordinate.

ACKNOWLEDGMENT

This work is partly supported by the Russian Foundation for Basic Research.

REFERENCES

- Schürmann, H. W., Y. Smirnov, and Y. Shestopalov, "Integral equation approach for the propagation of TE-waves in a nonlinear dielectric cylindrical waveguide," *J. Nonlinear Math. Phys.*, Vol. 11, 256–268, 2004.
- Xu, Z. and H. Han, "Absorbing boundary conditions for nonlinear Schrödinger equations," *Phys. Rev.*, Vol. 74, 037704, 2006.

3. Xu, Z., H. Han, and X. Wu, “Adaptive absorbing boundary conditions for Schrödinger-type equations: Application to nonlinear and multi-dimensional problems,” *J. Comput. Phys.*, Vol. 225, 1577–1589, 2007.
4. Fibich, G. and S. Tsynkov, “High order two-way artificial boundary conditions to nonlinear wave propagation with back-scattering,” *Commun. Comput. Phys.*, Vol. 171, No. 2, 632–677, 2001.
5. Antoine, X., A. Arnold, C. Besse, M. Ehrhardt, and A. Schadle, “A review on transparent and artificial boundary conditions technique for linear and nonlinear Schrödinger equations,” *J. Comput. Phys.*, Vol. 4, 729–796, 2008.
6. Tereshin, E. B., V. A. Trofimov, and M. V. Fedotov, “Conservative finite-difference scheme for the problem of propagation of a femtosecond pulse in a nonlinear photonic crystal with nonreflecting boundary conditions,” *Computational Mathematics and Mathematical Physics*, Vol. 46, No. 1, 152–164, 2006.
7. Trofimov, V. A. and A. D. Denisov, “Adaptive artificial boundary conditions for 2D Schrödinger equation,” *Proceedings of Fifth Conference on Numerical Analysis and Applications*, 50–51, Lozenetz, Bulgaria, 2012.

Benefits of Using Wireless Sensor Networks to Predict Plagues in Vineyards

I. Cuiñas, S. Cervera, and J. A. Gay-Fernández

Department Teoría do Sinal e Comunicacións, Universidade de Vigo, Spain

Abstract— Wireless sensor networks (WSN) are experienced an important development, as their applications grow and grow. Vineyards are one of the most popular scenarios to deploy WSN in order to tracking various botanic parameters. Agronomists could use the sensing capabilities to check the evolution of many parameters. Some of the measured parameters are closely related to various plant plagues, as mildew in vineyards. The usefulness of such tracking in plague prediction, and the possible benefits of controlling plagues by predicting their cycles with automatic data capture are the objective of the present work, which highlights both the botanic and the economic advantages of a fully performance WSN in a vineyard.

1. INTRODUCTION

Wireless sensor networks (WSNs) have been proposed as a key tool in improvement of agriculture goods quality, as a mean to control different parameters related to the biological activity and growing rhythm of the plants. Wine sector is especially interested in such technology: the final product (the wine) has important added value, but its quality is strongly dependent to the vines health and development during several months a year.

This paper is intended to describe the experience in installing and operating a WSN with different meteorological sensors in a vineyard at a Spanish denomination of origin area, as well as the processing of collecting data to analyze the most troublesome plague in the region, the mildew.

As described in Section 2, the basic system consists of a number of motes, each provided by a number of sensors (temperature, humidity, leaf wetness, and so on), a coordinator, and a gateway to link the data to the World (i.e., the Internet). This set of sensors is collecting data each a defined time gap, constructing what could be seen as time varying signals that could be processed and analyzed.

There are various mathematical models to predict plagues at vineyards, as indicated in Section 3. The application of methods as EPI, POM, Goidanich, RAI, Milvit, or Plasmo allows us to provide the biologists taking care of the vineyards with a mildew alert system, in order they to decide the actions or products to apply the plants each time. This scientific alert procedure could reduce the number of applied treatments, as it breaks the traditional period-based treatment and supports the decision of cure when it is need. Then, a reduction in costs could be obtained: both economics (products and work-time to apply them) and ecological (less chemical products incorporated to the soil and plants), as explained in Section 4.

2. FUNDAMENTALS OF WIRELESS SENSOR NETWORKS

The concept of WSN is an evolution of wireless networks with a clear orientation: the information transmitted from node to node in the network mainly come from sensors connected at each node. Thus, each node has a double mission: collecting the data provided by the plugged in sensors, and transmitting the own information or that received from other nodes to the adjacent ones. The goal is to minimize the capabilities of each node, reducing it to the minimum needed to perform its function: a small processing ability and short range transmitter/receiver. As a consequence, instead of talking about nodes, in WSN they are better known as motes. This is a word with a clear meaning: small, weightless, and inexpensive. The objective is to have a technology that allows the deployment of networks constructed by hundreds of motes at a low cost.

Whereas the motes assure the interconnectivity, the sensors provide the data to be transmitted. For agriculture applications there are a large collection of sensors, designing to measure a variety of parameters: temperature and humidity both at soil and air, solar irradiation, rain, leaf wetness, wind speed and direction, barometric pressure, rainfall and soil water content.

The motes carry the data towards the coordinator node. This coordinator works as a master node, and it is connected to a gateway that allows the transmission of data far away the location of the WSN. Depending on the installation, the gateway could be connected to a computer or server, to a modem to access terrestrial cellular networks, or to a dedicated radio link. Anyway,

independently of the physical communication method, finally data is stored in a data base, being available for agronomists, biologists, managers, and other people caring the crop under tracking. Besides, some WSN, as those based on IEEE 802.15.4 [1], have the ability of re-configuring its maps of links when some of the paths do not work. This feature provides robustness to the complete system.

3. PREDICTION OF PLAGUES ON VINEYARDS

WSN provides an exhaustive set of data, and up to date actualization, which is very good information for those persons that need to monitor the status of the crop. However, it is possible to go further: collected data could be analyzed by experts, but it also could be the input to mathematical models that would help in plague detection tasks.

Concretely, there are some well-known plagues attacking vineyards, and farmers are very afraid of them. Among those, mildew is probably the most studied, as it produces important economic losses in vineyards and, consequently, in wineries. Mildew is the result of the presence of a fungus in the green elements of the vines, and its life cycle is well defined [2]:

1. Contamination phase: in spring, zoospores are transported by rain and wind, reaching the vine green parts and colonizing them. The needed conditions for contamination are in fact a set: an air temperature around 10°C, a young plant of at least 10 cm, and a rain rate of at least 10 mm/day.
2. Incubation phase: it takes from 4 to 21 days, depending on atmospheric conditions.
3. Sporulation phase: during this step, the fungus is propagated along the vine.
4. Propagation phase: dissemination to nearby plants with the help of rebounding rain drops and wind. The optimal condition for ambience temperature is between 20 and 25°C, with the help of rain during night.

Table 1: Distribution of sensors plugged in to the nodes.

Sensor	nodes					
	1	2	3	4	5	6
Air temperature and humidity		X	X	X	X	X
Soil temperature and humidity	X	X	X	X	X	X
Solar radiation			X	X	X	
Soil water content	X	X				X
Leaf wetness	X	X	X	X	X	X
Weather station: barometric pressure, wind velocity and direction, rainfall, solar radiation, air temperature and humidity	X					

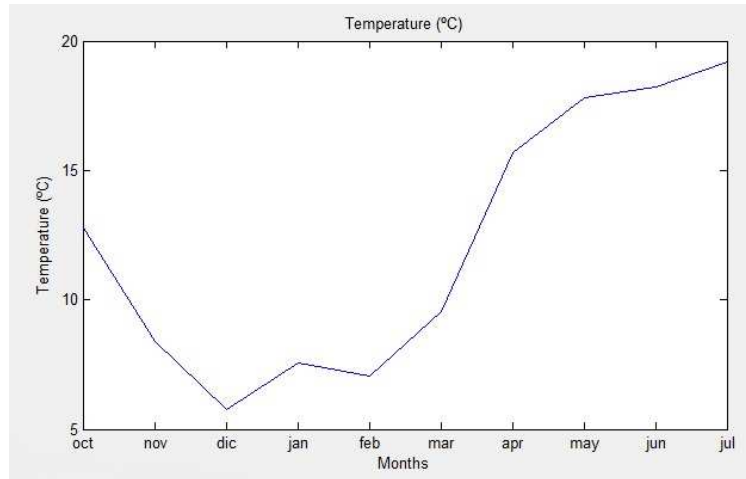


Figure 1: Evolution of mean air temperature temporal series, 2011 season.

Taking into account this process, most of the farmers apply preventive treatments to the complete vineyard, commonly at fixed dates selected with no scientific criteria. Generally, this system leads to a fixed number of treatments, in many cases more than needed, and not applied at the most effective instants.

In parallel, some models have been developed, based on the biology of the fungus and the evolution of meteorological parameters. Some of these models are IPS (Infection Potential State) [3], POM (Prevision of Optimal Maturation) [4], Goidanich [5], RAI (Risk Assessment Index), Milvit [7], and Plasmo [8]. They use different meteorological data, or various lengths in the time series, but they also look for helping the farmers to detect in advance the presence of mildew.

4. EXPERIENCE IN ACTUAL TESTS

A pilot WSN was installed in a vineyard of 210,670 square meters within a demarcated region, planted with vines of four different varietals. The yard is zoned and each zone is planted with only one vine varietal.

The network consists of six nodes, a coordinator, a gateway, and a link to GPRS public network, in order to use the Internet to transmit the data to the database at University facilities. This network has been working for more than two years, providing data each 5 minutes [9]. Table 1 summarizes the sensors connected to each node.

Some of the results could be observed in Figures 1 to 3. These data have been analyzed using both IPS and Goidanich methods. The IPS model indicates that the risk of mildew development was very low in 2011 season, as the index resulted to be below -10 in spring. However, using data

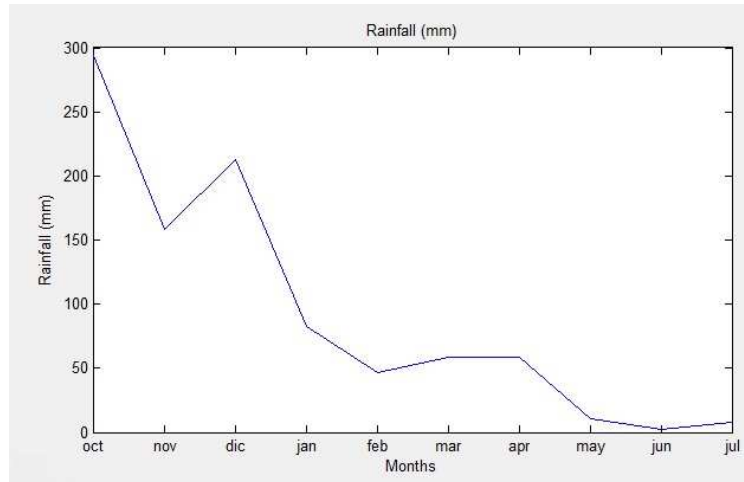


Figure 2: Evolution of mean rain falling temporal series, 2011 season.

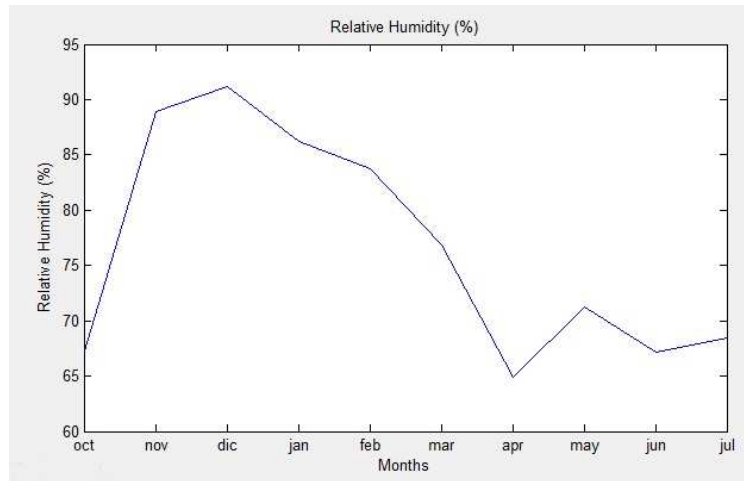


Figure 3: Evolution of humidity temporal series, 2011 season.

from previous years, in spring 2009 the risk was very high. Goidanich model also confirms a null risk of mildew infection during 2011 season. The tests developed allow us to conclude that both methods are complementary.

5. CONCLUSIONS

The use of WSN in vineyards could allow the farmers to improve the control of the vines health, and also to reduce costs, both economics and environmental.

A good knowledge of plague developments (the real-time condition of the vines, the exact days of mildew contamination risks, etc.) would allow the farmers to apply only the strictly needed treatments, instead of treating the plants in a calendar basis, which is pre-defined independently of the meteorological conditions. The scientific procedure provides important advantages for the agriculture exploitation:

1. Reduction of costs in chemical products: the treatments have to be applied only when they are strictly necessary. As an example, in 2011 season, no treatments were needed in the vineyard under test.
2. Reduction of chemicals in the soil: this redounds in less external elements in the environment, improving the ecological footprint of the crop.
3. Reduction of costs in terms of person-hours: each treatment that is not needed represents a number of working hours that could be used in other tasks.
4. Improvement in the quality of biologists work: they have up to the date information (i.e., each 5 minutes), what is impossible if they have to physically visit the vineyards.

ACKNOWLEDGMENT

This work was partially funded by Spanish Ministry of Economy and Competitiveness, State Secretary for Research under project TEC2011-28789-C02-02, that was co-funded using European Regional Development Funds (ERDF), as well as the Galician Regional Government under project CN 2012/260 “Consolidation of Research Units: AtlantTIC”.

REFERENCES

1. The Institute of Electrical and Electronics Engineers, IEEE 802.15.4-2003 Standard, 2003.
2. Goncal Barrios, J. R., “Modelización del Mildiu en la Vid,” *Phytoma*, No. 164, December 2004.
3. Molot, B., “La Modélisation du mildou de la vigne,” *Progres Agricole et Viticole*, Vol. 103, No. 15–16, 1986.
4. Tran, C. and S. Strizyk, “Simulation of the date of maturity of *Plasmopara viticola* oospores to predict the severity of primary infections in grapevine,” *The American Pytopathological Society*, 1990.
5. Goidanich, G., *Manuale di Patologia Vegetale*, Edizione Agricole, Bologna, 1964.
6. Bendek, C. E., P. A. Campbell, R. Torres, A. Donoso, and B. A. Latorre, “The risk assessment index in grape powdery mildew control decisions and the effect of temperature and humidity on conidial germination of *Erysiphe necator*,” Facultad de Agronomía e Ingeniería Forestal, Pontificia Universidad Católica de Chile, 2007.
7. Spencer-Phillips, P. and M. J. Jeger, *Advances in Downy Mildew Research*, Vol. 2, Kluwer Academic Publisher, 2004.
8. Orlandini, S., F. Rossi, and M. Magli, “Plasmo project,” web <http://plasmo.bo.ibimet.cnr.it/>.
9. Gay-Fernández, J. A. and I. Cuiñas, “Deployment of a wireless sensor network in a vineyard,” *International Conference on Wireless Information Networks and Systems, WINSYS 2011*, Seville, Spain, 2011.

GP GPU Acceleration of a PO Based RF Simulation Software Dedicated to Radar Simulation in Large Scale and Complex Environments

A. Boudet, N. Douchin, and P. Pitot

OKTAL Synthetic Environment, 11, avenue du Lac, Vigoulet-Auzil 31 320, France

Abstract— SE-RAY-EM software is based on a combination of Shooting and Bouncing Rays (SBR) technique, that has been optimized to calculate efficiently the intersections between rays from a transmitter towards a 3D database and back to a receiving point, and EM models for computing propagation, reflection and diffraction. These models are the formulations of Geometrical Optics (GO), Physical Optics (PO) and Equivalent Current Method (ECM). An operating strategy enables unified calculation for the near or far EM scattered fields from the scenes. The “forward scattering” approach based on the equivalence principle is also used to compute EM fields in the shadow region. Since it relies on asymptotic methods SE RAY-EM is well suited for computing the EM interactions of an incident wave with complex 3D models of large scale environments and objects at high frequencies typically in the 1–100 GHz range.

Existing works have shown that GP GPU acceleration is well suited for ray tracing applications. EM asymptotic simulations based on ray tracing simulation can benefit from that technology, with the following difficulties.

Computation of phases requires double precision: though GPU double precision capabilities are improved at each GPU generation, double precision numbers cost also twice as much registers than float numbers and twice as much memory bandwidth. So avoiding double computations while preserving phase precision is necessary.

For physical optics simulations, high frequency computation needs very precise surface sampling. To be efficient, it is necessary to reduce the number of samples to compute. As on existing SE-RAY-EM CPU renderer, we choose to implement an adaptive anti-aliasing process that reduces the samples number while achieving the precision requirements. Adaptive anti-aliasing process on a highly parallel architecture is not obvious as the number of rays to trace can actually explode. It must be controlled without consuming too much memory and keeping a high level of parallelism.

In this paper, we discuss on the way to solve such problems. We also present the SE-RAY-EM computation scheme on its existing CPU version and compare it to the new GP GPU version. Results and comparison with the CPU version of SE-RAY-EM are presented.

1. INTRODUCTION

In this paper, we first present the SE-RAY-EM software tool and its principle to handle electromagnetic computations. Then we discuss its current implementation and present the issues involved in its optimisation using Graphic Processor Unit (GPU) in the frame of EM simulation. Then we present a novel solution using cones for beam tracing and an adaptive anti-aliasing algorithm suited for massively parallel computation. Finally, we present some results to illustrate the efficiency of the new implementation.

2. STATE OF THE ART

2.1. Principle

SE-RAY-EM is an electromagnetic simulation code based on ray tracing [1] and asymptotic methods [2]. These methods are less physically rigorous than “exact” methods that are strictly based on the resolution of Maxwell equations. However, asymptotic methods as they are used in SE-RAY-EM enable to handle complex scenes that are very large compared to the wavelength with enough accuracy. That is when the main contributions to the electromagnetic field are correctly represented.

In the case of complex targets, SE-RAY-EM gives results very similar to the “exact” method for a much lower computation time. Where 600 MHz is a high limit for “exact” solutions used on this type of objects, it is almost a low limit in terms of physical validity for asymptotic methods. The standard computation range addressed by SE-RAY-EM is more between 1 to 100 GHz on far more complex scenes (natural terrain on several kilometres with several complex targets).

In SE-RAY-EM, rays are traced from transmitters towards reception points. These rays are grouped four by four in beams. Rays are traced from transmitters through a grid (Figure 1). The intersections of these beams are computed. They are two types of interactions (Figure 2):

- Geometrical Optics (GO) when the beam is reflected by a metallic or dielectric surface.
- Physical Optics (PO) towards the reception points at each interaction.

Using beams has three main interests. They enable to:

- Know the interaction contour of the incident wave with the surface, which is necessary for using PO.
- Detect edges.
- Detect the main aliasing cases: geometry, material, curvature of the surface.

As shown in Figure 3, the adaptive anti-aliasing mechanism of SE-RAY-EM consists in subdividing the computation grid as a “quadtrees”. So when aliasing is detected on the path of a beam, it is subdivided in four new beams.

Adaptive anti-aliasing is very interesting for EM computations as:

- The size of the primary grid can be coarse as the result of computation is a signal and not an image. The only constraint is that the grid is thin enough to detect important elements of the scene.
- The accuracy needed for EM computation is linked to the wavelength and object boundaries must be sampled at a fraction of the wavelength. For example, at 100 GHz, sampled element size can be less than 1 mm for a target of several meters. Without adaptive anti-aliasing, the computation should use a 100000×100000 pixel grid!
- Adaptive anti-aliasing enables to reduce the number of contributors for which EM models are applied. These complex computations have a cost that cannot be neglected and can be done for a lot of wavelengths. Reducing the number of contributors is then inevitable to reduce computing times.

2.2. SE-RAY-EM Discussion

The current anti-aliasing approach can miss some details or some small objects (e.g., mast of a boat). Actually, beams are built from a punctual sampling. On one hand, this forces the user to

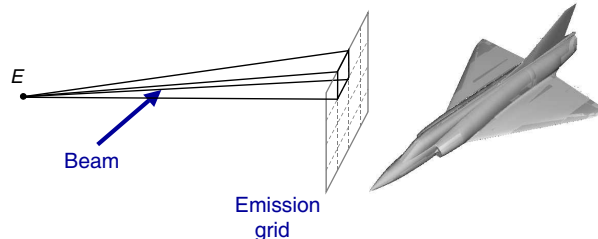


Figure 1: SE-RAY-EM emission grid.

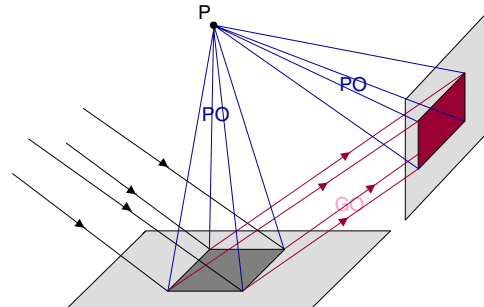


Figure 2: Principle of beam interactions.

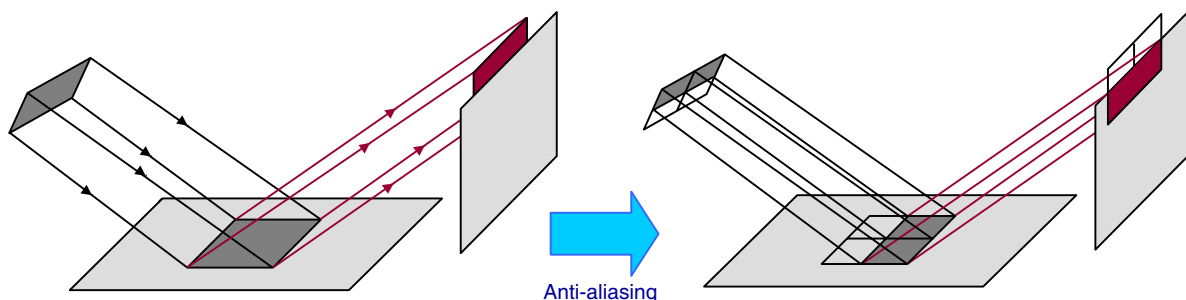


Figure 3: SE-RAY-EM adaptive anti-aliasing principle.

define a grid with a minimal resolution. On the other hand, the user has to use transparent faces (or wings) around small objects and edges in order to ensure their detection.

Another problem of the current anti-aliasing algorithm is that if the beam is aliased after several reflections, it is subdivided from the beginning. Even though the previous reflection levels are not aliased. The number of contributors can then be raised even if not necessary, and, more importantly, this can lead to unwanted artefacts when dealing with radar imagery cases.

3. MASSIVELY PARALLEL APPROACH

Nowadays, Graphic Processors Unit (GPU) have proven to be very efficient for optimising General Purpose (GP) computations, and particularly ray tracing applications [3] as SE-RAY-EM. However, the transition to GPU is not straightforward and several issues have to be taken into account.

3.1. Double versus Float

Historically, SE-RAY-EM performs all computations using double precision floating point operations (*double*). This permits to avoid naturally some problems of accuracy without any specific work. However, GPU are very efficient for single precision floating point (*float*) computation. Even though, *double* computations are now handled and tends to become faster, they should be used with parsimony. Also *double* data storage and transfer are more costly. Also *double* operations need twice as much registers as *float* ones. And registers are rare and precious when using GPUs. Our new implementation only uses *double* when it is absolutely necessary, mostly in the computations that involve the phase of the electromagnetic signal.

3.2. Object Instances and Moving Objects

SE-RAY-EM uses instances of objects in order to share geometries. Such objects can also reference underlying instances, which results in a hierarchical graph. A matrix defines the position of each instance. During raytracing, rays are transformed using these matrices in local space to perform intersection computation with the geometry. The hierarchical definition implies several transformations when a ray traverses the scene, which results in a lot of computation. This process has proven itself inefficient on the GPU. Then, we flattened the instance hierarchy before computation so that a ray is only transformed one time during ray tracing. This enables to handle both instances and moving object on the GPU with a small impact on performances.

3.3. Cone tracing

Instead of tracing individual rays, we use cones to trace beams. A cone will detect any geometric element in its volume. This way anti-aliasing is more reliable and small object and edges are detected directly without the need of any transparent wings. Besides the initial resolution can be really coarse. The only reason to increase the resolution will then be imposed if the GPU cannot be loaded enough.

Another advantage of using cones is that they can be processed independently of their neighbours, which is very interesting for parallelization. It is also simple to handle the generated contributors independently from one reflection level to another.

3.4. Adaptive Anti-aliasing

The difficulty when implementing adaptive anti-aliasing on GPUs consists essentially in managing the number of beams. Actually, when performing anti-aliasing, beams are cut in four sub-beams at each level, which can lead to an explosion of the number of beams to achieve the necessary accuracy. Unfortunately, these beams need to be stored in buffers to be handled on the GPU, which represents a lot of data.

In order to solve this issue, we use serialisation of the beams. Which means that when a beam is aliased, instead of generating the four beams at once, only the first child is generated, and when it is finished, it will launch his brother. With this approach, we ensure that the number of beams to treat never rises. However, if there is enough space left in the beam buffer, some beams may be de-serialised, in order to fill the buffer completely. Indeed, the GPU needs to be loaded enough to be efficient.

3.5. Multi-frequencies

Multi-frequencies computations consist in computing several (a lot, e.g., one to ten thousands) frequencies at the same time. Frequencies are independent in terms of electromagnetic computations, but share all the geometric computations (if we consider that anti-aliasing parameters given for the highest frequency are also valid for the smaller ones). In this new version, we postpone the

frequency computations as long as possible. The anti-aliasing process generates all geometrical contributors. These contributors are then used multiple times for applying EM models, one time per frequency.

4. RESULTS

We tested our new implementation of SE-RAY-EM versus the old one, in terms of accuracy and performances.

4.1. Accuracy

The first test consists in comparing qualitatively the results between the new implementation and both the standard version of SE-RAY-EM and the reference from the ELSEM3D software [4] which is based on Integral Equation EM approach and Moment Method numerical implementation. The test consists in the computation of the Radar Cross Section (RCS) computation of an aircraft for a frequency of 600 MHz (as represented in Figure 4). Figure 5 shows the results that are obtained. Some differences exist because signal of a complex object is noisy, but globally results computed by the three codes are very similar.

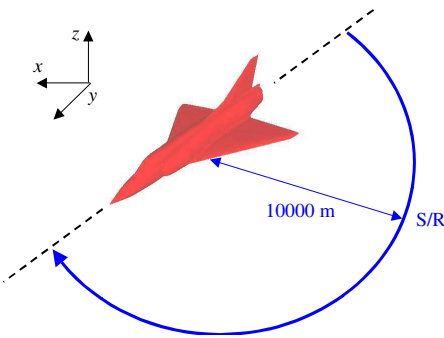


Figure 4: Aircraft RCS computation setup.

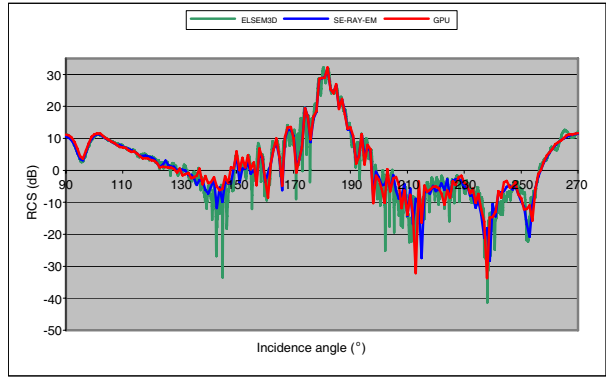


Figure 5: RCS of an aircraft computed with ELSEM3D (green), SE-RAY-EM (blue) and GPU version (red).

4.2. Performances

The test set up consists in the computation of the RCS at 10000 m of a tank with one or 151 frequencies from 8 to 11 GHz. Figure 6 shows the complex tank used for the simulation and an ISAR image generated from computed multi-frequencies and multiple angles results.

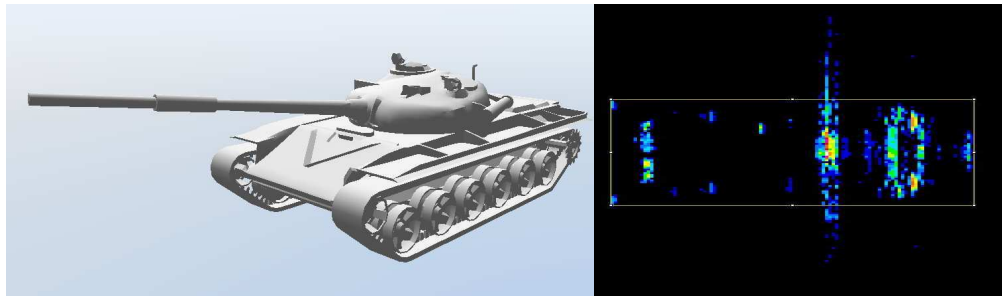


Figure 6: The tank used for test simulation and a computed ISAR image.

To compare the performances, the computations have been performed using the standard version of SE-RAY-EM and using the new parallel implementation with both a CPU and a GPU version. We performed the tests on two distinct computers:

- One laptop: Intel Core I7 2630QM and Nvidia GeForce 540M.
- One desktop: Intel Core i5 3470 and Nvidia GeForce GTX Titan.

Table 1: Computation times for one incidence in seconds with SE-RAY-EM standard version and with new parallel version in both CPU and GPU implementations.

	Standard Core I7	Standard Core I5	CPU Core I7	CPU Core I5	GPU GeForce 540M	GPU GeForce Titan
Mono-frequency	16.28	12.17	7.49	5.60	0.86	0.111
151 frequencies	109.00	80.40	97.85	70.4	7.62	0.735

Comparing the times of the standard version and the CPU new version, we can see that the new algorithm is more efficient than the previous one. The GPU implementation is 10 to 100 times faster than the standard SE-RAY-EM version.

5. CONCLUSION

Our new implementation of SE-RAY-EM is still on the road. It is now capable of handling multi-frequency RCS computations on complex targets with metallic or dielectric materials. This new version take benefits of a brand new algorithm that is massively parallel and takes advantage of the wide computing power available on GPUs, providing the same results as the previous version but in much shorter computation times (from ten to one hundred times faster computation).

Compared to SE-RAY-EM standard version, functionalities are still missing in the new version. They are planned for development in the forthcoming year: speckle materials, multi-texture, transparency, diffraction, optimisation of multiple reception points...

REFERENCES

1. Whitted, T., "An improved illumination model for shaded display," *Communications of the ACM*, Vol. 23, 343–349, 1980.
2. Mametsa, H. J., S. Laybros, T. Volpert, P. F. Combes, P. N. N'Guyen, and P. Pitot, "FER-MAT: A high frequency EM scattering code from complex scenes including objects and environment," *PIERS Proceedings*, 1–4, Pisa, Italy, March 28–31, 2004.
3. Aila, T. and S. Laine, "Understanding the efficiency of ray traversal on GPUs," *Proc. High-Performance Graphics*, 145–149, 2009.
4. Soudais, P., P. Leca, J. Simon, and T. Volpert, "Computation of the scattering from inhomogeneous objects with a discrete rotational symmetry and a nonsymmetric part," *IEEE Transactions on Antennas and Propagation*, Vol. 50, No. 2, February 2002.

Fe:BN Nanoceramic — Negative Refraction Material in the Wide Frequency Range

K. Oganisian¹, A. Vogt², P. Gluchowski¹, K. Orzechowski², and W. Strek¹

¹Institute of Low Temperature and Structure Research, PAS, Okolna 2, Wroclaw 50-422, Poland

²Faculty of Chemistry, Wroclaw University, F. Joliot-Curie 14, Wroclaw 50-383, Poland

Abstract— The measurements of frequency dependencies of permeability and permittivity of Fe:BN nanoceramic are reported. It was found that the values of the permittivity and permeability are negative in the wide frequency range. The refractive index was determined to be negative at frequencies above 10 MHz. It is concluded that Fe:BN nanoceramic is the naturally originated negative refraction material.

1. INTRODUCTION

At last decade the metamaterials are widely researching due to their unusual optical and physical properties that are very promising for applications [1–4]. At present time the many classes of metamaterials such as negative index materials (NIM) [1], single negative metamaterials [1, 5], electromagnetic bandgap metamaterials (photonic crystals) [1, 6] and many others are extensively studying. Unfortunately, the main properties of metamaterials cannot be reproduced in the naturally originated chemical compositions, therefore a common feature of all metamaterials is their artificial origin. However, the author of theory of the electrodynamics of negative refraction materials, V. Veselago has predicted and even performed an attempt to obtain a natural material with the negative refractive index [7, 8]. He unsuccessfully tried to synthesis the magnetic semiconductor CdCr₂Se₄ many years ago [7] and until now there are only few works have been published in which the negative refraction was observed for the natural chemical compositions [9–11].

Recently we showed that Fe:BN nanoceramic is the strong ferromagnetic material with very high saturation of magnetization and relatively high resistivity that made this material very attractive for radiofrequency application [12]. For determination of the field of application we performed the measurements of magnetic and electric impedance in the 1–1000 MHz frequency range. During this studies we found that Fe:BN nanoceramic reveals the negative values of permittivity and permeability simultaneously at least in the frequencies above 10 MHz. According to definition we estimated the negative refractive index for this material in the wide frequency range. Thus, we assume that Fe:BN nanoceramic can be concerned to the class of the naturally originated negative refraction material.

2. EXPERIMENT

Iron boron nitride nanoceramic has been obtained by application of hot pressing method (HPM) under a pressure of 8 GPa at 1450°C as described in Ref. [12]. The sample contained 7:1 of Fe and BN in molar ratio. The frequency dependences of permittivity and permeability have been measured by means of the lumped-capacitance method [13, 14]. The measurements of inductance and dissipation factor were performed on a HP-4191A RF Impedance in the 1–1000 MHz frequency range at room temperature using a simple “one-turn” model.

3. RESULT AND DISCUSSION

The structural investigation of the ferromagnetic Fe:BN revealed the clear core-shell structure in which iron core thoroughly covered by boron nitride shell [12]. The grain size of iron is varying from 10 nm up to 5 μm whereas the average thickness of BN coating was estimated of about 3.5 nm.

Frequency dependences of permittivity and permeability shown in Fig. 1.

The values of real part of permittivity are negative in the whole frequency range. Probably, the negative values of ϵ' are caused by plasmons despite of relatively low frequencies for their appearing. The values of μ' are also negative in the range above 10 MHz. It should be noted the values of ϵ'' are negative at frequencies above 10 MHz. The dissipation of permeability is also very small and even a little negative in the same frequency range. Such a behavior is unexpected one because the measurement set-up was carefully calibrated and we note that there is no phase effects is occurring during the measurements. At the moment we have no clear explanation of these dependences,

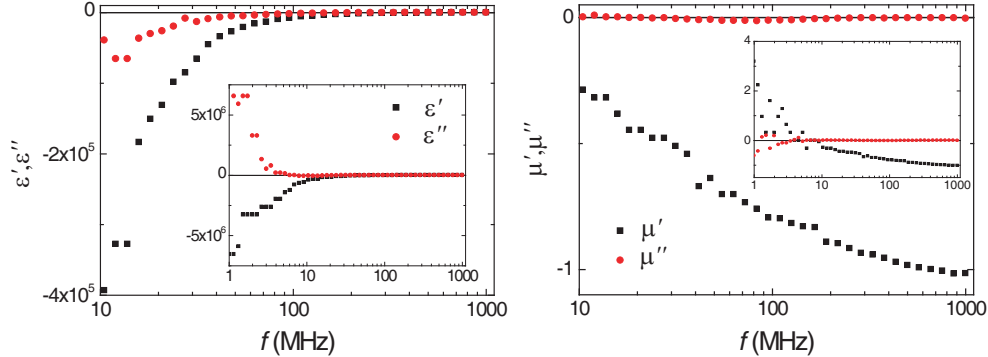


Figure 1: Frequency dependences of (a) permittivity and (b) of Fe:BN nanoceramic. Insets show these dependences at extended scales.

however, the negative values of both real and imaginary part of permittivity and permeability for left-handed materials have been recently predicted by V. Veselago [7]. Furthermore, he determined the left-handed materials as materials with negative $k = k' + ik''$, that, in turn, can be negative only in a case if k' and k'' are negative simultaneously. In Ref. [8] it was showed that k' and k'' can be negative only in a case when ϵ' , ϵ'' , μ' and μ'' are negative simultaneously. In the present case, the values of ϵ' , ϵ'' , μ' and μ'' are negative, thus, we suggest that obtained dependencies meets criterion of negative k for Fe:BN nanoceramic at least in the frequency range above 10 MHz.

The reason of occurring of the negative dissipations of permittivity can be explained in the terms of a quantum amplification. Indeed, Veselago noted that the materials with negative dissipations can be found among the compositions used in the quantum amplifiers [8]. It is possible that some of Fe³⁺ atoms are separated from grains and occasionally distributed on the BN grain boundaries. We assume that these atoms may be in the excited state due to the strain on the grain boundaries that occurred during the synthesis [12]. Due to the assumption that the incident wave is completely screened from Fe cores, it is possible, that propagation of this wave is occurring only in the BN medium. Therefore the impurity atoms of iron may play a role in the dissipations of the permittivity. We suppose that in this case $N_1 - N_2 < 0$, where N_1 — concentration of iron atoms in the ground state, N_2 — concentration of iron atoms in the excited state and as a result the incident wave can lead to the emission of energy equal the difference between excited and ground state, i.e., $E = E_2 - E_1$ for each atom in the excited state [16]. For verification of this assumption we performed the electron magnetic resonance measurements. A broad but very intensive resonant discontinuity has been observed at room temperature, that suggest to the existence of a large amount of the weak interacted paramagnetic ions. We relate it with ions of Fe³⁺ because nor B neither N does not to be appear in EPR measurements. But we note, for estimation of the amount of separated iron atoms and their contribution in the dissipation of permittivity the additionally investigation are strongly required.

Taking into account the structure of Fe:BN nanoceramic we suppose to the possibility of formation of mechanism of the plasma frequency depression into the far infra red and even GHz band as was predicted by Pendry et al. [15]. Moreover, roughly estimation of plasma frequency within their approach gives the value of about $\omega_p^2 \sim 10^{19}$ Hz, i.e., very similar to that calculated for the network of aluminium wires described in Ref. [15]. We propose the model in which a structure of iron spheres electrically isolated by boron nitride forms of some kind of weak interacting network that interacts with incident electromagnetic wave in the way the similar as metamaterial. Indeed, free electrons are localized inside iron spheres due to the boron nitride isolating. This may lead to the plasmon excitation caused by incident electromagnetic wave because the iron grain size is rather smaller than expected mean free path. Due to the movement of electrons inside the Fe grain the weak magnetic field is occurring and, it is possible, that the magnetic field induced by electrons can turn the total internal magnetic moments of iron particle in the opposite to the incident wave way. Thus, this can lead to the occurring of backward wave with the phase velocity opposite to the group velocity that propagates inside the material i.e., $k < 0$. Such a behavior is the same as defined for NIM, where the phase velocity opposite to the group velocity that is reason of the negative refraction. We expect that this model well describes the behavior of obtained dependences for Fe:BN nanoceramic and $k < 0$ in the frequencies above 10 MHz. However, for numerical confirmation the mean free path measurements are required.

According to Ref. [7] we calculated the refractive index as negative in a case where for $n = \sqrt{\epsilon\mu}$ the values of ϵ and μ are negative simultaneously. The frequency dependence of a complex refractive index shown in Fig. 2.

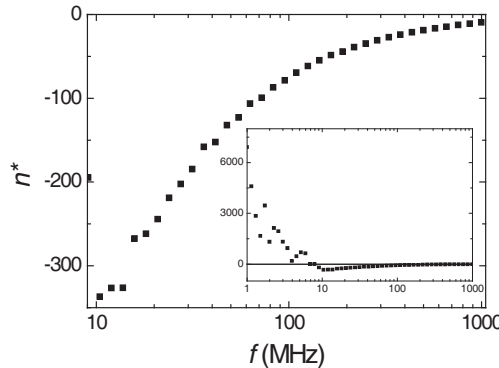


Figure 2: Complex refractive index $n^* = \sqrt{\epsilon^*\mu^*}$ of Fe:BN nanoceramic. Inset shows this dependence in the extended scale.

The sample reveals the negative refraction in the frequency range 9–1000 MHz. It looks like near the 10 MHz the refractive index has a minimum of about $n = -350$ then it rising up to $n = -20$ at 1 GHz. It should be noted, even at 1 GHz the refraction is still negative, therefore one can conclude, to estimation of the bandwidth of negative refraction of this material the additional investigations at the highest frequency are strongly required.

4. CONCLUSIONS

The frequency dependencies of permeability and permittivity of Fe:BN nanoceramic have been performed in the frequency range 1–1000 MHz. The sample revealed the negative values of permittivity and permeability in the wide frequency range. Application of simple model allows to describe the obtained dependencies in the terms of negative refraction. It is concluded that Fe:BN nanoceramic belong to the class of naturally originated negative refractive materials. The negative values of imaginary part of permittivity has to be discussed. One of the reason of such a behavior is the occurring of quantum amplification due to the feedback mechanism between excited Fe^{3+} ions distributed in the BN medium. But for making of any decisions the additional investigations of EPR are strongly required. The frequency dependence of refractive index n is nonlinear and its values are negative at frequencies above 9 MHz with minimum at about 10 MHz. It should be noted, that the ferromagnetic material could become to the diamagnetic one under the influence of incident electromagnetic wave. This allows to predict high potential applications for Fe:BN nanoceramic.

REFERENCES

1. Engheta, N. and R. W. Ziolkowski, *Metamaterials: Physics and Engineering Explorations*, John Wiley & Sons, 2006.
2. Saïd, Z., A. Sihvola, and A. P. Vinogradov, *Metamaterials and Plasmonics: Fundamentals, Modelling, Applications*, 106, Springer-Verlag, New York, Dec. 2008.
3. Shelby, R. A., D. R. Smith, and S. Schultz, *Science*, Vol. 292, 5514, 2001.
4. McPhedran, R. C., I. V. Shadrivov, B. T. Kuhlmeij, and Y. S. Kivshar, *NPG Asia Mater.*, Vol. 3, 100, 2011.
5. Eleftheriades, G. V. and K. G. Balmain, *Negative-refraction Metamaterials: Fundamental Principles and Applications*, Wiley, John & Sons, 2005.
6. Valentine, J., S. Zhang, T. Zentgraf, E. Ulin-Avila, D. A. Genov, G. Bartal, and X. Zhang, *Nature*, Vol. 455, 376, 2008.
7. Veselago, V., *Sov. Phys. Usp.*, Vol. 10, 509, 1966.
8. Veselago, V., L. Braginsky, V. Shklover, and C. Hafner, *J. Comput. Theor. Nanosci.*, Vol. 3, 1, 2006.
9. Pimenov, A., A. Loidl, K. Gehrke, V. Moshnyaga, and K. Samwer, *Phys. Rev. Lett.*, Vol. 98, 197401, 2007.
10. Shi, Z., R. Fan, Z. Zhang, K. Yan, X. Zhang, K. Sun, X. Liu, and C. Wang, *J. Mater. Chem. C*, Vol. 1, 1633, 2013.

11. Shi, Z., R. Fan, K. Yan, K. Sun, M. Zhang, C. Wang, X. Liu, and X. Zhang, *Adv. Funct. Mater.*, Vol. 23, 2013, DOI: 10.1002/adfm.201202895.
12. Organisian, K., P. Gluchowski, A. Vogt, and W. Strek, *Appl. Phys. Lett.*, under review.
13. Freundlich, P., H. A. Kolodziej, and E. Narewski, *J. Phys. E.*, Vol. 14, 1045, 1981.
14. Kornak, R., K. Maruszewski, W. Strek, K. Haimann, W. Dudzinski, A. Vogt, and H. Kolodziej, *Journal of Alloys and Compounds*, Vol. 380, 268, 2004.
15. Pendry, J. B., A. J. Holden, W. J. Stewart, and I. Youngs, *Phys. Rev. Lett.*, Vol. 76, 4773, 1996.
16. Stepin, L. D., *Quantum Radio Frequency Physics*, M.I.T. Press, 1965.

Bundle Block Adjustment with Optical and SAR Images

Shuai Xing, Qing Xu, Wei Sun, Jiansheng Li, and Yu He

Zhengzhou Institute of Surveying and Mapping, Zhengzhou, China

Abstract— The combined bundle block adjustment model with optical and SAR images has been constructed in this paper, and its some key problems have been studied, such as construction of observation equation, computation of weight matrix and the frame of computation process. Two experiments with the combination of different images (panchromatic SPOT-5 HRV, panchromatic SPOT-4 HRV, ERS-2 and RADARSAT-1) and different distributions of ground control points have been carried out. Preliminary experiment results with variant block adjustment schemes have proved the combined block adjustment model was feasible and correct. At last, the characteristics and application of the combined block adjustment have been summarized.

1. INTRODUCTION

Block adjustment is one of key techniques in photogrammetry, it is a procedure achieving orientation parameters of images and coordinates of pass points in a large area efficiently and simultaneously [7]. Up to now, what people focused on about block adjustment has not changed, it has been always the images photographed by one sensor at variant time and position. Since different photogrammetry and remote sensing sensors have been produced, the techniques processing different images achieved by different sensors have been proposed. Most works have been concentrated in radiative and physical processing, but a few people noticed multi-sensor images could be used to realize combined position.

Young-Ran Lee [10] has carried on experiments about combined block adjustment based on improved collinearity condition equations (CCE) with multi-satellite remote sensing images including Landsat-7, KOMPSAT-1, SPOT-1, IKONOS. And in planimetry accuracy of 2.76 m and in altimetry accuracy of 3.1 m have been obtained. Thierry Toutin [5] has studied to evaluate the spatiotriangulation applied to multi-sensor satellite images. The spatiotriangulation was applied to 49 images in six blocks (Landsat-7 ETM+, panchromatic SPOT-4 HRV, multiband ASTER, multimode radar RADARSAT-1, and ERS-1) acquired from different viewing/look angles. The most important results Toutin obtained were related to simultaneous bundle adjustments of the largest “master” Landsat-7 block using 25 ground control points (GCPs) in the two outer strips and the smallest “slave” block(s) using no GCP but only elevation tie points (ETPs). The errors, verified by a large number of independent check points (ICPs) in the “slave” blocks, were between 15–35 m (1.5–2 resolutions). And the internal accuracy of the blocks was better (around one resolution). In 2006 Thierry Toutin [6] has evaluated the spatiotriangulation applied to multi-sensor high resolution (HR) satellite images (SPOT-5 HRS, SPOT-5 HRG, IKONOS, Quick Bird). The errors obtained were 2.54 m in planimetry and 2.1 m in altimetry.

The research study above mentioned demonstrated the possibility to use the large block with a reduced number of GCPs to simultaneously adjust single image(s)/strip(s) or smallest block(s) with only tie points (TPs), and with no degradation in the accuracy. In this paper, the combined bundle block adjustment model with optical and SAR remote sensing images has been constructed, and its some key problems have been studied. First the imaging models for linear array push-broom imagery and SAR imagery are introduced in Section 2. Then the mathematical model of combined bundle block adjustment is constructed in Section 3. Section 4 shows experimental results with a large block and Section 5 shows conclusions.

2. TWO IMAGING MODELS

2.1. The Scanning Model

The linear array push-broom imagery is acquired with linear sensors by scanning the Earth surface. The relationship between ground and image is rigorous central projection. Each line of the image has different elements of exterior orientation. The collinearity equation of i line is expressed in the following way [1, 4, 9].

$$\left. \begin{aligned} x_i &= -f \frac{a_1(X-X_{si})+b_1(Y-Y_{si})+c_1(Z-Z_{si})}{a_3(X-X_{si})+b_3(Y-Y_{si})+c_3(Z-Z_{si})} \\ 0 &= -f \frac{a_2(X-X_{si})+b_2(Y-Y_{si})+c_2(Z-Z_{si})}{a_3(X-X_{si})+b_3(Y-Y_{si})+c_3(Z-Z_{si})} \end{aligned} \right\} \quad (1)$$

where a_i , b_i , c_i ($i = 1, 2, 3$) are elements of rotation matrix composed of φ_i , ω_i , κ_i , which are angle elements of exterior orientation.

The linearization equation of (1) is

$$\mathbf{A}^L \cdot \Delta^L + \mathbf{B}^L \cdot \mathbf{X}^L - \mathbf{L}^L = \mathbf{V}^L \quad (2)$$

where Δ^L and \mathbf{X}^L are separately correction matrixes of exterior orientation elements and ground point coordinates, \mathbf{A}^L and \mathbf{B}^L are separately coefficient matrixes of correction of exterior orientation elements and correction of ground point coordinates, \mathbf{L}^L is constant matrix and \mathbf{V}^L is correction matrix of image point coordinates.

2.2. F. Leberl Model

The geometry relation between ground and image points in a SAR image is established by the Doppler and Range equations proposed by F. Leberl [2, 8].

The range equation of slant range image is

$$(X - X_s)^2 + (Y - Y_s)^2 + (Z - Z_s)^2 = (y_s M_y + Ds_0)^2 \quad (3a)$$

where Ds_0 is the slant range delay, y_s is the across-track image coordinate of ground point P, M_y is the across-track pixel size, (X, Y, Z) are the object space coordinates of ground point P, (X_s, Y_s, Z_s) are the object space coordinates of radar antenna center.

The Doppler equation is

$$Xv(X - X_s) + Yv(Y - Y_s) + Zv(Z - Z_s) = -\frac{\lambda R_s}{2} f_{DC} \quad (3b)$$

where R_s is the slant range of ground point P, λ is the radar wavelength, f_{DC} is the Doppler frequency.

F. Leberl model is composed of formula (2) and (3). When $f_{DC} = 0$, they can be linearized to achieve elements of exterior orientation with GCPs.

The linearization equation of (3) is

$$\mathbf{A}^S \cdot \Delta^S + \mathbf{B}^S \cdot \mathbf{X}^S - \mathbf{L}^S = \mathbf{C} \cdot \mathbf{Vs}^S = \mathbf{V}^S \quad (4)$$

where the constructions of Δ^S , \mathbf{X}^S , \mathbf{A}^S , \mathbf{B}^S , \mathbf{L}^S , \mathbf{V}^S are similar with Δ^L , \mathbf{X}^L , \mathbf{A}^L , \mathbf{B}^L , \mathbf{L}^L , \mathbf{V}^L in (1).

3. MATHEMATICAL MODEL OF COMBINED BUNDLE BLOCK ADJUSTMENT

3.1. Observation Equations

Observation equations of each TP are as follows based on (2) and (4).

$$\begin{pmatrix} \mathbf{A}_P^L & 0 & \mathbf{B}_P^L \\ 0 & \mathbf{A}_P^S & \mathbf{B}_P^S \end{pmatrix} \begin{pmatrix} \Delta^L \\ \Delta^S \\ \mathbf{X}_P \end{pmatrix} - \begin{pmatrix} \mathbf{L}_P^L \\ \mathbf{L}_P^S \end{pmatrix} = \begin{pmatrix} \mathbf{V}_P^L \\ \mathbf{V}_P^S \end{pmatrix} \quad \text{Weight} \quad \begin{pmatrix} \mathbf{P}_P^L & 0 \\ 0 & \mathbf{P}_P^S \end{pmatrix} \quad (5)$$

And observation equations of each GCP are similar with (5).

$$\begin{pmatrix} \mathbf{A}_G^L & 0 & \mathbf{B}_G^L \\ 0 & \mathbf{A}_G^S & \mathbf{B}_G^S \end{pmatrix} \begin{pmatrix} \Delta^L \\ \Delta^S \\ \mathbf{X}_G \end{pmatrix} - \begin{pmatrix} \mathbf{L}_G^L \\ \mathbf{L}_G^S \end{pmatrix} = \begin{pmatrix} \mathbf{V}_G^L \\ \mathbf{V}_G^S \end{pmatrix} \quad \text{Weight} \quad \begin{pmatrix} \mathbf{P}_G^L & 0 \\ 0 & \mathbf{P}_G^S \end{pmatrix} \quad (6)$$

If coordinates of GCP are accurate in (6), \mathbf{X}_G is a zero matrix. Otherwise, when the error of GCP is not neglectful and \mathbf{X}_G is not a zero matrix, other observation equations of each GCP should be constructed.

$$\mathbf{E} \cdot \mathbf{X}_G - \mathbf{L}_G^X = \mathbf{V}_G^X \quad \text{Weight} \quad \mathbf{P}_G^X \quad (7)$$

Since there is strong correlation between some exterior orientation elements of the linear array push-broom image and it will affect the computation of exterior orientation elements, other observation equations, called fake observed value observation equations, would be constructed.

$$\mathbf{E} \cdot \Delta^L - \mathbf{L}_\Delta^L = \mathbf{V}_\Delta^L \quad \text{Weight} \quad \mathbf{P}_\Delta^L \quad (8)$$

where \mathbf{L}_Δ^L is usually a zero matrix.

Then all observation equations in one block with a linear array push-broom image and a SAR image are

$$\begin{pmatrix} \mathbf{A}_P^L & \mathbf{A}_P^S & \mathbf{B}_P^L \\ \mathbf{A}_G^L & \mathbf{A}_G^S & \mathbf{B}_G^L \\ \mathbf{E} & & \mathbf{E} \end{pmatrix} \begin{pmatrix} \boldsymbol{\Delta}^L \\ \boldsymbol{\Delta}^S \\ \mathbf{X}_P \\ \mathbf{X}_G \end{pmatrix} - \begin{pmatrix} \mathbf{L}_P^L \\ \mathbf{L}_P^S \\ \mathbf{L}_G^L \\ \mathbf{L}_G^S \\ \mathbf{L}_X^L \\ \mathbf{L}_X^S \\ \mathbf{L}_\Delta^L \end{pmatrix} = \begin{pmatrix} \mathbf{V}_P^L \\ \mathbf{V}_P^S \\ \mathbf{V}_G^L \\ \mathbf{V}_G^S \\ \mathbf{V}_X^L \\ \mathbf{V}_X^S \\ \mathbf{V}_\Delta^L \end{pmatrix} \text{Weight} \begin{pmatrix} \mathbf{P}_P^L & & & & \\ & \mathbf{P}_P^S & & & \\ & & \mathbf{P}_G^L & & \\ & & & \mathbf{P}_G^S & \\ & & & & \mathbf{P}_G^X \\ & & & & & \mathbf{P}_\Delta^L \end{pmatrix} \quad (9)$$

(9) is also expressed as follows.

$$\mathbf{A} \cdot \boldsymbol{\Delta} - \mathbf{L} = \mathbf{V} \quad \text{Weight} \quad \mathbf{P} \quad (10)$$

(10) will be normalized and the normal equations is

$$\mathbf{N} \cdot \boldsymbol{\Delta} = \bar{\mathbf{L}} \quad (11)$$

where

$$\mathbf{N} = \mathbf{A}^T \mathbf{P} \mathbf{A} = \begin{pmatrix} \mathbf{N}_{11} & \mathbf{N}_{12} \\ \mathbf{N}_{21} & \mathbf{N}_{22} \end{pmatrix}$$

$$\bar{\mathbf{L}} = \mathbf{A}^T \mathbf{P} \mathbf{L} = \begin{pmatrix} (\mathbf{A}_P^L)^T \mathbf{P}_P^L \mathbf{L}_P^L + (\mathbf{A}_G^L)^T \mathbf{P}_G^L \mathbf{L}_G^L + \mathbf{P}_\Delta^L \mathbf{L}_\Delta^L \\ (\mathbf{A}_P^S)^T \mathbf{P}_P^S \mathbf{L}_P^S + (\mathbf{A}_G^S)^T \mathbf{P}_G^S \mathbf{L}_G^S \\ (\mathbf{B}_P^L)^T \mathbf{P}_P^L \mathbf{L}_P^L + (\mathbf{B}_P^S)^T \mathbf{P}_P^S \mathbf{L}_P^S \\ (\mathbf{B}_G^L)^T \mathbf{P}_G^L \mathbf{L}_G^L + (\mathbf{B}_G^S)^T \mathbf{P}_G^S \mathbf{L}_G^S + \mathbf{P}_G^X \mathbf{L}_G^X \end{pmatrix}$$

The solution of (11) is

$$\boldsymbol{\Delta} = \mathbf{N}^{-1} \cdot \bar{\mathbf{L}}$$

3.2. Construction of Weight Matrixes

The 6 kinds of equations in (9) have different weight matrixes, which would be constructed based on the algorithms as following.

3.2.1. \mathbf{P}_P^L

\mathbf{P}_P^L is mainly determined by ground resolution of the linear array push-broom image. So the weight P_j of image j is computed by (12).

$$P_j = \left(\frac{r_{\max x}}{r_{jx}} \cdot \frac{r_{\max y}}{r_{jy}} \right) \cdot P_{\max} \quad (12)$$

where P_{\max} is the weight of the image with the highest ground resolution in the block, $r_{\max x}$ and $r_{\max y}$ are the ground resolution in x and y direction, r_{jx} and r_{jy} are the ground resolution of image j in x and y direction.

3.2.2. \mathbf{P}_G^L

$$\mathbf{P}_G^L = k^L \cdot \mathbf{P}_P^L \quad (13)$$

where k^L is a scale and usually higher than 1.

3.2.3. \mathbf{P}_P^S

Since \mathbf{V}^S in (4) is not the direct correction of observed values of image point, \mathbf{P}_P^S must be computed with the weight of observed values of image point by the relationship between weight and covariance [3].

$$\mathbf{P}_P^S = (\mathbf{Q}_P^S)^{-1} = \left(\frac{1}{\sigma_0^2} \sum \mathbf{V}^S \right)^{-1} \quad (14)$$

where $\sum \mathbf{V}^S$ is computed based on $\mathbf{C} \cdot \mathbf{V}\mathbf{s}^S = \mathbf{V}^S$ and variance-covariance propagation law [3].

$$\sum \mathbf{V}^S = \mathbf{C} \cdot \sum \mathbf{V}\mathbf{s}^S \cdot \mathbf{C}^T = \mathbf{C} \cdot (\sigma_0^2 \mathbf{E}) \cdot \mathbf{C}^T = \sigma_0^2 \cdot \mathbf{C}\mathbf{C}^T \quad (15)$$

Then \mathbf{P}_P^S is

$$\mathbf{P}_P^S = (\mathbf{C}\mathbf{C}^T)^{-1} \quad (16)$$

3.2.4. \mathbf{P}_G^S

$$\mathbf{P}_G^S = k^S \cdot \mathbf{P}_P^S \quad (17)$$

where k^S is a scale and usually higher than 1.

3.2.5. \mathbf{P}_G^X

\mathbf{P}_G^X is computed by the proportion between measurement accuracy of GCP and image point, usually in $[0, 1]$.

3.2.6. \mathbf{P}_Δ^L

In \mathbf{P}_Δ^L , the weight values of correction of exterior orientation elements are close to 0, and the weight values of correction of exterior orientation elements rates are close to 1.

3.3. The Frame of Computation Process

There are two steps in the frame of computation process of combined bundle block adjustment. The first step is block preliminary computation, which computes initial values of unknown elements. The second step is combined bundle block adjustment, which computes TPs' coordinates and exterior orientation elements of all images. The detailed frame is described in Fig. 1.

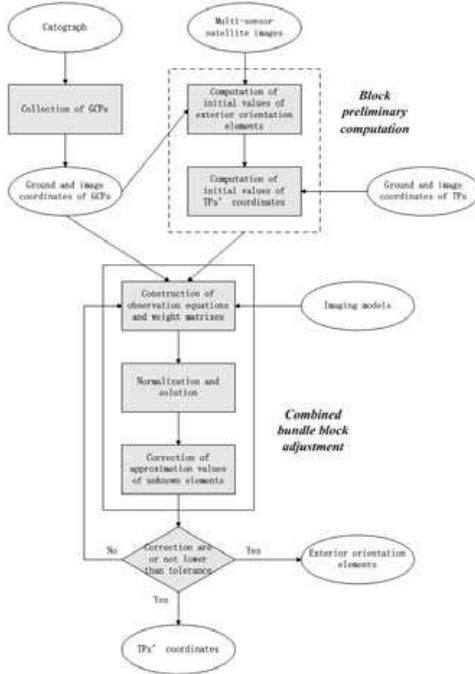


Figure 1: Flow chart of combined bundle block adjustment.

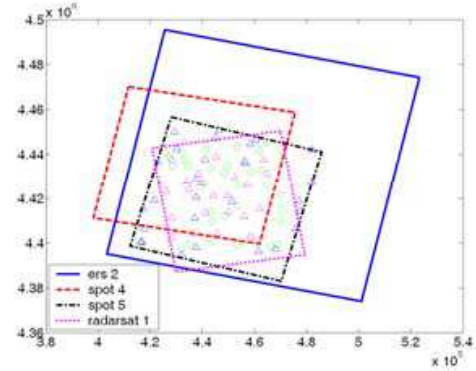


Figure 2: Distribution of four test images, GCPs and TPs.

4. EXPERIMENTS

4.1. Study Site and Dataset

The study site is located in Beijing, China. This area is characterized by the 1 : 25000 scale topographic maps where elevation ranges from 0–600 m.

4.2. Tests

Two combined bundle block adjustment experiments have been proposed to prove and analyze the performance and characteristics of combined bundle block adjustment.

Table 1: Characteristics of four test images.

Satellite	Time	Incidence angle (°)	Resolution (m)
SPOT-5	Feb. 10 2002	2.76	5
SPOT-4	Apr. 27 2005	15	10
ERS-2	Sep. 2 1998	22.9	Along track 12.5
			Across track 12.5
Radarsat-1	Nov. 6 2002	44.3	Along track 8.82
			Across track 5.56

4.2.1. Experiment 1

11 block adjustment schemes are constructed based on different combination of four images, which includes 6 block adjustment schemes based on arbitrary two images, 4 block adjustment schemes based on arbitrary three images and 1 block adjustment schemes based on four images. Initial values of exterior orientation elements of each image have been computed by space resection and initial coordinates of TPs have been computed by multi-image space intersection.

4.2.2. Experiment 2

4 block adjustment schemes with better accuracy ((2), (5), (6), (8)) have been chosen in 11 block adjustment schemes. They are used to test how different GCP distributions to affect the accuracy of combined bundle block adjustment. 6 kinds of GCP distribution have been proposed (Fig. 3), which include sparse surrounding GCPs, sparse surrounding GCPs and one central GCP, sparse surrounding GCPs and four central GCPs, dense surrounding GCPs, dense surrounding GCPs and one central GCP, dense surrounding GCPs and four central GCPs. Sparse surrounding GCPs means 8 well distributed GCPs, and dense surrounding GCPs means 24 well distributed GCPs. The number of TPs is not changed in 6 kinds of distribution.

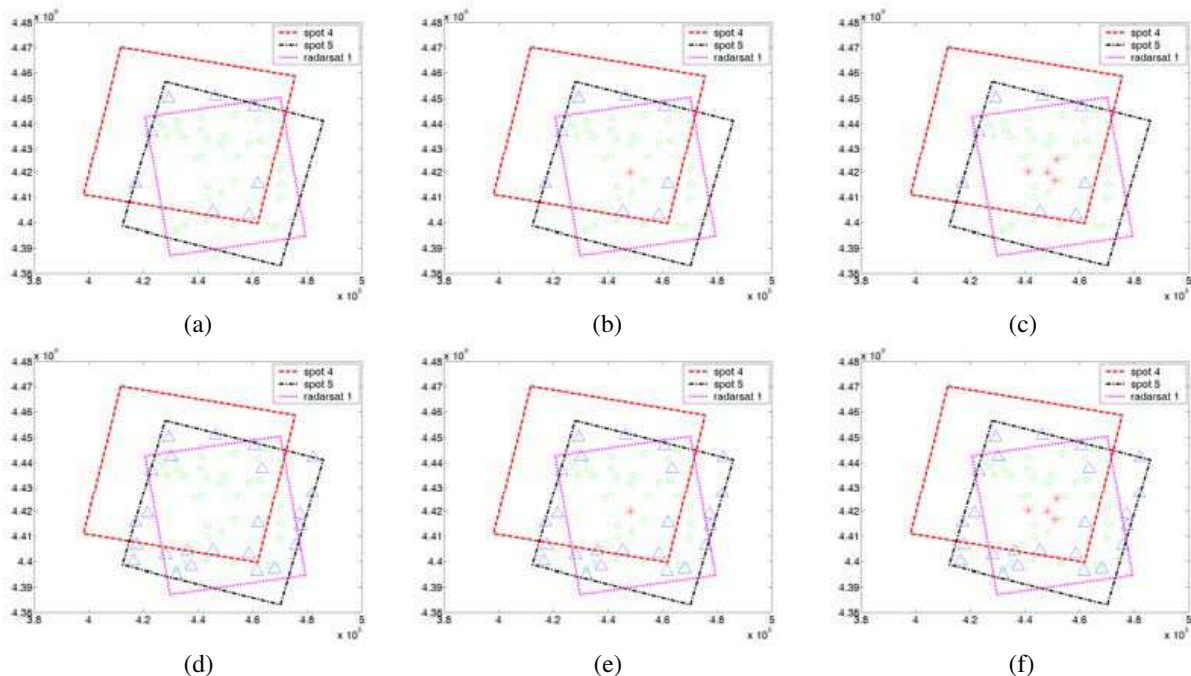


Figure 3: Distributions of three test images, GCPs and TPs in second experiment. (‘ Δ ’ represents surrounding GCP, ‘*’ represents central GCP, ‘o’ represents TP.) (a) Sparse surrounding GCPs, (b) sparse surrounding GCPs and one central GCP, (c) sparse surrounding GCPs and four central GCPs, (d) dense surrounding GCPs, (e) dense surrounding GCPs and one central GCP, (f) dense surrounding GCPs and four central GCPs.

4.3. Test Results

4.3.1. Experiment 1

In Table 2, root mean square (rms) errors of scheme (2), (5), (6), (8) are lower than other 7 schemes, the accuracy in planimetry is 20–30 m and in altimetry is 25–33 m. We found that this four schemes are all including SPOT-5, SPOT-4, Radarsat-1 images, and well distributed and highly accurate GCPs are important to the accuracy of combined bundle block adjustment.

Table 2: Statistics of the results of all block adjustment schemes in first experiment.

Block adjustment scheme	Image	Rms of exterior orientation elements (pixel)			Rms of ground coordinates of all pps (m)			
		RMS_X	RMS_Y	RMS_XY	RMS_X	RMS_Y	RMS_XY	RMS_Z
(1)	Radarsat1	2.954	2.005	3.571	98.182	30.332	102.761	102.423
	ERS2	16.159	952.714	952.851				
(2)	Radarsat1	2.954	2.005	3.571	14.640	16.718	22.222	21.953
	SPOT4	0.520	0.795	0.950				
(3)	SPOT4	0.751	1.536	1.710	14.693	48.906	51.066	18.520
	ERS2	3.332	1.207	3.544				
(4)	SPOT5	1216.186	316.861	1256.786	22.605	41.898	47.607	20.014
	ERS2	3.332	1.207	3.544				
(5)	SPOT5	0.994	1.059	1.452	10.722	18.683	21.541	21.663
	Radarsat1	2.954	2.005	3.571				
(6)	SPOT5	0.874	0.881	1.241	10.987	12.929	16.967	27.005
	SPOT4	0.528	0.784	0.945				
(7)	SPOT5	2.218	6.397	6.771	20.713	42.443	47.228	19.545
	SPOT4	5.884	1.672	6.117				
	ERS2	3.332	1.207	3.544				
(8)	SPOT5	0.992	1.062	1.454	10.225	18.580	21.208	21.653
	SPOT4	0.522	0.792	0.948				
	Radarsat1	2.954	2.005	3.571				
(9)	SPOT4	0.662	0.868	1.091	98.180	30.332	102.759	102.423
	Radarsat1	2.954	2.005	3.571				
	ERS2	16.159	58.955	61.130				
(10)	SPOT5	6.934	2.428	7.347	98.162	30.332	102.742	102.416
	Radarsat1	2.954	2.005	3.571				
	ERS2	16.159	839.882	840.037				
(11)	SPOT5	6.934	2.428	7.347	98.160	30.332	102.740	102.416
	SPOT4	0.662	0.868	1.091				
	Radarsat1	2.954	2.005	3.571				
	ERS2	16.159	41.206	44.261				

In other 7 schemes, ERS-2 image was the principal part for it covered the largest area in four images. But GCPs in ERS-2 image were all located on southwest of image because of less maps. Since the most part of the image was lost of control, the accuracy of other 7 schemes was worse.

4.3.2. Experiment 2

Combined bundle block adjustment experiments all have been finished with 6 kinds of GCP distributions. But the accuracy with sparse surrounding GCPs was evidently lower than with dense surrounding GCPs. This meant the increase of the number of surrounding GCPs would improve the accuracy of TPs' coordinates, especially planimetry coordinates, but not improve the accuracy of exterior orientation elements.

When we increased the number of GCPs in the center of the block, altimetry accuracy of TPs' coordinates were improved. Especially when we added one GCP in the center of the block, altimetry accuracy of the combined bundle block adjustment with sparse surrounding GCPs remarkably improved. But if we kept increasing the number of GCPs in the center of the block, the accuracy of the combined bundle block adjustment improved less.

It can be seen that the demand of the distribution of GCPs for the combined bundle block adjustment is consistent with the traditional bundle block adjustment. Just well distributed and dense surrounding GCPs and a few of central GCPs can ensure the accuracy of the combined bundle block adjustment.

5. CONCLUSIONS

A combined bundle block adjustment model has been proposed and the processing frame has been constructed. Experiment results with one block including four different images proved the model was correct and valid. Then we have drawn some conclusions as follows.

- Combined bundle block adjustment based on the model we proposed is feasible;
- Successful solution of combined bundle block adjustment is mainly determined by distribution of GCPs, but has nothing to do with types, number and combination modes of images;
- When overlays of images are different, GCPs should be collected surrounding the images covering with the largest area, which will improve the accuracy of combined bundle block adjustment;
- Accuracy of combined bundle block adjustment may be better than traditional bundle block adjustment with good ground control conditions;
- Distribution, number and accuracy of GCPs surrounding the block are important to the accuracy of combined bundle block adjustment.

ACKNOWLEDGMENT

This work was supported by National Natural Science Foundation Project (40901247).

REFERENCES

1. Chang, B., "The preliminary research on stereo plotting method of spot imagery," *Acta Geodetica et Cartographica Sinica*, Vol. 18, No. 3, 183–189, 1989.
2. He, Y., "SAR digital block triangulation," 7–9, Master Thesis, Zhengzhou Institute of Surveying and Mapping, 2005.
3. Huang, W.-B., *Theory and Applications of Modern Adjustment*, 23–29, PLA Press, 1992.
4. Qian, Z., J. Liu, and G. Xiao, *Space Photogrammetry*, 63–66, PLA Press, 1992.
5. Thierry, T., "Spatiotriangulation with multisensor VIR/SAR images," *IEEE Transactions on Geoscience and Remote Sensing*, Vol. 42, No. 10, 2096–2103, 2004.
6. Thierry, T., "Spatiotriangulation with multisensor HR stereo-images," *IEEE Transactions on Geoscience and Remote Sensing*, Vol. 44, No. 2, 456–462, 2006.
7. Wang, Z., *Principles of Photogrammetry*, 530–538, Surveying and Mapping Press, 1979.
8. Xiao, G. and C. Zhu, *Radargrammetry*, 54–56, Earthquake Press, 2001.
9. Yan, Q., Z. Zhang, and J. Zhang, "Orientation of remote sensing images taken by CCD from different orbit," *Geomatics and Information Science of Wuhan University*, Vol. 26, No. 3, 270–274, 2001.
10. Lee, Y.-R., "A study on aerial triangulation from multi-sensor imagery," *Korean Journal of Remote Sensing*, Vol. 19, No. 3, 255–261, 2003.

Micro-doppler Analysis of Rotating Targets in Dual-channel Bistatic SAR

Meng Lv

Department of Information Science and Electronic Engineering
Zhejiang University, Hangzhou 310027, China

Abstract— The micro-motions of structures in a target, such as the rotor of a helicopter, the scanning antenna of a ship, the vibrations of vehicle engines, may induce additional frequency modulations on the returned radar signals and generate sidebands about the center Doppler frequency of the target's body, which is known as the micro-Doppler effect. Extraction of micro-Doppler signature is very useful for target classification and recognition. In recent years, the researches of micro-Doppler extraction methods are widely discussed. However, few of them are based on bistatic SAR which has many advantages. Bistatic SAR may have a counter-stealth capability and the receivers are passive which is undetectable. Rotation is a typical micro-motion form. Most of the published researches on analysis of the rotation target did not pay enough attention to the interference of ground clutter. However, ground clutter caused by the presence of stationary targets makes the extraction of the micro-Doppler signature difficult, which may submerge the signals of rotating targets. In this paper, based on the configuration of bistatic SAR with a dual-channel fixed receiver, a new micro-Doppler signature extraction method is used to extract the micro-Doppler features and estimate parameters of rotating targets. The received signals' expressions of rotating targets are established in the case of dual-channel fixed-receiver bistatic SAR. With displaced phase center antenna technique, the ground clutter is suppressed and the signals of rotating targets are reserved in the range-compressed data domain. Then the mathematical expressions of micro-Doppler are derived. The fractional Fourier transform is adopted to compensate for the radar Doppler shift and the Gabor transform method is utilized for extraction of micro-Doppler information caused by rotating targets and parameter estimation. Finally, The effectiveness of the proposed method is evaluated through simulations.

1. INTRODUCTION

A common problem in synthetic aperture radar (SAR) system is the detection and identification of moving targets within a scene. Apart from target's bulk motion, the mechanical vibration and rotation on the target have been an issue ever since. These micro-motions induce phase modulations in the received signal and generate sidebands in the Doppler frequency spectrum of the target, which is known as micro-Doppler effect [1]. The micro-Doppler effect can be used to identify targets more effectively and accurately.

At present, the separation method of micro-Doppler information has advanced rapidly. There are several micro-Doppler studies based on synthetic aperture radar (SAR) or inverse synthetic aperture radar (ISAR) in the past few years [2, 3], but few researches analyze the micro-Doppler effect in the case of bistatic SAR. The rotation of a target is a typical micro-motion form [4, 5]. However, most of the micro-Doppler analysis of the rotation target did not pay much attention to the interference of ground clutter. Therefore, rotation target detection and parameters estimation algorithms in bistatic SAR with dual-channel fixed receiver which is utilized to remove the influence of ground clutter are analyzed.

2. SYSTEM GEOMETRY AND SIGNAL MODEL

As is shown in Figure 1, the transmitters A_1 and A_2 move along the azimuth direction with a velocity v , and the distance between A_1 and A_2 is d . The fixed receiver is located at (x_r, y_r, h_r) , and the scatterer P is rotating around $C(x_c, y_c, 0)$ with a rotation frequency f_r , radius r and initial phase θ_0 . The two channels transmit signals alternately, i.e., the pulse repetition interval (PRI) of the system is T and the PRI of each channel is $2T$. The displaced phase center antenna (DPCA) technique satisfy the relationship $d = mvT$ ($m = 1, 3, 5, \dots$).

It is equivalent that two transmitters observe the same scene at a time interval $\Delta\tau = mT$, thus the difference between the two transmitter echoes express the changes caused by the rotating target in the scene. In other words, the signals of clutter can be suppressed and the signals of rotating targets can be reserved accordingly.

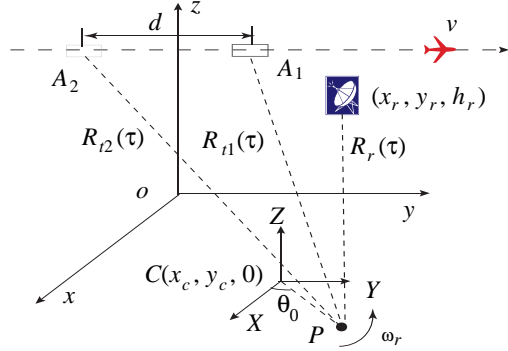


Figure 1: The geometry of bistatic SAR.

Suppose that the transmitters A_1 and A_2 move to the positions $(v\tau, 0, h)$ and $(v\tau - d, 0, h)$ at azimuth time τ respectively. The coordinate of rotating target P is expressed as

$$\begin{cases} x(\tau) = x_c + r \cos(\omega_r \tau + \theta_0) \\ y(\tau) = y_c + r \sin(\omega_r \tau + \theta_0) \\ z(\tau) = 0 \end{cases} \quad (1)$$

where the rotation angular velocity $\omega_r = 2\pi f_r$. The distance $R_{t1}(\tau)$ between the transmitter A_1 and the rotating target P and the distance $R_{r1}(\tau)$ between the fixed receiver and P are

$$R_{t1}(\tau) = \sqrt{(x(\tau))^2 + (v\tau - y(\tau))^2 + h^2} \quad (2)$$

$$R_{r1}(\tau) = \sqrt{(x_r - x(\tau))^2 + (y_r - y(\tau))^2 + h_r^2} \quad (3)$$

The distance $R_{t2}(\tau + \Delta\tau)$ between A_2 and P and the distance $R_{r2}(\tau + \Delta\tau)$ between the fixed receiver and P can be expressed analogously after the time interval $\Delta\tau$.

$p(t)$ is the transmitted radar signal, which is a linear frequency-modulated (LFM) signal as follows:

$$p(t) = \text{rect}\left(\frac{t}{T_r}\right) \exp(j(2\pi f_c t + \pi K_r t^2)) \quad (4)$$

where t is the range time, $\text{rect}(t) = 1$ for $-1/2 \leq t \leq 1/2$ and is zero otherwise, f_c is the carrier frequency, T_r is the chirp pulse duration and K_r is the chirp rate. In this paper, we only consider the phase factor [1]. Therefore, through demodulation and range compression, the baseband signals of the two channels are

$$s_1(t, \tau) = C \exp\left(-j \frac{2\pi R_{tr1}(\tau)}{\lambda}\right) \quad (5)$$

$$s_2(t, \tau + \Delta\tau) = C \exp\left(-j \frac{2\pi R_{tr2}(\tau + \Delta\tau)}{\lambda}\right) \quad (6)$$

where $R_{tr1}(\tau) = R_{t1}(\tau) + R_{r1}(\tau)$, $R_{tr2}(\tau + \Delta\tau) = R_{t2}(\tau + \Delta\tau) + R_{r2}(\tau + \Delta\tau)$ and C is a constant.

The initial phase θ_0 is assumed to be zero. Let $R_{t0} = \sqrt{h^2 + x_c^2}$, $R_{r0} = \sqrt{h_r^2 + (x_c - x_r)^2}$. The approximate expressions of $R_{tr1}(\tau)$ and $R_{tr2}(\tau + \Delta\tau)$ after Taylor series expansion are

$$R_{tr1}(\tau) \approx R_{t0} + R_{r0} + \frac{(v\tau - y(\tau))^2}{2R_{t0}} + \frac{(y_r - y(\tau))^2}{2R_{r0}} + 2r \cos(\omega_r \tau) \quad (7)$$

$$R_{tr2}(\tau + \Delta\tau) \approx R_{t0} + R_{r0} + \frac{(v\tau - y(\tau + \Delta\tau))^2}{2R_{t0}} + \frac{(y_r - y(\tau + \Delta\tau))^2}{2R_{r0}} + 2r \cos(\omega_r (\tau + \Delta\tau)) \quad (8)$$

3. MICRO-DOPPLER EFFECT

Let $\varphi_1 = 2\pi R_{tr1}(\tau)/\lambda$ and $\varphi_2 = 2\pi R_{tr2}(\tau + \Delta\tau)/\lambda$, so the different signal can be expressed as

$$\begin{aligned} \Delta s(t, \tau) &= s_1(t, \tau) - s_2(t, \tau + \Delta\tau) \\ &= -2C \sin\left(\frac{\varphi_1 - \varphi_2}{2}\right) \exp\left(j\left(\frac{\pi}{2} - \frac{\varphi_1 + \varphi_2}{2}\right)\right) \end{aligned} \quad (9)$$

where

$$\begin{aligned} \frac{\varphi_1 - \varphi_2}{2} &= \frac{4\pi r}{\lambda} \sin\left(\frac{2\omega_r\tau + \omega_r\Delta\tau}{2}\right) \sin\left(\frac{\omega_r\Delta\tau}{2}\right) \\ &\quad + \frac{2\pi r}{\lambda} \cos\left(\frac{2\omega_r\tau + \omega_r\Delta\tau}{2}\right) \sin\left(\frac{\omega_r\Delta\tau}{2}\right) \times \left(\frac{v\tau}{R_{t0}} - \frac{y_c}{R_{t0}} + \frac{y_r}{R_{r0}} - \frac{y_c}{R_{r0}}\right) \end{aligned} \quad (10)$$

$$\begin{aligned} \frac{\varphi_1 + \varphi_2}{2} &= \frac{\pi}{\lambda} \left(2R_{t0} + 2R_{r0} + 4r \cos\left(\frac{2\omega_r\tau + \omega_r\Delta\tau}{2}\right) \cos\left(\frac{\omega_r\Delta\tau}{2}\right)\right) \\ &\quad + \frac{(v\tau - y_c)^2}{R_{t0}} + \frac{(y_r - y_c)^2}{R_{r0}} + 2r \frac{y_c - v\tau}{R_{t0}} \sin\left(\frac{2\omega_r\tau + \omega_r\Delta\tau}{2}\right) \cos\left(\frac{\omega_r\Delta\tau}{2}\right) \\ &\quad + 2r \frac{y_c - y_r}{R_{r0}} \sin\left(\frac{2\omega_r\tau + \omega_r\Delta\tau}{2}\right) \cos\left(\frac{\omega_r\Delta\tau}{2}\right) \end{aligned} \quad (11)$$

It can be seen that if the target is static, i.e., $\omega_r = 0$, the amplitude of $\Delta s(t, \tau)$ is equal to zero all the time, which means the ground clutter is suppressed.

The phase of $\Delta s(t, \tau)$ is $\varphi(\tau) = \pi/2 - (\varphi_1 - \varphi_2)/2$. By taking the time derivative of the phase, the instantaneous Doppler frequency is

$$\begin{aligned} f &= \frac{1}{2\pi} \frac{d\varphi(\tau)}{d\tau} = -\frac{v^2\tau}{\lambda R_{t0}} + \frac{vy_c}{\lambda R_{t0}} + \frac{2r\omega_r}{\lambda} \sin\left(\frac{2\omega_r\tau + \omega_r\Delta\tau}{2}\right) \cos\left(\frac{\omega_r\Delta\tau}{2}\right) \\ &\quad - \frac{(y_c - y_r)r\omega_r}{\lambda R_{r0}} \cos\left(\frac{2\omega_r\tau + \omega_r\Delta\tau}{2}\right) \cos\left(\frac{\omega_r\Delta\tau}{2}\right) \end{aligned} \quad (12)$$

The first term in (12) is the linear Doppler shift caused by the radar's translation, which should be compensated in advance in order to avoid the m-D signature wrapping and to simply interpretation. The last terms are the micro-Doppler modulation induced by rotation. It can be seen that the m-D signature is a sinusoidal function of azimuth time τ . What's more, the offset $\Delta f = vy_c/\lambda R_{t0}$ along the frequency axis can be used to determine the azimuth position of the rotation center.

Let $k_a = -v^2\tau/R_{t0}$. The fractional Fourier transform (FRFT) [6] approach is utilized to estimate k_a .

$$\hat{k}_a = \frac{\tan((P-1)\pi/2)}{s^2} \quad (13)$$

where $s^2 = T_i/f_s$ is a scale factor, with T_i being the time of fight and f_s being the pulse repetition frequency of each channel.

Therefore, after the compensation for the radar Doppler shift, the different signal can be expressed as

$$\Delta s_c(t, \tau) = \Delta s(t, \tau) \exp(-j\pi\hat{k}_a\tau^2) \quad (14)$$

Then the m-D signature can be extracted from the signal $\Delta s_c(\tau)$ by using Gabor transform.

4. SIMULATIONS

The simulation parameters are $f_c = 9$ GHz, $T_r = 1$ μ s, $B = 150$ MHz, $PRF = 1800$ Hz, $T_i = 3$ s, $h = 4000$ m, $T = 1/1800$ s, $v = 200$ m/s, $d = 9vT = 1$ m and $(x_r, y_r, h_r) = (0, 0, 3000)$ m. There are six static scatterers and three rotating scatterers in the scene. The parameters of rotating scatterers are described in Table 1.

The module signal $s_1(t, \tau)$ in the range-compressed data domain is shown in Figure 2(a). Nine lines can be found along the azimuth direction. It is difficult to distinguish which one denote the

Table 1: Parameters of rotating scatterers.

Number	r (m)	f_r (Hz)	Scattering coefficient	Rotating center coordinate (m)
1	1	2	0.5	(1000, 30, 0)
2	1	1	0.3	(1050, 30, 0)
3	2	2	0.5	(950, 20, 0)

rotating scatterer. It can be seen that only the signals of rotating scatterers are clearly displayed and the ground clutter is almost eliminated after DPCA operation in Figure 2(b).

Figure 3 shows the normalized energy distribution of the different signal of the first rotating target projected onto the axis P [6]. The peak value appears at $P = 0.51$, then the estimation value of k_a is -290.5 Hz/s which is close to the true value -291.0 Hz/s . This approach can be also used to other rotating targets and the results are about the same.

The m-D signature of the first rotating target is shown in Figure 4(a), which is extracted by using Gabor transform (The negative frequency is upturned). In the meanwhile, the theoretical m-D signature of the first rotating target is illustrated in Figure 4(b). Compared Figure 4(a) with (b), it can be seen the theoretical result agrees well with the Gabor m-D signature.

A period value of 0.51 s can be obtained from Figure 4 by using the autocorrelation approach. In other words, the rotating frequency of the first target is 1.96 Hz , which is close to the true value

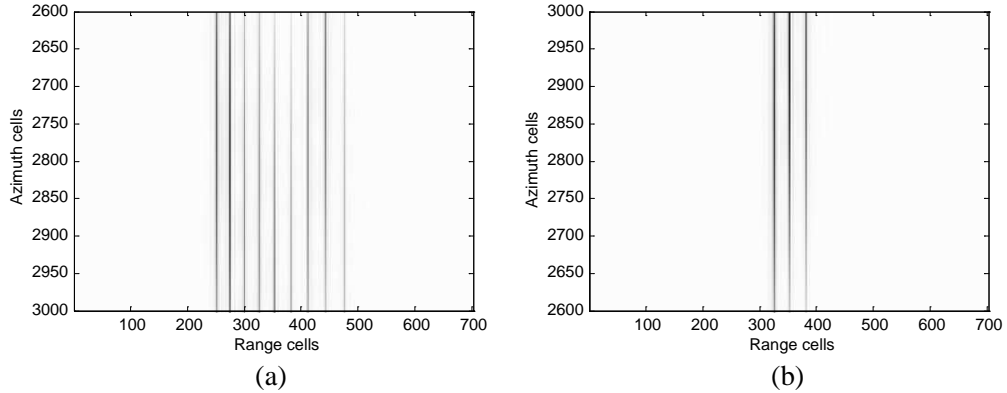


Figure 2: The signal $s_1(t, \tau)$ and $\Delta s(t, \tau)$ in the range-compressed data domain.

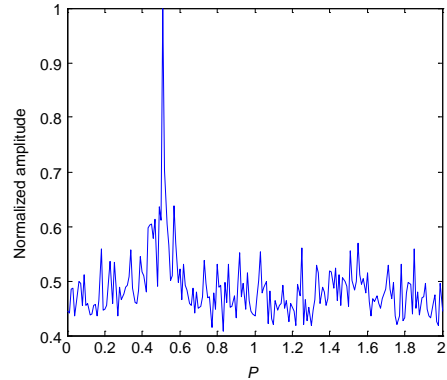


Figure 3: FRFT distribution of the different signal $\Delta s(t, \tau)$ of the first rotating target projected onto the axis P .

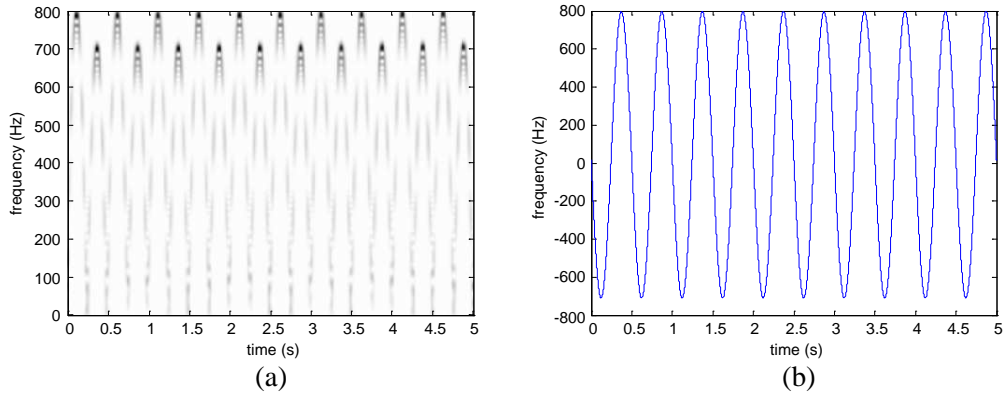


Figure 4: The Gabor transform outcome and the theoretical result of the first rotating target.

2 Hz. The m-D signature offset $\Delta f = 43.66$ Hz can be obtained. Then the position of the rotating center can be estimated by using the relationships $\hat{y}_c = -v\Delta f/\hat{k}_a$ and $\hat{x}_c = \sqrt{v^4/(\lambda^2\hat{k}_a) - h^2}$. The estimation of the first rotating target center position is (1002.49, 30.06, 0) m, which is close to the true values. The accurate results of other rotating targets can be obtained analogously.

5. CONCULSION

In this paper, the micro-Doppler effect of rotating targets is analyzed in the case of bistatic SAR with fixed receiver. The ground clutter is suppressed by DCPA technique and the theoretical expression of m-D signature is obtained. Gabor transform is utilized to extract the m-D signature. The simulation results demonstrate the validity of the method. The frequency and position of the rotating targets are estimated correctly.

REFERENCES

1. Chen, V. C., F. Li, S. S. Ho, and H. Wechsler, "Micro-Doppler effect in radar: Phenomenon, model, and simulation study," *IEEE Trans. Aerosp. Electron. Syst.*, Vol. 42, No. 1, 2–21, Jan. 2006.
2. Sparr, T. and B. Krane, "Micro-doppler analysis of vibrating targets in SAR," *Proc. Inst. Electr. Eng. — Radar Sonar Navig.*, Vol. 150, No. 4, 277–283, Aug. 2003.
3. Luo, Y., Q. Zhang, C. W. Qiu, X. J. Liang, and K. M. Li, "Micro-doppler effect analysis and feature extraction in ISAR imaging with stepped-frequency chirp signals," *IEEE Trans. Geosci. Remote Sens.*, Vol. 48, No. 4, 2087–2098, Apr. 2010.
4. Rüegg, M., E. Meier, and D. Nüesch, "Vibration and rotation in millimeterwave SAR," *IEEE Trans. Geosci. Remote Sens.*, Vol. 45, No. 2, 293–304, Feb. 2007.
5. Zhang, Q., T. S. Yeo, H. S. Tan, and Y. Luo, "Imaging of a moving target with rotating parts based on the Hough transform," *IEEE Trans. Geosci. Remote Sens.*, Vol. 46, No. 1, 291–299, Jan. 2008.
6. Deng, B., Y. L. Qiu, H. Q. Wang, and X. Li, "A modified method of SAR moving target detection and imaging based on fractional Fourier transform," *J. Electr. & Info. Tech.*, Vol. 30, No. 2, 326–330, Feb. 2008.

Snow Wetness Estimation from Polarimetric SAR Image

M. Surendar¹, G. Singh², A. Bhattacharya¹, G. Venkataraman¹, and P. A. Bharathi¹

¹Indian Institute of Technology, Bombay, Mumbai, India

²Niigata University, Niigata, Japan

Abstract— Snow pack parameters are very important for forecasting of snow avalanche and snow melt run off modeling in mountainous areas like Himalayan region of India. In this paper, a new algorithm for estimation of snow wetness based on SAR polarimetric decomposition has been described. This algorithm has been compared with the existing Shi and Dozier [1] inversion snow wetness method and validated with the field measurements.

1. INTRODUCTION

Avalanche modeling, snow melt runoff and hydrological investigation required timely information about spatial variability of snow properties. Among these properties, the snow wetness of snowpack is very important. Estimation of snow pack parameters is very complicated due to their continuous spatial and temporal variation. Various active microwave remote sensing systems have been used for estimating snow pack parameters. Shi and Dozier [1] used polarimetric Shuttle Imaging Radar-C (SIR-C) mission data to derive snow wetness by considering the surface and volume scattering powers. Shi and Dozier algorithm has been modified by Singh et al. [2] for dual polarization SAR data. But now the availability of fully polarimetric SAR data along with limited near-real time field observations insists and excites us to utilize full polarimetric SAR data for snow parameters estimation. Several assumptions have been made in the Shi and Dozier model to solve the regression equations. The second order statistics from the quad-pol SAR data can be used with an expectation to achieve a better accuracy. The scope of this study is to develop a methodology to retrieves snow wetness using decomposition scheme from full polarimetric SAR data. In this study the Radarsat-2 fine quad polarization data acquired on 7th February 2012 over Manali and Dhundi (center Lat/Long: N32°22'05"/77°15'00", Himachal Pradesh, India) has been used.

2. METHODOLOGY

2.1. G4U Based Snow Wetness Estimation

2.1.1. G4U Transformation

The fine quad polarization Radarsat-2 Single Look Complex (SLC) image was multilooked with the multilooking factor of 2 in range direction and 1 in azimuth direction and the coherency matrix (T_3) was generated. The ensemble averaged coherency matrix is defined as:

$$\langle [T_3] \rangle = \langle k_p k_p^\dagger \rangle = \begin{bmatrix} T_{11} & T_{12} & T_{13} \\ T_{21} & T_{22} & T_{23} \\ T_{31} & T_{32} & T_{33} \end{bmatrix} \quad (1)$$

where \dagger is transposed complex conjugate, $\langle \rangle$ indicates ensemble average, and k_p is the Pauli vector

which is represented as $k_p = \frac{1}{\sqrt{2}} \begin{bmatrix} S_{HH} + S_{VV} \\ S_{HH} - S_{VV} \\ 2S_{HV} \end{bmatrix}$.

In this study, general four component scattering power decomposition with unitary transformation (G4U) [3] has been used. In this decomposition, special unitary transformation has been applied to the rotated coherency matrix. The unitary transformations do not modify the coherency matrix information. So the rotated coherency matrix is transformed by a special unitary transformation. Due to this transformation T_{23} element in the coherency matrix becomes zero, which is directly related to the helix component of the scattering. The following rotation was applied in the

T_3 matrix [4]:

$$\left. \begin{aligned} \langle [T(\theta)] \rangle &= [R(\theta)] \langle [T] \rangle [R(\theta)]^\dagger; \\ \langle [T(\theta)] \rangle &= \begin{bmatrix} T_{11}(\theta) & T_{12}(\theta) & T_{13}(\theta) \\ T_{21}(\theta) & T_{22}(\theta) & T_{23}(\theta) \\ T_{31}(\theta) & T_{32}(\theta) & T_{33}(\theta) \end{bmatrix} \\ \text{where } [R(\theta)] &= \begin{bmatrix} 1 & 0 & 0 \\ 0 & \cos 2\theta & \sin 2\theta \\ 0 & -\sin 2\theta & \cos 2\theta \end{bmatrix} \\ 2\theta &= \frac{1}{2} \tan^{-1} \left(\frac{2\operatorname{Re}\{T_{23}\}}{T_{22}-T_{33}} \right) \\ T_{11}(\theta) &= T_{11}; \\ T_{12}(\theta) &= T_{12} \cos 2\theta + T_{13} \sin 2\theta; \quad T_{21}(\theta) = T_{12}^* \\ T_{13}(\theta) &= T_{13} \cos 2\theta - T_{12} \sin 2\theta; \quad T_{31}(\theta) = T_{13}^* \\ T_{22}(\theta) &= T_{22} \cos^2 2\theta + T_{33} \sin^2 2\theta + \operatorname{Re}(T_{23}) \sin 4\theta \\ T_{23}(\theta) &= j \operatorname{Im}(T_{23}); \quad T_{32}(\theta) = -j \operatorname{Im}(T_{23}) \\ T_{33}(\theta) &= T_{33} \cos^2 2\theta + T_{22} \sin^2 2\theta - \operatorname{Re}(T_{23}) \sin 4\theta \end{aligned} \right\} \quad (2)$$

The special unitary transformation applied to the rotated coherency matrix ($T(\theta)$) is:

$$\left. \begin{aligned} \langle [T(\varphi)] \rangle &= [U(\varphi)] \langle [T(\theta)] \rangle [U(\varphi)]^\dagger; \\ \langle [T(\varphi)] \rangle &= \begin{bmatrix} T_{11}(\varphi) & T_{12}(\varphi) & T_{13}(\varphi) \\ T_{21}(\varphi) & T_{22}(\varphi) & 0 \\ T_{31}(\varphi) & 0 & T_{33}(\varphi) \end{bmatrix} \\ \text{where } [U(\varphi)] &= \begin{bmatrix} 1 & 0 & 0 \\ 0 & \cos 2\varphi & j \sin 2\varphi \\ 0 & j \sin 2\varphi & \cos 2\varphi \end{bmatrix}; \\ 2\varphi &= \frac{1}{2} \tan^{-1} \left(\frac{2\operatorname{Re}\{T_{23}(\theta)\}}{T_{22}(\theta)-T_{33}(\theta)} \right) \\ T_{11}(\varphi) &= T_{11}(\theta); \\ T_{12}(\varphi) &= T_{12}(\theta) \cos 2\varphi - j T_{13}(\theta) \sin 2\varphi; \quad T_{21}(\varphi) = T_{12}^* \\ T_{13}(\varphi) &= T_{13}(\theta) \cos 2\varphi - j T_{12}(\theta) \sin 2\varphi; \quad T_{31}(\theta) = T_{13}^* \\ T_{22}(\theta) &= T_{22}(\theta) \cos^2 2\varphi + T_{33}(\theta) \sin^2 2\varphi + \operatorname{Im}(T_{23}(\theta)) \sin 4\varphi \\ T_{23}(\varphi) &= \operatorname{Re}(T_{23}(\theta)); \quad T_{32}(\varphi) = T_{23}^* \\ T_{33}(\varphi) &= T_{33}(\theta) \cos^2 2\varphi + T_{22}(\theta) \sin^2 2\varphi - \operatorname{Im}(T_{23}(\theta)) \sin 4\varphi \end{aligned} \right\} \quad (3)$$

The T_{23} (helix component) element of the coherency matrix becomes zero after the application of this transformation

$$T_{23}(\varphi) = \operatorname{Re}(T_{23}(\theta)) = \operatorname{Re}(j \operatorname{Im}(T_{23})) = 0 \quad (4)$$

Real rotation has been applied to the coherency matrix (T_3) to reduce the cross polarization components related to the volume scattering. This pseudo volume scattering may be occurred due to the snow covered terrain slope. The special unitary transformation helped to reduce the number of independent parameters to ease mathematical complexities and is accounted for utilizing all the parameters in the coherency matrix.

2.1.2. Snow Wetness Algorithm

In wet snow conditions, surface and volume scattering are the dominant scattering mechanisms. So the snow wetness algorithm developed here assumes that double bounce scattering is not present in the wet snow conditions. Generalized spheroid structure has been considered as the snow particle structure of wet snow. The volume scattering can be written as:

$$S_{vol} = S_{HH}^{vol} \left[\begin{array}{cc} 1 & 0 \\ 0 & A_P \end{array} \right]_{Spheroid} \quad (5)$$

Here A_P is the particle anisotropy which can be written as $A_P = \frac{\gamma_{VV}}{\gamma_{HH}}$. γ_{HH} , γ_{VV} are the Fresnel transmission coefficients.

$$\begin{aligned}\gamma_{HH} &= \frac{2\sqrt{\varepsilon_s - \sin^2\theta_i}}{\cos\theta_i + \sqrt{\varepsilon_s - \sin^2\theta_i}} \\ \gamma_{VV} &= \frac{2\sqrt{\varepsilon_s - \sin^2\theta_i}}{\varepsilon_s \cos\theta_i + \sqrt{\varepsilon_s - \sin^2\theta_i}}\end{aligned}\quad (6)$$

where ε_s is dielectric constant of snowpack volume and θ_i is the local incidence angle which has been converted into local refractive angle using Snell's law. The volume scattering component of the snow under uniform distribution condition is:

$$[T]_{vol}^{snow} = f_v \begin{bmatrix} |\gamma|^2 & 0 & 0 \\ 0 & \frac{1}{2} & 0 \\ 0 & 0 & \frac{1}{2} \end{bmatrix}, \quad f_v = 2T_{33}(\theta) - P_c, \quad |\gamma|^2 = \frac{|\gamma_{HH} + \gamma_{VV}|^2}{|\gamma_{HH} - \gamma_{VV}|^2} \quad (7)$$

$|\gamma|^2$ is a generalized Cloud's volume parameter which is used to estimate the volume dielectric constant of the snow pack.

$$|\gamma|^2 = \frac{T'_{11}}{f_v} - \frac{|T'_{12} + T'_{13}|^2}{f_v ((T'_{22} - T'_{33}) \cos 4\varphi)} \quad (8)$$

where $f_v = (T'_{22} + T'_{33}) - (T'_{22} - T'_{33}) \cos 4\varphi - f_c$.

Volume parameter can also be written as:

$$|\gamma|^2 = \frac{T_{11}(\theta)}{2T_{33}(\theta) - P_c} - \frac{|T_{12}(\theta) + T_{13}(\theta)|^2}{(2T_{33}(\theta) - P_c)(T_{22}(\theta) - T_{33}(\theta))} \quad (9)$$

The surface scattering is determined by the normal Bragg scattering model. The Bragg surface scattering can be written as:

$$S_{surf} = \begin{bmatrix} \alpha_{HH} & 0 \\ 0 & \alpha_{VV} \end{bmatrix} \quad (10)$$

where α_{HH} , α_{VV} are the Fresnel reflection coefficients for horizontally and vertically polarized waves.

The generalized Freeman surface parameter (β) can be written as:

$$|\beta|^2 = \frac{T_{22}(\theta) - T_{33}(\theta)}{T_{11}(\theta) - f_v |\gamma|^2} = \frac{|\alpha_{HH} - \alpha_{VV}|^2}{|\alpha_{HH} + \alpha_{VV}|^2} \quad (11)$$

Finally, the surface snow dielectric constant is derived by using generalized Freeman surface parameter (β) [5] and the volume snow dielectric constant is derived by using Cloude's volume parameter ($|\gamma|^2$) [6] through the iterative process with the help of Fresnel reflection and transmission coefficients. The snow dielectric constant is used for estimating snow wetness directly by using the following empirical relation developed in [7]:

$$W (\%) = 5.35[\varepsilon_s - (1 - 1.92\rho)] \quad (12)$$

where ρ is dry snow density.

3. RESULTS AND DISCUSSION

The generalized Freeman surface (β) and Cloude volume $|\gamma|^2$ parameter maps are shown in Figs. 1(a) and 1(b) respectively. The surface and volume snow wetness maps derived using the new methodology are shown in Figs. 1(c) and 1(d) respectively. In these maps, surface parameter shows very less value (< 0.5) and the volume parameter shows high value (> 1) over the snow covered area. The higher value of volume parameter is due to high volume backscattering from the snowpack. During the time of data acquisition and field measurements the weather data was recorded at the Dhundi observatory. Within an interval of two hours the air temperature varied from 5°C to 3°C

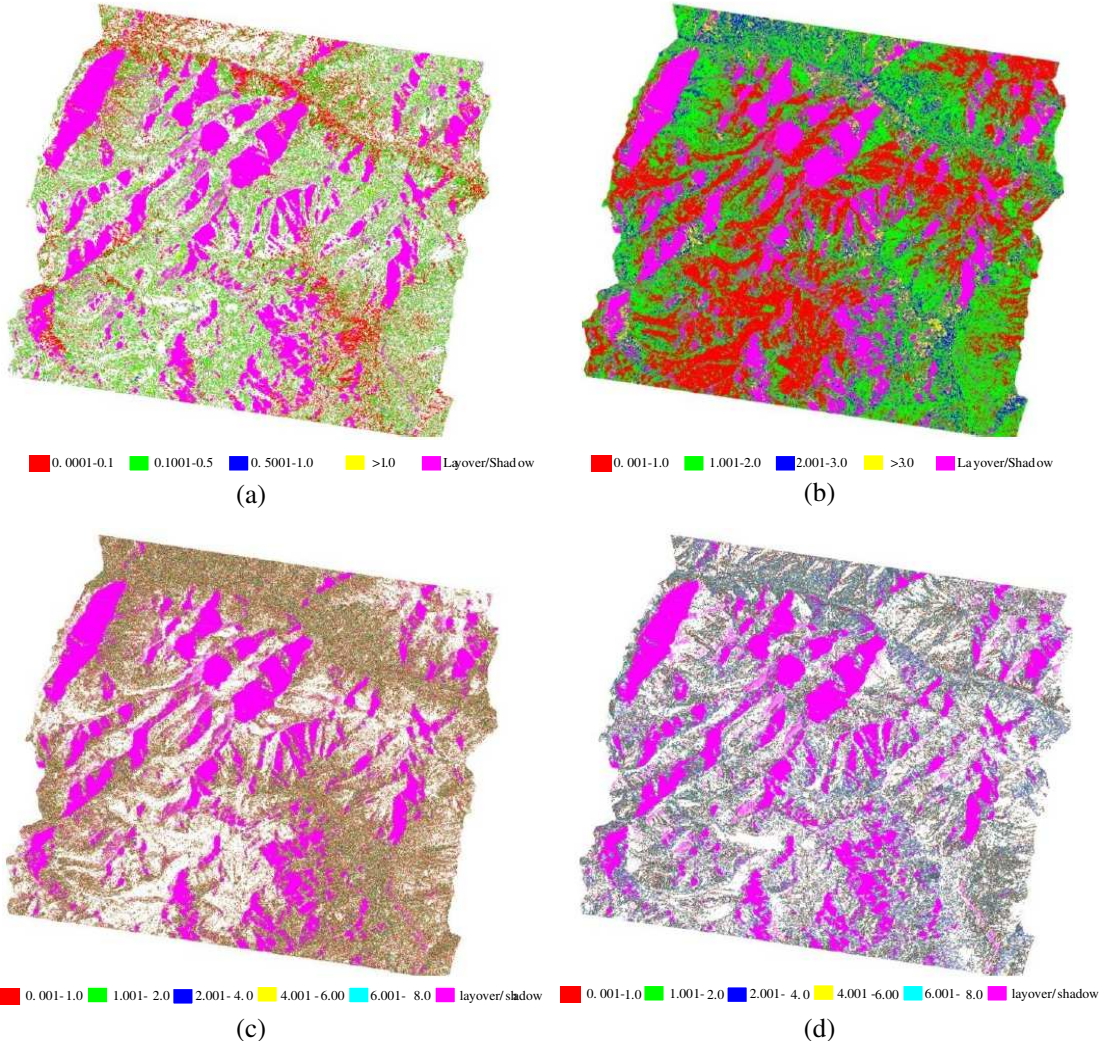


Figure 1: (a) Generalized Freeman surface parameter map. (b) Generalized cloud volume parameter map. (c) Surface snow wetness map. (d) Volume snow wetness map.

with a change in humidity from 76% to 62%. There was no variation in the snow temperature measured during this time interval. In these weather conditions the field measurements of the snow wetness were obtained for a depth of 1m with an interval of 10 cm. The newly developed G4U [4] pol-SAR decomposition technique was applied on the acquired Radarsat-2 quad pol data to estimate the snow wetness. The algorithm shows a Mean Absolute Error (MAE) of 1.218%. The comparison with the inversion model based snow wetness estimation [1] shows an increase in the

Table 1: Comparison of the snow wetness estimated by the two methods and validated by field measurements.

Location		Snow Wetness (% Volume)			Field Measurement (% Vol)	Error (G4U/Shi -Dozzier)	MAE (G4U/Shi -Dozzier)			
		G4U		Shi and Dozier						
		Surface	Volume							
Site 1	Manali (32°16'11.5"N 77°10'59.22"E)	1.412	3.350	2.382	10.266	2.82	0.438/7.446			
Site 2		1.293	2.936	2.115	3.017	1.634	0.481/1.383			
Site 3		1.926	3.266	2.596	5.864	4.37	1.774/1.494			
Site 4		1.433	2.696	2.065	7.447	3.47	1.405/3.977			
Site 5		2.231	4.559	3.395	7.949	5.17	1.775/2.779			
Site 6		2.411	2.744	2.577	4.141	1.511	1.066/2.630			
Site 7	Dhundi (32°21'19"N 77°07'35"E)	3.410	4.123	3.766	5.232	2.17	1.59/3.062			

MAE to 3.253% in Table 1. The volume scattering component is modeled by considering the snow particle as spheroids in the new methodology. This generalized snow structure might not hold true for all layers of snowpack. In future we would like to model the volume scattering component with snow structures derived from snow morphological analysis.

REFERENCES

1. Shi, J. and J. Dozier, “Inferring snow wetness using C-band data from SIR-C’s polarimetric synthetic aperture radar,” *IEEE Trans. Geosci. Remote Sens.*, Vol. 33, 905–914, 1995.
2. Singh, G. and G. Venkataraman, “Snow permittivity retrieval inversion algorithm for estimating snow wetness,” *Geocarto International*, Vol. 25, No. 3, 187–212, 2010.
3. Singh, G., Y. Yamaguchi, and S. Park, “General four-component scattering power decomposition with unitary transformation of coherency matrix,” *IEEE Trans. Geosci. Remote Sens.*, Vol. 19, 104–106, 2012.
4. Yamaguchi, Y., A. Sato, W.-M. Boerner, R. Sato, and H. Yamada, “Four-component scattering power decomposition with rotation of coherency matrix,” *IEEE Trans. Geosci. Remote Sens.*, Vol. 49, No. 6, 2251–2258, Jun. 2011.
5. Freeman, A., “Fitting a two-component scattering model to polarimetric SAR data from forests,” *IEEE Trans. Geosci. Remote Sens.*, Vol. 45, No. 8, 2583–2592, 2007.
6. Cloude, S. R., *Polarisation: Applications in Remote Sensing*, Oxford University Press, 2010.
7. Denoth, A., “An electronic device for long term snow wetness recording,” *Annual Glaciology*, Vol. 19, 104–106, 1994.

Optical Data Storage Using Diffractive Optical Elements

S. Yoshida, K. Yamada, N. Unno, J. Taniguchi, and M. Yamamoto
 Tokyo University of Science, 6-3-1 Niijuku, Katsushika-ku, Tokyo 125-8585, Japan

Abstract— The diffractive optical element (DOE) can transform wavefront and generate arbitrary intensity distribution. In this study, we focus on these functions of DOE, and examined the possibility as read-only memory (ROM) usage of the DOE. The DOE based optical data storage is thought of as a kind of holographic data storage (HDS) using thin holograms. In the HDS, digital data is recorded and read out as modulated two-dimensional page data, instead of bit-by-bit recording in conventional optical disks. We design and optimize the DOE using the iterative method with regularization. In the design and optimization process, we use iterative Fourier transform algorithm that is known as Gerchberg-Saxton algorithm. Designed and optimized DOE is fabricated by ultraviolet (UV) nanoimprinting technology. By adopting nanoimprinting technology, high productivity can be expected. Fabricated DOE is evaluated in the experiment. We verify that DOE for optical data storage can be actualized.

1. INTRODUCTION

The diffractive optical element (DOE) [1] has the wavefront transformation function, and can generate arbitrary intensity distribution. The DOE is used for various purposes, and its usage include beam shaper, beam splitter, beam homogenization, aberration correction. Especially, phase modulation type DOE is widely used because it can actualize high diffraction efficiency. And the DOE have a high degree of freedom for design. On the basis of these feature of DOE, we examine possibility as storage usage of the DOE.

The optical data storage using the DOE is thought of as a kind of holographic data storage (HDS) [2–4] using thin holograms. Features of HDS are large capacity and high transfer rate. In the HDS, digital data is recorded and read out as modulated two-dimensional page data, instead of bit-by-bit recording in conventional optical storages. Therefore, HDS actualize high data transfer rate. In this study, we focus on the read-only memory (ROM) type HDS which replaces conventional optical discs.

We design and optimize phase distribution of the DOE using the iterative method with regularization. In the optimization process, we use iterative Fourier transform algorithm (IFTA) that is known as Gerchberg-Saxton (GS) algorithm [5]. Designed and optimized DOE is fabricated by ultraviolet (UV) nanoimprinting technology [6]. High productivity can be expected by adopting nanoimprinting technology. DOEs are duplicated on the silicon (Si) substrate as reflection-type elements. In order to achieve large capacity, how small DOE can be fabricated is important. We attempt to produce the DOE has subwavelength structure.

2. DESIGN OF THE DOE

In this section, we explain design and fabrication process of the DOE. As discussed previously, we adopt GS algorithm for design and optimization. Designed DOE is formed as surface relief structure by ultraviolet (UV) nanoimprinting technology.

2.1. Design

Figure 1 illustrates the optimization procedure with GS algorithm. In the figure, U , A_t , A_s are complex wavefront, amplitude distribution at the target plane, and amplitude at the source plane, respectively. We set constraint conditions of the source and target, and the hologram is optimized in the iterative loop. In the loop, propagation and back-propagation of wavefront is calculated iteratively by angular spectrum method [7], and amplitude part of wavefront is replaced with the source and target constraint condition. On this occasion, phase part of wavefront is preserved. Iterative calculation is performed until convergence of the phase. Additionally, we adopt adaptive regularization parameter distribution (ARPD) [8] technique to suppress the oscillation and improve uniformity of the wavefront. The ARPD technique expresses as following equation

$$U_{n+1}(\mathbf{r}) = \begin{cases} \tau A_t \exp[i \arg(U_n)] + \left(1 - \tau - \tau \left\{ \frac{2\gamma}{\pi} \arctan \left[\frac{|U_n| - A_t}{A_t} \right] + \gamma - 1 \right\} \right), & \mathbf{r} \in S \\ U_n, & \mathbf{r} \notin S \end{cases}, \quad (1)$$

where, τ is the relaxation parameter, γ is a tuning parameter, index n is the iteration count, and S is the signal area. As a consequence, we obtain optimized hologram.

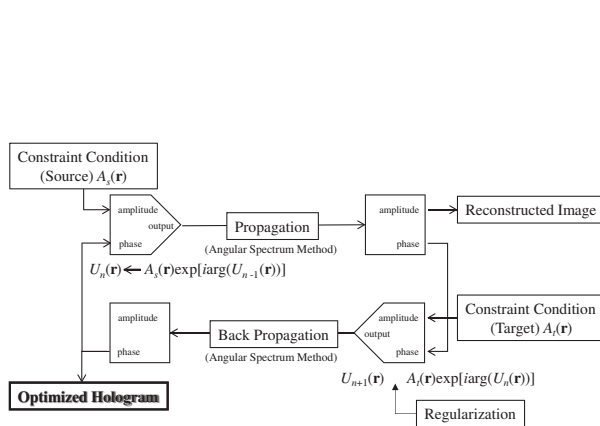


Figure 1: Optimization procedure of DOE.

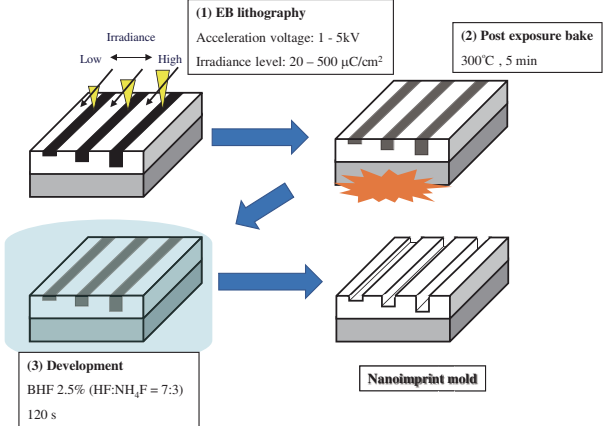


Figure 2: Manufacturing of nanoimprint mold.

2.2. Fabrication

Optimized hologram is quantized, and converted to the mask pattern for electron beam (EB) cutting. Molds for nanoimprint lithography are manufactured by EB cutting. The fabrication process of the mold consist of EB lithography, post exposure baking, and development process as shown in Fig. 2. The form of the mold is adjusted by switching the mask pattern. By using EB, high cutting accuracy can be actualized.

The DOE is fabricated by nanoimprint using the mold. Fig. 3 shows nanoimprint process. The mold is pressed into resist film, and the resist is exposed to UV. Hardened resist function as a DOE. The diagram of the reflective DOE on the Si substrate is shown in Fig. 4. As shown in the figure, phase of the hologram is expressed as height of the resist. In the figure, h is the height of resist and Λ is the pixel size. The height h is decided following equation

$$h = \frac{\lambda}{2(n-1)} \cdot \frac{\phi}{2\pi}, \quad (2)$$

where, λ is the wavelength, n is refractive index of resist, ϕ is phase of hologram. The height is formed in a step pattern with 4-stages by using 3 mask patterns.

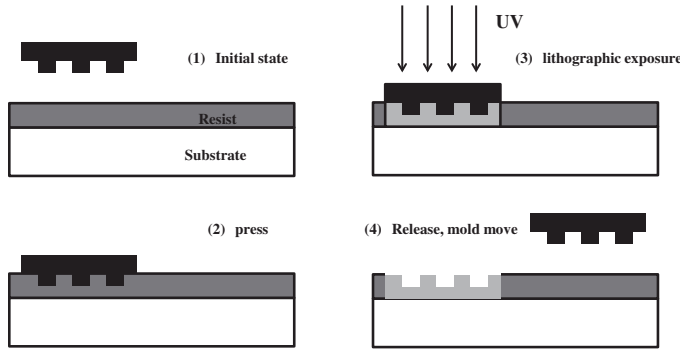


Figure 3: Nanoimprint process.

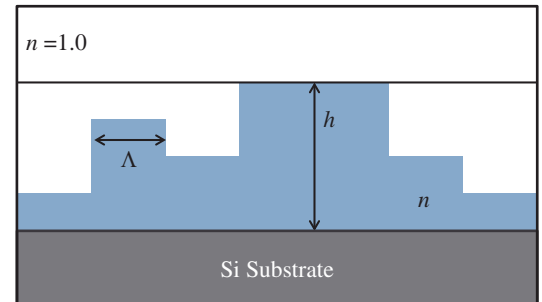


Figure 4: Diagram of DOE.

3. EXPERIMENTAL EVALUATION

Table 1 shows design conditions of the DOE, and Fig. 5 shows the target image. Pixel size of a DOE is a important factor that decides recording density. Therefore, we aim to produce the DOE with subwavelength structure and pixel size is set as 300 nm. The DOE is fabricated by nanoimprint lithography using optimized phase distribution. Optimized phase of the DOE is shown in Fig. 6. Optimized phase is quantized as 4 levels, and each quantized pattern is used as mask pattern for

EB cutting. Nanoimprint mold is manufactured according to lithography, baking, and development process as shown in Fig. 2. The DOE is fabricated with nanoimprint mold as shown in Fig. 3. We used PAK-01 (TOYO GOSEI Co. Ltd.) as nanoimprint resist. Refractive index of the resist is 1.52, and heights of surface relief h are 379.7 nm for $\phi = \pi/2$, 253.1 nm for $\phi = \pi$, and 126 nm for $\phi = 3\pi/2$ according to Eq. (2). Scanning electron microscope (SEM) image of the fabricated DOE is shown in Fig. 7.

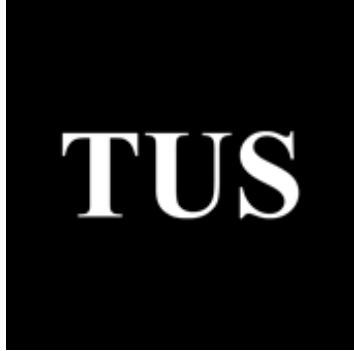


Figure 5: Target image.

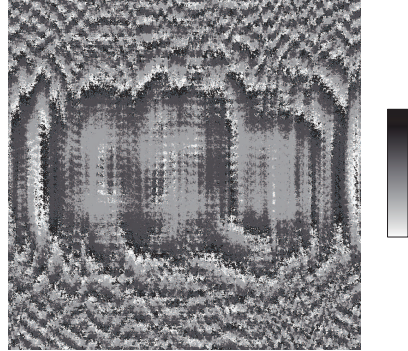


Figure 6: Optimized phase.

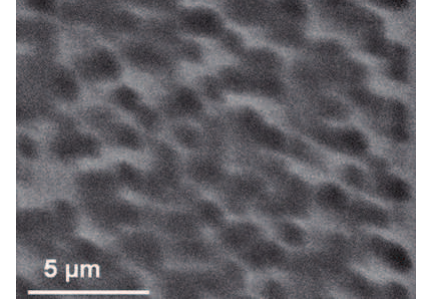


Figure 7: SEM image of DOE.

Table 1: Design and fabrication conditions.

DOE size	$300 \mu\text{m} \times 300 \mu\text{m}$
Pixel size Λ	$300 \text{ nm} \times 300 \text{ nm}$
Wavelength λ	405 nm
Working distance	5 mm
Quantization level	4
Acceleration voltage	10 kV
EB current	100 pA
Post exposure bake	300 °C
Resist thickness	1 μm
Development	Buffered HF 2.5%, 90 s
Release agent	Optool DSX 0.1% (Daikin Industries, Ltd.)
Nanoimprint resist	PAK-01 (TOYO GOSEI Co. Ltd.)

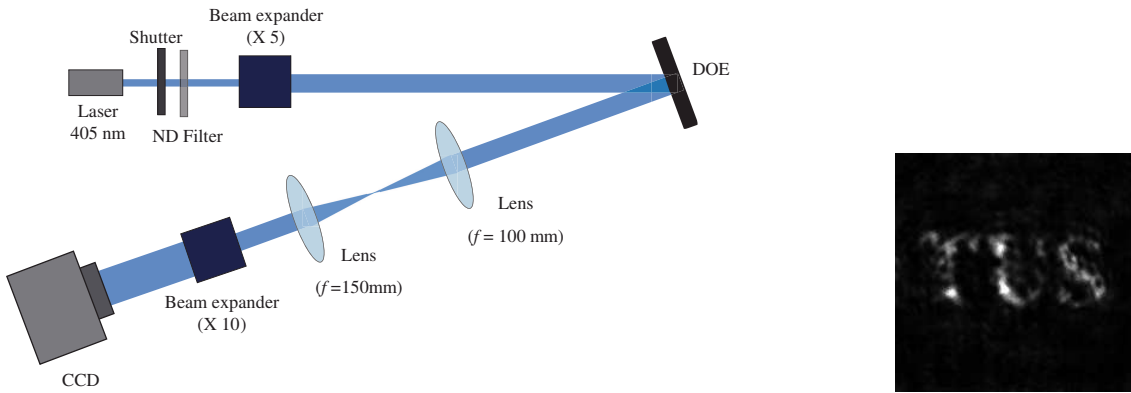


Figure 8: Experimental setup.

Figure 9: Reconstructed image.

Figure 8 shows the optical system for the evaluation experiment. We used a blue laser for readout of the DOE. The readout beam reflected by DOE is enlarged by beam expander and

lenses, and measured by the CCD. Reconstructed image by the experiment is shown in Fig. 9. The result shows that our approach is effective in principle. Especially, it is noteworthy that DOE with subwavelength structure can be actualized. However, we find room for improvement in image quality, and it is an issue in the future.

4. CONCLUSION

In this study, we consider capabilities of the ROM type HDS using the DOE. We designed the DOE by using GS algorithm and developed the trial model of ROM type HDS using nanoimprint lithography technology. We verify the effectiveness of our approach. Experimental results show our approach is effective. Especially, it is noteworthy that DOE with subwavelength structure can be actualized.

REFERENCES

1. Kress, B. C. and P. Meyrueis, *Digital Diffractive Optics: An Introduction to Planar Diffractive Optics and Related Technology*, Wiley, NY, 2010.
2. Psaltis, D., “Holographic data storage,” *Computer*, Vol. 31, No. 2, 52–60, 1998.
3. Coufal, H. J., D. Psaltis, and G. Sincerbox, *Holographic Data Storage*, Springer, Berlin, 2000.
4. Curtis, K., L. Dhar, A. Hill, W. Wilson, and M. Ayres, *Holographic Data Storage: From Theory to Practical Systems*, Wiley, NY, 2010.
5. Gerchberg, R. W. and W. O. Saxton, “A practical algorithm for the determination of the phase from image and diffraction plane pictures,” *Optik*, Vol. 35, No. 2, 237–246, 1972.
6. Chou, S. Y., P. R. Krauss, and P. J. Renstrom, “Imprint lithography with 25-nanometer resolution,” *Science*, Vol. 272, No. 5258, 85–87, 1996.
7. Goodman, J. W., *Introduction to Fourier Optics*, 3rd Edition, Roberts and Company, CO, 2004.
8. Kim, H. and B. Lee, “Iterative Fourier transform algorithm with adaptive regularization parameter distribution for optimal design of diffractive optical elements,” *Jpn. J. Appl. Phys.*, Vol. 43, No. 6A, L702–L705, 2004.

Multi-dimensional Shift Multiplexing for Holographic Data Storages

S. Yoshida, K. Yamamoto, H. Kurata, and M. Yamamoto

Tokyo University of Science, 6-3-1 Niijuku, Katsushika-ku, Tokyo 125-8585, Japan

Abstract— Holographic data storage (HDS) is a next-generation optical storage that uses the principles of holography. HDS recording density is potentially greater than that of a conventional optical disk. The multiplex holographic recording method is an important factor that affects the recording capacity of this storage. In this study, we focus on shift multiplexing with spherical waves and examined the possibility of high-density recording using this method. Since a spherical wave can be regarded in some locations as overlapping plane waves advancing in different directions, the shape of the diffraction grating recorded as a hologram is a function of the location in the recording medium. Therefore, multiplex recording is enabled in this system by simply displacing the recording medium. We propose a method of shift multiplex recording that combines the in-plane direction and depth direction of the recording medium. By focusing on the fact that shift selectivity is also in the depth direction, we examined the possibility of a multiplex recording method that combines multiple shift directions. We report on numerical and experimental evaluation results of our high-density recording and reproduction system based on this principle.

1. INTRODUCTION

Holographic data storage (HDS) [1–3] is a next-generation optical storage that uses the principles of holography. The multiplex holographic recording method is an important factor that affects the recording capacity of this storage. Various multiplex recording methods have been proposed so far. In this study, we focus on shift multiplexing with spherical waves [7] and examined the possibility of high-density recording using this method. We propose a method of shift multiplex recording that combines the in-plane direction and depth direction of the recording medium. In addition to those two types of direction, we combined with peristrophic multiplexing which is a recording method with rotating the medium.

By focusing on the fact that shift selectivity is also in the depth direction, we examined the possibility of a multiplex recording method that combines multiple shift directions and peristrophic method. We report on numerical and experimental evaluation results of our high-density recording and reproduction system based on this principle.

2. NUMERICAL EVALUATION

We have been developing HDS using shift multiplexing. In our simulation and experiment, holograms are recorded along three different directions which are x -axis (track direction), y -axis (horizontal direction) and z -axis (medium depth direction). Figure 1 shows the numerical evaluation for shift selectivity of each axis. This simulation is performed based on volume integral equation with Born approximation [4–6]. We assumed that wavelength is 405 nm and medium thickness is 1.5 mm. The vertical axis is normalized diffraction efficiency and the horizontal axis indicates shift value (μm). The shift selectivity of x -axis shown by red curve is about 3 μm , z -axis shown by green curve is about 5 μm , and y -axis shown in blue curve is much poorer than the other axis. The reason why the selectivity of y -axis is worse than the others is because Bragg condition only affects the plane which signal beam and reference beam create.

The characteristic feature of our method is using the depth medium direction. Making use of the depth direction, we can record holograms into some layers. Figure 2 shows the simulation result of diffraction efficiency when 2 layers holograms are recorded. 10 holograms are recorded at originally position which is $z = 0 \mu\text{m}$, after that other 10 holograms are recorded at the position $z = 200 \mu\text{m}$. This result indicates that it is possible to make records 2 layers so far without cross-talk.

3. EXPERIMENTAL EVALUATION

Our experimental setup is shown as Figure 3. Blue laser which is 405 nm is used for light source. The spherical reference beam is formed by using the objective lens which NA is 0.6. In this experiment, we verified 2 layers multiplexing, transmission and reflection type of recording, and peristrophic multiplexing with spherical reference beam.

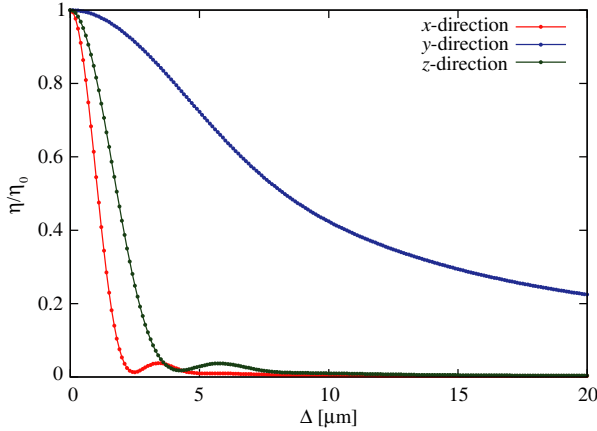


Figure 1: Shift selectivity of each direction.

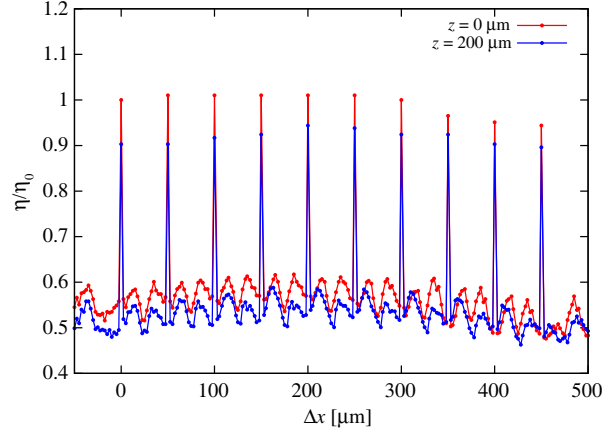


Figure 2: Write/read characteristics of multiplexing recording.

First of all, we examined about 2 layers multiplexing. shift-multiplexed holograms are recorded at primary position ($z = 0 \mu\text{m}$), after that another series of shift-multiplexed holograms are recorded at the position ($z = 200 \mu\text{m}$) by moving the recording medium. The red curve in Figure 4 shows the diffraction efficiency when 20 series of holograms were recorded at primary position ($z = 0 \mu\text{m}$) and the blue curve shows the diffraction efficiency when the other 20 holograms were recorded at the position ($z = 200 \mu\text{m}$) after initially recording. Each hologram is reconstructed independently without cross-talk. This results in the possibility of the recording track of a double layer system with changing the medium depth positions. The result of having conducted the record reproduction experiment of the double layer system on the actually same conditions as a simulation is shown in Figure 4. A simulation result similar with experimental result are obtained for the most part. However in both the simulation result and the experimentally result, the base noise level is increasing at $z = 0 \mu\text{m}$, and the analysis of the contents of this noise serves as a future subject.

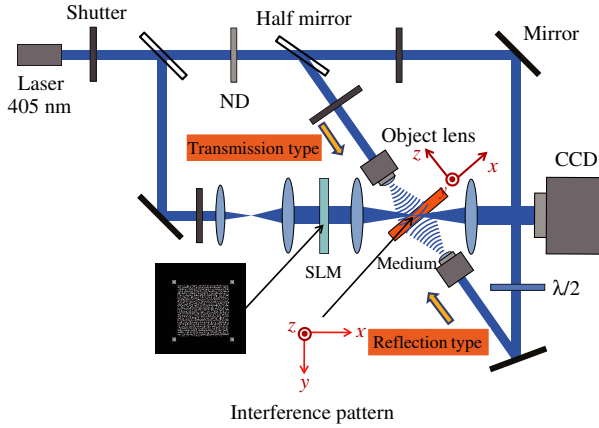


Figure 3: Experimental setup.

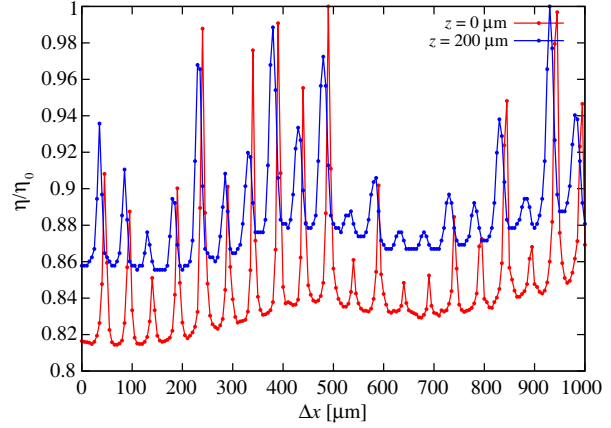


Figure 4: Multiplexing characteristics.

3.1. Transmission/Reflection Combination Recording

We examined the method using the transmission type recording together with the reflection type recording. This method has the advantage that the crosstalk does not appear even if the number of shift-multiplexed holograms increases because the directions of the interference fringe are different. Figure 5 shows the direction where an interference fringe is formed both transmission and reflection type of recording. Generally, it is a problem that noise increases and cross-talk appears when we write shift-multiplexed holograms with less than $5 \mu\text{m}$ shift pitch. However, this transmission/reflection combination recording has the advantage that the interval between holograms can be wider than conventional shift multiplexing because holograms are recorded both sides of the medium at the same place.

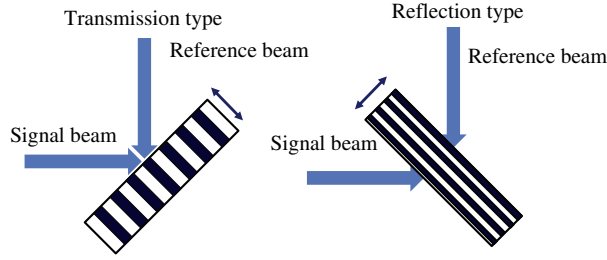


Figure 5: Grating of transmission and reflection hologram.

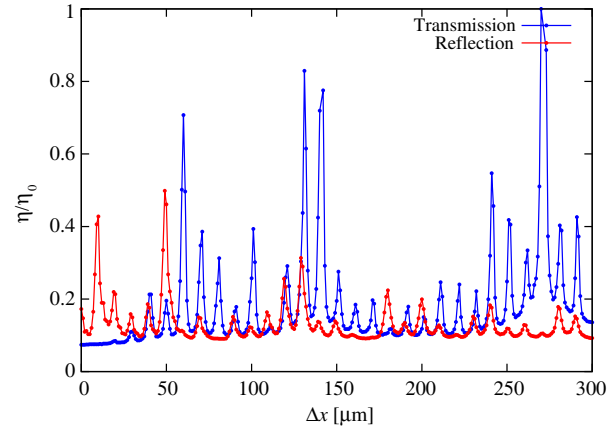


Figure 6: Characteristics of transmission/reflection combination recording.

In this experiment, we recorded 30 holograms with $10 \mu\text{m}$ shift pitch on rotating disk with transmission type of reference beam. After that we recorded 30 holograms with $10 \mu\text{m}$ shift pitch on rotating disk with reflection type of reference beam at the same spot previous holograms were recorded. Figure 6 shows relative amount of diffraction efficiency of transmission and reflective type recording. The vertical axis indicates normalized diffraction efficiency and horizontal axis indicates lateral shift pitch. SNR value of each hologram was enough for signal processing though the each hologram's diffraction efficiency did not stabilized. We can say that recording 30 holograms per sides at the same place of both sides with $10 \mu\text{m}$ shift pitch is same that we recorded totally 60 holograms with $5 \mu\text{m}$ shift pitch with only transmission type of recording.

3.2. Peristrophic Multiplexing with Spherical Reference Beam

This experiment examined the evaluation result of peristrophic multiplexing [8] with spherical reference wave. Figure 7 shows the principle of peristrophic multiplexing with spherical reference beam. Though conventional peristrophic multiplexing has been studied only using plane reference beam. We use spherical reference beam in order to combine with shift multiplexing. The rotation angle selectivity in peristrophic multiplexing using spherical reference beam shows in Figure 8. This graph shows next hologram can be recorded if rotation angle changed only 10 degree.

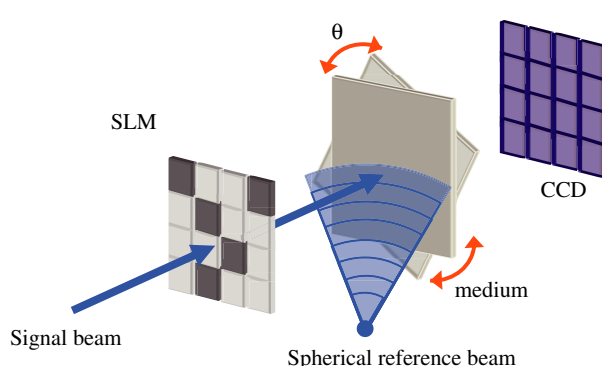


Figure 7: Peristrophic multiplexing with spherical multiplexing.

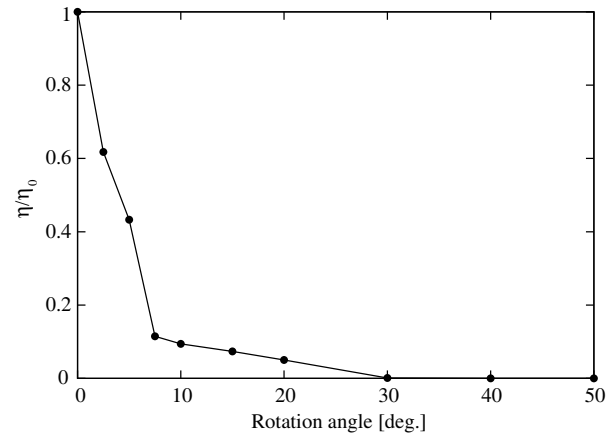


Figure 8: Rotational selectivity.

4. CONCLUSION

In this paper, we examined three kinds of experiments which are two layers recording, the method using the transmission type recording together with the reflection type recording, and peristrophic multiplexing with spherical reference beam to increase the storage capacity. Experimental results

indicated that the method using the transmission type recording together with the reflection type recording and peristrophic multiplexing are useful to increase the storage capacity. However two layers recording tend to raise noise levels as multiplexing hologram number increases. It is future problem about to lower noise. Combining these multiplexing method, we estimate that data capacity is over 1 TB/inch² or more.

REFERENCES

1. Psaltis, D., “Holographic data storage,” *Computer*, Vol. 31, No. 2, 52–60, 1998.
2. Coufal, H. J., D. Psaltis, and G. Sincerbox, *Holographic Data Storage*, Springer, Berlin, 2000.
3. Curtis, K., L. Dhar, A. Hill, W. Wilson, and M. Ayres, *Holographic Data Storage: From Theory to Practical Systems*, Wiley, NY, 2010.
4. Born, M. and E. Wolf, *Principles of Optics*, 7th Edition, Cambridge University Press, Cambridge, 1999.
5. Gombkötő, B., P. Koppa, P. Maák, and E. Lőrincz, “Application of the fast-Fourier-transform-based volume integral equation method to model volume diffraction in shift-multiplexed holographic data storage,” *J. Opt. Soc. Am. A*, Vol. 23, No. 11, 2954–2960, 2006.
6. Gombkötő, B., P. Koppa, A. Sütő, and E. Lőrincz, “Computer simulation of reflective volume grating holographic data storage,” *J. Opt. Soc. Am. A*, Vol. 24, No. 7, 2075–2081, 2007.
7. Barbastathis, G., M. Levene, and D. Psaltis, “Shift multiplexing with spherical reference waves,” *Appl. Opt.*, Vol. 35, No. 14, 2403–2417, 1996.
8. Curtis, K., A. Pu, and D. Psaltis, “Method for holographic storage using peristrophic multiplexing,” *Opt. Lett.*, Vol. 19, No. 13, 993–994, 1994.

On the Modeling of an External Cavity Tunable Laser ECTL Source with Finite Mirror Dimensions

Ahmed Fawzy¹, Salwa El-Sabban¹, Ibrahim Ismail¹, and Diaa Khalil²

¹Electronic and Communication Engineering Department, Faculty of Engineering
Helwan University, Helwan, Cairo, Egypt

²Electronic and Communication Engineering Department, Faculty of Engineering
Ain-Shams University, Abbassia, Cairo, Egypt

Abstract— In this work we study the diffraction effects on the performance of an external cavity tunable laser source taking into account the finite dimensions of the external mirror and in both strong and weak reflections regime. It is found that the strong reflection increases both the tuning range and the sensitivity. Taking into account the diffraction in the external cavity allows also better engineering of the ECTL dimensions.

1. INTRODUCTION

Communication, sensing and measurements are the three major application areas for tunable lasers [1–4]. In these directions, many specifications can be identified and the most important of them are the wide tuning range, high tuning speed and miniaturized device dimensions. These three specifications can be achieved using the Micro Electro Mechanical System (MEMS) technology.

MEMS technology makes use of photolithography to fabricate micromechanical structures, which are self-aligned and can be easily moved with fast response, high accuracy and enhanced mechanical stability. The MEMS technology can add a lot of features like the small size, low cost and weight as well as high tuning speed. For this purpose, MEMS based tunable laser structures have been proposed and tested in the literature using different structures [4]. These structures are mainly based on external cavity semiconductor laser in which the external cavity is formed by a moving MEMS mirror. One way to fabricate this moving mirror as well as its actuator is to use the Deep Reactive Ion Etching DRIE technology on SOI wafer. The objective of this paper is to study the diffraction in the MEMS based external cavity tunable laser source. For this purpose, a theoretical model is developed for the accurate simulation of the optical field propagation in the structure. The model is based on the use of an effective reflection coefficient to represent the external cavity using the plane wave expansion method. This effective reflection coefficient is then used for the calculation of the tuning range through an effective phase perturbation technique. In this technique we assume that the external cavity phase is a perturbation for the phase oscillation condition for the laser oscillator. Based on that, the new resonance frequency (emission wavelength) is then calculated as a function of the external mirror position and dimensions.

2. THEORETICAL MODEL

The studied configuration of the MEMS Tunable laser source is presented in Figure 1 with the external mirror assumed to have finite dimensions limited by the technological capabilities of the DRIE technology. In our formulation we assume that L is the primary cavity's length (containing the active medium), L_{ex} is the length of the external cavity, r_1 and r_2 are the reflectivities of the facets forming the original cavity and r_{2ext} is the reflectivity of external mirror. The external reflector can be combined with the second facet of the primary cavity yielding an effective reflectivity r_{eff} [5] that can be expressed as:

$$r_{eff}(\nu) = r_2 - \frac{1 - R_2}{r_2} \sum_{n=1}^{\infty} \left(-r_2 r_{2ext} e^{2i\theta_r} \right)^n \quad (1)$$

$$r_{eff}(\nu) = |r_{eff}| \exp(-j\phi_r) \quad (2)$$

r_{eff} , ϕ_r represent the amplitude and phase of effective reflectivity, R_2 is the power reflectivity of right facet of the primary cavity and θ_r represents the phase term corresponding to external cavity length at wavelength λ . In case of weak feedback, $r_{2ext} \ll r_2$ so we can neglect multiple reflection and can substitute in Equation (1) by $n = 1$. In case of strong feedback, $r_{2ext} \gg r_2$,

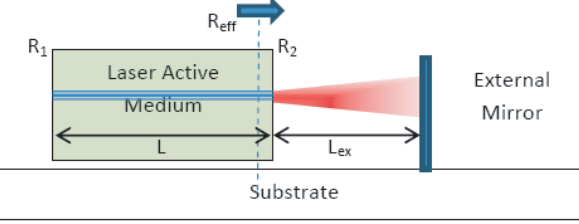


Figure 1: Schematic diagram of the studied ECTL source.

multiple reflections will affect the total amplitude and phase of effective reflectivity. As the optical frequency is mainly determined from the phase condition in the round trip of the laser cavity, we calculate the change in the round trip phase due to the existence of the external cavity. When this phase change is multiples of 2π , the oscillation condition can be satisfied again and a laser longitudinal mode oscillates. This change in the phase can be calculated as [6]:

$$\Delta\phi_l = 2\pi\tau_l (\nu - \nu_{th}) + \phi_r - \left[\alpha \left[\ln \frac{1}{r_1 |r_{eff}|} - \ln \frac{1}{r_1 |r_2|} \right] \right] \quad (3)$$

where τ_l is the round trip time delay of the optical beam inside the primary laser cavity given by: $\tau_l = \frac{2n_g L}{C}$ with n_g the group refractive index, ν is the new oscillation frequency and ν_{th} is the oscillation frequency before using an external cavity and α is the linewidth enhancement factor in the semiconductor material. From this relation, the frequency shift of the laser emission can be obtained as:

$$\text{Freq shift} = v - v_{th} = \frac{\left[\alpha \left[\ln \frac{1}{r_1 * (|r_{eff}|)} - \ln \frac{1}{r_1 * (|r_2|)} \right] - \phi_r \right]}{2\pi\tau_l} \quad (4)$$

This expression for the frequency shift is valid for both weak and strong feedback reflections. It can thus be used to study the effect of the diffraction on the frequency shift and hence on the resonance frequency of the laser.

To calculate this frequency shift, it is required to evaluate both the amplitude and phase of the reflected beam after travelling in the external cavity. For this purpose we use the plane wave expansion method. In this technique, the output beam from the active medium is analyzed as a superposition of plane waves. Each plane wave has its amplitude and phase determined from the field profile using the Fast Fourier Transform FFT technique. Propagation in the external cavity is represented for each plane wave component as a multiplication by a free space transfer function [7].

The total field composed of all the plan waves is then constructed again at the surface of the external reflector using the inverse Fourier transform IFFT to return to spatial domain. When the external mirror has finite dimensions, part of beam is reflected by mirror reflectivity and another part doesn't reflect due to finite mirror size and thus we have a truncated beam. The part that reflected from mirror is modulated by the shape of mirror. The reflected beam is then transformed again to the spectral domain and propagated in the free space as before. When arriving back to the laser diode surface, the beam is returned back to the spatial domain using the IFFT and its coupling to the cavity is calculated using the overlap integral with the cavity mode [8].

For the infinite mirror, the power coupling coefficient decreases as the length of the external cavity increases as shown in Figure 2. In our calculation we assume that the laser output is an elliptical Gaussian beam with a spot size of about $3.5 \mu\text{m}$ in the x direction and $1 \mu\text{m}$ in the y direction [9, 10]. The field distribution at the output of the laser diode can thus be expressed as

$$E(xy) = E_m e^{\frac{-x^2}{w_{ox}^2} + \frac{-y^2}{w_{oy}^2}} \quad (5)$$

where E_m is the field amplitude at the center of the beam, w_{ox} is the spot size in the x direction and w_{oy} is the spot size in the y direction and the beam phase front is assumed at the emitting edge of the laser diode surface. The laser source is emitting at the wavelength of 1550 nm . Because of the spot diffraction and in the absence of any focusing element, the external cavity length needs to be very short to maintain feedback efficiency acceptable. For a mirror with finite height, the power loss is more important as part of it is due to the diffraction effect and another part is due to truncation caused by the finite mirror height.

3. MULTIPLE REFLECTIONS

In the previous analysis we assume weak feedback with $|r_{2ext}| \ll |r_2|$ and thus, we assume only one round trip in the calculation. For an external mirror with high reflection coefficient, the optical beam intensity, after one round trip, may still be strong enough to perturb the operation of the laser. A model that accounts for the multiple reflections of the beam in the external cavity is thus developed. This situation is closer to the practical case as usually the mirror is coated by a metal to increase its reflection coefficient. We first examine the effect of multiple reflections on the laser performance when the external mirror reflection is weak and the obtained results are presented in Figure 3(a). It is clear that the effect of the multiple reflections on the frequency shift is nearly negligible as expected and the frequency shift is nearly sinusoidal with the external mirror position as predicted theoretically in Ref. 6 [11, 12]. On the other hand, when increasing the reflection coefficient of the external mirror to 0.5, we observe a change in the tuning behavior as the tuning is not symmetric with respect to the positive and negative frequency shift as seen in Figure 3(b). Also multiple reflections show a change in tuning sensitivity that can be expressed as the sensitivity of the wavelength to the mirror displacement $d\lambda/dx$ as can be seen in Figure 4 [3, 13]

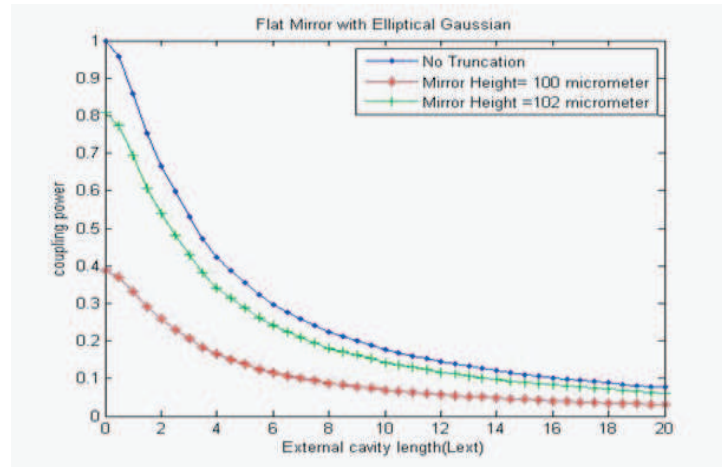


Figure 2: Power coupled from an external flat mirror back to an ECTL as a function of the external mirror position for different mirror dimensions.

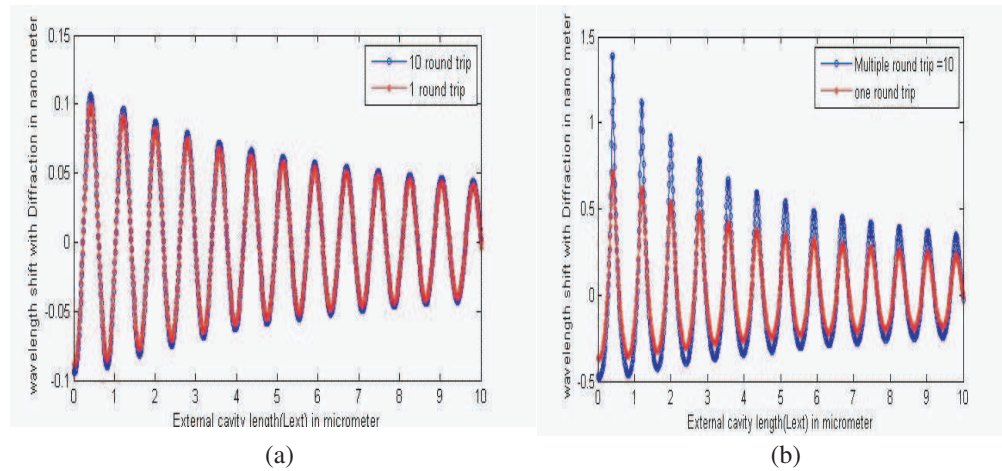


Figure 3: Comparison of Wavelength shift of an ECTL as a function of the external mirror position (a) for low reflection coefficient external mirror (0.1), (b) for moderate reflection coefficient external mirror (0.5).

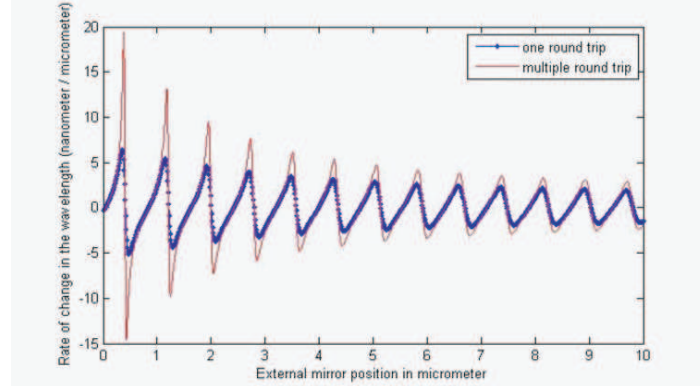


Figure 4: Comparison of wavelength variation predicted by the strong feedback model in case of one round trip and multiple round trips.

4. CONCLUSION

We developed a model to account for diffraction effects on the tuning behavior of an external cavity tunable laser. The model accounts also for strong and multiple reflections in the external cavity tunable laser. The model shows that strong reflection can increase the tuning range as well as the tuning sensitivity of the laser.

REFERENCES

1. Liu, A. Q., X. M. Zhang, V. M. Murukeshan, and Y. L. Lam, "A novel device level micro machined tunable laser using polysilicon 3D mirror," *IEEE Photon. Technol. Lett.*, Vol. 13, 427–9, 2001.
2. Zhu, W. M., W. Zhang, H. Cai, J. Tamil, B. Liu, T. Bourouina, and A. Q. Liu, "A MEMS Digital Mirror for tunable laser wavelength selection," *International Conference on Solid State Sensors and Actuators — TRANSDUCERS*, 2009.
3. Liu, A. Q., *Photonic MEMS Devices Design, Fabrication and Control*, CRC Press, 2009.
4. Liu, A. Q. and X. M. Zhang, "A review of MEMS external-cavity tunable lasers," *Journal of Micromechanics and Microengineering*, Vol. 17, No. 1, 2004.
5. Voumard, C., R. Salathe, and H. Weber, "Resonance amplifier model describing diode lasers coupled to short external resonators," *Applied Physics*, Vol. 12, No. 4, 369–378, April 1977.
6. Petermann, K., *Laser Diode Modulation and Noise*, Kluwer, London, 1988.
7. Saleh, B. E. A. and M. C. Teich, *Fundamentals of Photonics*, Wiley, 2007.
8. Solgaard, O., *Photonic Microsystems Micro and Nanotechnology Applied to Optical Devices and Systems*, Springer, 2008.
9. Bandres, M. A. and J. C. Gutiérrez-Vega, *Elliptical Beams*, Optical Society of America, 2008.
10. Marincic, A., "Huygens-Kirchhoff's theory in calculation of elliptical gaussian beam propagation through a lens," *Mikrotalasna Revija*, 2002.
11. Liu, A. Q., X. M. Zhang, D. Y. Tang, and C. Lu, "Tunable laser using micro machined grating with continuous wavelength tuning," *Applied Physics Letters*, Vol. 85, No. 17, 3684–3686, 2004.
12. Zhang, X. M., A. Q. Liu, D. Y. Tang, and C. Lu, "Discrete wavelength tunable laser using microelectromechanical systems technology," *Appl. Phys. Lett.*, Vol. 84, 329, 2004.
13. Heikkilä, V., J. K. Aikio, T. Alojoki, J. Hiltunen, A.-J. Mattila, J. Ollila, and P. Karioja, "Single-mode tuning of a 1540-nm diode laser using a Fabry-Pérot interferometer," *IEEE Photon. Technol. Lett.*, Vol. 16 1164–6, 2004.

Omnidirectional Absorber Based on Collision Plasma Heterostructures

Xiang-Kun Kong^{1, 2}, Shao-Bin Liu¹, Hai-Feng Zhang^{1, 3}, Bo-Rui Bian¹,
Hui-Chao Zhao¹, and Huan Yang¹

¹College of Electronic and Information Engineering

Nanjing University of Aeronautics and Astronautics, Nanjing 210016, China

²Jiangsu Key Laboratory of Meteorological Observation and Information Processing
Nanjing University of Information Science and Technology, Nanjing 210044, China

³Nanjing Branch, Artillery Academy of the PLA, Nanjing 211132, China

Abstract— A broadband omnidirectional absorber which is realized by hererostructures containing a collision plasma layer and a ternary plasma Bragg mirror is theoretically investigated. A collision plasma layer and an appropriate dielectric layer are put on the top of the ternary plasma photonic crystals to obtain a broadband omnidirectional absorption. It is shown to absorb roughly 70% of all available electromagnetic wave in a relative omnidirectional absorption band width 0.58 GHz with plasma width 3 mm in PCs. The band edges are impacted by the range of reflection band gap and the decrease of absorption range for TM wave at large incidence. This kind of hererostructures offer additional opportunities to design novel optoelectronic devices.

1. INTRODUCTION

High absorption efficiency is particularly desirable at present for various technologies such as photonic radiation detectors, efficient thermal emitters, and solar cells [1, 2]. Electromagnetic absorbers with enhanced absorption in a broad band or a wide range of angles of incidence have important applications such as electromagnetic invisibility cloak, aircraft stealth and functional detector/imager. To obtain high absorption, strong electromagnetic (EM) fields need be localized inside lossy materials.

In the past few years, much attention has been paid to design an absorber working at microwave band, terahertz wave band or light wave band. Since the pioneering work of Hojo et al. [3], the research on the plasma photonic crystals (PPCs) has enjoyed a rapid increase. As a type of metamaterial [4], plasma not only has a variable relative permittivity controlled by external parameters or even negative permittivity, but also can has a relatively high collision frequency comparable to plasma frequency. Therefore, it can combine with photonic band gap materials to form a broadband omnidirectional absorber. However, by far, no research on the broadband omnidirectional absorber based on a heterostructure composed of collision plasma layer and PPC has been conducted.

In this paper, a heterostructure contains a plasma film that has a relatively large collision frequency and a truncated one dimensional (1D) ternary PPC has been theoretically investigated. Under tunneling conditions, the localized EM fields can be formed for both transverse electric (TE) and transverse magnetic (TM) waves. Compared with the usual binary PCs, our previous work has proven that a ternary PPC have a superior feature in the enhancement of PBG and the modulation of the omnidirectional PBG [5]. Therefore, here, the width of the gap of the 1D PPC determines the width of the absorption band. If the 1D PPC has an omnidirectional gap, a wide total absorption band will be maintained for a wide range of incident angles. Specially, for TE waves, the absorption band is much broader at oblique incidence than it is at normal incidence.

2. TUNNELLING IN A COLLISION PLASMA LAYER PAIRED WITH A TERNARY PPC

Our previous research has proven that, compared with the usual binary PC, the ternary PPC has a superior feature in the enhancement of the high-reflection range and the modulation of the omnidirectional PBG [5]. Owning to the high reflective index contrast being realized by including plasma layer, the omnidirectional band gap utilized for absorption is obviously wider in ternary PPC than that in binary PC. In order to obtain a wider absorption band in the microwave frequency, we consider a heterostructure composed of a collision plasma film B and a truncated PPC denoted by $B(APC)^N$, where N is the periodic number. B and P are the plasma layers with different

permittivity described by the Drude model

$$\varepsilon(\omega) = 1 - \frac{\omega_{pe}^2}{\omega(\omega + i\nu)}. \quad (1)$$

Different from metal, here, $\omega_{pe} = \sqrt{n_e e^2 / m_e \varepsilon_0}$ is the electron plasma frequency being a function of the plasma density n_e and the collision frequency ν . Considering the density of non-fusion terrestrial plasmas ranges from 10^{15} m^{-3} to 10^{22} m^{-3} [6], the plasma frequency varies from $\omega_{pe} = 300 \text{ MHz}$ to $\omega_{pe} = 1 \text{ THz}$. A and C are the dielectric layers with low and high permittivity $\varepsilon_A = 2.56$ (polystyrene) and $\varepsilon_C = 21.16$ (tellurium), respectively. The thickness of A and C are selected to be $d_A = 15.2 \text{ mm}$ and $d_C = 6.4 \text{ mm}$, respectively. We choose cold, steady-state and collision plasma layer with $\omega_{peP} = 2\pi \times 15.9 \times 10^9 \text{ rad/s}$, $\nu_P = 2\pi \times 0.325 \times 10^7 \text{ rad/s}$ and $d_P = 3 \text{ mm}$, which is in the range of density of non-fusion terrestrial plasmas. The dispersion diagram of $(\text{APC})^N$ for both TE and TM waves are shown in Fig. 2 through the transfer matrix method [7]. The shaded region denotes the forbidden gap, which expands with the increase of plasma thickness. As is shown in Fig. 2, the frequency range from 7.85 GHz to 9.28 GHz indicated by the two dashed lines, are omnidirectional gap for all angles of incidence. When the frequency of incident wave is in this omnidirectional gap, the $(\text{APC})^N$ in the heterostructure denoted by $B(\text{APC})^N$, can be considered as a Bragg mirror.

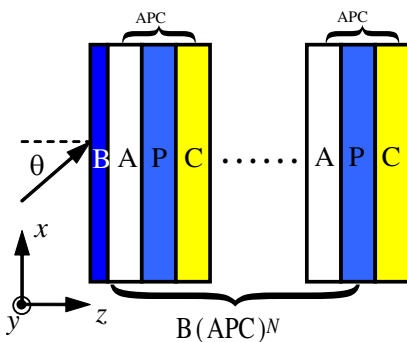


Figure 1: Schematic of the hetero-structure composed of a collision plasma and a ternary plasma. B and P is composed of unmagnetized plasma with different plasma frequency and collision frequency, A and C denotes two different dielectrics.

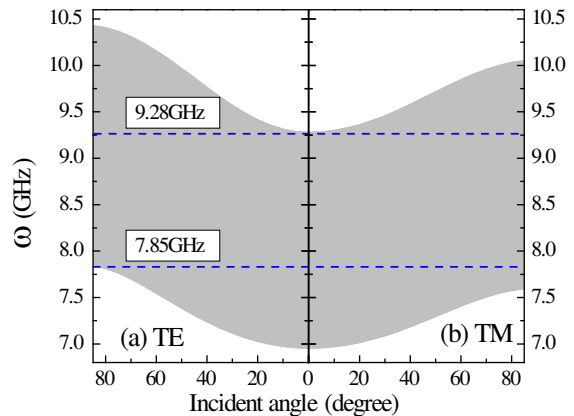


Figure 2: Dispersion diagram of $(\text{APC})^N$ for both TE and TM waves. In the region between the two dashed lines, an omnidirectional band gap exists.

3. OMNIDIRECTIONAL ABSORPTION BAND EXTENSION WITH A TOP APPROPRIATE DIELECTRIC LAYER

Next, we research on the extension of omnidirectional absorption in a wideband of frequencies and a large range of angles of incidence. The aforementioned results indicate that when the incident wave frequency is away from the tunneling frequency (ω_0), the absorption decreases.

Therefore, in order to realize the total absorption in a wideband, impedance matching with in the entire region of the gap of the ternary PPC should be met. Polystyrene is selected as the matching dielectric layer (denoted by D) that is also used to avoid plasma leakage. For the structure $DB(\text{APC})^N$, D and B are polystyrene layer and collision plasma layer with different thickness of $d_D = 3.638 \text{ mm}$ and $d_B = 3.3 \text{ mm}$, respectively. Figs. 3(a) and 3(b) show the spectra of absorbance (solid lines) of $DB(\text{APC})^N$ and reflectance (dashed lines) of $(\text{APC})^N$ for TE and TM waves at incident angles of 0° , 30° and 60° . As illustrated in Fig. 3, an omnidirectional absorption is realized for a broad band. Further, the absorption band is widened with the increase of incident angle for TE waves because the gap of the PPCs is broadened. The edges of absorption band coincide with those of the reflection band of the truncated PPCs. So the width of the photonic band gap determines that of the absorption band.

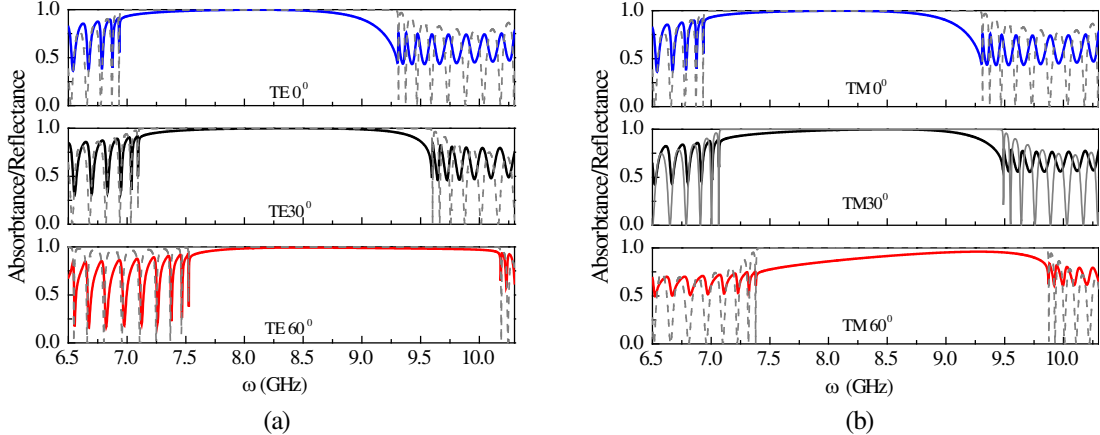


Figure 3: Absorbance (solid line) of DB(APC) 10 and reflectance (dashed line) of (APC) 10 as a function of frequency for TM and TE modes at incident angles of 0° , 30° and 60° . D is the matching dielectric film with $d_D = 3.64$ mm and $\epsilon_D = \epsilon_A$. $d_B = 3.3$ mm. All the other parameters are the same as those in Fig. 1.

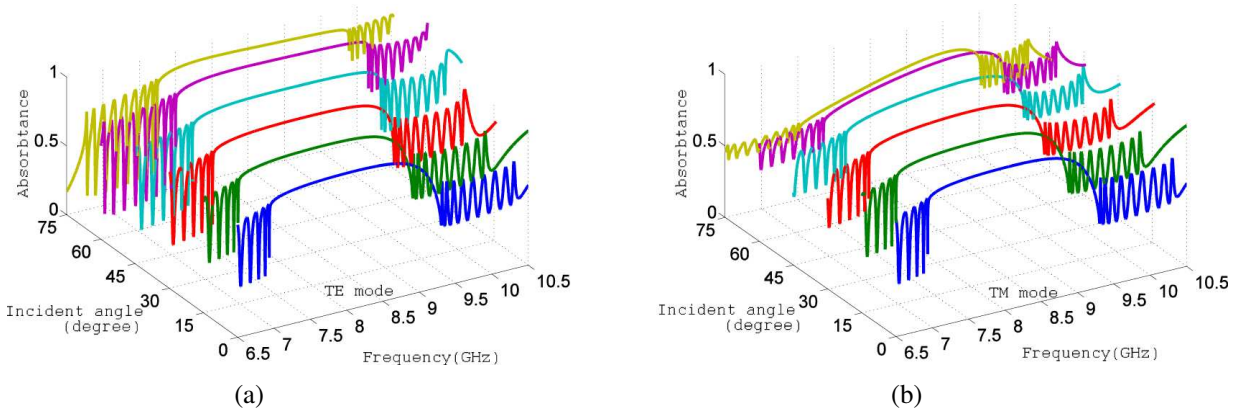


Figure 4: The absorbance as a function of the incident angle for the structure DB(APC) 10 for (a) TE mode and (b) TM mode.

All the results in Fig. 3 can be concluded in Fig. 4, in which the ternary PPC has a superior future in the enhancement of the absorption band. It is shown that the high absorption range shifts upward in frequency for both TE and TM waves when the incident angles increases. The high omnidirectional absorption band edge is primarily impacted by the band gap's high edge at normal incidence. However, owing to the reduction of the absorbance for TM wave at large incidence, the low one is impacted by the frequency in the absorption band. For example, the omnidirectional absorption band with absorbance over 70% is located from 8.64 GHz to 9.2 GHz with $d_P = 3$ mm, yielding an omnidirectional absorption bandwidth of about 0.58 GHz. The inclusion of a plasma layer causes the pass bands to be suppressed. As a result, the absorption band is increased. On the other hand, the absorption for TM wave at large incidence (75° incidence angle) can't be more than 80% in our research. Therefore, we only discussed the absorption band with absorption over 70%, which is an important criteria to evaluate an absorber.

4. CONCLUSIONS

In this paper, we have theoretically investigated a broadband omnidirectional absorber which is realized by hererostructures containing a collision plasma layer and a ternary plasma Bragg mirror. A collision plasma layer and an appropriate dielectric layer are put on the top of the ternary plasma photonic crystals to obtain a broadband omnidirectional absorption. The half-width of the absorption peak in the B(APC) N is much larger than that in the heterostructures B(AC) N . It is shown to absorb roughly 70% of all available electromagnetic wave in a relative omnidirectional absorption band width 0.58 GHz with plasma width 3 mm in PCs. The band edges are impacted by the range of reflection band gap and the absorption range for TM wave decreases at large

incidence. Compared with some previous conventional resonant absorbers, our proposed structure has a relative flatter total absorption spectrum over a broad frequency range in microwave. This kind of heterostructures offer additional opportunities to design novel optoelectronic devices.

ACKNOWLEDGMENT

We are grateful to the anonymous referees for their valuable comments and suggestions. This work was supported by the supports from Chinese Specialized Research Fund for the Doctoral Program of Higher Education (Grant No. 20123218110017), the Jiangsu Province Science Foundation (Grant No. BK2011727), the Foundation of Aeronautical Science (No. 20121852030), Open Research Program in Jiangsu Key Laboratory of Meteorological Observation and Information Processing (Grant No. KDXS1207) and Funding for Outstanding Doctoral Dissertation in NUAA (Grant No. BCXJ11-05).

REFERENCES

1. Yang, Z.-P., L. Ci, J. A. Bur, S.-Y. Lin, and P. M. Ajayan, “Experimental observation of an extremely dark material made by a low-density nanotube array,” *Nano Letters*, Vol. 8, 446–451, Feb. 1, 2008.
2. Garcia-Vidal, F. J., “Metamaterials: Towards the dark side,” *Nat. Photon.*, Vol. 2, 215–216, 2008.
3. Hojo, H. and A. Mase, “Dispersion relation of electromagnetic waves in one-dimensional plasma photonic crystals,” *Plasma Fusion Res.*, Vol. 80, 89–92, 2004.
4. Sakai, O. and K. Tachibana, “Plasmas as metamaterials: A review,” *Plasma Sources Science and Technology*, Vol. 21, 013001, 2012.
5. Kong, X. K., S. B. Liu, et al., “Omnidirectional photonic band gap of one-dimensional ternary plasma photonic crystals,” *Journal of Optics*, Vol. 13, 035101, 2011.
6. Bellan, P. M., *Fundamentals of Plasma Physics*, Cambridge University Press, Cambridge, 2006.
7. Orfanidis, S. J., *Electromagnetic Waves and Antennas*, Rutgers University Press, Piscataway, NJ, 2008.

Design of a Compact Dual-mode Dual-band Microstrip Bandpass Filter Based on Semi-fractal CSRR

Mushtaq A. Alqaisy¹, Jawad K. Ali², Chandan K. Chakrabarty¹, and Goh C. Hock¹

¹Department of Electronics and Communication Engineering

College of Engineering, Universiti Tenaga Nasional, Malaysia

²Microwave Research Group, Department of Electrical Engineering
University of Technology, Iraq

Abstract— Various complementary split ring resonators (CSRRs) are used as defected ground structures (DGSs) in the bandpass filter (BPF) design for different communication applications. In this paper, a hybrid CSRR has been introduced as a DGS in the ground plane of a dual-mode microstrip BPF to produce a new compact filter with dual band response. The proposed CSRR structure is essentially based on the conventional square double ring one, but with the inner ring made in the form Minkowski-like pre-fractal curve. Simulation and performance evaluation of the proposed filter have been carried out using a method of moment based EM simulator; the IE3D. Simulation results show that the resulting filter offers a dual passband response. The higher passband is attributed to the dual mode microstrip ring structure, while the lower passband is as a result of the embedded CSRR DGS structure, which implies an extra filter miniaturization. Results also show that the position of the lower passband could be varied, to certain extent, without affecting the position of the higher passband. This can be performed by the application of higher fractal iteration level to the inner split ring and/or dimension scaling of the whole CSRR structure. This feature makes the proposed filter suitable as a candidate for use in a wide variety of communication systems incorporating dual band operation.

1. INTRODUCTION

The conventional SRRs and CSRRs have been reported in [1–5] to design compact bandpass filters and microwave planar circuits. Hilbert fractal curve has been used as a DGS in the design of a microstrip lowpass filter operating at the L-band microwave frequency [6]. Sierpinski fractal geometry has been used in the implementation of a CSRR [7]. Split ring using square Sierpinski fractal curves has been proposed to reduce the resonant frequency of the structure and achieve improved frequency selectivity in the resonator performance. Minkowski, Koch and Peano fractal geometries have been successfully applied to the conventional square ring resonators to produce high performance miniaturized dual-mode microstrip bandpass filters [8–11]. Based on the conventional square patch, Sierpinski fractal curve has been applied to design a dual-mode microstrip bandpass filter [12]. Furthermore, other fractal geometries have been also adopted to design miniaturized dual-band dual-mode bandpass filters [13, 14].

On the other hand, split ring resonators, SSR, complementary split ring resonators, CSRR, and complementary single split ring resonators, CSSRR, have been used in the design of bandpass filters and band reject filters [15, 16]. On the basis of complementary split-ring resonator (CSRR) using Koch fractal curve, a bandpass filter based on such a structure is designed [15]. Hilbert fractal geometry has been applied as a DGS to produce miniaturized fractal spiral resonators [16].

In this paper, a compact dual-mode dual-band microstrip BPF, with its ground plane being defected using fractal based CSRR, is presented. The inner ring of the conventional square CSRR has been modified by applying Minkowski like pre-fractal curve to its sides. This results in a more compact microstrip BPF with dual passbands. The higher band is attributed by the dual-mode ring structure, and the other is a result of the embedded CSRR structure in the filter ground plane.

2. THE PROPOSED FILTER CONFIGURAION

The structure of the proposed filter consists of two parts as shown in Figure 1. The first part is the conventional microstrip dual-mode BPF configuration which constitutes the upper side of the whole structure. The second part represents the proposed CSRR as a DGS in the ground plane.

The details of the top dual-mode ring and the bottom CSRR structures are demonstrated in Figure 2. In fact, the dual-mode fractal based ring resonator, Figure 2(a), has been reported by one of the authors as a miniaturized dual-mode microstrip BPF [8]. The same filter structure is recalled here, but with the ground plane is perforated with CSRRs shown in Figures 2(b) and

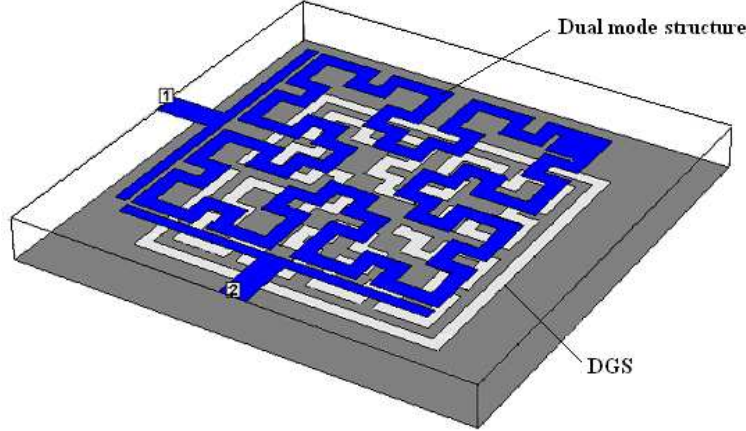


Figure 1: The layout of the proposed dual-mode dual-band BPF showing the top blue colored dual-mode structure and the bottom CSRR DGS in the ground plane.

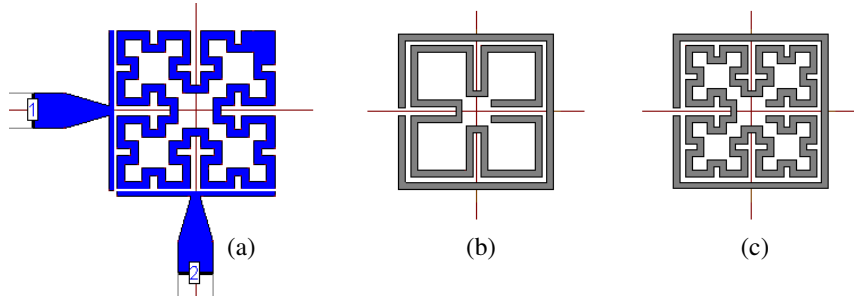


Figure 2: The proposed microstrip dual-band filter structure. (a) The dual-mode fractal based ring structure, (b) and (c) CSRR with Minkowski fractal shaped inner ring of the 1st and 2nd iterations respectively.

2(c). In practice, shape modification of the structure depicted in Figure 1(a) is a way to increase the surface current path length compared with that of the conventional square ring resonator; resulting in a reduced resonant frequency or a reduced resonator size, if the design frequency is to be maintained [8]. The same concept has been applied here to the conventional square CSRR so as to achieve further miniaturization.

It is expected then, that higher iterations will result in further miniaturization possibility owing to its extra space filling property. The increase in length decreases the required volume occupied for the pre-fractal bandpass filter at resonance. It has been found that [8, 17]:

$$P_n = \left(1 + 2 \frac{w_2}{L_o} \right) P_{n-1} \quad (1)$$

where P_n is the perimeter of the n th iteration pre-fractal structure, and w_2 and L_o are as depicted in Figure 3. Theoretically, as n goes to infinity, the perimeter goes to infinity. The ability of the resulting structure to increase its perimeter in the successive iterations was found very triggering for examining its size reduction capability as a microstrip bandpass filter. It should be reminded again that the same fractal has been applied to the dual-mode ring resonator (on the top of the filter structure) and the CSRR in the ground plane (on the bottom of the filter structure). However, this does not prevent the possibility to use other types of space filling fractal curves to achieve the same task.

3. THE FILTER DESIGN

The dual-mode fractal based microstrip ring resonator BPF with the ring has the structure corresponding to the 2nd iteration Minkowski pre-fractal geometry, Figure 2(a), has been designed for the ISM band applications at 2.45 GHz with its ground plane not defected. The filter structure has been supposed to be etched using a substrate with a relative permittivity of 2.65 and thickness of 1 mm. The input/output ports have 50Ω characteristic impedance. This corresponds to a trans-

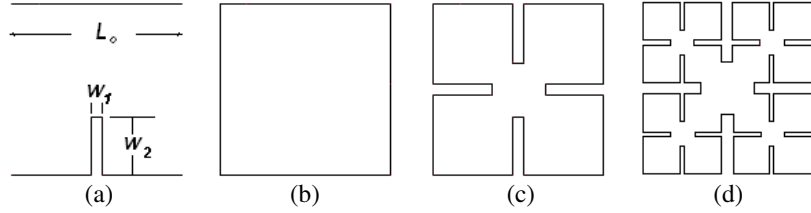


Figure 3: The generation process of the Minkowski-like pre-fractal structure, (a) the generator, (b) the square ring, (c) the 1st iteration, and (d) the 2nd iteration [8].

mission line width of about 2.8 mm. At resonance, the dual-mode resonator side length is found to be equal to 12.88 mm.

Based on this filter, two other filters with their ground planes being defected with the CSRRs corresponding to those depicted in Figures 2(b) and 2(c) have been modeled using the prescribed substrate. In both cases, the dimensions of the CSRR are such that the side length of the outer ring is exactly equal to that of the dual-mode resonator. The inner fractal shaped ring is a scaled down copy of the dual-mode resonator such that the spacing between the outer and the inner rings is found to be 0.5 mm to achieve the required coupling. The gaps in the two rings have been made equal to about 0.6 mm to reach the specified performance.

4. PERFORMANCE EVALUATION

At first, filter structure, depicted in Figure 2(a) with no CSRR in the ground plane, has been modeled and analyzed at the design frequency, using the commercially available EM simulator, IE3D [18]. This simulator performs electromagnetic analysis using the method of moments (MoM). The dual-mode resonator side length is found to be equal to 12.88 mm at resonance. This length represents about 0.15 the guided wavelength, λ_g , which is given by:

$$\lambda_g = \frac{\lambda_0}{\sqrt{\varepsilon_{eff}}} \quad (2)$$

where ε_{eff} is the effective dielectric constant, and can be calculated by empirical expressions reported in the literature [18]. However, most of the commercially available EM simulators can perform direct calculation of both λ_g and ε_{eff} , for given substrate parameters and the operating frequency. For the present case, λ_g has been found at the design frequency to be 82.74 mm.

Two other filters have been designed; both with the same dual-mode resonator depicted in Figure 2(a), but one of them has the DGS shown in Figure 2(b) while the other has the DGS shown in Figure 2(c). The corresponding simulation results of transmission responses of these filters are shown in Figure 4. It is demonstrated that the resulting pre-fractal based resonator bandpass filters offer adequate performance curves. As it is implied in Figure 4, the upper resonant band for the three filters, attributed by the dual-mode structure, is maintained; as if this resonator performs alone regardless of the existence of the DGS. The effect of the embedded CSRRs is confirmed by

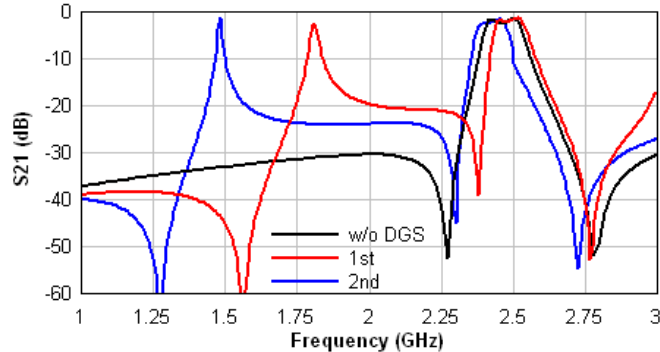


Figure 4: The simulated transmission S_{21} responses of the proposed filter without the DGS (black), and with DGS CSRR of the 1st (red) and 2nd (blue) iteration fractal curves depicted in Figures 3(c) and (d) respectively.

the appearance of the lower resonant bands. There is no such resonant band associated with the response of the filter with non-defected ground plane. Higher fractal iteration level of the CSRR leads to gain further miniaturization or, in other word, provides the designer with a practically useful means to tune the resulting filter response to the specified frequencies. The lower resonating bands as a result of the CSRRs depicted in Figures 2(b) and 2(c) are 1.81 and 1.45 GHz respectively. These are equivalent to size reductions, in terms of the corresponding guided wavelengths, of about $0.12\lambda_g$ and $0.09\lambda_g$ respectively.

5. CONCLUSIONS

A miniaturized dual-band microstrip BPF has been presented in this paper. Two miniaturization techniques have been simultaneously applied to construct this filter. The first is the use of the conventional dual-mode square ring resonator, and the other is application of a fractal based CSRR as a DGS in the filter ground plane. However, practical realization is required to confirm the results. Simulation results show that the proposed filter offers a transmission response with two passbands; the first one is that originally produced by the dual-mode ring resonator and the other is due to the DGS. The lower passband is that attributed by the CSRR. This means that the CSRR provides further miniaturization besides that produced by the dual-mode ring resonator. Simulation results show that two bands are independently produced. Application of higher fractal iteration levels results in further miniaturization depending on limitations imposed by the considered fabrication technique adopted to produce the filter prototype. It has been found that the frequency ratio of the two passbands can be varied to certain extent making the proposed filter suitable as a candidate for use in a wide variety of dual-band wireless applications. The proposed technique can be generalized to include other types of dual-mode BPFs to provide a suitable means of adding further resonant bands of these filters while maintaining their original sizes.

REFERENCES

1. Bonache, J., I. Gil, J. Garcia-Garcia, and F. Martin, “Complementary split rings resonators (CSRRs): Towards the miniaturization of microwave device design,” *Journal of Computational Electronics*, Vol. 5, 193–197, 2006.
2. Wu, G.-L., W. Mu, X.-W. Dai, and Y.-C. Jaio, “Design of dual-band bandpass filter with microstrip meander — loop resonator and CSRR DGS,” *Progress In Electromagnetics Research*, Vol. 78, 17–24, 2008.
3. Gil, M., J. Bonache, and F. Martin, “Ultra compact band pass filters implemented through complementary spiral resonators (CSRs),” *Proceedings of the IEEE MTT-S International Microwave Symposium Digest*, Bellaterra, Spain, June 2008.
4. Rodríguez, A., J. Selga, M. Gil, J. Carbonell, V. E. Boria, and F. Martin, “Automated synthesis of resonant-type metamaterial transmission lines using aggressive space mapping,” *Proceedings of the IEEE MTT-S International Microwave Symposium Digest*, Valencia, Spain, May 2010.
5. Aznar-Ballesta, F., O. Garcia-Perez, V. Gonzalez-Posadas, and D. Segovia-Vargas, “Recursive active filter with metamaterial unequal Wilkinson power divider,” *Proceedings of the 40th European Microwave Conference, EuMC*, Madrid, Spain, September 2010.
6. Chen, J., Z. B. Weng, Y. C. Jiao, and F. S. Zhang, “Lowpass filter design of Hilbert curve ring defected ground structure,” *Progress In Electromagnetics Research*, Vol. 70, 269–280, 2007.
7. Crnojevic-Bengin, V., V. Radonic, and B. Jokanovic, “Complementary split ring resonators using square Sierpinski fractal curves,” *Proceedings of the 36th European Microwave Conference, EuMC*, Manchester, UK, 2006.
8. Ali, J. K., “A new miniaturized fractal bandpass filter based on dual-mode microstrip square ring resonator,” *Proceedings of the 5th International Multi-Conference on Signals, Systems and Devices, IEEE SSD*, Amman, Jordan, July 2008.
9. Ali, J. K. and N. N. Hussain, “An extra reduced size dual-mode bandpass filter for wireless communication systems,” *PIERS Proceedings*, 1467–1470, Suzhou, China, September 12–16, 2011.
10. Ali, J. K., H. Alsaedi, M. F. Hasan, and H. A. Hammas, “A Peano fractal-based dual-mode microstrip bandpass filters for wireless communication systems,” *PIERS Proceedings*, 888–892, Moscow, Russia, August 19–23, 2012.
11. Ali, J. K. and N. N. Hussain, “A new fractal microstrip bandpass filter design based on dual-mode square ring resonator for wireless communication systems,” *Iraqi Journal of Applied Physics*, Vol. 5, 9–14, 2009.

12. Weng, M. H., D. S. Lee, R. Y. Yang, H. W. Wu, and C. H. Liu, "A Sierpinski fractal-based dual-mode bandpass filter," *Microwave and Optical Technology Letters*, Vol. 50, 2287–2289, 2008.
13. Liu, J. C., H. H. Liu, K. D. Yeh, C. Y. Liu, B. H. Zeng, and C. C. Chen, "Miniaturized dual-mode resonators with Minkowski-island-based fractal patch for WLAN dual-band systems," *Progress In Electromagnetics Research C*, Vol. 26, 229–243, 2012.
14. Ahmed, S. A., "Dual-mode dual-band microstrip bandpass filter based on fourth iteration T-square fractal and shorting pin," *Radioengineering*, Vol. 21, 617–623, 2012.
15. Li, T.-P., G.-M. Wang, K. Lu, H.-X. Xu, Z.-H. Liao, and B.-F. Zong, "Novel bandpass filter based on CSRR Koch fractal curve," *Progress In Electromagnetics Research Letters*, Vol. 28, 121–128, 2012.
16. Palandoken, M. and H. Henke, "Fractal spiral resonator as magnetic metamaterial," *Proceedings of Applied Electromagnetics Conference, AEMC*, Kolkata, India, December 2009.
17. Lee, E. C., P. J. Soh, N. B. Hashim, G. A. E. Vandenbosch, V. Volski, I. Adam, H. Mirza, and M. Z. A. A. Aziz, "Design and fabrication of a flexible Minkowski fractal antenna for VHF applications," *Proceedings of the 5th European Conference on Antenna and Propagation, EuCAP*, Rome, Italy, April 2011.
18. *IE3D User's Manual*, Release 12.3, Zeland Software, Inc., Fremont, CA, 2007.

Synthesis of Non-uniform Planar Lines and Coupled Line Filters Using Inverse Scattering Approach

Harishankar Prasad and M. Jaleel Akhtar

Department of Electrical Engineering, Indian Institute of Technology, Kanpur 208016, India

Abstract— A novel analytical approach for the synthesis of non-uniform planar line, and the coupled line filters is presented. The proposed method is based on the solution of the microwave inverse scattering problem, which requires the reconstruction of the impedance profile corresponding to the dimensions of the line in terms of its specified frequency response. For the synthesis of non-uniform line, the observed scattering coefficients are employed to reconstruct the impedance profile of the line, which is then transformed into the particular line geometry using the standard formulas. For the coupled line filter design, the procedure requires the synthesis of the parallel coupled line geometry in order to satisfy the specified frequency response over the given frequency band. The overall procedure requires the reformulation of Riccati equation in term of spectral domain reflection coefficient data and the impedance profile. The Riccati equation is solved using the renormalization approach in order to obtain a closed form expression of the impedance profile in terms of the inverse Fourier transform of the specified reflection coefficient data. The obtained impedance profile is then converted into the coupled line geometry using the available standard expressions. The advantage of the proposed approach is that even continuously varying transmission line structures can be designed and synthesized. The proposed approach is validated by designing a number of coupled line structures, and measuring the frequency approach of these structures using the network analyzer. A good match between the desired and obtained frequency response of these transmission line structures shows the applicability of the proposed approach.

1. INTRODUCTION

The design of filters in the RF/microwave frequency band is quite important as these filters play quite important role for many RF/microwave applications such as the microwave communication, radar, modern wireless communication etc.. The RF/microwave filters based on the planar technology is certainly advantageous because of smaller size, lighter weight, ease of fabrication and lower cost. The filters based on the coupled line topology are being used for certain applications, and the parallel coupled line microstrip filters proposed in [1] are amongst the most general used filters in microwave and radar engineering. In recent years, a number of methods have been developed to suppress the spurious transmission band [2] in parallel coupled microstrip filters. A number of standard methods to design various type of filters are available in text [3, 4], which usually start from the lumped design approach and then various forms of the transformation are being applied in order to make the design applicable for the RF/microwave frequency band.

In this paper, the inverse scattering approach is used to synthesize the coupled line geometry and filters. The advantage of the inverse scattering procedure as compared to the traditional low frequency approach for the filter design is that the line geometry can directly be obtained in terms of the desired scattering parameters, and planar lines of even continuously varying geometry can be reconstructed. The inverse scattering approach is usually being used to determine electrical properties of an object by illuminating it with electromagnetic wave and measuring scattering parameter of the scattered wave. The concept behind the microwave inverse scattering approach is to obtain the object's electrical and physical properties in terms of scattering parameters measured in the microwave frequency range using some appropriate reconstruction algorithm. This concept of inverse scattering is quite often being used in the field of microwave imaging and sensing problems, where the electrical/physical properties of an object are to be determined from measured scattering coefficients. In literature, one of the methods to solve one dimensional electromagnetic inverse problem is based on the solution of non linear Riccati differential equation using a renormalization approach [5, 6], where the basic idea is to obtain a unique closed form solution of the permittivity profile of the object in terms of measured scattering parameters [7]. In proposed work, the Riccati differential equation is reformulated in order to make them applicable for the analysis of planar structures. The inverse solution of Riccati equation is obtained using the renormalization technique in order to get closed form expression of the impedance profile in terms of inverse Fourier transform of the spectral domain reflection coefficient data. The impedance profile is then transformed into

geometry of the line corresponding to the coupled line structure satisfying the desired frequency response. The proposed approach provides an analytical solution, which is advantageous in terms of the stability and computational requirements as compared to some numerical optimization methods used by various authors in the past for the filter design using the inverse scattering approach [8, 9].

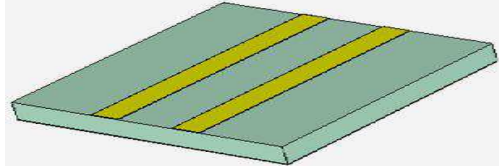


Figure 1: General microstrip coupled line.

2. THEORY

A typical microstrip parallel coupled line is shown in Figure 1. For known characteristics impedance Z_o and relative dielectric constant ϵ_r , the even mode impedances may be calculated as:

$$Z_{oe} = \frac{30\pi K(k'_e)}{\sqrt{\epsilon_r} K(k_e)} \quad (1)$$

where, $k_e = \tanh(\frac{\pi}{2} \cdot \frac{W}{b}) \cdot \tanh(\frac{\pi}{2} \cdot \frac{W+S}{b})$, and $k'_e = \sqrt{1 - k_e^2}$. Similarly, the odd mode impedance may be computed using the following expression:

$$Z_{oo} = \frac{30\pi K(k'_o)}{\sqrt{\epsilon_r} K(k_o)} \quad (2)$$

where, $k_0 = \tanh(\frac{\pi}{2} \cdot \frac{W}{b}) \cdot \coth(\frac{\pi}{2} \cdot \frac{W+S}{b})$, and $k'_o = \sqrt{1 - k_o^2}$. The expressions $K(k_e)$ and $K(k_o)$ in the above equations are the complete elliptical integral of the first kind. From above relations, the dimensions of microstrip may be calculated as

$$\frac{w}{b} = \frac{2}{\pi} \tanh^{-1} \sqrt{k_e \cdot k_o} \quad (3)$$

and

$$\frac{s}{b} = \frac{2}{\pi} \tanh^{-1} \left(\frac{1 - k_o}{1 - k_e} \sqrt{\frac{k_e}{k_o}} \right) \quad (4)$$

Now, for the parallel coupled microstrip filter, the physical length of coupled section are same for both the even and the odd mode. The coupling coefficient between parallel line is given as:

$$K_{n,n+1} = \frac{\text{BW}}{f_o \sqrt{g_n g_{n+1}}}. \quad (5)$$

Once the coupling coefficient is obtained, the dimensions of the microstrip line are computed using the standard curves [10].

3. THE DIRECT PROBLEM FORMULATION AND ITS INVERSE SOLUTION

The direct problem formulation requires the derivation of an equation relating the the impedance profile with the reflection coefficient data. This can be achieved by considering a half space inhomogeneous medium [5], where the impedance $\bar{Z}(x)$ varies continuously with respect to the distance x in the region $x \geq 0$, and the reflection coefficient $\Gamma(k_0)$ is measured at the input $x = 0$. For the planar structure, the half-space medium represents the nonuniform transmission line which is to be synthesized or designed. The Riccati differential equation for the reflection coefficient for these types of structures can be derived to have the following form:

$$\frac{d\Gamma(k_0, x)}{dx} = 2j\beta\Gamma(k_0, x) - \frac{1}{2} [1 - \Gamma^2(k_0, x)] \frac{d[\ln \bar{Z}(x)]}{dx} \quad (6)$$

where $\Gamma(k_0, x)$ is the local reflection coefficient, $\bar{Z}(x)$ is the normalized local intrinsic impedance, $\beta(k_0, x)$ is the local wave-number describing propagation along the x -direction, and k_0 is wave number of a monochromatic plane wave. The normalized impedance and the wave number are in general related to the impedance and the effective according to

$$\bar{Z}(x) = \frac{Z(x)}{Z_0} \quad \& \quad \beta(x) = \frac{k_0}{\bar{Z}(x)} \quad (7)$$

It may be noted here that in case of planar lines, the propagation constant can in general be defined in terms of the free-space wave number and the effective dielectric constant. It can be observed that (6) is a nonlinear equation, which does not have a generalized solution especially for solving the inverse problem. In the past, the inverse solution of the nonlinear differential equation given by (6) has been solved using the renormalization techniques as discussed in [5]. In this paper, the same approach has been used to solve the differential Equation (6) using appropriate boundary condition in order to obtain the expression of the spectral domain reflection coefficient defined at the input in terms of the impedance profile. For solving the inverse problem, the integral transform approach is used, which provides the expression for the impedance profile in terms of the inverse Fourier transform of the desired reflection coefficient data. A simplified form of the impedance profile can be derived to have the following form as a function of the electrical length, i.e.,

$$\bar{Z}(l) = \exp \left[2 \int_0^l \hat{r}(l') dl' \right] \quad (8)$$

where l is the electrical length depending upon the physical distance x and the dielectric properties of the substrate supporting the particular planar structure, $\hat{r}(l)$ is the input reflection coefficient transformed into the spatial domain using the inverse discrete Fourier transform, and l' is a dummy integration variable. The above equation assumes the impedance to be continuous at the interface between the unknown structure and the surrounding medium. In most of the planar structures including the microstrip line, the impedance of the connectors and cables are usually 50Ω at RF and microwave frequencies. Hence the filter and transmission lines are designed in such a way that a 50Ω impedance is maintained at the interface in order to avoid any reflection due to mismatch at the junction, and in this case the normalized impedance profile obtained using (8) should be multiplied with 50Ω in order to obtain the actual impedance profile. The impedance profile is finally transformed into the actual planar geometry using the standard formulas and curves as described earlier [4].

4. SIMULATION AND EXPERIMENTAL RESULTS

The proposed approach for the synthesis of nonuniform lines and coupled line microstrip filters is validated against both the independent simulation and the actual experimental data. The independent simulation in this paper is carried out using the CST microwave studio [11]. For the validation of our approach, firstly the synthesis of a continuously varying coplanar waveguide is

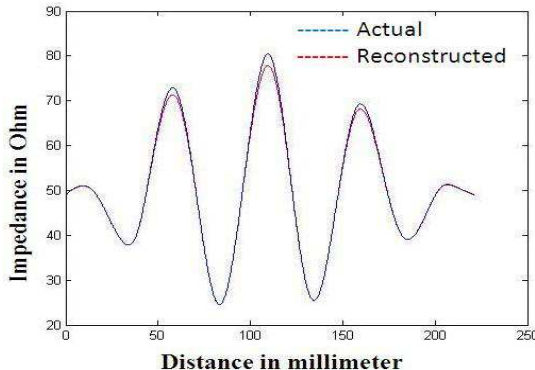


Figure 2: An impedance profile.

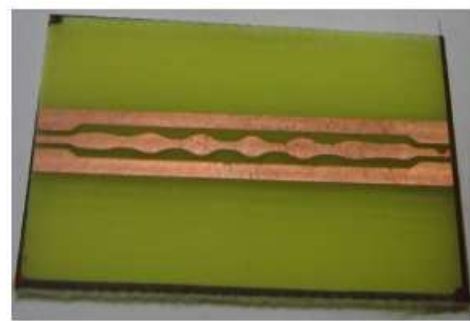


Figure 3: Fabricated structure of CPW on FR-4 substrate.

considered. The nonuniform coplanar line is simulated using the CST studio, and the reflection coefficient data obtained from the simulation is used in the proposed inverse algorithm to obtain the actual impedance profile of the line. This nonuniform line is then fabricated and the reflection coefficients of the fabricated line are measured, which are again used to reconstruct the impedance profile of this line. The actual and the reconstructed impedance profiles for this line are shown in Figure 2, where a good match between the two cases can be observed. The actual fabricated coplanar waveguide(CPW) is shown in Figure 3. After validity of proposed approach for synthesis of nonuniform line, a microstrip parallel coupled line band pass filter given in [4] has been designed on a FR-4 substrate having permittivity (ϵ_r) = 4.3 and substrate height as 1.0 mm. This filter is first simulated using the CST studio, and the frequency response of the simulated structure is shown in Figure 4. The simulated frequency response is used in the proposed inverse reconstruction algorithm in order to obtain the impedance profile, which is then transformed into the microstrip coupled line geometry using the standard curves. The obtained coupled line geometry is finally fabricated as shown in Figure 5. The scattering coefficients of the fabricated parallel line coupled filter shown in Figure 5 are then measured using the Agilent vector network analyzer, and the measured reflection and transmission coefficient data are shown in Figure 6. It can be observed from Figures 4 and 6 that the measured scattering coefficients of the designed filter match very closely with that of the simulated data thus verifying the accuracy of the proposed technique.

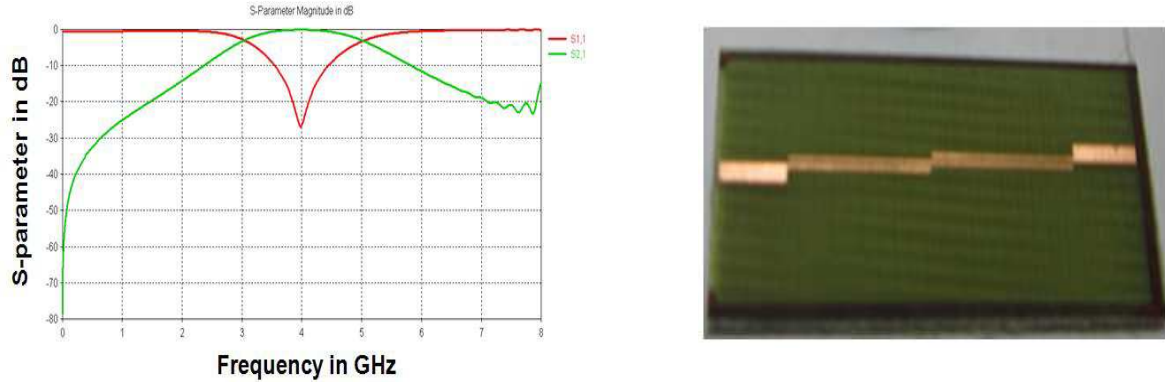


Figure 4: The scattering parameters of the simulated coupled line band pass filter.

Figure 5: Fabricated structure of coupled line filter : bpf 0 to 8 GHz.

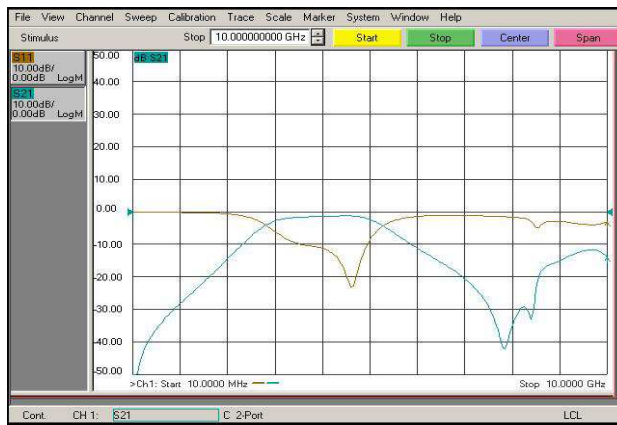


Figure 6: *S*-parameter of fabricated coupled line filter : bpf 0 to 8 GHz.

5. CONCLUSION

An analytical approach based on the microwave inverse scattering approach has been presented to design the microstrip coupled line filters working in the microwave frequency band. The presented technique is better than the conventional methods especially under situation where multiple discontinuities are present along the transmission line structure approximating a continuously varying

transmission line. The filters designed using the inverse scattering approach offer advantages such as the faithful frequency response over a wide frequency band, and no sharp impedance discontinuities. The proposed technique has been shown to be applicable to synthesize the structure of continuously varying transmission lines from the measured reflection coefficient data. The measured scattering data of the developed filters have been found to be within 2–3% of the specified frequency response.

REFERENCES

1. Cohn, S. B., "Parallel coupled transmission line resonator filters," *IEEE Transactions on Microwave Theory and Techniques*, April 1958.
2. Velazquez-Ahumada, M. C., et al., "Parallel coupled microstrip filters with floating ground plane conductor for spurious band suppression," *IEEE Transactions on Microwave Theory and Techniques*, Vol. 53, No. 5, May 2005.
3. Collin, R. E., *Foundation of Microwave Engineering*, McGraw-Hill, New York, 1966.
4. Pozar, D. M., *Microwave Engineering*, 3rd Edition, John Wiley and Sons, Singapore, 2004.
5. Akhtar, M. J. and A. S. Omar, "Reconstructing permittivity profiles using integral transforms and improved renormalization techniques," *IEEE Transactions on Microwave Theory and Techniques*, Vol. 48, No. 8, August 2000.
6. Akhtar, J., *Microwave Imaging: Reconstruction of One Dimension Permittivity Profiles*, Vdm Verlag Dr. Mueller, Germany, May 2008, ISBN 3639014553.
7. Cui, T. J. and C. H. Liang, "Novel application of an approximate profile inversion for one-dimensional medium," *IEEE Transactions on Antennas and Propagation*, Vol. 43, No. 3, March 1995.
8. Roy, M. L., Andre perennec, S. Toutain, and L. C. Calvez, "The continuously varying transmission line technique — Application to filter design," *IEEE Transactions on Microwave Theory and Techniques*, Vol. 47, No. 9, August 1999.
9. Roberts, P. P. and G. E. Town, "Design of microwave filters by inverse scattering," *IEEE Transactions on Microwave Theory and Techniques*, Vol. 43, 739–743, April 1995.
10. Wong, J. S., "Microstrip tapped line filters design," *IEEE Transactions on Microwave Theory and Techniques*, Vol. 27, January 1979.
11. CST Microwave Studio, Darmstadt, Germany, December 2011, available: <http://www.cst.com>.

Calculating the Scattering from Periodic Conducting Surfaces without Using Evanescent Modes, Part II: Formulation of the Solution

Dayalan Kasilingam and Christopher Goonan

Department of Electrical & Computer Engineering, University of Massachusetts Dartmouth, USA

Abstract— In part II of this paper, a new technique for finding the modal sub-space, which does not involve calculating the evanescent modes and is orthogonal to all the evanescent modes, is developed. In part I of this paper, the existence of this modal sub-space was shown. By projecting the boundary conditions on to this sub-space, the propagating scattered fields can be found in terms of the incident fields without calculating the evanescent modes. In this paper, it is shown that in the spectral domain, each mode resides in the null space of a matrix which depends only on the properties of the surface slopes and the components of the modal propagation constant. Since the method depends on the surface slopes, this technique works for surfaces with continuous slopes. The null space of each modal matrix is calculated and used to find the sub-space which is orthogonal to the evanescent modes. For this technique to be of practical value, it is critical that the method of finding the modal sub-space not involve calculating the evanescent modes directly. This technique accomplishes this by estimating the sub-space in terms of the propagation constants and surface slopes. The technique is shown to work for a variety of different surfaces with varying surface steepness. The proposed method reduces the computational complexity of the scattering problem significantly by eliminating the need for calculating the evanescent modes.

1. INTRODUCTION

The Rayleigh hypothesis for calculating the fields due to scattering from periodic surfaces was first formulated by Lord Rayleigh and applied to periodic gratings in the 1900's [1]. In the Rayleigh method, the fields are represented in terms of plane waves both above the periodic surface and inside the corrugated region of the periodic surface. Due to its compactness, the Rayleigh method is computationally more efficient than other semi-analytical methods such as the integral equation method [2]. However, in later years, the Rayleigh method was shown to be invalid for periodic surfaces with large steepness [3, 4]. Many researchers challenged Rayleigh's approach of using plane wave representations for the fields inside the corrugated region of the periodic surface. Several of these papers used extensive complex analysis to show that the solutions were unstable when the steepness of the periodic surface increased. However in the past decade, other researchers have shown that despite these apparent limitations, the Rayleigh hypothesis yields valid results even for steep surfaces [5].

In Part I of this paper [6], it was shown that the Rayleigh method can be used for calculating the fields from periodic conducting surfaces, using a modal sub-space which was orthogonal to all the evanescent modes. By projecting the boundary conditions on to this sub-space, it is shown that the propagating scattered fields can be found in terms of the incident fields. In the previous paper, this was accomplished by calculating the evanescent modes and using their functional form to derive the modal sub-space orthogonal to the evanescent modes.

In this companion paper, a new technique for finding the sub-space orthogonal to the evanescent modes without calculating the evanescent modes, is developed. For each Floquet mode [7], a matrix form of a difference equation whose null-space represents the functional form of that mode is derived. This matrix is generated using the modal propagation constants and the surface slopes. The proposed method reduces the computational complexity of the scattering problem significantly by eliminating the need for calculating the evanescent modes.

2. THEORY AND RESULTS

In this study, one considers scattering from a perfectly conducting, one-dimensional sinusoidal surface. For the purpose of clarity, the analysis will focus on horizontally polarized plane wave incidence. Figure 1 shows the incidence of the plane wave on the sinusoidal surface.

The surface profile is given by

$$h(x) = h_0 \cos k_L x, \quad (1)$$

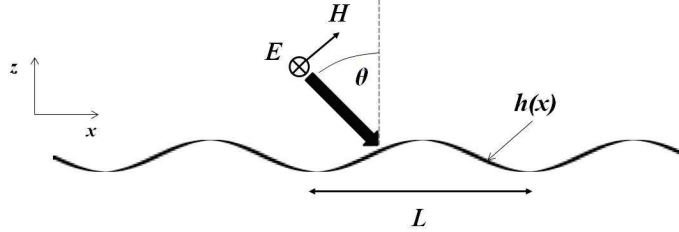


Figure 1: Geometry of the incident wave. The surface is a perfectly conducting sinusoidal surface. The periodicity is L .

where h_0 is the amplitude of the sinusoidal surface and $k_L = 2\pi/L$, where L is the periodicity. In the Rayleigh method, the fields are represented by discrete plane waves also known as Floquet modes [7]. The incidence fields are written as

$$E_i(x, z) = \hat{y} \sum_{n=-N_0}^{N_0} a_n \exp [-j(\alpha_n x + \beta_n z)], \quad (2)$$

where a_n is the amplitude and α_n and β_n are the x - and z -directed components on the propagation constant of the n th mode. α_n and β_n are given by $\alpha_n = 2\pi n/L$ and $\beta_n = \sqrt{k_0^2 - \alpha_n^2}$, respectively. $k_0 = 2\pi/\lambda_0$, where λ_0 is the electromagnetic wavelength. $2N_0+1$ is the total number of propagating Floquet modes (β_n is real) and depends on the magnitude of the periodicity, L , with respect to λ_0 . Similarly, the scattered fields can be written as

$$E_s(x, z) = \hat{y} \sum_{n=-N_0}^{N_0} b_n \exp [-j(\alpha_n x - \beta_n z)] + \hat{y} \sum_{|n|>N_0} c_n \exp [-j\alpha_n x - \gamma_n z], \quad (3)$$

where b_n and c_n represent the amplitude of the scattered propagating modes and scattered evanescent modes. The evanescent modes are non-propagating modes where $|\alpha_n| > k_0$ and $\gamma_n = \sqrt{\alpha_n^2 - k_0^2}$. The problem is solved by calculating the unknown amplitudes b_n and c_n by applying the boundary as follows,

$$E_i(x, h(x)) + E_s(x, h(x)) = 0. \quad (4)$$

Equation (4) can be solved using either the point matching method or the method of moments [2]. In the point matching method, the boundary condition is enforced at M observation points which are uniformly distributed across the surface, resulting in M linear equations. Using matrix representations these M equations can be written as

$$A\hat{a} + B\hat{b} + C\hat{c} = 0, \quad (5)$$

where \hat{a} , \hat{b} and \hat{c} are vectors representing the amplitudes of the incident mode, scattered propagating mode and scattered evanescent mode power waves, respectively.

If U is the basis representing sub-space orthogonal to the evanescent modes, then projecting Equation (5) on to this basis will yield

$$U^H A\hat{a} + U^H B\hat{b} = 0 \quad \text{or} \quad \hat{b} = W\hat{a}, \quad (6)$$

where $W = -(U^H B)^{-1} U^H A$ is the $(2N_0+1) \times (2N_0+1)$ scattering matrix which relates the scattered propagating modes to the incident modes. W is both unitary and symmetric, i.e., $W^H W = I$ and $W = W^T$.

The primary goal of this study is to find the basis, U , which spans the sub-space orthogonal to the evanescent modes without calculating the evanescent modes themselves. If U can be found directly, then one may use Equation (6) to solve the scattering problem without calculating the evanescent modes.

At the surface, each propagating mode can be represented as

$$\phi_n(x) = \exp [-j(\alpha_n x + \beta_n h(x))]. \quad (7)$$

Differentiating Equation (7), yields the first-order differential equation,

$$\frac{d\phi_n(x)}{dx} + j \left(\alpha_n + \beta_n \frac{\partial h}{\partial x} \right) \phi_n(x) = 0. \quad (8)$$

Since the boundary conditions are generally applied at discrete observation points, Equation (8) can be converted to a difference equation at each observation point. In the difference equation, the first derivative is replaced by the difference operator, K . The partial derivative, $\frac{\partial h}{\partial x}$, represents the tangent of the local surface slope and is represented by the function $s(x)$. Equation (8) is transformed into the spectral domain, by taking the Fourier transform and is now written as

$$jK\Phi(k) + j(\alpha_n I + \beta_n \bar{S}) \Phi(k) = 0 \quad \text{or} \quad (K + \alpha_n I + \beta_n \bar{S}) \Phi(k) = 0, \quad (9)$$

where the difference operator K is given by

$$K = \begin{bmatrix} \alpha_M & & & & \\ & \alpha_{M-1} & & & \\ & & \ddots & & \\ & & & 0 & \\ & & & & \ddots \\ & & & & & -\alpha_{M-1} \\ & & & & & & -\alpha_M \end{bmatrix}, \quad (10)$$

where M is determined by the number of observation points on the surface. $\Phi(k)$ is the spectral representation of the mode and is given by the Fourier transform of $\phi(x)$ and written as

$$\Phi(k) = F\phi(x), \quad (11)$$

where F is the Fourier operator. \bar{S} is a circular Toeplitz matrix obtained from the operation,

$$\bar{S} = F \text{diag}[s(x)] F^H \quad (12)$$

The operator \bar{S} represents the convolution operation between the spectrum of $s(x)$ and the modal function, $\Phi(k)$. The rows of \bar{S} are shifted versions of the spectrum of $s(x)$. Equation (9) shows that in the spectral domain, each mode resides in the null space of the matrix $A_n = (K + \alpha_n I + \beta_n \bar{S})$. Using Equation (9), the spectral representation of each mode can be found by estimating the null space of the matrix A_n . Since Equation (9) is the difference equation in the discrete domain which describes the first-order differential Equation (8) in the continuous domain, the nullity of A_n is unity. For evanescent modes, a similar matrix can be calculated and is given by $A_n = (K + \alpha_n I - j\gamma_n \bar{S})$.

It is important to note that finding the null space of A_n does not require calculating each mode directly. The matrix A_n depends only on the surface $s(x)$ and the propagation constants, α_n and β_n . Only the scalar quantities α_n and β_n need to be re-calculated for the different modes.

A sinusoidal surface with periodicity of $L = 5.5\lambda_0$, is used in simulations to test and verify this new technique. The scattered fields are calculated using the ‘full blown’ solution which is obtained by solving Equation (5) directly and using the ‘reduced’ solution which is calculated using Equation (9). In this paper, the ‘reduced’ solution is found by finding the null space of the matrix, A_n . In Part I [6], the ‘reduced’ solution was found by directly calculating the evanescent modes. The goal of this study is to reduce the computational complexity of the problem by estimating the sub-space orthogonal to the evanescent modes without calculating the evanescent modes directly.

Figure 2 shows the scattering patterns for different surface heights, using the ‘full blown’ solution and the ‘reduced’ solution. Clearly the two sets of solutions agree completely for three surface heights shown in Figure 3. This helps to verify the validity of the model by showing that by estimating the null space of the matrix A_n , the modal sub-space which is orthogonal to the evanescent modes can be found.

The power conservation test is used next to validate the ‘reduced’ solution approach. Figure 3 shows the power as a function of surface height. Shown in each figure is the power in the forward scattering component and the power in the backscattered component relative to the total incident power for both the ‘full blown’ solution and the ‘reduced’ solution. Clearly the results from the ‘reduced’ solution agree very well with the results from the ‘full blown’ solution. In Part I of this paper [6], scattered power calculations using the ‘full blown’ solution were generated to show the conservation of power. Figure 3 shows that the results obtained using the ‘reduced’ solution are consistent with those using the ‘full blown’ solution which has been tested and validated.

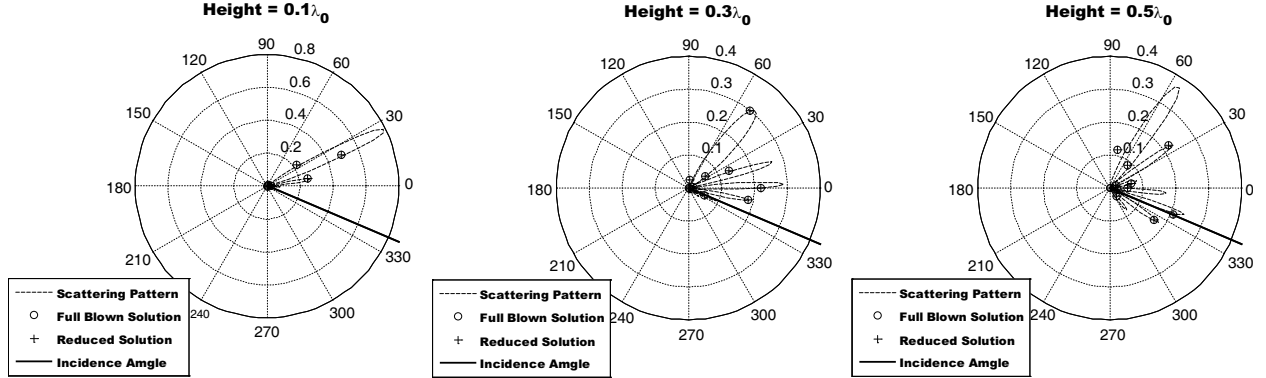


Figure 2: Scattering patterns calculated using the ‘full blown’ and ‘reduced’ solutions for different surface heights.

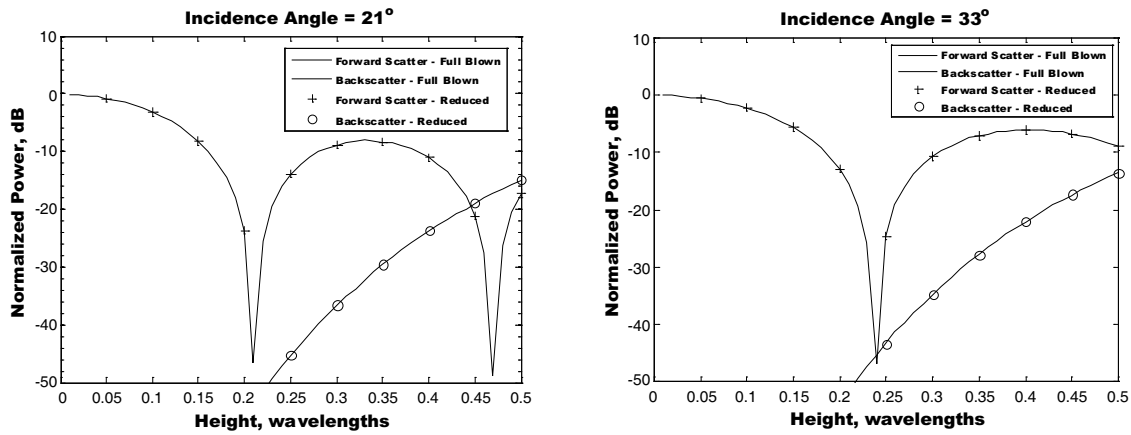


Figure 3: Scattered power relative to the total incident power as a function of surface height calculated using the ‘full blown’ solution and the ‘reduced’ solution.

3. CONCLUSION

In this paper, a new technique, for finding the finite dimensional sub-space which is spanned by the propagating Floquet modes and is orthogonal to all the evanescent modes, is developed. This sub-space is found without calculating the evanescent modes directly. The sub-space is found by estimating the one-dimensional, null spaces of a set of modal matrices which depend only on the properties of the surface slopes and the components of the modal propagation constant. By projecting the boundary conditions on to this sub-space, a set of equations which involve only the scattered propagating modes and the incident scattered modes is derived. The scattered propagating mode amplitudes are found in terms of the incident mode amplitudes and represented by a unitary scattering matrix which is also symmetric. Simulations show that the ‘reduced’ solution using the sub-space method agrees well with the ‘full blown’ solution which includes the evanescent modes. The proposed method reduces the computational complexity of the scattering problem significantly by eliminating the need for calculating the evanescent modes.

REFERENCES

1. Rayleigh, L., “On the dynamical theory of gratings,” *Proc. Royal Soc. A*, Vol. 79, 399–416, 1907.
2. Garg, R., *Analytical and Computational Methods in Electromagnetics*, Artech House, 2008.
3. Petit, R. and M. Cadilhac, “Sur la diffraction d’une onde plane par un réseau infiniment conducteur,” *C. R. Acad. Sci. B*, Vol. 262, 468–471, 1966.
4. Millar, R. F., “On Rayleigh assumption in scattering by a periodic surface,” *Proc. Camb. Phil. Soc.*, Vol. 65, 773–791, 1969.
5. Tishchenko, A. V., “Numerical demonstration of the validity of the Rayleigh hypothesis,” *Optic. Expr.*, Vol. 17, 17102–17117, 2009.

6. Kasingam, D. and C. Goonan, "Calculating the scattering from periodic conducting surfaces without using evanescent modes, Part I: Formulation of the solution," *PIERS Proceedings*, Stockholm, Sweden, August 12–15, 2013.
7. Eastham, M. S. P., "The spectral theory of periodic differential equations," *Texts in Mathematics*, Scottish Academic Press, Edinburgh, 1973.

Some Ideas Yet Unattempted in Georadar Full Waveform Inversion

G. Meles¹, S. Greenhalgh², H. Maurer², and A. Green²

¹School of Geosciences, University of Edinburgh

The Kings Buildings, West Mains Road, Edinburgh EH93JN, United Kingdom

²Institute of Geophysics, ETH Zurich, Sonneggstrasse 5, Zurich CH 8092, Switzerland

Abstract— Georadar full wave form inversion for elucidating the shallow subsurface is now commonplace. It yields significantly higher resolution images than conventional tomographic techniques based on first arrival times and pulse amplitudes, or reflection imaging techniques. Despite the successes, there are still a number of areas in need of extension or improvement. For a start, all approaches are generally based on a 2D model assumption. This assumption is often questionable but of equal concern is the infinite line source in the medium invariant (y) direction, which is implicit in 2D modeling. Actual antennae are better approximated as point sources, which give rise to quite different wave propagation characteristics. The 3D to 2D transformation filter which is normally applied to convert the point source field data to match the line source modeled data is strictly only valid in the far field for a homogeneous full space and does not account for interference effects in heterogeneous media. Nor are intrinsic 3D effects, like out of plane events (sideswipe) accommodated in the analysis. 3D and 2.5D inversion schemes are strictly needed but they are computationally demanding in terms of memory and run time. The 2.5D approach is a compromise approach when the assumption of a 2D model is valid, but it is still two orders of magnitude more demanding than 2D modeling.

In crosshole surveys, using vertical borehole dipole antennae, only TM modes involving both the vertical (z) and horizontal (x) components of the electric field in the medium, are taken into account, whereas in surface surveys in which the transmitter antenna can be oriented horizontally, TE modes with the electric field in the transverse y direction are exploited. Ideally, combined TE and TM mode inversions should be carried out, especially for borehole-to-surface experiments.

Nearly all GPR full waveform inversions are implemented in the time domain and assume constant (time invariant) values for the permittivity ϵ and conductivity σ at each cell. In the presence of material dispersion (frequency dependence of ϵ and σ) it is preferable to perform the inversion in the frequency domain where such frequency dependence can be readily accommodated. In the time-domain, it involves difficult and computer intensive convolutions. Other attractions of working in the frequency domain are that successful inversions can be achieved with just a few frequencies rather than the entire data as in a time domain approach, and the local minimum trapping problem is reduced by starting at low frequency.

An obvious future direction is to move away from gradient-based inversion schemes to more advanced Gauss-Newton or full Newton approaches. We have recently developed the necessary methodology for explicit computation of the Jacobian and pseudo-Hessian matrices but as yet have not implemented this approach because of the computational challenges associated with the large dimensions of the pseudo Hessian matrix to be inverted and multiplied. Emphasizing the later portions of the radargrams and compensation for radiation/reception pattern effects on sensitivity are also promising areas for further work. Without such time-variant boosting and gradient conditioning/normalization, the inversion is captured by the stronger direct arrivals and the more diagnostic later arriving reflected and diffracted signals are down-played.

Source signal estimation is a critical area in need of further research. Most finite difference time domain modeling schemes use what are called hard sources (impressing a specified electric field (or voltage) as a function of time at the source position in the grid), but the theory really requires that a soft source (impressing a given current density function) be used. To a first approximation, to generate the same electric field in the medium, the hard source has to be the time integral of the soft source waveform, but this is often overlooked. Transmitter and receiver coupling variations along the boreholes or at the surface of the Earth will cause different waveforms at each recording point and ideally these should be solved for in the inversion. A frequency-domain scheme to do this for seismic waveform inversion was recently developed by us and could be adapted to the GPR case.

1. INTRODUCTION

In recent years, we have developed improved 2D full waveform inversion methods for georadar data based on time domain solution of Maxwell's equations [10, 11]. They allow for simultaneous

inversion of both conductivity and permittivity parameters and honour the vectorial nature of the electric field in both the forward modeling and gradient calculations. Furthermore, they permit a progressive expansion of the bandwidth as iterations proceed, starting at low frequency, to tame the non-linearity local minimum trapping problem which afflicts all local search minimization inversion schemes. Several further developments are possible but because such scientific advances require considerable amounts of time and computer resources, they have not yet been implemented. Here we outline several of these possibilities. Some are merely technical, others are suggested from the seismic literature, whereas others are speculation.

2. COMBINED TE AND TM MODE INVERSION

For situations involving no model parameter variation in the y (or transverse) direction (i.e., 2D models) and for a constant source current distribution in this direction, two independent sets of field components (E_x, H_y, E_z) and (H_x, E_y, H_z) can be obtained. Therefore, for 2D simulations, the EM signal can be described as the superposition of decoupled TE and TM modes. In most GPR inversion schemes developed to date [6, 8, 10] the interest has been primarily on cross-hole imaging, so only TM modes involving the vertical component of the source electric field (corresponding to a borehole dipole transmitter) were taken into account. However, for surface surveys and borehole-to-surface surveys, in which the transmitter antenna can be oriented horizontally, TE modes with the electric dipole source oriented in the y direction could be profitably simulated and inverted [4]. Moreover, because TE modes only involve a single component of the electric field, namely E_y , only half of the memory requirements for TM modes are needed, thus enabling larger models to be inverted.

The implementation of TE modes in the inversion scheme of [10] would only involve a modest technical effort. An obvious next step would be to perform a combined TE and TM mode inversion, such as is commonplace in magnetotelluric investigations.

3. 3D AND 2.5D DATA INVERSION

All GPR full waveform inversions reported to date in the literature are based on 2D models, because simulations of GPR data would be extremely expensive for 3D models of realistic size. This, of course, makes the inversion of field data extremely problematic. The 2D assumption (medium properties invariant in the y -direction) is often questionable, but of equal concern is the infinite line source assumption that is implicit in 2D modeling. Actual transmitter antennae are much better approximated as point sources, which give rise to quite different wave propagation characteristics (spherical waves) compared to line sources (cylindrical waves). The current practice when inverting field data is to apply a crude 3D to 2D transformation (filter) that tries to convert the field data to 2D in order to match the modeled data [6]. The filter makes amplitude and phase adjustments to compensate for the differences between spherical and cylindrical spreading of the EM waves. Amongst others factors, the assumption of a scalar wavefield needs to be made. Therefore, for such single-component electric field data, the 3D to 2D transformation involved in real data inversion is probably more suitable than for the multicomponent TM modes.

Such approximation schemes are strictly only valid for a homogeneous full space in the far field and cannot adequately account for wave interference effects in heterogeneous media. Nor are intrinsic 3D effects, like out-of-plane events (sideswipe), accommodated in the analysis. The rapid growth in CPU performance and memory availability will likely make 2.5D or 3D inversion schemes feasible within a few years. The 2.5D approach is a compromise approach when the assumption of a 2D model is a valid approximation. It allows for the point source characteristic, by the artifice of constructing a spherical wave from a whole series of cylindrical waves. It entails taking a Fourier transform in the strike or y direction of the governing equations and then solving a whole series of 2D problems, one for each wavenumber. A final inverse Fourier transform of the various wavenumber spectra then yields the forward solution. As many as 50–200 wavenumbers may be required to obtain sufficient accuracy, so the computational effort (compared to 2D problems) is increased by approximatively two orders of magnitude.

4. OPTIMAL STEP LENGTHS BY PARABOLIC INTERPOLATION

In all current gradient-based inversion schemes, a line search algorithm is used for the determination of the step-length. The step-length ζ is found by following the approach introduced by [13], which

involves searching for a minimum of the objective function along the direction of the gradient:

$$S(\varepsilon + \zeta \nabla S_\varepsilon, \sigma + \zeta \nabla S_\sigma) \quad (1)$$

The function in (1) has just one independent variable (i.e., the step length ζ), whereas ε , σ , ∇S_ε and ∇S_σ are fixed.

A more complicated scheme than this can be considered. Because of the non-linearity of the forward problem, the one-variable function in (1) can be highly irregular, leading to local minimum trapping. At least on a broad scale, it is possible to assume a more regular trend of the misfit function (1). An alternative to the step-length defined in (1) of setting the first derivative to zero, an optimal value can be found by means of parabolic interpolation. This is illustrated schematically in Fig. 1. The cost function is evaluated at three different points, namely the current model (shown as the yellow dot) and two additional candidate points (shown in blue) along the gradient direction (i.e., at $(m, m + \lambda_1 \nabla S)$, and $m + \lambda_2 \nabla S$). The parabola that fits the three pairs of points $[m, \Phi(m)]$, $[m + \lambda_1 \nabla S, \Phi(m + \lambda_1 \nabla S)]$, $[m + \lambda_2 \nabla S, \Phi(m + \lambda_2 \nabla S)]$ is then constructed, and the model is updated at the optimal λ_{opt} extent corresponding to the minimum of such a parabola (the green point in Fig. 1). The extra computational effort needed to evaluate $\Phi(m + \lambda_1 \nabla S)$ and $\Phi(m + \lambda_2 \nabla S)$ could be compensated by faster convergence in the data space. The complexity of this scheme can be extended by considering additional search points, i.e., $(m + \lambda_i \nabla S)$ or by multiple choices of the search parameters λ_i . “An extension of this parabolic search method in global optimization was proposed by Bort et al. (2005) to mitigate the local minimum trapping problem”.

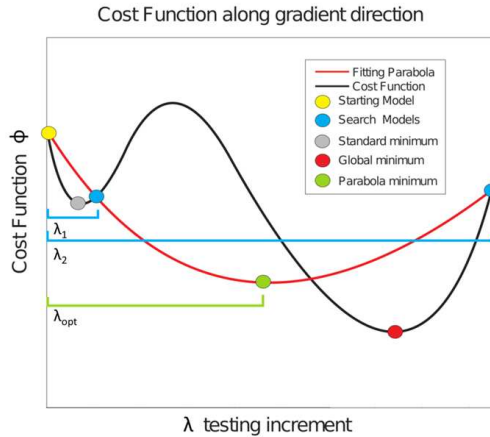


Figure 1: An optimal step-length can be determined by means of parabolic interpolation. The black line is the cost function along the gradient direction, whereas the curve shown in red is the parabola fit of the three points $[m, \Phi(m)]$, $[m + \lambda_1 \nabla S, \Phi(m + \lambda_1 \nabla S)]$, $[m + \lambda_2 \nabla S, \Phi(m + \lambda_2 \nabla S)]$. The yellow dot indicates the starting model, whereas the blue dots are selected search models along the gradient direction. The grey and green dots correspond to the standard and optimal updated models. The red dot indicates the global minimum along the gradient direction. The standard approach (grey dot) is caught in a local minimum.

5. TIME DOMAIN AND FREQUENCY-DOMAIN GAUSS-NEWTON INVERSIONS

The superiority of Gauss-Newton and full-Newton inversion schemes over gradient-based algorithms has been clearly demonstrated in a number of studies (e.g., [15]). The use of the inverse of the full Hessian matrix (full Newton approach) or the approximate Hessian matrix (Gauss-Newton approach) operating on the gradient of the cost function, as opposed to a simple step length multiplier (gradient approach) improves convergence in iterative inversion methods, focusing the gradient [14] and avoiding local minimum trapping, especially for highly-non-linear problems. Furthermore, Gauss-Newton and full Newton methods enable much more flexible regularization (damping, smoothing, and other constraints) compared to gradient-based methods which simply smooth the gradient. Because non-linearity is largely associated with the magnitude of the physical property contrasts and the degree of model complexity, Gauss-Newton and full-Newton methods extend the applicability of full-waveform inversion schemes to a much broader set of problems.

An obvious future direction concerns moving away from a gradient-based inversion scheme to a more advanced Gauss-Newton or full-Newton approach. The explicit sensitivity formulation presented by [12] provides the necessary methodology for the computation of the Jacobian (sensitivity)

matrix and related model appraisal. It will, therefore, allow time-domain Gauss-Newton inversion of GPR data, once a complete technical implementation is built. It should be appreciated, however, that the large dimensions of the pseudo-Hessian matrix to be inverted and multiplied would entail technical challenges, mainly associated with the current CPU and RAM limitations.

Further research could be devoted to a theoretical derivation of the second derivatives that form the elements of the full-Hessian matrix for the GPR case, based on an adjoint method. This has already been provided in the seismic case [1, 7] but has not yet been derived for the GPR case. The other promising option is to develop a frequency-domain Gauss-Newton or full-Newton inversion approach for GPR data. One attraction of working in the frequency domain is that successful inversions can be done with just a limited number of frequency components [9, 14, 16], rather than the entire data as in a time-domain approach. The forward modeling can be parallelised for each frequency component. Another advantage of working in the frequency domain is that material dispersion (i.e., frequency-dependent permittivity and conductivity) can be readily accommodated in this domain through the constitutive relationships, and the Green's functions need merely be multiplied with the source spectrum. By contrast, incorporating frequency-dependent electrical properties in the time domain involves difficult and computer-intensive convolutions. Recently, Felix has made a promising start in developing frequency-domain 2D inversion code.

6. EMPHASISING LATER PORTIONS OF THE WAVEFIELD AND RADIATION PATTERN COMPENSATION

In most situations involving full-waveform inversion, the cost function, which is a measure of the discrepancy between the simulated and the observed traces, is dominated by the direct transmitted wave. Because of the large amplitude differences between the direct wave and the later arriving reflected and diffracted signals, the inversion tends to minimize the misfit on the direct arrival and ignore the latter portions. Reflected events, despite their low amplitudes, are strongly indicative of the presence of any inhomogeneities (scatterers) in the medium. They are especially diagnostic in surface surveys where they constitute the real source of information. Different strategies can be considered in order to enhance the relative importance of this portion of the waveform and improve convergence in the model space.

We suggest two alternative strategies based on (1) time-variant amplitude boosting of the radarograms, and (2) gradient conditioning/radiation pattern normalization. The first approach is the most intuitive. It entails applying a gain function in order to increase the relative importance of later selected events. Such schemes are commonplace in seismic processing (migration procedures would not be effective without muting of direct arrivals (plus surface waves, guided waves, etc.) and enhancement of the weak reflection energy).

The second approach is more sophisticated than the first and could be applied to GPR data. It would quantitatively take into account the known radiation/reception patterns of the approximate dipole antennae and allow for these in the sensitivity calculations, as well as compensating for the geometric spreading of the wavefield (Gauthier et al., 1986). Such pre-treatment of the data would require almost the same computational effort as standard inversion.

7. HARD VERSUS SOFT SOURCES IN FDTD MODELING

Source implementations in FDTD modelling can be generally divided into two separate classes: a hard source, which consists of impressing a specified electric field (or voltage) as a function of time at the source position in the grid, or a soft source, which consists of impressing a given current density-time function (or antenna current) at the source position. The physical meaning of soft sources is well known, because current density J is commonly used in theoretical discussions of Maxwell's equations, where it appears explicitly as the right side source term, whereas no analytical solution or explicit expression exists for hard sources [5]. Hard and soft sources are differently implemented in FDTD modelling. Normally a hard source is assumed in GPR modeling and for a vertically oriented borehole, the value of the vertical electric field at the source position is set equal to a certain set of values at different times:

$$E_z^n(i_{trc}, j_{trc}) = E_s(t_n) \quad (2)$$

For soft sources, a more complex scheme is required (see [17]).

Hard sources are known to cause spurious reflections of fields propagating back at the transmitter location [3]. Soft sources, on the other hand, involve subtle problems in positioning of the Yee cell

and give rise to artificial non-propagating modes [17]. These modes, localized at the source position, exhibit substantial field divergence, implying charge deposition. In other words, with soft sources implemented numerically, transient or persistent artificial E - H fields can occur in the lattice, in addition to the desired propagating field; this affects the near-field only and can lead to errors of up to 20% of the corresponding analytical solution. It should be stressed that if the response to a specific electric current density J is desired, then only soft sources can be used.

A quantitative analysis of the relationship between hard and soft sources under special conditions is given by [5]. To a first approximation, in order to generate the same electric field in the medium, the hard source $I_H(t)$ has to be the temporal integral of the soft source waveform $I_S(t)$:

$$I_H(t) = \frac{1}{3\varepsilon_0\Delta x\Delta z} \int_{-\infty}^t I_S(t')dt' \quad (3)$$

Therefore, if we let \hat{G} and G denote the Green's operators for the two cases and we observe the

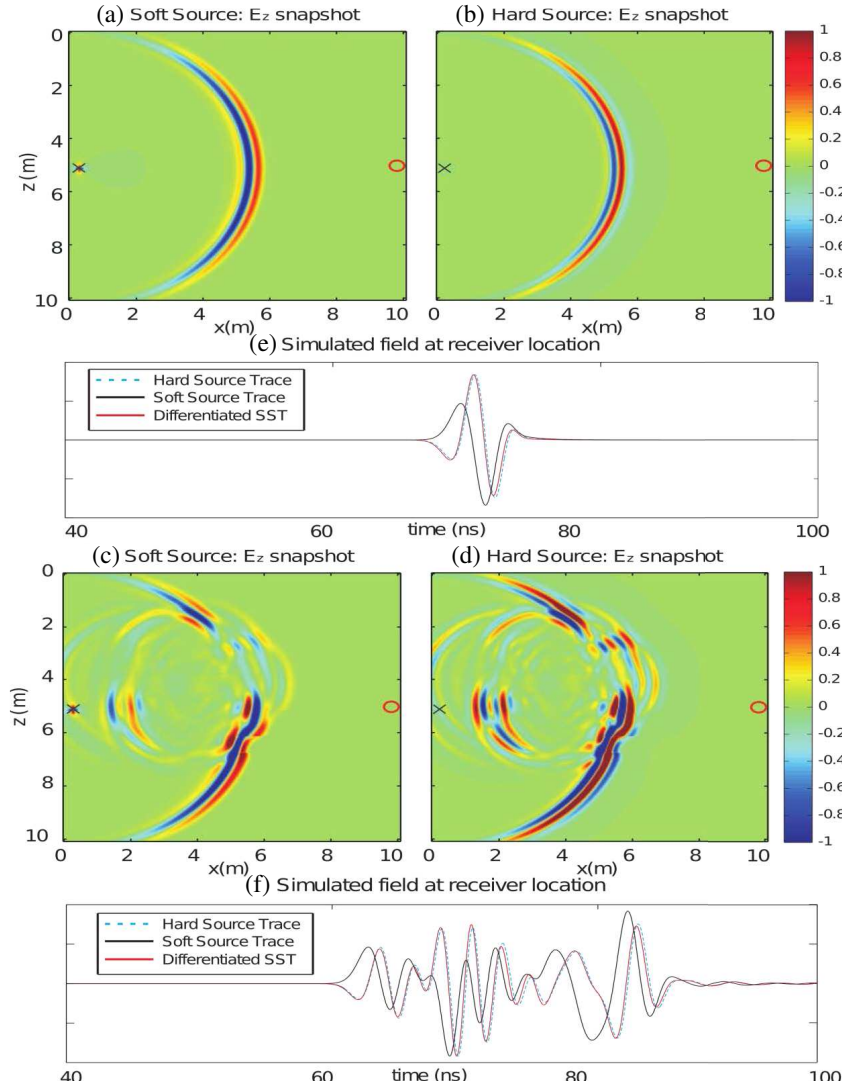


Figure 2: Snapshots of the vertical component of the E field corresponding to the same differentiated Gaussian pulse implemented as (a) a soft and (b) a hard source in a homogeneous model. Note the non-zero field in the proximity of the transmitter position in (a). (c) The corresponding radargram for the Tx and Rx indicated by a cross and circle. The dashed blue curve is for the hard source and the black curve for the soft source, whereas the red one is the derivative of the black curve. All curves are normalized. Note the large differences between the dashed blue and the black curves and the good fit between the dashed blue and the red curves in (c). (d)–(f), As for (a)–(c), but for a heterogeneous model.

same radargrams, i.e.,

$$\hat{G}(t) * I_H(t) = G(t) * I_S(t) \quad (4)$$

Then we have in the frequency domain

$$\hat{G}(\omega) \cdot \frac{I_S(\omega)}{i\omega} = G(\omega) \cdot I_S(\omega) \quad (5)$$

or

$$\hat{G}(\omega) \cdot I_S(\omega) = i\omega G(\omega) \cdot I_S(\omega) \quad (6)$$

Thus, we see that if the same source wavelet is used, then the hard source field can be found by time-differentiating the soft source field, as indicated in the frequency domain by $i\omega$ multiplication of the right side of (6). The red curve shown in Fig. 2(c) was obtained by differentiating the soft source trace, which corresponds to the right side of Equation (6). The dashed blue curve corresponds to the hard source trace and should be equal to the left side of Equation (6). Note the dashed blue and red traces are very similar. The experiment is for a heterogeneous double cross model discussed in [11]. The wavefields and the corresponding radar traces are shown in Figs. 2(d), (e) and (f). Again we see significant differences between the soft source (black) and hard source (dashed-blue) traces when using the same input signal, but upon differentiation of the soft source radargram (red trace) we obtain the approximate hard source trace (black). The large differences between the original dashed blue (hard source) and black (soft source) traces is strong justification for the need to implement soft sources when a proper characterization of the J term is given. However, we have shown that to a very good approximation we can obtain the radar traces for the hard source by temporal differentiation of the traces obtained for the soft source (red trace). This indicates that simple differentiation to a large extent properly accounts for the differences between soft and hard sources.

8. CONCLUSIONS

Future developments and implementations of GPR full-waveform inversion should be directed at 2.5D frequency-domain modeling, combined TE and TM mode exploitation, Gauss-Newton style parameter reconstruction, and boosting of later arrivals to compensate for reduced sensitivity. The forward modeling should also properly take into account the “soft” nature of the source.

REFERENCES

1. Bing, Z. and S. Greenhalgh, “Explicit expressions for the Fréchet and second derivatives in 2.5-D Helmholtz equation inversion,” *Geophys. Prosp.*, Vol. 47, 443–468, 1999.
2. Bort, E., G. Franceschini, A. Massa, and P. Rocco, “Improving the effectiveness of GA-based approaches to microwave imaging through an innovative parabolic crossover,” *IEEE Antennas and Wireless Propagation Letters*, Vol. 4, 138–142, 2005.
3. Buechler, D. N., D. H. Roper, C. H. Durney, and D. A. Christensen, “Modeling sources in the FDTD formulation and their use in quantifying source and boundary condition errors,” *IEEE Trans. Microwave Theory. Tech.*, Vol. 43, No. 4, 810–814, 1995.
4. Busch, S., J. van der Kruk, J. Bikowski, and H. Vereecken, “Quantitative conductivity and permittivity estimation using full-waveform inversion of on-ground GPR data,” *Geophysics*, Vol. 77, H79–H91, 2012.
5. Costen, F., J. P. Berenger, and A. K. Brown, “Comparison of FDTD hard source and FDTD soft source accuracy assessment in Debye media,” *IEEE Trans. Antennas & Prop.*, Vol. 57, No. 7, 2014–2022, 2009.
6. Ernst, J., A. G. Green, H. Maurer, and K. Holliger, “Application of a new 2D time-domain full-waveform inversion scheme to crosshole radar data,” *Geophysics*, Vol. 72, No. 5, J53–J64, 2007.
7. Fichner, A. and J. Trampert, “Hessian kernels of seismic data functionals based upon adjoint techniques,” *Geophys. J. Int.*, 775–798, 2010.
8. Klotzsche, A., J. van der Kruk, G. Meles, J. Doetsch, H. Maurer, and N. Linde, “Full-waveform inversion of crosshole ground penetrating radar data to characterize a gravel aquifer close to the Thur River, Switzerland,” *Near Surface Geophys.*, Vol. 8, 635–649, 2010.
9. Maurer, H., S. Greenhalgh, and S. Latzel, “Frequency and spatial sampling strategies for crosshole seismic waveform spectral inversion experiments,” *Geophysics*, Vol. 74, No. 6, 79–89, 2009.

10. Meles, G., J. van der Kruk, S. A. Greenhalgh, J. Ernst, H. Maurer, and A. G. Green, “A new vector waveform inversion algorithm for simultaneous updating of conductivity and permittivity parameters from combination crosshole/borehole-to-surface GPR data,” *IEEE Trans. Geosci. Remote Sens.*, Vol. 48, 3391–3407, 2010.
11. Meles, G., S. A. Greenhalgh, J. van der Kruk, and A. G. Green, “Taming the non-linearity problem in GPR full-waveform inversion for high contrast media,” *J. App. Geophys.*, Vol. 73, 174–186, 2011.
12. Meles, G., S. A. Greenhalgh, A. G. Green, H. Maurer, and J. van der Kruk, “GPR full waveform sensitivity and resolution analysis using an FDTD adjoint method,” *IEEE Trans. Geosci. Remote Sensing*, Vol. 50, No. 5, 1881–1896, 2012.
13. Pica, A., J. P. Diet, and A. Tranatola, “Nonlinear inversion of seismic reflection data in a laterally invariant medium,” *Geophysics*, Vol. 55, No. 3, 284–292, 1990.
14. Pratt, R. G., C. Shin, and G. J. Hicks, “Gauss-Newton and full Newton methods in frequency-space seismic waveform inversion,” *Geophys. J. Int.*, Vol. 133, No. 2, 341–362, 1998.
15. Sheen, D. H., K. Tuncay, C. E. Baag, and P. J. Ortoleva, “Time domain Gauss-Newton seismic waveform inversion in elastic media,” *Geophys. J. Int.*, Vol. 167, No. 3, 1373–1384, 2006.
16. Sirgue, L. and R. G. Pratt, “Efficient waveform inversion and imaging: A strategy for selecting temporal frequencies,” *Geophysics*, Vol. 69, No. 1, 231–248, 2004.
17. Taflove, A. and S. C. Hagness, *Computational Electrodynamics: The Finite Difference Time-domain Method*, Artec House Publishers, 2005.

Compton Effect in the Medium with Non-unity Refractive Index

S. G. Chefranov¹, A. G. Chefranov², and Vinay Venugopal³

¹A. M. Obukhov Institute of Atmospheric Physics, RAS, Moscow, Russia

²Eastern Mediterranean University, Famagusta, North Cyprus

³Division of Physics, VIT University, Chennai Campus, Chennai, India

Abstract— The foundations of the modern quantum theory of electro-magnetic radiation and its interaction with medium is constituted by the Einstein's theory of photo-effect and the theory of Compton effect. However, in the theory proposed by Compton and subsequent refinements, the medium features in explicit form are not generally accounted at all. This theory is based on the relationship between the photon momentum and its energy that may take place only in vacuum, but not in a medium with non-unity refractive index n . Here we use Abraham's representation for the momentum of a photon in medium for the creation of a new consistent Compton effect theory accounting for media features. A new condition under which anomalous Compton effect is possible, is defined. In our case, due to the photon scattering on a moving electron, the photon's energy can increase when the electron velocity is above a threshold value, in analogy with the Vavilov-Cherenkov radiation effect. In our theory we also provide a new description of the parameters for scattered electrons, which is important for the experimental determination of the dependence of the Compton effect in medium on refractive index n .

1. INTRODUCTION

Currently, the widely used electromagnetic field (EMF) theory in the medium is based on Minkowski's theory [1, 2] and its conclusions although more than forty years ago it's alternative Abraham's theory [3, 4] was confirmed experimentally. Actually, the experiments [5–7] could have ended the discussion that is on for the past sixty years on the so called Abraham-Minkowski dilemma since “the question is definitely solved on the benefit of Abraham's tensor” (see [8]), and Abraham's theory was accepted as the true one [8]. However, surprisingly Minkowski's theory up to now is not accepted as the false one and it continues to be used, as being “more convenient and even slightly differing from Abraham's theory in the most cases” [8, 9]. In the base of such positive relation to Minkowski's theory is as mentioned in [8, 9], its success in application of its conclusions to the building of quantum Vavilov-Cherenkov radiation (VCR) theory suggested by V. L. Ginzburg [8] in 1940 (see respective references in [8]), i.e., long before the experimental confirmation of Abraham's theory. More over, prior to appearance of the works [10–12], even attempts were not made based on Abraham's theory to create a quantum theory of VCR and its analogues including Compton effect in the medium theory. To do it, in [10–12] it was necessary to revise significantly the role of the medium energy change when a quantum of VCR is emitted, in spite of the fact that medium consideration as a direct VCR radiator was well known [13, 14]. Such accounting of the medium energy change while medium emitting a VCR quantum is not conducted in [8] and more over it is impossible, because of the complex value of effective photon rest mass which corresponds using in [8] a photon momentum in the medium representation based on the Minkowski's theory. When using in [10–12] (see also [15–17]) a photon momentum in the medium representation in a form corresponding to the Abraham's theory, there is no such difficulty since in this case photon in the medium effective rest mass value is real and has physical meaning. This, as it is shown in [10–12], is found to be important for the description of a non-stationary and non-equilibrium process defining physical mechanism and itself the threshold for VCR effect realization by the medium, contrary to the Tamm-Frank [13] VCR theory and corresponding to quantum VCR theory of Ginzburg which give only description of already stabilized equilibrium VCR field in the medium. The above mentioned “success” of Ginzburg quantum VCR theory is related in [8] with the presence of a correspondence of that VCR theory with initially stationary Tamm-Frank VCR theory [13]. This theories correspondence [8] and [12] now finds explanation on the base of conclusions of [18], where actually limits of the Minkowski theory applicability are established limiting the opportunity of its use only for the description of stabilized stationary electromagnetic processes with the medium participation.

Hence it is necessary to revise on the base of Abraham theory, all the theories for which the very non-stationary non-equilibrium effects of interaction of EMF and the medium may be essential. In

the present work (accounting conclusions of [19]) we propose a new Compton effect theory in the medium having refractive index n ($n > 1$ or $n < 1$) and the significant impact of that parameter on the experimentally measured values characterizing the effect is defined. Note that in [20], it is also proposed to account for the refractive index but without use of representation of photon momentum in the medium in the Abraham's form and without corresponding use of the finite and real photon rest mass in the medium with non-unity refractive index.

2. RESULTS AND DISCUSSION

Let us consider the energy-momentum balance equation for the Compton effect in the medium description. Energy-momentum balance equations are as follows:

$$\Delta E + E_1 + E_i = E_2 + E_r, \quad (1)$$

$$\vec{p}_1 + \vec{p}_i = \vec{p}_2 + \vec{p}_r, \quad (2)$$

where

$$\Delta E = (E_2 - E_1) \sqrt{n^2 - 1}/n, \quad n > 1 \quad (3)$$

is the energy change of medium (corresponding to the change of the value for rest mass of photon in medium with non-unity refractive index n), when a photon with energy E_1 is absorbed by medium and the photon with energy E_2 arises in this medium due to the interaction of absorbed photon with electron of medium that has initial energy E_i and momentum \vec{p}_i . In (1), (2), E_r, \vec{p}_r are energy and momentum of recoil electron in the corresponding Compton effect in medium with refractive index $n > 1$ (for $n < 1$, in all formulas n must be replaced by $1/n$).

In (1), (2), we use Abraham form for momentum presentation, when

$$p_1 = E_1/cn, \quad p_2 = E_2/cn, \quad \text{if } n > 1. \quad (4)$$

Also, for electron's momentum we have

$$p_i^2 c^2 = E_i^2 - m^2 c^4, \quad p_r^2 c^2 = E_r^2 - m^2 c^4. \quad (5)$$

If we consider the formula

$$p_r^2 = (\vec{p}_i + \vec{p}_1 - \vec{p}_2)^2 \quad (6)$$

on the basis of (1), (2), it is easy to obtain the following generalization for the Compton theory:

$$(N^2 - 1)(E_2 - E_1)^2 / 2mc^2 n^2 - N(E_2 - E_1)/n \sqrt{1 - V_i^2/c^2} \\ + (E_2 \cos \theta_2 - E_1 \cos \theta_1)V_i/nc \sqrt{1 - V_i^2/c^2} = E_1 E_2 (1 - \cos \theta)/mc^2 n^2 \quad (7)$$

In (7), V_i — is the value of initial electron velocity so that

$$p_i = mV_i / \sqrt{1 - V_i^2/c^2}, \quad (8)$$

$\theta, \theta_1, \theta_2$ — are the angles between \vec{p}_1 and \vec{p}_2 , \vec{p}_i and \vec{p}_1 , and \vec{p}_i and \vec{p}_2 respectively.

In (7), $N = n - \sqrt{n^2 - 1}$, where $N < 1$ for all n ($n > 1$ and for $n < 1$). We must also replace N on n if the value $\Delta E = 0$ in (1). Formula (7) may be presented in the form

$$(1 - N^2)x^2 - 2x \left(\frac{n(N - V_i \cos \theta_2/c)}{\varepsilon \sqrt{1 - V_i^2/c^2}} + 1 - \cos \theta \right) + 2(1 - \cos \theta) \\ = 2(\cos \theta_2 - \cos \theta_1)V_i n / c \varepsilon \sqrt{1 - V_i^2/c^2} \quad (9)$$

where $x = (E_1 - E_2)/E_1$, $\varepsilon = E_1/mc^2$. When in (9) $V_i = 0$ this formula is the same as (13) in [12] for the Compton effect in dielectric.

In the limit $(E_2 - E_1)/mc^2 \ll 1$ from (9) we have:

$$-x = (E_2 - E_1)/E_1 = \frac{V_i(\cos \theta_2 - \cos \theta_1)n/c - \varepsilon(1 - \cos \theta)\sqrt{1 - V_i^2/c^2}}{(N - V_i \cos \theta_2/c)n + \varepsilon(1 - \cos \theta)\sqrt{1 - V_i^2/c^2}} \quad (10)$$

Thus, anomalous Compton effect is realizable if the right hand side of (10) is positive, i.e., when the following inequalities are true:

$$n(V_i \cos \theta_2/c - N) < \varepsilon(1 - \cos \theta) \sqrt{1 - V_i^2/c^2} < V_i n(\cos \theta_2 - \cos \theta_1)/c, \quad (11)$$

or

$$n(V_i \cos \theta_2/c - N) > \varepsilon(1 - \cos \theta) \sqrt{1 - V_i^2/c^2} > nV_i(\cos \theta_2 - \cos \theta_1)/c. \quad (12)$$

From the condition providing positiveness of the left hand side of inequality (12) and its holding in principle, the restriction on the value of angle θ_2 follows that coincides with the VCR realization condition obtained in [10-12] and having the form:

$$1 > \cos \theta_2 > Nc/V_i; \quad 1 > \beta = V_i/c > N \quad (13)$$

Thus, as noted in [12], analogy of VCR effect and Compton effect is exhibited also in the form of necessary condition of realization of anomalous Compton effect in the form of inequality (13).

Because all the momentum vectors in (2) are in the same plane (only in the special case of the medium movement this condition maynot be valid), the angles θ , θ_1 , θ_2 are not independent and the value of angle $\theta_2 = \theta + \theta_1$ for some examples of electron and photon interaction (when $0 < \theta_1 < \pi/2$, $\theta > 0$ and $0 < \theta_2 < \pi/2$). Obviously in this case due to the positiveness of the parameter $\varepsilon > 0$, inequality (11) is not satisfied due to the negativeness of its right hand side, and the right hand side of (12), vice versa, always holds for $\cos \theta_2 < \cos \theta_1$. From the left hand side of (12)

$$\cos \theta > 1 - \frac{n(\beta \cos \theta_2 - N)}{\varepsilon \sqrt{1 - \beta^2}}, \quad (14)$$

where the right hand side exceeds -1 and really restricts range of θ only when holding the following complementing (13) inequality

$$\frac{2\varepsilon \sqrt{1 - \beta^2}/n + N}{\beta} > \cos \theta_2 \quad (15)$$

In its turn, inequality (15) can complement inequality (13) on the value of angle θ_2 , when its left hand side is less than 1 , i.e., under the following condition

$$\beta > \beta_1 = \frac{N \left[1 + \frac{2\varepsilon}{Nn} (4\varepsilon^2/n^2 + 1 - N^2)^{1/2} \right]}{1 + 4\varepsilon^2/n^2} > N \quad (16)$$

Inequality (16) is also take place when right hand side of (14) is smaller than -1 and we have:

$$1 > \cos \theta_2 > \left(N + 2\varepsilon \sqrt{1 - \beta^2}/n \right) / \beta, \quad (17)$$

when (14) give only condition $1 > \cos \theta > -1$. Thus conditions (16), (17) for anomalous Compton effect realizing have the direct analogy with VCR threshold conditions [10-12].

3. CONCLUSIONS

Thus we have considered the new theory of the Compton effect, which is based on Abraham theory for EMF in medium that should be experimentally verified.

REFERENCES

1. Minkowski, H., *Nach. Ges. Wiss. Gottingen*, K53, 1908.
2. Minkowski, H., *Math. Ann.*, Vol. 68, 472, 1910.
3. Abraham, M., *Rend. Circ. Matem. Palermo*, Vol. 28, 1, 1909.
4. Abraham, M., *Rend. Circ. Matem. Palermo*, Vol. 30, 5, 1910.
5. James, R. P., "Force on permeable matter in time-varying fields," Ph.D. Thesis, Department of Electrical Engineering, Stanford University, 1968.
6. Walker, G. B. and D. G. Lahoz, *Nature*, Vol. 253, 339, 1975.
7. Walker, G. B. and G. Walker, *Can. J. Phys.*, Vol. 55, 2121, 1977.
8. Ginzburg, V. L., *Theoretical Physics and Astrophysics*, Nauka, Moscow, 1981.

9. Brevik, I., *Phys. Rep.*, Vol. 52, 133, 1979.
10. Chefranov, S. G., *Phys. Rev. Lett.*, Vol. 93, 254801, 2004.
11. Chefranov, S. G., *JETP*, Vol. 126, 333, 2004.
12. Chefranov, S. G., “New quantum theory of the Vavilov-Cherenkov radiation and its analogues,” arXiv: 1205.3774v1[physics.gen-ph], May 16, 2012.
13. Tamm, I. E., *J. Phys. USSR*, Vol. 1, 439, 1939.
14. Landau, L. D. and E. M. Lifshitz, *Electrodynamics of Continuous Media*, Nauka, Moscow, 1982.
15. Chefranov, S. G., “The Vavilov-Cherenkov radiation by relict photon gas,” arXiv: 1009.0594v2 [astro-ph.HE], Oct. 7, 2010.
16. Chefranov, S. G., “Generalization of the Einstein-Plank-Richardson law for the photon energy in medium resolves Abraham-Minkowski dilemma in the electromagnetic field theory statement,” arXiv: 1202.0739v1 [physics.gen-ph], Feb. 2, 2012.
17. Chefranov, S. G., “The new microscopic Vavilov-Cherenkov radiation theory,” arXiv: 1204.0002v1 [physics.gen-ph], Mar. 30, 2012.
18. Pfeifer, P. N. C., T. A. Nieminen, N. R. Heckenberg, and H. Rubinsztein-Dunlap, “Constraining validity of the Minkowski energy-momentum tensor,” *Phys. Rev.*, Vol. A79, No. 2, 023813, arXiv: 0902.2605v2 [physics.class-ph], Feb. 22, 2009.
19. Venugopal, V. and P. S. Bhagdikar, “De Broglie wave length and frequency of the scattered electrons in compton effect,” *Physical Education*, Vol. 29, 34, arXiv: 1202.4572v3 [physics.gen-ph], Dec. 26, 2012.
20. Pardy, M., “Compton effect in dielectric medium,” arXiv: hep-ph/0406008 v1, Jun. 1, 2004.

An Acoustic Inverse Scattering Problem for Spherical Coating Materials with Radially Inhomogeneous Profile

E. Bilgin and A. Yapar

Electrical and Electronics Engineering Faculty, Istanbul Technical University, Istanbul, Turkey

Abstract— An acoustic inverse scattering problem which aims to reconstruct the acoustical parameters of the spherical coating material surrounding a sound-soft spherical object is investigated. The compressibility of the coating material is assumed to have one-dimensional variation along the radial direction. The coupled integral equations, the *object* and *data* equations, are reduced to one-dimensional form using the spherical symmetry. The inverse problem is then solved iteratively via Newton method. Numerical simulations demonstrate that the method is highly effective for profiles with smooth variation and provides a useful approximation for layered profiles. However, the success of the method depends on choosing an appropriate initial guess as expected for an iterative solution based on Newton algorithm.

1. INTRODUCTION

Aside from theoretical interest, the scattering and inverse scattering problems related to coated spherical objects have various practical applications such as acoustic cloaking and scattering cross-section reduction. Expressions of scattered pressure field and cross section are obtained for a sphere with penetrable coating illuminated by a plane acoustic wave in [1]. In [2], the case of a coated sound-soft or sound-hard sphere within point source wave field is investigated. The dependence of scattering cross section to the parameters of the coating material is also analysed in this work. The relationship between coating and scattering cross section forms the base for research in the field of acoustic cloaking [3, 4]. In [3] the theoretical principle of two dimensional acoustic cloaking is obtained via the transformation technique used for electromagnetic waves. The case of acoustic cloaking for a sphere is analysed in [4]. In [5], a method of the scattering reduction via an elastic cloaking layer is presented. The parameters of the single elastic layer are obtained through numerical minimization of scattering cross section.

A brief review of the literature presented here demonstrates that the inverse scattering problems related to the spherical coating materials have both theoretical and practical significance, and that the subject is still open to contributions. In the present study a sound-soft sphere coated by a spherical coating material with radially inhomogeneous compressibility is considered. The aim of the problem is to determine the acoustical profile of the coating material in the case of a point source excitation. The method applied here is first used in [6] to reconstruct the one-dimensional variation of the acoustical profile of a simple spherical object. Although the problem is a three dimensional one, it can be reduced to a one dimensional form by expressing the angular components of the field quantities in term of spherical harmonics and using the orthogonality of these functions over a spherical surface. As the acoustical profile is assumed to be a function of the radial distance, it is not affected by this operation. The solution of the inverse scattering problem is obtained via Newton method. In this method, one dimensional integral equation system formed by the *object* and *data* equations is iteratively solved, starting with an initial guess of unknown acoustical profile. The ill-posed nature of the data equation requires the use of a regularization technique, and the classical Tikhonov regularization is applied here for this purpose. Numerical simulations yields satisfactory results especially for smooth profiles, provided that an appropriate initial guess is chosen for unknown profile.

2. FORMULATION OF THE PROBLEM

Consider a sound-soft sphere of radius a as presented in Figure 1, coated by a concentric sphere of radius b whose acoustic parameters, the density $\rho(r)$ and the compressibility $b(r)$, are functions of radial distance r only. The region outside the spheres is assumed to be uniform with constant density ρ_0 and compressibility b_0 , therefore it is characterized by a constant wave number $k_0 = \omega\sqrt{b_0\rho_0}$. A time-harmonic point source located at the point $\mathbf{r}_s = (r_s, \theta_s, \phi_s)$, $r_s > b$, with strength P_0 is used for the excitation of the incident field.

As explained in [6] in the case of inhomogeneous density in the coating region, the inverse problem becomes very complicated. Therefore in the present study, the density of the coating

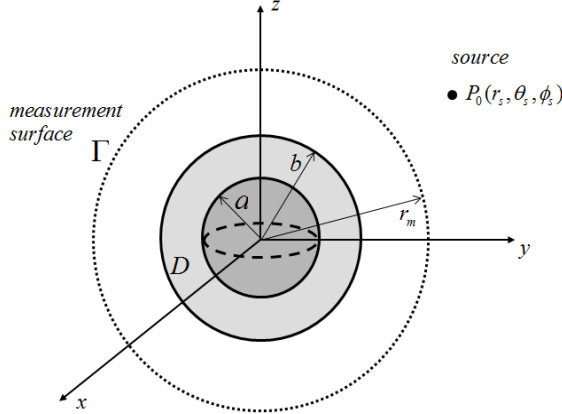


Figure 1: Geometry of the problem.

region is assumed to be constant and equal to the density of the outside region, namely $\rho(r) = \rho_0$. Consequently the aim of the inverse problem is to reconstruct the compressibility of the coating material $b(r)$ using the measurement of the scattered field over a spherical surface of radius $r_m > b$. The total field $u(\mathbf{r})$ inside the coating region is given by the object equation:

$$u(\mathbf{r}) = u^i(\mathbf{r}) + k_0^2 \int_D g_1(\mathbf{r}, \mathbf{r}') v(r') u(\mathbf{r}') dv'; \quad \mathbf{r} \in D \quad (1)$$

Here $u^i(\mathbf{r})$ is the incident field created by the point source and $v(r)$ is the so called object function

$$v(r) = \frac{\bar{k}^2(r)}{k_0^2} - 1. \quad (2)$$

where $\bar{k} = w\sqrt{\rho(r)b(r)}$ inside the coating region and $\bar{k} = k_0$ in the outside region. In Equation (1) $g_1(\mathbf{r}, \mathbf{r}')$ is the Green's function associated with a sound-soft sphere of radius a , with its center located at the origin of the coordinate system. This function can be expressed as

$$g_1(\mathbf{r}, \mathbf{r}') = g_0(\mathbf{r}, \mathbf{r}') + g_s(\mathbf{r}, \mathbf{r}'). \quad (3)$$

In Equation (3), $g_0(\mathbf{r}, \mathbf{r}')$ represent the free space Green's function which can be expressed in terms of spherical harmonics

$$g_0(\mathbf{r}, \mathbf{r}') = \frac{ik}{4\pi} \sum_{n=0}^{\infty} \sum_{m=-n}^n \frac{(2n+1)(n-|m|)!}{(n+|m|)!} j_n(k_0 r_<) h_n^{(1)}(k_0 r_>) P_n^{|m|}(\cos \theta) P_n^{|m|}(\cos \theta') e^{im(\phi-\phi')} \quad (4)$$

where $r_< = \min(r, r')$ and $r_> = \max(r, r')$. The term $g_s(\mathbf{r}, \mathbf{r}')$ in Equation (3) represents the scattered part and thus its radial dependence must be of the form $h_n^{(1)}(k_0 r) h_n^{(1)}(k_0 r')$. The coefficient of the function $g_s(\mathbf{r}, \mathbf{r}')$ is determined by applying the Dirichlet boundary condition to the entire function of $g_1(\mathbf{r}, \mathbf{r}')$ at the surface of the sound-soft sphere, $r = a$. Consequently, the scattered part of the function $g_1(\mathbf{r}, \mathbf{r}')$ is obtained as

$$\begin{aligned} g_s(\mathbf{r}, \mathbf{r}') = & \frac{-ik}{4\pi} \sum_{n=0}^{\infty} \sum_{m=-n}^n \left\{ \frac{(2n+1)(n-|m|)!}{(n+|m|)!} \frac{j_n(k_0 a)}{h_n^{(1)}(k_0 a)} \right. \\ & \times h_n^{(1)}(k_0 r) h_n^{(1)}(k_0 r') P_n^{|m|}(\cos \theta) P_n^{|m|}(\cos \theta') e^{im(\phi-\phi')} \left. \right\}. \end{aligned} \quad (5)$$

As a result of the spherical symmetry, the three-dimensional object equation given in Equation (1) has only radial inhomogeneity. Therefore, it can be reduced to a one-dimensional form by taking advantage of the orthogonality of the spherical harmonics. To express the field quantities in terms of spherical harmonics, a series expansion can be defined:

$$u(r, \theta, \phi) = \frac{1}{4\pi} \sum_{n=0}^{\infty} \sum_{m=-n}^n \hat{u}_{nm}(r) \frac{(2n+1)(n-|m|)!}{(n+|m|)!} P_n^{|m|}(\cos \theta) e^{im\phi} \quad (6)$$

where $\hat{u}_{nm}(r)$ is the series expansion coefficient for the field quantities

$$\hat{u}_{nm}(r) = \int_0^{2\pi} \int_0^\pi u(r, \theta, \phi) P_n^m(\cos \theta) \sin \theta e^{-im\phi} d\theta d\phi. \quad (7)$$

Substituting the expression for $u(\mathbf{r})$ given in Equation (6) and the Green's function $g_1(\mathbf{r}, \mathbf{r}')$ given in Equation (3) into the object equation in Equation (1) yields

$$\begin{aligned} \hat{u}_{nm}(r) = & \hat{u}_{nm}^i(r) + ik_0^3 \times \int_a^b \left\{ j_n(k_0 r_{<}) h_n^{(1)}(k_0 r_{>}) \right. \\ & \left. - \frac{j_n(k_0 a)}{h_n^{(1)}(k_0 a)} h_n^{(1)}(k_0 r) h_n^{(1)}(k_0 r') \right\} v(r') \hat{u}_{nm}(r') r'^2 dr'; \quad a < r < b \end{aligned} \quad (8)$$

This formulation is obtained by using the orthogonality of the Legendre polynomials and trigonometric functions over a spherical surface. The term $\hat{u}_{nm}^i(r)$ in Equation (8) represents the series expansion coefficient for the incident field. Equation (8) can be considered as the *reduced object equation*. The *data equation* which is the integral equation representing the scattered field can also be reduced to a one dimensional form in a similar way

$$\hat{u}_{nm}^s(r) = ik_0^3 \int_a^b \left\{ j_n(k_0 r') h_n^{(1)}(k_0 r) - \frac{j_n(k_0 a)}{h_n^{(1)}(k_0 a)} h_n^{(1)}(k_0 r) h_n^{(1)}(k_0 r') \right\} v(r') \hat{u}_{nm}(r') r'^2 dr'; \quad r > b. \quad (9)$$

3. SOLUTION OF THE INVERSE PROBLEM

The system formed by Equation (8) and Equation (9) can be used to solve the direct and inverse scattering problem. For the inverse problem, the coefficients for the scattered field over the measurement surface Γ , $\hat{u}_{nm}^s(r_m)$, are needed. To this end we assume that the scattered field $u^s(r_m, \theta, \phi)$ is measured over Γ and then the coefficients $\hat{u}_{nm}^s(r_m)$ are obtained using Equation (7). In practice the field quantities can be measured at a finite number of points, therefore the integral is evaluated numerically by Simpson's rule.

The unknowns for the inverse problem, $v(r)$ and $\hat{u}_{nm}(r)$, can be determined by applying a linearization technique to the non-linear system formed by Equation (8) and Equation (9). An iterative Newton algorithm, used in [6], is applied in the present study in order to reconstruct the object function $v(r)$. The presentation of the algorithm given below follows the notation of [6]. We first define an operator for reduced *data equation* given in Equation (9) as

$$Lv = ik_0^3 h_n^{(1)}(k_0 r_m) \int_a^b \left\{ j_n(k_0 r') - \frac{j_n(k_0 a)}{h_n^{(1)}(k_0 a)} h_n^{(1)}(k_0 r') \right\} v(r') \hat{u}_{nm}(r') r'^2 dr'. \quad (10)$$

The iterative process starts with solving the reduced *object equation* using an initial guess $v^{(0)}(r)$ for the object function in order to obtain the initial variation of the function $\hat{u}_{nm} = \hat{u}^{(0)}(r)$. The linearization of the *data equation* in Newton sense is obtained by expanding the operator L into a Taylor series around the initial guess $v^{(0)}(r)$

$$Lv^{(0)} + L_\partial \delta v(r) = \hat{u}^s, \quad (11)$$

where $\delta v(r)$ corresponds to the update amount of the object function and L_∂ stands for the Fréchet derivative of the operator L . The increment $\delta v(r)$ can be determined by solving Equation (11), however as it is an ill-posed integral equation a regularization technique must be applied. By applying the classical Tikhonov regularization we obtain the first update increment as

$$\delta v^{(1)} = (\alpha I + L_\partial^* L_\partial)^{-1} L_\partial^* \left(\hat{u}^s - Lv^{(0)} \right) \quad (12)$$

where α is the regularization parameter and $*$ corresponds to the conjugate transpose of the related matrices. Now the object function can be updated as $v^{(1)} = v^{(0)} + \delta v^{(1)}$. The iterative process is continued until the ℓ^2 norm of the ratio $\delta v/v$ becomes smaller than a predetermined threshold ϵ .

4. NUMERICAL RESULTS

In this section some numerical results are presented in order to analyse the accuracy of the method. First, in order to check the validity of the method, a direct scattering problem involving a comparison with the analytical solution is considered. A sound-soft sphere of radius $a = 0.1$ m is coated by a homogeneous sphere of radius $b = 0.2$ m, described by the compressibility $b(r)/b_0 = 2$. Here b_0 is the compressibility of the surrounding medium which is assumed to be homogeneous and is characterized by a constant wave number of $k_0 = 10\pi$. The point source is situated at the point $r_s = 0.4$ m; $\theta_s = \frac{\pi}{3}$; $\phi_s = \frac{\pi}{2}$. The variation of the total field in the coating region with respect to the radial distance r is calculated via the presented method (integral equation) and analytical solution. The curves presented in Figure 2 demonstrate that the solution with integral equation is in perfect agreement with the analytical one and therefore we can conclude that the method is suitable to be applied in inverse scattering problems.

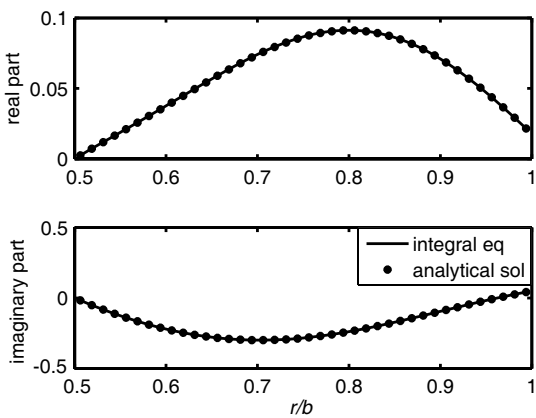


Figure 2: Real and imaginary parts of the total field inside a two layered sphere ($\theta = \phi = \frac{\pi}{6}$); solution with integral equation and analytical solution.

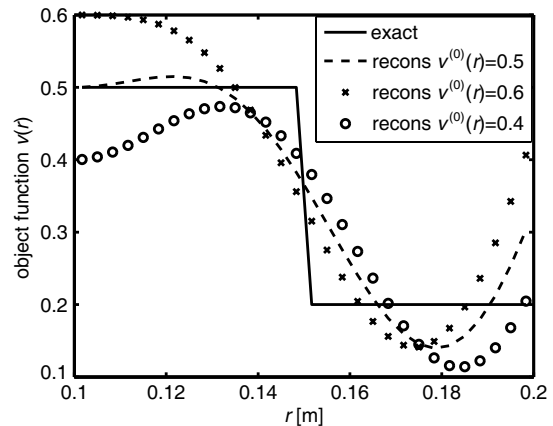


Figure 3: Exact and reconstructed values of the object function for a two layered coating region with three different initial guesses.

Three different profiles (two layered piecewise homogeneous, sinusoidally varying and linearly varying) are considered as examples for the inverse problem. In all cases the radius of the sound-soft sphere is chosen as $a = 0.1$ m and the radius of the coating region as $b = 0.2$ m. The surrounding homogeneous medium has again a constant wave number of $k_0 = 10\pi$ and the point source is located at the same point of $r_s = 0.4$ m; $\theta_s = \frac{\pi}{3}$; $\phi_s = \frac{\pi}{2}$. A random term $0.05|u^s|e^{i2\pi r_n}$ which corresponds to additive noise is added to the simulated scattered field in order to model a realistic case with a 5% noise level, r_n 's being normally distributed random numbers. The regularization parameter is chosen as $\alpha = 0.1$ at the beginning of the iteration procedure and then updated in every iteration as $\alpha = \frac{0.1}{i_n}$. Here i_n is the number of iterations. The threshold for stopping the iteration is chosen as $\epsilon = 10^{-3}$. The highest number of n for the coefficients \hat{u}_{nm}^s is determined as $n_{\max} = 3$ for all examples and the integrals are evaluated by a discretization of 30 points along the radial distance.

As a first example we consider a two layered piecewise homogeneous sphere described by $b(r)/b_0 = 1.5$ for $0.1 \leq r \leq 0.15$, and $b(r)/b_0 = 1.2$ for $0.15 < r \leq 0.2$. The three different initial guesses for the object function are chosen as $v^{(0)}(r) = 0.4$, $v^{(0)}(r) = 0.5$ and $v^{(0)}(r) = 0.6$. The exact and reconstructed profiles are depicted in Figure 3. As expected the method is not capable of catching the sharp transition perfectly, nonetheless it provides a smoothed approximation of the exact profile. The figure also shows that the performance of the method is strongly dependant to the choice of initial guess. The best result is obtained in the case of optimum initial guess of $v^{(0)}(r) = 0.5$. For the second example, a sinusoidally varying profile described by $\frac{b(r)}{b_0} = 1.5 + 0.5 \cos(3\pi \frac{r-a}{b-a})$ is reconstructed with the initial guesses of $v^{(0)}(r) = 0.75$, $v^{(0)}(r) = 1$ and $v^{(0)}(r) = 1.25$. Through the results presented in Figure 4 it can be concluded that the method is useful in reconstructing continuous profiles. However, the success of the method still diminishes for non-optimal initial guesses. It should be noted that for more rapidly oscillating profiles the method fails to converge to a meaningful solution. When the compressibility of the coating region becomes smaller than the compressibility of the surrounding medium the object function take negative values. In the third example, a linearly varying compressibility described by $\frac{b(r)}{b_0} = 0.5 + 0.5 \frac{r-a}{b-a}$ is

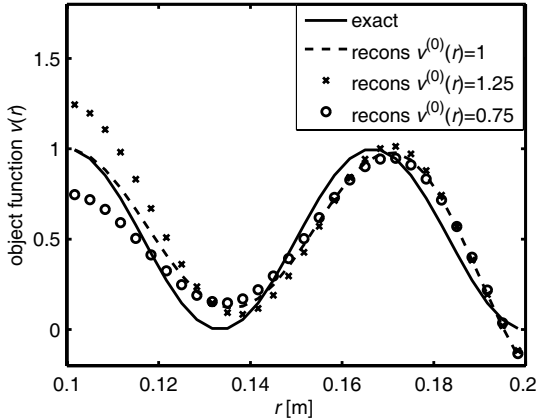


Figure 4: Exact and reconstructed values of the object function for a sphere described by $\frac{b(r)}{b_0} = 1.5 + 0.5 \cos(3\pi \frac{r-a}{b-a})$ with three different initial guesses.

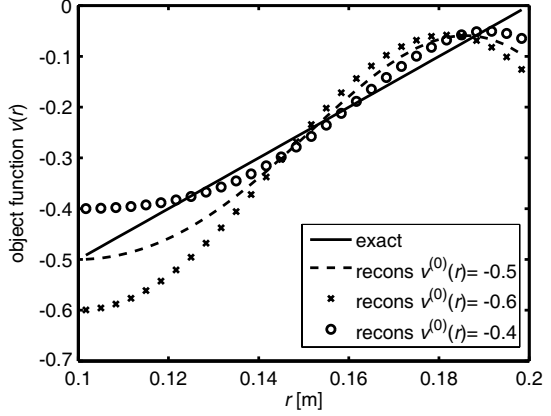


Figure 5: Exact and reconstructed values of the object function for a sphere described by $\frac{b(r)}{b_0} = 0.5 + 0.5 \frac{r-a}{b-a}$ with three different initial guesses.

considered. For this example the initial guesses for the object function are chosen as $v^{(0)}(r) = -0.4$, $v^{(0)}(r) = -0.5$ and $v^{(0)}(r) = -0.6$. The results presented in Figure 5 demonstrates that the method is also applicable for materials having smaller compressibility than the surrounding medium.

5. CONCLUSION

A method to reconstruct the acoustical profile of a radially inhomogeneous spherical coating region surrounding a sound-soft sphere is presented. The density of the region is assumed to be constant and equal to that of the surrounding medium, in order to obtain one dimensional *object* and *data* equations using orthogonality of spherical harmonics. The inverse problem is then solved by applying an iterative Newton algorithm to these equations. Numerical simulations show that although it can not detect sharp transitions in layered profiles; the method is quite reliable in reconstructing continuous profiles. However, the success of the method depends on an appropriate choice of the initial guess, which is expected for an iterative solution.

REFERENCES

1. Kakogiannos, N. B. and J. A. Roumeliotis, "Acoustic scattering from a sphere of small radius coated by a penetrable one," *J. Acoust. Soc. Am.*, Vol. 98, No. 6, 3508–3515, 1995.
2. Arnaoudov, Y., G. Dassios, and V. Kostopoulos, "The soft and the hard coated sphere within a point source wave field," *J. Acoust. Soc. Am.*, Vol. 104, No. 4, 1929–1942, 1998.
3. Cummer, S. A. and D. Schurig, "One path to acoustic cloaking," *New J. Phys.*, Vol. 9, No. 45, 2007.
4. Norris, A. N., "Acoustic cloaking theory," *Proc. R. Soc. A*, Vol. 464, 2411–2434, 2008.
5. Guild, M. D., A. Alu, and M. R. Haberman, "Cancellation of acoustic scattering from an elastic sphere," *J. Acoust. Soc. Am.*, Vol. 129, No. 3, 1355–1365, 2011.
6. Bilgin, E., A. Yapar, and T. Yelkenci, "An acoustic inverse scattering problem for spheres with radially inhomogeneous compressibility," *J. Acoust. Soc. Am.*, Vol. 133, No. 4, 2097–2104, 2013.

Properties of One-way Magnetooptic Nanostructures in THz Range

P. Kwiecien¹, V. Kuzmiak², I. Richter¹, and J. Čtyroký²

¹Department of Physical Electronics, Faculty of Nuclear Sciences and Physical Engineering
Czech Technical University in Prague, Břehová, 11519 Prague 1, Czech Republic

²Department of Guided-Wave Photonics, Institute of Photonics and Electronics AS CR, v.v.i.
Chaberská 57, 182 51 Prague 8, Czech Republic

Abstract— We have studied guiding structures based on the highly-dispersive polaritonic InSb semiconductor material, in the presence of an external magnetic field. The Voigt magnetooptic configuration has been imposed to enable nonreciprocity (and one-way propagation) bringing new interesting phenomena in connection with magnetoplasmons (MSP), with reasonably large magnetic fields applied for functioning. For that purpose, we have recently also developed an efficient two dimensional numerical technique based on the magnetooptic (MO) aperiodic rigorous coupled wave analysis (MOaRCWA), capable of numerically handling such problems. Taking into account the InSb permittivity tensor dispersions, together with corresponding nonreciprocal dispersion diagrams, we have explored — via the MOaRCWA technique — nonreciprocal behavior of the MSP. It reflects variety of interesting features associated with both surface and bulk polaritonic modes within the THz frequency range. In particular, we have investigated an Au/dielectric/InSb sandwiched guiding structures.

1. INTRODUCTION

For photonics to become a realistic alternative to electronics compact integrated optical analogs of one-way electronic devices such as diodes and transistors, are needed. Most of the nonreciprocal devices and one-way devices are based on nonlinear optics and magnetooptical (MO) effects. Using MO effects, unidirectional propagation can arise from a strong electromagnetic spectral asymmetry in the presence of an external magnetic field based on the simultaneous breaking of space and time-reversal symmetry [1]. Many conventional metal surfaces support localized surface plasmon polariton modes that can be excited using prism-coupling methods which, however cannot be applied in THz frequency range. Unlike metals, the dielectric properties of semiconductors can be adjusted by controlling the dopant concentration which in turn determines the degree of confinement and the loss for the plasmonic wave. Surface plasmon polaritons in the THz range are technologically important because they provide a possibility to develop subwavelength-scale device and offer the only possibility to investigate nanoscale systems in THz frequencies. In this paper, by extending our previous work, we developed an efficient 2D numerical technique based on the MO aperiodic rigorous coupled wave analysis. Specifically, we have focused on the structures containing an InSb/dielectric interface.

2. TWO DIMENSIONAL MAGNETOOPTIC APERIODIC RIGOROUS COUPLED WAVE ANALYSIS

By extending our previous work on RCWA/aRCWA techniques [2–7], we have recently also developed an efficient 2D numerical technique based on the magnetooptic (MO) aperiodic rigorous coupled wave analysis (2D MOaRCWA) [8]. This technique, in which critical key improvements have been implemented, too, namely allows dealing with fully anisotropic medium described by a general form of permittivity and/or permeability tensor. Inspired in [9], we have derived and implemented a general form of the eigenvalue equation, taking into account both proper Fourier factorization rules as well as the ASR techniques. Similarly to the standard case, first step of our 2D MOaRCWA was the periodic 1D MORCWA method. With the interest in MO nanostructures, we have successfully applied this method for calculations of effective propagation constants/waveguide losses. The technique has been tested on many examples, including gyrotropic diffraction gratings, planar anisotropic/MO waveguides, MO polarization TE-TM converters, etc., with a very good performance and convergence. Clearly, such technique also allows analyzing SPP propagation in nanostructures in the presence of the external magnetic field in all three possible MO configurations, i.e., transversal (or Voigt), longitudinal (Faraday), and polar configuration (see Fig. 1).

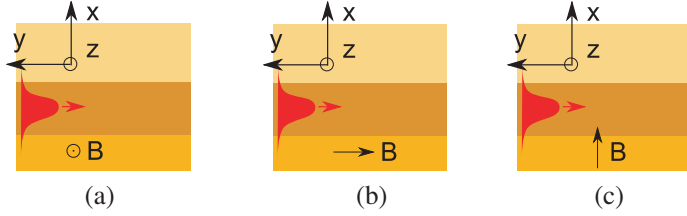


Figure 1: Schematic drawing of three possible MO waveguide configurations: (a) transversal (Voigt), (b) longitudinal (Faraday), (c) polar configuration.

3. ANALYSIS OF MAGNETOOPTIC INSB NONRECIPROCAL STRUCTURES

In the following, we present the results of numerical modeling and analysis of light propagation in a special MO waveguiding InSb-based structure operating in THz range. In THz spectral region, magnetoplasmon (MSP) components have become of particular interest due to rich physics, sub-wavelength confinement, and one-way-propagating properties, along the increasing needs for functional devices (such as isolators, switches, splitters), controlled via the magnetooptic effect with the external magnetic field. Here, the unidirectional propagation can arise from a strong electromagnetic spectral asymmetry in the presence of that external magnetic field, based on the simultaneous breaking of space and time-reversal symmetry [10–13]. Although many conventional nanostructures with metal surfaces, based on propagating and/or localized surface plasmon polariton modes, are easily excitable with, e.g., prism-coupling methods, they cannot be applied in THz frequency range. On the other hand, unlike metals, the dielectric properties of semiconductors can be adjusted by controlling the dopant concentration. This in turn determines the degree of confinement and also the losses of plasmonic waves. For the analysis of unidirectional properties in terahertz frequency range, we have combined the MOaRCWA technique-based simulations with (quasi) analytical predictions in order to study MSP performance of plasmonic nanostructures with highly-dispersive polaritonic InSb material [14, 15], in the presence of external magnetic field [16, 17]. Here, transversal (Voigt) magnetooptic configuration can be used to impose nonreciprocity (one-way propagation), together with bringing new interesting phenomena in connection with MSP, associated with both surface and bulk polaritonic modes within the THz frequency range.

To study unidirectional properties in THz range, we applied both analytical methods [17] and numerical simulations by using 2D MOaRCWA technique [8]. Specifically, based on our previous investigation of one-way waveguides consisting of metal/MO photonic crystal interface [18], we focused on the structures containing InSb/dielectric/metal interfaces. The dispersion relation of such structures are known to exhibit a number of interesting features [14, 19] which are shown to be revealed in their transport properties. Our work has been also partially motivated by recent investigations of Au/dielectric/InSb sandwiched guiding structures [20–24]. The results obtained demonstrate variety of interesting features for both planar and structured interfaces.

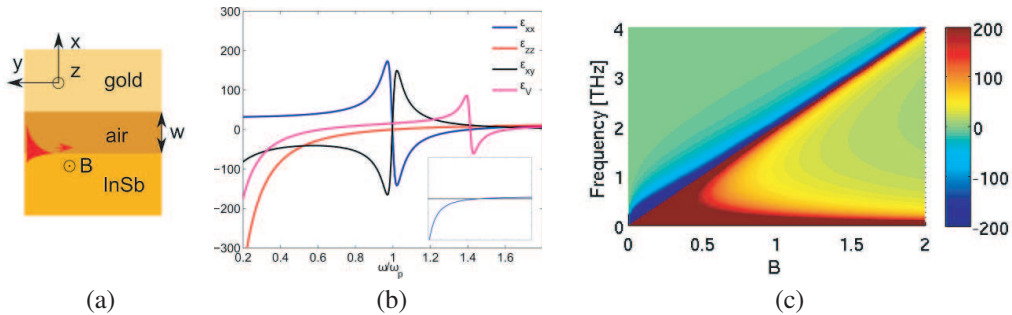


Figure 2: (a) Schematic picture of the one-way MO InSb waveguide structure of interest, operating within the THz range, (b) frequency dependence of the dielectric tensor components, with InSb loss γ taken into account, $(\epsilon_{xx}, \epsilon_{yy}, \epsilon_{zz}, \epsilon_{xy})$ and the corresponding Voigt dielectric constant ϵ_V of InSb material; the inset shows the case with no magnetic field applied ($\omega_c/\omega_p = 0$), i.e., $\epsilon_{xx} = \epsilon_{zz}$, $\epsilon_{xy} = \epsilon_V$), (c) frequency-magnetic field contour plot of the real part of $\epsilon_{xy} = \epsilon_V$ (with loss γ).

Schematic picture of the MO guiding structure of interest is shown in Fig. 2. Here, the width w_0 and the length of the waveguide are $w_0 = 15.68 \mu\text{m}$ and $300 \mu\text{m}$, respectively. The guide consists of magnetized InSb substrate, separated from gold cover with an air guide (with the relative permittivity of air equal 1). It should be noted that, within the THz frequency range, gold resembles a perfect conductor. Also in Fig. 2(b), spectral dispersion of the dielectric tensor components according to the MO Drude model (with InSb loss γ taken into account), together with the corresponding Voigt dielectric constant ε_V , is depicted. According to the MO Drude dispersion model [20], with the damping taken into account, the frequency dependence is given as

$$\begin{aligned} \varepsilon &= \varepsilon_\infty \begin{pmatrix} \varepsilon_{xx} & i\varepsilon_{xy} & 0 \\ -i\varepsilon_{xy} & \varepsilon_{xx} & 0 \\ 0 & 0 & \varepsilon_{zz} \end{pmatrix}, \quad \varepsilon_{xx} = 1 - \frac{\omega_p^2(\omega + i\gamma)}{\omega[(\omega + i\gamma)^2 - \omega_c^2]}, \\ \varepsilon_{xy} &= \frac{\omega_p^2\omega_c}{\omega[(\omega + i\gamma)^2 - \omega_c^2]}, \quad \varepsilon_{zz} = 1 - \frac{\omega_p^2}{\omega(\omega + i\gamma)^2} \end{aligned} \quad (1)$$

where ε_∞ is high-frequency limit permittivity, ω_p the plasma frequency, γ is the collision damping, $\omega_c = eB/m^*$ is the cyclotron frequency (e and m^* are the charge and the effective mass of an electron, respectively). The following parameters of InSb material as the input into the model (@ room temperature and magnetic field $B = 1 \text{ T}$) were chosen: $\varepsilon_\infty = 15.68$, $\omega_p = 12.6 \text{ THz}$, $\gamma = (0.1\pi) \text{ THz}$, $\omega_c = 12.56 \text{ THz}$. As can be seen, in Fig. 2(b), the resonant position of the Voigt dielectric constant $\varepsilon_V = \varepsilon_{xx} + \varepsilon_{xy}^2/\varepsilon_{xx}$ is shifted from the value $\omega/\omega_p = 1$ to the hybrid frequency $\omega_H = \sqrt{\omega_c^2 + \omega_p^2}$. Additionally, in Fig. 2(c), the frequency-magnetic field contour plot of the real part of ε_{xy} (with loss γ taken into account) is shown. Here, the displacement of the Voigt dielectric constant with respect to the applied magnetic field is clearly visible. Next, in Fig. 3, an example of the performance of MO InSb waveguide structure is shown. First, the nonreciprocal dispersion diagram (with respect to the direction of propagation) for the waveguiding structure was calculated; the results are shown in Fig. 3(a) where a comparison with the case of no applied magnetic field (and this with the symmetric dispersion curve) is shown, too. It can be seen that without the magnetic field applied, the dispersion curves behave symmetrically, for both the forward and backward propagating waves. On the other hand, when magnetic field is applied, the dispersion curves of the two propagating waves act quite differently. For that purpose, apart from the MOaRCWA technique, a dispersion equation for a MO boundary [17], that can be generalized to a waveguiding case [21], was used:

$$\left\{ \frac{\kappa_2\kappa_3}{\kappa_1^2} + \frac{1}{\varepsilon_d^2} - i\frac{\beta\kappa_2}{\kappa_1^2} \frac{\varepsilon_{xy}}{\varepsilon_m\varepsilon_V\varepsilon_{xx}} \right\} \tanh(\kappa_1 w) + \left\{ \frac{\kappa_3}{\kappa_1} \frac{1}{\varepsilon_d\varepsilon_V} + \frac{\kappa_2}{\kappa_1} \frac{1}{\varepsilon_m\varepsilon_d} - i\frac{\beta}{\kappa_1} \frac{\varepsilon_{xy}}{\varepsilon_d\varepsilon_V\varepsilon_{xx}} \right\} = 0 \quad (2)$$

where $\kappa_1^2 = \beta^2 - k_0^2\varepsilon_d$, $\kappa_2^2 = \beta^2 - k_0^2\varepsilon_m$, $\kappa_3^2 = \beta^2 - k_0^2\varepsilon_V$. We applied this dispersion equation technique also as a test for our numerical MOaRCWA data; in fact, for the two approaches, a

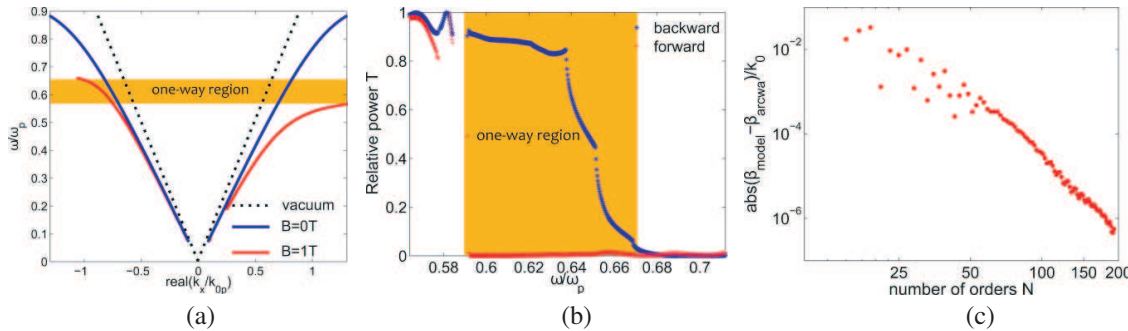


Figure 3: Example of the performance of MO InSb waveguide structure: (a) Dispersion diagram with nonreciprocity behavior with respect to the direction of propagation, (b) relative power T of the forward and backward propagating waves, (c) convergence of the magnetoplasmon mode relative error ($\omega/\omega_p = 0.6$) versus the number of Fourier orders of MOaRCWA.

perfect agreement was found. To support this, the convergence of the magnetoplasmon mode relative error (for $\omega/\omega_p = 0.6$), i.e., the difference between the analytical data from the dispersion equation and the numerical results, versus the number of Fourier orders of MOaRCWA, is shown in Fig. 3(c).

Most importantly in Fig. 3(b), the relative power transmittance of the forward and backward propagating waves (or for the appropriate change of the direction of the magnetic field) is shown, revealing clearly the behavior within the one-way region. Additionally, we have studied the dependences on the parameters of interest that influence the performance of the one-way propagating frequency band, specifically the cutoff frequencies of the forward and the backward propagating modes versus the applied magnetic field, the permittivity of the guiding dielectric layer, as well as the thickness of this guide; the results are shown in Fig. 4. As was expected, the external magnetic field (see Fig. 4(a)) influences the cutoff frequencies of both the propagating modes dramatically, in the same fashion, with quite strong decrease, keeping the bandwidth of the one-way-propagating band the same. On the contrary, the effect of the permittivity of the dielectric guiding layer ϵ_d , shows the opposite tendencies in the cutoff frequencies (see Fig. 4(b)), thus increasing the one-way bandwidth. Finally, the effect of the guide thickness on the cutoff frequencies has been considered (see Fig. 4(c))). Clearly, these parametrical dependences will enable to understand the physics and to design MO InSb guiding structures with proper parameters to ensure an efficient one-way performance of tunable THz plasmonic devices. In conclusion to this part, with our techniques, we have been able to analyze a one-way propagating plasmonic waveguide in the THz range, based on the nonreciprocal MPS.

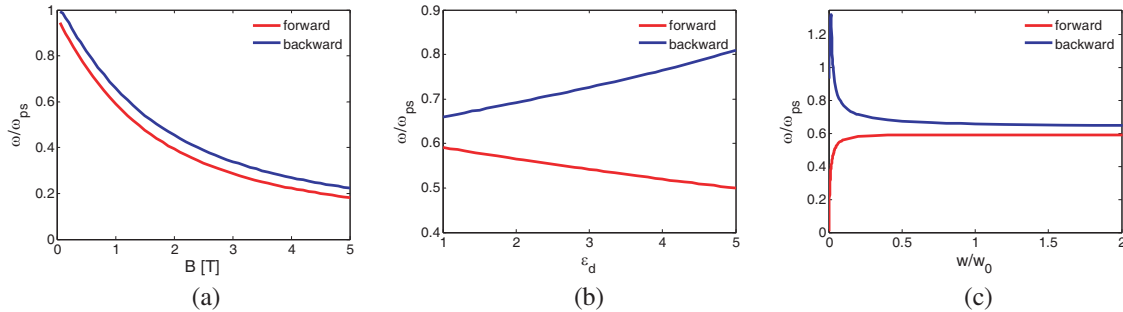


Figure 4: Influence of MO InSb waveguide design parameters on the cutoff frequencies of forward and backward propagating modes: (a) the effect of external magnetic field B , (b) the effect of the permittivity of the dielectric waveguide layer ϵ_d , and (c) the effect of the dielectric waveguide thickness.

Finally, we have also looked at another promising configuration — a symmetric configuration of the structure (see Fig. 23(a)), i.e., the upper metallic part (gold) — guide superstrate — has been replaced with the same InSb material, as in the substrate. As was expected, in this case, the one-way dispersion relation and nonreciprocal propagation has been ensured with the antiparallel orientation of the applied magnetic field. Also, in this case, the effective thickness of the waveguide has been reduced twice, due to the horizontal symmetry of the structure.

4. CONCLUSIONS

The 2D Fourier-based modal method MOaRCWA capable of rigorously treating magnetooptical effects in photonic and plasmonic nanostructures, developed within the research in our cooperating research laboratories, have been recently applied, together with the (quasi) to the analysis of a special type of MO nanostructure, with novel physical properties, namely 2D planar magnetooptic nonreciprocal one-way waveguides, based on a semiconductor InSb — dielectric — metal interfaces, exhibiting a number of interesting features associated with both surface and bulk polaritonic modes, reflected in their transport properties.

ACKNOWLEDGMENT

This work was financially supported by the Czech Science Foundation within the project No. P205/10/0046.

REFERENCES

1. Figotin, A. and I. Vitebsky, "Nonreciprocal magnetic photonic crystals," *Phys. Rev. E*, Vol. 63, 066609, 2001.
2. Čtyroký, J., P. Kwiecien, and I. Richter, "Fourier series-based bidirectional propagation algorithm with adaptive spatial resolution," *Journal Lightwave Technology*, Vol. 28, 2969–2976, 2010.
3. Kwiecien, P., I. Richter, and J. Čtyroký, "Comparison of 2D and 3D Fourier modal methods for modeling subwavelength-structured silicon waveguides," *Proceedings of SPIE*, Vol. 8306, 83060Y, 2011.
4. Maes, B., J. Petráček, S. Burger, P. Kwiecien, J. Luksch, and I. Richter, "Simulations of high-Q optical nanocavities with a gradual 1D bandgap," *Optics Express*, Vol. 21, 6794–6806, 2013.
5. Čtyroký, J., P. Kwiecien, and I. Richter, "Analysis of hybrid dielectric-plasmonic slot waveguide structures with 3D Fourier Modal Methods," *J. Europ. Opt. Soc. Rap. Public.*, Vol. 8, 13024, 2013.
6. Čtyroký, J., P. Kwiecien, I. Richter, J. Petráček, and J. Luksch, "Modal methods for 3D modeling of advanced photonic structures," *ICTON 2012 Proceedings*, paper Tu.C5.2, invited, Coventry, United Kingdom, July 2012.
7. Petráček, J., B. Maes, S. Burger, J. Luksch, P. Kwiecien, and I. Richter, "Simulation of high-Q nanocavities with 1D photonic gap," *ICTON 2012 Proceedings*, paper Tu.C6.4, invited, Coventry, United Kingdom, July 2012.
8. Kwiecien, P., V. Kuzmiak, I. Richter, and J. Čtyroký, "Nonreciprocal waveguiding EM surfaces and structures for THz region," *Proceedings of 21st International Workshop on Optical Wave Theory and Numerical Modeling*, Vol. 21, 05, Enschede, The Netherlands, April 2013.
9. Li, L., "Use of Fourier series in the analysis of discontinuous periodic structures," *J. Opt. Soc. Am. A*, Vol. 13, 1870–1876, 1996.
10. Armelles, G., A. Cebollada, A. García-Martín, J. M. García-Martín, M. U. González, J. B. González-Díaz, E. Ferreiro-Vila, and J. F. Torrado, "Magnetoplasmonic nanostructures: Systems supporting both plasmonic and magnetic properties," *J. Optics A: Pure Applied Optics*, Vol. 11, No. 114023, 1–10, 2009.
11. Armelles, G., A. Cebollada, A. García-Martín, and M. U. González, "Magnetoplasmonics: Combining magnetic and plasmonic functionalities," *Advanced Optical Materials*, Vol. 1, 10–35, 2013.
12. Belotelov, V. I., I. A. Akimov, M. Pohl, V. A. Kotov, S. Kasture, A. S. Vengurlekar, A. V. Gopal, D. R. Yakovlev, A. K. Zvezdin, and M. Bayer, "Enhanced magneto-optical effects in magnetoplasmonic crystals," *Nature Nanotechnology*, Vol. 6, 370–376, 2011.
13. Temnov, V. V., "Ultrafast acousto-magneto-plasmonics," *Nature Photonics*, Vol. 6, 728–736, 2012.
14. Wallis, R. F., "Theory of surface polaritons in anisotropic dielectric media with application to surface magnetoplasmons in semiconductors," *Physical Review B*, Vol. 9, 3424–3437, 1974.
15. Aers, G. C. and A. D. Boardman, "The theory of semiconductor magnetoplasmon-polariton surface modes: Voigt geometry," *J. Physics C: Solid State Physics*, Vol. 11, 945–959, 1978.
16. Boardman, A., N. King, Y. Rapoport, and L. Velasco, "Gyrotropic impact upon negatively refracting surfaces," *New Journal of Physics*, Vol. 7, No. 191, 1–24, 2006.
17. Dmitriev, V. A. and A. O. Silva, "Nonreciprocal properties of surface plasmon-polariton at the interface between two magnetized media: Exact analytical solutions," *Progress In Electromagnetics Research Letters*, Vol. 21, 177–186, 2011.
18. Kuzmiak, V., S. Eyderman, and M. Vanwolleghem, "Controlling surface plasmon polaritons by a static and/or time-dependent external magnetic field," *Physical Review B*, Vol. 86, No. 045403, 1–9, 2012.
19. Kong, F. M., K. Li, H. Huang, B.-I. Wuand, and J. A. Kong, "Analysis of the surface magnetoplasmon modes in the semiconductor slit waveguide at THz frequencies," *Progress In Electromagnetics Research*, Vol. 82, 257–270, 2008.
20. Hu, B., Q. J. Wang, and Y. Zhang, "Broadly tunable one-way terahertz plasmonic waveguide based on nonreciprocal surface magneto plasmons," *Optics Letters*, Vol. 37, 1895–1897, 2012.
21. Rivas, J. G., C. Janke, P. Bolivar, and H. Kurz, "Transmission of THz radiation through InSb gratings of subwavelength apertures," *Optics Express*, Vol. 13, 847–859, 2005.

22. Fan, F., S. J. Chang, W. H. Gu, X. H. Wang, and A. Q. Chen, "Magnetically tunable terahertz isolator based on structured semiconductor magneto plasmonics," *IEEE Photonics Technology Letters*, Vol. 24, 2080–2083, 2012.
23. Fan, F., S. Chen, X. H. Wang, and S. J. Chang, "Tunable nonreciprocal terahertz transmission and enhancement based on metal/magneto-optic plasmonic lens," *Optics Express*, Vol. 21, 8614–8621, 2013.
24. Hu, B., Q. J. Wang, and Y. Zhang, "Slowing down terahertz waves with tunable group velocities in a broad frequency range by surface magneto plasmons," *Optics Express*, Vol. 20, 10071–10076, 2012.

Broadband Characterization Using stripline Structure

Ellen Yoshie Sudo Lutif^{1,2}, Alberto José de Faro Orlando¹,
and Antonio Carlos da Cunha Migliano²

¹Aerospace Technological Institute (ITA), CTA, Brazil

²Institute of Advanced Studies (IEAv), CTA, Brazil

Abstract— The finite difference time domain method has been used to design, simulate, and validate the measurement results for the stripline structure. An analysis of the resonant characteristics for a broadband waveguide by using the finite difference time domain method for the description of the electromagnetic behavior of the cell discontinuities in the analysis of the transmission and reflection coefficients, permits in the 500 MHz–50 GHz frequency band the achievement of a good precision for the results. We will analyses the relation $w/h = 1.1$. The sample shows a good transmission in the PCB stripline structure. An electromagnetic wave is formattted of the type TEM $50 \times 50 \text{ mm}^2$. The results show that Stripline EM field distribution is more symmetrical offering better control over even/odd mode impedance. Characteristic impedance is very sensitivity to the ratio of center conductor width to dielectric thickness and relativity insensitive to the ratio of center-conductor thickness to dielectric thickness. The stripline structure is then implemented on Alumina substrate and measured in the laboratory. The measurement and simulation results are found to be close in the frequency range of 1.5 GHz to 2.5 GHz.

1. INTRODUCTION

Electromagnetic compatibility (EMC) analysis of integrated circuits (IC) is an important factor of IC performance. Due to the rapid increase in operation frequencies, RF interference and decrease in overall dimensions of the electronic circuits, the EMC performance of ICs can have great impact on system reliability. Any change in the component values in RF system affects the performance and can cause catastrophic failures. This can be prevented by using a material which has good thermal characteristics as a substrate and accurate design technique to design and implement the stripline at RF range.

The stripline typically consists of a line conductor trace sandwiched between two reference planes and a dielectric material. The transmission line, i.e., the trace and planes, form the controlled impedance. The value of the impedance will be determined by its physical construction and electrical characteristics of the dielectric material. The fundamental propagation mode for a stripline is TEM. The S -parameter measurement benches employ a vector network analyzer and high-quality on-wafer system covering 0.05–10 GHz. They allow fast and easy measurements of the S -parameters.

If the width of the central conductor satisfies the condition $\frac{W}{b-t} \geq 0.35$, we can assume that the field at right side and left side do not interfere. The distributed capacitance C_1 mainly consists of two parallel plate capacitors and four edge capacitors:

$$C_1 = 2C_p + 4C'_f \quad (1)$$

with

$$C_p = \frac{0.0885\epsilon_r w}{\frac{b-t}{2}} \quad (\text{pF/cm}) \quad (2)$$

$$C'_f = \frac{0.0885\epsilon_r}{\pi} \left\{ \frac{2}{1 - \frac{t}{b}} \ln \left(\frac{1}{1 - \frac{t}{b}} + 1 \right) - \left(\frac{1}{1 - \frac{t}{b}} - 1 \right) \ln \left[\frac{1}{(1 - \frac{t}{b})^2} - 1 \right] \right\} \quad (\text{pF/cm}) \quad (3)$$

Therefore the characteristic impedance can be calculated using

$$Z_c = \frac{94.15}{\sqrt{\epsilon_r} \left(\frac{\frac{w}{b}}{1 - \frac{t}{b}} + \frac{C'_f}{0.0885\epsilon_r} \right)} \quad (\Omega) \quad (4)$$

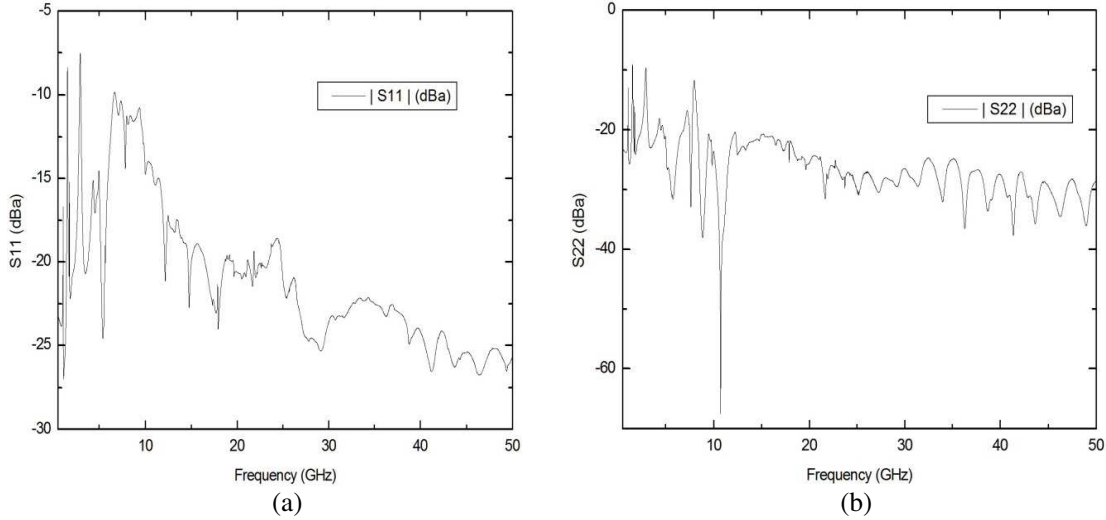


Figure 1: (a) Power reflected from port 1 as a function of frequency. (b) Power reflected from port 2 as a function of frequency.

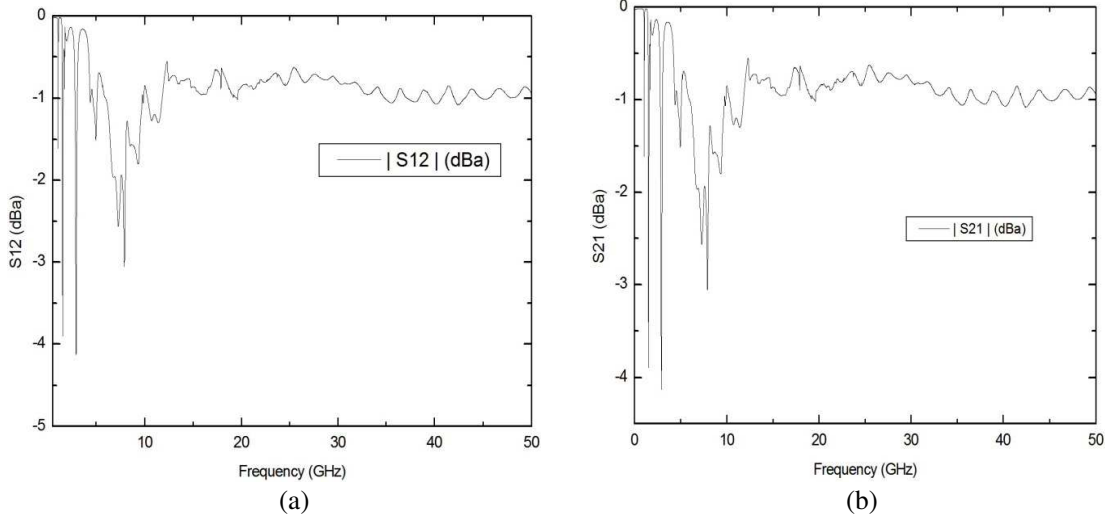


Figure 2: (a) Power transmitted from port 1 to port 2 as a function of frequency. (b) Power transmitted from port 2 to port 1 as a function of frequency.

2. METHODOLOGY

FDTD is used to solve Maxwell's equations for arbitrary model spaces. Indeed, FDTD allows us to solve models that would be difficult or impossible with analytical methods. FDTD is a direct time-domain solution to Maxwell's curl equations [1]. The continuous-time expressions of Maxwell's equations for linear, isotropic, non-dispersive materials which will be discretized in XFDTD are:

$$\frac{\partial \bar{E}}{\partial t} = \frac{1}{\varepsilon} \nabla \times \bar{H} - \frac{1}{\varepsilon} (\overline{J_{source}} + \sigma \bar{E}) \quad (5)$$

$$\frac{\partial \bar{H}}{\partial t} = \frac{1}{\mu} \nabla \times \bar{E} - \frac{1}{\mu} (\overline{M_{source}} + \sigma \bar{H}) \quad (6)$$

A vector analyzer is a versatile measurement system, which comprises of a two or four channels for microwave receiver designed to process the magnitude and phase of transmitted and reflected waves of the network. When dealing with vector measurement quantities, such as complex reflection and transmission coefficients (i.e., S-parameters) in RF and microwave metrology, several important factors need to be considered such as the expression form of the complex quantities (either in the real and imaginary components or magnitude and phase components) and correlation between these

components [2]. The critical dimensions for the stripline sample holder are as follows: The housing is perfect electrical metal with inside dimensions of $(50 \times 50 \times 10)$ mm, the permittivity relative of the air equal 1.0. The stripline was meshed with cells, each of which are $(0.6 \times 0.6 \times 0.6)$ mm in size for FDTD simulation and center conductor was excited for a source of radio frequency of 1 volt operating in scale from 500 MHz to 10 GHz.

3. RESULTS

The Figure 3 shows that VSWR is less than 3.0 over the specified frequency range. This VSWR specifications also implies that the reflection coefficient is less than 0.5 over the quoted frequency range. The minimum VSWR is 1.0. In this case, no power is reflected, which is ideal.

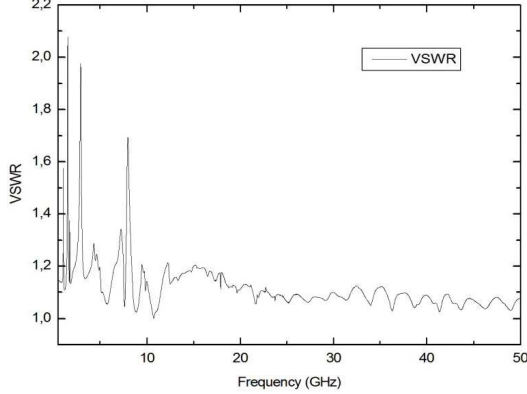


Figure 3: Standing wave ratio (VSWR) as a function of frequency.

The goal of this paper was to perform a physical design of stripline according to the ISO standard [3] by which the improvements of S_{11} and S_{21} parameters were achieved by an application of the experience from numerical simulations.

The Stripline design assures a perfect matching with 50 Ohms in the frequency of 500 MHz to 50 GHz.

4. CONCLUSIONS

Stripline structure using simplified equivalent circuit is designed, simulated, built and measured at RF range. The numeric study of the stripline structure using FDTD software shows that the measured and simulation results are found to be very close in the frequency range of 1.5 GHz to 2.5 GHz [4]. The numerical results have a resonant behavior with good transmission in some frequencies range according to Figures 1, 2 and 3.

ACKNOWLEDGMENT

The authors wish to thank the laboratory of electromagnetic systems at Advanced Study Institute for infrastructure offered. And, they wish to thank Microwave Department at Aerospace Technological Institute for the realization of this work.

REFERENCES

1. Jackson, J. D., *Classical Electrodynamics*, John Wiley & Sons, Inc., New York, 1999.
2. Ridler, N. M. and M. J. Salter, “An approach to the treatment of uncertainty in complex S -parameter measurements,” *Metrologia*, Vol. 39, 295–302, 2002.
3. ISO 11452-5, “Road vehicles — Component test methods for electrical disturbances from narrowband radiated electromagnetic energy — Part 5: Stripline,” Geneva, 2002.
4. Lutif, E. Y. S., A. K. Hirata, A. J. De Faro Orlando, and A. C. da Cunha Migliano, “Design of stripline structure for electromagnetic characterization at microwave frequency,” *PIERS Proceedings*, 1036–1039, Moscow, Russia, Aug. 19–23, 2012.

Design and Simulation of Optimized Ultra-wideband Saddle Antenna

A. Sudhakar¹ and D. Madhavi²

¹Department of ECE, RVR & JC College of Engineering Chowdavaram, GUNTUR-522019, Andhra Pradesh, India

²Department of Physics, RVR & JC College of Engineering Chowdavaram, GUNTUR-522019, Andhra Pradesh, India

Abstract— A novel design of a simple saddle antenna is presented and discussed. The antenna geometrical and numerical models are created. Its performance is predicted with time domain and TLM full-wave solvers of CST software. The antenna design is numerically optimized by profound analysis of the effects of parameters on antenna radiation characteristics. The terminal characteristics and radiation patterns of the optimized saddle antenna in the ultra wideband range are presented. The antenna offers excellent performance for UWB system ranging from 3.7 GHz to 10.2 GHz. The consistent directivity of the antenna ensures it a prominent place in the field of wireless communication.

1. INTRODUCTION

Saddle antenna [1, 2] is a unique kind of flared antenna. This ultra wideband antenna is based on using of two smoothly shaped flares of a simple geometrical structure — the saddle. The first flare, larger in size, serves as an antenna base, reflector and one of the radiator arms. The second flare, smaller in size, operates as other arm of the radiator. An apparent idea is exploited in this design that an ideal UWB antenna would operate as a broadband well matched transformer for the current at its driving ports to the radiated fields that leave the antenna aperture. Besides terminal matching, the antenna would provide a necessary spatial distribution of the radiated energy. The antenna is studied through numerical full wave simulations. The achieved directivity in the band is uniform, greater than 5 dB with considerably low VSWR involves constant beam width and suitability for pulse transmission with minimized distortions. Unlike traditional narrow-band systems, their UWB counterparts [3–7] operate by employing very short electrical pulses of nanosecond and sub nanosecond duration resulting in very wide transmission bandwidths ranging from several hundred megahertz up to several gigahertz. Such huge bandwidths must be supported with suitable UWB antennas that behave unavoidably as band pass filters. The saddle antenna is a blend of all the characteristics making it a novel compact flared UWB antenna. The antenna has been developed to provide a well-behaved radiator operating as a single element and/or array element in UWB time domain radar and telecommunication systems.

2. GEOMETRICAL MODEL OF THE ANTENNA FLARE

The saddle antenna is based on flares of a simple geometrical structure — the saddle. The antenna has several prototypes, classified upon the basis of the alignment of the flares and the type of excitation provided. The simple saddle surface with saddle point located at the origin is given by

$$z(x, y) = k(x^2 - y^2); \quad -s < x, \quad y < s \quad (1)$$

A simple saddle has 2 minima and 2 maxima along a circle centered at the origin.

Since $\cos(n\phi)$ have n minima and n maxima as ϕ varies from 0 to 2π , any function in polar coordinates (r, ϕ) of the form.

$z(r, \phi) = Z(r) \cos[n(\phi + \phi_0)]$ corresponds to saddle of order n .

By taking $z(r) = r^n$ and $\phi_0 = 0$ to get $z_n(r, \phi) = r^n \cos n\phi$.

Converting directly to Cartesian coordinates we get

$$z_n(x, y) = (x^2 + y^2)^{n/2} \cos [n(\arctan(y/x))] \quad (2)$$

Slope, $s(x, y)$ can be defined for each point on a surface $z(x, y)$

$$s(x, y) = \sqrt{z_x^2 + z_y^2} \quad (3)$$

The slope for any of the saddle surfaces depends only on the distance from the origin.

The curvature k gives a measure of the overall or net curvature at a point (x, y) and can be computed for a surface $z(x, y)$ as

$$k = \frac{z_{xx}z_{yy} - z_{xy}^2}{(1 + s^2)^2} \quad (4)$$

A point (x, y) is classified as elliptic if $k > 0$, parabolic if $k = 0$ and hyperbolic if $k < 0$.

It can be shown that all points on a simple saddle ($n = 2$) are hyperbolic. A typical saddle flare with $k = 0.25$ and $s = 4$ is shown in Fig. 1. The saddle antenna [2] can be classified based on the excitation source employed as wave guide port aided feed and a discrete source feed as shown in Fig. 2. The radiation characteristics of both the prototypes vary over a wide extent despite the fact that the only change in either of the prototypes is the feed only. The geometrical as well as the radiation characteristics of the entire model can be deduced on the following parameters.

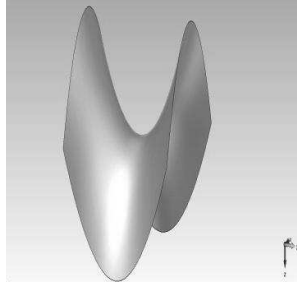


Figure 1: Typical Saddle Antenna.

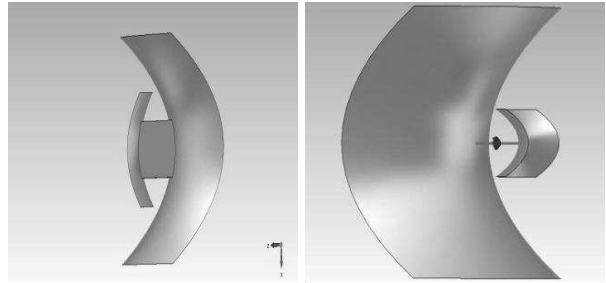


Figure 2: Different designs of saddle antenna.

Distance between the flares is d , i.e., distance between the centers of first flare to the second flare. Dimension of the smaller flare s_{rad} which is referred to as radiator.

Dimension of the larger flare s_{ref} which is referred to as reflector.

Coefficient of the curvature of the radiator is k_{rad} .

Coefficient of the curvature of the reflector is k_{ref} .

All the parameters augment the space requirement with their enhancement. The coefficients of curvature are the worst of all as they make the fabrication more complex owing to the fact that the non-uniformity of the curvature increases with the increase in coefficients of curvature. However, they cannot be compressed to smaller values as that would destroy the shape of the flare, turning into a uniform planar structure. Thus the radiation efficiency of the saddle antenna depends on the careful optimization of these parameters.

3. SIMULATED RADIATION AND TERMINAL CHARACTERISTICS OF THE SADDLE ANTENNA

The wave guide port excited saddle antenna shown in Fig. 3 has higher directivity when compared with its counterpart and has considerably low VSWR. The topology of the antenna differs from previously proposed antennas because the bent profiles of the flares enhance its bandwidth and radiation characteristics, which cannot be obtained at an equivalent level with just flat flare surfaces. Comparing to other antenna geometries, the present design is also relatively simple and suitable for quite easy prototyping and manufacturing.

The antenna simulated here requires a space of $32 \times 32 \times 32$ mm. The distance between the flares is taken as 10 mm while the total length of the flared wave guide is 16 mm. The area of cross section of wave guide is around 8×8 mm with the thickness of the walls being 0.3 mm. The wave guide ends are saddle flared so that the flares can be easily merged in and effectively connected to the

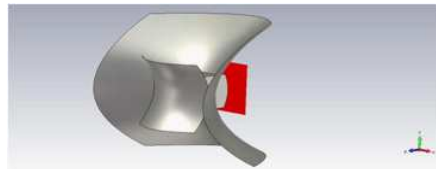


Figure 3: Wave guide port excited saddle antenna.

wave guide port. The size of the smaller flare is 16×16 mm. The antenna terminal characteristics were obtained as shown in Fig. 4.

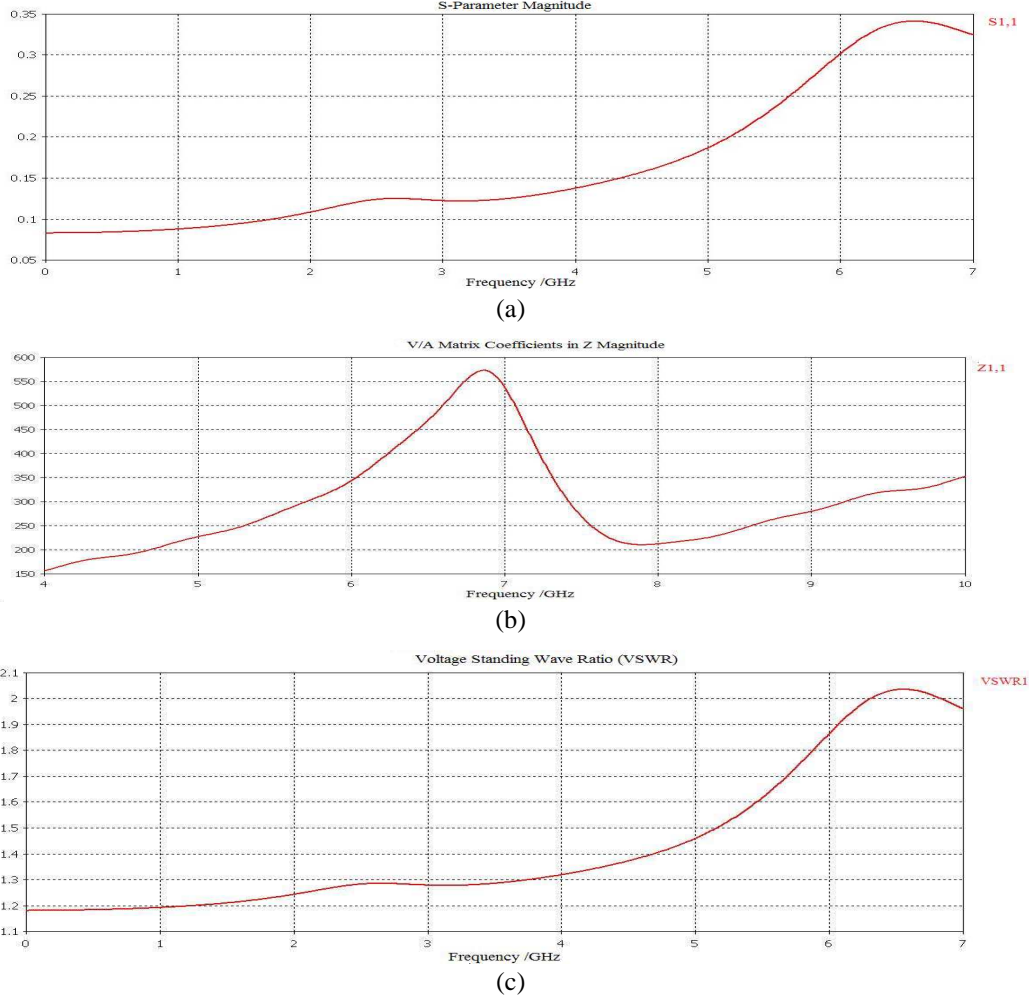


Figure 4: Antenna terminal characteristics. (a) S -parameter magnitude. (b) Impedance. (c) VSWR.

4. OPTIMIZATION

Optimization has been done after proper analysis of effects of various antenna parameters on the antenna's radiation and terminal characteristics with special emphasis on directivity and VSWR. This data is shown in the Table 1.

5. DISCUSSION

The terminal parameters as observed are almost uniform over the band. The band width for the antenna would be around 2 to 8 GHz. The highly volatile impedance of the antenna, which plays a vital role in deciding the efficiency of matching between terminals, is almost uniform within the range of 200 to 300 ohms excluding the slight deviation in the 6–7 GHz range.

The most important parameter of all, the VSWR, i.e., the actual measure of reflection losses arising from terminal impedance mismatch has been uniform and to the best been conformed to value closer to 1, which is generally observed in a perfect and near ideal model. The uniform distribution of the s -parameter magnitude curve also ensures a promising compatibility of the antenna in a wide range of applications. The performance characteristics of the UWB antennas have been compared with the optimized saddle antenna modeled in this paper. The radiation patterns (3 dimensional) at 2.8 GHz and 8 GHz are shown in Fig. 5. The radiation characteristics shown in Fig. 5 to Fig. 7 of the antenna ensure parameters that are best desired from a saddle UWB antenna. The directivity is almost equal to or greater than 5 dB over the entire band.

Table 1: Effect of antenna's physical parameters on VSWR and Gain.

Parameter	Variation	VSWR	GAIN
k_{rad}	increases	increases	decreases
k_{rad}	decreases	constant	constant
k_{ref}	increases	increases	decreases
k_{ref}	decreases	decreases	decreases
s_{rad}	increases	increases	increases
s_{rad}	decreases	decreases	decreases
s_{ref}	increases	constant	constant
s_{ref}	decreases	constant	constant
d	increases	increases slightly up to certain extent (but stays constant for the remaining part)	decreases
d	decreases	increases	decreases

The antenna designed in this paper is unique when compared with conventional antennas as it can provide very wide bandwidth in combination with the unidirectional pattern (about 10 dB front to back ratio) and the planar structure. This antenna has negligible group delay (sub-nanosecond level), compact size (less than one free-space wave length at center frequency) and low cross polarization level (less than -15 dB).

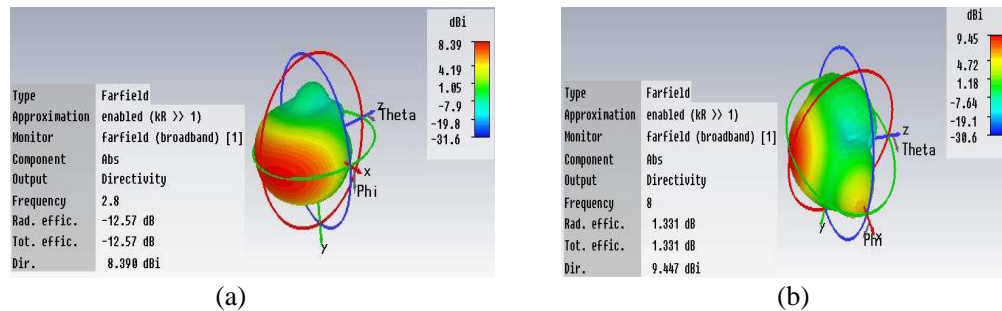
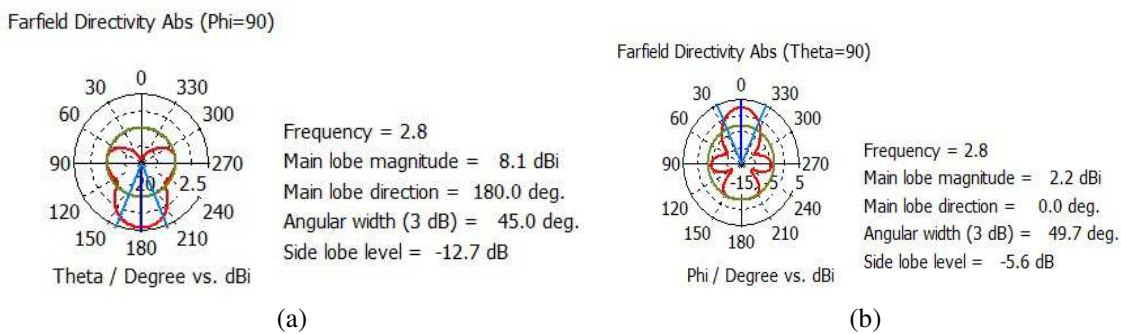
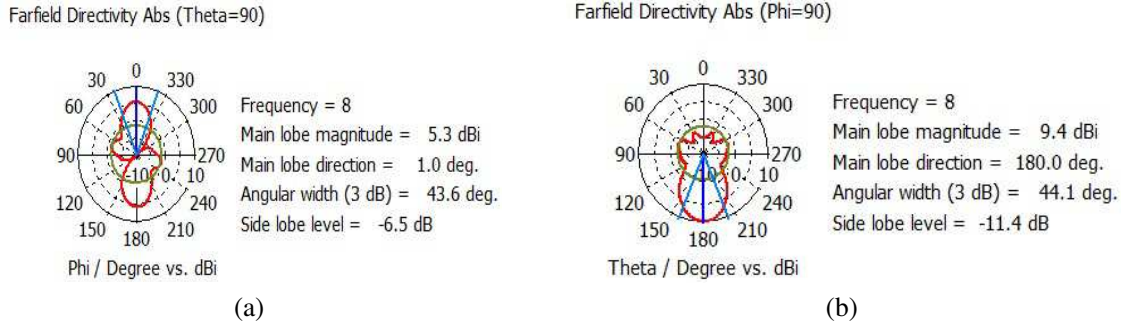


Figure 5: Radiation (3 dimensional) patterns (a) at 2.8 GHz, (b) at 8 GHz.

Figure 6: Simulated radiation patterns in the (a) E -plane and (b) H -plane at 2.8 GHz.

Figure 7: Simulated radiation patterns in the (a) *H*-plane, (b) *E*-plane at 8 GHz.

6. CONCLUSION

This antenna presents a relatively compact physical structure to operate in UWB. In particular, this antenna demonstrates a frequency independent behavior holding small variations for the input impedance and constant beam width as demonstrated. In general, the presented antenna exhibits an efficient use of occupied physical space, beam stability and approximately 5 dB gain with more than 10 dB front to back ratio. Main goals for a later design would be to achieve a lower SWR across the band width and better proximity insensitivity to make it more suitable for indoor wireless communication.

ACKNOWLEDGMENT

Authors thank the University Grants Commission, Govt. of India, New Delhi and the Management of R.V.R & J.C. College of Engineering, Guntur for their financial support for this work.

REFERENCES

1. Peckham, S. D., "Profile, plan and streamline curvature: A simple derivation and applications," *Proceedings of Geomorphometry*, 27–30, Redlands, CA, 2011.
2. Peckham, S. D., "Monkey, starfish and octopus saddles," *Proceedings of Geomorphometry*, 31–34, Redlands, CA, 2011.
3. Chen, Z. N., X. H. Wu, N. Yang, and M. Y. W. Chia, "Considerations for source pulses and antennas in UWB radio systems," *IEEE Trans. Antennas Propagat.*, Vol. 52, No. 7, 1739–1748, 2004.
4. Qing, X. M. and Z. N. Chen, "Transfer functions measurement for UWB antenna," *IEEE Int. Symp. Antennas Propagat.*, 2532–2535, 2004.
5. Ammann, M. J., "Impedance bandwidth of the square planar monopole," *Microw. Opt. Techno. Letters*, Vol. 24, 185–187, 2000.
6. Chen, Z. N. and M. Y. W. Chia, "Impedance characteristics of trapezoidal planar monopole antenna," *Microw. Opt. Techno. Letters*, Vol. 27, 120–122, 2000.
7. Ammann, M. J. and Z. N. Chen, "Wideband monopole antennas for multiband wireless systems," *IEEE Antennas Propagat. Magazine*, Vol. 45, No. 2, 146–150, 2003.

Digital Public Safety Radio Communication

E. Nascimento Junior¹, H. Tertuliano Filho¹, J. R. Descardeci²,
C. A. Dartora¹, T. M. Sanchez Otobo¹, and E. C. Rolin¹

¹Department of Electrical Engineering, Federal University of Paraná, Brazil

²Department of Electrical Engineering, Federal University of Tocantins, Brazil

Abstract— Big events such as the World Cup and the Olympics bring international responsibilities to the country hosting them. Investments have been made in infrastructure in general. Public safety radio communications is a special area that requires studies, resource, adequacy to international standards, and integration between new and current systems. This article is a measurement exercise test that partially compares the performance of APCO, TETRA and TETRAPOL standards used in public safety. The main objective of this exercise was to contribute to the Federal Government providing additional guidelines for choosing the system to be deployed in these big events.

1. INTRODUCTION

The digital radio communication widely used in various industries due to advantages in performance, equipment with reduced dimensions compared to analog systems. Law enforcement agencies use radio communication networks and therefore require adaptation and modernization of their equipment. In this way the process of digitalization of radio communication networks of public security organs in Brazil is to meet current standards, increase the capacity and integrate the systems of different law enforcement institutions.

1.1. The Standards Used in Brazil

On a wide range of digital radio standards and systems available for use in public security, proprietary systems and open standards. One of the most widely used open standards in Brazil are the APCO-25, the TETRAPOL and TETRA.

The APCO-25 is installed in the public security departments of various Brazilian States, being the most important structure found in the State of São Paulo, with conventional and trunking systems operating in phases 1 and 2, on VHF and 800 MHz [2].

The pattern APCO-25 evolved from APCO project 16—that was an analog troncalizada structure. For this reason the APCO-25 maintains compatibility with analog systems, being one of the most relevant characteristics. In this system the voice packets are prioritized in relation to data packets. Each packet has a header with 12 octets, octets 10 information and control, and 2 octets of cyclic redundancy check [3]. Figure 1 presents the packages in one of the frames of the system.

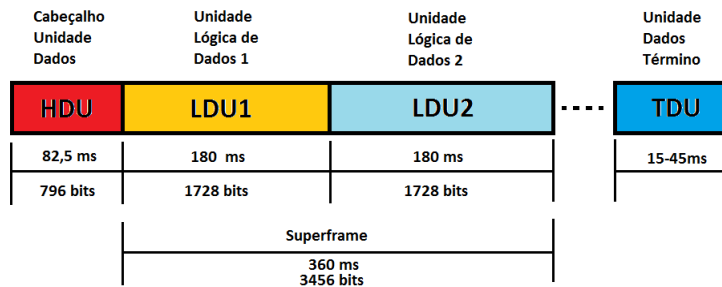


Figure 1: Header and frame of APCO-25.

The unit logical data 1, is located in the first half of the superframe, containing 48 bits of the 64-bit identification, 1296 bits synchronization voice codes, 240 bits link control and 32 bits of low-speed data [1].

The TETRAPOL is used by the Federal Police in the 27 capitals of Brazilian States in the 450 MHz band, and will migrate to 380 MHz range in resolution 557 attendances of Anatel. This pattern emerged in early 1990, a partnership between the security forces and the French defence and the company Matra communications. In France have been installed radio networks for military

use and the ACROPOL network for use in public safety. In this system the encryption is end-to-end type, with extensive key algorithm, which makes the system more secure than the other. The Tetrapol standard air interface is presented in Figure 2.

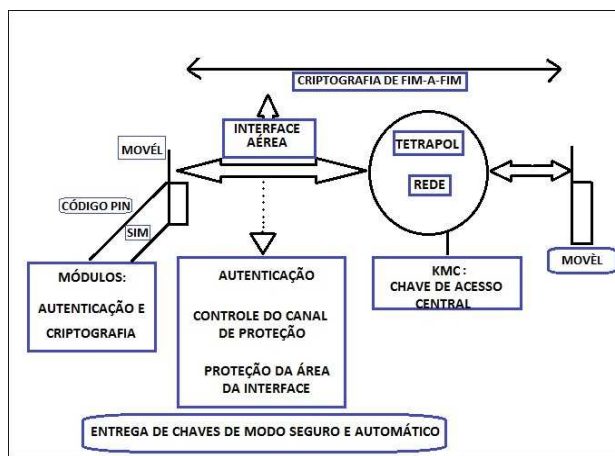


Figure 2: Tetrapol network air interface.

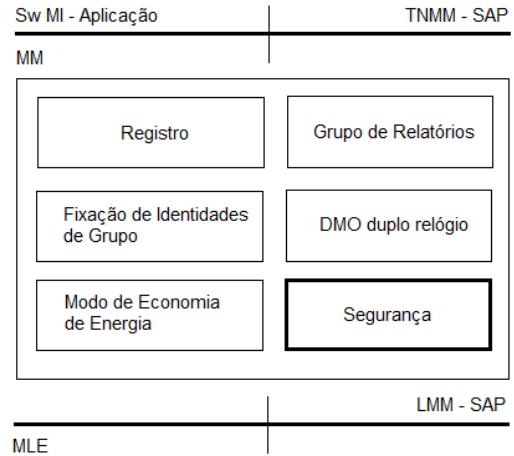


Figure 3: Registration, authentication protocol, signaling and power control TETRA.

The TETRAPOL has multiple access FDMA technique, and their mode of operation is trunked only.

The TETRA is used by the department of public security of the State of Rio de Janeiro, as a legacy of the 2007 Pan-American Games, is operated in the 450 MHz band, and also is in the process of migrating to 380 MHz range, resolution 557 to Anatel. The TETRA appeared in 1994, has been standardized by ETSI, its operation is in the trunked form and the constant communication with the terminal carrier. Your registration protocol performs authentication control, energy saving, safety and use in direct mode [6].

The access to the technical means is TDMA with data transmission rate of 28,800 bps. The PI/4 is DQPSK modulation scheme with a synchronization period between 800 and 25,000 symbols [4]. Has an air interface, peripheral equipment interface, man-machine interface, infrastructure, network management, system-to-system interface with PSTN networks, ISDN connections, and IP networks [7]. Figure 3 summarizes these interfaces.

O tetra uses the TEA protocol for encryption end-to-end [5].

Table 1 presents a comparison between digital radio standards used in public security in their respective stages.

Table 1: Comparison between standards

	APCO-25 1	APCO-25 2	TETRA 1	TETRA 2	TETRAPOL
Modulação	C4FM	CQPSK	π/4 DQPSK	π/4 DQPSK	GMSK
Faixa de Frequência	1,2,3,4	1,2,3,4	6	6	5
Espaçamento do canal (kHz)	12,5	6,25	6,25	6,25	12,5
Canal de Controle (kHz)	12,5	6,25	6,25	6,25	12,5
Canais em 25 kHz	2	4	4	4	2
Potência Portátil (W)	5	5	3	3	5
Potência Móvel (W)	45	45	10	10	10
Potência Repetidor (W)	45	45	75	75	75
Compatível com Analógicos	sim	sim	não	não	Não
Sistema Convencional	sim	sim	não	não	Não
Sistema Troncalizado	sim	sim	sim	sim	Sim
Técnica de Múltiplo Acesso	FDMA	TDMA	TDMA	TDMA	FDMA
Codificador de Voz	IMBE	AMBE	ACELP	ACELP	RPCELP
Criptografia	DES-OFB/AES	DES-OFB/AES	TEA	TEA	
Taxa de Tx. Dados (kbps)	9,6	9,6	28,8	518	7,2
Controle de Potencia Portátil	Não	Não	Sim	Sim	Sim

Id	1	2	3	4	5	6
MHz	136-174	380-512	746-806	806-870	70-520	299-800

1.2. Standards Test

LabTelecom-Telecommunications Laboratory, Department of electrical engineering from UFPR elaborated a test routine for comparison between the standards used in public safety. This routine was approved by ANATEL in the form of technical note. Was chosen for the testing of systems, by the National Secretariat of public safety the city of Oriximiná in Pará. It was during the testing phase, the observation of the behavior not only of technologies but also the behavior of the electrical components, mechanical parts, antenna, types of power equipment and the frequency of operation. The development of numerical solutions for coverage analysis depends not only on the identification and solution for integration of propagation models, but also from the database to the proper design of the project were used two softwares. The Radiomóbil developed by Canadian Roger Coudé using SRTM data base and Longley-Rice propagation model and the Celplanner, Brazilian commercial product that supports multiple Celplan technologies. The use of the same allowed then the measurement of altimetry and fundamental factors on morphology analysis of results. The databases used in the analysis of the results were raster or vector, i.e., made up of pixels.

Figure 4 shows the topography of Oriximiná used by Celplanner.

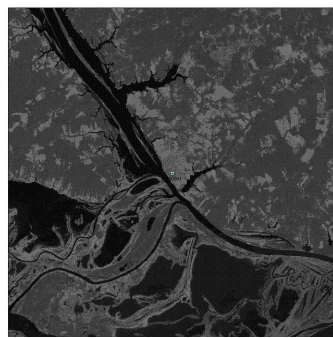


Figure 4: Image from topography of Oriximiná in Celplanner.

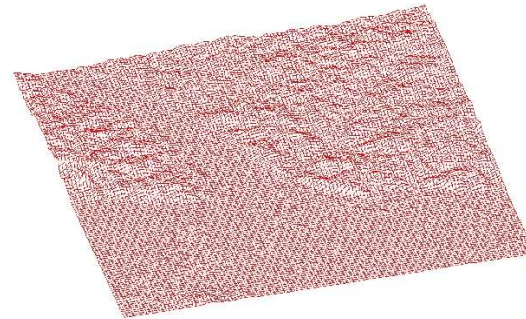


Figure 5: Image monochrome 3D of Oriximiná in Celplanner.

The Figures 5 and 6 show the same region of Figure 4, but in 3D, the first being monochrome, the second color. These figures were also generated in Celplanner.

At the same time in the LabTelecom, an algorithm was written in Matlab®, able to reproduce the results of the tests in Oriximiná, in the same way as commercial programs used. With the use of the Google maps API's were extracted data from street of the city as well as its geographical limits. These data were then entered into the algorithm developed and the results can be seen in Figure 7.

Likewise the terrain profile of measurement points and the decay of power in dBm, this algorithm to a radius of 10.8 miles away are shown in Figure 8.

The measuring points are shown in Table 2. It should be noted that during the test, a team of

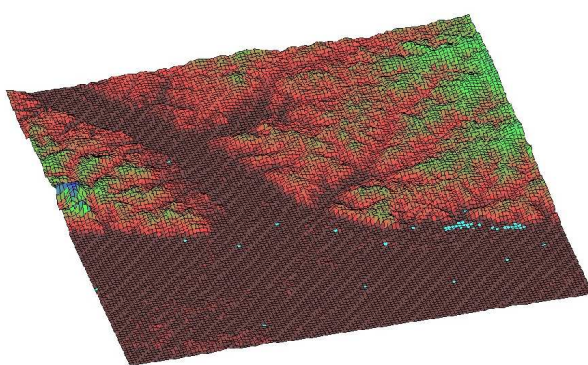


Figure 6: Image color 3D of Oriximiná in Celplanner.

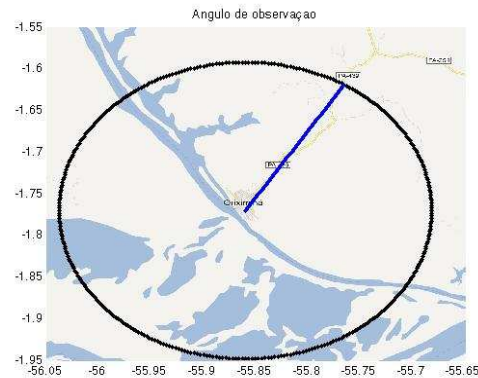


Figure 7: Map of Oriximiná with coverage circle and observation angle in the algorithm.

Anatel and representatives of companies remained in the ERB and another was the field making the offset with the measuring equipment on the vehicle, on a trajectory over the measuring points.

In the algorithm was also possible to obtain a 3D image in the region, and the points of measurement which can be seen in Figure 9.

The Figure 10 shows the antenna-Spectrum Analyzer.

The Tower in which the equipment was installed had 80 m high, however for testing the standard height was 36 m from the foot of the Tower. At the end of the test, to the participating companies delivered reports containing results of the measurements. From these data was generated Figure 11, where we have the power levels measured in dBm in ordered, what shows the differences of mea-

Table 2: Points mensured

ID	LATITUDE	LONGITUDE	(Km)
BASE	1,770416667	55,859694444	
L01	1,773861111	55,857111111	0,479022522
L02	1,777305556	55,854000000	0,994364334
L03	1,778583333	55,852805556	1,188653384
L04	1,767166667	55,862972222	0,513513024
L05	1,763972222	55,865833333	0,990174972
L06	1,760777778	55,868694444	1,467119466
L07	1,758638889	55,870611111	1,786583456
NS1	1,760388889	55,862472222	1,157832276
NS2	1,757250000	55,859500000	1,465293609
NS3	1,754083333	55,856555556	1,850734605
NS4	1,750750000	55,853500000	2,294317647
NS5	1,747583333	55,850555556	2,736579125
NS6	1,744138889	55,847500000	3,223330262
NS7	1,740555556	55,844777778	3,713992297
NS8	1,737111111	55,842250000	4,183272662
NS9	1,733472222	55,839611111	4,678696314
NS10	1,729888889	55,837000000	5,168118134
NS11	1,726222222	55,834555556	5,657073519
NS12	1,722583333	55,831916667	6,154393739
NS13	1,718388889	55,830222222	6,65305477
NS14	1,714361111	55,830222222	7,046533773
NS15	1,710333333	55,826750000	7,624105149
NS16	1,701222222	55,809305556	9,523419308
NS17	1,679500000	55,791638889	12,63519319
NS18	1,668972222	55,780000000	14,35264502
NS19	1,647972222	55,778305556	16,35829022
RS01	1,744138889	55,855444444	2,962047396
RS02	1,805888889	55,839166667	4,559951302
RS03	1,816694444	55,827472222	6,27392126
RS04	1,843055556	55,796277778	10,80110559

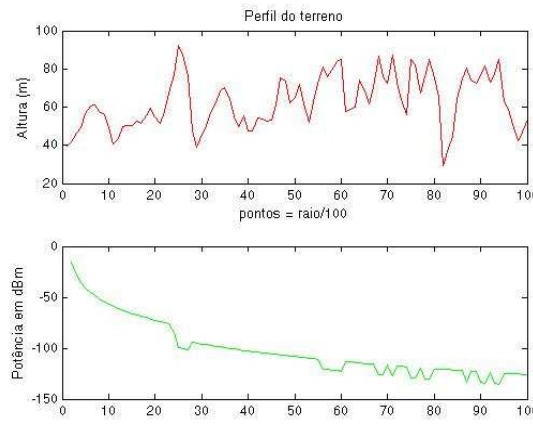


Figure 8: Terrain profile and power decay on the algorithm.

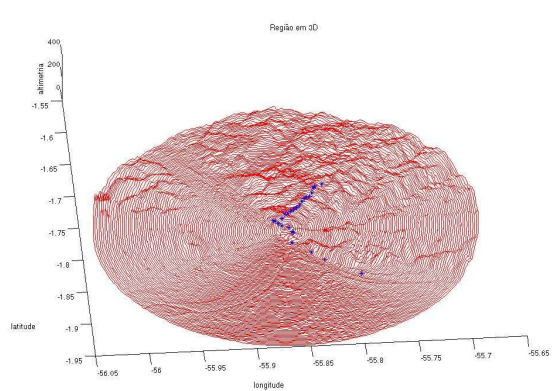


Figure 9: Image monochrome 3D of Oriximiná in the algorithm.

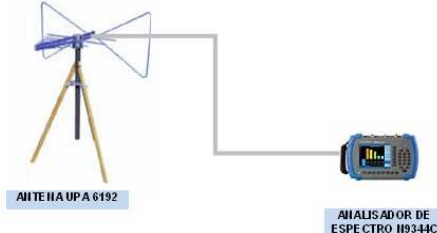


Figure 10: Spectrum analyzer antenna scheme.

surement and measurement between the representatives the APCO-25 because it operated with the same frequency and power, but the results showed differences in potencies received.

In Figure 12 where it has the measurements carried out by Anatel is possible to see the collected data and compare the performance of systems along the way.

Upon completion of the tests, sought a similar configuration and calibration of the parameters tested to perform the Celplaner coverage prediction. The result of the APCO-25 is presented in Figure 13.

In turn the result of TETRA is shown in Figure 14.

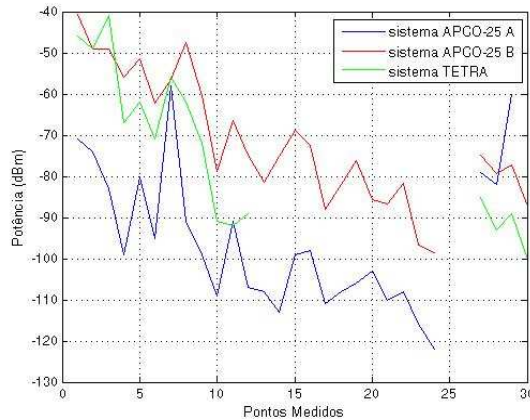


Figure 11: Measures put forward by the manufacturers.

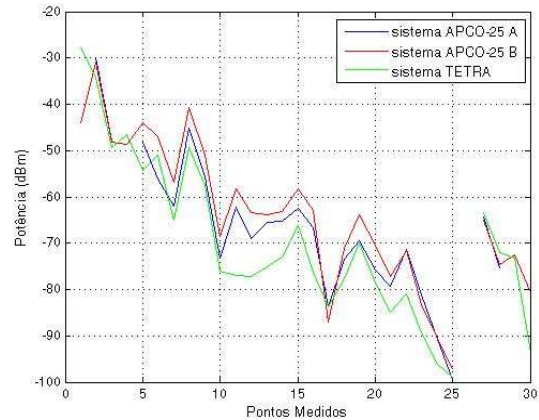


Figure 12: Measures presented by Anatel.

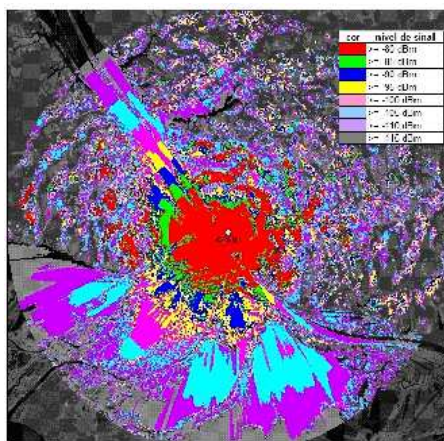


Figure 13: Predição de cobertura do APCO-25 no Celplanner.

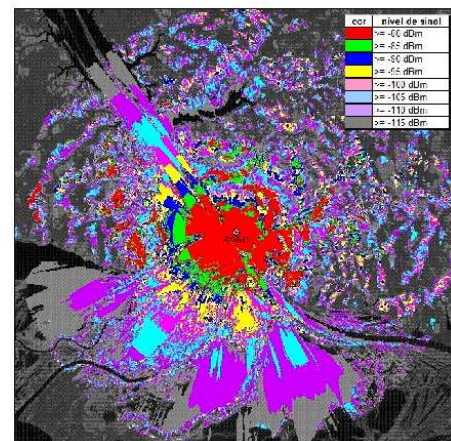


Figure 14: Predição de cobertura do TETRA no Celplanner.

2. CONCLUSIONS

In the face of efforts to adapt and standardization of digital radio systems, the need to use an integrated and interoperable digital system, with robust infrastructure for use throughout the national territory, at the federal, State and municipal levels so shared and controlled by security agencies involved.

About the tests, it is worth noting that companies that represented the APCO-25 system, presented conventional structure with repeaters configured in 100 W, and the TETRA system was configured with 10 W, being the native troncalizada operation of this standard.

The TETRA and APCO-25 systems tested in Oriximiná demonstrated satisfactory performance under the aspect of radio propagation in accordance with Friis's formula, as was expected. The tests were carried out with different powers, of course configured with the system configured with greater power (APCO-25) presented greater coverage, however it was found that if they are with the same parameters of frequency, power and linkage geometry, the result will be similar coverage, with difference in other parameters such as traffic and data transmission rate. It has not been possible to perform the measurement of bit error rate (BER), data transmission rates among others, leaving these indicators to be assessed at the next opportunity.

ACKNOWLEDGMENT

The SENASP, ANATEL, the Electrical Engineering Department of the UFPR, Department of electrical engineering of the UFT, Motorola Solutions, Tait Radiocommunications and Teltronic S.A. And everyone who contributed to the performance of the tests in remote and inhospitable region like the Amazon rainforest around the city of Oriximiná in Pará State.

REFERENCES

1. Ramsey, E. R., W. Thomas Miller III, and A. L. Kun, "A software based implementation of an APCO Project 25 compliant packet data transmitter," *IEEE Conference on Technologies for Homeland Security*, 410–414, Department of Electrical & Computer Engineering, University of New Hampshire, 2008.
2. Diab, T., P. Martins, and P. Godlewski, "Control channel scheduling for apco Phase 2 air interface," *The 17th Annual IEEE International Symposium on Personal, Indoor and Mobile Radio Communications (PIMRC'06)*, 2006.
3. Kiley, P. and T. Benedett, "Public safety interoperability with an SCA military radio using the P25 waveform," *IEEE Military Communications Conference*, 2007.
4. Miculić, M. and B. Modilic, "General system architecture of tetra network for public safety services," *50th IEEE International Symposium ELMAR-2008*, 207–210, Zadar, Croatia, Sep. 10–12, 2008.
5. Buric, M., "Voice end-to-end encrypted for TETRA radiocommunication system," *8th IEEE International Conference on Communications*, 419-422, 2010.
6. Xin, S., "Research on energy economy mode in TETRA digital trunking system," *IEEE First International Conference on Pervasive Computing, Signal Processing, and Applications*, 1180–1183, Scholl of Eletronic and Information Engineering, Beijing Jiao Tong University, China, 2010.
7. Salkintzis, A. K., "Evolving public safety communication systems by integrating WLAN and TETRA networks," *IEEE Communications Magazine*, 38–46, 2006.

A Compact UWB Antenna with Wide Band-notch at 5 GHz for WLAN Band

Qurratulain and Neela Chatteraj

ECE Department, Birla Institute of Technology, Mesra, Ranchi-835215, India

Abstract— In this paper, the design of a novel and compact ultra-wideband (UWB) printed monopole antenna having an overall size of $24 \times 32 \text{ mm}^2$ with band notch characteristic is proposed. This antenna consists of a tapered square radiating patch with a U shaped slot to provide band notching in the 5.15–5.825 GHz band which includes WLAN (IEEE 802.11a) and HIPER-LAN/2 applications. The simulated impedance bandwidth results of proposed antenna with the U shaped slot are well supported by measured results with successful band notching. The measured group delay and radiation pattern results are also presented and performance of the antenna is analyzed/discussed. The effect of the slot is discussed in terms of current distribution.

1. INTRODUCTION

Ultra-wideband (UWB) has come up as a revolutionary and contemporary wireless technology in the last decade. It has generated a great deal of interest for use in the industry and academia. Ultra-Wideband (UWB) commonly refers to signal or system that either has a large relative bandwidth or a large absolute bandwidth [1].

The release of a bandwidth of 7.5 GHz (from 3.1 GHz to 10.66 GHz) for ultra wideband (UWB) applications by the Federal Communications Commission (FCC), by far the largest spectrum allocation for unlicensed use the FCC has ever granted [2], has led to significant UWB researches.

As is the case in any conventional wireless communication system, an antenna plays a very fundamental role in UWB systems also. Although the challenges faced in designing a UWB antenna are many more. A good candidate for UWB applications are printed monopole antennas due to their compactness, light weight and simple structure. Many kinds of UWB antenna designs with different sizes and shapes have been designed and presented in recent years [3–12].

Interference is a serious problem for UWB application systems. The existing Wireless Local Area Network (WLAN) for 802.11a and HIPERLAN/2 systems operating in the frequency band 5.150–5.825 GHz can cause interference with UWB systems. Therefore a band stop filter is required to reduce interference between the UWB systems and these existing wireless systems.

In this paper, we propose a single wide band-notched compact UWB antenna having a broad impedance bandwidth. A partial ground plane is used to increase the bandwidth of the antenna. The band-notching is obtained by embedding a U shape slot in the radiating patch. UWB performance parameters of return loss, radiation pattern, group delay and current distribution are studied. The simulated results are well supported and justified by measured results of the fabricated antenna. The simulated current distribution is also discussed to understand the physical concept of frequency band notching.

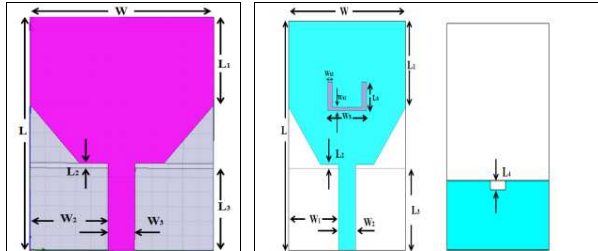
2. UWB ANTENNA DESIGN

The geometry of the proposed antennas and the snapshot of the fabricated antennas are shown in Figures 1(a) & (b) and Figures 2(a) & (b) respectively. To obtain the frequency rejection characteristic a U slot is inserted in the patch as shown in Figure 1(b). It is fabricated on a $24 \times 32 \text{ mm}^2$ Glass epoxy substrate with a dielectric constant of 4.36 and substrate thickness of 1.567 mm. The radiating patch is in the form of a rectangle with a U-slot on it for frequency filtering. Tapering is used to improve the matching over the entire bandwidth.

To obtain the frequency rejection characteristic a U slot is inserted in the patch as shown in Figure 1. The rejected frequency is assumed to be as

$$f_{center} = \frac{c}{2L_{slot}\sqrt{\epsilon_{eff}}} \quad (1)$$

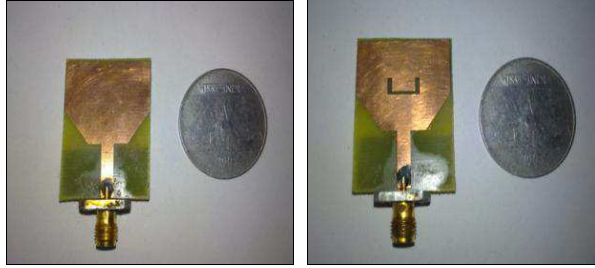
where L_{slot} is the total length of the slot, ϵ_{eff} is the effective dielectric constant, and c is the speed of light. We take the total slot length calculated from (1) into account initially and then adjust the geometry of the design. The parameters of the proposed antenna are given in Table 1.



(a) Without Slot

(b) With Slot

Figure 1: Geometry for the proposed antenna.



(a) Without Slot

(b) With Slot

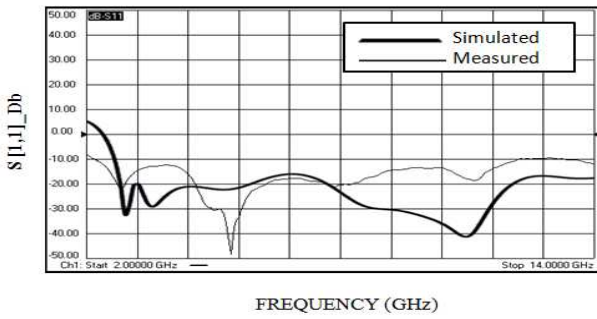
Figure 2: Snapshot of the fabricated antennas.

Table 1: Detailed parameters for the proposed UWB antenna.

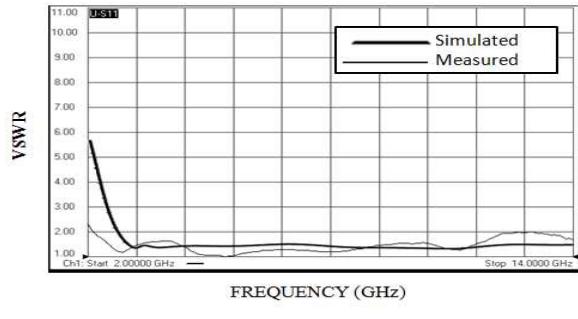
Serial No.	Symbols Used	Dimensions (mm)
1	L	32
2	W	24
3	L_1	18.7
4	L_2	0.5
5	L_3	11.5
6	L_4	1.5
7	W_1	10.25
8	W_2	3.5
9	L_s	4
10	W_s	9
11	W_{s1}	1
12	W_{s2}	0.5

3. RESULTS AND DISCUSSION

The measurements are done using vector network analyser (PNA N5230A, Agilent Technologies) in uncontrolled environment. The Return loss curves and the VSWR curves of the proposed antennas without slot and with slot are shown in Figures 3(a) & (b) and Figures 4(a) & (b) respectively. The fabricated antenna achieves a bandwidth of 3.1 to 14 GHz successfully and also a band-notching effect in the frequency range from 5.1 to 5.9 GHz is obtained.



(a) Return loss curve



(b) VSWR curve

Figure 3: Comparison of simulated and measured results of proposed antenna without slot.

The radiation patterns have been measured using C-band (4–8 GHz) and X-band (8–12.4 GHz) Microwave benches (Vidyut Yantra Udyog). Figure 5 shows the simulated radiation patterns of the proposed antenna at 4.5, 6.5, 8.5 and 10.5 GHz. The measured far field radiation patterns of the proposed antenna at 6.5, 8.5, 10.5 GHz are plotted in Figure 6. It is clearly seen that the radiation patterns of E -plane are monopole like and H -plane radiation patterns show almost omni-directional characteristic.

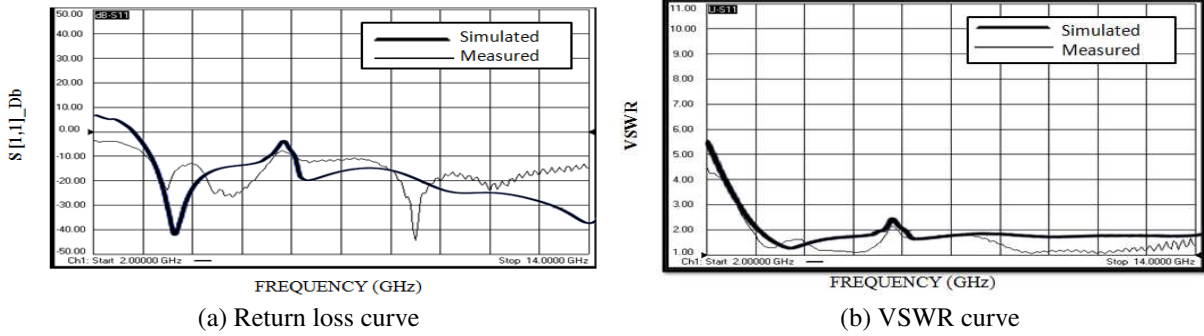


Figure 4: Comparison of simulated and measured results of proposed antenna with slot.

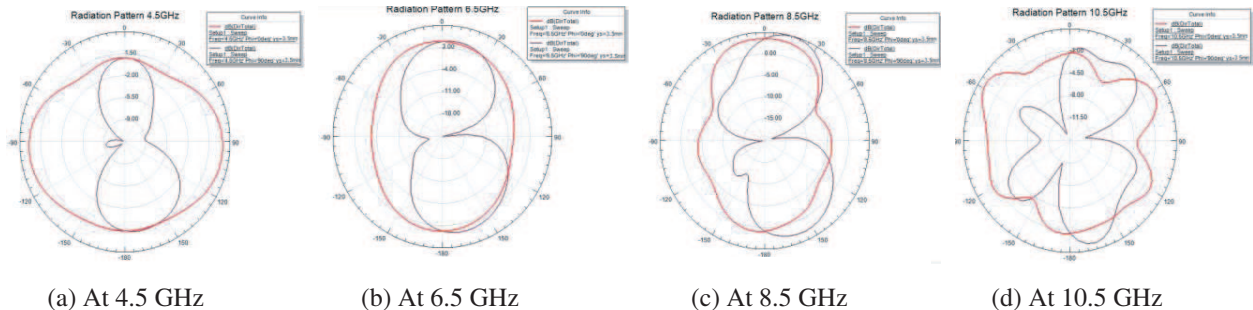


Figure 5: Simulated radiation patterns of the proposed UWB antenna.

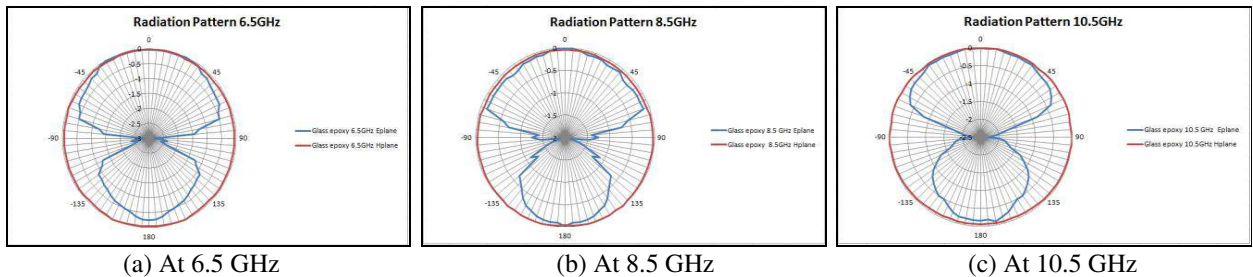


Figure 6: Measured Radiation patterns of the proposed UWB antenna. (a) At 6.5 GHz. (b) At 8.5 GHz. (c) At 10.5 GHz.

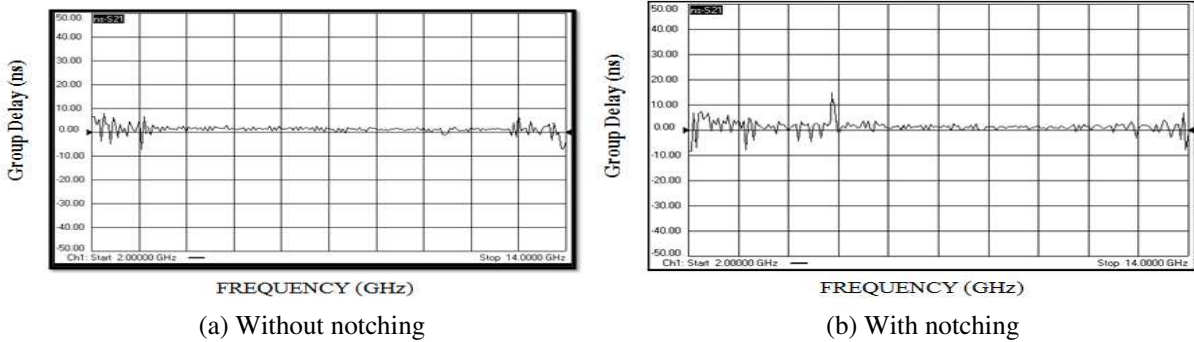


Figure 7: Measured group delay of fabricated UWB antennas. (a) Without notching. (b) With notching.

Figure 7 shows the measured group delay for the proposed antenna with and without the slot. It is seen that group delay variation is abruptly increased at the notched frequency band.

In order to understand the effect of slot in getting the notch function or notch band the surface current distributions on the radiating patch of the proposed antenna are shown at four different frequencies are shown in Figure 8. At the pass band frequencies of 4.5 GHz, 6.5 GHz, 8.5 GHz (outside the notched band) the surface current distribution is uniform. At 5.5 GHz the concentration

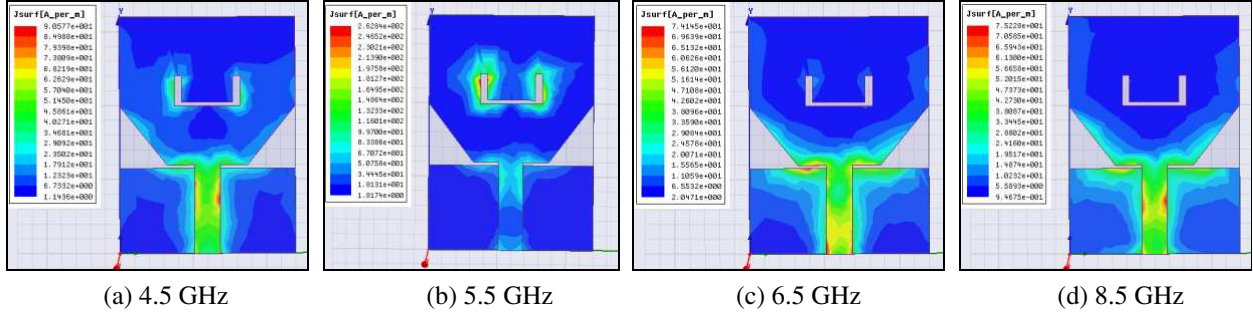


Figure 8: Surface current distributions on the antenna at (a) 4.5 GHz, (b) 5.5 GHz, (c) 6.5 GHz, (d) 8.5 GHz.

of current around the U shaped slot is the strongest indicating a notched band. This shows the effect of notching in the antenna.

Some discrepancies are seen between simulated and measured results which can be due to fabrication faults, misalignment because of etching on both sides of the substrate, measurement in uncontrolled environment and connector losses.

4. CONCLUSION

A new single wide band-notched UWB antenna has been designed, simulated, measured and fabricated. The frequency notch function is obtained by adding a U shape slot in the radiating patch. The simulation results obtained by Ansoft HFSS software show good agreement with the measured results. The proposed antenna shows good UWB performance in the range of 3.1–14 GHz and achieves band notching from 5.1–5.9 GHz to avoid interference with lower and upper WLAN (IEEE 802.11a) and also HIPERLAN/2. Thus this antenna could be good for UWB application.

ACKNOWLEDGMENT

The authors would like to acknowledge and thank the support of Birla Institute of Technology (Mesra) for providing the facility and equipment for this work.

REFERENCES

- Schantz, H., *The Art and Science of Ultra Wideband Antennas*, Artech House Inc., Norwood, MA, 2005.
- “Federal communications commission revision of Part 15 of the commission’s rules regarding ultra-wideband transmission system from 3.1 to 10.6 GHz,” *FEDERAL Communications Commission*, 98–153, FCC, ET-Docket, Washington, DC, 2002.
- Choi, J., K. Chung, and Y. Roh, “Parametric analysis of a band rejection antenna for UWB application,” *Microwave and Optical Technology Letters*, Vol. 47, No. 3, 287–290, Nov. 5, 2005.
- Chen, H.-D., J.-N. Li, and Y.-F. Huang, “Band-notched ultra-wide band square slot antenna,” *Microwave and Optical Technology Letters*, Vol. 48, No. 12, 2427–2429, Dec. 2006.
- Su, S.-W. and K.-L. Wong, “Printed band-notched ultrawideband quasi-dipole antenna,” *Microwave and Optical Technology Letters*, Vol. 48, No. 3, 418–420, Mar. 2006.
- Chair, R., A. A. Kishk, K. F. Lee, C. E. Smith, and D. Kajfez, “Microstrip line and CPW fed ultra wideband slot antennas with U-shaped tuning stub and reflector,” *Progress In Electromagnetics Research*, Vol. 56, 163–182, 2006.
- Choi, J., S. Hong, and U. Kim, “The design of an UWB antenna with notch characteristic,” *PIERS Online*, Vol. 3, No. 7, 987–990, 2007.
- Wang, F-J. and J.-S. Zhang, “Study of a band-notched double printed dipole antenna,” *Microwave and Optical Technology Letters*, Vol. 50, No. 11, 2986–2989, Nov. 2008.
- Chen, W-S. and C.-H. Lin, “A planar hybrid antenna for UWB application,” *Microwave and Optical Technology Letters*, Vol. 51, No. 5, 1243–1246, May 2009.
- Li, P., L. Ma, and J.-S. Li, “A hexagonal ultra-wideband antenna with notched band,” *Microwave and Optical Technology Letters*, Vol. 51, No. 12, 2917–2921, Dec. 2009.
- Lim, E. G., Z. Wang, C.-U. Lei, Y. Wang, and K. L. Man, “Ultra wideband antennas — Past and present,” *IAENG International Journal of Computer Sciences*, 2010.
- Bazaz, R., S. K. Koul, M. Kumar, and A. Basu, “An ultra-wideband antenna with band reject capability and its characterization in time domain,” *Progress In Electromagnetics Research C*, Vol. 19, 223–234, 2011.

Effect of Stationary Magnetic Fields on Different Bacterial Strains

P. Krepelka¹, E. Hutova¹, and K. Bartusek²

¹Department of Theoretical and Experimental Electrical Engineering
Brno University of Technology, Technicka 12, Brno 612 00, Czech Republic
²Institute of Scientific Instruments, Academy of Sciences of the Czech Republic
Kralovopolska 147, Brno 612 64, Czech Republic

Abstract— The authors discuss the effects of stationary magnetic fields on the growth, morphology, and chemical composition of colonies of bacteria. Homogeneous and gradient stationary magnetic field modified these bacterial cells by exhibiting the magnetic flux density value of 5.5 to 8 T/m. The modified bacterium was compared with a reference sample placed in the same conditions outside the magnetic field. Using neodymium magnets, we generated ten different magnetic field types of diverse densities and defined configurations. The model of the magnetic field structure was computed by means of a finite element method (ANSYS) and experimentally verified via measurement with a Hall effect sensor. Within the follow-up stages of the research, changes in the chemical composition of bacterial cells will be monitored. We used NIR spectroscopy to examine the influence of a magnetic field on the metabolism of the bacteria. Although the interpretation of the NIR spectra is a difficult task, this method is suitable for the measurement of water-based samples. The changes are to be evaluated via an analysis of the principal components.

1. INTRODUCTION

The bacterial strains applied in the experiment were *Lactobacillus acidophilus*, *Staphylococcus epidermidis*, *Enterococcus durans*, and *Escherichia coli*, all in the form of colonies cultivated on the growth medium and in an isotonic diluent. We examined the effect of a magnetic field on these bacterial strains. Growth suppression caused by the elimination of the bacteria via the magnetic field [1] was anticipated. The experiment was carried out under stable ambient conditions to exclude possible effects of the environment. We used standard image processing methods to observe the structure and size of the bacterial colonies on Petri dishes. These variations will bring an effect on the number and strength of the molecular bonds. An appropriate technique for the determination of these changes appears to consist in the vibration spectrum; the observation of the variations is performed by means of the NIR spectrum.

2. IMAGE PROCESSING TECHNIQUES

A special algorithm is required for the counting and measurement of the colony radius. The described technique is based on standard image processing methods. The image of the Petri dish was taken by an HP scanjet G3110 with 600DPI (bottom down). The process of evaluating the size of the colony radius is shown in Figure 1.

The preprocessing procedure first requires us to decrease the image size to optimalize the computation speed. Then, the image is converted to grayscale. In some cases, converting the image by means of classic algorithms [2] may be sufficient. However, if the color of the colonies is known, the conversion based on HSL components [3] is desirable. This is the best method of highlighting the colonies against the background. In the next step, it is necessary to binarize the image. The conversion to a black-and-white (binary) image can be performed using thresholding algorithms. For this case, balanced histogram thresholding [4] is used. This method works with the image histogram and checks the balance of this histogram. To achieve the balanced state, the technique removes components on both sides of the histogram. When this iterative process finishes, the result threshold is known.

After that, image segmentation is needed. Firstly, blobs are isolated by method introduced at [5]. We have the set of blobs with one or more colonies. To determine whether we are dealing with a single colony, the circularity criterion is used. This criterion is based on computing with the blob perimeter and area. Equation (1) expresses the relation between these variables (a — blob area, p — perimeter). Lower values reflect bigger circularity.

$$f_c = \left(1 - \frac{4\pi a}{p^2}\right)^2 \quad (1)$$

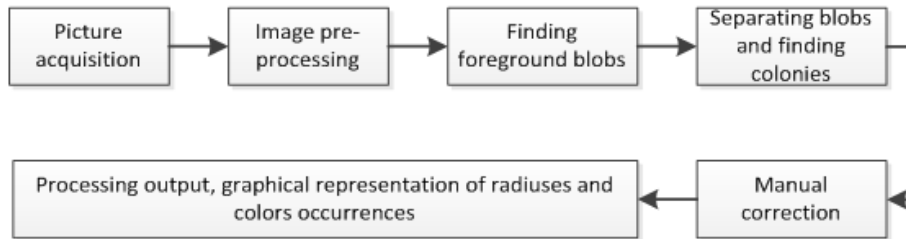


Figure 1: Evaluation of the size of the colony radius.

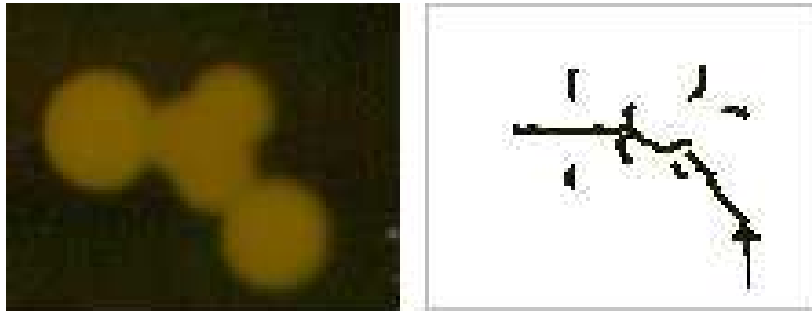


Figure 2: The formation and skeleton of a colony.

If the measured blob has a sufficient circularity, it is regarded as a colony, and its radius is measured. Otherwise, the algorithm for connected colonies was used. This algorithm computes the skeleton of the formation. At each point of skeleton, it creates a shape vector [6] and determines the probability of circle appearance. This probability is defined by the occurrence of a number of the same value. If the probability is high enough, the related part of the formation is declared as a colony with a defined radius, and this part is then removed from the formation. This procedure is repeated until all formations are removed.

3. DETERMINING THE CHEMICAL COMPOSITION OF BACTERIAL CELLS

The chemical variations are observed by means of the NIR spectrum. The magnetic field influencing the metabolism of the bacteria changes their membrane structure and ratio of lipids, proteins and polysaccharide. These variations will bring an effect on the number and strength of the molecular bonds, which will affect the NIR spectrum. Near-infrared spectroscopy is a spectroscopic method that uses a narrow region of the electromagnetic spectrum (900 nm to 2500 nm). The generated light passes over the sample. According to the strength and type of the molecular bonds, the spectrum will absorb some of the light wavelength. We used a transmission method to acquire the spectra; the length of the measuring path was 2 mm. The maximum recovery diluent (water, peptic digest of an animal tissue, sodium chloride) was used for the storage and measurement. All samples were stored in an Eppendorf micro test tube 1 ml. The Varian Cary 5E spectrometer gained a spectrum with 3 nm spectral resolution and 0.1 s average reading time. The preprocessing of the acquired spectra was performed using normalization and the smooth first derivate (Savitzky-Golay) [7]. In this experiment, the standard normal variate (SNV) was used for the analysis. The result of the SNV expressed zero mean data with a normalized variance. After that, orthogonal signal correction was used to increase the prediction accuracy. This orthogonal signal correction is based on a simple idea related to suppressing the part of input variables that is unrelated to the predicted value. Within the process, a signal correction is performed that does not remove useful information from the input data. For the analysis, the classic chemometric method of principal component analysis (PCA) is used. All the above-mentioned algorithms were implemented in Mathworks MATLAB 7.9.0.

Figure 3 shows a slight shift of the peak near 1385 nm between the reference sample and the sample affected by a magnetic field on the *Enterococcus durans*. A similar effect was observed in all measured bacteria strains. Another singularity was observed at 1185nm; in all affected

samples, we measured the absorption increase. These changes in the spectra may be caused by changes in the chemical composition of a bacterial cell. A peak shift is observed at the edge of a strong O-H first overtone peak of water; this anomaly can be caused by different concentrations of organic compounds. The peak around 1190 nm can be associated with the second overtone of the C-H stretching molecule bond. The C-H bonds occurs in amino acids found in proteins. The described situation can be a proof of a different biochemical process inside bacteria cells. For meaningful results, more measurements would be needed with a focus on the different bacteria concentrations and various temperatures. These changes were confirmed by the PCA analysis. The PCA is a well-known technique applied to identify statistical trends in data. This method provides a procedure for the reduction of a complex data set to a lower dimension to reveal the sometimes hidden dependencies. The goal of the PCA is to reduce the number of variables to a smaller set of components by analyzing the variance in the variables. The components are created as linear combinations of the variables. The weight of these combinations is shown in Figure 4(a). We can notice negative peaks at 1390 nm and 1180 nm, which confirms our previous observations. The middle section of Figure 4 expresses the residual error of the constructed model (affected vs. unaffected) according to number of components. With more components involved in the creation of the model, the residual error decreases. By two components unaffected and affected bacterial strains can be distinguished using computed weights at mentioned peaks (Figure 4(b)).

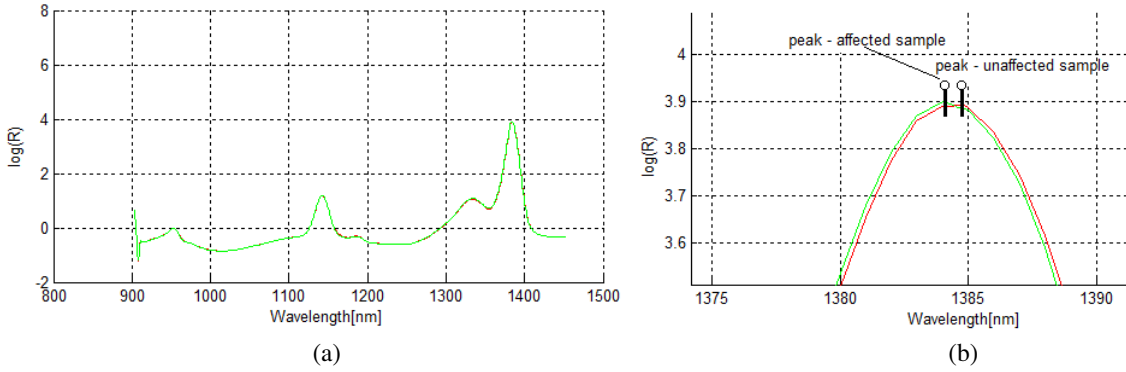


Figure 3: (a) The preprocessed difference spectrum, (b) detail of peak shift.

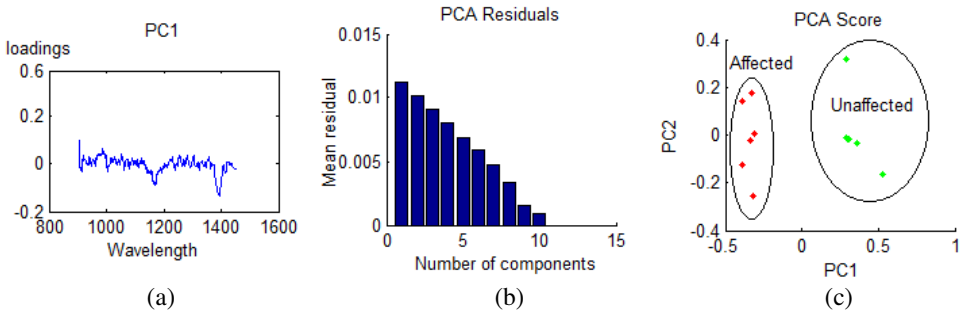


Figure 4: (a) The weight of component 1; (b) mean residual error of the model; (c) classification by the PCA.

4. MODEL OF THE MAGNETIC FIELD

The characteristics of the applied magnetic fields were determined using the finite element method in the ANSYS system. The representation of the resulting magnetic flux density vectors is shown in Figure 5. In the experimental measurement of the magnetic flux density gradient, we assumed that the highest value of the gradient will be achieved between the magnets [8].

5. CHARACTERIZATION OF THE EXPERIMENT

The experiment was conducted in steps as shown in Figure 6.

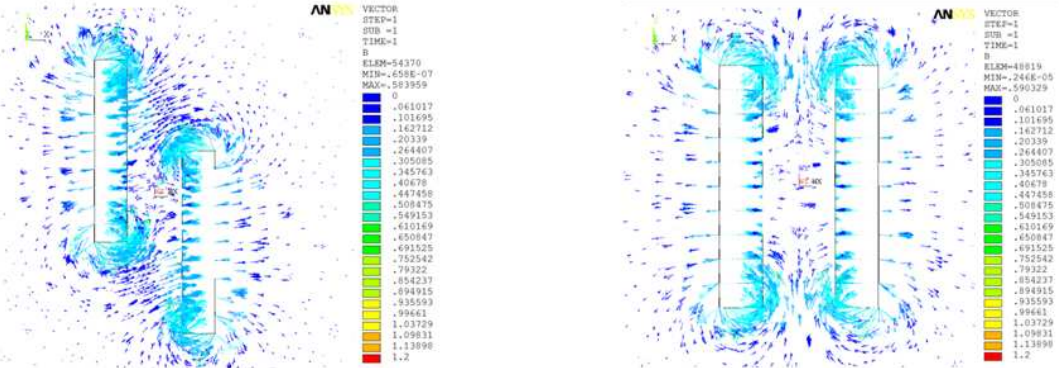


Figure 5: The results of the ANSYS-based modeling [8].

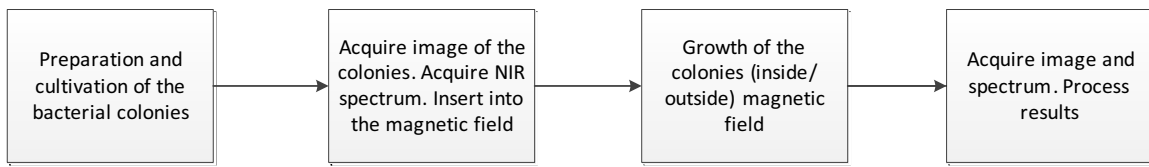


Figure 6: Description of the experiment.

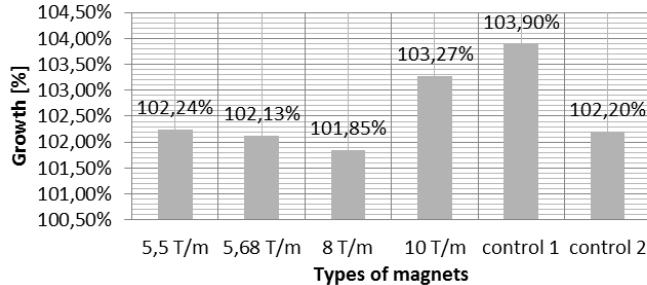


Figure 7: Percentage growth of bacteria on the of experiment.

We used two types of stationary magnetic fields. The first type was created at the ferrite magnet exhibiting the magnetic field gradient value of 5.5 and 5.68 T/m. The second type was created by the neodymium magnets. Magnets exhibit the magnetic field gradient. Density values are from 10 to 11 T/m. The third group of Petri dishes were used as a reference. Experiment takes 7 days at laboratory temperature (22°C).

6. RESULTS AND CONCLUSION

Four bacterial strains were stored in a maximum recovery diluent. The solution was used to prepare the colonies and to facilitate the NIR measurement. After the formation of the colonies, the first image of the reference and the exposed samples was acquired, and the NIR spectra were measured. The experiment lasted for 7 days at a laboratory temperature (22°C). At the end of the experiment, another image was acquired and the resultant spectrum obtained. As expected, the magnetic field had suppressed the growth of the colonies. To highlight the differences, a longer time or higher temperature would be necessary. The *Enterococcus durans* and the *Staphylococcus epidermidis* increased their radii by about 3% in the reference sample and 1–2% in the exposed sample. The other set strains exhibited similar results. Because of the inappropriately selected conditions, the growth was negligible and difficult to measure. For a convincing proof of growth suppression by the magnetic field, more measurements should be performed. The biological effect of the electromagnetic field may be based on the interference among ionic channels in the membrane, which affect the transportation of ions into the cells. Another explanation lies in the formation of free radicals caused by the magnetic field [1].

More interesting results were obtained by examining the NIR spectra. Two significant changes

were observed in the spectrum. First, there occurred changes in the compound concentration proved by the motion of the absorption peak to 1385 nm. Second, the ratio of proteins changed, it demonstrates decrease of peak at 1185 nm. This could constitute the proof of a different biochemical process inside bacteria cells.

ACKNOWLEDGMENT

The research described in the paper was financially supported by project of the BUT Grant Agency, No. FEKT-S-11-5/1012 and project from Education for Competitiveness Operative Programme CZ.1.07.2.3.00.20.0175 (Electro-researcher).

REFERENCES

1. Strasak, L., V. Vetterl, and J. Smarda, "Effects of low-frequency magnetic fields on bacteria *Escherichia coli*," *Bioelectrochemistry*, Vol. 55, No. 1–2, 161–164, Jan. 2002.
2. Bovik, A., *Handbook of Image and Video Processing*, Academic, New York, 2000, ISBN: 978-0-12-119792-6.
3. Bovic, A. C., M. Clark, and W. S. Geisler, "Multichannel texture analysis using localized spatial filters," *IEEE Trans. PAMI*, Vol. 12, No. 1, 55–73, 1991.
4. Sahoo, P. K., S. Soltani, and A. K. C. Wong, "A survey of thresholding techniques, computer vision," *Graphics, and Image Processing*, Vol. 41, No. 2, 233–260, 1998, ISSN 0734-189X.
5. Iwaki, O., K. Kubota, and H. Arakawa, "A character/graphic segmentation method using neighborhood line density," *IEICE Trans. Inform. Process.*, Vol. 68, No. 4, 821–828, 1985.
6. Sun, C. C. and S. C. Tai, "Beat-based ECG compression using gain-shape vector quantization," *IEEE Trans. Biomed. Eng.*, Vol. 52, No. 11, 1882–1888, Nov. 2005.
7. Savitzky, A. and M. J. E. Golay, "Smoothing and differentiation of data by simplified least squares procedures," *Analytical Chemistry*, Vol. 36, 1627–1639, 1964, doi:10.1021/ac60214a047.
8. Hutova, E., K. Bartusek, and J. Mikulka, "Study of the influence of magnetic fields on plants tissues," *PIERS Proceedings*, 57–60, Taipei, Mar. 25–28, 2013.

Enhanced Spectrum Planning in Cognitive System Based on Reinforcement Learning

R. Urban, E. Hutova, and D. Nespor

Department of Theoretical and Experimental Electrical Engineering
Brno University of Technology, Technicka 12, Brno 612 00, Czech Republic

Abstract— This paper presents preliminary results of interference less spectrum planning which is performed by reinforcement learning. The frequency planning of the wireless services is very difficult in current overfilled spectrum situation since it is nearly impossible to find spectral hole worldwide to deploy a new wireless service. The possible solution is an open dynamic spectrum access which could be implemented as a part of cognitive radio. Moreover, the modern wireless standards such as LTE-A partly implement cognitive radio improvements, e.g., carrier aggregation system, which enables using unused parts of the frequency spectrum to decrease interference and increase data throughput. It could be realised both the intra-band and the inter-band solution. According to the measured data of the spectrum situation in various environments, we prepared best case of channel switching in LTE-A and WI-FI systems, which is based on the reinforcement learning to minimize interference with primary users represented by measured data. Using this technique, we are capable to obtain very low misdetection probability and large variety in channel switching.

1. INTRODUCTION

Currently generally acceptable approach of spectrum allocation is very inefficient. Frequency spectrum is allocated according to the global frequency plans for large geographical areas. This method leads to blocking some parts of the spectrum in large areas. On the other hand, some spectrum parts could be over utilized by aggregation of several base stations at the same place. Regarding to these facts, deploying of the new worldwide wireless service is now nearly impossible due to the totally overfilled frequency spectrum plans around. One possible solution of this issue in frequency spectrum is offered by using dynamic spectrum sharing or resource management, which could be operated by cognitive system [1].

Cognitive radio is an intelligent autonomous system capable of adapting to the current area and time [1, 2]. It is possible to change transmitter parameters such as the operation frequency and radiation power, which are crucial parameters for dynamic spectrum sharing. These systems are using white spaces in the frequency spectrum (unused bandwidth) or rarely used parts of the spectrum in time, so called grey space. To find out these sharing possibilities, it is necessary to sense the environment and aware spectrum holes. It is obvious, that real-time sensing costs a lot of energy and also processing time. From this reason radio environment maps and spectrum usage, based on off-line spectrum surveys [3], models should be used instead of the sensing [4, 5]. Spectrum data are managed by a cognitive engine that controls available resources. In a cognitive system, we define primary users (wireless devices using the spectrum according to the assigned licence) and secondary or cognitive users (new entrants to the shared frequency spectrum whose traffic is coordinated by the cognitive engine). In this paper, we are focusing on LTE and WIFI cognitive users, who have dynamically assigned channel to maximize SINR and minimize interference caused by or to other systems by cognitive engine. It is obvious that the spectrum sensing is a crucial feature for correct operation of the cognitive radio. Real-time wideband spectrum sensing is still one of the main challenges for system developers. Therefore, cognitive radio is now fully working in limited bands [6] and simulations are provided in a large scale.

This paper introduces new approach of finding the best available channel for secondary users, which is based on reinforcement learning from spectrum survey data introduced in [3]. The reinforcement learning algorithm returns the vector of the scored channels based on possible interference in particular channel. Based on this statistical information we are able to plan secondary users' frequency allocation and minimize chance of interference between both primary and secondary users. Nonetheless to say, that better spectrum planning brings decline of the radiation power and decline of the microwaves smog to biological issues as well. The effects of the enormous electromagnetic radiation are widely discussed in [4].

2. SYSTEM DEFINITION

In simulation we suppose to deploy LTE-A and WI-FI service over the real measured data partly presented in [3]. We assume the distribution of primary users based on the 24 hour measurement sample of the frequency spectrum background from urban area. The measurement was performed in the frequency band from 800 MHz up to 2800 MHz, which covers the most common LTE bands and also WI-FI band. Presented simulation process has several steps. Firstly, the measured data are processed and potential primary users are marked as “interference possibility” or occupied part of the spectrum. Secondly, the reinforcement algorithm (see below) is periodically applied to obtain actual scores for each channel of specific services working under LTE and WI-FI technology (see below). The channel with lowest score is chosen and used until another channel got lower score. Finally, interference counts for selected channel combination are calculated as a comparison parameter.

2.1. Long Term Evolution (LTE)

Long Term Evolution (LTE) [7] is a modern standard for cellular telecommunications. It was designed to provide connectivity 100 Mbit in downlink and 50 Mbit in uplink for mobile user equipment's (UE). There is also an implementation of MIMO (4×4). Commonly it uses 64QAM modulation for downlink and QPSK modulation respectively for uplink stream. The next step cellular networks evolution is LTE-A, truly 4G system, which is capable of 10 times higher transmission speeds. For our simulations we choose 3 MHz channel bandwidth.

2.2. WI-FI

One of the most common worldwide wireless standard is definitely WI-FI [8]. It was firstly introduced in 1985 and nowadays it is included in nearly all mobile devices (smart phones, cameras, cars, TVs, etc.). This technology is mainly using OFDM technique in shared open spectrum ISM (Industrial, Science and Medical) bands – 2.4 GHz and 5 GHz respectively. The massive spread of the WI-FI systems causes overfilled in the shared designed spectrum and it is very difficult to find “interference less” channel.

2.3. Reinforcement Learning

Reinforcement learning is one of the machine learning technique [9], which provides us fast estimation of the channels behaviour. The crucial parameter of reinforcement learning is weight function (W_t) which is defined as:

$$W_t = CW_{t-1} + I(t, t-1), \quad (1)$$

where W_{t-1} is the value of the weight function in previous time step, C is constant (in this paper $C = 1$) and I is increment of the weight function for current time step with memory of the onetime step.

Generally, the scores of reinforcement learning should be set by many ways. We have decided to use dominant punishment algorithm and we have also used memory where the channel situation is stored from previous time ($t-1$). If we detect repetitive interference possibility, scores are increased by value 1000. Hence, single interference count add to total channel score 100. Finally, when the channel is empty in 2 following time steps, we decrease score by 1. This logic minimizes interference possibility. Unfortunately, it minimizes improvements of the channels scores as well.

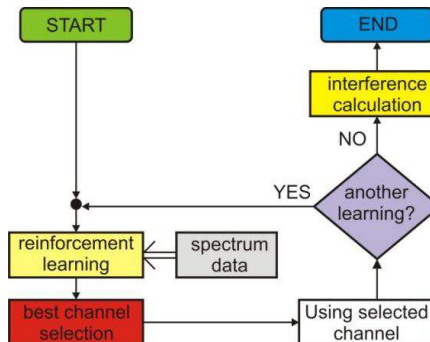


Figure 1: Simulation flowchart.

3. SIMULATION RESULTS

It is obvious, that intelligent spectrum utilization is a great opportunity how to increase performance of the wireless system. Each part of our simulation (see Fig. 1) is described below.

Firstly, the input parameters such as learning duration, learning repetition, etc. need to be selected. Afterwards, the band selection is crucial. In this paper we are limited only for intra-band channel switching, but in further work we would like to extend the scope of this work also for inter-band switching. Learning duration defines, how many measured samples will be used for reinforcement learning algorithm. On the other hand, learning repetition is describing duration, how long the selected “best” channel is used. After setting parameters of the simulation, we are able to start the initial learning. Based on the reinforcement learning (Chapter 2), we got initial

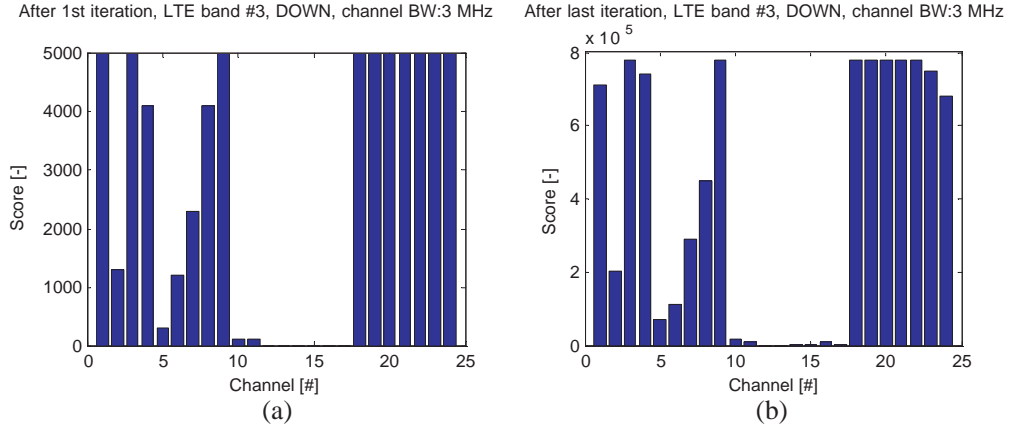


Figure 2: Reward/punishment score after 1st iteration and last iteration respectively for one LTE band.

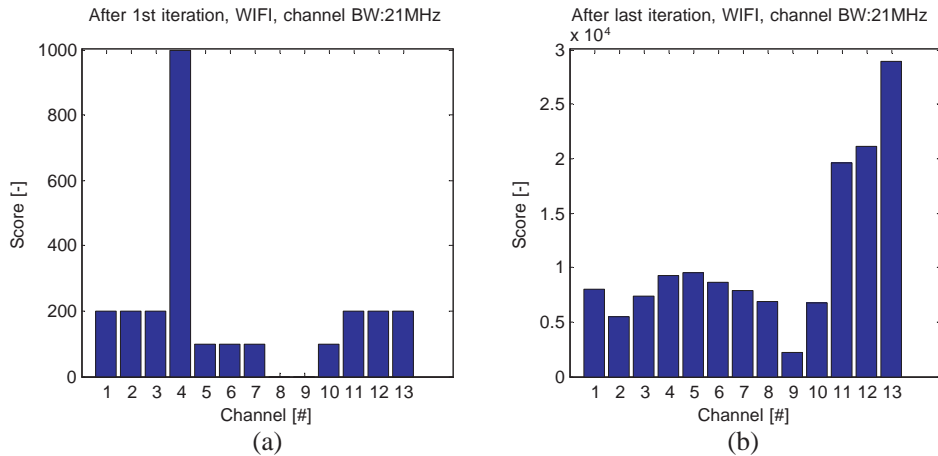


Figure 3: Reward/punishment score after 1st iteration and last iteration respectively for WI-FI service.

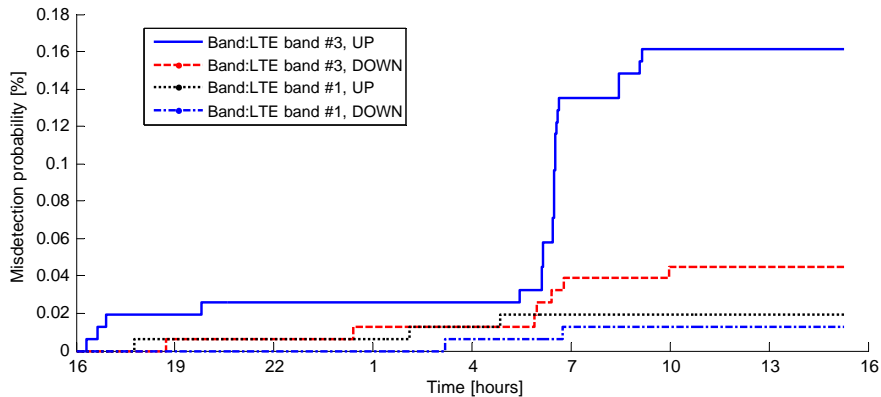


Figure 4: The best channel interference probabilities for selected LTE bands.

score table (Fig. 2(a)) for all channels in selected band. In second step, we choose the channel with lowest score. When more channels with equal scores exist, we choose the lowest channel. In following example we start with channel #12 for LTE service and channel #8 for WI-FI (Fig. 3) Until the next learning sequence, we are using selected channel. The channel preference is changed according to updated scores from weight function (1). The final scores after all possible learning sequences for current data set are presented in Fig. 2 and Fig. 3(b).

Finally the interference count is calculated as a number of detected primary user's radiation (for both frequency and time domain) in selected channel as misdetection probability. The results are presented in Fig. 4 and Fig. 5.

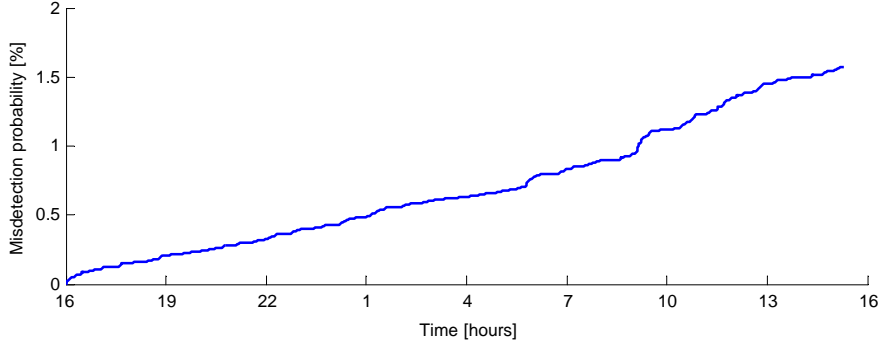


Figure 5: The best channel for WI-FI technology.

4. CONCLUSION

First results of the enhanced spectrum planning using reinforcement learning were presented. Based on the measured result, the algorithms for spectrum diagnosis were prepared and presented. It was proved, that this technique enables nearly interference less channels planning in various systems. It takes into account changes in the environment in both time domain and frequency domain. Preliminary results indicate that proposed technique nearly eliminates interferences in narrows LTE bands (less than 0.5%). The misdetection probability is less than 0.2% for LTE service and less than 2% for WI-FI service. The intra- and inter-channel aggregation enables additional bandwidth for fast data transfers. The same system was also tested for WI-FI band where the sufficient misdetection probability in various environments was obtained.

Further work will be focused not only on physical layer, but more factors will be taken into account, such as data transmission, carrier aggregation for LTE systems, channel aggregation for WI-FI service and environment simulation via game-theory.

REFERENCES

1. Mitola, J., *Cognitive Radio Architecture: The Engineering Foundations of Radio XML*, Wiley-Interscience, Hoboken, NJ, 2006.
2. Mitola, J., "Cognitive radio architecture evolution," *Proceedings of the IEEE*, Vol. 97, 626–641, 2009.
3. Urban, R., T. Korinek, and P. Pechac, "Broadband spectrum survey measurements for cognitive radio applications," *Radioengineering*, Vol. 21, 2012.
4. Urban, R., P. Fiala, T. Kriz, and J. Mikulka, "Stochastic description of wireless channel for cognitive radio," *PIERS Proceedings*, 38–42, Taipei, Taiwan, March 25–28, 2013.
5. Urban, R., T. Kriz, and M. Cap, "Indoor broadband spectrum survey measurements for the improvement of wireless systems," *PIERS Proceedings*, 376–280, Taipei, Taiwan, 2013.
6. "Cognitive radio experimentation platform," 2011, Available: <http://asgard.lab.es.aau.dk/joomla/index.php/home>.
7. Kumar, A., J. Sengupta, and Y.-F. Liu, "3GPP LTE: The future of mobile broadband," *Wirel. Pers. Commun.*, Vol. 62, 671–686, 2012.
8. IEEE, "Part 11: Wireless LAN medium access control (MAC) and physical layer (PHY) specifications," *Amendment 4: Further Higher Data Rate Extension in the 2.4 GHz Band*, Ed.: The Institute of Electrical and Electronics Engineers, Inc., 2003.
9. Bublin, M., J. Pan, I. Kambourov, and P. Slanina, "Distributed spectrum sharing by reinforcement and game theory," Fifth Karlsruhe Workshop on Software Radio, Karlsruhe, Germany, 2008.

2D Simulations of Bioelectrical Properties of Thorax by EIT

K. Ostanina, J. Dedkova, and T. Kriz

Department of Theoretical and Experimental Electrical Engineering
Brno University of Technology, Technicka 3082/12, Brno 616 00, Czech Republic

Abstract— The conventional Electrical Impedance Tomography (EIT) is a non-invasive imaging method of internal structure of the investigated object using spatial conductivity and relative permittivity distributions obtained from measurements of surface voltages and the known injected current. The EIT image reconstruction is an ill-posed inverse problem of finding such internal admittance distribution, which minimizes certain optimization criteria.

In the article, the improved EIT algorithm for images reconstruction of an internal admittance distribution of the human thorax tissue is described. This approach of imaging was applied to the several computer simulations, which demonstrate the real range of application of the proposed algorithm. The obtained results were presented. The properties of reconstruction process were also discussed.

1. INTRODUCTION

The imaging of electrical properties of the biological tissue like conductivity or permittivity has been the main topic of EIT investigations for many years. A lot of different algorithms based on EIT, which were used for numerical mapping of electrical tissue properties inside the investigated objects, were developed. The basic principle of EIT is described for example in [1]. One of the main advantages of this method is a non-invasive measurement of surface voltages. Furthermore, EIT has a relatively low cost and does not require using the sophisticated equipment.

The image reconstruction algorithm of the internal admittance

$$\mathbf{y} = \sigma + j \cdot 2\pi f \varepsilon_0 \varepsilon_r, \quad (1)$$

where σ is the conductivity, ε_r is the relative permittivity, ε_0 is the permittivity of free space and f is the frequency, includes two similar techniques, namely the conductivity and the permittivity reconstruction algorithms (Electrical Resistance Tomography and Electrical Capacitance Tomography). The both techniques require a system of conducting electrodes attached to the surface of the investigated object. In the case of conductivity imaging, the current is injected in electrode pairs and the resulting voltage is measured in the remaining electrodes. In the case of permittivity imaging, the voltage is supplied in turn to each electrode and the current is measured under the condition that other electrodes are grounded. In this paper the algorithm based on combination of these techniques was used.

2. BASIC THEORY

The electrical systems of imaging usually employ an alternating current at a fixed frequency f , which is sufficiently small. Thereby, the quasi-static approximation is valid and the magnetic field can be neglected. The conductivity and permittivity imaging (or reconstruction of the admittance distribution) can be represented as solution the following equation:

$$\operatorname{div}(\sigma + j \cdot 2\pi f \varepsilon_0 \varepsilon_r) \operatorname{grad} \mathbf{U} = 0. \quad (2)$$

The combination of Dirichlet and Neumann boundary conditions is described a complete boundary value problem, which can be solved for \mathbf{U} .

The determination of admittance distribution (imaging of internal structure of the object) represents the minimization of suitable objective function based on the Least Squares method (LSM). For the solution of minimization problem, the Newton-Raphson method was applied. In order to provide a stability of the reconstruction process, the Tikhonov regularization method (TRM) and an auxiliary filter are introduced in this EIT algorithm. After the linearization, the iteration procedure is used. And the unknown admittance distribution can be described by this equation:

$$\mathbf{y}_{i+1} = \mathbf{y}_i + (\mathbf{J}_i^T \mathbf{J}_i + \alpha \mathbf{L}^T \mathbf{L})^{-1} (\mathbf{J}_i^T (\mathbf{U}_M - \mathbf{U}_{\text{FEM}}(\mathbf{y}_i)) - \alpha \mathbf{L}^T \mathbf{L} \mathbf{y}_i) \quad (3)$$

where i is the number of iteration, \mathbf{J} is the Jacobian, \mathbf{U}_M is the vector of measured voltages on the surface object, $\mathbf{U}_{\text{FEM}}(\mathbf{y})$ is the vector of computed peripheral voltage relatively to \mathbf{y} , which can be obtained using the Finite Element method (FEM); α is a regularization parameter and \mathbf{L} is a regularization matrix.

3. MODEL

The numerical model for simulations is a 2D finite element model (FE model) which represents a simplified horizontal slice of the human thorax. This model consisting of 208 elements and 121 nodes is shown in Figure 1. Sixteen electrodes have been used for the voltage measurements on the surface of the investigated object. This is a simplified model of the human thorax, which consists of three homogeneous isotropic layers: lungs, heart and muscle.

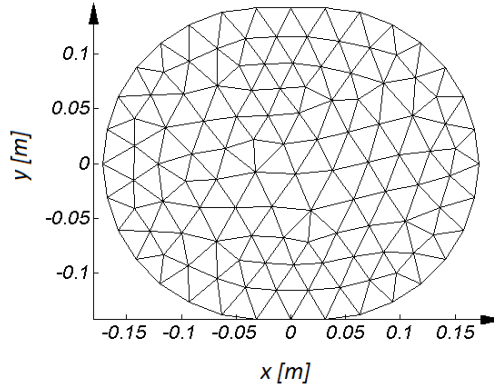


Figure 1: A 2D FE model for the modeling of human head tissue.

The conductivity and relative permittivity values of these biological tissues for frequencies of 1 kHz and 10 kHz used for the following simulations are presented in Table 1. These values were adopted from literature previously published [2].

Table 1: The conductivity and relative permittivity values of biological tissues.

Tissue name	1 kHz		10 kHz	
	Conductivity [S/m]	Relative permittivity	Conductivity [S/m]	Relative permittivity
Lung (inflated)	7.954e-2	1.415e+5	9.317e-2	1.717e+4
Heart	1.063e-1	3.529e+5	1.542e-1	7.005e+4
Muscle	3.212e-1	4.349e+5	3.408e-1	2.591e+4

4. SIMULATIONS RESULTS

The original admittance distributions, namely distribution of the real component of admittance — impedivity, demonstrating horizontal slice of the human thorax for frequencies of 1 kHz and 10 kHz are shown in Figures 2(a) and 2(d).

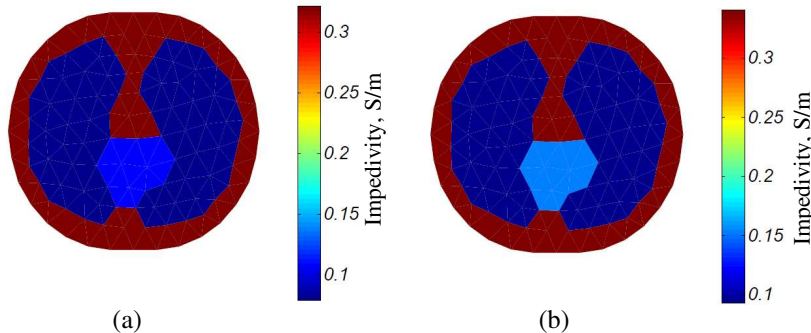


Figure 2: An original impedivity distribution for frequencies of (a) 1 kHz and (b) 10 kHz.

The experimental part of this paper bases on two groups of simulations. In the first group, a simple constraint, namely the impedivity has to be a positive number or equal to zero only, was introduced. In the second, the number of unknown (the so called Degrees of Freedom — DOFs) was reduced. All parameters of these reconstruction processes are given in Tables 2 and 3.

Table 2 presents data obtained after imaging of the impedivity distribution, which correspond the original distribution in Figure 1(a). The information in Table 3 describes the reconstruction process of distribution demonstrated in Figure 2(b).

Table 2: The parameters of reconstruction process (frequency — 1 kHz).

Parameters	without a reduction of DOFs			with a reduction of DOFs		
Regularization parameter, α_0	$5 \cdot d - 6$			$2 \cdot d - 6$		
Change of reg. parameter, $d\alpha^*$	0.1	0.3	0.7	0.1	0.3	0.6
Objective function, $\Psi(\sigma)$	4.142e-24	3.743e-7	1.236e-6	1.296e-24	2.665e-7	1.210e-22
Number of iteration	60	60	140	55	55	170
Relative error, Err [%]	1.334e-9	1.725	2.844	4.501e-10	1.851	4.571e-8
Time**, [sec]	0.87	0.88	1.58	0.76	0.87	1.87
Image of reconstruction result	original ¹	Figure 3(a)	Figure 3(b)	original ¹	Figure 3(c)	original ¹

Note: DOFs is Degrees of Freedom.

* $d\alpha$ ensures dynamic change of regularization parameter within the duration of the iteration process.

** Time of the reconstruction process depends on the parameters of hardware.

¹ “Original” means that the final impedivity distribution is identical with the original distribution.

Table 3: The parameters of reconstruction process (frequency — 10 kHz).

Parameters	without a reduction of DOFs			with a reduction of DOFs		
Regularization parameter, α_0	$7 \cdot d - 6$			$5 \cdot d - 6$		
Change of reg. parameter, $d\alpha^*$	0.1	0.3	0.6	0.1	0.3	0.6
Objective function, $\Psi(\sigma)$	6.311e-24	5.412e-24	2.236e-23	2.588e-23	1.732e-23	2.454e-23
Number of iteration	50	90	195	55	95	185
Relative error, Err [%]	2.466e-9	3.670e-9	2.252e-8	2.316e-9	3.568e-9	2.921e-8
Time**, [sec]	0.84	1.14	2.26	0.82	1.12	2.06
Image of reconstruction result	original ¹	original ¹	original ¹	original ¹	original ¹	original ¹

Note: DOFs is Degrees of Freedom.

* $d\alpha$ ensures dynamic change of regularization parameter within the duration of the iteration process.

** Time of the reconstruction process depends on the parameters of hardware.

¹ “Original” means that the final impedivity distribution is identical with the original distribution.

The simulation results, illustrated reconstructions of the impedivity distribution of biological tissues inside human thorax for different parameters by applying the proposed algorithm are present in Figure 3.

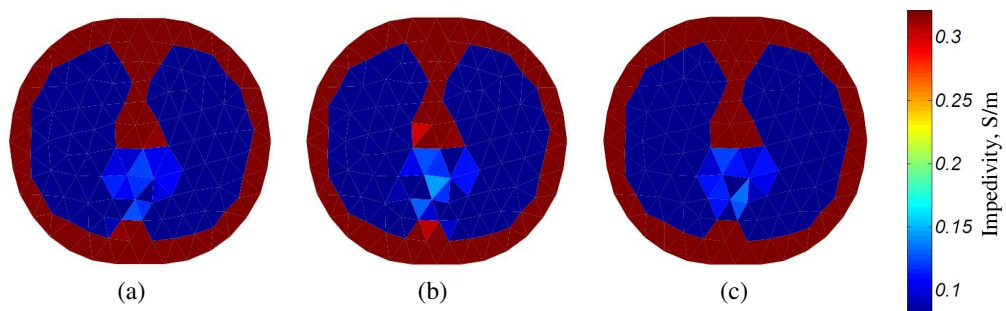


Figure 3: The reconstruction results (frequency — 1 kHz) in the cases: (a) $\alpha_0 = 5 \cdot d - 6$, $d\alpha = 0.3$; (b) $\alpha_0 = 5 \cdot d - 6$, $d\alpha = 0.7$; (c) $\alpha_0 = 2 \cdot d - 6$, $d\alpha = 0.3$.

The behavior of the objective function $\Psi(\sigma)$, condition number $ncond$ and regularization parameter α during the reconstruction process is compared in Figure 4. This characteristics were obtained by using EIT algorithm with a reduction of DOFs for parameters: (a) $\alpha_0 = 2 \cdot d - 6$, $d\alpha = 0.6$, frequency — 1 kHz and (b) $\alpha_0 = 5 \cdot d - 6$, $d\alpha = 0.6$, frequency — 10 kHz.

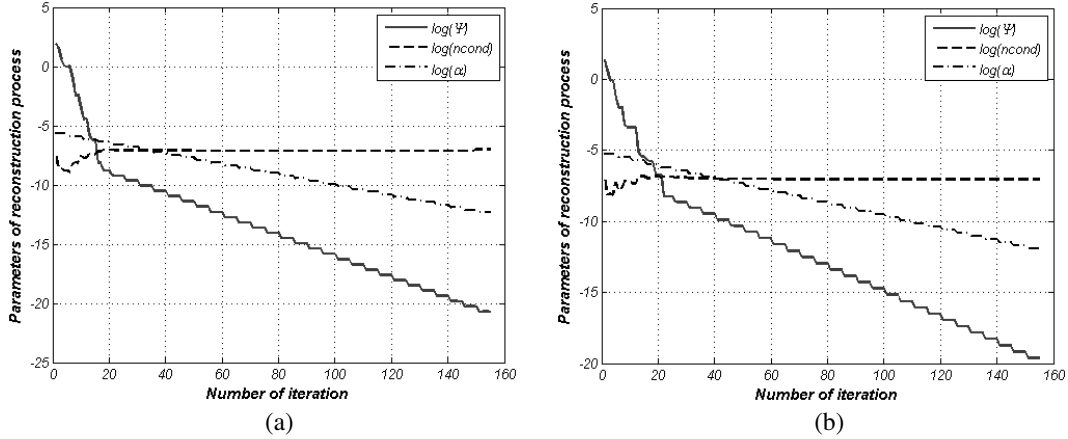


Figure 4: The characteristics of reconstruction in the cases using a reduction of DOFs: (a) $\alpha_0 = 2 \cdot d - 6$, $d\alpha = 0.6$, frequency — 1 kHz; (b) $\alpha_0 = 5 \cdot d - 6$, $d\alpha = 0.6$, frequency — 10 kHz.

5. CONCLUSION

In this paper, the algorithm for images reconstruction of an internal admittivity distribution of the human thorax tissue based on the Electrical Impedance Tomography with using the Tikhonov regularization method is presented.

The realized simulations demonstrated that the use of admittivity values of the biological tissues of higher frequencies (10 kHz) for the images reconstruction has significant influence on the increase of stability and accuracy of a reconstruction process. By using the admittivity of lower frequencies (1 kHz) in imaging, the stability and accuracy can be provided by introduction an auxiliary technique, such as the Level Set method or the Fuzzy filters. Also, this problem can be solved by using an additional refinement of mesh and subsequent reduction of DOFs.

ACKNOWLEDGMENT

The research described in the paper was financially supported by project of the BUT Grant Agency FEKT-S-11-5/1012 and projekt CZ.1.07.2.3.00.20.0175, Elektro-vyzkumník.

REFERENCES

- Holder, D. C., ed., *Electrical Impedance Tomography. Methods, History and Applications*, Institute of Physics Publishing, London, 2005.
- Andreuccetti, D., R. Fossi, and C. Petrucci, “An internet resource for the calculation of the dielectric properties of body tissues in the frequency range 10 Hz–100 GHz,” Website at <http://niremf.ifac.cnr.it/tissprop/>, IFAC-CNR, Florence, Italy, 1997 (based on data published by C. Gabriel et al. in 1996).

Estimation of the Air Ion Mobility Spectrum by Means of a Gerdien Tube with a Segmented Inner Electrod

Z. Roubal and P. Křepelka

Department of Theoretical and Experimental Electrical Engineering
Brno University of Technology, Kolejní 2906/4, Brno 612 00, Czech Republic

Abstract— Light negative air ions demonstrably exhibit positive influence on the human organism. The concentration of these ions can be effectively used as the integral criterion for the evaluation of air purity, and there also exists a multitude of other applications. The presented aspiration method enables us to establish the concentration of air ions in the atmosphere. In a gerdien tube fitted with a one-piece inner electrode, measurement of the saturation characteristics must be performed to facilitate the determination of the air ion mobility spectrum. The characteristics represent the relation of the measured current through the inner electrode to the polarization voltage. The measurement is time-intensive and sensitive to temporal fluctuations of the air ion concentration during the measurement. For this reason, a gerdien tube of the first type is used; the device comprises a segmented inner electrode, and the air ion mobility spectrum can be estimated (for two polarization voltages) from individual currents of the inner electrode segments. However, due to the overlapping between the functions G that characterize the transmission functions of the individual electrodes, estimation of the air ion spectrum is not an explicit task. The simulation electrostatic field and air flow is shown in this paper.

1. INTRODUCTION

In industrial zones, where the environment air is often polluted with dust and smog, the concentration of air ions can be regulated or measured only with difficulty. Any thus impaired area shows an inherent deficiency of negative ions and, conversely, an abundance of positive ions complementing the nano and microscopic dust particles. Significantly, the described aspects have a markedly negative effect on the overall degree of fatigue and professional performance of a human being [1, 2]. The impact of environment on a human organism has been analyzed in studies [1, 2]. In the DTEEE laboratories, the methodology supporting the measurement of air ions concentration and mobility spectrum utilizes an aspiration condenser [3–9], this method is dependent upon a suitable approximation of saturation characteristics.

2. GERDIEN TUBE

A Gerdien tube (GT) is instrumental used for the measurement of air ions concentration assuming that the volume of tested air has not been limited or the ions are continuously generated. In the time domain, it is possible to measure by means of an GT only ions of one polarity; then, following a certain interval, ions of the other polarity can be measured. Ionized air is sucked into the GT by a ventilator. The homogeneous electric field is set between the inner and the outer electrode. If an electric ion shows a negative electric charge and the collecting inner electrode has a positive electric potential, the ion is progressively attracted to the inner electrode. Provided that the ion impinges upon the electrode, it will induce an electric current that is measured by the help of a sensitive electrometric picoampermeter [4]. The velocity of the ions motion in the electric field can be described by mobility k [$\text{m}^2 \cdot \text{V}^{-1}\text{s}^{-1}$].

It is possible to determine boundary mobility k_m for every GT configuration.

All ions showing an index of mobility greater than k_m will impinge upon the inner electrode; however, only a proportionate part of them will impinge in ions which mobility is smaller than k_m . Based on the aspiration condenser parameters, the air flow volume rate is defined as

$$M = (r_2^2 - r_1^2) \cdot \pi \cdot v_x, \quad (1)$$

where M , r_2 , r_1 , v_x , ... are the air flow volume rate, the outer electrode radius, the inner electrode radius, and the air flow velocity, respectively.

The main parameter applied for the definition of air ions mobility consists in boundary mobility k_m ,

$$k_m = \frac{\varepsilon_0 \cdot \varepsilon_r \cdot M}{C_{AK} \cdot U_{AK}}, \quad (2)$$

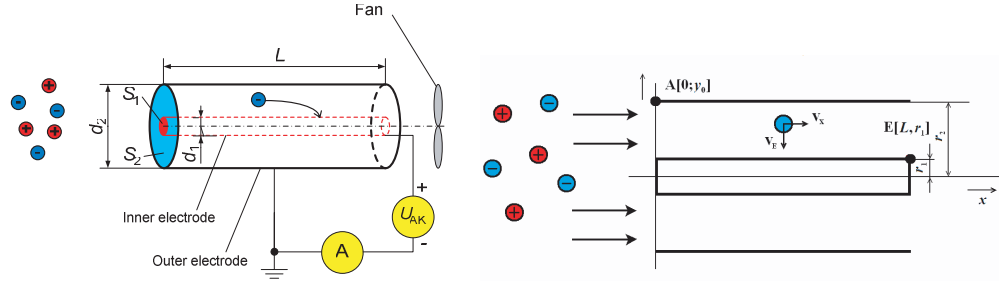


Figure 1: The basic principle of an gerdien tube.

where $\varepsilon_0, \varepsilon_r, C_{AK}, U_{AK}, \dots$ are the vacuum permittivity, the relative permittivity, the GT capacity, and the GT polarization voltage, respectively. Then, for current I measured by the electrometric picoampermeter, we can define

$$I_{k < k_m} = \frac{k}{k_m} \cdot n \cdot q \cdot M, \quad I_{k \geq k_m} = n \cdot q \cdot M, \quad (3)$$

where n, q, \dots are the volume concentration of ions and the elementary charge, respectively.

3. CONCENTRATION OF THE VOLUME DENSITY OF IONS

The condition of equivalence between an ion charge and an electron elementary charge is satisfied only in light ions, which implies that the condition is not valid in heavy ions that contain several charges of the described type. Then, the relevant situation is referred to as relative number of ions per volume unit. The starting point for the determination of an ion mobility consists in the quantity of charge q and volume concentration of electric charge ρ [10–12].

$$n_{+-}(k_1, k_2) = \frac{\rho_{+-}(k_1, k_2)}{q}. \quad (4)$$

Now, net electric current in the circuit can be written in the form of

$$I = M \cdot \frac{1}{k_m} \int_0^{k_m} k \cdot \rho(k) dk + M \cdot \int_{k_m}^{\infty} k \cdot \rho(k) dk. \quad (5)$$

It is advantageous [4] to express the characteristics of the aspiration condenser by the help of function G . Equation (5) can be modified to the form

$$I = \int_0^{\infty} G(k) \cdot \rho(k) \cdot dk, \quad (6)$$

for the gerdien tube with non divided inner electrode, function G is given

$$G = \begin{cases} \frac{C \cdot U \cdot k}{\varepsilon_0} & k < k_m \\ M & k \geq k_m \end{cases} \quad (7)$$

4. THE ELECTROSTATIC FIELD IN GERDIEN TUBE

Using a simulation in ANSYS (based on the FEM), we calculated the electrostatic field inside the Gerdien tube in relation to two conditions. In the first one, the electrostatic potential for the measurement of positive ions was simulated; the voltage on the outer and the inner electrodes was 25 V and 0 V, respectively. The voltage of the shielding electrode was 0 V. The described situation is shown in Fig. 2. However, if negative ions are not measured, the voltage on the outer electrode is 0 V; the inner electrode then exhibits the voltage of 25 V. This configuration is indicated in Fig. 3.

The electric field intensity inside cylindrical capacitor is described by equation

$$E = \frac{U_{AK}}{y \cdot \ln \left(\frac{r_2}{r_1} \right)} \quad (8)$$

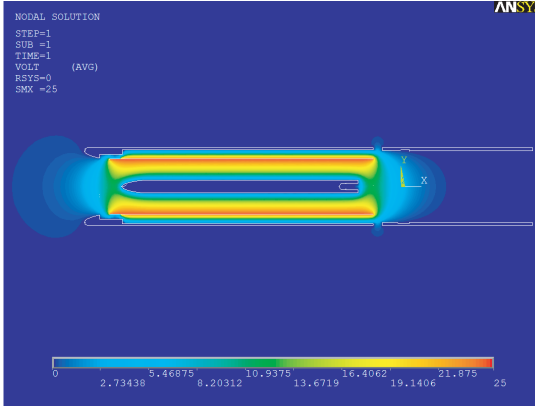


Figure 2: The electric potential for the measurement of positive ions.

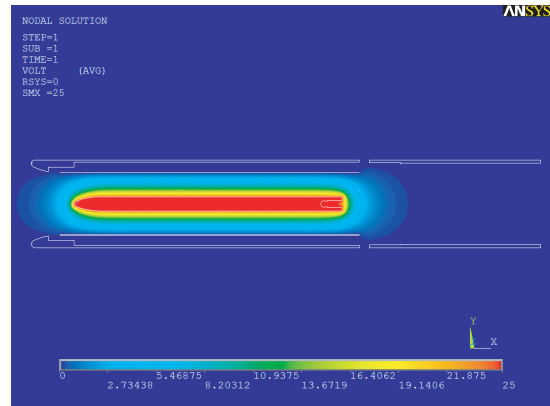


Figure 3: The electric potential for the measurement of negative ions.

The simulated electric field intensity for both measurements shown in Fig. 4.

Based on the simulation in Ansys, it is possible to compare the electric field intensity in the defined path with the ideal equation (8). The maximum error at the edges of the inner electrode is smaller than 15% (Fig. 6). In the center of the inner electrode, the error (below 1%) is caused by inaccurate approximation provided by the FEM.

5. AIR FLOW IN THE GERDIEN TUBE

The air flow in the Gerdien tube was simulated using the CFX program; the predicted flow type was laminar. The corresponding results are presented in Figs. 7 and 8.

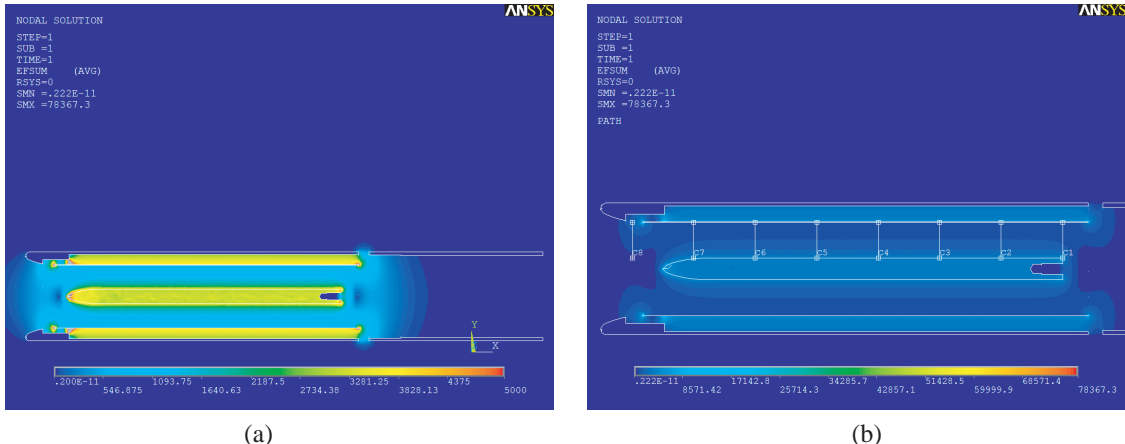


Figure 4: (a) The electric electric field intensity for $U_{AK} = 25$ V. (b) The defined path in the GT.

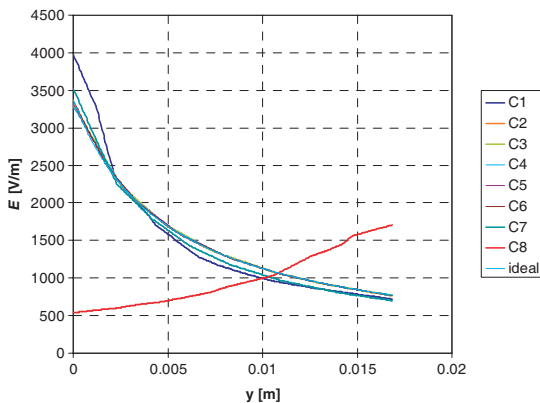


Figure 5: The electric field intensity for the for defined path.

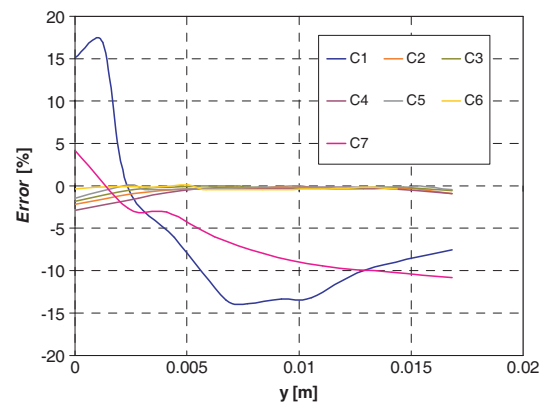


Figure 6: The error between ideal and real electric field.

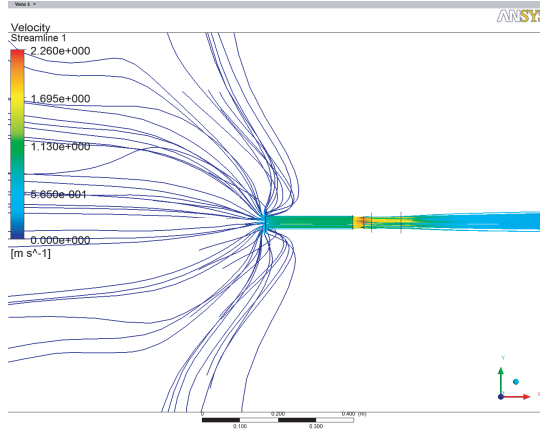


Figure 7: The slice air flow velocity in GT.

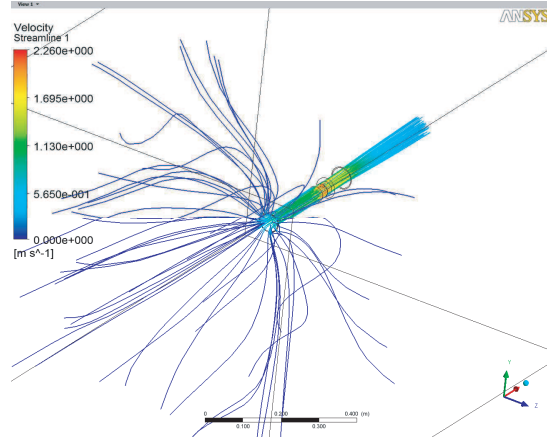


Figure 8: The air flow velocity in GT and streamline.

Figures 9 and 10 show a slice through the GT in the defined path. The laminar flow assumption expected for a GT by the authors of [13] was confirmed.

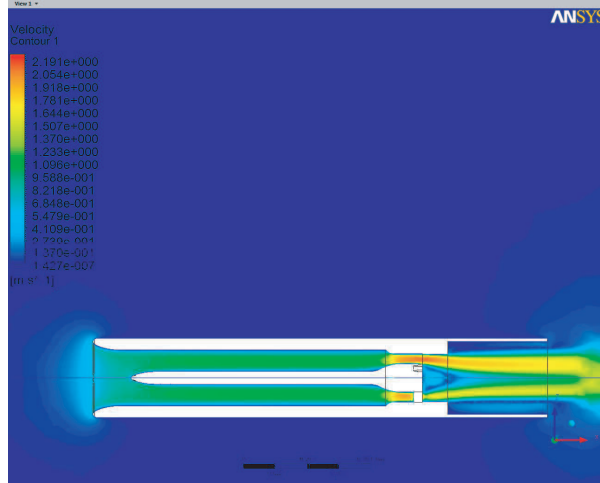


Figure 9: A longitudinal slice through the air flow velocity in the GT.

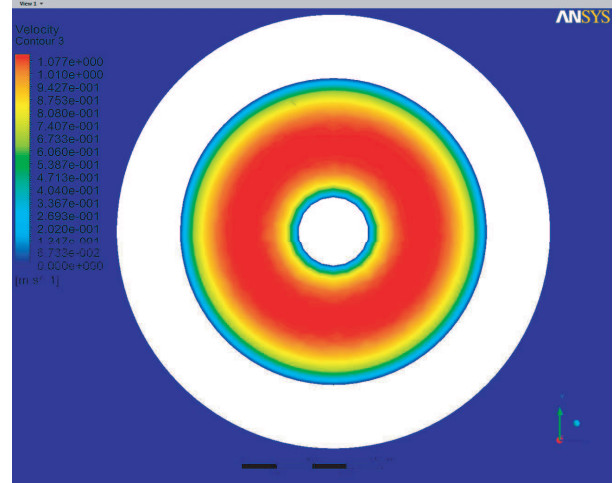


Figure 10: The C4 slice through the air flow velocity in the GT.

6. CONCLUSION

The ANSYS program was applied to facilitate the simulation of the electrostatic field and air flow inside the examined GT. Thus, the above-shown equation 8 and the predicted laminar flow were confirmed to be valid [13]. This confirmation is important for the determination of function G in our Gerdien tube. The new electrometric amplifier will include an integrator to eliminate the white noise. The elimination of the $1/f$ noise of the operational amplifier will be performed by using a modulated amplifier to compensate the offset voltage. The electrometric amplifier will employ a cooling Peltier element to decrease the input current of the operational amplifier and the input noise current [14].

ACKNOWLEDGMENT

The research described in the paper was financially supported by project of the BUT Grant Agency, FEKT-S-11-5/2012 project from Education for Competitiveness Operative Programme CZ.1.07.2.3.00.20.0175, (Electro-researcher).

REFERENCES

1. Tikhonov, V. P., A. A. Temnov, V. A. Kushnir, T. V. Sirota, E. G. Litvinova, M. V. Zakharchenko, and M. N. Kondrashova, "Complex therapeutical effect of ionized air: Stimulation

- of the immune system and decrease in excessive serotonin. H₂O₂ as a link between the two counterparts," *IEEE Trans. Plasma Scien.*, Vol. 32, No. 4, 1661–1667, 2004.
2. Kondrashova, M. N., E. V. Grigigorako, A. N. Tikhonov, T. V. Sirota, A. V. Temnov, I. G. Stavrovskaya, N. I. Kosyakova, N. V. Lange, and V. P. Tikonov, "The primary physicochemical mechanism for the beneficia biological/medical effects of negative air ions," *IEEE Trans. Plasma Scien.*, Vol. 28, No. 1, 230–237, 2000.
 3. Roubal, Z., M. Steinbauer, and Z. Szabó, "Modeling of saturation characteristic of an aspiration condenser," *PIERS Proceedings*, 216–220, Xi'an, China, March 22–26, 2010.
 4. Roubal, Z. and M. Steinbauer, "Design of electrometric amplifier for aspiration condenser measurement," *PIERS Proceedings*, 1430–1434, Xi'an, China, March 22–26, 2010.
 5. Bartušek, K., P. Fiala, T. Bachorec, and E. Kadlecová, "Numerical modeling of accuracy of air ion field measurement," *PIERS Proceedings*, 578–581, Beijing, China, March 26–30, 2007.
 6. Steinbauer, M., P. Fiala, Z. Szabó, and K. Bartušek, "Experiments with accuracy of the air ion field measurement," *Advances in Electrical and Electronic Engineering*, Vol. 08, No. 7, 276–681, 2008, ISSN 1336-1376.
 7. Mikulka, J., M. Steinbauer, and Z. Szabó, "Application of low-level measurement principles to air ion field characterization," *The 18th International Conference "Electromagnetic Disturbances EMD' 2008" Proceedings*, 137–140, Vilniaus Gedimino Technikos Universiteto Leidykla "Technika", Vilnius, Lithuania, 2008, ISSN 1822-3249.
 8. Szabó, Z. and K. Bartušek, "Effect of air-ion concentration on microflora in living spaces," *Sborník konference Measurement 2009*, 141–144, Institute of Measurement Science, Bratislava, 2009, ISBN 978-80-969672-1-6.
 9. Sedláček, J., Z. Szabó, and R. Kadlec, "Optimized ARC filters using goal-lossy GIC," *PIERS Proceedings*, 591–596, Beijing, China, March 23–27, 2009.
 10. Tammet, H. F., *The Aspiration Method for Determination of Atmospheric Spectra*, IPST, Jerusalem, 1970.
 11. Kadlec, R., E. Kroutilová, and P. Fiala, "Multiple reflection from layered heterogeneous medium," *PIERS Proceedings*, 87–90, Suzhou, China, September 12–16, 2011.
 12. Bartušek, K., "Meření spektrálních charakteristik iontových polí," *Elektrorevue*, 2001, <http://www.elektro-revue.cz/clanky/01038/index.html>.
 13. Roubal, Z. and K. Bartušek, "The determination of function G and air ion mobility spectrum in an aspiration condenser with segmented inner electrode," *PIERS Proceedings*, Kuala Lumpur, Malaysia, 374–379, March 27–30, 2012.
 14. Roubal, Z. and R. Kadlec, "Evaluation of characteristics of HV electrometric amplifier with low input current," *PIERS Proceedings*, 995–999, Suzhou, China, September 12–16, 2011.

Study about Effects Induced by Temporal-variability of Ionosphere on Medium-Earth-Orbit SAR Azimuth Imaging

Liang Li^{1, 2, 3}, Jun Hong^{1, 2}, and Feng Ming^{1, 2}

¹Institute of Electronics, Chinese Academy of Sciences, Beijing 100190, China

²Sciences and Technology on Microwave Imaging Laboratory, Beijing 100190, China

³University of Chinese Academy of Sciences, Beijing 100049, China

Abstract— An analysis model for ionospheric effects on azimuth imaging of Medium-Earth-Orbit SAR (MEOSAR) is established based on the system characteristics of MEOSAR and the temporal-variability of ionosphere. The effects caused by the quadratic and cubic phase errors induced by ionosphere gradients on azimuth imaging are analyzed. The results of the analysis show that both the quadratic phase error and the cubic phase error being neglected for Low-Earth-orbit SAR (LEOSAR) will deteriorate the azimuth imaging for MEOSAR. Moreover, the ionospheric effects become more and more serious with the increasing of SAR altitude.

1. INTRODUCTION

Resolution and swath are important performance indicators for spaceborne Synthetic Aperture Radar (SAR), but they are contrary to each other for LEOSAR. It is an effective method for solving the contradiction through heightening the orbit of SAR. With the development of the technology in radar, the possibility for MEOSAR has been accepted and much attention is paid to it since the 21th century [1–3]. Many researcher have studied MEOSAR on synchronization technology, orbit design, performance analysis, imaging process, moving target detection and so on [4, 5]. And MEOSAR has been one of the most popular spaceborne SAR sensors.

Spaceborne SAR is often works above the ionosphere and radio signal will be inevitably affected by the ionosphere, which will cause ionosphere-induced effects such as phase fluctuation, group delay, Doppler frequency-shift, dispersive and Faraday rotation. Study about the ionospheric effects on spaceborne LEOSAR have been made by many researchers [6, 7], but the paper about ionospheric effects on MEOSAR is few. Only S. H. Hobbs et al. discussed the effects of ionospheric perturbations over long integration time on geosynchronous SAR imaging performance [8]. In this paper, an analysis model for ionospheric effects on MEOSAR azimuth imaging is established based on the system characteristics of MEOSAR and the temporal-variability of ionosphere. The effects caused by the quadratic and cubic phase errors induced by ionosphere gradients on azimuth imaging are analyzed.

2. ANALYSIS ABOUT SPECIFICATIONS OF MEOSAR [4]

2.1. Azimuth Resolution

The resolution in azimuth can be expressed as Eq. (1).

$$\rho_a = V_g/B_a \quad (1)$$

where B_a is the Doppler bandwidth and V_g is the velocity of the beam projected on ground.

Assuming the rotation of the earth can be neglected, the value of V_g can be estimated from Eq. (2).

$$V_g \approx R_e \sqrt{\mu/R_s^3} \quad (2)$$

where $\mu = 3.986 \times 10^{14}$ is the gravitation constant of the earth. R_e and R_s are radius of the earth and SAR orbit respectively.

Equation (2) implies V_g will decreases with the increasing of SAR altitude. From Eq. (1), we know the Doppler bandwidth needed can be less for MEOSAR than LEOSAR when azimuth resolution is same, that is to say, when the Doppler bandwidth is same, azimuth resolution of MEOSAR is better than LEOSAR.

2.2. Synthetic Time

The echo of spaceborne SAR in azimuth is also the linear frequency-modulated signal approximately. The rate of frequency modulated in azimuth at the center of azimuth beam can be expressed approximately as Eq. (3).

$$K_a = 2V_r^2 / (\lambda R_c) \quad (3)$$

where $V_r \approx \sqrt{V_g V_s}$ is the equivalent velocity and $V_s = \sqrt{\mu/R_s}$ is the velocity of SAR. R_c is the range from SAR to the target at the center of azimuth beam.

The synthetic time described as Eq. (4) can be estimated from Eq. (1) and Eq. (3).

$$T_a \approx \lambda R_c / (2\rho_a V_s) \quad (4)$$

For MEOSAR, R_c is larger and V_g is smaller than they are for LEOSAR, so synthetic time for MEOSAR will be larger than for LEOSAR for a given azimuth resolution. Therefore, the effects on azimuth imaging induced by the changing of ionosphere in the synthetic time will increase.

3. IONOSPHERIC EFFECTS ON PROPAGATION OF SIGNAL [9]

3.1. Group Delay

The refractive index can be expressed as Eq. (5) based on the theory of Appleton-Hartree [10].

$$n \approx 1 - \omega_p^2 / 2\omega^2 \quad (5)$$

where $\omega_p = \sqrt{e^2 N_e / m \epsilon_0}$ is the angular plasma frequency, and e and m are the charge and mass of an electron respectively. ϵ_0 is the electric permittivity of free space, N_e is the electron density and ω is the angular frequency of electromagnetic wave.

The velocity of electromagnetic wave in the ionosphere is

$$v_{ion} = c \cdot n = c \left(1 - \omega_p^2 / 2\omega^2 \right) \quad (6)$$

The two-way extra delay introduced by the presence of ionosphere is

$$\tau_{gi} = \frac{\int_s (1-n)dl}{c} \approx \frac{80.6}{cf^2} \cdot TEC \quad (7)$$

where s is the ray path and $TEC = \int_s N_e dl$ is the total electron content along the path. c is the velocity of light and f is the frequency of electromagnetic wave.

The group delay induced by ionosphere will introduce a range shift in the focused image.

3.2. Phase Advance

There will be phase advance for wave propagating in ionosphere because the refractive index in ionosphere is less than one, which will introduces the phase error. The phase advance induced by ionospheric TEC can be evaluated from Eq. (8) [10].

$$\phi_{ion} = -\frac{2\pi \cdot 80.6}{cf} \cdot TEC_s \quad (8)$$

How does the phase error affect the image quality depends on not only the magnitude but also the function form of the phase error. If the phase error only depends on frequency and is time-independent, only the image quality in range is affected. Otherwise, if the phase error is time-dependent, the image quality in azimuth is also affected.

Because the change of TEC in synthetic time cannot be neglected for MEOSAR, from Eq. (8) we know the phase error induced by ionosphere is not only a function of frequency but also varies with azimuth positions. Therefore, both range imaging and azimuth imaging will be affected. In this paper, only the influence on azimuth imaging is analyzed.

4. EFFECTS ON MEOSAR AZIMUTH IMAGING

4.1. Model for Analysis

The ideal SAR echo can be expressed as Eq. (9)

$$s_0(\tau, \eta) = A_0 \cdot \exp \{-j4\pi f_0 R(\eta)/c\} \cdot \exp \{j\pi k_r(\tau - 2R(\eta)/c)^2\} \quad (9)$$

where τ is the fast time and η is the slow time. k_r is the rate of frequency modulated. f_0 is the center frequency operated and $R(\eta)$ is the distant from SAR to target.

Considering the group delay and phase advance induced by ionosphere, Eq. (9) will be expressed as Eq. (10).

$$s_{0ion}(\tau, \eta) = A_0 \cdot \exp \{-j4\pi f_0 R(\eta)/c\} \cdot \exp \{j\pi k_r \tau_{ion}^2\} \cdot \exp \{j\phi_{ion}(f, \eta)\} \quad (10)$$

where $\tau_{ion} = \tau - 2R(\eta)/c - \tau_{gi}$, $f = f_0 + k_r \tau_{ion}$ and $\phi_{ion}(f, \eta)$, which is the function of frequency and slow time, is the phase error induced by ionosphere.

Ionospheric TEC will affect the azimuth image, and for SAR sensor, TEC is a function of slow time in azimuth. A Taylor expansion about TEC at $\eta = 0$ is performed [13]:

$$TEC_s(\eta) = TEC_s(0) + TEC'_s(0) \cdot \eta + TEC''_s(0) \cdot \eta^2/2 + TEC'''_s(0) \cdot \eta^3/6 + \dots \quad (11)$$

where $TEC(0)$ is the TEC at $\eta = 0$. $TEC'(0)$, $TEC''(0)$ and $TEC'''(0)$ are one-order, two-order and three-order derivative of TEC. And η is the slow time in azimuth.

From Eq. (11) we can see the phase errors induced by ionospheric TEC include constant error, linear, quadratic, cubic and high-order phase errors. The first two terms don't impact the image quality. The quadratic phase error will cause mainlobe widening and sidelobes rising and the cubic phase error will induce an asymmetrical distortion in azimuth image. The high-order error is usually small.

For LEOSAR, synthetic time is usually less than one second, so ionospheric TEC can be considered as a constant and the effects induced by background ionosphere can be ignored. However, for MEOSAR, synthetic time increase a lot compared to LEOSAR, then the phase error induced by ionosphere will increases accordingly. In this section, only the ionospheric effects induced by the quadratic and the cubic phase errors are considered.

4.2. Simulation

In this section, the quadratic and cubic phase errors induced by ionosphere are analysed with regard to SAR sensors which altitude are 600 km, 1300 km, 3000 km and 10000 km respectively. The parameters are listed in Table 1.

Table 1: Parameters of SAR for simulation.

Altitude (km)	600	1300	3000	10000
Frequency (GHz)	1.25	1.25	1.25	1.25
Azimuth Resolution (m)	5	5	5	5
Slant Angle (°)	0	0	0	0
Scene Incidence Angle (°)	45	45	45	45
d^2TEC/dt^2	0.01TECu	0.01TECu	0.01TECu	0.01TECu
d^3TEC/dt^3	0.003TECu	0.003TECu	0.003TECu	0.003TECu

From Eq. (8) and Eq. (11), we can calculate the quadratic phase error Φ_2 and cubic phase error Φ_3 in azimuth induced by TEC. Expressed as Eq. (12).

$$\Phi_2 = -\pi \cdot 80.6 \cdot TEC''_s \cdot \eta^2 / (c f_0), \quad \Phi_3 = -\pi \cdot 80.6 \cdot TEC'''_s \cdot \eta^3 / (3 \cdot c f_0) \quad (12)$$

Assuming the ionospheric state is same, the longer synthetic time for MEOSAR will introduce a larger peak quadratic and cubic phase errors and the azimuth imaging will be affected more seriously. Fig. 1 gives the simulation results of image in azimuth affected by the quadratic and cubic phase errors. Table 2 quantificationally presents the degradation in PSLR and resolution caused by the quadratic and cubic phase error. The results from simulation show that the influence on azimuth imaging caused by the quadratic and cubic phase errors becomes more and more serious with the rising of orbit on condition of the same ionosphere state for L-band SAR sensor.

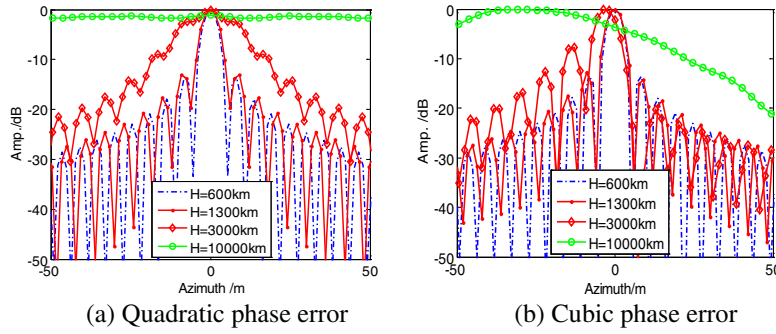


Figure 1: Distortion caused by phase errors in azimuth image.

Table 2: Effects of resolution and PSLR caused by quadratic and cubic phase error.

SAR Altitude		600 km	1300 km	3000 km	10000 km	
Resolution/m	Quadratic	4.72	5.24	18.38	657.22	
	Cubic	4.72	5.23	6.61	46.08	
PSLR/dB	Quadratic	Left	13.45	12.98	9.02	/
		Right	13.45	12.98	9.02	/
	Cubic	Left	13.40	12.78	7.41	2.08
		Right	13.54	14.06	20.35	32.48

5. CONCLUSION

In this paper, the model for analyzing ionospheric effects on MEOSAR is established. On base of this model, we analyzed the influences on L-band MEOSAR azimuth imaging caused by ionosphere-induced phase errors. The results of simulation show that the quadratic and cubic phase errors neglected for LEOSAR will introduce a serious distortion in azimuth image for MEOSAR. Moreover, the ionospheric effect becomes more and more serious with the increasing of SAR altitude. So measures must be taken to correct the ionospheric effect especially for low-frequency high-resolution MEOSAR.

REFERENCES

1. Bruno, D., S. Hobbs, and G. Ottavianelli, "Geosynchronous synthetic aperture radar: Concept design, properties and possible applications," *Acta Astronautica*, Vol. 59, 149–156, 2006.
2. Yu, Z., et al.. "Concepts, properties and imaging technologies for GEO SAR," *Proceedings of SPIE*, Vol. 7494, 749707/1–749407/8, 2009.
3. Edelstein, W., S. Madsen, A. Moussessian, and C. Chen, "Concepts and technologies for synthetic aperture radar from MEO and geosynchronous orbits," *Proceedings of SPIE*, Vol. 5659, 195–203, Bellingham, USA, 2005.
4. Huang, L. J., "Imaging algorithm for Medium-Earth-Orbit SAR," Institute of Electronics, Chinese Academy of Sciences, Beijing, 2010.
5. Zheng, J. B., H. J. Song, X. Q. Shang, et al., "Doppler properties analysis of GEO spaceborne SAR," *Journal of Electronics & Information Technology*, Vol. 33, No. 4, 810–815, 2011.
6. Jun, S. K., D. Andreas, and P. Konstantinos, "Correction of ionospheric distortions in low frequency interferometric SAR data," *IEEE International Geoscience and Remote Sensing Symposium*, 1505–1508, Vancouver, Canada, Jul. 24–29, 2011.
7. Li, L. L., "Spaceborne SAR signals propagation in the ionosphere and ionosphere image by spaceborne SAR," Institute of Electronics, Chinese Academy of Sciences, Beijing, 2006.
8. Bruno, D. and S. E. Hobbs, "Radar imaging from geosynchronous orbit: Temporal decorrelation aspects," *IEEE Transactions on Geoscience and Remote Sensing*, Vol. 48, No. 7, 2924–2929, 2010.
9. Li, L., J. Hong, F. Ming, et al., "An approach for ionospheric effects correction on spaceborne SAR calibration based on active radar calibrator," *Journal of Electronics & Information Technology*, Vol. 34, No. 5, 1096–1101, 2012.
10. Chen, A. C. and H. A. Zebker, "Reducing ionospheric effects in InSAR data using accurate coregistration," *IEEE Transactions on Geoscience and Remote Sensing*, 1–11, 2012.

Design and Synthesis of Multi Resonant Planar Antenna Using Particle Swarm Optimization Method

B. Rama Sanjeeva Reddy, D. Vakula, and N. V. S. N. Sarma

National Institute of Technology, Warangal, India

Abstract— This paper presents a novel technique for design of multi resonant planar antenna for mobile communication applications using particle swarm optimization (PSO) algorithm. Based on a planar antenna structure, the predetermined geometrical parameters are extracted initially by Particle Swarm Optimization. The planar antenna structure is modified in obtaining satisfactory return loss and bandwidth for three frequency bands and further performed by means of an iterative based optimization strategy. The fitness function of the optimization is calculated by generated code. The feasibility of this algorithm allows improved optimization efficiency and less computational time.

1. INTRODUCTION

The design of multi resonant antennas enticed the focus of several researchers due to demand of radiating devices able to provide multiple transmission and reception functions [1]. The challenge is to determine the antenna geometry parameters such as dimensions of the patch and feed position, to achieve the best design to satisfy the desired criterion. Many efforts have been investigated in parametric study of the different planar antenna structures. However, a trial-and-error process is inevitable in most of the patch antenna designs [2].

The PSO concept was developed in 1995 as a novel evolutionary optimization methodology over a complex solution space and is applied to many EM applications. PSO takes the advantage of its algorithm simplicity and robustness, compared to conventional optimization algorithms such as genetic algorithms (GA). A fitness function is defined to quantify the performance of each candidate design [3]. Towards the end of the optimization, most particles converge to the global optimum, which better fit in to best design. This paper presents the application of PSO in multi band planar and fractal antenna designs. The multi objective optimizations further enhance the performance of PSO by exploiting its inherit versatility and using multiple fitness functions.

In this paper, a low profile slit loaded square patch antenna design method is proposed using Electro Magnetic simulation software and evolutionary optimization algorithm (PSO) possesses desirable attributes [4]. The EM simulation is most time consuming part in the optimization. The invisible boundary condition applied in EM simulator reduces the unnecessary fitness evaluations to achieve an efficient optimization.

2. DESIGN OF MULTIRESONANT PLANAR ANTENNA

The geometry of the proposed multi resonant, slit loaded low profile square patch antenna is shown in Fig. 1(a) with 1.6 mm thickness and relative permittivity of 4.4. The size of the substrate is $40 \times 40 \text{ mm}^2$. Four T-shaped slits are inserted at the edge centres; their upper arms have the same dimensions, a narrow width L_1 , and their center arms have dimensions D_3 and W_1 , with the slit along the positive y axis having a different arm width D_1 ($\neq D_3$). The size of the slot centered on the patch is 12.5 mm with a thickness of 1 mm. The antenna can cover the lower frequency band (GSM) and the upper frequency band (PCS, UMTS, WLAN and WiMax). Fig. 1(b) represents the feed position change for which the geometrical perimeters to be optimized for best solution.

The design parameters for the antenna are listed in Table 1. This arrangement is very effective for fine tuning the perturbed TM_{03} mode (upper operating band) and perturbed TM_{01} mode (lower operating band). The patch size is characterized by (W, L, h) . The slot at the center incorporated diagonally inside the patch is placed with slant angle of 45° position of the feed located gives the best return loss to be achieved.

3. OBJECTIVE FUNCTION USED TO OPTIMIZE THE STRUCTURE

The key features of the Particle Swarm Optimization algorithm used for the planar antenna are: (1) The main algorithm of PSO is relatively simple (since in its original version, it only adopts one operator for creating new solutions, unlike most evolutionary algorithms) and its implementation is, therefore straight forward. Equations, figures, tables and references should follow (2) PSO has

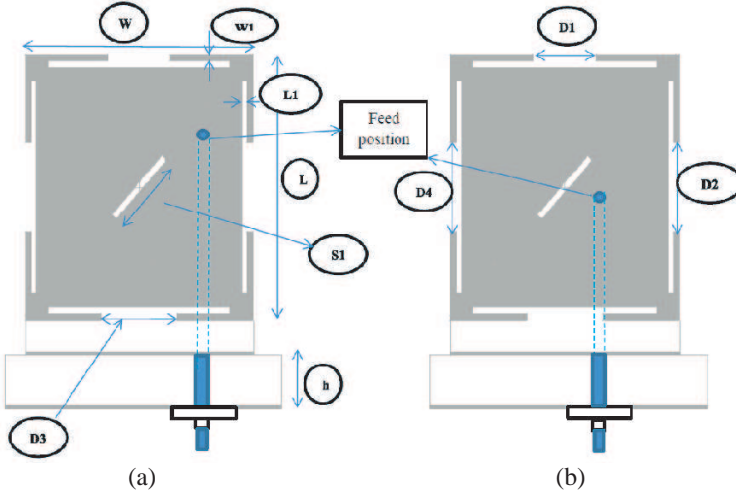


Figure 1: (a) Geometry of proposed multiresonant antenna structure, (b) feed position change.

Table 1: Design parameters of the slit loaded square patch antenna (Unit: Millimeters).

Design	L	W	L_1	W_1	S_1	D_1	$D_2 = D_3 = D_4$	Feed point (x, y)
Antenna 1	30	25	0.8	0.8	10.5	10.5	11.5	(8.5, 5.5)
Antenna 2	40	37	1	1	12.5	12.5	13.5	(5.5, -0.5)

been found to be very effective in a wide variety of applications, being able to produce very good results at a very low computational cost [5].

In PSO, particles are flown through hyper dimensional search space. Changes to the position of the particles with in the search space are based on the social psychological tendency of individuals to emulate the success of other individuals.

The position of each particle is changed according to its own experience and that of its neighbours. a sequential numerical scheme in order to ensure a logical development of subject matter.

Let $x_i(t)$ denote the position of particle p_i , at the time step t . The position of p_i is then changed by adding a velocity $v_i(t)$ to the current position [6],

$$x_i(t) = x_i(t-1) + v_i(t) \quad (1)$$

The velocity vector reflects the socially exchanged information and, in general, is defined in the following way:

$$v_i(t) = Wv_i(t-1) + C_1r_1(x_{pbest(i)} - x_i(t)) + C_2r_2(x_{leader} - x_i(t)) \quad (2)$$

where $r_1, r_2 [0, 1]$ are random values. First the swarm is initialized and it included both the positions and velocities [7]. The corresponding pbest position of each particle is initialized and the leader is located (gbest solution is selected as leader). Then for a maximum number of iterations, each particle flies through the search space updating the position (using Eqs. (1) and (2)) and its pbest and gbest are updated. In this paper, the number of particle dimensions is set to 8, as listed in Table 1. The number of particles in a swarm and the maximum iteration times depends on the dimension of the fitness function and the particles. Therefore, the number of particles in swarm is set to 8 and the maximum iteration times is set to 1000 for the particles to get converged. The fitness function for the antenna designed is given as

$$f_1 = \max(S_{11n}) \quad (3)$$

where the subscript n refers to sample points in the return loss versus frequency. Multiple frequency bands 40 MHz, 41 MHz and 40 MHz are set in IE3D for the antenna optimization. Due to the low profile of patch, the antenna has relatively narrow bandwidth. Due to the geometrical complexity, it is difficult to estimate the desired performance of antenna quantitatively.

4. DESIGN RESULTS AND DISCUSSION

It is noted that the S_{11} is extracted from EM simulation result as shown in Fig. 2. It is shown that the best particle position is obtained after 710 iteration. The parameters for the slit loaded square patch antenna obtained using PSO method are listed in Table 2. Fig. 3 shows the simulated S_{11} using EM simulator.

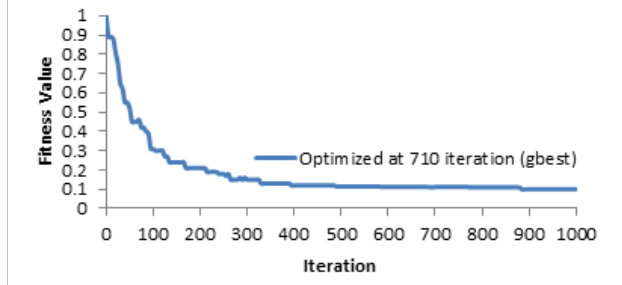


Figure 2: Optimized antenna using fitness function.

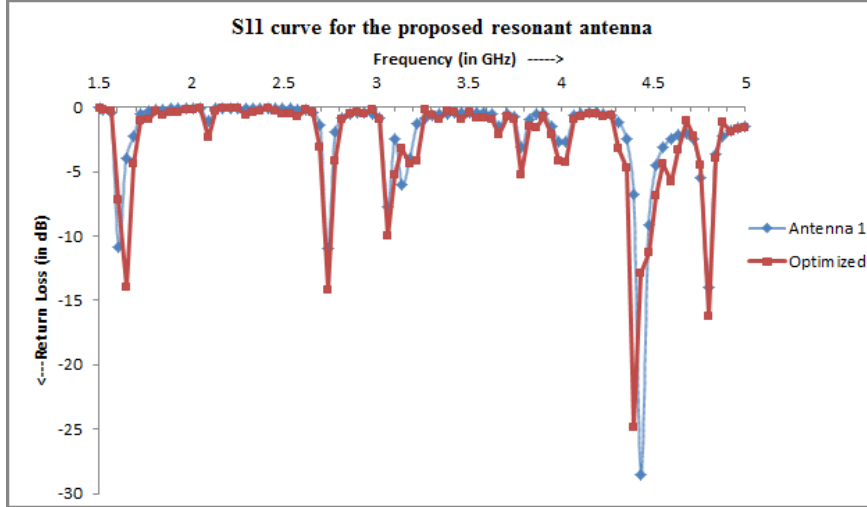


Figure 3: Return loss curve of the optimized antenna and antenna 1 (Ref).

It is observed that the optimized antenna has a simulation return loss of $S_{11} < -26.5$ dB (VSWR < 1.55) in the band of 4434–4474 MHz, return loss of $S_{11} < -14.92$ dB (VSWR < 1.05) in the band of 2737–2778 MHz, return loss of $S_{11} < -14.2$ dB (VSWR < 1.75) in the band of 1606–1646 MHz. The results shows the better optimization values except a slight frequency shift.

Table 2: Optimized design parameters antenna (Unit: Millimetre's).

Design	L	W	L_1	W_1	S_1	D_1	$D_2 = D_3 = D_4$	Feed point (x, y)
Optimized	37.5	32	0.85	0.87	11.1	10.7	11.9	(5.5, -0.5)

5. CONCLUSION

In this paper, a optimization method is proposed for slit loaded square shaped planar antenna. The procedure for the usage of PSO is briefly described and extracted the required parameters of the antenna design. The return loss and bandwidth values for the proposed antenna are satisfied with the optimized values. The accuracy, robustness and ease to implement PSO algorithm, validate its potential application in multi resonant antenna. The solution set of a problem with multiple objectives cannot found in single solution. Considering this challenge, the PSO can be further modified in applying for multi-objective optimization.

REFERENCES

1. Liu, W.-C., "Design of multiband CPW-fed monopole antenna using a PSO approach," *IEEE Trans. on Antennas and Prop.*, Vol. 53, No. 5, 3273–3279, 2005.
2. Wong, K.-L., *Compact and Broad Band Microstripantennas*, John Wiley Sons, Inc., New York, 2002.
3. Azaro, R., G. Boate, M. Bonelli, A. Massa, and E. Zeri, "Design of prefractalmonopolar antenna for 3.4–3.6 GHz Wi-Max band portable devices," *IEEE Antennas Wireless Propag. Lett.*, No. 5, 116–119, 2006.
4. Nanbo, J. and Y. Rahmat-Samii, "Parallel particle swarm optimization and FDTD algorithms for multiband and wide band patch antenna designs," *IEEE Trans. on Antennas and Prop.*, Vol. 53, No. 11, 3459–3468, 2005.
5. Robinson, J. and Y. Rahmat-Samii, "Particle swarm optimization in electromagnetics," *IEEE Trans. on Antennas and Prop.*, Vol. 52, No. 2, 397–407, 2004.
6. Boeringer, D. W. and D. H. Werner, "Particle swarm optimization versus genetic algorithms for phased array synthesis," *IEEE Trans. on Antennas and Prop.*, Vol. 52, No. 3, 771–779, 2004.
7. Kennedy, J. and R. Eberhart, "Particle swarm optimization," *Proc. 1995 Int. Conf. Neural Network*, Vol. 4, 1942–1948, 1995.

Advanced Photonic Crystal Structures for Nano-scale Photonic Integrated Circuitry

Imanol Andonegui¹, Isidro Calvo², and Angel J. Garcia-Adeva¹

¹Departamento de Fisica Aplicada I, E.T.S. Ingenieria de Bilbao

Universidad del Pais Vasco (UPV/EHU), Alda. Urquijo s/n, Bilbao 48013, Spain

²Departamento de Ingenieria de Sistemas y Automatica, E.U. Ingenieria Tecnica de Vitoria

Universidad del Pais Vasco (UPV/EHU), C/Nieves Cano 12, Vitoria 01006, Spain

Abstract— We report on the design of high-bandwidth photonic crystal (PC) devices based on disordered topologies that perform the essential functionalities required in a photonic integrated circuit (PIC) such as light guiding through curved paths, light injection/extraction to/from an input/output channel and (de)multiplexing of light power. We used various heuristic optimization methods as well as a genetic algorithm approach as an inverse design (ID) engine for engineering these, apparently counter-intuitive, PC structures. This method leads to promising topologies that outperform previous models based on intuition. In addition, we demonstrate the validity of the ID method for designing PC structures that fulfil multiple conflicting objectives. PC topologies proposed throughout this manuscript are constrained in order to satisfy the limitations imposed by lithographic manufacturing techniques. Therefore, these designs are not only interesting from a theoretical point of view but also of great practical importance, since they can be readily manufactured.

1. INTRODUCTION

The prospect of attaining a fully functional photonic device that tackles light propagation in sub-wavelength scale requires breaking the spatial symmetry of PCs. These topologies enhance additional functionalities and enable a higher level of control in complex light paths. However, creating novel designs based upon aperiodic PC clusters entails dealing with numerous sensitive and correlated parameters. In such situations, a thorough study of the entire set of feasible parameters turns out to be a class of an NP-hard problem and so, it is impractical to solve the problem in a polynomial amount of time. Currently, the process of designing a PC structure that ultimately complies with a certain required objective is still based on intuitive assumptions rather than using a rigorous mathematical technique. Owing to this fact, numerous previous studies report on several PC devices wherein the variation of a few of their constituents yields to interesting optical devices. However, achieving a significant enhancement of the transmittance spectra over a wide bandwidth is a very challenging task for such trial-and error guided design techniques. In contrast, as reported in this work, an inverse design (ID) approach based on a global optimization heuristic algorithm yields to excellent results while needing only minimal computational resources. Besides, the ID techniques used for modelling the reported PC structures support a constrained search of the parameter space and hence they can render PC topologies that are fully compatible with CMOS fabrication technology.

2. DESIGNING A SIMPLE FOUR CHANNEL ADD-DROP MODEL DEVICE

In 2D PCs, in which a few of its constituents are taken into account, it is still possible solve and predict the configuration that leads to a successful device. Up to this date, many authors have reported studies about light tunnelling on add/drop PC topologies. Most of them make use of a time coupled mode theory to explore the resonant states that enforce the light leakage to a neighbour channel. Fan et al. did much the same in a four channel add/drop configuration [1] in order to get to a complete channel drop tunnelling.

The schematic diagram of the generic coupled system used by Fan et al. is illustrated in Fig. 1(b). They suggested a PC topology consisting of two waveguides and a pair of cavities. The twofold symmetry of the model permits to couple and uncouple light to the target ports. Noticeably, even in this simplified model, the exploration of the feasible solutions would take a very high number of calculations. However, when using the ID methodology to this problem, the solution is quickly achieved taking into account only those combinations of parameters that yield promising results. In Fig. 1(a), we show both the transmittance results for the naive geometry proposed by Fan et al. and the improved results obtained by means of the ID method. When setting the topology with

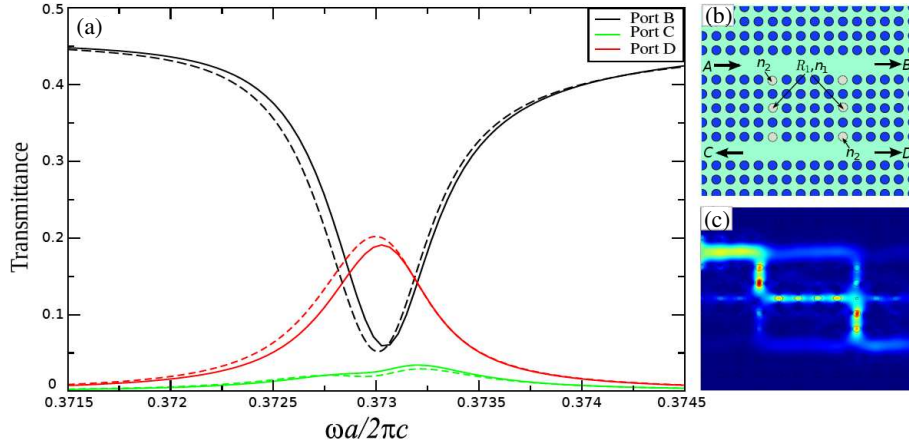


Figure 1: (a) Transmittance calculation through the ports B, C, D , for the light tunnelling scheme suggested by Fan et al. (solid lines) and the one provided by the IHS algorithm (dashed lines). (b) Schematic illustration of two parallel waveguides that comprise the basic configuration used for designing a working add-drop device according to [1], where n_1 and n_2 stand for the dielectric index of the rods that determine the light leakage to the output ports and R_1 is the radius of the rod labelled as 1. (c) Time averaged power distribution showing light coupling though port D .

the parameters found by the ID method the interference pattern at the sharp drop frequency range interacts destructively and minimizes the amount of light redirected to channel C and B while it acts constructively in port D producing a complete transfer of light.

In summary, we achieved a very accurate and efficient transfer of light using ID methods to improve the cavity light leakage design proposed by Fan et al.. It seems that these models, which are the subject of analytical studies, are an easy matter to be solved using the ID approach proposed in this paper. Besides, in this case, our solution yields to slightly better results than the one proposed in [1]. In the following section, we will show that using the ID method is even more valuable when addressing much more complex configurations that can not be solved so easily using semi-analytic approaches due to the large number of degrees of freedom involved.

3. EFFICIENT SHARP PCWG BENDS

The ability to guide light waves in sharp bends of PC integrated circuits is one of the most advantageous properties of PC waveguides. Traditional waveguide systems rely on the index guiding mechanism for steering light through bends and, as a result, the bending efficiency is highly affected by a critical bending angle that prevents total internal reflection (TIR) in sharp bends. Most of the theoretical studies reported so far focus on PCs made of dielectric rods in air. Waveguides created in this fashion are normally single mode. Then, it is relatively easy to carry out a significant enhancement of PCWG bends therein. However, reducing the reflection from a bend region in a large bandwidth using a multi-mode holes-etched-in-dielectric-type PC is not as straightforward. In a simple bend structure, the coupling of energy between the Γ - M direction waveguide and the waveguide oriented according to the curvature is not efficient and, therefore, the transmission of the bend is low. Following an analogous approach as the one reported in the previous section, topologies comprising 60° and sharp 120° curved paths are considered for optimization using the ID approach. In Figs. 2(b) and 2(c), the resulting topologies obtained by means of the ID process for a 60° and a 120° twisted waveguides are shown, respectively. These optimized topologies exhibit a significant improvement in the transmittance spectrum for the normalized frequency range [0.26–0.28] with respect to the non-optimized ones (see Fig. 2(a)). The optimized bending topologies achieve an almost perfect mode coupling between the regular straight waveguide and the waveguide following a distinct crystalline direction. Moreover, the transmittance spectra is almost flat in the whole target frequency range.

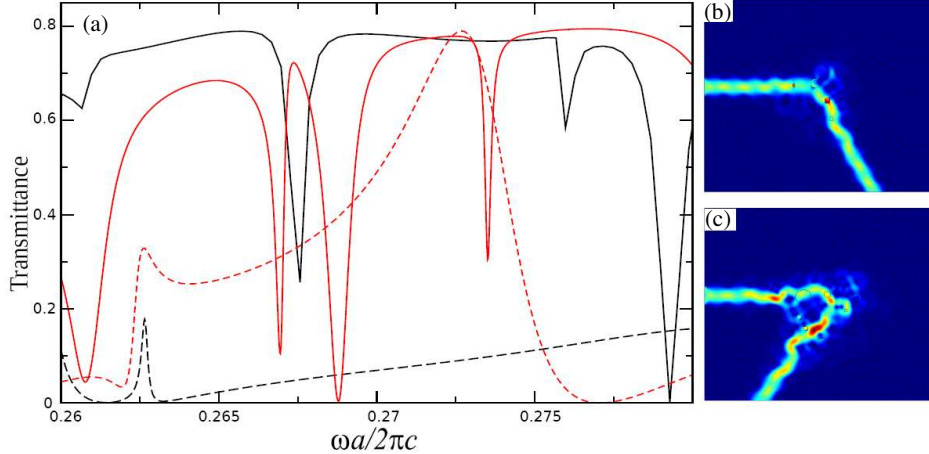


Figure 2: (a) Comparison of the transmittance spectra obtained using different bending configurations. The black solid and dashed lines depict the transmittance spectra for the case of the optimized topology and for the non-optimized 60° bend waveguide, respectively. Red solid and dashed lines correspond to the transmittance calculations for the optimized topology and for the non-optimized 120° sharply bend waveguide, respectively. (b) Time averaged power distribution for a 60° bend PCWG at $a/\lambda = 0.27$ and for (c) a 120° twisted PCWG at the same normalized frequency.

4. INVERSE DESIGN OF AN OPTICAL CROSS-CONNECT AND WAVELENGTH MULTIPLEXING STRUCTURES

Enhancing broadband light guiding through PC paths is essential for communication network applications. In the same way, creating highly selective filters is particularly important for adding and extracting light from waveguides. Furthermore, such channel-drop filter devices are key elements for exploiting the spectral bandwidth capabilities in dense wavelength demultiplexing systems (DWDM) [2, ?]. PCs are specially well suited for investigating such devices: on the one hand, the PBG performs an efficient discrimination of light power at a high-range of wavelengths and, on the other hand, minimal structural modification of the periodic arrangement leads to light localization with high Q-factors. In this regard, we devised a PC system that permits to determine the path of the light flow according to the wavelength, much in the same way as nowadays electronic interconnectors do. So far, some early studies have demonstrated PC WDM designs based on superprism effects [4, ?] and there are quite some studies that make use of resonances to perform similar performance [6, ?]. The former tend to have large areas and thus they seem to be too bulky for a PIC module; the later provide a large integration area but do not support a high bandwidth operation. In contrast, a PCWG coupler consisting of an input waveguide followed by two parallel output waveguides, offers a high bandwidth starting point for designing a high efficiency WDM system. In this context, we used the ID method and we succeeded to devise a high performance duplexer shown in Fig. 3. The operational frequency range of this device is specially important because for typical lattice parameters it spans the optical telecom window. For example, for $a = 405$ nm, it allows to commute signals corresponding to 1500 and 1550 nm wavelength within the [1470–1560] nm wavelength interval. Moreover, at this frequency range, these configurations exhibit almost single-mode operation with near-zero group velocity dispersion (GVD).

Optical cross-connect interconnects (OXC) are a fundamental element for a high-speed all-optical signal switching system. In contrast with the present digital OXC systems, this PC based optical OXC deals with multiple high speed optical signals that are switched in the optical domain in their entirety and do not require any prior multiplexing stage or optical-to-electrical conversion. In this regard, we present a fully bidirectional WDM and OXC compatible with chip-scale silicon photonics. This device is comprised by two parallel PCWG sections joined by an inverse designed interference stage that produces a mode matching between opposite waveguides through a reasonable bandwidth. In addition, the most widespread configuration of add/drop multiplexing devices that, in general, are constructed including an array waveguide diffraction grating or fiber gratings, demand a significantly large bend radius, and so the overall device dimensions scale accordingly. Our simulations reveal that this component outperforms previous approaches, as it permits to couple waveguide modes using a short and compact PC geometry comprised by only a few holes and

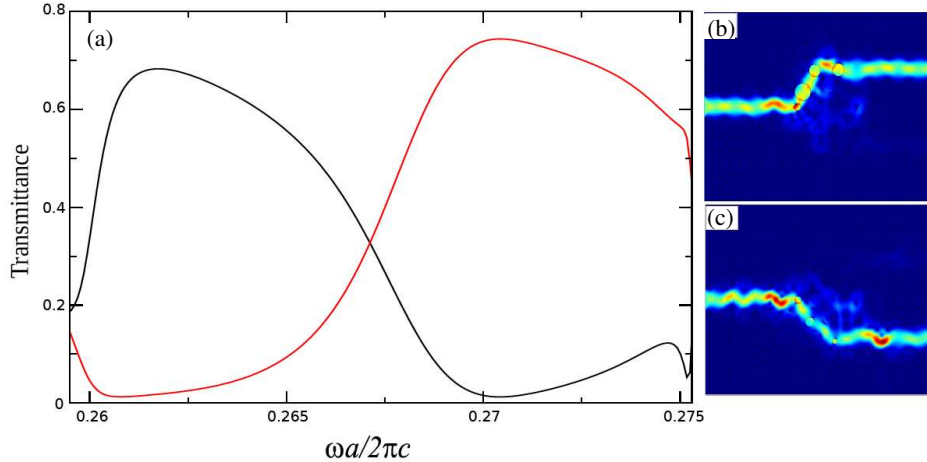


Figure 3: (a) Transmittance spectra calculated at the upper output waveguide (coloured in black) and at the lower waveguide port (coloured in red). (b) Time averaged power flow at $a/\lambda = 0.263$. Almost all the light power follows the upper path, and conversely, at (c) $a/\lambda = 0.273$ the light power is steered through the opposite waveguide.

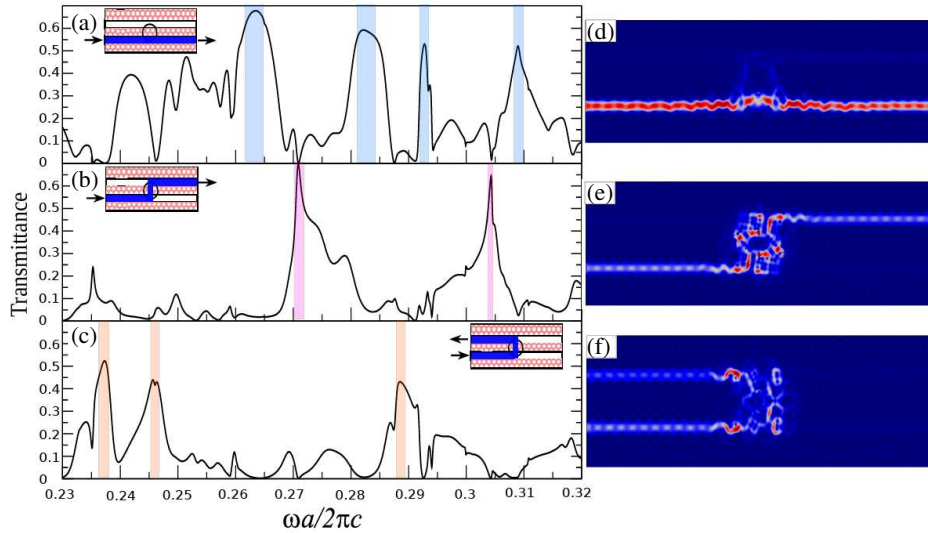


Figure 4: (a)–(c) Transmittance spectra for the cross-connect system designed using ID proceeding. The incoming light is routed to one of the output ports according to the wavelength. Noticeably, reflection and cross-talk losses are almost negligible. (d)–(f) Time averaged power distribution that shows the versatility of the device.

allows miniaturizing the crossing and multiplexing functionalities, as shown in Fig. 4. Besides, this structure routes the light flow in a selective way, bypassing it at some frequencies as shown in Fig. 4(d), almost completely coupling light to an adjacent waveguide (Fig. 4(e)) and selectively filtering some other frequencies as it is sketched in Fig. 4(f).

Figure 4 depicts the transmittance flux calculated at the boundary of each output port. Therein, it is shown that almost the entire input power is redirected through a unique port and moreover, this structure changes this procedure according to the input signal wavelength. We believe that this system could serve as an optical signal encoding source for a OCDMA system, as long as it allows for an efficient, low loss and fast routing of WDM signals through an optical networks architecture.

5. CONCLUSION

In this paper we demonstrate the usefulness of employing an inverse design approach for designing novel complex light guiding structures in photonic crystal materials. These topologies support low losses and high bandwidth requirements within very compact modelling. The ID methodology is a well known tool in other engineering disciplines, but there have been very few attempts to

use it in the design of complex photonic devices based on PCs. In contrast with intuition-based approaches, we show in the present manuscript that global optimization heuristic and evolutionary algorithms are specially well suited to deal with the noisy and non-linear nature of disordered PCs. The optimized complex systems obtained by means of these technique clearly outperform intuitive based models. These procedure supports a constrained search of the parameter space and hence it leads to PC topologies that are fully compatible with CMOS fabrication technology. We found that this method is easily applicable to most PC engineering design problems since it does not require any detailed knowledge of the structure of the problem and it can rely on the solver of the system as a blackbox.

ACKNOWLEDGMENT

We would like to thank the Basque Government for financial support under the SAIOTEK 2012 (ref. S-PE12UN043) programme. One of us, I.A., wants to thank the Vicerrectorado de Euskara y Plurilinguismo de la UPV/EHU for financial support under the PhD Fellowships 2011 programme.

REFERENCES

1. Fan, S., P. R. Villeneuve, and J. D. Joannopoulos, “Channel drop tunneling through localized states,” *Phys. Rev. Lett.*, Vol. 80, 960–963, 1998.
2. Ren, H., C. Jiang, W. Hu, M. Gao, and J. Wang, “Photonic crystal channel drop filter with a wavelength-selective reflection micro-cavity,” *Opt. Express*, Vol. 14, 2446–2458, 2006.
3. Sharkawy, A., S. Shi, and D. W. Prather, “Multichannel wavelength division multiplexing using photonic crystals,” *Appl. Opt.*, Vol. 40, 2247–2252, 2001.
4. Chung, K. B. and S. W. Hong, “Wavelength demultiplexers based on the superprism phenomena in photonic crystals,” *Appl. Phys. Lett.*, Vol. 81, 1549–1551, 2002.
5. Jugessur, A., L. Wu, A. Bakhtazad, A. Kirk, T. Krauss, and R. De La Rue, “Compact and integrated 2-D photonic crystal super-prism filter-device for wavelength demultiplexing applications,” *Opt. Express*, Vol. 14, 1632–1642, 2006.
6. Kuo, C. W., C. F. Chang, M. H. Chen, S. Y. Chen, and Y. D. Wu, “A new approach of planar multi-channel wavelength division multiplexing system using asymmetric super-cell photonic crystal structures,” *Opt. Express*, Vol. 15, 198–206, 2006.
7. Liu, V., Y. Jiao, D. A. B. Miller, and S. Fan, “Design methodology for compact photonic-crystal-based wavelength division multiplexers,” *Opt. Lett.*, Vol. 36, 591–593, 2011.

Simulation of Motional Averaging with a Superconducting Circuit

J. Li¹, M. P. Silveri², K. S. Kumar¹, J.-M. Pirkkalainen¹, A. Vepsäläinen¹, W. C. Chien³, J. Tuorila², M. A. Sillanpää⁴, P. J. Hakonen¹, E. V. Thuneberg², and G. S. Paraoanu¹

¹O. V. Lounasmaa Laboratory, Aalto University, P. O. Box 15100, Aalto FI-00076, Finland

²Department of Physics, University of Oulu, P. O. Box 3000, FI-90014, Finland

³Department of Physics, National Chung Hsing University

250 Kuo Kuang Road, Taichung 40227, Taiwan

⁴Department of Applied Physics, Aalto University, Aalto FI-00076, Finland

Abstract— The possibility of using a quantum system to simulate another one has been recognized for a long time as an important research direction in quantum information and quantum computing. In Ref. [1], a superconducting circuit (a transmon) was employed to simulate an NMR (nuclear magnetic resonance) effect known as motional averaging. In this paper we analyze the results of numerical integration of the time evolution of the density matrix of a qubit with random frequency fluctuations, and compare the results with those obtained by using the method of quantum trajectories. We show that both methods produce equivalent results, although some differences may appear in the range of intermediate modulation frequencies.

1. INTRODUCTION

The generic problem of frequency-modulation of the characteristic or proper frequency of a physical system appears in a vast variety of contexts. In the field of superconducting circuits [2, 3], frequency modulation is typically realized by changing the magnetic field that penetrates a SQUID (superconducting interference device) loop. One phenomenon associated with the change in frequency is parametric amplification, either of a classical input signal or of vacuum fluctuations [4]. Another important phenomenon is motional averaging and narrowing. This phenomenon has been first observed [5] and described theoretically [6] in ensembles of nuclei measured by NMR (nuclear magnetic resonance) techniques. Today it is one of the textbook results in the field of NMR [7]. More recently, the phenomenon of motional averaging has been demonstrated with the protons in water molecules [8], and in ensembles of two-level systems consisting of ultracold ⁸⁷Rb atoms [9].

In contrast to the experiments involving ensembles of particles, our realization of motional averaging [1] uses a single quantum system, whose transition frequency between the ground state and the first excited state can be controlled externally. This system is a superconducting circuit consisting of a capacitively-shunted charge qubit (a transmon) embedded in a superconducting waveguide resonator [10]. Two microwave fields are applied to the system: one, at the frequency of the resonator, is used for measurement, while the other, around the qubit frequency, is used for driving. In addition, the qubit frequency is modulated by a random telegraph noise with externally-controlled amplitude and characteristic jumping frequency χ , defined more precisely below. Surprisingly, by adding noise in this way a new, “motional averaged” spectral line is formed, with a linewidth smaller than the amplitude of the random modulation [1]. We have also succeeded in driving Rabi oscillations on the motional averaged line, demonstrating the formation of hybrid states of the transmon and the modulation field. The fact that quantum coherence persists in the presence of noise and that a spectral line appears at an average frequency where — at least ideally — the qubit only crosses very fast without spending any time in is a rather counterintuitive feature of this effect, adding up to the list of other unexpected quantum effects that were demonstrated in recent times with superconducting qubits, such as interaction-free [11] and partial [12] measurements, reversal of nonunitary transformations [13], and the violation of Leggett-Garg inequalities [14].

When modulating the system sinusoidally, we observe a rich spectral structure, resembling a Landau-Zener interference pattern. However, direct Landau-Zener transitions are prohibited in our system by the fact that the frequency of the modulation is much smaller than the energy level separation. We were able to show that in this case the transitions occur through the absorption of photons from the driving field; we call this process **photon-assisted Landau-Zener effect**.

Finally, for the values of the fields used in our experiment we show that, in a rotating frame, the system reaches the ultrastrong coupling regime. Our setup can also be seen as the simulation of the effect of coupling an externally-controlled fluctuation to a qubit. We have also suggested that

the experimental demonstration of motional averaging shown here could provide a novel route to improving the dephasing times of existing superconducting qubits.

In this contribution we analyze the simplest theoretical model for motional averaging, consisting of a frequency-modulated two-level system under driving and with dissipation. We present the results of two methods used for calculating the time-evolution of this system, namely direct numerical integration and the method of quantum trajectories. The two methods produce overall the same spectra, but for certain parameter choice some differences may appear in the regime of intermediate modulation frequencies.

2. MODEL AND RESULTS

We consider a generic qubit Hamiltonian with bare (unmodulated) frequency ω_0 ,

$$H_0 = \frac{\hbar}{2}\omega_0\sigma_z, \quad (1)$$

on top of which we add a frequency-modulated term $\xi(t)$, resulting in a total time-dependent Hamiltonian

$$H(t) = \frac{\hbar}{2}[\omega_0 + \xi(t)]\sigma_z. \quad (2)$$

For the modulation, we consider a stochastic Poisson process in which $\xi(t)$ switches randomly between two values, $\pm\xi$, with mean jumping frequency denoted by χ . For such processes, the probability of n jumps within a time interval t is given by

$$P_n(t) = \frac{1}{n!}(\chi t)^n e^{-\chi t}. \quad (3)$$

The correlations between the jumping events at times t_n are maximally anti-correlated, namely $\langle \xi(t_{n+1})\xi(t_n) \rangle = -\xi^2$. In addition, the qubit is driven by a σ_x -coupled tone with angular frequency ω ,

$$H_{\text{drive}}(t) = \hbar g \cos(\omega t)\sigma_x, \quad (4)$$

where g is the strength of the coupling (the Rabi frequency). It is useful to truncate the driving Hamiltonian to energy-conserving terms, by employing a rotating-wave approximation,

$$H_{\text{drive}}(t) \approx H_{\text{drive}}^{\text{RWA}}(t) = \frac{\hbar g}{2} [\sigma e^{i\omega t} + \sigma^+ e^{-i\omega t}]. \quad (5)$$

Thus the total Hamiltonian in the rotating-wave approximation reads

$$H_{\text{tot}}^{\text{RWA}}(t) = H_{\text{drive}}^{\text{RWA}}(t) + H(t). \quad (6)$$

Finally, dissipation is introduced via the standard Liouvillean approach to superconducting qubits, see e.g., [15]. The time-dependent equation satisfied by the density matrix ρ takes the form

$$\dot{\rho}(t) = -\frac{i}{\hbar} [H_{\text{tot}}^{\text{RWA}}(t), \rho(t)] + \mathcal{L}[\rho(t)], \quad (7)$$

where the Liouvillean superoperator at zero temperature is

$$\mathcal{L}[\rho(t)] = \frac{\Gamma_1}{2}[2\sigma\rho(t)\sigma^+ - \sigma^+\sigma\rho(t) - \rho(t)\sigma^+\sigma] + \frac{\Gamma_\varphi}{2}[\sigma_z\rho(t)\sigma_z - \rho(t)]. \quad (8)$$

Here σ and σ^+ are the lowering and raising Pauli matrices, Γ_1 is the relaxation rate, and Γ_φ is the dephasing rate. The Liouvillean can be written in the matrix form as

$$\mathcal{L}[\rho(t)] = \frac{1}{2} \begin{bmatrix} 2\Gamma_1\rho_{11}(t) & -(\Gamma_1 + 2\Gamma_\varphi)\rho_{01}(t) \\ -(\Gamma_1 + 2\Gamma_\varphi)\rho_{10}(t) & -2\Gamma_1\rho_{11}(t) \end{bmatrix}. \quad (9)$$

Equation (7) can be directly solved numerically, by using the standard Runge-Kutta method [16]. In contrast, in [1] we have solved the evolution by using the quantum trajectories technique [17], see [18]. We have run in parallel several simulations using these methods, demonstrating that they

yield very similar-looking spectra. There are however some interesting differences, that appear more visibly for a certain range of parameters. Here we present such an example.

In Fig. 1 we show the result of simulations using the two methods described above. The direct integration technique using the standard Runge-Kutta method for solving differential equations produces the spectrum shown in Fig. 1(b). Interestingly, this shows that the two lines in the spectrum at low jumping frequencies spread up a bit when χ increases, before collapsing into the motional-averaged line. Also, the probability of qubit excitation at frequencies between the two initial values $\pm\xi = \pm 71$ MHz tends to be larger. This can be understood as coming from multiple-photon processes which are not completely extinct as one would expect for ideal random pulses. Indeed, one sees clearly these multiple-photon spectral lines when modulating the qubit frequency with a sine wave [16]. An ideal random telegraph-noise pulse can be expanded in an infinite number of frequency components, each of them producing a set of sidebands. Since they are at different frequencies, all these sidebands will average out, with the exception of the middle one (the zero-photons sideband), which is common to all frequencies and which produces the motional-averaged line. Interestingly, the feature described above (slight up-spreading of the two spectral lines) appears also in some of the experimental data, see [16]. The advantage for using the method of quantum trajectories is that the computer runtime is much shorter, since it can be easily parallelized. The simulation for a $50(x\text{-axis}) \times 101(y\text{-axis})$ points and using the mirror symmetry with respect to the $\omega = \omega_0$ -line, as presented here, would have taken 378 hours for a single CPU but by parallelizing for 21 CPUs it took only approx 18 hours. The number of averaged traces was 1000.

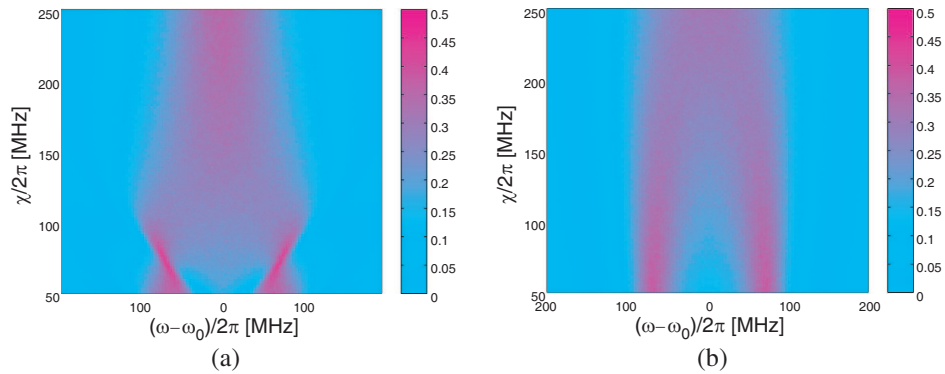


Figure 1: Results of simulations for the qubit population for $\pm\xi = 71$ MHz, $\Gamma_1 = 2\pi \times 1$ MHz, $\Gamma_\varphi = 2\pi \times 2.5$ MHz. (a) Simulation using the method of quantum trajectories. The raise/fall time was 2 ns, and it was sampled in three intermediate steps, each of them with width of 0.5 ns. The figure is obtained with 1000 averages. (b) Simulation by direct numerical integration using the Runge-Kutta method, with 100 averages. The rise/fall time was 1.6 ns, and the width of the time step was 0.1 ns. The two spectra are quite similar, but there are some differences in the intermediate jump frequency regime. The direct simulation partly retains the multiple-photon sidebands, which, at low jumping frequencies, tend to blur the space between the two jump frequencies, and also somewhat extend the two spectral lines sideways. These features are almost completely washed out in (a). At high jump frequencies, the results of these simulations are nearly identical.

3. SUMMARY AND CONCLUSION

When the frequency of an artificial atom realized as a superconducting qubit is varied fast enough by the application of a sequence of random pulses, a single line emerges in the absorption spectrum. This phenomenon is known as motional averaging. Since in general the linewidth of quantum systems is determined by such random processes (e.g., $1/f$ noise), this process is often referred to as motional narrowing, since it appears as the narrowing of the spectral line when these processes are fast enough. Our experiment can be seen as simulating the above phenomenon using a superconducting circuit. In this contribution we have discussed the numerical predictions for the spectra using two different techniques, one which is a direct numerical calculation and the other which employs the method of quantum trajectories. We found that the two methods give equivalent results, showing the consistency of these theoretical approaches. The differences between the two can be explained by the incomplete averaging out of multiple-photon sidebands in the case of the direct integration method. Also, the second method is faster and can be easily parallelized.

ACKNOWLEDGMENT

The work was supported by the Academy of Finland, through projects 135135, 141559, 263457 and the Center of Excellence “Low Temperature Quantum Phenomena and Devices” project 250280. W. C. Chien was supported from Academy of Finland project 253094, related to the cooperation between Finland and Taiwan. G. S. P. would like to thank Watson Kuo for useful comments.

REFERENCES

1. Li, J., M. P. Silveri, K. S. Kumar, J.-M. Pirkkalainen, A. Vepsäläinen, W. C. Chien, J. Tuorila, M. A. Sillanpää, P. J. Hakonen, E. Thuneberg, and G. S. Paraoanu, “Motional averaging in a superconducting qubit,” *Nat. Commun.*, Vol. 4, 1420, 2013.
2. Buluta, I., S. Ashhab, and F. Nori, “Natural and artificial atoms for quantum computation,” *Rep. Prog. Phys.*, Vol. 74, 104401, 2011.
3. Wendin, G. and V. S. Shumeiko, “Superconducting quantum circuits, qubits and computing,” *Handbook of Theoretical and Computational Nanoscience*, Vol. 3, edited by M. Rieth and W. Schommers, American Scientific Publishers, 2006.
4. Lähteenmäki, P., G. S. Paraoanu, J. Hassel, and P. Hakonen, “Dynamical Casimir effect in a Josephson metamaterial,” *Proc. Natl. Acad. Sci.*, Vol. 110, No. 11, 4234–4238, 2013.
5. Bloembergen, N., E. M. Purcell, and R. V. Pound, “Relaxation effects in nuclear magnetic resonance absorption,” *Phys. Rev.*, Vol. 73, 679–712, 1948.
6. Anderson, P. W., “A mathematical model for the narrowing of spectral lines by exchange or motion,” *J. Phys. Soc. Jpn.*, Vol. 9, 316, 1954.
7. Abragam, A., *Principles of Nuclear Magnetism*, Oxford University Press, New York, 1961.
8. Kohmoto, K., Y. Fukuda, M. Kunitomo, K. Ishikawa, M. Tanigawa, K. Ebina, and M. Kaburagi, “Hole burning in well-defined noise fields: Motional narrowing,” *Phys. Rev. B*, Vol. 49, 15352, 1994.
9. Sagi, Y., R. Pugatch, Y. Almog, and N. Davidson, “Spectrum of two-level systems with discrete frequency fluctuations,” *Phys. Rev. Lett.*, Vol. 104, 253003, 2010.
10. Koch, J., T. M. Yu, J. Gambetta, A. A. Houck, D. I. Schuster, J. Majer, A. Blais, M. H. Devoret, S. M. Girvin, and R. J. Schoelkopf, “Charge insensitive qubit design derived from the Cooper pair box,” *Phys. Rev. A*, Vol. 76, 042319, 2007.
11. Paraoanu, G. S., “Interaction-free measurements with superconducting qubits,” *Phys. Rev. Lett.*, Vol. 97, 180406, 2006.
12. Katz, N., M. Ansmann, R. C. Bialczak, E. Lucero, R. McDermott, M. Neeley, M. Steffen, E. M. Weig, A. N. Cleland, J. M. Martinis, and A. N. Korotkov, “Coherent state evolution in a superconducting qubit from partial-collapse measurement,” *Science*, Vol. 312, 1498–1500, 2006.
13. Katz, N., M. Neeley, M. Ansmann, R. C. Bialczak, M. Hofheinz, E. Lucero, A. OConnell, H. Wang, A. N. Cleland, J. M. Martinis, and A. N. Korotkov, *Phys. Rev. Lett.*, Vol. 101, 200401, 2008.
14. Groen, J. P., D. Riste, L. Tornberg, J. Cramer, P. C. de Groot, T. Picot, G. Johansson, and L. DiCarlo, “Partial-measurement back-action and non-classical weak values in a superconducting circuit,” arXiv:1302.5147v1, 2013.
15. Li, J., G. S. Paraoanu, K. Cicak, F. Altomare, J. I. Park, R. W. Simmonds, M. A. Sillanpää, and P. J. Hakonen, “Decoherence, Autler-Townes effect, and dark states in two-tone driving of a three-level superconducting system,” *Phys. Rev. B*, Vol. 84, 104527, 2011.
16. Li, J., “Decoherence in superconducting quantum circuits,” No. 102, Aalto University Doctoral Dissertation, 2012.
17. Gardiner, C. W. and P. Zoller, *Quantum Noise: A Handbook of Markovian and Non-Markovian Quantum Stochastic Methods with Applications to Quantum Optics*, Springer-Verlag, Berlin, 2004.
18. Silveri, M., “Nonlinear and stochastic driving of a superconducting qubit,” No. 82, Report Series in Physical Sciences, Oulu University, 2013.

Quantum Deformed Richardson-Gaudin Model

P. Kulish¹, A. Stolin², and H. Johansson²

¹Steklov Mathematical Institute, St. Petersburg, Russia

²University of Gothenburg, Sweden

Abstract— The Richardson-Gaudin model describes strong pairing correlations of fermions confined to a finite chain. The integrability of the Hamiltonian allows for its eigenstates to be constructed algebraically. In this work, we show that quantum group theory provides a possibility to deform the Hamiltonian preserving integrability. More precisely, we use the so-called Jordanian r -matrix to deform the Hamiltonian of the Richardson-Gaudin model. In order to preserve its integrability, we need to insert a special nilpotent term into the auxiliary L-operator which generates integrals of motion of the system. Moreover, the quantum inverse scattering method enables us to construct the exact eigenstates of the deformed Hamiltonian. These states have a highly complex entanglement structure which require further investigation.

1. INTRODUCTION

The Richardson-Gaudin model [1, 2] is an integrable spin- $\frac{1}{2}$ periodic chain with Hamiltonian

$$H = \sum_{j=1}^N \epsilon_j S_j^z + g \sum_{j, k=1}^N S_j^- S_k^+, \quad (1)$$

where g is a coupling constant and $S_l^\pm = (S_l^x \pm iS_l^y)$, with S_l^α N copies of the Lie algebra $su(2)$ generators

$$[S_l^\alpha, S_{l'}^\beta] = i\epsilon^{\alpha\beta\gamma} S_l^\gamma \delta_{ll'}, \quad \alpha, \beta, \gamma = x, y, z. \quad (2)$$

As shown by Cambiaggio et al. [3], by introducing fermion operators c_{lm}^\dagger and c_{lm} related to the $sl(2)$ generators by

$$S_l^z = \frac{1}{2} \sum_m c_{lm}^\dagger c_{lm} - \frac{1}{2}, \quad S_l^+ = \frac{1}{2} \sum_m c_{lm}^\dagger c_{l\bar{m}}^\dagger = (S_l^-)^\dagger \quad (3)$$

the Richardson-Gaudin model in Eq. (1) gets mapped onto the pairing model Hamiltonian

$$H_P = \sum_l \epsilon_l \hat{n}_l + \frac{g}{2} \sum_{l, l'} A_l^\dagger A_{l'}. \quad (4)$$

Here c_{lm}^\dagger (c_{lm}) creates (annihilates) a fermion in the state $|lm\rangle$ (with $|l\bar{m}\rangle$ the time reversed state of $|lm\rangle$), and $n_l = \sum_m c_{lm}^\dagger c_{lm}$ and $A_l^\dagger = (A_l)^\dagger = \sum_m c_{lm}^\dagger c_{l\bar{m}}^\dagger$ are the corresponding number- and pair-creation operators. The pairing strengths $g_{ll'}$ are here approximated by a single constant g , with ϵ_l the single-particle level corresponding to the m -fold degenerate states $|lm\rangle$.

As is well-known, the pairing model in Eq. (4) is central in the theory of superconductivity. Richardson's exact solution of the model [1], exploiting its integrability, has been important for applications in mesoscopic and nuclear physics where the small number of fermions prohibits the use of conventional BCS theory [4]. Moreover, its (pseudo)spin representation in the guise of the Richardson-Gaudin model, Eq. (1), provides a striking link between quantum magnetism and pairing phenomena, both central concepts in the physics of quantum matter.

The eigenstates of the Richardson-Gaudin Hamiltonian, Eq. (1), can be constructed algebraically using the quantum inverse scattering method (QISM) [5, 6]. The main objects of this method are the classical r -matrix

$$r(\lambda, \mu) = \frac{4}{\lambda - \mu} \sum_\alpha S^\alpha \otimes S^\alpha \Big|_{s=\frac{1}{2}} \simeq \frac{1}{\lambda - \mu} \begin{pmatrix} 1 & 0 & 0 & 0 \\ 0 & -1 & 2 & 0 \\ 0 & 2 & -1 & 0 \\ 0 & 0 & 0 & 1 \end{pmatrix}. \quad (5)$$

and the L -matrix of the loop algebra $\mathcal{L}(sl(2))$ generators $h(\lambda)$, $X^+(\lambda)$, $X^-(\lambda)$

$$L(\lambda) = \begin{pmatrix} h(\lambda) & 2X^-(\lambda) \\ 2X^+(\lambda) & -h(\lambda) \end{pmatrix}. \quad (6)$$

The commutation relations (CR) of loop algebra generators are given in compact matrix form

$$[L_1(\lambda), L_2(\mu)] = -[r_{12}(\lambda, \mu), L_1(\lambda) + L_2(\mu)], \quad (7)$$

where $L_1(\lambda) = L(\lambda) \otimes \mathbb{I}$, $L_2(\mu) = \mathbb{I} \otimes L(\mu)$ and $r(\lambda, \mu)$ is the 4×4 c -number matrix in Eq. (5). A consequence of this form is the commutativity of transfer matrices,

$$t(\lambda) = \frac{1}{2} \text{tr}_0 (L^2(\lambda)) \in \mathcal{L}(sl(2)), \quad [t(\lambda), t(\mu)] = 0 \quad (8)$$

The corresponding mutually commuting operators extracted from the decomposition of $t(\lambda)$ define a Gaudin model [2, 7]. However, to get Richardson Hamiltonian a mild change of the L -operator is necessary

$$L(\lambda) \rightarrow L(\lambda; c) := c h_0 + L(\lambda)$$

where $h_0 = \sigma_0^z$ in auxiliary space \mathbb{C}_0^2 of spin $\frac{1}{2}$. This transformation does not change the CR of matrix elements of this matrix $L(\lambda; c)$ due to the symmetry of the r -matrix (5):

$$[Y \otimes \mathbb{I} + \mathbb{I} \otimes Y, r(\lambda, \mu)] = 0, \quad Y \in sl(2). \quad (9)$$

The resulting transfer matrix obtains some extra terms

$$t(\lambda; c) = \frac{1}{2} \text{tr}_0 (L(\lambda; c))^2 = c^2 \mathbf{1} + c h(\lambda) + h^2(\lambda) + 2 (X^+(\lambda) X^-(\lambda) + X^-(\lambda) X^+(\lambda)). \quad (10)$$

Let us consider a spin- $\frac{1}{2}$ representation on auxiliary space $V_0 \simeq \mathbb{C}^2$ and spin ℓ_k representations on quantum spaces $V_k \simeq \mathbb{C}^{\ell_k+1}$ with extra parameters ϵ_k corresponding to site $k = 1, 2, \dots, N$. The whole space of quantum states is $\mathcal{H} = \otimes_1^N V_k$ and the highest weight vector (highest spin, “ferromagnetic state”) $|\Omega_+\rangle$ satisfies

$$X^+(\lambda) |\Omega_+\rangle = 0, \quad h(\lambda) |\Omega_+\rangle = \rho(\lambda) |\Omega_+\rangle, \quad (11)$$

where

$$\rho(\lambda) = \sum_{k=1}^N \frac{\ell_k}{\lambda - \epsilon_k},$$

It is useful to introduce notation for global operators of $sl(2)$ -representation on $\mathcal{H} = \otimes_1^N V_k$

$$Y_{gl} := \sum_{k=1}^N Y_k$$

To find the eigenvectors and spectrum of $t(\lambda)$ on \mathcal{H} one requires that vectors of the form

$$|\mu_1, \dots, \mu_M\rangle = \prod_{j=1}^M X^-(\mu_j) |\Omega_+\rangle \quad (12)$$

are eigenvectors of $t(\lambda)$:

$$t(\lambda) |\{\mu_j\}_{j=1}^M\rangle = \Lambda(\lambda; \{\mu_j\}_{j=1}^M) |\{\mu_j\}_{j=1}^M\rangle, \quad (13)$$

provided that the parameters μ_j satisfy the Bethe equations:

$$2c + \sum_{k=1}^N \frac{\ell_k}{\mu_i - \epsilon_k} - \sum_{j \neq i}^M \frac{2}{\mu_i - \mu_j} = 0, \quad i = 1, \dots, M. \quad (14)$$

The realization of the loop algebra generators on the space \mathcal{H} is as follows

$$h(\lambda) = \sum_{k=1}^N \frac{h_k}{\lambda - \epsilon_k}, \quad X^-(\lambda) = \sum_{k=1}^N \frac{X_k^-}{\lambda - \epsilon_k}, \quad X^+(\lambda) = \sum_{k=1}^N \frac{X_k^+}{\lambda - \epsilon_k}. \quad (15)$$

The coupling constant g of (1) is connected with parameter $c = \frac{1}{g}$ while the Hamiltonian (1) is obtained as operator coefficient of term $\frac{1}{\lambda^2}$ in expansion of $t(\lambda; c)$ at $\lambda \rightarrow \infty$.

The eigenvalues for the vectors (12) are

$$\begin{aligned} \Lambda_0(x) &= c\rho(\lambda) + \rho^2(\lambda) - 2 \frac{d}{d\lambda} \rho(\lambda), \\ \Lambda_M(\lambda; \{\mu_j\}) &= \Lambda_0 - (c + 2\rho(\lambda)) \sum_{j=1}^M \frac{2}{\lambda - \mu_j} + \sum_{k \neq j}^M \frac{4}{(\lambda - \mu_k)(\lambda - \mu_j)} \end{aligned}$$

Quantum group theory provides a possibility to deform the Hamiltonian preserving integrability [8, 9]. More exactly, we use the so-called Jordanian r -matrix to quantum deform the Hamiltonian of Richardson-Gaudin model (1). We add to $sl(2)$ symmetric r -matrix (5) the Jordanian part which does not depend on spectral parameters λ, μ :

$$r^J(\lambda, \mu) = \frac{C_2^\otimes}{\lambda - \mu} + \xi (h \otimes X^+ - X^+ \otimes h), \quad (16)$$

with Casimir element C_2^\otimes in the tensor product of two copies of $sl(2)$

$$C_2^\otimes = h \otimes h + 2(X^+ \otimes X^- + X^- \otimes X^+).$$

After Jordanian twist the r-matrix (16) is commuting with the nilpotent generator X_0^+ only

$$[X_0^+ \otimes \mathbb{I} + \mathbb{I} \otimes X_0^+, r^{(J)}(\lambda, \mu)] = 0. \quad (17)$$

Hence, one can add the term $cX_0^+ + L(\lambda, \xi)$ to the L -operator, where $X_0^+ = \sigma_0^+$ in auxiliary space \mathbb{C}_0^2 of spin 1/2 representation. This yields the twisted transfer-matrix

$$\begin{aligned} t^{(J)}(\lambda) &= \frac{1}{2} \text{tr}_0 (cX_0^+ + L(\lambda, \xi))^2 \\ t^{(J)}(\lambda) &= cX^+(\lambda) + h(\lambda)^2 - 2h'(\lambda) + 2(2X^-(\lambda) + \xi)X^+(\lambda) \end{aligned} \quad (18)$$

The corresponding commutation relations between the generators of the twisted loop algebra are explicitly given by

$$\begin{aligned} [h(\lambda), h(\mu)] &= 2\xi (X^+(\lambda) - X^+(\mu)) \\ [X^-(\lambda), X^-(\mu)] &= -\xi (X^-(\lambda) - X^-(\mu)), \\ [X^+(\lambda), X^-(\mu)] &= -\frac{h(\lambda) - h(\mu)}{\lambda - \mu} + \xi X^+(\lambda), \\ [X^+(\lambda), X^+(\mu)] &= 0, \\ [h(\lambda), X^-(\mu)] &= 2 \frac{X^-(\lambda) - X^-(\mu)}{\lambda - \mu} + \xi h(\mu), \\ [h(\lambda), X^+(\mu)] &= -2 \frac{X^+(\lambda) - X^+(\mu)}{\lambda - \mu}. \end{aligned} \quad (19)$$

Realization of the Jordanian twisted loop algebra $\mathcal{L}_J(sl(2))$ with CR (19) is given similar to (15) with extra terms proportional to the deformation parameter ξ

$$h(\lambda) = \sum_{k=1}^N \left(\frac{h_k}{\lambda - \epsilon_k} + \xi X_k^+ \right), \quad X^-(\lambda) = \sum_{k=1}^N \left(\frac{X_k^-}{\lambda - \epsilon_k} - \frac{\xi}{2} h_k \right), \quad X^+(\lambda) = \sum_{k=1}^N \frac{X_k^+}{\lambda - \epsilon_k}. \quad (20)$$

To construct eigenstates for the twisted model in the framework of QISM one has to use creation operators of the form [9, 10]

$$B_M(\mu_1, \dots, \mu_M) = X^-(\mu_1)(X^-(\mu_2) + \xi) \dots (X^-(\mu_M) + \xi(M-1)) \quad (21)$$

acting by these operators on the ferromagnetic state $|\Omega_+\rangle$.

The deformed Richardson-Gaudin model Hamiltonian can now be extracted from the transfer-matrix $t^{(J)}(\lambda)$ as the operator coefficient in its expansion $\lambda \rightarrow \infty$.

According to (8) and (18) one can also extract quantum integrals of motion J_k using the realization (20). It would yield rather cumbersome expressions for J_k :

$$t^{(J)}(\lambda) = J_0 + \frac{1}{\lambda} J_1 + \frac{1}{\lambda^2} J_2 + \dots \quad (22)$$

The corresponding quantum deformed Hamiltonian

$$H \simeq J_2 = c \sum_{j=1}^N \epsilon_j X_j^+ + 2\xi \left\{ \left(\sum_{j=1}^N \epsilon_j h_j \right) X_{gl}^+ - h_{gl} \sum_{j=1}^N \epsilon_j X_j^+ \right\} + \frac{g}{2} \left(h_{gl}^2 + 2h_{gl} + 4X_{gl}^- X_{gl}^+ \right).$$

Let us write down a simplified case without the Jordanian twist: $\xi = 0$. Then one gets

$$J_0 = 0, \quad J_1 = X_{gl}^+, \quad J_2 \simeq \sum_{k=1}^N \epsilon_k X_k^+ + \frac{g}{2} \left(h_{gl}^2 + 2h_{gl} + 4X_{gl}^- X_{gl}^+ \right). \quad (23)$$

More complicated deformations of the Richardson-Gaudin model can be obtained using r -matrices related to the higher rank Lie algebras [11]. The structure of the eigenstates of the transfer matrix and their entanglement properties [12] are under investigation.

ACKNOWLEDGMENT

This work was supported by RFBR grants 11-01-00570-a and 12-01-00207-a (P.K.), and by STINT grant IG2011-2028 (A.S and H.J.).

REFERENCES

1. Richardson, R. W., “Exact eigenstates of pairing force hamiltonian,” *J. Math. Phys.*, Vol. 6, No. 7, 1034–1051, 1963.
2. Gaudin, M., *La Fonction D’onde de Bethe*, Chapter 13, Masson, Paris, 1983.
3. Cambiaggio, M. C., A. M. F. Rivas, and M. Saraceno, “Integrability of the pairing hamiltonian,” *Nucl. Phys. A*, Vol. 624, 157, 1997.
4. Dukelsky, J., S. Pittel, and G. Sierra, “Exactly solvable Richardson-Gaudin models for many-body quantum systems,” *Rev. Mod. Phys.*, Vol. 76, 643, 2004.
5. Faddeev, L. D., “How algebraic Bethe ansatz works for integrable models,” *Quantum Symmetries/Symétries Quantiques, Proceedings of the Les Houches Summer School, Session LXIV*, A. Connes, K. Gawedzki, and J. Zinn-Justin, Eds., 149–219, North-Holland, Amsterdam, 1998.
6. Kulish, P. P. and E. K. Sklyanin, “Quantum spectral transform method. Recent developments,” *Lecture Notes in Physics*, Vol. 151, 61–119, Springer, New York, 1982.
7. Sklyanin, E. K., “Generating function of correlators in the \mathfrak{sl}_2 Gaudin model,” *Lett. Math. Phys.*, Vol. 47, 275–292, 1999.
8. Kulish, P. P. and A. A. Stolin, “Deformed yangians and integrable models,” *Czech. J. Phys.*, Vol. 12, 207–1212, 1997.
9. Kulish, P. P., “Twisted $sl(2)$ Gaudin model,” Preprint PDMI, Aug. 2002.

10. Antonio, N. C. and N. Manojlovic, “ sl_2 Gaudin model with Jordanian twist,” *J. Math. Phys.*, Vol. 46, 102701, 2005.
11. Stolin, A. A., “On rational solutions of Yang-Baxter equation for $sl(n)$,” *Math. Scand.*, Vol. 69, 57–80, 1991.
12. Dunning, C., J. Links, and H.-Q. Zhou, “Ground-state entanglement of the BCS model,” *Phys. Rev. Lett.*, Vol. 94, 227002, 2005.

Proton Beam Induction of Quantum Correlations in Silicon Nanocrystal

Vesna I. Berec^{1, 2}

¹Department of Physics, University of Belgrade, Serbia

²Institute of Nuclear Sciences, Vinča, P. O. Box 522, Belgrade 11001, Serbia

Abstract— Permanent system size decreasing trend of communication systems defined by Moore’s Law, by 2015 will imply the implementation of elements as memory units comparable to individual atoms and charge. Accordingly, the quantum effects at the subatomic level will have a decisive influence on the development of information technology. We investigate induction-generation of mutual quantum correlations — entanglement, which implies accurate control, manipulation and transfer of quantum information — qubits addressable for modeling and implementation in quantum channels and network systems. The proposed investigation employs the quantum communication protocol based on the transmission model of hyperchanneled protons and the Monte Carlo simulations of spin systems in silicon nanocrystals.

The quantum electrodynamical nature of entanglement as an essential quantum property that establishes mutual predictable correlation of particles of energy/matter is investigated using the precisely guided proton beam through a ²⁹Si nanocrystal axial channel on a basis of screened Moliere’s interaction potential. Numerical solutions of equations of motion of protons correspond to hyperchanneled proton spatial and angular distributions in the phase space.

1. INTRODUCTION

Information on the spin state of a particle in the quantum entanglement state — whether the given particle spin is oriented parallel or anti-parallel — allows simultaneous information about the spin of the other particle which belongs to entanglement pair. Quantum entanglement allows qubits to simultaneously interact and to transfer the quantum state information regardless to the distance between them, in the process of communication that is not limited by the speed of light. The correlated particles will retain the status of entanglement if they are in isolated environment. In accordance with afore mentioned, the great potential of quantum entanglement lies in quantum information storage and processing [1], development and implementation of chip integrated quantum network protocols and quantum cryptography.

In order to prevent alteration or loss of quantum information that is extremely fragile, it is necessary to achieve precise control over all elements of quantum network(s) along with high degree of transmission fidelity. The noise reduction through the transmission process could be achieved by establishing the specific circumstances when two quantum objects — spin qubits form a unique mixed quantum state in the composite system, type: singlet-triplet. In that context, the process of coupling of electron with 1/2 nuclear quantum spin states [2] in silicon nanocrystal target, mediated by the polarized nuclear spin states of hyperchanneled protons through the quantum entanglement, could allow the transfer of information originally deposited in the electrons to the spin state of the host ²⁹Si. The result is an extremely fast transfer of quantum information in long-lived quantum state (polarization) of a nuclear spin, further addressable to a photon, with corresponding polarization/frequency.

Motivated by the fact that direct induction of ion-atom entanglement and coherent storage of quantum bits (qubits) quantum state information could permit the precise qubit manipulation, and single qubit measurement for times which could exceed seconds, we have investigated the features and benefits of hybrid qubits [2], under ion channeling regime, based on coupling of electron spin to nuclear spin in the isotopic, ~ 99% pure ²⁹Si nanocrystal target. Obtained results reveal a pathway for production of a new type of memory unit for quantum processing in silicon.

2. RESULTS AND DISCUSSION

The nuclear spins in case system are “locked” via the hyperchanneled proton beam in a desired state between $m_I = +1/2$ and $m_I = -1/2$ on the nanosecond time scale. This approach can provide a fast and efficient way of controlling nuclear spin qubits and thus enable the generation of switchable spin-based quantum gates by addressing the electron spin. The anisotropic hyperfine

coupling which allows strong mixing of quantum states is achieved by the control mechanism of spin qubit based on the 2 MeV proton pulse sequence through nanosilicon crystal channel according to a modified Meiboom-Gillecho regime.

The main Hamiltonian includes: the ion-atom confinement potential [4], acting inside the silicon nanocrystal cavity, and the internal-spin-degree of freedom which refers to hybrid electron-nuclear system [2]. The system properties and dynamics of the continuum ion-atom interaction potential in the nanocrystal are based on Lindhard continuum model for the ion-atom interactions in the impulse approximation [3]. The Hamiltonian governing the oscillatory motion of ions is

$$H = (1/2) m (p_{\perp}^2 + U(r)) = E (\psi_x^2 + \psi_y^2) + U(r), \quad E_{\perp} = E\psi^2 + U(r) \quad (1)$$

where E_{\perp} and p_{\perp} are ion transverse energy and momentum, ψ_x and ψ_y are x and y components of scattering small angle with respect to the low index channel axis. The proton trajectories are determined using the Moliere's approximation of the Thomas Fermi interaction potential [4]

$$U_i(r) = \frac{2Z_1Z_2e^2}{d} \sum_{i=1}^3 \alpha_i K_0 \left(\beta_i \frac{r}{a} \right), \quad (2)$$

where Z_1 and Z_2 are the atomic numbers of the proton and the atom, respectively, e is the electron charge, d is the quantum displacement from the harmonic oscillator ground state, r is the distance between the proton and atomic strings, a_0 is the Bohr radius, $a = [9\pi^2/128Z_2]^{1/3} \cdot a_0$ is the atom screening radius, and K_0 is the zero order modified Bessel function of the second kind with the fitting parameters: $(\alpha_i) = (0.35, 0.55, 0.10)$, $(\beta_i) = (0.30, 1.20, 6.00)$ [4]. The internal-spin-Hamiltonian for the case system placed in an external magnetic field B_x , is

$$H = \omega_e S_z + \omega_H I_z^H + \omega_S I_z^{Si} + S_z \otimes \left[\sum_{n \in Si, H} [A_n I_z^n + B_n I_x^n] \right]. \quad (3)$$

S_z is the electron spin component along the direction \hat{z} of the static external field \mathbf{B}_0 . The operator of the nuclear 1/2 spins I^n refers to: hyperchanneled protons, (¹H), and the ²⁹Si nuclei (99% abundance in target). ω_e , ω_H and ω_S are e⁻, ¹H and ²⁹Si Zeeman frequencies, respectively. A_n and B_n are hyperfine coupling coefficients. The system primary orientation depends on the coefficients of the hyperfine interaction. The hyperfine anisotropic term $BS_z I_x$ couples the longitudinal component of the electron spin with the transverse component of the ²⁹Si nuclear spin. The B_x field is applied perpendicular to \hat{z} axis which corresponds to the excitation laser propagation. To perform the atom-cavity experiment we have used the field stored in the cavity mode to manipulate charged particles at ideal conditions for separate qubit control. The optically generated states in that sense afterward can be transferred as a wavepackets along the transmission line for the multiple-qubit sessions. Investigation is initially processed according to Monte Carlo simulation of the quantum communication protocol of hybrid spin system in axial <100> silicon nanocrystal [4] based on the transmission model of hyper channeled protons. This implies precise guidance of the proton beam through a ²⁹Si nanocrystal single channel. Numerical simulation of the $m_S = 0$ and $m_S = \pm 1$ states, which are mapped on the two photon count-down emission probability as a read out, represents a function of the time interval τ obtained using a superoperator density matrix tomography in x - y plane, for the corresponding hyperfine transition frequency. Quantum transition probabilities are established via proton trajectory parameterization. The mapping of the quantum trajectories in phase space is carried out in a two-stage process: in the coordination phase space — the transverse position plane, and angular phase space, i.e., in the exit plane of scattering [4], for certain values of the 2 MeV proton beam relative to low index axial axis according to the parameters: tilt angle and the 92 nm thickness of the silicon nanocrystal.

3. EXPERIMENTAL PROTOCOL

All atoms are initially prepared in the ground state $|g\rangle$ by the laser excitation at a 221.7 nm, the off-resonant light pulse is applied to the $g-e$ transition, where $|e\rangle$ corresponds to the first excited state transition, inducing Raman scattering into the triplet state-metastable level $|s\rangle$. A short proton pulse synchronously follows a Ti: sapphire transfer pulse initializing the $|s\rangle$ state where the polarization states are $|s_0\rangle = -\sin\theta|e_{\vartheta}\rangle$ and $|s_{\pm}\rangle = e^{\pm i\varphi}/\sqrt{2}(\cos\theta|e_{\vartheta}\rangle \pm i|e_{\varphi}\rangle)$. A

transition from the system's singlet to triplet state is provided with the spin precession by the angle $\vartheta = 2\pi$, $\varphi = 6.09$ mrad around z axis, in conjunction with 2 T B_x field. Distribution of transition amplitudes obtained from 2 MeV proton beam source with a 92 nm ^{29}Si target is presented in Figure 1. The spherical polar and azimuthal angles of the electron spin, θ and φ , i.e., the polarization states, depend on change in angular momentum, Δm of the ^{29}Si atom excited along the $\langle 100 \rangle$ axis of target (following the direction/angle of the incident proton beam: $\vartheta = \pi$, $\varphi = 0.05\psi_c$, $\varphi = 0.1\psi_c$, $\varphi = 0.15\psi_c$ and $\varphi = 0.20\psi_c$).

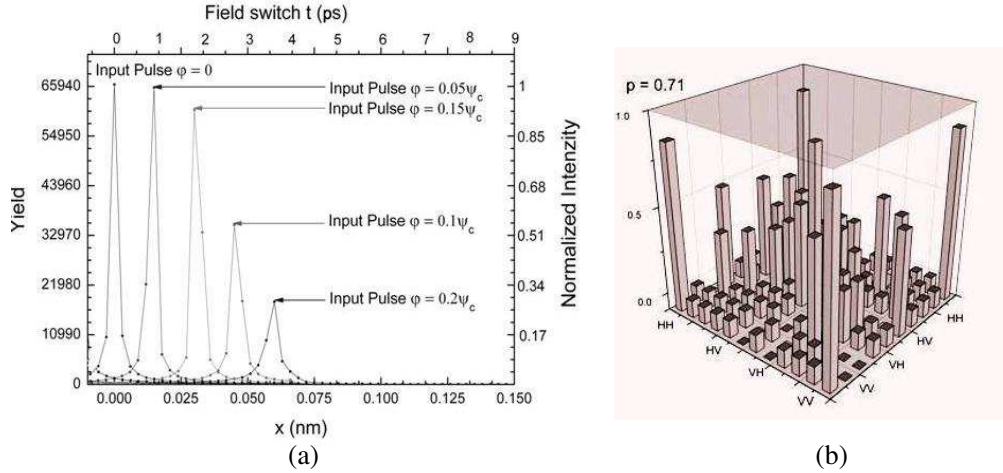


Figure 1: (a) The proton beam focusing spot associated with the tilt angles: $\varphi = 0.05\psi_c$, $\varphi = 0.1\psi_c$, $\varphi = 0.15\psi_c$ and $\varphi = 0.20\psi_c$, “covers” the area in the vicinity of the low index $\langle 100 \rangle$ nanocrystal axis and allows the control for two-qubit entanglement with inhibition of the new spin polarizations for the nuclear ^{29}Si spins in adjacent sites. (b) Tomography superoperator results which confirm quantity measure of established mixed state entanglement for nuclear spins — the concurrence, for the real components of the Werner states. Silicon nanocrystal is tilted along the θ_x axis corresponding to the limit $p > 1/3$ which defines the maximal quantity of entanglement. $p = 0.71$ corresponds to the ion beam incident angle at $\varphi = 0.1\psi_c$, where $\psi_c = [2Z_1Z_2e^2/(dE)]^{1/2} = 6.09$ mrad.

4. CONCLUSIONS

We have examined the isotopically purified silicon nanocrystal (in the 2 T magnetic field) as a medium for the direct generation of an atom-photon entanglement obtained as a mixed quantum state of hyperpolarized $1/2$ nuclear spins hyperfine-coupled with electron spin, using the super focusing channeling effect. Experimental modeling and characterization of entanglement as a state vector in the Hilbert space $\mathcal{H}_1 \otimes \mathcal{H}_2$ of the composite system that cannot be expressed as the direct tensor product of states $|\varphi\rangle_1$, $|\varphi\rangle_2$ in a given case include mixed quantum state induced by the superimposed hyperchanneled proton beam of 2 MeV energy over electron spin states in silicon nanocrystal. Obtained results support further exploration toward implementation of single memory unit below atomic scale aimed for information storage and quantum processing based on silicon, since the achieved robust entanglement of nuclear states becomes far more isolated from destructive interactions.

REFERENCES

1. Kimble, H. J., “The quantum internet,” *Nature*, Vol. 453, 1023–1030, 2008.
2. Morton, J. J. and B. W. Lovett, “Hybrid solid-state qubits: The powerful role of electron spins,” *Annu. Rev. Condens. Matter Phys.*, Vol. 2, 189–212, 2011.
3. Guidi, V., A. Mazzolari, D. De Salvador, and L. Bacci, “Deflection of MeV protons by an unbent half-wavelength silicon crystal,” *Phys. Rev. Lett.*, Vol. 108, 014801, 2012.
4. Berec, V., “Quantum entanglement and spin control in silicon nanocrystal,” *PLoS ONE*, Vol. 7, No. 9, e45254, 2012, doi:10.1371/journal.pone.0045254.

Optical Sensor Based on LSPR Phenomenon to Reveal Cholesterol Concentrations for Biomedical Applications

R. Tarporelli, R. Iovine, and L. Vegni

Department of Engineering, University of Roma Tre, Via Vito Volterra 62, Rome 00146, Italy

Abstract— In this contribution a nanodevice based on Localized Surface Plasmon Resonance (LSPR) phenomenon for biological characterization operating in the Visible and Near Infrared frequency Regime is proposed. The device consists of coupled biconical nanoparticles deposited on a silica substrate. By using a very small inter-particle distance it is possible to obtain a strong near electric field enhancement at the resonant wavelength suitable for ultra-sensitive biosensing applications. Full-wave simulations confirm the possibility to use the device as an optical sensor to detect in a ultra-sensitive way different cholesterol concentrations of the lipid membrane.

1. INTRODUCTION

Cholesterol is a main component of the plasma membranes of eukaryotic cells and plays an important role in maintaining membrane integrity and fluidity [1]. Nowadays, it is observed that elevate levels in the cholesterol contents of the lipid membrane can be associated to a tumor initial stage [2, 3]. For example, it is referred that the breast cancer and the prostate cancer cell contained lipid with high values of cholesterol. The main reasons are:

- cancer cells tend to accumulate cholesterol in their cell membrane which facilitates procarciogenic cell signaling;
- high cholesterol level is vital for carcinogenesis because it activates several protein signals such as Sonic Hedgehog (SH) and Protein Kinase B (PKB).

Therefore, these results indicate the importance of the evaluation of cholesterol concentrations of the lipid membrane.

For this purpose, an LSPR device to evaluate different cholesterol concentration by permittivity measurements is proposed. Nowadays, it is well known that the optical properties of nanoparticles depend on the dielectric properties of the background environment. This behavior is already exploited in several sensing applications based on LSPR phenomenon [4, 5].

In this work an electromagnetic enhancement of this mechanism is necessary because the permittivity of the lipid membrane shows small changes when different values of cholesterol are considered. This enhancement is obtained by arranging the nanoparticles in a linear array configuration.

In the following subsection it will be shown a numerical electromagnetic analysis of biconical nanoparticles, the array design (coupled particles) representing the sensing platform and the possibility to use it as an ultra-sensitive sensing platform.

Full-wave simulations confirm that in this configuration the device is able to reveal small changes of cholesterol concentration of the lipid membrane.

2. SINGLE PARTICLE ANALYSIS

The particle consists of a pair of opposing gold truncated nanocones excited by an impinging plane wave, having the electric field parallel to the cone principal axis as shown in Figure 1.

The electromagnetic analysis is carried out through full-wave numerical simulations by varying the geometrical parameters of the particle. We have assumed:

- for gold the experimental values as reported in [6];
- the surrounding dielectric medium is to be vacuum.

As depicted in Figure 2 it is possible to note that:

- by increasing h (apothem of the truncated nanocone) the extinction cross-section spectrum increases (stronger dipole moment of biconical nanoparticles) — Figure 2(a);
- by increasing r_1 (longer radius of the truncated nanocone) the extinction cross-section spectrum shifts towards longer wavelength — Figure 2(b).

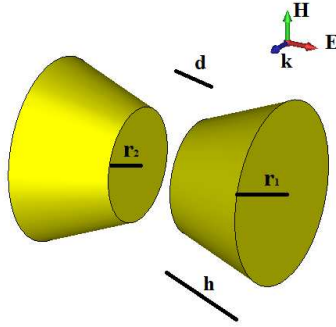
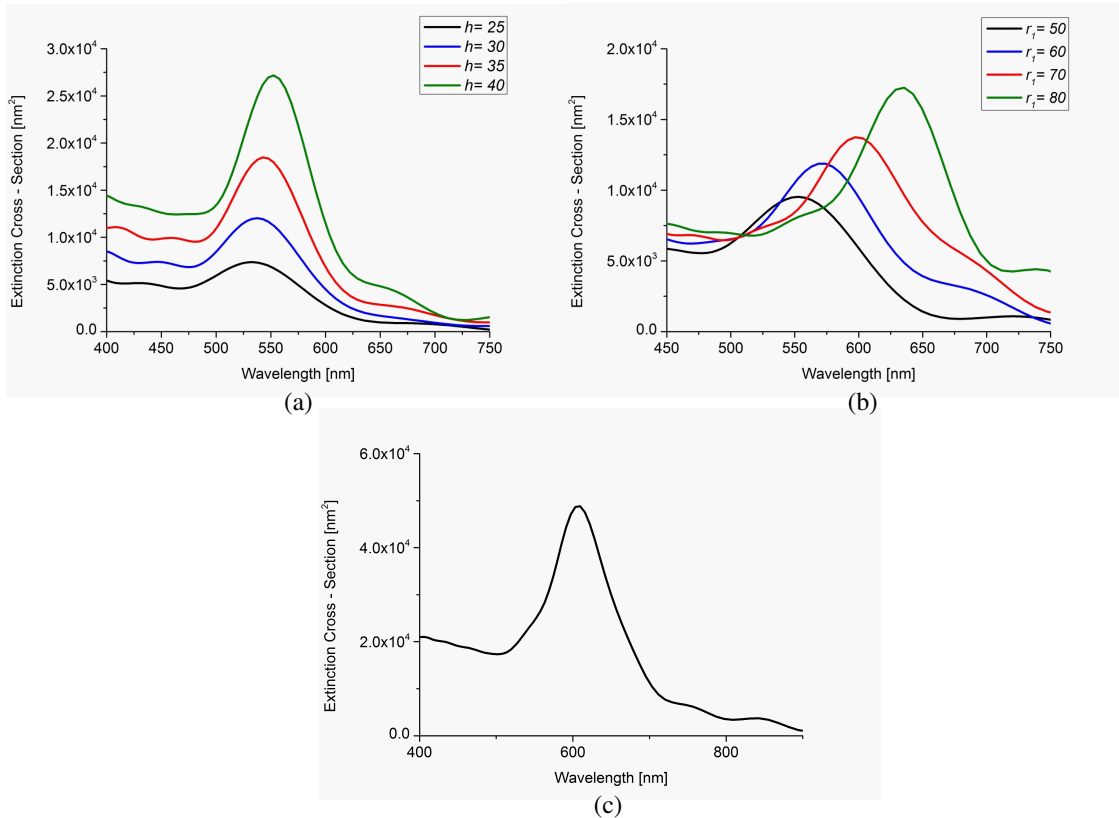


Figure 1: Geometrical sketch of biconical nanoparticles.

Figure 2: Extinction Cross – Section spectra for (a) $r_1 = 40$, $r_2 = 25$, $d = 10$, $25 < h < 40$, (b) $50 < r_1 < 80$, $d = 10$, $h = 25$ and (c) $r_1 = 80$ nm, $r_2 = 25$ nm, $d = 10$ nm, $h = 40$ nm.

In the following section it is analyzed the possibility to arrange the proposed biconical particles in a linear array configuration in order to obtain an additional electromagnetic field enhancement. In this way, it has been verified the capability to reveal small changes by refractive index measurements, as the evaluation of different cholesterol concentrations of the lipid membrane.

3. COUPLED BICONICAL PARTICLES AS AN ULTRASENSITIVE BIOSENSING PLATFORM

In this section we analyze the possibility to enhance the electromagnetic LSPR phenomenon by using coupled biconical nanoparticles deposited on a silica substrate. The device is shown in Figure 3. In this configuration the enhancement originates from the charge induction among the nanoparticles which interact stronger as they get closer to each other. As an example we show in Figure 4 the electromagnetic field enhancement for the linear arrangement of nanoparticles with $r_1 = 80$ nm, $r_2 = 25$ nm, $d = 10$ nm, $h = 40$ nm and an inter-particle distance between coupled biconical particles equals to 30 nm.

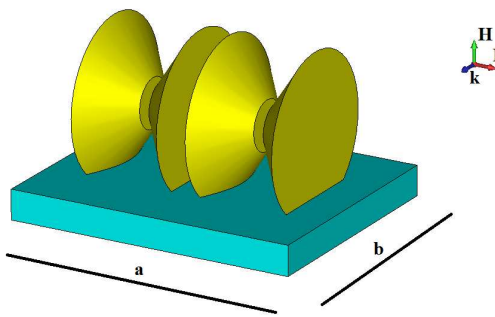


Figure 3: Coupled biconical nanoparticles arranged in a linear chain configuration. Geometrical parameters: $a = 290$; $b = 240$; $r_1 = 80$; $r_2 = 25$; $h = 40$. All the dimensions are expressed in nm.

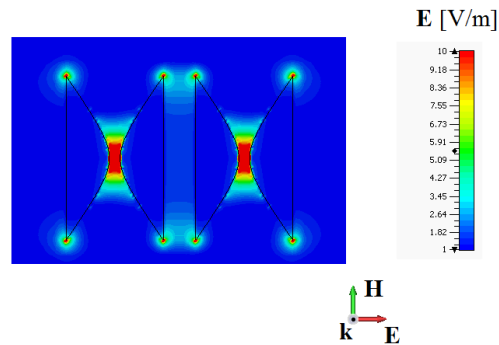


Figure 4: Near electric field distribution at the resonant wavelength (609 nm). The incident electric field amplitude is 1 V/m.

To test the device sensitivity, the Refractive Index (RI) values of different cholesterol concentrations of the lipid membrane have been used [7]. In this way a shift in the position of the spectra response is related to the different concentration of the compound under test.

It is possible to observe (Figure 5) that the proposed device allows the detection of different cholesterol concentrations of the lipid membrane (lecithin and cholesterol mixture) despite of the refractive index shows small changes when different concentrations are considered.

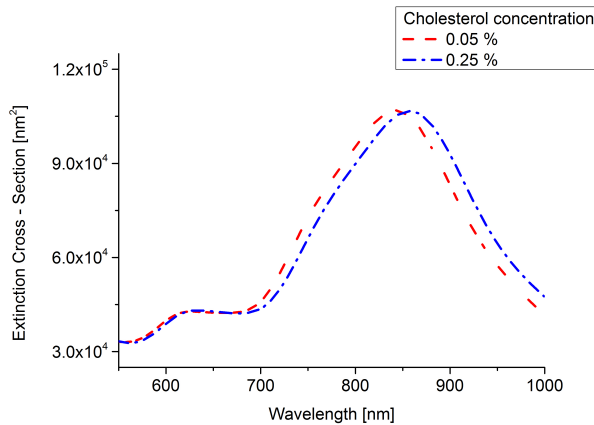


Figure 5: Extinction cross section spectra for different cholesterol concentrations of the lipid membrane. The geometrical parameters of the cone particles are: $r_1 = 80$, $r_2 = 25$, $d = 10$, $h = 40$, *inter-particle distance between coupled biconical particles* = 30. All the dimensions are expressed in nm.

4. CONCLUSION

In this contribution we have proposed biconical nanoparticles arranged in a linear chain configuration as an ultra-sensitive biosensing platform. By using full-wave simulations the electromagnetic properties of the device are evaluated. Numerical results encourage the possibility to use such device for the recognition of different cholesterol concentrations of the lipid membrane.

REFERENCES

1. Silvius, J. R., "Role of cholesterol in lipid raft formation: Lessons from lipid model systems," *Biochim. Biophys. Acta*, Vol. 1610, No. 2, 174–183, 2003.
2. Freeman, M. R. and K. R. Solomon, "Cholesterol and prostate cancer," *J. Cell. Biochem.*, Vol. 91, 54–69, 2004.
3. Kolanjiappan, K., C. R. Ramachandran, and S. Manoharan, "Biochemical changes in tumor tissues of oral cancer patients," *Clin. Biochem.*, Vol. 36, 61–65, 2003.

4. Iovine, R., L. La Spada, and L. Vegni, “Modified bow-tie nanoparticles operating in the visible and near infrared frequency regime,” *Advances in Nanoparticles*, Vol. 2, 21–27, 2013.
5. La Spada, L., R. Iovine, and L. Vegni, “Nanoparticle electromagnetic properties for sensing applications,” *Advances in Nanoparticles*, Vol. 1, 9–14, 2012.
6. Johnson, P. B. and R. W. Christy, “Optical constants of the noble metals,” *Phys. Rev. B*, Vol. 6, 4370–4379, 1972.
7. Jin, Y. L., J. Y. Chen, L. Xu, and P. N. Wang, “Refractive index measurements for biomaterial samples by total internal reflection,” *Phys. Med. Biol.*, Vol. 51, N371–N379, 2006.

Casimir Friction for Media of Finite Density

Johan S. Høye¹ and Iver Brevik²

¹Department of Physics, Norwegian University of Science and Technology, Trondheim, Norway

²Department of Energy and Process Engineering, Norwegian University of Science and Technology
Trondheim, Norway

Abstract— This work is a continuation of our papers from the last couple of years on the Casimir friction for a pair of particles at low relative velocity. The new element in the present analysis is to allow the media to be dense. Then the situation becomes more complex due to induced dipolar correlations, both within the two planes, and between the planes. We show that the structure of the problem can be simplified by regarding the two plates to be a generalized version of a pair of particles. The force is predicted to be usually very small, but can for very small separations become large.

1. INTRODUCTION

The typical situation envisaged in connection with Casimir friction is the one where two parallel semi-infinite dielectric nonmagnetic plates at micron or semi-micron separation are moving longitudinally with respect to each other, one plate being at rest, the other having a nonrelativistic velocity \mathbf{v} . Usually the plates are taken to have the same composition, their permittivity $\varepsilon(\omega)$ being frequency dependent.

Most previous works on Casimir friction are formulated within the framework of macroscopic electrodynamics. Some references in this direction are [1–7]. In particular, the application of the theory to graphene materials is a very promising avenue of approach; cf., for instance, Ref. [4]. In the present paper we focus on the following themes:

- We make use of *statistical mechanical methods* for harmonic oscillators, moving with respect to each other with constant velocity \mathbf{v} , at a finite temperature T . We claim that such a strategy is quite powerful. We have used this method repeatedly in previous recent investigations [8–12]; cf. also the earlier papers [13, 14] in which the foundations of the method were spelled out. The essence of the method is to generalize the statistical mechanical Kubo formalism to time-dependent cases.
- These methods are then used to generalize the theory to the case of *dense* media. This is a nontrivial task, as the additivity property holding for dilute media is no longer valid. One will have to deal with a more complicated form of the Green function. The atomic polarizabilities appearing in the theory of dilute media have to be replaced by functions based upon the frequency dependent permittivity.
- It turns out that the friction force becomes finite at finite temperature, although very small usually. The force is however very sensitive to the values of the input parameters, and can under special circumstances, such as for small separations, become quite large.

We mention that the microscopic approach has been followed by other investigators also, especially by Barton [15–17]. The equivalence between our approach and that of Barton is actually not so straightforward to verify, but has been shown explicitly [10].

2. DILUTE MEDIA

For a pair of polarizable particles the electrostatic dipole-dipole pair interaction perturbs the Hamiltonian by an amount

$$-AF(t) = \psi_{ij}s_{1i}s_{2j}, \quad (1)$$

where the summation convention for repeated indices i and j is implied. The s_{1i} and s_{2j} are components of the fluctuation dipole moments of the two particles ($i, j = 1, 2, 3$). With electrostatic dipole-dipole interaction we can write

$$\psi_{ij} = -\frac{\partial^2}{\partial x_i \partial x_j} \psi, \quad \psi = \frac{1}{r}, \quad (2)$$

(i.e., $\psi_{ij} = -(3x_i x_j / r^5 - \delta_{ij} / r^3)$). Here $\mathbf{r} = \mathbf{r}(t)$ with components $x_i = x_i(t)$ is the separation between the particles. The time dependence in Eq. (1) is due to the variation of \mathbf{r} with time t , and the interaction will vary as

$$-AF(t) = \left[\psi_{ij}(\mathbf{r}_0) + \left(\frac{\partial}{\partial x_l} \psi_{ij}(\mathbf{r}_0) \right) v_l t + \dots \right] s_{1i}s_{2j}, \quad (3)$$

where v_l are the components of the relative velocity \mathbf{v} . The components of the force \mathbf{B} between the oscillators are

$$B_l = -T_{lij}s_{1i}s_{2j}, \quad T_{lij} = \frac{\partial}{\partial x_l} \psi_{ij}. \quad (4)$$

The friction force is due to the second term of the right hand side of Eq. (3), and for dilute media the first term can be neglected.

For the time dependent part of Eq. (3) we may write $-AF(t) \rightarrow -A_l F_l(t)$ where $A_l = B_l$ and $F_l(t) = v_l t$. According to the Kubo formula the perturbing term leads to a response in the thermal average of B_l given by

$$\Delta \langle B_l(t) \rangle = \int_{-\infty}^{\infty} \phi_{BAq}(t-t') F_q(t') dt', \quad (5)$$

where the response function is ($t > 0$)

$$\phi_{BAq}(t) = \frac{1}{i\hbar} \text{Tr} \{ \rho [A_q, B_l(t)] \}. \quad (6)$$

Here ρ is the density matrix and $B_l(t)$ is the Heisenberg operator $B_l(t) = e^{itH/\hbar} B_l e^{-itH/\hbar}$ where B_l like A_q are time independent operators. With Eqs. (3) and (4) expression (6) can be rewritten as

$$\phi_{BAq}(t) = T_{lij} T_{qnm} \phi(t) \delta_{in} \delta_{jm}, \quad (7)$$

$$\phi(t) \delta_{in} \delta_{jm} = \text{Tr} \{ \rho \frac{1}{i\hbar} [s_{1i}s_{2j}, s_{1n}(t)s_{2m}(t)] \} \quad (8)$$

(i.e., the situation with scalar polarizability is assumed such that $\langle s_{ai}s_{an}(t) \rangle = 0$ for $i \neq n$). Further following Refs. [11] and [18] one can introduce the correlation function $g(\lambda)$ in imaginary time $\lambda = it/\hbar$ where

$$\phi(t) = \frac{1}{i\hbar} [g(\beta + \lambda) - g(\lambda)] \quad (9)$$

$$g(\lambda) \delta_{in} \delta_{jm} = \text{Tr} [\rho s_{1n}(t) s_{2m}(t) s_{1i} s_{2j}] \quad (10)$$

with Fourier transforms

$$\tilde{\phi}(\omega) = \int_0^\infty \phi(t) e^{-i\omega t} dt \quad \text{and} \quad \tilde{g}(K) = \int_0^\beta g(\lambda) e^{iK\lambda} d\lambda. \quad (11)$$

Here $K = i\hbar\omega$ and $\beta = 1/(k_B T)$, where k_B is Boltzmann's constant and T the temperature. Then one has [14]

$$\tilde{\phi}(\omega) = \tilde{g}(K). \quad (12)$$

Further we now have

$$g(\lambda) = g_1(\lambda) g_2(\lambda) \quad \text{and} \quad \tilde{g}(K) = \frac{1}{\beta} \sum_{K_0} \tilde{g}_1(K_0) \tilde{g}_2(K - K_0) \quad (13)$$

where for a simple harmonic oscillator with zero frequency polarizability α_a and eigenfrequency ω_a ($a = 1, 2$)

$$\tilde{g}_a(K) = \alpha_{aK} = \frac{\alpha_a (\hbar\omega_a)^2}{K^2 + (\hbar\omega_a)^2}. \quad (14)$$

Altogether following Ref. [11] the friction force is then given by

$$F_{fl} = -iG_{lq}v_q \frac{\partial \tilde{\phi}(\omega)}{\partial \omega} \Big|_{\omega=0} = -G_{lq}v_q H \frac{\pi\beta}{2} \delta(\omega_1 - \omega_2), \quad (15)$$

where

$$G_{lq} = T_{lij} T_{qij}, \quad H = \left(\frac{\hbar\omega}{2 \sinh(\frac{1}{2}\beta\hbar\omega)} \right)^2 \alpha_1 \alpha_2, \quad (16)$$

and $\omega_1 - \omega_2 = \omega$.

The treatment above can be extended to more general polarizability that can be written as ($a = 1, 2$)

$$\alpha_a(K) = \int \frac{\alpha_{Ia}(m^2)m^2}{K^2 + m^2} d(m^2). \quad (17)$$

This will generalize Eq. (15) to oscillators with a band of eigenfrequencies.

Finally by integrating G_{lq} over space one obtains for dilute media the friction force F (per unit area) between two half-planes that move parallel to each other [11]

$$F = -GvH, \quad G = \frac{3\pi}{8d^4} \rho_1 \rho_2, \quad (18)$$

where now with $m = \hbar\omega$

$$H = \frac{\pi\beta\hbar}{2} \int \frac{m^4 \alpha_{I1}(m^2) \alpha_{I2}(m^2)}{\sinh^2(\frac{1}{2}\beta m)} dm. \quad (19)$$

Here v is the relative velocity in the x direction. Moreover ρ_1 and ρ_2 are the particle densities in the half-planes, and d is the separation between the half-planes.

When v is low, there is according to (16) no friction. Physically this is understood by the circumstance that excitations of the quantized system require disturbances with frequencies matching the energy difference $\hbar(\omega_1 - \omega_2)$. Low constant velocity represents the limit of zero frequency.

3. DENSE MEDIA

For higher densities, separate oscillators both within each plane and between planes will be correlated. This will add to the complexity of the problem. Some simplification can be achieved, however, by regarding the two half-planes as a generalized version of a pair of particles. A detailed exposition of the theory for this case is given in [18]. Here, we sketch some points.

Expression (10) is a thermal average of four oscillating dipole moments. They have Gaussian distributions since they represent coupled harmonic oscillators. This means that averages can be divided into averages of pairs of dipole moments. To better see the structure of these correlations one-dimensional oscillators with interaction energy $\phi s_1 s_2$ were considered [11]. Then non-zero averages $\langle s_1 s_2 \rangle$ as well as $\langle s_1^2 \rangle$ and $\langle s_2^2 \rangle$ could be evaluated from which $\langle s_1 s_2 s_1 s_2 \rangle - \langle s_1 s_2 \rangle \langle s_1 s_2 \rangle = \langle s_1^2 \rangle \langle s_2^2 \rangle + \langle s_1 s_2 \rangle \langle s_1 s_2 \rangle$ and its structure was obtained. This was further extended to obtain the expression and the structure for $\langle s_1(t) s_2(t) s_1 s_2 \rangle - \langle s_1(t) s_2(t) \rangle \langle s_1 s_2 \rangle$. Then the ϕ was replaced by the electrostatic interaction (1) and (2), and the two particles were replaced by the two half-planes. The corresponding correlation function is then found by the Green function solution of Maxwell's equations for the electrostatic problem [19]. At the end of this evaluation the effect of mutual correlations ($\langle s_1 s_2 \rangle \neq 0$) could be neglected, keeping only pair correlations within each half-plane. The result of all this was then that the low density expressions of the previous section are kept except that the polarizability is replaced by

$$4\pi\rho_a \alpha_{aK} \rightarrow \frac{2(\varepsilon_a - 1)}{\varepsilon_a + 1}. \quad (20)$$

where ε_a is the dielectric constant or relative permittivity where for low density $\varepsilon_a - 1 = 4\pi\rho_a \alpha_a$.

Assume now that the plates are equal, and assume the Drude model for the permittivity ($\varepsilon_a = \varepsilon$)

$$\varepsilon = 1 + \frac{\omega_p^2}{\zeta(\zeta + \nu)}, \quad (21)$$

where $\zeta = i\omega$, and where ν represents damping of plasma oscillations due to finite conductivity of the medium. With this one finds

$$\frac{\varepsilon - 1}{\varepsilon + 1} = \frac{q^2}{K^2 + q^2 + \sigma|K|} \quad (22)$$

where $q^2 = (\hbar\omega_p)^2/2$ and $\sigma = \hbar\nu$. The physical interpretation of this is that the electron plasma acts as set of damped harmonic oscillators that all have the same eigenfrequency $\omega_p/\sqrt{2}$ (replacing the zero eigenfrequency of expression (21)). This is the eigenfrequency of surface plasma waves.

With relations (21) and (22) we can repeat the calculations that led to the friction force per unit area F (18). Then the frequency distribution $\alpha_I(m^2)$ of Eq. (19) is needed. With expression (22) it is (for small ν) [11]

$$m^2\alpha(m^2) = \frac{q^2}{2\pi\rho} \frac{\sigma q}{x^2 + (\sigma q)^2}, \quad x^2 = m^2 - q^2. \quad (23)$$

With this some calculation leads to the following force expression per unit area ($\rho_1 = \rho_2 = \rho$)

$$F = -\frac{3kTv}{128\pi\nu d^4} \left(\frac{\frac{1}{2}\beta q}{\sinh(\frac{1}{2}\beta q)} \right)^2. \quad (24)$$

It is noteworthy that the particle density ρ does not occur explicitly in this expression. It is present indirectly, though, in the plasma frequency ω_p which decreases with decreasing density with the consequence that F even increases with decreasing density due to the $\sinh(\cdot)$ term.

Also it may not be so obvious why F is inversely proportional to ν that represents damping of plasma oscillations due to finite conductivity. The point here is that ν represents the width of the frequency spectrum of plasma oscillations. For small ν the friction is due to overlapping frequencies, and small ν means narrow frequency band and large overlap of frequencies.

Consider, as an example, gold at $T = 300$ K, corresponding to $kT = 25.86$ meV. Then $\hbar\omega_p = 9.0$ eV, $\hbar\nu = 35$ meV, $q = \hbar\omega_p/\sqrt{2} = 6.36$ eV, $\frac{1}{2}\beta q = 123$. We can then calculate the first factor in the expression (24). Choosing $v = 100$ m/s for the relative velocity and a small separation $d = 10$ nm between the plates, the first factor in (24) becomes 5.81 mPa. The second factor in (24), however, containing the $\sinh(\cdot)$ term, washes the friction force out for all practical purposes.

4. CONCLUSION

There have been various approaches to the Casimir friction problem in the literature, and they are actually quite difficult to compare. The statistical mechanical approach which we have presented above, can be related to that of Barton since they both use a microscopic description [15–17]. As mentioned above, we have shown in an earlier work that our approaches lead to the same result [10].

In the case of dilute media, the friction force is given by the expression (15). For low velocities v , the force is zero. For high velocities, making the disturbance large enough to excite frequencies comparable to the excitation frequencies for the molecules, the friction force is finite.

For dense media, the force expression (24) is overwhelmingly suppressed by the $\sinh(\cdot)$ factor. It is far beyond measurability for typical metals.

In Ref. [18], we made an attempt to compare our results with related ones of Volokitin and Persson [3], and the interested reader may consult that source. Their approach was within macroscopic electrodynamics, a method quite different from that followed by us above.

Note added in the proof: A remark should be added concerning the numerics: Recent considerations have shown that it is the case of low frequencies that is of primary importance here. Taking that into account, the expression (24) will be replaced by a different, and much larger, estimate. Our analytical considerations above remain however unchanged.

REFERENCES

1. Pendry, J. B., *J. Phys.: Condens. Matter*, Vol. 9, 10301, 1997.
2. Pendry, J. B., *New J. Phys.*, Vol. 12, 033028, 2010.
3. Volokitin, A. I. and B. N. J. Persson, *Rev. Mod. Phys.*, Vol. 79, 1291, 2007.
4. Volokitin, A. I. and B. N. J. Persson, *Phys. Rev. Lett.*, Vol. 106, 094502, 2011.
5. Dedkov, G. V. and A. A. Kyasov, *Surface Science*, Vol. 605, 1077, 2011.
6. Dedkov, G. V. and A. A. Kyasov, *Surface Science*, Vol. 606, 46, 2012.
7. Philbin, T. G. and U. Leonhardt, *New J. Phys.*, Vol. 11, 033035, 2009.
8. Høye, J. S. and I. Brevik, *EPL*, Vol. 91, 60003, 2010.
9. Høye, J. S. and I. Brevik, *Eur. Phys. J. D*, Vol. 61, 335, 2011.
10. Høye, J. S. and I. Brevik, *Eur. Phys. J. D*, Vol. 64, 1, 2011.

11. Høye, J. S. and I. Brevik, *Eur. Phys. J. D*, Vol. 66, 149, 2012.
12. Høye, J. S. and I. Brevik, *Int. J. Mod. Phys. A*, Vol. 27, 1260011, 2012.
13. Høye, J. S. and I. Brevik, *Physica A*, Vol. 181, 413, 1992.
14. Brevik, I. and J. S. Høye, *Physica A*, Vol. 153, 420, 1988.
15. Barton, G., *New J. Phys.*, Vol. 12, 113044, 2010.
16. Barton, G., *New J. Phys.*, Vol. 12, 113045, 2010.
17. Barton, G., *New J. Phys.*, Vol. 13, 043023, 2011.
18. Høye, J. S. and I. Brevik, arXiv:1305.4269 [quant-ph].
19. Høye, J. S. and I. Brevik, *Physica A*, Vol. 259, 165, 1998.

VHF EMF Portable Radio Assessment

Nina Rubtsova¹, Sergey Perov¹, Elena Bogacheva¹, Quirino Balzano², and Niels Kuster³

¹Federal State Budgetary Institution ‘Research Institute of Occupational Health’ under the Russian Academy of Medical Sciences, Moscow, Russian Federation

²Department of Electrical and Computer Engineering, University of Maryland, Maryland, USA

³Foundation for Research on Information Technologies in Society, Zurich, Switzerland

Abstract— The safety of the users of portable transmitter in the occupational and general public conditions is of actual concern, because such radiofrequency (RF) devices are operated in the vicinity of human body. Portable transmitters are the essential personal communication devices for different kinds of professions. For the safety evaluation of such devices in Russia there is an exposure limit value for the electric field strength measured near the head and at a control point. The Specific Absorption Rate (SAR) is used as the basic restriction. In our investigation, the electric field strength was measured at the recommended control point in free space and SAR from the portable radio transmitters model “Radyo-301” was measured in a flat phantom. The evaluation has shown that this type of RF exposure may exceed Russian permissible levels, but less than basic restriction of ICNIRP guidelines. Therefore the use of these devices should be considered a health risk factor according to the Russian regulatory approach.

1. INTRODUCTION

In recent years portable radio frequency (RF) devices have found increasing use in the occupational and general public conditions. Such mobile communication devices are various and include walkie-talkie cellular phones wireless hand free equipment, etc.. Hand-held radio devices operate in different frequency band — from very high frequency (VHF) to ultra-high frequency (UHF).

During the last twenty years there have been a lot of publications reporting the human safety assessment of hand held mobile communication devices, but mainly the tested frequency range was higher than 300 MHz. In the VHF band there are several wireless communication standards, one of them is TETRA and others involving FM portable radio transmitters. Portable devices are RF sources, normally used in the vicinity of the human body. This causes a concern about the safe occupational exposure of such devices. However this safety assessment is not a simple task, because electromagnetic waves have a complex structure in the near field [4] and, so, it is necessary to make a dosimetry assessment of the electromagnetic field (EMF) exposure. It involves the evaluation of Specific Absorption Rate (SAR) using a standard homogenous flat phantom. There are relatively few reports of portable transmitter SAR evaluation in the VHF band [1–3].

In the Russian Federation the mobile communication reference level control point is located at 4.5 meters from the sources for 170 MHz [5]. This approach is not correct, because it is far from user and source. But, in Russia, this measurement approach applies to all RF communication devices used in the vicinity of the human body and head. We are interested in evaluating the real exposure condition at the user location and the absorption of energy from this type of source. So, the portable radios were tested for SAR performance and for electric field strength at the control point. Measured data have been compared with the ICNIRP basic restriction and the Russian permissible levels.

2. MATERIALS AND METHODS

The device under test (DUT) was the portable radio transmitter “Radyo-301” manufactured by Izhevkiy Radiozavod (Russia). Such transceiver is the recommended mobile communication device for railways, police and some other operational structures in Russia. This type of communication is used for local networking in the VHF radiofrequency range (149–171 MHz). This EMF source is a hand held (or body mounted) transmitter, usually placed near the head and torso.

In our investigations two identical models of portable radio transmitter “Radyo-301” (*DUT 1* and *DUT 2*) were used for the specific absorption rate (SAR) assessment. These DUT’s operate over several RF channels, but in our research the DUT’s worked at a single frequency (171.25 MHz) in simplex mode with 5 W transmitted output power.

Free space measurements of electric field strength were carried out with the broadband field meter Narda NBM-550 (Narda Safety Test Solutions, USA) with electric probe EF0391. The portable

radio transmitters worked at maximum output power. The distance from DUT to measured point (control point) was 4.5 meters for 170 MHz. The method and distance of measurement were coincide completely with requirements of SanPiN 2.1. 8/2.2.4.1190-03 [5]. This is the distance the of the recommended measurement point from the center of the loudspeaker in front of the DUT. The DUT is placed in a low loss energy holder and the *E*-field Narda probe is located at 4.5 meter from DUT.

The absorbed energy investigations were carried out with the dosimetric system DASY 52 NEO (SPEAG AG, Zurich, Switzerland). The portable radio transmitters were placed in a low loss energy holder under a flat phantom (ELI4, SPEAG AG) with a bottom-wall thickness of 2.0 mm. The portable radio transmitters worked at maximum output power as in previous measurements. The phantom was filled with a liquid simulating tissue with the dielectric properties of tissue at 170 MHz [HSL175, SPEAG AG]: $\epsilon_r = 52.58$; $\sigma = 0.80 \text{ S/m}$. The dosimetric isotropic probe used was the ET3DV6 (SPEAG AG) with 2.7 mm distance from probe tip to dipole sensor centers. The DUT's were located under the ELI4 phantom as shown in Fig. 1.

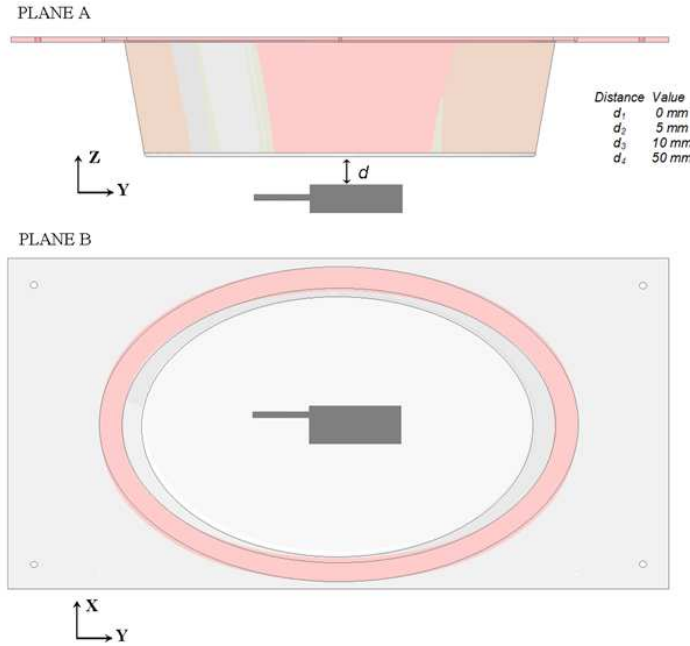


Figure 1: The flat phantom set-up.

The DUTs were located parallel to the phantom bottom surface. The DUT's were placed at distances d below the flat phantom. The area scan grid covered all parts of the device including the antenna. The measured areas were at the front and back sides of the device. The penetrated EMF distribution in the flat phantom plane (Area Scan) was carried out in 15 mm steps. In pre-evaluation of the area scans, the SAR distribution was out of boundaries for back side position. Therefore we used a larger size of area scan. The front side area scan dimension was $15 \times 28.5 \text{ cm}^2$ and included 190 measured points. The back side area scan dimension was $15 \times 34.5 \text{ cm}^2$ with 230 measured points.

The area scan is used to evaluate the SAR distribution and to reveal the maximum absorption locations where the peak SAR (the "hot spot") is located.

In the scanned areas where the maximum SAR ("hot spot") was detected, the peak spatial average SAR was evaluated (zoom scan). The size of zoom scan was $4 \times 4 \times 3 \text{ cm}^3$ with 252 measured points. Volume measurements were performed at every peak absorption point for both sides of the radios.

3. RESULTS AND DISCUSSION

As Narda NBM-550 is broadband field meter, we include the correction factor for the DUT frequency. The *E*-field measurements were performed several times and the rms *E* field values at the control point ranged from 2.08 to 2.25 V/m. The measured electric field strength is higher than

reference level at the control point. The maximum permissible electric field strength at the control point is 1.5 V/m [5].

During the SAR measurements, “hot spots” are detected on the flat phantom surface at distances “ d ” up to 50 mm from the radio case (Fig. 1). Without a gap between flat phantom and *DUT 1* there are three “hot spots” in the front side of the radio. The first “hot-spot” (maximum absorption) depends on strength of reactive fields between device and phantom. For *DUT 2* there were two “hot spots” for two positions: without air gap and at 10 mm distance. In all other cases was detected only one “hot spot”.

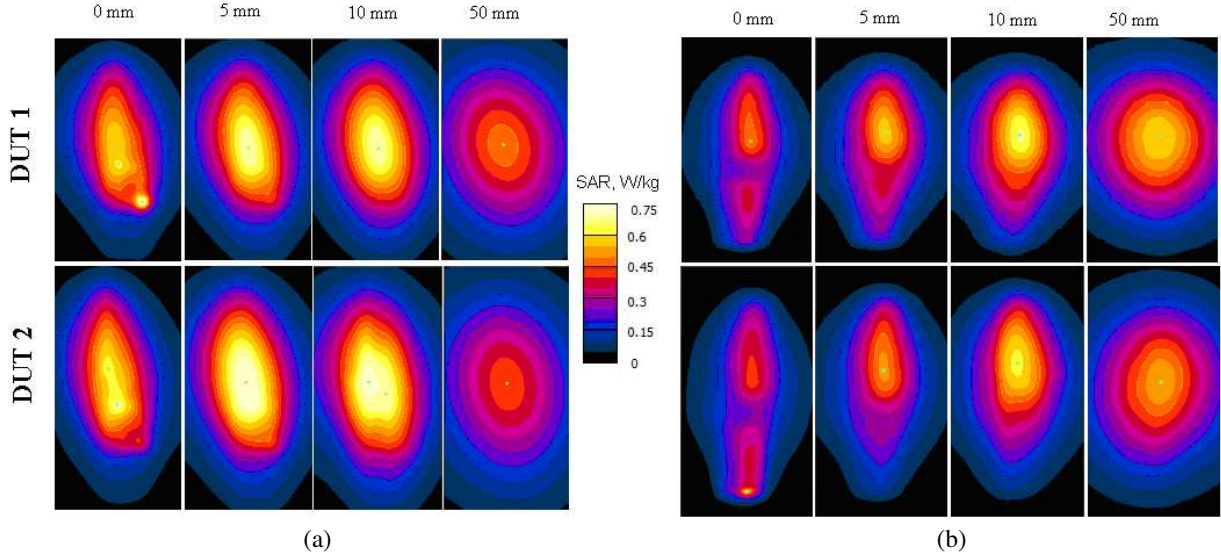


Figure 2: SAR distribution. (a) Front side. (b) Back sides.

Table 1 presents the maximum recorded values of SAR for each “area scan”. The peak SAR’s on the front side have been registered at 5 mm distance from the phantom, and they were 0.687 W/kg and 0.766 W/kg. The peak SAR’s on the back side have been recorded at the bottom part of portable radio transmitter. It is interesting to note that the maximum SAR values from the back of both radios have been registered at 10 mm distance from the phantom, and they were 0.65 W/kg and 0.62 W/kg. It appears that the radio battery near the phantom causes either a substantial distortion in the electric field distribution or a large mismatch of the antenna impedance.

Table 1: Summary of the area scan results for all measurements.

Distance, mm	SAR, W/kg (Front side)			SAR, W/kg (Back side)		
	<i>DUT 1</i>	<i>DUT 2</i>	dB	<i>DUT 1</i>	<i>DUT 2</i>	dB
0	0.603	0.665	0.43	0.467	0.432	0.34
5	0.687	0.766	0.47	0.563	0.512	0.41
10	0.687	0.719	0.20	0.652	0.621	0.21
50	0.483	0.436	0.44	0.592	0.53	0.48

Table 2: Summary of the zoom scan results for all measurements.

Distance, mm	SAR (10 g), W/kg					
	Front area			Back area		
	<i>DUT 1</i>	<i>DUT 2</i>	dB	<i>DUT 1</i>	<i>DUT 2</i>	dB
0	0.396	0.453	0.58	0.313	0.234	1.26
5	0.481	0.532	0.44	0.394	0.342	0.61
10	0.45	0.499	0.45	0.44	0.438	0.02
50	0.353	0.316	0.48	0.425	0.42	0.05

Table 2 summarizes the zoom scan results, the peak spacial-average (ps-) SAR's for all measurements. It shows that the maximum ps-SAR values were recorded in the front of the radio (area potentially in the front of the user's head). The comparison of results show that the maximum ratio of the 10 g ps-SAR measured using the two radios is less than 1.3 dB.

The maxima of the mass -averaged SAR's in 10 g were observed at the distance of 5 mm from phantom's shell bottom at front side, and 10 mm — at back side for both radios.

4. CONCLUSIONS

In this paper the VHF portable radio transmitter exposure has been evaluated using the maximum mass-averaged SAR in 10 g at different distances. The maximum values were detected at distances 5 mm and 10 mm from flat phantom. The maximum mass-averaged SAR's in 10 g were 0.5 W/kg at front side and 0.44 W/kg at back side.

This investigation shows the real exposure EMF levels for the user of portable transmitters. The SAR data show that the levels of human body exposure under normal DUT usage are from 0.5 to 0.2 W/kg which are not above the EU limits, but for the Russian regulations the measured electric field strength is higher than the permissible level.

According to these results and the Russian hygienic regulations, this model of portable transmitters can be a potentially harmful device for human health. Therefore, the work time with these radios needs to be regulated in Russia. For this reason, the exposure time must be restricted and, for a proper safety enforcement in the work place, timers are necessary to limit the RF transmission intervals over a working day.

These two approaches to EMF assessment show that a dual evaluation (dosimetry and free space measurements) is necessary for such RF transmitters in the Russian Federation. But for their detail hygienic assessment, it is necessary to find the correlation between basic restrictions and reference levels.

REFERENCES

1. Cleveland, Jr., R. F. and T. W. Athey, "Specific absorption rate (SAR) in models of the human head exposed to hand-held UHF portable radios," *Bioelectromagnetics*, 173–186, 1989.
2. Martens, L. and G. Vermeeren, "Electromagnetic dosimetry of the SAR for a walkie-talkie set-up," *XXVIIth General Assembly of International Union Radio Sciense*, October 23–29, 2005.
3. Vermeeren, G. and L. Martens, "Assessment of the SAR in the SAM head phantom for a PMR446 radio held in four typical positions close to the head," *Abstract Book The Bioelectromagnetics Society 28th Annual Meeting*, 42–45, June 11–15, 2016.
4. Balzano, Q., O. Garay, and R. F. Steel, "Energy deposition in biological tissue near portable radio transmitters at VHF and UHF," *Proceeding of the 27th Conference of IEEE VT-G Orlando*, 25–39, FL, March 16–18, 1977.
5. SanPiN 2.1.8/2.2.4.1190-03, "Hygiene requirements for placement and operation of land mobile radio," Moscow, 2003.

Conductivity and Permittivity Measurements of Children and Adult's Hands Covering Mobile Communications Frequency Bands

Chinthana Panagamuwa, Ian Howells, and William Whittow

Centre for Mobile Communications Research, School of Electronic, Electrical and Systems Engineering
Loughborough University, Loughborough, LE11 3TU, United Kingdom

Abstract— This paper investigates the use of a simple open-ended coaxial line probe for measuring *in vivo* the relative permittivity and conductivity of human hands at microwave frequencies. In particular, we investigate how these properties are affected by the force with which the probe is pushed into the skin and the time over which the probe is in contact with the skin. Results show these two variables have a large influence on the measured results. We identify a suitable test procedure for use on a large scale volunteer study and present initial relative permittivity and conductivity results from more than 150 volunteers, ranging from ages 11 to 65.

1. INTRODUCTION

Smart phones have become more than simple communication devices; for many they are indispensable accessories capable of running sophisticated applications. The use of these smart phones by children is becoming more widespread. In this changing climate, possible health effects of radiation from mobile phones on children in particular, takes on an added importance. In order to assess the Specific Absorption Rate (SAR) in human tissue, the relative permittivity and conductivity of the tissue must be studied. These properties of biological tissues at microwave frequencies have been investigated over a number of decades [1–4]. Researchers have used live and dead animals as well as adult volunteers to measure the electrical properties of tissues.

Numerous full-body human phantom models are now available for EM simulations of SAR. Although a number of studies have developed mathematical functions to extrapolate child data from adult, actual measured conductivity and permittivity data for children is much harder to source.

As part of a large volunteer based study looking at how the hand holding a mobile phone affects the power absorbed in the head, this study evaluates the use of the open-ended coaxial line (OECL) probe technique for measuring palm relative permittivity and conductivity of human participants. First we investigate how the force with which the probe is pushed into the palm affects the relative permittivity and conductivity. With increasing force, we expect the blood to be forced away and the contact point to become closer to the underlying muscle, which will then change the dielectric properties. With the probe making contact with the palm, we also investigate how the measured results change with time. The aim is to develop a suitable measurement protocol that can be used on child and adult volunteers. Finally, we present relative permittivity and conductivity data collected from more than 150 participants and demonstrate how these properties change with age.

2. OPEN-ENDED COAXIAL LINE PROBE CONSTRUCTION AND CALIBRATION

The use of an open-ended coaxial line probe for measuring the dielectric properties of materials, especially liquids, has been studied for over three decades. Burdette et al. in 1980, were the first to demonstrate the use of an OECL probe [2]. The inner conductor of their probe protruded beyond the outer, in effect creating a miniature monopole. Further work by Athey et al. [3] and Stuchly et al. [4] eventually led to the more familiar flush OECL probe. Marsland et al. [5] carried out a detailed analysis of the use of an OECL probe for dielectric measurements. In [6], Blackham et al. presented the OECL probe technique with an added flange.

For our study, an OECL probe was produced by cleaving a RG-402 semi-rigid cable. A SMA connector was fixed to the other end. A flange was omitted from our probe design because there is limited space on the palm for taking a measurement, especially in the case of children. The natural creases in the skin also make it difficult to have a flange completely flush against the palm surface.

Calibration of the probe is a critical part of the measurement process. An Anritsu Lightning 37397D vector network analyser was set for CW signal at 1710 MHz (GSM 1800 frequency for channel 512) and calibrated at the end of the cable. Measuring a single data point minimises the

sweep time of the VNA allowing repeat measurements to be taken at short intervals. Once the OECL probe was connected to the cable, it was secured as shown in Figure 1 to minimise movement.

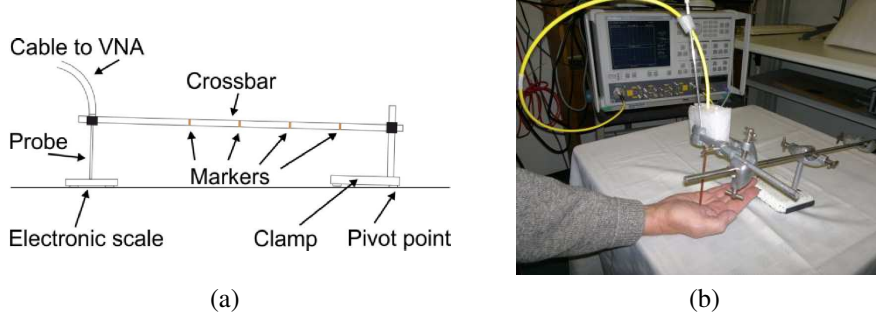


Figure 1: (a) Experimental setup for calibrating the probe weight; (b) photograph of the probe being used on a volunteer.

Calibration of the probe itself was conducted by measuring the complex reflection coefficient Γ^* with three different calibration standards, namely open, short and deionised water. Open Γ^* was recorded with the probe left open-ended in free space. Short Γ^* was recorded with aluminium foil pushed against the cleaved end. Finally, the Γ^* was measured with the probe dipped into pure deionised water to a depth of 3 cm below the surface. Kraszewski et al. [7] concluded that deionised water was the most suitable standard liquid for probe calibration based on a study of polar liquids. The depth to which the probe should be submerged is dependent on the diameter of the probe and in [8], Anderson et al. suggested that a 6.4 mm diameter probe only needs to be 6 mm below the surface of the liquid.

The complex permittivity of deionised water is calculated using the Debye Equation [10]

$$\varepsilon_w^* = \varepsilon' + j\varepsilon'' = \varepsilon_\infty + \frac{\varepsilon_s - \varepsilon_\infty}{1 + j\omega\tau}$$

where ε_w^* is the complex relative permittivity with ε' and ε'' are the real and imaginary parts respectively. ε_∞ is the relative permittivity at high frequencies and ε_s is the static permittivity at low frequencies. τ is the relaxation time. From [11], $\varepsilon_\infty = 4.6$, $\varepsilon_s = 78.3$, and $\tau = 8.08$ ps. The complex relative permittivity (ε_m^*) and the effective conductivity (σ_m) of the material under test, in this instance the participant's palm, is calculated from [5]

$$\begin{aligned} \varepsilon_m^* &= -\frac{\Delta_{m2} \times \Delta_{13}}{\Delta_{m1} \times \Delta_{32}} \varepsilon_w^* - \frac{\Delta_{m3} \times \Delta_{21}}{\Delta_{m1} \times \Delta_{32}} \\ \sigma_m &= \omega \varepsilon_0 \varepsilon'' \\ \Delta_{ij} &= \Gamma_i^* - \Gamma_j^* \end{aligned}$$

where Γ_1^* , Γ_2^* , Γ_3^* , Γ_m^* are the measured complex reflection coefficients for the short, open, deionised water and material under test respectively.

3. FORCE AND SAMPLE TIME STUDY

The palm relative permittivity and conductivity was calculated by measuring the Γ^* when the probe was placed on the palm of the volunteer. In order to change the force applied by the probe on the skin, the experimental setup given in Figure 1 was used. The point at which the clamp base pivots on the table was adjusted while the probe tip rested on an electronic scale. Markers were drawn on the crossbar of the clamp at locations where the readout on the scale corresponded to 50 g (0.49N) to 400 g (3.92N) in steps of 50 g (0.49N).

The VNA was set to display both the real and imaginary parts of the Γ^* . A digital video camera was placed in front of the display in order to record the change in Γ^* over time. With the camera recording, the probe was placed on the centre of the volunteer's palm ensuring the tip was not overlapping any of the natural creases in the skin. The video recording was made over a period of 50 seconds. The process was repeated with the clamp positioned at each of the markers on the crossbar, which corresponded to 0.49N to 3.92N. Following all the measurements, video editing software was used to tabulate the real and imaginary parts of Γ^* at different periods. Readings were taken every 0.2s for the first 2s, every 0.4s from 2 to 6s and every 2s from 6s to 50s.

3.1. Relative Permittivity and Conductivity Results

The calculated results for the relative permittivity and conductivity are shown in Figures 2 and 3 respectively. It is important to note that the skin surface of the palm is not smooth. For an accurate measurement, the probe tip needs to be flush against the material's surface. Even when the obvious large creases in the palm are avoided, there are small ridges in the skin that are unavoidable. These introduce tiny air gaps between the bottom of the probe and the surface of the skin and will thus reduce the calculated relative permittivity and conductivity results.

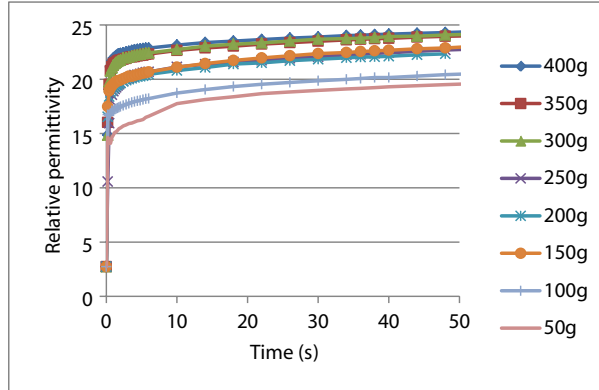


Figure 2: Palm relative permittivity of participant at 1710 MHz measured over time with different probe effective masses.

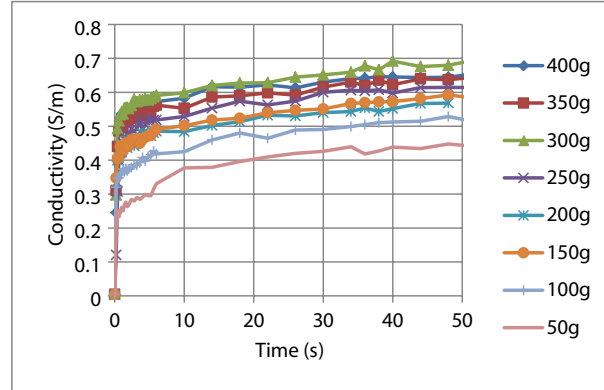


Figure 3: Palm conductivity of participant at 1710 MHz measured over time with different probe effective masses.

The volunteer reported that it was difficult to keep the hand perfectly still for 50 seconds. Small involuntary movements will have an effect on the measured reflection coefficient, and thus introduce ripples in the presented results.

In comparison to results presented in the literature for dry skin ($\epsilon_r \approx 39$, $\sigma \approx 1.15 \text{ S/m}$) [12], our results appear significantly lower but when compared to dry palm results from the literature [13], our results are consistent.

Both relative permittivity and conductivity increase with time. Each plotted result shows a rapid change in the first 3 to 4 seconds followed by a gradual increase that tends to plateau. With increasing time, more blood is pushed away from the contact point and the underlying muscle relaxes which causes the probe to sink further into the palm. The gradual increase in the relative permittivity and conductivity may also be due to the small ridges in the skin flattening out, thus reducing the air gaps and improving the contact between the probe and the skin.

Both relative permittivity and conductivity increase with applied force. As the force applied by the probe increases, the displaced tissue engulfs the inserted probe tip. This has the effect of increasing the volume through which the fringing electric fields propagate. For an accurate measurement, all the electric fields emanating from the probe tip should propagate through the test material. We expected the relative permittivity and conductivity to increase with increasing force and this is observed in the measurements.

In order to minimise the escape of the electric fields into the air, the probe should be pushed firmly into the palm. However, there are obvious limits to the force that can be applied. A force of 3.92N (400 g) was uncomfortable to the participant and therefore is unsuitable for use in a volunteer study involving the public. Similarly, the time at which the VNA is sampled should be delayed to ensure the measurement has stabilised to its final value, but this delay also has limitations. The participants are unlikely to endure long periods with the probe pushing into their palms.

4. VOLUNTEER BASED STUDY OF PALM PROPERTIES

Based on our above findings, an effective mass of 300 g (2.94N) was chosen as the most suitable test setup for the large scale volunteer study; results presented for 350 g and 400 g are similar to those taken with 300 g. Eight seconds was chosen as the delay period before recording the complex reflection coefficient off the VNA in order to reduce the discomfort caused.

Initial relative permittivity and conductivity data taken from more than 150 volunteers is presented in Figures 4 and 5. The results are grouped into 5 age brackets and for each bracket, an

average value has been calculated for the right and left hand. Each age bracket has at least 10 volunteers; the 20–30y bracket has the largest dataset with 79 volunteers.

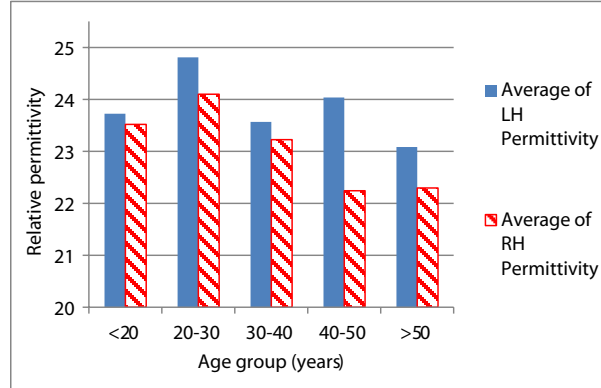


Figure 4: Left and right hand palm relative permittivity plotted by age groups.

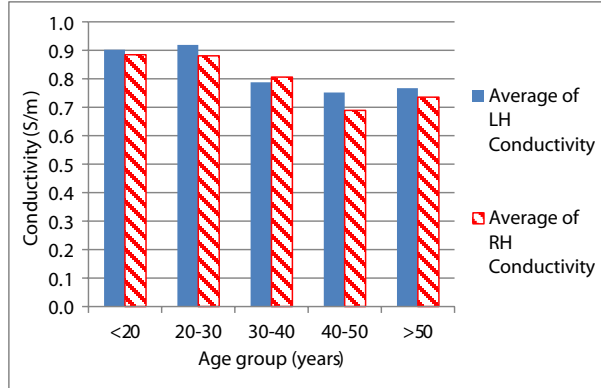


Figure 5: Left and right hand palm conductivity plotted by age groups.

The general trend in both graphs is to show a decrease in palm relative permittivity and conductivity with increasing age. With increasing age, in general the skin becomes dryer and in the palm the skin becomes thicker and rougher. Therefore, we expect to see the conductivity and permittivity decrease with age. Somewhat surprisingly, in a majority of the age brackets, the right hand on average has a lower relative permittivity and conductivity compared to the left. We note that more than 90% of the volunteers were right handed. We could speculate that the right hand, as a result of being used more than the left hand, has thicker skin and thus lower relative permittivity and conductivity. There are likely to be unavoidable measurement variations between left and right hands caused by differing sweat and dirt levels as well as differing tension levels in the palm muscles during measurements. However, with further data collection from more volunteers, we can expect the influence of some of these uncontrollable variables to reduce.

5. CONCLUSIONS

In this study we have shown when measuring the relative permittivity and conductivity of the palm, the force applied to an OECL probe and the time at which the measurement is taken has a large impact on the results. Identifying the optimum force and time to collect the data is not a simple task. The time taken for the complex reflection coefficient measurement to reach a plateau is dependent on a large number of factors such as the suppleness of the skin and the tension in the underlying muscle. The effect of many of these uncontrollable variables can only be minimised by collecting a sufficiently large dataset and currently this is an on-going study. It is important to note that, the probe's electric field penetrates not just the palm skin but also into the deeper tissue. Therefore the complex reflection coefficient captured during a palm measurement is the result of many electric field reflections from multiple tissue layers and as such, represents the relative permittivity and conductivity of a hand region rather than the skin alone.

REFERENCES

1. Gabriel, S., R. W. Lau, and C. Gabriel, "The dielectric properties of biological tissues: II. Measurements in the frequency range 10 Hz to 20 GHz," *Phys. Med. Biol.*, Vol. 41, No. 11, 1996.
2. Burdette, E. C., F. L. Cain, and J. Seals, "In vivo probe measurement technique for determining dielectric properties at VHF through microwave frequencies," *IEEE Transactions on Microwave Theory and Techniques*, Vol. 28, No. 4, 414–427, Apr. 1980.
3. Athey, T. W., M. A. Stuchly, and S. S. Stuchly, "Measurement of radio frequency permittivity of biological tissues with an open-ended coaxial line: Part I," *IEEE Transactions on Microwave Theory and Techniques*, Vol. 30, No. 1, 82–86, Jan. 1982.
4. Stuchly, M. A., A. Kraszewski, S. S. Stuchly, and A. M. Smith, "Dielectric properties of animal tissues in vivo at radio and microwave frequencies: Comparison between species," *Phys. Med. Biol.*, Vol. 27, No. 7, 927–936, Jul. 1982.

5. Marsland, T. P. and S. Evans, "Dielectric measurements with an open-ended coaxial probe," *IEE Proceedings H — Microwaves, Antennas and Propagation*, Vol. 134, No. 4, 341–349, Aug. 1987.
6. Blackham, D. V. and R. D. Pollard, "An improved technique for permittivity measurements using a coaxial probe," *IEEE Transactions on Instrumentation and Measurement*, Vol. 46, No. 5, 1093–1099, Oct. 1997.
7. Kraszewski, A., S. S. Stuchly, M. A. Stuchly, and S. A. Symons, "On the measurement accuracy of the tissue permittivity *in vivo*," *IEEE Transactions on Instrumentation and Measurement*, Vol. 32, No. 1, 37–42, Mar. 1983.
8. Anderson, L. S., G. B. Gajda, and S. S. Stuchly, "Analysis of an open-ended coaxial line sensor in layered dielectrics," *IEEE Transactions on Instrumentation and Measurement*, Vol. 35, No. 1, 13–18, Mar. 1986.
9. Bartley, P. G., S. O. Nelson, and R. W. McClendon, "Dimensional analysis of a permittivity measurement probe," *IEEE Transactions on Instrumentation and Measurement*, Vol. 51, No. 6, 1312–1315, Dec. 2002.
10. Debye, P., *Polar Molecules*, The Chemical Catalog Company, New York, 1929.
11. Schwan, H. P., R. I. Sheppard, and E. H. Grant, "Complex permittivity of water at 25°C," *Journal of Chemical Physics*, Vol. 64, No. 5, 2257–2258, Mar. 1976.
12. Andreuccetti, D., R. Fossi, and C. Petrucci, "An internet resource for the calculation of the dielectric properties of body tissues in the frequency range 10 Hz–100 GHz," Website at <http://niremf.ifac.cnr.it/tissprop/>, IFAC-CNR, Florence, Italy, 1997. Based on data published by C. Gabriel et al., in 1996.
13. Gabriel, C., "Compilation of the dielectric properties of body tissues at RF and microwave frequencies," Report N.AL/OE-TR-1996-0004, Occupational and environmental health directorate, Radiofrequency Radiation Division, Brooks Air Force Base, Texas, USA, Jan. 1996.

Characterization of HF RFID Tags Exposed to Moisture Based on Threshold Power Measurement

Toni Björninens¹, Jukka Voutilainen², Lauri Sydänheimo¹, and Leena Ukkonen¹

¹Department of Electronics and Communications Engineering, Tampere University of Technology
P. O. Box 692, FI-33101, Tampere, Finland
²Voyantic Ltd., Kutojantie 11, FI-02630, Espoo, Finland

Abstract— We investigated the impact of moisture on the operation of fully assembled high-frequency (HF) ISO 15693 compliant radio-frequency identification (RFID) tags operating at the frequency of 13.56 MHz. In the tag performance characterization, we use an active measurement technique based on the ramping of the output power of the reader during wireless communication with the tag under test.

1. INTRODUCTION

Radio-frequency identification (RFID) makes use of electromagnetic fields to track objects equipped with electronic transponders, commonly known as tags. In passive RFID systems, the tags are remotely powered and they are composed of only two components: an antenna and an application specific integrated circuit (tag IC). At high frequency regime (HF) this technology enables localized identification at the distances up to tens of centimeters based on inductive coupling. This technology does not require line-of-sight and the maintenance-free tags have long life-time. The passive HF tags have currently wide range of applications in access control, ticketing, alarm systems, animal tagging, and item level identification. In the future, the low-cost passive tags capable of ultra-low-power data transmission are envisioned to provide platforms for wireless sensor nodes operating as a part of the prospected internet of things [1, 2].

RFID tags sold in mass markets are typically general purpose labels, which are not optimized for operation on a specific platform, but maintain sufficient performance when mounted on common low-permittivity platforms, such as cardboard and plastic packages. However, in real application environments RFID tags may become in contact with materials, such as water and metals, which have drastically different electromagnetic properties. This is problematic for the reliability of the system. In this article, we analyze the impact of moisture on HF RFID tags. In the tag performance characterization, we use a novel measurement technique based on the ramping of the output power of the reader during wireless communication with the tag under test.

Figure 1 shows an equivalent presentation of an HF RFID tag where the near field coil is loaded with the tag microchip. Nominally, the inductance of the coil (L) and capacitance from the IC input (C_{ic}) form a resonant circuit. When the tag is exposed to moisture, the leakage current and distributed capacitance in between the adjacent coil traces increase. In the circuit model shown in Fig. 1, the impact of these phenomena is modelled with C_p and R_p . Moreover, R_s represents the series resistance of the coil conductor. As the amount of moisture soaked into the tag increases, C_p increases and R_p decreases. This lowers the resonance frequency and reduces the sensitivity of the tag. Both these impact negatively on the wireless operation.

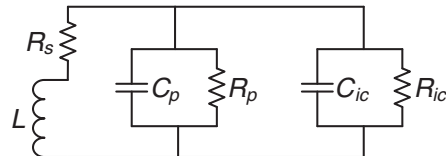


Figure 1: Equivalent circuit representation of a passive HF RFID tag.

2. MEASUREMENT-BASED CHARACTERIZATION OF HF RFID TAGS

Conventionally, the frequency tuning of HF tags is measured indirectly based on how they affect the input impedance of a reader coil. In this characterization, the input impedance of the reader coil is measured with and without a tag in its near field. The measurement can be conducted with a vector

signal analyzer (VNA), for instance, at low enough output power so that the non-linearity of the tag IC frontend does not affect the result. The frequency of the peak magnitude of the impedance difference is then used as a design parameter for the tag coil: the chip manufacturers typically provide a target frequency, which will lead to optimal resonance frequency in the active operation mode of the tag. We conducted this measurement on Smartrac BlockTM tag. The measurement result is shown in Fig. 2. The peak impedance difference occurred at 13.8 MHz.

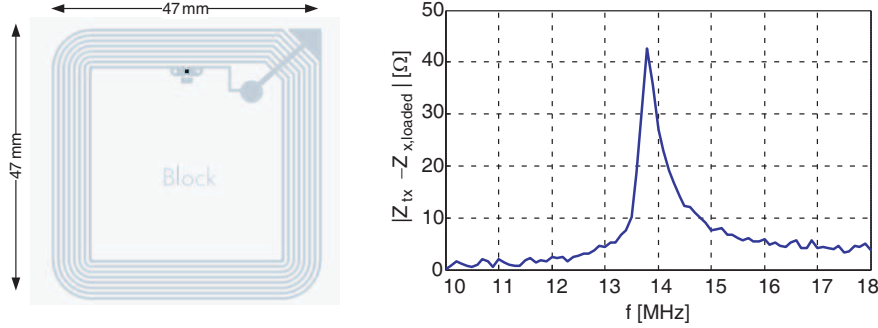


Figure 2: The tested tag and the impact of a coupled tag on the reader coil input impedance.

The threshold power measurement proposed in this paper provides a direct approach for the HF tag performance analysis. It will not only provide information of the tag resonance frequency, but also on the activation sensitivity of the tag. Moreover, compared with the VNA measurement it requires simple hardware. Previously, similar measurement systems have been used to characterize ISO 18000-6 compliant passive UHF RFID tags communicating with the reader via propagating electromagnetic waves in regionally regulated sub-bands of 840–960 MHz range [3]. However, to our knowledge this approach has not been applied in the characterization of HF tags.

The threshold power measurement technique is applicable to fully assembled RFID tags. During the measurement, the tags are interrogated while the output power of the reader is ramped down. The smallest output power at which a valid response from the tag was acquired is the threshold power (P_{th}) of the tag. Repeating this procedure over a range of frequencies provides the key-information on the tag performance: the frequency of the minimum threshold power is the optimal operation frequency of the tag. At this frequency the wireless power transfer efficiency from the reader output to the tag chip in its active operation mode is the highest. With the additional knowledge of the loss in the cable connecting the reader coil the output of the transmitter and the exact geometry of the reader coil, we can transform the measured threshold power to magnetic field intensity (H_{th}). In our test setup, we used a circular coil. In this case, the threshold magnetic field intensity at the tag location is given by [1]

$$H_{th} = \frac{NR^2 I_{th}}{2(z^2 + R^2)^{3/2}}, \quad (1)$$

where H_{th} is the magnetic field strength at an axial distance z from the center of the reader coil, R is the coil radius, N is the number of turns, and I_{th} is the rms current in the coil corresponding to the threshold power.

3. MEASUREMENT RESULTS

We used the threshold power measurement to analyze the impact of moisture on the Smartrac BlockTM tag. We conducted the measurement with Voyantic Tagformance HF measurement device [4], which automates the power-frequency sweep procedure. In the test, the tag was attached to a compact disc jewel case, which was placed at a distance of 6 cm from the reader coil. The tag was first measured dry and then soaked with tap water. Next, the threshold power was measured repeatedly until the tag had completely dried out. Fig. 3 shows the threshold power and magnetic field intensity of the studied tag during the wetting test.

As seen from the results in Fig. 3, in the initial dry state the tested tag has the best sensitivity at the frequency of 13.8 MHz. At this frequency, $P_{th} = -4$ dBm. The soaked tag experienced a frequency down-shift of 0.5 MHz and a notable 12.4 dB reduction in the tag sensitivity. While this is an extreme case of a soaking wet tag, also smaller amounts of moisture cause a visible change in

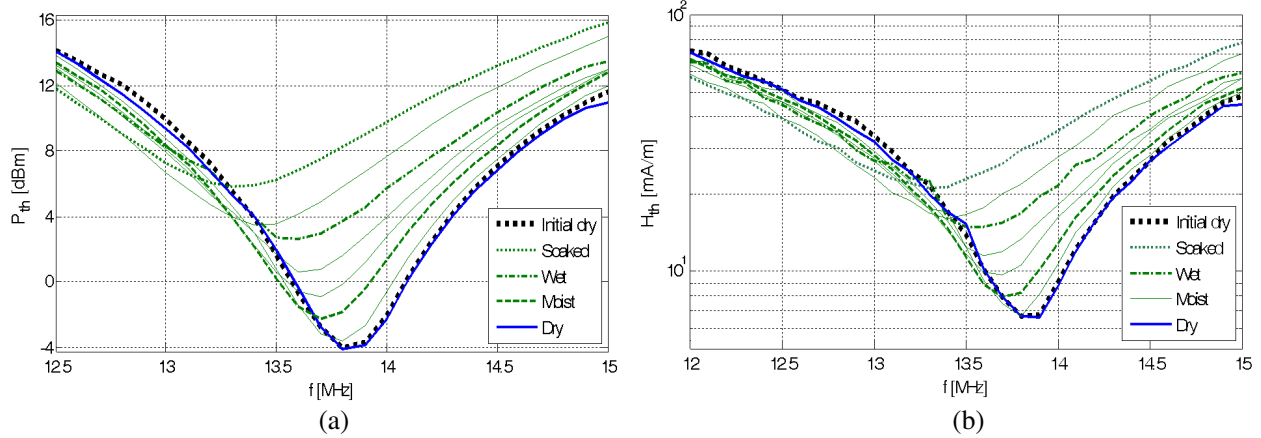


Figure 3: (a) The threshold power and (b) magnetic field intensities of the studied tag during the wetting test.

the tag performance. When the tag had dried out, the measured P_{th} was the same as in the initial dry state before the wetting test. This confirms that the tag IC was not damaged during the test. Hence the observed variation in the measured threshold power can be attributed completely to the impact of moisture on the tag coil. Moreover, the observed variability agrees with the prediction based on the equivalent circuit model representation of the tag discussed in Introduction (Fig. 1).

Based on the results presented in Fig. 3, it can be concluded that a way to alleviate the performance variation due to moisture is to purposefully tune the tag to a higher frequency in the nominal dry conditions. This way, smaller performance variation at the actual operation frequency (13.56 MHz) is attained: P_{th} varied 8.3 dB instead of the 12.4 dB at the optimum operation frequency of 13.8 MHz. Moreover, if the extreme case of a soaked tag is excluded, this variability reduces to only 4.1 dB at 13.56 MHz. This design choice, however, comes with the cost of reduced tag sensitivity.

Alternatively, the observed frequency-shift in the tag's response can be exploited in the development of inductively powered low-cost wireless humidity sensor tags. The threshold power based sensing may provide a simpler mechanism for sensor readout compared with the reader antenna input impedance based method utilized earlier in vapour and pressure sensors based on 13.56 MHz tags [5, 6]. Compared with ISO 18000-6 compliant UHF RFID humidity sensor tags [7, 8], the implementation at 13.56 MHz could provide a more reliable readout since the near field wireless channel is localized and thus free from multipath.

4. CONCLUSIONS

We presented a measurement-based performance characterization of an HF RFID tag exposed to moisture. The proposed new measurement technique is based on the ramping of the output power of the reader during wireless communication with the tag under test. Unlike conventional HF tag measurement techniques based on evaluation of the impact of a coupled tag on the reader coil input impedance, the presented measurement method provides direct measurement of both the sensitivity and frequency response of the tag under test. This enabled a full analysis of the varying moisture levels on the tag performance. The results demonstrated the possibility of exploiting standard HF RFID tags as low-cost moisture sensors.

REFERENCES

1. Finkenzeller, K., *RFID Handbook: Fundamentals and Applications in Contactless Smart Cards and Identification*, John Wiley & Sons, Ltd., Chichester, West Sussex, UK, 2003.
2. Kortuem, G., F. Kawsar, D. Fitton, and V. Sundramoorthy, "Smart objects as building blocks for the Internet of things," *IEEE Internet Computing*, Vol. 14, No. 1, 44–51, Jan.–Feb. 2010.
3. Nikitin, P., K. V. S. Rao, and S. Lam, "UHF RFID tag characterization: Overview and state-of-the-art," *Antenna Measurement Techniques Association Symposium*, 289–294, Seattle, WA, USA, Oct. 21–26, 2012.
4. Voyantic, Ltd., Espoo, Finland: <http://www.voyantic.com/>.

5. Potyrailo, R. A., C. Syrman, W. G. Morris, S. Go, Y. Lee, J. Cella, and K. S. Chichak, “Selective quantitation of vapors and their mixtures using individual passive multivariable RFID sensors,” *IEEE RFID Conf.*, 22–28, Orlando, FL, USA, Apr. 14–16, 2010.
6. Surman, C., R. A. Potyrailo, W. G. Morris, T. Wortley, M. Vincent, R. Diana, V. Pizzi, J. Carter, and G. Gach, “Temperature-independent passive RFID pressure sensors for single-use bioprocess components,” *IEEE RFID Conf.*, 78–84, Orlando, FL, USA, Apr. 12–14, 2011.
7. Virtanen, J., L. Ukkonen, T. Björninen, A. Z. Elsherbeni, and L. Sydänheimo, “Inkjet printed humidity sensor for passive UHF RFID systems,” *IEEE Trans. Instrum. Meas.*, Vol. 60, No. 8, 2768–2777, Aug. 2011.
8. Gao, J., J. Sidén, H.-E. Nilsson, and M. Gulliksson, “Printed humidity sensor with memory functionality for passive RFID tags,” *IEEE Sensors*, Vol. 13, No. 5, 1824–1834, May 2013.

Non-invasive Antenna Pattern Characterization Using Time-domain and Frequency-domain Measurement Techniques

T. H. Loh, D. A. Humphreys, and P. Miller

National Physical Laboratory, Teddington, Middlesex, United Kingdom

Abstract— We investigated the performance limitations due to time-domain multi-sine stimuli with different Peak-to-Average-Power Ratios (PAPRs) on non-invasive radiation pattern measurements of a broadband antenna over 500 MHz to 4500 MHz and compare these results with frequency domain quasi-CW measurements using a vector network analyser. Both measurements are made in the same environment, an anechoic chamber using an opto-electric field sensor system to minimize distortion of the antenna pattern. The PAPR of the time domain stimulus waveform directly affects the system dynamic range and the uncertainty of the results.

1. INTRODUCTION

The wireless communications landscape is changing as a result of deregulation of additional RF spectrum resources and development of multiple-input-multiple-output (MIMO) systems, driving the need for over-the-air (OTA) testing of complete systems. In an anechoic chamber at the UK National Physical Laboratory (NPL), we have replaced the standard metal coaxial feed by an optical fibre system that has minimal effect on the antenna radiation-pattern [1]. This system is particularly useful for measuring antenna systems where the impact of the RF feed is significant.

The well-established closed-loop, swept-frequency CW testing, using a vector network analyser (VNA), i.e., frequency domain (FD) testing is ideal for passive antenna testing but is not compatible with highly modulated signals in an active system and this will be especially true for MIMO, where multiple simultaneous data-channels are present. We have previously investigated scalar OTA testing of the antenna system radiation pattern where the signal is often modulated, bursty and intermittent [2] but as the phase information is lost these techniques cannot be used for MIMO systems. In time domain (TD) antenna characterizations [3] the frequency content is embedded in the source and received waveforms. Provided the TD measurement system is linear, equivalent results are expected for either TD or FD stimulus. In this paper we will explore the impact of waveform Peak-to-Average-Power-Ratio (PAPR), and noise on time-domain antenna measurement dynamic range using a broadband antenna and compare the results with FD results.

2. TIME-DOMAIN WAVEFORMS

The time-domain waveforms must comprise sufficient frequency components to characterize the antenna and these components are all simultaneously present in the waveform.

2.1. Waveform Design

The relative phase of the frequency components determines the shape of the waveform envelope and hence the PAPR, which is an important consideration for the choice of waveforms because of the voltage limits set by the RF power amplifiers in the system. The waveforms we have used (see Table 1) have a uniform RF amplitude distribution with complex Fourier coefficients, $V(f)$, and corresponding TD waveform $v(t)$, that can be expressed as follows:

$$V(f) = \exp \left[j\pi a^2 \frac{(2f - f_{\max} - f_{\min})^2}{4(f_{\max} - f_{\min})\Delta f} \right] \quad (1)$$

$$v(t) = F^{-1}[V(f)] \quad (2)$$

where $F^{-1}[]$ denotes the inverse-Fourier transform. The parameters f , f_{\max} , f_{\min} , and Δf , are the operating, maximum, minimum, and step frequencies, respectively. By retaining the parabolic phase/frequency relation [4] and altering the coefficient a over the range from $a = 0$ (impulse) to $a = 1$ (Schroeder multi-sine [4]), the PAPR can be varied between two extremes.

2.2. Uncertainty Estimation

If the measurement epoch exceeds twice the waveform period ($2/\Delta f$) then there will be frequencies that do not coincide with comb frequencies and can be used to estimate the noise. Assuming that the noise is not shaped then the rms noise is a good estimate of the uncertainty of the measured response. Assuming that the expected value of these components are zero and they are uncorrelated and are drawn from the same Rayleigh distribution,

$$\langle V_{\text{meas}} \rangle_\infty = 0 \quad (3)$$

then the uncertainty estimate for the voltage uncertainty components in the frequency domain, u_V is

$$u_V = \left(\frac{1}{2N_{\text{freq}}} \sum_{j=0}^{N_{\text{freq}}} |V_{\text{meas}_j}|^2 \right)^{1/2} \quad (4)$$

where N_{freq} is the number of frequencies and V_{meas} , is the noise frequency component of the Fourier transform of the measured time-domain voltage waveform, which is the average of 256 traces.

3. MEASUREMENT DETAILS

All measurements were conducted using the Small-Antenna Radiated Testing (SMART) fully anechoic chamber (FAC) at NPL. This test range contains an automated roll-over-azimuth positioner system, shown in Figure 1(a) and is housed in a screened anechoic room 7.15 m long \times 6.25 m high \times 6.25 m wide, covered with pyramidal absorber [1]. Figure 1 shows the experimental setup in the NPL SMART chamber. All measurements were made to have strong correspondent frequency-domain signals between 500 MHz and 4.5 GHz with 20 MHz frequency resolution. The radiation pattern measurements were made for the Schwarzbeck 9113 biconical antenna using both the TD and FD measurement systems. The measurement setup within the FAC remains unchanged while interchanging the TD and FD equipment.

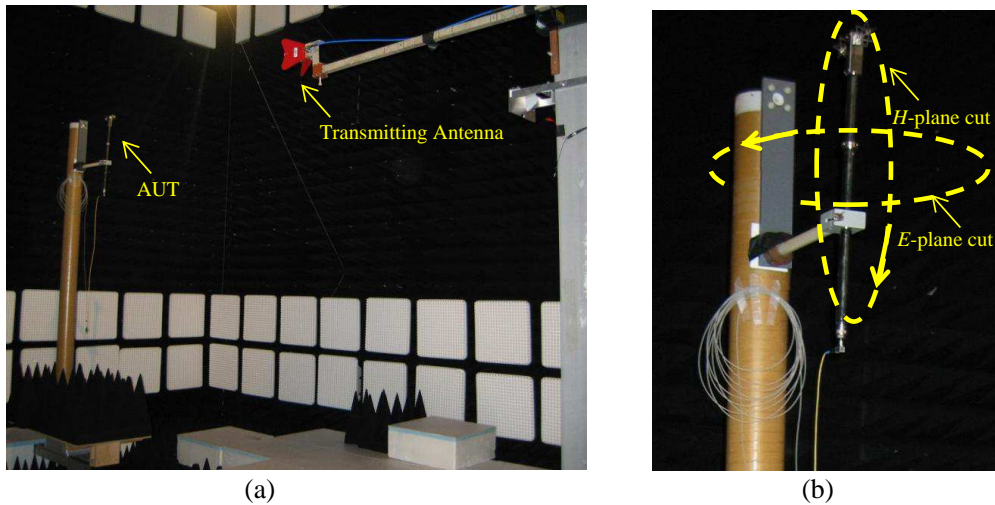


Figure 1: Photographs. (a) The experimental setup in the NPL SMART FAC. (b) Scanning axes.

3.1. Measurement Systems and Instrumentation

Figure 2 shows the physical layout of the measurement system used for both the TD and FD methods. As depicted Figure 2, the Antenna Under Test (AUT) was setup as receiving device connected to an opto-electric field sensor (OEFS) system and oriented with its conical arms point towards the receiving tower so to have minimal effect from the tower. An ETS-Lindgren 3117 double-ridged waveguide horn was used as transmitting antenna and was mounted on a low permittivity polystyrene walkover block. The distance between the source antenna and the DUT was 2 m and the height of the antennas above the top of the walkover foam was 2.53 m. The AUT was placed over the centre of rotation of the positioner. For each set of measurements, the AUT was rotated on the positioner with the pattern acquired at 5° steps.

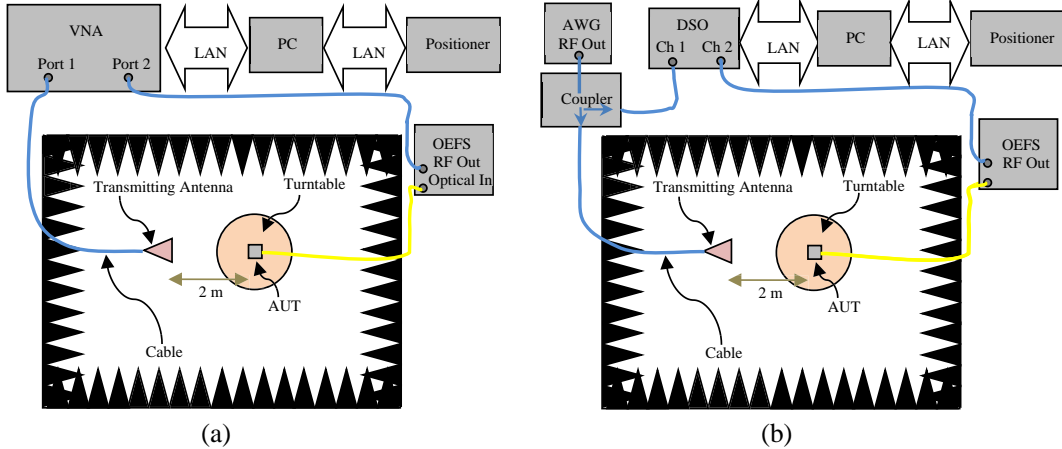


Figure 2: Layout of the measurement system used for: (a) VNA-based FD method; (b) AWG-DSO-based TD method.

The instrumentation for the time-domain measurements is an assembly of general equipment, rather than a single dedicated instrument. The RF source waveforms were directly generated using an Arbitrary Waveform Generator (AWG) with a 12 GSamples/s sample rate and resolution of 8-bits. Additional amplification increased the amplitude to $22V_{p-p}$. A digital sampling oscilloscope (DSO), with a bandwidth of 12.4 GHz, and the OEFS system, with a bandwidth of > 10 GHz, was used as the receiver. A second DSO channel monitored the transmit signals and the remaining two DSO channels provided timebase correction [5].

A two-port VNA was configured at 0 dBm power level and 15 Hz IF-bandwidth and used with the OEFS system to provide the reference frequency-domain measurements of the antenna radiation pattern. No additional amplification was required for this system.

3.2. Stimulus Waveforms

The stimulus waveforms covered the range 500 MHz to 4.5 GHz with an evenly spaced, 20 MHz frequency grid. The parameters for the multi-sine waveforms are given in Table 1.

Table 1: Waveform parameters and PAPR.

Waveform Name	<i>Waveform 1</i>	<i>Waveform 2</i>
Coefficient, a	0.98	0.25
PAPR	1.7	20

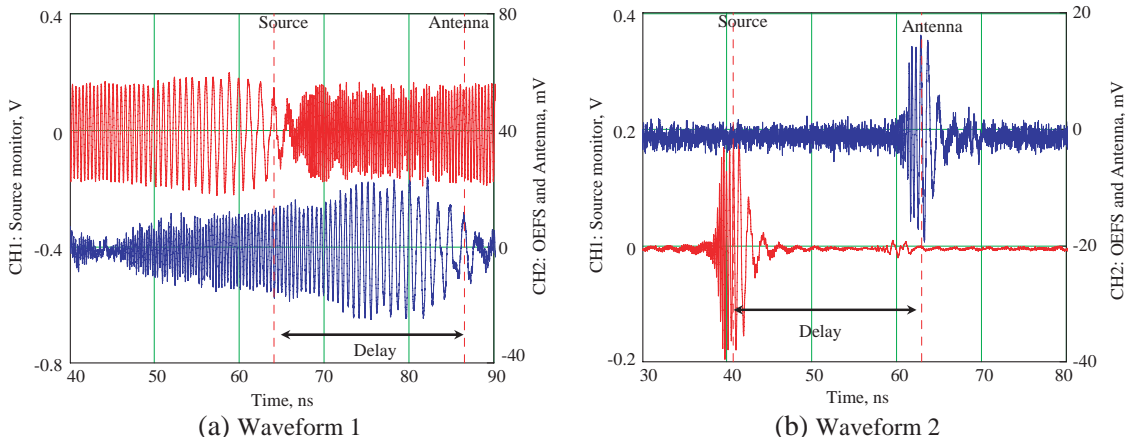


Figure 3: Measured TD results for E -plane cut at $\theta = 90^\circ$ at DSO channels 1 and 2 inputs shown in Figure 2(b) for: (a) *Waveforms 1*; (b) *Waveforms 2*.

4. RADIATION PATTERN OF SCHWARZBECK 9113 BICONICAL ANTENNA

The Schwarzbeck 9113 biconical antenna was measured for both the TD stimulus and validated with the FD measurement. Figure 3 shows, for *Waveforms 1* and *2*, the measured TD results obtained from the DSO for *E*-plane cut at $\theta = 90^\circ$. Figure 4 shows a comparison of the co-polar antenna radiation pattern measurement in the *H*-plane and *E*-plane cut between the FD and the frequency counterpart of the TD stimulus following a Fourier Transform. The results show that the AWG-DSO-based TD *Waveform 1* stimulus agrees very closely with the VNA-based method using a CW signal.

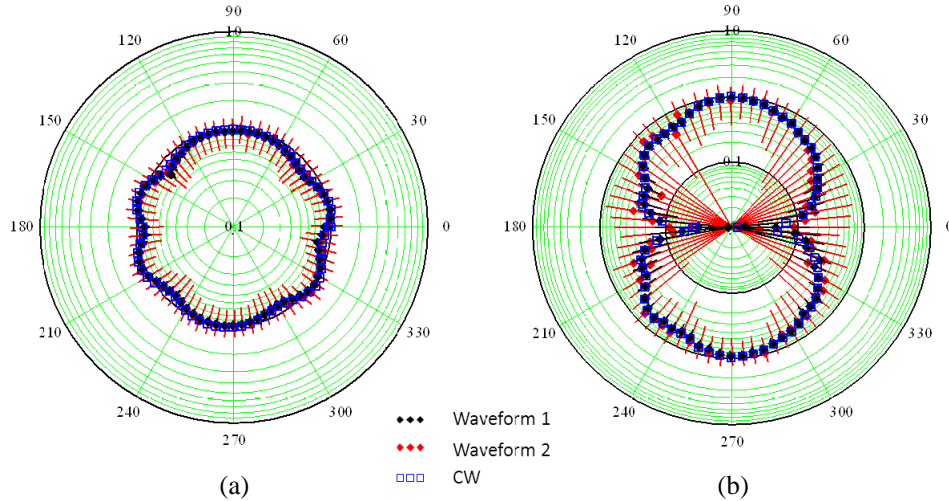


Figure 4: Radiation pattern measurement of Schwarzbeck 9113 biconical antenna normalized to the 90° CW result. Standard uncertainties shown for time-domain results. (a) *H*-plane at 1.2 GHz. (b) *E*-plane at 2.9 GHz.

The two waveforms have average signal to noise ratios of 36 dB (*Waveform 1*) and 21 dB (*Waveform 2*) and the ratio of the PAPR signals is 10.7 dB, which is in broad agreement with the ratio of the transmit signals (11.1 dB). The noise-floor of the *Waveform 2* measurements is 3.3 dB higher than the *Waveform 1* result but the reason for this has not yet been identified.

5. CONCLUSIONS

The results show that the Schroeder multi-sine results (*Waveform 1*) were superior to the high-PAPR stimulus (*Waveform 2*) because of the higher average power. Including a filter to restrict the system bandwidth would improve the noise performance of the DSO receiver by limiting the OEFS noise contribution. This is not an issue for the VNA as the noise is limited by the IF bandwidth. The time-domain (TD) approach can be used to measure modulated waveforms and provide results equivalent to a VNA but have the disadvantage of additional complexity and the choice of TD stimuli will affect measurement accuracy.

ACKNOWLEDGMENT

This work was funded by the National Measurement Office, an Executive Agency of the UK Department for Business, Innovation and Skills.

REFERENCES

1. Loh, T. H., M. Alexander, P. Miller, and A. Betancort, “Interference minimisation of antenna-to-range interface for pattern testing of electrically small antennas,” *4th European Conf. on Antennas and Propagation (EuCAP 2010)*, 1–5, Barcelona, Spain, Apr. 2010.
2. Loh, T. H. and M. Collett, “A rigorous measurement technique for radiation pattern characterisation of embedded wireless communication systems,” *PIERS Proceedings*, 1405–1408, Kuala Lumpur, Malaysia, Mar. 27–30, 2012.
3. Allen, O. E., D. A. Hill, and A. R. Ondrejka, “Time-domain antenna characterizations,” *IEEE Trans. on EMC*, Vol. 35, No. 3, 339–346, Aug. 1993.

4. Schroeder, M. R., "Synthesis of low-peak-factor signals and binary sequences with low auto-correlation," *IEEE Trans. on Information Theory*, Vol. 16, 85–89, Jan. 1970.
5. Humphreys, D. A and F. Bernard, "Compensation of sampling oscilloscope trigger jitter by an in-phase and quadrature referencing technique," *ARMMS Meeting*, Abingdon, Oxfordshire, UK, Apr. 18–19, 2005.

Far Field Gain Estimation Method for Japanese Broadband Antenna Standard Using Time-frequency Analysis

S. Kurokawa, M. Ameya, and M. Hirose

National Institute of Advanced Industrial Science and Technology, Tsukuba, Ibaraki, Japan

Abstract— We are developing a far field gain and antenna factor estimation method for Japanese broadband antenna standards. We have already proposed a method for estimating the free space antenna factor of broadband antennas using a time-domain analysis and a pulse compression technique. However to estimate the antenna factor and gain, we are using fixed antenna distance. In this paper, we propose a new estimation method for determining the antenna distance at each frequency that to estimate the far field antenna gain. Our proposed method is based on the techniques of a time domain analysis and a time-frequency analysis using a short time Fourier transform. In the case of biconical antenna, the difference between far-field gain and the estimated near-field gain using our proposed method is less than 0.05 dB at 10 m antenna distance and less than 0.25 dB at 3 m antenna distance in the frequency range from 30 MHz to 220 MHz.

1. INTRODUCTION

We are developing a far field gain estimation method for Japanese broadband antenna standards, such as biconical antenna [1], log-periodic dipole array antenna (LPDA) [2], LPDA with bow-tie antenna [3]. We have already proposed a method for estimating the free space antenna factor of biconical antenna and LPDA using a time-domain analysis and a pulse compression technique [4, 5]. However to estimate the antenna factor and gain, we are using fixed antenna distance. For this reason, main source of measurement uncertainty of antenna factor and antenna gain is dependence of antenna distance. In order to decrease a measurement uncertainty, we propose a new estimation method for determining the antenna distance at each frequency that to estimate the far field antenna gain. Our proposed method is based on the techniques of a time domain analysis and a time-frequency analysis using a short time Fourier transform for biconical antenna. This method can be determined the antenna distance at each frequency. In this paper, our proposed method is first explained. Next, difference between the far field gain and the estimated gain is explained.

2. OUTLINE OF ANTENNA DISTANCE DETERMINATION METHOD USING TIME FREQUENCY ANALYSIS

2.1. Friis Transmission Formula and near Field Gain of Broadband Antenna

In order to determine the antenna distance at each frequency for estimating the far field antenna gain of a biconical antenna at near antenna distance, two antenna are set face to face and same polarization in antenna distance $z = D$ m. In this case, frequency domain receiving signal $S_{21}(\omega, z)$ is shown Equation (1) using the Friis transmission formula [6] as

$$|S_{21}(\omega, z)|^2 = M_1 M_2 \left(\frac{\lambda}{4\pi z} \right)^2 G_{\text{NF1}}(\omega, z) \cdot G_{\text{NF2}}(\omega, z) \quad (1)$$

where $G_{\text{NF1}}(\omega, z)$ and $G_{\text{NF2}}(\omega, z)$ are the near field antenna gains of the transmitting and receiving antennas, respectively. ω is the frequency, λ is the wave length, $M_i = (1 - |\Gamma_i(\omega, z)|^2)$, ($i = 1, 2$) is an antenna miss much loss. In the case of using method of moment for estimating the frequency response $S_{21}(\omega, z)$, transmitting antenna and receiving antenna assume the same antennas. In this case, we can assume $G_{\text{NF1}}(\omega, z) = G_{\text{NF2}}(\omega, z) = G_{\text{NF}}(\omega, z)$, $\Gamma_1(\omega, z) = \Gamma_2(\omega, z) = \Gamma(\omega, z)$. Then, the near field antenna gain can be obtained by the following equation,

$$G_{\text{NF}}(\omega, z) = \frac{4\pi z}{\lambda} |S_{21}(\omega, z)| \cdot \left(1 - |\Gamma(\omega, z)|^2 \right)^{-1} \quad (2)$$

In this paper, our estimating biconical antenna is BBA9106 of Schwarzbeck Mess-Elektronik Inc.

2.2. Antenna Distance Determination Using Time-frequency Analysis

Antenna distance of transmitting and receiving antenna set $z = 1 \text{ m}, 2 \text{ m}, 3 \text{ m}, 4 \text{ m}, 5 \text{ m}, 10 \text{ m}, 20 \text{ m}$. First, the frequency response $S_{21}(\omega, z)$ is calculated by FEKO [7]. Then, the time-domain $S_{21}(t, z)$ is calculated by the inverse Fourier transform with a Hamming window [8] $H(\omega)$ as

$$S_{21}(t, z) = F^{-1} \{ S_{21}(\omega, z) \cdot H(\omega) \} \quad (3)$$

Figures 1 and 2 show calculated frequency domain $S_{21}(\omega, z)$ and time domain $S_{21}(t, z)$, respectively.

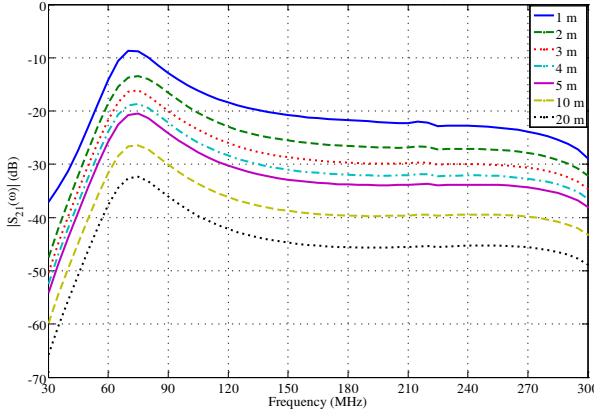


Figure 1: $S_{21}(\omega, z)$ calculation results.

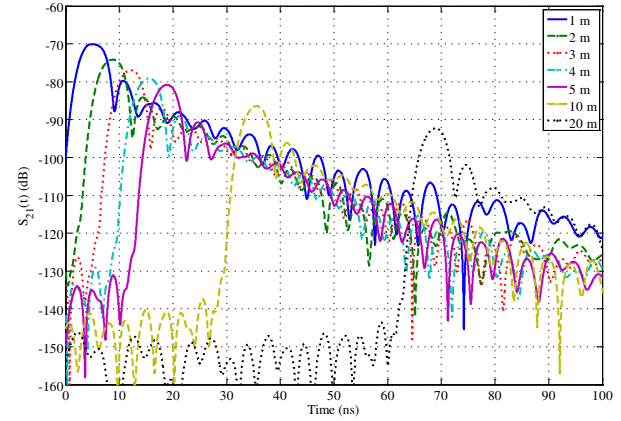


Figure 2: $S_{21}(t, z)$ calculation results.

In order to determine the antenna distance at each frequency, we calculate time-frequency response of $S_{21}(t, z)$ using the short time Fourier transform (STFT) with hamming type time window. The time domain hamming window width is $w = 128, 700$, Number of Fourier transform is 8196. Figures 3 and 4 show the calculated time-frequency analysis of $z = 3 \text{ m}$ and 10 m for the case of $w = 128$, respectively. In the case of frequency range from 30 MHz to 220 MHz, traveling time of peak level is increased as a frequency range increase. Figures 5 and 6 show the estimated difference length $d_{\text{STFT}}(\omega)$ from the incident point to the peak point of each frequency for the case of $w = 128$ and $w = 700$, respectively. Figure 7 shows the estimated ideal deference length $d_{\text{ideal}}(\omega)$ from the incident point to the peak point of each frequency that estimated by

$$z = \frac{\lambda}{4\pi} |S_{21}(\omega, z)|^{-1} \cdot \left(1 - |\Gamma(\omega, z)|^2\right) \cdot G_{\text{far}}(\omega) \quad (4)$$

where, $G_{\text{far}}(\omega)$ and $\Gamma(\omega, z)$ is far field gain and reflection coefficient of biconical antenna, respectively.

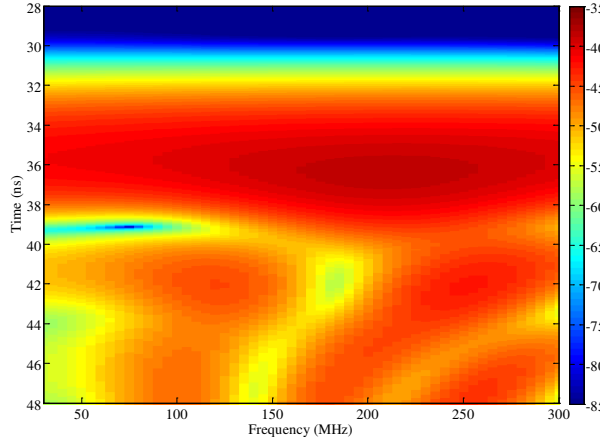


Figure 3: Short time Fourier transform results at $z = 3 \text{ m}$.

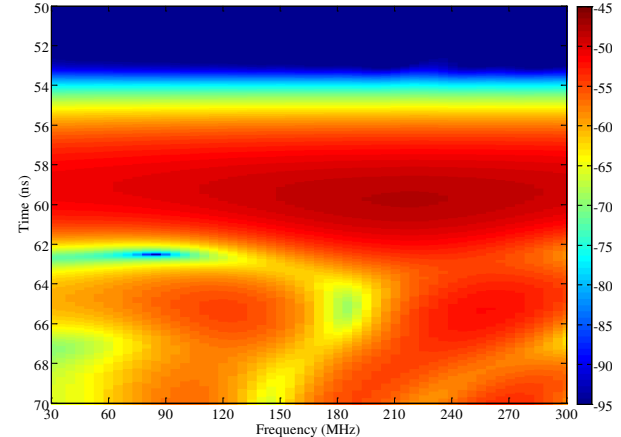


Figure 4: Short time Fourier transform results at $z = 10 \text{ m}$.

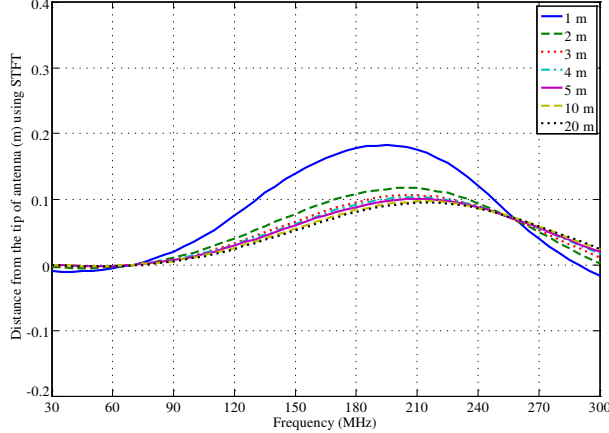


Figure 5: Estimated $d_{\text{STFT}}(\omega)$ using STFT results ($w = 128$).

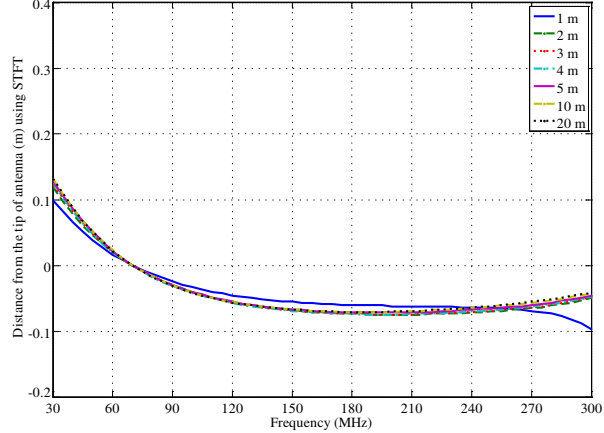


Figure 6: Estimated $d_{\text{STFT}}(\omega)$ using STFT results ($w = 700$).

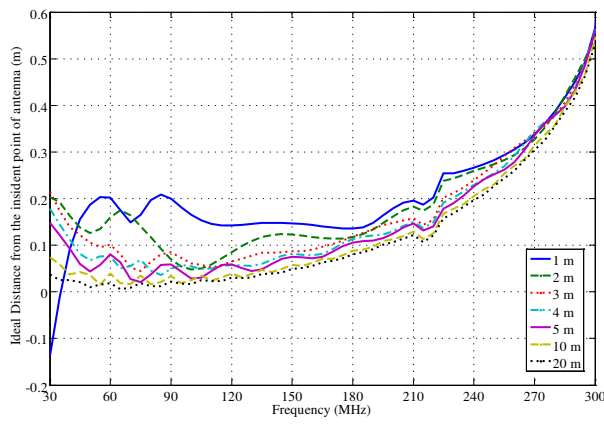


Figure 7: Estimated results of $d(\omega)$ using Equation (4).

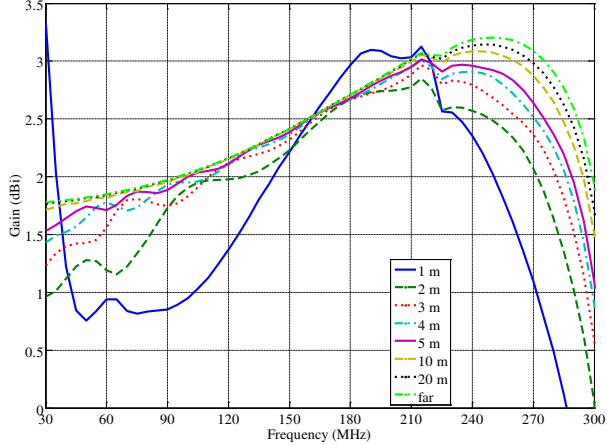


Figure 8: Estimated antenna gain using $d_{\text{STFT}}(\omega, z)$ ($w = 128$).

We compare the ideal antenna distance with estimated antenna distance. In the frequency range below 70 MHz, estimated antenna distance of $w = 700$ has good agreement of ideal antenna distance at antenna distance more than $z = 3$ m. In the frequency range from 70 MHz to 220 MHz, estimated antenna distance of $w = 700$ has good agreement of ideal antenna distance at antenna distance more than $z = 3$ m.

3. ANTENNA GAIN ESTIMATION

We estimate the antenna gain from the estimated antenna distance using Equation (2). Further, we show another far field antenna gain estimation method that uses antenna phase center location as Equation (5) [9, 10]

$$|S_{21}(\omega, z)|^2 = (1 - |\Gamma_1(\omega)|)(1 - |\Gamma_2(\omega)|) \left(\frac{\lambda}{4\pi(z + d_1(\omega) + d_2(\omega))} \right)^2 G_{\text{far1}}(\omega) \cdot G_{\text{far2}}(\omega) \quad (5)$$

where $G_{\text{far1}}(\omega, z)$ and $G_{\text{far2}}(\omega, z)$ are the far field antenna gains of the transmitting and receiving antennas, respectively. $d_1(\omega)$ and $d_2(\omega)$ are the distance from the incident point to the phase center of the transmitting and receiving antennas, respectively. In the case of the transmitting antenna and the receiving antenna assume the same antennas, we can assume $G_{\text{far1}}(\omega) = G_{\text{far2}}(\omega) = G_{\text{far}}(\omega)$, $\Gamma_1(\omega) = \Gamma_2(\omega) = \Gamma(\omega)$. Then, the far field antenna gain can be obtained by the following equation,

$$G_{\text{far}}(\omega) = \frac{4\pi(z_1 - z_2)}{\lambda} \left(1 - |\Gamma(\omega)|^2 \right)^{-1} \frac{|S_{21}(\omega, z_1)| |S_{21}(\omega, z_2)|}{|S_{21}(\omega, z_2)| - |S_{21}(\omega, z_1)|} \quad (6)$$

Figure 8 shows the estimated antenna gain for the case of $w = 128$ and far field gain. Figures 9 and 10 show the difference between the far field gain and estimated antenna gain using our proposed method for the case of $w = 128$ and $w = 700$, respectively. In the frequency range below 70 MHz, difference of antenna gain of $w = 700$ is less than 0.25 dB at antenna distance more than $z = 3$ m. In the frequency range from 70 MHz to 220 MHz, difference of antenna gain of $w = 128$ is less than 0.25 dB at antenna distance more than $z = 3$ m. estimated antenna distance of $w = 700$ has good agreement of ideal antenna distance at antenna distance more than $z = 3$ m. Figure 11 shows the difference between the far field antenna gain and estimated antenna gain using phase center location. In the frequency range from 100 MHz to 300 MHz, difference of antenna gain is less than 0.2 dB using $S_{21}(\omega)$ of $z = 3$ m and 4 m. These results show the fact that our proposed method can be estimate the antenna gain less than 0.25 dB difference from the far field gain in the frequency range from 30 MHz to 220 MHz at $z = 3$ m.

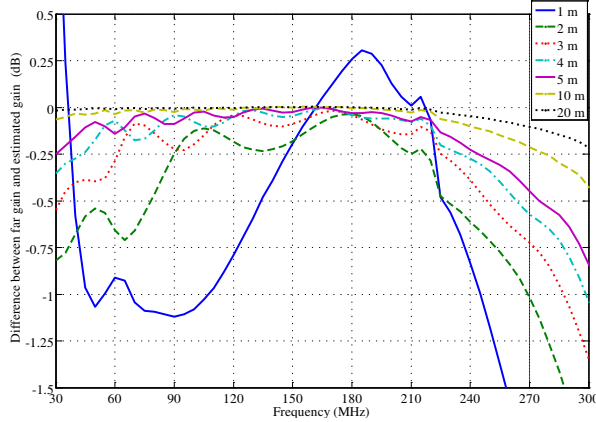


Figure 9: Difference between far field gain and estimated gain using $d_{\text{STFT}}(\omega)$ ($w = 128$).

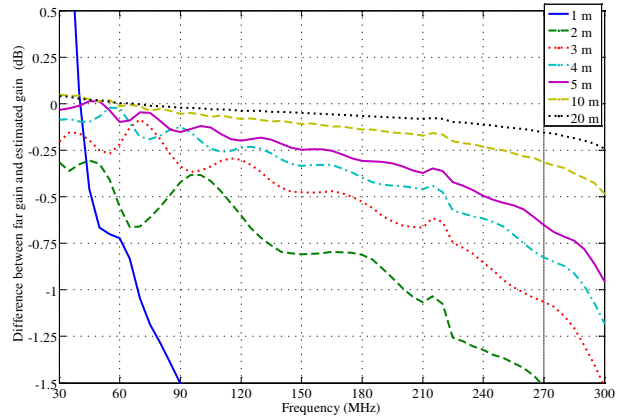


Figure 10: Difference between far field gain and estimated gain using $d_{\text{STFT}}(\omega)$ ($w = 700$).

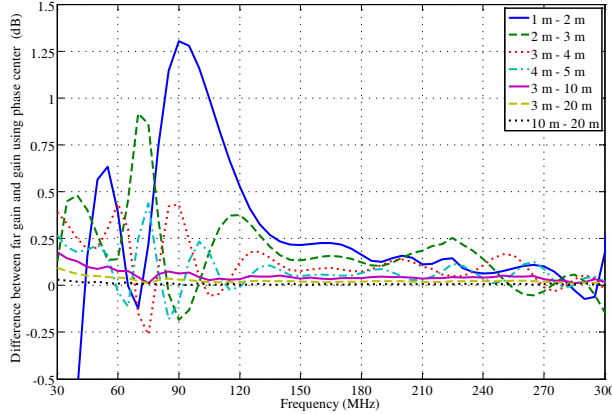


Figure 11: Difference between far gain and estimated gain using the phase center.

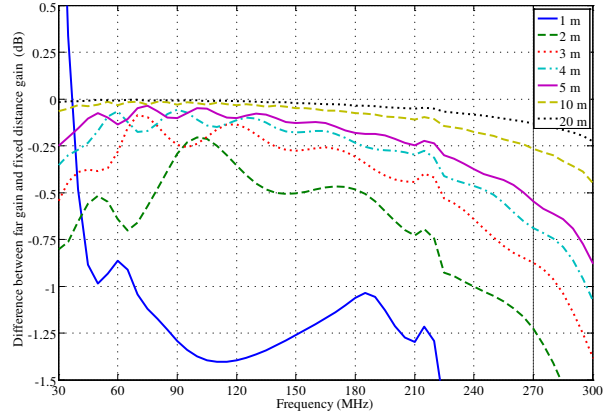


Figure 12: Difference between far gain and estimated gain from the fixed antenna physical distance.

4. CONCLUSION

We propose a new method for estimating an antenna gain of biconical antenna. The method combines the time domain analysis and time-frequency analysis to obtain the antenna distance at each frequency. The estimated antenna gain by our proposed method has good agreement with far field gain, that is less than 0.25 dB difference in the frequency range from 30 MHz to 220 MHz at 3 m antenna distance. And, the estimated antenna gain by using phase center equation is comparable has good agreement with far field gain, that is less than 0.2 dB difference in the frequency range from 100 MHz to 300 MHz using the $S_{21}(\omega)$ s of 3 m and 4 m antenna distance.

REFERENCES

1. Biconical Antenna BBA9106+VHA9103B, Schwarzbeck-Mess Elektronik OHG, <http://www.schwarzbeck.de/Datenblatt/91039106.pdf>.
2. Logarithmic Periodic Broadband Antennas UHALP9108A, Schwarzbeck-Mess Elektronik OHG, <http://www.schwarzbeck.de/Datenblatt/k9108a1.pdf>.
3. CBL6111C classic Bilog antenna 30 MHz–1 GHz, Teseq Inc.
4. Kurokawa, S., M. Hirose, and K. Komiyama, “Measurement and uncertainty analysis of free-space antenna factors of a log-periodic antenna using time-domain techniques,” *IEEE Trans. Instrum. Meas.*, Vol. 58, No. 4, 1120–1125, 2009.
5. Kurokawa, S., M. Ameya, and M. Hirose, “Time-domain three antenna method for biconical antenna,” *Proc. CPEM2010*, 2010.
6. Collin, R. E., *Antennas and Radiowave Propagation*, 303–304, McGraw-Hill, 1985.
7. FEKO, EM Software & Systems-S.A. (Pty) Ltd., <http://www.feko.info/>.
8. Oppenheim, A. V. and R. W. Schafer, *Discrete-time Signal Processing*, 713–718, Prentice-Hall, Englewood Cliffs, NJ, 1989.
9. Harima, K., “Accurate gain determination of LPDA by considering the phase center,” *IEICE Electronics Express*, Vol. 7, No. 23, 1760–1765, Oct. 2010.
10. Hirose, M., S. Kurokawa, and M. Ameya, “Theoretical investigation on relationship between near-field gain and far-field gain using phase center,” *Technical Report of IEICE, AMT2012-02*, Jun. 2012 (in Japanese).

Extended *S*-parameter Method for Radiation Characteristics and Mutual Coupling of Multiport Antennas

T. Yanagi, T. Fukasawa, and H. Miyashita

Mitsubishi Electric Corporation, Japan

Abstract— When a coaxial cable is connected to an antenna, unbalanced current may be induced on the outside of the cable and causes a measurement error. This error becomes large in the case that an antenna and a ground plane are small. Therefore, it is important for antenna measurement to eliminate influence of coaxial cables connected to antennas. The *S*-parameter method is known as one of the methods to reduce influence of coaxial cables for measurement of a balanced antenna impedance. This method is useful and widely used to measure the impedance characteristics of many kinds of antennas because it does not require any special equipment for measurement except two cables. However, it has been applied for measurements of impedance and radiation pattern of only one antenna element. In this paper, an extended *S*-parameter method (ESPM) for accurate measurements of reflection, mutual coupling and radiation characteristics of multiport antennas that can reduce the influence of the coaxial cables is proposed. First, the ESPM for multiport antennas is formulated. Two coaxial cables are connected to each antenna in this method. Impedance and mutual coupling characteristics with reducing influence of the coaxial cables are obtained by synthesizing measured *S*-parameters under the condition that unbalanced currents on the outside of the coaxial cables are canceled. Radiation pattern with reduced unbalanced currents can be calculated from array patterns with excitation coefficients derived by the measured *S*-parameters. Next, we apply the proposed method to two close-positioned monopole antennas mounted on a small ground plane and demonstrate the validity and effectiveness of the proposed method by measurement. It is shown that accurate measurement results can be obtained using the proposed method.

1. INTRODUCTION

A vector network analyzer is usually used for measurements of antenna characteristics. If a coaxial cable is connected to a small antenna, unbalanced current will be induced on the outside conductor of the coaxial cable and causes a measurement error. As a result, it may not be possible to measure the original antenna characteristics. In order to reduce the unbalanced current, ferrite chokes and balun chokes are often used. However, power absorption due to ferrite chokes causes error in reflection and transmission characteristics. Additionally, the operation frequency range of a balun is limited in principle because the effect of current reduction depends on a resonance of a quarter-wavelength. Another way to eliminate influence of coaxial cables is using fiber optics [1]. However, it was reported that impedance is altered by the influences of the optical/electric (o/e) converter mounted on the ground plane when the size of the antenna or the ground plane is much smaller than a wavelength. The *S*-parameter method [2] is known to be one way to reduce the influence of an unbalanced current. Although the *S*-parameter method is an effective and useful method, it has only been applied for impedance measurements.

In this paper, an extended *S*-parameter method (ESPM) for accurate measurements of reflection, mutual coupling and radiation characteristics is proposed. First, the formulation of the proposed method is shown. Further, the effectiveness of the proposed method is experimentally confirmed.

2. EXTENDED *S*-PARAMETER METHOD FOR MULTIPORT MEASUREMENT

2.1. Impedance and Mutual Coupling

Consider a case in which small n -element antennas are mounted on a small ground plane. Fig. 1 shows the measurement model for the *S*-parameter method at k -th antenna element ($k = 1, 2, \dots, n$). In this case, the n -element antenna system is expressed as $2n$ -port network. The incident waves at Port: $2k - 1$ and Port: $2k$ are defined as a_{2k-1} and a_{2k} , and the reflected waves at Port: $2k - 1$ and Port: $2k$ are defined as b_{2k-1} and b_{2k} ($k = 1, 2, \dots, n$), respectively. The incident waves, reflected waves, and *S*-parameters can be related as follows.

$$\mathbf{B} = \mathbf{S}\mathbf{A} \quad (1)$$

S is the scattering matrix, **A** is a column vector in which the element is the incident wave at each port, and **B** is a column vector in which the element is the reflected wave at each port.

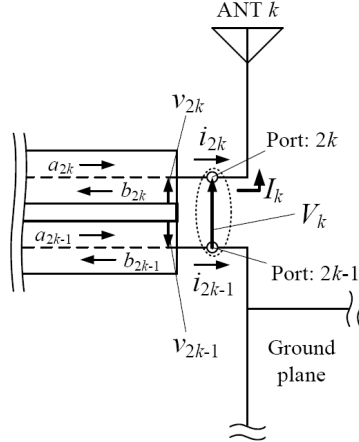


Figure 1: Measurement model for S -parameter method.

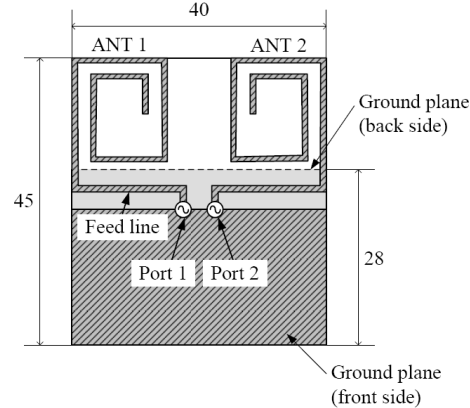


Figure 2: The measurement model for S -parameter between two antennas.

The current on the inner conductor of the cable connected to Port: l is defined as i_l . The condition in which the currents on the outside of two cables cancel each other is expressed below.

$$i_{2k-1} = -i_{2k} \quad (2)$$

If the characteristic impedance is normalized to 1, this condition is rewritten as follows.

$$a_{2k-1} + a_{2k} - b_{2k-1} - b_{2k} = 0 \quad (3)$$

When the m -th antenna is measured, the other ports have to be reflection-free termination. Therefore, the incident wave at the measurement port of antenna k , A_k , must satisfy the following equation.

$$A_k = (V_k + I_k)/2 = 0 \quad (k \neq m) \quad (4)$$

From Equation (4), we obtain

$$-a_{2k-1} + 2a_{2k} - b_{2k-1} = 0 \quad (k \neq m). \quad (5)$$

As mentioned above, $4n - 1$ equations are defined from Equations (1), (3) and (5). Because the number of unknowns is $4n$ ($a_1, \dots, a_{2n}, b_1, \dots, b_{2n}$), we can solve the system of equations by normalizing other unknowns using one certain unknown. Here, we choose a_{2m-1} as the unknown to normalize and represent the normalized unknowns using the symbol “ \hat{a} ”. In this case, Equations (1), (3) and (5) are rewritten as following equations.

$$\sum_{j=1}^{2n} (1 - \delta_{2m-1,j}) S_{i,j} \hat{a}_j - \hat{b}_i = -S_{i,2m-1} \quad (6)$$

$$\hat{a}_{2k} - \hat{b}_{2k-1} - \hat{b}_{2k} = -1 \quad (7)$$

$$\hat{a}_{2k-1} + \hat{a}_{2k} - \hat{b}_{2k-1} - \hat{b}_{2k} = 0 \quad (8)$$

$$-\hat{a}_{2k-1} + 2\hat{a}_{2k} - \hat{b}_{2k-1} = 0 \quad (9)$$

the reflection coefficient at Port: m , $S_{m,m}$, and the transmission coefficient from Port: m to Port: k , $S_{k,m}$, are provided by the following equations.

$$S_{m,m} = \frac{-1 - \hat{b}_{2m-1} + 2\hat{b}_{2m}}{-1 + 2\hat{a}_{2m} - \hat{b}_{2m-1}} \quad (m = 1, 2, \dots, n) \quad (10)$$

$$S_{k,m} = \frac{-\hat{a}_{2k-1} - \hat{b}_{2k-1} + 2\hat{b}_{2k}}{-1 + 2\hat{a}_{2m} - \hat{b}_{2m-1}} \quad (k \neq m) \quad (11)$$

2.2. Radiation Pattern

If the antenna except ANT m (under the test) is terminated, we obtain the following equations from Equation (1).

$$\begin{aligned} b_{2m-1} &= S_{2m-1,2m-1}a_{2m-1} + S_{2m-1,2m}a_{2m} \\ b_{2m} &= S_{2m,2m-1}a_{2m-1} + S_{2m,2m}a_{2m} \end{aligned} \quad (12)$$

Eliminating b_{2m-1} and b_{2m} from Equation (12) by using Equation (3), the following equation can be obtained.

$$\alpha = \frac{a_{2m}}{a_{2m-1}} = \frac{1 - S_{2m-1,2m-1} - S_{2m,2m-1}}{1 - S_{2m,2m} - S_{2m-1,2m}} \quad (13)$$

Equation (13) means that two ports, i.e., Port: $2m - 1$ and Port: $2m$, are excited by a_{2m-1} and αa_{2m-1} . During actual measurements, it is difficult to excite both ports with an arbitrary amplitude and phase. The offline synthesis of array-element patterns for each port is a useful and practical method. E_{2m-1} and E_{2m} are defined as array-element patterns for Port: $2m - 1$ and Port: $2m$, respectively, and a synthesized array pattern E_t can be obtained as follows.

$$E_t = E_{2m-1} + \alpha E_{2m} \quad (14)$$

From (14), we obtain the radiation pattern with a cancelled current on the outside of the coaxial cables.

2.3. Actual Gain

When two ports are excited by a_{2m-1} and αa_{2m-1} , the reflected waves b_{2m-1} and b_{2m} can be described as follows.

$$\begin{aligned} b_{2m-1} &= (S_{2m-1,2m-1} + S_{2m-1,2m}\alpha)a_{2m-1} \equiv \beta a_{2m-1} \\ b_{2m} &= (S_{2m,2m-1} + S_{2m,2m}\alpha)a_{2m-1} \equiv \gamma a_{2m-1} \end{aligned} \quad (15)$$

To subtract the reflected power from the incident power for both ports results in the total incident power, P_{in} .

$$P_{in} = |a_{2m-1}|^2 + |a_{2m}|^2 - |b_{2m-1}|^2 - |b_{2m}|^2 = |a_{2m-1}|^2 (1 + |\alpha|^2 - |\beta|^2 - |\gamma|^2) \quad (16)$$

If a standard gain antenna with a gain of G_d is connected to Port: $2m - 1$, the input power to the antenna, P_{ind} , becomes $P_{ind} = |a_{2m-1}|^2$. If E_d is the observed level for the standard gain antenna, the absolute gain of the antenna under the test, G_a , can be expressed as follows.

$$G_a = \frac{|E_t|^2}{P_{in}} / \frac{|E_d|^2}{G_d P_{ind}} = G_d \frac{|E_t|^2}{|E_d|^2 (1 + |\alpha|^2 - |\beta|^2 - |\gamma|^2)} \quad (17)$$

Because the gain calculated by Equation (17) is normalized by the actual power supplied to the antenna during the test, mismatch loss is not taken into account. G_a divided by the mismatch loss M (positive in dB expression) results in an actual gain G_{act} , which can be expressed as follows,

$$G_{act} = \frac{G_a}{M} = G_a \left(1 - \left| \frac{Z_m - Z_0}{Z_m + Z_0} \right|^2 \right) \quad (18)$$

where Z_m is the input impedance of ANT m and Z_0 is the characteristic impedance.

3. MEASUREMENT RESULTS

3.1. Impedance and Mutual Coupling

Measured impedance characteristics (S_{11}) and mutual coupling (S_{21}) for the model of Fig. 2 are shown in Fig. 3. The measured frequency range is from 700 MHz to 900 MHz. For comparison, the measurement results obtained using the proposed method and those obtained using the conventional method (connect coaxial cable directly) are shown in the same figure. Concerning the reflection characteristics, it turns out that resonance frequency is drastically shifted from near 800 MHz to the low frequency using the conventional method, and a correct measurement has not been performed. Meanwhile, the results using the proposed method are in good agreement with the calculated results, and measurement accuracy of both of amplitude and phase is improved.

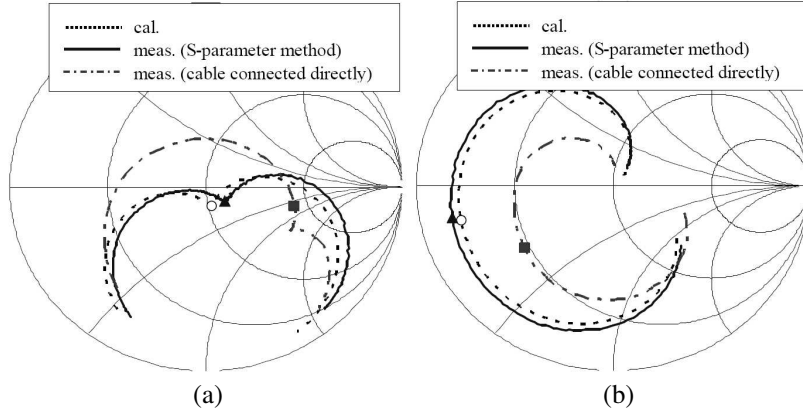


Figure 3: Measurement results of S -parameter between two antennas. (a) S_{11} , (b) S_{21} .

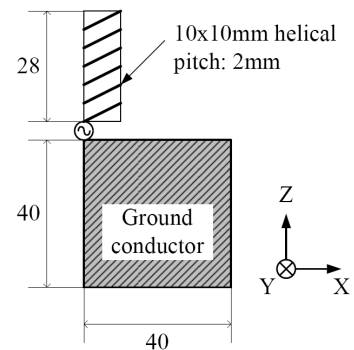


Figure 4: The measurement model for radiation pattern.

3.2. Radiation Characteristics

The measured radiation pattern for the model of Fig. 4 is shown in Fig. 5. The patterns are normalized by the peak value in the z - x plane. The result obtained using the proposed method provides close agreement with the calculated result. On the other hand, the results of the conventional method are influenced by the cable connected to the antenna, and the degree of coincidence is lower than that of the proposed method. Fig. 6 shows the frequency characteristics of the average of actual gain in the z - x plane. The frequency is normalized by the resonant frequency. For reference, the result obtained using the measurement system of fiber optics [1] is shown in Fig. 6. An o/e converter required for measurement by fiber optics is put in a small metal case on the ground plane. Because the resonant frequency is shifted due to the influence of the metal case, the input impedance of the antenna is tuned by adjustment of the antenna length and matching circuit. Both results shown in Fig. 6 are in good agreement and the validity of the results obtained using the proposed method is confirmed.

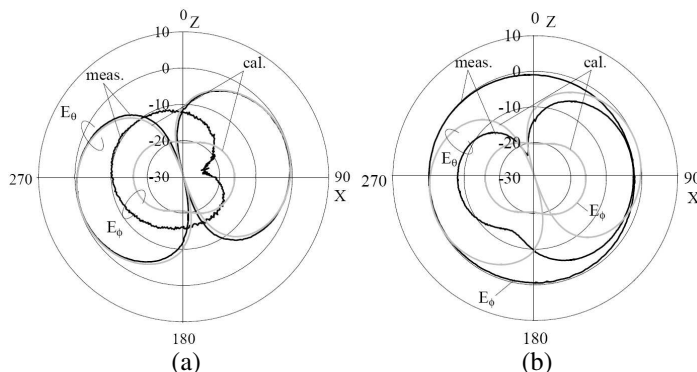


Figure 5: Measurement results of radiation pattern. (a) S -parameter method, (b) cable connected directly.

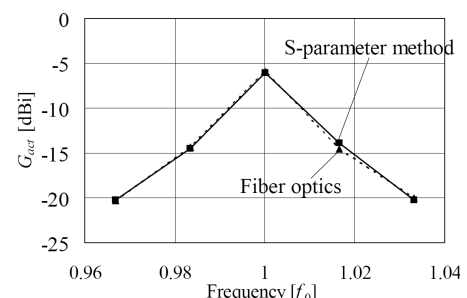


Figure 6: Measurement results for antenna gain.

4. CONCLUSION

The accurate measurement method by applying S -parameter method to reflection, mutual coupling and radiation characteristics has been proposed. The validity and effectiveness have been confirmed experimentally.

REFERENCES

1. Fukasawa, T., K. Shimomura, and M. Otsuka, "Accurate measurement method for characteristics of an antenna on a portable telephone," *IEICE Trans. on Commun. (JPN Edition)*, Vol. J86-B, No. 9, 1895–1905, Sep. 2003 (in Japanese).
2. Meys, R. and F. Janssens, "Measuring the impedance of balanced antennas by an S -parameter method," *IEEE Antennas Propagat. Mag.*, Vol. 40, No. 6, 62–65, 1998.

Path Loss Characteristics in a Civil Laboratory Building at a Frequency of 2.4 GHz

Supachai Phaiboon¹ and Adchara Kampan²

¹Electrical Engineering Department, Faculty of Engineering

Mahidol University, Salaya, Nakhon Pathom 73170, Thailand

²Technology of Information System Management, Faculty of Engineering

Mahidol University, Salaya, Nakhon Pathom 73170, Thailand

Abstract— This paper presents indoor radio wave propagation characteristics of a large laboratory at a frequency of 2.4 GHz. We performed path loss measurements in two categories namely LOS, NLOS same room and LOS, NLOS different rooms. These categories provide different path loss characteristics in each environment. The measured data was fixed with linear regression in order to provide path loss exponents, n and wall attenuation factor (WAF). From the results, it is found that the path loss exponent is still less than 2 for only LOS and about 2.24 for LOS and NLOS in the same room. Additionally, the $WAFs$ for the metal grid wall and the solid wall are 5.5 dB and 21.53 dB respectively.

1. INTRODUCTION

Indoor path loss model has been an active area of research in recent years. Various measurement campaigns have been executed to determine propagation characteristics of electromagnetic waves in office and also factory buildings. These measurements resulted in propagation models which support the coverage prediction of wireless networks operating in these environments. For laboratory applications, monitoring and control of testing between machine lab and quality control centers requires wireless connection in order to save cost and time consuming comparing with cable connection. While wireless communication between two pieces of machinery is needed for rerouting when production lines are often changed, improved, or moved. On the other hand, energy management centers need to incorporate wireless network in their energy conservation processes.

2. PATH LOSS MODELS

Indoor path loss is a function of distance to the power n as below:

$$PL(d) = PL(d_0) + 10n \log_{10} \left(\frac{d}{d_0} \right) \quad (1)$$

where PL is the path loss approximation at distance d from the transmitter, and $PL(d_0)$ is the path loss at the reference distance, d_0 from the transmitter. The value of n depends on the surroundings and building structure. Because of walls between the transmitter and the receiver, propagation loss as a function of distance and wall attenuation can be calculated as follows:

$$PL(d) = PL(d_0) + 10n \log_{10} \left(\frac{d}{d_0} \right) + \sum_{i=1}^k WAF_i \quad (2)$$

where WAF_i is wall attenuation factors of i th wall in dB which depend on their structure and material.

3. MEASUREMENT PROCEDURE

3.1. Description of the Civil Laboratory Buildings

The laboratory building is in the faculty of engineering, Mahidol university. Figure 1 shows the photo of the building with ceiling height of 12 m. There are three areas in the same roof which are separated by walls. The first area with a dimension of 40×32 m is a typical laboratory building of civil engineering where is in Bay 3 and Bay 4. This area consists of a large open space surrounding with machinery laboratory and small rooms with aluminium and glass walls. The main structure consists of concrete walls and cement floors.

The second area with dimension of 18×32 m is a typical retail store namely Bay 2. This area is surrounded by metal racks, metal rolls, wooden sheets and machineries. This area consists of metal



Figure 1: A photo of the civil laboratory with metal grid wall and the solid wall (isowall).



Figure 2: The equipment apparatus.

grid wall located at the entrance of the area and isowall walls located at the entrance to the retail store and office building. The third area with a dimension of 22×32 m is a typical retail store and office building namely Bay 1. This area consists of a large open space with storage and cleaning rooms. All walls in this area are made of isowall.

3.2. Measurement Apparatus and Method

Propagation experiments in civil laboratory environment were carried out with measurement apparatus as shown in Figure 2, consists of a transmitter and a receiver parts. The transmitter part consists of a transmitting antenna (Tx) and a signal generator. As the Tx, omnidirectional vertically polarized antenna quarter wavelength dipole with ground plane was used. The Tx is mounted on a telescopic mast at a height of 3.0 m above the floor in factory building. A Hewlett-Packard 83732B synthesized signal generator with a 30 dB low noise amplifying (LNA) was used to inject a continuous wave signal with constant power of about 18 dBm into the Tx antenna. The transmitter was placed at a fixed location in the measurement environment. The receiver part consists of a receiving antenna (Rx) mounted on a wooden mast at a height of about 1.71 m above the floor for all measurements. As the Rx, an omnidirectional antenna of the same type as the Tx was connected to a Hewlett-Packard 83732B spectrum analyzer which showed the received power level at the transmitting frequency. The receiver unit was moved to the measurement points as shown by circular dots in Figure 1. For each measurement point, at least 36 samples were taken over 40 wavelengths and averaged to the local average power. Therefore the distance between two adjacent samples was 0.8λ in order to fulfill Lee's criteria [5].

4. PATH LOSS CHARACTERISTIC RESULTS

The path-loss samples at 2400 MHz are discussed in two different categories as follows.

4.1. LOS and NLOS in Same Room

Path loss for LOS was shown in Figure 3(a). From the figure, the path loss exponent is about 1.9 ($7.6032 \times 2.5/10$). This is because of the wave guiding effect from the roof and the machineries. In order to obtain overall characteristics of radio waves, the measured path losses in the same room (Bay 3 and 4) were classified equally into 11 LOS and NLOS points and distributed over measurement distance. Figure 3(b) shows graph of path loss and distance for LOS and NLOS. The results show that path loss characteristic provides mixed properties between LOS and NLOS. In this case, the path loss exponent is increased about 2.24 ($8.9422 \times 2.5/10$).

4.2. LOS and NLOS in Different Rooms

Radio waves propagate into different room via two different walls, a metal grid wall and a solid wall in Bay 2 and 1 respectively as shown in Figure 1. These make received signal strength decrease because of wall attenuation factor (*WAF*). Two categories are considered, NLOS via the metal grid wall and NLOS via the two different walls. It is found that the wall attenuation factors are 5.5 dB and 21.53 dB for the metal grid wall (*WAF1*) and the solid wall (*WAF2*) respectively as shown in Figure 4. Note that y-intercept value of 40.004 is fixed for convenient calculation.

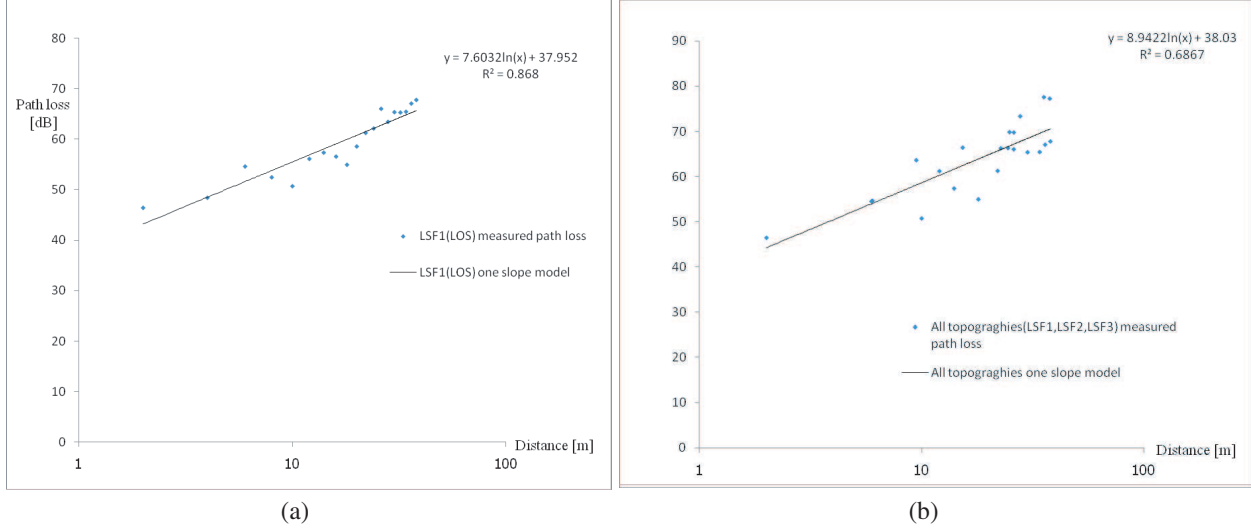


Figure 3: (a) LOS and (b) LOS + NLOS path loss in function of distance.

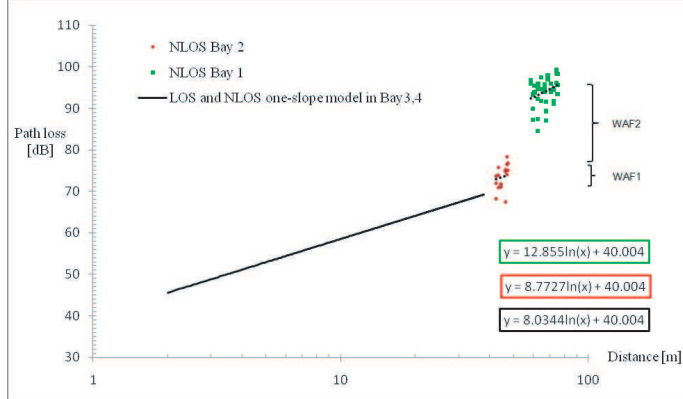


Figure 4: LOS and NLOS path loss and distance in all Bays.

5. CONCLUSION

This paper presented results of path loss characteristics experiments performed in a civil laboratory at a frequency of 2.4 GHz. The measurements were conducted at several locations in the plant both in the same room and different room.

The path loss exponent n for LOS is found to be less than 2, it results from the waveguide effect of the metal machine and roof. While the NLOS path loss exponent, n is found to be 2.10 to 2.52. Also, the transmitting height is not significant to path loss exponent.

Additionally, the wall attenuation factor (WAF) for the metal grid wall and the solid wall are found to be 2.88 dB and 14.53 dB respectively.

ACKNOWLEDGMENT

This research project has received research funding from Faculty of Engineering, Mahidol University under contract No. EG R02-02/2553.

REFERENCES

1. Rappaport, T. S. and C. D. McGillem, "UHF fading in factories," *IEEE J. Select. Areas Commun.*, Vol. 7, No. 1, 40–48, Jan. 1989.
2. Kjesbu, S. and T. Brunsvik, "Radiowave propagation in industrial environments," *Proc. 26th Annual Conference of the IEEE Industrial Electronics Society*, Vol. 4, 2425–2430, Oct. 2000.
3. Tanghe, E., W. Joseph, L. Verloock, L. Martens, H. Capoen, K. Van Herwegen, and W. Vantomme, "The industrial indoor channel: Large-scale and temporal fading at 900, 2400 and 5200 MHz," *IEEE Trans. Wireless Commun.*, Vol. 7, No. 7, 2740–2750, Jul. 2008.

4. Rappaport, T. S., *Wireless Communications Principles and Practice*, 2nd Edition, Prentice Hall PTR, 2002.
5. Lee, W. C. Y., “Estimate of local average power of a mobile radio signal,” *IEEE Trans. Veh. Technol.*, Vol. 34, No. 1, 22–27, Feb. 1985.

Detection Reliability Analysis of Passive DAS RFID System

Abdelmoula Bekkali^{1,*}, Abdullah Kadri¹, Michael Crisp², and Richard V. Penty²

¹Qatar Mobility Innovations Center (QMIC), Doha, Qatar

²Electrical Division, Department of Engineering, University of Cambridge, UK

*abdelmoulab@qmic.com

Abstract— Recently, it has been shown that improved wireless communication coverage can be achieved by employing distributed antenna system (DAS). The DAS RFID system is based on a novel technique whereby two or more spatially separated transmit and receive antennas are used to enable greatly enhanced tag detection performance over longer distances using antenna diversity combined with frequency and phase hopping. In this paper, we present a detection reliability evaluation of the DAS RFID in a typical lab environment. We conduct an extensive experimental analysis of passive RFID tag detection with different locations and orientations. The tag received signal strengths corresponding to various tag locations on one of the six different sides of a cube, and for different reader transmit power are collected and analyzed in this study.

1. INTRODUCTION

Radio Frequency Identification (RFID) is a rapidly developing technology which uses wireless communication for automatic identification of objects. RFID technology has been widely adopted as an attractive and cost effective technology for applications such as asset management, access control, and industrial automation [1]. The RFID tag detection and reader reliable reading range remain the most critical issues for successful deployment of passive ultra high frequency (UHF) RFID systems. The main factors influencing the tag response reliability include tag location and orientation, impedance mismatch between tag antenna and chip [2], and multipath fading and communication blind spot [3]. Furthermore, tag placement on highly dielectric materials (i.e., liquids) or conductors (i.e., metals) can drastically change the properties of a tag antenna and therefore, it reduces reading efficiency and shortens reading distance. Usually, these factors are beyond the control of the system user, hence for a maximum detection rate, proper conditions should be analyzed and defined before any implementation of the RFID system.

Several research works have studied the possibility of enhancing the passive RFID reliable coverage by improving the hardware performance in the presence of these propagation obstacles [4–11]. In [4], the authors suggested methods to increase the reading range by improving the power sensitivity of the passive RFID tag while other research efforts have focused on improving the reading range of RFID reader [5–7]. A reconfigurable antenna architecture has been proposed in [5] where an antenna array with a steerable high gain beam is used. The reading range can also be increased by boosting the reader signal with an external auxiliary continuous wave (CW) transmitter [6] and multi-sine signals [7]. Alternative methods have been proposed to improve the reliability of RFID systems by using phased array antennas [8] and optimizing the placement of multiple RFID antennas [9, 10].

Recently, it has been shown that improved communication coverage can be achieved by employing distributed antenna system (DAS) [11, 12]. By applying concepts of DAS system to RFID system, it is possible to overcome the shortcomings of the existing passive UHF RFID systems, enabling a few reader antennas to provide reliable coverage over a wide area [11, 12]. The DAS RFID system is based on a novel technique whereby two or more spatially separated transmit and receive antennas are used to enable greatly enhanced tag detection performance over longer distances using antenna diversity combined with frequency and phase hopping. By expanding the field of view of a single RFID reader, as well as improving reading reliability, one can envisage RFID systems with wide coverage areas as opposed to the portal systems currently in use today where sensitivity constraints require the objects to pass close to the reader antennas for detection.

In this paper, we present a detection reliability evaluation of the DAS RFID in a lab environment. We conduct an extensive experimental analysis of passive RFID tag detection with different locations and orientations. The tag received signal strengths corresponding to various tag locations on one of the six different sides and reader transmit power are collected and analyzed in this study.

The remainder of this paper is organized as follows. The background and description of the DAS RFID system is given in Section 2. The test-bed environments considered in this study for

RFID tag detection and the performance evaluation with the results obtained from experimental approach is presented in Section 3. Conclusions are drawn in Section 4.

2. DAS RFID SYSTEM DESCRIPTION

The DAS RFID system is a wide area passive UHF RFID system which uses antenna diversity combined with phase and frequency hopping [12]. It is based on an intelligent DAS signal processing that can lead to power efficiency for passive UHF RFID systems and thus, enhance the probability of successful tag detection. Since the protocols are unchanged by the DAS, the system remains standard-compliant and allows the use of low cost, off-the-shelf RFID tags.

It is well known that using several antennas can mitigate RF dead zones compared to a single antenna due to spatial diversity. However, the existing RFID systems apply time division multiplexing between diversity antennas to prevent interference occurring between signals from different antennas [12]. In the DAS RFID system, the deep fades caused by self interference are controlled by the variation of the amplitude and the relative phase difference of the transmitted signals at each antenna. Coupled with frequency hopping, which can cause shifts in the environmental multi-path fading, deep nulls can be eliminated. In addition, the system makes use of multi-cast signals such that the power sum can be exploited to provide maximum power at the tag.

As shown in Figure 1, the DAS RFID consists of a base station (BS) containing an RFID Impinj R2000 transceiver [13], an RF processing unit, UHF RFID patch antennas and UHF passive tags. The antennas are distributed over the interrogation area using coaxial cables. The DAS RFID controller is connected to a centralized server via an Ethernet interface allowing tag information to be uploaded to a server for processing, analysis and display. The RF processing unit consists of phase shifters, RF switches, and splitters and combiners to perform the frequency and phase shifts closely synchronized with the tag interrogation attempts by the RFID controller. In addition, the RF processing unit is designed to switch antennas so each can perform either transmit (Tx.) or receive (Rx.) operations in successive tag interrogations. Since the number of tags and their locations are usually unknown and the RF environment (the location of nulls) is unknown, the relative phase and absolute frequency are randomly dithered. Over time, the randomization of the null locations allows a tag at any location to be read [12].

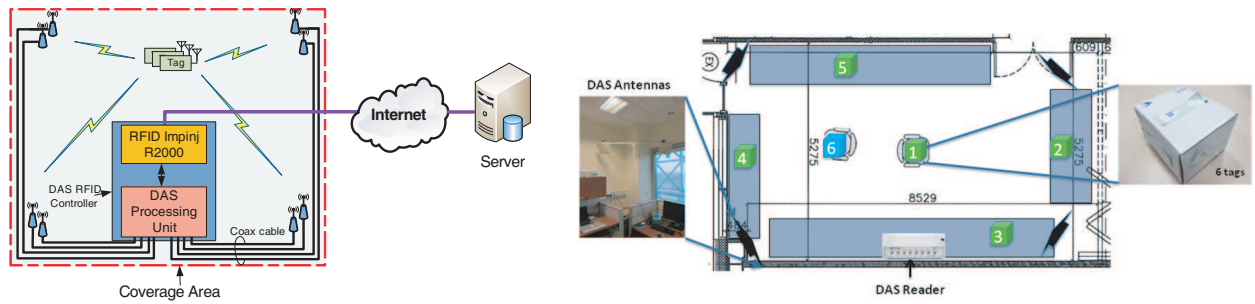


Figure 1: DAS RFID system architecture.

Figure 2: Experimental test bed.

3. DAS RFID SYSTEM PERFORMANCE EVALUATION

We designed several tests to assess the effect of the environmental factors on detection reliability of the DAS RFID system. Tests were carried out in a typical lab room with metallic objects such as desks and computer equipment. The lab is 45 m² located at Qatar Mobility Innovations Centre (QMIC). In the field tests, a DAS RFID Controller, 4 patch antennas pairs, and 36 tags were deployed in the lab as shown in Figure 2. The DAS RFID controller is configured to hop in the EU band (i.e., 865 MHz–868 MHz) with 100 ms dwelling time and an inventory period of 3 s so that each channel is visited multiple times within an inventory. Each antenna pair consists of two Tx./Rx. patch antennas separated by 1.5 m and placed at a height of 2.5 m. The antennas are circularly polarized with 6 dBi gain. Figure 3 shows the antennas locations where four are transmitting +33 dBm ERP and four are receiving the tag backscattered signals. It should be noted that the EU regulations allow 2 W ERP transmission [14]. The antennas are distributed using 30 m lengths of LMR-400 coaxial cable and their locations are chosen and pointed towards the centre of the interrogation area to achieve overlapping areas of coverage within the constraints of a cluttered room.

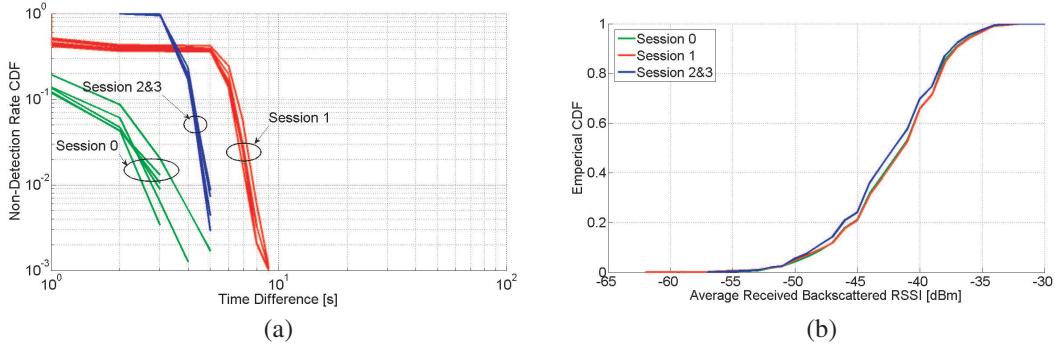


Figure 3: (a) Non-detection rate CDF for tags attached to Box-1, for reader Tx. power = +27 dBm and for different session, (b) corresponding received backscattered RSSI CDF.

For all field tests, 30 UPM Raflatac Dogbone (Tag type-1) tags and 6 Alien ALN-9629 (Tag type-2) tags are placed at a height of 1 m and distributed as shown in Figure 2. Each 6 tags are placed on 6 sides of a ($15\text{ cm} \times 15\text{ cm} \times 10\text{ cm}$) carton box and remained fixed throughout the experiment. The goal is to study the DAS RFID system performance corresponding to various tag orientation on one of the six different sides.

In the following we describe the performance of the DAS RFID system in term of tags detection reliability. The detection reliability is defined as the probability or percentage that an RFID reader successfully detects and identifies an RFID tag when it is in the reader RF field.

The session concept is one of the most important settings in passive RFID systems. The session setting is used to categorize tag populations and makes inventory events easier to manage so that the reader does not continue to re-read tags which have already been read in a given inventory, allowing a greater opportunity of unread tags to respond.

There are four session types specified in the EPCglobal Class1Gen2 specifications, which describes tag behavior when the tag is inside (energized) or outside (de-energized) of the RF field: *Session 0 (S0)*: persist indefinitely when powered; when no power from the reader it loses state; *Session 1 (S1)*: limited persistence when tag powered or not power ($500\text{ ms} < t < 5\text{ s}$); *Session 2 (S2)*: persist indefinitely when powered and at least 2 s after losing power; *Session 3 (S3)*: persist indefinitely when powered and at least 2 s after losing power.

In order to understand the effect of the sessions selection on the reading reliability of the DAS RFID system, we set the reader transmission power to be +27 dBm, the minimum and the maximum of Q parameter are 3 and 9 respectively, and the inventory period is 3 s. Figure 3(a) plots the non-detection rate cumulative distribution function (CDF) of tags on Box-1 and for different sessions from 0 to 3 over a number of inventories. The x -axis represents the time inbetween reads, or the observation period where a tag may not be seen with a probability given by the y -axis. Figure 3(b) depicts the average received backscattered RSSI CDF. It is fairly easy to see that although the received RSSI is almost identical for all sessions, the session S0 outperforms sessions S2 and S3 and far better than session S1. This is due to the fact that the number of tags being inventoried is small (less than 50 tags). For instance, for session S0, the system requires 2 s to read 99% of tags and 4 s to read 99.9% of tags, while for sessions S2 and S3, it requires 4 s to read 99% of tags and about 5 s to read all the tags. For session S1, the system requires about 7 s and about 9 s to read 99% and 99.9%, respectively. In practice, the session S0 is not good for reading large number of tags at once because if a tag is de-energized momentarily, it will reset and participate in the anti-collision algorithm again.

To assess how the number of RFID reader antennas affects the detection reliability, performance comparison of DAS RFID system with 4 antennas and 8 antennas is plotted in Figure 4. In the experiment, the tags are placed on Box 1, the reader transmission power is +33 dBm and session S2 is selected. From the figure, we observe that for a detection rate equal to 100%, the system requires about 7 s when 8 antennas are deployed and more than 500 s when only 4 antennas are used. However, the 4 antennas configuration requires only 160 s to achieve 99% detection rate. This suggests that it is possible to use 4 antennas for applications that require 100% detection rate with a long inventory period. Furthermore, from the figure, it can be observed that when the power is normalised (8 antennas at +18 dBm), the 8 antennas still outperform the 4 antennas configuration by quite a large margin.

We also evaluated the effect of the reader transmission power on the reading reliability. The reader transmission power is changed and session S2 is selected. Figure 5 plots the non-detection rate cumulative distribution function (CDF) of tags on Box 1 for different reader transmission power levels $\{+33 \text{ dBm}, +27 \text{ dBm}, +18 \text{ dBm}\}$. As expected, the detection reliability drops as the transmission power level decreases. For instance, the system can achieve 100% detection rate within 5 s for the reader Tx. Power = $+33 \text{ dBm}$ and drops to 93% for the Tx. Power = $+18 \text{ dBm}$ for the same period. For the reader Tx. Power = $+18 \text{ dBm}$, the system requires less than 20 s to achieve 100% detection rate.

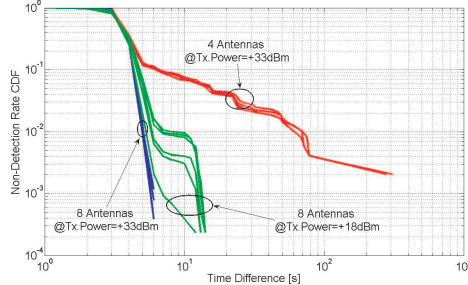


Figure 4: Non-detection rate CDF for tags attached to Box-1 and measured for 8 and 4 RFID DAS antennas respectively.

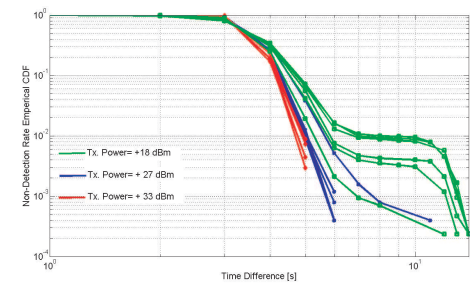


Figure 5: Non-detection rate CDF for each tag attached to Box-1 measured for each reader transmission power $+33 \text{ dBm}$, $+27 \text{ dBm}$, $+18 \text{ dBm}$.

To analyze the performance of the detection reliability using the DAS RFID reader inside the lab, we placed 30 tags of type-1 (i.e., *UPM Raflatac Dogbone*) on carton boxes 1 to 5 and 6 tags of type-2 (*Alien ALN-9629*) on Box 6. The boxes 1 through 6 are distributed inside the area as shown in Figure 2. It should be noted that the boxes remains fixed throughout the experiment. Table 1 summarizes the mean and the variance of the tags backscattered RSSI attached at each box. The backscattered RSSI data is measured over one hour period for different reader transmission power levels $\{+33 \text{ dBm}, +30 \text{ dBm}, +27 \text{ dBm}, +24 \text{ dBm}, +21 \text{ dBm}, \text{ and } +18 \text{ dBm}\}$. The table shows the measured backscattered RSSI in terms of the mean and variance and their corresponding

Table 1: Average backscattered RSSI and detection rate for tags attached to each box from 1 through 6.

Tx.Pw = +18 dBm			Tx.Pw = +21 dBm			Tx.Pw = +24 dBm			
Received RSSI		Detection rate at 10 sec (100% detection rate required time)	Received RSSI		Detection rate at 10 sec (100% detection rate required time)	Received RSSI		Detection rate at 10 sec (100% detection rate required time)	
Mean (dBm)	Var (dB)		Mean (dBm)	Var (dB)		Mean (dBm)	Var (dB)		
Box 1	-46	27	95% (20 sec)	-44.5	24.3	100% (7 sec)	-43.25	21.72	100% (7 sec)
Box 2	-47.88	29	90% (80 sec)	-46.34	26	99% (11 sec)	-44.79	22.43	100% (7 sec)
Box 3	-45.35	30.5	97% (20 sec)	-43.6	30	100% (7 sec)	-41.86	27.42	100% (7 sec)
Box 4	-44.37	32	99% (11 sec)	-42.76	31	100% (7 sec)	-41.41	29	100% (5 sec)
Box 5	-49.73	23.3	80% (120 sec)	-48.42	25	94% (11 sec)	-46.8	21.62	100% (8 sec)
Box 6	N/A	N/A	N/A	-47.72	23	60% (120 sec)	-46	21	99% (13 sec)

Tx.Pw = +27 dBm			Tx.Pw = +30 dBm			Tx.Pw = +33 dBm			
Received RSSI		Detection rate at 10 sec (100% detection rate required time)	Received RSSI		Detection rate at 10sec (100% detection rate required time)	Received RSSI		Detection rate at 10 sec (100% detection rate required time)	
Mean (dBm)	Var (dB)		Mean (dBm)	Var (dB)		Mean (dBm)	Var (dB)		
Box 1	-42	18	100% (4 sec)	-40.5	19	100% (4 sec)	-40	22	100% (5 sec)
Box 2	-43.33	18.8	100% (6 sec)	-41.22	19.5	100% (6 sec)	-40.8	21.52	100% (8 sec)
Box 3	-40	24.8	100% (4 sec)	-39	26	100% (4 sec)	-38.44	29.33	100% (6 sec)
Box 4	-40	25	100% (5 sec)	-39	28	100% (5 sec)	-38.4	30.5	100% (7 sec)
Box 5	-45	18.5	100% (6 sec)	-43	17.4	100% (6 sec)	-42.8	20	100% (9 sec)
Box 6	-43	18	100% (10 sec)	-43	17	100% (10 sec)	-42	19	100% (10 sec)

detection rate for each box and each reader transmission power level. The obtained results show that the mean RSSI variation inside the experiment area is not high, and for a quarter of the maximum Tx. power level (i.e., +27 dBm), 100% of detection rate in less than 6 s and 10 s for tag type-1 and type-2, respectively. Furthermore, a slight performance degradation at less than the maximum Tx. power (i.e., +33 dBm) can be observed, this is due to insufficient antenna isolation causing a reduction in sensitivity as the leakage is increased. It should be noted that an additional performance improvement can be obtained by having better DAS antenna configuration deployment and an optimal Q value selection.

4. CONCLUSION

An experimental evaluation of the DAS RFID system to achieve reliable tag detection in a lab environment is presented. Important performance metrics such as the RSSI and tag detection rate have been measured and analyzed. The obtained results show that the DAS RFID system can achieve 100% detection rate over an area of 35 m^2 even with a quarter of the maximum transmission power level within a 6 s observation period. It is expected that with an optimized Q value and best configuration deployment of the DAS RFID antennas, the system will be able to achieve 100% detection in shorter inventory period and wider reliable coverage area.

ACKNOWLEDGMENT

This work was made possible by NPRP grant # NPRP4-726-2-272 from the Qatar National Research Fund (a member of The Qatar Foundation). The statements made herein are solely the responsibility of the authors.

REFERENCES

1. Finkenzeller, K., *RFID Handbook: Radio-frequency Identification Fundamentals and Applications*, John Wiley & Sons, 2000.
2. Pillai, V., "Impedance matching in RFID tags: To which impedance to match?," *IEEE AP-S International Symposium*, 3505–3508, 2006.
3. Loo, C. H., A. Z. Elsherbeni, F. Yang, and D. Kajfez, "Experimental and simulation investigation of RFID blind spots," *Journal of Electromagnetic Waves and Applications*, Vol. 23, Nos. 5–6, 747–760, 2009.
4. Trotter, M. and G. Durgin, "Survey of range improvement of commercial RFID tags with power optimized waveforms," *IEEE RFID Conference*, 195–202, 2010.
5. Abbak, M. and I. Tekin, "RFID coverage extension using microstrip patch antenna array," *IEEE Antennas Propag. Mag.*, Vol. 51, No. 1, 185–191, February 2009.
6. Park, J.-S., J.-W. Jung, S.-Y. Ahn, H.-H. Roh, H.-R. Oh, Y.-R. Seong, Y.-D. Lee, and K. Choi, "Extending the interrogation range of a passive UHF RFID system with an external continuous wave transmitter," *IEEE Trans. Instrum. Meas.*, Vol. 59, No. 8, 2191–2197, August 2010.
7. Boaventura, A. and N. Carvalho, "Extending reading range of commercial RFID readers," *IEEE Transaction on Microwave Theory and Techniques*, Vol. 61, No. 1, January 2013.
8. Sadr, R., "RFID beam forming system," U.S. Patent 2011/0090059A1, 2011.
9. Wang, L., B. A. Norman, and J. Rajgopal, "Maximizing read accuracy by optimally locating RFID interrogators," *RFID Handbook: Applications, Technology, Security, and Privacy*, 181–198, CRC Press, 2008.
10. Bhattacharya, I. and U. K. Roy, "Optimal placement of readers in an RFID network using particle swarm optimization," *International Journal of Computer Networks and Communications*, 225–234, 2010.
11. Sabesan, S., M. Crisp, R. Penty, and I. H. White, "Demonstration of improved passive UHF RFID coverage using optically-fed distributed multi-antenna system," *Proc. IEEE International Conference on RFID 2009*, 217–224, 2009.
12. Sabesan, S., M. Crisp, R. Penty, and I. H. White, "An error free passive UHF RFID system using a new form of wireless signal distribution," *Proc. IEEE International Conference on RFID 2012*, 58–65, 2012.
13. http://www.impinj.com/Indy_RFID_Reader_Chips.aspx.
14. EPCglobal Specification for RFID Air Interface, http://www.epcglobalinc.org/standards/uhfc-1g2/uhfc1g2_1.2.0-standard-20080511.pdf.

High-frequency Scattering by Strongly Elongated Spheroids

I. V. Andronov¹ and F. Molinet²

¹University of St. Petersburg, Russia

²Société MOTHESIM, France

Abstract— For strongly elongated bodies the usual asymptotic approach fails because the parameter characterizing the rate of elongation counteracts the asymptotic parameter which is the large wave size of the object. The most interesting case is the case of strongly elongated body when the length of the object measured in wavelength is proportional to the square of its cross-section. This case was studied in the previous papers and the derived there leading term of the asymptotics provides a very good approximation for the induced current on the surface.

In this paper using that results we derive the asymptotics of the total scattering cross-section for axial incident plane wave on a strongly elongated spheroid.

1. INTRODUCTION

Many advances in the theory of diffraction were due to the high-frequency asymptotic methods, which provide relatively simple formulae for the fields in the form of series by inverse fractional powers of the large parameter $k\rho$, where k is the wave number and ρ is the characteristic radius of surface curvature in the plane of incidence. However for strongly elongated bodies the usual asymptotic approach fails. This happens because besides $k\rho$ another large parameter ρ/ρ_t , where ρ_t is the radius of transverse curvature, which characterizes the rate of elongation, is present in the problem formulation. Bodies with $\rho/\rho_t = O((k\rho)^\delta)$, $\delta < 1/3$ do not present difficulties and usual asymptotics are valid for such problems. When $1/3 \leq \delta < 2/3$ we deal with moderately elongated bodies in the terminology of [1]. In this case the structure of asymptotic expansions does not change and the influence of the large transverse curvature can be taken into account by introducing effective impedance in the boundary conditions [2]. Bodies with $\delta \geq 1$ have transverse dimensions of the order of the wavelength or smaller.

The most interesting case is the case of strongly elongated body when $2/3 \leq \delta < 1$. The asymptotic technique for the description of diffraction by bodies of revolution characterized by the relation

$$\chi \equiv k\rho \left(\frac{\rho_t}{\rho} \right)^{3/2} = O(1), \quad (1)$$

which corresponds to $\delta = 2/3$, was developed in [3, 4], where induced currents on a perfectly conducting surface were studied.

In this paper we extend the approach to describe far fields.

2. PROBLEM OF SCATTERING

Let a plane electromagnetic wave be axially incident on a prolate perfectly conducting spheroid with semiaxes a and b . The time factor is assumed in the form $e^{-i\omega t}$, where the frequency ω is large, so that $ka \gg 1$ and $kb \gg 1$, where $k = \omega\sqrt{\epsilon\mu}$ is the wave number. In view of (1) we assume that $kb = \chi(ka)^2$. We use Cartesian coordinates with z -axis coincident with the axis of the spheroid, $z = 0$ in its center, and x -axis be directed along the magnetic field of the incident wave.

The asymptotics of the field near the surface of the spheroid is derived in [3, 4]. It is written in spheroidal coordinates with stretched radial coordinate. Namely, we introduce spheroidal coordinates (η, ξ, φ) by the usual formulae

$$r = p\sqrt{1 - \eta}\sqrt{\xi^2 - 1}, \quad x = r \cos \varphi, \quad y = r \sin \varphi, \quad z = p\eta\xi,$$

where $p = \sqrt{b^2 - a^2}$ is the half focal distance. Then we pass from ξ to stretched coordinate τ by the formula

$$\xi = 1 + \frac{\chi}{2kb}\tau.$$

Coordinate τ is equal to zero on the axis and it is equal to one on the surface of the spheroid.

By the parabolic equation method which is appropriately modified we get at the leading order by kb , which is the large asymptotic parameter,

$$H_\varphi = H \sin \varphi, \quad E_\varphi = E \cos \varphi,$$

where

$$\begin{pmatrix} H \\ E \end{pmatrix} = \frac{e^{ikb\eta - i\chi\eta/2 + i\pi/4}}{\sqrt{\chi\tau} \sqrt{1-\eta^2}} \int_{-\infty}^{+\infty} \left(\frac{1-\eta}{1+\eta} \right)^{it} \Omega(t) \left\{ M_{it,0}(-i\chi\tau) + R(t) W_{it,0}(-i\chi\tau) \pm T(t) W_{it,1}(-i\chi\tau) \right\} dt, \quad (2)$$

$$\begin{aligned} \Omega(t) &= \frac{1}{\pi} \Gamma\left(\frac{1}{2} + it\right) \Gamma\left(\frac{1}{2} - it\right) = \frac{1}{\cosh(\pi t)}, \\ R(t) &= -\frac{M_{it,0}(-i\chi) \dot{W}_{it,1}(-i\chi) + \dot{M}_{it,0}(-i\chi) W_{it,1}(-i\chi)}{W_{it,0}(-i\chi) \dot{W}_{it,1}(-i\chi) + \dot{W}_{it,0}(-i\chi) W_{it,1}(-i\chi)}, \\ T(t) &= -\frac{1}{\Gamma\left(\frac{1}{2} - it\right)} \frac{1}{W_{it,0}(-i\chi) \dot{W}_{it,1}(-i\chi) + \dot{W}_{it,0}(-i\chi) W_{it,1}(-i\chi)}, \end{aligned}$$

$M_{it,\ell}()$ and $W_{it,\ell}()$ are Whittaker functions and dot denotes derivative. Plus in formula (2) is taken for H and minus for E .

We shall also need the expression for the H_η component of the field on the surface. Up to smaller order terms it is given by the formula (n is the normal to the surface)

$$H_\eta = -\frac{i}{k} \left\{ \frac{\partial E_\varphi}{\partial n} - \frac{1}{r} \frac{\partial H_\varphi}{\partial \varphi} \right\} = -\frac{i}{ka\sqrt{1-\eta^2}} \left\{ \frac{\partial E_\varphi}{\partial \tau} - \frac{\partial H_\varphi}{\partial \varphi} \right\} \Big|_{\tau=1}.$$

3. THE FAR FIELD

We use Stratton-Chu [5] formula for the scattered field

$$\vec{H}^s = -\frac{1}{4\pi} \iint_S [\vec{J}, \nabla G] dS. \quad (3)$$

Here $[\cdot, \cdot]$ denotes vector product, $\vec{J} = [\vec{n}, \vec{H}]$ is the induced current on the surface and

$$G(\vec{r}, \vec{r}') = \frac{e^{ikZ|\vec{r}-\vec{r}'|}}{|\vec{r}-\vec{r}'|}$$

is the scalar Green function. The electric vector can be also expressed via the induced current, but for our purposes it is sufficient to work with magnetic field only.

The field \vec{H}^s scattered from a finite body has the asymptotics

$$\vec{H}^s = \frac{e^{ikr}}{r} \vec{\Psi} \left(\frac{\vec{r}}{r} \right)$$

at large distances $r = |\vec{r}|$ from the body. The scattering cross-section Σ is defined as

$$\Sigma = \frac{4\pi}{k} \text{Im}(\Psi, \vec{a}),$$

where $\vec{\Psi}$ is taken in the direction of incidence and \vec{a} is the polarization of the magnetic field in the incident wave. One can tend the point of observation in formula (3) to infinity. The limit can be taken under the sign of integration, which yields

$$\Sigma = -\frac{1}{k} \text{Im} \left(\iint [\vec{J}, \nabla \Psi_G] dS, \vec{a} \right), \quad (4)$$

where Ψ_G is the far field amplitude from the asymptotics

$$G = \frac{e^{ikr}}{r} \Psi_G + O(r^{-2}), \quad |r| \rightarrow +\infty.$$

By reciprocity Ψ_G coincides with the field of the plane wave incident from the opposite direction. We use the results from [6], where scalar waves diffraction on an elongated spheroid is studied. In the representation of the incident plane wave in the boundary layer near the surface we change the direction, that is replace η with $-\eta$. This results in the following asymptotic formula

$$\Psi_G = \frac{e^{-ikb\eta+i\chi\eta/2+i\pi/4}}{\sqrt{\chi\tau}\sqrt{1-\eta^2}} \int_{-\infty}^{+\infty} \left(\frac{1-\eta}{1+\eta} \right)^{-is} \Omega(t) M_{is,0}(-i\chi\tau) ds. \quad (5)$$

Now we substitute asymptotics (2) and (5) into formula (4) which we rewrite in projections. The current \vec{J} has two components J_η in longitudinal direction and J_φ in the transverse cross-section. Thus we have

$$\Sigma = -\frac{1}{k} \text{Im} \left\{ \iint \left(J_\varphi \frac{\partial G}{\partial s} \cos^2 \varphi - J_\eta \frac{\partial G}{\partial n} \sin^2 \varphi \right) dS \right\}.$$

Differentiation by the arc-length s results in the leading order in multiplication by ik . Further, $dS = ba\sqrt{1-\eta^2}d\eta d\varphi$. The integral by φ can be computed and gives the multiplier π . So, we get

$$\Sigma = \frac{\pi b}{k} \text{Im} \left\{ \int_{-1}^1 \left(2H \frac{\partial \Psi_G}{\partial \tau} + H\Psi_G - 2\Psi_G \frac{\partial E}{\partial \tau} \right) d\eta \right\}. \quad (6)$$

Due to $E|_{\tau=1} = 0$, we can represent the subintegral expression in (6) as $H\mathcal{L}\Psi_G - \Psi_G\mathcal{L}E$, where $\mathcal{L} = 1 + 2\partial/\partial\tau$. Functions E and Ψ_G depend on τ by means of expressions $\tau^{-1/2}M_{it,0}(-i\chi\tau)$, and $\tau^{-1/2}W_{it,\ell}(-i\chi\tau)$, therefore the representations for $\mathcal{L}E$ and $\mathcal{L}\Psi_G$ differ from (2) and the second component of (5) by replacing Whittaker functions with their derivatives and by the additional factor $-2i\chi$.

Further we change the order of integration and compute first the integral by η . In view of the formula

$$\int_{-1}^1 \left(\frac{1-\eta}{1+\eta} \right)^{i(s-t)} \frac{d\eta}{1-\eta^2} = \pi\delta(s-t),$$

which can be checked by the substitution $\eta = -\tanh(\alpha/2)$, we get

$$\begin{aligned} \Sigma = & \frac{2\pi^2 b}{k} \text{Im} \int_{-\infty}^{+\infty} \Omega^2(t) \left\{ (M_{it,0}(-i\chi) + R(t)W_{it,0}(-i\chi) + T(t)W_{it,1}(-i\chi)) \dot{M}_{it,0}(-i\chi) \right. \\ & \left. - (\dot{M}_{it,0}(-i\chi) + R(t)\dot{W}_{it,0}(-i\chi) - T(t)\dot{W}_{it,1}(-i\chi)) M_{it,0}(-i\chi) \right\} dt. \end{aligned} \quad (7)$$

We see that the contribution of the incident field disappears in (7). Using the formula

$$\dot{M}_{it,0}W_{it,0} - M_{it,0}\dot{W}_{it,0} = \frac{1}{\Gamma(\frac{1}{2}-it)}$$

for the Wronskian of Whittaker functions, we simplify formula (7) to

$$\Sigma = -\frac{4\pi^2 b}{k} \text{Im} \int_{-\infty}^{+\infty} \frac{\Omega^2(t)}{\Gamma(\frac{1}{2}-it)} \frac{\dot{M}_{it,0}(-i\chi)\dot{W}_{it,1}(-i\chi) + \dot{M}_{it,0}(-i\chi)W_{it,1}(-i\chi)}{\dot{W}_{it,0}(-i\chi)\dot{W}_{it,1}(-i\chi) + \dot{W}_{it,0}(-i\chi)W_{it,1}(-i\chi)} dt.$$

Finally we rewrite Whittaker functions via Coulomb wave functions F and H^+ [7] and normalize the effective cross-section by the visible section of spheroid πa^2 . This results in the desired asymptotic formula

$$\Sigma' = -\frac{8}{\chi} \text{Im} \left(\int_{-\infty}^{+\infty} \frac{\dot{F}_{-\frac{1}{2}}\left(t, \frac{\chi}{2}\right) H_{\frac{1}{2}}^+\left(t, \frac{\chi}{2}\right) + F_{-\frac{1}{2}}\left(t, \frac{\chi}{2}\right) \dot{H}_{\frac{1}{2}}^+\left(t, \frac{\chi}{2}\right)}{\dot{H}_{-\frac{1}{2}}^+\left(t, \frac{\chi}{2}\right) H_{\frac{1}{2}}^+\left(t, \frac{\chi}{2}\right) + H_{-\frac{1}{2}}^+\left(t, \frac{\chi}{2}\right) \dot{H}_{\frac{1}{2}}^+\left(t, \frac{\chi}{2}\right)} \frac{dt}{1+e^{-2\pi t}} \right). \quad (8)$$

4. NUMERICAL RESULTS

Analysis of formula (8) shows that subintegral expression rapidly decreases at $\pm\infty$. For numerical computations we restricted the domain of integration to the segment $[-2-\chi/2, 2]$ and used the code from [8] for the computation of Coulomb wave functions. The dependence of the total normalized scattering cross-section on the parameter of elongation is presented on the Figure 1. We see that when $\chi \rightarrow \infty$, that is the body becomes not elongated, the total scattering cross-section Σ' tends to the well known classical limit of 2. For finite values of the elongation parameter $\Sigma' > 2$ if $\chi > \chi_0$ and $\Sigma' < 2$ if $\chi < \chi_0$, where $\chi_0 \approx 1.95$. The total scattering cross-section reaches its maximal value of approximately 2.0778 at $\chi \approx 4.36$.

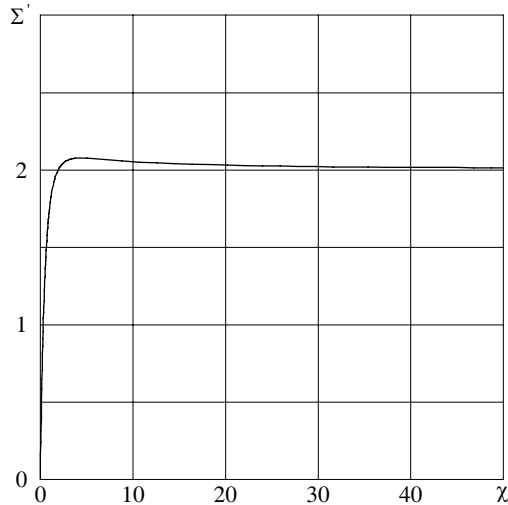


Figure 1: Normalized total scattering cross-sections as function of elongation.

REFERENCES

1. Andronov, I. V. and D. Bouche, "Asymptotic of creeping waves on a strongly prolate body," *Ann. Télécommun.*, Vol. 49, No. 3–4, 205–210, 1994.
2. Molinet, F., I. Andronov, and D. Bouche, *Asymptotic and Hybrid Methods in Electromagnetics*, The IEE, London, 2005.
3. Andronov, I. V., "High frequency asymptotics of electromagnetic field on a strongly elongated spheroid," *PIERS Online*, Vol. 5, No. 6, 536–540, 2009.
4. Andronov, I. V., D. P. Bouche, and M. Duruflé, "High-frequency diffraction of plane electromagnetic wave by an elongated spheroid," *IEEE Transactions on Antennas and Propag.*, Vol. 60, No. 11, 5286–5295, 2012.
5. Stratton, J. A. and L. J. Chu, "Diffraction theory of electromagnetic waves," *Phys. Review*, Vol. 56, No. 1, 99–107, 1939.
6. Andronov, I. V., "Diffraction by a strongly elongated body of revolution," *Acoustical Physics*, Vol. 57, 121–126, 2011.
7. Abramowitz, M. and I. Stegun, *Handbook of Mathematical Functions*, Chap. 9, 13, 1046, National Bureau of Standards, New York, 1964.
8. Thompson, I. J. and A. R. Barnett, "COULCC: A continued-fraction algorithm for Coulomb functions of complex order with complex arguments," *Comput. Phys. Commun.*, Vol. 36, 363–372, 1985.

Diffraction by an Acute-angled Dielectric Wedge: The H -polarization Case

M. Frongillo¹, G. Gennarelli², and G. Riccio¹

¹D.I.E.M., University of Salerno, Via Ponte Don Melillo, Fisciano (SA) 84084, Italy

²Institute for Electromagnetic Sensing of the Environment
National Research Council, Via Diocleziano 328, Naples 80124, Italy

Abstract— The goal of this work is to propose a useful formulation for the field diffracted by an acute-angled lossless dielectric wedge illuminated by a H -polarized plane wave. Two problems relevant to the dielectric region and the surrounding space are tackled and solved by formulating the corresponding radiation integrals in terms of electric and magnetic equivalent Physical Optics (PO) surface currents lying on the internal and external faces of the wedge. For each observation domain, the solution for the diffracted field is derived in the Uniform Geometrical Theory of Diffraction (UTD) framework by means of a useful approximation, analytical manipulations and uniform asymptotic evaluations of the resulting integrals. This leads to closed form expressions containing the reflection and transmission coefficients of the structure and the UTD transition function.

1. INTRODUCTION

Diffraction by penetrable wedges formed by dielectric materials represents a canonical problem having an important role in many applications. The existing approaches provide approximate analytical or heuristic solutions, or attempt to solve the problem in an exact sense by using function theoretic techniques or by combining analytical and numerical techniques to compute integral equations. Uniform Asymptotic Physical Optics (UAPO) solutions were proposed in [1, 2] for evaluating the field diffracted by right- and obtuse-angled lossless dielectric wedges when a plane wave impacts on them at normal incidence. They were expressed in closed form and given in terms of the Geometrical Optics (GO) response of the structure and the UTD transition function [3]. As a consequence, they resulted to be manageable and easy to implement in a computer code. Numerical tests and comparisons with Finite Difference Time Domain (FDTD) data assessed their accuracy. The time domain UAPO diffraction coefficients associated to the right-angled geometry were derived in [4] by taking advantage of the knowledge of their frequency domain counterparts [1].

UAPO solutions for evaluating the diffracted field in the dielectric region and the surrounding free-space are here obtained in the case of an acute-angled lossless wedge illuminated by a H -polarized plane wave at normal incidence.

2. PROBLEM DESCRIPTION AND UAPO APPROACH

The geometry of the considered problem and the related parameters are shown in Fig. 1. The wedge-shaped dielectric region and its surfaces are denoted by Ω_d , S_0 and S_n , respectively. It has internal apex angle $\alpha < \pi/2$ and is filled by a lossless non-magnetic ($\mu_r = 1$) material having relative permittivity ε_r . The Ω_0 indicates the free-space region surrounding the wedge. The incidence direction is assumed perpendicular to the edge and defined by the angle ϕ' , which is here considered in the range from $\pi/2$ to $\pi - \alpha$, so that only S_0 is illuminated by the incident H -polarized plane wave having the magnetic field $\underline{H}^i = H_0^i e^{j\varphi} \hat{z}$. The observation point is $P(\rho, \phi)$.

If $\theta^i = \phi' - \pi/2$ is the incidence angle, the wave penetrates into Ω_d according to the transmission angle $\theta_0^t = \sin^{-1}(\sin \theta^i / \sqrt{\varepsilon_r})$, and undergoes multiple reflections (see Fig. 2) until the reflection angle $\theta_p^r = \theta_p^i = p\alpha + \theta_0^t$ is greater than $\pi/2 - \alpha$. The number of total internal reflections is given by $M = \text{Int}[(\pi/2 - \theta_0^t)/\alpha]$, where $\text{Int}[\cdot]$ denotes the integer part of the argument.

Waves transmitted through S_0 and S_n define shadow boundaries in Ω_0 and exist until $\theta_p^i < \theta_c = \sin^{-1}(1/\sqrt{\varepsilon_r})$, with $p = 1, \dots, M^* = \text{Int}[(\theta_c - \theta_0^t)/\alpha] \leq M$.

The approach for determining the diffracted field is the same adopted in [1, 2]. The starting

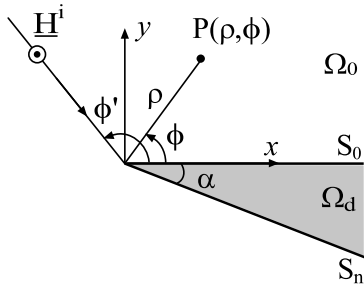


Figure 1: Geometry of the problem.

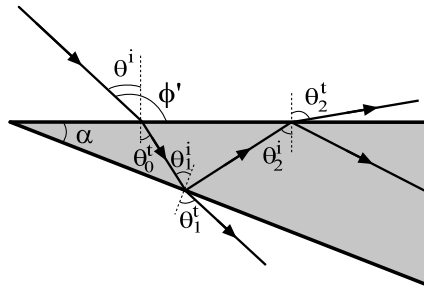


Figure 2: GO propagation mechanisms.

point is the PO radiation integral for evaluating the scattered electric field in Ω_0 and Ω_d :

$$\begin{aligned} \underline{E}^s &\cong -jk \left[(\underline{\underline{I}} - \hat{s}\hat{s}) \zeta \tilde{\underline{J}}_{s_0} + \tilde{\underline{J}}_{ms_0} \times \hat{s} \right] I_0 - jk \left[(\underline{\underline{I}} - \hat{s}\hat{s}) \zeta \tilde{\underline{J}}_{s_n} + \tilde{\underline{J}}_{ms_n} \times \hat{s} \right] I_n \\ &= -jk \left[(\underline{\underline{I}} - \hat{s}\hat{s}) \zeta \tilde{\underline{J}}_{s_0} + \tilde{\underline{J}}_{ms_0} \times \hat{s} \right] \iint_{S_0} e^{j\varphi_0} \frac{e^{-jk|\underline{r}-\underline{r}'|}}{4\pi |\underline{r}-\underline{r}'|} dS_0 \\ &\quad - jk \left[(\underline{\underline{I}} - \hat{s}\hat{s}) \zeta \tilde{\underline{J}}_{s_n} + \tilde{\underline{J}}_{ms_n} \times \hat{s} \right] \iint_{S_n} e^{j\varphi_n} \frac{e^{-jk|\underline{r}-\underline{r}'|}}{4\pi |\underline{r}-\underline{r}'|} dS_n \end{aligned} \quad (1)$$

where \hat{s} is the unit vector in the diffraction direction, $\underline{J}_s = \tilde{\underline{J}}_s e^{j\varphi}$ and $\underline{J}_{ms} = \tilde{\underline{J}}_{ms} e^{j\varphi}$ are the electric and magnetic equivalent PO surface currents on $S = S_0 \cup S_n$. Moreover, ζ and k are the impedance and propagation constant in Ω_0 or Ω_d , \underline{r} and \underline{r}' denote the observation and source points, respectively, and $\underline{\underline{I}}$ is the 3×3 identity matrix. The integrals I_0 and I_n can be manipulated in order to apply the Steepest Descent Method, so that uniform asymptotic evaluations give the UAPO diffraction terms I_0^d and I_n^d . Accordingly, $\underline{H}^d = \hat{s} \times \underline{E}^d / \zeta$, with

$$\underline{E}^d = -jk \left[(\underline{\underline{I}} - \hat{s}\hat{s}) \zeta \tilde{\underline{J}}_{s_0} + \tilde{\underline{J}}_{ms_0} \times \hat{s} \right] I_0^d - jk \left[(\underline{\underline{I}} - \hat{s}\hat{s}) \zeta \tilde{\underline{J}}_{s_n} + \tilde{\underline{J}}_{ms_n} \times \hat{s} \right] I_n^d = \underline{E}_{S_0}^d + \underline{E}_{S_n}^d \quad (2)$$

3. UAPO DIFFRACTED FIELD

The expressions of the UAPO diffracted field in Ω_d and Ω_0 are reported in terms of the UTD transition function $F_t(\cdot)$ [3].

$$\begin{aligned} (\underline{E}_{S_0}^d)_{\Omega_d} &= \hat{\phi} \zeta_d H_0^i T_0 \frac{e^{-j\pi/4}}{2\sqrt{2\pi k_d}} \frac{e^{-jk_d\rho}}{\sqrt{\rho}} \left\{ (\sin \phi - \cos \theta_0^t) \frac{F_t \left(2k_d \rho \cos^2 \left(\frac{(2\pi-\phi)+(\theta_0^t+\pi/2)}{2} \right) \right)}{\cos \phi + \cos(\theta_0^t + \pi/2)} \right. \\ &\quad \left. + \sum_{m=1}^M \left(\prod_{p=1}^{m-1} R_p \right) [(1+R_m) \sin \phi + (1-R_m) \cos \theta_m^i] \frac{F_t \left(2k_d \rho \cos^2 \left(\frac{(2\pi-\phi)+(\theta_m^i+\pi/2)}{2} \right) \right)}{\cos \phi + \cos(\theta_m^i + \pi/2)} \right\} \end{aligned} \quad (3)$$

$$\begin{aligned} (\underline{E}_{S_n}^d)_{\Omega_d} &= \hat{\phi} \zeta_d H_0^i T_0 \frac{e^{-j\pi/4}}{2\sqrt{2\pi k_d}} \frac{e^{-jk_d\rho}}{\sqrt{\rho}} \left\{ \sum_{m=1}^M \left(\prod_{p=1}^{m-1} R_p \right) [(1-R_m) \cos \theta_m^i - (1+R_m) \sin(\phi + \alpha)] \right. \\ &\quad \left. \cdot \frac{F_t \left(2k_d \rho \cos^2 \left(\frac{\phi-(2\pi-\alpha)+(\theta_m^i+\pi/2)}{2} \right) \right)}{\cos(\phi + \alpha) + \cos(\theta_m^i + \pi/2)} \right\} \end{aligned} \quad (4)$$

$$\begin{aligned} \left(\underline{\underline{E}}_{S_0}^d\right)_{\Omega_0} = & \hat{\phi}\zeta_0 H_0^i \frac{e^{-j\pi/4}}{2\sqrt{2\pi k_0}} \frac{e^{-jk_0\rho}}{\sqrt{\rho}} \left\{ \left[(1-R_0)\sin\phi' - (1+R_0)\sin\phi \right] \frac{F_t\left(2k_0\rho\cos^2\left(\frac{\phi+\phi'}{2}\right)\right)}{\cos\phi + \cos\phi'} \right. \\ & \left. - T_0 \sum_{\substack{m=1 \\ m \text{ even}}}^{M^*} \left(\prod_{p=1}^{m-1} R_p \right) T_m (\sin\phi + \cos\theta_m^t) \frac{F_t\left(2k_0\rho\cos^2\left(\frac{\phi\pm(\theta_m^t+\pi/2)}{2}\right)\right)}{\cos\phi + \cos(\theta_m^t + \pi/2)} \right\} \end{aligned} \quad (5)$$

Note that the sign + (−) must be used in (5) when $0 < \phi < \pi$ ($\pi < \phi < 2\pi - \alpha$).

$$\begin{aligned} \left(\underline{\underline{E}}_{S_n}^d\right)_{\Omega_0} = & \hat{\phi}\zeta_0 H_0^i T_0 \frac{e^{-j\pi/4}}{2\sqrt{2\pi k_0}} \frac{e^{-jk_0\rho}}{\sqrt{\rho}} \left\{ \sum_{\substack{m=1 \\ m \text{ odd}}}^{M^*} \left(\prod_{p=1}^{m-1} R_p \right) T_m [\sin(\phi + \alpha) - \cos\theta_m^t] \right. \\ & \left. \cdot \frac{F_t\left(2k_0\rho\cos^2\left(\frac{(\phi+\alpha)\pm(\theta_m^t+\pi/2)}{2}\right)\right)}{\cos(\phi + \alpha) + \cos(\theta_m^t + \pi/2)} \right\} \end{aligned} \quad (6)$$

The sign + (−) in (6) applies to $0 < \phi < \pi - \alpha$ ($\pi - \alpha < \phi < 2\pi - \alpha$). If $\theta_p^t = \sin^{-1}(\sqrt{\varepsilon_r} \sin\theta_p^i)$, the reflection and transmission coefficients used in (3)–(6) are so defined:

$$T_0 = \frac{2\sqrt{\varepsilon_r} \cos\theta^i}{\sqrt{\varepsilon_r} \cos\theta^i + \cos\theta_0^t}; \quad R_0 = \frac{\sqrt{\varepsilon_r} \cos\theta^i - \cos\theta_0^t}{\sqrt{\varepsilon_r} \cos\theta^i + \cos\theta_0^t} \quad (7)$$

$$T_p = \frac{2\cos\theta_p^i}{\cos\theta_p^i + \sqrt{\varepsilon_r} \cos\theta_p^t}; \quad R_p = \frac{\cos\theta_p^i - \sqrt{\varepsilon_r} \cos\theta_p^t}{\cos\theta_p^i + \sqrt{\varepsilon_r} \cos\theta_p^t} \quad (8)$$

4. NUMERICAL EXAMPLE

The example refers to a lossless wedge characterized by $\varepsilon_r = 2.5$ and $\alpha = 15^\circ$ in the case of plane wave impinging at $\phi' = 100^\circ$. The magnetic field levels are collected on a circular path with $\rho = 3\lambda_0$, λ_0 being the free-space wavelength. The black arrows in Fig. 3(a) indicate (from left to

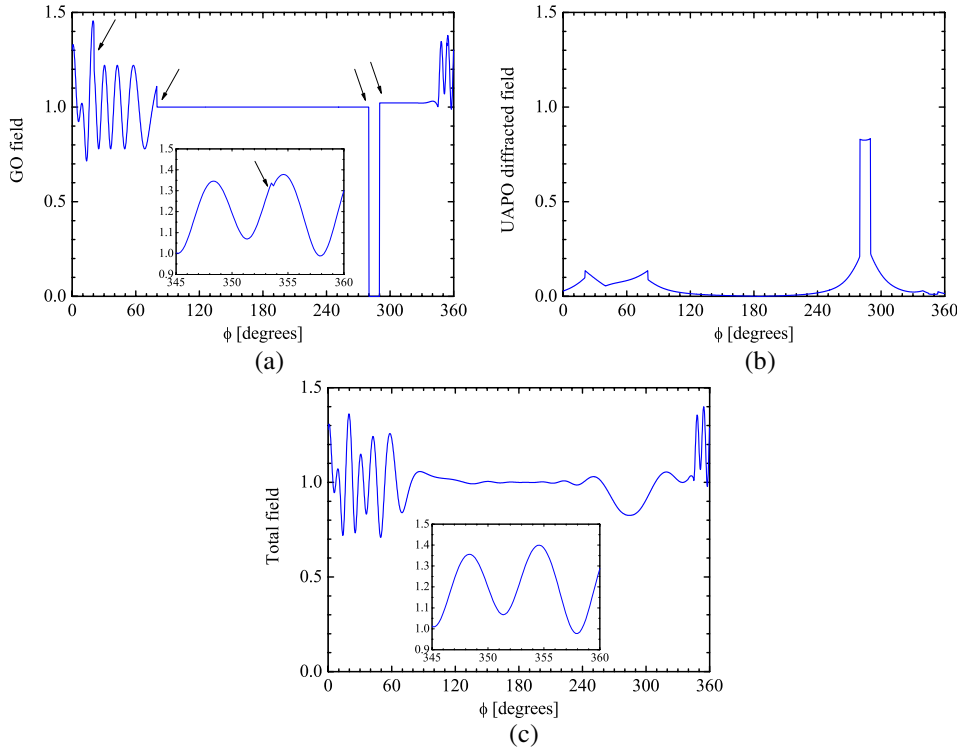


Figure 3: Magnetic field amplitude. (a) GO field; (b) UAPO diffracted field and (c) total field.

right) the boundaries of the GO field. 1) Transmitted through S_0 , 2) reflected by S_0 , 3) incident on the wedge, 4) transmitted through S_n , and 5) reflected by the internal faces. As can be seen in Fig. 3(c), the total field is everywhere continuous, thus confirming that the UAPO diffraction contribution is able to compensate the discontinuities of the GO field. Moreover, the proposed solutions are in closed form and easy to handle.

REFERENCES

1. Gennarelli, G. and G. Riccio, "A uniform asymptotic solution for diffraction by a right-angled dielectric wedge," *IEEE Trans. Antennas Propagat.*, Vol. 59, 898–903, 2011.
2. Gennarelli, G. and G. Riccio, "Plane-wave diffraction by an obtuse-angled dielectric wedge," *J. Opt. Soc. Am. A*, Vol. 28, 627–632, 2011.
3. Kouyoumjian, R. G. and P. H. Pathak, "A uniform geometrical theory of diffraction for an edge in a perfectly conducting surface," *Proc. of IEEE*, Vol. 62, 1448–1461, 1974.
4. Gennarelli, G. and G. Riccio, "Time domain diffraction by a right-angled penetrable wedge," *IEEE Trans. Antennas Propagat.*, Vol. 60, 2829–2833, 2012.

Conductor Locations Reconstruction in a Cylindrical Winding Model

M. Dalarsson and M. Norgren

Division of Electromagnetic Engineering, School of Electrical Engineering
Royal Institute of Technology, Stockholm SE-100 44, Sweden

Abstract— A study of a novel method to detect mechanical deformations of windings in a power transformer, while in operation, is presented. We employ an approximate model of a transformer winding surrounded by the transformer-tank wall and the magnetic core. The transformer winding is viewed as a structure consisting of thin conducting cylindrical rings (winding segments or turns) situated within a coaxial cylindrical waveguide, where the inner conducting cylinder represents the iron core that conducts the magnetic flux and the outer conducting cylinder represents the wall of the transformer tank. The idea is to insert antennas inside the transformer tank above and below the winding to radiate and measure microwave fields that interact with the metallic structure and the insulation. The responses from the radiated waves are assumed to be sensitive to any mechanical deformations that could be caused by electromagnetic forces due to short-circuit currents and possible manufacturing weaknesses. The goal is to determine the radial locations of the individual winding segments or individual turns from measurements of the scattered fields at both ends. The propagation problem is solved by conventional waveguide theory, including mode-matching and cascading techniques. We utilize optimization as a suitable method to solve the inverse problem and obtain an agreement between the reconstructed and true positions of the winding segments.

1. INTRODUCTION

Power transformers are critical components in the electric power grid and their occasional failures may result in major electricity shortages in their geographical areas. In operation, power transformers are subject to several degradation mechanisms, including thermal degradation at hot spots, partial discharges due to local electric field surges, increased levels of moisture in the cellulose insulation due to decomposition ([1, 2]) as well as winding deformations due to mechanical forces from short circuit currents.

In this paper, we focus on detecting the mechanical winding deformations in power transformers. The method can in principle be used to detect the effects of other degradation mechanisms mentioned above, but the current investigation is limited to detection of mechanical deformation of windings only [3]. Similar investigations for diagnostics of partial discharges have recently been reported in [4].

The diagnostic methods for power transformers, currently available on the market, are either coarse methods or off-line methods that require disconnection from the grid. The off-line methods generally imply a non-service stress of a transformer [2, 5–7]. Furthermore, methods that offer an on-line monitoring of possible winding deformations due to the mechanical forces from short circuit currents are generally not available.

The idea of our approach is to insert antennas inside the transformer tank, above and below the transformer windings, to radiate and measure microwave fields that interact with the winding structure. The analysis of the measured signals and their relations to the structure parameters, being the signatures of mechanical deformations, is an inverse electromagnetic problem [8] that typically is not straightforward to solve mathematically.

We model a transformer winding structure as a coaxial cylindrical waveguide where the inner conducting cylinder represents the iron core that conducts the magnetic flux and the outer conducting cylinder represents the wall of the transformer tank, as shown in Fig. 1. In between there is a set of conducting cylindrical rings (winding segments or turns) that are situated within a coaxial cylindrical waveguide. From Fig. 1, we see that our coaxial cylindrical model is best suited for some designs of practical power transformers. Such designs include for example the single-phase overhead (pole-mounted) distribution transformers [9] that could be considered to actually resemble our ideal structure, as shown in Fig. 2(a). Furthermore, some large single-phase shunt reactors may also be considered to show a closer resemblance to our ideal structure. On the other hand, a large three-phase power transformer has a more complex mechanical structure [10] as shown in Fig. 2(b). In these more complex transformers the tank wall often does not possess a cylindrical

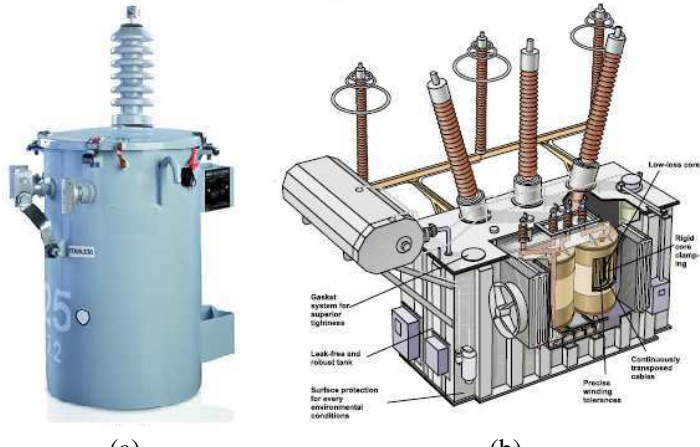
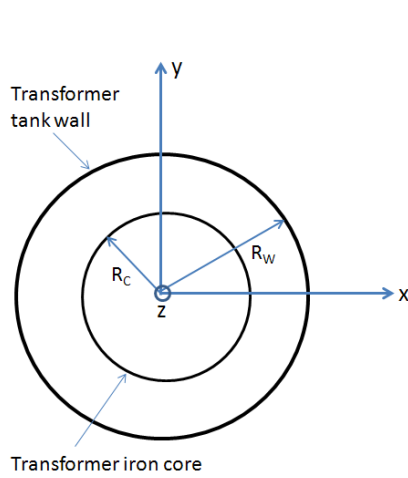


Figure 1: The power transformer as a coaxial cylindrical waveguide.

Figure 2: (a) Single-phase overhead distribution transformer.
(b) Large power transformer.

symmetry. Furthermore, the tank wall (even if it has a suitable circular shape) does not encircle the entire core and windings.

The more complex power transformers, as the one shown in Fig. 2(b), would require some modifications to our basic model depicted in Fig. 1. Despite this idealization in our model, with a favorable deployment of microwave antennas and certain empirical corrections, our method may provide an accurate and stable diagnosis of mechanical deformations of transformer windings even in the more mechanically complex cases. Furthermore, as the present model is the first step towards the establishing of the principles for the solution of the inverse electromagnetic problem at hand, we have deliberately chosen a simple symmetric model, in order to avoid a high numerical calculation complexity and more advanced code optimization.

In the present paper, we solve the propagation problem by conventional waveguide theory, including mode-matching and cascading techniques [11]. We use a parametric study of an appropriate optimization function for solving the inverse problem in order to reconstruct the actual positions of the irradiated winding segments.

2. PROBLEM FORMULATION

The geometry of our approximate model is shown in Fig. 3. We denote the four regions (1–4) between the two cylindrical conductive surfaces of the coaxial waveguide (iron core and tank wall) and the conductive obstacle (winding segment or turn) as indicated in Fig. 3.

For the propagation problem we only consider TM-modes ($H_z = 0$) as they include the dominant TEM-mode which propagates at all frequencies. Following [12], in the lossless case ($\sigma = 0$), the longitudinal component of the electric field, for progressive waves traveling in positive z -direction,

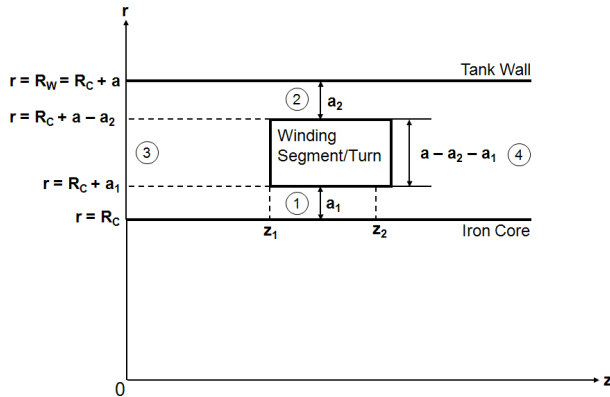


Figure 3: Cross section of a coaxial waveguide as a model of a transformer winding.

is given by

$$E_z = \frac{1}{j\omega\epsilon} \left(\frac{d^2\Lambda}{dz^2} + k^2\Lambda \right) T(r, \varphi), \quad \Lambda(z) = \exp(-jk_z z), \quad k^2 = \omega^2\mu\epsilon \quad (1)$$

In the present paper, the complete winding insulation consisting typically of transformer oil, insulating paper and pressboard, is approximated by a single homogeneous material with μ and ϵ being the effective permeability and permittivity, respectively. The transverse components of the fields can be obtained using

$$H_r = \frac{1}{r} \frac{\partial T}{\partial \varphi} \Lambda(z), \quad H_\varphi = -\frac{\partial T}{\partial r} \Lambda(z), \quad E_r = Z H_\varphi, \quad E_\varphi = -Z H_r. \quad (2)$$

The wave impedance Z and the longitudinal component k_z of the wave vector are given by

$$Z = \frac{k_z}{\omega\epsilon} = \frac{\sqrt{k^2 - \gamma^2}}{\omega\epsilon} = \frac{\sqrt{\omega^2\mu\epsilon - \gamma^2}}{\omega\epsilon}, \quad k_z = \sqrt{\omega^2\mu\epsilon - \gamma^2} = \sqrt{\frac{\omega^2}{c^2} - \gamma^2} = \frac{\omega}{c} \sqrt{1 - \frac{c^2\gamma^2}{\omega^2}}, \quad (3)$$

as expected for the TM-waves, where γ is the transverse wave number. The TM-waves can only propagate when $\omega > \omega_{\text{cutoff}} = c\gamma$. Otherwise the waves are evanescent and decay exponentially. The scalar transverse function denoted by $T(r, \varphi)$ in (1) and (2) for TM-waves in a coaxial wave guide is a solution of the transverse wave equation in cylindrical coordinates as indicated below

$$\frac{1}{r} \frac{\partial}{\partial r} \left(r \frac{\partial T}{\partial r} \right) + \frac{1}{r^2} \frac{\partial^2 T}{\partial \varphi^2} + \gamma^2 T = 0 \Rightarrow T(r, \varphi) = [P J_n(\gamma r) + Q N_n(\gamma r)] \cos(n\varphi), \quad (4)$$

where P and Q are arbitrary constants, $J_n(\gamma r)$ is the Bessel function of integer order while $N_n(\gamma r)$ is the Neumann function of integer order. From (1), we see that the longitudinal component of the electric field E_z , being tangential to both cylindrical boundaries of the coaxial waveguide, is directly proportional to the scalar transverse function $T(r, \varphi)$. Thus for any polar angle φ and any value of z , we must have

$$E_z(R_I, \varphi, z) = 0, \quad E_z(R_O, \varphi, z) = 0 \Rightarrow T(R_I, \varphi) = 0, \quad T(R_O, \varphi) = 0, \quad (5)$$

where we denote the inner and outer radius of the coaxial region by R_I and R_O respectively. This implies

$$-\frac{Q}{P} = \frac{J_n(\gamma R_I)}{N_n(\gamma R_I)} = \frac{J_n(\gamma R_O)}{N_n(\gamma R_O)}. \quad (6)$$

If we restrict our present analysis to mechanical deformations that possess cylindrical symmetry and are independent on the angle φ , we can assume $n = 0$ and obtain the TM-modes

$$T^{(m)}(r) = P \left[J_0(\gamma_m r) - \frac{J_0(\gamma_m R_I)}{N_0(\gamma_m R_I)} N_0(\gamma_m r) \right], \quad (7)$$

where γ_m ($m = 1, 2, 3, \dots$) is a discrete set of solutions of the Equation (6), given by [13]

$$\gamma_m R_I = \frac{m\pi}{\lambda - 1} - \frac{1}{8\lambda} \frac{\lambda - 1}{m\pi} + \left[\frac{25(\lambda^3 - 1)}{6(4\lambda)^3(\lambda - 1)} - \frac{1}{(8\lambda)^2} \right] \frac{(\lambda - 1)^3}{m^3\pi^3} + \dots, \quad (8)$$

with $\lambda = R_O/R_I > 1$. Using now the definitions (2) as well as the formulae $J'_0(w) = -J_1(w)$ and $N'_0(w) = -N_1(w)$, we see that in our case we have

$$\mathbf{E}^{(m)} = E_r^{(m)} \mathbf{e}_r \sim \frac{\partial T^{(m)}}{\partial r} \sim J_1(\gamma_m r) - \frac{J_0(\gamma_m R_I)}{N_0(\gamma_m R_I)} N_1(\gamma_m r), \quad (9)$$

$$\mathbf{H}^{(m)} = H_\varphi^{(m)} \mathbf{e}_\varphi \sim \frac{\partial T^{(m)}}{\partial r} \sim J_1(\gamma_m r) - \frac{J_0(\gamma_m R_I)}{N_0(\gamma_m R_I)} N_1(\gamma_m r). \quad (10)$$

Based on the results (9) and (10), we can define the orthonormal basis functions for TM_m modes in the coaxial waveguide, as follows

$$\psi_m(r) = \psi_m(\gamma_m, R, r) = A_m \left[J_1(\gamma_m r) - \frac{J_0(\gamma_m R)}{N_0(\gamma_m R)} N_1(\gamma_m r) \right], \quad m = 1, 2, 3, \dots, \quad (11)$$

where $R = \{R_I \text{ or } R_O\}$ and A_m are normalization constants obtained from normalization conditions for basis functions (11). If we now refer to Fig. 3, the basis functions in the regions 1 (below the conductive obstacle) and 2 (above the conductive obstacle), are given by

$$\psi_m^{(1)}(r) = \psi_m \left(k_{Tm}^{(1)}, R_C, r \right), \quad \psi_m^{(2)}(r) = \psi_m \left(k_{Tm}^{(2)}, R_W, r \right), \quad m = 1, 2, 3 \dots \quad (12)$$

while in the regions 3 and 4, with no obstacle present, the basis functions are given by

$$\psi_m^{(3)}(r) = \psi_m \left(k_{Tm}^{(3)}, R_C, r \right), \quad \psi_m^{(4)}(r) = \psi_m \left(k_{Tm}^{(4)}, R_C, r \right), \quad m = 1, 2, 3 \dots \quad (13)$$

with $k_{Tm}^{(i)} = \gamma_m^{(i)}$ defined using (8), (12) and (13), where

$$\lambda_1 = 1 + \frac{a}{R_C}, \quad \lambda_2 = \frac{R_C + a}{R_C + a - a_2}, \quad \lambda_3 = \lambda_4 = \frac{R_W}{R_C}, \quad m = 1, 2, 3 \dots \quad (14)$$

Using the definition of the transverse wave number γ_m in the lossless case, i.e., $\gamma_m^2 = \omega^2 \mu \epsilon - k_{zm}^2$, where we denote the longitudinal wave number for the m -th mode by k_{zm} , the longitudinal wave numbers $k_{zm}^{(i)}$ and the TM _{m} -mode impedances for the four regions ($i = 1, 2, 3, 4$) are given by

$$k_{zm}^{(i)2} = \omega^2 \mu \epsilon - \gamma_m^{(i)2}, \quad Z_m^{(i)} = \frac{k_{zm}^{(i)}}{k} \eta, \quad \eta = \sqrt{\frac{\mu}{\epsilon}}. \quad (15)$$

The transverse electric fields $E_{rm}^{(i)}$ and magnetic fields $H_{\varphi m}^{(i)}$ are linear combinations of the basis functions $\psi_m^{(i)}(r)$ for the respective region. The transverse fields can then be expanded, in terms of the basis functions, as follows [11]:

$$E_r^{(i)}(r, z) = \sum_{m=0}^{N_i} \left[c_m^{(i)+}(z) + c_m^{(i)-}(z) \right] Z_m^{(i)} \psi_m^{(i)}(r), \quad H_{\varphi}^{(i)}(r, z) = \sum_{m=0}^{N_i} \left[c_m^{(i)+}(z) - c_m^{(i)-}(z) \right] \psi_m^{(i)}(r). \quad (16)$$

where we truncated the sums to a finite number of modes ($0 \leq m_i \leq N_i$) required for the numerical calculations. For each mode and each region $E_{rm}^{(i)} = Z_m^{(i)} H_{\varphi m}^{(i)}$ and $c_m^{(i)\pm}(z)$ are the coefficients for the modes propagating in $\pm z$ -direction. Thus, with a finite number of modes ($0 \leq m_i \leq N_i$), we introduce the mode coupling integral and the mode coupling matrix elements by

$$\left\langle \psi_{m_i}^{(i)}(r) | \psi_{m_j}^{(j)}(r) \right\rangle_i = 2\pi \int_{I_i} \psi_{m_i}^{(i)}(r) \psi_{m_j}^{(j)}(r) r dr, \quad K_{(i,j)m_i,m_j} = Z_{m_i}^{(i)} \langle \psi_{m_i}^{(i)}(r) | \psi_{m_j}^{(j)}(r) \rangle_i. \quad (17)$$

where I_i denotes the interval of integration for each of the regions. For example for the region 1, we have $I_1 = [R_C, R_C + a_1]$. The mode coupling matrix elements are collected into the mode coupling $\mathbf{K}_{(i,j)}$ -matrices, where $m_i = 0, 1, 2, \dots, N_i$, $m_j = 0, 1, 2, \dots, N_j$, $i = 1, 2$, $j = 3, 4$, which indicates that any of the regions $i = 1, 2$ couples to any of the regions $j = 3, 4$. On the other hand there is no direct coupling between regions 1 and 2 or between regions 3 and 4 respectively. The mode impedances in the four regions can also be collected into four diagonal impedance matrices as follows:

$$\mathbf{D}_{(i)} = \text{diag} \left\{ Z_n^{(i)} \right\}_{n=0}^{N_i}. \quad (18)$$

Using the above notation, the boundary conditions at the planes $z = z_1$ and $z = z_2$, with continuity of E_r over the entire surface and the continuity of H_{φ} over the aperture parts of the surface, result

in six matrix equations

$$\mathbf{D}_{(3)} \left[\mathbf{c}_{(3)}^+(z_1) + \mathbf{c}_{(3)}^-(z_1) \right] = \mathbf{K}_{(1,3)}^T \left[\mathbf{c}_{(1)}^+(z_1) + \mathbf{c}_{(1)}^-(z_1) \right] + \mathbf{K}_{(2,3)}^T \left[\mathbf{c}_{(2)}^+(z_1) + \mathbf{c}_{(2)}^-(z_1) \right] \quad (19)$$

$$\mathbf{D}_{(1)} \left[\mathbf{c}_{(1)}^+(z_1) - \mathbf{c}_{(1)}^-(z_1) \right] = \mathbf{K}_{(1,3)} \left[\mathbf{c}_{(3)}^+(z_1) - \mathbf{c}_{(3)}^-(z_1) \right] \quad (20)$$

$$\mathbf{D}_{(2)} \left[\mathbf{c}_{(2)}^+(z_1) - \mathbf{c}_{(2)}^-(z_1) \right] = \mathbf{K}_{(2,3)} \left[\mathbf{c}_{(3)}^+(z_1) - \mathbf{c}_{(3)}^-(z_1) \right] \quad (21)$$

$$\mathbf{D}_{(4)} \left[\mathbf{c}_{(4)}^+(z_2) + \mathbf{c}_{(4)}^-(z_2) \right] = \mathbf{K}_{(1,4)}^T \left[\mathbf{c}_{(1)}^+(z_2) + \mathbf{c}_{(1)}^-(z_2) \right] + \mathbf{K}_{(2,4)}^T \left[\mathbf{c}_{(2)}^+(z_2) + \mathbf{c}_{(2)}^-(z_2) \right] \quad (22)$$

$$\mathbf{D}_{(1)} \left[\mathbf{c}_{(1)}^+(z_2) - \mathbf{c}_{(1)}^-(z_2) \right] = \mathbf{K}_{(1,4)} \left[\mathbf{c}_{(4)}^+(z_2) - \mathbf{c}_{(4)}^-(z_2) \right] \quad (23)$$

$$\mathbf{D}_{(2)} \left[\mathbf{c}_{(2)}^+(z_2) - \mathbf{c}_{(2)}^-(z_2) \right] = \mathbf{K}_{(2,4)} \left[\mathbf{c}_{(4)}^+(z_2) - \mathbf{c}_{(4)}^-(z_2) \right] \quad (24)$$

where the vectors $\mathbf{c}_{(i)}^\pm(z)$ are defined by ($i = 1, 2, 3, 4$)

$$\mathbf{c}_{(i)}^\pm(z) = \begin{bmatrix} c_1^{(i)\pm}(z) & c_2^{(i)\pm}(z) & \dots & c_{N_i}^{(i)\pm}(z) \end{bmatrix}^T. \quad (25)$$

The propagation equations for different modes and regions are summarized into the following matrix equation

$$\mathbf{c}_{(i)}^\pm(z_2) = \mathbf{P}_{(i)}^\pm(z_2 - z_1) \mathbf{c}_{(i)}^\pm(z_1), \quad \mathbf{P}_{(i)}^\pm(z_2 - z_1) = \text{diag} \left\{ \exp[\mp jk_{zm}^i(z_2 - z_1)] \right\}_{m=0}^{N_i}. \quad (26)$$

where $i = 1, 2, 3, 4$.

3. SCATTERING ANALYSIS

Let us now consider the scattering of TM_n waves from the conductive obstacle depicted in Fig. 4 above. From the geometry of the problem we see that it is convenient to use the same number of modes at each side of the conductive obstacle, i.e., in the regions 3 and 4. Thus we assume that $N_3 = N_4 = N_0$. Hence, we can write

$$\mathbf{D}_{(3)} = \mathbf{D}_{(4)} = \mathbf{D}_{(0)}, \quad \mathbf{K}_{(1,3)} = \mathbf{K}_{(1,4)} = \mathbf{K}_{(1)}, \quad \mathbf{K}_{(2,3)} = \mathbf{K}_{(2,4)} = \mathbf{K}_{(2)}. \quad (27)$$

Furthermore, in the regions 1 and 2, we can define the shorthand notation

$$\mathbf{P}_{(1)} = \mathbf{P}_{(1)}^+(z_2 - z_1) = \mathbf{P}_{(1)}^-(z_1 - z_2), \quad \mathbf{P}_{(2)} = \mathbf{P}_{(2)}^+(z_2 - z_1) = \mathbf{P}_{(2)}^-(z_1 - z_2). \quad (28)$$

With the above notations and after some algebra, we obtain

$$\begin{bmatrix} \mathbf{c}_{(3)}^-(z_1) \\ \mathbf{c}_{(4)}^+(z_2) \end{bmatrix} = \mathbf{S}' \begin{bmatrix} \mathbf{c}_{(3)}^+(z_1) \\ \mathbf{c}_{(4)}^-(z_2) \end{bmatrix} = \begin{bmatrix} \mathbf{S}'_{11} & \mathbf{S}'_{12} \\ \mathbf{S}'_{21} & \mathbf{S}'_{22} \end{bmatrix} \begin{bmatrix} \mathbf{c}_{(3)}^+(z_1) \\ \mathbf{c}_{(4)}^-(z_2) \end{bmatrix} \quad (29)$$

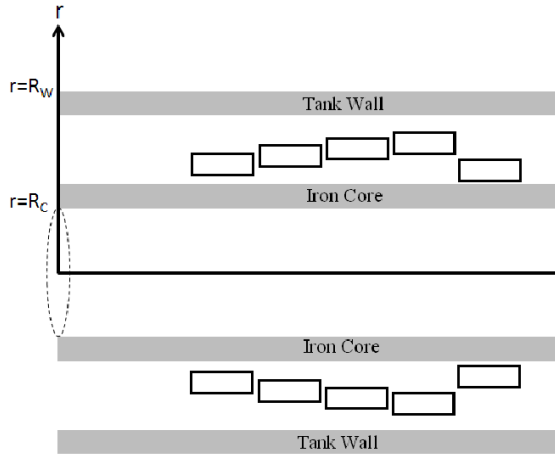


Figure 4: Effective problem geometry.

with

$$\mathbf{S}' = \begin{bmatrix} \mathbf{D}_{(0)} + \mathbf{M} & \mathbf{N} \\ \mathbf{N} & \mathbf{D}_{(0)} + \mathbf{M} \end{bmatrix}^{-1} \times \begin{bmatrix} \mathbf{D}_{(0)} - \mathbf{M} & -\mathbf{N} \\ -\mathbf{N} & \mathbf{D}_{(0)} - \mathbf{M} \end{bmatrix}, \quad (30)$$

where

$$\mathbf{M} = \mathbf{K}_{(1)}^T \mathbf{A}_{(1)} + \mathbf{K}_{(1)}^T \mathbf{P}_{(1)} \mathbf{B}_{(1)} + \mathbf{K}_{(2)}^T \mathbf{A}_{(2)} + \mathbf{K}_{(2)}^T \mathbf{P}_{(2)} \mathbf{B}_{(2)} \quad (31)$$

$$\mathbf{N} = \mathbf{K}_{(1)}^T \mathbf{B}_{(1)} + \mathbf{K}_{(1)}^T \mathbf{P}_{(1)} \mathbf{A}_{(1)} + \mathbf{K}_{(2)}^T \mathbf{B}_{(2)} + \mathbf{K}_{(2)}^T \mathbf{P}_{(2)} \mathbf{A}_{(2)} \quad (32)$$

with

$$\mathbf{A}_{(1)} = (\mathbf{I} - \mathbf{P}_{(1)}^2)^{-1} \mathbf{D}_{(1)}^{-1} \mathbf{K}_{(1)}, \quad \mathbf{B}_{(1)} = (\mathbf{I} - \mathbf{P}_{(1)}^2)^{-1} \mathbf{P}_{(1)} \mathbf{D}_{(1)}^{-1} \mathbf{K}_{(1)}. \quad (33)$$

This scattering Equation (29) describes the propagation over the metal obstacle (from z_1 to z_2). Since the conductor is immersed in a “cell” extending from z_L ($< z_1$) to z_R ($> z_2$), we need to find the scattering matrix for the propagation over the entire “cell”, that is from z_L to z_R . In order to do that, we introduce the matrices

$$\mathbf{P}_L = \mathbf{P}_{(0)}^+ (z_1 - z_L), \quad \mathbf{P}_R = \mathbf{P}_{(0)}^+ (z_R - z_2). \quad (34)$$

Using these matrices, we can write

$$\begin{bmatrix} \mathbf{c}^-(z_L) \\ \mathbf{c}^+(z_R) \end{bmatrix} = \mathbf{S} \begin{bmatrix} \mathbf{c}^+(z_L) \\ \mathbf{c}^-(z_R) \end{bmatrix} = \begin{bmatrix} \mathbf{S}_{11} & \mathbf{S}_{12} \\ \mathbf{S}_{21} & \mathbf{S}_{22} \end{bmatrix} \begin{bmatrix} \mathbf{c}^+(z_L) \\ \mathbf{c}^-(z_R) \end{bmatrix}. \quad (35)$$

Thus we obtain the complete scattering matrix elements for propagation over the entire “cell”, i.e., from z_L to z_R , in the form

$$\mathbf{S}_{11} = \mathbf{P}_L \mathbf{S}'_{11} \mathbf{P}_L, \quad \mathbf{S}_{12} = \mathbf{P}_L \mathbf{S}'_{12} \mathbf{P}_R, \quad \mathbf{S}_{21} = \mathbf{P}_R \mathbf{S}'_{21} \mathbf{P}_L, \quad \mathbf{S}_{22} = \mathbf{P}_R \mathbf{S}'_{22} \mathbf{P}_R. \quad (36)$$

The cascading of one cell denoted by a , with scattering matrix \mathbf{S}^a and situated in the interval $z_1 \leq z \leq z_2$, with a neighboring cell denoted by b , with scattering matrix \mathbf{S}^b and situated in the interval $z_2 \leq z \leq z_3$, gives the following scattering equation:

$$\begin{bmatrix} \mathbf{c}^-(z_1) \\ \mathbf{c}^+(z_3) \end{bmatrix} = \mathbf{S}^c \begin{bmatrix} \mathbf{c}^+(z_1) \\ \mathbf{c}^-(z_3) \end{bmatrix} = \begin{bmatrix} \mathbf{S}_{11}^c & \mathbf{S}_{12}^c \\ \mathbf{S}_{21}^c & \mathbf{S}_{22}^c \end{bmatrix} \begin{bmatrix} \mathbf{c}^+(z_1) \\ \mathbf{c}^-(z_3) \end{bmatrix}, \quad (37)$$

where

$$\mathbf{S}_{11}^c = \mathbf{S}_{11}^a + \mathbf{S}_{12}^a \left(\mathbf{I} - \mathbf{S}_{11}^b \mathbf{S}_{22}^a \right)^{-1} \mathbf{S}_{11}^b \mathbf{S}_{21}^a, \quad \mathbf{S}_{12}^c = \mathbf{S}_{12}^a \left(\mathbf{I} - \mathbf{S}_{11}^b \mathbf{S}_{22}^a \right)^{-1} \mathbf{S}_{12}^b, \quad (38)$$

$$\mathbf{S}_{21}^c = \mathbf{S}_{21}^b \left(\mathbf{I} - \mathbf{S}_{22}^a \mathbf{S}_{11}^b \right)^{-1} \mathbf{S}_{21}^a, \quad \mathbf{S}_{22}^c = \mathbf{S}_{22}^b + \mathbf{S}_{21}^b \left(\mathbf{I} - \mathbf{S}_{22}^a \mathbf{S}_{11}^b \right)^{-1} \mathbf{S}_{22}^a \mathbf{S}_{12}^b. \quad (39)$$

Using the cascading formula (37) with (38)–(39), it is possible to cascade together any number of cells by iteration.

4. OPTIMIZATION RESULTS

The computer simulation geometry of our two-dimensional transformer winding model is shown in Fig. 4. The transformer is modeled as a coaxial waveguide, where the outer cylinder represents the wall of the transformer tank and the inner cylinder represents the iron core that conducts the magnetic flux. As we are mainly concerned with investigating the principles, the chosen dimensions do not correspond to any particular real transformer.

The inverse problem to determine the studied parameters $\mathbf{x} = (r_1, r_2, \dots, r_n)$ is based on minimizing the optimization function J , defined by

$$J(\mathbf{x}) = \sum_{i,j} \left| S_{ij}^{\text{calc}}(\mathbf{x}) - S_{ij}^{\text{meas}} \right|^2, \quad (40)$$

where $S_{ij}^{\text{calc}}(\mathbf{x})$ are the elements of the calculated scattering matrix and S_{ij}^{meas} are the corresponding elements of the measured scattering matrix. In the present paper the studied parameters are the radial positions of the winding segments. The multi-parameter algorithm aiming to minimize $J(\mathbf{x})$ with respect to variation of all radial conductor positions is developed. In order to minimize $J(\mathbf{x})$ with respect to variation of multiple conductor positions, we use a modified steepest-descent optimization method where we first compute the gradient of J , and then seek a minimum of the function by stepping from an initial guess x_0 in the direction of the negative of the gradient. The developed method is programmed to be quasi-genetic, so that if the number of iterations is exceeded and the gradient of J hasn't reached a value near zero, the algorithm restarts itself with a new initial guess. All restarts are saved, and the one with the lowest J -value is printed. Finally, the algorithm can sweep over a range of frequencies.

The optimization model has been tested by comparing our calculated scattering data with synthetic measurement data from the commercial program HFSS. The S -parameters are determined directly using HFSS by defining two ports at the two sides of the waveguide. The results of the comparison of our calculated scattering data with the HFSS synthetic measurement data, for $f = 1200$ MHz, are shown in Table 1.

Table 1: Recreation of 3 cells in Fig. 4, using HFSS data at $f = 1200$ MHz.

Conductor	1	2	3
True \mathbf{x} value	1.5000	1.6000	1.7000
Computed \mathbf{x} value	1.4912	1.6472	1.6627

From the results shown in Table 1 we see that in this case we have a good agreement between the theory and the HFSS data. We note also that our model can in general handle any number of conductor cells.

5. DISCUSSION AND CONCLUSIONS

The present optimization method is quite sensitive to the choice of the initial guess and likely to stop at the local minima. In order to illustrate the differences compared to the parallel-plate waveguide model [3], we can consider a single-cell optimization and compare the examples of J -functions from the parallel-plate waveguide model (Fig. 5(a)) with an example of J -function from the proper coaxial waveguide model presented here (Fig. 5(b)). In both Figs. 5, the global minimum is attained at the correct position of the middle conductor (here zero due to the perfect model).

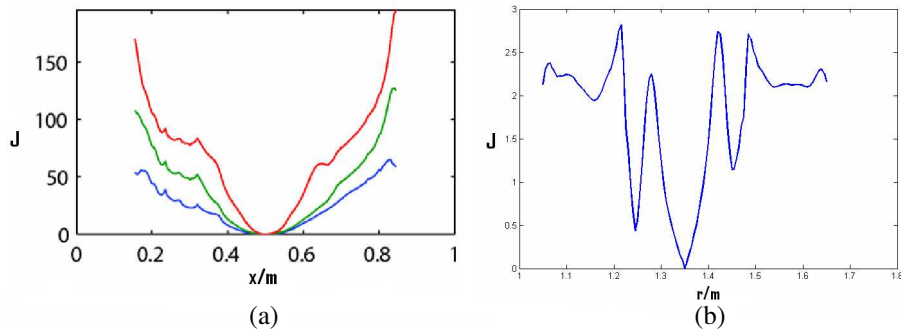


Figure 5: Comparison between the parallel plate waveguide model and the proper coaxial waveguide model.

In the parallel-plate waveguide model, we see that the local minima occurred some distance away from the global minimum, such that a good initial guess, which lies in the global “well”, can make a local optimization method converge towards the global minimum. In the proper coaxial waveguide model presented here, this is not so easy. We note that the local minima are very distinct and give deeper wells such that the use of the same (or slightly modified) optimization algorithm as the one used in [3] easily tends to detect spurious local minima. In some cases of the proper coaxial waveguide model a wider global well could be found while in many practical cases the occurrence of a very close local minima effectively prevents a reliable optimization. It indicates that further efforts are needed to reduce the stochastic behavior of the J -function and develop a more

robust algorithm. Other efficient optimization methods can be considered to improve efficiency and accuracy of the calculations (e.g., the method of conjugate gradients based on the quadratic polynomial fit of J etc.). The study of these potential improvements of the present analysis will be the objective of our continued efforts.

ACKNOWLEDGMENT

This work was funded by the Swedish Energy Agency, Project Nr 34146-1.

REFERENCES

1. Wang, M., A. J. Vandermaar, and K. D. Srivastava, "Review of condition assessment of power transformers in service," Feature Article, *IEEE Electrical Insulation Magazine*, Vol. 18, No. 6, 12–25, Nov./Dec. 2002.
2. Tenbohlen, S., D. Uhde, J. Poittevin, H. Borsi, P. Werle, U. Sundermann, and H. Matthes, "Enhanced diagnosis of power transformers using on- and off-line methods: Results, examples and future trends," *Cigre, Session 2000*, Paper 12-204, 2000.
3. Dalarsson, M., A. Mottevasselian, and M. Norgren, "On using multiple modes to reconstruct conductor locations in a power transformer winding," *PIERS Proceedings*, 516–523, Kuala Lumpur, Malaysia, Mar. 27–30, 2012.
4. Myska, R. and P. Drexler, "Simulation and verification of methods for partial discharge source localization," *PIERS Proceedings*, 704–708, Kuala Lumpur, Malaysia, Mar. 27–30, 2012.
5. Mackenzie, E. A., J. Crossey, A. de Pablo, and W. Ferguson, "On-line monitoring and diagnostics for power transformers," *Conference Record of the 2010 IEEE International Symposium on Electrical Insulation (ISEI)*, 1–5, San Diego, CA, Jun. 6–9, 2010.
6. Shao, Y., Z. Rao, and Z. Jin, "Online state diagnosis of transformer windings based on time-frequency analysis," *WSEAS Transactions on Circuits and Systems*, Vol. 8, No. 2, 227–236, Feb. 2009.
7. Abeywickrama, N., Y. V. Serdyuk, and S. M. Gubanski, "High-frequency modeling of power transformers for use in frequency response analysis (FRA)," *IEEE Trans. on Power Delivery*, Vol. 23, No. 4, 2042–2049, 2008.
8. Colton, D. and R. Kress, *Inverse Acoustic and Electromagnetic Scattering Theory*, Springer, Berlin, 1992.
9. Figure Modified from Open Internet Marketing Presentation by ABB Corporation, "Single phase overhead (polemounted) distribution transformers," Courtesy of ABB Corporation.
10. Figure Modified from Open Marketing Materials by ABB Corporation, "Liquid-filled power transformers," Courtesy of ABB Corporation.
11. Masterman, P. H. and P. J. B. Clarricoats, "Computer field-matching solution of waveguide transverse discontinuities," *Proc. IEE*, Vol. 118, 51–63, 1971.
12. Schelkunoff, S. A., *Electromagnetic Waves*, D. Van Nostrand Company, Inc., New York, 1943.
13. Abramowitz, M. and I. A. Stegun, *Handbook of Mathematical Functions*, Applied Mathematics Series 55, US Department of Commerce, National Bureau of Standards, Washington, D.C., 1964.

The Eigenvalue Problem for a Bianisotropic Cavity

E. Argyropoulou¹ and A. D. Ioannidis²

¹National and Kapodistrian University of Athens, Greece

²Linnaeus University, Sweden

Abstract— We discuss the eigenvalue problem for a perfectly conducting bianisotropic cavity. We formulate the corresponding mathematical problem and we give a characterization of the eigenelements (non-zero eigenfrequencies and modes) via a perturbation argument involving the eigenelements of the hollow cavity.

1. FORMULATION

In this section, we formally deduce the equation that is used in the paper. Our starting point is the source free, time harmonic Maxwell system (time convention is taken to be $e^{-i\omega t}$)

$$i\omega \mathbf{D} = -\operatorname{curl} \mathbf{H}, \quad (1)$$

$$i\omega \mathbf{B} = \operatorname{curl} \mathbf{E}. \quad (2)$$

The fields take values in \mathbb{C}^3 and are functions of the spatial variable $\mathbf{r} \in \Omega$, $\Omega \subset \mathbb{R}^3$ is an open set, and the angular frequency $\omega \in \mathbb{C}$. Equation (1) is Ampère's law and (2) is Faraday's law.

Maxwell's equations are supplemented with the two Gauss laws

$$\operatorname{div} \mathbf{D} = 0, \quad (3)$$

$$\operatorname{div} \mathbf{B} = 0. \quad (4)$$

Note that \mathbf{D} , \mathbf{B} automatically satisfy (3), (4) whenever \mathbf{D} , \mathbf{B} , \mathbf{E} , \mathbf{H} satisfy (1), (2) for $\omega \neq 0$.

We assume that the domain Ω is filled with a bianisotropic material. Materials of this kind are optically active in the sense that they can twist the polarization plane of light in either refraction or transmission. This is a consequence of the fact that electric and magnetic fields are coupled. In this work, we consider the most general case of a linear medium where the constitutive relations, *e.g.*, see [10], are

$$\mathbf{D} = \boldsymbol{\epsilon} \mathbf{E} + \boldsymbol{\xi} \mathbf{H}, \quad (5)$$

$$\mathbf{B} = \boldsymbol{\zeta} \mathbf{E} + \boldsymbol{\mu} \mathbf{H}. \quad (6)$$

The parameters $\boldsymbol{\epsilon}$, $\boldsymbol{\xi}$, $\boldsymbol{\zeta}$ and $\boldsymbol{\mu}$, which characterize the behavior of the material, are 3×3 matrices having as entries complex functions of \mathbf{r} and ω .

In the six vector notation, the problem is stated as follows:

$$i\omega \begin{bmatrix} \boldsymbol{\epsilon} & \boldsymbol{\xi} \\ \boldsymbol{\zeta} & \boldsymbol{\mu} \end{bmatrix} \begin{pmatrix} \mathbf{E} \\ \mathbf{H} \end{pmatrix} = \begin{bmatrix} 0 & -\operatorname{curl} \\ \operatorname{curl} & 0 \end{bmatrix} \begin{pmatrix} \mathbf{E} \\ \mathbf{H} \end{pmatrix}, \quad (7)$$

and can be considered as a generalized eigenvalue problem, where ω acts as the eigenvalue and $(\mathbf{E}, \mathbf{H})^T$ as the eigenvector; observe that the matrix in the left hand side depends on the eigenvalue ω .

To make things more precise, let us denote by $\mathbf{e} := (\mathbf{E}, \mathbf{H})^T$ the electromagnetic (EM) field, by

$$\mathbf{M} = \mathbf{M}(\omega) := \begin{bmatrix} \boldsymbol{\epsilon} & \boldsymbol{\xi} \\ \boldsymbol{\zeta} & \boldsymbol{\mu} \end{bmatrix},$$

the material matrix and by

$$\mathcal{Q} := i \begin{bmatrix} 0 & \operatorname{curl} \\ -\operatorname{curl} & 0 \end{bmatrix}$$

the formal Maxwell operator. With this notation, the formal eigenvalue problem under consideration is written as

$$\mathcal{Q}\mathbf{e} = \omega \mathbf{M}(\omega)\mathbf{e}. \quad (8)$$

2. THE MATHEMATICAL PROBLEM

We are now going to formulate (8) in a Hilbert space setting. We focus in the case of a cavity, and more precisely,

Assumption 1. Ω is a bounded Lipschitz domain in \mathbb{R}^3 .

As a consequence, an exterior normal $\hat{\mathbf{n}}$ is defined on almost all points of Γ . We further assume that the “wall” $\Gamma := \partial\Omega$ is perfectly conducting,

Assumption 2. $\hat{\mathbf{n}} \times \mathbf{E} = \mathbf{0}$ on Γ .

Note that the above assumption also implies that $\hat{\mathbf{n}} \cdot \mathbf{H} = 0$ on Γ . Our exposition and notation generally follows [2]. We work in the product space $\mathcal{X} := L^2(\Omega; \mathbb{C}^3) \times L^2(\Omega; \mathbb{C}^2)$ with its natural inner product. The *curl* operator is understood in the weak sense and, in the same sense, \mathcal{Q} is understood as a maximally defined operator matrix. Namely, the domain of \mathcal{Q} is

$$D(\mathcal{Q}) := H_0(\text{curl}; \Omega) \times H(\text{curl}; \Omega).$$

Proposition 1. \mathcal{Q} is a selfadjoint operator.

Assumption 3. The entries of $\boldsymbol{\epsilon}$, $\boldsymbol{\xi}$, $\boldsymbol{\zeta}$ and $\boldsymbol{\mu}$ are $L^\infty(\Omega)$ functions (with respect to \mathbf{r}).

Corollary 1. M defines a bounded multiplication operator on \mathcal{X} .

Proposition 2. $H^1(\Omega) \hookrightarrow L^2(\Omega)$ with a compact injection.

As a consequence of the above result, the spectrum of \mathcal{Q} is discrete and consists with a sequence of eigenvalues with no accumulation point. Actually, the non-zero eigenvalues of \mathcal{Q} , *i.e.*, the eigenfrequencies of the hollow cavity, appear as a bilateral sequence $(\omega_n^0)_{n \in \mathbb{Z}^*}$, where $(\omega_n^0)_{n \in \mathbb{N}^*}$ is an increasing sequence of non-negative numbers, thus diverging at infinity, and $\omega_{-n}^0 = -\omega_n^0$. Each ω_n^0 , $n \neq 0$, is counted as many times as its multiplicity. $\omega_0^0 := 0$ is always an eigenvalue but needs a special treatment, since the kernel (null space) $\ker \mathcal{Q}$ is infinite dimensional. Nevertheless, divergence free fields in $\ker \mathcal{Q}$ still generate a finite dimensional space, which describes the EM statics in Ω . For a detailed treatment of the matter, we refer to [3], see also [2].

Let us now focus on the corresponding eigenvectors, *e.g.*, see [1, 3] or [4] for a rigorous justification. Let then $\mathbf{e}_n := (\mathbf{E}_n, \mathbf{H}_n)^T$ be the normalized eigenvector corresponding to some ω_n^0 , $n = 1, 2, \dots$, as it is obtained by solving an eigenvalue problem for the minus vector Laplacian:

$$-\nabla^2 \mathbf{E}_n = (\omega_n^0)^2 \mathbf{E}_n \text{ on } \Omega, \quad \text{div } \mathbf{E}_n = 0 \text{ on } \Omega, \quad \hat{\mathbf{n}} \times \mathbf{E}_n = \mathbf{0} \text{ on } \Gamma \quad \text{and} \quad \mathbf{H}_n := \frac{i}{\omega_n^0} \text{curl} \mathbf{E}_n.$$

The eigenvector for $\omega_{-n}^0 = -\omega_n^0$ is then given by $\mathbf{e}_{-n} = (\mathbf{E}_n, -\mathbf{H}_n)$. Eigenvectors corresponding to different eigenvalues are orthogonal, so $(\mathbf{e}_n^0)_{n \in \mathbb{Z}^*}$ can be chosen as an orthonormal sequence.

Let now $\mathcal{H} := [\dots, \mathbf{e}_{-n}, \dots, \mathbf{e}_{-2}, \mathbf{e}_{-1}, \mathbf{e}_1, \mathbf{e}_2, \dots, \mathbf{e}_n, \dots]$, see the following section for the notational conventions. The restriction of \mathcal{Q} on \mathcal{H} is denoted by $\mathcal{Q}_{\mathcal{H}}$.

Proposition 3. $\mathcal{Q}_{\mathcal{H}}$ is a self-adjoint operator in \mathcal{H} and has a compact inverse. The sequence of eigenvalues of $\mathcal{Q}_{\mathcal{H}}$ is $(\omega_n^0)_{n \in \mathbb{Z}^*}$ and the sequence of the corresponding eigenvectors is $(\mathbf{e}_n^0)_{n \in \mathbb{Z}^*}$. The latter is an orthonormal basis for \mathcal{H} .

Then (8) is restricted on \mathcal{H} and is written $\mathbf{e} = \omega \mathcal{Q}_{\mathcal{H}}^{-1} M(\omega) \mathbf{e}$. Let $\mathcal{F}(\omega) := \omega \mathcal{Q}_{\mathcal{H}}^{-1} M(\omega)$; we then conclude to the eigenvalue problem for a linear pencil

$$(I - \mathcal{F}(\omega)) \mathbf{e} = 0. \tag{9}$$

Observe that $\mathcal{F}(\omega)$ is a compact operator in \mathcal{X} , since it is the product of a compact and a bounded operator. Problem (9) can be treated in the spirit of the following section.

3. THE ABSTRACT FRAMEWORK

Let $(X, \langle \cdot, \cdot \rangle)$ be a separable Hilbert space. For a set $U \subset X$, we denote by \overline{U} the closure, by U^\perp the orthogonal complement and by $[U]$ the linear span of U ; the closed linear span is then $\overline{[U]}$. $B(X)$ stands for the Banach algebra of bounded operators in X and $K(X)$ for the ideal of compact operators. Given $T \in B(X)$, we denote by $R(T)$ the range and by $\ker T$ the null space of T . T^* stands for the adjoint operator.

Consider a domain (open and connected set) $D \subset \mathbb{C}$ and an operator-valued function $F : D \rightarrow B(X)$. We have the following important result [9, Theorem VI.14].

Proposition 4. (Analytic Fredholm Alternative) *Let F be analytic and $F(\omega) \in K(X)$ for all $\omega \in D$. Then either*

- a) $I - F(\omega)$ is not injective for every $\omega \in D$, or
- b) $(I - F(\omega))^{-1} \in B(X)$ for all $\omega \in D \setminus S$, where $S \subset \mathbb{C}$ is a countable set without any limit point. In case (b), the operator-valued function $(I - F(\cdot))^{-1}$ is analytic in $D \setminus S$, meromorphic in D and the residues at the poles are finite rank operators.

Practically, the above reads as follows: if one can manage to count out case (a), then equation $F(\omega)x = x$ has non-trivial solutions only for $\omega \in S$. The solutions corresponding to a specific $\omega \in S$ form a finite-dimensional subspace.

Definition 1. Values in S are called eigenvalues of the pencil $I - F(\cdot)$. A non-trivial solution of $F(\omega)x = x$, $\omega \in S$, is called an eigenvector corresponding to ω and the linear span of the eigenvectors is called the eigenspace corresponding to ω .

We now focus in the special case $F(\omega) := AB(\omega)$, $\omega \in D$, where A is a compact self-adjoint operator with dense range and $B(\omega) \in B(X)$. The spectral theorem [5] ensures that A is represented as

$$Ax = \sum_n \lambda_n \langle x, e_n^0 \rangle e_n^0, \quad (10)$$

where (λ_n) is the sequence of (non-zero real) eigenvalues of A , in an absolutely descending order and counted as many times as their multiplicity, and (e_n^0) is the sequence of corresponding eigenvectors. The latter is an orthonormal basis for $\overline{R(A)} = X$. Here we assume that A has infinitely many eigenvalues and thus $\lambda_n \rightarrow 0$.

The problem $F(\omega)x = x$, i.e., $AB(\omega)x = x$, can now be written as

$$\sum_n \lambda_n \langle B(\omega)x, e_n^0 \rangle e_n^0 = \sum_n \langle x, e_n^0 \rangle e_n^0,$$

or, equivalently, as

$$\sum_n \lambda_n \left\langle x, \left(B(\omega) - \frac{1}{\lambda_n} I \right)^* e_n^0 \right\rangle e_n^0 = 0. \quad (11)$$

Let $f_n = f_n(\omega) := (B(\omega) - \frac{1}{\lambda_n} I)^* e_n^0 = (B(\omega)^* - \frac{1}{\lambda_n} I)e_n^0$. The left hand side of (11) is a multiplier operator

$$S = S(\omega) := \sum_n \lambda_n \langle \cdot, f_n \rangle e_n^0,$$

corresponding to sequences $(\lambda_n) \subset \mathbb{R}$, $(f_n) \subset X$, $(e_n^0) \subset X$. S is then an everywhere defined operator (and thus bounded). To say that (11) admits non-trivial solutions is equivalent to S being not injective; in other words, the inverse of S does not exist. The invertibility of multipliers is studied in [11].

Proposition 5. *The following are equivalent:*

- a) S is injective.
- b) (f_n) is a complete sequence, i.e., $\overline{[f_1, f_2, \dots, f_n, \dots]} = X$.
- c) $\langle x, f_n \rangle = 0$ for every n , implies $x = 0$.

Corollary 2. ω is an eigenvalue of $I - F(\cdot)$ if and only if the sequence $(f_n(\omega))$ is not complete. The corresponding eigenspace is $\ker S(\omega)$. Moreover, $x \in \ker S(\omega)$ if and only if $\langle x, f_n(\omega) \rangle = 0$ for every n and, consequently,

$$\ker S(\omega) = [f_1(\omega), f_2(\omega), \dots, f_n(\omega), \dots]^{\perp}.$$

Let us now consider the inverse problem, that is to reconstruct the operator $B(\cdot)$ by the knowledge of the eigenelements of the problem $F(\omega)x = x$. Actually, let us consider an eigenvalue ω and the corresponding eigenspace $\ker S(\omega)$. Then

$$\ker S(\omega)^{\perp} = \overline{[f_1(\omega), f_2(\omega), \dots, f_n(\omega), \dots]},$$

and assume that there is a way to calculate the sequence $(f_n(\omega))$. The straightforward relation

$$\langle B(\omega)e_n^0, e_m^0 \rangle = \langle e_n^0, f_m(\omega) \rangle + \frac{\delta_{nm}}{\lambda_n}, \quad (12)$$

(δ stands for the Kronecker delta) allows the recovery of the operator $B(\omega)$.

4. EIGENFREQUENCIES AND MODES OF THE BIANISOTROPIC CAVITY

We now return to problem (9). In order to apply the results of the previous paragraph, we have to make one additional assumption.

Assumption 4. M is an analytic function $D \ni \omega \mapsto M(\omega) \in B(\mathcal{X})$, where D is a domain in the complex plane, such that $0 \in D$.

The above is a very reasonable assumption, since $M(\omega)$ usually arises by a Fourier transform. Consequently, \mathcal{F} defines an analytic function $D \ni \omega \mapsto \mathcal{F}(\omega) \in K(\mathcal{X})$. Moreover, $\mathcal{F}(0) = 0$ and thus $I - \mathcal{F}(0)$ is invertible. The Analytic Fredholm Alternative then gives

Proposition 6. *The pencil $I - \mathcal{F}(\cdot)$ has countably many eigenvalues with finite dimensional corresponding eigenspaces. They form a sequence (ω_n) of non-zero complex numbers, diverging at infinity.*

Each ω_n is called an eigenfrequency of the cavity and, from the physical point of view, it provides an angular frequency where propagation inside the cavity is possible. The above result reveals that such frequencies exist and are countably many. The eigenvectors corresponding to an eigenfrequency ω_n are called the corresponding modes. Note that $\omega_n \neq 0$ and the corresponding modes satisfy (3), (4), but possible modes corresponding to the static case $\omega_0 = 0$ in general do not; this case needs special treatment.

Let now $\mathcal{A} := \mathcal{D}_{\mathcal{X}}^{-1}$, $B(\omega) := \omega M(\omega)$. The eigenvalues of \mathcal{A} are calculated as follows

$$\lambda_n := \frac{1}{\omega_n^0}, \quad n = \pm 1, \pm 2, \dots,$$

and the sequence of the corresponding eigenvectors is again (e_n) . Consequently, one has the expansion

$$\mathcal{A}x = \sum_{n \in \mathbb{Z}^*} \lambda_n \langle x, e_n^0 \rangle e_n^0.$$

Now $\mathcal{F}(\omega) = \mathcal{A}B(\omega)$ and problem (9) is reformulated with the aim of the multiplier operator

$$\mathcal{S}x = \mathcal{S}(\omega)x := \sum_{n \in \mathbb{Z}^*} \lambda_n \langle x, f_n \rangle e_n^0,$$

where

$$f_n = f_n(\omega) := \left(B(\omega) - \frac{1}{\lambda_n} I \right)^* e_n^0 = (\bar{\omega} M(\omega)^* - \omega_n^0 I) e_n^0, \quad n = \pm 1, \pm 2, \dots$$

Proposition 7. $\omega \neq 0$ is an eigenfrequency of the cavity if and only if $\mathcal{S}(\omega)$ is not an injective operator, if and only if $(f_n(\omega))_{n \in \mathbb{Z}^*}$ is not complete. The corresponding subspace of modes is finite dimensional and is given by

$$\ker \mathcal{S}(\omega) = [\dots, f_{-n}(\omega), \dots, f_{-2}(\omega), f_{-1}(\omega), f_1(\omega), f_2(\omega), \dots, f_n(\omega), \dots]^\perp.$$

Moreover, the following equality applies

$$\langle M(\omega)e_n^0, e_m^0 \rangle = \frac{1}{\omega} (\langle e_n^0, f_m(\omega) \rangle + \omega_n^0 \delta_{nm}),$$

from which the material matrix can be recovered.

5. CONCLUSION

This paper discusses the rigorous mathematical formulation of the eigenvalue problem for the perfect conducting bianisotropic cavity. More precisely, we prove that under appropriate mild assumptions on the material matrix, the cavity has an infinite countable number of non-zero eigenfrequencies with no accumulation point. For each eigenfrequency, there is a finite number of corresponding modes for which we provide a characterization by using the eigenelements of the hollow cavity. We also provide an argument for the inverse problem, *i.e.*, how to reconstruct the material matrix by using the eigenelements of the cavity.

ACKNOWLEDGMENTS

The authors would like to thank Professor Ioannis Stratis at Department of Mathematics, National and Kapodistrian University of Athens, Greece for his motivating supervision. ADI also acknowledges inspiring collaboration with Professors Börje Nilsson and Sven Nordebo at Faculty of Technology, Linnaeus University, Sweden. EA's research has been co-financed by the European Union (European Social Fund, ESF) and Greek national funds through the Operational Program "Education and Lifelong Learning" of the National Strategic Reference Framework (NSRF) — Research Funding Program: Heracleitus II. Investing in knowledge society through the European Social Fund.

REFERENCES

1. Aksoy, S. and O. A. Tretyakov, "The evolution equations in study of the cavity oscillations excited by a digital signal," *IEEE Trans. Antennas Prop.*, Vol. 52, No. 1, 2004.
2. Dautray, R. and J. L. Lions, *Mathematical Analysis and Numerical Methods for Science and Technology, Vol. 3: Spectral Theory*, Springer, Berlin, 1990.
3. Costanza, G. and A. D. Ioannidis, *Remarks on the Mathematical Solution of the Hollow Cavity Eigenvalue Problem*, this volume.
4. Geyi, W., "Time-domain theory of metal cavity resonator," *Progress In Electromagnetics Research*, Vol. 78, 219–253, 2008.
5. Helmberg, G., *Introduction to Spectral Theory in Hilbert Spaces*, North Holland, Amsterdam, 1969.
6. Ioannidis, A. D., "On the cavity problem for the general linear medium in electromagnetic theory," *Bull. Greek Math. Soc.*, Vol. 57, 199–209, 2010.
7. Ioannidis, A. D., G. Kristensson, and I. G. Stratis, "On the well-posedness of the Maxwell system for linear bianisotropic media," *SIAM J. Math. Anal.*, Vol. 44, No. 4, 2459–2473, 2012.
8. Omar, A., *Electromagnetic Scattering and Material Characterization*, Artech House, Boston, 2011.
9. Reed, M. and B. Simon, *Methods of Modern Mathematical Physics I: Functional Analysis*, Academic Press, San Diego, 1980.
10. Roach, G. F., I. G. Stratis, and A. N. Yannacopoulos, *Mathematical Analysis of Deterministic and Stochastic Problems in Complex Media Electromagnetics*, Princeton U.P., New Jersey, 2012.
11. Stoeva, D. T. and P. Balazs, "Invertibility of multipliers," *Appl. Comput. Harmon. Anal.*, Vol. 33, 292–299, 2012.

Wide-field Circular SAR Imaging Studies Based on Ground-based Experiments

S. Demirci¹, E. Yigit², B. Yilmaz¹, and C. Ozdemir¹

¹Department of Electrical-Electronics Engineering, Mersin University, Mersin, Turkey

²Vocational School of Technical Sciences, Mersin University, Mersin, Turkey

Abstract— Circular synthetic aperture radar (CSAR) imaging systems collect data by moving the radar antenna along a circular path around the scene. These spotlight systems provide very high resolution imagery due to 360° observation of scenes. Nevertheless, a major challenge inhibiting successful imaging is encountered when the scene's dimension is a significant fraction of the scanning path's radius (i.e., wide-field scenario). In this case, layover effects become more significant and may severely degrade image quality. In this paper, various simulation and real imaging experiments of wide-field CSAR are studied to characterize these effects. A ground-based, short-range scanning system (small LOS distance and small scanning radius) is assumed and two-dimensional (2D) monostatic CSAR imaging of isotropic point targets as well as a real complex target is analyzed to characterize image defocusing effects. The results demonstrate difficulties in obtaining successful 2D representations of targets from a single-pass CSAR data.

1. INTRODUCTION

Circular synthetic aperture radar (CSAR) is a term generally used to refer to synthetic aperture radar (SAR) systems wherein the radar-carrying platform at a fixed height moves along a circular path while the radar beam illuminates the ground region that falls inside the scanning circle [1–4]. Since this type of a spotlight scenario provides observation of targets over a complete azimuthal coverage of 360 degrees, it can achieve highly sharp resolved images when compared to linear SAR scenarios. Additionally, the resolution in vertical direction and hence the height information of the scene can be obtained by the help of a single pass of the radar only.

Despite these unique features, a major challenge for CSAR is encountered while obtaining two-dimensional (2D) images of large scenes. More clearly, if the scene's extent (in any direction) is a significant fraction of the SAR path's radius (i.e., wide-field scenario), various contributions from the scatterers superpose in the same range-azimuth cell, resulting in layover phenomenon [5]. Layover effects actually arise from the 2D representation of a three-dimensional (3D) object and can significantly degrade the SAR imaging quality. In this work, it is aimed to quantify these layover effects through ground-based, short-range (i.e., small LOS distance and small scanning radius) CSAR imaging studies of point targets as well as a complex car vehicle. In all image reconstruction tasks, a spherical back-projection algorithm [6] is used to focus wide-angle CSAR data.

2. IMAGING MODEL FOR A SINGLE-PASS CSAR

Data collection geometry for a single-pass, monostatic CSAR imaging is shown in Figure 1. The antenna and the radar platform located at a fixed height Z_c moves along a circular path with radius R_g while illuminating the desired ground target [1]. Hence, the targets can be observed over a full span of the azimuth (view or aspect) angles, i.e., $\emptyset = 0 \sim 360^\circ$ with this type of scanning geometry. The reflectivity function of the target to be imaged is represented by $g(x, y, z)$ and the line-of-sight (LOS) distance from the antenna to the origin of the target is termed as the slant-range R_0 given as $R_0 = \sqrt{R_g^2 + Z_c^2}$. The corresponding depression (slant) angle θ can be calculated as $\theta = \tan^{-1}(Z_c/R_g)$. The received echo signal at a particular viewpoint (θ, \emptyset) , can then be written for a frequency domain radar system as

$$E_{\theta, \emptyset}(k_r) = \iiint_{-\infty}^{\infty} g(x, y, z) \exp(-jk_r d) dx dy dz \quad (1)$$

where k_r is the radial wavenumber defined for the two-way propagation as $k_r = 4\pi f/c$, f is the frequency, c is the speed of the light and d is the distance from the antenna to the scatterers that

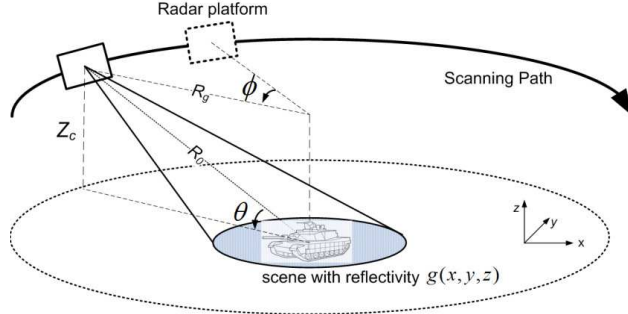


Figure 1: Data collection geometry for a 2D monostatic CSAR imaging.

lie within the radar footprint. Assuming the illuminated target is in the near-field region of the antenna, d can be expressed as

$$d = \sqrt{(x - R_g \cos \theta)^2 + (y - R_g \sin \theta)^2 + (z - Z_c)^2} \quad (2)$$

The range profile $e_{\theta, \phi}(r)$ of the illuminated scene can be obtained by applying one-dimensional (1D) inverse Fourier transform (IFT) to the frequency data given in Equation (1) as follows

$$e_{\theta, \phi}(r) = \iiint_{-\infty}^{\infty} g(x, y, z) \delta(d - r) dx dy dz \quad (3)$$

Equation (3) is the so-called Radon transform of the target scene which represents a projection of the 3D target reflectivity function into a 1D function for that particular viewpoint. Obtaining an estimate of the target reflectivity can then be thought as a process of inverting this transform. This task; however, is known to be a difficult process due to the range-migration effects occurred in wide-angle and/or near-field data collections. Among the SAR imaging methods that fully accounts these effects, and perhaps the most widely used method for this purpose is the back-projection algorithm, sometimes abbreviated BPA [6]. Due to the 2D data collection geometry of the current single-pass scenario, the 2D formulation of this BPA can be readily used to find the reflectivity map on an any desired imaging plane (i.e., focal plane $z_f = z$). The obtained image $g(x, y)$ then represents the projection of the 3D target reflectivity function $g(x, y, z)$ onto that chosen plane, which may utilize major image degradations for wide-field imaging scenarios.

3. SIMULATION RESULT

In the simulation experiment, it was aimed to evaluate the ground-plane imagery of various isotropic point targets located at different heights and locations. The targets were placed at 20 distinct locations of the 3D space as shown in Figure 2(a) and then the backscattering data were acquired for two different values of the depression angle, i.e., $\theta = 23.5^\circ$ and $\theta = 45^\circ$. For the first case, the depression angle value of 23.5° was obtained by setting these values to $Z_c = 9.54$ m and $R_g = 21.9$ m. In the latter case of $\theta = 45^\circ$, both the height Z_c of the radar from the ground and the radius of the

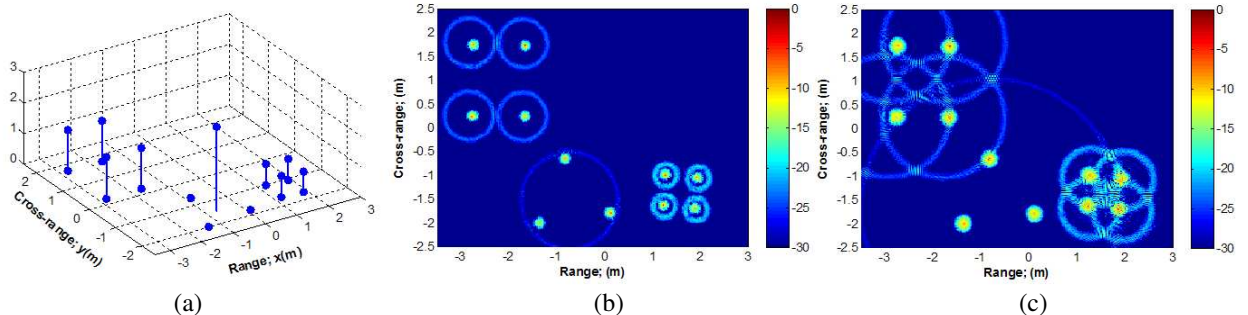


Figure 2: (a) Multiple point targets in 3D space. Ground plane imaging results for the depression angle values of (b) $\theta = 23.5^\circ$ and (c) $\theta = 45^\circ$.

circular path R_g was set to 21.9 m. In both situations, the frequency data were collected within the bandwidth of 4.5 to 6 GHz sampled at 501 points and the azimuth data were collected within the full aperture of 360° sampled with 0.25° steps. The ground plane imaging results obtained by application of the spherical BPA to the simulated data are shown in Figures 2(b) and 2(c). Some observations from these results are as follows: (i) The response is focused when the height of the target z_t is equal to the height of the imaging plane z_f otherwise it is shown up a defocused ring. (ii) As the difference between the z_f and z_t increases, the radius of the defocusing ring increases and its width decreases. (iii) The radius of the defocusing ring is also shown to be larger for the $\theta = 45^\circ$ case.

4. EXPERIMENTAL RESULT

The imaging challenges of wide-field CSAR geometries were also investigated through real CSAR imaging studies. For this purpose, a circular-shaped balcony of a building that is located within the Mersin University campus was exploited to collect single-pass CSAR data. As shown from the schematic diagram given in Figure 3(a), the balcony is at a height of $Z_c = 9.54$ m from the ground surface and has a rotational structure that allows up to 270° azimuthal observations of targets with a scanning radius of $R_g = 21.9$ m. With this geometry, 2D CSAR imaging experiments for various kinds of vehicles were conducted by placing the targets at the center of the scanning circle that is projected onto the ground plane. Considering typical vehicle sizes, this deployed geometry results in a wide-field application such as a target scene with an 4 m radius corresponds to a 18.2% fraction of the scanning path radius. An example imaging result for a sedan car (Scoda Octavia) is shown in Figure 3(b). In data collection, the depression angle was set to $\theta = 23.5^\circ$ and the frequency was stepped from 4.5 to 6 GHz at 501 points while the azimuth angle was varied from 0° to 180° with 0.25° steps. It is shown from Figure 3(b) that the car's shape, especially its front part, is well reconstructed due to the chosen orientation of the target w.r.t. the scanning aperture. The width of the car measured from the obtained image is shown to be in consistent with its true value. This shows that the reconstructed image is not mostly dominated by considerable defocusing effects due to layover. However, the quality of the obtained image is also shown to be worse when compared to the ones obtained in coplanar ISAR imaging, thereby demonstrating the difficulties in obtaining accurate 2D imagery from wide-field CSAR data.

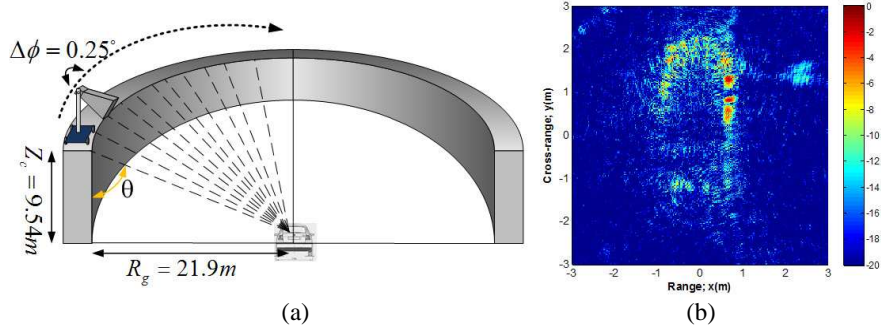


Figure 3: Ground-based CSAR imaging of a sedan car: (a) geometry, (b) BPA imaging result reconstructed from 180° aperture data.

5. CONCLUSIONS

In this paper, the challenges encountered in 2D CSAR imaging of large scenes have studied through numerical as well as real imaging experiments. Simulation results have demonstrated that the imagery possesses ring-shaped defocusing effects when the chosen imaging plane is not equal to the height of the target. Besides, as the difference between the imaging plane and height of the target increases, the radius of this defocusing ring increases while its width decreases. Additionally the radius of the defocusing ring is also shown to be larger for a value of the depression angle that is more closer to 45° . The real experimental result for a complex target has shown that these defocusing effects may not severely affect the whole target identification performance, when the scene radius (in any direction) is not so large w.r.t. the scanning radius and/or when the low values of the depression angle are used in data collection.

REFERENCES

1. Soumekh, M., *Synthetic Aperture Radar Signal Processing with MATLAB Algorithms*, Wiley, New York, 1999.
2. Yu, L. and Y. Zhang, “A 3D target imaging algorithm based on two-pass circular SAR observations,” *Progress In Electromagnetics Research*, Vol. 122, 341–360, 2012.
3. Yan, W., J.-D. Xu, G. Wei, L. Fu, and H.-B. He, “A fast 3D imaging technique for near-field circular SAR processing,” *Progress In Electromagnetics Research*, Vol. 129, 271–285, 2012.
4. Tan, W., W. Hong, Y. Wang, and Y. Wu, “A novel spherical-wave three-dimensional imaging algorithm for microwave cylindrical scanning geometries,” *Progress In Electromagnetics Research*, Vol. 111, 43–70, 2011.
5. Dungan, K. E. and L. C. Potter, “Classifying civilian vehicles using a wide-field circular SAR,” *Algorithms for Synthetic Aperture Radar Imagery XVI, Proc. SPIE*, E. G. Zelnio and F. D. Garber, Eds., Vol. 7337, 2009.
6. Demirci, S., H. Cetinkaya, M. Tekbas, E. Yigit, C. Ozdemir, and A. Vertiy, “Back-projection algorithm for ISAR imaging of near-field concealed objects,” *2011 URSI General Assembly and Scientific Symposium*, Istanbul, Turkey, August 13–20, 2011.

An Accurate High Resolution ISAR Image Reconstruction Method Based on 2-D Nonuniform Fast Fourier Transform

X. Y. He and K. Cai

Science and Technology on Electromagnetic Scattering Laboratory, China

Abstract— We present a new method to reconstruct high resolution inverse synthetic aperture radar (ISAR) images. When the far-field data arranged in the polar format, the two-dimensional (2-D) image can be reconstructed by a 2-D Fourier transform directly. But the fast Fourier transform (FFT) is failed for the data do not falling on a Cartesian grid. We introduce the 2-D nonuniform fast Fourier transform (NUFFT) to reconstruct the ISAR image. It is the first time to use NUFFT technology to achieve ISAR imaging. Instead of interpolating the input data, NUFFT interpolate the exponential function for each sampling point. The technology could easily extend to high dimensional by tensor product. The 2-D NUFFT is very suitable to reconstruct ISAR image. An example will be shown to demonstrate that the reconstructed images have higher resolution than the general method when using the same data.

1. INTRODUCTION

Synthetic aperture radar (SAR) is an instantaneous sensor, which has been wildly used in the complicated civilian and battle environment for the ability of working under almost all weather conditions. The SAR images are powerful visualization tools that can provide high-resolution two dimensional (2-D) electromagnetic (EM) image of an area or a target of interest. There are many different work-modes in SAR system according to different imaging geometric constructions, including strip-map mode, scan mode, spotlight mode, turntable mode, bistatic mode, interference mode, etc. The different imaging algorithm is suitable to different work-mode. For example, the Range-Dopple algorithm is suitable to strip-map mode, the SPECAN algorithm to Scan-SAR mode, the polar format algorithm to spotlight mode and truntable mode (ISAR). From the point of Green function view of the SAR system [1], when the data arranged in the polar format, the Green function could be so simple that a 2-D Fourier transform can achieve the image reconstruction. In the strip-map mode and the spotlight mode, after the spectral analysis [2], the data will be arranged in the polar format. So the polar format algorithm has special significance. Walker et al. discussed the polar format algorithm used in the turntable mode SAR imaging in 1980 [3]. W. G. Carrara et al. used the polar format algorithm in airborne spotlight SAR imaging system [4].

In the polar format, the k -space data do not fall on a Cartesian grid, but collected as a sector, so image reconstruction requires more sophisticated processing techniques rather than a direct 2-D fast Fourier transform (FFT). The general method to evaluate the nonuniform discrete Fourier transform (NUDFT) is linear interpolating the polar data into rectangular format [4]. During polar to rectangular interpolation, the value of each sample on the rectangular output grid obtained from an appropriately weighted neighborhoods of polar input samples. Following the polar interpolation step, the data uniformly resampled in the k -space and 2-D FFT can reconstruct the image. The disadvantages of the method are the numerical error of the interpolation, and the inefficiency of the utilization of data, which deteriorates image resolution.

A fast numerical algorithm named nonuniform fast Fourier transform (NUFFT) [5–12] is more efficient to evaluate the NUDFT. NUFFT calculates complex kernels based on the given sampling pattern to minimize the interpolation error. Instead of interpolating the input data, NUFFT interpolate the exponential function for each sampling point. The NUFFT algorithm has firstly been addressed by Dutt and Rokhlin [5]. Later, Liu and Nguyen optimized the method in the least-square sense [7] and extended it to the multiple dimensions [10–12]. The NUFFT algorithms have been applied to biomedical image reconstruction [11, 12] and subsurface sensing for landmine detection [10]. Here, we successfully applied the 2-D NUFFT algorithm to the ISAR image simulation system and have obtained good results. The reconstructed images have higher resolution than the general method when using the same data.

This paper is organized as follows. In Section 2, the ISAR image reconstruction formula has been stated. In Section 3, we present the details of the derivation of the 2-D NUFFT formulas. In Section 4, the 2-D NUFFT algorithm is introduced to realize the ISAR image reconstruction. Finally we present an example in Section 5, followed by the conclusions and future work.

2. SAR IMAGE RECONSTRUCTION FORMULA

The 2-D object function $O(x, y)$ can be reconstructed through a 2-D Fourier transform of the scattered far-field [13] as Equation (1):

$$O(x, y) = \iint \hat{p} \cdot \mathbf{E}^s e^{-j(k_x x + k_y y)} dk_x dk_y \quad (1)$$

where (k_x, k_y) is the coordinate variables of the k -space, $\hat{p} \cdot \mathbf{E}^s$ is the observed component of the scattered field in the \hat{p} direction (\hat{p} can be $\hat{\theta}$ or $\hat{\phi}$). In the mode of circular monostatic radar, the locus of the backscattering data

$$k_x^2 + k_y^2 = (2k_0)^2 \quad (2)$$

is traced out in the k -space, which defines a circle with radius $2k_0$ and center at origin. k_0 is the incident wavenumber. The collected data arranged as a sector, shown in Figure 1. $\alpha = \text{atan}(k_y/k_x)$ is the incident direction in imaging plane. α_c is the center angle. k_c is the center wavenumber. $\Delta\alpha$ is the width of imaging aperture, Δk is the width of incident wavenumber. The small black dots stand for sampling points. We need only Fourier transforming the data in k -space and the ISAR image will be reconstructed.

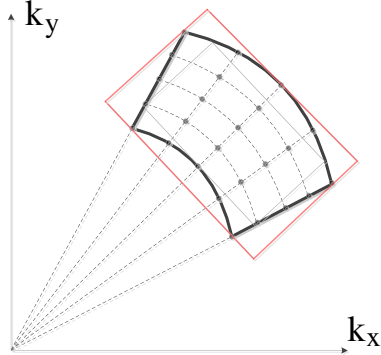


Figure 1: Polar formatting for sample imaging geometry.

3. 2-D NUFFT

The trigonometric functions $e^{-j\omega x}$ are eigen-functions of the differentiation operator and can be effectively used to model solutions of differential equations. Rewrite function (1) into the 2-D discrete form:

$$u(n_1, n_2) = \sum_{l_1=1}^{N_1} \sum_{l_2=1}^{N_2} U(l_1, l_2) e^{-j2\pi v_{l_1} n_1 - j2\pi v_{l_2} n_2} \quad (3)$$

where $n_1 = -N_1/2, N_1/2 - 1, N_1$ is the frequency sampling number, $n_2 = -N_2/2, N_2/2 - 1, N_2$ is the azimuth sampling number. U is the co-polarization far-field data. Normalize $k \cos(\alpha_{l_1})$ and $k \sin(\alpha_{l_1})$ to closed interval $[-1/2, 1/2]$, then ω_{l_1} and ω_{l_2} constituted.

Let $\bar{v} = (v_{l_1}, v_{l_2})$ be the k -space coordinate variables, which is nonuniform as shown in Figure 1, $\bar{n} = (n_1, n_2)$ be the reconstructed image space coordinate variables, which is uniformly grid. The 2-D exponent kernel [8] satisfies Equation (4):

$$s_{\bar{n}} e^{-j2\pi \bar{v} \cdot \bar{n}} = \sum_{\bar{r} \in [-q/2, q/2]^2} \Phi_{\bar{r}}(\bar{v}) e^{-j2\pi([\mu \bar{v}] + \bar{r}) \cdot \bar{n}} \quad (4)$$

where $s_{\bar{n}}$ is a 2-D scaling factor, which controls the calculation accuracy. μ is the oversampling factor, and $(q+1) \times (q+1)$ is the kernel size. $[a]$ denotes the nearest integer of a . Formula (4) is an over-determined set of simultaneous equations. Ref. [8] proposed its least-square solution. The solution of $\Phi_{\bar{r}}$ is the tensor product of 1-D solution in each dimension [10–13].

$$\Phi_{\bar{r}}(\bar{v}) = \Phi_{r_1}(\bar{v}) \otimes \Phi_{r_2}(\bar{v}) \quad (5)$$

The process of solving the 1-D least-square kernel is detailed in [5,8]. We present the result here,

$$\Phi_{r_i}(\bar{v}) = F_i^{-1}\alpha(v_{l_i}) \quad (6)$$

where $i = 1, 2$ denote the two dimension, F_i is a $(q + 1) \times (q + 1)$ Toeplitz matrix which only dependent with (μ, N_i, q) ,

$$F_i = \begin{cases} N_i & m = k \\ \frac{e^{-j\frac{2\pi}{\mu N_i}(m-k)\frac{N_i}{2}} - e^{-j\frac{2\pi}{\mu N_i}(k-m)\frac{N_i}{2}}}{1 - e^{-j\frac{2\pi}{\mu N_i}(k-m)}} & m \neq k \end{cases} \quad m, k = 1, \dots, q+1 \quad (7)$$

Vector $\alpha(v_{l_1})$ will like the following,

$$\alpha_k(v_{l_i}) = -j \left(\frac{\sin\left(\frac{\pi}{2\mu}(2k-1-q-2\{\mu N_i v_{l_i}\})\right)}{1 - e^{-j\frac{\pi}{\mu N_i}(2\{\mu N_i v_{l_i}\}+q-2k+1)}} + \frac{\sin\left(\frac{\pi}{2\mu}(2k+1-q-2\mu N_i v_{l_i})\right)}{1 - e^{-j\frac{\pi}{\mu N_i}(2\{\mu N_i v_{l_i}\}+q-2k-1)}} \right), \quad k=1, \dots, q+1 \quad (8)$$

Substituting (4) into (3), we get the uniform sampling data \tilde{U} . Then use the regular FFT to calculate u ,

$$u = \text{FFT2D}(\tilde{U}) \quad (9)$$

At last, scaling the values lie in $[-\pi, \pi]$ by the accuracy factor,

$$s_{\bar{n}}^{-1} = \sec \frac{\pi n_1}{\mu N_1} \otimes \sec \frac{\pi n_2}{\mu N_2} \quad (10)$$

Suppose N_1 and N_2 being in the same order N , the 2-D NUFFT have a total complexity of $O(\mu^2 \log(\mu^2 N) + 2Nq)$.

4. SAR IMAGE RECONSTRUCTION WITH 2-D NUFFT TECHNOLOGY

We use the 2-D NUFFT to reconstruct the ISAR image with oversampling factor $\mu = 2$, the kernel size $q = 2$. Reference to Figure 1 and the discrete Fourier transform theory, the resolution in range direction is entirely decided by width of frequency,

$$\delta r = \frac{c}{2B} \quad (11)$$

where c is the speed of light in vacuum, and $B = (c\Delta k)/2\pi$. The azimuth resolution is decided by center wavenumber and the synthetic aperture width $\Delta\alpha$,

$$\delta xr = \frac{c}{4f_c \sin \Delta\alpha} \quad (12)$$

The expressions are consisting with the actual measurement experience.

We will show an aircraft as example to demonstrate the mentioned method is suitable to reconstructed ISAR images. We have also calculated the same image by the general interpolation method and used DFT directly. The comparison will show that the NUFFT method have higher resolution than the general method. Two measure of accuracy are defined by the formulae

$$\text{ERR}_{\infty} = \max_{1 \leq j \leq N} |\tilde{u}_j - u_j| / \sum_{j=1}^N |u_j| \quad (13)$$

$$\text{ERR}_2 = \sqrt{\sum_{j=1}^N |\tilde{u}_j - u_j|^2 / \sum_{j=1}^N |u_j|^2} \quad (14)$$

The geometrical model of the aircraft is shown in Figure 2. The center frequency is 30 GHz, pitch angle is 90° , and the center of azimuth angle is 0° . The width of frequency is 1.5GHz which make the range resolution 0.1 m. The azimuth accumulate width is 2.866° which make the azimuth

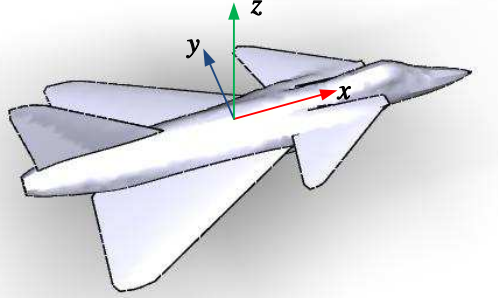


Figure 2: The geometrical model of the aircraft.

resolution 0.1 m too. The three images are reconstructed by 2-D NUFFT, linear interpolation and FFT and DFT, and shown in Figures 3(a), (b) and (c) respectively. The numerical errors between (a) and (c) are $\text{ERR}_{\infty} = 0.0158$, $\text{ERR}_2 = 0.0923$, between (b) and (c) are $\text{ERR}_{\infty} = 0.1723$, $\text{ERR}_2 = 0.8691$. All of the three images can reflect the scattering feature of the target. The 2-D NUFFT method has lower numerical error than the general interpolation method.

The range of data used in 2-D NUFFT technique is the sectors minimum enclosing rectangular, and in interpolation and FFT method is the sectors inscribed rectangular, as shown in Figure 1, which means the range of data used in Figure 3(a) is larger than in Figure 3(b), and result in the resolution of Figure 3(a) is higher than Figure 3(b).

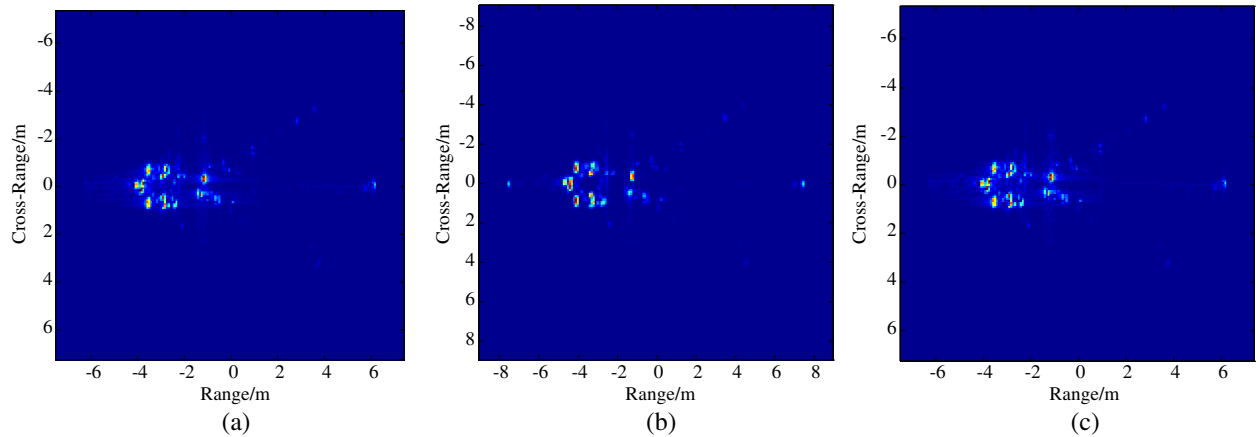


Figure 3: The ISAR images of the aircraft by (a) 2-D NUFFT, (b) interpolation and FFT, (c) DFT.

5. CONCLUSION

Previously, the nonuniform nature of the wavenumber space required interpolation before the regular fast Fourier transform be applied. However, linear interpolation usually degrades the quality of reconstructed images. The NUFFT method mitigates such errors by using high-order spatial-varying kernels. It is the first time to use the 2-D NUFFT in ISAR image reconstruction. The new method makes the ISAR image reconstruction much progress.

REFERENCES

1. Curlander, J. C. and R. N. McDonough, *Synthetic Aperture Radar: Systems and Signal Processing*, John Wiley, Inc., New York, 1991.
2. Sack, M., M. R. Ito, and I. G. Gummung, “Application of efficient linear FM matched filtering algorithms to synthetic aperture radar processing,” *IEE Proc.*, No. 1, 45–57, 1985.
3. Walker, J. L., “Range-doppler imaging of rotating objects,” *IEEE Trans. Aero. And Elec. Sys.*, Vol. 16, No. 1, 23–52, 1980.

4. Carrara, W. G., R. S. Goodman, and R. M. Majewski, *Spotlight Synthetic Aperture Radar: Signal Processing Algorithms*, Artech House, Norwood, MA, 1995.
5. Dutt, A. and V. Rokhlin, "Fast Fourier transforms for nonequispaced data," *SIAM J. Sci. Comp.*, Vol. 14, 1368–1393, 1993.
6. Beylkin, G., "On the fast fourier transform of functions with singularities," *Appl. Comput. Harmonic Anal.*, Vol. 2, 363–382, 1995.
7. Liu, Q. H. and N. Nguyen, "An accurate algorithm for nonuniform fast fourier transforms (NUFFTs)," *IEEE Microw. Guided Wave Lett.*, Vol. 8, No. 1, 18–20, 1998.
8. Nguyen, N. and Q. H. Liu, "The regular fourier matrices and nonuniform fast fourier transforms," *SIAM J. Sci. Comput.*, Vol. 21, No. 1, 283–293, 1999.
9. Fessler, J. A. and B. P. Sutton, "Nonuniform fast Fourier transform using minmax interpolation," *IEEE Trans. Signal Process.*, Vol. 51, No. 2, 560–574, 2003.
10. Song, J., Q. H. Liu, K. Kim, and W. Scott, "High-resolution 3-D radar imaging through nonuniform fast Fourier transform (NUFFT)," *Communications in Computational Physics*, Vol. 1, No. 1, 176–191, 2006.
11. Song, J., Y. Liu, S. L. Gewalt, G. Cofer, G. A. Johnson, and Q. H. Liu, "Least-square NUFFT methods applied to 2-D and 3-D radially encoded mriimage reconstruction," *IEEE Transactions on Biomedical Engineering*, Vol. 56, No. 4, 1134–1142, 2009.
12. He, X. Y., X. B. Wang, X. Y. Zhou, B. Zhao, and T. J. Cui, "Fast ISAR image simulation of targets at arbitrary aspect angles using a novel SBR method," *Progress In Electromagnetics Research B*, Vol. 28, 129–142, 2011.
13. He, X. Y., X. Y. Zhou, and T. J. Cui, "Fast 3D-ISAR image simulation of targets at arbitrary aspect angles through nonuniform fast Fourier transform (NUFFT)," *IEEE Transactions on Antennas and Propagation*, Vol. 60, No. 5, 2012.

Short-range Ground-based SAR Imaging Experiments: Application of Back-projection Algorithm

Enes Yigit¹, Sevket Demirci², Betul Yilmaz², and Caner Ozdemir²

¹Vocational School of Technical Sciences, Mersin University, Mersin, Turkey

²Department of Electrical-Electronics Engineering, Mersin University, Mersin, Turkey

Abstract— In this paper, an experimental study on ground based-synthetic aperture (GB-SAR) radar imagery was accomplished to image terrestrial regions by the help of a GB-SAR data collection setup. Experiments are realized with the help of a Vector Network Analyzer (VNA-Anritsu MS2026C), antennas (C-band), manual controlled rail-scanner, and the control computer. VNA is used as the stepped frequency continuous wave radar system operating between 5 kHz and 6 GHz. GB-SAR image of motor way is reconstructed by applying Back-projection algorithm to the collected data set. Thus, the short-range GB-SAR imaging techniques were investigated through both simulated and real ground-based imaging experiments and some imaging difficulties such as layover effects are exhibited.

1. INTRODUCTION

Synthetic aperture radar (SAR) is an important remote sensing and imaging technique capable of generating high resolution images of stationary target on the ground, and it becomes an important tool in military intelligence, surveillance, and reconnaissance [1, 2]. Since conventional SAR systems has an implementation difficulty, high cost and long data collection time; ground based SAR (GB-SAR) systems; however, are easier to implement, cheaper in hardware and faster in data collection and therefore they become more preferable recently [3, 4]. Also; maintenance and improvement of the system are clearly versatile providing arbitrary choices in frequency, interferometry, polarimetry and incidence angle so, it can be used as a test-bed for an advanced concept design of airborne or space borne SAR system. Unlike conventional SAR systems that observe large regions of earth, GB-SAR systems can acquire high resolution images of interested earth portions of limited sizes. Therefore; it may be used in many specialized applications such as unstable slopes monitoring, environment monitoring, investigation of artificial structures, observation of mature grain and etc. [5, 6]. In spite of these unique features, a major challenge for GB-SAR is encountered while obtaining short range two-dimensional (2D) images of large scenes. The variability of the azimuth resolution in the reconstructed image is the one of the most important effect. This phenomenon resulted from the equation of the range dependent azimuth resolution [7]. In addition to variable azimuth resolution, the flat-ground assumption leads to an effect known as layover. For scatterers outer surface the ground plane, the range measured by each measurement is a bit different than if the target was in the ground plane. In typical airborne SAR situation, a high scatterer such as a mountain or top of skyscraper appears closer to the radar, causing the image of such structures to “layover” towards the radar in the reconstructed imagery [8]. In this work, it is aimed to quantify these layover effects through short-range GB-SAR imaging studies of manmade terrestrial targets. In order to image reconstruction tasks, back-projection algorithm (BPA) [9] is used to focus GB-SAR images.

The outline of the paper is as follows: Section 2 provides the geometry of GB data collection scheme and simulation of the GB-SAR experiment. In Section 3, measurement result of the GB-SAR is presented and the conclusions are given in the last section.

2. SIMULATION RESULTS

In the simulation experiment, it was aimed to evaluate the ground-plane imagery of various isotropic point targets located at different heights and locations. The targets were placed at 11 distinct locations of the 3D space as shown in Figure 1 and then the backscattering data were acquired for two different values of the depression angle, i.e., $\theta = 0^\circ$, $\theta = 45^\circ$ and $\theta = 58^\circ$. For the first case, the depression angle value of $\theta = 0^\circ$ was obtained by setting these values to $Z_1 = 0$ m as it seen in Figure 1(a). In the latter case of $\theta = 45^\circ$ was obtained by setting these values to $Z_2 = 5$ m. And in the third situation the depression angle value of $\theta = 58^\circ$ was obtained by setting these values to $Z_3 = 8$ m as it seen in Figure 1(a). In all situations, the frequency data were collected within the

bandwidth of 3 to 6 GHz sampled at 512 points and the length of synthetic aperture was 10 m for a total 501 discrete points. The ground based imaging results obtained by application of BPA to the simulated data are shown in Figure 2. Some observations from these results are as follows: (i) The response is focused when the height of the target antenna equal to the height of the imaging plane $z = 0$ (see in Figure 2(a)), otherwise it is shown up a defocused effect in range direction which is known as a layover effect. (ii) As the difference between the height of the antenna and imaging plane increases, the distance of the defocusing effect increases as seen in Figures 2(b)–(c). (iii) The distance of the defocusing effect is also shown to be larger for the $\theta = 58^\circ$ case.

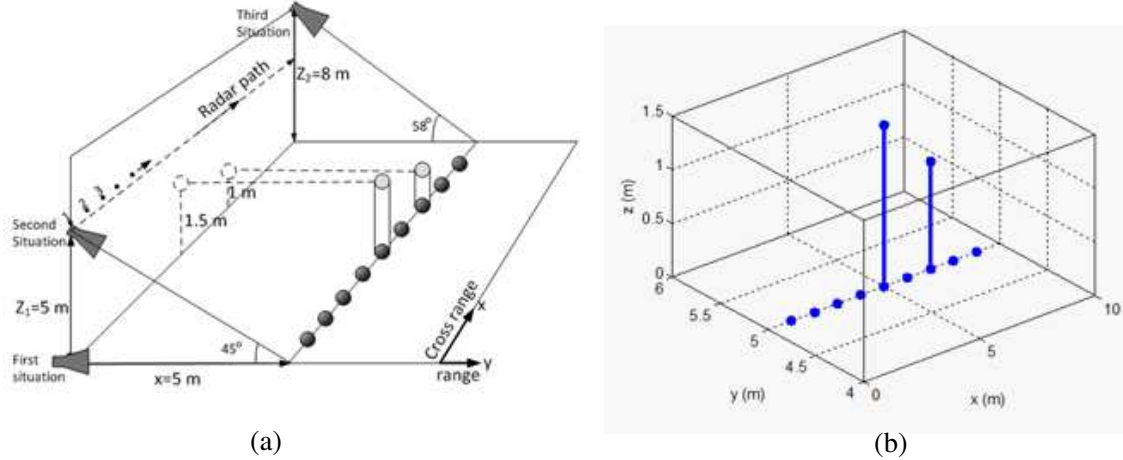


Figure 1: (a) Data collection geometry for a 2D monostatic GB-SAR imaging, (b) multiple point targets in 3D space.

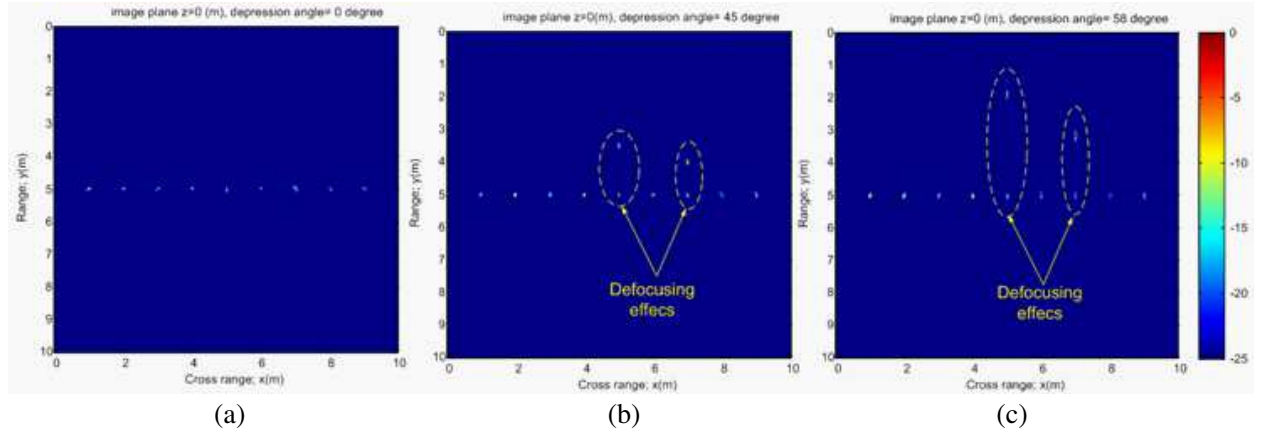


Figure 2: Ground plane imaging results for the depression angle values of (a) $\theta = 0^\circ$, (b) $\theta = 45^\circ$, (c) $\theta = 58^\circ$.

3. MEASUREMENT RESULTS

In order to perform the GB-SAR survey, the measurement setup shown in Figure 3(a) was assembled. The setup consists of Vector Network Analyzer of (VNA-Anritsu MS2026C), antennas (C-band), manual controlled rail-scanner, and the control computer as seen in Figure 3(a). VNA is used as the stepped frequency continuous wave radar system operating between 5 kHz and 6 GHz. The antennas that were used in the quasi-monostatic mode are of pyramidal horn types that have half-power beam widths of approximately 23° at 5 GHz. The system was installed on a balcony of a 9 m-high building and look angle of the antennas were arranged 23° as shown in Figure 3(b). The length of synthetic aperture was 10 m for total of 200 discrete measurement points. The frequency of VNA was altered with 5 MHz discrete steps ranging from 4.5 GHz to 6 GHz for a total of 301 frequencies. The final SAR image of the road, reconstructed by back-projection algorithm (BPA), is shown in Figure 3(c). Some observations from this result are as follows: The responses

from ground targets like rubbish bin, sidewalk and safety zone are focused when the heights of the targets are approximately equal to the height of the imaging plane; otherwise it is shown up a defocused reflection. As seen from the Figure 3(b), the position of the pole is approximately $x = 4.25$ m and $y = 16.5$ m. However; the reflection from the pole is seen approximately at $x = 4.25$ m and $y = 14$ m as seen in Figure 3(c). This is because of the layover effect resulted from height of the pole and depression angle of the antenna. When the depression angle gets closer to the 0° the defocusing distance is also shown to be smaller. Hence, when the short range GB-SAR image is interpreted, this depression angle effect must be taken in to account.

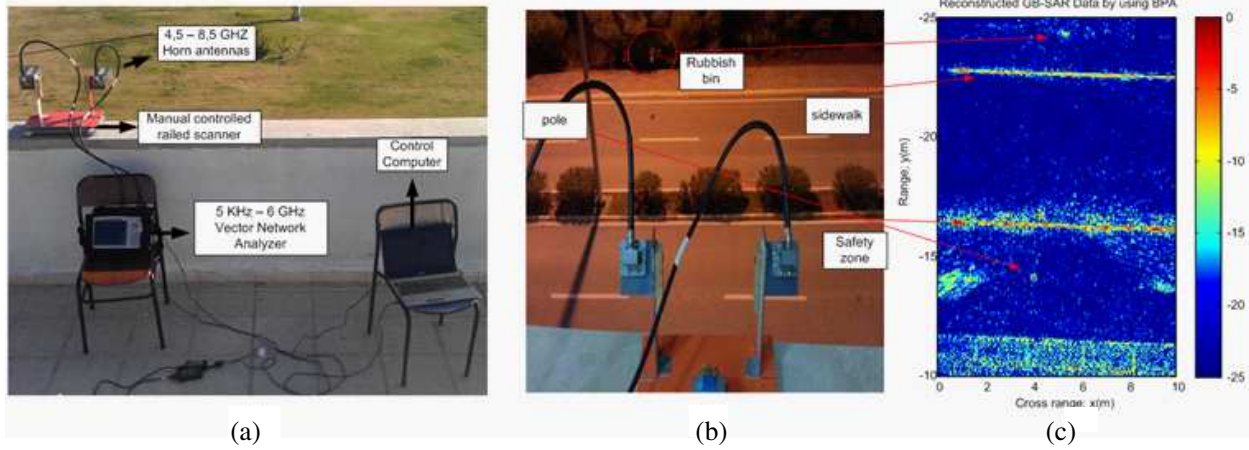


Figure 3: (a) Ground Based SAR imaging setup, (b) the road to be imaged, (c) GB-SAR image of the road.

4. CONCLUSIONS

In this paper, the 2D GB-SAR imaging of large scenes have studied through numerical as well as real imaging experiments. Simulation results have demonstrated that the imagery have defocusing effects when the chosen imaging plane is not equal to the height of the target. Besides, as the difference between the height of the antenna and imaging plane increases, the distance of the defocusing effect increases. Furthermore, the distance of the defocusing effect is also shown to be larger for a higher value of the depression angle. The real experimental result for a GB-SAR data has shown that these defocusing effects on the pole because of its tallness. In addition to these results, the variable azimuth resolution can be noticed when the pole and rubbish bin reflections are compared against each other. Since the rubbish bins location was farther than the pole location with respect to the antenna, the azimuth resolution of the bin is shown worst than the pole. Consequently the short-range GB-SAR imaging techniques were investigated through real, ground-based imaging experiments and some imaging difficulties are exhibited.

REFERENCES

1. Mao, X., D.-Y. Zhu, and Z.-D. Zhu, "Signatures of moving target in polar format spotlight SAR image," *Progress In Electromagnetics Research*, Vol. 92, 47–64, 2009.
2. Chan, Y. K. and V. C. Koo, "An introduction to synthetic aperture radar (SAR)," *Progress In Electromagnetics Research B*, Vol. 2, 27–60, 2008.
3. Cazzani, L., C. Colesanti, D. Leva, G. Nesti, C. Prati, F. Rocca, and D. Tarchi, "A ground-based parasitic SAR experiment," *IEEE Trans. Geosci. Remote Sensing*, Vol. 38, No. 5, 2132–2141, 2000.
4. Cho, B. L., Y. K. Kong, H. G. Park, and Y. S. Kim, "Automobile-based SAR/InSAR system for ground experiments," *IEEE Trans. Geosci. Remote Sensing*, Vol. 3, No. 3, 401–405, 2006.
5. Pieraccini, M., G. Luzi, D. Mecatti, L. Noferini, and C. Atzeni, "Ground-based SAR for short and long term monitoring of unstable slopes," *Proceedings of the 3rd European Radar Conference*, 92–95, 2006.
6. Zhou, Z. S., V. Boerner, and M. Sato, "Development of a ground-based polarimetric broadband SAR system for non-invasive ground-truth validation in vegetation monitoring," *IEEE Trans. Geosci. Remote Sensing*, Vol. 42, No. 9, 1803–1810, 2004.

7. Yigit, E., S. Demirci, A. Unal, C. Ozdemir, and A. Vertiy, "Millimeter-wave ground-based synthetic aperture radar imaging at short ranges," *Journal of Infrared, Millimeter, and Terahertz Waves*, Vol. 33, No. 12, 1227–1238, December 2012.
8. Luminati, J. E., "Wide-angle multistatic synthetic aperture radar: Focused image formation and aliasing artifact mitigation," Ph.D. Thesis, Department of the Air Force Air University at Air Force Institute of Technology, July 2005.
9. Yiğit, E., Ş. Demirci, C. Özdemir, A. Ünal, and A. Vertiy, "Application of efficient back projection algorithm to millimeter wave ground based synthetic aperture radar systems," *Mediterranean Microwave Symposium (MMS 2012)*, İstanbul, September 2–5, 2012.

Compressed Sensing Based Near-field Inverse Synthetic Aperture Radar Imaging

C. Ozdemir¹, S. Demirci¹, E. Yigit², and B. Yilmaz¹

¹Department of Electrical-Electronics Engineering, Mersin University, Mersin, Turkey

²Vocational School of Technical Sciences, Mersin University, Mersin, Turkey

Abstract— In this paper; the capability of compressed sensing (CS) for near-field inverse synthetic aperture radar (ISAR) imaging is addressed. Considering two-dimensional, millimeter-wave ISAR imaging geometry, a CS-based reconstruction technique is developed and its potential is assessed through numerical simulations and measurements applied to hypothetical as well as various complex targets. It is shown for most cases that the target shapes can be accurately and sufficiently reconstructed from a very low number of samples of the whole collected data (e.g., 1.7%) thereby demonstrating the validity of the CS technique. Nevertheless, it is also shown that, the increasing complexity (i.e., low sparsity) of the target scene may somewhat degrade the success of the approach.

1. INTRODUCTION

The newly developed theory of compressed sensing (CS) states that it is possible to reconstruct sparse or compressible signals from a small set of linear measurements [1, 2]. Besides, if properly selected (i.e., random, noisy-like), the number of these measurements can be much smaller than the Nyquist rate, which may then provide distinct advantages over conventional systems in terms of data acquisition and processing. In the context of synthetic aperture radar (SAR), this high under-sampling capability may give rise to a reduction in transmission/reception of radar signals, a reduction in storage constraints, etc.. Consequently, the feasibility of using CS in SAR imaging has become a trending topic and an increasing research has begun to benefit from this new framework. Various SAR imaging modalities have been tested for this purpose. Among these are traditional airborne/spaceborne SAR [3–5], circular SAR (CSAR) [6, 7], ground-penetrating radar (GPR) [8], ground-based linear-SAR [9] and inverse synthetic aperture radar (ISAR) [10]. These studies, however, have shown the application of CS to SAR imaging to be difficult in practice. This is due to the fact that most of the encountered SAR signals have sparsity levels that are not high enough to generate efficient CS solutions. This sparsity, in turn, depends on the utilized imaging geometry, radar parameters and structure and reflectivity of the investigated scene. For example, in conventional SAR imaging, speckle noise and as well as low energy reflection that happens in natural areas may strictly limit the success of the CS method. On the other hand, in turntable-based ISAR or equivalently ground-based annular/circular motion SAR imaging, images usually contain a relatively small number of scattering centers resulting in highly sparse (i.e., compressible) backscattering data. Thus, the CS approach may be readily applied to backscattering data of such scanning geometries to improve data acquisition and processing procedures.

In this contribution, the value of CS in two-dimensional (2D) millimeter-wave ISAR imaging is investigated through both simulation and real imaging experiments. For this task, a CS-based image reconstruction algorithm that uses only very few samples of the whole ISAR data is developed and applied to W-band backscattering data of various targets collected over wide angular apertures. In all examples, near-field illumination is assumed and the results for an imaging procedure based on a spherical back-projection algorithm [11] are also presented for comparison purposes. The outline of the paper is as follows: Section 2 provides a brief formulation of the CS-based ISAR imaging algorithm. In Section 3, the validation results of the proposed algorithm are demonstrated for hypothetical and real targets. Conclusions are given in the last section.

2. COMPRESSED SENSING BASED IMAGING OF ISAR DATA

2.1. ISAR Signal Model

Data collection geometry for a 2D monostatic ISAR measurement set-up is shown in Figure 1. The target is represented by a reflectivity function $\sigma(x, y)$ and is assumed to be in the near-field of the antenna positioned at the Cartesian coordinates of $(x, y) = (R \cos \theta, R \sin \theta)$ where R is the range from the antenna location to the scene center (i.e., coordinate origin) and θ is the instantaneous

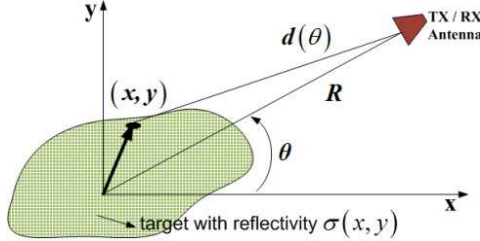


Figure 1: Data collection geometry for a 2D monostatic ISAR imaging.

look-angle. Let's assume that the frequency (wavenumber) and the angular data is collected for a total of K and L points respectively, thereby producing a $K \times L$ size matrix data of the echo signal $\mathbf{y}(\mathbf{k}, \theta)$. Representing the imaging area with $M \times N$ pixels, the received signal at a particular measurement point (k_u, θ_v) can be expressed as

$$y(k_u, \theta_v) = \sum_{n=1}^N \sum_{m=1}^M \sigma(x_{mn}, y_{mn}) \cdot \exp\{-jk_u d_{mn}(\theta_v)\} \quad (1)$$

where (x_{mn}, y_{mn}) denotes the pixel coordinates, k is the wavenumber defined for the two-way propagation as $k = 4\pi f/c$, f is the frequency, c is the speed of light, $d_{mn}(\theta_v)$ is the near-field range from antenna to the pixel point given as $d_{mn}(\theta_v) = \sqrt{(x_{mn, \theta_v} - x)^2 + (y_{mn, \theta_v} - y)^2}$, $u = 1, 2, \dots, K$ and $v = 1, 2, \dots, L$. Let's define $\mathbf{A} \in \mathbb{C}^{KL \times MN}$ as the measurement matrix of the echo signal with elements $A_{uv}(x_{mn}, y_{mn}) = \exp\{-jk_u R_{mn}(\theta_v)\}$ and reshape 2D matrices $\mathbf{y} \in \mathbb{C}^{K \times L}$ and $\boldsymbol{\sigma} \in \mathbb{C}^{M \times N}$ as one-dimensional (1D) vectors that are formed by stacking their columns. In this case, Equation (1) can be written in vector form as

$$\mathbf{y} = \mathbf{A}\boldsymbol{\sigma} \quad (2)$$

2.2. Compressed Sensing for ISAR Imaging

Let's assume that the target reflectivity σ is an S -sparse vector that can be expressed in an orthonormal basis $\Psi \in \mathbb{C}^{MN \times MN}$ as $\sigma = \Psi\alpha$ where α is the coefficient sequence of σ whose non-zero entries represent the S strongest scattering centers. So, the linear representation model of the measured signal given in Equation (2) can be written as $y = \mathbf{A}\Psi\alpha$. Now, according to the CS theory, it is possible to reconstruct the sparse vector α with a very small number of samples of the measured signal y . For this purpose, $J(S \leq J \ll KL)$ rows of the measurement matrix \mathbf{A} and corresponding values of y can be selected randomly which yields to new signal model for CS reconstruction given as

$$y_p = \Phi \mathbf{A} \Psi \alpha = \Theta \alpha \quad (3)$$

where $\Phi \in \mathbb{R}^{J \times KL}$ is the orthonormal basis matrix formed by random selection of the J rows of a $KL \times KL$ size identity matrix and Θ is the final measurement matrix. With this constructed model for the ISAR echo signal, a sparse approximation of the unknown vector α can be found via either solving an optimization problem with ℓ_1 -norm or by using a one kind of greedy algorithm. Finally, the desired complex reflectivity function σ can be subsequently derived from the found solution.

3. RESULTS

The validity of the proposed CS-based imaging technique was tested through simulation and experimental imaging examples. In all examples, wide-angle near-field ISAR data collection geometry was assumed together with millimeter-wave usage. The sparse approximations of the target reflectivity functions were found by using a widely-known greedy reconstruction algorithm, namely COSAMP [12].

3.1. Numerical Simulated Results

A hypothetical target model for an *f-35* aircraft was constructed with ideal point scatterers of equal magnitudes as shown in Figure 2(b). In collection, frequency f was varied from 37.5 to 42.5 GHz for a total of 401 sampling points and azimuth angle θ was varied between 0 to 180° for a total of 721 sampling points, thereby producing $K \times L = 289121$ distinct measurements of (f, θ) pair. The imaging result for the BP algorithm and full data usage case is shown in Figure 2(a), while the CS

result obtained by using only the 2200 random samples of the whole data is shown in Figure 2(c). It is shown that the CS image is sufficiently accurate and precise to identify the target shape.

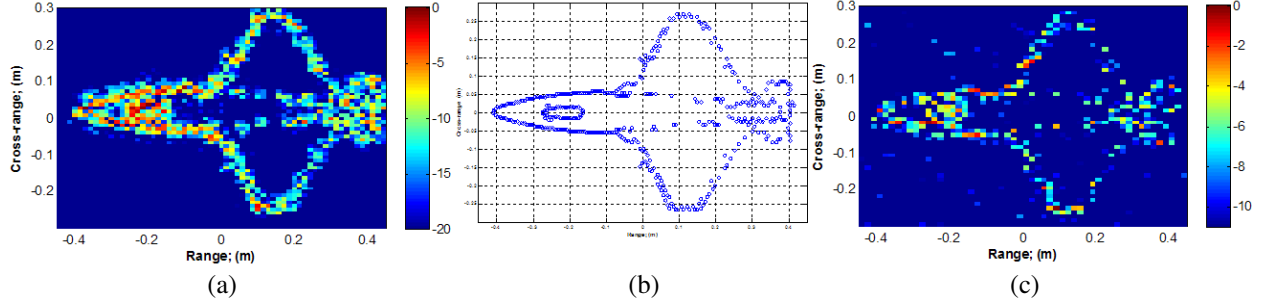


Figure 2: Images for the simulation target. (a) BP result, (b) point scatterer model, (c) CS result.

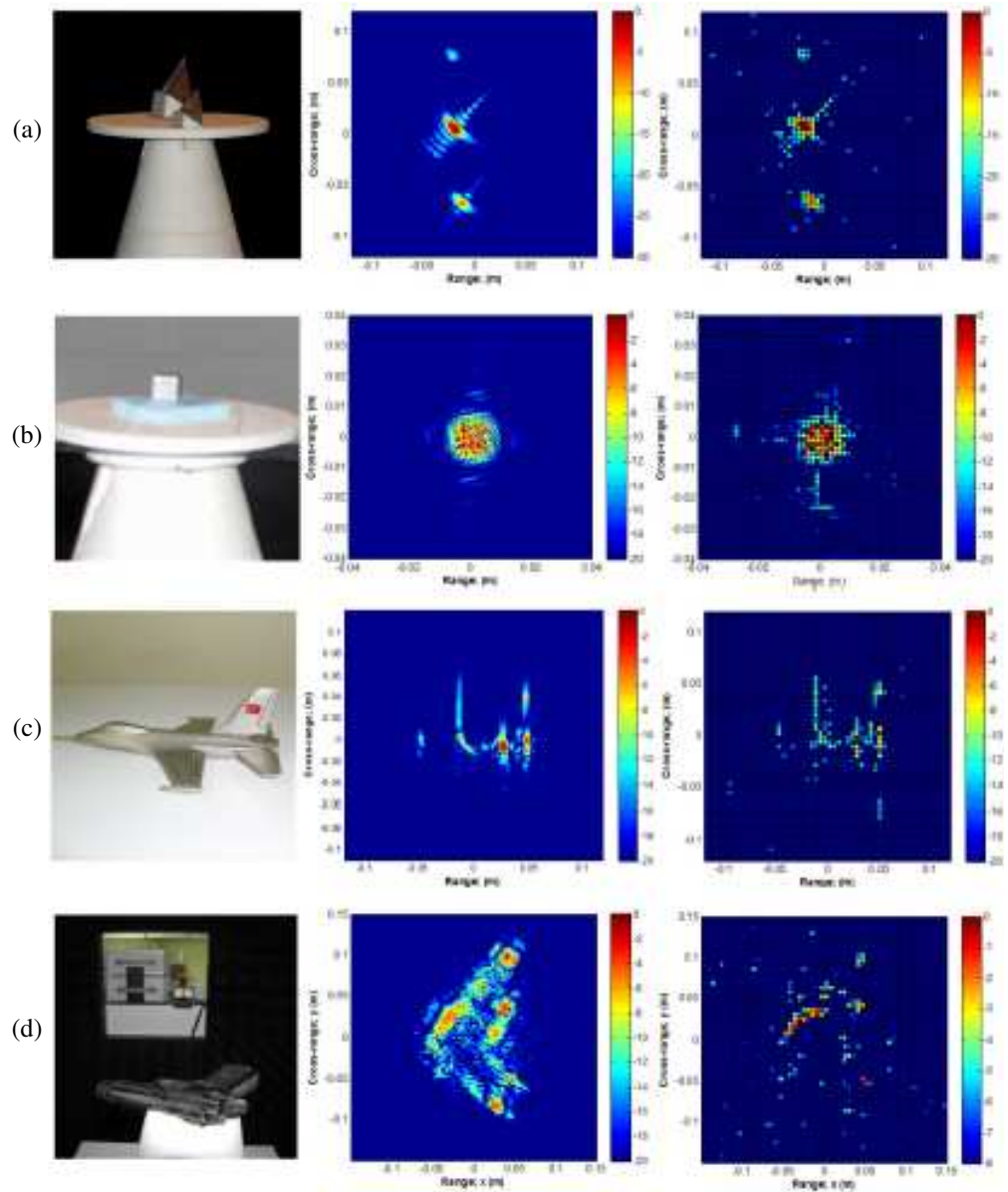


Figure 3: Photos and imaging results of various target scenes (left: sample photo of the target scene, middle: BP result, right: CS result). (a) Two corner reflectors, (b) 1 cm³ metal cube, (c) an aircraft prototype, (d) a handgun.

Compared to the BP result, the CS image is also shown to have better resolution characteristics.

3.2. Experimental Measured Results

To experimentally verify the validity of the CS technique, real ISAR data of various test objects were acquired within the indoor anechoic chamber facility of the *International Laboratory for High Technologies (ILHT) at Scientific and Research Council of Turkey-Marmara Research Center (TUBITAK-MRC)*. The investigated targets whose pictures are shown in the left-column figures of Figure 3 are; two corner reflectors, 1cm³ metal cube, a prototype of an f-16 aircraft and a handgun. In all experiments, antenna-to-target distance was kept fixed to a value of 1.3 m and the bandwidths and the sampling intervals of frequency/angular measurements were selected appropriately that all satisfy the Nyquist criteria. The corresponding ISAR images obtained by applying the BP algorithm to the full data set are shown in the middle-column figures of Figure 3 whereas CS-based imaging results are shown in the right-column figures. The percentages of the ratio of the echo samples used in CS-based reconstructions to the total number of corresponding whole data are; 9.4% for reflector targets, 6.29% for the cube target, 9.4% for the aircraft target and 1.68% for the gun target. It can be commented that, the CS method provides well reconstructed images except for the one wherein the handgun is the imaging target. Compared to the BP result, the CS result for this case contains considerably less target features. Yet, the strong scattering centers can be clearly identified within the dynamic range. This degradation shows that the performance of the CS method can become worse for a highly complex target.

4. CONCLUSIONS

In this paper, we have demonstrated a CS-based ISAR imaging algorithm that has the capability of forming sufficiently accurate images from a limited number of data samples. The algorithm was tested and validated for varying degrees of the complexity of the test scenes that contain canonical targets such as cube and corner reflectors and as well as more complex targets such as an aircraft prototype and a handgun. The algorithm is shown only to have difficulties while reconstructing the weak scatterings of the handgun target, though the dominant scatterings are precisely imaged.

ACKNOWLEDGMENT

The authors are grateful to International Laboratory for High Technologies (ILHT) of TUBITAK Marmara Research Center for providing laboratory facilities for the conducted experiments. The authors also wish to acknowledge ILHT employees; Mr. Harun ÇETINKAYA and Mr. Mustafa TEKBAS for their contributions to the experimental study.

REFERENCES

1. Candes, E., J. Romberg, and T. Tao, "Stable signal recovery from incomplete and inaccurate measurements," *Commun. Pur. Appl. Math.*, Vol. 59, No. 8, 1207–1223, 2006.
2. Donoho, D. L., "Compressed sensing," *IEEE Transactions on Information Theory*, Vol. 52, 1289–1306, 2006.
3. Stojanovic, I., W. C. Karl, and M. Cetin, "Compressed sensing of mono-static and multi-static SAR," *Proc. Algorithms Synthetic Aperture Radar Imagery XVI, SPIE*, 7337, 2009.
4. Bhattacharya, S., T. Blumensath, B. Mulgrew, and M. Davies, "Fast encoding of synthetic aperture radar raw data using compressed sensing," *The 2007 IEEE Workshop on Statistical Signal Processing*, 448–452, Madison, USA, August 2007.
5. Rilling, G., M. Davies, and B. Mulgrew, "Compressed sensing based compression of SAR raw data," *Signal Processing with Adaptive Sparse Structured Representations — SPARS'09*, Saint-Malo (F), 2009.
6. Wei, S.-J., X.-L. Zhang, J. Shi, and G. Xiang, "Sparse reconstruction for SAR imaging based on compressed sensing," *Progress In Electromagnetics Research*, Vol. 109, 63–81, 2010.
7. Yu, L. and Y. Zhang, "Random step frequency CSAR imaging based on compressive sensing," *Progress In Electromagnetics Research C*, Vol. 32, 81–94, 2012.
8. Gurbuz, A. C., J. McClellan, and R. Scott, Jr., "A compressive sensing data acquisition and imaging method for stepped frequency GPRs," *IEEE Transactions on Information Theory*, Vol. 57, 2640–2650, 2009.
9. Wei, S.-J., X.-L. Zhang, and J. Shi, "Linear array SAR imaging via compressed sensing," *Progress In Electromagnetics Research*, Vol. 117, 299–319, 2011.

10. Patel, V. M., G. R. Easley, D. M. Healy, Jr., and R. Chellappa, “Compressed sensing for synthetic aperture radar imaging,” *IEEE International Conference on Image Processing (ICIP 2009)*, 2141–2144, Cairo, Egypt, 2009.
11. Demirci, S., H. Cetinkaya, E. Yigit, C. Ozdemir, and A. A. Vertiy, “A study on millimeter-wave imaging of concealed objects: Application using back-projection algorithm,” *Progress In Electromagnetics Research*, Vol. 128, 457–477, 2012.
12. Needell, D. and J. A. Tropp, “CoSaMP: Iterative signal recovery from incomplete and inaccurate samples,” *Appl. Comput. Harmon. A*, Vol. 26, No. 3, 301–321, 2009.

Huynen Dichotomy-based Radar Target Adaptive Extraction

Dong Li and Yunhua Zhang

Key Laboratory of Microwave Remote Sensing
Chinese Academy of Sciences, Beijing 100190, China

Abstract— Huynen dichotomy is extended to the scattering scenarios of irregularity and non-symmetry for a Huynen canonical dichotomy and further for a generalized Huynen dichotomy based on the wave dichotomy and N -target invariance. The generalized dichotomy includes nine dichotomy sub-algorithms which cover all of the existing Huynen-like dichotomies and can achieve a good consistency with the Cloude decomposition on the extraction of single target scattering. By adaptively filtering the noisy scattering, the dichotomy can well strengthen the target scattering.

1. INTRODUCTION

It was Dr. J. R. Huynen [1] in 1970 who first introduced the concept of target decomposition, since then this area has been attracting extensive focuses particularly after the invention of PolSAR. Huynen dichotomy corresponds to the real world of symmetry and regularity, however, it has not been used in practice as widely as its theoretic reputation because it cannot obtain stable and unique decomposition for some real radar targets. Besides this, there still exist other target dichotomies such as the Holm-Barnes decomposition and Yang decomposition. We consider the main reason restricting the application is its preference for symmetry and regularity but many radar targets are not such ideal [2]. This paper thus develops a generalized Huynen dichotomy in consideration of the integrated target scattering scenarios of symmetry, regularity, non-symmetry, irregularity, and their hybrids. It is hoped to unify the existing Huynen-like target dichotomies and be well used for adaptive target extraction.

The rest of the paper is arranged as follows. Section 2 gives a concise review on the existing Huynen-like target dichotomies, and the generalized dichotomy is presented in Section 3. Section 4 tests the algorithm on the real PolSAR data, and the paper is finally concluded in Section 5.

2. THE HUYNEN-LIKE DICHOTOMY OF RADAR TARGET

Huynen initiated the decomposition by first formulating the physical realizability conditions on Kennaugh matrix for both the single and distributed targets. The obtained conditions can be equivalently expressed by the target coherence matrix. When the target scattering is measured through the reciprocal propagation medium by monostatic radar, the Hermitian coherence matrix \mathbf{T} can be expressed as:

$$\mathbf{T} = \langle \mathbf{k} \cdot \mathbf{k}^H \rangle = \begin{bmatrix} 2A_0 & C - jD & H + jG \\ C + jD & B_0 + B & E + jF \\ H - jG & E - jF & B_0 - B \end{bmatrix} \quad (1)$$

where \mathbf{k} is the Pauli vector of \mathbf{T} , $\langle \dots \rangle$ denotes the ensemble average, and the nine parameters on the right side are called the “Huynen parameters”, which contain the physical information of radar targets and are useful for general analysis without reference to any scattering model. According to Huynen phenomenological theory [1], parameters A_0 , $B_0 + B$, and $B_0 - B$ are the generators of target symmetry/regularity, irregularity, and non-symmetry, respectively, and the others denote the pairwise couplings among the three generators. As for the single target, the ensemble average operation in (1) can be removed, and the physical realizability of single target Kennaugh matrix derived by Huynen is equivalent to requiring coherence matrix \mathbf{T} be of rank one, thus there exist nine equations among the Huynen parameters because all the nine second-order minors of \mathbf{T} should be zero, but only five of them are independent. Thus we can extract the following three condition

groups:

$$\begin{cases} \begin{aligned} 2A_0(B_0 - B) &= H^2 + G^2 \\ 2A_0(B_0 + B) &= C^2 + D^2 \\ 2A_0(E + jF) &= (C + jD)(H + jG) \end{aligned} \end{cases} \quad \begin{cases} \begin{aligned} 2A_0(B_0 - B) &= H^2 + G^2 \\ (B_0 - B)(B_0 + B) &= E^2 + F^2 \\ (B_0 - B)(C - jD) &= (H + jG)(E - jF) \end{aligned} \end{cases} \quad (2)$$

$$\begin{cases} \begin{aligned} 2A_0(B_0 + B) &= C^2 + D^2 \\ (B_0 + B)(B_0 - B) &= E^2 + F^2 \\ (B_0 + B)(H + jG) &= (C - jD)(E + jF) \end{aligned} \end{cases}$$

Each group in (2) is self-contained and can independently define a monostatic target structure. From them we can further obtain the following three equations, respectively:

$$\begin{cases} (B_0 - B)(B_0 + B) = E^2 + F^2 \\ 2A_0(B_0 + B) = C^2 + D^2 \\ 2A_0(B_0 - B) = H^2 + G^2 \end{cases} . \quad (3)$$

As for the general distributed target, the physical realizability of Kennaugh matrix is equivalent to requiring the coherence matrix \mathbf{T} be positive semidefinite, and this can be directly obtained from (1). Thus all the three second-order principal minors of \mathbf{T} have to be nonnegative:

$$\begin{cases} (B_0 - B)(B_0 + B) > E^2 + F^2 \\ 2A_0(B_0 + B) > C^2 + D^2 \\ 2A_0(B_0 - B) > H^2 + G^2 \end{cases} . \quad (4)$$

From (3) and (4) we can see that the same four parameters, such as (B_0, B, E, F) , behave differently for the two target scenarios, which are similar to the four components of Stokes vector for the two wave scenarios of full and partial polarizations. The wave dichotomy enables us to always decompose a partially polarized wave Stokes vector as the sum of a fully polarized wave vector and a fully depolarized wave vector. Thus analogous to wave dichotomy, Huynen focused on developing a target dichotomy to decompose the distributed target Kennaugh matrix into the incoherent sum of an equivalent single target Kennaugh matrix and a remnant N -target Kennaugh matrix. Huynen insisted that the real world physically prefers symmetry and regularity, the related parameters $(2A_0, C, D, G, H)$ should be fully reserved in the single target Kennaugh matrix, thus he chose to decompose the parameters (B_0, B, E, F) . Huynen dichotomy can be equivalently expressed on target coherence matrix \mathbf{T}

$$\mathbf{T} = \mathbf{T}_S + \mathbf{T}_N = \begin{bmatrix} 2A_0 & C - jD & H + jG \\ C + jD & B_{0S} + B_S & E_S + jF_S \\ H - jG & E_S - jF_S & B_{0S} - B_S \end{bmatrix} + \begin{bmatrix} 0 & 0 & 0 \\ 0 & B_{0N} + B_N & E_N + jF_N \\ 0 & E_N - jF_N & B_{0N} - B_N \end{bmatrix} \quad (5)$$

where subscripts S and N index the coherence matrix parameters of equivalent single target \mathbf{T}_S and N -target \mathbf{T}_N , respectively, and parameters (B_{0S}, B_S, E_S, F_S) of \mathbf{T}_S can be inverted from the 1st condition group of (2).

Huynen dichotomy has clear physical significance, however, it cannot extract a desired target when $2A_0$, i.e., the first component of \mathbf{T} , is small or even zero. Thus Yang et al. proposed a modified Huynen dichotomy in terms of two simple transforms of Kennaugh matrix [3]. It is shown that the decomposition can achieve consistent target dichotomy even if parameter $2A_0$ is small or null [3]. The N -target coherence matrix \mathbf{T}_N in Huynen dichotomy only contains the non-symmetric and irregular Huynen parameters. From the group structure of SU (2), \mathbf{T}_N is also found to be invariant to antenna rotation [4]. From the invariance, Holm and Barnes found there exist three different target dichotomies with the corresponding single target scattering Pauli vectors shown as follows:

$$\begin{aligned} \mathbf{k}_{\text{Shn1}} &= \frac{1}{\sqrt{2A_0}} \begin{bmatrix} 2A_0 \\ C + jD \\ H - jG \end{bmatrix} & \mathbf{k}_{\text{Shn2}} &= \frac{1}{\sqrt{2(B_0 - F)}} \begin{bmatrix} C - G + jH - jD \\ B_0 + B - F + jE \\ E + jB_0 - jB - jF \end{bmatrix} \\ \mathbf{k}_{\text{Shn3}} &= \frac{1}{\sqrt{2(B_0 + F)}} \begin{bmatrix} C + G - jH - jD \\ B_0 + B + F - jE \\ E - jB_0 + jB - jF \end{bmatrix} \end{aligned} \quad (6)$$

where \mathbf{k}_{Shn1} just corresponds to the single target extracted by Huynen dichotomy. The dichotomies corresponding to \mathbf{k}_{Shn2} and \mathbf{k}_{Shn3} are the Holm-Barnes decompositions I and II.

3. THE GENERALIZATION OF HUYNEN TARGET DICHOTOMY

Huynen dichotomy behaves well on the symmetrical and regular targets, such as the rough extended surface. However, with the development of airborne and spaceborne polarimetric technique, the observable radar targets are not so simple and ideal anymore but of complex irregularity and non-symmetry, such as the crowded forests and buildings, on which Huynen dichotomy will fail. Huynen has pointed out that in these cases the N -target should be focused instead of the single target [1], however, from (5) we can see that the target irregularity- and non-symmetry-related parameters $B_0 + B$ and $B_0 - B$ are not fully reserved in the coherence matrix of N -target but also decomposed into the coherence matrix of the single target. Thus focuses on single target or N -target are all inappropriate to achieve an integrated characterization of radar targets in these cases. Huynen dichotomy should be extended. We still have two inequations in (4) with their corresponding equations shown in (3), thus we can also obtain two other target dichotomies analogous to the wave dichotomy:

$$\mathbf{T} = \mathbf{T}'_{\mathbf{S}} + \mathbf{T}'_{\mathbf{N}} = \begin{bmatrix} 2A_{0S} & C_S - jD_S & H + jG \\ C_S + jD_S & B_{0S} + B_S & E + jF \\ H - jG & E - jF & B_0 - B \end{bmatrix} + \begin{bmatrix} 2A_{0N} & C_N - jD_N & 0 \\ C_N + jD_N & B_{0N} + B_N & 0 \\ 0 & 0 & 0 \end{bmatrix} \quad (7)$$

$$\mathbf{T} = \mathbf{T}''_{\mathbf{S}} + \mathbf{T}''_{\mathbf{N}} = \begin{bmatrix} 2A_{0S} & C - jD & H_S + jG_S \\ C + jD & B_0 + B & E + jF \\ H_S - jG_S & E - jF & B_{0S} - B_S \end{bmatrix} + \begin{bmatrix} 2A_{0N} & 0 & H_N + jG_N \\ 0 & 0 & 0 \\ H_N - jG_N & 0 & B_{0N} - B_N \end{bmatrix}. \quad (8)$$

The dichotomy (7) reserves the non-symmetry-related parameters ($B_0 - B$, E , F , G , H) into the coherence matrix of single target, thus it prefers the non-symmetric target. Based on the reserved parameters and the 2nd condition group of (2), the decomposed parameters ($2A_{0S}$, $B_{0S} + B_S$, C_S , D_S) can be retrieved. The dichotomy (8) reserves the irregularity-related parameters ($B_0 + B$, C , D , E , F) into the single target coherence matrix, it prefers the irregular target. Based on the reserved parameters and the 3rd condition group, the decomposed parameters ($2A_{0S}$, $B_{0S} - B_S$, G_S , H_S) can be retrieved. The dichotomies (7) and (8) along with Huynen dichotomy enable us an adaptive target dichotomy. For a given target coherence matrix \mathbf{T} , we first use the three dichotomies to decompose it for the equivalent single targets $\mathbf{T}_{\mathbf{S}}$, $\mathbf{T}'_{\mathbf{S}}$, and $\mathbf{T}''_{\mathbf{S}}$, respectively. Among them we then select the target whose total power, i.e., the *SPAN* is the maximum as the optimal single target, and we call this algorithm the Huynen canonical dichotomy. It is easy to validate that the dichotomies (7) and (8) are consistent with the Huynen dichotomies of the two modified Kennaugh matrices of Yang decomposition.

The N -target coherence matrices $\mathbf{T}'_{\mathbf{N}}$ and $\mathbf{T}''_{\mathbf{N}}$ are found to be invariant to the absolute phase unitary transform and ellipticity unitary transform, respectively. From the invariance of $\mathbf{T}'_{\mathbf{N}}$, we can also obtain three dichotomies:

$$\begin{aligned} \mathbf{k}_{\mathbf{Shn4}} &= \frac{1}{\sqrt{B_0 - B_0}} \begin{bmatrix} H + jG \\ E + jF \\ B_0 - B \end{bmatrix} & \mathbf{k}_{\mathbf{Shn5}} &= \frac{1}{\sqrt{2A_0 + B_0 + B + 2C}} \begin{bmatrix} 2A_0 + C - jD \\ B_0 + B + C + jD \\ E + H - jF - jG \end{bmatrix} \\ \mathbf{k}_{\mathbf{Shn6}} &= \frac{1}{\sqrt{2A_0 + B_0 + B - 2C}} \begin{bmatrix} 2A_0 - C + jD \\ -B_0 - B + C + jD \\ -E + H + jF - jG \end{bmatrix} \end{aligned} \quad (9)$$

Pauli vector $\mathbf{k}_{\mathbf{Shn4}}$ just corresponds to dichotomy (7). Similarly, according to the invariance of $\mathbf{T}''_{\mathbf{N}}$, we also have:

$$\begin{aligned} \mathbf{k}_{\mathbf{Shn7}} &= \frac{1}{\sqrt{B_0 + B}} \begin{bmatrix} C - jD \\ B_0 + B \\ E - jF \end{bmatrix} & \mathbf{k}_{\mathbf{Shn8}} &= \frac{1}{\sqrt{2A_0 + B_0 - B + 2H}} \begin{bmatrix} 2A_0 + H + jG \\ C + E + jD + jF \\ B_0 - B + H - jG \end{bmatrix} \\ \mathbf{k}_{\mathbf{Shn9}} &= \frac{1}{\sqrt{2A_0 + B_0 - B - 2H}} \begin{bmatrix} 2A_0 - H - jG \\ C - E + jD - jF \\ -B_0 + B + H - jG \end{bmatrix} \end{aligned} \quad (10)$$

Pauli vector $\mathbf{k}_{\mathbf{Shn7}}$ just corresponds to dichotomy (8). By combining dichotomies (6), (9), and (10), we can also take an adaptive strategy to select the dichotomy among the nine whose single target has the maximum *SPAN* as the optimal dichotomy, and we call it the generalized Huynen dichotomy.

The existing target dichotomies such as Huynen dichotomy, Holm-Barnes decomposition, and Yang decomposition can all be unified in it.

Huynen dichotomy reserves parameter $2A_0$ into the single target, this can be interpreted as the preference for the symmetric and regular targets. The other eight dichotomy sub-algorithms in generalized dichotomy also have certain invariance, thus they prefer the right-wound helicity, left-wound helicity, volume scatterer, horizontal dipole, vertical dipole, irregular dihedral, rotated horizontal dipole, and rotated vertical dipole, respectively [2].

4. EXPERIMENT AND ANALYSIS

In this section, we test the developed target dichotomy using a PolSAR data acquired by DLR's E-SAR sensor at L-Band over Oberpfaffenhofen, Germany. The Pauli RGB presentation of the data is displayed in Figure 1(a). The single targets extracted by the generalized Huynen dichotomy is displayed in Figure 1(b). We can see that the generalized dichotomy makes the signature of target scattering much clear by adaptively filtering out the unwanted noise scatterings. This may greatly improve the identification capability for radar targets. Since each of the nine dichotomy sub-algorithms prefers a kind of target scatterings, thus the generalized dichotomy enables us to coarsely attribute a target into nine different classes directly from its coherence matrix. We find that the symmetric and regular targets cover only 47.16% of the Oberpfaffenhofen scene. This means more than half of the scene is inappropriate for Huynen dichotomy, which illustrates why its application is restricted in a sense.

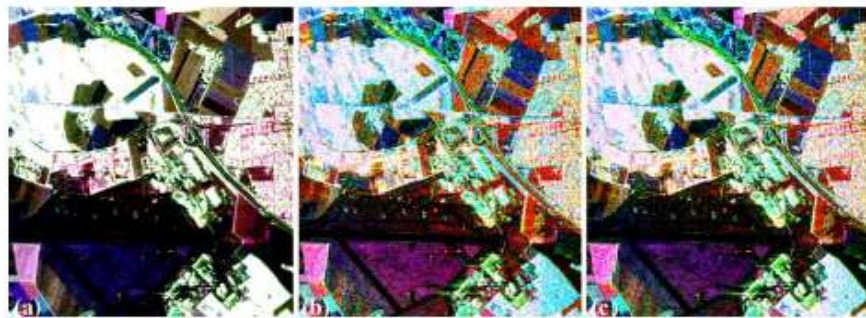


Figure 1: Single target scattering extractions on the Oberpfaffenhofen data. (a) The Pauli image of the original data, and the Pauli images of the extractions from (b) generalized Huynen dichotomy and (c) Cloude decomposition.

To further test the dichotomy, we also process the data with the Cloude decomposition [5] for comparison. The algorithm conducts decomposition via eigendecomposing of target coherence matrix:

$$\mathbf{T} = \sum_{i=1}^3 \lambda_i \mathbf{u}_i \cdot \mathbf{u}_i^H, \quad \mathbf{T}_{\text{Scd}} = \mathbf{k}_{\text{Scd}} \cdot \mathbf{k}_{\text{Scd}}^H = \sqrt{\lambda_1} \mathbf{u}_1 \cdot \sqrt{\lambda_1} \mathbf{u}_1^H, \quad \mathbf{k}_{\text{Scd}} = \sqrt{\lambda_1} \mathbf{u}_1, \quad \lambda_1 \geq \lambda_2 \geq \lambda_3 \quad (11)$$

where λ_i is the i th nonnegative eigenvalue, and \mathbf{u}_i is the corresponding unit eigenvector. Cloude selected \mathbf{u}_1 as the dominant single target scattering because it is the optimal estimation to the single target scattering, and \mathbf{T}_{Scd} is the dominant single target coherence matrix with the Pauli vector of \mathbf{k}_{Scd} . The dominant single target extraction of the Oberpfaffenhofen scene by Cloude decomposition is shown in Figure 1(c). It is nearly the same as the extraction of generalized Huynen. To further validate this consistency, we compare the Huynen-like dichotomies with Cloude decomposition on the extraction of single target Pauli vector at each pixel of Oberpfaffenhofen scene. We compare the moduli of Pauli vector \mathbf{k}_{Shn} extracted by each of the Huynen-like dichotomies which include Huynen dichotomy, Holm-Barnes decompositions I and II, Huynen canonical dichotomy (or Yang decomposition), and the generalized Huynen dichotomy, with the moduli of Pauli vector \mathbf{k}_{Scd} extracted by Cloude decomposition. Figures 2(a), (b), and (c) show the relations between moduli of the three components of \mathbf{k}_{Shn} and moduli of the corresponding components of \mathbf{k}_{Scd} on the whole image, respectively. The relation on the Frobenius norm of the extracted Pauli vectors is shown in Figure 2(d). We can see that from Huynen dichotomy, Holm-Barnes decomposition to Huynen canonical dichotomy, and further to the generalized Huynen dichotomy, a clear convergence to

Cloude decomposition is attained. Especially for the generalized dichotomy, the achieved average relative residue on Frobenius norm between it and Cloude decomposition is just 1.3854%. To eliminate the potential influences from dataset, we also compare the algorithms on the NASA/JPL L-band AIRSAR data of San Francisco, and the similar convergence trend is also clearly observed. It is shown that the average relative residue on the Frobenius norm of Pauli vectors extracted by generalized dichotomy and Cloude decomposition on this data is also as tiny as 0.99%. These observations show that by generalizing the Huynen dichotomy, we can finally yield a consistency with the Cloude decomposition.

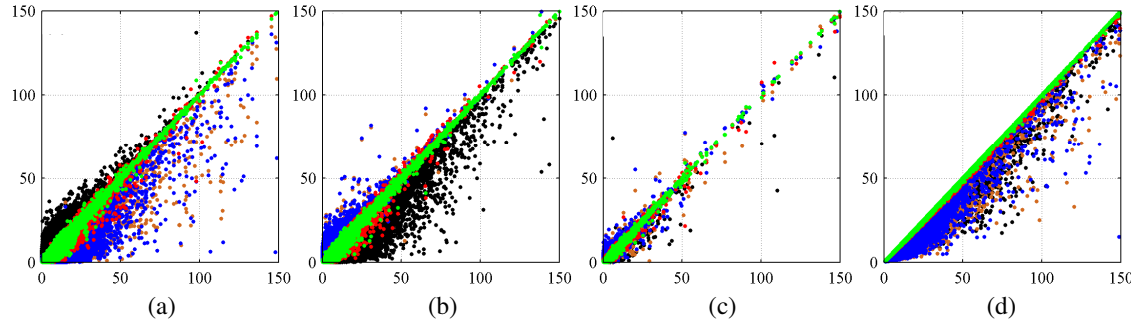


Figure 2: Comparison of the Huynen-like target dichotomies including (black) the Huynen dichotomy, the Holm-Barnes (chocolate) decomposition I and (blue) decomposition II, (red) the Huynen canonical dichotomy or Yang decomposition, and (green) the generalized Huynen dichotomy with the Cloude decomposition on the (a), (b), (c) moduli of the three components and (d) Frobenius norm (F-norm) of the extracted single target Pauli vectors on the Oberpfaffenhofen data.

5. CONCLUSIONS

Huynen dichotomy is the first formalized polarimetric decomposition. But it has not been widely used because it may not obtain stable and unique target dichotomy. We think the main reason restricting its application is the preference for symmetry and regularity. By generalizing the dichotomy to the scattering scenarios of irregularity, non-symmetry, and their hybrids, an adaptive extraction of single radar target scattering scheme is achieved and it is consistent with the Cloude decomposition. From Cloude decomposition, Cloude and Pottier developed the widely-used $H/\bar{\alpha}$ classification. In another paper [6] we will show that the generalized dichotomy can provide us an unsupervised terrain classification scheme which is well consistent with $H/\bar{\alpha}$.

REFERENCES

1. Huynen, J. R., "Phenomenological theory of radar targets," Ph.D. Dissertation, Delft University of Technology, Delft, The Netherland, 1970.
2. Li, D., "Stereo processing and polarimetric analysis of synthetic aperture images," Ph.D. Dissertation, University of Chinese Academy of Sciences, Beijing, China, 2013.
3. Yang, J., Y.-N. Peng, Y. Yamaguchi, and H. Yamada, "On Huynen's decomposition of a Kennaugh matrix," *IEEE Geoscience and Remote Sensing Letters*, Vol. 3, No. 3, 369–372, Jul. 2006.
4. Holm, W. A. and R. M. Barnes, "On radar polarization mixed target state decomposition techniques," *Proceedings of IEEE National Radar Conference*, 249–254, Ann Arbor, MI, 1988.
5. Cloude, S. R., "Target decomposition theorems in radar scattering," *Electronics Letters*, Vol. 21, No. 1, 22–24, Jan. 1985.
6. Li, D. and Y. Zhang, "Huynen dichotomy-based unsupervised terrain classification," *PIERS Proceedings*, Stockholm, Sweden, Aug. 12–15, 2013.

Huynen Dichotomy-based Unsupervised Terrain Classification

Dong Li and Yunhua Zhang

Key Laboratory of Microwave Remote Sensing
Chinese Academy of Sciences, Beijing 100190, China

Abstract— A Huynen target dichotomy-based nine-symbol Bernoulli statistical model is developed to characterize the random scattering of mixed target. From the model two characteristic parameters, i.e., the Huynen alpha angle and the scattering fraction of polarization (*FoP*) are derived which are consistent with the Cloude-Pottier alpha angle and scattering entropy in the identification of scattering mechanism and target randomness, respectively. A Huynen *FoP*/alpha unsupervised terrain classification scheme is finally obtained and demonstrated to be well consistent with the widely-used entropy/alpha classifier.

1. INTRODUCTION

Since Dr. S. R. Cloude proposed using the target coherence matrix to analyze the depolarization phenomena, the decomposition of target Kennnaugh matrix developed by Huynen [1] can be then equivalently transformed to the decomposition of this matrix. By eigendecomposing the matrix, Cloude and Pottier developed a three-symbol Bernoulli random scattering model to probabilistically interpret the mixed target scattering as three single target scatterings represented by the three unit orthogonal eigenvectors of coherence matrix appearing with the probabilities proportional to the eigenvalues [2]. Two parameters, i.e., the $\bar{\alpha}$ angle and the scattering entropy H are then extracted to index the scattering mechanism and randomness, and their combinations construct the $H/\bar{\alpha}$ classification scheme which has been widely used in SAR polarimetry. This paper revisits the Cloude-Pottier decomposition from the viewpoint of Huynen target dichotomy. A nine-symbol Bernoulli statistical modeling of mixed target random scattering is developed, and two parameters, i.e., the Huynen $\bar{\alpha}$ angle and scattering fraction of polarization (*FoP*) are extracted and shown to be consistent with the Cloude-Pottier $\bar{\alpha}$ angle and entropy H in the description of scattering mechanism and target purity. The parameters provide us an unsupervised *FoP*/ $\bar{\alpha}$ classifier which is well agreed with $H/\bar{\alpha}$.

The rest of the paper is arranged as follows. Section 2 concisely presents the Cloude-Pottier decomposition, and Section 3 presents and validates the Huynen *FoP*/ $\bar{\alpha}$ unsupervised classifier. The paper is concluded in Section 4.

2. THE CLOUDE-POTTIER POLARIMETRIC DECOMPOSITION SCHEME

The physical realizability of scattering wave Stokes vector shows that the coherence matrices of mixed target and single target are positive semidefinite and of rank one, respectively. Thus based on the eigendecomposition of coherence matrix \mathbf{T} , the mixed target can be decomposed into the sum of three single targets:

$$\mathbf{T} = \begin{bmatrix} T_{11} & T_{12} & T_{13} \\ T_{21} & T_{22} & T_{23} \\ T_{31} & T_{32} & T_{33} \end{bmatrix} = \sum_{i=1}^3 \mathbf{T}_{\text{Sedi}} = \sum_{i=1}^3 \sqrt{\lambda_i} \mathbf{u}_i \cdot \sqrt{\lambda_i} \mathbf{u}_i^H = \sum_{i=1}^3 \mathbf{k}_{\text{Sedi}} \cdot \mathbf{k}_{\text{Sedi}}^H, \\ \text{with } \mathbf{k}_{\text{Sedi}} = \sqrt{\lambda_i} \mathbf{u}_i, \quad \lambda_1 \geq \lambda_2 \geq \lambda_3 \quad (1)$$

where λ_i is the i th nonnegative real eigenvalue of \mathbf{T} , \mathbf{u}_i is the unit eigenvector and corresponds to a single target coherence matrix \mathbf{T}_{Sedi} with the Pauli vector \mathbf{k}_{Sedi} . Cloude and Pottier gave a statistical interpretation of (1) using a three-symbol Bernoulli scheme, and the mixed target scattering is modeled as three single target scatterings represented by eigenvector \mathbf{u}_i occurring with the probability P_i given by

$$P_i = \frac{\lambda_i}{\sum_{i=1}^3 \lambda_i} \quad \text{with} \quad \sum_{i=1}^3 P_i = 1. \quad (2)$$

Cloude and Pottier found that each eigenvector \mathbf{u}_i in (1) can be parameterized in the following form if a revised Bragg scattering model is considered [2]:

$$\mathbf{u}_i = e^{j\varphi_i} \begin{bmatrix} \cos \alpha_i & \sin \alpha_i \cos \beta_i e^{j\delta_i} & \sin \alpha_i \sin \beta_i e^{j\gamma_i} \end{bmatrix}^T, \quad i = 1, 2, 3. \quad (3)$$

In this way, any target parameter in (3), such as the α angle, can be treated as a random sequence of α_1 , α_2 , and α_3 with the corresponding probabilities of occurrence P_1 , P_2 , and P_3 , thus the best estimation of each target parameter can be obtained by the mean of the sequence [2]:

$$\bar{\alpha} = \sum_{i=1}^3 P_i \alpha_i \quad \bar{\beta} = \sum_{i=1}^3 P_i \beta_i \quad \bar{\delta} = \sum_{i=1}^3 P_i \delta_i \quad \bar{\gamma} = \sum_{i=1}^3 P_i \gamma_i. \quad (4)$$

The $\bar{\alpha}$ angle in (4) is related to the physical scattering mechanism because it corresponds to a continuous change from surface scattering ($\bar{\alpha} = 0^\circ$) to dihedral scattering ($\bar{\alpha} = 90^\circ$) [2]. Thus it can associate observables with the physical properties of target. Besides this, Cloude and Pottier further defined a scattering entropy H [2]:

$$H = - \sum_{i=1}^3 P_i \log_3 P_i. \quad (5)$$

For single target, the entropy H is zero, for the unpolarized target it is 1, and for the partially polarized target it is between 0 and 1. Thus it can describe the purity and disorder of the mixed target scattering [2].

The scattering $\bar{\alpha}$ angle and entropy H compose a 2D $H/\bar{\alpha}$ description plane, as shown in Figure 2(b). Cloude and Pottier further subdivided it into eight effective zones, as indexed by Z1 to Z8. $H = 0.5$ and $H = 0.9$ are selected as the boundaries along the entropy axis; while along the alpha axis, the boundaries are as follows [2]. $\bar{\alpha} = 55^\circ$ for Z1 and Z2, $\bar{\alpha} = 50^\circ$ for Z3 and Z4, $\bar{\alpha} = 40^\circ$ for Z4 and Z5, $\bar{\alpha} = 47.5^\circ$ for Z6 and Z7, and $\bar{\alpha} = 42.5^\circ$ for Z7 and Z8. It is found that each of the partitioned zones can describe a class of different scattering behaviors. Take Z8 as an example, scatterer attributed to this zone has small $\bar{\alpha}$ angle and low entropy, so it corresponds to the low entropy Bragg surface scatterer, such as the rough land and sea surface. It has been validated that these boundaries are not dependent on a particular dataset although there is some degree of arbitrariness on the setting of them [2].

3. THE HUYNEN FoP/ALPHA UNSUPERVISED TERRAIN CLASSIFICATION SCHEME

Huynen dichotomy is the first formalized polarimetric decomposition. But it has not been widely used because it may not obtain stable and unique target dichotomy [3]. A generalized Huynen dichotomy is proposed [4], which includes nine independent target dichotomies with different scattering preference. The equivalent single target scatterings \mathbf{k}_{Shni} of the nine dichotomies are shown in (6), and they provide nine different understandings of the real single target scattering. We further normalize the Pauli vector of each target scattering with its Frobenius norm as shown in (7). In this way, nine unit target vectors are obtained and they can be also parameterized in accordance with the revised Bragg scattering model, as shown in (8). We treat each $\mathbf{k}_{\text{nShni}}$ as a potential form of the original target scattering occurring with the probability P_i shown in (9), where $SPAN_i$ is

the total power of the single target scattering \mathbf{k}_{Shni} and it is the square of the Frobenius norm of

$$\left\{ \begin{array}{l} \mathbf{k}_{\text{Shn1}} = \frac{1}{\sqrt{T_{11}}} \begin{bmatrix} T_{11} \\ T_{21} \\ T_{31} \end{bmatrix} \quad \mathbf{k}_{\text{Shn2}} = \frac{1}{\sqrt{T_{22}+T_{33}-2\text{Im}(T_{23})}} \begin{bmatrix} T_{12}+jT_{13} \\ T_{22}+jT_{23} \\ T_{32}+jT_{33} \end{bmatrix} \\ \mathbf{k}_{\text{Shn3}} = \frac{1}{\sqrt{T_{22}+T_{33}+2\text{Im}(T_{23})}} \begin{bmatrix} T_{12}-jT_{13} \\ T_{22}-jT_{23} \\ T_{32}-jT_{33} \end{bmatrix} \quad \mathbf{k}_{\text{Shn4}} = \frac{1}{\sqrt{T_{33}}} \begin{bmatrix} T_{13} \\ T_{23} \\ T_{33} \end{bmatrix} \\ \mathbf{k}_{\text{Shn5}} = \frac{1}{\sqrt{T_{11}+T_{22}+2\text{Re}(T_{12})}} \begin{bmatrix} T_{11}+T_{12} \\ T_{21}+T_{22} \\ T_{31}+T_{32} \end{bmatrix} \quad \mathbf{k}_{\text{Shn6}} = \frac{1}{\sqrt{T_{11}+T_{22}-2\text{Re}(T_{12})}} \begin{bmatrix} T_{11}-T_{12} \\ T_{21}-T_{22} \\ T_{31}-T_{32} \end{bmatrix} \\ \mathbf{k}_{\text{Shn7}} = \frac{1}{\sqrt{T_{22}}} \begin{bmatrix} T_{12} \\ T_{22} \\ T_{32} \end{bmatrix} \quad \mathbf{k}_{\text{Shn8}} = \frac{1}{\sqrt{T_{11}+T_{33}+2\text{Re}(T_{13})}} \begin{bmatrix} T_{11}+T_{13} \\ T_{21}+T_{23} \\ T_{31}+T_{33} \end{bmatrix} \\ \mathbf{k}_{\text{Shn9}} = \frac{1}{\sqrt{T_{11}+T_{33}-2\text{Re}(T_{13})}} \begin{bmatrix} T_{11}-T_{13} \\ T_{21}-T_{23} \\ T_{31}-T_{33} \end{bmatrix} \end{array} \right. \quad (6)$$

$$\mathbf{k}_{\text{nShni}} = \frac{\mathbf{k}_{\text{Shni}}}{\|\mathbf{k}_{\text{Shni}}\|_F}, \quad i = 1, 2, \dots, 9 \quad (7)$$

$$\mathbf{k}_{\text{nShni}} = e^{j\varphi_i} \begin{bmatrix} \cos \alpha_i & \sin \alpha_i \cos \beta_i e^{j\delta_i} & \sin \alpha_i \sin \beta_i e^{j\gamma_i} \end{bmatrix}, \quad i = 1, 2, \dots, 9. \quad (8)$$

$$P_i = \frac{\text{SPAN}_i}{\sum_{i=1}^9 \text{SPAN}_i} \quad \text{with} \quad \left\{ \begin{array}{l} \text{SPAN}_i = \|\mathbf{k}_{\text{Shni}}\|_F^2 \\ \sum_{i=1}^9 P_i = 1 \end{array} \right. , \quad i = 1, 2, \dots, 9 \quad (9)$$

\mathbf{k}_{Shni} . In this way, the real unit target scattering \mathbf{k}_{nShn} is modeled as a random sequence of $\mathbf{k}_{\text{nShni}}$ with the corresponding probability of occurrence P_i , and we name this the nine-symbol Bernoulli scattering model. Then the best estimation of each target parameters in (8) can be obtained by

$$\bar{\alpha} = \sum_{i=1}^9 P_i \alpha_i \quad \bar{\beta} = \sum_{i=1}^9 P_i \beta_i \quad \bar{\delta} = \sum_{i=1}^9 P_i \delta_i \quad \bar{\gamma} = \sum_{i=1}^9 P_i \gamma_i. \quad (10)$$

It can be easily validated that for the surface scattering the $\bar{\alpha}$ angle in (10) is 0° , for the dihedral scattering the value is 90° , and for the other scattering cases it ranges from 0° to 90° . Thus this $\bar{\alpha}$ angle may be also used to simply identify the mechanism of target scattering. In order to differentiate (10) from the $\bar{\alpha}$ angle (4) proposed by Cloude and Pottier, we call (10) the Huynen $\bar{\alpha}$ angle and (4) the Cloude-Pottier $\bar{\alpha}$ angle hereafter.

Besides this, motivated by the parameter degree of polarization (*DoP*) which is used to evaluate the purity of the polarized wave, here we propose a target scattering fraction of polarization (*FoP*) parameter to indicate the purity and disorder of the mixed target scattering. It is defined as the ratio between the *SPAN* of each of the nine extracted single target scatterings and the *SPAN* of the original mixed target scattering:

$$FoP_i = \frac{\text{SPAN}_i}{\text{SPAN}}, \quad i = 1, 2, \dots, 9. \quad (11)$$

Thus we can obtain the following average estimation of the scattering *FoP*:

$$FoP = \sum_{i=1}^9 P_i FoP_i = \sum_{i=1}^9 \frac{(\text{SPAN}_i)^2}{\text{SPAN} \sum_{i=1}^9 \text{SPAN}_i}. \quad (12)$$

The *FoP* for single target is 1, for unpolarized target it is $1/3$, and for the partially polarized target it is between $1/3$ and 1. Thus *FoP* may characterize the target randomness as the entropy *H* does.

In the following we investigate the relationship between Huynen $\bar{\alpha}$ angle and Cloude-Pottier $\bar{\alpha}$ angle as well as the relationship between *FoP* and entropy *H* on the AIRSAR L-band data of San Francisco. Figures 1(a) and (d) display the $\bar{\alpha}$ angle from Cloude-Pottier and Huynen estimations,

respectively, from which we can see that the two $\bar{\alpha}$ angles behave nearly the same. Figure 2(a) further shows the strong correlation between them. The mean and standard deviation of the residue between the two $\bar{\alpha}$ angles are 0.52° and 2.48° , respectively. Thus we think Huynen $\bar{\alpha}$ angle is a good alternative to Cloude-Pottier $\bar{\alpha}$ angle for identifying the scattering mechanism.

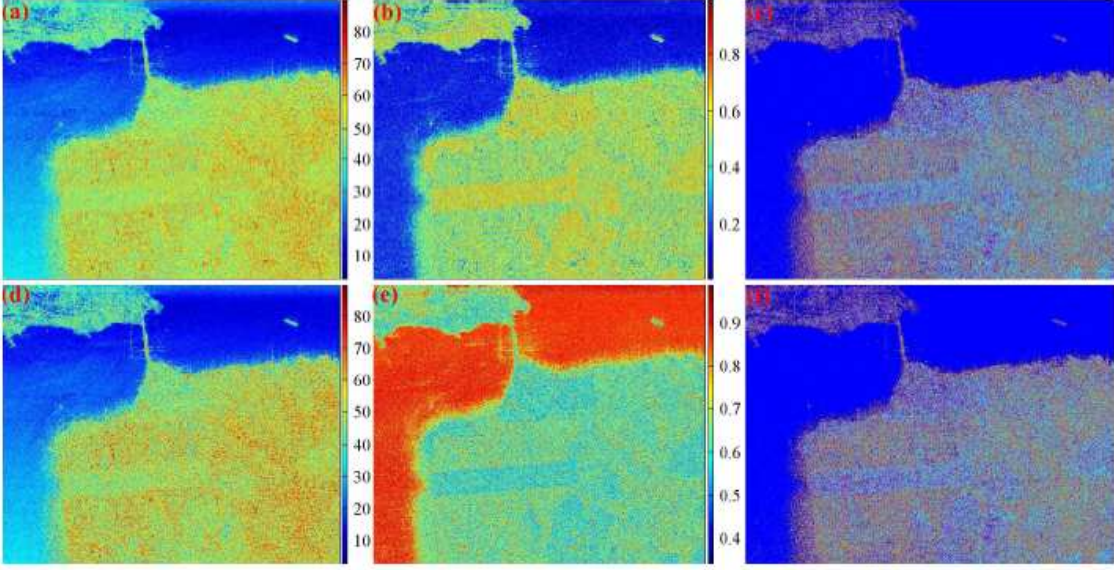


Figure 1: (a) The Cloude-Pottier alpha angle, (b) the entropy, and (c) the entropy/alpha classification of the San Francisco PolSAR data, (d) the Huynen alpha angle, (e) the scattering fraction of polarization (FoP), and (f) the Huynen FoP /alpha classification of the data.

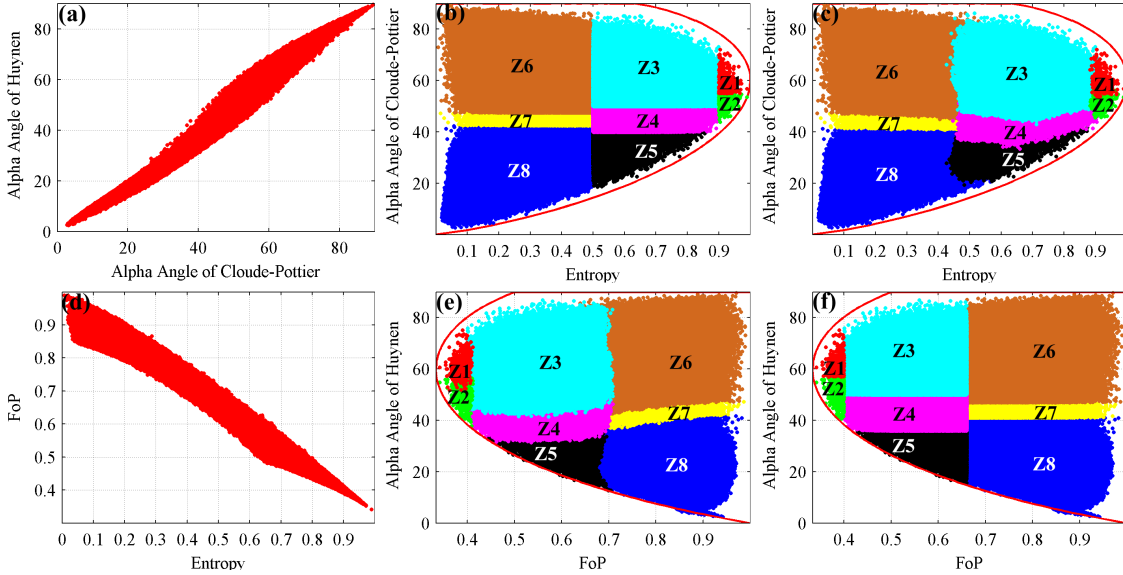


Figure 2: (a) The relationship between Huynen alpha angle and Cloude-Pottier alpha angle, as well as (d) the relationship between Huynen fraction of polarization (FoP) and Cloude-Pottier entropy, (b) the entropy/alpha classification plane of the data and (e) its equivalent presentation in FoP /alpha plane, as well as (f) the FoP /alpha classification plane of the data and (c) its equivalent presentation in entropy/alpha plane.

As for the entropy H and scattering FoP , they are displayed in Figures 1(b) and (e), respectively. It is interesting to observe that the entropy and FoP behave completely reversely. The area of high entropy is of low FoP and the area of high FoP is of low entropy. This correlation is further shown in Figure 2(d), and we can see that the two have a good correspondence for targets of high entropy or much lower entropy, but the correspondence is ambiguous for targets of low or

medium entropy. Nevertheless, we will show in the following that the ambiguity can be resolved by combining the $\bar{\alpha}$ angle. Thus FoP can alternate entropy to describe the target purity.

We above show the usefulness of Huynen $\bar{\alpha}$ angle and FoP by relating them to the Cloude-Pottier $\bar{\alpha}$ angle and entropy. From them we can see that the combination of FoP and Huynen $\bar{\alpha}$ angle, i.e., the Huynen $FoP/\bar{\alpha}$, may provide an unsupervised terrain classification. In the following we investigate $FoP/\bar{\alpha}$ by relating it to $H/\bar{\alpha}$. The 2D $H/\bar{\alpha}$ plane on the San Francisco data is shown in Figure 2(b), which is further subdivided into eight basic zones to characterize classes of different scattering behaviors and represented in eight different colors. Based on these, the scene is classified into eight classes in an unsupervised way, as shown in Figure 1(c). We transfer and show the classification result to the space of $FoP/\bar{\alpha}$ in Figure 2(e) still using the same color indexes as the $H/\bar{\alpha}$ classification. As shown, the nine target zones are well separated in the $FoP/\bar{\alpha}$ plane with slight mixture near class borders, which indicates the combination of Huynen FoP and $\bar{\alpha}$ angle can be well used for classification. Based on Figure 2(e), we can determine some hard boundaries on FoP and Huynen $\bar{\alpha}$ angle to coarsely classify the terrain into eight classes: $FoP = 0.40$ and $FoP = 0.66$ are selected as the boundaries along the FoP axis; while along $\bar{\alpha}$ axis, the boundaries are as follows: $\bar{\alpha} = 57^\circ$ for Z1 and Z2, $\bar{\alpha} = 50^\circ$ for Z3 and Z4, $\bar{\alpha} = 36^\circ$ for Z4 and Z5, $\bar{\alpha} = 47^\circ$ for Z6 and Z7, and $\bar{\alpha} = 41^\circ$ for Z7 and Z8. Therefore, we obtain a $FoP/\bar{\alpha}$ classification scheme as shown in Figure 2(f). Figure 2(c) shows the corresponding $H/\bar{\alpha}$ classification plane under this $FoP/\bar{\alpha}$ classification, clearly, it is consistent with the original $H/\bar{\alpha}$ plane shown in Figure 2(b). This can be further demonstrated if we classify the San Francisco scene using $FoP/\bar{\alpha}$, as shown in Figure 1(f). By comparing it with the classification of $H/\bar{\alpha}$ in Figure 1(c) we can see that the two can achieve a perfect consistency, and the sea, urban area, and vegetable area are all well separated. The total classification consistency between the two classifiers is 93.38%. To eliminate the potential influences from dataset, we also apply the two classifiers to ESAR L-band data of Oberpfaffenhofen and AIRSAR L-band data of Flevoland, and the classification consistencies are still as high as 91.64% and 91.29%, respectively. All these show that Huynen $FoP/\bar{\alpha}$ can achieve an unsupervised classification independent of a particular data, therefore, we think it is a good alternative to $H/\bar{\alpha}$.

4. CONCLUSIONS

The $H/\bar{\alpha}$ classifier is one of the most successful polarimetric algorithms and has been widely used in many aspects. This paper is dedicated to develop an alternative to it from the viewpoint of Huynen target dichotomy. A nine-symbol Bernoulli scheme is proposed to statistically model the mixed target scattering. From the model, two parameters, the Huynen $\bar{\alpha}$ angle and the scattering FoP are extracted to describe the scattering mechanism and target randomness, respectively. A Huynen $FoP/\bar{\alpha}$ unsupervised classification scheme is finally obtained and shown to be well consistent with the $H/\bar{\alpha}$ classifier.

REFERENCES

1. Huynen, J. R., "Phenomenological theory of radar targets," Ph.D. Dissertation, Tech. Univ. Delft, Delft, The Netherland, 1970.
2. Cloude, S. R. and E. Pottier, "An entropy based classification scheme for land applications of polarimetric SAR," *IEEE Trans. Geosci. Remote Sens.*, Vol. 35, No. 1, 68–78, Jan. 1997.
3. Li, D., "Stereo processing and polarimetric analysis of synthetic aperture (SAR) images," Ph.D. Dissertation, University of Chinese Academy of Sciences, Beijing, China, 2013.
4. Li, D. and Y. Zhang, "Huynen dichotomy-based radar target adaptive extraction," *PIERS Proceedings*, Stockholm, Sweden, Aug. 12–15, 2013.

Scattered Intensity Distribution at near the Glass Transition of Charged Fibrous Virus (fd) Suspensions

Kyongok Kang

Forschungszentrum Juuelich, Institute of Complex Systems (ICS-3)

Soft Condensed Matter, ICS-3 52425 Juuelich, Germany

Abstract— The scattered intensity distributions are discussed at near the glass transition of charged fibrous virus (fd) suspensions. Unusual scattered intensity peaks are observed by approaching the glass transition at higher concentration, for longer waiting time, of 100–300 hours, in the dynamic light scattering. In this paper, both time-averaged and ensemble-averaged intensity correlation functions are provided for non-ergodic systems that have different orientations of neighboring domains of charged chiral rods.

1. INTRODUCTION

The observations of a glass transition in suspensions of very long and thin rod-like, highly charged colloids at low ionic strength, where thick electric double layers are present. Below the glass-transition concentration, the morphology of the system therefore consists of many nematic domains with different orientations. The initial morphology with large shear-aligned domains breaks up in smaller domains, where equilibrium is reached after typically after 80–100 hours. As a model system for very long and thin, stiff, highly charged colloidal rods, we use fd-virus particles at a low ionic strength, where the particles consist of a protein-coated DNA strand with a length of 880 nm and with a cross-sectional diameter of 6.8 nm [1, 2]. The persistence length is about 3000 nm. A detailed preparation of the dispersions of fd-virus suspension and the analysis of effect of dissolved carbon dioxide on both the ionic strength and pH can be found in Ref. [3]. For lowering the ionic strength, below the 0.16 mM, the effective diameter becomes larger than the core of the bare diameter, and it leads to apparently less volume fraction to feel the interactions, corresponding to a Debye length if 27 nm. This large Debye length and the high charge density of fd particles (about 8 elementary charges per nm [4]) lead to strong long-ranged repulsive electrostatic interactions between fd-rods, which in turn lead to glassy behavior at sufficiently high fd concentration. The glass transition concentration (of 11.7 mg/ml) is found far above the isotropic-nematic coexistence region (1.5–3.4 mg/ml), where both the particle dynamics and the domain-texture dynamics freeze in [5, 6].

In the present paper, the experimental evidences of scattered intensity distributions at below and near the glass transition concentration of charged fibrous viruses (fd), where the long ranged electrostatic repulsion lead to structural arrest and to freezing of the domain texture. The ensemble-averaged intensity correlation functions at below the glass transitions concentration have shown that apparent fast and slow dynamical mode serves as the long-time sustainable elasticity that are responsible the slowing down behaviors. However, at near the glass transition concentration, different mechanism is observed.

2. SCATTERED INTENSITY AND ENSEMBLE AVERAGED CORRELATION FUNCITON

Vertically aligned small angle dynamic light scattering [6, 7] is used at a given wavevector through the commercially available 1 mm thickness cuvette. The wavelength of the laser beam is 633 nm, and the scattering angle is chosen as corresponding to a length scale of 1 μm , which is the length of a single fd-virus particle. The scattering experiments are done in VV polarization. Since the depolarized scattering of fd-virus particles is very weak, and the length scale that is probed is comparable to the length of the rods. Correlation functions therefore only probe translational motion over typical distances of the order of the length of single rods. This implies that, whenever the ensemble averaged correlation function exhibits no decay during a certain time interval; single rods are not able to diffuse over distances larger or comparable to their own length during that time. In that case the sample behaves as a glass, that is, particle motion is frozen-in during such time intervals. The “brute force averaging”, in order to obtain ensemble averaged correlation functions from a series of single time averaged correlation functions (shown in the lower right plot in Figure 1),

reads,

$$\hat{g}_E(t) = \frac{\sum_{n=1}^N \langle i^2 \rangle_{T,n} \hat{g}_{T,n}(t)}{\sum_{n=1}^N \langle i^2 \rangle_{T,n}} \quad (1)$$

where time-averaged correlation function (in lower left in Figure 1) is defined as

$$\hat{g}_T(t) = \frac{\langle i(t)i(t=0) \rangle}{\langle i(t)^2 \rangle_{T,n}} \quad (2)$$

For non-ergodic samplings are also discussed in other polymeric and metallic gels, and globular suspensions for [8–11].

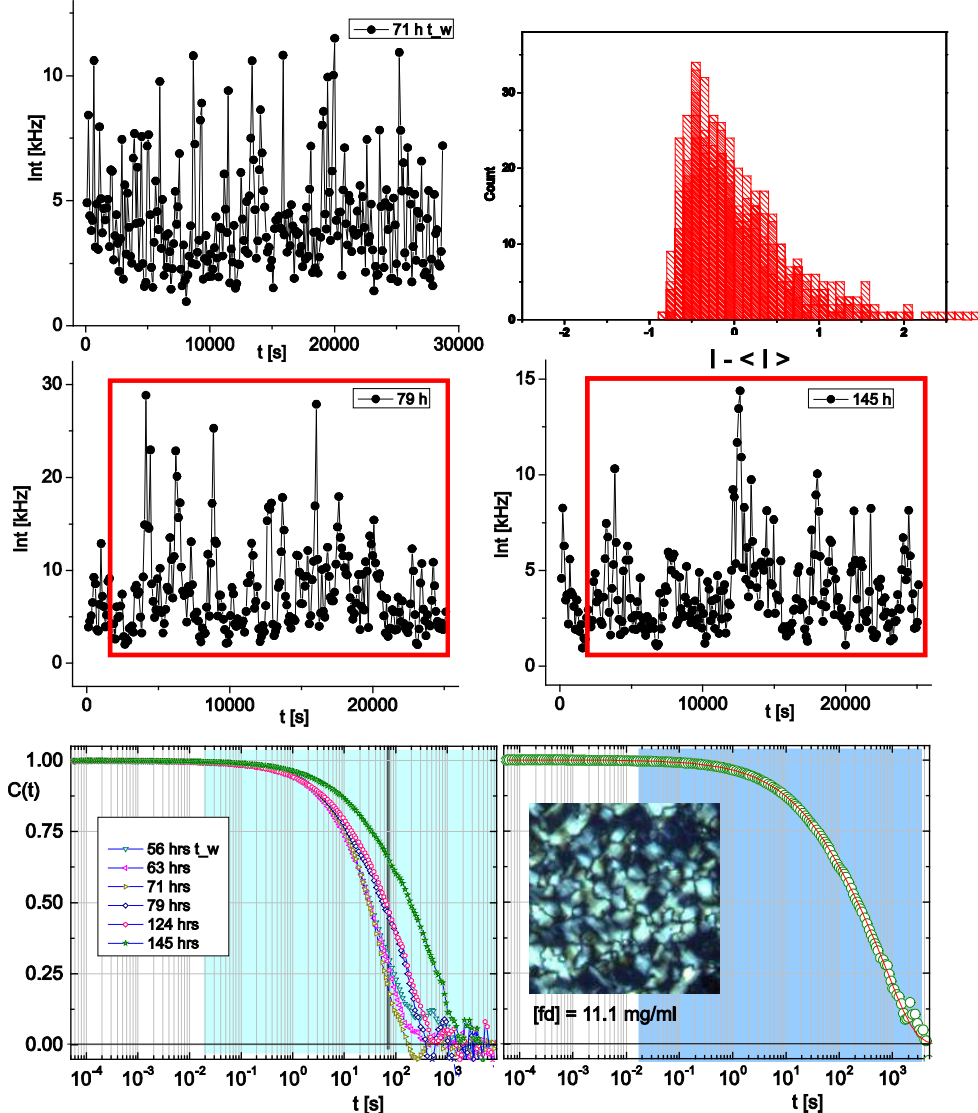


Figure 1: (Upper) Time-averaged scattered intensity and the deviation from the average distribution at different waiting time in the equilibrium state of the concentration at just below the glass transition concentration, 11.1 mg/ml. (Lower) Time-averaged normalized, and ensemble-averaged normalized correlation functions are shown in left and right, respectively. The equilibrated orientation texture is shown in the inset ($7 \times 7 \text{ mm}^2$).

3. SCATTERED INTENSITY PEAKS AT NEAR THE GLASS TRANSITION CONCENTRATION

The time-averaged scattered intensities are shown at below and above the glass transition concentration, in Figure 1 and Figure 2, respectively. The glass state has shown the initial cage due to the structural arrest can be noticeably distinguished in both textures and the microscopic dynamics [5, 6]. The trace of time averaged scattered intensity has been served as the representative scattering events for a given waiting times, and the corresponding normalized correlation functions are interpreted as a particle dynamics within the structural arrest. At the concentration of near, but just below the glass transition concentration, of 11.1 mg/ml, time-averaged scattered intensity and their corresponding normalized correlation functions are shown for an increase of the waiting time, where quite asymmetric distribution is found for the scattered intensity distribution func-

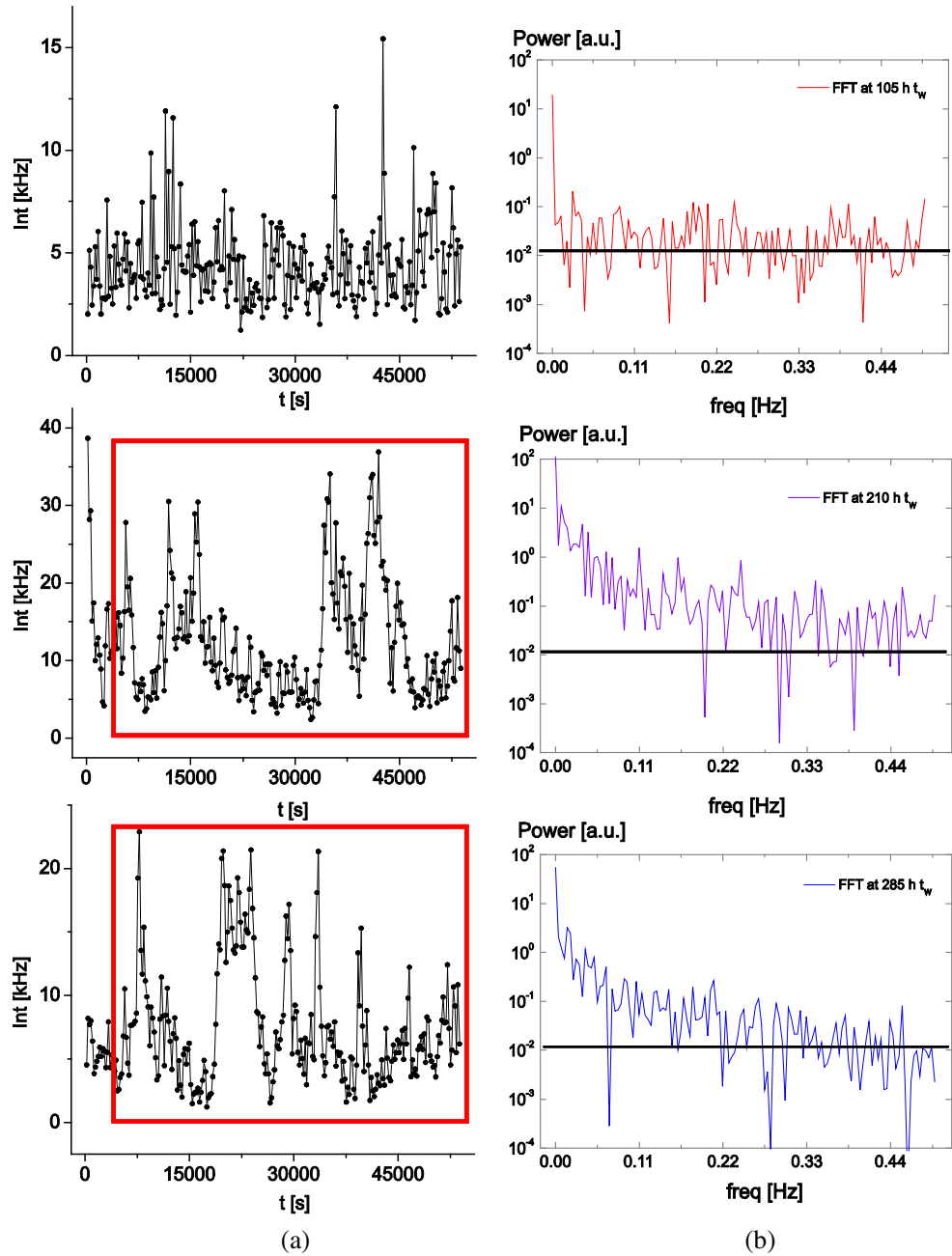


Figure 2: (a) Time-averaged scattered intensity in time at different waiting time of the concentration of 13.6 mg/ml, in the glass state, after the long-time structural arrest. (b) Power spectrum in the Fourier transform of the scattered time-averaged intensity at much long waiting time, suggests evidently the “repulsive” feature of glass.

tions. However, significantly different behavior is seen in the above glass transition concentration of 13.6 mg/ml, Figure 2, where much broader scattered intensity in time is observed at far long waiting time. Power spectrum is presented via Fourier transform of this broader scattered intensity distribution, which is depicted in the right plot of Figure 2. Not only the amplitude of power is increased as an increase of waiting time, but also the somewhat coherence of the power “drop” has been observed in the mean profile, suggesting that the possibility of a condensed “gas” phase or “super cooled” liquid state. The system slows down up to typically 200–300 hours. Much longer time is needed for escaping the local cage due to the structural arrest from the beginning, and followed by the slower motion at larger waiting times.

4. CONCLUSION

The resulting long-ranged electrostatic interactions give rise to structural arrest above a fd-concentration of 11.7 ± 0.6 mg/ml, where each rod is caged due to strong double-layer overlap. Structural arrest is probed by means of dynamic light scattering. The glass transition is found to occur far above the isotropic-nematic coexistence region. The dynamics of the domain texture is found to freeze at the same concentration where structural arrest occurs, as quantitatively probed by means of image time correlation. There are thus two features of the glass transition of charged chiral fd-rods: structural arrest and freezing of the orientation texture. Right after filling the cuvette, for small waiting times, a fast decay of image time correlation functions is found. The decay slows down for longer waiting time, followed by a transient faster decay, before the equilibrium is reached, where the decay rates are significantly smaller as compared to the initial rates. For the particle dynamics as probed by dynamic light scattering, however, the relaxation times of correlation functions are very large for small waiting times. There is a faster decay for increasing waiting times, followed by a decrease of decay rates, and reaching the plateau value for the equilibrated state. However, in the glass concentration, different mechanisms are responsible for the slowing down behaviors; (i) the initial caging due to the structural arrest, (ii) the propagation of a mechanical flow that sets in relatively faster, and finally (iii) reaching the slow in time metastable state. Here, intriguingly, the power is generated in the glass concentration, after extended waiting times, the slow dynamics takes over for much longer time as 200–300 hours. This may be due to the strong repulsive interaction of charged chiral fd-rods that are embedded in the density-orientation order such that effectively self-organize them in bulk.

ACKNOWLEDGMENT

Author thanks to Dr. H. Kriegs for his assistance on a synchronization of the beam shutter for long time slow measurements in automated data acquisition.

REFERENCES

1. Marzec, C. J. and L. A. Day, *Biophys. J.*, Vol. 42, 171–180, 1983.
2. Marzec, C. J. and L. A. Day, *Biophys. J.*, Vol. 53, 425–440, 1988.
3. Kang, K., J. K. G. Dhont, A. Wilk, A. Patkowski, and J. K. G. Dhont, *J. Chem. Phys.*, Vol. 126, 214501, 2007.
4. Zimmermann, K., J. Hagedorn, C. C. Heuck, M. Hinrichsen, and J. Ludwig, *J. Bio. Chem.*, Vol. 261, 1653, 1986.
5. Kang, K. and J. K. G. Dhont, *Phys. Rev. Lett.*, 2013.
6. Kang, K. and J. K. G. Dhont, *Soft Matt.*, 2013.
7. Kang, K., *Rev. Sci. Instrum.*, Vol. 82, 053903, 2011.
8. Fang, L. and W. Brown, *Macromolecules*, Vol. 25, 6897, 1992.
9. Xue, J.-Z., D. J. Pine, S. T. Miller, X.-J. Wu, and P. M. Chaikin, *Phys. Rev. A*, Vol. 46, 6550, 1992.
10. Rodd, A. B., D. E. Dunstan, D. V. Boger, J. Schmidt, and W. Burchard, *Macromolecules*, Vol. 34, 3339–3352, 2001.
11. Kulkarni, A. M., N. M. Dixit, and C. F. Zukoski, *Farady Discuss.*, Vol. 123, 37–50, 2003.

Deep Field Penetration in Cylindrical Conductors

F. E. M. Silveira

Centro de Ciências Naturais e Humanas, Universidade Federal do ABC, Santo André, Brazil

Abstract— Recent investigations in the phenomenon of deep field penetration in cylindrical conductors have been motivated by the possibility of optically manipulating power flows in photonic nanowires. The basic aspects of the subject are rediscussed by taking into account inertial effects due to charge carriers. Inertial effects are described by introducing a finite relaxation time for the current density. The resulting generalized Ohm's law can be rigorously justified in the framework of extended irreversible thermodynamics. A generalization of the diffusion equation is derived and its solution is parametrized in terms of the surface current and impedance. The real and imaginary parts of the latter are related, as usual, to the surface resistance and inductance, respectively. It is found that the surface inductance attains a minimum if the radius of the conductor acquires a critical value. It is also shown that such a situation should occur at low frequencies, for which the relaxation time is of the order of the diffusion time of the electric field. The proposed formulation is then applied to aluminum at room temperature, and it is found that the minimum inductance scales as 22.1 fH for a critical radius of the order of 35.1 nm. This shows that inertial effects should be important at the nanoscale. The results presented here may be of interest for investigations in the subject of nanophotonics. More generally, the experimental validation of the proposed theory would suggest that extended irreversible thermodynamics is the basic theory that determines the constitutive relations, which describe dissipative processes.

1. INTRODUCTION

Some time ago, the limiting situation of electromagnetic diffusion, for which the fields penetrate deeply into a rigid conductor, had been examined for cylindrical structures [1, 2]. Recent investigations in the subject have been motivated by the possibility of optically manipulating power flows in photonic nanowires [3–5].

In the classical approach to the problem, the induced current density \vec{J} is related to the applied electric field \vec{E} through the standard Ohm's law,

$$\vec{J} = \sigma \vec{E}, \quad (1)$$

where σ is the electric conductivity. Such an expression is widely known to describe satisfactorily the dissipative processes which occur at sufficiently low frequencies. Actually, if the field were suddenly turned off, Eq. (1) predicts that the current would vanish instantaneously. This shows that the ordinary Ohm's law ignores inertial effects due to charge carriers.

Inertial effects may be included in the discussion with basis on extended irreversible thermodynamics. This approach treats the dissipation function of linear processes as the average of the statistically fluctuating dissipation rate on either coarse or small spatial scales [6, 7]. In recent years, a link has been established between such a formulation and the possibility of extending some constitutive relations of matter to describe dissipative processes occurring at sufficiently fast rates [8, 9].

In the framework of extended irreversible thermodynamics, Eq. (1) may be generalized to

$$\left(1 + \tau \frac{\partial}{\partial t}\right) \vec{J} = \sigma \vec{E}, \quad (2)$$

where τ is a constant with dimension of time. Actually, in the limit $\tau \rightarrow 0$, Eq. (2) recovers Eq. (1). Now, if the electric field is suddenly removed from the conductor, Eq. (2) leads to

$$\vec{J} = \vec{J}_0 e^{-t/\tau}. \quad (3)$$

This shows that any initial current density \vec{J}_0 dissipates in the conductor in a time scale of the order of τ . Therefore, τ may be physically interpreted as the relaxation time of the current density, which is driven by inertial effects of charge carriers at sufficiently high frequencies.

In a previous work, the attenuation and damping of electromagnetic fields had been discussed with basis on Eq. (2) [10]. Subsequently, the skin effect and related dissipative processes were

examined for conductors of arbitrary shape [11]. Recently, an extension of Hagen-Rubens relation was obtained up to the near-infrared [12]. More recently, the phenomena of resistive heating and magnetic diffusion were investigated for good conductors [13]. Only still more recently, the two limiting situations of electric diffusion, namely, the skin effect and field penetration, have been explored in cylindrical configurations for the first time [14].

This work rediscusses inertial effects of charge carriers on the process of deep field penetration in cylindrical conductors at the quasi-static limit with basis on Eq. (2). A generalization of the diffusion equation is derived and its solution is parametrized in terms of the surface current and impedance. The real and imaginary parts of the latter are related, as usual, to the surface resistance and inductance, respectively. It is found that the surface inductance attains a minimum if the radius of the conductor acquires a critical value. It is also shown that such a situation should occur at low frequencies, for which the relaxation time is of the order of the diffusion time of the electric field.

2. ELECTRIC DIFFUSION

The magnetic \vec{H} and electric \vec{E} fields are related through the curl Maxwell's equations, namely, Faraday and Ampère-Maxwell laws,

$$\mu \frac{\partial \vec{H}}{\partial t} = -\nabla \times \vec{E}, \quad \nabla \times \vec{H} = \vec{J} + \epsilon \frac{\partial \vec{E}}{\partial t}, \quad (4)$$

respectively, where μ and ϵ are the magnetic permeability and electric permittivity, respectively. Then, by combining Eqs. (2) and (4) (on neglect of the displacement current $\epsilon \partial_t \vec{E}$ — the quasi-static approximation), we get

$$\left(1 + \tau \frac{\partial}{\partial t}\right) \nabla^2 \vec{E} = \mu \sigma \frac{\partial \vec{E}}{\partial t}, \quad (5)$$

where \vec{E} has been assumed to be a divergenceless field (the bulk of the medium does not contain any free charge — the good conductor limit). To the best of our knowledge, Eq. (5) had not been previously derived in the literature. Such an expression extends the usual relation governing the electric diffusion in good conductors, by taking into account inertial effects due to charge carriers. Actually, in the limit $\tau \rightarrow 0$, inertial effects can be fully neglected and Eq. (5) recovers the standard result [15, 16] $\nabla^2 \vec{E} = \mu \sigma \partial_t \vec{E}$.

Next, if we regard the electric field as varying harmonically in time, $\sim e^{-i\omega t}$, the extended formula can be written as an eigenvector equation,

$$\nabla^2 \vec{E} = -k^2 \vec{E}, \quad (6)$$

where the complex eigenvalue,

$$k = \sqrt{\frac{\mu \sigma}{\tau}} (\sin \varphi)^{1/2} e^{i\varphi/2} e^{i\pi/4}, \quad (7)$$

may be read in terms of the time dephasing angle of the current density with respect to the electric field, $\varphi = \tan^{-1}(\omega \tau)$ — see Eq. (2).

3. CYLINDRICAL CONDUCTORS

Let us consider a cylindrical conductor of circular cross-section with radius a . Then, by symmetry, the electric and magnetic fields over the surface of the cylinder vary only with time. Given these boundary conditions, the unique solution of $\nabla \cdot \vec{E} = 0$ and $\nabla \times \vec{E} = 0$ outside the conductor is $\vec{E} = \text{constant}$ (though its value also varies with time), and \vec{H} must be the same as it would be outside a cylinder carrying a constant current equal to the instantaneous value of the variable current $I e^{-i\omega t}$. Inside the conductor, with the z -axis along the axis of the cylinder and ϕ denoting the azimuthal angle, the harmonic electric and magnetic fields depend only on the radial coordinate r ,

$$\vec{E}(r, t) = \hat{z} E_z(r) e^{-i\omega t}, \quad \vec{H}(r, t) = \hat{\phi} H_\phi(r) e^{-i\omega t}, \quad (8)$$

respectively. Thus, the eigenvector Eq. (6) and Faraday's law, the first of Eq. (4), lead to

$$\frac{1}{r} \frac{d}{dr} \left(r \frac{dE_z}{dr} \right) = -k^2 E_z, \quad H_\phi = -\frac{\tau}{\mu} \frac{e^{-i\pi/2}}{\tan \varphi} \frac{dE_z}{dr}, \quad (9)$$

respectively.

The solutions of these equations, which remain finite along the z -axis, are

$$E_z = (R - \imath\omega L) \frac{I}{2\pi a} \frac{\mathcal{J}_0(kr)}{\mathcal{J}_0(ka)}, \quad H_\phi = \frac{I}{2\pi a} \frac{\mathcal{J}_1(kr)}{\mathcal{J}_1(ka)}, \quad (10)$$

respectively, where the complex constant of proportionality (the surface impedance) between the surface current, $I/2\pi a$, and electric field is given by

$$R - \imath\omega L = \sqrt{\frac{\mu}{\sigma\tau}} \left(\frac{\tan \varphi}{\cos \varphi} \right)^{1/2} e^{-\imath\varphi/2} e^{\imath\pi/4} \frac{\mathcal{J}_0(ka)}{\mathcal{J}_1(ka)}, \quad (11)$$

with $\mathcal{J}_1(kr) = -\mathcal{J}'_0(kr)$ denoting Bessel functions. As usual, R and L describe the surface resistance and inductance, respectively.

4. DEEP FIELD PENETRATION

For the limiting situation in which $|k|a \ll 1$, one can take just the first few terms of the expansion for the Bessel function at every point of the cross-section [17]:

$$\mathcal{J}_0(kr) \sim 1 - \left(\frac{kr}{2} \right)^2 + \frac{1}{4} \left(\frac{kr}{2} \right)^4 - \frac{1}{36} \left(\frac{kr}{2} \right)^6 \pm \dots \quad (12)$$

Then, on the assumption of (12), it follows from Eq. (11) that

$$R = \frac{2}{\sigma a} \left(1 + \frac{\mu^2 \sigma^2 a^4}{48\tau^2} \sin^2 \varphi \right), \quad L = \frac{\mu a}{4} + \frac{2\tau}{\sigma a}. \quad (13)$$

These are the values attained by the surface resistance R and inductance L when the electric field deeply penetrates in the cylindrical conductor.

5. CRITICAL RADIUS AND MINIMUM INDUCTANCE

We arrive now at the main result of this work. Quite interestingly, we see that the inclusion of inertial effects due to charge carriers into the problem leads to a critical value for the radius of the cylindrical conductor, for which the surface inductance attains its minimum. Indeed, by requiring that the derivative of L with respect to a , as it can be computed from the second of Eq. (13), vanishes, the critical radius can be calculated as

$$a_c = \sqrt{\frac{8\tau}{\mu\sigma}}, \quad (14)$$

such that the minimum inductance becomes

$$L_m = \sqrt{\frac{2\mu\tau}{\sigma}}. \quad (15)$$

This means that $\tau \sim \mu\sigma a_c^2$, the diffusion time of the electric field, for $a \sim a_c$, the critical radius of the cylindrical conductor. According to Eq. (7), this situation should occur at still low frequencies, $\omega\tau \ll 1$, provided the condition $|k|a_c \ll 1$ is satisfied.

For a typical non magnetic good conductor such as aluminum, we have [12, 13] $\tau \sim 6.91 \times 10^{-15}$ s, $\mu \sim 1.26 \times 10^{-6}$ H/m and $\sigma \sim 35.7 \times 10^6$ S/m, at room temperature. In this case, we find that $a_c \sim 35.1 \times 10^{-9}$ m and $L_m \sim 22.1 \times 10^{-15}$ H. This shows that inertial effects of charge carriers should be important at the nanoscale. Actually, the assessment of inductances of the order of fH fits perfectly within the present day laboratory capabilities [18–20].

We stress that the existence of the critical radius (14) and minimum inductance (15) necessarily requires the assumption of a finite relaxation time for the current density. Therefore, the experimental validation of the proposed theory would strongly suggest that the extended formulation of irreversible thermodynamics is the underlying fundamental theory that determines the constitutive relations of matter, which, in turn, describe appropriately the associated dissipative phenomena.

In Fig. 1, we show the surface inductance L as a function of the radius a of the cylindrical conductor, as given by the second of Eq. (13).

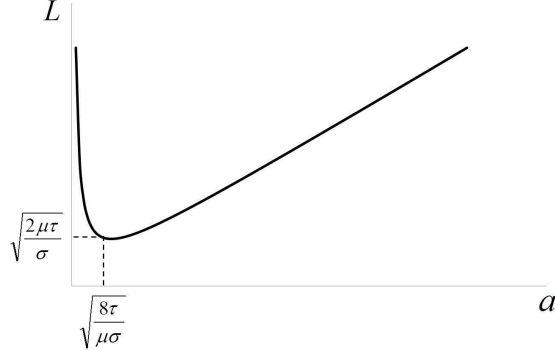


Figure 1: The surface inductance L as a function of the radius a of the cylindrical conductor, as given by the second of Eq. (13). The units are arbitrary. When $a = (8\tau/\mu\sigma)^{1/2}$, the critical radius a_c , $L = (2\mu\tau/\sigma)^{1/2}$, its minimum value L_m , as predicted by Eqs. (14) and (15), respectively.

6. CONCLUSION

This work has rediscussed inertial effects of charge carriers on the process of deep field penetration in cylindrical conductors at the quasi-static limit. Inertial effects have been included into the problem by introducing a finite relaxation time, τ , for the current density — see Eq. (2).

It has been shown that the surface inductance attains a minimum, L_m — see Eq. (15), if the radius of the conductor acquires a critical value, a_c — see Eq. (14). It has been also noticed that such a situation shall occur at low frequencies, for which τ is of the order of the diffusion time of the electric field.

The proposed formulation has been applied to aluminum at room temperature and it has been found that $L_m \sim 22.1$ fH for $a_c \sim 35.1$ nm, thereby showing that inertial effects should be important at the nanoscale. The results presented here may be of interest for investigations in the subject of nanophotonics — see Refs. [3–5]. More generally, as we have mentioned, the experimental validation of the proposed theory would suggest that extended irreversible thermodynamics is the basic theory that determines the constitutive relations, which describe dissipative processes.

ACKNOWLEDGMENT

This work is partially supported by FAPESP, Brazilian government agency, under grant number 2013/06945-7.

REFERENCES

1. Van Bladel, J. G., *IEEE Trans. Electromagn. Compat.*, Vol. 38, 549, 1996.
2. Shumpert, J. D., *IEEE Trans. Antennas Propag.*, Vol. 46, 1612, 1998.
3. Lockyear, M. J., A. P. Hibbins, and J. R. Sambles, *Phys. Rev. Lett.*, Vol. 102, 073901, 2009.
4. Ye, F., D. Mihalache, B. Hu, and N. C. Panoiu, *Phys. Rev. Lett.*, Vol. 104, 106802, 2010.
5. Morgado, T. A., J. S. Marcos, M. G. Silveirinha, and S. I. Maslovski, *Phys. Rev. Lett.*, Vol. 107, 063903, 2011.
6. Ziegler, H., *An Introduction to Thermomechanics*, North-Holland, Amsterdam, 1983.
7. Ziegler, H. and C. Wehrli, “The derivation of constitutive relations from the free energy and the dissipation functions,” *Adv. Appl. Mech.*, Vol. 25, 183, Academic Press, New York, 1987.
8. Grinstein, G. and R. Linsker, *J. Phys. A: Math. Theor.*, Vol. 40, 9717, 2007.
9. Ostoja-Starzewski, M. and A. Zubelewicz, *J. Phys. A: Math. Theor.*, Vol. 44, 335002, 2011.
10. Silveira, F. E. M. and J. A. S. Lima, *J. Phys. A: Math. Theor.*, Vol. 42, 095402, 2009.
11. Silveira, F. E. M. and J. A. S. Lima, “Skin effect from extended irreversible thermodynamics perspective,” *Journal of Electromagnetic Waves and Applications*, Vol. 24, Nos. 2–3, 151–160, 2010.
12. Silveira, F. E. M. and S. M. Kurcbart, *Europhys. Lett.*, Vol. 90, 44004, 2010.
13. Silveira, F. E. M. and S. M. Kurcbart, *Int. J. Eng. Sci.*, Vol. 52, 22, 2012.
14. Silveira, F. E. M., *Physica A*, Vol. 392, 1818, 2013.
15. Sommerfeld, A., *Electrodynamics*, Academic Press, New York, 1964.

16. Landau, L. D., E. M. Lifshitz, and L. P. Pitaevskii, *Electrodynamics of Continuous Media*, Butterworth-Heinemann, Oxford, 1984.
17. Abramowitz, M. and I. A. Stegun, *Handbook of Mathematical Functions: With Formulas, Graphs, and Mathematical Tables*, Dover Publications, New York, 1972.
18. Chen, H.-K., H.-J. Chen, D.-C. Chang, Y.-Z. Juang, and S.-S. Lu, *IEEE Microw. Wirel. Compon. Lett.*, Vol. 18, 467, 2008.
19. Matko, V. and K. Jezernik, *Sensors*, Vol. 10, 3954, 2010.
20. Augustine, C., X. Fong, B. Behin-Aein, and K. Roy, *IEEE Trans. Nanotech.*, Vol. 10, 778, 2011.

NMR Lens — Mapping of the Magnetic Field

D. Nespor, T. Kriz, R. Kubasek, and P. Fiala

Department of Theoretical and Experimental Electrical Engineering
Brno University of Technology, Technická 3082/12, Brno 616 00, Czech Republic

Abstract— Paper presents measurement methodology for mapping of the magnetic flux density in the reactive field of the resonators. Measuring workplace simulates RF electromagnetic field in NMR system with frequency sweeping possibility. This makes it possible to monitor manipulation of the magnetic field and dependence of the resonant frequency of the resonators interacting with surrounding objects.

1. INTRODUCTION

Electromagnetic field is possible to manipulate by means of dielectric materials [1]. Electromagnetic field will be affected due to values of dielectric constant ϵ_r and permeability μ_r . The lens was constructed as periodic structure of single split ring resonators (SSR). A negative effective permeability μ_r can be imposed on this structure [1, 2]. The main problem is to set up the resonance frequencies of the resonators [3, 4]. The resonance frequency is very sensitive and it is possible to very easily change it by the interaction with others resonators or by the interactions with objects in the surrounding area (parts of the NMR system, measured object, probe sensors etc.). This is the reason, why is so complicated to set resonant frequency exactly. NMR system has one disadvantage and that it is not possible to change frequency of the RF electromagnetic field. So it is impossible to find out resonant frequency of the resonators interaction with NMR system and eventually with measured object.

2. MEASURING STATION

The mapping of the magnetic flux density is a step by step measuring of the 2D area with the defined numbers of the measured points. The measuring station contains RF generator, transceiver of the electromagnetic field, measured sample, measuring sensor, RF spectrum analyser and xy position device. Schematic representation of the measuring chain is shown in Figure 1.

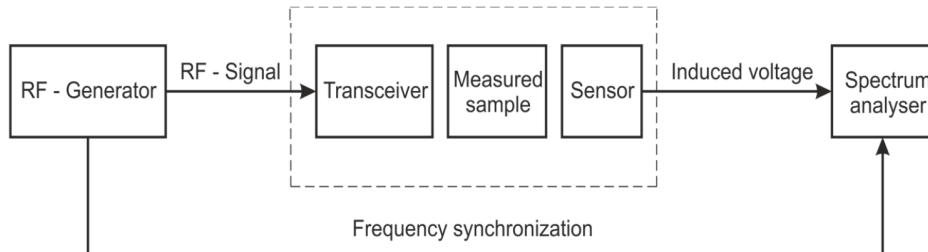


Figure 1: Schematic representation of the measuring chain.

One loop magnetic antenna, with diameter $d = 30$ mm was used as a transceiver. The antenna was realized by PCB technology on FR4. The antenna impedance was tuned to 50Ω by using capacitors. The magnetic antenna is shown in Figure 2.

The resonant frequency of the measured object is very sensitive on the interactions with objects in the surrounding area. This also applies to measuring sensor. For minimal affection measured object is necessary to have a sensor with induction much smaller than the induction of the measured object. But for maximum signal it is necessary to have sensor with maximal induction. So that is the compromise which is needful to resolve. The NMR system works with frequency $f = 197.25$ MHz, but for these measuring the frequency $f = 100$ MHz was used. This allows the use the twice bigger SSR and to simplify the measuring sensor construction. As measuring sensor was used fundamental one loop coil combined with a twisted wire to minimize inductance and for a precise definition of the measurement area. This sensor measures magnetic flux density only in direction perpendicular on the surface of the measured sample. For the other direction of the magnetic flux density measuring,

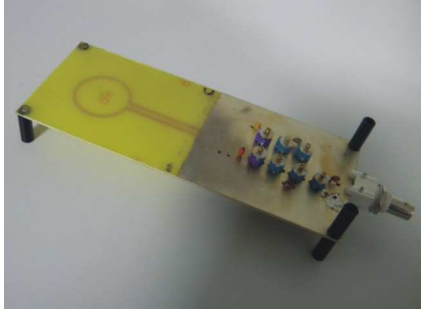


Figure 2: Magnetic antenna.



Figure 3: One loop sensor.

it is necessary to construct a sensor with corresponding loop direction. The one loop sensor is shown in Figure 3.

The position device was realized like cross — table with two stepper motors. Motors are controlled using microcontroller. The position device is shown in Figure 4. The whole measuring station is shown in Figure 5. Measurement is performed so, that the device performs one step then followed by a time delay to stabilize the magnetic field. After the time delay the microcontroller generates measuring pulse and the RF spectral analyser measures one value of the electric power P . After measuring, follows the next step. In this manner, step by step, is measured, the whole area. Data are written to a text file in one column. A matrix of the measured values is created from the text file after the end of the measuring.



Figure 4: Position device.



Figure 5: Measuring station.

3. VERIFICATION OF THE MEASURING METHOD

To verify the accuracy of the measurements was used measurement of the magnetic flux density of the transmitting antenna. The measured area was 80×80 mm, increments of 1 mm. Measuring was made for different distances d from the magnetic antenna. Magnetic flux density B is linearly dependent on the induced current in the measuring loop. Magnetic flux density ratio corresponds to the ratio of currents. This dependence was used for calculation of the normalized magnetic flux density B_n (1).

$$B_n = \frac{B}{B_{\max}} = \frac{I}{I_{\max}}, \quad (1)$$

where I is induced current, I_{\max} is maximal induces current, B is magnetic flux density and B_{\max} is maximal magnetic flux density. Induced current I was calculated using the Equation (2).

$$I = \sqrt{\frac{P}{Z}}, \quad (2)$$

where P is electric power and Z is impedance of the sensor. The measured magnetic flux density B_n of the magnetic antenna at a distance of 1 mm is shown in Figure 6.

Measured results were compared with numerical simulations. Simulated magnetic flux density B_{ns} is shown in Figure 7. Simulated normalized flux density B_{ns} was calculated analogously like B_n but directly from magnetic flux density B . A comparison of simulation and measurement is

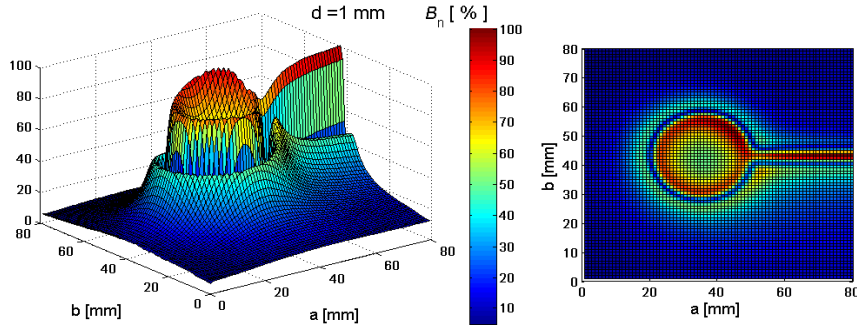


Figure 6: Measured magnetic flux density B_n of the magnetic antenna.

obvious, that the results are almost identical. The slight differences are caused by two main reasons. The first reason is finite size of the sensor. The second reason is that, the numerical model was based in the middle of the perfectly matched layers and therefore the structure is not influenced by reflected electromagnetic waves and electromagnetic smog.

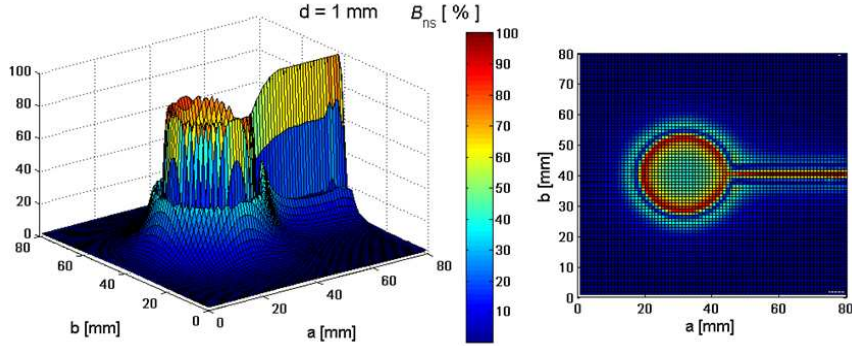


Figure 7: Simulated magnetic flux density B_{ns} of the magnetic antenna.

4. RESULTS

The measured sample was 2D structure of the SSR resonators. The structure was realized like uniform matrix of the 5×5 resonators. Resonators have diameter $d_r = 10$ mm and distances between resonators is $l = 10$ mm. The resonators were tuned to the resonant frequency $f_r = 100$ MHz by a ceramic chip capacitor. The ceramic chip capacitors have been assembled over the interspaces. Value of capacitance of the capacitor was determined by a analytical calculation. The measuring was made for wide frequency spectrum around the predicted resonant frequency. The exact resonant frequency which was determined from results is $f_r = 91$ MHz. Magnetic flux density B_n at frequency which is equal the resonant frequency of the resonators is shown in Figure 8.

The measured results correspond with theoretical premises and with numerical simulations. The results also showed that the resonators have no exactly uniform resonant frequencies. It is caused by

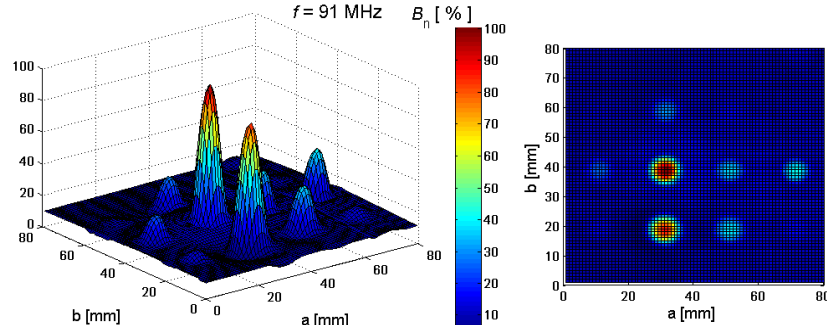


Figure 8: Magnetic flux density B_n at resonant frequency.

inaccuracies of the chip capacitors. Magnetic flux density B_n at frequency lower than the resonant frequency of the resonators is shown in Figure 9.

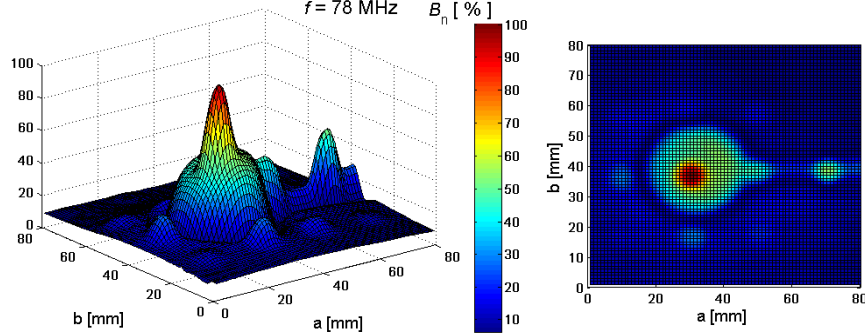


Figure 9: Magnetic flux density B_n at frequency lower than resonant frequency.

The figure shows magnetic flux density of the antenna and magnetic flux density of the resonators. When resonators resonate at a frequency lower than the resonant frequency, then the magnetic flux density of these resonators has the same direction as the magnetic flux density of the antenna. The resulting magnetic flux density is then the sum of these two magnetic flux densities.

Magnetic flux density B_n at frequency higher than the resonant frequency of the resonators is shown in Figure 10. When resonators resonate at a frequency higher than the resonant frequency, then the magnetic flux density of these resonators has the opposite direction as the magnetic flux density of the antenna. The resulting magnetic flux density is then the difference of these two magnetic flux densities. This effect is most evident in the central resonator, where the magnetic flux density crosses zero around this resonator.

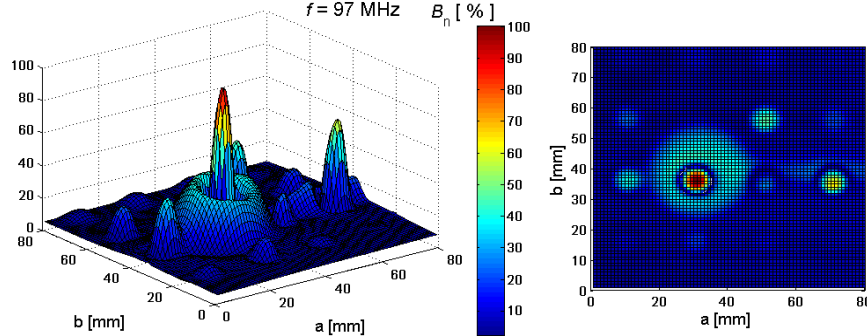


Figure 10: Magnetic flux density B_n at frequency higher than resonant frequency.

5. CONCLUSION

Measuring method for mapping of a magnetic flux density in the close field of the SSR was defined in this paper. As is evident from comparison with numerical simulations this method is accurate. There is possible to measure only absolute value of the magnetic flux density with one loop sensor. Therefore is not possible to determine the positive or negative direction of the magnetic flux density. This is the biggest disadvantage of this method. But the problem with determining the direction can be quite simply solved using knowledge about behaviour of the magnetic flux density around resonance frequency. This is demonstrated in the results of measurements above.

This work will be continued to measuring different configurations of the resonators to find optimal structure.

ACKNOWLEDGMENT

The research described in the paper was financially supported by project of the Czech Science Agency Nr. 13-09086S, “An Investigation of Artificial Electromagnetic Materials and Metamaterials with Applied Numerical and Imaging Methods”.

REFERENCES

1. Pendry, J. B., “Negative refraction makes a perfect lens,” *Phys. Rev. Lett.*, Vol. 85, No. 18, 3966–3969, Oct. 2000.
2. Freire, M. J., L. Jelinek, and R. Marques, “On the applications of $\mu = -1$ metamaterial lenses for magnetic resonance imaging,” Departamento de Electronica y Electromagnetismo, Facultad de Fisica, Universidad de Sevilla, 2009.
3. Bartusek, K., P. Drexler, P. Fiala, R. Kadlec, and R. Kubasek, “Magnetoinductive lens for experimental mid-field MR tomograph,” *PIERS Online*, Vol. 6, No. 7, 621–624, 2010.
4. Nespor, D., P. Drexler, P. Fiala, and K. Bartusek, “Using metamaterials as electromagnetic lens for MR tomograph,” *PIERS Proceedings*, 1158–1161, Marrakesh, Morocco, Mar. 20–23, 2011.

A Measurement System for Electrical Impedance Tomography

T. Kříž, Z. Roubal, and J. Rez

Department of Theoretical and Experimental Electrical Engineering
Brno University of Technology, Kolejná 2906/4, Brno 612 00, Czech Republic

Abstract— The authors present a measurement system designed to facilitate tests within electrical impedance tomography (EIT). More concretely, this system provides the input data for EIT-based conductivity image reconstruction. The realized setup includes a generator, a voltage-to-current converter, a switching unit, an accurate AC multimeter, and a measuring vessel. This vessel contains 16 stainless steel electrodes; a pair of the directly opposed electrodes is connected to the converter, and voltage is measured on the other electrodes. The current electrodes are periodically excited. For each instance of current excitation, a set of voltages is measured; thus, we obtain $n(n - 1)$ of measured voltage values, where n expresses the number of the electrodes. The measurement system is fully automated. To control the measurement, we created a program in the HP VEE environment. The measured sample consists in a saline solution, in which agar-based objects exhibiting different conductivity are placed; these objects then form defects. The applied intermittent excitation prevents the occurrence of electrolysis. The measurement is realized with several conductivity values as well as with various locations and number of defects in the saline solution.

1. INTRODUCTION

Electrical Impedance Tomography EIT is a tomographic diagnostic method. It is based on the detection of potential changes at the boundary of the diagnosed environment. These changes are caused by the existence of locations with a different electric conductivity. Electrical impedance tomography can be used to detect defects in materials or generally to provide the distribution of conductivity inside the measured object. In practice, this means that the diagnosed object is surrounded by a group of electrodes and measured the electric potential (voltage). When the selected pair of electrodes is attached as the current power source, the other electrodes are used for measuring the potential at the location boundary. The electric current field is created in the diagnosed object. Distribution of this field depends on the configuration of the electrodes and on the homogeneity or inhomogeneity of the object internal conductivity.

Thus, the obtained data allow us to use computing methods to determine the conductivity distribution (cracks or inhomogeneities) inside the measured object. To eliminate undesirable galvanic phenomena and electrolysis, we supply alternating current at lower frequencies of up to tenths of units of Hz to kHz and, less intensely, tens of mA. As the EIT method considerably depends upon the noise level and the accuracy of the measured values, it was necessary to use the principles of low-level measurement. The paper describes the application of these principles to the switching unit. Within the follow-up stages of the research, the measured voltage values will be compared to the numerical model of the measured task, and we will evaluate the measurement accuracy and errors as well as their influence on the instability of conductivity reconstruction.

2. DESIGNED ELECTRICAL IMPEDANCE TOMOGRAPHY MEASURING SYSTEM

A measuring system has been designed and realized for the purposes of EIT. This system will be used for experimental verification of the results obtained from the mathematical solution of the



Figure 1: Overall configuration of the measuring system for the EIT method.

current field in an environment with an inhomogeneous conductivity. The measuring system was created for this purpose. The designed system consists of 16 electrodes with supporting electronics. The layout of the workstation is shown in Figure 1.

The block diagram is shown in Figure 2. The measuring system consists of a PC with the control program created in HP VEE 3.2. The program written in the QBasic interpreter controls the Agilent 33120A generator and the switching unit for the switching of voltage electrodes; the measuring station also includes an Agilent 34401A multimeter. The function generator works on the DDS principle. It provides a stable output voltage amplitude. Thanks to an A/D converter with multiple integration MultiScope III, the used multimeter strongly suppresses the mains interference of 50 Hz and its harmonics. This provides high accuracy measurements required for the correct reconstruction of conductivity. The generator and the multimeter are connected via a GPIB bus, and the EIT switching unit is controlled via an LPT port. The measuring vessel with the 16 electrodes is shown in Figure 3. The vessel dimensions are shown in Figure 4. Each measurement is performed 5 times to increase the accuracy. The voltage results are calculated as the arithmetic mean of the obtained values. Moreover, the calculated standard deviation of each measurement shows the effect of random variables.

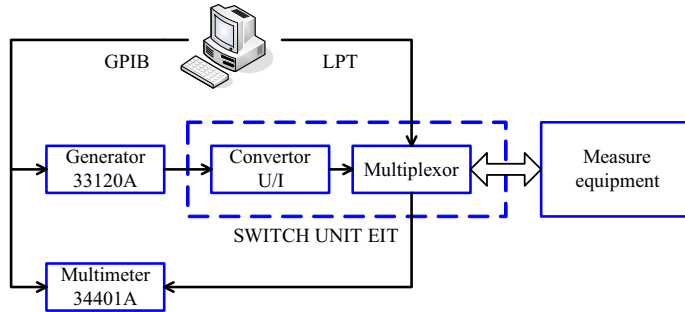


Figure 2: Block diagram of the EIT measuring system.



Figure 3: Measuring vessel with 16 electrodes.

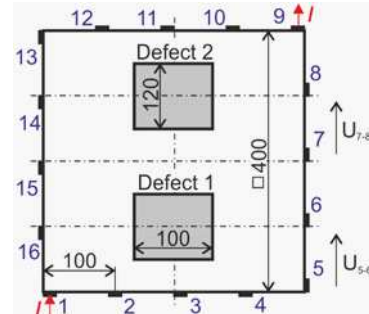


Figure 4: Measuring vessel with dimensions.

The switching unit selects a pair of opposing electrodes in the measurement to function as the current exciting elements; then, neighbouring pairs of electrodes are sequentially connected to the multimeter to measure the AC voltage between them. It is only possible to measure the voltage between neighbouring electrodes. AC voltage is used to prevent the electrolysis, even at the expense of slower measurement. For a correct reproducible measurement, it is necessary to choose the suitable measurement frequency. Distilled water with NaCl is used as the basic solution. The measured dependence on the frequency of the relative permittivity and conductivity is shown in Figures 5 and 6.

For the purposes of the EIT has been used saline with a specific conductivity 0.871 S/m. As a compromise was chosen frequency 510 Hz, when it is not applied so much change in the relative permittivity and the frequency is not a multiple of 50 Hz. This was increased repeatability compared to the originally selected frequency in [1].

The control and the analog (measured) signals were galvanically isolated to application of the low-level measurement principle. Due to, the switching unit contains of double reed relay in the package DIL. The connectors are gold-plated to minimize interference. The internal arrangement of

the switching unit with converter V/I is shown in the Figure 6. The front panel shows measurement electrodes (red LED) is in the Figure 7. A pair of the current electrode is indicated by a green LED. If we need to test the function of the device, excitation and measurement electrodes can be switched manually. The converter V/I is composed of a monolithic IC TDA2030 and the conversion constant 30 mA/1 V. It's output impedance 2 k Ω is sufficient for the necessary stability of the excitation current.

3. EVALUATION AND COMPARISON OF THE MEASURED DATA

The values of voltage between electrodes were measured for cyclic change of excitation electrodes (1–9 to 8–16). There were made three measurements. The measuring vessel was filled the saline

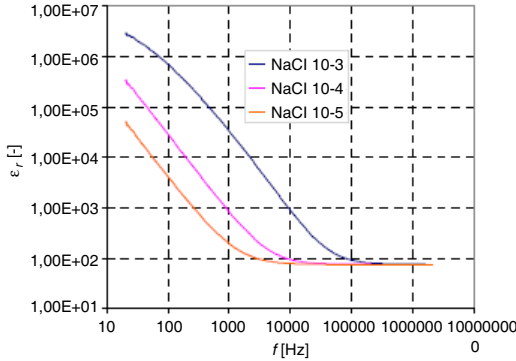


Figure 5: The permittivity dependence of NaCl on the frequency.

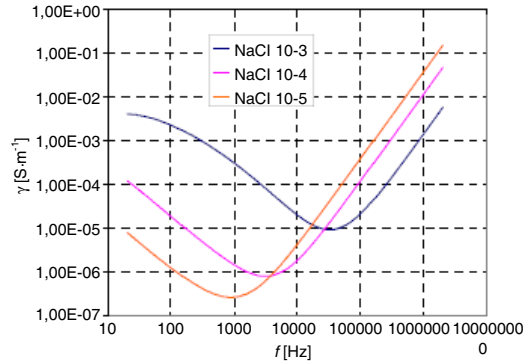


Figure 6: The dependence of saline conductivity on frequency.



Figure 7: The internal arrangement of the switching unit.

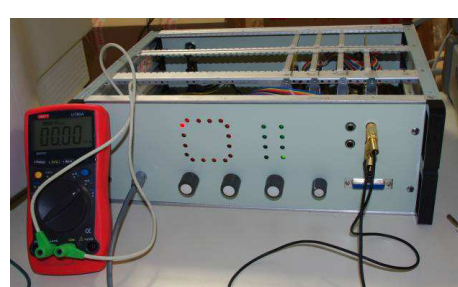


Figure 8: The front panel switching unit.

Table 1: Results for the current electrode voltage 1-9.

Electrodes		V_{1-2}	V_{2-3}	V_{3-4}	V_{4-5}	V_{5-6}	V_{6-7}	V_{7-8}	V_{8-9}
V_m	[V]	2.04	0.31	0.15	0.05	0.05	0.16	0.31	1.99
S.D.		236	9	177	33	221	18	7	31
V_a	[V]	1.78	0.30	0.15	0.05	0.05	0.15	0.31	1.76
V_{ael}	[V]	2.12	0.30	0.15	0.05	0.05	0.15	0.31	2.10
Err	[%]	14.5	2.87	4.73	6.13	2.95	2.97	2.17	13.2
Err_{el}	[%]	3,79	1.16	3.05	4.45	1.29	1.28	0.46	5.14
Electrodes		V_{9-10}	V_{10-11}	V_{11-12}	V_{12-13}	V_{13-14}	V_{14-15}	V_{15-16}	V_{16-1}
V_m	[V]	2.01	0.31	0.15	0.05	0.05	0.16	0.32	1.99
S.D.		16	7	7	13	17	2	14	309
V_a	[V]	1.78	0.30	0.15	0.05	0.05	0.15	0.31	1.76
V_{ael}	[V]	2.12	0.30	0.15	0.05	0.05	0.15	0.31	2.10
Err	[%]	12.7	3.20	3.88	6.98	6.67	3.96	3.22	12.7
Err_{el}	[%]	5.37	1.52	2.20	3.29	3.95	2.27	1.53	5.48

only, height of the saline was 50 mm for the first measurement. At the second measurement was placed in the measuring vessel defect, filled with air ($\sigma = 0 \text{ S/m}$) with dimensions $120 \times 100 \text{ mm}$ and third measurements were placed two defects of the same size. Location of the defect is in Figure 3. To evaluate the measured data for EIT reconstruction and the influence of the contact resistance was created numerical model in the ANSYS, which was solved current field described by the Laplace equation $\operatorname{div} \sigma \operatorname{grad} \phi = 0$. The numerical model was created as a three-dimensional geometry with respect to the measuring vessel and electrodes. At first, numerical model was created. This numerical model have not been considered in the contact resistance of the measuring electrodes. The second model was created with respect to the contact resistance. Voltage was measured 5 times on each pair of electrodes and the mean and standard deviation have been calculated. The measured values and the results of both numerical models are summarized in the Table 1. There is evaluated relative error between the measured value and the value obtained from the numerical model without the inclusion of contact resistance with it. The effect of contact resistance is very significant as you can see in the Figure 5. Contact resistance was calculated from the two measurements with two conductivity of saline. The first was measured voltage on the current electrodes for conductivity of saline 0.666 S/m and the second measurement with half value of the conductivity of saline. The current values for both measurements was equal. With these measurements we can obtain a system of two linear equations with two variables that it describes the resistance of electrodes and saline:

$$2R_s + 2R_{el} = V_1/I \quad (1a)$$

$$R_s + 2R_{el} = V_2/I, \quad (1b)$$

where R_s is resistance of saline and R_{el} is resistance of electrodes.

After solving system of equations we get contact resistance of the electrode, which was 5.89Ω . For the purposes of the numerical model contact resistance was converted to conductivity through the electrode dimensions.

The changes of the voltages on the electrodes were evaluated for voltage values obtained by measurements for one defect and two defects, the change was related to the values of the voltage without defects. Changes in voltage units amounted to hundreds of percent compared to the

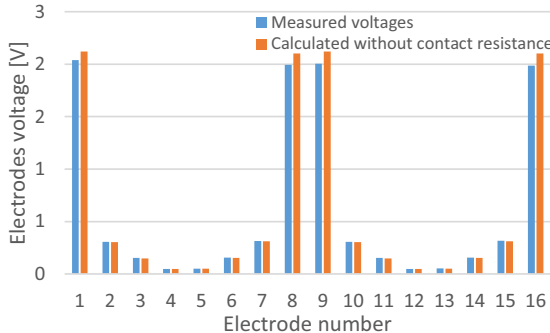


Figure 9: Measured and calculated electrode voltages.

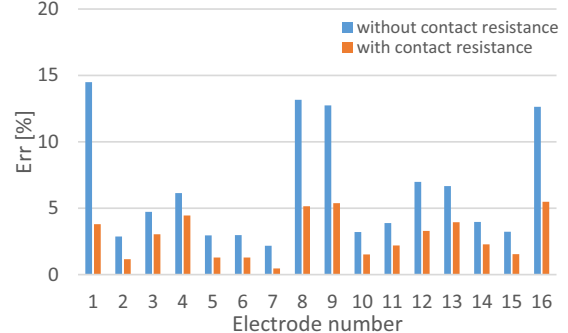


Figure 10: Relative error — with/without contact resistance.

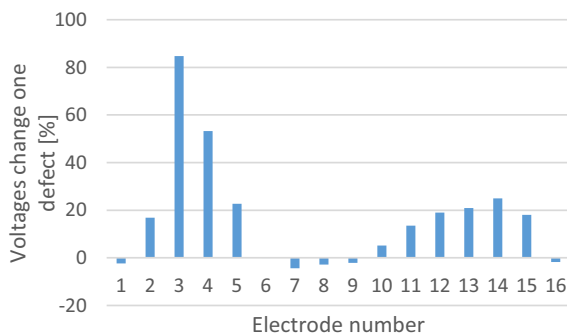
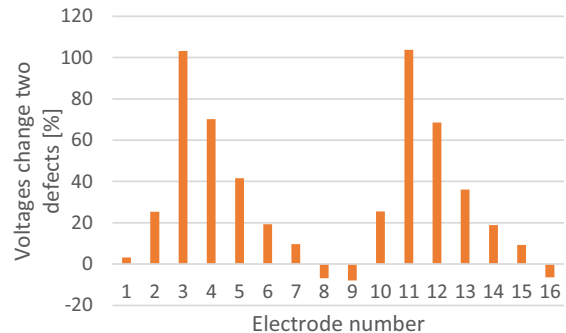


Figure 11: Electrode voltages changes for one and two defect relative to measured data without defects.



measured sample without inhomogeneities. Changes of electrodes voltage are in Figure 10.

4. CONCLUSION

The measuring system has been designed and realised for measuring voltages on electrically conductive materials.

The obtained voltage values for three different configurations of conductivity were compared with the values obtained from the numerical model. The relative error on the impact of contact resistance reached several percent. With such a small relative error, measured data can be used to reconstruction of the conductivity using algorithms based on EIT.

ACKNOWLEDGMENT

The research described in the paper was financially supported by project of the BUT Grant Agency FEKT-S-11-5/1012 and projekt CZ.1.07.2.3.00.20.0175, Elektro-vyzkumník.

REFERENCES

1. Rez, J., "Impedanční tomografie a její použití," *Defektoskopie 2005*, nedestruktivní defektoskopie, magnetické metody, 44–52, VM print Leopoldov, 2005.
2. Mikulka, J., E. Gescheidtova, and K. Bartusek, "Soft-tissues image processing: Comparison of traditional segmentation methods with 2D active contour methods," *Measurement Science Review*, Vol. 12, No. 4, 153–161, 2012.
3. Fiala, P., E. Kroutilová, M. Steinbauer, P. Dohnal, M. Hadinec, and K. Bartušek, "Experiments with the effect of non-homogenous parts in materials," *PIERS Proceedings*, 1081–1084, Hangzhou, China, March 24–28, 2008.

Identification of Bacteria Strains via Advanced Methods for the Statistical Processing of Near-infrared Spectra

Pavel Krepelka

Department of Theoretical and Experimental Electrical Engineering
Brno University of Technology, Technicka 12, Brno 616 00, Czech Republic

Abstract— The NIR absorption spectrum contains information related to molecular bonds of the examined sample. When the energy quantum from a source of light equals the energy necessary for the transition of a bond to a higher vibration level, the light is absorbed; in the measured spectrum, this effect can be observed in the form of an absorption band. Based on the interpretation of these bands, chemical compounds can be determined or quantified. However, the processes become more complicated in the NIR part of the spectrum. Because the value of the delivered energy is higher, most absorption bands are caused by overtones rather than by the fundamental transition of vibration conditions. Due to these effects, the absorption bands overlap, gain in width, and are difficult to interpret. The classification is usually carried out by means of traditional chemometric methods such as principal component analysis and partial least squares regression; these techniques were used for the identification of bacterial strains in a fluid medium during the transmission measurement. Improvements of this method are presented within the paper. The authors also introduce other processing methods, for example the artificial neural net and fuzzy logic techniques. The main advantage of the neural net approach consists in its simplicity and ability to provide high-speed evaluation. Fuzzy modelling then respects the shape and position of the absorption peaks, which enables us to easily interpret the acquired spectrum. All the above-described methods are employed (and subsequently compared) in the process of identifying some bacterial strains.

1. INTRODUCTION

Infrared spectroscopy is a frequently used chemometric method for determining the composition of a material and detecting or quantifying any impurities present. The acquired spectrum contains information about the chemical structure of the sample; this information is based on the IR wavelength absorption by the molecule bonds. Infrared spectroscopy is also a common spectroscopic technique for organic research. The bacterial cell identification based on IR spectroscopy has been known since 90 century. At that time, a spectral database of dry bacterial films was created [1]. In this paper, the near-infrared analysis is introduced. The instrumentation for NIR measuring is faster and more accessible. Another advantage of this method consists in the possibility of measuring bacteria directly in a water-based solution. However, the NIR spectrum contains more wide and overlapping peaks, which causes interpretation difficulties. To eliminate this problem, chemometric statistical methods are utilized. The most common techniques comprise principal component analysis and the partial least squares regression method. Any improper use of these methods leads to a decrease in the accuracy of prediction. In discrimination problems, the correct application of discriminant analysis and appropriate encoding of the predicted values is a crucial factor. In the paper, other techniques such as neural net classification and fuzzy logic processing are also introduced.

A bacterial cell consists mainly of bounded and unbounded water. A substance with IR active molecule bonds (C-H, N-H, O-H) are presented in amino acid, nucleic acid, polysaccharide, fats and lipids. An overtone and combination bands would be detectable in the NIR spectrum. As these spectral changes are negligible and difficult to detect, sophisticate methods for the NIR spectra interpretation must be utilized.

2. MATERIAL AND METHODS

Spectra of the *Lactobacillus acidophilus*, *Staphylococcus epidermidis*, *Enterococcus durans*, and *Escherichia coli* suspensions were collected and examined. A transmission technique for the spectra acquirement was chosen due to its simplicity and the without preprocessing feature. The maximum recovery diluent (water, peptic digest of an animal tissue, sodium chloride) was used for the storage and measurement. The Varian Cary 5E spectrometer gained a spectrum with 3 nm resolution and 0.1 s average time. The raw spectral data (the logarithm of transmittance related to the blank

sample) were transformed using the Savitzsky-Golay algorithm the (first derivative). The data were processed and visualized via Mathworks MATLAB 7.9.0.

A frequently used statistical analysis is the PCA [2]. In this experiment, the z-score was used for the analysis. The Z-score expressed the “zero mean” data with a normalized variance. The PCA searched for the maximum variance in the variables and computed a new orthogonal system for expressing the value (score). The analysis is based on the covariance matrix treatment. It is important to note that the PCA does not include the spread in the predicted variables. Figure 1 shows the scores of the first two components. Although some bacterial strains seem to be separable, the separability usually decreases with the increasing number of observations (measurements). This is due to the growing variance in the data independent of the output predicted variable. Figure 2(b) illustrates the loading (weight) of the first — and the most important — component. At 1130 nm and 950 nm, the variances in the measured data stand at their highest level, which may be a good starting point for changes in the examination of bacterial cells.

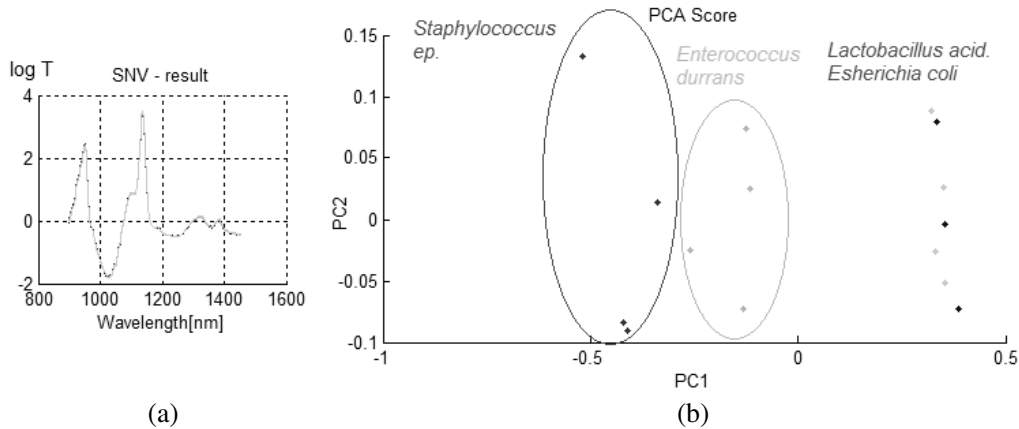


Figure 1: The Z-score of (a) the difference spectrum and (b) the PC score plot.

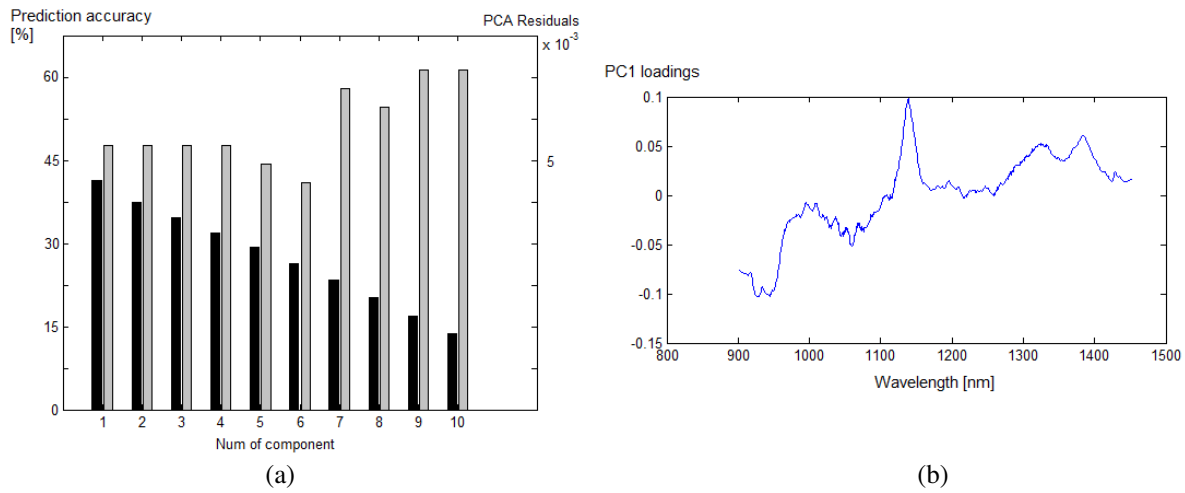


Figure 2: The reliability of (a) the PCA model and (b) PC1 loadings.

In some publications, only the two-component score is illustrated. For a reliable prediction, we nevertheless need enough components. Reliability can be expressed as the model residuum graph (Figure 2). In this example, the linear discrimination analysis was used for the classification. Validating of created model ensured cross validation (“leave one out” technique). Figure 2 shows the dependencies of the model residuum and prediction accuracy on the number of components. This graph formulates the importance of choosing the right number of principal components.

The partial least square method (PLS) appears to be a more suitable technique for the bacterial identification [4]. The method considers variance in the input variables and the predicted variables.

In chemometrics, there are two common types of algorithm: the PLS and PLS2. The PLS2 assumes the case when more predicted (output) variables are used. The spectral data can be regarded as collinear data. Generally, the PLS offers better performance in handling the collinearity problem than the PCA with a regression. The PLS usually needs less components to reach the same minimal square error than the PCR (principal component regression). Compared to the PCA, the PLS ensures a smoother choice of factors. The important aspect of PLS-based computation is the coding of the predicted value. The application of this technique with a discrimination analysis is known as the PLS-DA. Unfortunately, an approach frequently used to express the output variable is the use of “dummy” variables. The ordinal number then reflects each discriminant group. Because the order of the number does not express any trend in the classification group, the method attempts to find these non-existent dependencies, and the resulting accuracy rapidly decreases. A better way of coding the predicted value consists in expressing the degree of affiliation to each class (0–1). The output vector has number of dimension matched to number of classes. In this case, we need to apply the PLS2 in the event of classifying into more classes. Another approach to increasing the prediction accuracy is to take advantage of the orthogonal signal correction [3]. The filter-based signal correction (smoothing, derivation, baseline correction, standard normal variate etc.) offers a corrected signal with better properties. However, these properties are difficult to determine, and the determination process can degrade the spectrum and remove some information that carry the characteristics. The orthogonal signal correction is based on the simple idea related to the suppression of the part of input variables that is unrelated to the predicted value. It removes from the input matrix bilinear components (observations) which are orthogonal to the output matrix (predicted values). By another definition, it makes signal correction that does not remove any useful information from the input data. This technique can be realized by the modified NIPALS algorithm or via applying the direct orthogonal signal correction. This approach is based solely on the least squares steps. A comparison of the “dummy coded”, “degree of affiliation coded” without and with OSC is shown in Figure 3.

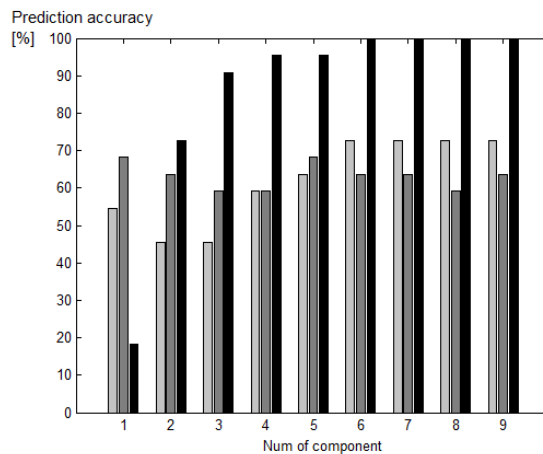


Figure 3: The accuracy of prediction. The degree of affiliation-coded variable (lightest); “dummy”-coded variable; degree of affiliation-coded variable with orthogonal signal correction (darkest).

An alternative approach to creating the prediction model is to utilize the artificial neural network. The ANN can be employed in signal processing (noise suppression, blind source separation), control, robotics (navigation, vision recognition), pattern recognition, speech production etc.. The neural network is a computational model applied for artificial intelligence; this model is inspired by the functions of a biological brain. Neural networks are characterized predominantly by their ability to learn and perform massive parallel computations. A neural network can involve non-linearity dependencies. In this example, we use a multi-layer network with the learning method based on the backward propagation of errors. The number of neurons in the hidden layer was determined as a half of the input layer neuron count. The mean absolute error was used as a performance function. The threshold to stop the learning was assigned to 0.01. These parameters have to be chosen carefully to avoid over-fitting problem. With 10 PLS components applied as the input to the ANN, the prediction accuracy computed by cross validation achieved 92%.

The last investigated method was fuzzy modelling. This technique can be applied in solving

data inaccuracy and processing their vague formulation. A prominent advantage of the described modelling approach consists in the peak shape approximation realized by the membership function. Each spectral artifact was approximated by the Gaussian distribution. The parameters of this distribution determine the degree of the membership in the given class. With the database of inference rules, the fuzzy set representing the shape of parts of the spectra can be estimated. Generally, the inference engine comprises procedures capable of handling the problem via manipulation with the knowledge base. The rules were defined experimentally in the form of production elements (IF-THEN) and the Mamdani implication. The disadvantage of this approach consists in the fact that the rules must be created manually for each classification problem. A different approach to the procedure of knowledge database building can be identified in the use of a neural network and the construction of neuro-fuzzy systems (Figure 4). The fuzzed variables were submitted to the ANN. After learning, the network was capable of performing correct classification of the data into classes representing the bacterial strains. The disadvantage of this technique lies in its sensitivity related to the selection of the training data and other network parameters. This technique achieved 100% accuracy, but it still needs to be tested on a wider set of data.

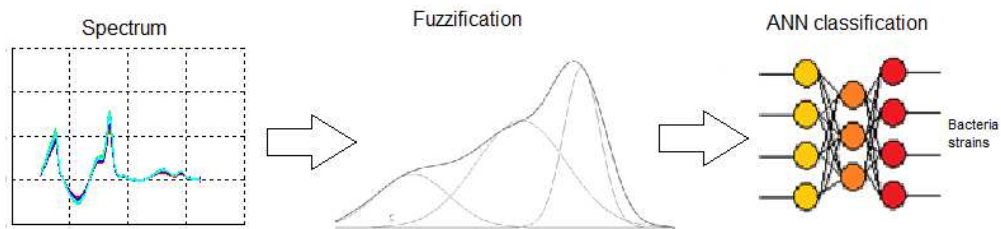


Figure 4: The neuro-fuzzy system.

3. CONCLUSION

NIR spectroscopy is a powerful and simple technique for analyzing various types of industrial processes. The method became very popular because of its non-destructive and high-speed character. The NIR spectra are not easily readable, and therefore statistical treatment is needed. In this paper, the identification of four bacterial strains was introduced. The bacteria cells produce only neglectable changes of the spectra, and that is also why advanced methods were applied. Some basic pre-processing techniques (the standard normal variate, the Savitzsky-Golay derivative) were shown; these methods improve the accuracy of most subsequently used methods. The principal component analysis appears to be a good starting point towards satisfactory orientation in the data. By the help of a discriminant analysis, it can be used as a classification tool; despite this fact, the PCA cannot reach a degree of accuracy comparable to regression techniques, which are able to compute even with output data. The maximum accuracy rate (60%) was achieved using 9 components.

The partial least squares methods is a classic chemometric approach used for calibration and discrimination. For discrimination problems, it is important to choose suitable coding of the predicted value. The coding to "dummy" variables is unsuitable, because the order of the number does not express any trend in the classification group. Better results can be achieved with the coding of the output value to express the degree of affiliation to each class. By means of the orthogonal signal correction, the achieved accuracy rate rapidly increased to a value approaching 100%.

Also, two other rarely used methods were introduced in the paper. The artificial neural network is an advantageous solution thanks to its ability to process non-linear dependencies, but it possesses a large number of parameters to be estimated. With the neural net, we reached an accuracy rate close to 100%, but more validating data would have to be submitted for precise determination of accuracy. Fuzzy modeling appears to be a very interesting alternative to spectra processing. However, its main disadvantage consists in the fact that the technique needs manual tuning of the parameters. Interesting results can be obtained on the basis of connecting the fuzzy system and the neural network. In some cases, the classification based on the neural net with fuzzed inputs can provide better accuracy than letting the neural net work directly with the spectrum.

Although the model was validated via cross validation, insufficient number of the measured data makes it impossible to perform the computing with reasonable accuracy. But it is sufficient

to compare the different approaches. The classic statistical methods to calibrate the spectra were shown together with their regular results and improved performance. The neural nets and fuzzy logic appear to offer a remarkable alternative with interesting results.

ACKNOWLEDGMENT

The research described in the paper was financially supported by a project of the BUT Grant Agency, No. FEKT-S-11-5/1012.

REFERENCES

1. Helm, D., H. Chinski, G. Schallehn, and D. Naumann, “Classification and identification of bacteria by Fourier-transform infrared spectroscopy,” *Journal of General Microbiology*, Vol. 137, 61–79, 1991.
2. Abdi, H. and L. J. Williams, “Principal component analysis,” *Wiley Interdisciplinary Reviews: Computational Statistics*, Vol. 2, 433–459, 2010.
3. Wold, S., H. Antti, F. Lindgren, and J. Öhman, “Orthogonal signal correction of near-infrared spectra,” *Chemometrics and Intelligent Laboratory Systems*, Vol. 44, 175–185, 1998, ISSN 0169-7439.
4. Helland, I. S., “PLS regression and statistical models,” *Scandinavian Journal of Statistics*, Vol. 17, 97–114, 1990.

The Effect of a Magnetic Field on the Speed of Temperature Change

E. Hutova, K. Bartusek, and P. Fiala

Department of Theoretical and Experimental Electrical Engineering
Brno University of Technology, Technická 3084/12, Brno 616 00, Czech Republic

Abstract— The paper presents the micro/nanoscopic model of a material inserted in a magnetic field. The model accepts the time component of an electromagnetic field from the perspective of relative motion of systems. The relatively moving systems were derived and tested [1], and the influence of the motion on the superposed electromagnetic field was proved to exist already at relative motion speeds in the order of units of ms^{-1} . In micro- and nanoscopic objects such as biological tissues, the effect of an external magnetic field on the growth and behaviour of the biological system needs to be evaluated. We designed the model based on a description using Maxwell's equations of the electromagnetic field, and we also extended the monitored quantities to include the various flux densities; moreover, the time flux density $\tau()$ was monitored as a quantity. This quantity was then experimentally examined on the physical problem of the speed of heating a defined volume of a homogeneous material in relation to the magnitude and type of the surrounding magnetic field. Experiments were conducted with growth properties of simple biological samples in pre-set external magnetic fields.

1. INTRODUCTION

When the temperature in animal cells and organisms containing water drops below $0\pm\text{C}$, the water will freeze, resulting in the death of the living structures. Experiments performed on living organisms show that the magnetic field reduces the effects of hypothermia affecting the cells of these living organisms and decreases the mortality in the cells. This fact is caused by a large number of influences, which include the effect of the external magnetic field, its form, and distribution over the space in which the microscopically conceived system is located. Due to the effect of the external magnetic field, the hypothetical particles of the model of the system (a homogeneous material, a heterogeneous structure — biological units — a cell, ...) change their dynamics, thus changing the entire microscopically interpreted system.

This paper analyzes the influence of a magnetic field on inanimate objects. Using physical parameters, we created a mathematical model which describes the rate of temperature change in the defined material sample. Experimental measurement of the temperature change of a copper sensor in a stationary homogeneous and gradient magnetic field was performed. Up to 10 times, the sample was cooled down to the nitrogen boiling point ($-195.80\pm\text{C}$ to 77.35K); at the pre-selected time, the sample was then removed and placed in an area where it was heated to the temperature of $-20\pm\text{C}$. Using the measuring centre and 4 temperature sensors (2 sensors measuring the temperature of the sample and 2 others for the measurement of the ambient temperature), we recorded the temperature change in the sample and the time required to heat it. This experiment was repeated in the presence of two magnetic fields. The results of the experiment were consistent with the mathematical model and contribute to the description of physical processes during the cooling of the biological tissues.

2. MODEL OF THE ELECTROMAGNETIC FIELD AND PARTICLES

For the model with distributed parameters of the electromagnetic field, it is possible to use partial differential equations based on the theory of the electromagnetic field to formulate a coupled model with concentrated parameters (in our case, particles). The model scale at the level of nanometers was also determined using the partial differential equations. The forces acting on a moving electric charge in the electromagnetic field can be expressed by means of the formula

$$f_e = \rho(\mathbf{E} + \mathbf{v} \times \mathbf{B}) \quad \text{in } \Omega, \quad (1)$$

where \mathbf{B} is the magnetic flux density vector in the space of a moving electrically charged particle with the volume density ρ , \mathbf{v} the mean velocity of the particle, $\mathbf{v} = \mathbf{ds}/dt$, \mathbf{s} the position vector from the beginning of the coordinate system o , t the time, \mathbf{E} the electric intensity vector, Ω the definition region of the independent variables and functions. Then the specific force acting on the

moving electrically charged particles with the charge q_e , number N_e , and — in the monitored area — volume V is

$$\int_0^\Omega \frac{f_e}{q_e} dV = (\mathbf{E} + \mathbf{v} \times \mathbf{B}) \quad \text{in } \Omega. \quad (2)$$

For the quantum mechanical model described by the concentrated parameters, this force will initiate a change of the charged particle energy W_e , thus causing a change of particle oscillation frequency ω . This can be written in the expression

$$\Delta\omega_0 = \frac{\partial\omega}{\partial W_e} \Delta W_e, \quad (3)$$

where ω_0 is the oscillation frequency of the electrically charged particle, $\Delta\omega_0$ the change of the particle oscillation frequency, ΔW_e the change of energy of the electrically charged particle. The change of oscillation frequency of the electrically charged particle can be directed upwards in the damping of the electric charge movement or downwards during its acceleration. The dependence of an electrically charged particle frequency on the steady-state values of the electromagnetic field can be expressed as

$$\omega_0 \approx \sqrt{\frac{|q_e(\mathbf{E} + \mathbf{v} \times \mathbf{B})|}{m_e s}}, \quad (4)$$

where s is the characteristic mean distance of the oscillation of a particle with the electric charge q_e which moves at a steady-state velocity \mathbf{v} , m_e the mass of an electrically charged particle in the magnetic field with magnetic flux density \mathbf{B} . The numerical model in Ω is based on the formulation of the electromagnetic field equations for the quantities of the intensities and inductions

$$\text{rot } \mathbf{E} = -\frac{\partial \mathbf{B}}{\partial t} + \text{rot}(\mathbf{v} \times \mathbf{B}). \quad \text{rot } \mathbf{H} = \mathbf{J}_+ \frac{\partial \mathbf{D}}{\partial t} + \text{rot}(\mathbf{v} \times \mathbf{D}) \quad (5)$$

$$\text{div } \mathbf{B} = 0, \quad \text{div } \mathbf{D} = \rho, \quad (6)$$

where \mathbf{H} is the magnetic field intensity vector, \mathbf{J} the current density vector, \mathbf{D} the electric flux density vector. Respecting the continuity equation

$$\text{div } \mathbf{J}_T = -\frac{\partial \rho}{\partial t} \quad \text{where } \mathbf{J}_T = \mathbf{J} + \rho \mathbf{v} + j c \rho \mathbf{u}_t, \quad (7)$$

where j is the symbol of the imaginary component of the quantity complex shape and c the velocity of light module in the vacuum, the above-written formulas (5) will assume the form

$$\begin{aligned} \text{rot } \mathbf{E} &= -\frac{\partial \mathbf{B}}{\partial t} + \text{rot}(\mathbf{v} \times \mathbf{B}) - \frac{1}{\gamma} \text{rot}(\rho \mathbf{v} + j c \rho \mathbf{u}_t + \mathbf{J}), \\ \text{rot } \mathbf{H} &= \gamma \mathbf{E} + \rho \mathbf{v} + \gamma(\mathbf{v} \times \mathbf{B}) + j c \rho \mathbf{u}_t + \frac{\partial \mathbf{D}}{\partial t} + \text{rot}(\mathbf{v} \times \mathbf{D}). \end{aligned} \quad (8)$$

Here, γ is the conductivity of environment from the macroscopic point of view. After connecting the macroscopic concept of the EMHD model with the microscopic approach, the coupling with the moving particle and its dynamics will manifest itself in the current flux \mathbf{J}_T from the expression (7):

$$\mathbf{J}_T = \gamma \mathbf{E} + \rho \mathbf{v} + j c \rho \mathbf{u}_t + \frac{\gamma}{q_e} \left(\frac{m_e d\mathbf{v}}{dt} + l \mathbf{v} + k \int_t \mathbf{v} dt \right), \quad (9)$$

where m_e is the quantity of the model with concentrated parameters — the particle mass which is given by the relation

$$m_e = m_0 \sqrt{\left(1 - \frac{v^2}{c^2}\right)}, \quad (10)$$

where l is the damping coefficient, k the coefficient of stiffness of the ambient environment. The material relations for the macroscopic part of the model are represented by the expressions

$$\mathbf{B} = \mu_0 \mu_r \mathbf{H}, \quad \mathbf{D} = \epsilon_0 \epsilon_r \mathbf{E}, \quad (11)$$

where the indexes of the quantities of the permeabilities and permitivities r denote the quantity of the relative value and the 0 value of the quantity for vacuum. The linkage between the macroscopic and the microscopic (dynamics of particles in the electromagnetic field) parts of the model is described by the relations of force action on the individual electrically charged particles in the electromagnetic field, and the effect is respected of the movement of electrically charged particles on the surrounding electromagnetic field from (8).

$$\begin{aligned} \text{rot} \mathbf{E} &= -\frac{\partial \mathbf{B}}{\partial t} + \text{rot}(\mathbf{v} \times \mathbf{B}) - \frac{1}{\gamma} \text{rot} \left(\rho \mathbf{v} + jc\rho \mathbf{u}_t + \mathbf{J} + \frac{\gamma}{q_e} \left(\frac{m_e d\mathbf{v}}{dt} + l\mathbf{v} + k \int_t \mathbf{v} dt \right) \right), \\ \text{rot} \mathbf{H} &= \gamma \mathbf{E} + \rho \mathbf{v} + \gamma(\mathbf{v} \times \mathbf{B}) + \frac{\gamma}{q_e} \left(\frac{m_e d\mathbf{v}}{dt} + l\mathbf{v} + k \int_t \mathbf{v} dt \right) + jc\rho \mathbf{u}_t + \frac{\partial \mathbf{D}}{\partial t} + \text{rot}(\mathbf{v} \times \mathbf{D}). \end{aligned} \quad (12)$$

The coupling of both models is formulated using Equation (9) and the formula

$$q_e (\mathbf{E} + \mathbf{v} \times \mathbf{B}) + \frac{q_e}{\gamma} \left(\rho \mathbf{v} + jc\rho \mathbf{u}_t - \frac{\partial(\varepsilon \mathbf{E})}{\partial t} \right) = \frac{m_e d\mathbf{v}}{dt} + l\mathbf{v} + k \int_t \mathbf{v} dt. \quad (13)$$

The effect of the behaviour of the macroscopic model describing the mass with the quantum mechanical model of elements of the system can be observed using the fluxes of quantities. The known quantities are magnetic flux ϕ , current flux I , and electric flux having the magnitude q :

$$\phi = \iint_{\Gamma} \mathbf{B} \cdot d\mathbf{S}, \quad I = \iint_{\Gamma} \mathbf{J} \cdot d\mathbf{S}, \quad q = \iint_{\Gamma} \mathbf{D} \cdot d\mathbf{S}, \quad (14)$$

where \mathbf{S} is the vector of the oriented boundary (in a 3D model of the plane), and Γ is the boundary of the area Ω , in which the flux is evaluated. If there is a moving element of the system in the model with a scale difference expressed in orders, it is easier to describe the state and effect of the superposed electromagnetic field by expressing the time flux density τ . The time flux can be different or inhomogeneous in parts of the area Ω . It is then possible to write

$$t = \iint_{\Gamma} \tau \cdot d\mathbf{S}. \quad (15)$$

After expanding the expression with the time flux density for the Cartesian coordinate system o, x, y, z , we have

$$t = \iint_{\Gamma} \frac{\mathbf{u}_z}{dz} \frac{1}{v_z(t)} \cdot (dx \times dy), \quad (16)$$

where $\mathbf{v}(t)$ is the instantaneous velocity vector, $v(t)$ the module of the instantaneous velocity vector, and dx, dy, dz are the vectors of differences in the coordinate system. Then the time flux density in the direction of the z -axis is

$$\tau_z = \frac{1}{v_z(t) dz} \mathbf{u}_z, \quad (17)$$

where \mathbf{u}_z is the base vector of the applicable coordinate system. To respect the other directions, we can write

$$\tau = \frac{1}{v_x(t) dx} \mathbf{u}_x + \frac{1}{v_y(t) dy} \mathbf{u}_y + \frac{1}{v_z(t) dz} \mathbf{u}_z, \quad (18)$$

where $\mathbf{u}_x, \mathbf{u}_y$ are the base vectors of the coordinate system. Time density depends on the instantaneous velocity of the particle motion in the quantum mechanical model and on the element of length. If there occur regions with different instantaneous velocities at elementary sections within the area Ω of the system described by the quantum mechanical model (atoms, molecules etc.), then the space is characterized by an uneven time flux density according to the expression (18). The relation between the time flux density τ and the quantities of the electromagnetic field of the model of the system (12) is evident. The impact of specific force on the moving electric charge

q_e can be defined according to the above-shown formulas (1) and (13). To evaluate the effect of the properties of the distribution of the magnetic field having a magnetic flux density \mathbf{B} and to assess the influence of the electric charge q_e moving at the instantaneous velocity \mathbf{v} in this field, the expressions (1), (2) for the area Ω can be formulated as

$$\mathbf{E} = q_e (\mathbf{v} \times \mathbf{B}) \quad \text{in } \Omega. \quad (19)$$

Then, for the motion of the electrically charged particle along the element of the closed curve $d\ell$ (according to the microscopic interpretation), it is possible to rewrite the above formula (19) as

$$\begin{aligned} \mathbf{E} d\ell &= q_e (\mathbf{v} d\ell \times \mathbf{B}) \quad \text{in } \Omega, \text{ and after modification from the formulas (17), (18) we have} \\ \frac{\mathbf{E}}{q_e} d\ell &= (\tau^{-1} \times \mathbf{B}) \quad \text{in } \Omega. \end{aligned} \quad (20)$$

If an electrically charged particle moves in the magnetic field having a magnetic flux density \mathbf{B} , and if the dimensions of the area Ω are multiply larger than the electrically charged particle or groups of particles, it is necessary to consider the questions of how the motion of the particle is influenced and what are the observable oscillation changes, namely the time flux density changes in parts of the area Ω . According to formula (3), respecting the conservation the external energies (heat, motion), it is possible to say that the properties of the charged particles depend on the characteristics of the external magnetic field. There are three basic variants of the state of the macroscopically interpreted distribution of the external magnetic field having a magnetic flux density \mathbf{B} :

1. The external magnetic field exhibits low values of magnetic flux density \mathbf{B} , and its distribution is homogeneous on the microscopic scale. Then we have $B = \min$, $\partial B_x / \partial x = 0$, $\partial B_y / \partial y = 0$, $\partial B_z / \partial z = 0$ or, in at least one direction of the coordinate system and respecting the curl character of the field, formula (6).
2. The external magnetic field exhibits higher values of magnetic flux density \mathbf{B} , and its distribution is homogeneous on the microscopic scale. Then we have $B = \max$, $\partial B_x / \partial x = 0$, $\partial B_y / \partial y = 0$, $\partial B_z / \partial z = 0$ or, in at least one direction of the coordinate system and respecting the curl character of the field, formula (6).
3. The external magnetic field is inhomogeneous on the macroscopic scale. Then we have $\partial B_x / \partial x \neq 0$, $\partial B_y / \partial y \neq 0$, $\partial B_z / \partial z \neq 0$ and, respecting the curl character of the field, (6).

3. NUMERICAL MODEL ANALYSIS

We performed a simple analysis of the FeNdB permanent magnet blocks having the dimensions $15 \times 10 \times 40$ mm, surface magnetic flux density $B_r = 1.2$ T, and intensity $H_{co} = 850$ kA/m.

Figure 1 shows a configuration with the minimum and, in a certain part, homogeneous magnetic field. A setup for the inhomogeneous magnetic field with a high gradient distribution is presented in Figure 2.

During the experiment, an element evaluating the observed macroscopic behaviour of mass was inserted in the red-marked areas.

4. EXPERIMENTS

The verification of the difference in the properties of the microscopic model of mass under the pre-defined condition of the external magnetic field was performed using a copper element having

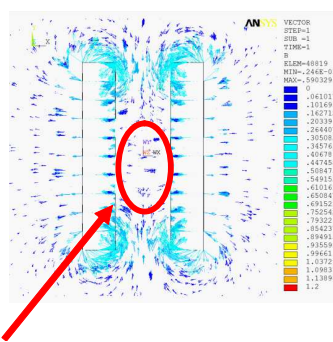


Figure 1: Permanent magnet configuration: a weakly homogeneous field.

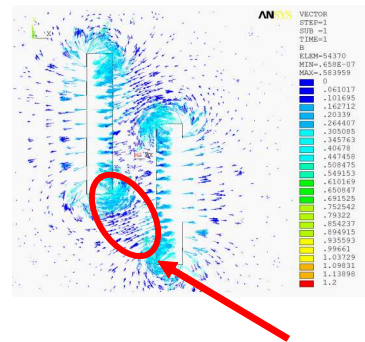


Figure 2: Permanent magnet configuration: a strong magnetic field with a high gradient.

the dimensions $10 \times 10 \times 10$ mm. This element was cooled down to -193°C and then heated at the ambient temperature of 20°C . The heating period was measured repeatedly, starting from -180°C and proceeding to -20°C . These limits had been chosen with respect to suppressing the systematic measurement error in the experiment; the actual experiment is shown in Figure 3.



Figure 3: Configuration of the permanent magnets during the experiment.

The aim of the experiment was to compare three different settings of the external magnetic field according to the Section 2 above and to indicate their impact on the speed of heating. If, in any of the cases, under repeated measurement in the given space there occurs a decrease of the statistically significant deviation of the heating period with respect to the reference measurement, it is possible to assume according to formula (16) that a lower time density was reached in the sample than in the reference measurement. Conversely, with a significantly longer heating time there occurs an increase of the time density in the measured sample as compared to the reference measurement.

5. COMPARISON OF THE ANALYSES

It follows from the conducted experiments that, in a strong magnetic field with a high gradient character of the magnetic flux density \mathbf{B} , $d\mathbf{B}/dx$; 200 Tm^{-1} is the lowest density of the time flux τ (setting 3, Section 2). A higher value of the time flux density τ can be found in a magnetic homogeneous field with a low magnetic flux density \mathbf{B} , B ; $2 \mu\text{T}$ (setting 1, Section 2), and the highest value is detected in a homogeneous magnetic field with the magnitude of the Earth's field $-B$; $50 \mu\text{T}$. (setting 2, Section 2).

Table 1: Data of the comparison of the different settings.

Homogeneous field			Gradient field			No external field		
Measurment no.	min	s	Measurment no.	min	s	Measurment no.	min	s
10	0:06:20	380	10	0:06:15	375	10	0:06:30	390
9	0:06:11	390	9	0:05:21	321	9	0:06:16	376
8	0:06:12	390	8	0:05:02	302	8	0:06:13	373
7	0:06:10	376	7	0:05:10	310	7	0:06:11	371
6	0:06:21	373	6	0:05:15	315	6	0:06:06	366
5	0:06:18	371	5	0:05:07	307	5	0:05:54	354
4	0:06:12	366	4	0:04:47	287	4	0:05:50	350
3	0:06:14	354	3	0:04:43	283	3	0:06:25	385
2	0:06:24	350	2	0:04:02	242	2	0:06:25	385
1	0:06:16	385	1	0:03:44	224	1	0:06:16	376
Average:	0:06:16	373.5	Average:	0:04:57	296.6	Average:	0:06:13	372.6
Median:	0:06:15	374.5	Median:	0:05:02	304.5	Median:	0:06:13	374.5
Standard deviation:	5.25E-05	13,11678	Standard deviation:	4.22E-04	39,90789	Standard deviation:	1.31E-04	12,39516
Maximum:	0:06:24	390	Maximum:	0:06:15	375	Maximum:	0:06:30	390
Minimum:	0:06:10	350	Minimum:	0:03:44	224	Minimum:	0:05:50	350

6. CONCLUSION

A model of the macroscopic setting of a magnetic field was formulated, and the time flux density τ was observed within the microscopic concept of the quantum mechanical model of mass. Time flux density is a quantity introduced to monitor the influence of an external magnetic field on the behaviour of elements of mass or their groups at the level of atoms. The experiment showed a simple task of evaluating the behaviour of anorganic mass during changes in the energy of the sample. The aim of the research was to prepare the already built-up model for use in classifying the behaviour of simple biological materials in an externally defined magnetic field.

ACKNOWLEDGMENT

The research described in the paper was financially supported by a grant of the Czech Science Foundation, No. GACR 13-09086S, a project of the BUT Grant Agency, No. FEKT-S-11-5/1012, and projects from the Education for Competitiveness Operative Programme, Nos. CZ.1.07.2.3.00.20.0175 and CZ.1.07/2.3.00/30.0005.

REFERENCES

1. Fiala, P., Z. Szabo, and M. Friedl, “EMHD models respecting relativistic processes of trivial geometries,” *PIERS Proceedings*, 95–98, Suzhou, China, Sep. 12–16, 2011.

Response of a Layered Medium to an Obliquely Incident Wave

R. Kadlec, P. Fiala, and I. Běhunek

Department of Theoretical and Experimental Electrical Engineering
Brno University of Technology, Technická 3082/12, Brno 616 00, Czech Republic

Abstract— The authors report on an analytical solution of the propagation, reflection and refraction of broadband electromagnetic signals within multilayered optical materials. The presented solution is processed in the Matlab program, which is suitable for a specifically oriented detailed analysis of a general problem.

The paper includes a theoretical analysis and references to the generated algorithms. The presented comparison of the parameter changes is supported by graphical outputs of the algorithms. The algorithms created in the Matlab environment are verified by means of programs based on the finite element method, namely the ANSYS program.

The response of the layered material depends on the thickness of each layer. The resulting algorithms show the response of layers with different thickness. The wave is sent from a source in the form of a single pulse. The response is shown for the electric field strength \mathbf{E} and magnetic field strength \mathbf{H} , i.e., the amplitude and the phase.

The methods described in this paper are well-suited for the analysis of beam refraction to the other side from the perpendicular line during the passage through the boundary. This phenomenon occurs in metamaterials.

1. INTRODUCTION

Inhomogeneities and regions with different parameters generally appear even in the cleanest materials. During the electromagnetic wave passage through a material, there occur an amplitude decrease and a wave phase shift. These phenomena are due to the material characteristics such as conductivity, permittivity, or permeability [1]. If a wave impinges on an inhomogeneity, there occurs a change in its propagation. The change manifests itself in two forms, namely in reflection and refraction. In addition to this process, polarization and interference may appear in these waves [2].

In the Matlab program, algorithms were created that simulate reflection and refraction in a lossy environment on the boundary between two dielectrics. The reflection and refraction are in accordance with Snell's law for electromagnetic waves as shown in Fig. 1(a). The form of Snell's law is as follows [3]:

$$\frac{\sin \theta_0}{\sin \theta_2} = \frac{\mathbf{k}_2}{\mathbf{k}_1} = \frac{\sqrt{j\omega\mu_2 \cdot (\gamma_2 + j\omega\varepsilon_2)}}{\sqrt{j\omega\mu_1 \cdot (\gamma_1 + j\omega\varepsilon_1)}}, \quad (1)$$

where \mathbf{k} is the wave number, γ the conductivity, ε the permittivity, μ the permeability, θ_0 the angle of incidence, and θ_2 the angle of refraction. Relation (1) is defining for the boundary line between the dielectrics medium. The interpretation of the Fresnel equations and Snell's laws is simple in the case of the refraction on boundary line between the dielectrics medium. In the case of refraction in a lossy medium, according to relation (1), the angle θ_2 depends on the wave numbers \mathbf{k}_1 a \mathbf{k}_2 , which are generally complex; then, an inhomogeneous wave is propagated in medium 2.

For simplicity, we will analyze separately the \mathbf{E} vector parallel to the boundary (also known as the TE wave) as indicated in Fig. 1(a) and the \mathbf{H} vector parallel to the boundary (also known as the TM wave). For the TE wave, the electric field strength of the reflection and transmission beams is expressed according to the equation

$$\mathbf{E}_r = \mathbf{E}_1 e^{-jk_1 \mathbf{u}_{n1} \times \mathbf{r}}, \quad \mathbf{E}_t = \mathbf{E}_2 e^{-jk_2 \mathbf{u}_{n2} \times \mathbf{r}}, \quad (2)$$

where \mathbf{E}_1 is calculated from the intensity on the boundary line \mathbf{E}_0 and the reflection coefficient ρ_E , and \mathbf{E}_2 is calculated from the intensity on the boundary line \mathbf{E}_0 and the transmission factor τ_E . For the modelling, there is a suitable relation in the forms

$$\mathbf{E}_r = \frac{\mu_2 k_1 \cos \theta_0 - \mu_1 \sqrt{k_2^2 - k_1^2 \sin^2 \theta_0}}{\mu_2 k_1 \cos \theta_0 + \mu_1 \sqrt{k_2^2 - k_1^2 \sin^2 \theta_0}} \mathbf{E}_0 \cdot e^{-j\mathbf{k}_1 \mathbf{u}_{n1} \times \mathbf{r}},$$

$$\mathbf{E}_t = \frac{2\mu_2 k_1 \cos \theta_0}{\mu_2 k_1 \cos \theta_0 + \mu_1 \sqrt{k_2^2 - k_1^2 \sin^2 \theta_0}} \mathbf{E}_0 \cdot e^{-j\mathbf{k}_2 \mathbf{u}_{n2} \times \mathbf{r}}.$$
(3)

The interpretation of the propagation of electromagnetic waves on a layered heterogeneous medium is expressed by the relation

$$\mathbf{E}_{rl} = \mathbf{E}_{il} \rho_{El} \cdot e^{-j\mathbf{k}_l \mathbf{u}_{nrl} \times \mathbf{r}_l}, \quad \mathbf{E}_{tl} = \mathbf{E}_{il} \tau_{El} \cdot e^{-j\mathbf{k}_l \mathbf{u}_{ntl} \times \mathbf{r}_l},$$
(4)

where \mathbf{E}_{rl} a \mathbf{E}_{tl} are the reflection and refraction electromagnetic waves on the boundary line ($l = 1, \dots, \text{max}$) according to Fig. 1(a)), \mathbf{E}_{il} is the amplitude electric field strength on the boundary line l , ρ_{El} and τ_{El} are the reflection coefficient and transmission factor on the boundary line l , \mathbf{k}_l is the wave number of the layer, \mathbf{r}_l is the electromagnetic wave positional vector on the boundary line l , \mathbf{u}_{ntl} and \mathbf{u}_{nrl} are the unit vectors of the propagation direction.

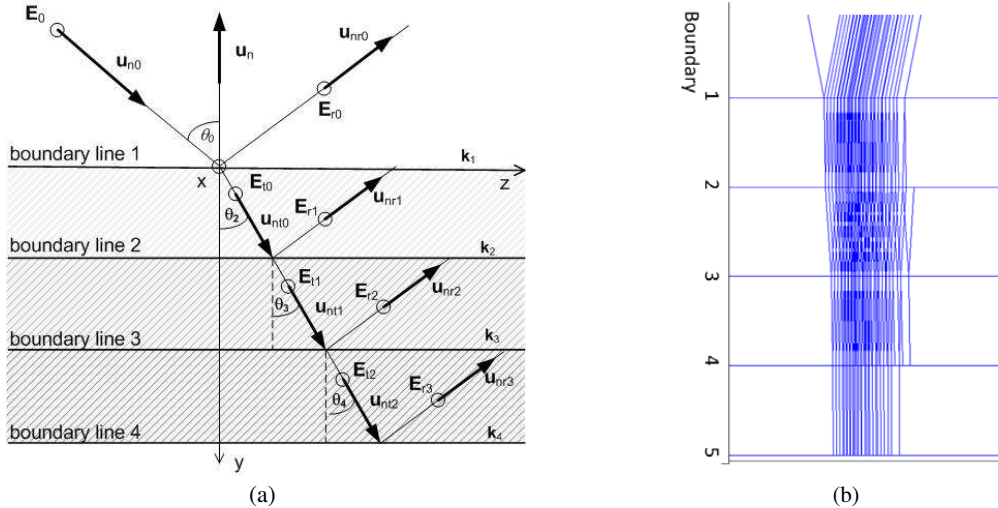
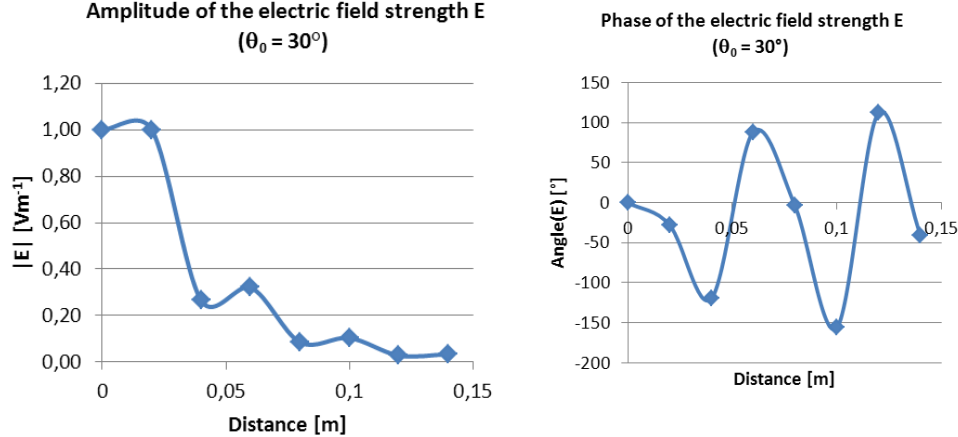
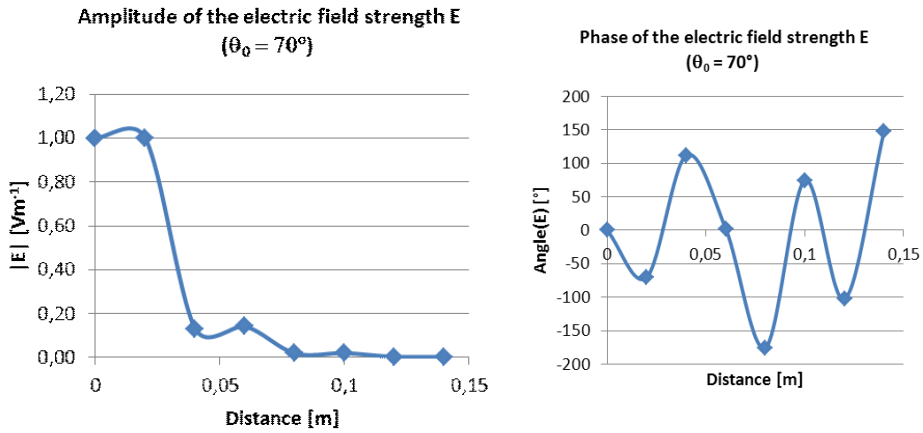


Figure 1: Reflection and refraction of the electric component of an electromagnetic wave on a layered medium: (a) layout, (b) Matlab for 5000 cycles.

2. OBLIQUE INCIDENT WAVE ON A LAYERED MEDIUM

The Matlab-based analysis using Equations (3) and (4) was performed in the planar layers. Figs. 2 and 3 show the response of the environment of 5 layers with the same thickness $d = 20$ mm. During the transmission, the wave at the frequency of 1 GHz passes from the surrounding environment with the parameters $\epsilon_{r0} = 1$, $\mu_{r0} = 1$, and $\gamma_0 = 0$ S/m at the incidence of the wave on the boundary 1 at the angle of θ_0 (according to Fig. 1(a)) into a material 1 with parameters $\epsilon_{r1} = 1$, $\mu_{r1} = 1$ and $\gamma_1 = 1.10^{-9}$ S/m, where the wave is reflected and refracted. Furthermore, the wave propagates through material 2 with parameters $\epsilon_{r2} = 81$, $\mu_{r2} = 0.999991$, and $\gamma_2 = 1.10^{-9}$ S/m; after that, the wave passes through materials 3 and 5 having the same parameters as material 1 and via material 4 with the same parameters as material 2. The selection of the material parameters is only a test, and thus it does not have any special meaning.

From the complex form of the angle of reflection θ_r and angle of refraction θ_t , we determine the intensity of the reflected and refracted waves. To derive the direction of the propagation of the electromagnetic waves, we cannot use the real part of the angle, because the part changes with any change of the direction of the propagation constant amplitude. It is necessary to separate the complex angle from the real angle and analyze them separately. By retrospective evaluation of the direction of propagation from the complex form of the angle, the error is up to 50%. This value is not negligible.

Figure 2: The strength of the electric component of the TE wave on a layered medium at the angle $\theta_0 = 30^\circ$.Figure 3: The strength of the electric component of the TE wave on a layered medium at the angle $\theta_0 = 70^\circ$.

Figures 2 and 3 show the response of the separate layers to the primary refraction electromagnetic wave. The response of the material is the response to an electromagnetic wave of the pulse source. Fig. 2 and Fig. 3 do not show the interferences for a more descriptive interpretation of the attenuation of the electromagnetic waves. However, the algorithm evaluates all of the reflected and refracted waves.

3. FEM MODEL OF A LAYERED MEDIUM

In order to verify the properties of the analytical model of an accurate evaluation of wave propagation in a layered environment, another model was used. This numerical model utilizes the finite element method (FEM) and has the same properties as the previous model. As the mathematical model, we applied the enhanced wave equation for a lossy environment:

$$\nabla^2 u + f \frac{\partial u}{\partial t} + g \frac{\partial^2 u}{\partial t^2} - f_c(x, y, z, t) = 0, \quad \forall g(x, y, z) \neq 0, \quad \forall f(x, y, z) \neq 0, \quad \text{in } \Omega \quad (5)$$

where u is the searched functional, f a function of the electromagnetic wave damping, g a function of the electromagnetic wave excitation, f_c a function of the lossy environment, Ω the defining domain of variables and functions.

The FEM numerical method with defined boundary conditions is applied to Equation (5), and an incident electromagnetic wave is also defined. The distribution of the electric field \mathbf{E} and its phase ϕ were evaluated within the model analysis. Fig. 3 shows the distribution of the electric field strength \mathbf{E} in dependence on the initial angle of the electromagnetic wave incidence. For similar incidence angles of the electromagnetic wave, the strength and phase of the electric field are shown in Fig. 4. The characteristics in Fig. 4 correspond to the axis direction perpendicular to the layer plane.

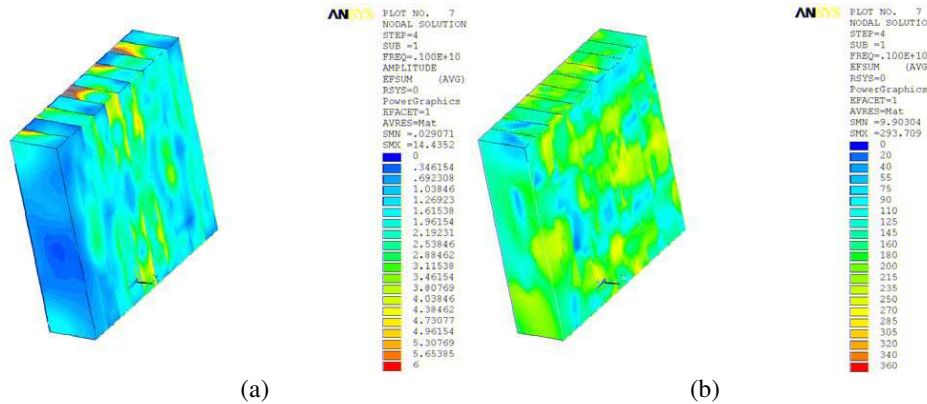


Figure 4: The distribution of the electric field strength \mathbf{E} : (a) amplitude, and (b) phase for $\theta_0 = 30^\circ$.

4. CONCLUSIONS

The article presents a comparison of two approaches to the analysis of wave propagation in a layered material structure. The first of these techniques is based on the propagation of electromagnetic waves as defined by analytical formulas (3), (4) and was solved in the Matlab program. The second approach utilizes the FEM applied to the wave equation. The FEM-based solution was conducted using the Ansys system. The comparison of the results provided by both approaches cannot be performed directly.

Numerical modelling carried out by means of the wave equation and ANSYS produces a continuous source of electromagnetic waves. Interference effects between the reflected and refracted waves arise on the boundary between the layers. Moreover, the interference process is also entered by the time-delayed waves from the source and interface reflections [4].

A complex form of the angle of reflection and refraction is considered in the case of the analytical approach, which allows accurate determination of the size and intensity of the reflected and refracted waves. In order to determine the direction of the constant phase propagation in a lossy medium, we consider only real parts of the wave number. The analytical solution and its algorithms process the time-varying phenomena of the pulsed source. The analytical solution includes the effect of time-dependent propagation of electromagnetic waves in a heterogeneous medium, and it results in the distribution of the electromagnetic field at the boundaries during certain moments of time.

The results of the ANSYS-based analysis of the propagation of electromagnetic waves in a material in the time-domain corresponds to the resulting distribution of the superimposed field intensities on individual boundaries of the analytical model. In the case of evaluation of the impulse phenomenon, it can be concluded that the ANSYS method is disadvantageous, because the phase change behaviour is non-uniform due to the multiple interference and the different propagation speeds. By contrast, the analysis of the pulsed source of the electromagnetic wave by means of an analytical model provides expectable results in heterogeneous structures since the behavior of phase change is uniform. The analytical solution allows us to analyze the response of the material in detail for the individual parts.

ACKNOWLEDGMENT

The research described in the paper was financially supported by Czech Science Foundation (13-09086S), a project of the BUT Grant Agency, No. FEKT-S-11-5/1012, and a project from the Education for Competitiveness Operative Programme, No. CZ.1.07.2.3.00.20.0175 (Electro-researcher).

REFERENCES

1. Roubal, Z., M. Steinbauer, and Z. Szabó, "Modeling of saturation characteristic of an aspiration condenser," *PIERS Proceedings*, 216–220, Xian, China, March 22–26, 2010.
 2. Steinbauer, M. and K. BArtušek, "Numerical method of simulation of material influences in MR tomography," *PIERS Proceedings*, 1077–1080, Hangzhou, China, March 24–28, 2008.
 3. Dedek, L. and J. Dedková, *Elektromagnetismus*, 232, Brno, VITIUM, 2000, ISBN 80-214-1548-7.
 4. Drexler, P. and R. Kubásek, "Pulsed magnetic field fiber optic sensor based on orthoconjugate retroreflector," *Proceedings of SCS 2009 International Conference on Signals, Circuits and Systems*, 52–57, Tunisia, 2009, ISBN: 978-1-4244-4398-7.

Low-level Measurement of the Electric Field Intensity around a Heterogeneous Structure

P. Fiala, M. Friedl, J. Mikulka, I. Behunek, and Z. Szabo

Department of Theoretical and Experimental Electrical Engineering

Brno University of Technology, Technická 3082/12, Brno 616 00, Czech Republic

Abstract— The paper presents the measurement of the electric field intensity in the area of a biological structure. The measured quantity can be evaluated remotely, without touching the plant, and this is a factor of exceptional importance for field applications. But the decisive aspect consists in the possibility of deciphering the information (about a living object) that may be carried by the electric field. Therefore, the most vital problem is to find out whether the electric field could be utilized for contactless diagnostics. The principle of the method will consist in electric charge measurement on the electrodes of a capacitive sensor exhibiting the elimination of interferences and leakage currents. Theoretical analysis will be performed to enable the setting of the measurement method sensitivity with respect to the anticipated diurnal magnitudes of the electric field in different instantaneous weather conditions. The measurement method using one test tree within a tree stand will be analyzed; the group of other related steps comprises modification proposals for the sensor and the measurement methodology, comparison with the theoretical model, and direct comparison with the data evaluated by other laboratory or experimental techniques.

1. INTRODUCTION

Within biological structures, the investigation of the properties of cells and higher organizational units such as tissues or organs can be advantageously supported by the monitoring of quantities or aspects that include electric field intensity \mathbf{E} , electric potential φ , oxygen density in tissues, and the content and distribution of proteins, enzymes, or insulin [1–3]. For these purposes, however, the researchers need to have a good command of the metrology and measuring methods related to low-level measurement. One of the activities subsumed under biological research [4] consists in the measurement of fluid circulation in wood, which is realized at various rates ranging between 0.1–1 m/hour. This activity is further complemented with the monitoring of the electric field intensity distribution in the vicinity of the examined region. In the described biological materials, electric field intensity must be monitored not only in close vicinity of the tree and its parts (a cell, a tracheid, the root system components, the trunk, branches, leaves, and needles), but also in entire tree groups and stands. The electric field intensity vector \mathbf{E} in the biological structure of a tree is related to a specific density of the fluid and the pace of its flow within the system of the given biological material.

The measurement of fluid concentration and its circulation through tree structure tissues constitutes a rather difficult task that cannot be realized in a simple manner if the planned measurement process is conceived as non-destructive. The measurement method is based upon the monitoring of impedance changes that occur within the sensor environment, namely in the sensor resonance area above the porous material [2–4].

Electric field intensity \mathbf{E} is a quantity that records the microscopic and macroscopic characteristics of a biologically active system such as a tree, in which the process of growth can be observed [5]. The basic concept for the measurement of electric field intensity \mathbf{E} was outlined in paper [6]. It has been proved that a convenient opto-electronic measuring method with an active sensor or detection or air properties [6] (the Raman scattering spectrum detection). constitutes a feasible solution for external applications in various weather conditions in various weather conditions. The authors of this paper have concentrated mainly on the opto-electronic method including an active sensor.

2. OPTO-ELECTRONIC MEASUREMENT OF THE ELECTRIC FIELD INTENSITY

Electro-optical crystals exhibit electro-optical properties; owing to the influence of the external magnetic field, there occurs a change of the refractive index known as the Pockels effect. The optical properties of an electro-optical crystal can be described according to the relation known as index ellipsoid. The following formula is given by the equation derived in detail within [7]:

$$\left(\frac{1}{n_x^2}\right)x^2 + \left(\frac{1}{n_y^2}\right)y^2 + \left(\frac{1}{n_z^2}\right)z^2 = 1, \quad (1)$$

where x , y and z are the main (or crystallographic) axes of the crystal, and n_x , n_y and n_z are the main refractive indexes in the directions x , y and z . This equation holds true for zero intensity of the applied electric field. The formula of the crystal for the applied electric field E (E_x , E_y , E_z) is as follows:

$$\left(\frac{1}{n^2}\right)_1 x^2 + \left(\frac{1}{n^2}\right)_2 y^2 + \left(\frac{1}{n^2}\right)_3 z^2 + 2\left(\frac{1}{n^2}\right)_4 yz + 2\left(\frac{1}{n^2}\right)_5 xz + 2\left(\frac{1}{n^2}\right)_6 xy = 1, \quad (2)$$

and if x , y and z are aligned with the main axes of the crystal and $E = 0$, then the equation must be reduced to the above-shown formula (1). The change of the refractive index is defined as

$$\Delta \left(\frac{1}{n^2}\right)_i = \sum_{j=1}^3 r_{ij} E_j, \quad (3)$$

where the value $j = 1, 2, 3$ represents the directions x , y and z . This definition allows us to express the formula (3) as a matrix in the following manner:

$$\begin{bmatrix} \Delta \left(\frac{1}{n^2}\right)_1 \\ \Delta \left(\frac{1}{n^2}\right)_2 \\ \Delta \left(\frac{1}{n^2}\right)_3 \\ \Delta \left(\frac{1}{n^2}\right)_4 \\ \Delta \left(\frac{1}{n^2}\right)_5 \\ \Delta \left(\frac{1}{n^2}\right)_6 \end{bmatrix} = \begin{bmatrix} r_{11} & r_{12} & r_{13} \\ r_{21} & r_{22} & r_{23} \\ r_{31} & r_{32} & r_{33} \\ r_{41} & r_{42} & r_{43} \\ r_{51} & r_{52} & r_{53} \\ r_{61} & r_{62} & r_{63} \end{bmatrix} \cdot \begin{bmatrix} E_x \\ E_y \\ E_z \end{bmatrix}, \quad (4)$$

where the 6×3 matrix with elements r_{ij} is referred to as an electro-optical tensor matrix of the crystal. By simplification we have:

$$\left(\frac{1}{n_0^2}\right) x^2 + \left(\frac{1}{n_0^2}\right) y^2 + \left(\frac{1}{n_0^2}\right) z^2 + 2r_{41}E_x yz + 2r_{41}E_y xz + 2r_{41}E_z xy = 1 \quad (5)$$

Let us assume a beam of light linearly polarized along the crystallographic x -axis and travelling in the z -direction. We then have the following formula:

$$\varepsilon_x = A e^{i(\omega t - k_x z)}. \quad (6)$$

The beam can be decomposed into two polarized components along the main dielectric axes x' and y'

$$\begin{aligned} \varepsilon_{x'} &= A e^{i(\omega t - k_{x'} z)} \\ \varepsilon_{y'} &= A e^{i(\omega t - k_{y'} z)}, \end{aligned} \quad (7)$$

where $k_{x'} = (2\pi/\lambda_0) n_{x'}$ a $k_{y'} = (2\pi/\lambda_0) n_{y'}$. After modifying the formula (7), we obtain the phase change equation

$$\begin{aligned} \varepsilon_{x'} &= A \exp \{ i [\omega t - (2\pi/\lambda_0) (n_0 - 1/2n_0^3 r_{41} E_z) z] \} = A \exp (i\phi_{x'}) \\ \varepsilon_{y'} &= A \exp \{ i [\omega t - (2\pi/\lambda_0) (n_0 + 1/2n_0^3 r_{41} E_z) z] \} = A \exp (i\phi_{y'}). \end{aligned} \quad (8)$$

The difference of the phases between the components is referred to as retardation and defined in the following way:

$$\delta_E = \phi_{x'} - \phi_{y'} \quad (9)$$

$$\delta_E = \frac{2\pi n_0^3 r_{41} V}{\lambda_0}, \quad (10)$$

where $V = E_z$ for the given length. The difference of the phases induces phase delay between the orthogonal polarizations, which is denoted as double refraction. In electro-optical crystals, such double refraction is caused by the applied electric voltage. Some materials exhibit the basic type of this phase delay; for example, limestone, firestone, and margarite are materials in which natural double refraction occurs.

3. DESCRIPTION AND ARRANGEMENT OF THE EXPERIMENT

The main component of the entire experiment consists in a BSO electro-optical crystal, whose dimensions are $2 \times 4 \times 8$ mm, and the half-wave voltage attains the value of 965.39 V. Electrodes made of an electrically conductive material should be placed transversely on the crystal; however, we will not utilize this solution because a high voltage power supply will be applied as the source of the electric field intensity. The power supply is capable of generating voltage between 500 V and 20 kV; thus, we will induce a suitably large intensity of the field E in free space by means of the pre-set electrode system sphere/plate, and no steamed electrodes will be necessary.

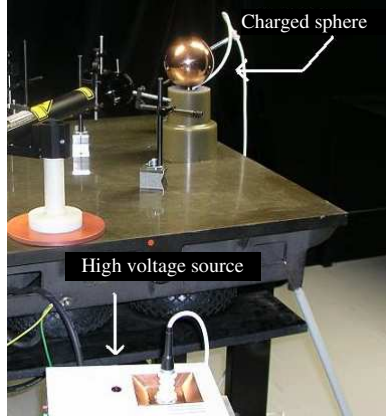


Figure 1: The high voltage supply that charges a spherical electrode — the source of the electric field E intensity..

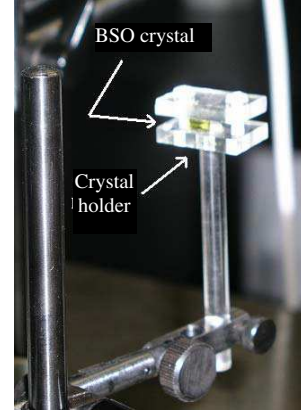


Figure 2: The BSO crystal and its positioning in the holder.

The crystal is placed in a special holder, Fig. 2. Within the experiment, we will verify a system with one junction and a $\lambda/4$ plate; this configuration was selected based on the availability of the required plate and with the aim to ensure linearity in the range of 0 V–107.3 V. In the experimental setup, a He-Ne radiation source is followed by a polarizer and the $\lambda/4$ plate, the crystal placed in the holder, an analyzer, and a PIN-type photodiode connected to an oscilloscope. The arrangement is shown in Fig. 3 below.

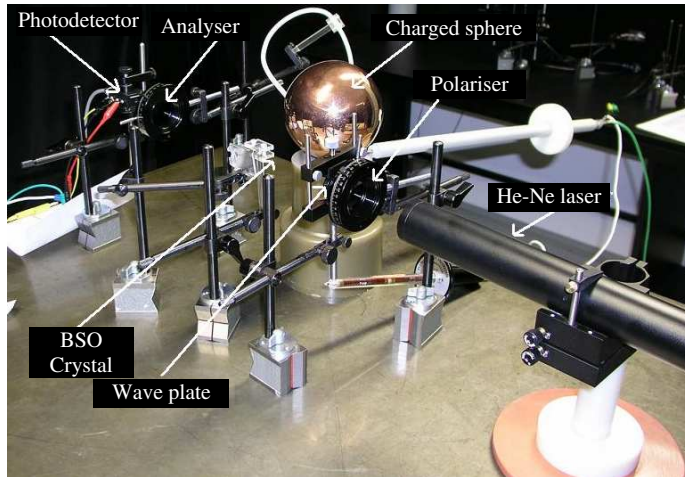


Figure 3: Configuration of the experiment.

4. THEORETICAL MINIMUM DETECTABLE VALUE OF THE METHOD

Based on a detailed schedule [7], the expected output power of the system with one junction P_{out} is as follows:

$$P_{out} = P_{in} 10^{\frac{-dB_{ztrat}}{10}} \left(1 + \pi \frac{U}{U_\pi} \right), \quad (11)$$

where P_{in} is the input power of the laser beam, dB_{loss} represents the power loss of the system in dB, U expresses the voltage applied to the electrodes of the crystal, and U_π is the half-wave voltage. For a two-junction system, the expected output voltage is

$$P_{out} = P_{in} 10^{\frac{-\text{dB}_{ztrat}}{10}} \left(1 + 2\pi \frac{U}{U_\pi} \right). \quad (12)$$

If we concentrate on determining the minimum detectable value of the voltage U_{\min} , then the output power P_{out} is the sum of the minimum detectable value and the noise-equivalent power

$$P_{out} = P_{out\min} + NEP \quad (13)$$

For the system with one junction, we then have

$$P_{out\min} + NEP = P_{in} 10^{\frac{-\text{dB}_{ztrat}}{10}} \left(1 + \pi \frac{U_{\min}}{U_\pi} \right), \quad (14)$$

and the formula for the two-junction system is

$$P_{out\min} + NEP = P_{in} 10^{\frac{-\text{dB}_{ztrat}}{10}} \left(1 + 2\pi \frac{U_{\min}}{U_\pi} \right). \quad (15)$$

After modification, we obtain a formula for the system with one laser beam junction; in this formula, NEP is the noise-equivalent power. The power is expressed from the known bandwidth for the given photodetector, namely $B = 3.5 \text{ MHz}$ [7], and from the value of the spectral power of the noise NEP_{SPEKT} .

$$NEP = NEP_{SPEKT} \cdot \sqrt{B} = 4.1 \cdot 10^{-14} \cdot \sqrt{3.5 \cdot 10^6} = 76.7 \text{ nW} \quad (16)$$

If the loss of the system amounted to 10 dB (which is an achievable value in the given case) and the output power were set to the maximum of 15 mW at the half-wave voltage of $U_\pi = 965.4 \text{ V}$, the value of the minimum detectable voltage for the system with one junction would be

$$U_{\min} = U_\pi \frac{NEP}{\pi \cdot P_{in} 10^{\frac{-\text{dB}_{ztrat}}{10}}} = 965.4 \frac{76.7 \cdot 10^{-9}}{\pi \cdot 15 \cdot 10^{-3} \cdot 10^{\frac{-10}{10}}} = 16 \text{ mV}. \quad (17)$$

For the two-junction system, we would then have

$$U_{\min} = U_\pi \frac{NEP}{2\pi \cdot P_{in} 10^{\frac{-\text{dB}_{ztrat}}{10}}} = 965.4 \frac{76.7 \cdot 10^{-9}}{2\pi \cdot 15 \cdot 10^{-3} \cdot 10^{\frac{-10}{10}}} = 8 \text{ mV}. \quad (18)$$

5. CONCLUSION

The paper discusses the classification of methods for the contactless measurement of the electric field strength in external applications requiring a high degree of sensitivity. In view of the opto-electronic methods with a sensor and considering detectable changes of the opto-electronic properties of air, the authors have concentrated on the technique using a sensor.

The above-described method was experimentally analyzed in laboratory conditions, and its sensitivity was determined to range within units of mV in a two-junction system. Such sensitivity is sufficient for capturing the magnitude or changes of the intensity of the electric field E in the vicinity of plants, for example trees. The research is being continued to enable wide application of this technique to external tests conducted in various weather conditions.

Moreover, the investigation will be also centered on the opto-electronic methods that, without using any opto-electronic sensors, utilize the properties of thin air layers in the region of the electric field with intensity E .

ACKNOWLEDGMENT

The research described in the paper was financially supported by the GACR 13-09086S grant, a project of the BUT Grant Agency No. FEKT-S-11-5/1012, and projects from the Education for Competitiveness Operative Programme, Nos. CZ.1.07.2.3.00.20.0175 and CZ.1.07/2.3.00/30.0005.

REFERENCES

1. Meleschenko, S. N., "Nature of changes in electrical properties of plant tissue with change in the external conditions," *Biofyzika*, Vol. 10, No. 3, 507–513, 1965.
2. Aubrecht, L., Z. Stanek, and J. Koller, "Systematic study of the characteristics of the point to-plane corona on natural objects," *Proceedings of the International Congress on Plasma Physics 25th EPS Conference on Controlled Fusion and Plasma Physics*, 2431–2433, ECA 22C, Prague, 1998.
3. Aubrecht, L., J. Koller, and Z. Staněk, "Onset voltages of atmospheric corona discharges on coniferous trees," *Journal of Atmospheric and Solar Terrestrial Physics*, Vol. 83, 1901–1906, 2001.
4. Steinbauer, M., P. Fiala, K. Bartušek, and Z. Szabó, "Experiments with accuracy of air ion field measurement," *PIERS Proceedings*, 1062–1066, Hangzhou, China, March 24–28, 2008.
5. Vojtek, T., M. Steinbauer, P. Fiala, and K. Bartušek, "Gerdien condenser measuring and numerical modeling of air ion fields," *Applied Electronics*, 225, 2006, ISBN: 978-80-7043-442-0.
6. Fiala, P., M. Friedl, and J. Mikulka, "Low-level measurement of electric field intensity," *PIERS Proceedings*, 178–181, Moscow, Russia, August 19–23, 2012.
7. Dordova, L., "Electric charge measurement using special techniques," Diploma Thesis, Brno University of Technology, Czech Republic, May 2007.

Consequences of the Extended Field Theory

Konstantin Meyl

Faculty of Computer and Electrical Engineering, Furtwangen University, Germany

Abstract— We all learned from our textbooks, that the field equations according to Maxwell do not describe potential vortices in the dielectric such as vortex losses in capacitors. But this was yesterday. Since Science and Nature have reported in 2009 about the development of magnetic monopoles by the German Helmholtz Society [12] the 3rd Maxwell equation ($\operatorname{div} B = 0$) is describing only a special case and we have to consider about the consequences and the impact to what we learned about electrodynamics.

In the contribution in PIERS 2012 in Moscow [1] from the new and extended field equations the pointing vector was derived with one loss term in addition, based on the new development but avoiding any postulates. The present contribution at PIERS 2013 is continuing the published ideas from 2012, with the aim, to prove the losses of capacities.

It will be shown, that still visible proves are published, like vortex spots in high voltage capacities. The frequency dependence of the loss factor, calculated by the Lorentz model, compared with calculations as vortex losses, according to the new and extended field theory show very clear the importance and power of this new theory.

Thus the calculated potential-vortex and its effect on the dielectric medium can be measured and its existence made evident through observable natural phenomena.

1. INTRODUCTION (ABOUT VORTEX LOSSES)

Conductive materials like silver, copper or aluminum heat up by electrical currents and eddy-currents. Dielectrics, as they are used in capacitors and insulating materials, distinguish themselves by a low electric conductivity which is why no eddy-currents are to be expected. Besides, potential-vortices and the accompanying vortex losses are totally unknown in the valid field theory which is why we must continue to search for the reasons why a non-conductor gets hot.

Electrets and other ferroelectric materials with distinctive hysteresis $D(E)$ -characteristics [i.e., barium titan-ate] are extremely rare. Because the material should be blamed for the measurable losses, the polarization of the material still remains as a possible reason for losses.

As a consequence of change in polarity with high frequencies, the dielectric displacement D follows the electric field strength E time-delayed. The produced loss factor δ represents the dielectric losses. This is what we learn from our textbooks [2]. However, this entails a complex dielectric coefficient:

$$\varepsilon = \operatorname{Re}\{\varepsilon\} + j\operatorname{Im}\{\varepsilon\} \quad (1)$$

with the loss factor

$$\tan \delta = \operatorname{Im}\{\varepsilon\}/\operatorname{Re}\{\varepsilon\}. \quad (2)$$

which results directly in a complex speed of light c according to the definition

$$\varepsilon \cdot \mu = 1/c^2, \quad (3)$$

which is an offence against the basic principles of physics!

A transient hysteresis $D(E)$ -characteristic would also have to appear in dielectric, but non-ferroelectric, materials. This is verified by the frequency dependency, because a direct proportionality to an increasing frequency would be expected. However, the technologically important insulating materials show a widely constant loss factor. Leaving the question, which physical phenomenon heats up an insulator?

In spite of offence against the constance of the speed of light, the complex epsilon belongs to the inalienable toolbox of every electrical engineer. He will not want this tool to be taken from him. Practical people think and act pragmatically: “*if no better theory is available*”, many argue, “*then a wrong theory is still better than none*”.

With this reasoning, even dielectric losses that have not yet been investigated, are considered and summed up under the loss factor (2).

2. THE FIELD THEORY FROM MAXWELL'S DESK

At least, this physically wrong model is in many cases able to deliver useful arithmetic values [2]. We can say, “*the description is harmlessly wrong*”, from the mathematics’ point of view.

However for a member of theoretical physics, who is confronted with a complex speed of light, the complex dielectricity ϵ marks the end of all efforts. If the result of a derivation turns out wrong the mistake is either in the approach or in the derivation.

The latter is presumably perfect, after generations of students had to check the calculations year after year. At some point a mistake had to appear. Under these circumstances the mistake quite obviously lies in the approach, in the basic acceptance of classical electrodynamics [3].

Here the vector potential \mathbf{A} is introduced mathematically correct. Physically speaking, this is still a foreign body in the field theory. In addition, vector potential and potential-vortex exclude themselves mutually. We will have to decide whether to calculate dielectric losses with a complex Epsilon or with the vortex decay, because doing so both ways at the same time is mathematically impossible.

With his book “*A Treatise on Electricity and Magnetism*” [4] from 1865 *James Clerk Maxwell*, professor of mathematics, pursued an ambitious aim to derive the wave equation of *Laplace* from an equation sentence about the electric and magnetic field, to describe light as an electromagnetic wave.

The enlarged representation by means of quaternions from 1874 with its mathematical description of potential-vortices, scalar waves and many unconfirmed phenomena exceeded the physical phenomena experimentally provable in the past. Therefore, a vector potential was not necessary in the depiction.

Only in 1888 was one of the numerous phenomena proven experimentally by *Heinrich Hertz* in Karlsruhe (Germany), concerning the electromagnetic wave. Eddy-currents were also recognized together with the laws by *Ampère*, *Faraday*, and *Ohm*. This is why *Heaviside* suggested shortening the field equations of *Maxwell* to both proven phenomena. Professor Hertz agreed and professor Gibbs wrote down the truncated field equation in its currently still commonly used notation of vector-analyses.

Since then the field theory has not been able to describe longitudinal waves even though they had been proven by *Tesla* in 1894 [5]; and they had to be postulated over and over again, for example for the near field of an antenna [6].

3. THE VECTOR POTENTIAL

To describe other secured facts of electrodynamics, for example dielectric losses, *Maxwell* had already considered the introduction of a vector potential \mathbf{A} :

$$\mathbf{B} = \text{curl} \mathbf{A} \quad (4)$$

As a consequence of this mathematical statement the divergence of the magnetic flux density \mathbf{B} is zero.

$$\text{div} \mathbf{B} = \text{div curl} \mathbf{A} = 0 \quad (5)$$

J. D. Jackson [3] and his followers [11] thought $\text{curl} \mathbf{B}$ to be magnetic monopoles. As long as they do not exist, the field physicists want to see a confirmation for the correctness of Eq. (5) (3rd Maxwell equation). This has been the presumption until now.

On September 3rd 2009, the *Helmholtz centre* in Berlin, Germany, announced [9 Science, and others]: “*Magnetic monopoles proven for the first time*”. With this discovery in a magnetic solid state the vector potential with all its calculations is no longer viable, in spite of the correctness and verifiability of all present results. One can also say, “*we must start all over again and consider a new approach*”.

I suggest a vortex description completely without vector potential \mathbf{A} and with

$$\text{div} \mathbf{B} \neq 0 \quad (6)$$

With my approach even the *Aharonov Bohm* effect is explainable, generating scalar waves, that are verified after they have tunneled through a screening. According to today’s interpretation [11] this effect with no measurable field is assigned to the vector potential and even spoken of as evidential value.

4. HELMHOLTZIAN RING-LIKE VORTICES IN THE AETHER

The doubts about classical electrodynamics are not new. In 1887 *Nikola Tesla* demonstrated his scalar wave experiments to the theoretical physicist *Lord Kelvin* in his lab in New York. He told Kelvin about the meeting with the German Professor *Hermann von Helmholtz* on the occasion of the World's Fair in Chicago 1893. Kelvin knew him very well and had cooperated with him in the past. Now the vortex concept of his colleague and his model of stable vortex rings were very helpful.

In the case of a standing wave the impulse is passed on from one particle to the next. In the case of acoustics we are dealing with a shock wave where one air molecule knocks the next. In this way sound propagates as a longitudinal wave. Correspondingly the question is raised: “*What sort of quanta are the ones, which in the case of the Tesla radiation carry the impulse?*”

Lord Kelvin deduced: “*The Tesla experiments prove the existence of longitudinal standing waves in space*”.

Through the question, what passes on the impulse, Kelvin comes to the conclusion: it is *vortices in the aether!* With that he had found an answer to his contemplations.

With his students he built boxes, with which he could produce smoke rings, to be able to study and demonstrate in experiments the special properties of ring-like vortices as a fluid dynamics analogy.

But he didn't have a suitable field theory. For a short time Germany exported vortex physics to England, before it was buried by the German quantum physicists. A primary advocate was *James Clerk Maxwell*, who held the vortex theory for the best and most convincing description of matter [8, 9]: James Clerk Maxwell: “... *the vortex rings of Helmholtz, which Thomson imagines as the true form of the atom, fulfil more conditions than any other previous concept of the atom.*”].

As his successor at the *Cavendish laboratory in Cambridge J. J. Thomson* was appointed to a professorship. As a young man he received an award for a mathematical treatise about vortices. He discovered the electron and imagined it, how could it be otherwise, as a field vortex. [10: J. J. Thomson: “*the vortex theory is of much more fundamental nature than the usual theory of solid particles*”].

The crucial weakness of vortex physics, the lacking of an usable field theory, was of benefit to the emerging quantum physics. This could change fundamentally with the discovery of the potential-vortex, the vortex of the electric field.

In addition, the experimental proof of a vortex transmission as a longitudinal wave through air or a vacuum, as accomplished by Tesla already 100 years ago, is neither with Maxwell's field theory nor with the currently used quantum theory explicable or compatible. We are faced with an urgent need for a new field theory.

5. NOISE INTENSITY OF THE CAPACITOR

So we apply vortex physics to a dielectric with a suitable model representation.

The wave will now rotate around a stationary point, the vortex centre. The propagation with the speed of light c is maintained as the rotary-velocity. For a plane circular vortex, where the path for one revolution on the out-side is a lot longer than near the vortex centre, arises a longer wave length and as a consequence a lower frequency on the outside, then on the inside.

With this property the vortex proves to be a *converter of frequency*: the vortex transforms the frequency of the causing wave into an even spectrum, that starts at low frequencies and stretches to very high frequencies.

This property we observe as “*white noise*”. The consistent conclusion would be that this concerns the vortex of the electric field. Anyone can, without big expenses, convince him or her-self that the property to change frequency is dependent on position and of the circumstance that vortices can be very easily influenced and that they avoid or whirl around a place of disturbance (i.e., an antenna).

For that, one only needs to tune a radio receiver to a weak and noisy station and move oneself or some objects around, then one is able to directly study the effect of the manipulation of the receiving signal.

But already the fact that the use and measuring of signals is limited by noise, highlights the need to pay attention to the potential-vortex.

Within a limited frequency range the power of the Nyquist or resistance noise is *independent of frequency*.

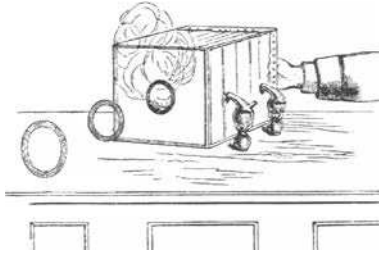


Figure 1: [7]: Vortex rings from a smoke vortex gun.

This should be clarified particularly by the term “*white noise*” analogous to white light, where all visible spectral ranges independent of frequency have the same energy density.

But this relation doesn't hold for high frequencies of any magnitude. Here another noise-effect appears that is said to have its cause in the quantum structure of energy [2]. Untouched by possible interpretations an increasing power of the noise is measured, that is more and more proportional to its frequency (Fig. 2, curve a). Interestingly this curve shows a remarkable *duality* to the power output curve of eddy currents, likewise plotted alongside the frequency, which can for instance be measured on eddy current couplings [13] (Fig. 2, curve b).

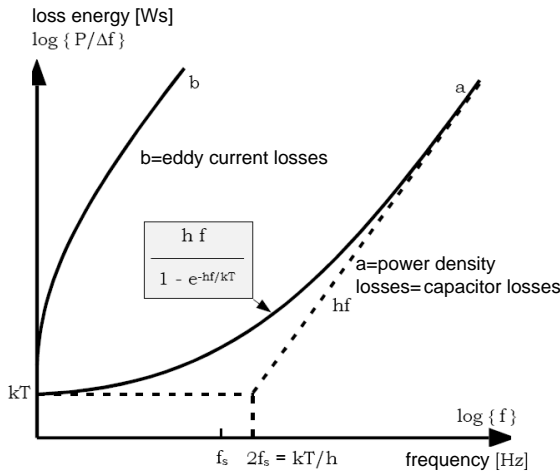


Figure 2: The power density shown against frequency (a) for noise according to Küpfmüller [2], as well as for dielectric losses of a capacitor (also a) and (b) for eddy current losses according to Meyl [13], (b in visible duality to a).

This circumstance suggests a dual relationship of the potential-vortex of the electric field in weakly conducting media on the one hand and the eddy current in conductive materials on the other hand [14].

6. CAPACITOR LOSSES

Next, the dielectric losses in a capacitor supplied with an alternating current, are measured and also plotted alongside the frequency. At first their progressions are independent of the frequency, but towards the higher frequencies they increase and show the same characteristic course of the curve referring to the power of the noise (Fig. 2, curve a).

This excellent correlation leads to the assumption that the dielectric losses are nothing but *vortex losses*.

These vortex phenomena, caused by time-varying fields, are not only found in ferromagnetic and conductive materials but equally as dual phenomena in dielectric and non-conductors.

Examples of practical applications are induction welding and the microwave oven. The process can be described in other words as follows: in both examples the cause is posed by high-frequency alternating fields that are irradiated into a dielectric as an electromagnetic wave, there roll up to potential-vortices and eventually decay in the vortex centre. The desired and used thermal effect arises during this diffusion process.

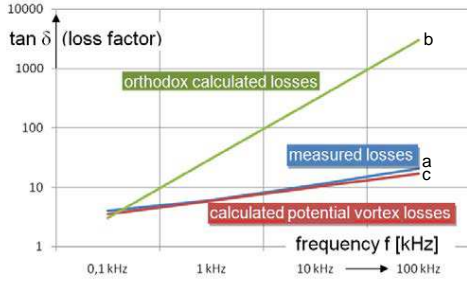


Figure 3: Experimental prove of calculated losses (qualitative comparison) with a MKT capacitor [17] (siemens). (a) Measured dielectric losses of the MKT-capacitor. (b) Standard calculation according to Lorentz-model. (c) Calculation as potential-vortex-losses acc. to Meyl-model.

The author, in collaboration with a college at the university for theoretical physics in Konstanz as part of a bachelor thesis, recently succeeded in finding a conclusive proof. For this purpose the measured dielectric losses of a standard MKT capacitor were calculated from their frequency dependence and compared. This systematically designed case deviates starkly from the conventionally derived characteristics in accordance with the Lorenz-model, the latter of which is at odds with reality and has long been known to be so and criticized by experts. In contrast to that, the characteristic of the potential-vortex losses come much closer to the truth (Fig. 3).

7. THE VISIBLE PROOF

The striving in the direction of the vortex center gives the potential-vortex of the electric field a *structure shaping property*. As a consequence of this *concentration effect* circular vortex structures are to be expected comparable to the visible vortices in flow dynamics (i.e., tornadoes and whirlwinds).

At the same time as the dual anti-vortex arises, so does the diverging eddy current. It takes on, as is well-known, the given structure of the conductor, which in the technical literature is referred to as “*skin effect*”.

Now if conductor and non-conductor meet, as they do in a capacitor, then at the boundary area visible structures will form. Circles would be expected, if the eddy current on the inside striving towards the outside is as powerful as the compressing *potential-vortex* drawing in from the outside. Actually such circular structures are observed on the aluminium of high tension capacitors when they are in operation for a longer period of time. The formation of these circles, the cause of which until now is considered to be unsolved, is already experimentally investigated and discussed on an international level by scientists (Fig. 4, [16, 17]). These circular vortex structures can be seen as a visible proof for the existence of potential-vortices of the electric field [14].

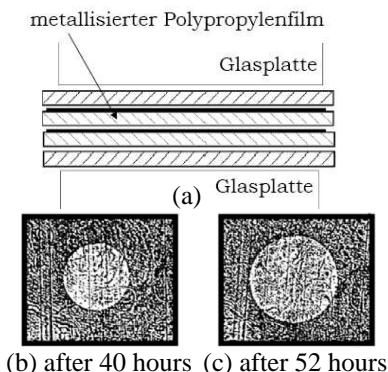


Figure 4: (a) Measurement set up and (b) and (c) photo of vortex structure in a metallized polypropylene layer capacitor at 450 V/60 Hz/100°C and 110 fold magnification observation of the formation of a vortex. According to Yializis et al. [16].

REFERENCES

1. Meyl, K., "Self-consistent electrodynamics," *PIERS Proceedings*, 172–177, Moscow, Russia, August 19–23, 2012.
2. Küpfmüller, K., *Einführung in Die Theoretische Elektrotechnik*, Springer, Verl. 12, Aufl. 1988.
3. Jackson, J. D., *Classical Electrodynamics*, 2nd Edition, Wiley & Sons, NY, 1975.
4. Maxwell, J. C., *A Treatise on Electricity and Magnetism*, Dover Publications, New York, Orig. 1873.
5. Meyl, K., *Scalar Wave Transponder*, 3rd Edition, Villingen-Schwenningen, INDEL Verlag, 2012.
6. Zinke, Brunswig: *Lehrbuch der Hochfrequenztechnik, Band 1*, 3rd Edition, 335, Springer-Verlag, 1986.
7. Ash, D. and P. Hewitt, *Science of the Gods*, Gateway Books, Bath, England, 1990.
8. Thomson, W., *Philosophical Magazine*, July 1887.
9. Maxwell, J. C., "Atoms," *Encyclopaedia Britannica*, Vol. 2, 467, 1798.
10. Thomson, J. J., *On the Motion of Vortex Rings*, London, 1883.
11. Lehner, G., *Elektromagnetische Feldtheorie*, 1st Edition, 541, Springer Verlag, 1990.
12. Morris, D. J. P., et al., "Magnetische monopole in magnetischem Festkörper entdeckt," Pressemitteilung vom 3.9.09 der *Hermann von Helmholtz-Gemeinschaft e.V. Berlin*, 2009.
13. Meyl, K., *Dreidimensionale Nichtlineare Berechnung Von Wirbelstromkupplungen*, Diss. Universität Stuttgart, (Wirbelströme, INDEL Verlag 1991), 1984.
14. Meyl, K., "Wirbel des elektrischen feldes," *EMC Journal*, Vol. 1, 56–59, 1995, 6. J, ISSN 0945-3857.
15. Treskatis, T., "Frequenzabhängigkeit der dielektrischen Verluste eines metallisierten Kunststoff-Folienkondensators," University Konstanz, 2010.
16. Yializis, A., S. W. Cichanowski, and D. G. Shaw, "Electrode corrosion in metallized polypropylene capacitors," *Proceedings of IEEE, International Symposium on Electrical Insulation*, Boston, Mass., 1980.
17. Taylor, D. F., "On the mechanism of aluminium corrosion in metallized film capacitors," *IEEE Transactions on Electrical Insulation*, Vol. EI-19, No. 4, 288–293, 1984.

Automated Segmentation of Brain Tumor Edema in FLAIR MRI Using Symmetry and Thresholding

P. Dvorak^{1,2}, K. Bartusek², and W. G. Kropatsch³

¹Department of Telecommunications, Faculty of Electrical Engineering and Communication
Brno University of Technology, Technická 12, Brno 612 00, Czech Republic

²Institute of Scientific Instruments of the ASCR, v.v.i., Královopolská 147, Brno 612 64, Czech Republic

³Pattern Recognition and Image Processing Group, Institute of Computer Graphics and Algorithms,
Faculty of Informatics, Vienna University of Technology, Favoritenstr. 9/186-3, Vienna A-1040, Austria

Abstract— Nowadays, the brain tumor detection and segmentation in MR images is a developing issue. There are many research teams producing different and interesting methods and algorithms for this particular task of medical image processing. Many of them are semi-automatic, but the aim of current research, and of this work, is to find a fully automatic method.

This paper focuses on the automatic edema segmentation in FLAIR images. This type of contrast images was selected because of the visibility and manifestation of edema in this image type. Since in axial plane of healthy brain, the approximate left-right symmetry exists, it is used as the prior knowledge for searching the approximate edema location. It is assumed that the edema is not located symmetrically in both hemispheres, which is met in most cases. For the detection, the multi-resolution approach is used. Since the edemas manifest as a hyperintense area in FLAIR images, it is extracted using thresholding. For the automatic determination of the threshold, the Otsu's algorithm is used. This work does not deal with the tumor presence detection. One of our previous work focuses on this topic. The main reason for the edema segmentation is for the tumor classification. This will be carried out by applying the resulting mask of the proposed method to perfusion MR images. Since perfusion images are of very low contrast, the pathological area, it means the tumor and a potential edema around it, has to be detected and segmented in another type of MR images.

1. INTRODUCTION

The aim of this work is to develop a fully automatic method for peritumoral region segmentation. This work does not focus on tumor presence detection. This preprocessing step was studied in our previous work [1].

The general properties of healthy brain are widely used as a prior-knowledge. One of them is the probability of tissues locations using probability brain atlas, which is used e.g., in [2]. Another widely used knowledge, which is used in this article, is the approximate left-right symmetry of a healthy brain. This approach is also used e.g., in [3, 4]. The areas that break this symmetry are most likely parts of a tumor.

There are also many other methods relying on machine learning algorithms such as SVM used e.g., in [5]. For this purpose, many algorithms need to have a patient-specific training dataset. This makes the method more demanding for the experts. These methods usually rely on other contrast images, such as combination of T2-weighted and T1-weighted contrast enhanced images.

The method proposed in this work is fully automatic. The detection process is independent on the type of the tumor. It can correctly detect anomalies in images containing a tumor, a tumor with edema or only an edema. But the segmentation step relies on higher intensity of a pathological area and can be used for areas manifesting as a hyperintense area in FLAIR images, such as edema.

2. PROPOSED METHOD

The proposed method is based on our previous work [6]. The input of the whole process is a stand-alone 2D magnetic resonance image containing a tumor. It means that no neighbor slices are considered. This method works for both axial and coronal planes, where the approximate symmetry for healthy brains exist. At first, the image is filtered by Wiener filter [8], which suppresses the noise. This causes the particular tissues to be more compact.

The edema segmentation process consists of several steps. The first step is the extraction of skull followed by cutting the image. In this cut image, the asymmetric parts are detected and then the pathological area is segmented and extracted. The detection of the symmetry axis is skipped because the input data were aligned in previous processing. The only assumption of proposed

method is a vertically aligned head. For the purpose of detecting the symmetry axis, the method described in [9] could be used. An addition of this or similar method as a preprocessing step will be one of the aims of the future work.

2.1. Brain Extraction

The extraction of brain is based on the technique used in [10] and is done by the well-known Chan-Vese algorithm of Active contour segmentation method [11]. At first, the points of background are filtered out. Since the level of noise is much lower than the signal of tissues, the computation is not complicated. The threshold is computed as an average value from the region multiplied by two, where no tissue is present. Since the tissues cannot be present in top corners of the image, the threshold is computed from these parts. The image is then thresholded and the segmentation algorithm is executed with this initial mask. Even though some points of background could remain in the initial mask, they are eliminated by segmentation. Since the skull border does not produce very high gradient in FLAIR images, the result of the segmentation is brain mask.

The smallest rectangle surrounding the brain is then extracted. Assuming that the brain is approximately symmetric, the symmetry axes is set to be parallel to the vertical axis and to divide the detected rectangle into two parts of the same size. The operation of logical conjunction is performed with this segment and its symmetric flipped image. This causes that points that are not on one side will not be considered also on the other side. Even if the mask is not so precise, the future results are not so influenced because the asymmetries caused by tumors are much higher.

2.2. Detection of Symmetric Anomalies

The process of asymmetry detection is similar to our previous work [6] and is based on multi-resolution image analysis [7]. At first, the input image is divided into two approximately symmetric halves. Assuming that the head is not rotated, the symmetry axis is parallel to vertical axis and divide the image of detected brain into two parts of the same size.

The algorithm goes through both halves symmetrically by a square block. The size of the block is computed from the size of the image. The step size is smaller than the block size to ensure the overlapping of particular areas. These areas are compared with its opposite symmetric part using by Bhattacharya coefficient [12]. Normalized histograms with the same range are computed from both parts and the Bhattacharya coefficient (BC) is computed from these histograms as follows [12]:

$$BC = \sum_{i=1}^N \sqrt{l(i) \cdot r(i)}, \quad (1)$$

where N denotes the number of bins in the histogram, l and r denote histograms of blocks in left and right half, respectively.

The range of values of Bhattacharya coefficient is $\langle 0, 1 \rangle$, where the smaller value, the bigger difference between histograms. For the next computation, the asymmetry is computed as:

$$A = 1 - BC. \quad (2)$$

The comparison is done in multi-resolution way, it means that different sizes of the block area are considered. The block side lengths are $1/4$, $1/8$, $1/16$, and $1/32$ of the smaller image side length. The results of the computation are asymmetry maps for every block size. Every asymmetry map is thresholded by a value T determined from healthy brains as:

$$T = \frac{\sum_h^H (2\mu_h + \max(AM_h))}{3H}, \quad (3)$$

where H determines number of available images of healthy brain, μ is an average value of asymmetry map AM for particular image h . Every block size has a different value of T . A conjunction of all binary masks for particular image are computed. Since in case of small tumor, the asymmetry for large block can be small, it is included for conjunction only if the mask is non-empty. If this condition is not met, only asymmetry maps for smaller block sizes are considered.

The results of the pathological area detection by symmetry analysis is shown in Figure 1.

2.3. Edema Segmentation

After the detection of symmetric anomalies, the pathological area can be segmented. For this purpose, simple thresholding is used. Since the output of asymmetry detection is both-sided mask,

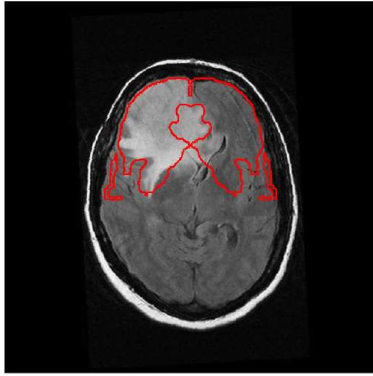


Figure 1: Results of pathological area detection process.

healthy and pathological areas are included. The threshold is determined automatically by Otsu's algorithm [13], but any other automatic method can be also used.

The threshold is determined from the image points inside the resulting mask of asymmetry detection, but the thresholding process is applied to the whole image. The conjunction of these masks is found. Since some incorrect small areas could be extracted, only the largest region of the conjunction is labeled as pathological. Since the edema could extend beyond the asymmetry area border, the whole region acquired by the thresholding is extracted. Morphological erosion and dilation are performed with the resulting mask to smooth the region borders.

3. RESULTS

The final results of the edema segmentation are shown in Figure 2. The algorithm was tested on images acquired in The University Hospital Brno and images from Radiopaedia database, the on-line collaborative radiology resource. Every image contained a tumor with an edema or only an edema. Various shapes, locations, and sizes of these pathological areas and various image resolution were tested. Even relatively small edemas were segmented correctly, but in case of very small edema, or large asymmetry in another parts, the algorithm can fail. For this purpose, the extension into 3D can significantly improve the results.

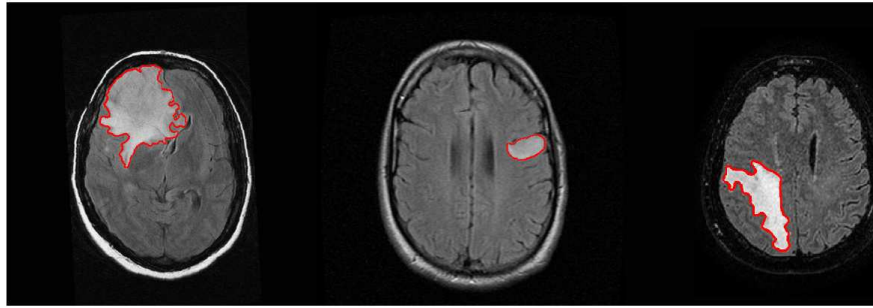


Figure 2: Results of region extraction process.

4. CONCLUSION AND FUTURE WORK

Fully automatic brain tumor edema extraction technique from FLAIR axial slices was proposed in this work. The technique is based on the multiresolution symmetry analysis and the thresholding using Otsu's algorithm.

The future work will consist of the automatic symmetry axis detection and the tumor extraction. The attention in the future work will also be paid on searching for the relations between neighbor slices and the work will be extended into 3D MR images by combining axial and coronal planes and neighbor slices.

ACKNOWLEDGMENT

This research is part of the project reg. No. CZ.1.07/2.3.00/20.0094 “Support for incorporating R&D teams in international cooperation in the area of image and audio signal processing” and is co-financed by the European Social Fund and the state budget of the Czech Republic. The described research is funded by projects SIX CZ.1.05/2.1.00/03.0072, project GACR 102/12/1104, and project CZ.1.05/2.1.00/01.0017 (ED0017/01/01).

REFERENCES

1. Dvorak, P., W. G. Kropatsch, and K. Bartusek, “Automatic detection of brain tumors in MR images,” *36th International Conference on Telecommunications and Signal Processing (TSP)*, July 2013.
2. Cuadra, M. B., C. Pollo, A. Bardera, O. Cuisenaire, J. G. Villemure, and J. P. Thiran, “Atlas-based segmentation of pathological MR brain images using a model of lesion growth,” *IEEE Trans. on Med. Imaging.*, Vol. 23, No. 1, 1301–1314, 2004.
3. Cap, M., P. Marcon, E. Gescheidtova, and K. Bartusek, “Automatic detection and segmentation of the tumor tissue,” *PIERS Proceedings*, 53–56, Taipei, March 25–28, 2013.
4. Pedoia, V., E. Binaghi, S. Balbi, A. De Benedictis, E. Monti, et al., “Glial brain tumor detection by using symmetry analysis,” *Proc. SPIE 8314, Medical Imaging 2012: Image Processing*, 831445, February 23, 2012.
5. Mikulka, J. and E. Gescheidtova, “An improved segmentation of brain tumor, edema and necrosis,” *PIERS Proceedings*, 25–28, Taipei, March 25–28, 2013.
6. Dvorak, P., W. G. Kropatsch, and K. Bartusek, “Pathological area detection in MR images of brain,” *Elektrorevue*, Vol. 4, No. 1, 17–21, April 2013.
7. Kropatsch, W. G., Y. Haxhimusa, and A. Ion, “Multiresolution image segmentations in graph pyramids,” *Applied Graph Theory in Computer Vision and Pattern Recognition Studies in Computational Intelligence*, Vol. 52, 3–41, 2007.
8. Lim, J. S., *Two-dimensional Signal and Image Processing*, Englewood Cliffs, NJ, Prentice Hall, 1990.
9. Ruppert, G. C. S., L. Teverovskiy, C. Yu, A. X. Falcao, and Y. Liu, “A new symmetry-based method for mid-sagittal plane extraction in neuroimages,” *International Symposium on Biomedical Imaging: From Macro to Nano*, 2011.
10. Ray, N., B. N. Saha, and M. R. Graham Brown, “Locating brain tumors from MR imagery using symmetry,” *Conference Record of the Forty-first Asilomar Conference on Signals, Systems and Computers*, 224–228, November 2007.
11. Chan, T. F. and L. A. Vese, “Active contours without edges,” *IEEE Transactions on Image Processing*, 266–277, 2001.
12. Bhattacharyya, A., “On a measure of divergence between two statistical populations defined by their probability distribution,” *Bulletin of the Calcutta Mathematical Society*, Vol. 35, 99–110, 1943.
13. Otsu, N., “A threshold selection method from gray-level histograms,” *IEEE Transactions on Systems, Man, and Cybernetics*, Vol. 9, No. 1, 62–66, 1979.

Hypothesis for the Identity of the $L_2(c, \rho, n)$ and $\hat{L}_2(\hat{c}, \hat{\rho}, \hat{n})$ Numbers and Its Application in the Theory of Waveguides

Georgi Nikolov Georgiev¹ and Mariana Nikolova Georgieva-Grosse²

¹Faculty of Mathematics and Informatics
University of Veliko Tarnovo “St. St. Cyril and Methodius”
Veliko Tarnovo BG-5000, Bulgaria
²Consulting and Researcher in Physics and Computer Sciences
Gerlingen D-70839, Germany

Abstract— A guess is made that if for the limited arbitrary real numbers c and \hat{c} , for the less than unity real positive ones ρ and $\hat{\rho}$, and for the natural n and the positive integer \hat{n} it holds: $c = \hat{c}$, $\rho = \hat{\rho}$ and $n = \hat{n}$, then the real positive numbers $L_2(c, \rho, n)$ and $\hat{L}_2(\hat{c}, \hat{\rho}, \hat{n})$, connected with the positive purely imaginary, resp. real zeros in x , resp. in \hat{x} of a special function, devised by two complex $\Phi(a, c; x)$ and $\Phi(a, c; \rho x)$, resp. real $\hat{\Phi}(\hat{a}, \hat{c}; \hat{x})$ and $\hat{\Phi}(\hat{a}, \hat{c}; \hat{\rho} \hat{x})$ Kummer, and two complex $\Psi(a, c; x)$ and $\Psi(a, c; \rho x)$, resp. real $\hat{\Psi}(\hat{a}, \hat{c}; \hat{x})$ and $\hat{\Psi}(\hat{a}, \hat{c}; \hat{\rho} \hat{x})$ Tricomi confluent hypergeometric ones of suitably selected complex a and real c , resp. real \hat{a} and \hat{c} parameters and a positive purely imaginary x or ρx , resp. real \hat{x} or $\hat{\rho} \hat{x}$ variable, coincide. This assumption, called Hypothesis for the identity of the $L_2(c, \rho, n)$ and $\hat{L}_2(\hat{c}, \hat{\rho}, \hat{n})$ numbers, is substantiated numerically with a higher or lower accuracy, depending on the value of c (\hat{c}). The curve of equation, written through any of the quantities $L_2(c, \rho, n)$ or $\hat{L}_2(\hat{c}, \hat{\rho}, \hat{n})$ which separates the domains of propagation of the normal TE_{0n} and of the one of the two possible slow $\widehat{TE}_{0\hat{n}}$ modes — the $\widehat{TE}_{0\hat{n}}^{(1)}$ wave ($n = \hat{n}$) in the coaxial waveguide with ferrite, magnetized azimuthally in negative (clockwise) direction, is interpreted as a physical image of the result obtained in case $c = \hat{c} = 3$, postulating ρ ($\hat{\rho}$) as a relative thickness of the central conductor of the structure and n (\hat{n}) as an order of the mode.

1. INTRODUCTION

The Georgiev and Georgieva-Grosse's $L_2(c, \rho, n)$ and $\hat{L}_2(\hat{c}, \hat{\rho}, \hat{n})$ numbers [1, 2] (denoted also through $L(c, \rho, n)$ and $\hat{L}(\hat{c}, \hat{\rho}, \hat{n})$ [3–7]) are finite real positive ones, determined like the attained under certain conditions common limits of some infinite sequences of real numbers, whose terms are proportional to the positive purely imaginary, resp. real zeros of a complex, resp. real transcendental function, involving four complex, resp. real Kummer and Tricomi confluent hypergeometric functions $\Phi(a, c; x)$ and $\Psi(a, c; x)$ [8] of appropriately chosen parameters and variable [1–7]. (Hats “ $\hat{\cdot}$ ” are put above the symbols, relevant to the second class of numbers [2, 4].) The quantities c and \hat{c} (the second parameters of confluent functions) are bounded arbitrary real, ρ and $\hat{\rho}$ (parameters, multiplying the independent variable of functions x , resp. \hat{x}) are real, positive, smaller than unity, while n and \hat{n} (the numbers of the zeros in question of the general function) — a natural number and a positive integer.

In this study a Hypothesis is formulated and corroborated numerically to the degree to which this approach allows it, asserting that if $c = \hat{c}$, $\rho = \hat{\rho}$ and $n = \hat{n}$, it is valid: $L_2(c, \rho, n) \equiv \hat{L}_2(\hat{c}, \hat{\rho}, \hat{n})$. The eventualities c (\hat{c}) — different or equal to a positive, negative integer or zero, are considered. It is shown that the theory of the azimuthally magnetized coaxial ferrite waveguide that sustains rotationally symmetric TE modes [1–7] may serve as a field of employment of the outcome spoken of.

2. $L_2(c, \rho, n)$ AND $\hat{L}_2(\hat{c}, \hat{\rho}, \hat{n})$ NUMBERS

Definition 1: *The $L_2(c, \rho, n)$ numbers in which c is a restricted arbitrary real, positive, negative or zero, ρ is real, positive, $0 < \rho < 1$ and n is a natural number, are finite real positive ones, specified in the following way:*

i) In case $c \neq l$, $l = 0, -1, -2, \dots$ [1, 7]:

$$L_2(c, \rho, n) = \lim_{k_- \rightarrow -\infty} K_{2-}(c, \rho, n, k_-) = \lim_{k_- \rightarrow -\infty} M_{2-}(c, \rho, n, k_-), \quad (1)$$

where $K_{2-}(c, \rho, n, k_-) = |k_-| \chi_{k_-, n}^{(c)}(\rho)$, $M_{2-}(c, \rho, n, k_-) = |a_-| \chi_{k_-, n}^{(c)}(\rho)$ and $\chi_{k_-, n}^{(c)}(\rho)$ is the n th positive purely imaginary zero of the function $F_2(a, c; x, \rho) = \Phi(a, c; x)\Psi(a, c; \rho x) - \Phi(a, c; \rho x)\Psi(a, c; x)$

in x , ($n = 1, 2, 3, \dots$) in which $\Phi(a, c; x)$ and $\Psi(a, c; x)$ are the Kummer and Tricomi confluent hypergeometric functions with $a = a_-$, $a_- = c/2 - jk_-$ — complex, $c = 2\text{Re}a$ ($c = 2\text{Re}a_-$), $x = jz$ — positive purely imaginary, z — real, positive, k_- — real, negative, $-\infty < k_- < 0$, ρ — real, positive, (c, n — fixed).

ii) On the understanding that $c = l$ and ε is an infinitesimal real positive number [1, 7]:

$$L_2(c, \rho, n) = \lim_{\varepsilon \rightarrow 0} L_2(l - \varepsilon, \rho, n) = \lim_{\varepsilon \rightarrow 0} L_2(l + \varepsilon, \rho, n) = L_2(2 - l, \rho, n), \quad (2)$$

where $L_2(l - \varepsilon, \rho, n)$ and $L_2(l + \varepsilon, \rho, n)$ are finite real positive quantities, determined in the sense of point i).

iii) When $c = g$, $g = 2 - l$ ($g = 2, 3, 4, \dots$):

$$L_2(g, \rho, n) = \lim_{\varepsilon \rightarrow 0} L_2(g - \varepsilon, \rho, n) = \lim_{\varepsilon \rightarrow 0} L_2(g + \varepsilon, \rho, n). \quad (3)$$

[$L_2(g - \varepsilon, \rho, n)$, $L_2(g + \varepsilon, \rho, n)$ and ε are specified like in the previous item.]

Besides, it is carried out, too [1, 7]:

$$L_2(c, \rho, n) = L_2(2 - c, \rho, n), \quad c \neq l, \quad (4)$$

$$L_2(1 + h, \rho, n) = L_2(1 - h, \rho, n), \quad h \neq l, \quad (5)$$

$$L_2(1 + l, \rho, n) = L_2(1 - l, \rho, n), \quad (6)$$

h — real number.

Definition 2: The $\hat{L}_2(\hat{c}, \hat{\rho}, \hat{n})$ numbers in which \hat{c} is a restricted arbitrary real, positive, negative or zero, $\hat{\rho}$ is real, positive, $0 < \hat{\rho} < 1$ and \hat{n} is a positive integer, are finite real positive ones, advanced, as follows:

i) If $\hat{c} \neq \hat{l}$, $\hat{l} = 0, -1, -2, \dots$ [2]:

$$\hat{L}_2(\hat{c}, \hat{\rho}, \hat{n}) = \lim_{\hat{k}_- \rightarrow -\infty} \hat{K}_{2-}(\hat{c}, \hat{\rho}, \hat{n}, \hat{k}_-) = \lim_{\hat{k}_- \rightarrow -\infty} \hat{M}_{2-}(\hat{c}, \hat{\rho}, \hat{n}, \hat{k}_-), \quad (7)$$

where $\hat{K}_{2-}(\hat{c}, \hat{\rho}, \hat{n}, \hat{k}_-) = |\hat{k}_-| \hat{\chi}_{\hat{k}_-, \hat{n}}^{(\hat{c})}(\hat{\rho})$, $\hat{M}_{2-}(\hat{c}, \hat{\rho}, \hat{n}, \hat{k}_-) = |\hat{a}_-| \hat{\chi}_{\hat{k}_-, \hat{n}}^{(\hat{c})}(\hat{\rho})$ and $\hat{\chi}_{\hat{k}_-, \hat{n}}^{(\hat{c})}(\hat{\rho})$ is the \hat{n} th real positive zero of the function $\hat{F}_2(\hat{a}, \hat{c}; \hat{x}; \hat{\rho}) = \hat{\Phi}(\hat{a}, \hat{c}; \hat{x}) \hat{\Psi}(\hat{a}, \hat{c}; \hat{\rho}\hat{x}) - \hat{\Phi}(\hat{a}, \hat{c}; \hat{\rho}\hat{x}) \hat{\Psi}(\hat{a}, \hat{c}; \hat{x})$ in \hat{x} in which $\hat{\Phi}(\hat{a}, \hat{c}; \hat{x})$ and $\hat{\Psi}(\hat{a}, \hat{c}; \hat{x})$ are the Kummer and Tricomi confluent hypergeometric functions with $\hat{a} = \hat{c}/2 + \hat{k}_-$ — real, negative, ($\hat{a} \neq -\hat{m}$, $\hat{m} = 1, 2, 3, \dots$), $\hat{c} > 0$ or $\hat{c} < 0$ (in both cases $\hat{a} < \hat{c}$), \hat{x} — real, positive, $\hat{k}_- = \hat{a} - \hat{c}/2$ — real, negative, $\hat{n} = 1, 2, \dots, \hat{t}$, \hat{t} — a finite positive integer, whose numerical equivalent is determined by the parameters of \hat{F}_2 ($\hat{a}_- \equiv \hat{a}$), (\hat{c}, \hat{n} — fixed).

ii) Provided $\hat{c} = \hat{l}$ and $\hat{\varepsilon}$ is an infinitesimal real positive number [2]:

$$\hat{L}_2(\hat{c}, \hat{\rho}, \hat{n}) = \lim_{\hat{\varepsilon} \rightarrow 0} \hat{L}_2(\hat{l} - \hat{\varepsilon}, \hat{\rho}, \hat{n}) = \lim_{\hat{\varepsilon} \rightarrow 0} \hat{L}_2(\hat{l} + \hat{\varepsilon}, \hat{\rho}, \hat{n}) = \hat{L}_2(2 - \hat{l}, \hat{\rho}, \hat{n}), \quad (8)$$

where $\hat{L}_2(\hat{l} - \hat{\varepsilon}, \hat{\rho}, \hat{n})$ and $\hat{L}_2(\hat{l} + \hat{\varepsilon}, \hat{\rho}, \hat{n})$ are finite real positive numbers in the meaning of point i).

Moreover, it is implemented, as well [2]:

$$\hat{L}_2(\hat{c}, \hat{\rho}, \hat{n}) = \hat{L}_2(2 - \hat{c}, \hat{\rho}, \hat{n}), \quad \hat{c} \neq \hat{l}, \quad (9)$$

$$\hat{L}_2(1 + \hat{h}, \hat{\rho}, \hat{n}) = \hat{L}_2(1 - \hat{h}, \hat{\rho}, \hat{n}), \quad \hat{h} \neq \hat{l}, \quad (10)$$

$$\hat{L}_2(1 + \hat{l}, \hat{\rho}, \hat{n}) = \hat{L}_2(1 - \hat{l}, \hat{\rho}, \hat{n}), \quad (11)$$

\hat{h} — real number.

Comments: Items i) and ii) both in **Definition 1** and in **Definition 2** are of a principle nature. The first sets the notion $L_2(c, \rho, n)$ [$\hat{L}_2(\hat{c}, \hat{\rho}, \hat{n})$] number over the field of all admissible values of its parameters and the second extends its existence area with the poles of Kummer function [8]. Point iii) in **Definition 1** is introduced because of computational reasons. This is a new original idea in the Theory of $L_2(c, \rho, n)$ numbers. It is in fact a special case of sentence i), i.e., the Definition referred to involves two different specifications of the quantities $L_2(c, \rho, n)$ in

the instance talked over. The grounds for its formulation are the striving to avoid the calculational problems which arise at $c = g$, due to the complicated logarithmic character of the representation of $\Psi(a, c; x)$ [8]. They entail a decrease of the accuracy of the results obtained, when the limiting approach *i*) is employed. Note, however, that the latter is applicable, if $c = 1$.

In addition, the symmetry relations (4)–(6) make possible to shrink the process of reckoning up of $L_2(c, \rho, n)$ at certain ρ and n to the numerical equivalents of c larger or equal to 1 only.

Unlike the complex region, in the real one Eq. (7) yields $\hat{L}_2(\hat{c}, \hat{\rho}, \hat{n})$ for any $\hat{c} \neq \hat{l}$, inclusive for $\hat{c} = \hat{g}$ ($\hat{g} = 2 - \hat{l}$, $\hat{g} = 2, 3, 4, \dots$). Accordingly, it is not necessary to bring in a separate text for it in **Definition 2**.

3. BASIC HYPOTHESIS

3.1. Formulation

Hypothesis 1: *On condition that $c = \hat{c}$, $\rho = \hat{\rho}$ and $n = \hat{n}$, where c and \hat{c} are limited arbitrary real, ρ and $\hat{\rho}$ are real, positive, less than unity, n is a natural number and \hat{n} — a positive integer (n and \hat{n} — restricted), the $L_2(c, \rho, n)$ numbers in the sense of **Definition 1** and the $\hat{L}_2(\hat{c}, \hat{\rho}, \hat{n})$ ones in that of **Definition 2**, are identical. Accordingly, it is fulfilled:*

$$L_2(c, \rho, n) \equiv \hat{L}_2(\hat{c}, \hat{\rho}, \hat{n}). \quad (12)$$

If beside the above assumptions for the parameters it is imposed, as well that $c = \hat{c} \neq l$ ($l = \hat{l}$) and $k_- = \hat{k}_-$ is large negative, then it is true:

$$\chi_{k_-, n}^{(c)}(\rho) \approx \hat{\chi}_{\hat{k}_-, \hat{n}}^{(\hat{c})}(\hat{\rho}), \quad (13)$$

$$K_{2-}(c, n, \rho, k_-) \approx M_{2-}(c, n, \rho, k_-) \approx \hat{K}_{2-}(\hat{c}, \hat{n}, \hat{\rho}, \hat{k}_-) \approx \hat{M}_{2-}(\hat{c}, \hat{n}, \hat{\rho}, \hat{k}_-). \quad (14)$$

(The meaning of all tokens is as in **Definitions 1 and 2**.)

Note: Affirmation (1) could also be tracked down in Refs. [3–6] and assertion (7) — in Ref. [6]. Further, the identity (12) and the approximate equality (13) in case $c = \hat{c} = 3$ have been treated initially in Ref. [6]. In all cited papers the subscript “2” is omitted in the relevant symbols, wherever it appears above, except in relation (3) which is not discussed before.

3.2. Numerical Substantiation

Tables 1, 2 and 3 corroborate the above statements for $c = \hat{c} = 1$ and 3 (positive integers), $c = \hat{c} = -8.0791324685$ and 10.0791324685 (arbitrary real negative and positive numbers, resp.),

Table 1: Numbers $\chi_{k_-, n}^{(c)}(\rho)$, $K_{2-}(c, \rho, n, k_-)$, $M_{2-}(c, \rho, n, k_-)$, $\hat{\chi}_{\hat{k}_-, \hat{n}}^{(\hat{c})}(\hat{\rho})$, $\hat{K}_{2-}(\hat{c}, \hat{\rho}, \hat{n}, \hat{k}_-)$ and $\hat{M}_{2-}(\hat{c}, \hat{\rho}, \hat{n}, \hat{k}_-)$ for $c = \hat{c} = 1$ and 3, $\rho = \hat{\rho} = 0.1$, $n = \hat{n} = 1$ and large negative $k_- = \hat{k}_-$.

k_-	$\chi_{k_-, n}^{(c)}(\rho)$	$K_{2-}(c, \rho, n, k_-)$	$M_{2-}(c, \rho, n, k_-)$	$\hat{\chi}_{\hat{k}_-, \hat{n}}^{(\hat{c})}(\hat{\rho})$	$\hat{K}_{2-}(\hat{c}, \hat{\rho}, \hat{n}, \hat{k}_-)$	$\hat{M}_{2-}(\hat{c}, \hat{\rho}, \hat{n}, \hat{k}_-)$
	$c = 1$					
-1.10^1	(-1) 5.08599 55657	5.08599 55657	5.09234 90917	(-1) 5.14448 80360	5.14448 80360	4.88726 36342
-1.10^2	(-2) 5.11462 21493	5.11462 21493	5.11468 60817	(-2) 5.11520 69833	5.11520 69833	5.08963 09484
-1.10^3	(-3) 5.11491 16094	5.11491 16094	5.11491 22488	(-3) 5.11491 74578	5.11491 74578	5.11235 99990
-1.10^4	(-4) 5.11491 45044	5.11491 45044	5.11491 45108	(-4) 5.11491 45628	5.11491 45628	5.11465 88171
-1.10^5	(-5) 5.11491 45333	5.11491 45333	5.11491 45334	(-5) 5.11491 45339	5.11491 45339	5.11488 89593
-1.10^6	(-6) 5.11491 45336	5.11491 45336	5.11491 45336	(-6) 5.11491 45336	5.11491 45336	5.11491 19761
	$c = 3$					
-1.10^1	(-1) 7.58292 06953	7.58292 06953	7.66775 40201	(-1) 7.71969 87233	7.71969 87233	6.56174 39148
-1.10^2	(-2) 7.64943 86487	7.64943 86487	7.65029 91622	(-2) 7.65080 59201	7.65080 59201	7.53604 38313
$-4.46 \cdot 10^2$	(-2) 7.171526 63224	7.65008 77980	7.65013 10641	(-2) 7.71528 17341	7.65015 65341	7.62442 73081
-1.10^3				(-3) 7.65012 90021	7.65012 90021	7.63865 38086
-1.10^4				(-4) 7.65012 22341	7.65012 22341	7.64897 47158
-1.10^5				(-5) 7.65012 21664	7.65012 21664	7.65000 74146
-1.10^6				(-6) 7.65012 21658	7.65012 21658	7.65011 06906

and $c = \hat{c} = -1, 0, 1, 2$ and 3 (negative, positive integers and zero), (cf. the underlined digits and the ones, marked by bold face type), assuming $\rho = \hat{\rho} = 0.1$, $n = \hat{n} = 1$ and $\varepsilon = \hat{\varepsilon} = 1.10^{-1}$ to 1.10^{-5} . The analysis indicates that it is possible to substantiate numerically the statements of **Hypothesis 1**, using the infinite power series, defining $\Phi(a, c; x)$ and $\Psi(a, c; x)$ [8], provided $c \neq g$ with 10 and even 12 decimal places (for $k_- = \hat{k}_- = -1.10^6$). The same approach could be applied for $c = g$ maximum up to $k_- = \hat{k}_- = -4.49 \cdot 10^2$ and $-4.46 \cdot 10^2$, when $g = 2$ and 3 , resp., (cf. Table 3). At larger $|k|$ the computer programmes, worked out at present, cease to operate for complex parameters. The reason for this fact is that the calculations for $c = g$ are effectuated, harnessing the more complicated representation of the Tricomi function by a power series, involving a logarithmic term [8], as debated above. The accuracy in this instance could be increased, counting $L_2(g + \varepsilon, \rho, n)$ and $L_2(g - \varepsilon, \rho, n)$, e.g., for $\varepsilon = 1.10^{-5}$ and taking the arithmetic mean of them. For example, if $c = g = 2, 3, 4$ and 5 , the results are correspondingly: **5.76140 47863** and **5.76137 91022**, resp. **5.76139 19443**; **7.65014 68658** and **7.65009 74658**, resp. **7.65012 21658**; **10.64667 39621** and **10.64660 40904**, resp. **10.64663 90263**; **14.58038 02020** and **14.58029 32419**, resp. **14.58033 67220** against **5.76137 33273**, **7.65008 79516**, **10.64656 89163** and **14.58019 73524**, cast up directly from the power series in the complex case for $k_- = -4.49 \cdot 10^2 \div -4.46 \cdot 10^2$. For real parameters, however, the programmes in question, using the logarithmic series, run, giving practically the same numerical equivalents for $\hat{L}_2(\hat{c}, \hat{\rho}, \hat{n})$ with $\hat{c} = c = g$, as the arithmetic mean: **5.76139 19442**, **7.65012 21658**, **10.64663 90263**, **14.58033 67226**. The blank boxes in the left-hand lower part (middle line) of Table 1 (Table 3) conform to such k_- for which $\chi_{k_-, n}^{(c)}(\rho)$, resp. $K_{2-}(c, \rho, n, k_-)$ and $M_{2-}(c, \rho, n, k_-)$, i.e., $L_2(c, \rho, n)$ cannot be figured out from (does not exist in the sense of) Eq. (1). Table 4 lists the values of $L_2(c, \rho, n)$ [of $\hat{L}_2(\hat{c}, \hat{\rho}, \hat{n})$] for $c = 1.0$ (0.1) 7.0 . The outcomes for any c (\hat{c}), save for $c = 2(1)7$ (without exception) are found from Eq. (1) [Eq. (7)], assuming $L_2(c, \rho, n) = K_{2-}(c, \rho, n, k_-) = M_{2-}(c, \rho, n, k_-)$ [$\hat{L}_2(\hat{c}, \hat{\rho}, \hat{n}) = \hat{K}_{2-}(\hat{c}, \hat{\rho}, \hat{n}, \hat{k}_-) = \hat{M}_{2-}(\hat{c}, \hat{\rho}, \hat{n}, \hat{k}_-)$] for $k_- = -1.10^6$ ($\hat{k}_- = -1.10^6$). In view of identity (12) $L_2(c, \rho, n)$ for $c = 2(1)7$ is taken equal to $\hat{L}_2(\hat{c}, \hat{\rho}, \hat{n})$. For further information see also Refs. [1-7]. [Throughout the paper the digits in a given result, being identical with these in the final one for the $L_2(c, \rho, n)$ and $\hat{L}_2(\hat{c}, \hat{\rho}, \hat{n})$ numbers of the very c (g), ρ , n , resp. \hat{c} (g), $\hat{\rho}$, \hat{n} , are distinguished by bold face type. The alike digits of $\chi_{k_-, n}^{(c)}(\rho)$ and $\hat{\chi}_{\hat{k}_-, \hat{n}}^{(\hat{c})}(\hat{\rho})$ with $c = \hat{c}$, $\rho = \hat{\rho}$, $n = \hat{n}$ and $k_- = \hat{k}_-$ in Tables 1 and 2, are underlined. The same holds for the twin digits of $L_2(l \pm \varepsilon, \rho, n)$ and $L_2(l, \rho, n)$, resp. of $L_2(2 - (l \pm \varepsilon), \rho, n)$ and $L_2(2 - l, \rho, n)$, i.e., $L_2(g, \rho, n)$ in Table 3 and in the numerical findings, presented in this Section.]

Table 2: Numbers $\chi_{k_-, n}^{(c)}(\rho)$, $K_{2-}(c, \rho, n, k_-)$, $M_{2-}(c, \rho, n, k_-)$, $\hat{\chi}_{\hat{k}_-, \hat{n}}^{(\hat{c})}(\hat{\rho})$, $\hat{K}_{2-}(\hat{c}, \hat{\rho}, \hat{n}, \hat{k}_-)$ and $\hat{M}_{2-}(\hat{c}, \hat{\rho}, \hat{n}, \hat{k}_-)$ for $c = \hat{c} = -8.07913 24685$ and 10.0791324685 , $\rho = \hat{\rho} = 0.1$, $n = \hat{n} = 1$ and large negative $k_- = \hat{k}_-$.

k_-	$\chi_{k_-, n}^{(c)}(\rho)$	$K_{2-}(c, \rho, n, k_-)$	$M_{2-}(c, \rho, n, k_-)$	$\hat{\chi}_{\hat{k}_-, \hat{n}}^{(\hat{c})}(\hat{\rho})$	$\hat{K}_{2-}(\hat{c}, \hat{\rho}, \hat{n}, \hat{k}_-)$	$\hat{M}_{2-}(\hat{c}, \hat{\rho}, \hat{n}, \hat{k}_-)$
	$c = \hat{c} = -8.07913 24685$					
-1.10^1	(<u>-1</u>) 42.33045 01549	42.33045 01549	45.65375 75431	(<u>-1</u>) 48.95708 52835	48.95708 52835	68.73362 41473
-1.10^2	(<u>-2</u>) 45.14869 81866	45.14869 81866	45.18552 02092	(<u>-2</u>) 45.21338 20011	45.21338 20011	47.03980 65138
-1.10^3	(<u>-3</u>) 45.18067 18986	45.18067 18986	45.18104 05284	(<u>-3</u>) 45.18131 87352	45.18131 87352	45.36383 16648
-1.10^4	(<u>-4</u>) 45.18099 20782	45.18099 20782	45.18099 57646	(<u>-4</u>) 45.18099 85466	45.18099 85466	45.19924 97102
-1.10^5	(<u>-5</u>) 45.18099 52801	45.18099 52801	45.18099 53170	(<u>-5</u>) 45.18099 53448	45.18099 53448	45.18282 04610
-1.10^6	(<u>-6</u>) 45.18099 53121	45.18099 53121	45.18099 53125	(<u>-6</u>) 45.18099 53128	45.18099 53128	45.18117 78244
$c = 10.0791324685$						
-1.10^1	(<u>-1</u>) 42.33045 01549	42.33045 01549	47.40202 06038	(<u>-1</u>) 48.95708 52835	48.95708 52835	24.28483 78913
-1.10^2	(<u>-2</u>) 45.14869 81866	45.14869 81866	45.20599 44192	(<u>-2</u>) 45.21338 20011	45.21338 20011	42.93482 36684
-1.10^3	(<u>-3</u>) 45.18067 18986	45.18067 18986	45.18124 56269	(<u>-3</u>) 45.18131 87352	45.18131 87352	44.95362 44869
-1.10^4	(<u>-4</u>) 45.18099 20782	45.18099 20782	45.18099 78156	(<u>-4</u>) 45.18099 85466	45.18099 85466	45.15822 92831
-1.10^5	(<u>-5</u>) 45.18099 52801	45.18099 52801	45.18099 53375	(<u>-5</u>) 45.18099 53448	45.18099 53448	45.17871 84186
-1.10^6	(<u>-6</u>) 45.18099 53121	45.18099 53121	45.18099 53127	(<u>-6</u>) 45.18099 53128	45.18099 53128	45.18076 76201

Table 3: $L_2(c, \rho, n)$ numbers with $c = l - \varepsilon$, l , $l + \varepsilon$, $c = 2 - (l - \varepsilon)$, $2 - l$ and $2 - (l + \varepsilon)$ in case $l = 0, -1$, and $c = 1 - \varepsilon$, 1 and $1 + \varepsilon$, $\varepsilon = 1.10^{-i}$, $i = 1, 2, \dots, 5$, $\rho = 0.1$ and $n = 1$.

$\varepsilon \setminus l$	k_-	-1	k_-	0	k_-	1	k_-	0	k_-	-1
$L_2(l - \varepsilon, \rho, n)$										
1.10 ⁻¹	-1.10 ⁶	7.90264 84872	-1.10 ⁶	5.89604 30797	-1.10 ⁶	5.12142 31165	-1.10 ⁶	5.89604 30797	-1.10 ⁶	7.90264 84872
1.10 ⁻²	-1.10 ⁶	7.67487 76625	-1.10 ⁶	5.77429 64467	-1.10 ⁶	5.11497 96239	-1.10 ⁶	5.77429 64467	-1.10 ⁶	7.67487 76625
1.10 ⁻³	-1.10 ⁶	7.65259 27191	-1.10 ⁶	5.76267 67729	-1.10 ⁶	5.11491 51845	-1.10 ⁶	5.76267 67729	-1.10 ⁶	7.65259 27191
1.10 ⁻⁴	-1.10 ⁶	7.65036 91711	-1.10 ⁶	5.76152 03708	-1.10 ⁶	5.11491 45401	-1.10 ⁶	5.76152 03708	-1.10 ⁶	7.65036 91711
1.10 ⁻⁵	-1.10 ⁶	7.65014 68658	-1.10 ⁶	5.76140 47863	-1.10 ⁶	5.11491 45337	-1.10 ⁶	5.76140 47863	-1.10 ⁶	7.65014 68658
$L_2(l, \rho, n)$										
					-1.10 ⁶	5.11491 45336	$-4.49 \cdot 10^2$	5.76137 33273	$-4.46 \cdot 10^2$	7.65008 79516
$L_2(l + \varepsilon, \rho, n)$										
1.10 ⁻⁵	-1.10 ⁶	7.65009 74658	-1.10 ⁶	5.76137 91022	-1.10 ⁶	5.11491 45337	-1.10 ⁶	5.76137 91022	-1.10 ⁶	7.65009 74658
1.10 ⁻⁴	-1.10 ⁶	7.64987 51715	-1.10 ⁶	5.76126 35301	-1.10 ⁶	5.11491 45401	-1.10 ⁶	5.76126 35301	-1.10 ⁶	7.64987 51715
1.10 ⁻³	-1.10 ⁶	7.64765 27233	-1.10 ⁶	5.76010 83651	-1.10 ⁶	5.11491 51845	-1.10 ⁶	5.76010 83651	-1.10 ⁶	7.64765 27233
1.10 ⁻²	-1.10 ⁶	7.62547 77605	-1.10 ⁶	5.74861 24018	-1.10 ⁶	5.11497 96239	-1.10 ⁶	5.74861 24018	-1.10 ⁶	7.62547 77605
1.10 ⁻¹	-1.10 ⁶	7.40870 46824	-1.10 ⁶	5.63923 60849	-1.10 ⁶	5.12142 31165	-1.10 ⁶	5.63923 60849	-1.10 ⁶	7.40870 46824

Table 4: Values of $L_2(c, \rho, n)$ as a function of c for $\rho = 0.1$ in case $n = 1$.

c	L_2	c	L_2	c	L_2	c	L_2	c	L_2	c	L_2
1.0	5.11491 45336	2.0	5.76139 19442	3.0	7.65012 21658	4.0	10.64663 90263	5.0	14.58033 67226	6.0	19.29960 51768
1.1	5.12142 31165	2.1	5.89604 30797	3.1	7.90264 84872	4.1	11.00064 51495	5.1	15.01902 12459	6.1	19.81035 31159
1.2	5.14094 34972	2.2	6.04308 37217	3.2	8.16611 45545	4.2	11.36383 20114	5.2	15.46538 94535	6.2	20.32782 38093
1.3	5.17345 95901	2.3	6.20239 95490	3.3	8.44034 81171	4.3	11.73603 03769	5.3	15.91932 02062	6.3	20.85194 95883
1.4	5.21894 46455	2.4	6.37386 81019	3.4	8.72517 44114	4.4	12.11707 43959	5.4	16.38069 80900	6.4	21.38266 72573
1.5	5.27736 13406	2.5	6.55735 92267	3.5	9.02041 68096	4.5	12.50680 20386	5.5	16.84941 34118	6.5	21.91991 78804
1.6	5.34866 19056	2.6	6.75273 55542	3.6	9.32589 74684	4.6	12.90505 54883	5.6	17.32536 21597	6.6	22.46364 65643
1.7	5.43278 82861	2.7	6.95985 30069	3.7	9.64143 79728	4.7	13.31168 14901	5.7	17.80844 59307	6.7	23.01380 22397
1.8	5.52967 23425	2.8	7.17856 13357	3.8	9.96685 99696	4.8	13.72653 16537	5.8	18.29857 18292	6.8	23.57033 74430
1.9	5.63923 60849	2.9	7.40870 46824	3.9	10.30198 57855	4.9	14.14946 27103	5.9	18.79565 23397	6.9	24.13320 81007
2.0	5.76139 19442	3.0	7.65012 21658	4.0	10.64663 90263	5.0	14.58033 67226	6.0	19.29960 51768	7.0	24.70237 33172

4. APPLICATION

The zeros of $F_2(a, c; x, \rho)$ determine the eigenvalue spectrum $\bar{\beta}_2 = \chi_{k,n}^{(c)}(\rho)/(2\bar{r}_0)$ of the coaxial ferrite waveguide with azimuthal magnetization for the normal TE_{0n} modes, if it holds: $k = \alpha\bar{\beta}/(2\bar{\beta}_2)$, $c = 3$, $x = jz_0$, $z_0 = 2\bar{\beta}_2\bar{r}_0$, $\rho = \bar{r}_1/\bar{r}_0$, $\bar{\beta} = \beta/(\beta_0\sqrt{\varepsilon_r})$, $\bar{\beta}_2 = \beta_2/(\beta_0\sqrt{\varepsilon_r})$, $\bar{r}_0 = \beta_0 r_0 \sqrt{\varepsilon_r}$, $\bar{r}_1 = \beta_0 r_1 \sqrt{\varepsilon_r}$, r_0 and r_1 are the outer and inner conductor radii, $\alpha = \gamma M_r / \omega$ is the off-diagonal element of Polder permeability tensor of the ferrite (γ — gyromagnetic ratio, M_r — remanent magnetization, ω — angular frequency of the wave), $0 < |\alpha| < 1$, ε_r is its relative permittivity, β is the phase constant of the wave, $\beta_2 = [\omega^2 \varepsilon_0 \mu_0 \varepsilon_r (1 - \alpha^2) - \beta^2]^{1/2}$ is the radial wavenumber, $\beta_0 = \omega \sqrt{\varepsilon_0 \mu_0}$ is the free space phase constant [3, 5–7]. Likewise, the zeros of $\hat{F}_2(\hat{a}, \hat{c}; \hat{x}, \hat{\rho})$ yield the eigenvalue spectrum $\bar{\beta}_2 = \hat{\chi}_{\hat{k}, \hat{n}}^{(\hat{c})}(\hat{\rho})/(2\hat{\bar{r}}_0)$ of the configuration considered for slow $\widehat{TE}_{0\hat{n}}$ modes, provided $\hat{c} = 3$, $\hat{k} = \hat{\alpha}\bar{\beta}/(2\bar{\beta}_2)$, $\hat{x} = \hat{x}_0$, $\hat{x}_0 = 2\bar{\beta}_2\bar{r}_0$, $\hat{\rho} = \hat{r}_1/\bar{r}_0$. Here $\bar{\beta} = \hat{\beta}/(\beta_0\sqrt{\varepsilon_r})$, $\bar{\beta}_2 = \hat{\beta}_2/(\beta_0\sqrt{\varepsilon_r})$, $\bar{r}_0 = \beta_0 \hat{r}_0 \sqrt{\varepsilon_r}$, $\bar{r}_1 = \beta_0 \hat{r}_1 \sqrt{\varepsilon_r}$. The quantities \hat{r}_0 , \hat{r}_1 , $\hat{\alpha}$, $\hat{\beta}$ and $\hat{\beta}_2$ have the same sense as that of the ones without hats “ \wedge ”, but related to the slow waves, save for the fact that $|\hat{\alpha}|$ could be less or larger than 1 [2, 6]. Moreover, it is assumed that: $\hat{r}_0 = r_0$, $\hat{r}_1 = r_1$. The normal TE_{0n} modes might propagate both for positive and negative ferrite magnetization [3, 5–7]. The slow ones split in two sets, denoted by the symbols $\widehat{TE}_{0\hat{n}}^{(1)}$ and $\widehat{TE}_{0\hat{n}}^{(2)}$ which might exist exclusively for negative magnetization [2, 6].

There are En_{1-} — (\hat{En}_{1-} —) envelope curves in the $\bar{\beta}(\bar{r}_0) — [\bar{\beta}^{(1)}(\bar{r}_0^{(1)}) —]$ phase diagram

of the TE_{0n} ($\widehat{TE}_{0n}^{(1)}$) modes of equation $\bar{\beta}_{en-} = \bar{\beta}_{en-}(\bar{r}_{0en-})$ [$\bar{\beta}_{en-}^{(1)} = \bar{\beta}_{en-}^{(1)}(\bar{r}_{0en-}^{(1)})$], written in parametric form as: $\bar{r}_{0en-} = L_2(c, \rho, n)/[|\alpha_{en-}|(1 - \alpha_{en-}^2)^{1/2}]$, $\bar{\beta}_{en-} = (1 - \alpha_{en-}^2)^{1/2}$ ($\bar{r}_{0en-}^{(1)} = \hat{L}_2(\hat{c}, \hat{\rho}, \hat{n})/\{|\hat{\alpha}_{en-}^{(1)}|[1 - (\hat{\alpha}_{en-}^{(1)})^2]^{1/2}\}$, $\bar{\beta}_{en-}^{(1)} = [1 - (\hat{\alpha}_{en-}^{(1)})^2]^{1/2}$), restricting from the side of higher (lower) frequencies the characteristics for negative magnetization, (α_{en-} and $\hat{\alpha}_{en-}^{(1)}$ — parameters, relevant to the modes referred to and connected with the envelopes) [2–7]. The coincidence of these curves for $c = \hat{c} = 3$, $\rho \equiv \hat{\rho}$, $n = \hat{n}$ and $\alpha_{en-} \equiv \hat{\alpha}_{en-}^{(1)}$ is a direct corollary of **Hypothesis 1**.

5. CONCLUSION

It is demonstrated numerically that the real positive numbers $L_2(c, \rho, n)$ and $\hat{L}_2(\hat{c}, \hat{\rho}, \hat{n})$ (the limits of specially constructed sequences of real numbers with terms, involving the zeros of certain complex, resp. real functions, incorporating several Kummer and Tricomi ones) concur, if their parameters c and \hat{c} (arbitrary real), ρ and $\hat{\rho}$ — real, positive, less than unity and n and \hat{n} — bounded natural number and a positive integer, are the same to certain degree of accuracy. This is formulated as a Hypothesis for identity of $L_2(c, \rho, n)$ and $\hat{L}_2(\hat{c}, \hat{\rho}, \hat{n})$. It is shown that the peculiarities of the rotationally symmetric TE modes transmission in the coaxial waveguide, entirely filled with azimuthally magnetized ferrite are directly linked with this mathematical outcome. From a physical point of view its validity when $c = \hat{c} = 3$ and $\rho = \hat{\rho}$ for each $n = \hat{n}$ means existence of a curve in the phase portrait of geometry for negative magnetization of the load at which the propagating mode is transformed from normal to slow.

ACKNOWLEDGMENT

We express our gratitude to our mother Trifonka Romanova Popnikolova and to our late father Nikola Georgiev Popnikolov for their self-denial and for their tremendous efforts to support all our undertakings.

REFERENCES

1. Georgiev, G. N. and M. N. Georgieva-Grosse, “Theory of the L numbers: Definition, computational modeling, properties and application,” *Proc. Thirteenth Int. Conf. Electromagn. Adv. Applicat. ICEAA’11*, 544–547, Turin, Italy, September 12–16, 2011, (Invited Paper in the Special Session “Future challenges in mathematical and computational electromagnetics and its applications” organized by G. N. Georgiev and M. N. Georgieva-Grosse).
2. Georgiev, G. N. and M. N. Georgieva-Grosse, “Theory of the $\hat{L}_2(\hat{c}, \hat{\rho}, \hat{n})$ numbers and its application to the slow wave propagation in the coaxial ferrite waveguide,” *Progress In Electromagnetics Research Symposium Abstracts*, 249–250; *PIERS Proceedings*, 450–455, Moscow, Russia, August 19–23, 2012, (in the Special Session: “Advanced mathematical and computational methods in the electromagnetic theory and their applications,” organized by M. N. Georgieva-Grosse and G. N. Georgiev).
3. Georgiev, G. N. and M. N. Georgieva-Grosse, “New elements in the theory of the coaxial waveguide with azimuthally magnetized ferrite,” *Proc. Int. Sem. Days Diff. 2005 DD’05*, 81–93, in Abstracts, 29, St. Petersburg, Russia, June 28–July 1, 2005.
4. Georgiev, G. N. and M. N. Georgieva-Grosse, “Some classes of real numbers and their application to waveguide propagation,” *Conf. Proc. 11th Int. Conf. Math. Meth. Electromagn. Theory MMET*06*, 393–395, Kharkov, Ukraine, June 26–29, 2006.
5. Georgiev, G. N. and M. N. Georgieva-Grosse, “ L numbers method for analysis of azimuthally magnetized coaxial ferrite waveguide phase shifter,” *Proc. 30th ESA Antenna Worksh. Antennas Earth Observ., Sci., Telecomm. Navig., Space Missions*, 156–159, also in CDROM, ESA/ESTEC, Noordwijk, The Netherlands, May 27–30, 2008.
6. Georgiev, G. N. and M. N. Georgieva-Grosse, “A property of the $L(c, \rho, n)$ numbers and its application to waveguide propagation,” *Proc. XXIX URSI General Assembly*, BK.6(120), in CDROM, Chicago, IL, USA, August 7–16, 2008.
7. Georgiev, G. N. and M. N. Georgieva-Grosse, “Theorem for the $L(c, \rho, n)$ numbers,” *Progress In Electromagnetics Research Symposium Abstracts*, 743; *PIERS Proceedings*, 1478–1482, Moscow, Russia, August 18–21, 2009.
8. Tricomi, F. G., *Funzioni Ipergeometriche Confluenti*, Edizioni Cremonese, Rome, Italy, 1954.

An Analysis of a Strip Antenna Located at an Interface between Free Space and a Magnetoplasma

A. V. Kudrin¹, T. M. Zaboronkova², and A. S. Zaitseva¹

¹University of Nizhny Novgorod, Russia

²Technical University of Nizhny Novgorod, Russia

Abstract— We consider the problem of finding the current distribution of a linear antenna in the form of an infinitesimally thin, perfectly conducting, narrow strip located at a plane interface between free space and a magnetoplasma. The strip is infinitely long and perpendicular to an external dc magnetic field superimposed on the plasma medium. The current on the strip surface is excited by a time-harmonic voltage creating a given electric field which is aligned with the strip and differs from zero in a narrow gap of it. The problem is reduced to a system of integral equations for the current. It is shown that solutions of these equations can be obtained in analytical form in the case where the semi-infinite magnetoplasma occupying one half-space is resonant.

1. INTRODUCTION

Much previous work on the electrodynamic characteristics of antennas operated in a magnetoplasma refers to the case where the plasma parameters are independent of the spatial coordinates (see, e.g., [1, 2] and references therein). In the past decade, a substantial degree of interest has been shown in the characteristics of antennas in inhomogeneous plasma media [3]. Of special interest is the case where the antenna is located on the boundary of free space and a magnetoplasma. It is the purpose of the present work to find the electrodynamic characteristics of a linear antenna located at a plane interface between free space and a magnetized plasma medium. The semi-infinite magnetoplasma occupying one half-space is assumed resonant. By resonant magnetoplasma, we mean a cold, collisionless magnetized plasma in which the refractive index of one of the characteristic modes tends to infinity at a certain angle between the wave vector and an external dc magnetic field [1, 2].

2. FORMULATION OF THE PROBLEM

Consider a straight antenna of infinite length, which is aligned with the x axis and lies in the xz plane (see Fig. 1). The antenna having the form of an infinitesimally thin, perfectly conducting, narrow strip of half-width d is located at an interface between free space and a magnetoplasma. It is assumed that an external static magnetic field \mathbf{B}_0 is aligned with the z axis. The semi-infinite magnetoplasma occupying one half-space ($y < 0$) is described by a general dielectric tensor

$$\boldsymbol{\varepsilon} = \varepsilon_0 \begin{pmatrix} \varepsilon & -ig & 0 \\ ig & \varepsilon & 0 \\ 0 & 0 & \eta \end{pmatrix}, \quad (1)$$

where ε_0 is the permittivity of free space. The elements ε , g , and η of tensor (1) are functions of the angular frequency ω , and expressions for them can be found elsewhere [3]. We restrict ourselves to consideration only of the case where the magnetoplasma is resonant. For such a plasma, the diagonal elements ε and η of the dielectric tensor have opposite signs [3]. For definiteness, in what follows we will be discussing the case where $\varepsilon > 0$ and $\eta < 0$, which is encountered in many important applications [1, 2].

The current on the strip surface is excited by a time-harmonic ($\sim \exp(i\omega t)$) voltage that is applied over a narrow interval (gap) $|x| \leq \Delta$ and creates an electric field with the only nonzero component E_x^{ext} on the surface of the strip (i.e., at $y = 0$ and $|z| < d$):

$$E_x^{\text{ext}}(x, 0, z) = \frac{V_0}{2\Delta} [U(x + \Delta) - U(x - \Delta)] [U(z + d) - U(z - d)]. \quad (2)$$

Here, $V_0 = \text{const}$ is a constant amplitude of the given voltage, U is a Heaviside function, and Δ is the half-width of the gap.

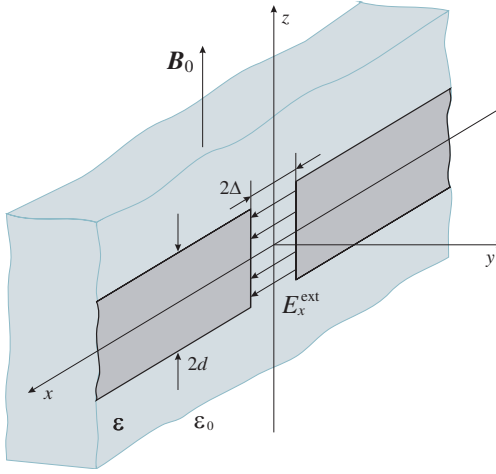


Figure 1: Geometry of the problem.

3. INTEGRAL EQUATIONS FOR THE ANTENNA CURRENT

Using the Fourier transform technique, we represent the excitation field E_x^{ext} for $|z| < d$ in the form

$$E_x^{\text{ext}}(x, 0, z) = \frac{k_0}{2\pi} \int_{-\infty}^{\infty} \mathcal{E}_x^{\text{ext}}(n_x) \exp(-ik_0 n_x x) dn_x, \quad (3)$$

where

$$\mathcal{E}_x^{\text{ext}}(n_x) = V_0 \frac{\sin(k_0 n_x \Delta)}{k_0 n_x \Delta} \quad (4)$$

and $k_0 = \omega/c$ is the wave number in free space.

The density \mathbf{J} of the electric current excited on the antenna by field (2) can be sought as

$$\mathbf{J} = \mathbf{x}_0 I(x, z) \delta(y), \quad (5)$$

where $|z| < d$, δ is a Dirac function, and $I(x, z)$ is the surface current density which admits the following representation:

$$I(x, z) = \frac{k_0}{2\pi} \int_{-\infty}^{\infty} I(n_x, z) \exp(-ik_0 n_x x) dn_x. \quad (6)$$

To find $I(x, z)$, we express the tangential components E_x and E_z of the electric field excited by current (5) in terms of the unknown quantity $I(n_x, z)$ and then use the boundary conditions at the interface between two media ($y = 0$) along with the boundary conditions on the antenna surface ($y = 0$ and $|z| < d$):

$$E_x + E_x^{\text{ext}} = 0, \quad E_z = 0. \quad (7)$$

The described procedure makes it possible to obtain integral equations for $I(n_x, z)$ and then reduce the problem of finding the antenna current to solving the corresponding integral equations.

After some lengthy algebra, the tangential components of the antenna-excited electric field at the boundary $y = 0$ can be written as

$$\begin{bmatrix} E_x(x, 0, z) \\ E_z(x, 0, z) \end{bmatrix} = -\frac{k_0}{2\pi} \int_{-\infty}^{\infty} dn_x \int_{-d}^d \begin{bmatrix} K_x(n_x, z - z') \\ K_z(n_x, z - z') \end{bmatrix} I(n_x, z') \exp(-ik_0 n_x x) dz'. \quad (8)$$

Here,

$$K_x(n_x, \zeta) = \frac{i Z_0 k_0}{2\pi} \int_{-\infty}^{\infty} \sum_{k=1}^2 \frac{e_k B_k}{\Delta} \exp(-ik_0 n_z |\zeta|) dn_z, \quad (9)$$

$$K_z(n_x, \zeta) = \text{sgn } \zeta \frac{i Z_0 k_0}{2\pi \eta} \int_{-\infty}^{\infty} \sum_{k=1}^2 \frac{n_k B_k}{\Delta} \exp(-ik_0 n_z |\zeta|) dn_z, \quad (10)$$

where

$$\begin{aligned}
B_1 &= -i\eta h_2 \frac{n_2 n_y}{n_\perp^2} + \eta e_2 \frac{n_x n_z}{n_\perp^2} + n_2 \frac{1 - n_x^2}{n_\perp^2}, \quad B_2 = i\eta h_1 \frac{n_1 n_y}{n_\perp^2} - \eta e_1 \frac{n_x n_z}{n_\perp^2} - n_1 \frac{1 - n_x^2}{n_\perp^2}, \\
\Delta &= n_2 \left[\eta e_1 h_2 + \frac{i n_y}{n_\perp^2} (e_1 + \eta h_2) \right] - n_1 \left[\eta e_2 h_1 + \frac{i n_y}{n_\perp^2} (e_2 + \eta h_1) \right] \\
&\quad - (n_2 - n_1) \frac{1 - n_x^2}{n_\perp^2} + \eta \frac{n_x n_z}{n_\perp^2} (e_1 + h_1 - e_2 - h_2), \\
n_k &= -\frac{\varepsilon}{n_z g} \left[n_z^2 + n_{\perp k}^2 (n_z) + \frac{g^2}{\varepsilon} - \varepsilon \right], \quad e_k = \frac{i n_{y,k} + n_x \alpha_k}{n_{\perp k}^2}, \quad h_k = \frac{i n_{y,k} - n_x \beta_k}{n_{\perp k}^2}, \\
n_{\perp k}^2 &= (2\varepsilon)^{-1} \left\{ \varepsilon^2 - g^2 + \varepsilon\eta - (\eta + \varepsilon)n_z^2 \right. \\
&\quad \left. + (-1)^k \left[(\eta - \varepsilon)^2 n_z^4 + 2(g^2(\eta + \varepsilon) - \varepsilon(\eta - \varepsilon)^2) n_z^2 + (\varepsilon^2 - g^2 - \varepsilon\eta)^2 \right]^{1/2} \right\}, \tag{11}
\end{aligned}$$

and Z_0 is the impedance of free space. Other quantities in (11) are defined as

$$\begin{aligned}
n_\perp^2 &= 1 - n_z^2, \quad n_y = (1 - n_x^2 - n_z^2)^{1/2}, \quad n_{y,k} = (n_{\perp k}^2 - n_x^2)^{1/2}, \\
\alpha_k &= (n_z^2 + n_{\perp k}^2 - \varepsilon) g^{-1}, \quad \beta_k = n_z n_k^{-1}. \tag{12}
\end{aligned}$$

In the above formulas, n_y and $n_{y,k}$ are defined so as to ensure the conditions $\text{Im } n_y < 0$ and $\text{Im } n_{y,k} < 0$.

Using the boundary conditions (7) for the tangential components of the electric field on the antenna surface and allowing for Eqs. (3), (4), and (8), we obtain the following integral equations for the Fourier transform $I(n_x, z)$ of the surface current density:

$$\int_{-d}^d K_x(n_x, z - z') I(n_x, z') dz' = \mathcal{E}_x^{\text{ext}}(n_x), \tag{13}$$

$$\int_{-d}^d K_z(n_x, z - z') I(n_x, z') dz' = 0, \tag{14}$$

where $|z| < d$.

4. SOLUTION OF THE INTEGRAL EQUATIONS

The behavior of solutions of the obtained integral equations is determined by the properties of their kernels. We can represent the kernels $K_x(n_x, \zeta)$ and $K_z(n_x, \zeta)$ of integral Eqs. (13) and (14) as the sums of singular and regular parts:

$$\begin{aligned}
K_x(n_x, \zeta) &= K_x^{(s)}(n_x, \zeta) + K_x^{(r)}(n_x, \zeta), \\
K_z(n_x, \zeta) &= K_z^{(s)}(n_x, \zeta) + K_z^{(r)}(n_x, \zeta).
\end{aligned}$$

The singular parts $K_x^{(s)}(n_x, \zeta)$ and $K_z^{(s)}(n_x, \zeta)$ tend to infinity for $\zeta \rightarrow 0$, whereas the regular parts $K_x^{(r)}(n_x, \zeta)$ and $K_z^{(r)}(n_x, \zeta)$ remain finite in this limit and can be taken at $\zeta = 0$ if the antenna is so narrow that the following conditions take place:

$$d \ll 2\Delta, \quad (k_0 d)^2 \max\{|\varepsilon|, |g|, |\eta|\} \ll 1. \tag{15}$$

The singular part of $K_x(n_x, \zeta)$ is written as

$$\begin{aligned}
K_x^{(s)}(n_x, \zeta) &= \frac{i Z_0 k_0}{2\pi} \left\{ \left[1 + \frac{2n_x^2}{1 + |\varepsilon\eta|} \right] \int_{|n_x|}^\infty \frac{\sqrt{n_z^2 + n_x^2}}{n_z^2} \cos(k_0 n_z |\zeta|) dn_z \right. \\
&\quad \left. - \frac{2i n_x^2}{\sqrt{|\varepsilon\eta|}} \int_{\tilde{n}_z}^\infty \frac{\cos(k_0 n_z |\zeta|)}{\sqrt{n_z^2 - |\varepsilon/\eta| n_x^2}} dn_z \right\}, \tag{16}
\end{aligned}$$

where $\bar{n}_z = |\varepsilon/\eta|^{1/2}|n_x|$. The regular part $K_x^{(r)}(n_x, \zeta)$ of the kernel $K_x(n_x, \zeta)$ is determined by the integral over n_z , the integrand of which is given by the difference of the respective quantities entering rigorous formula (9) for the kernel $K_x(n_x, \zeta)$ and those entering relation (16).

Under conditions (15), the singular part (16) of the kernel $K_x(n_x, \zeta)$ in the limit $\zeta \rightarrow 0$ can be represented as

$$\begin{aligned} K_x^{(s)} = & -\frac{iZ_0k_0}{2\pi} \left\{ \left(1 + \frac{2n_x^2}{1+|\varepsilon\eta|} \right) \left[\ln \frac{k_0|\zeta|}{2} + \ln |n_x| + \gamma \right] \right. \\ & \left. - \frac{2in_x^2}{\sqrt{|\varepsilon\eta|}} \left[\ln \frac{k_0|\zeta|}{2} + \ln \sqrt{\frac{|\varepsilon|}{|\eta|}} + \ln |n_x| + \gamma \right] \right\}, \end{aligned} \quad (17)$$

where $\gamma = 0.5772\dots$ is Euler's constant. As a result, integral Eq. (13) takes the form

$$\int_{-d}^d I(n_x, z') \ln \frac{k_0|z-z'|}{2} dz' = \chi \frac{2i\pi V_0}{Z_0 k_0} \frac{\sin(k_0 n_x \Delta)}{k_0 n_x \Delta} - S(n_x) \int_{-d}^d I(n_x, z') dz', \quad (18)$$

where

$$\chi = \frac{i\varepsilon_{eff}}{n_x^2 + i\varepsilon_{eff}}, \quad \varepsilon_{eff} = \frac{(1+|\varepsilon\eta|)\sqrt{|\varepsilon\eta|}}{2(1+|\varepsilon\eta|+i\sqrt{|\varepsilon\eta|})}, \quad (19)$$

$$S(n_x) = \gamma + \ln |n_x| - \frac{2in_x^2}{\sqrt{|\varepsilon\eta|}} \chi \ln \sqrt{\frac{|\varepsilon|}{|\eta|}} + \frac{2i\pi}{Z_0 k_0} \chi K_x^{(r)}(n_x, 0). \quad (20)$$

In turn, Eq. (14) under conditions (15) is transformed to the following form:

$$\int_{-d}^d n_x \frac{I(n_x, z')}{z-z'} dz' = 0. \quad (21)$$

When deriving Eq. (21), we took into account the relation $K_z^{(r)}(n_x, 0) = 0$. It can be shown that the solutions of Eqs. (18) and (21) are the main terms of the asymptotics of exact solutions to initial integral Eqs. (13) and (14) under conditions (15). It is a straightforward matter to verify that the solution to Eq. (18) with the logarithmic kernel automatically satisfies the singular integral Eq. (21) with the Cauchy kernel [2]. This fact allows us to consider only Eq. (18). The solution to Eq. (18) can be found using the techniques discussed in [2] and has the form

$$I(n_x, z) = -\frac{2i}{Z_0 k_0 \sqrt{d^2 - z^2}} \frac{\chi V_0}{\ln(4/k_0 d) - S(n_x)} \frac{\sin(k_0 n_x \Delta)}{k_0 n_x \Delta}. \quad (22)$$

Substituting Eq. (22) into Eq. (6), we obtain the following formula for the linear current density $I(x, z)$:

$$I(x, z) = -\frac{iV_0}{Z_0 \pi \sqrt{d^2 - z^2}} \int_{-\infty}^{\infty} \frac{\sin(k_0 n_x \Delta)}{k_0 n_x \Delta} \frac{\chi \exp(-ik_0 n_x x)}{\ln(4/k_0 d) - S(n_x)} dn_x. \quad (23)$$

It is seen from the formulas obtained that the surface current density tends to infinity near the edges of a perfectly conducting strip. Such behavior of the current density corresponds to the well-known Meixner condition at the edge [4]. Note that despite the divergence of $I(x, z)$ for $|z| \rightarrow d$, the total current $I_{\Sigma}(x)$ in the cross section $x = \text{const}$, which is determined by integration of the surface current density $I(x, z)$ with respect to z from $-d$ to d , is finite:

$$I_{\Sigma}(x) = \int_{-d}^d I(x, z) dz.$$

Note that in a general case, the integration over n_x in the current representation (23) can be made only numerically. Simple analytical expression for the antenna current distribution can be obtained if the strip is so narrow that the condition $\ln(4/k_0 d) \gg |S(n_x)|$ is fulfilled for $|n_x| < (k_0 \Delta)^{-1}$. In

this case, it is possible to neglect the quantity $S(n_x)$ and analytically evaluate the integral with respect to n_x in Eq. (23). For $|x| > \Delta$, we obtain in the limit $\Delta \rightarrow 0$ that

$$I_\Sigma(x) = \frac{V_0\pi h}{Z_0 k_0 \ln(4/k_0 d)} \exp(-ih|x|), \quad (24)$$

where

$$h = k_0 \frac{1-i}{\sqrt{2}} \sqrt{\varepsilon_{eff}}. \quad (25)$$

It is evident that Eq. (24) corresponds to the transmission line theory with the complex current propagation constant given by Eq. (25). Upon calculation of $I_\Sigma(x)$, the input impedance $Z = R+iX$ of the antenna can be found in a standard way as $Z = V_0/I_\Sigma(0)$. It follows from Eq. (24) that in the case considered, it is inexpedient to increase the antenna length to values substantially exceeding the characteristic scale $|h|^{-1}$ of the current decrease along the antenna, because the real part of the antenna input impedance and, hence, the power radiated by the antenna stop to increase with the antenna length.

5. CONCLUSION

The problem of determining the current distribution and input impedance of a perfectly conducting strip antenna located at an interface between free space and a magnetoplasma has been considered. The main attention has been focused on the case of a resonant magnetoplasma. The problem has been reduced to solving a system of singular integral equations. On the basis of the solution of these equations, expressions for the current distribution and the antenna input impedance have been obtained. It is shown that in the considered case, the properties of the integral equations admit an analytical solution for the antenna current if the strip is sufficiently narrow. The obtained closed-form solution describes the current distribution both along and across the strip and makes it possible to find the electrodynamic characteristics of the considered strip antenna.

ACKNOWLEDGMENT

This work was supported by the Russian Foundation for Basic Research (project Nos. 12-02-00747-a and 13-02-97035-a), the Government of the Russian Federation (contract No. 14.B25.31.0008), and the Russian Ministry of Science and Education (contract No. 14.B37.21.0901).

REFERENCES

1. Kudrin, A. V., E. Yu. Petrov, and T. M. Zaboronkova, “Current distribution and input impedance of a loop antenna in a cold magnetoplasma,” *Journal of Electromagnetic Waves and Applications*, Vol. 15, No. 3, 345–378, 2001.
2. Zaboronkova, T. M., A. V. Kudrin, and E. Yu. Petrov, “Electrodynamic characteristics of a strip antenna in a magnetoplasma,” *J. Commun. Technol. Electron.*, Vol. 57, No. 3, 296–300, 2012.
3. Kudrin, A. V., A. S. Zaitseva, T. M. Zaboronkova, C. Krafft, and G. A. Kyriacou, “Theory of a strip loop antenna located on the surface of an axially magnetized plasma column,” *Progress In Electromagnetics Research B*, Vol. 51, 221–246, 2013.
4. Meixner, J., “The behavior of electromagnetic fields at edges,” *IEEE Trans. Antennas Propagat.*, Vol. 20, No. 4, 442–446, 1972.

Exactly Solvable High Frequency Model of a Coil of Finite Length

Dierk Bormann^{1,2}

¹ABB Corporate Research, Power Technologies, Västerås S-721 78, Sweden

²Royal Institute of Technology, School of Electrical Engineering, Stockholm S-100 44, Sweden

Abstract— A simple high-frequency model of a homogeneous coil is proposed and analyzed. The model describes a transmission line, supplemented by homogeneously distributed stray capacitances connecting subsequent sections of the line (“series capacitance”), as well as mutual inductances between different sections. It has been argued repeatedly in the literature that adding series capacitance to a transmission line model (as a means to describe a transformer winding) should lead to a finite upper limit frequency for propagating modes. At frequencies above that limit, the winding should instead behave essentially as a capacitance network. Using our model, we show that this effect is suppressed (i.e., the limit frequency is shifted to infinity) by the presence of mutual inductance of essentially any kind. Furthermore, we show that the model can be solved analytically for a coil of finite length, with a much more general form of mutual inductances than commonly believed so far, and therefore is an ideal tool for the detailed study of coil-end effects.

1. INTRODUCTION

The so-called “classical” transformer theory [1–5] was born out of the necessity to make predictions about fast surge phenomena in coils, before the advent of digital computers. It is based on integro-differential equations which generalize the usual transmission line equations by taking into account capacitances and mutual inductances between the individual turns of a winding, and aims at approximate analytical solutions of these equations. Nowadays the most popular tools for investigating surge phenomena rely instead on the numerical solution of detailed discretized models. However, exact or approximate analytical solutions of simple models are still very valuable since they (i) allow a deeper understanding of generic phenomena and their parameter dependencies, and (ii) may serve as test and/or calibration cases for the numerical algorithms.

An example of an interesting generic phenomenon is the purported upper limit frequency for propagating modes in coils with series capacitance. Such a limit frequency was predicted in 1915 by Wagner [1] on the basis of a simplified equation in which mutual inductances between turns were replaced by effective self inductances. Later (in 1940) Rüdenberg [2] provided more detailed arguments why this simplification ought to be allowed, at least when studying long-wavelength modes. A more general treatment of the problem including mutual inductances was attempted by Steidinger [3] in 1924, this time leading to arguments *against* the existence of a limit frequency.

Wagner’s view had also been opposed already in 1919 by Blume and Boyajian [6], whose approximate treatment of mutual inductance predicted an unlimited spectrum of propagating modes. Their model was later adopted for instance by Bewley [7, 8], and recently used by Akbari et al. [9] for electrical PD localization in transformer windings. More accurate treatments of mutual inductance have been described in works by Pirenne [4] and by Abetti and Maginniss [5], but these authors neglected the series capacitances from the start in order to obtain integral equations of the Fredholm type (which was justified since these authors were mainly interested in low-order resonances of the coil, i.e., standing waves of long wavelengths), and therefore their work made no reliable predictions regarding the high-frequency modes. To the best of our knowledge, the issue was never clearly resolved. The idea that mutual inductances are essentially irrelevant for the high-frequency coil behavior, and therefore that in the presence of series capacitance there should be an upper frequency limit, survived in the literature and still seems to be widely accepted today. For example, the approximate arguments of Wagner and Rüdenberg were repeated, essentially unchanged, as late as 1991 in the influential textbook by Greenwood [10].

In the present paper, we will revisit the “classical” integro-differential equations for simple coils [1–5]. The equations we study can be viewed as describing a simple linear transmission line, supplemented by homogeneously distributed stray capacitances which connect different sections of the line (“series capacitance”), as well as mutual inductances between different sections. We will then argue that, while a model including series capacitance but without mutual inductances has the “classical” limit frequency [1], the presence of any reasonable form of mutual inductances in

the equations will actually shift the limit frequency to infinity. Moreover, we will show that for a certain, quite general class of mutual inductance expressions the model can be solved *analytically*, not only in the hypothetical case of a coil of infinite length but even when its length is *finite*, and so it provides a flexible tool for the detailed study of coil-end effects and their influence on the frequency-dependent characteristic terminal impedances and transfer functions of the coil.

2. BASIC EQUATIONS

We consider the “continuum limit” description of a homogeneous helical coil of length ℓ (in axial direction), valid on length scales much larger than the inter-turn spacing, taking both series capacitance and mutual inductance between the turns into account. It is given by a system of integro-differential equations in one spatial dimension x (corresponding to the axial position of a turn along the coil) for the local voltage $U(x, t)$ and the local current $I(x, t)$ of the following general form [3, 4]:

$$\frac{\partial}{\partial x} \left(I - C_s \frac{\partial^2 U}{\partial x \partial t} \right) = -C_g \frac{\partial U}{\partial t}, \quad (1)$$

$$\frac{\partial U}{\partial x}(x, t) = \int_0^\ell dx' M(x - x') \frac{\partial I}{\partial t}(x', t), \quad (2)$$

where C_g , C_s are the distributed capacitance (per unit length) to ground, and the series capacitance (times unit length) of the coil, respectively, and $M(x - x')$ is the mutual inductance (per unit length squared) of two turns of the coil located at the positions x , x' . The second term in the current continuity Equation (1) is the displacement current between turns through the series capacitance, and (2) describes the induced voltage in a turn at position x , due to a varying current in a turn at x' . Both equations can be combined into a single integro-differential equation for $U(x, t)$,

$$\frac{\partial^2 U}{\partial x^2}(x, t) = C_g \int_0^\ell dx' M(x - x') \left(1 - a^2 \frac{\partial^2}{\partial x'^2} \right) \frac{\partial^2 U}{\partial t^2}(x', t), \quad (3)$$

where we have introduced the usual “capacitive voltage decay length” $a = \sqrt{C_s/C_g}$ of a fast surge. A similar equation holds for $I(x, t)$.

This kind of integro-differential equation is usually very difficult to solve because of the finite integration bounds 0 and ℓ . But there are two simple approximations which allow circumventing this problem. The first one is that by Wagner and Rüdenberg (WR) [1, 2], which assumes that the mutual inductance function has a sufficiently short range to be replaced by a Dirac delta function, $M(x) = L_{\text{WR}}\delta(x)$, with the constant L_{WR} being an effective self inductance (per unit length). The second approximation is that by Blume and Boyajian (BB) [6], which implicitly assumes that the mutual inductance function decreases linearly with distance, $M(x) = \text{const} - \frac{1}{2}L_{\text{BB}}|x|$, leading to $d^2 M/dx^2 = -L_{\text{BB}}\delta(x)$. The latter assumption is unrealistic for an infinitely long coil (since $M(x)$ would become negative and very large for large enough $|x|$), but may be acceptable if the coil length ℓ is finite. For each of these approximations, (3) simplifies to a pure differential equation with no explicit dependence on ℓ anymore:

$$\frac{\partial^2 U}{\partial x^2} = L_{\text{WR}} C_g \left(1 - a^2 \frac{\partial^2}{\partial x^2} \right) \frac{\partial^2 U}{\partial t^2}, \quad (\text{WR}) \quad (4a)$$

$$-\frac{\partial^4 U}{\partial x^4} = L_{\text{BB}} C_g \left(1 - a^2 \frac{\partial^2}{\partial x^2} \right) \frac{\partial^2 U}{\partial t^2}. \quad (\text{BB}) \quad (4b)$$

Passing over to Fourier space, i.e., looking for plane-wave solutions of the form

$$I(x, t) = I_{k\omega} e^{j(\omega t - kx)} \quad \text{and} \quad U(x, t) = U_{k\omega} e^{j(\omega t - kx)}, \quad (5)$$

with frequency ω and wave number k , we find that Eqs. (4a), (4b) have solutions with the dispersion

relations

$$\omega^2 = \frac{k^2}{L_{\text{WR}}\tilde{C}(k)}, \quad (\text{WR}) \quad (6a)$$

$$\omega^2 = \frac{k^4}{L_{\text{BB}}\tilde{C}(k)}, \quad (\text{BB}) \quad (6b)$$

where $\tilde{C}(k) = C_g(1 + a^2 k^2)$ is an effective, wave-number dependent capacitance (per unit length).

3. COIL OF INFINITE LENGTH

In general, our Equation (3) with finite integration bounds has no plane-wave solutions, but for a hypothetical, infinite (in both directions) coil it has. Moving the bounds 0, ℓ to $-\infty, \infty$ leads to solutions with the dispersion relation

$$\omega^2 = \frac{k^2}{\tilde{M}(k)\tilde{C}(k)}, \quad (7)$$

where $\tilde{M}(k) = \int_{-\infty}^{\infty} dx M(x) e^{ikx}$ denotes the Fourier transform of the mutual inductance function $M(x)$. Note that $k^2/\tilde{C}(k)$ approaches the finite, nonzero limit C_s^{-1} for large k . Consequently, if $\tilde{M}(k)$ goes to zero for $k \rightarrow \infty$, expression (7) will diverge in that limit, implying that there is no finite upper limit frequency ω_c ; otherwise there is one. For instance, The WR approximation (6a) corresponds to a constant $\tilde{M}(k) = L_{\text{WR}}$ and thus has an upper limit frequency (namely, $\omega_c = (L_{\text{WR}}C_s)^{-1/2}$), whereas the BB approximation (6b) with $\tilde{M}(k) = L_{\text{BB}}/k^2$ does not. In general, a non-vanishing $k \rightarrow \infty$ limit of $\tilde{M}(k)$ means that $M(x)$ has a delta-function contribution at $x = 0$, which is physically inconsistent with the continuum limit ($M(x)$ can diverge at most logarithmically for $x \rightarrow 0$), and so any physically sensible $\tilde{M}(k)$ must vanish for $k \rightarrow \infty$, implying that ω_c is infinite. Furthermore, if we assume that $\tilde{M}(k)$ has a finite limit for $k \rightarrow 0$ (namely, the total inductance per unit length of the infinite coil), then expression (7) goes to zero in that limit and there is no lower limit frequency either; at any given real frequency ω there is (at least) one pair of real solutions $\pm k$.

Although the high-frequency behavior of the WR approximation thus appears somewhat unphysical, it has a very interesting feature. At frequencies above ω_c it has, instead of propagating modes, exponentially decaying “boundary modes” with purely imaginary wave vector $k = j\kappa$ (κ real). This can be seen easily by solving (6a) for k^2 :

$$k^2 a^2 = \frac{\omega^2}{\omega_c^2 - \omega^2}, \quad (\text{WR}) \quad (8)$$

which shows that $k^2 = -\kappa^2$ is *negative* for any given $\omega > \omega_c$. Both k and κ diverge as ω approaches ω_c (from below and above, respectively). In the high-frequency limit $\omega \gg \omega_c$, κ approaches the constant value $1/a$, which reflects the fact that the voltage distribution caused by a very fast transient or high frequency disturbance is governed only by the capacitive network formed by the distributed ground and series capacitances, with negligible influence of inductances.

Inspired by this, we may ask whether also the infinite-length version of our more general model (3) has other solutions than plane waves, or more specifically, whether for any given real ω the general dispersion relation (7) has solutions with complex k , in addition to the real solutions $\pm k$ identified above. In order to investigate this question, we have to choose a specific form of the mutual inductance function $M(x)$. We consider the following form which is simple enough for calculations albeit still quite general. To a delta-function contribution (which may also be chosen equal to zero), describing self inductance, is added an arbitrary number n of exponential terms, describing mutual inductance which decreases with distance:

$$M(x) = L_0 \delta(x) + \sum_{i=1}^n \frac{L_i}{2b_i} e^{-|x|/b_i}. \quad (9)$$

where L_0 , L_i , and b_i are real and positive constants. The Fourier transform of (9) is a rational function of k^2 of the simple form

$$\tilde{M}(k) = L_0 + \sum_{i=1}^n \frac{L_i}{1+k^2b_i^2}. \quad (10)$$

Obviously, the WR and BB approximations both are special cases of (9) or (10): WR corresponds to $n = 0$ and $L_0 \neq 0$, whereas BB corresponds to $n = 1$ and $L_0 = 0$ in the limit $b_1 \rightarrow \infty$ with L_1/b_1^2 kept constant.

With (10), the dispersion relation (7) can now be written in the form

$$\omega^2 C_g \left(L_0 + \sum_{i=1}^n \frac{L_i}{1+k^2b_i^2} \right) = \frac{k^2}{1+k^2a^2}, \quad (11)$$

which is equivalent to a polynomial equation of degree $n+1$ in k^2 , and so for given ω always must have $n+1$ (complex) solutions for k^2 . It turns out that for real and positive coefficients C_g , L_i , and b_i ($i = 1, \dots, n$), all of these solutions are again real. Their location is shown graphically in Figure 1. As long as $\omega^2 L_0 C_g a^2 < 1$, i.e., for frequencies ω below an upper limit frequency $\omega_c = (L_0 C_g a^2)^{-1/2}$, exactly one of these solutions is positive (denoted $k^2 = p^2$ with real $p > 0$ in Figure 1), corresponding to the propagating mode, whereas the other n solutions are negative (denoted $k^2 = -q_i^2$ with real $q_i > 0$, $i = 1, \dots, n$). For $\omega \rightarrow \omega_c$, p^2 diverges and at frequencies above ω_c , all $n+1$ solutions are negative ($k^2 = -q_i^2$ with real $q_i > 0$, $i = 0, \dots, n$). Note that if the delta-function contribution in (9) is set to zero ($L_0 \rightarrow 0$), then the upper limit frequency ω_c moves to infinity and, as argued above, there is a propagating mode at all frequencies.

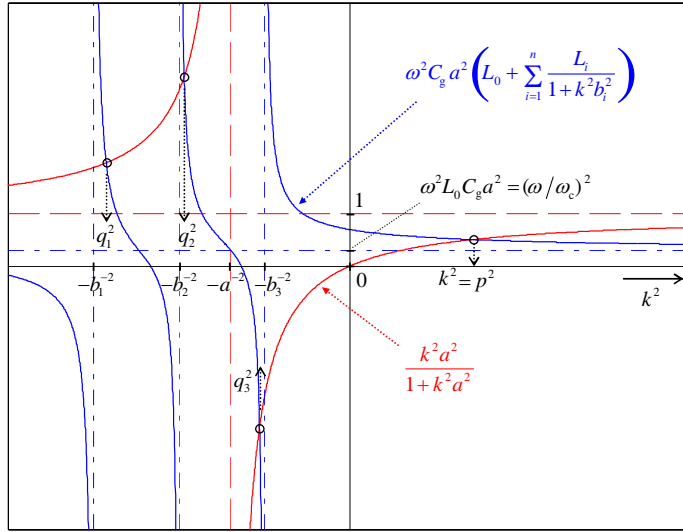


Figure 1: Graphical solution of the dispersion relation for k^2 . Blue/red curve: left/right side of Equation (11).

In summary, our Equations (1)–(3) with integration bounds moved to infinity have $2(n+1)$ linearly independent solutions of the form (5) with $k = \pm p$ or $k = \pm jq_i$. The solutions with imaginary wave numbers $k = \pm jq_i$ are exponentially increasing in either positive or negative x direction and thus, strictly speaking, physically meaningless for a system which is infinitely extended in both directions. As we will see in the next section they are, however, very useful to describe boundary effects in finite systems.

4. COIL OF FINITE LENGTH

We return to the integro-differential Eqs. (1)–(3), now assuming *finite* integration bounds $0, \ell$. Remarkably, it turns out that the exact solution of the *finite* system, including the effects of the boundaries, is a particular superposition of the solutions which we derived above for the infinitely extended system. The reason for this, as was already noticed by Steidinger [3], is that any solution of (2) also must obey a certain linear and homogeneous differential equation with constant coefficients, which is obtained from (2) by expressing the function $M(x)$ in terms of its Fourier transform

$\tilde{M}(k)$ and substituting the differential operator $-j\frac{\partial}{\partial x}$ for k :

$$\begin{aligned}\frac{\partial U}{\partial x}(x, t) &= - \int_0^\ell dx' \left(\int_{-\infty}^{\infty} \frac{dk}{2\pi} \tilde{M}(k) e^{-jk(x-x')} \right) \frac{\partial I}{\partial t}(x', t) \\ &= -\tilde{M} \left(-j\frac{\partial}{\partial x} \right) \int_0^\ell dx' \left(\int_{-\infty}^{\infty} \frac{dk}{2\pi} e^{-jk(x-x')} \right) \frac{\partial I}{\partial t}(x', t) = -\tilde{M} \left(-j\frac{\partial}{\partial x} \right) \frac{\partial I}{\partial t}(x, t). \quad (12)\end{aligned}$$

Since $\tilde{M}(k)$ is a rational function of k^2 , (12) is equivalent to a linear and homogeneous differential equation of finite degree with constant coefficients, and so the exact solution of (1)–(3) at a given frequency ω can be written as a superposition of harmonic terms with wave numbers k obeying the dispersion relation (7). But these are just the two propagating modes with real wave numbers $k = \pm p$ and the $2n$ exponential “boundary modes” with imaginary wave numbers $k = \pm jq_i$ discussed earlier. The relative amplitudes of these modes are determined by the voltage or current boundary conditions imposed at the coil ends; in practice, they can be calculated for instance by inserting a general linear combination (with constant coefficients) of the above modes into (1)–(3), and solving the resulting set of linear equations for the coefficients.

In principle, this idea has already been described in [3]; however, neither Steidinger nor any of the later authors working on this problem seem to have realized the full potential of this approach. The crucial point is that our assumption in (9) of L_i and b_i being real constants actually was used only to conclude that all the solutions k^2 of (11) also must be real. But there is no reason to reject complex values of k^2 , so we can relax this condition and start with *complex* values of L_i and b_i instead ($\text{Re}b_i > 0$ in order to avoid divergence of $M(x)$ as $|x| \rightarrow \infty$), allowing to describe non-monotonic or even oscillatory mutual-inductance functions $M(x)$. This generalization can for instance be used to analyze the detailed local voltage and current distributions within individual turns of a finite helical coil. We plan to present such an analysis in a forthcoming paper. Interestingly, both $\tilde{M}(k)$ and $\tilde{C}(k)$ become *oscillating* functions of k in this case, allowing within in a certain frequency range multiple real solutions of the dispersion relation (7), i.e., several propagating modes with different k .

The exact solutions described above for simple finite coils are extremely useful as starting points and reference cases for modeling and understanding the general behavior of more complex types of coils in real transformers or electrical machines, and in particular for studying coil-end effects.

REFERENCES

1. Wagner, K. W., “Das eindringen einer elektromagnetischen Welle in eine Spule mit Windingskapazität,” *Elektrotechnik und Maschinenbau*, Vol. 33, No. 8, 89–92 and No. 9, 105–108, 1915.
2. Rüdenberg, R., “Performance of traveling waves in coils and windings,” *Trans. AIEE*, Vol. 59, 1031, 1940.
3. Steidinger, W., “Das elektromagnetische Verhalten der einlagigen Zylinderspule,” *Archiv für Elektrotechnik*, Vol. XIII, 237, 1924.
4. Pirenne, M. J., “Théorie générale des phénomènes oscillatoires dans les enroulements des transformateurs,” *Revue Générale de l’Électricité*, 19–29 and 53–63, Jan. 1940.
5. Abetti, P. A. and F. J. Maginniss, “Fundamental oscillations of coils and windings,” *IEEE Trans. PAS*, Vol. 73, 1–10, 1954.
6. Blume, L. F. and A. Boyajian, “Abnormal voltages within transformers,” *AIEE Transactions*, Vol. 38, Part 1, 577–614, 1919.
7. Bewley, L. V., “Transient oscillations in distributed circuits with special reference to transformer windings,” *AIEE Transactions*, Vol. 50, 1215–1233, Dec. 1931.
8. Bewley, L. V., *Travelling Waves on Transmission Systems*, 2nd Edition, Dover Publication Inc., 1951.
9. Akbari, A., P. Werle, H. Borsi, and E. Gockenbach, “Transfer function-based partial discharge localization in power transformers: A feasibility study,” *IEEE Electrical Insulation Magazine*, Vol. 18, No. 5, 22–32, Sep.–Oct. 2002.
10. Greenwood, A., *Electrical Transients in Power Systems*, 2nd Edition, John Wiley, New York, 1991.

Complex Permittivity Determination of Homogeneous Objects Loaded in Circular Waveguide via Integral Equation Method

A. Aydogan^{1,2} and F. Akleman²

¹Electrical and Electronics Engineering Department, Marmara University, Istanbul, Turkey

²Electronics and Communication Engineering Faculty, Istanbul Technical University, Istanbul, Turkey

Abstract— An integral equation approach is presented for the complex permittivity determination of arbitrarily shaped homogenous objects loaded in circular waveguide. In order to formulate the integral equation based inverse algorithm, first the well-known data and object equations, containing electric type dyadic Green's function of empty waveguide are obtained. It should be noted that the data and object equations can be solved with different techniques to determine the permittivity of the objects partially/fully loaded in a waveguide. In this paper, a Newton based iterative algorithm is applied where the nonlinear data equation is linearized by first order Taylor expansion using Frechet derivative of the integral operator. In this study, complex permittivity determination of non-magnetic, arbitrarily shaped and homogeneous material using the scattered electric fields in the circular waveguide is considered. The inverse algorithm for partially filled circular waveguide is applied for objects with different geometries and satisfactory results are obtained also in the presence of random noise.

1. INTRODUCTION

Determination of complex permittivity is an important topic in microwave and electromagnetic studies due to its wide range of applications, such as non-destructive testing, filter design and biomedical applications, etc.. The integral equation based reconstruction algorithm has been introduced for similar inverse problems in rectangular waveguides [1, 2] and it can easily be shown that the proposed method is applicable to waveguides with arbitrary cross sections if the related dyadic Green's function of the empty waveguide is known.

In this study, a three dimensional dielectric object with constant complex permittivity is considered. Location and shape of the object is assumed to be known. Scattered field data is obtained synthetically via solution of direct scattering problem instead of a real-measurement. Related integral equations are converted into matrix equations through a Moment Method based approach, where integration of dyadic Green's function at each discrete cell is required. The main problem encountered in the solution of direct scattering problem by means of Method of Moments is the integration of dyadic Green's function of empty circular waveguide in the source region, which is handled using a pie-type meshing to obtain an analytical integration [3]. The time dependency is chosen to be $e^{-i\omega t}$ and omitted.

2. FORMULATION OF THE PROBLEM

The problem to be considered is shown in Fig. 1. An arbitrarily shaped, homogeneous, non-magnetic lossy dielectric object is loaded inside a circular waveguide with radius a .

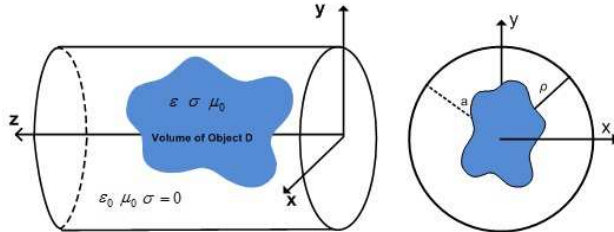


Figure 1: Geometry of the problem.

Total electric field inside the waveguide at any point is given by

$$\vec{E}(\vec{r}) = \vec{E}^i(\vec{r}) + \vec{E}^s(\vec{r}) \quad (1)$$

where \vec{r} is the position vector. Equivalent volume current density $\vec{J}(\vec{r})$ is related to total field as;

$$\vec{J}(\vec{r}) = -i\omega\varepsilon_0(\varepsilon_r - 1)\vec{E}(\vec{r}) \quad (2)$$

where ε_r is the relative dielectric constant of the homogeneous object D . Eq. (2) can be rearranged to relate $\vec{J}(\vec{r})$ and $\vec{E}(\vec{r})$ directly via so-called object function as $\vec{J}(\vec{r}) = -i\omega\varepsilon_0\vec{E}(\vec{r})v(\vec{r})$. For clarity, the well-known object function is given below

$$v(\vec{r}) = \frac{\varepsilon}{\varepsilon_0} - 1 \quad (3)$$

In (2), $\varepsilon = \varepsilon_r\varepsilon_0$ is the complex permittivity of the object D . The well-known data equation is given by (4) where $\vec{E}^s(\vec{r})$ and $\bar{G}(\vec{r}, \vec{r}')$ are the scattered field and dyadic Green's function of the empty circular waveguide, respectively. The explicit expression of $\bar{G}(\vec{r}, \vec{r}')$ is given in [3]. Position vectors r and r' denote the observation and source points respectively. Note that $\vec{E}^s(\vec{r})$ is the contribution of the object D to the total field.

$$\vec{E}^s(\vec{r}) = k_0^2 \int_{r' \in D} \bar{G}(\vec{r}, \vec{r}') \vec{E}(\vec{r}') v(\vec{r}') dv', \quad r \notin D \quad (4)$$

where k_0 is the wavenumber of free-space. Integral equation of scattered field due to the Green's theorem is also valid in object D . Substituting (4) into (1) in domain of object D , one obtains well-known object equation;

$$\vec{E}(\vec{r}) = \vec{E}^i(\vec{r}) + k_0^2 \int_{r' \in D} \bar{G}(\vec{r}, \vec{r}') \vec{E}(\vec{r}') v(\vec{r}') dv', \quad r \in D \quad (5)$$

First, the object equation is taken into account in order to obtain unknown equivalent volume current density via Moment Method. As mentioned before, self-cells should be treated carefully due to the singularity. To this aim, a principle volume with pill-box shape is considered [4] when source and observation points coincide where contribution of self-cells are added independently. Regarding to the source region singularity, the integral equation to be solved for direct problem becomes,

$$-\vec{E}^i(\vec{r}) = \frac{\vec{J}(\vec{r})}{i\omega[\varepsilon(\vec{r}) - \varepsilon_0]} + i\omega\mu_0 \lim_{\delta \rightarrow 0} \int_{V_D - V_\delta} \bar{G}(\vec{r}, \vec{r}') \vec{J}(\vec{r}') dv' + \frac{J_\partial}{i\omega\varepsilon_0} \quad (6)$$

where V_δ represents the source region which is an infinitesimally small volume and treated separately from the volume integral as a contribution term. J_∂ stand for the contribution of the source region which is the longitudinal component of $\vec{J}(\vec{r})$ in the direction of propagation, i.e., z component for given geometry. Obtaining current density, one can calculate scattered field through data equation as given in (5). So, synthetic scattered field data is obtained to reconstruct the complex permittivity.

3. NEWTON BASED INVERSE ALGORITHM

In this section, a Newton-type algorithm to reconstruct the complex permittivity of the object under interest is presented. Similar algorithm is applied to inhomogeneous objects loaded in rectangular waveguide in [2] and satisfactory results are reported. In this study, presented algorithm in [2] is adapted for homogeneous case and applied to circular waveguide.

Relation between current density based function and total electric field given in (2) can be written in operator form as;

$$\Phi_f(\vec{r}) = v_f(\vec{r})E_f(\vec{r}), \quad f = 1, 2, \dots, F \quad (7)$$

where f represents different operating frequency values. Assuming real part of object function or relative permittivity is independent from frequency, one should do the following normalization for frequency-dependent imaginary part;

$$v_f(\vec{r}) = \text{Re}[v_1(\vec{r})] + i\frac{\omega_1}{\omega_f}\text{Im}[v_1(\vec{r})], \quad f = 1, 2, \dots, F \quad (8)$$

Data and object equations, given in (4) and (5) respectively, can be written in operator form

$$G_f^D \Phi_f(\vec{r}') = E_f^s(\vec{r}'), \quad f = 1, 2, \dots, F \quad (9)$$

$$E_f(\vec{r}) = E_f^i(\vec{r}) + G_f^O \Phi_f(\vec{r}'), \quad f = 1, 2, \dots, F \quad (10)$$

Integral operators G_f^D and G_f^O with kernel $G(\vec{r}, \vec{r}')$, acting on Φ_f are defined as

$$G_f^D = k_0^2 \int_D \bar{G}(\vec{r}, \vec{r}') dv', \quad r \notin D, \quad f = 1, 2, \dots, F \quad (11)$$

$$G_f^O = k_0^2 \int_D \bar{G}(\vec{r}, \vec{r}') dv', \quad r \in D, \quad f = 1, 2, \dots, F \quad (12)$$

In order to obtain a first initial value for current density based function, back-propagation algorithm is used, which maps the scattered field back into the spatial domain of object D . Initial guess for current density can be obtained through conjugate gradient method as given below [5]

$$\Phi_f^0(\vec{r}') = \frac{\|G_f^{D*} E_f^s\|_2}{\|G_f^D G_f^{D*} E_f^s\|_2} G_f^{D*} E_f^s \quad (13)$$

where G_f^{D*} is the adjoint of data operator and $\|\cdot\|_2$ denotes L_2 norm. Initial guess for total electric field can be obtained as

$$E_f^0(\vec{r}) = \vec{E}_f^i(\vec{r}) + G_f^O \Phi_f^0 \quad (14)$$

where E_f^0 is the initial guess for total electric field inside object D in operator form at operating frequency. Relation in (7) is an over-determined system. Minimizing the residual error, $\Phi_f(\vec{r})$ is projected onto the subspace spanned by the columns of $E_f(\vec{r})$ and initial guess for object function can be obtained in least square sense as given below

$$\text{Re}(v^0) = \frac{\sum_{n=1}^N \sum_{p=1}^3 \sum_{f=1}^F \text{Re}(\Phi_{n,p,f}^0 \bar{E}_{n,p,f}^0)}{\sum_{k=1}^K \sum_{p=1}^3 \sum_{f=1}^F \text{Re}(E_{n,p,f}^0 \bar{E}_{n,p,f}^0)} \quad (15)$$

$$\text{Im}(v^0) = \frac{\sum_{n=1}^N \sum_{p=1}^3 \sum_{f=1}^F \frac{\omega_1}{\omega_f} \text{Im}(\Phi_{n,p,f}^0 \bar{E}_{n,p,f}^0)}{\sum_{n=1}^N \sum_{p=1}^3 \sum_{f=1}^F \left(\frac{\omega_1}{\omega_f}\right)^2 \text{Im}(E_{n,p,f}^0 \bar{E}_{n,p,f}^0)} \quad (16)$$

where k , p and over-bar stand for k th subcell of total K discretized cells, normalized vectors in cylindrical coordinates (ρ, ϕ, z) and complex conjugate, respectively. Obtaining initial values, an iterative algorithm can be carried out. A first order Taylor expansion is considered as an acceptable approximation to linearize the non-linear data equation given in (9) as follows

$$G_f^D \Phi_f(\vec{r}') + G_f^{D'} \Delta \Phi_f(\vec{r}') = E_f^s(\vec{r}'), \quad f = 1, 2, \dots, F \quad (17)$$

where $G_f^{D'} \Delta \Phi_f(\vec{r}')$ is Frechét derivative of integral operator $G_f^{D'}$ with respect to object function $v(\vec{r})$, which are related as

$$G_f^{D'} \Delta \Phi_f^{n+1} = k_f^2 \int_D \bar{G}_f(\vec{r}, \vec{r}') \vec{E}_f^n(\vec{r}') \Delta v_f^n(\vec{r}') dv', \quad r \in D \quad (18)$$

Here n denotes the step number of recursive algorithm which is “0” for first iteration and $\Delta v(\vec{r}')$ is the update amount of object function, related to $\Delta \Phi_f(\vec{r}')$ through the total electric field as

$$\Delta \Phi_f(\vec{r}') = E_f^n \Delta v_f^n(\vec{r}'). \quad (19)$$

Thikonov regularization [5] is applied to obtain a stable solution for update amount of current density based function $\Delta\Phi_f^n(\vec{r}')$ as follows

$$\Delta\Phi_f^n(\vec{r}') = [\alpha I + G_f^{D'*}G_f^D]^{-1} [G_f^{D'*}(E_f^s - G_f^D\Phi_f^n)] \quad (20)$$

where I and α are identity matrix and regularization parameter. Morozov discrepancy rule is used to determine α which minimizes residual error in (18) as a posteriori choice based on noise level in practice instead of a priori asymptotic approach, namely

$$\|G_f^{D'}\Delta\Phi_f^n(\vec{r}') - (E_f^s(\vec{r}) - G_f^D\Phi_f^n(\vec{r}))\| \leq \delta \quad (21)$$

where σ is the expected noise level. Obtaining $\Delta\Phi_f^n(\vec{r}')$ through a suitable regularization parameter α , one easily determines the update amount of object function via (15) and (16) for real and imaginary parts, respectively. Note that, (15) and (16) are written for first iteration with superscript 0 which should be replaced with n for n th iteration. Object function can be updated via $v^{(n+1)}(\vec{r}) = v^n(\vec{r}) + \Delta v^{(n+1)}$. Then, total electric field can be updated through object equation given in (10). Newton-based iteration continues until $\frac{\|\Delta\|}{\|v\|} < b$ where b is an arbitrary defined real number, e.g., 10^{-2} .

4. NUMERICAL RESULTS

The radius of waveguide is chosen as 0.15 m. For this geometry, dominant mode region is between 586 MHz–765 MHz. Operating frequency is taken as 700 MHz for dominant mode excitation TE_{11} , regarding to the waveguide stability. A high lossy dielectric object is considered with different geometries. A noise of 1% magnitude of scattered field with normally distributed random phase variation is added to synthetic scattered field data. Reflected and transmitted fields are observed at $z = 0$ and $z = \lambda + w$ planes where w is the length of the object. Front side of object is located at $z = \lambda/2$. To avoid inverse crime, mesh number for inverse problem is chosen less than of direct problem.

Two different homogeneous objects which are shown in Fig. 2 are examined. First object is fully loaded in tangential direction and leaned toward the guide wall with $a/4$ width and $\lambda/6$ length. Second object is half loaded in radial direction and has $\pi/4$ width in tangential direction with $\lambda/3$ length in propagation direction. Complex permittivity of the objects are chosen as $2.1 + 1i$. For the

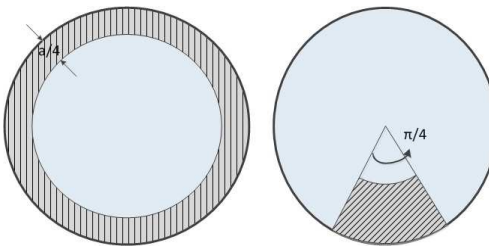


Figure 2: Object 1 & object 2.

analysis of object 1, reconstruction domain is divided into 120 and 96 cells for direct and inverse problems, respectively while these values are 140 and 112 for object 2. $\frac{\|\Delta\|}{\|v\|}$ reached a desired level of 10^{-2} at 4th and 3rd iteration for object 1 and object 2, respectively. Reconstructed permittivity for two objects with relative error are given with Table 1.

Table 1: Exact & determined complex permittivity.

	Exact Value	Determined Value	Relative Error (%)
Object 1	$2.1 + 1i$	$2.091 + 1.013i$	0.679%
Object 2	$2.1 + 1i$	$2.094 + 0.996i$	0.305%

5. CONCLUSION

In this study, determination of complex permittivity of a homogeneous object, arbitrarily loaded in a circular waveguide is analyzed. Through Moment Method procedure, related integral equations are converted into matrix equations. Scattered field data is produced synthetically as a direct scattering problem. Using scattered field data, the well-known Newton Algorithm is carried out to determine complex permittivity. Satisfactory results are obtained in the presence of noise. Future studies will be focused on reconstruction of inhomogeneous objects through the algorithm used in this study.

REFERENCES

1. Akleman, F., “Reconstruction of complex permittivity of a longitudinally inhomogeneous material loaded in a rectangular waveguide,” *IEEE Microwave and Wireless Components Letters*, Vol. 18, No. 3, 158–160, Mar. 2008.
2. Kilic, E., F. Akleman, B. Esen, D. M. Ozaltin, O. Ozdemir, and A. Yapar, “3-D imaging of inhomogeneous materials loaded in a rectangular waveguide,” *IEEE Transactions on Microwave Theory and Techniques*, Vol. 58, No. 5, 1290–1296, May 2010.
3. Aydogan, A. and F. Akleman, “Validation of mom-based direct scattering analysis in circular waveguide for appropriate mesh-type decision,” *2012 International Conference on Mathematical Methods in Electromagnetic Theory (MMET)*, 275–278, Aug. 28–30, 2012.
4. Yaghjian, A. D., “Electric dyadic Green’s functions in the source region,” *Proceedings of the IEEE*, Vol. 68, No. 2, 248–263, Feb. 1980.
5. Van den Berg, P. M., “Nonlinear scalar inverse scattering: Algorithms and applications,” *Scattering and Inverse Scattering in Pure and Applied Science*, R. Pike and P. Sabatier, Eds., Vol. 1, 142–161, Academic Press, London, 2002.

Current Density Estimation and Visualization for Exposed Live Transmission Line Workers

C. A. Belhadj¹ and N. Maalej²

¹Electrical Engineering Department

King Fahd University of Petroleum and Minerals, Dhahran 31261, Saudi Arabia

²Physics Department, King Fahd University of Petroleum and Minerals, Dhahran 31261, Saudi Arabia

Abstract— This paper is about estimation and visualization of the current densities for live transmission line workers body tissues. The purpose of this investigation work was to evaluate the safety level of an exposed high voltage transmission line worker externally and internally. A typical utility 132-kV, 60 Hz transmission line was considered. The charge simulation method was used to compute the external electric field and Biot-Savart law was used for the magnetic field estimation. The live-line worker exposure simulation was conducted using EPRI's WorkStation. To estimate the organs internal induced electric field and current densities, Finite Difference Time Difference computational algorithm method was implemented using EMPIRE commercial software. Visible Human was used to investigate several tissues. The obtained values of external and internal exposure fields level were well below the recommended international standards limits for the scenarios considered in this study.

1. INTRODUCTION

The concern among workers of Saudi Electricity Company (SEC) regarding possible health hazards due to the exposure power Frequency electric and magnetic Fields (ELF-EMF) is growing. Limited knowledge and information available for live-line workers tends to magnify intensively the risk of exposure to extremely low frequency fields. The SEC transmission networks above 110 kV spans a total length of 33,685 circuit-km (ckm) [1]. There has been a rising interest over the years in determining the safe exposure levels of people, mainly workers, and the general public, to power frequency electric and magnetic fields [2–8]. Several organizations have developed standards and guidelines for such permissible exposure levels.

By far, the most important organizations that have contributed to the establishment of these standards and guidelines are the Institute of Electronic and Electrical Engineers (IEEE) [2], and the International Commission on Non-Ionizing Radiation Protection (ICNIRP) [3]. There are other organizations such as the American Conference of Governmental Industrial Hygienists (ACGIH) [4], and the National Radiological Protection Board (NRPB) that have major contribution [5, 6]. There are many government agencies and organizations that have published articles in this subject [7, 8].

The permissible levels quoted in many countries refer to the permissible levels set by the IEEE standard, and the ICNIRP guideline. Table 1 lists a summary of occupational external exposure limits for 60 Hz for the IEEE, ICNIRP, ACGIH and NRPB.

Table 1: Summary of external exposure limits for live-line workers.

Organization	Electric Field (kV/m)	Magnetic Field $\times 10^4$ (mG)
IEEE	20	2.71 (Head & Torso)
ICNIRP	8.333	0.417
ACGIH	25	1
NRPB	12	1.6

In recent years, a number of laboratories have developed heterogeneous models of the human body with an anatomical shape and numerous tissues to study the EMF exposure. Most of these models have been developed by computer segmentation of data from MRI and allocation of proper tissue type [22–25]. These groups and others have used the high resolution human body models to study the EMF's exposures of the human body to low and high frequencies. Hand reviewed the different calculation method and anatomical models for high frequency electromagnetic exposure [26]. Several methods have also been developed to study electric fields and current densities

induced in anatomic models of the human body for low frequency exposure [27–30]. Gandhi used the quasi-static impedance method to calculate the currents induced in the nominal $2 \times 2 \times 3$ and 6 mm resolution anatomically based models of the human body for exposure to magnetic fields at 60 Hz from homogeneous and non-homogeneous magnetic fields [28]. Dimbylaw used both the impedance method and the scalar potential finite difference methods in a fine-resolution (2 mm) anatomically realistic voxel model [30].

Table 2: Summary of internal exposure limit for live-line workers.

Organization	Organ	Electric Field/Current Density
IEEE	Brain	53.1 mV/m
	Heart	943 mV/m
	Hands, wrists, feet and ankles	2100 mV/m
	Other tissue	2100 mV/m
ICNIRP	Central Nervous System (CNS)	10 mA/m ²
NRPB	Central Nervous System (CNS)	10 mA/m ²

This paper introduces detailed system study data and three practical scenarios. Profiles calculation are then presented and discussed. The internal field and current density estimation and visualization are then displayed and discussed. Conclusions are then drawn. The paper terminates with acknowledgment, and references.

2. SYSTEM & EXPOSURE SCENARIOS

Detailed line data and tower dimension are illustrated in Fig. 1 and line details are delineated in Table 3.

Table 3: Transmission line data for the 132 Kv line

Line Ratings		
Rating (MVA)		293 MVA
Nominal Line Voltage (kVL-L)		132 kV
Actual Line Voltage (kVL-L)		132 kV
Nominal Line Current (kA)		1.284 kA
Peak Load Current (kA), for Both Circuits		Circuit 1 Circuit 2
		603 A 603 A
Line Conductor and Overhead Ground Wire Parameters		
Conductor/Ground Wire	Conductor	Ground Wire
Diameter (cm)	2.773 cm	1.03 cm
Number of Sub-conductors	SINGLE	
Phase Relation of Conductors	VERTICAL (R-Y-B)	
Right of Way	40 m	
Full span (m)	305 m	
Mid Span height (m) or Sag (m) (lowest point)	10 m	

The three selected scenarios are described in Table 4. The computation of the external electric and magnetic fields have been conducted for all three scenarios. These scenarios cover the most probable locations near a transmission line where live line workers are likely to be exposed for activities such as live insulator washing or live visual inspection.

The height of a typical worker (human body) is assumed to be 1.75 m. The computation for both electric and magnetic fields is conducted from 0.5 m to 1.75 m of the human body using a step

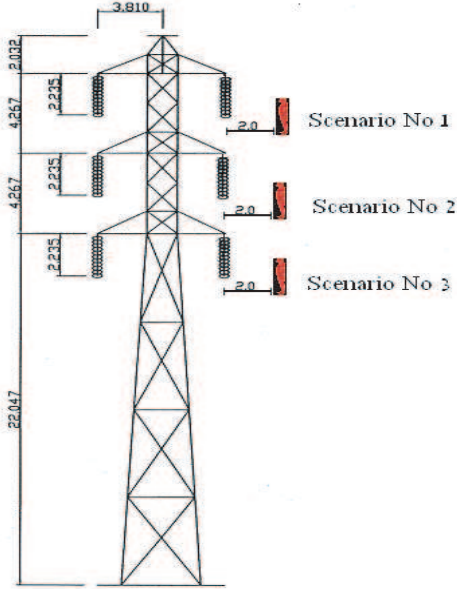


Figure 1: Tower dimension for the 132 kV transmission line.

Table 4: Selected exposure scenarios for simulation studies.

No.	Description of Exposure Scenario
1.	A worker is standing in the bucket close to conductor phase A and about 2 m away from the conductor.
2.	A worker is standing in the bucket close to conductor phase B and about 2 m away from the conductor.
3.	A worker is standing in the bucket close to conductor phase C and about 2 m away from the conductor.

of 0.25 m. After computation of field's values at these points along the human body, the maximum value of the electric is also recorded.

3. ELECTRIC AND MAGNETIC FIELD CALCULATIONS

The basic physics of quasi-static fields allow separate discussion of power frequency electric and magnetic fields [9].

3.1. Charge Simulation Méod

The solution methodology for electric field is based on two-dimensional charge simulation method. This commonly used approach consists essentially of two stages: (1) calculation of the equivalent charges per unit length of conductor and (2) calculation of the electric field produced by these charges. A detailed treatment of the calculations is given in [10–17].

3.2. BIOT-SAVART Law

The basic equation for calculating the magnetic field of a long, straight wire is derived from Ampere's Law. Detailed treatment of the calculations is given in [11, 13, 18].

In this study the electric and magnetic fields produced by the transmission line have been modeled using the subroutine EXPOCALC of the EPRI's software EMF Workstation, Version 2.51 [18–21]. The software package used, starts by setting the general required parameters such as the designated area of concern parameters, the structure position, boundary area, as well as the field calculation height. The line design parameters are entered in a detailed manner and that includes phase structure of the line, conductor size, applied voltage and the operating current. The span specifications are then taken in to consideration.

Scenario 1 was about a live line worker standing in the bucket close to conductor of phase A and about 2 m away from the conductor. The clearance of the line worker is at 93 feet (28.27 m) from

ground to middle of the body length. Scenario 2 and 3 were about a live line worker standing in the bucket close to conductor of phase B and C respectively and about 2m away from the conductor. The clearance of the line worker for scenario 2 is at 79 feet (24 m) from ground to middle of the body length while the clearance of the line worker for scenario 3 is at 65 feet (19.76 m) from ground to middle of the body. Fig. 1 depicts these three scenario worker position.

The simulations were performed for both electric and magnetic fields for each scenario, along the human body model as displayed by Fig. 2. and Fig. 3, respectively. The profile taken is covering the human boy length from 0.5 m to 1.75 m by a step of 0.25 m. This coverage includes the brain (nervous system), chest (lungs), hands, stomach, reproduction organs, leg and to the knee. These different human tissues are exposed to different level of induced electric fields and current densities in human body tissues.

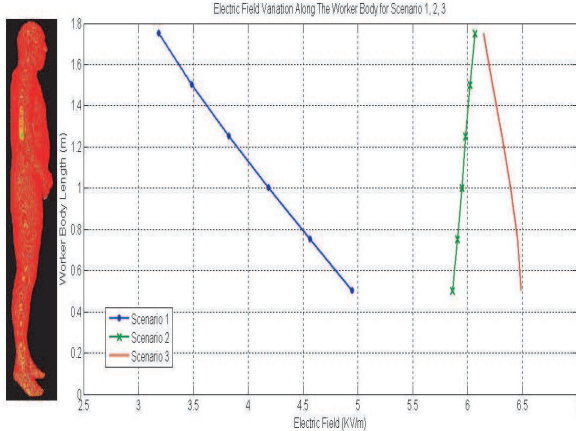


Figure 2: Electric field variation along the worker body for scenario 1, 2, 3.

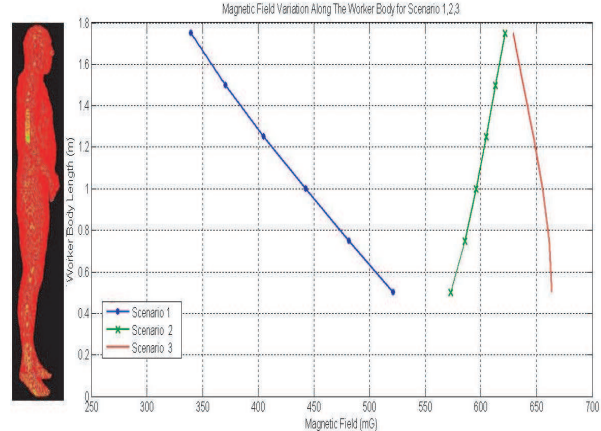


Figure 3: Magnetic field variation along for worker body (scenario 1, 2, 3).

Figures 2 and 3 reveal relatively lower profile values for both fields for scenario 1 than both profile values relevant to scenario 2 and 3. Scenario 1 results show a descending profile of both electric and magnetic fields going from the less sensitive to the most sensitive tissue of the human body, from knee to brain. The variation is 1.763 kV/m and 181.75 mG respectively. The gradient across the body relatively is high in both fields.

Scenario 2 profile show an ascending profile of both electric and magnetic fields going from the less sensitive to the most sensitive tissue of the human body, from knee to brain. The gradients are 0.204 kV/m and 48.56 mG respectively. Though the values are higher than scenario 1 profile values but the gradients across the body are relatively low in both fields.

Scenario 3 displays the highest profile values for both fields with a descending profile of both electric and magnetic fields going from the less sensitive to the most sensitive tissue of the human body, from knee to brain. The gradients are 0.341 kV/m and 34.62 mG respectively. Though the values are higher than scenario 1 profile values but the gradients across the body are relatively low in both fields and in the same range as for scenario 2.

4. COMPLIANCE WITH THE STANDARDS

The exposure profile levels computed in Section 3 for the three scenarios 1, 2 and 3 are compared to the universal standards such as IEEE Standard C95.6, ICNIRP guidelines ACGIH threshold Limit Values and to NRPB. These standards recommend limits on exposures to electric and magnetic fields in the frequency range of 0 to 3000 hertz (Hz) and derived for both controlled (occupational, live line workers) and uncontrolled (publicly accessible) environments, for uniform and non-uniform fields, for whole-body and extremity exposures.

The highest computed values for the electric field were 4.949 kV/m, 6.065 kV/m and 6.485 kV/m for scenarios 1, 2 and 3 respectively. The Maximum Permissible Level according to the ICNIRP guidelines for occupational exposure is 8.333 kV/m, which is very conservative. The limit according to the ACGIH Guidelines for Exposure to 60 Hz EMF is 25 kV/m while the NRPB limits is 12 kV/m.

The maximum magnetic field simulation results were 521.47 mG, 621.51 mG and 663.51 mG for scenarios 1, 2 and 3 respectively however, the Maximum Permissible Exposure for the power

frequency magnetic field and for exposure to whole body are 2.71×104 mG, 0.417×104 mG, 1×104 mG and 1.6×104 mG for IEEE, ICNIRP, ACGIH, ACGIH and NRPB respectively.

The highest electric and magnetic fields exposure level for the SEC 132 kV transmission line, therefore, is well below the limits set by the different standards.

5. INTERNAL FIELD CALCULATIONS

Scenario 3 is selected as study candidate for the internal field and current density study. In this scenario the worker is exposed to the strongest and worst fields. The external electric field is taken from front to back ($E_y = 6.485$ kV/m). The external magnetic field is taken from head to feet ($B_z = 664$ mG). The voxel size is 6 mm. The human body is in free space and not in contact with electrical ground. The above entries are taken by EMPIRE software in order to compute the induced tissue electric field and current density.

Table 5 shows the induced maximum current density and the induced maximum electric field for selected body organs. The values for all the voxels in each organ are used to calculate the maximum values of the current density and electric field. The values for the induced electric fields are obtained by dividing the current density at each voxel by the conductivity of that voxel as specified by the human body model.

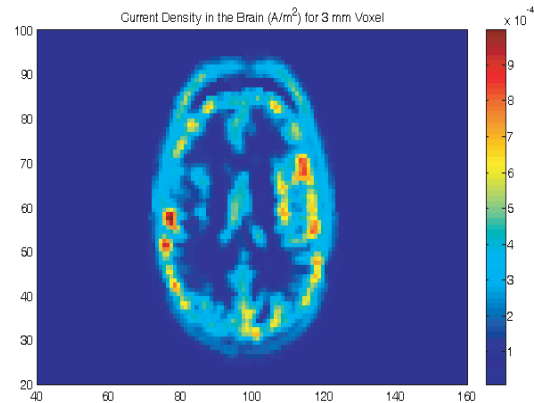
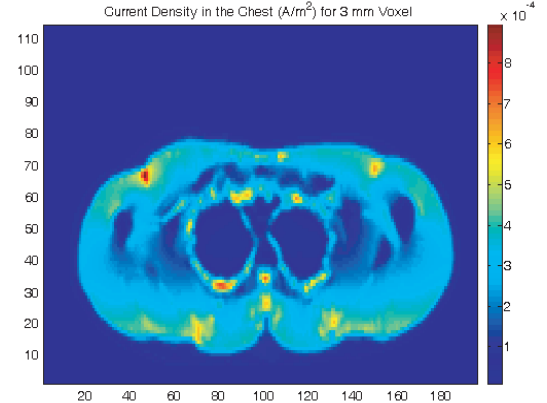
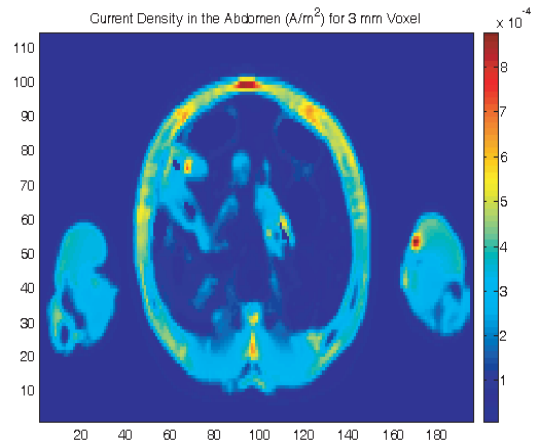
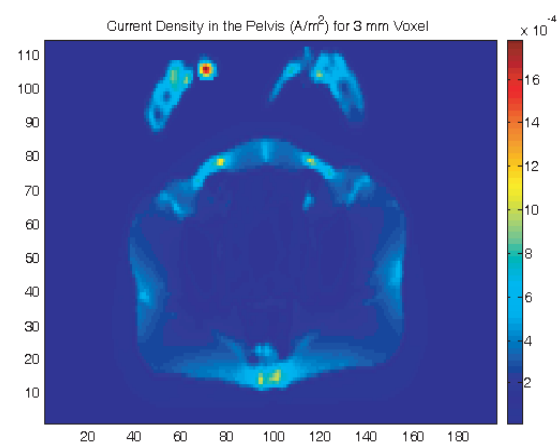
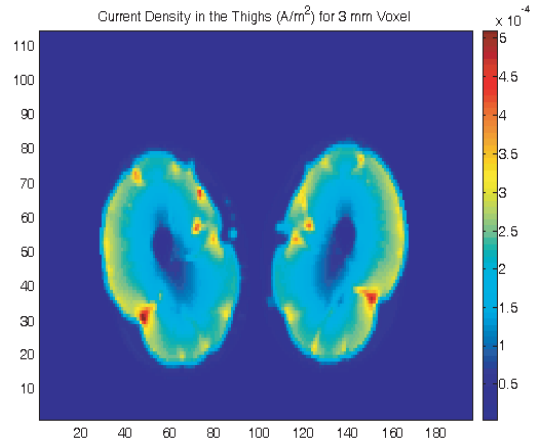
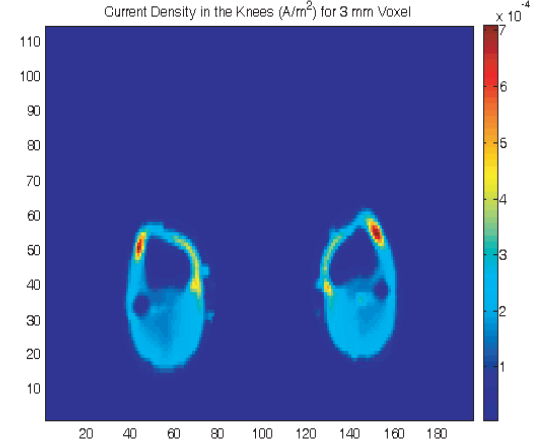
Table 5: Scenario 3: Organ maximum current density J_{\max} , and maximum induced electric field E_{\max} .

Tissue Type	J_{\max} (mA/m ²)	E_{\max} (mV/m)
Cerebellum	0.90	8.99
Gray Matter	1.49	18.59
White Matter	1.26	22.93
Heart	1.11	12.88
Nerve (Spine)	1.06	38.47
Cerebral Spinal Fluid	1.49	0.75
Eye (Aqueous Humor)	0.69	0.46
Kidneys	0.38	4.07
Liver	1.83	49.39
Lung (Inner)	1.81	25.83
Lung (Outer)	1.62	7.88
Pancreas	0.64	1.23
Spleen	1.18	13.18
Feet and Ankles	1.89	1111.95
Hands and Wrist	2.68	1041.19

In all tissue type listed in Table 5 the maximum current densities and the corresponding electric fields are found to be below the exposure limit of 10 mA/m² for the current density and of 2100 mv/m for the tissue electric field. Several tissues in the list such as ankle, knees, Hands, Wrist and Feet show higher current density due to the small body cross section at.

6. CURRENT DENSITY VISUALIZATION

The figures from 4 to 9 show the anatomical structure of selected representative body tissues. Respectively the figures are relevant to the brain, the chest, the abdomen, the pelvis, the thighs and the knees. Each figure associated color bar represents the variation of the current density value. The dark blue color shows the lowest current density value while the dark red shows the maximum current density value. Such visualization gives the relative intensity value of the current density as well as its location in the tissue section. As a matter of fact the maximum value is represented by the dark red color. Usually, the maximum values occur at the boundaries between different tissues.

Figure 4: Current density in the brain (A/m^2).Figure 5: Current density in the chest (A/m^2).Figure 6: Current density in the abdomen (A/m^2).Figure 7: Current density in the pelvis (A/m^2).Figure 8: Current density in the thighs (A/m^2).Figure 9: Current density in the knees (A/m^2).

7. CONCLUSION

Practical exposure scenarios profiles for electric and magnetic fields representing actual working conditions for live-line workers have been presented. Both scenarios 3 and 2 present relatively strong live-line workers exposures for both electric and magnetic fields. The highest computed values of 6.485 kV/m and of 663.51 mG respectively for the external electric and magnetic fields are both relevant to scenarios 3. Both fields values are found to be below their respective Maximum Permissible Level according to the IEEE, ICNIRP, ACGIH, NRPB guidelines for occupational

exposure for power frequency. The highest induced maximum current density in all the tissues was found to be below the ICNIRP and the NRPB limit of 10 mA/m^2 . The visualization of the anatomical structure of the tissue has revealed the location of the maximum current density value as well the relative intensity value of the current density at each voxel in the layer. In general the highest values for each organ are obtained at the border between different tissues.

ACKNOWLEDGMENT

The authors acknowledge the support of King Fahd University of Petroleum & Minerals, Dhahran, Saudi Arabia.

REFERENCES

1. Saudi Electricity Company, "Annual report," Saudi Arabia, 2004.
2. IEEE Std C95.6., "IEEE standard for safety levels with respect to human exposure to electromagnetic fields, 0–3 kHz," 2002.
3. International Commission on Non-Ionizing Radiation Protection, "Guidelines limiting exposure to time-varying electric, magnetic, and electromagnetic fields (up to 300 GHz)," *Health Physics*, Vol. 74, No. 3, 494–522, 1998.
4. American Conference of Governmental Industrial Hygienists, "TLVs and BEIs," ACGIH, Cincinnati, 2001.
5. Advisory Group on Non-Ionizing Radiation (AGNIR) of the UK National Radiological Protection Board (NRPB), "Limiting exposure to electromagnetic fields (0–300 GHz)," *Doc. NRPB*, Vol. 15, No. 2, 2004.
6. National Radiological Protection Board, "Restrictions on human exposure to static and time varying electromagnetic fields and radiation: Scientific basis and recommendation for implementation of the Board's statement," *Doc. NRPB*, Vol. 4, 8–69, 1993.
7. Olden, K. O., "Health effects from exposure to power-line frequency electric and magnetic fields," NIH Publication 99-4493, National Institute of Environmental Health Sciences, 1999.
8. International Agency for Research on Cancer (IARC), "Non-ionizing radiation, part 1: Static and extremely low frequency electric and magnetic fields," Publication 80, 2002.
9. Electric Power Research Institute, *Transmission Line Reference Book 345 kV and Above*, Fred Weidner and Sons, New York, NY, 1975.
10. Singer, H., H. Steinbigler, and P. Weiss, "A charge simulation method for the calculation of high voltage fields," *IEEE Trans. PAS*, Vol. 93, 1660–1668, 1974.
11. Shen, L. and J. Kong, *Applied Electromagnetics*, Brooks/Cole Engineering Division, 1983.
12. Foe, P. Y. and S. Y. King, "Bundle conductors electric field by integral equations method," *Proc. IEE*, Vol. 123, No. 7, 702–706, 1976.
13. Maruvade, P. S. and W. Janischweskyj, "Electrostatic field of system of parallel cylindrical conductors," *IEEE Trans. PAS*, Vol. 88, No. 7, 1069–1078, 1969.
14. Singer, H., H. Steinbigler, and P. Weiss, "A charge simulation method for the calculation of high voltage fields," *IEEE Trans. PAS*, Vol. 93, 1660–1668, 1974.
15. El-Araby, A., M. Abdel-Salam, and E. Mansour, "Electric field and corona threshold levels on HV bipolar transmission lines-calculations vs. experiment," *IEEE Trans. PAS*, Vol. 77, 236–3, 1977.
16. Sendaula, H. M., "Electric field induced by EHV transmission over irregular terrain," *IEEE Trans. PAS*, Vol. 102, No. 5, 1452–1458, 1983.
17. ERRI, *Transmission Line Reference Book 345 kV and Above*, Fred Weidner and Sons, New York, NY, 1975.
18. Electric Power Research Institute (EPRI), "Electric and magnetic fields workstation (EMF WORKSTATION)," Users Manual Version 2.51, 2012.
19. Deno, D. W. and L. E. Zaffanella, "Electrostatic effects of overhead transmission lines and stations," *Transmission Line Reference Book: 345 kV and Above*, EPRI Report RP-68, 248-2801975, Electric Power Research Institute, 2006.
20. Electric Power Research Institute, *Transmission Line Reference Book, 345 kV and Above*, 2nd Edition, Project UHV, 1982.
21. Electric Power Research Institute, *Electrostatic and Electromagnetic Effects of Ultra High Voltage Transmission Lines*, Project 566, 1978.

22. Gandhi, O. P. and J. Y. Chen, "Numerical dosimetry at power line frequencies using anatomically based models," *Bioelectromagn. J. Supp.*, Vol. 1, 43–60, 1992.
23. Dawson, T. W., J. DeMoerloose, and M. A. Stuchly, "Comparison of magnetically induced ELF fields in humans computed by FDTD and scalar potential FD codes," *Appl. Comput. Electromag. Soc. (ACES)*, Vol. 11, 63–71, 1996.
24. Zubal, I. G., C. R. Harrell, E. O. Smith, Z. Rattner, G. R. Gindi, and P. H. Hoffer, "Computerized three-dimensional segmented human anatomy," *Med. Phys. Biol.*, Vol. 21, 299–302, 1994.
25. Dimbylow, P. J., "FDTD calculations of the whole-body averaged SAR in an anatomically realistic voxel model of the human body from 1 MHz to 1 GHz," *Phys. Med. Biol.*, Vol. 42, 479–490, 1997.
26. Hand, J. W., "Modeling the interaction of electromagnetic fields (10 MHz–10 GHz) with the human body: Methods and applications," *Phys. Med. Biol.*, Vol. 53, R243–R286, 2008.
27. Furse, C. M. and O. P. Gandhi, "Calculation of electric fields and currents induced in a millimeter resolution human model at 60 Hz using the FDTD method," *Bioelectromagnetics*, Vol. 19, 293–299, 1998.
28. Gandhi, O. P., "Some numerical methods for dosimetry: Extremely low frequencies to microwave frequencies," *Radio Science*, Vol. 30, 161–177, 1995.
29. Gandhi, O. P., G. Kang, D. Wu, and G. Lazzi, "Currents induced in anatomic models of the human for uniform and nonuniform power frequency magnetic fields," *Bioelectromagnetics*, Vol. 22, 112–121, 2001.
30. Dimbylow, P. J., "Induced current densities from low-frequency magnetic fields in a 2 mm resolution, anatomically realistic model of the body," *Phys. Med. Biol.*, Vol. 43, 221–230, 1998.

An Efficient Implementation of Yasuura's Method of Modal Expansion by Sequential Accumulation

M. Kawano¹, T. Matsuda², and Y. Okuno³

¹Lumerical Solutions Inc., Canada

²Kumamoto National College of Technology, Japan

³Graduate School of Science and Technology, Kumamoto University, Japan

Abstract— As an efficient numerical implementation of the large-sized least-squares problem that arises in Yasuura's method, the sequential accumulation processing is introduced. We describe the numerical algorithm of the QR decomposition method with sequential accumulation to solve the large-sized least-squares problem whose Jacobian is a dense matrix or a banded one. It is shown that computer storage required at one time is significantly saved in comparison with that of the implementation without sequential accumulation. The proposed numerical algorithm enables us to apply Yasuura's method to large-sized problems such as scattering by a cluster of nanoparticles or diffraction from multilayered periodic structures.

1. INTRODUCTION

Yasuura's method [1] is one of the efficient numerical techniques for the boundary value problems of the Helmholtz equation and has been applied to various electromagnetic problems such as diffraction gratings [2–4], scattering by a three-dimensional scatterer [5], and dielectric waveguides [6], etc.. In that method, the approximate solution is formed as a linear combination of modal functions and the expansion coefficients are determined so that the approximate solution satisfies the boundary conditions in a least squares sense. The numerical algorithm of Yasuura's method, thus, reduces to the usual least-squares problem. Further, it is proved that the sequence of solutions determined by the method converges to the true solution uniformly [1].

Yasuura's method is applicable to the problems of a cluster of nanoparticles or multilayered periodic structures, which are recently of great interest in the field of nanotechnologies [7]. However, the numerical implementation of Yasuura's method in such problems may require a large amount of memory and takes a long computation time as the number of nanoparticles or the number of layers increases. This is because the size of the least-squares problem to be solved becomes to be large and thus the amount of numerical computations considerably increases.

We therefore need to attain the improvement in the numerical implementation of the large-sized least-squares problem that arises in Yasuura's method. In this presentation, we consider two types of the large-sized least-squares problem whose Jacobian [8] is a dense matrix or a banded one, respectively, which is formulated in the application of Yasuura's method to the scattering problem by a cluster of nanoparticles or the diffraction problem from multilayered periodic structures. We introduce the sequential accumulation processing [8] to solve such least-squares problems. As a result, computer storage required at one time is significantly saved and then the amount of computation is reduced in comparison with that of the implementation without sequential accumulation.

2. NUMERICAL IMPLEMENTATION OF YASUURA'S METHOD

The numerical algorithm of Yasuuras's method is formulated as the least squares problem:

Find the solution vector \mathbf{A} minimizing the Euclidean norm

$$I = \|\Phi\mathbf{A} - \mathbf{b}\|^2. \quad (1)$$

In Eq. (1), Jacobian Φ is a $J \times M$ matrix, the solution vector \mathbf{A} and the driving vector \mathbf{b} are an M - and J -dimensional column vector, respectively. We here deal with two types of Jacobian Φ , a dense matrix and a banded one:

$$\Phi = \begin{bmatrix} \Phi_1 \\ \Phi_2 \\ \vdots \\ \Phi_L \end{bmatrix} \quad (J \times M) \quad (2)$$

and

$$\Phi = \begin{bmatrix} \Phi_{11} & \Phi_{12} & 0 & \dots & 0 \\ 0 & \Phi_{22} & \Phi_{23} & \ddots & \vdots \\ \vdots & \ddots & \ddots & \ddots & 0 \\ 0 & \dots & 0 & \Phi_{LL} & \Phi_{LL+1} \end{bmatrix} \quad (J \times M). \quad (3)$$

When we apply Yasuura's method to a scattering problem of plane wave by a cluster of nanoparticles, Jacobian Φ consists of L block matrices Φ_ℓ ($\ell = 1, 2, \dots, L$) with L being the number of particles as shown in Eq. (2) (Appendix A). The size of Jacobian $J \times M$ is $J \times M = 24(N+1)^2L \times 4N(N+2)^2L$ with N is the truncation number of multipole expansions.

On the other hand, in the case of a diffraction problem by a multilayered bi-grating which is stacked thin-films periodically corrugated, Φ becomes to be a block bi-diagonal matrix of Eq. (3) where L is the number of layers (Appendix A). The size of Jacobian is then given by $J \times M = (24N^2L) \times (4N^2L)$ with N being the truncation size of modal expansions.

We hereafter explain an efficient implementation to numerically solve the large-sized least-squares problem in which Jacobian Φ is given by Eq. (2) or (3). We can suppose that Jacobian Φ is a matrix of full rank.

2.1. QR Decomposition Method

Least squares problems can be solved by the orthogonal transformation of Jacobian such as a QR decomposition method [8]. In this method, the Jacobian matrix is decomposed as a product of a unitary matrix $\mathbf{Q}(J \times J)$ and an upper triangular matrix $\mathbf{R}(M \times M)$

$$\Phi = \mathbf{Q}^* \mathbf{R} \quad \text{or} \quad \mathbf{Q}\Phi = \mathbf{R} \quad (4)$$

with $*$ being the conjugate transpose. The solution \mathbf{A} is then obtained by solving

$$\mathbf{R}\mathbf{A} = \mathbf{Q}^*\mathbf{b}. \quad (5)$$

The application of a QR decomposition method to the entire matrix Φ of Eq. (2) or (3), however, requires a large amount of memory at one time and takes a long computation time when L becomes to be large. For instance, in the problem of a multilayered bi-grating the size of Φ is $105,840 \times 17,640$ for $L = 10$ and $K = 21$ and the amount of memory size easily exceeds 30 GB. Thus, the increment of L may cause a serious problem of lack of computer storage and extremely time-consuming computations. This problem can be removed by the introduction of the sequential accumulation in the QR decomposition method [8] as we show next.

2.2. Sequential Accumulation of Dense Matrix

We describe the sequential accumulation for the QR decomposition of the Jacobian matrix Φ is given in Eq. (2). We write the driving vector \mathbf{b} in a partitioned form as follows

$$\mathbf{b} = \begin{bmatrix} \mathbf{b}_1 \\ \mathbf{b}_2 \\ \vdots \\ \mathbf{b}_L \end{bmatrix} \quad (J \times 1) \quad (6)$$

where the dimension of each \mathbf{b}_ℓ ($\ell = 1, 2, \dots, L$) is denoted in J_ℓ and $J = \sum_{\ell=1}^L J_\ell$. Note that J_ℓ is the same as the number of rows of the block matrix Φ_ℓ in Eq. (2).

The QR decomposition method with sequential accumulation is executed in the following iteration scheme:

Step 1. We first consider the combination consisting of Φ_1 and \mathbf{b}_1

$$\tilde{\Phi}^{(1)} = \begin{bmatrix} \Phi_1 & \vdots & \mathbf{b}_1 \end{bmatrix} \quad (J_1 \times (M+1)). \quad (7)$$

Using a usual algorithm of the QR decomposition, we obtain

$$\mathbf{Q}^{(1)} \tilde{\Phi}^{(1)} = \begin{bmatrix} \mathbf{R}^{(1)} & \vdots & \mathbf{g}^{(1)} \\ 0 & \vdots & 0 \end{bmatrix} \quad (8)$$

where $\mathbf{Q}^{(1)}$ is the orthogonal matrix is an upper triangular matrix.

Step 2. Next, appending the combination $[\Phi_2 : \mathbf{b}_2]$ to the first-line member o the right side of Eq. (8) we have

$$\tilde{\Phi}^{(2)} = \begin{bmatrix} \mathbf{R}^{(1)} & \vdots & \mathbf{g}^{(1)} \\ \Phi_2 & \vdots & \mathbf{b}_2 \end{bmatrix} \quad ((M + J_2) \times (M + 1)) \quad (9)$$

and apply the QR decomposition to $\tilde{\Phi}^{(2)}$. The result is given by

$$\mathbf{Q}^{(2)}\tilde{\Phi}^{(2)} = \begin{bmatrix} \mathbf{R}^{(2)} & \vdots & \mathbf{g}^{(2)} \\ 0 & \vdots & 0 \end{bmatrix}. \quad (10)$$

Step L. Repeating the same procedure L times, we finally obtain

$$\mathbf{Q}^{(L)}\tilde{\Phi}^{(L)} = \begin{bmatrix} \mathbf{R}^{(L)} & \vdots & \mathbf{g}^{(L)} \\ 0 & \vdots & e \end{bmatrix}, \quad (11)$$

where

$$\tilde{\Phi}^{(L)} = \begin{bmatrix} \mathbf{R}^{(L-1)} & \vdots & \mathbf{g}^{(L-1)} \\ \Phi_L & \vdots & \mathbf{b}_L \end{bmatrix} \quad ((M + J_L) \times (M + 1)). \quad (12)$$

Step $L + 1$. We solve the set of linear equations

$$\mathbf{R}^{(L)}\mathbf{A} = \mathbf{g}^{(L)}. \quad (13)$$

When Jacobian Φ is full rank, the coefficient matrix $\mathbf{R}^{(L)}$ is the regular upper triangular matrix.

It is proved that the solution of Eq. (13) is equivalent to that of the original least-squares problem in Eq. (1) and the mean-square error is then given by $I = |\mathbf{e}|^2$. The significant point permitting a saving of storage is the fact that for each step ℓ the matrix $[\mathbf{R}^{(\ell)} : \mathbf{g}^{(\ell)}]$ can be constructed by the QR decomposition of $\tilde{\Phi}^{(\ell)}$ and store in the storage space previously occupied by $\tilde{\Phi}^{(\ell)}$. Consequently, computer storage required is significantly saved and then the amount of computation is reduced.

2.3. Sequential Accumulation of Banded Matrix

We next explain the sequential accumulation for Jacobian Φ having a banded structure Eq. (3). The solution vector \mathbf{A} is partitioned as follows:

$$\mathbf{A} = \begin{bmatrix} \mathbf{A}_1 \\ \mathbf{A}_2 \\ \vdots \\ \mathbf{A}_L \\ \mathbf{A}_{L+1} \end{bmatrix} \quad (M \times 1). \quad (14)$$

where the dimension of each \mathbf{A}_ℓ is M_ℓ and $M = \sum_{\ell=1}^{L+1} M_\ell$. As for the driving vector, we use the partitioned form \mathbf{b} defined in Eq. (6).

Step 1. We first consider the combination

$$\tilde{\Phi}^{(1)} = [\Phi_{11} \quad \Phi_{12} \quad \vdots \quad \mathbf{b}_1] \quad (J_1 \times (M_1 + M_2 + 1)). \quad (15)$$

Using the algorithm of the QR decomposition, we obtain

$$\mathbf{Q}^1\tilde{\Phi}^{(1)} = \begin{bmatrix} \mathbf{R}_{11}^{(1)} & \mathbf{R}_{12}^{(1)} & \vdots & \mathbf{g}_1^{(1)} \\ 0 & \mathbf{R}_{22}^{(1)} & \vdots & \mathbf{g}_2^{(1)} \\ 0 & 0 & \vdots & \mathbf{e}^{(1)} \end{bmatrix}. \quad (16)$$

Step 2. From the second-line member on the right side of Eq. (16) we set

$$\tilde{\Phi}^{(2)} = \begin{bmatrix} \mathbf{R}_{22}^{(1)} & 0 & \vdots & \mathbf{g}_2^{(1)} \\ \Phi_{22} & \Phi_{23} & \vdots & \mathbf{b}_2 \end{bmatrix} \quad ((M_2 + J_2) \times (M_2 + M_3 + 1)). \quad (17)$$

and have

$$\mathbf{Q}^{(2)} \tilde{\Phi}^{(2)} = \begin{bmatrix} \mathbf{R}_{22}^{(2)} & \mathbf{R}_{23}^{(2)} & \vdots & \mathbf{g}_2^{(2)} \\ 0 & \mathbf{R}_{33}^{(2)} & \vdots & \mathbf{g}_3^{(1)} \\ 0 & 0 & \vdots & \mathbf{e}^{(2)} \end{bmatrix}. \quad (18)$$

Step L. In the L th step, we obtain

$$\mathbf{Q}^{(L)} \tilde{\Phi}^{(L)} = \begin{bmatrix} \mathbf{R}_{LL}^{(L)} & \mathbf{R}_{LL+1}^{(L)} & \vdots & \mathbf{g}_L^{(L)} \\ 0 & \mathbf{R}_{L+1L+1}^{(L)} & \vdots & \mathbf{g}_{L+1}^{(L)} \\ 0 & 0 & \vdots & \mathbf{e}^{(L)} \end{bmatrix} \quad (19)$$

where

$$\tilde{\Phi}^{(L)} = \begin{bmatrix} \mathbf{R}_{LL}^{(L-1)} & 0 & \vdots & \mathbf{g}_L^{(L-1)} \\ \Phi_{LL} & \Phi_{LL+1} & \vdots & \mathbf{b}_L \end{bmatrix} \quad ((M_L + J_L) \times (M_L + M_{L+1} + 1)). \quad (20)$$

Step $L+1$. Each \mathbf{A}_ℓ of the solution vector is founded by back substitution, i.e., as the solution of a set of linear equations with upper triangular coefficient matrices:

$$\begin{cases} \mathbf{R}_{L+1L+1}^{(L)} A_{L+1} = \mathbf{g}_{L+1}^{(L)} \\ \mathbf{R}_{\ell\ell}^{(\ell)} \mathbf{A}_\ell = \mathbf{g}_\ell^{(\ell)} - \mathbf{R}_{\ell\ell+1}^{(\ell)} \mathbf{A}_{\ell+1} \quad (\ell = L, L-1, \dots, 1) \end{cases}. \quad (21)$$

The coefficient matrix $\mathbf{R}_{\ell\ell}^{(\ell)}$ ($\ell = L+1, L, L-1, \dots, 1$) is regular, i.e., $\text{rank}(\mathbf{R}_{\ell\ell}^{(\ell)}) = M_\ell$ as Jacobian Φ is full rank. Then the mean square error is given by $I = \sum_{\ell=1}^L |\mathbf{e}^{(\ell)}|^2$.

In the sequential accumulation of a banded matrix stated above, the QR decomposition of $\tilde{\Phi}^{(\ell)}$ is executed L times. Consequently we remove difficulties in the numerical implementation of the least-squares problem in Eq. (1) by the increment of L and/or M .

3. CONCLUSION

As an efficient implementation of the large-sized least-squares problem that arises in Yasuura's method, we have described the QR decomposition method with the sequential accumulation processing. It is demonstrated that computer storage required at one time is significantly saved in comparison with that of the implementation without sequential accumulation. Consequently, the proposed algorithm enables us to implement on a desk top computer such as PC.

ACKNOWLEDGMENT

This work is supported in part by a grant-in-aid 22560045 from Japan Society for the Promotion of Science.

APPENDIX A. NUMERICAL ALGORITHM OF YASUURA'S METHOD

We briefly describe the application of Yasuura's method to the problem of scattering by a cluster of nanoparticles and diffraction from a multilayered bi-grating.

Figure 1 shows the scattering problem of plane wave by a cluster consisting of L nanoparticles. In Yasuura's method, the scattered electric field is formed in the multipole expansion and its expansion coefficients are determined so that the boundary condition is satisfied in a least squares

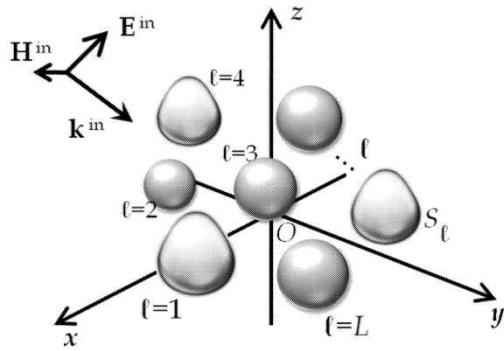


Figure 1: A cluster of nano-sized particles.

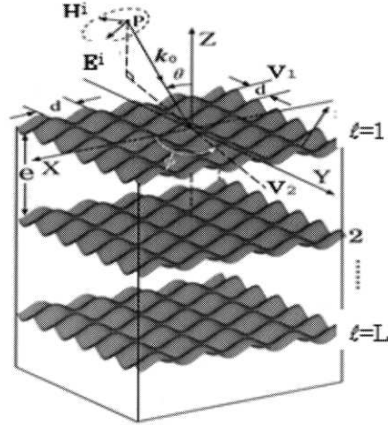


Figure 2: A multilayered bi-grating.

sense. This leads us to the least-squares problem whose Jacobian Φ is a dense matrix given in Eq. (2). When the truncation number of the multipole expansion is N , the size of Φ is $J \times M = 24(N+1)^2L \times 4N(N+2)^2L$.

Figure 2 shows the diffraction problem of plane wave from a multilayered bi-grating. The grating consists of a stack of L thin-films periodically corrugated in both the x and y directions. The diffracted electric fields are expanded in vector modal functions which are separated solutions of the Helmholtz equations satisfying the periodic conditions. When we apply Yasuura's method to the diffraction problem, Jacobian Φ of the least-squares problem is finally formulated as a block bi-diagonal matrix given in Eq. (3). The size of Φ becomes to be $J \times M = (24N^2L) \times (4N^2L)$ with N being the truncation size of modal expansions.

REFERENCES

- Yasuura, K., "A view of numerical methods in diffraction problems," *Progress in Radio Science 1966–1969*, 257–270, W. V. Tilson and M. Sauzade, Eds., 1986.
- Ikuno, H. and K. Yasuura, "Improved point-matching method with application to scattering from a periodic surface," *IEEE Trans. Antennas Propag.*, Vol. 21, No. 5, 657–662, 1973.
- Matsuda, T. and Y. Okuno, "Numerical evaluation of plane-wave diffraction by a doubly periodic grating," *Radio Sci.*, Vol. 31, 1791–1798, 1996.
- Suyama, T., Y. Okuno, and T. Matsuda, "Surface plasmon resonance absorption in a multilayered thin-film grating," *Journal of Electromagnetic Waves and Applications*, Vol. 23, No. 13, 1773–1783, 2009.
- Kawano, M., H. Ikuno, and M. Nishimoto, "Numerical analysis of 3-D scattering problems using the Yasuura method," *IEICE Trans. Electron.*, Vol. E-79-C, 1358–1363, 1996.
- Yasumoto, K. and M. Murayama, "A rigorous analysis of a thin-film dielectric wave guide with a sinusoidal surface corrugation," *Radio Sci.*, Vol. 22, 1013–1017, 1987.
- Luk'yanchuk, B., N. I. Zheludev, S. A. Maier, N. J. Halas, P. Nordlander, H. Giessen, and C. T. Chong, "The Fano resonance in plasmonic nanostructures and metamaterials," *Nature Materials*, Vol. 9, 707–715, 2010.
- Lawson, C. L. and R. J. Hanson, *Solving Least Squares Problems*, Prentice-Hall, Englewood Cliffs, 1974.

A Grating-based Plasmon Biosensor via Phase Detection with Wide Measurement Range

Ziqian Luo¹, Taikei Suyama², Xun Xu³, Yoichi Okuno⁴, and Sailing He^{1,5}

¹Academy of Advanced Optoelectronics, South China Normal University, Guangzhou, China

²Akashi National College of Technology, Akashi, Japan

³Faculty of Engineering, Kyushu Sangyo University, Fukuoka, Japan

⁴Graduate School of Science and Technology, Kumamoto University, Kumamoto, Japan

⁵Centre for Optical and Electromagnetic Research, Zhejiang University, Hangzhou, China

Abstract— We scan the surface plasmonic resonance phenomenon around the environment index range as $1.27 < n < 1.35$, and find very similar patterns of phase shift. We summarize rules of phase shift patterns between different index range, and recommend an optical set-up method that can determine a wide measurement range of refractive index by combining all small workspaces.

1. INTRODUCTION

The Surface plasmon resonance (SPR) absorption occurs on a metal grating when a phase-matching condition is satisfied: the phase constant of an evanescent order coincides with the real part of an eigenvalue of surface plasmons. It causes an obvious change in the reflected phase as the material index changed [1]. The phase detection has already been employed in prism-based biosensors and works to improve the resolution of the sensors to 10^{-7} refractive index units (RIU) [2–4]. Thus, grating-based plasmon biosensors via phase detection were reported to have great potential on medical and physiological applications [5–8].

According to our previous research, we can determine the refractive index of the material with an accuracy of seven digits by measuring the phase shift of zeroth-order diffraction light alone, considering the trade-off between high resolution and experimental practicability [8]. The seven-digit resolution is sufficient for practical applications, for example, in clinical medicine or physiology [1, 9]. However, the magnitude of a phase shift cannot be more than 180° , high resolution means a narrow measurement range in refractive index.

In the following sections, we examine the possibility of measurement range extension of the phase detection employed in the grating-based plasmon biosensor. We will formulate the problem of diffraction by a metal grating placed in conical mounting and describe the method of solution employed [10–12]. We will also show the numerical results and will make discussions from the viewpoint of sensor applications.

2. FORMULATION OF THE PROBLEM AND THE METHOD OF SOLUTION

Figure 1 shows the schematic representation of diffraction by a layered grating made of a metal and having an over-coating made of another metal. The grating is uniform in the Y direction and is periodic in X . The surface profiles are given by

$$S_1: z_1 = \eta_1(x) = h \sin(2\pi x/d) \quad (1a)$$

$$S_2: z_2 = \eta_2(x) = h \sin(2\pi x/d) - e \quad (1b)$$

where h , d , and e are the amplitude (half depth) of the surface modulation, the period, and the thickness of the coating. Note that the small letters (x, y, z) denote a point on the surfaces.

The surfaces separate the whole space into three regions:

$$\begin{aligned} V1: & Z > \eta_1(X) \\ V2: & \eta_1(X) > Z > \eta_2(X) \\ V3: & \eta_2(X) > Z \end{aligned} \quad (2)$$

We assume that V_1 , V_2 , and V_3 , respectively, are filled with a dielectric (with a positive refractive index n_1), a metal (having a complex-valued index n_2), and another metal (with n_3). The capital letters (X, Y, Z) show the coordinates of a point in these regions. A convention $\mathbf{P} = (X, Y, Z)$ will be used as well.

The electric field of an incident light is given by

$$\mathbf{E}^i(\mathbf{P}) = \mathbf{e}^i \exp(i\mathbf{k}^i \cdot \mathbf{P} - i\omega t) \quad (3)$$

where

$$\mathbf{k}^i = (\alpha, \beta, -\gamma) \quad (4)$$

with $\alpha = n_1 k^i \sin \theta \cos \phi$, $\beta = n_1 k^i \sin \theta \sin \phi$, $\gamma = n_1 k^i \cos \theta$, and $k^i = 2\pi/\lambda$. As shown in Fig. 1, θ is the polar angle between the Z -axis and the incident wave-vector φ is the azimuth angle between the X -axis and the plane of incidence, and λ is the wavelength in vacuum.

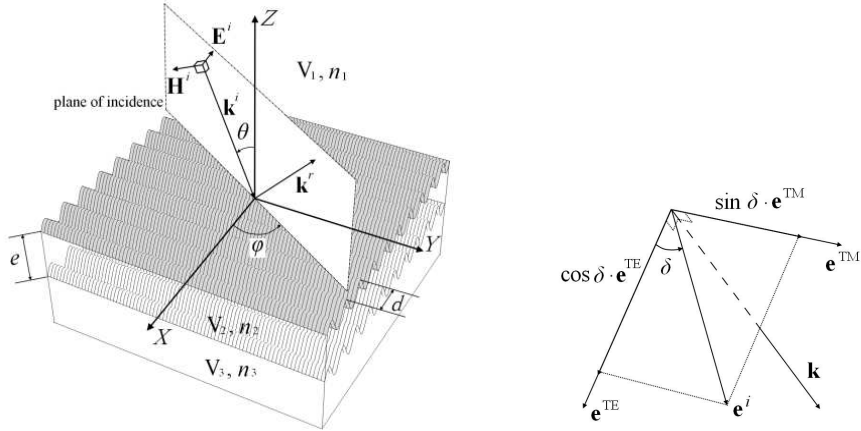


Figure 1: Schematic representation of diffraction by a layered metal grating and definition of the polarization angle.

When $\varphi = 0^\circ$, the incident light comes from a direction orthogonal to the grooves and the diffracted waves propagate in directions in the plane of incidence. This arrangement is called the *planer mounting* (or classical mounting). While if $\varphi \neq 0^\circ$, as shown in Fig. 1, the directions lie on a cone centered at the origin. This is termed the *conical mounting*.

Let us decompose the amplitude \mathbf{e}^i appeared in (3) into a TE- and a TM-component, where TE (or TM) means the absence of the Z -component in the relevant electric (or magnetic) field. To do this, we first define two unit vectors that span a plane orthogonal to \mathbf{k}^i :

$$\mathbf{e}^{\text{TE}} = (\sin \varphi, -\cos \varphi, 0) \quad (5a)$$

$$\mathbf{e}^{\text{TM}} = (\cos \theta \cos \varphi, \cos \theta \sin \varphi, \sin \theta) \quad (5b)$$

They are the unit vectors in the direction of the TE- and TM-component in the sense above. The amplitude \mathbf{e}^i is decomposed as

$$\mathbf{e}^i = \mathbf{e}^{\text{TE}} \cos \delta + \mathbf{e}^{\text{TM}} \sin \delta \quad (6)$$

where δ , which is termed a polarization angle, is the angle between \mathbf{e}^{TE} and \mathbf{e}^i (see Fig. 1). The incident light is specified by the wavelength λ , the polar angle θ , the azimuth angle φ , and the polarization angle δ .

We consider the problem to seek the diffracted electric and magnetic fields in V_j ($j = 1, 2, 3$). Note that they consist of both TE- and TM-components because we assume the conical mounting. The solutions should satisfy the following requirements:

- (D1) the Helmholtz equations in each region;
- (D2) a radiation condition in the Z -direction that the diffracted waves in V_1 (or V_3) propagate or attenuate in positive (or negative) Z direction;
- (D3) a periodicity condition that the relation $f(X+d, Y, Z) = \exp(i\alpha d) f(X, Y, Z)$ holds and the phase constant in Y is β for any component of diffracted light;
- (D4) the boundary conditions on S_1 and S_2 that the tangential components of the electric and magnetic fields must be continuous across the boundary.

3. NUMERICAL RESULTS AND DISCUSSION

In the following, we consider a commercial grating made of aluminum with a gold over-coating. The parameters are $2h = 0.072 \mu\text{m}$, $d = 0.556 \mu\text{m}$ and $e = 0.778 \mu\text{m}$. The incident light is a monochromatic plane wave from a laser diode with a wavelength of $0.633 \mu\text{m}$. As for the value taken in our computation, we assume that the refractive indices of Al and Au at this wavelength are $n_2 = 0.1594 + i3.2166$ and $n_3 = 1.2078 + i7.0148$ [12]. However, it should be noted that the index of a metal film depends not only on the wavelength but also on the thickness of the film when the film is extremely thin. It may take unusual values if circumstances require. When dealing with a thin metal structure, hence, we should be careful in using the index value given in the literature.

As shown in our former works, for a given $n_1 = n$, there would be an incident condition can excite the SPR absorption. And while n_1 changes around n , the TM_0 diffraction light would show an obvious phase shift [8]. Fig. 2 shows some similar patterns of phase shift while n_1 changes around in different region. The refractive index of the material over the grating surface can be accurately determined by the almost linear parts of these curves. The range covered by the almost linear part of each curve will be called a workspace below. Without changing the structure parameters but only the incident angle, we can shift the workspace in a large range while the sensor resolution can remain in a high level. Combining all the small workspaces, a wide range of refractive index can be determined respectively.

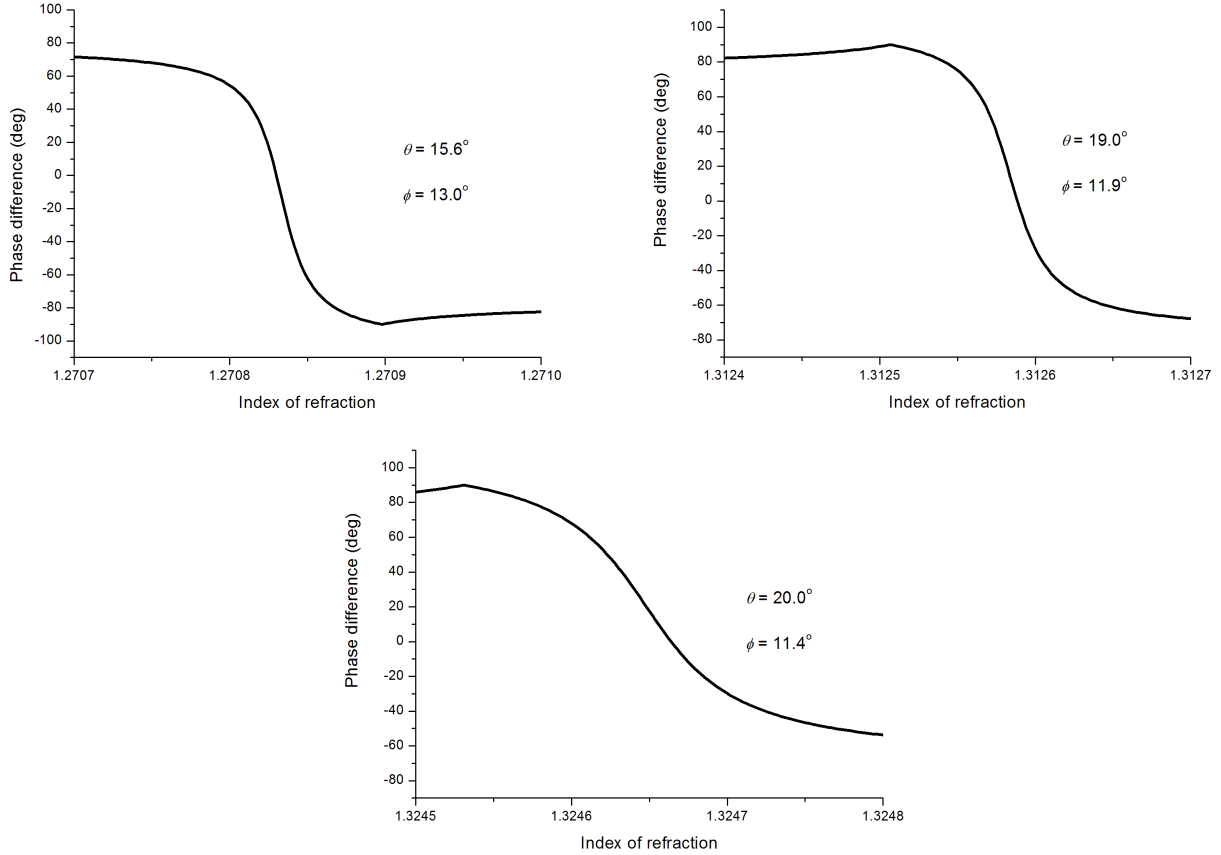


Figure 2: Similar phase shift patterns in different refractive index environment.

Another question is that while we shift the workspace, is the sensor resolution able to keep in a same high level? Let's consider workspaces whit a unit length as $\Delta n = 0.0005$. If the SPR phase shift can reach 100° , the sensor can keep a 2.5×10^{-8} RIU resolution. We scanned every SPR component in each workspace, and recorded all the largest extents of phase shift we can reach in different workspaces (Fig. 3). The result is not so smooth as we expected. Two fifth of them can merely reach 100° , while others can reach 120° . One fifth of them can reach 150° or even more than 170° . If we choose the optical set-up which pursues the extreme slope of phase shift curve in each workspace, it would be impossible to keep the resolution of all workspaces in a same high level. Thus, as the short board effect, we can only keep the sensor resolution as 2.5×10^{-8} RIU level.

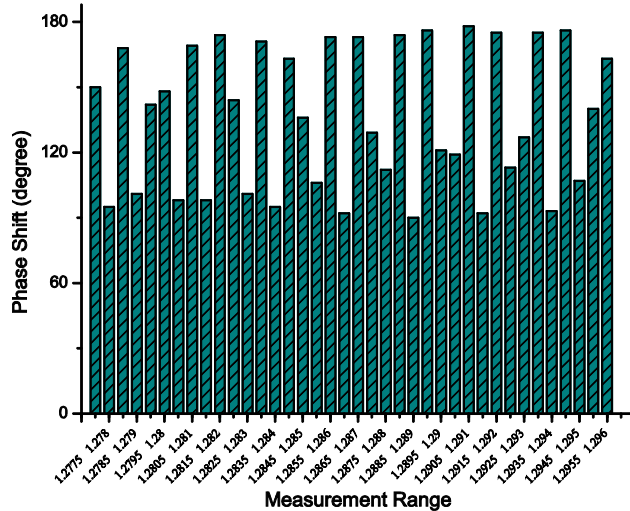


Figure 3: Different extents of phase shift in different workspace.

Figure 3 also shows that the high extents of phase shift appear periodically. Every 5 workspaces are one period, within which the third and fifth workspaces always have high extents of phase shift. For example, in the first period of Fig. 3 (n_1 from 1.2770 to 1.2795), the third workspace (n_1 from 1.2780 to 1.2785) has an 168° phase shift, and the fifth workspace (n_1 from 1.2790 to 1.2795) has an 142° phase shift. Another example is that the fifth period (n_1 from 1.2895 to 1.2920), the third workspace (n_1 from 1.2905 to 1.2910) has an 178° phase shift, and the fifth workspace (n_1 from 1.2915 to 1.2920) has an 175° phase shift.

Table 1: Workspaces and recommended settings for polar angle θ and azimuth angle φ .

Workspace (index range)	θ	φ	Workspace (index range)	θ	φ
1.2770 ~ 1.2795	16.2°	6.4°	1.3320 ~ 1.3345	20.4°	5.5°
1.2795 ~ 1.2820	16.4°	6.5°	1.3345 ~ 1.3370	20.6°	5.6°
1.2820 ~ 1.2845	16.6°	6.3°	1.3370 ~ 1.3395	20.8°	5.5°
1.2845 ~ 1.2870	16.8°	6.3°	1.3395 ~ 1.3420	21.0°	5.4°
1.2870 ~ 1.2895	17.0°	6.3°	1.3420 ~ 1.3445	21.2°	5.4°
1.2895 ~ 1.2920	17.2°	6.3°	1.3445 ~ 1.3470	21.4°	5.3°

In our former work, after considering the trade off between high resolution and low reflection, we extended workspace to a unit length as $\Delta n = 0.003$ [8]. By now it seems to be not resonable because the grating structure exhibits a periodical SPR behavior with a period as $\Delta n = 0.0025$. Thus, we optimized the recommended optical set-up table, shown as Table 1. It would improve the sensor resolution (from 1.5×10^{-7} RIU to 1.25×10^{-7} RIU) and let the workspace shifts more smoothly.

4. CONCLUSION

Since the sample index n_1 has large influence on the phase modulation of the diffracted TM mode, the phase detection is a strong way to find the index. We observed a periodical SPR behavior on a metal grating structure. It helps us to revise the optical set-up scheme, improve the possible grating-based bio-sensor's resolution from 1.5×10^{-7} RIU to 1.25×10^{-7} RIU, and let the workspace can shift more smoothly. This means more than 7-digit determination of the index with wide measurement range can be employed for medical and physiological applications.

ACKNOWLEDGMENT

This work is supported by Guangdong Innovative Research Team Program (No. 201001D0104799318).

REFERENCES

1. Nelson, S. G., K. S. Johnston, and S. S. Yee, "High sensitivity surface plasmon resonance sensor based on phase detection," *Sensors and Actuators B*, 35–36, 187–191, 1996.
2. Ho, H. P., W. C. Law, S. Y. Wu, C. Lin, and S. K. Kong, "Real-time optical biosensor based on differential phase measurement of surface plasmon resonance," *Biosensors and Bioelectronics*, Vol. 20, 2177–2180, 2005.
3. Ho, H. P., W. Yuan, C. L. Wong, S. Y. Wu, Y. K. Suen, S. K. Kong, and C. Lin, "Sensitivity enhancement based on application of multi-pass interferometry in phase-sensitive surface plasmon resonance biosensor," *Optics Communications*, Vol. 275, 491–496, 2007.
4. Wong, C. L., H. P. Ho, Y. K. Suen, S. K. Kong, Q. L. Chen, W. Yuan, and S. Y. Wu, "Real-time protein biosensor arrays based on surface plasmon resonance differential phase imaging," *Biosensors and Bioelectronics*, Vol. 24, 606–612, 2008.
5. Homola, J., "On the sensitivity of surface plasmon resonance sensors with spectral interrogation," *Sensors and Actuators B*, Vol. 41, 207–211, 1997.
6. Homola, J., I. Koudela, and S. Yee, "Surface plasmon resonance sensor based on diffraction gratings and prism couplers: Sensitivity comparison," *Sensors and Actuators B: Chemical*, Vol. 54, Nos. 1–2, 1624, 1999.
7. Kuo, W.-K. and C.-H. Chang, "Phase detection properties of grating-coupled surface plasmon resonance sensors," *Optics Express*, Vol. 18, No. 19, 19656–19664, 2010.
8. Luo, Z., T. Suyama, X. Xu, and Y. Okuno, "A grating-based plasmon biosensor with high resolution," *Progress In Electromagnetics Research*, Vol. 118, 527–539, 2011.
9. Banerjee, A., "Enhanced refractometric optical sensing by using one-dimensional ternary photonic crystals," *Progress In Electromagnetics Research*, Vol. 89, 11–22, 2009.
10. Yasuura, K. and T. Itakura, "Approximation method for wave functions (I), (II) and (III)," *Kyushu Univ. Tech. Rep.*, Vol. 38, No. 1, 72–77, 1965; Vol. 38, No. 4, 378–385, 1966; Vol. 39, No. 1, 51–56, 1966.
11. Okuno, Y. and H. Ikuno, "Yasuura's method, its relation to the fictitious source methods, and its advancements in solving 2-D problems," *Generalized Multipole Techniques for Electromagnetic and Light Scattering*, T. Wriedt, Ed., 111–141, Elsevier, Amsterdam, 1999.
12. Hass, G. and L. Hadley, "Optical properties of metals," *American Institute of Physics Handbook*, D. E. Gray, Ed., 2nd Edition, 6–107, McGraw-Hill, New York, 1963.